NASA/CP—1999–209261

3 04141999 NASA-CP-209261 - 10
NASA
MARSHALL SPACE FLIGHT CENTER
ATTN : AT01/LIBRARY
HUNTSVILLE AL 35812-0001

# 11th International Conference on Atmospheric Electricity

*Compiled by*
*H.J. Christian*
*Marshall Space Flight Center, Marshall Space Flight Center, Alabama*

Proceedings of a conference held
in Guntersville, Alabama,
June 7–11, 1999

***June 1999***

## The NASA STI Program Office...in Profile

Since its founding, NASA has been dedicated to the advancement of aeronautics and space science. The NASA Scientific and Technical Information (STI) Program Office plays a key part in helping NASA maintain this important role.

The NASA STI Program Office is operated by Langley Research Center, the lead center for NASA's scientific and technical information. The NASA STI Program Office provides access to the NASA STI Database, the largest collection of aeronautical and space science STI in the world. The Program Office is also NASA's institutional mechanism for disseminating the results of its research and development activities. These results are published by NASA in the NASA STI Report Series, which includes the following report types:

- TECHNICAL PUBLICATION. Reports of completed research or a major significant phase of research that present the results of NASA programs and include extensive data or theoretical analysis. Includes compilations of significant scientific and technical data and information deemed to be of continuing reference value. NASA's counterpart of peer-reviewed formal professional papers but has less stringent limitations on manuscript length and extent of graphic presentations.

- TECHNICAL MEMORANDUM. Scientific and technical findings that are preliminary or of specialized interest, e.g., quick release reports, working papers, and bibliographies that contain minimal annotation. Does not contain extensive analysis.

- CONTRACTOR REPORT. Scientific and technical findings by NASA-sponsored contractors and grantees.

- CONFERENCE PUBLICATION. Collected papers from scientific and technical conferences, symposia, seminars, or other meetings sponsored or cosponsored by NASA.

- SPECIAL PUBLICATION. Scientific, technical, or historical information from NASA programs, projects, and mission, often concerned with subjects having substantial public interest.

- TECHNICAL TRANSLATION. English-language translations of foreign scientific and technical material pertinent to NASA's mission.

Specialized services that complement the STI Program Office's diverse offerings include creating custom thesauri, building customized databases, organizing and publishing research results...even providing videos.

For more information about the NASA STI Program Office, see the following:

- Access the NASA STI Program Home Page at ***http://www.sti.nasa.gov***

- E-mail your question via the Internet to help@sti.nasa.gov

- Fax your question to the NASA Access Help Desk at (301) 621-0134

- Telephone the NASA Access Help Desk at (301) 621-0390

- Write to:
  NASA Access Help Desk
  NASA Center for AeroSpace Information
  800 Elkridge Landing Road
  Linthicum Heights, MD 21090-2934

NASA/CP—1999–209261

# 11th International Conference on Atmospheric Electricity

*Compiled by*
*H.J. Christian*
*Marshall Space Flight Center, Marshall Space Flight Center, Alabama*

Proceedings of a conference held
in Guntersville, Alabama,
June 7–11, 1999

National Aeronautics and
Space Administration

Marshall Space Flight Center • MSFC, Alabama 35812

***June 1999***

Available from:

NASA Center for AeroSpace Information
800 Elkridge Landing Road
Linthicum Heights, MD 21090-2934
(301) 621-0390

National Technical Information Service
5285 Port Royal Road
Springfield, VA 22161
(703) 487-4650

**11th International Conference**
**on**
**Atmospheric Electricity**

**June 7-11, 1999**
**Lake Guntersville State Park**
**Guntersville, Alabama, USA**

Organized by:

International Commission on Atmospheric Electricity
Global Hydrology and Climate Center

Sponsored by:

National Aeronautics and Space Administration (NASA)
Marshall Space Flight Center
National Science Foundation

Conference Chairman:

Hugh J. Christian, Jr. (NASA Marshall Space Flight Center)

International Commission:

P. Krider, President

E.Williams, Secretary

S. Anisimov *(Russia)*
S. Chauzy *(France)*
C-M. Guo *(China)*
R. Jayaratne *(Botswana)*
P. Laroche *(France)*
M. Nakano *(Japan)*
H. Tammet *(Estonia)*

M. Baker *(USA)*
H. Christian *(USA)*
J. Hughes* *(USA)*
Z. Kawasaki *(Japan)*
J. Latham* *(U.K.)*
L. Ruhnke *(USA)*
W. Winn *(USA)*

M. Brook* *(USA)*
H. Dolezalek* *(USA)*
S. Israelsson *(Sweden)*
N. Kitagawa* *(Japan)*
S. Michnowski *(Poland)*
C. Saunders *(U.K.)*

* *Honorary Member*

## Preface

The 11th International Conference on Atmospheric Electricity (ICAE), held in 1999 at Lake Guntersville, Alabama, USA, builds on the traditions established by a long line of preceding conferences. Since 1954, conferences have typically been held every four years. They have been hosted by research groups active in the field of Atmospheric Electricity from around the world. Host countries have included the United States, Switzerland, Japan, Germany, United Kingdom, Sweden, and Russia. The prime objective for each conference has been to provide a forum for discussions of current research and challenging problems in Atmospheric Electricity.

We are presently in an era where Atmospheric Electricity is becoming important to wide ranging disciplines. Recent advances in remote sensing have provided researchers with the ability to make high quality lightning measurements around the globe, both from space and on the ground. These new measurements provide a global perspective that has heretofore been unavailable. Using these new data sets of the distribution and intensity of lightning, we are now identifying relationships between lightning activity and the variability of large-scale weather systems. Consequently, a measure of lightning activity could become an important remote sensing variable for global change research.

On a smaller scale, techniques are rapidly evolving for in-cloud lightning mapping, *in situ* microphysical and electrical measurements, cloud dynamics, modeling, laboratory measurements, and in fair weather ions and chemistry. We are truly undergoing a renaissance in Atmospheric Electricity.

The unique organization of the 11th ICAE was intended to foster individual and group discussion rather than extensive formal presentations. We had hoped that this would maximize interactions between the participants and thus build global collaborations to pursue the many new and exciting scientific developments. Indeed almost 300 abstracts were received from scientists living in 28 different countries. Of these, over 200 were selected by the Conference referees for presentation and 194 extended abstracts are published in these Proceedings.

The local organizing committee has prepared the Proceedings. The Conference owes its success to the organizing committee, the referees, the International Commission on Atmospheric Electricity and to NASA and the National Science Foundation for providing valuable financial support. Of course, the key to the success of any conference is the quality of the invited and contributed papers and the quality of the participating scientists. The 11th ICAE has been truly blessed.

Hugh J. Christian, Jr.

## Table of Contents

**Sessions I and II—Lightning Characteristics** ..... 1

Broadband Interferometer and 3D Observations
*R. Mardiana, Y. Ota, Z. Kawasaki, M. Murakami, K. Matsuura* ..... 2

Observations and Inferred Physical Characteristics of Compact Intracloud Discharges
*D. Smith, R. Massey, K. Wiens, K. Eack, X. Shao, D. Holden, P. Argo* ..... 6

Height of Radiation Sources Associated with Lightning Discharges
*M. Ishii, J. Hojo, K. Shimizu, K. Sato, K. Shinjo* ..... 10

VHF Observations During a Spider Lightning Flash
*E. Defer, C. Thery, P. Blanchet, P. Laroche* ..... 14

Broad Band Interferometric Measurement of Intra-Cloud Lightning in Chinese Inland Plateau
*T. Ushio, Z. Kawasaki, M. Chen, D. Wang, N. Takagi, T. Watanabe, X. Liu, Q. Xiushu, C. Guo* ..... 18

The Inception Phase of Positive Leaders in Triggered Lightning: Comparison of Modeling with Experimental Data
*A. Bondiou-Clergerie, P. Lalande, P. Laroche, J. Willett, D. Davis, I. Gallimberti* ..... 22

Computer Simulation of a Downward Negative Stepped Leader
*V. Mazur, L. Ruhnke, A. Bondiou-Clergerie, P. Lalande* ..... 26

1997 Triggered Lightning Experiment in the Inland Plateau of China
*X. Liu, C. Wang, X. Qie, Y. Zhang, W. Dong, Q. Xiao, G. Zhang, C. Guo, M. Chen, T. Watanabe, D. Wang, N. Takagi, M. Nakano, K. Nakamura, Z. Kawasaki, S. Sumi* ..... 30

Verification of Bi-directional Leader Concept Using Interferometric Measurement
*S. Yoshihashi, Z. Kawasaki* ..... 34

On Lightning Current Probability Distribution from Southeastern Brazilian Measurements
*O. Mendes, Jr., M. Domingues, I. Pinto, O. Pinto, Jr., J. Diniz, A. Carvalho, A. Cazetta* ..... 38

Analysis of Negative Downward Lightning Current Curves form 1985 to 1994 at Morro Do Cachimbo Research Station (Brazil)
*M. Lacerda, O. Pinto, Jr., I. Pinto, J. Diniz, A. Carvalho* ..... 42

Lightning Subsequent Strokes Producing New Terminations to the Ground
*S. Davis, E. Thomson* ..... 46

Photographic Documentation of Two Return Strokes Along the Same Channel Separated by About a Millisecond
*V. Idone, D. Davis* ..... 50

3D Imaging of Lightning Channel and Leader Progression Velocity
*Z. Kawasaki, H. Isoda, S. Yoshihashi* ..... 54

Positive Leaders in Rocket-Triggered Lightning: Propagation Velocity from Measured Current and Ambient-Field Profile
*J. Willett, D. Davis, P. Laroche* ..... 58

Cloud-to-Ground Lightning Flash Characteristics Obtained in the Southeastern Brazil Using the LPATS Technique and the New Hybrid Lightning Location Methodology
*O. Pinto, Jr., I. Pinto, J. Diniz, A. Carvalho, A. Filho* ..... 62

Conditions of Plasma Channels Required for Triggered Lightning
*M. Miki, A. Wada, H. Goshima, T. Shindo* ..... 65

Calculation of Electric Field Strength Necessary for Altitude Discharge above Thunderstorms
*V. Morozov* ..... 69

On the Temporal Evolution of Red Sprites, Runaway Theory versus Data
*V. Yukhimuk, R. Roussel-Dupre, E. Symbalisty* ..... 72

On the Nature of Mesospheric Electric Fields
*A. Zadorozhny* ..... 76

Satellite Detection of Sprites and Other Middle Atmospheric Storm Effects
*S. Clodman* ..... 80

Characteristics of Thunderstorms and Lightning Flashes which Produce Mesospheric Transient Luminous Events
*W. Lyons, T. Nelson, R. Armstrong, E. Williams, D. Suszcynsky, R. Strabley, M. Taylor, L. Gardner* ..... 84

Parameterization of Sprites and Their Parent Discharges
*M. Stanley, P. Krehbiel, M. Brook, W. Rison, C. Moore, R. Thomas* ..... 88

Ionization in the Middle Atmosphere Associated with Thunderstorms-- Multi-Color Photometric Analysis of Sprite Emissions
*R. Armstrong, D. Suszcynsky, R. Strabley, W. Lyons, T. Nelson* ..... 92

EM Radiation Associated with Sprites?
*T. Otsuyama, Y. Hobara, M. Hayakawa* ..... 96

Propagation Characteristics of Return Strokes and M-Components in Florida Rocket-Triggered Lightning
*D. Wang, T. Ito, N. Takagi, T. Watanabe, V. Rakov, M. Uman* ..... 99

An Analysis of Natural Lightning Discharge to the Ground in Chinese Inland Plateau
*X. Qie, X. Liu, G. Zhang, Y. Yu, C. Guo, D. Wang, T. Watanbe, N. Takagi, Z. Kawasaki, T. Ushio, M. Nakano, K. Nakamura* ..... 103

Broad Band Interferometric Measurement of Rocket Triggered Lightning
*W. Dong, X. Liu, X. Qie* ..... 107

About the Positive Leader Propagation Mechanism
*A. Ivanovsky* ..... 111

Properties of Leader Development in Altitude-Triggered Lightning
*M. Chen, T. Watanabe, N. Takagi, D. Wang, X. Liu, Y. Zhang, L. Zhou, D. Zhong* ..... 115

Peak Radiation Fields of Lightning Return Strokes over Finitely Conducting Ground
*V. Cooray* ..... 119

Return Stroke Current Modeling of Lightning Striking a Tall Tower Accounting for Reflections Within the Growing Channel and for Upward-Connecting Discharges.
*V. Shostak, W. Janischewskyj, A. Hussein, J. Chang, B. Kordi* ..... 123

Magnetic Field of a Branching Discharge
*V. Borisov, A. Utkin* ..... 127

Thin Structure of Atmospherics
*Y. Krasnitsky* ..... 131

Investigation of a Frequency Spectrum of Discharges Generated by a Charged Aerosol Cloud
*A. Orlov, A. Temnikov* ..... 135

Formation of Plasma Space Stems in Charged Aerosol Clouds: Experimental Results and Theoretical Explanation
*A. Temnikov, A. Orlov, V. Syssoev* ..... 138

Statistical Analysis and Polymer-Composite Structure of Ball Lightning
*A. Amirov, V. Bychkov* ..... 142

Current Measurements of Upward Negative Leaders in Rocket Triggered Lightning
*M. Nakano, S. Sumi, K. Nakamura* ..... 146

Lightning, the Global Circuit and the Middle Atmosphere
*L. Hale* ..... 150

Multiple-Station Measurements of Triggered Lightning Electric and Magnetic Fields
*D. Crawford, V. Rakov, M. Uman, G. Schnetzer, K. Rambo, M. Stapleton* ..... 154

Positive Leaders in Triggered Lightning: Propagation Velocity from Measured Current and Electric Field Derivative at Ground
*D. Davis, P. Laroche* ..... 158

Signal Strength of Return Strokes Occurring Over the Sea and Over Land: A Sensitivity Analysis
*A. Galvan, V. Cooray, T. Gotschl, V. Scuka* ..... 162

An Intercomparison of Ground, Airborne, and Space Instrumentation Definitions of the Lightning Element
*D. Mach, W. Boeck, H. Christian* ..... 166

**Session III—Lightning Detection and Protection** ..... **171**

Comparison of Ground-Based 3-Dimensional Lightning Mapping Observations with Satellite-Based LIS Observations in Oklahoma
*R. Thomas, P. Krehbiel, W. Rison, T. Hamlin, D. Boccippio, S. Goodman, H. Christian* ..... 172

TRMM/LIS Observations of Lightning Activity
*Z. Kawasaki, S. Yoshihashi* ..... 176

Towers, Lightning and Human Affairs
*L. Byerley, W. Brooks, R. Noggle, K. Cummins* ..... 180

"ORAGES": A Project for Space-Borne Detection of Lightning Flashes Using Interferometry in the VHF-UHF Band
*A. Bondiou-Clergerie, P. Blanchet, C. Thery, A. Delannoy, J. Lojou, A. Soulage, P. Richard, F. Roux, S. Chauzy* ..... 184

Lightning First Pulses Used in the "LASI" (Time of Arrival) and "ATLAS" (Single Station) Total Lightning Mapping Systems
*R. Markson, L. Ruhnke* ..... 188

A Spherical Earth Solution for TOA Lightning Location Retrieval
*W. Koshak, R. Solakiewicz* ..... 192

Performance of the New LLP-Impact System in Finland
*T. Tuomi* ..... 196

Demographics of U.S. Lightning Casualties and Damages from 1959-1994
*R. Holle, R. Lopez, E. Curran* ..... 200

Results of Investigations into Annual USA Lightning Costs and Losses
*R. Kithil* ..... 204

The Two Important Characteristics of Ground Flashes for the Human Safety
*N. Kitagawa, A. Sugita, S. Takahashi* ..... 207

Comments on the E.S.E. Air Terminals
*C. Guo* ..... 211

Lightning Injuries to Humans in France
*E. Gourbiere* ..... 214

An Integrated North American Lightning Detection Network
*K. Cummins, R. Pyle, G. Fournier* ..... 218

Electric-Field Changes of Lightning Observed with Balloon-Borne Slow Antennas
*W. Beasley, K. Eack, H. Morris, D. Rust, D. MacGorman* ..... 222

A New, High Voltage, Arbitrary Waveform Generator for Simulating Pre-Return Stroke C-G Lightning Electric Fields
*F. D'Alessandro, J. Gumley* ..... 226

A Preliminary Assessment of the Long-Term Performance in the Field of an Enhanced Air Terminal and the Lightning Protection Design Method
*F. D'Alessandro* ..... 230

Operational LPATS Network in Australia
*A. Sharp* ..... 234

Lightning Launch Commit Criteria for America's Space Program
*W. Roeder, J. Sardonia, S. Jacobs, M. Hinson, D. Harms, J. Madura, S. DeSordi* ..... 238

New Mechanism of Thundercloud Electricity and Lightning Production
*V. Ermakov, Y. Stozhkov* ..... 242

Preliminary FAA Investigations Into Using Total Lightning to Improve Convective Forecasting for Aviation
*A. Nierow, R. Showalter, C. Souders* ..... 246

Long-Range and Trans-Oceanic Lightning Detection
*J. Cramer, K. Cummins* ..... 250

A Diagnostic Analysis of the Kennedy Space Center LDAR Network
*D. Boccippio, S. Heckman, S. Goodman* ..... 254

**Session IV—Thunderstorm Electrification ..... 259**

Aircraft Measurements of Particle Image and Charge Inside a New Mexico Thundercloud
*W. Murray, W. Winn, R. Thomas, A. Ebneter, P. Fleishhacker, R. Lawson, K. Weaver, R. Stewart, C. Wieland* ..... 260

An Experimental Study of Charge and Mass Transfer During Ice Contact Interactions
*B. Mason, J. Dash* ..... 264

Vapor and Heat Supply to Riming Graupel: Effect on Charging
*C. Saunders, E. Avila, S. Peck, N. Castellano, G. Varela* ..... 268

Turbulent Electric Dynamo in Thunderstorm Clouds
*E. Mareev* ..... 272

Inferring Selected Cloud Properties from Satellite Lightning Data
*V. Schroeder, M. Baker* ..... 276

Contact Time in Ice-Ice Collisions
*G. Caranti, G. Varela, R. Pereyra* ..... 280

Electrical Structure of Clouds and Thundercloud Electrification
*P. Handel* ..... 284

An Examination of the Convective Charging Hypothesis
*J. Helsdon, S. Gattaleeradapan, R. Farley* ..... 288

The Effect of the Cloud Droplet Spectrum on Electrical Charge Transfer During Individual Ice-Ice Collisions
*R. Pereyra, E. Avila, G. Caranti, G. Varela* ..... 292

Charge Transfer Process During Collision of Riming Graupel Pellet with Small Ice Crystals Within a Thundercloud
*S. Datta, U. De, K. Goswami, L. Jones* ..... 296

Electric Charge on Raindrops During Thunderstorm Precipitations
*P. Baranski* ..... 300

Reversal of the Sign of Charge on Graupel During Riming Electrification: Measurements in Hokuriku Winter Clouds and in a Wind Tunnel
*T. Takahashi* ..... 304

Separation of Charge During Rebounding Collisions Between Graupel as a Possible Mechanism of Thunderstorm Electrification
*R. Jayaratne* ..... 308

Thunderstorm Electrification: The Effect of Chemical Impurities in Cloud Water
*R. Jayaratne* ..... 312

Estimation of the Total Corona Charge Transfer from the Surface to the Thundercloud
*S. Chauzy, S. Soula* ..... 316

Discharge Initiation by Uncharged Raindrops Falling at Terminal Velocity in a Horizontal Electric Field
*S. Coquillat, S. Chauzy, J. Georgis, B. Combal, X. Silvani* ..... 320

Effect of Droplet Size on Graupel Surface Properties in Connection with Noninductive Charge Transfer
*R. Mitzeva, T. Kassabova, C. Saunders* ..... 324

On Charging Phenomena in Snowstorm
*H. Shio* ..... 328

The Electric Charge's Separation During Break-up of the Electrolyte Solutions
*A. Kolpakov, L. Maliarova, E. Titova* ..... 332

Thunderstorm and Lightning Development: Modeling and Observations
*R. Solomon, C. Thery, E. Defer, A. Bondiou-Clergerie* ..... 335

Simulation Study of Non-Inductive Charging and Discharge Processes in the Thunderstorm
*Y. Zhang, M. Yan, X. Liu* ..... 339

Rate of Evaporation of the Charged and Uncharged Water Drops Suspended in the Air Stream of a Wind Tunnel
*A. Kamra, R. Bhalwankar, A. Sathe* ..... 343

A Study of the Ion Attachment by Droplets in Cloud Conditions: Implication for Pollutant Transport
*G. Caranti, S. Masuelli* ..... 347

To Selective Ion Charging of Water Drops in Thunderstorms
*A. Sorokin* ..... 351

Charge Generation With and Without Secondary Ice Production
*J. Hallett* ..... 355

Simulation of Early Electrification in a Three-Dimensional Dynamic Cloud Model
*C. Ziegler, J. Straka, D. MacGorman* ..... 359

Determination of Thunderstorm Anvil Ice Contents and Other Cloud Properties from Satellite Observations of Lightning
*A. Blyth, H. Christian, J. Latham* ..... 363

**Session V and VI—Thunderstorm Characteristics ..... 367**

Lightning and Radar Characteristics of the Bow Echo Event of May 24-25, 1998
*N. Murray, R. Orville* ..... 368

Combined Microwave and Sferics Measurements as a Continuous Proxy for Latent Heating in Mesoscale Model Predictions
*D. Chang, C. Morales, J. Weinman, W. Olson* ..... 372

Three-Dimensional Lightning Mapping Observations During MEaPRS in Central Oklahoma
*P. Krehbiel, R. Thomas, W. Rison, T. Hamlin, J. Harlin, M. Davis* ..... 376

Characteristics of "Superbolt" Related Winter Thunderclouds Over the Japan Sea
*T. Shimura, F. Kobayashi, T. Shindo, A. Wada, T. Sakai* ..... 380

Some Aspects of Correlation Between Lightning Activity and Rainfall in Thunderstorms
*S. Soula, G. Molinie, S. Defoy, S. Chauzy, N. Simond* ..... 384

An Investigation of the Horizontal Extent of Charge Regions in One Thunderstorm
*T. Marshall, M. Stolzenburg, D. Bartels, D. Rust* ..... 388

Lightning Characteristics in the 1992-1996 Period in the Basque Country Area: Lightning-Precipitation Relationships
*J. Areitio, I. Herrero, A. Ezcurra* ..... 392

First Measurements of the Atmospheric Electric Field in the Spanish Basque Country
*I. Herrero, J. Areitio, A. Ezcurra* ..... 396

Lightning in the Hurricane Core: Distribution and Significance
*J. Molinari, M. Black, P. Black, V. Idone* ..... 400

A Multi-Platform Study of the February 10, 1998, Squall Line Event and TRMM Overpass of Southeast Texas
*D. Wolff, R. Orville, E. Zipser* ..... 404

Cloud-to-Ground Lightning Activity in Mesoscale Convective Complexes in Southeastern Brazil in 1993-94
*I. Pinto, O. Pinto, Jr., J. Conforte, J. Diniz, A. Carvalho, A. Filho* ..... 408

Lightning Ground Flash Measurements over the Contiguous United States: A Ten Year Summary 1989-1998
*R. Orville, G. Huffines* ..... 412

Vertical Profile of Space Charge Near Ground Surface Estimated with Corona Current
*K. Narita, Y. Goto, N. Takeuchi, N. Honma, N. Suzuki* ..... 416

Optical Observations of Lightning in Northern India, Himalayan Mountain Countries and Tibet
*W. Boeck, D. Mach, S. Goodman, H. Christian, Jr.* ..... 420

Thunderstorm Development in Convective Clouds
*A. Adzhiev, R. Kalov, S. Sizhazhev, M. Agzagova, Kh. Kumykov* ..... 424

The Characteristics of Positive Ground Discharges of Tropical Thunderstorms at Ibadan, Nigeria
*E. Oladiran, U. Akpan, E. Numphas, S. Israelsson* ..... 428

3-Deminsional Lightning and Dual-Polarization Observations of Thunderstorms in Central New Mexico
*W. Rison, R. Scott, R. Thomas, P. Krehbiel, T. Hamlin, J. Harlin* ..... 432

Characteristics of Cloud-to-Ground Lightning in the Contiguous U.S. from 1995-1997
*B. Zajac, S. Rutledge, L. Carey* ..... 436

Lightning and 85-GHz MCSs in the Global Tropics
*R. Toracinta, E. Zipser* ..... 440

Electric Field Profiles and Lightning In Storms with Frequent Positive Cloud-to-Ground Lightning
*D. MacGorman, D. Rust, P. Krehbiel, R. Thomas, W. Rison, M. Lockwood, W. Beasley, K. Eack* ..... 444

Thunderstorm Activity over Land and Sea Regions of India and the Sensitivity of Wet-Bulb and Sea Surface Temperatures to their Occurrence
*G. Manohar, S. Kandalgaonkar, M. Tinmaker* ..... 448

Lightning Activities of Winter Thundercloud Observed by Dual-Polarization Doppler Radar on the Hokuriku Coast of Japan
*K. Kami, K. Shinjo, T. Sakai, T. Wakai* ..... 452

Development of Heat Thunderstorms and Distribution of Lightning Strokes around the Northern Part of the Kanto Plain, Japan
*T. Suzuki, F. Kobayashi, T. Shimura, T. Miyazaki, T. Hirai* ..... 456

Two Types of PGF-Producing Clouds in Winter Thunderstorms in Israel
*Y. Yair, O. Altaratz, Z. Levin* ..... 460

Relation Between Lightning Activity of Summer and Winter Thunderclouds and Surface Electric Field Variation, Japan
*K. Michimoto, T. Shimura, T. Suzuki* ..... 464

Electrical and Radar Observations of Thunderstorms in the Eastern Mediterranean
*O. Altaratz, Z. Levin, Y. Yair* ..... 468

Cloud-to-Ground Lightning at Low Surface Temperatures
*P. Moore, V. Idone* ..... 472

Lightning in Supercell Storms
*G. Reuter, S. Kozak* ..... 476

Polarimetric Radar Observations and Cloud Modeling Studies of Low Lightning Producing Convection in the Fort Collins Flash Flood
*W. Peterson, L. Carey, S. Rutledge* ..... 480

Observations of Thunderclouds and Lightning Activity in Winter by Dual Polarization Radar and SAFIR
*Y. Sonoi, H. Uyeda, Z. Kawasaki, Y. Maekawa, S. Fukao, T. Takahashi* ..... 484

A Possible Mechanism of Gushes of Rain or Hail after Lightning
*N. Singh, A. Mohan* ..... 488

Results of Electrical Field Strength Investigations in Convective Clouds
*A. Sinkevich, Ju. Dovgaluk, Yu. Ponomarev, V. Stepanenko* ..... 492

Studies of Florida Thunderstorms using LDAR, LLP, and Single Doppler Radar Data
*G. Forbes, S. Hoffert* ..... 496

Combined Dual-Doppler, Multiparameter Radar, and Lightning Observations of a Severe Convective Storm
*T. Lang, S. Rutledge, P. Kennedy* ..... 500

Relationship Between Initial Development of Precipitation and Onset of Cloud Electrification and the Observed Behaviour of Point Discharge Current During "Rain" and "No-Rain" Situations in the Thunderstorms at Pune
*S. Kandalgaonkar, M. Tinmaker, G. Manohar* ..... 503

Electric Field Profiles in a Mesoscale Convective System with Multiple Bow Echoes 25 May 1998 during the MCS Electrification and Polarization Radar Study (MEaPRS)
*D. Rust, T. Marshall, M. Stolzenburg, D. Jorgensen, T. Shepherd, D. MacGorman* ..... 507

Cloud-to-Ground Lightning Characteristics of a Major Tropical Cyclone Tornado Outbreak
*E. McCaul, D. Buechler, S. Goodman* ..... 511

Total Lightning Activity Associated with Tornadic Storms
*S. Goodman, D. Buechler, S. Hodanish, D. Sharp, E. Williams, R. Boldi, A. Matlin, M. Weber* ... 515

The 1997-98 El Nino Event and Related Lightning Variations in the Southeastern United States
*D. Buechler, S. Goodman, E. McCaul, K. Knupp* ..... 519

A Comparison Between Lightning Activity and Passive Microwave Movements
*K. Driscoll* ..... 523

High-Altitude Aircraft-Based Electric Field Measurements above Thunderstorms
*M. Bateman, R. Blakeslee, J. Bailey, M. Stewart, A. Blair* ..... 527

Lightning Discharge Locations Relative to Reflectivity and Updraft/Downdraft Structures in a Colorado Thunderstorm
*J. Dye, T. Matejka, P. Laroche, E. Defer, G. Hubler, S. Rutledge* ..... 530

**Session VII—Fair Weather Electricity** ..... **535**

Data Processing at Special Data Center on the Surface Layer Atmospheric Electricity, A.I. Voeikov MGO RC ARS
*Ya. Shvarts, I. Petrenko, G. Shchukin* ..... 536

Effect of Coagulation on the Particle Charge Distribution and Air Conductivity
*S. Dhanorkar, A. Kamra* ..... 539

Natural Atmospheric Ions as Electrostatic Systems
*V. Klingo* ..... 543

On Factors Determining the Variations of the Electric Characteristics of a Surface Layer
*A. Petrov, G. Petrova, I. Panchishkina* ..... 547

On the Description of Atmospheric Electric Field and Current Under Inhomogeneous Conductivity
S. Davydenko, P. Bespalov ..... 551

Global Variations of Ionospheric Potential in Surface Layer
G. Kupovykh ..... 555

A Sensor for Balloon Measurements of the Air Conductivity
V. Struminsky ..... 559

Seasonal Dependence of Electrical Mobility Spectra of Small Air Ions
*T. Parts* ..... 563

The String Fluxmeter: How to Make and How to Use
*V. Struminsky* ..... 567

Structures and Spectra of Aeroelectric Field Pulsations
*S. Anisimov, S. Bakastov, E. Dmitriev, E. Mareev* ..... 571

Turbulent Transfer of Space Charge in the Atmospheric Surface Layer
*J. Barlow, R. Harrison* ..... 575

Properties of Ion-Induced Nucleation Obtained from Mobility Measurements
*K. Hara, S. Nakae, K. Miura* ..... 579

Enhanced Fair-Weather Electric Fields Soon After Sunrise
*T. Marshall, D. Rust, M. Stolzenburg, W. Roeder, P. Krehbiel* ..... 583

On Electric Properties of Radiation Fog
*S. Israelsson* ..... 587

Measurement of Atmospheric Electrical Conductivity During Monsoon Period
*J. Rai, A. Kumar, A. Singh* ..... 591

The Atmospheric Electric Fog Effect
*J. van der Hage, T. de Bruin* ..... 595

Ion-Aerosol Interactions in Atmospheric Air
*K. Aplin, R. Harrison* ..... 598

South Pole Electric Field Responses to Changes in Overhead Ionospheric Potential
*B. Tinsley* ..... 602

Stratospheric Balloon Measurements of Conductivity and Electric Fields Associated with Sferics in Brazil
*M. Saba, O. Pinto, Jr., I. Pinto, O. Mendes, Jr.* ..... 606

Effect of Wind on Horizontal Wire Antenna Collecting Atmospheric Air-Earth Current
*R. Lelwala, T. Tuomi, S. Israelsson, K. Jayaratne* ..... 610

Synergetic Models of Space Charge Structures in the Atmosphere
*O. Mareeva, E. Mareev, S. Israelsson, S. Anisimov* ..... 614

Classification of Natural Air Ions Near the Ground
*U. Horrak, J. Salm, H. Tammet* ..... 618

Atmospheric Electricity as a Factor of Dry Deposition of Particulate Pollution
*H. Tammet, S. Israelsson* ..... 622

The Limits of Air Ion Mobility Resolution
*H. Tammet* ..... 626

Aeroelectrical Measurements in Geoelectromagnetic Complete Set of Geophysical Observatory "Borok"
*S. Anisimov, S. Bakastov, E. Dmitriev, E. Anisimova* ..... 630

Simulation of the Universal-Time Diurnal Variation of the Global Electric Circuit Charging Rate
*D. Mackerras, M. Darveniza, R. Orville, E. Williams, S. Goodman* ..... 634

A Study of the Atmospheric Electrical Parameters and the Meteorological Conditions During some Intense Air Pollution Episodes in Athens
*D. Retalis, A. Retalis* ..... 638

Ionospheric Potential as a Measure of Global Temperature Variation
*R. Markson, D. Vogel* ..... 642

Evidence for the Absence of Conductivity Variations Above Thunderstorms
*J. Bailey, R. Blakeslee, K. Driscoll* ..... 646

**Session VIII—Global Lightning; Chemistry ..... 651**

Enhanced NOx by Lightning in the Upper Troposphere and Lower Stratosphere Inferred from the Global NO2 Measurements of the Upper Atmosphere Research Satellite (UARS)
*N. Sanger, R. Zhang, R. Orville, X. Tie, W. Randel, E. Williams* ..... 652

Evaluation of NOx Produced by Storms Based on 3d VHF Lightning Mapping
*P. Laroche, E. Defer, P. Blanchet, C. Thery* ..... 656

Impact of Lightning Discharge on Stratospheric Ozone
*B. Klumov* ..... 660

An Estimation of Nitric Oxide Variation Caused by Lightning over a Bulgarian Area Based on Experimental and Model Data
*S. Kolev* ..... 664

Recent Results of the FORTE rf Payload
*A. Jacobson* ..... 668

Thunderstorm and Lightning Studies using the FORTE Optical Lightning System (FORTE/OLS)
*D. Suszcynsky, M. Kirkland, P. Argo, R. Franz, A. Jacobson, S. Knox, J. Guillen, J. Green, R. Spaulding* ..... 672

Detection Rates of Lightning Generated Radio Emissions by FORTE
*R. Zuelsdorf, A. Jacobson, M. Kirkland, R. Strangeway, C. Russell* ..... 676

Satellite Observations of Transient Radio Impulses from Thunderstorms
*P. Argo, M. Kirkland, A. Jacobson, R. Massey, D. Suszynsky, K. Eack, T. Fitzgerald, D. Smith* ... 680

Operation of an Array of Field-Change Detectors to Provide Ground Truth for FORTE Data
*R. Massey, K. Eack, M. Eberle, X. Shao, D. Smith, K. Wiens* ..... 684

Investigation of Possibilities to Obtain Information on Thunderstorm Clouds by Satellite Radar TRMM
*V. Stepanenko* ..... 688

El Nino Related Meridional Shifts in the Global Position of the Worldwide Thunderstorm Activity
*G. Satori, B. Zieger* ..... 691

A New Schumann Resonance Station in the Negev Desert for Monitoring Global Lightning Activity
*C. Price, M. Finkelstein, B. Starobinets, E. Williams* ..... 695

Schumann Resonances and the Temporal-Spatial Dynamics of Global Thunderstorm Activity
*V. Mushtak, R. Boldi, E. Williams* ..... 698

Periodic Variations of Solar and Tropospheric Origins in Schumann Resonances
*B. Zieger, G. Satori* ..... 701

Comparisons of Long-Term Schumann Resonance Records in Europe and North America
*G. Satori, E. Williams, B. Zieger, R. Boldi, S. Heckman, K. Rothkin* ..... 705

Global Lightning Triangulation
*M. Fullekrug* ..... 709

The European Lightning NOx Project—First Results of the Field Experiment 1998
*U. Finke, P. Laroche, H. Holler, H. Huntrieser, T. Fehr* ..... 712

Optical Detection of Lightning From Space
*H. Christian* ..... 715

An Optimal Relation of Radar Reflectivity to Lightning Rate
*S. Heckman* ..... 719

Optical Transient Detector (OTD) Observations of a Tornadic Thunderstorm
*D. Buechler, S. Goodman, H. Christian, K. Driscoll* ..... 722

Global Frequency and Distribution of Lightning as Observed by the Optical Transient Detector (OTD)
*H. Christian, R. Blakeslee, D. Boccippio, W. Boeck, D. Buechler, K. Driscoll, S. Goodman, J. Hall, W. Koshak, D. Mach, M. Stewart* ..... 726

Lightning Production of NOx in a 3D Storm Model
*J. Helsdon, X. Zhang, R. Farley* ..... 730

Land-Ocean Differences in LIS and OTD Tropical Lightning Observations
*D. Boccippio, W. Koshak, H. Christian, S. Goodman* ..... 734

Initial Comparison of the Lightning Imaging Sensor (LIS) with Lightning Detection and Ranging (LDAR)
*T. Ushio, K. Driscoll, S. Heckman, D. Boccippio, W. Koshak, H. Christian* ..... 738

Diurnal Lightning Distribution as Observed by the Optical Transient Detector (OTD)
*R. Blakeslee, K. Driscoll, D. Buechler, D. Boccippio, W. Boeck, H. Christian, S. Goodman, J. Hall, W. Koshak, D. Mach, M. Stewart* ..... 742

The Lightning Imaging Sensor
*H. Christian, R. Blakeslee, S. Goodman, D. Mach, M. Stewart, D. Buechler, W. Koshak, J. Hall, W. Boeck, K. Driscoll, D. Boccippio* ..... 746

Global Lightning Variations Caused by Changes in Flash Rate and by Changes in the Number of Thunderstorms
*E. Williams, K. Rothkin, D. Stevenson, D. Boccippio* ..... 750

The Role of the Boundary Layer Aerosol in the Vertical Development of Precipitation and Electrification: Another Look at the Contrast between Lightning over Land and Over Ocean
*E. Williams, D. Rosenfeld, N. Madden, C. Labrada, J. Gerlach, L. Atkinson* ..... 754

The Relationship between the Background and Transient Signals in Schumann Resonances
*E. Williams, D. Castro, R. Boldi, T. Chang, E. Huang, V. Mushtak, W. Lyons, T. Nelson, S. Heckman, D. Boccippio* ..... 758

Long-Term SR and ELF Transients Observed in a Japanese Site
*M. Hayakawa, A. Nickolaenko, Y. Hobara, E. Williams* ..... 762

**Author Index** ..... **767**

**Subject Index** ..... **773**

# Sessions I and II:

# Lightning Characteristics

# Broadband Interferometer and 3D Observations

**R. Mardiana, Y. Ota, Z-I Kawasaki, M. Murakami, K. Matsuura**
Osaka University, JAPAN

ABSTRACT: Lightning observations to image lightning channel progression in 3D by means of broadband radio interferometer is performed. Using two sets of broadband system at two different sites, we observed many lightning discharges during a field campaign in Darwin Australia in 1998. We carried out the data processing to investigate the development of lightning discharges. The system shows that for several tens kilometers, lightning discharges can be detected, their progression can be reconstructed and their positions can be mapped into three-dimensionally spatial format and in time sequence.

## INTRODUCTION

Lightning breakdown processes emit electromagnetic radiation with broadband spectrum in the frequency range of VHF/UHF. Several techniques have been developed for locating 3D lightning radiation sources. Narrow-band interferometer has showed its great capability for imaging lightning channel in 3D and explained the lightning progression for ground and cloud flashes. Laroche et.al.[1996] has employed this technique operated at the center frequency of 110-118 MHz. Onuki et.al.[1996] used the same technique but using a center frequency of 327 MHz.. Different technique based on time of arrival also was used by Proctor at.al.[1988] and LDAR system to observe a 3D electromagnetic sources emitted from lightning [Maier, 1996]. Recently, the broadband interferometer has been manufactured and its capability to locate and reconstruct the lightning progression in 2D or azimuth-elevation format has been demonstrated by Ushio et.al.[1997] and Mardiana et.al.[1998]. This paper presents the three-dimensional observations of broadband system and an experimental result will be discussed.

## MEASUREMENT SYSTEM

To realize 3D lightning channel reconstruction, a field campaign was conducted with two observation sites in Darwin, Australia in 1998. The distance between two sites was 23.1 km, site 1 was named Middle Point (latitude 12.581S and longitude 131.101E) and site 2 was Humpty Doo (latitude 12.579S and longitude 131.314E). Each site employed three broadband flat plane antennas having logarithmic amplifier, those were separated horizontally with the baseline's length of 10 meters and aligned at three apexes of a square. The broadband lightning signals were digitized at 500 MHz sampling rate. The digitizer was divided into 1500 segments, and one segment can record one broadband electromagnetic pulse for 1 microsecond. Once the electromagnetic pulse from lightning flash is detected, the triggering circuit is turned on to record a waveform and save it as one segment (referred to as an EM source). The minimum time between two consecutive EM sources is about 70 μs due to instrumentally dead time. The system was operated to record radiation sources from 10 to 200 MHz. A slow antenna having a time constant of 10s, sampling rate 1 MHz and 12-bit resolution was equipped at each site to record electrostatic field changes for 1 second. A GPS at each site was also setup to get time-synchronization to confirm that the radiation sources captured at both sites are from the same lightning flash. A triangulation scheme was used to image 3D lightning progression and to map lightning radiation positions. For each EM source, both sites provide data in azimuth-elevation format that are required to participate in the x-y-z solution. If the EM source is saturated and if its timing from both sites are not consistent with a location solution, the location is not available. A successful EM source into location solution is referred to as an event. The system succeeded to locate a number of events along the lightning channel, depicting flashes in 3D spatial

location and temporal progression. No comparison result was done with other lightning position system.

RESULTS

A four-stroke negative ground flash will be discussed. This flash occurred on November 27, 1998 at 04:54:53 (UTC) as recorded by the GPS installed at both sites. During this flash period, the system at site 1 detected 1500 EM sources or reached the maximum memory size of digitizer and site 2 detected 802 EM sources. During post analysis, first, the data from each site is processed to have an azimuth-elevation position, any data having saturated EM source will be not be considered. Next each EM source of both sites, whose the difference of incident time does not exceed 76 μs, can be candidate to be paired. The 76 μs is the maximum arrival time delay of an EM source to travel for one site to another. Using these criteria, of those EM sources detected, 510 events can be mapped into 3D-image. Figure 1 shows the angular position of this flash in hemispherical parabolic projection as recorded at two sites. Approximate lightning strike in azimuth direction is 225 degrees from site 1 and 340 degrees from site 2. We chose east as zero degree of azimuth direction and rotated counterclockwise. Full scale of electric field waveform at both sites for this lightning is shown in Figure 2. The classic atmospheric electricity convention was applied for explanation of electric field change. Electric field change of both sites, figure 2a and 2b, are identical and four return strokes can be recognized as indicated by the abrupt positive change of electric field, but only the first-three has emitted very strong radiation during leader progression as shown in time-altitude plot in figure 2c.

Figure 3 shows the extended scale of time-altitude plot of lightning progression in figure 2c. The system mapped the initial stepped leader L1, in figure 3a, from an altitude of 6.5 km downward to 2 km. Using the time and altitude of the first located event and the time of the ground strike, the first leader velocity was ~$1.9 \times 10^5$ m/s, typical of initial leaders. The leader culminated with an abrupt change of electric field change caused by a return stroke. This initial leader was followed after 20-25 ms quiet intervals by the second leader L2 in figure 3b. The second leader was mapped from approximately 6.5 km downward to 2.5 km, with a relative slow speed of ~$1.0 \times 10^5$ m/s.

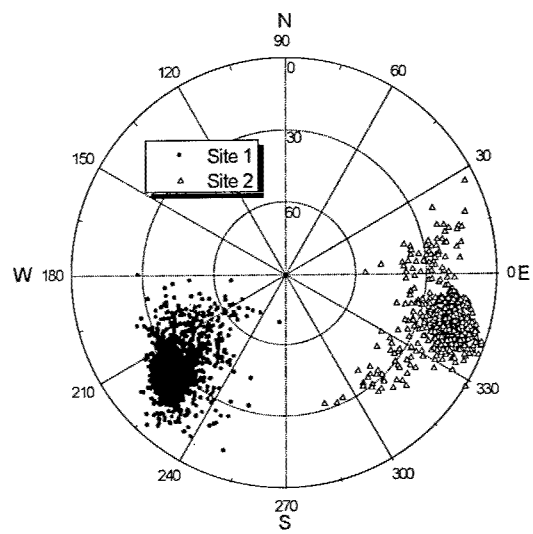


**Figure 1. Hemispherical parabolic projection of radiation sources for both sites. A dot or a triangle represents a position of an EM source.**

Radiation likely from "J-change" were detected prior to the third leader L3 in figure 3c, just after 10-15 ms from last event of stepped leader L2. These radiation J have a tendency to move upward and emitted approximately from altitude of 5 to 7 km and occurred in nearly the same region as origin of the initial leader L1. The third leader L3 was detected from approximately 7 km moving downward to 3.5 km, with a corresponding velocity of ~$1.1 \times 10^5$ m/s. A 20-25 ms after leader L3, a leader was detected at a short period of about ~1.8 ms. This leader moved downward from approximately 6.6 km to 4.2 km but no return stroke signature was detected as shown in figure 3d. The absence of a return stroke led us to conclude that it is so-called an attempted leader AL [Shao, 1995]. The last leader L4 was likely a dart leader and initiated a continuing current. Not so many events of this leader were captured and mapped. Coarse approximation of the velocity of this leader was $2.1 \times 10^6$ m/s.

Figure 4 displays the 3D-plan view of L1, L2 and L3 of this flash in x-y-z format. It is interesting to note we found the first stroke on ground following L1 has nearly or exactly the same spatial position with the second stroke, but the third has a different position with previous ones. From the aspect of the leader velocity, L1 and L2 have a possibility to have a different striking point, but their spatial positions do not likely support it. In case of L3, since its striking point position is different with the former strokes, the leader velocity has a typical stepped leader velocity. The distance of the first stroke can be estimated as indicated by a circle S1 on x-y plot, and it is 8.7 km and 17.4 km from site 1 and site 2, respectively. Third stroke point S3 has a distance of 5.5 km from site 1 and 18.9 km from site 2. The distance between S1 and S3 is 2.8 km and S3 is closer to site 1. The fourth stroke has not so many events during its leader progression, but we argue that it has the same leader channel path with L3 and striking point with S3. From x-z and y-z plots the flash has a vertical channel length of about 8 km, but ~2 km above the ground EM sources could not be detected due to many trees surrounding observation sites or radiation was too weak. Histogram shows the group of events based on altitude position. It is clearly seen that between 4.5 to 5.5 km, most numerous sources were observed. Laroche et.al.[1996] has observed 3D lightning structure in Florida and the result that 5 to 7 km was the most active zone. Stanley et.al.[1996] used NEXRAD radar scan to observe lightning radiation position at KSC, Florida and his result displayed that 6 to 9 km was the most active zone. Our result needs more lightning data to confirm the altitude position of the most numerous sources during lightning activity.

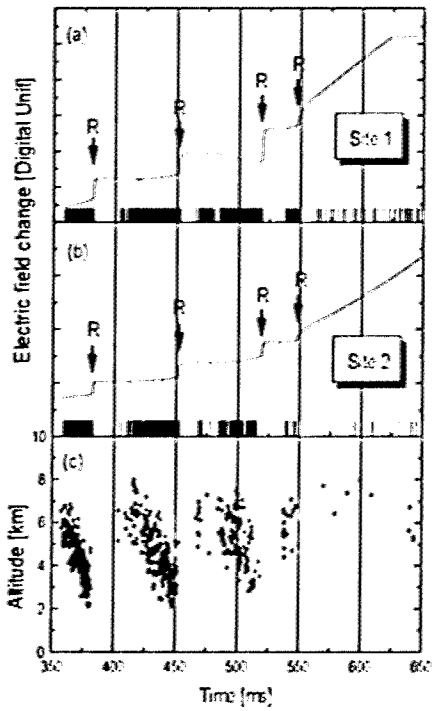


**Figure 2. Figure (a) and (b) are overall electric field change of both sites. The times for which broadband system for each site detected EM sources are shown as thin lines above each x-axis. Four return strokes were indicated by arrows. In figure (c), a total of 510 events can be located. The leader progression in time-altitude plot indicates that the first three leaders emit very strong radiation.**

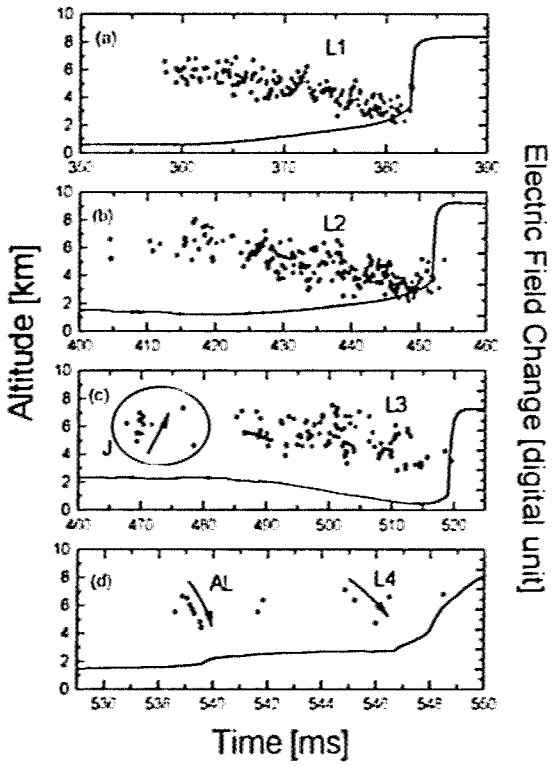


**Figure 3. Detail Leader progression in time-altitude plot and their associated electric field change in extended scale. Labels L1, L2, K, L3, AL and L4 are used to simplify explanation. L = leader, J = J-change, AL = attempted leader.**

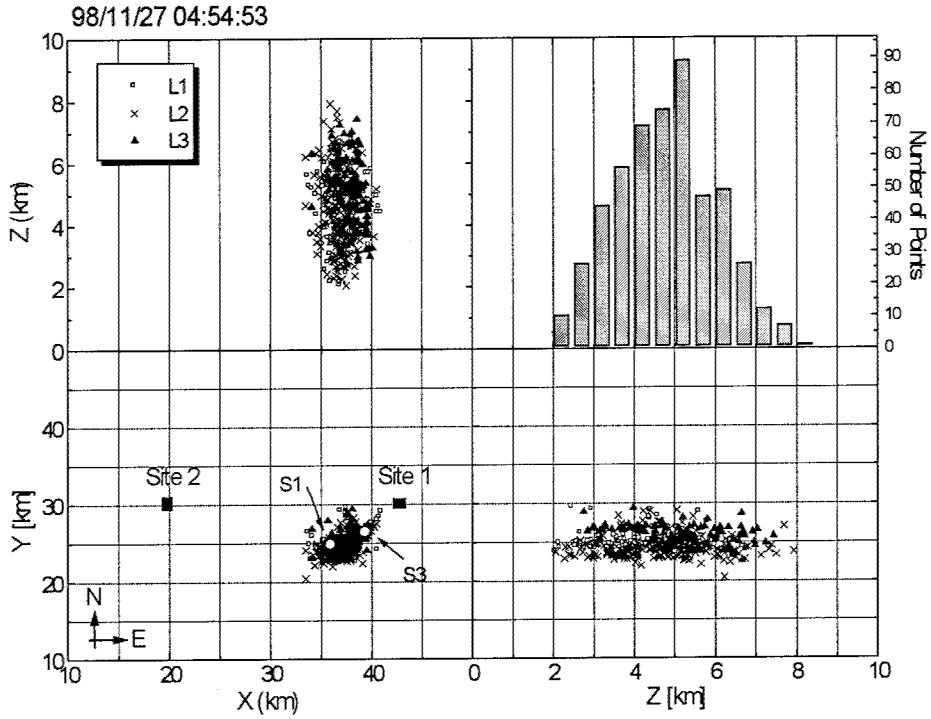


**Figure 4. Three-dimensionally plan view for the discussed L1, L2 and L3. Circles on x-y plot represent the position of the striking point on ground of the first stroke S1 and the third stroke S3. We chose x-y position for site 1 at (43.1, 30) km and site 2 at (20, 30) km. Histogram shows the number of events or points for every 0.5 km of altitude.**

## CONCLUSIONS

Observing lightning in 3D and its progression using two sets of broadband systems has been demonstrated. A negative cloud to ground flash, as an example, has been detected with this system and it were mapped in either azimuth-elevation or three-dimensionally format. This four-stroke flash was unusual in that subsequent return strokes were initiated by stepped leaders (L2 and L3) and the occurrence of multipoint strokes on ground. The first stroke is approximated to have a same position with the second, but the third has a different position. The system has enough temporal resolution, but spatial resolution should be compared with other lightning position systems.

## REFERENCES


Proctor, D.E., R. Uytenbogaardt, M. Meredith, VHF Radio Pictures of Lightning Flashes to Ground, *J. Geophys. Res.*, 93, 12, 683-12,727-2783, 1988.

Laroche, P., A. Bondiou, P. Blanchet, M. Weber, B. Boldi, 3D Structure of Lightning Discharge Within Storms, *10th ICAE*, Osaka, Japan, 330-332, 1996.

Maier, L., C. Lennon, P. Krehbiel, M. Maier, Lightning as Observed by a Four-Dimensional Lightning Location System at Kennedy space center, *10th ICAE*, Osaka, Japan, 280-283, 1996.

Onuki, J., Z-I. Kawasaki, M. Wada, K. Matsuura, Imaging of Lightning in Three Dimensions using Interferometer, *10th ICAE*, Osaka, Japan, 325-328, 1996.

Shao, X.M., P.R. Krehbiel, R.J. Thomas and W. Rison, Radio interferometric observations of cloud-to-ground lightning phenomena in Florida, *J. Geophys. Res.*, 100, 2749-2783, 1995.

Stanley, M., P. Krehbiel, L. Maier, C. Lennon, Comparison of Lightning Observations from the KSC LDAR System with NEXTRAD Radar Observations, *10th ICAE*, Osaka, Japan, 224-225, 1996.

Ushio, T., Z. Kawasaki, Y. Ohta and K. Matsuura, Broadband interferometric measurement of rocket triggered lightning in Japan, *Geo. Res. Lett*, 24, 2769-2772, 1997.

Mardiana, R., Y. Ota, M. Murakami, T. Ushio, Z. Kawasaki, K. Matsuura, A Broadband Radio Interferometer for Observing Lightning Discharge Processes, *J. Atmph. Elect.*, 18, 2, 111-117, 1998.

# OBSERVATIONS AND INFERRED PHYSICAL CHARACTERISTICS OF COMPACT INTRACLOUD DISCHARGES

D. A. Smith[1], R. S. Massey[1], K. C. Wiens[2], K. B. Eack[1], X. M. Shao[1], D. N. Holden[1], P. E. Argo[1]

[1]Space and Atmospheric Sciences, Los Alamos National Laboratory
Los Alamos, New Mexico, U.S.A.
[2]Department of Physics, New Mexico Institute of Mining and Technology
Socorro, New Mexico, U.S.A.

ABSTRACT: Compact intracloud discharges (CIDs) represent a distinct class of electrical discharges that occur within intense regions of thunderstorms. They are singular discharges that produce brief (typically 3 μs in duration) broadband RF emissions that are 20 to 30 dB more powerful than radiation from all other recorded lightning processes in the HF and VHF radio spectrum. Far field electric field change recordings of CIDs consist of a single, large-amplitude, narrow bipolar pulse (NBP) that begins to rise during the RF-producing phase of the CID and typically lasts for 20 μs. During the summer of 1998 we operated a 4-station array of electric field change meters in New Mexico to support FORTÉ satellite observations of transient RF and optical sources and to learn more about the phenomenology and physical characteristics of CIDs. Over 800 CIDs were detected and located during the campaign. The events were identified on the basis of their unique field change waveforms. CID source heights determined using the relative delays of ionospherically reflected source emissions were typically between 4 and 11 km above ground level. Events of both positive and negative polarity were observed with events of initially-negative polarity (indicative of discharges occurring between underlying positive and overlying negative charge) occurring at slightly higher altitudes. Within CID field change waveforms the CID pulse was often followed within a few ms by one or more smaller-amplitude pulses. We associate these subsequent pulses with the initial activity of a "normal" intracloud flash, the inference being that some fraction of the time, a CID initiates an intracloud lightning flash.

## INTRODUCTION

During the summer of 1996, two ground-based receiver arrays in NM were used to record the electric field change signals and broadband HF emissions from lightning discharges. The arrays were fielded in support of the satellite-borne Blackbeard broadband radio receiver to try to identify the sources of powerful VHF pulse pairs called TIPP (transionospheric pulse pair) events [*Holden et al.*, 1995; *Massey and Holden*, 1995]. A distinct class of thunderstorm events was identified as the most likely source of the powerful TIPP emissions; these events were dubbed compact intracloud discharges (CIDs) [*Smith*, 1998; *Smith et al.*, 1999]. CIDs produced broadband HF radiation bursts that lasted a few microseconds and were at least 20 dB more powerful than the radiation from other recorded lightning processes. The electric field change emissions from CIDs were distinct, large-amplitude bipolar pulses that closely resembled waveforms previously identified by *LeVine* [1980] and *Willett et al.* [1989]. *Willett et al.* dubbed the field change waveforms narrow bipolar pulses (NBPs).

During the 1996 campaign, differential time of arrival techniques were used to determine the 3-D locations of CIDs, with accurate altitude determinations made possible by considering the relative delays of ionospheric reflections from the source. Twenty-four CIDs, which were recorded from three thunderstorms in New Mexico and West Texas, were studied in detail. The events occurred at altitudes between 8 and 11 km above mean sea level. Event altitudes, in conjunction with the initially-positive polarities of their field change waveforms, suggested that the events occurred between the main negative and upper positive charge regions in their parent thunderstorms. Radar reflectivity data from two of the storms showed that CIDs occurred in close spatial proximity to thunderstorm cores with peak radar reflectivities of 47 to 58 dBZ.

Among the conclusions reached by *Smith* [1998] and *Smith et al.* [1999] were that the discharges were vertically oriented, had spatial extents of several hundred meters, and consisted of average currents

on the order of 100 kA that lasted for approximately 15 μs. Based on the results of a charge distribution model, it was concluded that the events occurred in thunderstorm regions with charge densities as high as several tens of $nC/m^3$ and peak electric fields strengths on the order of 1 MV/m. Both of these values are an order of magnitude greater than values previously measured or inferred from *in situ* thunderstorm measurements. The unique radio emissions from CIDs, in combination with their unprecedented physical characteristics, were concluded to clearly distinguish the events from other types of previously observed thunderstorm electrical processes.

1998 OBSERVATIONS

In May of 1998 the Space and Atmospheric Sciences Group at Los Alamos National Laboratory began continuous operation of a four-station array of electric field change meters in New Mexico to provide ground-based measurements in support of RF and optical observations by the FORTÉ satellite. The array and FORTÉ observations are discussed in other papers in these Proceedings (see *Massey et al.*, *Jacobson et al.*, *Suszcynsky et al.*, and *Argo et al.*). During 1998, nearly 128,000 events were detected, recorded, and located by the array. Of these events, over 800 (0.7%) were classified as narrow bipolar pulses (NBPs), the distinct field change waveforms associated with compact intracloud discharges. Two representative NPB waveforms are shown in Figure 1.

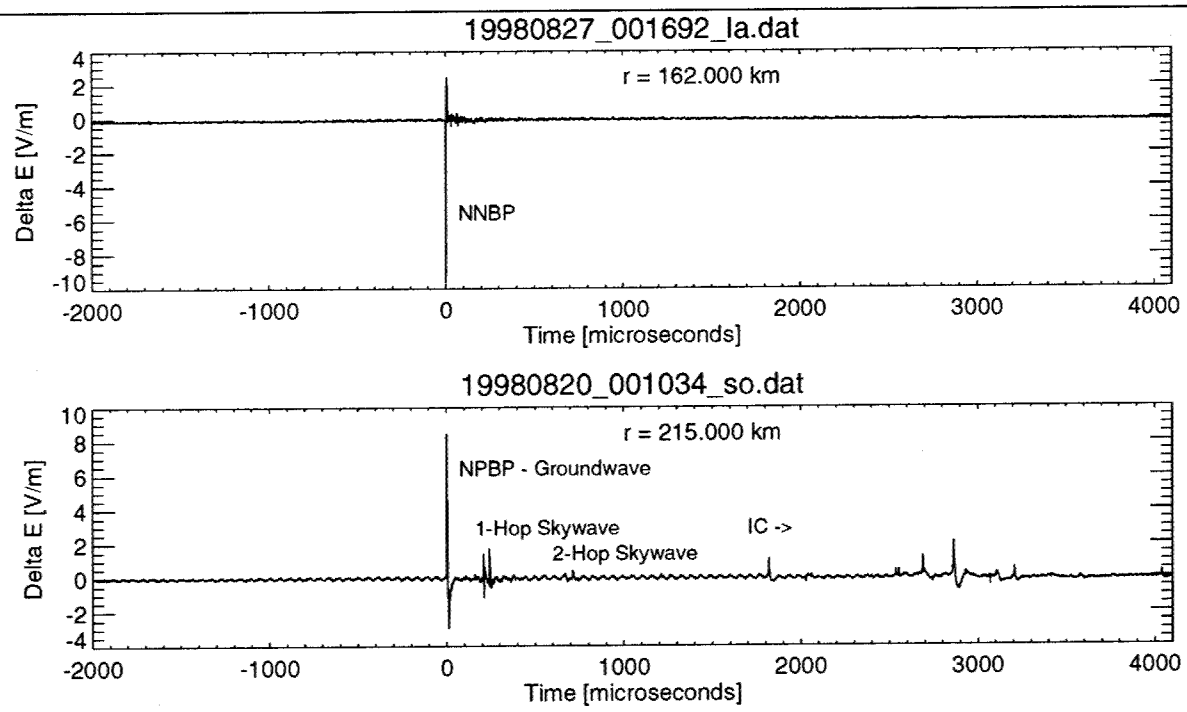


Figure 1. Electric field change recordings of narrow bipolar pulses. The upper waveform features an isolated narrow negative bipolar pulse. The lower waveform features a narrow positive bipolar pulse followed by two sets of ionospherically reflected pulse pairs and pulses corresponding to the initial activity of an intracloud stroke.

NPBs were identified on the basis of their fast rise and fall times and their isolation in contrast to other classes of events. We have shown that, in combination, these two traits serve as a good discriminant for NBPs. Rise plus fall times of NBPs were typically less than 10 μs. Isolation was parameterized by computing the ratio of the average power within a 10 μs window centered on the peak absolute amplitude in field change records to the average power occurring after the window in the record. The value of this isolation parameter (or SNR) was typically greater than 500 for CIDs and less for other types of events.

During the 1998 campaign, NPBs of both initially-positive and initially-negative polarities were observed: we refer to these events as narrow positive and narrow negative bipolar pulses respectively (NPBPs and NNBPs). Under our polarity convention, NPBPs occur between regions of underlying negative and overlying positive charge. The reverse is true for NNBPs. NPBPs were recorded three times as often as NNBPs. The upper waveform of Figure 1 features a NNBP and illustrates the fast rise and fall times characteristic of the events, in addition to their isolation. The lower waveform of the figure features a NPBP followed by a coda of additional waveform features, described below.

Although quantitatively more isolated than other classes of recorded waveforms (e.g. waveforms from positive and negative cloud-to-ground return strokes), two notable classes of post-trigger features were often discernable in NBP waveforms (post-trigger times were 4 or 12 ms). The lower waveform of Figure 1 illustrates both of these classes. The first features to note are the two pulse pairs (the second is quite weak) that occur at delays of 210 and 660 μs from the groundwave signal. These pairs are 1-hop and 2-hop reflections of the CID emissions from the ionosphere and ground. Within each pair, the first pulse is the direct ionospheric reflection, and the second is the ionospheric reflection of a ground reflection. The second feature to note in the lower waveform are the weak, initially-positive pulses that begin after 1800 μs. These pulses resemble normal intracloud (IC) pulses and suggest that some fraction of the time NBPs initiate, or at least serve as a precursor to, an IC flash. Our attention was drawn to the subsequent, smaller amplitude pulses as a result of collaboration with the New Mexico Tech (NMT) research group. Their Lightning Mapping System imaged IC strokes that occurred immediately following NBPs identified by the array and made clear an association between NBPs and "normal" intracloud lightning strokes [*Rison et al.*, these Proceedings]. The data indicate that not all IC flashes begin with a NBP. It has yet to be determined whether all, or even most, NBPs are followed by an IC flash.

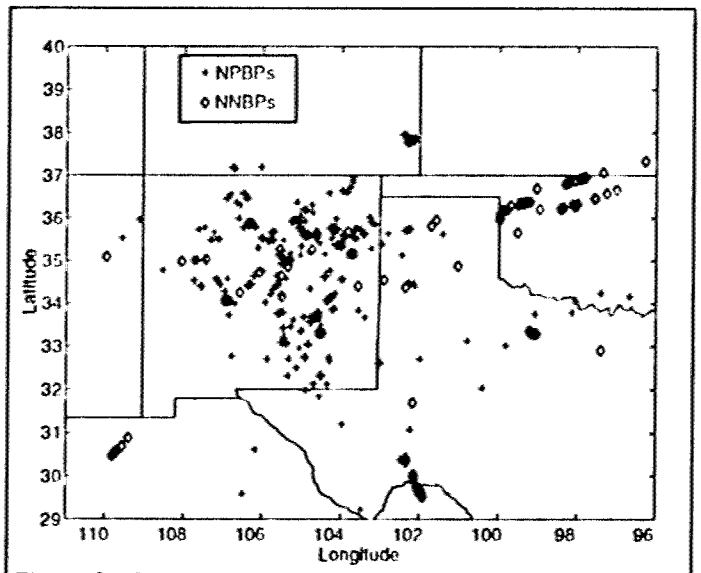

Figure 2. Locations of positive and negative narrow bipolar pulses recorded during 1998.

## CID LOCATIONS

The locations of CIDs recorded during 1998 are shown in Figure 2. *Massey et al.* [these Proceedings] describe the method used to determine 2-D source locations. In the figure, NPBPs and NNBPs are represented by plus symbols and diamonds respectively (the four array stations are shown as shaded circles). It is interesting to note that the negative events exhibited clustering to a larger degree than the positive events. That is, the negative events were produced during a relatively small number of storms, most of which produced many negative events.

Over half of the NBPs recorded featured ionospheric reflections that we were able to identify and time tag. Source heights and ionosphere virtual heights were computed for these events using the differential times of arrival between the groundwave signal and the reflected skwave signals. Histograms of source heights above ground level for both NPBPs and NNBPs are shown in Figure 3. As of this writing, we have not yet converted the heights to altitudes above mean sea level. Note that in general, the negative-polarity events occurred at higher altitudes. This observation was also true for individual storms that produced NBPs of both polarities. Because events of opposite polarity indicate a reversed charge structure, it is thought that that NNBEs occur between the upper positive thunderstorm charge region and an overlying region of negative charge, or that the events occur in thunderstorms with inverted charge

structures. The fact that negative events occur higher than positive events provides some support for the former hypothesis, as does the fact that events of both polarities were observed in some storms.

## SUMMARY AND DISCUSSION

During 1998, we recorded and located over 800 narrow bipolar pulses associated with CIDs. Most of the events occurred at altitudes between 4 and 12 km above ground level. Events of both positive and negative polarities were observed with the negatives occurring less often and in temporal clusters. Negatives also occurred at higher altitudes than positives, both in general and within individual storms. We also found that NBPs often initiate or serve as a precursor to regular intracloud discharges. It is not yet known whether this is always the case.

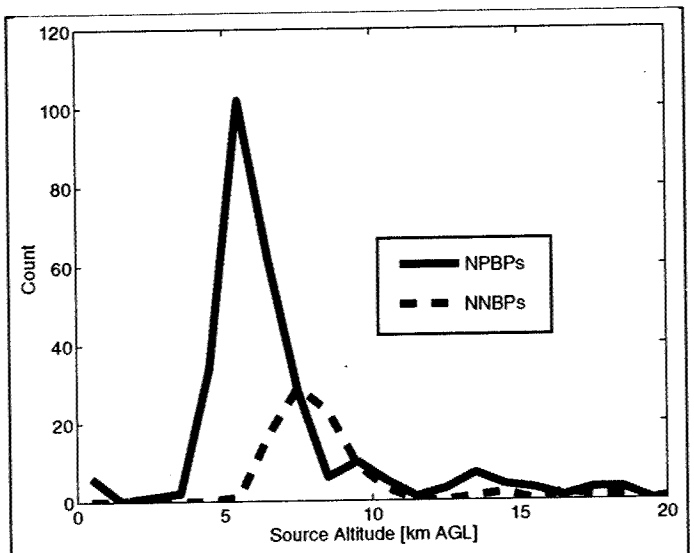


Figure 3. Altitudes (above ground level) of positive and negative bipolar pulses recorded during 1998.

The remarkable physical characteristics of NBPs continue stand out from those of other lightning processes. Their breakdown RF radiation is over 20 dB more powerful than that from other lightning. Their inferred discharge current moments are an order of magnitude greater . Among our planned activities for 1999 are the implementation of a second array in Florida to increase the likelihood of coincident detections with FORTÉ and utilize lightning research assets located there; the addition of at least one broadband RF channel (50 MHz to 1 GHz bandwidth) at a station in New Mexico to attempt to discern intra-CID temporal structure; and further collaboration with NMT and their Lightning Mapping System to study CIDs and their relationship to intracloud strokes.

ACKNOWLEDGEMENTS: The authors thank the other members of the FORTÉ Science Team and our colleagues at the New Mexico Tech for their support and helpful discussions. We also express our gratitude to NMT, Eastern New Mexico University, and Mesa Technical College for hosting remote field change stations and thus, contributing to the success of the array. This work was supported by the U.S. Department of Energy.

## REFERENCES

Holden, D. N., C. P. Munson, and J. C. Devenport, Satellite observations of transionospheric pulse pairs, *Geophys. Res. Lett., 22*, 889-892, 1995.

Le Vine, D. M., Sources of the strongest RF radiation from lightning, *J. Geophys. Res., 85*, 4091-4095, 1980.

Massey, R. S., and D. N. Holden, Phenomenology of transionospheric pulse pairs, *Radio Sci., 30*, 1645-1659, 1995.

Smith, D. A., Compact intracloud discharges, Ph.D. Dissertation, Dept. of Electrical Engineering, University of Colorado, Boulder, 1998 (.pdf avail. from http://edot.lanl.gov/).

Smith, D. A., X. M. Shao, D. N. Holden, C. T. Rhodes, P. R. Krehbiel, M. Stanley, M. Brook, R. Thomas, Observations and analysis of distinct thunderstorm radio emissions, *J. Geophys. Res., 104*, 4189-4212, 1999.

Willett, J. C., J. C. Bailey, and E. P. Krider, A class of unusual lightning electric field waveforms with very strong high-frequency radiation, *J. Geophys. Res., 94*, 16,255-16,267, 1989.

# HEIGHT OF RADIATION SOURCES ASSOCIATED WITH LIGHTNING DISCHARGES

M. Ishii[1], J. Hojo[1], K. Shimizu[1], K. Sato[1], and K. Shinjo[2]

[1]The University of Tokyo, Tokyo, Japan
[2]Hokuriku Electric Power Co., Toyama, Japan

ABSTRACT: Radiation sources of in-cloud discharges are located three-dimensionally by the TOA technique using data from a network of fast antennas and VHF receivers. The location accuracy of most of the analyzed radiation sources was within 0.5 km in the z-direction. The sources of VHF pulses, radiated within 50 microseconds of a bipolar pulse observed by a fast antenna, were located mostly within 0.5 km from the source of the bipolar pulse. The distributions of the height of the origins of bipolar pulses are clearly separated depending on the initial polarity of a bipolar pulse, regardless of the seasons or the kinds of flashes. The polarity of the bipolar pulses is consistent with the hypothesis that there is a negative charge center at the temperature height of about −5 to −10°C. The peaks of the two distributions correspond to the peaks of the reported bimodal distribution of VHF sources in the beginning of flashes.

## INTRODUCTION

Location of in-cloud discharges of lightning flashes has been observed by VHF radiation, and the results were discussed in conjunction with the electric field changes observed by fast and slow antennas [Proctor, 1981; Shao and Krehbiel, 1994]. Electric field observed by a fast antenna contain narrow pulses, which also can be located by the time-of-arrival (TOA) technique with reasonable accuracy. In addition, a bipolar pulse has information on its polarity, which may be related to the direction of the pulse current as the source of radiation observed by a fast antenna. Thus, the distributions of the heights of the radiation sources of bipolar pulses are examined for lightning flashes in summer and winter. The relationship between the positions of a bipolar pulse and VHF pulses occurred within a short period is also examined.

## INSTRUMENTATION

An eight-station network of fast antennas and VHF receivers was constructed on the coast of the Sea of Japan at about 36°E and 136°N for three-dimensional location of electromagnetic radiation sources associated with lightning discharges. The spacings between the stations are between 5 to 10 km. Electric field observed by five fast antennas in the frequency range of 0.32 kHz to 1.2 MHz is digitized every 0.18 microseconds with 12 bit resolution and is recorded for 3.9 ms. The envelope of VHF radiation amplitude at 250MHz observed at eight stations is similarly recorded. These records are time-stamped with 0.2 microsecond accuracy and processed later.

Isolated VHF pulses and narrow pulses observed by fast antennas embedded in bipolar pulses are located. The location accuracy depends on the position relative to the network. Error is within 0.5 km in the horizontal direction and mostly within 0.5 km in the vertical direction, for the data in this report. Figure 1 shows an example of a bipolar pulse with narrow pulses in the beginning of a cloud flash. The polarity of the vertical electric field follows the atmospheric convention, that is, downward electric field is positive. In this report, that of the initial half cycle defines the polarity of a bipolar pulse. The bipolar pulse in Fig. 1 is an example of a negative bipolar pulse.

## POSITION OF RADIATION SOURCES OF VHF AND BIPOLAR PULSES

Bipolar pulses are frequently seen in the beginning of either cloud-to-ground (C-G) flashes or cloud flashes, and were attributed to developing lightning channels in the cloud [Villanueva et al., 1994]. VHF pulses are usually observed at about the same time. These pulses are located three-dimensionally and the relative position of these pulses is examined. The position of these VHF and bipolar pulses turned out to be close each other. Figure 2 shows the distribution of the distance between a VHF pulse and a bipolar pulse occurred within 50 microseconds. These data are from 9 lightning flashes including +CG, −CG and cloud flashes through the year, and about 70% of the distances of the two kinds of pulses were within 1 km. Thus, in the beginning of a flash, the area in the cloud where discharges take place can be located either by using VHF pulses or bipolar pulses observed by fast antennas.

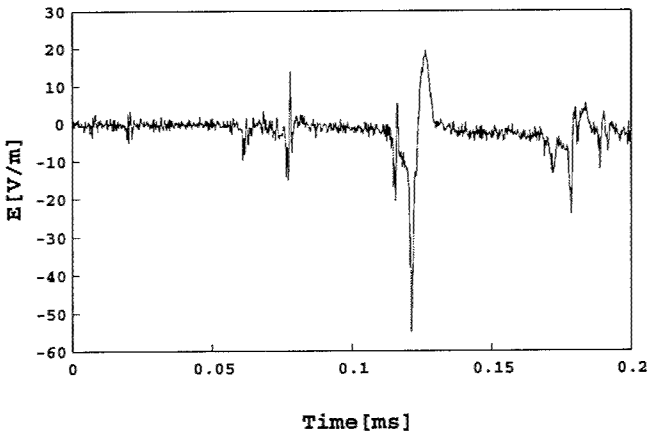


Fig. 1. Example of Negative Bipolar Pulse.

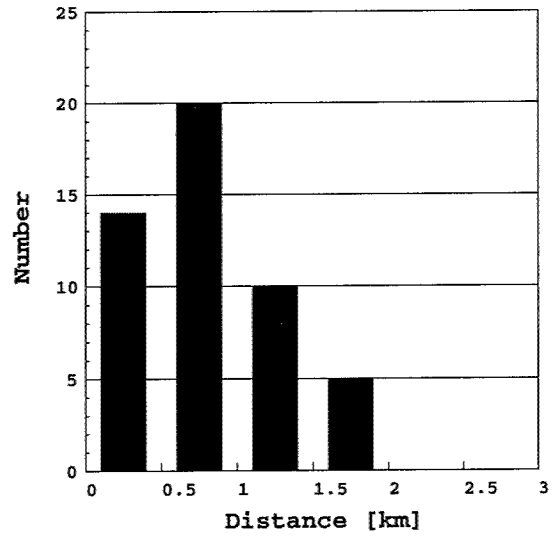


Fig. 2. Total Distance between Sources of Bipolar Pulse and of VHF Radiation.

HEIGHT OF BIPOLAR PULSES

Bipolar pulses in the beginning of about70 lightning flashes in summer (July – August) and winter (December – February) are located three-dimensionally. Figure 3 shows distribution of the temperature heights of the sources of bipolar pulses preceding 23 negative first C-G strokes in summer. Because they are mostly positive as was reported by Weidman and Krider [1979], there are not many data of negative bipolar pulses (NBP) (three flashes out of 23). But it is recognized that the distributions of the heights of positive bipolar pulses (PBP) and NBP are clearly separated. The median height of the distribution of PBP is –1.3°C, and that for NBP is –24°C, which correspond to the peaks of the bimodal distribution of the heights of initial VHF pulses, –3.3°C and –27.7°C, in the beginning of CG and cloud flashes in summer observed in South Africa [Proctor, 1991]. If the number of the bipolar pulses only is concerned, the distribution of Fig. 3 resembles that of the initial VHF pulses for negative ground flashes of South Africa.

In Fig. 4, the distribution of the height of the sources of negative bipolar pulses in the beginning of cloud flashes in summer is shown. No PBP was found out of the analyzed 6 cloud flashes, and this tendency is consistent with our previous observation that cloud flashes began with PBP were rare in summer [Ishii et al., 1994]. The analyzed distribution of NBP resembles that of NBP preceding –CG strokes in summer.

The height of the earliest bipolar pulse located in each flash distributes similarly to the distributions in Figs. 3 and 4. But the distributions for the earliest bipolar pulses are not shown here due to the small sample size. The initial VHF pulses in the beginning of flashes distributed in a similar manner [Proctor, 1991]. From these results, it is inferred that the heights of the bipolar pulses in the beginning of a flash distribute around the height of the initial breakdown. If the polarity of the bipolar pulse is related to the vertical direction of the pulse current of the source, a PBP corresponds to upward current. Existence of a negative charge center at a height around the temperature of –5°C to –10°C accords with this observation.

Regarding lightning flashes in winter, bipolar pulses associated with +CG flashes and NBP associated with cloud flashes have been analyzed. Few other types of flashes have been analyzed so far. Figure 5 shows distributions of the temperature heights of bipolar pulses in the beginning of +CG flashes in winter. Positive CG strokes preceded by PBP are more frequent in winter than in summer [Ishii et al., 1994]. Here also are found two distributions having their peaks at different heights depending on the pulse polarity. The temperature heights of the peaks lie at slightly higher altitudes than, but do not much differ from, those of –CG flashes in summer seen in Fig. 3. The lower end of the distribution of PBP may be cut off due to the low temperature on the surface, usually around 0°C in winter.

Figure 6 shows the distribution of the temperature heights for the bipolar pulses in the beginning of cloud flashes in winter. Though, different from summer, cloud flashes contain PBP should frequently be observed in winter [Ishii et al., 1994], only one cloud flash of this kind has been analyzed so far. The distribution of NBP in Fig. 6 is quite similar to that of NBP in Fig. 5 preceding –CG strokes.

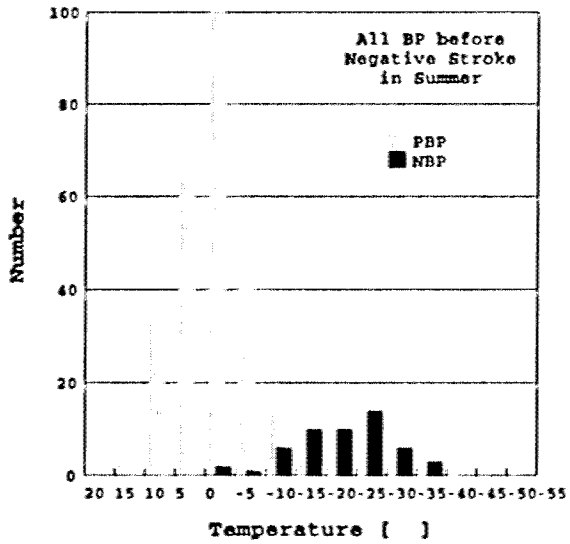


Fig. 3. Distribution of Temperature Height of Bipolar Pulses Preceding Negative C-G Strokes in Summer.

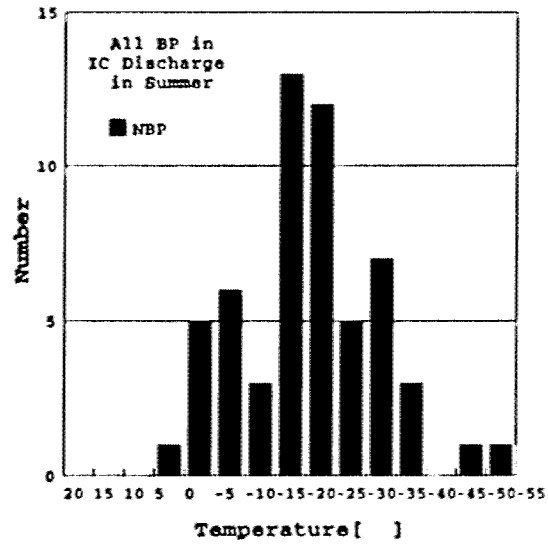


Fig. 4. Distribution of Temperature Height of Bipolar Pulses in the Beginning of Cloud Flashes in Summer.

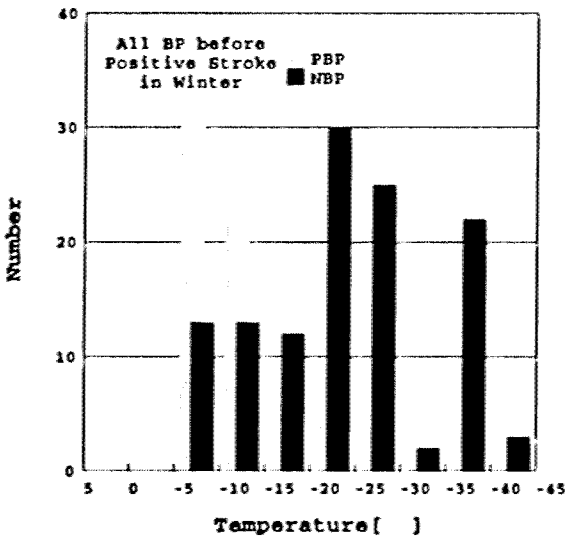


Fig. 5. Distribution of Temperature Height of Bipolar Pulses Preceding Positive C-G Strokes in Winter.

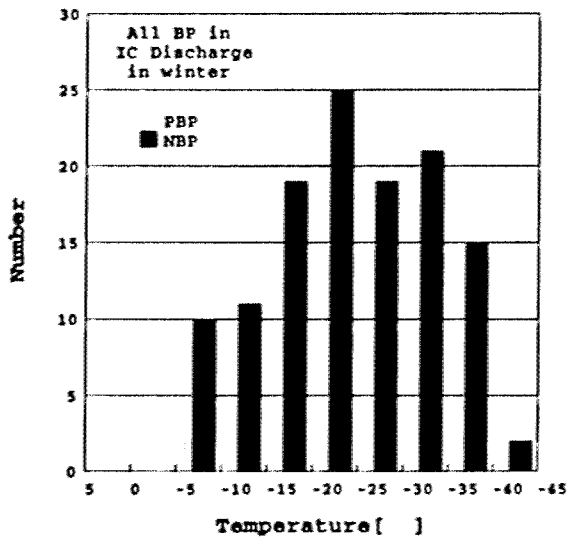


Fig. 6. Distribution of Temperature Height of Bipolar Pulses in the Beginning of Cloud Flashes in Winter.

## CONCLUSION

The spatial positions of initial VHF pulses and bipolar pulses observed by a fast antenna in the beginning of a lightning flash are not much apart. The region of the initial breakdown in the cloud can be studied either by using the VHF pulses or the bipolar pulses.

The temperature heights of the initial breakdown pulses of lightning flashes are not much affected by the seasons, except that the high-temperature end of the distribution may be cut off due to the low surface temperature in winter. Bipolar pulses distribute depending on the polarity of the initial half cycle. Positive bipolar pulses are most frequent at around the temperature height of –5°C, and negative ones distribute around the height of about –25°C. These distributions are almost independent of the seasons or of the kinds of lightning flashes, and the peaks correspond to those of the bimodal distribution of the height of initial VHF pulses observed in summer in South Africa by Proctor [1991]. If the initial polarity of the bipolar pulses corresponds to the direction of the source pulse current in the discharge channel in the cloud, the distributions of the initial bipolar pulses accord with the existence of a negative charge center at the temperature height of about –5 to –10°C.

## REFERENCES


Ishii, M., Hojo, J. and Sato, S., Electromagnetic pulses radiated from in-cloud discharges preceding first return strokes, 22nd Int. Conf. on Lightning Protection, Budapest, R1a-02, 1994.

Proctor, D. E., VHF radio pictures of cloud flashes, J. Geophys. Res., **86**, 4041-4071, 1981.

Proctor, D. E., Regions where lightning flashes began, J. Geophys. Res., **96**, 5099-5112, 1991.

Shao, X. M. and Krehbiel, P. R., The spatial and temporal development of intracloud lightning, J. Geophys. Res., **101**, 26641-26668, 1996.

Villanueva, Y., Rakov., V. A. and Uman, M. A., Microsecond-scale electric field pulses in cloud lightning discharges, J. Geophys. Res., **99**, 14353-14360, 1994.

Weidman, C. D. and Krider, E. P., The radiation field wave forms produced by intracloud lightning discharge processes, J. Geophys. Res., **84**, 3159-3164, 1979.

# VHF OBSERVATIONS DURING A SPIDER LIGHTNING FLASH

E. Defer, C. Thery, P. Blanchet and P. Laroche

ONERA, Chatillon, France.

ABSTRACT : We have analyzed VHF radiations detected during a spider lightning flash with the ONERA three-dimensional interferometric mapper. Two states have been identified during this horizontal extended flash. First, a 40 km long horizontally extended event that lasted 130 ms was recorded. Then, few tens of milliseconds later, some short duration events were recorded. The first event exhibited the same characteristics as observed during a negative downward stepped leader occurring during a negative cloud-to-ground lightning flash, i.e. a 4 $10^5$ $m.s^{-1}$ global velocity and a continuous radiation recorded on our narrow band interferometer.

## INTRODUCTION

Spider lightning flashes occur generally during decaying stage of storm, propagate roughly just above the cloud base and can be observed from ground (Mazur *et al.*, 1998). Spider events had been already observed with interferometric instruments (Mazur *et al.*, 1998). They consist in a extended event with a high continuous VHF radiation. We present observations recorded by the ONERA interferometric mapper during a spider lightning flash which occurred during the final stage of a Florida storm.

## INSTRUMENT

The ONERA lightning mapper uses the interferometric technique to retrieve in three-dimensional locations of VHF radiating sources (Laroche *et al.*, 1994). This technique provides the directions of VHF radiations by analyzing the phase difference of an incident wave on an array of antennas (Richard *et al.*, 1986; Rhodes *et al.*, 1994). The ONERA lightning mapper consists in two independent stations, 40 km distant. Each station retrieves azimuth of VHF sources. One station, labeled ST1, is equipped with a second sensor which provides elevation of VHF sources. These sets of angles are combined to obtain three-dimensional VHF locations. Each station detected VHF emission at 114 MHz, with 1 MHz bandwidth and 23 µs time resolution. VHF records were stored when VHF magnitude, measured at the receiver inputs, exceeded an adjustable threshold. Figure 1 shows the locations of the VHF sensors in Florida in 1992 and 1993.

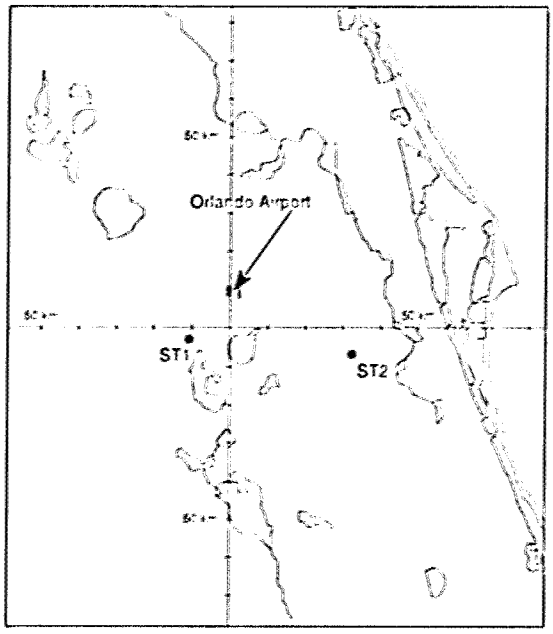


*figure 1 : locations of different sensors. Filled circles locate ST1 and ST2 stations. VHF sources are reconstructed in the gray area. Orlando, Central Florida.*

## OBSERVATION OF THE LIGHTNING FLASH

This flash occurred the 14th August 1992 in Florida, at 21:41:29 UT with a 1.2 s duration (deduced from VHF measurements). Figures 2*a* and 2*b* show temporal evolution of VHF magnitude recorded respectively by the ST1 and ST2 stations. These figures show a continuous VHF emission during a 130 ms period, followed by short duration emissions. Figures 2*c* and 2*d* show measured azimuth of VHF sources (clockwise direction with respect to the North). The continuous emission was associated with a well defined progressing event. Figure 2*e* shows the temporal evolution of elevation angle, measured by the ST1 elevation sensor. During the continuous emission, elevation increased and then decreased. It is explained by a progression toward then forward the ST1 station. Figure 2*f* shows location of all VHF sources in the azimuth-elevation ST1 axis. This figure shows that the event propagated from the South to the North with a long part at a roughly constant elevation. Figures 2*c*, 2*d* and 2*e* show that short duration emission occurred either at the ending

extremity of first event or around parts of channel created during the continuous emission. Some sources were located at low elevation (figure 2*f*). A low signal to noise ratio and the poor sensitivity of the elevation sensor for low elevation explain these mislocated sources. We removed all VHF sources with a retrieved elevation lower than 5 degrees during the process of three-dimensional location.

Figures 3*a*, 3*b* and 3*c* show the three-dimensional locations of the entire flash deduced from angular measurements. A 50 km long horizontal extension characterizes this flash. Z1, Z2 and Z3 zones correspond to the continuous emission. No locations were reconstructed between Z1 and Z2 zones. It is explained by a non-storage of the VHF signal (received at ST2 station) probably due to its magnitude lower than the threshold (see figures 2*b* and 2*d*, blanking period at the beginning of the long VHF emission). This flash progressed to the North. It traversed the baseline and the internal lobe. This explains why no VHF sources have been reconstructed between Z2 and Z3 zones. Note that when the flash crossed the baseline, VHF sources were located at 20° elevation (figure 2*f*). Figures 3*b* and 3*c* show an artificial spreading (R1) due to a less accurate location from ST1 station (low signal received at ST1 station). Ground projection of VHF sources is deduced from azimuth measurements. Altitude is computed by using elevation measurements and the distance between ground projection and the ST1 station. If the ground projection is slightly shifted from its real location, the retrieved altitude of VHF source is slightly erroneous. In our case, the sources are shifted to the West and their altitudes are retrieved with low values. Note that the measured elevation is constant during R1 period (figure 2*f*, ST1 azimuth at 80°). However, figure 3*c* shows that the flash propagated at roughly 5 km AMSL high between 0°C and -10°C levels. Z4 group shows a more extended lightning activity associated to VHF angular measurements recorded at the ending extremity of the continuous emission (ST1 azimuth between 0° and 50°).

XY locations of the long VHF emission are plotted in figure 4*a*. At t=556 ms, VHF sources are located in the southern part of the flash (figure 4*a*). The discharge progressed to the North with a 3.5 $10^5$ m.s$^{-1}$ speed. Between t=596 and 606 ms, the discharge seems to propagate more rapidly (7.5 $10^5$ m.s$^{-1}$ speed) while the propagation is slower between 636 and 656 ms (3.8 $10^5$ m.s$^{-1}$ speed). The speed of the discharge increased one more time between 656 and 666 ms (5.4 $10^5$ m.s$^{-1}$ speed). During the last ten milliseconds of the long discharge, between 666 and 676 ms, the discharge moved to the East with 3 $10^5$ m.s$^{-1}$ speed.

Short duration events radiated from two distant zones. Part of them developed near the final location of the long discharge 350 ms after it stopped. Other bursts were located in the vicinity of the starting zone of Z2. Analyzes of ST1 station data had shown that burst duration evolved between 23 µs (time resolution of each interferometric station) and 1.7 ms while inter-burst duration evolved between 1.3 ms and 160 ms. Analyzes of ST2 station data are more difficult but inter-burst duration is lower than 148 ms.

## DISCUSSION

The panels in figure 2 show that ST2 station recorded more samples than ST1 during the second part of the flash. As angular measurements are combined to retrieve the three-dimensional locations of VHF sources, it is obvious that the under-sampling of the flash by one station limits the three-dimensional description of this flash.

The first event exhibited the same impulsive process as recorded during a negative downward stepped leader and propagated at about 4 $10^5$ m.s$^{-1}$ velocity. These characteristics suggest also that the first event is a negative intra-cloud stepped leader. Laroche *et al.* (1994) and Mazur *et al.* (1998) have already noted that spider discharge exhibits characteristics similar to the downward negative stepped leader occurring during a negative cloud-to-ground flash. Massachusetts Institute of Technology (MIT) corona point ground based sensors, located at the Orlando Airport and close to the final location of the long discharge, exhibited a positive response indicating the motion of negative charges above the MIT network (measurements not shown). It is also consistent with a negative intra-cloud stepped leader process. Mazur (1989) suggests that lightning flash channel is created by a bi-leader discharge. In the case described here, the positive leader may have propagated in the cloud or connected to the ground. Unfortunately we have no means to identify any connection to the ground.

The interferometric system did not record any long recoil streamers propagating in the leader channel, but short duration events were located at two distant zones. Negative charge transfer due to the progression of the intra-cloud leader has modified the charge structure of the cloud. Negative charge brought by the long negative leader may have increased the ambient electric field in Z4 area and trigger new lightning discharges.

The origin of the southern short duration events is not clear. These short duration events occurred in the vicinity of the start of Z2 group. Z2 occurred after a period of low level VHF emission of the propagating leader. The first recorded event of these short duration discharges occurred about 130 ms after the beginning of the intra-cloud negative leader, when the leader stopped its progression. May be other events occurred during the leader

development, but these events may have emitted VHF radiation which was masked by the VHF emission of the negative leader.

Mazur *et al.* (1998) have detailed VHF radiation of spider discharges recorded during lightning flashes. In the present case, the spider event seems to be the first component of the flash. Further investigations with concurrent measurements like other interferometric data, ground based E field records, NLDN reports and radar observations should complete this study by identifying the type of flash (positive cloud-to-ground or intra-cloud flash) and its successive components, by analyzing cloud characteristics around the path of this lightning flash and by relating lightning activity to the storm history.

ACKNOWLEGDEMENTS : We thank Earle Williams and Dennis Boccippio for providing MIT corona point data.

REFERENCES

Laroche P., A. Bondiou, P. Blanchet and, J. Pigère, 3D VHF mapping of lightning discharge within a storm, *Proceedings SEE "lightning and mountains", Chamonix, France*, 1994.

Mazur V., 1989, Triggered lightning strikes to aircraft and natural intracloud discharges, *J. Geophys. Res.*, **94**, 3311-3325.

Mazur V., X.-M. Shao, and P. Krehbiel, 1998, « Spider » lightning in intracloud and positive cloud-to-ground flashes, *J. Geophys. Res.*, **103**, 19811-19822.

Richard P., A. Delannoy, G. Labaune and, P. Laroche, 1986, Results of spatial and temporal characterization of the VHF-UHF radiation of lightning, *J. Geophys. Res.*, **91**, 1248-1260.

Rhodes C. T., X. M. Shao, P. R. Krehbiel, R. J. Thomas and, C. O. Hayenga, 1994, Observation of lightning phenomena using radio interferometry, *J. Geophys. Res.*, *99*, 13,059-13,082.

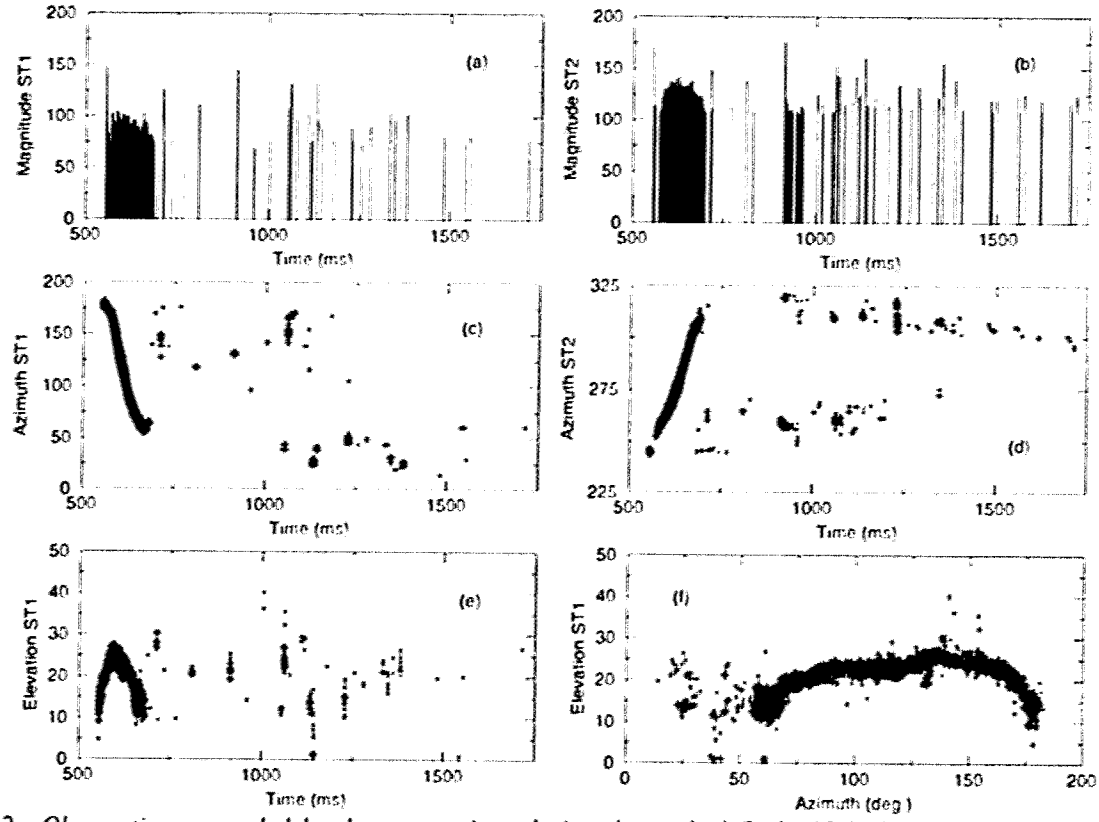


*figure 2 : Observations recorded by the two stations during the studied flash (08/14/92 21:41:29 UT, Florida). Temporal evolution in ST1 of magnitude (in an arbitrary unit, (a)), azimuth (c) and elevation (e); temporal evolution in ST2 of magnitude (in an arbitrary unit, (b)) and azimuth (d) and elevation (e); (f) VHF source locations in the azimuth-elevation axis (ST1).*

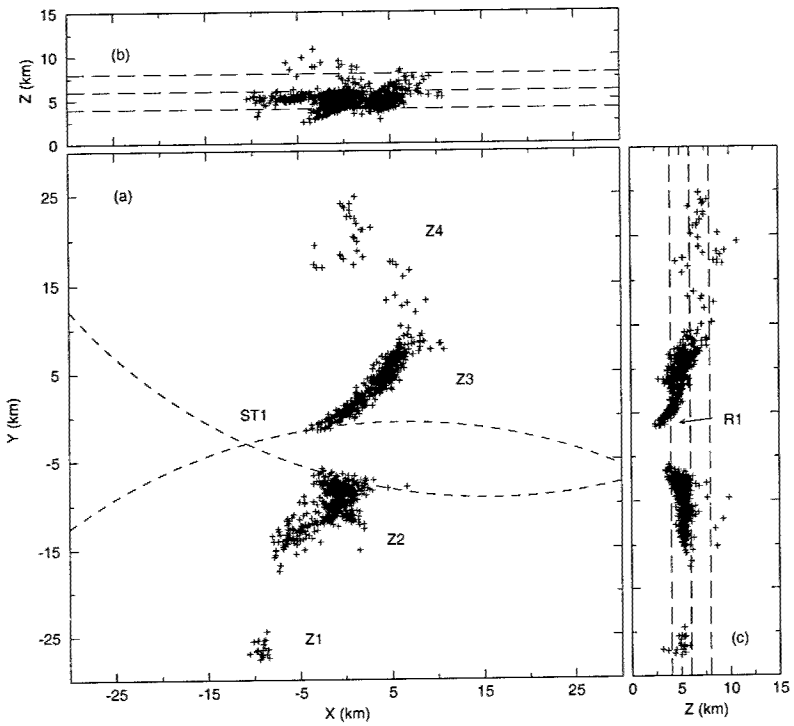


*figure 3 : three-dimensional VHF sources. (a) : XY projection; (b) : XZ projection; (c) : YZ projection (08/14/92 21:41:29 UT, Florida). Long dashed lines plot temperature level (0°C at 4 km AMSL, -10°C at 6 km AMSL and -20°C at 8 km AMSL).*

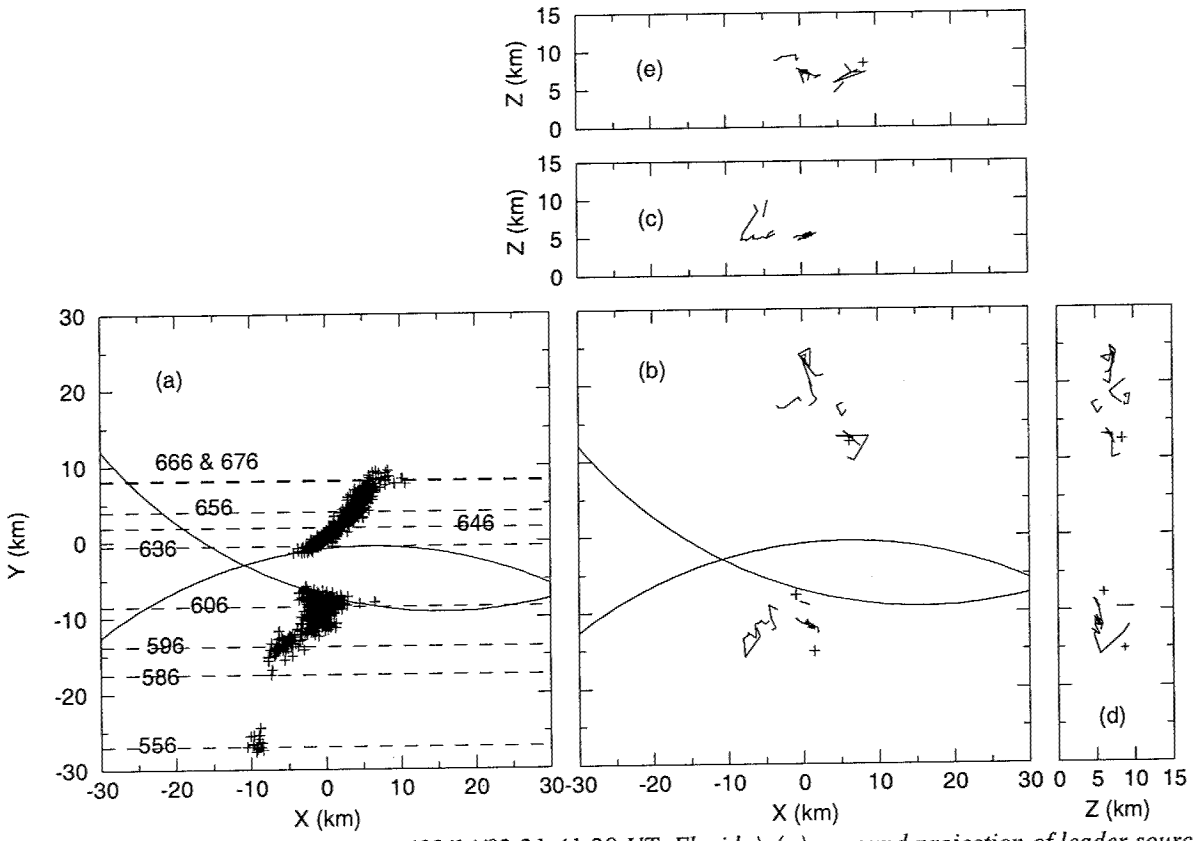


*figure 4 : XY views of successive events (08/14/92 21:41:29 UT, Florida). (a) : ground projection of leader sources, dashed lines indicate time (ms); (b), (c), (d) and (e) show respectively XY, XZ (Y<0 km), XZ (Y>0 km) and YZ projection views of reconstructed (crosses locate reconstructed isolated sources). Successive sources with a temporal gap lower than 1 ms are joined.*

# Broad Band Interferometric Measurement of Intra-cloud Lightning in Chinese Inland Plateau Area

Tomo Ushio*, and Z-I. Kawasaki Dept. of Electrical Eng., Osaka University, Osaka, Japan
(* Now at Global Hydrology and Climate Center, Huntsville, Alabama, USA)
M. Chen, D. Wang, N. Takagi and T. Watanabe Gifu University, Gifu, Japan
X. Liu and Q. Xiushu Lanzhou Institute of Plateau and Atmospheric Physics, Lanzhou, China
C. Guo Shanghai Meteorological Bureau, Shanghai, China

**Abstract** We have measured the characteristics of intra-cloud lightning at Pingliang, a plateau area in north-western China, using a broad band interferometer system developed by Ushio et al. (1997). This system, using a 500 MHz digitizer with 8 Megabyte memory and operating at the frequencies from 30 to 250 MHz, measures the two dimensional direction of arrival of the radiation from lightning discharges. A detailed study of two intra-cloud lightnings has shown that the intra-cloud lightning usually begins with an activity which lasts a few hundred milliseconds and involves the development of several horizontal streamers at the lower part inside the cloud. Since the similar initial activity to this has not been observed from the summer storms either in Florida or in New Mexico by Shao et al.(1996), our results appear to support the unique charge structure of the thunderstorms around Pingliang area as suggested by Liu et al. (1989). Followed this initial activity, the most active stage was observed to occur simultaneously in two directions, one tracing the previously-produced horizontal channel and the other connecting to the upper part of the cloud. From our electric field data which have been simultaneously recorded with the broad band interferometer data, the latter is inferred to transfer negative charge upward. As a whole, the intra-cloud lightning studied here exhibits a two-level structure in which the two levels were connected by a single upward channel as reported by Shao et al. (1996). In addition, in a comparison to the narrow band interferometer and the time of arrival system, the advantage and the disadvantage of our system are also discussed.

**Introduction** Thunderstorm in northern part of china is suggested to take the unique charge structure [Liu et al., 1989]. The experimental results of rocket triggered lightning obtained by Liu et al. [1994] support in part the features of lower positive charge of Gansu thunderstorms. Even though such experimental results are obtained, only a few studies have been conducted in the inland plateau area of China to investigate the characteristics of lightning flashes [Liu et al., 1989; Liu et al., 1994; Takeda et al., 1998]. Recently, Shao et al. [1996] have described the basic principle of a broad band interferometer[Kawasaki et al., 1991] for lightning observation in one spatial dimension, and Ushio et al. [1998] have developed two dimensional broad band interferometer using a sequential triggering method. The broad band interferometer has an advantage to locate the source of each pulse in both the isolated impulsive radiation events and radiation bursts compared to narrow band interferometry and time-of-arrival system. On the other hand, broad band interferometry can not record all of the radiation events due to the high digitization rate such as several hundred MHz. For example, Ushio et al. [1997] can capture only 50 broad band signal emitted by lightning, which is not sufficient to capture all the pulses from lightning flash.

In this paper we describe radiation location results obtained for intra-cloud lightning in Gansu thunderstorm by using a broad band interferometric technique which can record 2000 pulses from lightning. In addition, in a comparison to the narrow band interferometer and the time of arrival system, the advantage and the disadvantage of our system are also discussed.

**Instrumentation** The observations were made at Pinglyang near Gansu in the inland plateau area of People's Republic of China, at an altitude of 1630 m above sea level. The broad band interferometer system is described by Ushio et al. [1997] and measures the two dimensional direction of arrival of the radiation sources with submicrosecond resolution, using an array of antennas along two orthogonal baselines. The length of the baseline is 10 meters long in this experiment. The data is digitized at 500 MHz sampling rate. The number of pulses which we can capture for one flash is changed to two thousand from 50 pulses, and the recording time for one pulse is 1 microsecond. The processing of the broad band signal is similar to that described by Shao et al. [1996], and identical to that by Ushio et al. [1997]. The electric field change caused by lightning flash is also recorded by using fast antenna with a recording duration of 1 second. The frequency range of the antenna is from 200 Hz to 500 kHz. No absolute-amplitude calibration of the recorded E-field change data is obtained. The polarity of the vertical electric

field pointing downward is defined as positive.

**Results** Figure 1 shows electric field change for an intra-cloud lightning that occurred at 15:41:40 on 27 July, 1997. Vertical lines mark a sequence of occurrence times of the broad band electromagnetic pulses emitted by lightning flash. This flash occurred in a mature stage of a large storm about one hour after onset of lighting in the storm. The field change is initially negative going (opposite in polarity to the field change due to a cloud to ground discharge lowering negative charge to earth). After that, the field change (550 to 680 millisecond) shows large negative going slope, during which the broad band signal are emitted intensively. In the latter part of the flash, some abrupt positive field changes attributable to K changes appear in the record. Microsecond-scale pulses do not appear in the overall flash electric field change shown in Figure 1.

Figure 2 shows an overview of all the radiation sources for the flash in azimuth and elevation format. This flash exhibited a two-level structure in which the two levels were connected by a single upward channel as reported by Shao et al. [1996]. During the first 200 millisecond, radiation progressed horizontally from the starting point S along the path a1, and developed along path a2 and b. In the most active stage of the flash (570 to 680 millisecond), the breakdown progressed upward in elevation to the upper level, where it extends to the channels c1 and c2. In the latter part of the flash, we have difficulty to locate the radiation sources attributable to K changes due to the digitizer's dead time of 70 microseconds.

Figure 3 shows radiation source locations during the most active period (550 to 680 millisecond), along with fast electric field change (a), and azimuth and elevation of the broad band pulses versus time (b). During the 590 to 620 millisecond in figure 3, the channel progressed horizontally from the starting point S along the path a2. After that during the 620 to 650 millisecond, the radiation sources retraced the previously formed channel a2 again, and developed upward in elevation along the path b simultaneously. From 650 to 680 millisecond the breakdown progressed to the upper level and extended horizontally along the path c1, and then developed to the channel c2, whose elevation decreases appeared to result from component away from the observation site. Note that the a2 and b breakdown occurred simultaneously, showing that the broad band interferometer can locate the simultaneously on-going radiation sources separate in space.

## Discussion

Proctor [1981, 1983] analyzed IC flashes in South Africa using a long base line time-of-arrival system, and shown that most of flashes he studied were initiated by negative breakdown which propagate horizontally. To the contrary, Shao et al. [1996] found that IC flash in Florida often had a bilevel structure connected by a single upward channel and the initial breakdown began at the lower level and propagated upward. Liu and Krehbiel [1985] and Shao et al. [1996] interpret that the difference comes from the fact that the discharges studied by Proctor occurred in the dissipating stage of storms and those by Shao occurred in the early stage of storms. The initial breakdown of the IC flashes analyzed in this experiment were horizontally oriented in three flashes. The polarity of the electric field change indicates that the initial horizontal breakdown transfers negative charge slightly downward and the activity would be concerned with the discharge process between major negatively charged region and the minor lower positively charged region in the cloud. Liu et al. [1989] suggest that the dominant positive charge often exists in the lower part of Gansu thunderstorms based on the results of multipoint electric field measurement and [Wang et al., 1990] rocket triggered lightning experiment. The result in this paper is consistent with the unique charge structure of thunderstorms in Gansu or the stage of the thunderstorm. In the most active part of the flash, negative charge is transported upward in the cloud, and the overview of all the radiation sources for the flash cleary shows the bilevel structure reported by Shao et al. [1996].

**Acknowledgments** This research is supported in part by the grant-in-aid for Scientific Research of Ministry of Education, Science and Culture. We would like to thank all the participants in this project for helping pursuing this experiment.

## References

Kawasaki, Z.-I., J.-M. Li, K. Matsuura, M. Kawasaki, and O. Sugimoto, Localization of partial discharges using time difference of arrival of radiation fields, *Proc. 3rd Int. Conf. on Properties and Applications of Dielectric Materials*, Tokyo, Japan, 1991

Liu, X., Z. Ye, X. Shao, C. Wang, M. Yan, and C. Guo, Intracloud lightning discharges in the lower part of

thundercloud, *Acta Meteorol. Sinica*, 3, 212-219, 1989

Liu, X., C. Wang, Y. Zhang, Q. Xiao, D. Wang, Z. Zhou, and C. Guo, Experiment of artificially triggering lightning in China, *J. Geophys. Res.*, 99, 10727-10731, 1994

Proctor, D. E., VHF radio pictures of cloud flashes, *J. Geophys. Res.*, 86, 4041-4071, 1981

Proctor, D. E., Lightning and precipitation in a small multicellular thunderstorms, *J. Geophys. Res.*, 88, 5421-5440, 1983

Shao, X. M., and P. R. Krehbiel, The spatial and temporal development of intracloud lightning, *J. Geophys. Res.*, 101, 26641-26668, 1996

Shao, X. M., D. N. Holden, and C. T. Rhodes, Broad band radio interferometry for lightning observations, *Geophys. Res. Lett.*, 23, 1917-1920, 1996

Takeda, M., D. Wang, N. Takagi, T. Watanabe, M. Chen, T. Ushio, Z.-I. Kawasaki, M. Nakano, K. Nakamura, X. Liu, X. Qie, and C. Guo, Some results of investigation on slow front of return stroke electric waveform, *J. Atmos. Electr.*, 18, 31-39, 1998

Ushio, T., Z-I Kawasaki, Y. Ohta, and K. Matsuura, Broad band interferometric measurement of the rocket triggered lightning in Japan, *Geophys. Res. Lett.*, 24, 2769-2772, 1997

Ushio, T., A study on broad band lightning electro-magnetic field, Ph.D. dissertation, Osaka University, Japan, 1998

Wang, D., X. Liu, and C. Wang, A preliminary analysis of the characteristics of ground discharges in thunderstorms near Zhongchuan, Gansu Province, Plateau Meteorol., 9, 405-410, 1990

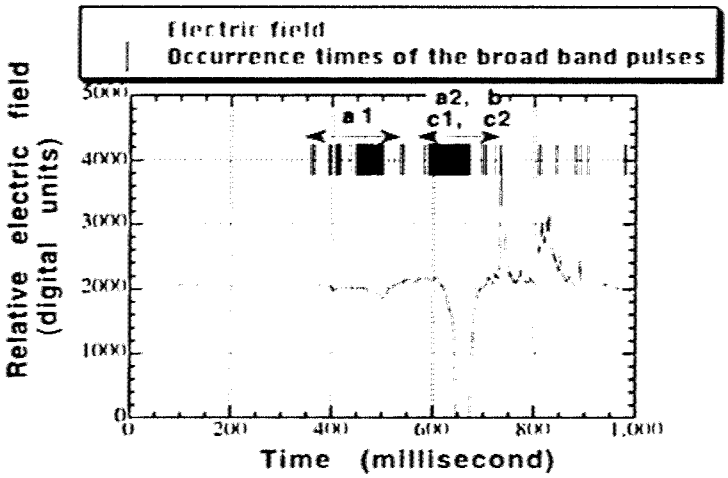


Fig. 1 Whole electric field change due to intra-cloud lightning recorded by fast antenna at 15:41:40 on 27 July. Occurrence times of the broadband pulses captured by our system are also shown with vertical bars.

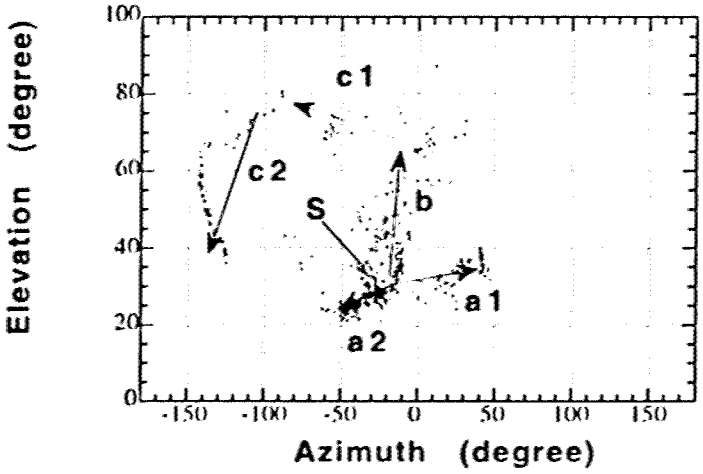


Fig. 2 Overview showing all the radiation sources for flash in Fig. 8 in azimuth and elevation format. S denotes the region where the flash started. The flash begins at S, and develops horizontally as labelled a1 and a2. After the a1 and a2 leaders develop horizontally, b and c1 leaders go upward.

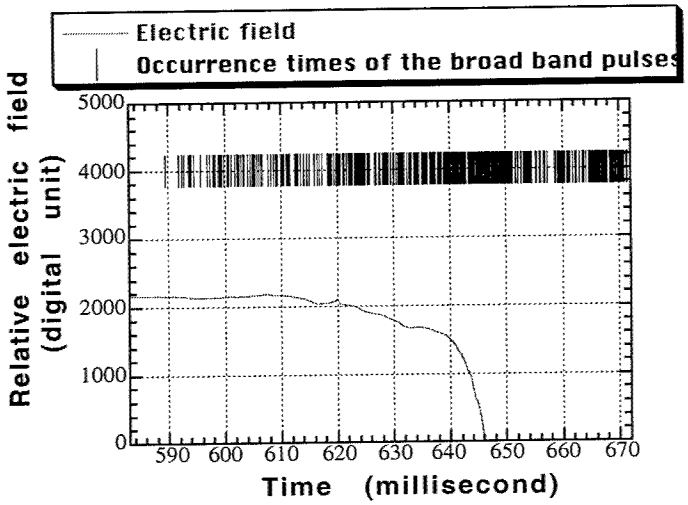


(a) Time waveforms of electric field change

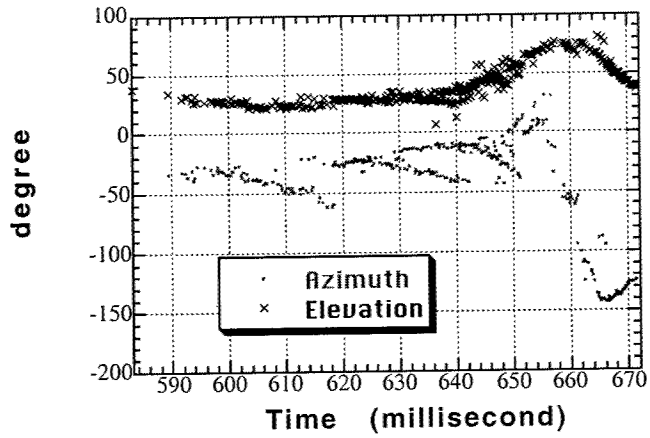


(b) Azimuth and elevation of the broad band pulses versus time.

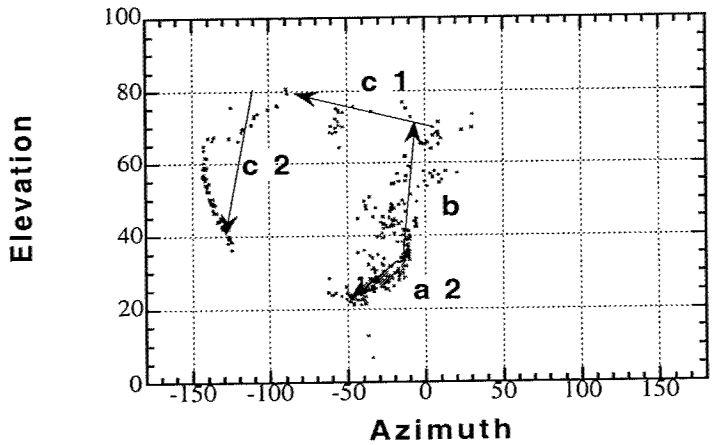


(c) Radiation source locations in azimuth and elevation format.

Fig. 3. Results for the most active stage of the flash. Note that the a2 and b breakdowns occur simultaneouly, showing that the broad band interferometer can locate the on-going radiation sources separate in space.

# THE INCEPTION PHASE OF POSITIVE LEADERS IN TRIGGERED LIGHTNING : COMPARISON OF MODELING WITH EXPERIMENTAL DATA

A. Bondiou-Clergerie[1], P. Lalande[1], P. Laroche[1], J.C. Willett[2], D. Davis[3], I. Gallimberti[4]
[1]Onera, Chatillon, France
[2]AFRL, Boston, U.S.A.
[3]SUNYA, Albany, U.S.A
[4] University of Padova, Padova, Italy

ABSTRACT : A self consistent model simulating inception and development of positive leaders has been previously derived from theoretical studies of laboratory long sparks. The model was successfully tested in the case of positive leaders in long laboratory gaps and has been extended to the positive leaders in triggered lightning flashes by including channel thermalization processes. In this last case, full testing and validation of the model requires measurement of the vertical profile of ambient electric field prior to the triggering of the flash. A recent experiment has provided ambient field profiles a few seconds before nine lightning flashes triggered by the rocket-and-wire technique. This paper presents a comparison between calculated and measured features of the positive leader during its inception and first few milliseconds of propagation in one of these cases. Relationships between average ambient field and wire length at inception are analyzed over the whole set of data and the concept of a « leader stabilization field » is presented.

## 1. INTRODUCTION

Triggered lightning flashes allow a detailed study of the positive leader properties and therefore provide a valuable opportunity to test self-consistent physical models that simulate the discharge inception and development. In the present paper, comparisons between experimental and theoretical results are made from a set of triggered lightning flashes performed in measured ambient field profiles. The purpose of this paper is to use these measured profiles as model inputs to perform numerical simulations of the successive phases of the positive leader inception and propagation. A detailed analysis of the model outputs will be given here in a single case. The same model may be used to derive a simple criterion giving the minimum electrical conditions for actual positive leader inception : this criterion will be compared to the experimental results.

## 2. EXPERIMENTAL SET-UP AND MEASUREMENTS

A major field experiment was conducted during the summer of 1996 to obtain simultaneous, collocated measurements of ambient, electrostatic-field profiles and rocket-triggered-lightning phenomenology beneath Florida thunderstorms [Willett *et al.*, in press]. First, nearly vertical profiles of the ambient electrostatic field were measured with sounding rockets very similar to those described by Marshall *et al.* [1995]. A few seconds later triggering rockets were fired, towing grounded conducting wires aloft [e.g., Laroche *et al.*, 1989]. The phenomenology of the triggered lightning was documented with still and video cameras, and the currents and field changes produced by the positive leaders that initiated these discharges were recorded.

One event from this experiment (Flight 13) will be examined in detail here. The measured ambient-field and potential profiles for this flight can be found in Willett *et al.* [in press, Figure 18]. Briefly, the field aloft in this case was nearly vertical up to cloud base, starting from about 7 kV/m at the surface and increasing monotonically to a relatively uniform value of about 23 kV/m above 500 m altitude. The potential at the observed triggering altitude of 230 m was -3.6 MV relative to ground.

## 3. SELF-CONSISTENT MODELING OF A POSITIVE LEADER

The model is originally based on experimental and theoretical studies of positive leaders in laboratory long gaps. These studies have shown that the discharge develops through complex mechanisms that lead to a basic structure made of a corona region at the discharge head, followed by the leader filamentary channel. This leader channel includes a cold, moderately conductive part and, if high currents are flowing, a hot thermalized part of high conductivity[*Gallimberti, 1979*]. The self consistent, time dependent simulation of all these processes is based on the solution of classical equations for conservation of mass, momentum and energy, together with Poisson's equation for the electric field distribution along the propagation axis. These equations are simplified according to the dominant processes in each discharge region, leading to a set of coupled equations for leader and corona front velocities, leader current, deposited space charge, channel temperature and conductivity, etc. The resulting model is essentially self-consistent using as its main input the initial electric field distribution prior to the discharge inception. As the

model is one dimensional (along the propagation axis), all processes that occur in the radial direction are not simulated : as a consequence, the corona width and its number of filaments have to be provided as inputs of the calculation. Under laboratory conditions, these parameters can be derived from experimental results over a large set of experiments.

Depending on the electric field distribution, this self-consistent model indicates that the dynamic behavior of the coupled leader filament/corona head system may be different, leading to continuous or discontinuous propagation modes. In laboratory long gaps, with average ambient fields usually around 200 kV/m, the model predicts a stable continuous propagation of the positive leader discharge, consistent with experimental results [*Bondiou and Gallimberti, 1994; Goelian et al, 1997*]. On the contrary, in much lower external ambient fields, the modeling of the leader/corona system shows that the propagation is mainly discontinuous, being made of successive « restrikes » [*Bondiou et al, 1994*]. This is consistent with the observed behavior of positive leaders in triggered lightning flashes and with the discontinuous propagation of laboratory discharges in point to plane gaps subjected to very slow rise-time voltages [*Les Renardieres, 1973*].

*Adaptation of the model to the triggered lightning leader case: E-field calculation method*

In the case of laboratory discharge modeling, the calculation of field and potential distributions can be performed using an analytical solution of Poisson's equation within an ellipsoidal-hyperboloidal coordinate system [*Bondiou and Gallimberti, 1994]*. In this case, the electrode and the leader are represented as semi-infinite hyperboloids, while the corona region is represented as a frustum of ellipsoid. When successive restrikes are involved, however, it is necessary to develop specific methods in order to take into account the different E-field components (see Figure 1). At a given time t of the positive leader development the electrostatic configuration is made of conductors and space charge regions that modify the initial ambient field distribution:

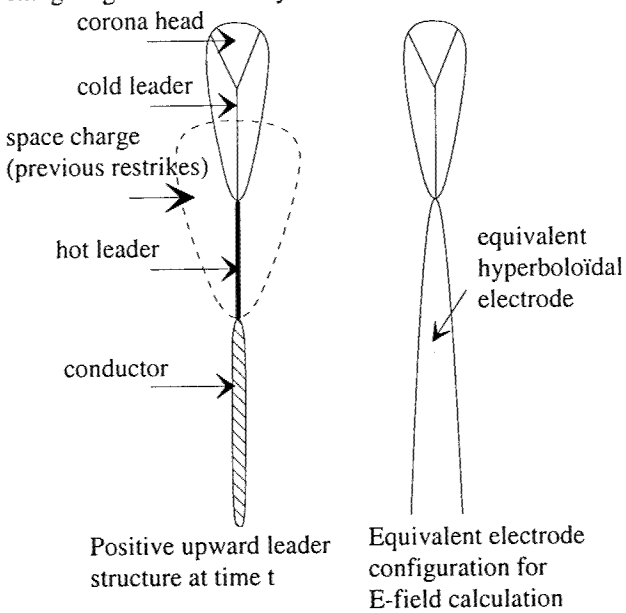


- a corona/cold leader system at its head
- a hot leader section in which temperature has exceeded the threshold for thermalization during the previous restrikes. Its internal field is assumed here to be negligible.
- the space charge left by the preceeding restrikes
- the electrode (wire+rocket)

The E-field distribution due to the last 3 items can be calculated periodically using a numerical method derived from the classical « Charge Simulation Method ». The curvature radius and potential of a conductive semi-infinite hyperboloid giving the same E-field distribution are then calculated by a best-fit method. This « equivalent electrode », whose tip is located at the hot leader head, is then used to perform an analytical calculation of the total driving electric field along the corona/cold leader system every 500ns during its development between 2 restrikes. After each restrike, a new equivalent electrode is calculated taking into account the new corona charge and a new section of hot leader.

Figure 1 : Discharge structure and E-field approximation

*Stable or unstable propagation*

Whatever the propagation mode may be, the model is also able to predict the existence of arrest or instability conditions for the discharge. Under laboratory conditions, for a given gap length, it is possible to calculate the critical voltage under which the positive leader stops before reaching the cathode. Similarly, under triggered lightning conditions, the model predicts the existence of « attempted leaders » that develop and stop for rocket altitudes well below the one of the stable leader onset. It has been demonstrated in [*P. Lalande, 1996*] that the self-consistent model described above may be also used to derive a « stabilization field » criteria that gives in a simple formula, the conditions for stable propagation of a positive leader discharge.

## 4. COMPARISONS BETWEEN MODEL AND EXPERIMENT

### 4.1. Detailed study of flash n°13

The results presented here are obtained by introducing the measured vertical ambient field profile as an input of the calculation. For a given rocket altitude, the calculation of initial field distribution is made by representing the rocket and wire using the conventional Charge Simulation Method. It is important to note that the space-charge clouds left behind by permanent « glow » corona and previous attempted leaders are not taken into account in the calculation of initial field distribution. Under these assumptions, it is not possible to calculate accurately the inception altitudes of all the successive attempted leaders, or « precursors ». Numerical simulations are then performed for different rocket altitudes regularly spaced between $H_{min}$ -minimum altitude for inception of a precursor- and $H_{max}$ -altitude for inception of the stable leader.

Figure 2 shows the results of the simulation performed for the rocket at H=140m. The representation of the discharge tip position versus time indicates that the discharge propagation mode is discontinuous, i.e. made of 4 successive restrikes. The detailed interpretation for this behavior has been given in [*Bondiou et al. 1994*]. For altitudes $H<H_{max}$, the discharge stops after several restrikes because the field at the tip of the leader channel is not sufficient to generate a new corona discharge initiating a new restrike. This is due to the effect of the corona space charge accumulated during the restrikes : it creates a space charge field that exceeds the driving field, the latter being due to the ambient field amplified by the presence of the wire plus the leader conductive channel.

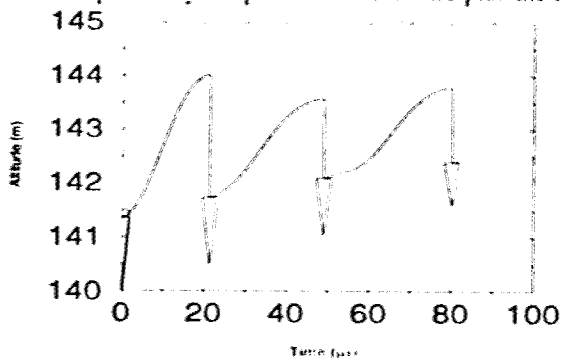


Figure 2a :« Streak » representation of the calculated positions of the corona and leader heads. H= 140m; ambient field profile #13

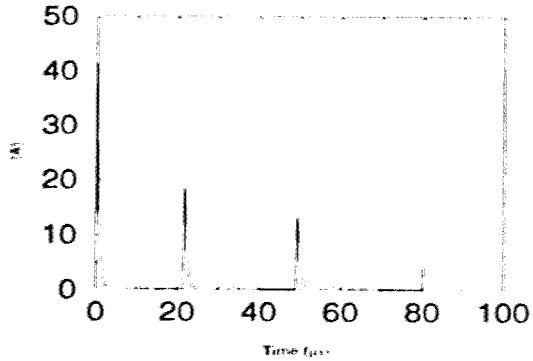


Figure 2b : Calculation of the discharge current. H= 140m; ambient field profile #13

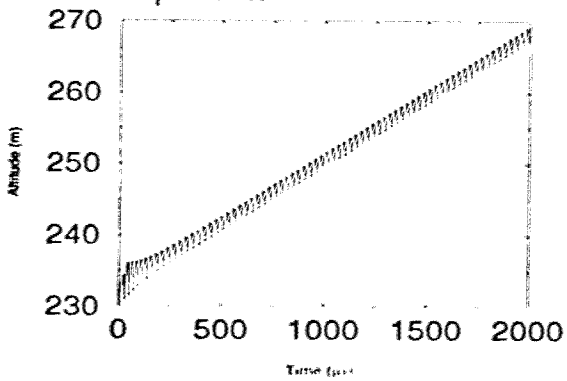


Figure 3a :« Streak » representation of the calculated positions of the corona and leader heads. H= 230m; ambient field profile #13

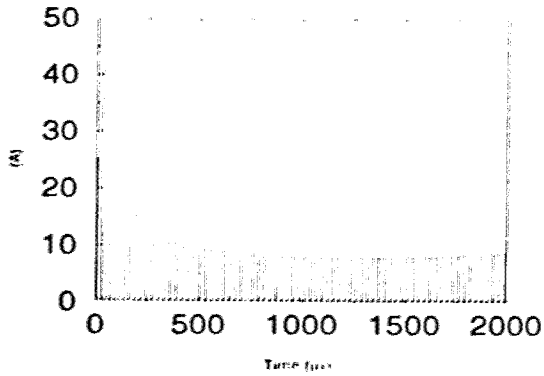


Figure 3b : Calculation of the discharge current. H= 230m; ambient field profile #13

For altitudes $H \geq H_{max}$, this ambient field amplification remains sufficient to balance the corona space charge effect : the discharge is then stabilized and may propagate over very long distances. The corresponding model outputs for $H=H_{max}$=230m for the flash #13 are given on Figure 3. Note that these results are obtained for the following parameters setting : the number of filaments is set to 1500, instead of 1000 under laboratory conditions, and the width of the corona envelope was set around 1m. These parameters have a noticeable influence only on the calculated values of charges, currents and propagation velocities; the choice is done in order to maximize the agreement between model and experimental results.

| | Experiment | Model |
|---|---|---|
| **Precursors** | (mean ± std.) | |
| Charge per pulse | 19 ± 10 μC | 20 to 35 μC |
| Peak current | 16 ± 11 A | 10 to 30 A |
| Δt between pulses | 29 ± 7 μs | 20 to 25 μs |
| **Actual leader** | | |
| Onset altitude | 230 m | 230m |
| Charge per pulse | 52 ± 11 μC (averaged over the first 15 pulses) | 37.5 μC (averaged over the first 4 pulses) |
| Peak current | 18 ± 18 A (id.) | 38.5 A (id.) |
| Average current | 1.5A (first 875μs) | |
| Δt between pulses | 32 ± 5μs (first 15 pulses) | 29 μs |

A quantitative comparison between model-predicted and measured values is shown in the adjacent table. Relative uncertainties in the experimental values are estimated at 50% for charge and peak current, 30% for average current and 5% for the onset altitude,. Inter-pulse intervals are accurate to ~1μs. Although good agreement exists among the listed parameters, the model predicts precursors of regularly increasing pulse number, peak current, and charge with increasing height, whereas the observed increase in these quantities is irregular. Further, the number of pulses within a predicted precursor at a given altitude exceeds that observed. These discrepancies are likely due to the model's neglect of glow corona and prior precursor space charge, and to the assumption of purely vertical propagation.

4.2. Study of inception conditions

The model can be used to calculate the minimum ambient field necessary to initiate a stable leader from a vertical linear structure of height H (in this calculation, the ambient field is supposed to be uniform along the propagation axis). Using the set of parameters validated above, this « stabilization field » is plotted in figure 4 as a function of height. On the same figure, averages between ground and leader-onset height of the ambient field measured prior to the different flashes triggered in the reported experiment are given as function of the altitude of the actual leader onset, from Willett *et al.* [in press, Table 2]. Although the data set corresponds to a limited range of the whole curve, this comparison shows that the calculated stabilization field is in good agreement with experimental results.

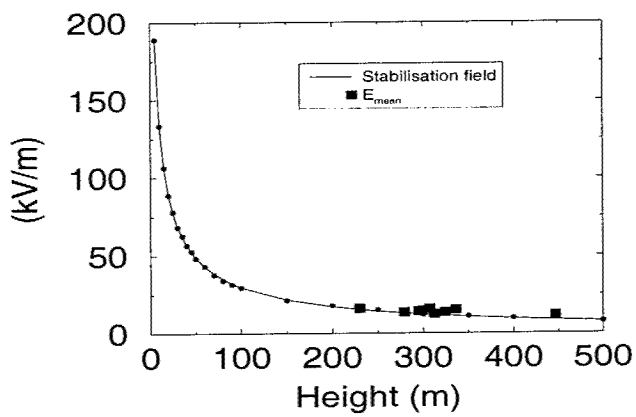


Figure 5 : Stabilization field as function of structure height. Comparison with measurements.

5. CONCLUSION

This study represents the first attempt to validate quantitatively a self-consistent model simulating the inception and development of the positive upward leader in triggered lightning. In spite of some simplifying assumptions, it is shown that the model is in good agreement with the reported data. The stabilization field criteria seems to be a valuable tool that can be easily used to predict inception conditions from a grounded structure.

6. REFERENCES


Gallimberti I., « The mechanism of the long spark formation » *Journal de Physique, N°7, Tome 40,* 1979

Bondiou A. Gallimberti I., « Theoretical modeling of the development of positive sparks in long gaps » *J. Phys. D: Appl. Phys. 27,* 1994.

Bondiou A., P. Laroche, I. Gallimberti, "Modeling of the positive leader development in the case of long air gap discharge and triggered lightning" *22nd ICLP, Budapest Hungary, Sept. 19-23,* 1994

N. Goelian, P.Lalande, A.Bondiou-Clergerie, G.-L. Bacchiega, A. Gazzani, I. Gallimberti « A simplified model for the simulation of the positive spark development in long air gaps » *J. Phys. D: Appl. Phys. 30, pp 2441-2452,* 1997

Lalande P. « Etude des conditions de foudroiement d'une structure au sol » PhD Report, Orsay University, N° 4458, Sept 1996.

Laroche, P., A. Bondiou, A. Eybert-Bérard, L. Barret, J.P. Berlandis, G. Terrier, and W. Jafferis, Lightning flashes triggered in altitude by the rocket and wire technique, ICOLSE, *University of Bath, UK, September 26-28*, 1989.

Les Renardieres Group, *Electra n°23*, 1972

Marshall, T.C., W. Rison, W.D. Rust, M. Stolzenburg, J.C. Willett, and W.P. Winn, Rocket and balloon observations of electric field in two thunderstorms, *J. Geophys. Res., 100*, 20,815-20,828, 1995.

Willett J.C., Davis D.A., and Laroche P., "An experimental study of positive leaders initiating rocket-triggered lightning ," *Atmospheric Research*, in press.

# COMPUTER SIMULATION OF A DOWNWARD NEGATIVE STEPPED LEADER

V. Mazur[1], L. H. Ruhnke[2], A. Bondiou-Clergerie[3], and P. Lalande[3]
[1]NOAA/National Severe Storms Laboratory, Norman, OK 73069, U.S.A.
[2]Reston, VA, 20190, U.S.A.
[3]Office National d'Etudes et de Recherche Aerospatiales, Chatillon, France

## INTRODUCTION

In a realistic computer simulation (model) of interaction between a downward negative stepped leader and a ground structure, the results will depend heavily upon the assumptions made about the manner of propagation of both the downward and upward induced leaders. It is important to base these assumptions on descriptions that are physically sound and which have emerged from theoretical modeling of negative and positive leaders, as well as laboratory experiments on long sparks [Bacchiega et al. 1994, Bondiou and Gallimberti, 1994]. The objective of this study is twofold: (1) to develop a scheme of computer simulation for negative lightning leader interaction with a ground structure that reflects known physical concepts, and which is reasonably simple to model; and, (2) to determine the dominant factors affecting interception of the downward negative leader with a ground structure.

## PHYSICAL DESCRIPTION OF THE NEGATIVE LEADER PHASES[1]

The negative filament breakdown starts near the tip of the leader when the E-field exceeds the breakdown field of 2.6 MV/m. The length of the corona avalanche is determined by the ambient potential profile ahead of the leader and by a constant E-field maintained inside the established negative corona region, which is 750 kV/m ("Gallimberti criterion"). To determine the length of the negative corona avalanche ("Gallimberti length"), one should (1) draw a line from the tip of the negative leader with a slope of 750 kV/m on the graph of the ambient potential profile, and (2) determine the abscissa, L, of the crossing point of this line with the ambient potential profile (Fig. 1). The process of the negative corona avalanche is very fast in comparison with other processes in negative leader propagation. The avalanche region has a net negative charge that migrates in the corona process from the tip of the negative leader.

Following the end of the avalanche, space charges in the negative corona region begin to redistribute according to the distribution of the conductivity and dielectric constant in the zone (the so called "relaxation process"). In addition, a current will flow into the zone from the tip, due to the existing conductivity and electric field. The tendency of this relaxation process is to increase the potential at the outer corona region; this makes the electric field beyond the end of the corona zone increase, and also produces an electric field of the opposite polarity. This process will lead to the breakdown conditions of, first, a new negative corona at the end of the corona zone, and then, a positive corona toward the leader. These events start a single cycle of the bipolar corona process (also called a "pilot system"). There may be as many as several such cycles of bipolar corona formation, with relaxation processes in between. At the starting point of this bipolar corona region, thermalization sets in to create a conducting "space" leader. The bi-directional development of this space leader occurs with unequal speed toward and away from the leader; the speed toward the leader is twice that of the movement away from the leader. There is also unidirectional development of the thermalized stem from the tip of the negative leader. The interstep process ends with the junction of the space and negative leaders.

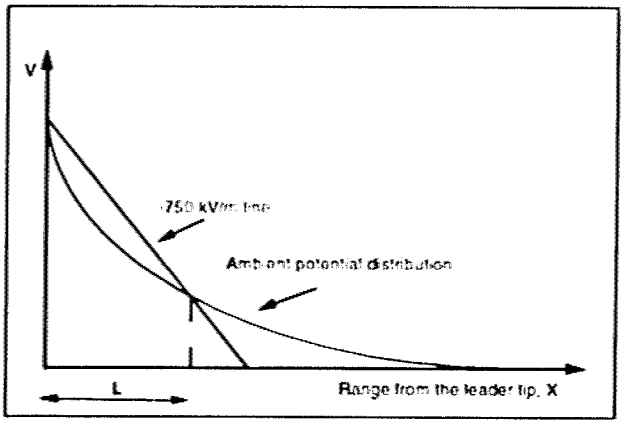


Figure 1. Determining the length L of the negative corona avalanche.

[1] Based on studies of the laboratory-produced positive and negative leaders [Bacchiega et al. 1994; Bondiou and Gallimberti,1994].

## ASSUMPTIONS FOR COMPUTER SIMULATION

In the electrostatic model we employ in computer simulation of a negative leader, the diameter of the leader's corona shell is the diameter of the leader in our model. Channels of several meters in diameter are required if the surface electric field on the channel is to be below the breakdown value [Schonland, 1953; Uman, 1969]. Although, generally, the leader potential changes during leader progression, for the last 200 meters one may assume it to be constant. In our model, we considered a leader of 10 m diameter[2] with - 40 MV potential at a height of 200 m above the ground, propagating downward with an average speed of $10^6$ m $s^{-1}$[3]. Numerical solutions for 3-dimensional potential distributions were obtained using the charge simulation method [e.g., Malik, 1989].

## RESULTS OF COMPUTER SIMULATIONS

### Modeling of the Stepping Process

In modeling of the stepping process, we simplified the sequence of processes described earlier, with an emphasis on the dominant features of these processes, namely, development of the space leader. The space leader is represented by an electrically floating conducting element of the same diameter as the leader that starts at the distance L ahead of the leader channel, and grows toward the leader tip with a constant speed of $1 \times 10^6$ m $s^{-1}$. The potential of the floating element is determined by the ambient potential distribution, and is changing throughout its development. The junction occurs at the very end of this development[4]. Figure 2 shows the waveform of the E-field on the ground during the single interstep development of the negative leader, normalized to the highest value of the electric field at the end of the step cycle and to the duration of the interstep period. The normalized curve is shown to be independent of the height of the leader tip above the ground, as well as independent of the leader potential.

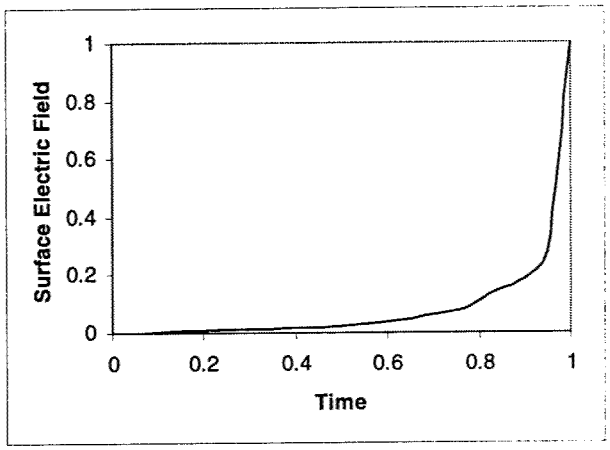


Figure 2. Standardized waveform of the surface E-field change during the interstep period.

### Modeling of the Negative Stepped Leader Moving toward the Ground

Two scenarios for the negative leader's interaction with a ground structure were selected for modeling, plus one without a ground structure (for comparison): (1) a ground with a 20-m high metal mast placed 20 m away from the leader axis, assuming no upward leader development; (2) the metal mast with an upward leader developing; and (3) a ground without any structure, The numerical solution for the 3-dimensional potential and electric field distribution was obtained for the sequence of leader steps starting from a height of 200 m above the ground and continuing untill the final "jump" to the ground. The variation of the E-field between steps was calculated by applying the normalized curve from the single step simulation to the actual length of each individual step. The direction of negative leader propagation was determined by the direction of the longest Gallimberti length. A similar process was used to determine the direction of the positive leader.

The leader makes 6 steps before the jump-over to the ground in Case 3 or to the mast in Case 1 at the height of 33.7 m and 41 m above the ground (Fig 3), respectively. In Case 2, the initiation of the upward positive leader at the tip of the mast occurs when the downward leader is 162 m above the ground. Both the negative and upward positive leaders are propagating on a straight line until the final jump after 4 steps (Fig. 4). For Case 1, we plotted for the last step the sequence of the boundaries for the negative corona region from the tip of the space leader (Fig. 5). There is a clear indication that the influence of the mast became noticeable only at the very close proximity of the leader tip to it. The surface electric field under the leader, prior to the jump, (- 306 kV/m) is the highest in Case 3 (the

---

[2] The diameters of luminous stepped leaders have been measured photographically to be between 1 and 10 m [Schonland, 1953].

[3] The speed in the range of $6 \times 10^5$ and $15 \times 10^5$ m $s^{-1}$ was reported by Schonland et al.[1935].

[4] The arc during the junction illuminates the entire region of length L, so it produces a bright step propagating outward with a velocity similar to that of a return stroke.

flat ground) and is only about 45% of this value in Case 2 of the upward leader from the mast (see Fig. 6).

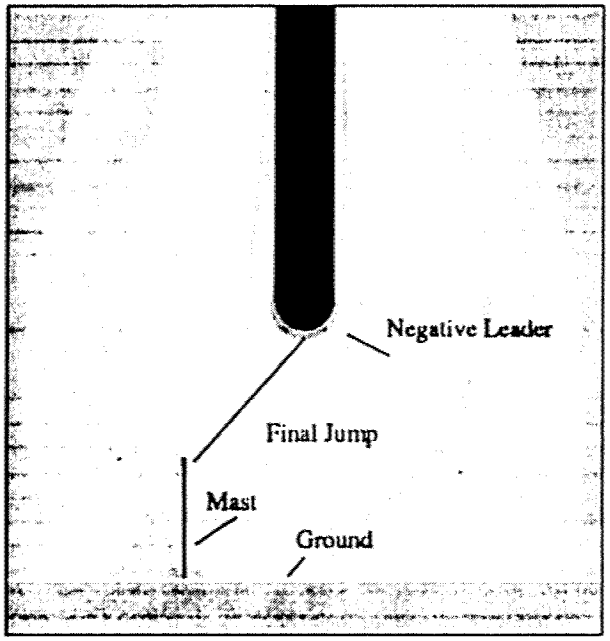


Figure 3. Negative leader prior to the final jump to the mast in Case 1 (no upward emitted leader from the mast).

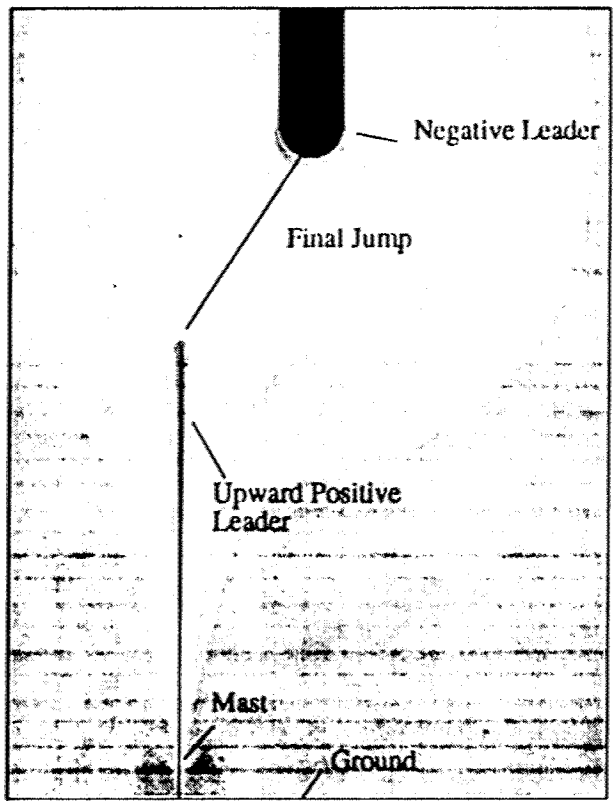


Figure 4. Negative leader prior to the final jump too the mast with upward positive leader (Case 2).

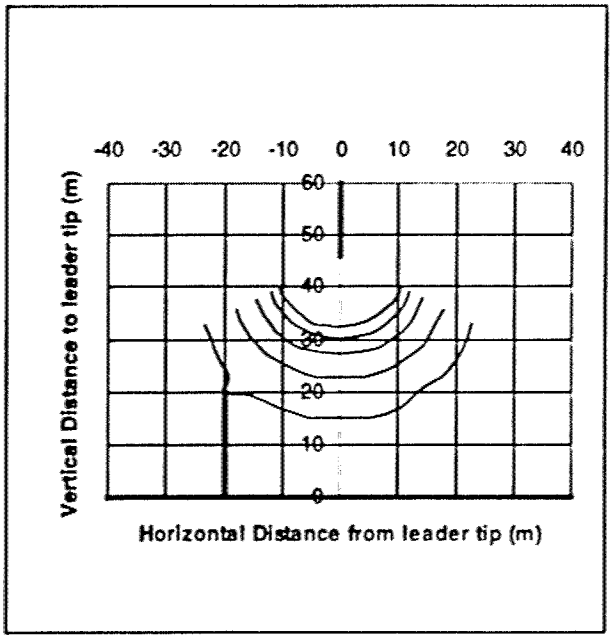


Figure 5. Development of the corona wavefront during the final jump to the tower (Case 1).

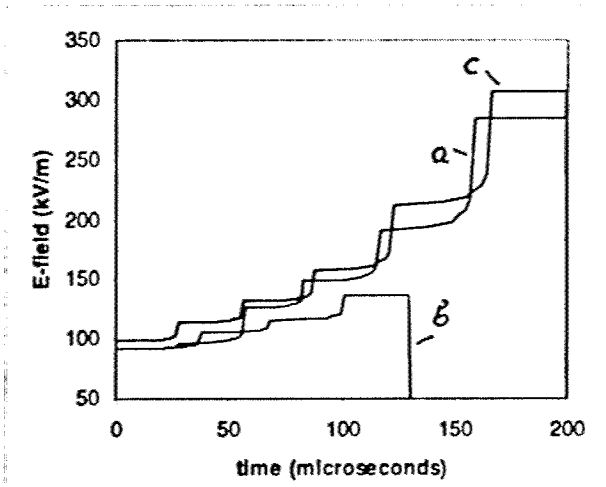


Figure 6. Electric field waveforms on the ground surface, under the leader, during the downward progression of the negative leader for Case 1 (a), Case 2 (b), and Case 3 (c).

## SUMMARY AND DISCUSSION

In an interaction between a downward moving negative leader and a mast, the leader does not react to the mast until the final jump, regardless of the emission of the upward positive leader. Our results (1) do not support the assumption that both the negative

downward and positive upward leaders gradually converge toward each other, and (2) do show the critical role of the final jump. Thus, the dominant factor in the interaction of a leader with a ground structure is the leader's potential that determines the length of the leader step. This also means that the height of the mast is not the critical factor in the mast's effectiveness as a protecting device.

Our results show that under the assumption of a constant potential of the leader and a constant velocity of the space leader development, the step length increases with the leader tip approaching the ground. This trend is also observed in laboratory-produced negative stepped leaders [Bacchiega et al, 1994].

REFERENCES

Bacchiega, G. L., A. Gazzani, M. Bernardi, I. Gallimberti, A. Bondiou, Theoretical modeling of the laboratory negative stepped leader, 1994 Internatl. Aerospace and Ground Conf. on Lightning and Static Electricity, Mannheim (Germany), May 24-27, 1994.

Bondiou, A. and I. Gallimberti, Theoretical modeling of the development of the positive spark in long gaps, J. Phys. D: Appl. Phys. , 27, 1252-1266, 1994.

Malik, N. H., A review of the charge simulation method and its applications, IEEE Trans. Electrical Insulation, Vol. 24, No.1, 3-20, 1989.

Schonland, B. F. J., D. J. Malan, and H. Collens, Progressive Lightning, Pt. 2, Proc. Soc. London Ser. A, 152, 595-625, 1935.

Schonland, B. F. J., The pilot streamer in lightning and the long spark, Proc. Soc. London Ser. A, 220, 25-38, 1953.

Schonland, B. F. J. , The lightning discharge, Handbk. Phys., 22, 576-628, 1956.

Uman, M. A., Lightning, pp.54, 211-214, McGraw-Hill, New York, 1969.

# 1997 TRIGGERED LIGHTNING EXPERIMENT IN THE INLAND PLATEAU OF CHINA

X. Liu[1], C. Wang[1], X. Qie[1], Y. Zhang[1], W. Dong[1], Q. Xiao[1], G. Zhang[1], C. Guo[2], M. Chen[1,3], T. Watanabe[3], D. Wang[3], N. Takagi[3], M. Nakano[4], K. Nakamura[5], Z. Kawasaki[6] and S. Sumi[7]

[1] Lanzhou Institute of Plateau Atmospheric Physics, Chinese Academy of Sciences
[2] Shanghai Meteorological Institute, China
[3] Gifu University, Japan
[4] Toyota National College of Technology, Japan
[5] Nagoya Institute of Technology, Japan
[6] Osaka University, Japan
[7] Chubu University, Japan

ABSTRACT: This paper presents main results of triggered lightning experiment conducted in 1997 in the inland plateau of China, with the emphases on the characteristics of an altitude triggered lightning. The bi-directional leader propagation was identified by simultaneous electrical and photographic observation. After initiation the downward moving positive leader, which produced at the lower end of aloft steel wire under the action of dominated lower positive charge of thundercloud, connected in the period of 0.7 ms to the upward moving attachment negative leader and occurred a junction process, similar to in some respects but actually different from in the strict sense return stroke of natural lightning discharges.

## INTRODUCTION

In the summer of 1997, Chinese and Japanese scientists conducted jointly a comprehensive observation of positive lightning in Pingliang, Gansu province which is located on the east verge of Qinghai-Tibet Plateau. The main objective of the experiment was to investigate the mechanism of positive lightning discharges which often take a considerable percentage in winter storms in Japan and in summer storms in northern China. During the experiment the technique of lightning artificial triggering was used and two cases of triggered lightning were obtained. Among them the so-called 'altitude triggering technique' was used in one case, i.e., the lower end of still wire trailed by ascending rocket was attached to the ground not directly but through a length of nylon line. This paper describes the field experiment, measuring technique and main results obtained.

## EXPERIMENT ARRANGEMENT AND MEASURING SYSTEM

The experiment site was located in a relatively even terrain with the height of 1797 msl on the east side of Liupan Mountain, also the east verge of Qinghai-Tibet Plateau. Local thunderstorms in summer season are quite frequent in this region and appear often to have special electrical structure. Lower positive charge large in amount and spread in dimension often exists in the bottom of thundercloud during its development. Triggered lightning technique in this condition provides an effective means to investigate the mechanism of positive lightning discharge.

Lightning triggering facilities and measuring system in 1997 experiment were similar to those used in previous years in China (Liu and Zhang, 1998), but added more advanced measuring instruments. Both 'classical' and 'altitude' triggering technique were used in the experiment, for the latter the lower end of still wire trailed by ascending rocket attached through a length of isolated nylon line to the ground. In this way the initiation of downward step leader of natural lightning can be simulated more truly. Lightning current was measured with a shunt(5.47 m Ω), fiber optical link and 8 channel DL708 digital recorder system operating at 10 MHz sampling rate, 12 bit resolution and 8 Mb/channel memory. The digital recorder was placed in the rocket igniting and instrumentation room located 80m away from the rocket launcher. Besides coaxial shunt a Hall effect device and Rogowski coil were also used for current measurement. In the instrumentation room also placed were instruments for measuring E-field, field change and step voltage caused by triggered lightning discharge. The electric field change was measured by a slow antenna system with 100 ms integrator time constant. The signal was recorded also in the DL708 digital recorder synchronized with lightning current. At a distance of 780m away from rocket launcher there were automatic lightning discharge progressing feature observation system(ALPS), streak camera, slow antenna and a wide bandwidth interferometer system. In addition an EG&G Reticon CCD high speed digital camera system was placed at a distance of 3.5 km away from the rocket launcher. The camera is operating in a 256 ×256 CCD array in synchronous mode with 1000 f/s framing rate and 0.08 shutter time. The total recording period of the high speed digital camera can be as long as 2s.

DATA AND ANALYSIS

A multi-cell thunderstorm, identified by a 5cm weather radar located 15 km away from the experiment site, developed on the northwest in the afternoon on July 26, 1997. The storm was approaching the site around 15:40 BT( Beijing Time). Evolution of ground E-field measured by a field mill near the triggered lightning channel showed that the ground E-field was dominated by bottom positive charge of thundercloud during active stage of storm development. Total of four rockets were launched in attempting to trigger lightning. Among them 9703 at 16:02:21 BT and 9704 at 16:09:49 BT were successful respectively.

Altitude triggering technique was used in the case of 9703, in which the still wire in a length of 486m trailed by rocket was connected via a length of 86m nylon line and another piece of 30m still wire to the shunt and current measuring system. The triggering height of 9703 event was 550m (the altitude of rocket lifted when triggering occurred). Fig. 1 shows the record of base channel current , relative step voltage and relative luminosity, the latter was obtained by the high speed digital camera at the distance of 3.5 km away from triggered lightning channel. It can be seen that there was good correlation between current, step voltage and relative luminosity.

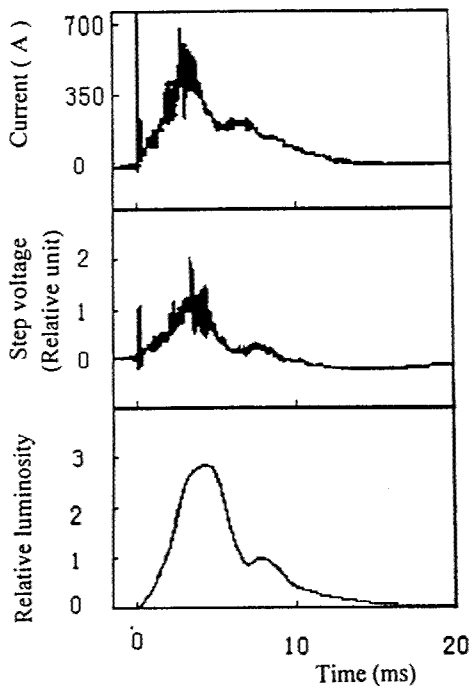


Fig.1 Record of current, step voltage and relative luminosity for triggered lightning 9703

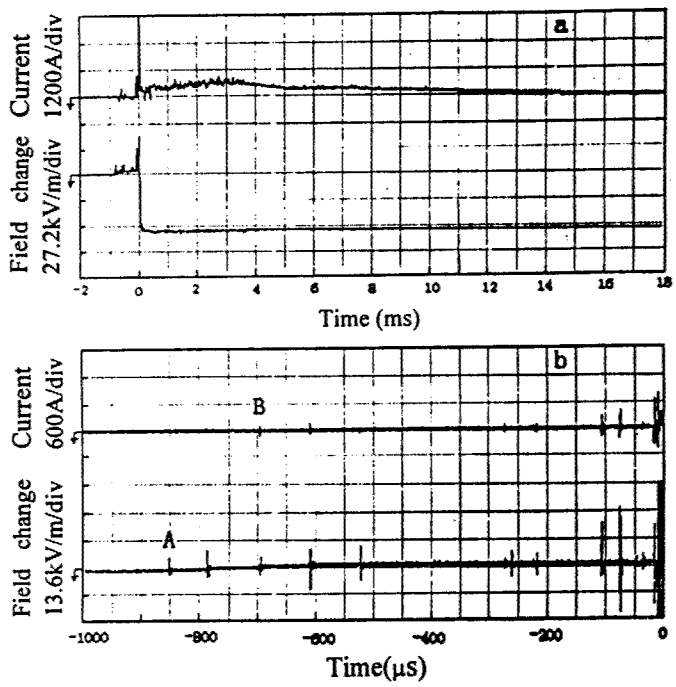


Fig. 2 Current and electric field change records of altitude-triggered lightning flash 9703 (a) and their expanded scale view before the time origin "0" (b)

A sharp peak appears at the beginning of current record with the amplitude of over 1 kA. The peak consists of oscillating pulses as viewed from the expanded time scale which lasted only several tens microsecond. The high speed digital camera operating at the time resolution of 1 ms was not able to capture those pulses. The current starts to increase after the initial peak and reaches the main peak in 3-4 ms with the amplitude of 600 A. The triggered lightning lasted only about 15 ms and appeared to be a small continuously discharging process without return strokes. In fig.2 shown are a simultaneous records of current and E-field change measured at the distance of 70 m from lightning channel (a) and its expanded time scale view before the time origin 'o' (b) respectively. The downward positive leader was inferred to start from the lower end of aloft steel wire at the moment 'A' as shown in the fig. 2(b). This fact can be easily understood because that positive streamer can produce and self-sustaining propagation at lower ambient field compared with that of negative streamer. The negative leader should produce at the upper end of elevated steel wire thereafter and propagate towards the thundercloud simultaneously with downward positive leader. An attached negative leader produces at the moment 'B', which lagged 160 μs of the moment 'A', from the upper end of the grounded steel wire under the action of downward positive leader. The attachment process lasted about 700 μs and followed a junction process which caused

a surge current when both the downward positive leader and upward negative leader met together at the moment 'o' as shown in the fig. 2(b). The junction process, also identified as initial peak of current record in the fig. 1 and fig. 2(a), was regarded as return stroke by Uman et al (Uman et al. 1997). Its characteristic is similar in some respects to but actually different from in the strict sense that of natural lightning, because the dowmward positive leader originated not from thundercloud.

The initiation of both downward positive leader and upward negative leader and their bi-directional propagation can be easily seen in the high speed digital camera record. Fig. 3 shows the high speed camera pictures in the initial two frames with the vertical visual field about 1200 m and time interval of 1 ms. The distinct luminescence can be seen emerged from both end of aloft steel wire[fig. 3 (a)]. The luminescent part aloft was the upward-going negative leader initiated from upper end of the wire which had reached at the height of 550 m, while the lower one was the downward-moving leader which already attached to the upward-going negative leader initiated from upper end of grounded wire. There was no detectable luminosity in most part of aloft wire between the luminous segments, indicating that the current flowing through this portion of the wire at the moment was not large enough to vaporize it. This fact implied that the current density along the channel was not uniform at the moment when downward leader touched the ground. To the best of our knowledge, this is the only picture up to date showing the simultaneous propagation of bi-directional leader. However the duration of bi-directional leader propagation was less than 1 ms. Fig. 3(b) shows the next picture of the flash which was taken 1 ms later. The luminosity of the leader channel increased significantly implying that the negative leader current flowing upward along the aloft wire had been large enough at this moment and the physical process thereafter was similar to that of classical triggering. The top front of the negative leader had reached the altitude of 1000 m and a branch appeared at the height of 625 m. The successive pictures exhibit (not shown here) that the leader propagated upward continuously thereafter (Wang et al. 1998).

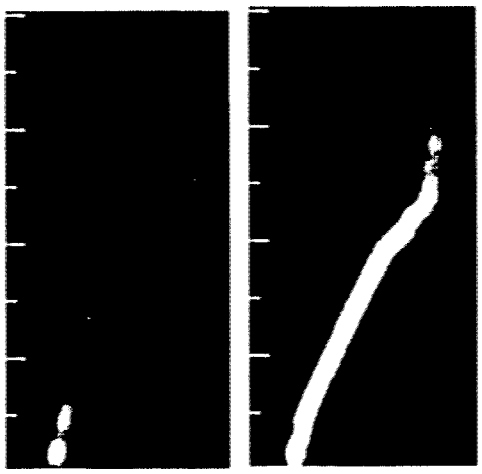

Fig. 3 High speed digital camera pictures of initial leader of triggered lightning flash 9703 (a), (b).

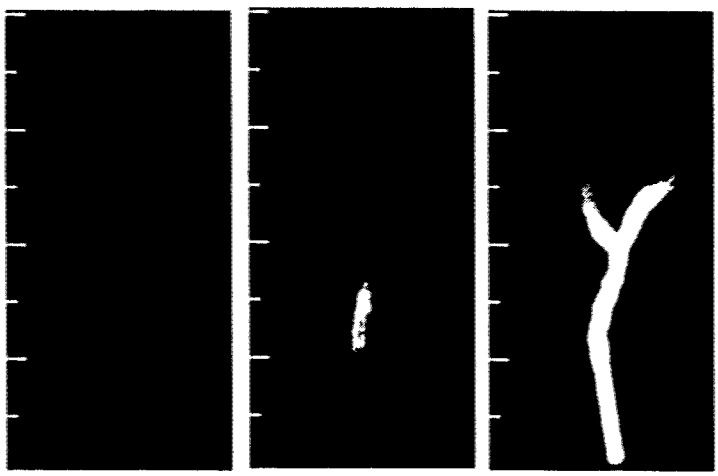

Fig. 4 Same as fig. 4 but for the grounded-triggered lightning flash 9704 (a), (b), (c).

The 9704 event was a traditional grounded triggered lightning flash. Fig. 4(a)-(c) are pictures of its initial leader. In the fig. 4(a) shown was the onset of the upward-going negative leader which was originated from the top of grounded wire in the height about 300 m and was very dim in luminosity. One ms later its front reached 600 m and a branch appeared[fig. 4(b)]. The wire was not luminous due to low current. Fig. 4(c) is the picture of the next millisecond, the leader progressed upwards for more than 300 m and the third branch occurred. The leader current at that time was already strong enough to vaporize the wire and make it luminous brilliantly. The record of current (not shown here) reveals that the event 9704 was also a small lightning flash with the characteristics similar to those in the northern China (Liu et al. 1994).

## CONCLUSION AND DISCUSSION

The main results of 1997 triggered lightning experiment have been presented and analyzed in this paper, with the emphasis on the characteristics of an altitude triggered lightning flash. The bi-directional propagation of both the positive and negative leader was identified by the simultaneous electric and photographic observation. The results of this paper

differ from that conceptualized by Mazur and Ruhnke (Mazur and Ruhnke, 1993). They emphasized the 'screening effect' of leader branches in the upper level on the lower parts of lightning channel, which results in current cutoff and the accumulation of charges with opposite polarity and finally leads to the occurrence of bi-directional leader. In our case, the upward-going leader did produce a lot of branches on its way to cloud, but there was no evidence showing the current cutoff in the lower parts of the channel and the production of bi-directional leader in this way. The concept of bi-directional leader of altitude triggered lightning is different from that of natural lightning, which should be verified by further observation.

ACKNOWLEDGEMENTS: This work was supported by the Chinese Academy of Sciences, the Natural Science Foundation of China and Japanese Ministry of Education, Science and Culture.

REFERENCES

Liu, X., and Y. Zhang, Review of artificially triggered lightning study in China, T. IEE Japan, 118-B, 24-29, 1998.

Liu, X., C. Wang, Y. Zhang, Q. Xiao, D. Wang, Z. Zhou and C. Guo, Experiment of artificially triggering lightning in China, J. Geophys. Res., 99, 10727-10731, 1994.

Mazur V, and L. H. Ruhnke, Common physical processes in natural and artificially triggered lightning, J. Geophys. Res., 98, 12913-12930, 1993.

Uman M. A., V. A. Rakov, K. J. Rambo, T. W. Vaught, M. I. Fernandez, D. J. Cordier, R. M. Chandler, R. Bernstein, and C. Golden, Triggered lightning experiments at Camp Blinding, Florida (1993-1995), T. IEE Japan, 117-B, 446-452, 1997.

Wang C., X. Liu, W. Dong, C. Zhang and Q. Xiao, The initiation and propagation of lightning leader in positive ambient elecctric field, Plateau Meterology, 17,66-74, 1998 (in Chinese).

# Verification of Bi-directional Leader Concept Using Interferometric Measurement

Sachi Yoshihashi Zen Kawasaki

Department of Electrical Engineering
Faculty of Engineering, Osaka University
Yamada-Oka 2-1, Suita Osaka 565 0871, JAPAN

**Abstract.** Bi-directional leader concept is discussed from the aspects of field observations. For this purpose field observations are conducted during winter and summer thunderstorm seasons at Hokuriku in Japan and Darwin in Australia respectively. The main instrument presented in this paper is UHF interferometers, and 2D and 3D lightning channel images are shown in terms of UHF radiation sources. Currents of lightning discharges triggered from a tip of a high artificial construction are measured to confirm the polarity of upward initiating leaders, and features of UHF radiation depending on the polarity are given. Three-dimensional UHF radiation source images during leader progression for "negative" and "positive" cloud-to-ground flashes are shown, and the correctness of the bi-directional leader concept is shown.

## 1 Introduction

Figure 1 shows a lightning strike that is triggered by an ascending airplane. It is noticed that there are branches both above and below the airplane. This means both the upward and downward propagating leaders are initiated by the airplane summltaniously. Since a flying airplane is not grounded to the earth, original charges on the airplane should be conserved during leader development phase. To concerve the charges it is required that negative and positive leaders are initiated simultaniously and propagated to opposite directions. It is believed to be "Bi-directional leader concept". To evaluate the Bi-directional leader concept field observations are carried out during summer and winter thunderstorm seasons. The campaign sites for summer observations are at Darwin in Australia, and for winter at Hokuriku Coast in Japan.The discussion is mainly based on the interpretation of 2D and 3D images of UHF radiation sources by means of interferometers. The lightning current measurements on a top of a tower are used to confirm the polarity of upward initiating leaders and features of UHF radiaion. Radiation source images during "negative" and "positive" leader developing stages are given to support the correctness of the bi-directional leader concept.

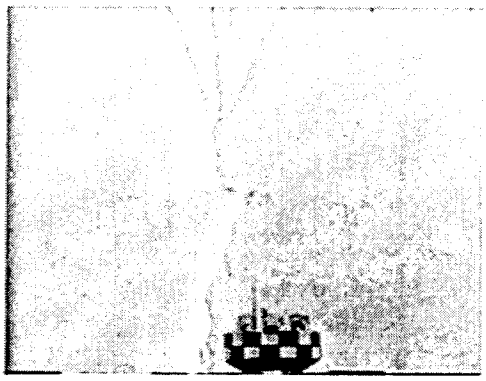

Fig. 1 A lightning strike that is triggered by an ascending airplane

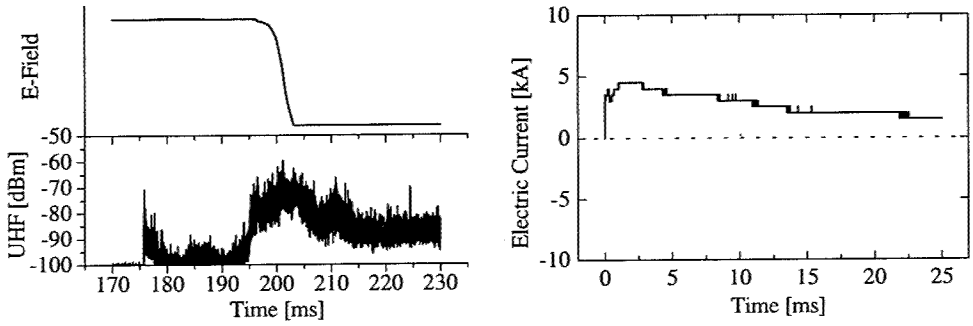


(a) Electric filed change and UHF radiation (b) Electric current

Fig. 2 Negative upward leader

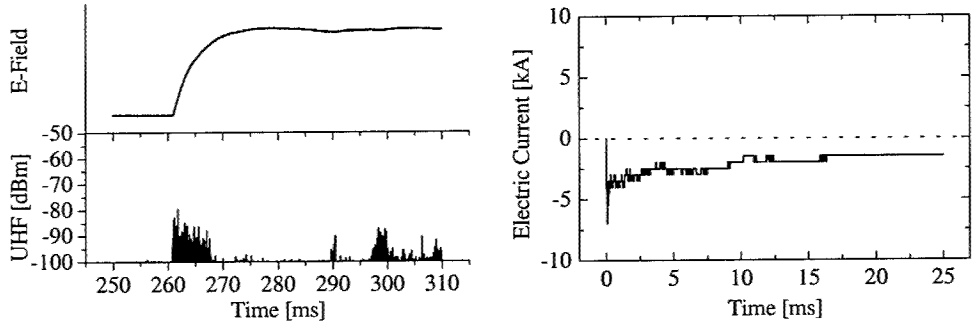


(a) Electric filed change and UHF radiation (b) Electric current

Fig. 3 Positive upward leader

## 2 UHF radiation of upward initiated discharges

The currents, electric field changes and UHF radiation of upward initiating lightning discharges from the tower tip toward thunderclouds are shown in Figure2 and 3. We apply the traditional atmospheric convention to present electric field changes in this paper, and the negative field change means the lowering positive charges toward the ground. The event of Figure 2 corresponds to the positive charges lowered and the event of Figure 3 negative charges lowered.

The UHF radiation for the positive upward leader shows the features of shorter duration than those of the negative one. The maximum amplitudes of the currents for positive and negative upward leaders are -7.0 kA and 4.5kA respectively. Though the amplitude of the current for the positive leader are larger than that of the negative one, UHF radiation intensity for the former is 10dBm weaker than that of the latter.

We know that the UHF radiations associated with negative leader progressions are stronger than those of positive leader through our experiences, and the results presented here show no contradictions at all. During the laser triggered lightning experiment we obtained the upward positive leader, and the features are the consistent with the above presented results.

## 3 Result of Interferometer observations

**3.1 Negative cloud-to-ground strike** An image of a lightning channel in three-dimension (3D) is realized by observations using two sets of UHF interferometers. As one of examples of observations for negative CG strikes during summer thunderstorms is shown in Figure 4(a) and (b). Figure 4(a) shows the electric field change and the UHF radiation intensity. It is obvious that the features of UHF radiation which we can see in Figure 4(a) are typical for negative CG. Figure 4(b) shows the 3D channel image of the leader. It is clear that we can see the propagation of the leader channel, time sequence and a touch down to the ground. We can conclude that these are the same to the previous observations by other investigators.

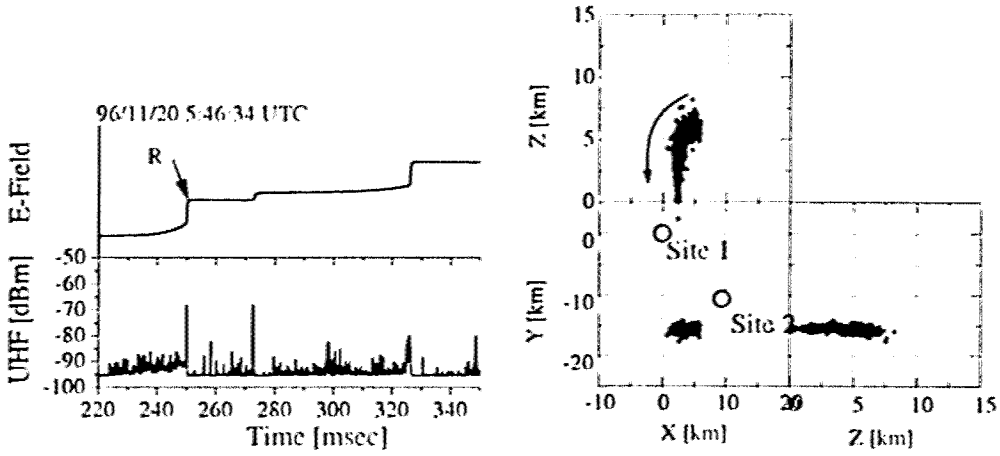


(a) Electric filed change and UHF radiation (b) 3D images

Fig. 4 Negative CG flash

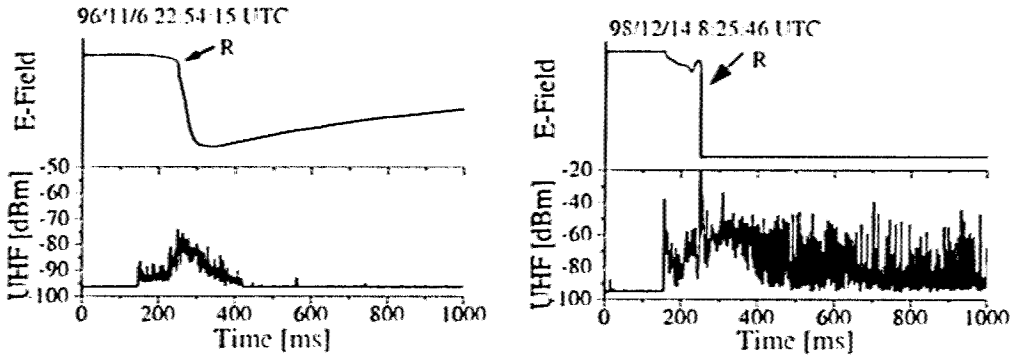


(a) Summer thunderstorm (b) Winter thunderstorm

Fig. 5 Electric field change and UHF radiation of positive CG flashes

**3.2 Positive cloud-to-ground strike** The electric field change and UHF radiation associated with positive CG flashes during summer and winter thunderstorm are shown in Figure 5(a) and (b). It is noticed that the UHF radiation intensity increases immeadiately after retrun strokes, and this phenomenon is discovered by authors. Figure 6(a) and (b) show the mapping of UHF radiation sources corresponds to the leader progression phase. It is interesting that the performance of UHF radiation source location and time sequence during positive leader propagation is completely different from those of the negative leader that we can see in Figure 4(b). If we think about the traditional senario of leader progressions, it should be uni-directional. That means in case of the negative CG we have the negative leader progression, and in case of positive CG we have the positive leader progression and/or time sequence. If this is true, we can see only UHF radiation sources for negative CG, because we know the intensity associated with the positive leader is rather weak as shown in the previous section. However we can still see the UHF radiation sources even during leader progression for positive CG.It is noticed that the time sequence is quite different between negative and positive leaders as we can see in Figure 4 (b) and Figure 6. To interpret above mentioned discrepancy we have no way except accepting the concep of the bi-directional leader progression. During the positive downward leader development the upward negative leader may exist to conserve the charge at the point where the initiation of the leader occures. According to our model both positive and negative leaders should exist, but the intensity of UHF radiation by negative leader is stronger than that of positive one. That is why we can see only the radiation sources associated with negative leader progression. Figure 7 shows a model of the positive leader progression to interpret the concept the bi-directional progression. Moreover it is noticed that the veloicty of the negative leader progression is ten times faster than that of the positive

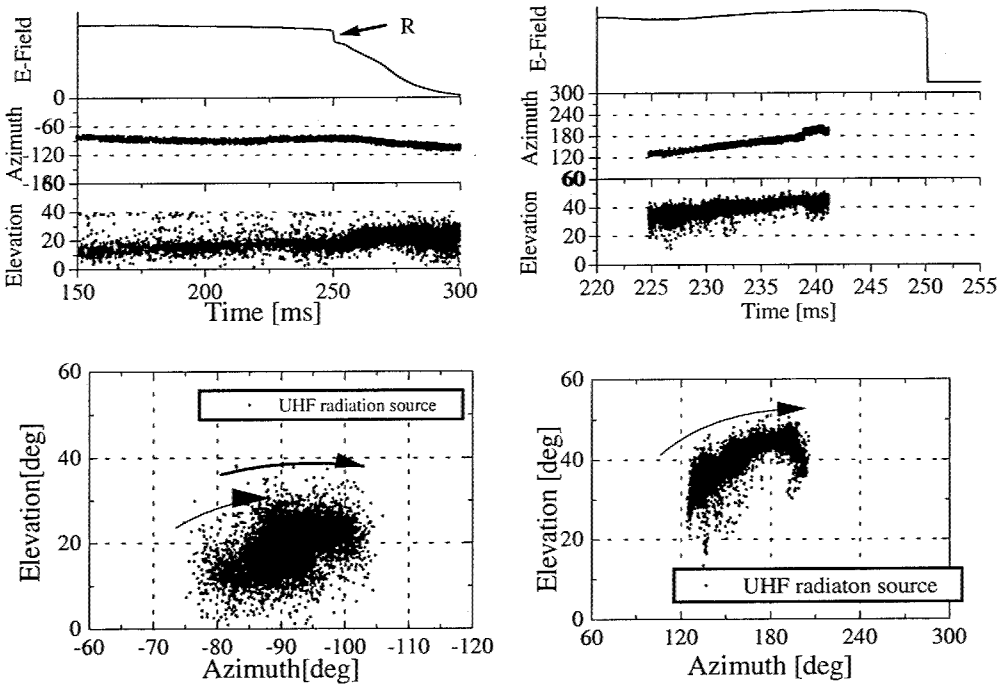


(a) Summer thunderstorm (b) Winter thunderstorm

Fig. 6 The mapping results of positive CG flashes

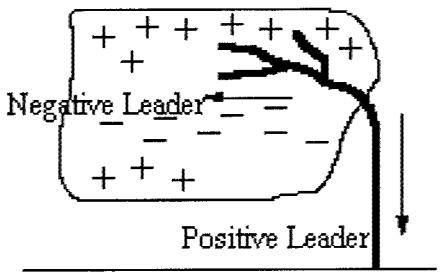


Fig. 7 A model of the positive leader progression

leader. This feature explains that the negative leader is more visible than the positive leader.

## 4 Conclusions

This paper presented characteristics of UHF radiation of upward initiating lightning strikes from the tower tip toward the thundercloud, and showed UHF radiation source mapping during leader progression for positive and negative CG strikes by interferometers in three dimensions. For negative CG we see the ordinary leader development, and for positive CG we see rather stationary and scattered radiation sources. We imagine UHF radiation sources are due to negative leader in both cases, and we can not see the tip of a positive leader. We can conclude that the concept of the bi-directional leader is correct from the aspects of observations by interferometers.

## References

Wada, M., Z-I. Kawasaki, K. Matsuura, T. Matsui, T. Musasiya, and K. Yamamoto, UHF Interferometer System and Observation of Lightning Discharge, T.IEE Japan, 116B, No.1, 322-331, 1996( in Japanese)

Ohnuki J., Z-I. Kawasaki, M. Wada, K. Matsuura, T. Matsui and M. Adachi, 3D imaging of lightning channels by means of interferometers, T.IEE Japan, 116B, No.4, 475-481, 1996(in Japanese)

Kawasaki, Z-I., V. Mazur, Common Physical Processes in Natural and Triggered Lightning in Winter Storms in Japan, J. Geophys. Res., .97, 12935-12945, 1992

# ON LIGHTNING CURRENT PROBABILITY DISTRIBUTION FROM SOUTHEASTERN BRAZILIAN MEASUREMENTS

O. Mendes Jr.[1], M. O. Domingues[2], I. R. C. A. Pinto[1], O. Pinto Jr.[1], J. H. Diniz[3], A. M., Carvalho[3], A. M., Cazetta[3]

[1]Divisão de Geofísica Espacial, Instituto Nacional de Pesquisas Espaciais (INPE), Brazil
[2]Divisão de Ciências Meteorológicas, INPE, Brazil
[3]Companhia Energética de Minas Gerais (CEMIG), Brazil

ABSTRACT: The estimated peak-current amplitude of brazilian southeastern lightning occurrences measured by LPATS, from 1988 to 1995, is analysed here. So the Log Normal and the three parameter Weibull Probability Density Functions are used to investigate this data set. This work identified $\sim 62\%$ of negative, $\sim 37\%$ of positive and $\sim 1\%$, of bipolar lightning flashes. The mode of negative flashes is higher than the mode of positive ones. All lightning current distributions are leptokurtic distributions. The Log Normal PDF fits better this current data set than the three parameter Weibull PDF. However, in consequence of its representative behaviour, the last one could be very usefull as an index for classification of thunderstorm events.

## INTRODUCTION

In a few words, lightning consists basically of a high current ($\sim kA$), transient atmospheric electric discharge with a path length of about several kilometers. It is a consequence of a great amount of electric charge ($\sim 10 - 100C$) accumulated in the thunderclouds (cumulonimbus) and it occurs when the electric field exceeds locally the electric air insulation ($> 400\,kV/m$) – (Uman, 1987). Most of the fundamental physical processes of lightning are not well known yet. However a great amount of natural phenomena seem to follow a probability distribution function (PDF). So sometimes when an adequate PDF can be achieved, hidden physical mechanisms could be investigated or specific features could be quantified.

Adding a contribution to this understanding, this paper aims to examine two distribution functions: the more commonly used Log Normal PDF (Wilks, 1995) and the recently improved three parameter Weibull PDF (Qiao and Tsokos, 1994, 1995). They are used to analyze the estimated peak-current amplitude of lightning flashes measured in the period from 1988 to 1995 in a wide region of the Southeastern Brazil. Thus concerning to the current distribution a result from the PDF comparison and some features of lightning are presented here.

## DATA

During the last two decades, detection and location systems have been used in different parts of the world to determine the characteristics of cloud to ground lightning flashes. One of these systems, the Lightning Positioning and Tracking System (LPATS), is based on time-of-arrival of lightning electric signature (Bent and Lyons, 1984). This system records data of return stroke, which consist of date, time, sensors used to resolve stroke, latitude, longitude and estimated peak-current amplitude.

The data set used in this work, October–March (warm season) from 1988 – 1989 to 1994 – 1995, are from the Companhia Energética de Minas Gerais (CEMIG), Minas Gerais, Brazil. In this period the system worked with four sensors under the same technical condition (Diniz et al., 1996). In this work the region of strokes was limited to 14 – 23°S and 39 – 52°W to take advantage of estimated global efficiency of LPATS ($> 50\%$).

Lightning phenomena should be analysed as a whole because strokes are not an isolated element in the physical processes. For these analyses it was necessary to recuperate lightning flashes from

stroke records through a numerical process, named lightning classification (Mendes and Domingues, 1998). So the following empirical criteria were adopted for the time and distance between strokes: subsequent strokes in a flash were considered to be within $500ms$ of the previous stroke and within $2s$ and $10km$ of the first stroke (Cook and Casper, 1992; Pinto et al., 1996). In this classification no restriction was imposed on the polarity of subsequent strokes, allowing to join strokes with different polarities in the same lightning (the so called bipolar lightning). For positive lightning perhaps a contamination by non–cloud–to–ground lightning occurs below $15kA$ (Zaima et al., 1997). However, no correction for this effect is made here.

## METHODOLOGY

PDFs are abstract mathematical tools used to represent feature distribution of elements or events in a set of occurrences. Several PDFs have the properties of nonnegativity and positive skewness, that provide the adequate shape for the representation of lightning distributions. Among them there are: (1) the commonly used Log–normal PDF and (2) the flexible but laborious three parameter Weibull PDF.

The Log-Normal PDF is written as:

$$g(x;\sigma,\mu) = \frac{1}{x\,\sigma\sqrt{2\,\pi}} \exp\left[-\frac{(\log x - \mu)^2}{2\,\sigma^2}\right], \tag{1}$$

where $x$ is the variable, $\mu$ and $\sigma$ are the mean and standard deviation, respectively, of the variable $\log(x)$. It is often used in lightning research in order to provide distributions of some lightning measurements (Cianos and Pierce, 1972; Uman, 1987).

The other function is the Weibull PDF written as:

$$f(x;x_0,\alpha,\beta) = \alpha\frac{(x-x_0)^{\alpha-1}}{\beta^\alpha} \exp\left[-\left(\frac{x-x_0}{\beta}\right)^\alpha\right], \tag{2}$$

where $x$ is the variable, $x_0$, $\alpha$ and $\beta$ are the location, shape and scale parameters, respectively, and $(x - x_0) \geq 0$, $\alpha > 0$, $\beta > 0$. It has the advantage of having three adjustable parameters which allow to model satisfactorily several sets of measured data; but fitting parameters for the Weibull distribution requires interative methods. Recently this PDF was improved by new techninques of parameter estimation (Qiao and Tsokos, 1994, 1995).

So this work uses a large data set and does a lightning classification before any stroke distribution analysis. Next, using this adequate approach, it takes into account the single stroke flashes and the first to the fifth stroke of multiple stroke flashes for both positive and negative lightning. Finally, concerning to the estimated peak-current distribution this work examines those distribution functions, analysing the performances and some characteristics, and also allows to obtain some features of these brazilian lightning.

## RESULTS AND DISCUSSIONS

This eigth year analysis identified $4,951,480$ flashes: $\sim$ 62% of negative polarity, $\sim$ 37% of positive polarity and $\sim$ 1% of bipolar polarity lightning. Due to the ambiguity and small percentage of bipolar lightning, only the negative and positive lightning are considered in this study.

Lightning flashes can be formed by multiple strokes. Figure 1 presents the distribution of strokes per flash. The $\sim$ 69% of lightning flashes consist of only one stroke (single stroke). Negative flashes present more multiple events than the positive ones. Although the multiplicity distribution for negative flashes seems to obey a discrete exponential-kind PDF, a fitting for multiplicity was not found yet.

Figures 2 and 3 present the current distribution for negative and positive flashes, respectively. According to the importance of the multiplicity discussed earlier, from the identified lightning flashes the first five strokes in multiple flashes and the single stroke are analysed. All distribution are leptokurtic, although the shapes of higher order strokes seem to be platykurtic due to the figure scale. The mode of higher order strokes presents a tendency to shift slightly to low values of current. For all order of stroke in negative lightning the mode ($\sim 20\,kA$) is higher than the mode for positive lightning ($\sim 10\,kA$).

Table 1 shows the calculated distribution parameters of Log Normal and three parameter Weibull PDF for negative flashes. For positive flashes there is a similar result. A calculation is made for negative and positive flashes taking into account the first five and three strokes, respectively. The Log-Normal PDF gives a better fit to the analysed data set than the three parameter Weibull (an example is shown in Figure 4).

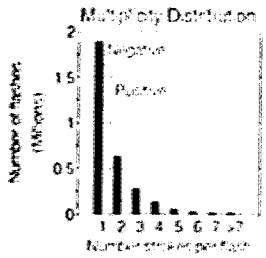


Figure 1. Flash Distribution.

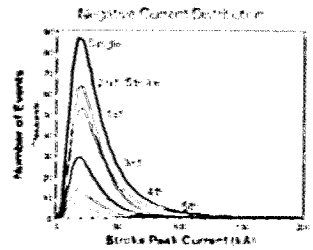


Figure 2. Negative Current Distribution.

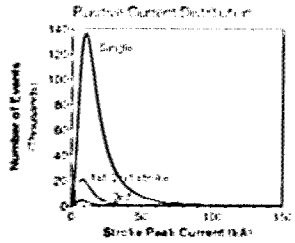


Figure 3. Positive Current Distribution.

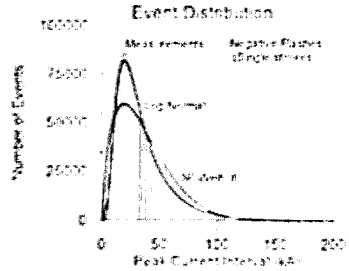


Figure 4. PDFs.

TABLE 1. Parameters of Probability Density Function from Negative Flashes, Oct. Mar., 1988 1995.

| Stroke | Log Normal | | 3p Weibull | | |
|---|---|---|---|---|---|
| | $\mu$ | $\sigma$ | $x_0$ | $\alpha$ | $\beta$ |
| Single | 1.453 | 0.292 | $\sim 5$ | 1.427 | 38.713 |
| $1^{st}$ | 1.478 | 0.286 | $\sim 5$ | 1.449 | 40.896 |
| $2^{nd}$ | 1.413 | 0.242 | $\sim 5$ | 1.768 | 33.196 |
| $3^{rd}$ | 1.404 | 0.247 | $\sim 5$ | 1.721 | 32.668 |
| $4^{th}$ | 1.393 | 0.256 | $\sim 5$ | 1.651 | 32.241 |
| $5^{th}$ | 1.379 | 0.257 | $\sim 5$ | 1.635 | 31.201 |

## CONCLUSIONS

The data distribution shows that for all order of stroke the mode of negative ligthning is higher than the mode for positive lightning and the mode of higher order strokes shift slightly to lower values of current. All strokes present leptokurtic distribution.

The Log–Normal PDF fits better this current data set than the three parameters Weibull PDF. However, in consequence of its representative behaviour, the last one could be very usefull as an index for classification of thunderstorm events.

So this work motivates the investigation of other physical features of lightning and also contributes to a preliminary picture of climatology of lightning in brazilian region.

## ACKNOWLEDGEMENTS:

One of the authors (Dr. Odim Mendes Jr.) wishes to thank FAPESP for support under grant 1998 – 3860 – 9.

## REFERENCES:

Bent, R. B.; Lyons, W. A. Theoretical Evaluations and Initial Operational Experiences of LPATS (Lightning Position and Tracking System) to Monitor Lightning Ground Strikes using a Time–of–Arrival (TOA) Technique. VII International Conference on Atmospheric Electricity. Proceedings. 317–324. American Meteorological Society, 1984.

Cianos, N.; Pierce, E. T. A ground-lightning Environment for Engineering Usage. Stanford Research Institute Project 1834, Technical Report 1, Stanford Research Institute, Menlo Park, California 94025, Aug. 1972.

Cook, B.; Casper, P. U.S.A. National Lightning Data Service. In: Proc. Int. Conf. Lightning Prot., 21:351–356, 1992.

Diniz, J. H.; Carvalho, A. M.; Cherchiglia, L. C.; Filho, J. J. S.; Amorim, G. E. S. Lightning Research Carried out by Companhia Energética de Minas Gerais–Brazil. International Conference on Lightning Protection (JCLP). Proceedings. Firenze, Italy, 1996.

Mendes, O. Jr.; Domingues, M. O. Algoritmo Eficiente de Classificação de Relâmpagos. XX Congresso Nacional de Matemática Aplicada e Computacional. Proceedings. Caxambu, Minas Gerais, 14-18 de setembro, 1998.

Qiao, H.; Tsokos, C. P. Parameter Estimation of the weibull probability distribution. Mathematics and Computers in Simulation, 37:47–55, 1994.

Qiao, H.; Tsokos, C. P. Estimation of the three parameter weibull probability distribution. Mathematics and Computers in Simulation, 39:173-185, 1995.

Pinto, O. Jr.; Gin, R. B. B.; Pinto, I. R. C. A.; Mendes, O. Jr. Cloud–to–ground lightning flash characteristics in Southeastern Brazil for the 1882-1993 summer season. Journal of Geophysical Research,101(D23):29,627–29,635, 1996.

Uman, M. A. The lightning discharge. International Geophysics Series, 39. Florida, Academic Press. pp. 377, 1987.

Wilks, D. Statistical Method in the Atmospheric Sciences. New York, Academic Press. pp. 467, 1995.

Zaima, E. I.; Mochizuki, A.; Fukiyama, N.; Hojo, J. I.; Ishii, M. Observations of Lightning Location System. Electrical Engineering in Japan, 120(1):9-15, 1997.

# ANALYSIS OF NEGATIVE DOWNWARD LIGHTNING CURRENT CURVES FROM 1985 TO 1994 AT MORRO DO CACHIMBO RESEARCH STATION (BRAZIL)

Moacir Lacerda[1], Osmar Pinto Jr.[1], Iara R.C.A. Pinto[1], José H. Diniz[2] and André M.Carvalho[2]
[1]Instituto Nacional de Pesquisas Espaciais-INPE, São José dos Campos, SP-Brazil
[2]Companhia Energética de Minas Gerais (CEMIG)Belo Horizonte, MG-Brazil

ABSTRACT: This paper presents an analysis of negative descendent cloud to ground lightning captured by a 60 m metalic tower between 1985 and 1994 in the "Morro do Cachimbo", research station (43° 58' 26" W, 20° 00'39" S) of the Companhia Energética de Minas Gerais (CEMIG), Brazil. From the comparison of return strokes with those of another station in Switzerland, it was noted that electric current wave forms are similar in both countries, although the mean peak current in Brazil (41 kA) is greater than that in Switzerland (30 kA) and the time to peak is greater in Brazil (22 μs) than in Switzerland (13 μs). Differences in subsequent strokes were observed too. It was found that the time to peak current is correlated to the time to peak of derivative current with a linear correlation coeficient of about 94%.The mean third return stroke current was found to be stronger than the second and an explanation for that was suggested. M-components recorded at about 200 μs (geometric mean peak current of 2.37 kA) had time to peak lower than those obtained after 1 ms in Florida and Alabama.

## INTRODUCTION

We analyze electric current waveform of 22 negative downward lightning obtained in the CEMIG LIGHTNING RESEARCH STATION (CLRS) in Brazil, between 25/Nov/1985 and 26/Feb/1994. To analyze that, we repeat the same method used for Berger et al (1975) in Switzerland to obtain average curves and then compare both results. The CLRS was acquired from the National Electric Engineering Research Institute (NEERI), Pretoria, South Africa, and installed under orientation of Dr. A. J. Eriksson, and allow to record: a) lightning ground flash activity; b) atmospheric electric field; c) photographic records and video images of lightning within view of two video cameras; d) current waveform and current wavefront to a metallic tower. A 60 m metallic tower is located on the top of a mountain about 1600 m above sea level and 200 m above any other mountain in the region. It captures the discharge and conductes the electric current through a transformer that generates a voltage proportional to the current, before to dissipate it on ground. (NEERI, 1985). The precision in measurements of current and time was initially 760 A and 1 μs and now is 116 A and 0.2 μs, respectively. The data are digitized and stored in a 32 bit HP computer. The collected discharges were summarized by Diniz et al. (1995): 63 discharges (mean number of discharge for year, 7) with 27 (43%) of the negative downward type; there were 17 (63%) negative discharge with only one stroke and 10 (37%) with more than one; median peak current for first and subsequent strokes were 41.3 kA and 16.0 kA respectivly; the mean density of dischage in the region was 5.5 disc./km$^2$/year.

## RESULTS

A) Average curves. To obtain average curves we considered 22 descendent negative discharge, corresponding to 22 first strokes and 50 subsequent strokes. In figures 1a and 2a we show average curves without normalization for CLRS first and subsequent strokes, respectively. We compared the shape of waveform and three parameters were used to characterize these differences: peak current ($I_{peak}$), time to peak ($T_{peak}$) and time to half value ($T_{hpeak}$, the time when $I = 0.5*I_{peak}$, decreasing). Differences are shown in figures 1b and 2b, where normalized curves are presented. For first strokes the inclination of the tail in a mono-log paper are different, although in both cases (Switzerland and Brasil) they are closed to straight lines. In figure 2a we present average curves for all subsequent strokes (full line, 50 strokes), for second (10 strokes) and third strokes (10 strokes). There was no significative difference in shape between curves 1a and 2a when normalized compared with curves 1b and 2b, respectively, obtained using Berger's method of pre-normalize curves before averaging them. Strokes in CLRS showed higher $I_{peak}$ and $T_{peak}$ than Switzerland data for first and subsequent strokes. The values obtained for first strokes were, respectivley:41 kA, 22 μs ($T_{hpeak}$ = 88 μs) in Brazil versus 30 kA, 13 μs ($T_{hpeak}$ =112 μs) for Switzerland and for subsequent 14 kA and 4 μs ($T_{hpeak}$ =60 μs) in Brazil versus 12 kA and 1 μs ($T_{hpeak}$= 37 μs) in Switzerland. The third strokes average waveform presented itself more intense than second in CLRS (Lacerda et al. 1997a, and Lacerda, 1998).

B) Derivative current for first and subsequent strokes. In figures 3a and 3b we show the normalized average derivative current (di/dt) for first and subsequent strokes, respectively. The dashed line is the average normalized current. Peak values used for normalizing curves were around 5.76 kA/μs and 4.92 kA/μs for first and subsquent strokes, respectively. As we used the worst time scale precision for obtaining the derivative current pattern showed

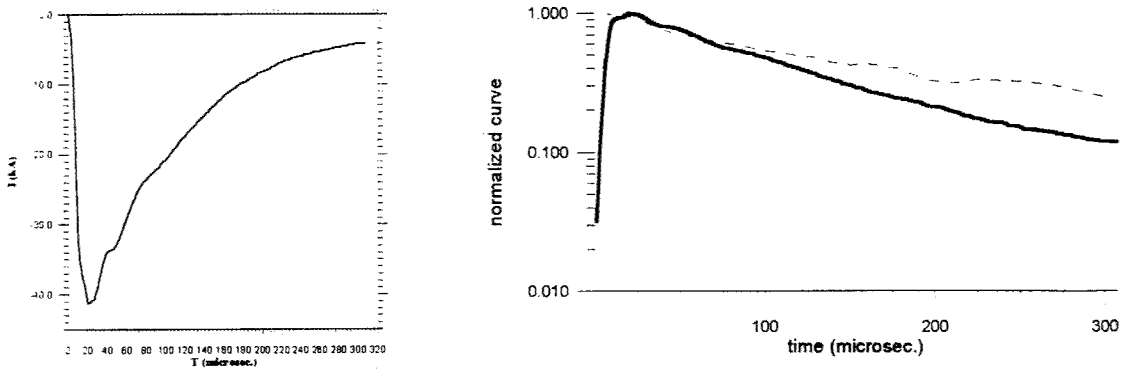


(a) (b)

Figure 1 a) Average waveform for first return strokes of CLRS; b) Comparison of CLRS normalized waveform (full line) with Berger's data (dashed line).

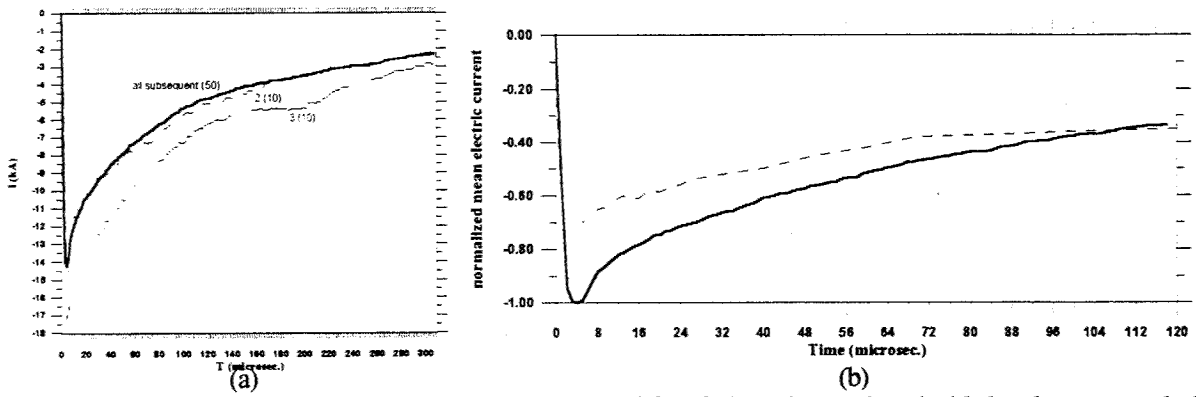


(a) (b)

Figure 2 a) Average waveform for subsequent return strokes of CLRS data; the numbers inside brackets are total of analyzed data and outside brackets refer to the order of stroke; b) Comparison with Berger's data (dashed line) for subsequent normalized waveform.

in figures 3a and 3b, the absolute values of di/dt before normalization are probably underestimated. Mean value for maximum di/dt in subsequent strokes calculated using individual curves is around 32.82 kA/μs (Lacerda et al 1997b). This means that these values may be at least 7 times bigger. Even so, we believe that the normalized pattern obtained is still representative of an average pattern.

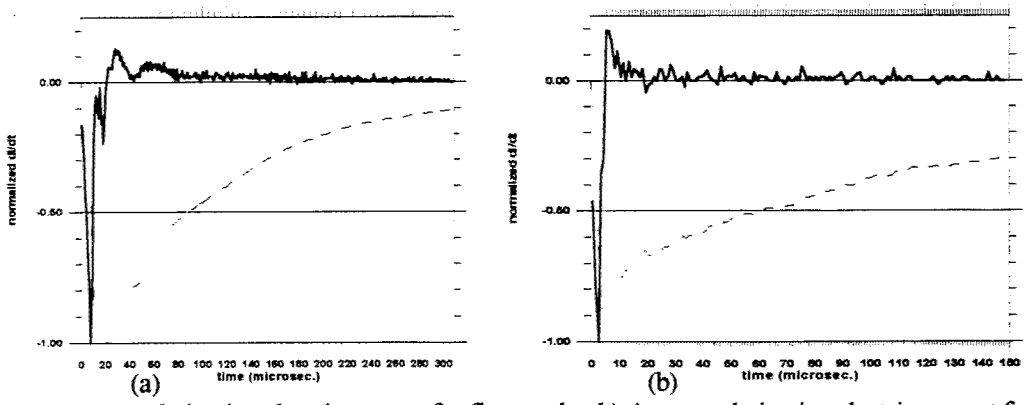


(a) (b)

Figure 3 a) Average derivative electric current for first stroke; b) Average derivative electric current for subsequent strokes; in both cases (a) and (b) dashed lines are curves 1a and 2a normalized.

c) Correlation between $T_{peak}$ and $T_{dm}$; m-components. The figure 4a shows the correlation between $T_{peak}$ and the time when occurs the maximum derivative current for subsequent strokes ($T_{dm}$). The fit equation is $T_{peak}=1.1397*T_{dm}+0.51$, and the coefficient of determination, R-squared is 93,66% (Lacerda et al, 1997b).In 11 return stroke waveforms of subsequent strokes of order higher than 2 we found 13 m-component like those shown in figure 4b,

where two strokes, 4004, and 4005 are presented. A detailed study of all m-component can be found in Lacerda et al (1997c) and Lacerda (1998). In table 3 we summarize the parameters studied and compare them with the same parameters obtained in Florida and Alabama (Fisher et al. 1993). The elapsed time $\Delta t_m$, is the instant of time when the M-component starts after the beginning of return stroke. $I_{cc}$ is the continuing current level. $I_m$ is the magnitude of m component (peak value) (Thottappillil et al. 1995) with mean value of 308.09 µs, 5.03 kA and 3.22 kA respectively.

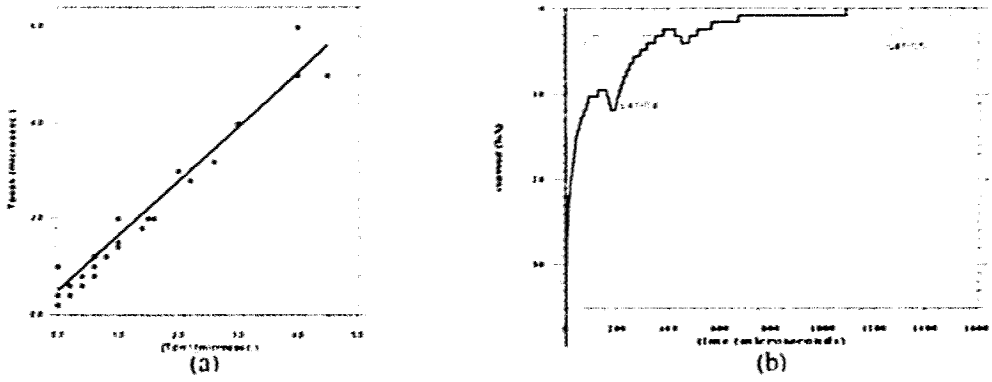

(a) (b)

Figure 4 a)Correlation between the time to peak current ($T_{peak}$) and maximum derivative current ($T_{dm}$); b) Four m-component in 2 strokes. The first two numbers beside the curve represent the discharge and the last two, the stroke.

Geometrical means (GM) are 237.56 µs, 3.69 kA and 2.37 kA, respectively. These differences occur because CLRS m-components are near m-components, while those of Florida and Alabama are far m-components (Lacerda et al 1997c). Near m-components are faster and stronger than the far m-components. The total analyzed data are presented between brackets.

TABLE 1. Parameters of m-component in CLRS compared with Florida and Alabama.

| m-component | $\Delta t_m$ | $I_{cc}$ | $I_m$ | $t_{1/2}$ |
|---|---|---|---|---|
| CLRS | 237.57 µs (13) | 3.69 kA (13) | 2.37 kA (13) | 120 µs (13) |
| Florida | 11 ms (80) | 195 A (55) | 84 A (62) | 874 µs (59) |
| Alabama | 7 ms (78) | 159 A (66) | 164 A (62) | 757 µs (54) |

DISCUSSION

Differences between CLRS and Switzerland data presented in this paper are important because they put several questions: a)are these differences due to systems of measurement used to capture and record data, or they are related to the lightning discharge itself? b) are lightning discharge waveform latitude dependent? c)Will differences remain when we extend data analysis of CLRS to cover the period between 1994 to 1999?The answer to the these questions includes to examine normalized average waveform of other set of data obtained in different conditions (Eriksson, 1979; Garbagnati and Lo Piparo, 1970; Fisher et al. 1993; Zundl, 1994; Montandon and Beyeler, 1994) in order to note the similarities or differences between them and increase data set of CLRS with data collected between 1994 and 1999.Trying to solve the second question, Pinto et al (1997) have argued that peak current may be latitude dependent. Peak current has a value of 40 kA from the equador to the latitude of 30° and a value of 30 kA for higher latitudes (Pinto et al. 1997).Third strokes were more intense than second. Rakov and Uman (1990) found similar result analyzing geometrical mean of electric-field peak. In CLRS all the average curve of third stroke are bigger than second. This fact suggests that may be there is a possible new mechanism not well understood between second and third strokes.The CLRS has collected waveforms in a better precision (116 A x 200 ns) after 1994 and will allow to improve the calculus of di/dt. This result could be used to establish voltage across indutive path in direct strokes, and calculate distant radiation in some particular cases.The instant of time of maximum derivative current is correlated to the instant of peak current. This fact may indicate that the current waveform presentes approximatly the same shape, for all discharges (Lacerda et al. 1997b). Near m-component could be better understood from analysis of current waveform in other research stations. M-components introduce a large variety of rate of increase in current waveform which could difficult the performance of electronic devices used in surge protection systems.

CONCLUSION

In this paper is presented an analysis of negative descendent cloud to ground lightning captured by a 60 m metalic tower between 1985 and 1994 in the "Morro do Cachimbo", research station. The main conclusions of this analysis

are: 1) Strokes in CLRS showed higher $T_{peak}$ and $I_{peak}$ than Switzerland data for first and subsequent strokes average normalized waveforms. The values found are 22 μs, 41 kA, for first strokes, respectively and 4 μs, 14 kA for subsequent strokes, respectively; $T_{hpeak}$ were smaller (88 μs) in first and higher (60 μs) in subsequent strokes than in Switzerland. 2) The third strokes average waveform presented itself more intense than second; 3) The obtained normalized pattern for di/dt was established and even considering that calculated values are underestimated, this average pattern is still representative; 4) Near m-components registered in CLRS are faster and stronger than far m-components registered in Florida and Alabama.

ACKNOWLEDGMENTS: To Fundação de Amparo à Pesquisa do Estado de São Paulo (**FAPESP**) for financial support (project 98/11958-9).We acknowledge all the personnel of CEMIG involved in the project "CAXIMBO", for laborious work in maintaining the Caximbo's station and specially to Eng. Jacinto Soares Filho (in memorian) and Eng. Carlos Alexandre M. do Nascimento. ***This work is dedicated to the memory of Jacinto.***

REFERENCES

Berger, K.; Anderson, R. B.; Kroninger, H. Parameters of lightning flashes. **Electra, v. 41, p.** 23-37, 1975.

Diniz, J.H.; Carvalho, A.M.; Soares Filho, J.J. Parâmetros de descargas atmosféricas: resultados de 9 anos de pesquisa na Estação do Cachimbo período 1985-1994. Relatório nº 02.110 ST/DN1-001 CEMIG, Dez 1995.

Eriksson, A. J. ELEK 189. **The lightning ground flash - an engeneering study**. Pretória. 400 p. South Africa. Thesis (Ph. D. in Philosophy in the Faculty of Engineering) - University of Natal, Dec. 1979.

Fisher, R.J.; Schnetzer, G.H.;Thottappillil, R.; Rakov, V.A.; Uman, M.A.; Goldberg, D.J. Parameters of triggered-lightning flashes in Florida and Alabama. **Journal of Geophysical Research**, 98, D12, 22.887-22.902, Dec. 1993.

Garbagnati, E.; Lo Piparo, G. B. Stazione sperimentale per il relievo delle caratteristiche dei fulmini. **L'Elettrotecnica,** v. 57, n. 7, 1970.

Lacerda,M. **Análise e modelagem de curas de corrente de relâmpagos negativos descendentes entre 1985 e 1994, na Estação de Pesquisa do Morro do Caximbo (MG)**. São José dos Campos. Tese (Doutorado em Ciência Espacial/Geofísica Espacial) - Instituto Nacional de Pesquisas Espaciais, 1998.

Lacerda, M., Pinto Jr., O., Pinto, I. R. C. A., Diniz, J. H., Carvalho, A. M. Direct lightning current measurements in southeastern Brazil I. current waveform. In: Congresso Internacional da Sociedade Brasileira de Geofísica. 5., São Paulo. 1997. **Anais.** São Paulo: 1997a. v. 2, p. 1176-1178.

Lacerda, M., Pinto Jr., O., Pinto, I. R .C. A., Diniz, J. H., Carvalho, A. M. Direct lightning current measurements in southeastern Brazil II. correlations. In: Congresso Internacional da Sociedade Brasileira de Geofísica. 5., São Paulo. 1997. **Anais.** São Paulo: 1997b. v. 2, p. 1179-1181.

Lacerda, M., Pinto Jr., O., Pinto, I. R. C. A., Diniz, J. H., Carvalho, A. M., Direct lightning current measurements in southeastern Brazil III. M-component. In: Congresso Internacional da Sociedade Brasileira de Geofísica. 5., São Paulo. 1997..**Anais.** São Paulo: 1997c. v. 2, p. 1182-1184.

Montandon, E.; Beyeler, B. The lightning measuring equipment on the Swiss PTT Telecommunications tower at St. Chrischona, Switzerland. In: International Conference on Lightning Protection. 22., Budapest, 1997. **Proceedings.** Hungary: 1994. p. R 1c-06.

National Electrical Engineering Research Institute (NEERI). **CEMIG ligthning research station system operation manual: Eletric Power**. Pretoria, South Africa, 1985.

Pinto, O.; Pinto, I.R.C.A.; Lacerda, M.; Carvalho, A.M.; Diniz, J. H.; Cherchiglia, L.C.L. Are equatorial negative lightning flashes more intense than those at higher latitudes? **Journal of Atmospheric and Solar-Terrestrial Physics**, v. 59, n. 15, p. 1881-1883, 1997.

Rakov, V. A., Uman, M. Some properties of negative cloud-to- ground lightnig flashes versus stroke order. **Journal of Geophysical Research,** v. 95, n. D3, p. 5447-5453, Apr. 1990.

Thottappillil, R.; Goldberg , J. D.; Rakov, V., A.;Uman, M.A.; Fisher, R. J., Schnetzer, G. H. Properties of M components from currents measured at triggered lightning channel base. **Journal of Geophysical Research** v. 100, n. D12, p. 25.711-25.720, Dec. 1995.

Zundl, T. First results of the coordinated lightning current and LEMP Measurements at Peissenberg Tower. In: International Conference on Lightning Protection. 22., Budapest, 1997. **Proceedings.** Hungary: 1994. R 1c-09.

# LIGHTNING SUBSEQUENT STROKES PRODUCING NEW TERMINATIONS TO GROUND

Stephen M. Davis and Ewen M. Thomson

University of Florida, Gainesville, FL.

ABSTRACT: We analyze results from 16 flashes to ground containing dE/dt pulse trains prior to subsequent strokes in new terminations. Strokes in new terminations were preceded by leaders that were dart-stepped in nature, producing the observed pulse trains, prior to adopting a new path to ground via a stepped leader. Locations of individual sources in the trains were obtained using the time of arrival method from dE/dt measured at five ground stations. Point-to-point source velocities in trains ranged from $1.0 \times 10^6$ m/s to $1.2 \times 10^7$ m/s. All dE/dt waveforms from strokes creating a new termination to ground contained fine structure after the return stroke peak, similar to that seen in first strokes. However, fine structure accompanying new terminations to ground was shorter, with a median duration of 37 μs, than that of first strokes, median value 141 μs. Sources of fine structure were located in the channel apparently formed by the stepped leader portion of the leader.

## 1. INTRODUCTION

Subsequent leaders in a discharge may adopt a new path to ground (via a stepped leader) and form a new channel near ground [*Schonland et al.*, 1938b; *Schonland*, 1956]. We call this new channel a "new termination". A possible explanation for the observation of multiple channels below cloud base has been proposed by *Thomson et al.* [1984]. Thomson et al. suggested that multiple channels may be due to a subsequent leader following an old channel in the cloud and then branching before reaching cloud base.

*Willett et al.* [1995] found that both first strokes and new terminations to ground exhibit fine structure after the return stroke peak in the dE/dt waveform. Subsequent strokes following the same channel as an earlier stroke were associated with a "quiet" dE/dt waveform after the return stroke peak. In one case, an "anomalous" waveform was recorded in which the dE/dt waveform was initially noisy after the return stroke peak but became quiet 12 μs afterwards. *Willett et al.* [1995] suggest that fine structure in the dE/dt signature arises from new channels to ground while old channels produce a quiet dE/dt signature. They suggest a critical test of this hypothesis may come from the "anomalous" type signature they record.

## 2. INSTRUMENTATION AND DATA

The measurement system comprised five flat plate antennas in a 15 km x15 km network at Kennedy Space Center, Fl. [*Thomson et al.*, 1994]. The time derivative of the electric field (dE/dt) was measured at each station by sensing the displacement current through the antenna. Signals were digitized at the rate of 20 MHz for 4096 samples, yielding 204.8 μs records. There was a 30 μs dead time between consecutive trigger records. The upper 6-dB cutoff frequency for sites 2 - 5 was 4 MHz while the central recording site had a 6-dB cutoff frequency of 2 MHz owing to an additional antialiasing filter. The lower 6 dB cutoff frequency was a few hertz for all sites. Locations of individual pulse sources were found using the time-of-arrival method described by *Thomson et al.* [1994]. Typical pulse timing errors were 30 ns and errors in spatial locations were 30-45 meters in x, y, and z for sources at altitudes of several kilometers and near the network. Sources below 1 km had height errors on the order of several hundred meters.

## 3. RESULTS AND DISCUSSION

The dE/dt traces of three of six strokes to ground of flash 1403 are shown in Figure 1. Stroke 1 was the first of the flash sequence and contained fine structure that persisted for at least 83 μs. The second stroke in the sequence occurred in a new termination, displaced 1.1 km from the first stroke. Fine structure following this stroke lasted for just 33 μs. Strokes 3 through 6 followed the channel of the second stroke and were not accompanied by fine structure as evidenced by the dE/dt waveform of stroke 5.

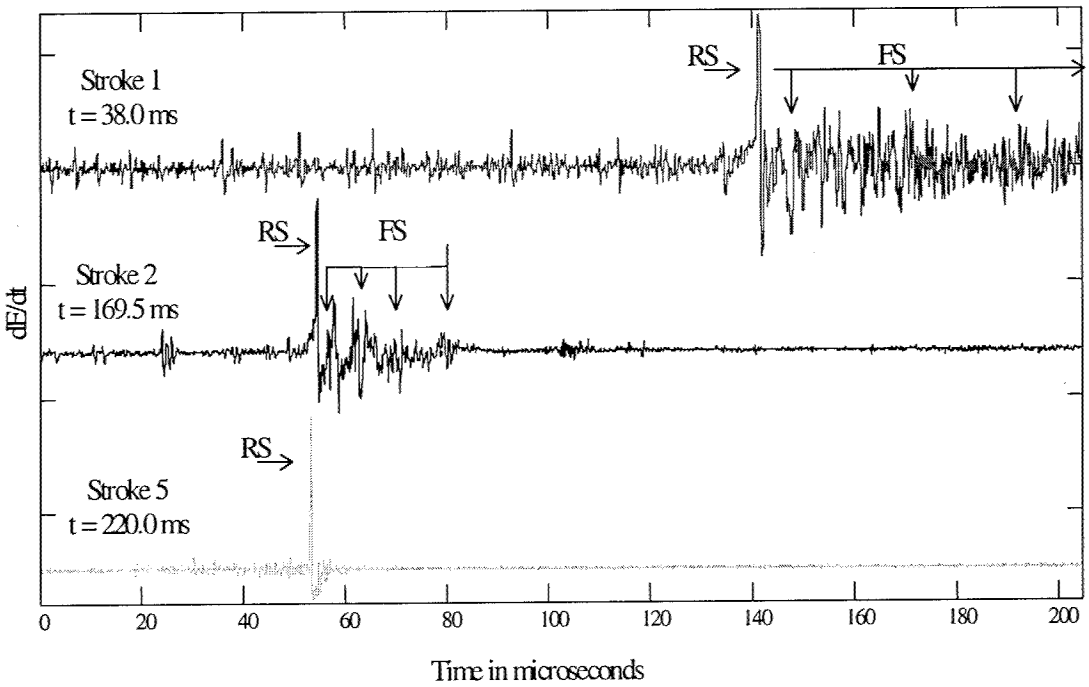


Figure 1. dE/dt traces for three of the six strokes in flash 1403. Time from the beginning of the flash is shown on each trace. The second stroke occurred in a new termination while the fifth occurred in the channel established by the second. Return stroke peak is marked "RS" and fine structure "FS".

The second stroke of the flash was preceded by the leader shown in Figure 2. Individual pulse sources were located between 2.6 and 0.9 km high and progressed downward. The average point-to-point speed calculated over each record was between $1.5 \times 10^6$ m/s and $2.5 \times 10^6$ m/s, consistent with that of a dart-stepped leader. Pulse amplitudes became smaller during the sixth record of the leader and fell below our triggering threshold four milliseconds prior to the second stroke. The time interval and distance between the last pulse in Figure 2 and the second stroke yield a speed of $2.3 \times 10^5$ m/s, consistent with that of a stepped leader.

The locations of all dE/dt sources in flash 2541403 are depicted in Figure 3. Source locations prior to and including the first stroke are marked as "O" while strokes 2-6 were co-located and are marked as "◊". Three sources during the fine structure after the first stroke (see Figure 1) were located to a height of 2.6 km and are represented by "X". Locations of leader sources preceding the second stroke (see Figure 2) are represented by "+" and span heights between 2.6 and 0.9 km. Several sources were located during the fine structure following the second stroke and are indicated by " " in Figure 3. Notice the concentration of these sources between ground and the last sources of the leader. These are consistent with originating from the region of the stepped portion of the leader creating the new termination to ground.

A total of seventeen strokes occurring in new terminations to ground in 16 flashes were preceded by a dE/dt pulse train. Point-to-point speeds in trains were between $1.0 \times 10^6$ m/s and $1.2 \times 10^7$ m/s, in good agreement with those of dart-stepped leaders. In each case, however, pulse amplitudes near the end of trains fell below the trigger threshold of the system several milliseconds prior to the following return stroke. The average velocity between the last recorded pulse in the train and the following return stroke was between $0.8 - 5.8 \times 10^5$ m/s, consistent with that of a stepped leader. Final sources in pulse trains were located between 0.7 km and 3.4 km high with a median value of 1.1 km.

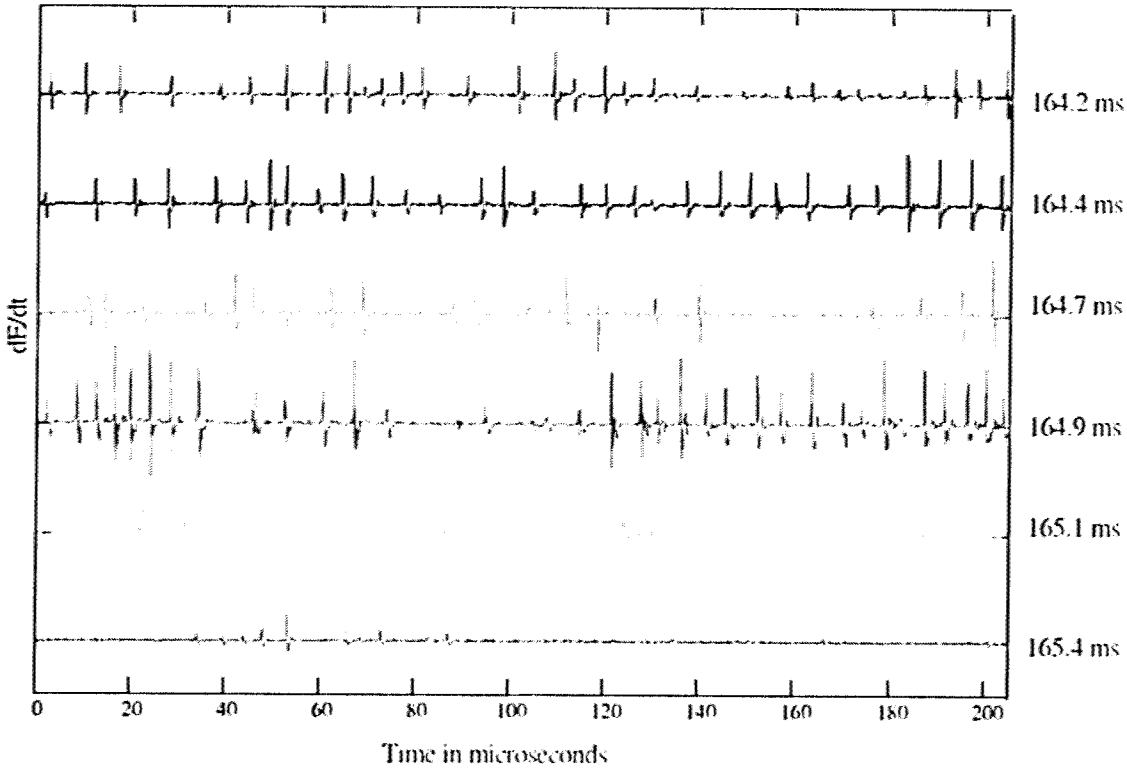


Figure 2. dE/dt trace of the leader recorded at station 5 preceding the second stroke of flash 2541403. Time at start of each trace is shown to the right.

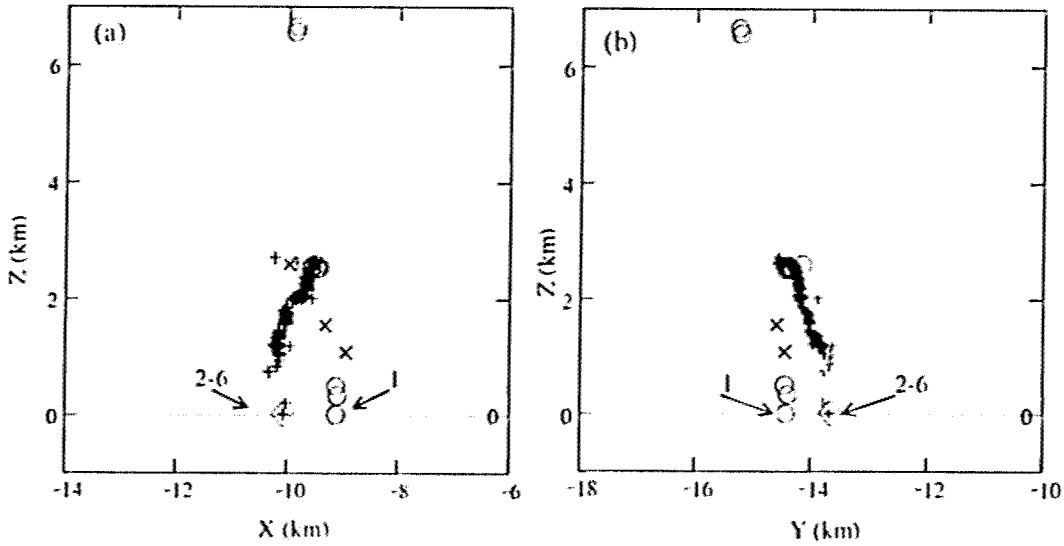


Figure 3. Locations of dE/dt sources in flash 2541403. (a) Z vs. X and (b) Z vs. Y . X and Y are oriented east and north respectively with reference to the central recording stations. See *Thomson et al.* [1994] for station layout.

Fine structure was present in waveforms of both first strokes of a flash and in strokes in new terminations, but its duration was shorter for new terminations (median value 37 μs in 17 strokes) than in first strokes of a flash (median value 141 μs in 17 strokes). Source locations during the fine structure in new terminations were consistent with inferred stepped leader sources between ground and the lowest sources in pulse trains.

## 4. CONCLUSIONS

We find evidence to support the hypothesis of *Thomson et al.* [1984] that multiple channels below cloud base may be due to a leader following an old path in the cloud and later adopting a new path to ground creating a new termination. Strokes occurring in new terminations were associated with a shorter fine structure duration, 37 μs (median), than first strokes in flashes, 141 μs (median). The shorter duration fine structure is a result of the small stepped leader path between the end of the dart-stepped leader portion of the leader and the following return stroke. Sources of fine structure were located in the channel apparently formed by the stepped leader portion of the leader.

## REFERENCES


Schonland, B., D. Malan, and H. Collens, Progressive lightning VI, *Proc. R. Soc. London Ser. A*, 168: 455-469, 1938b.

Schonland, B., The lightning discharge, *Handb. Phys.*, 22: 576-628, 1956.

Thomson, W., M. Galib, M. Uman, W. Beasley, and M. Master, Some features of stroke occurrence in Florida lightning flashes, *J. Geophys. Res.*, 89, 4910-4916, 1984.

Thomson, E., P. Medelius, and S. Davis, System of locating the sources of wideband dE/dt from lightning, *J. Geophys. Res., 99,* 22,793-22,802, 1994.

Willett, J., D. Le Vine, and V. Idone, Lightning-channel morphology revealed by return-stroke radiation field waveforms, *J. Geophys. Res.,* 100, 2727-2738, 1995.

# PHOTOGRAPHIC DOCUMENTATION OF TWO RETURN STROKES ALONG THE SAME CHANNEL SEPARATED BY ABOUT A MILLISECOND

Vincent P. Idone and Daniel A. Davis

Department of Earth and Atmospheric Sciences
University at Albany, SUNY
Albany, New York, USA

ABSTRACT: Two strokes in a triggered lightning flash initiated in 1996 at Camp Blanding, Florida, were recorded with a time-resolved photographic system that unequivocally documents the occurrence of these strokes along the same channel with an interstroke interval of only 1.09 ms. Each stroke has a distinct downward leader phase. This observation appears to confirm effectively the hypothesis of *Rakov and Uman* [1994] that such stroke couplets, consisting of a primary and secondary stroke, can occur with an interval of a millisecond or less. We reproduce these records and provide analyses of the leader propagation speeds of the primary and secondary stroke: $0.96 \times 10^7$ m/s and $1.4 \times 10^7$ m/s, respectively. We also present qualitative analyses of the difference in optical characteristics of the two strokes, which may be typical of such short interstroke interval events.

## INTRODUCTION

Recently, *Rakov and Uman* [1994] have presented evidence for the occurrence of two strokes along the same channel with the time interval between the strokes being a millisecond or less. Their observations were based upon simultaneous single-station electric field and multiple-station video records from 76 negative cloud-to-ground flashes in Florida. A total of 15 such double-field waveforms were recorded, with six of these showing only a single channel in the video records. This latter observation led *Rakov and Uman* to conclude that two full stroke sequences (consisting of a downward leader and an upward return) could propagate along the same channel at such short interstroke intervals. This further implies that the channel can decay to a condition suitable to support a leader process much more quickly than previously thought. Though their hypothesis seemed credible based upon the available evidence, *Rakov and Uman* admitted that "...further observations are needed before it can be positively proven."

Here we present time-resolved photographic records of a pair of strokes along the same channel, these strokes having an interstroke interval of just 1.09 ms with both strokes imaging a distinct downward leader. Although this separation interval is technically not less than 1 ms, the observed interval is effectively within the regime of intervals discussed by *Rakov and Uman* [1994] and is certainly likely to be eclipsed by still shorter intervals given the miniscule fraction of events we have sampled in obtaining this example from the parent population. Hence, our principal objective here is to present the fundamental photographic evidence for the occurrence of this stroke "couplet" along with associated characteristics of the strokes as derived from analysis of the streak records.

## OBSERVATIONS

The recordings presented here were made during the summer of 1996 when the authors participated in a triggered lightning experiment carried out at Camp Blanding, Florida, under the direction of Dr. J. Willett of the Air Force Geophysics Directorate. This particular field study was located on a different part of the Camp Blanding facility, several kilometers distant from the University of Florida lightning research facility which was in simultaneous but independent operation.

The particular pair of consecutive strokes of interest occurred in the seventh trigger attempt, flash 9607, which was initiated at 18:35 GMT on August 11. Highly time-resolved photography of this flash was obtained from a distance of 1.97 km using a Hycam II 16-mm high-speed framing camera modified to run in streak mode. The film used was Kodak SO-078 (a 400 ASA T-grain emulsion) which was run through the camera at a writing rate of 21.5 m/s. The camera was equipped with a conventional 24-mm Pentax lens. The strokes of interest were the third and fourth strokes in the flash, the flash having been triggered in the "classical" manner via the rocket-trailing wire technique.

The time-resolved records of this stroke couplet (the primary and immediately following secondary) are shown in Figures 1 and 2, respectively. These are positive renditions of the film negative as digitized with a Xillix Microimager camera at 100 pixels/mm. The Xillix camera scanned the images at 1344x1047 pixels at 12 bits/pixel. However, we cropped the images to a size of 1300x950 pixels. Further, our image analysis software necessarily converted the original 12-bit values to 8-bit output (256 levels). Though not optimal, this conversion is adequate for

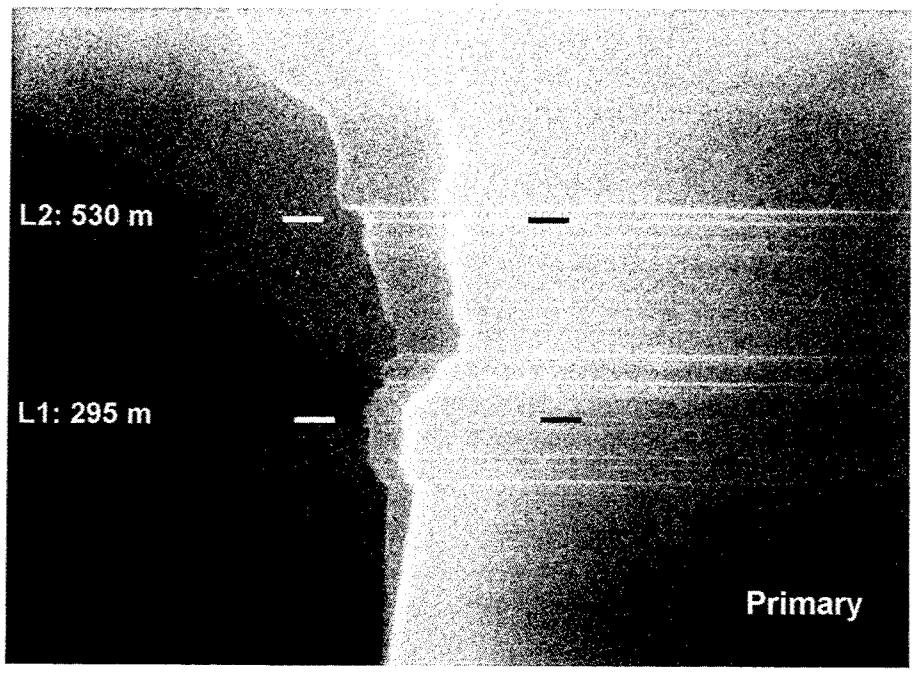


**Figure 1.** Time-resolved image of the third stroke (primary) in triggered flash 9607. Time increases to the right with 140 μs (300 pixels) between the inner limits of the dashes at levels L1 and L2; level heights above ground as indicated.

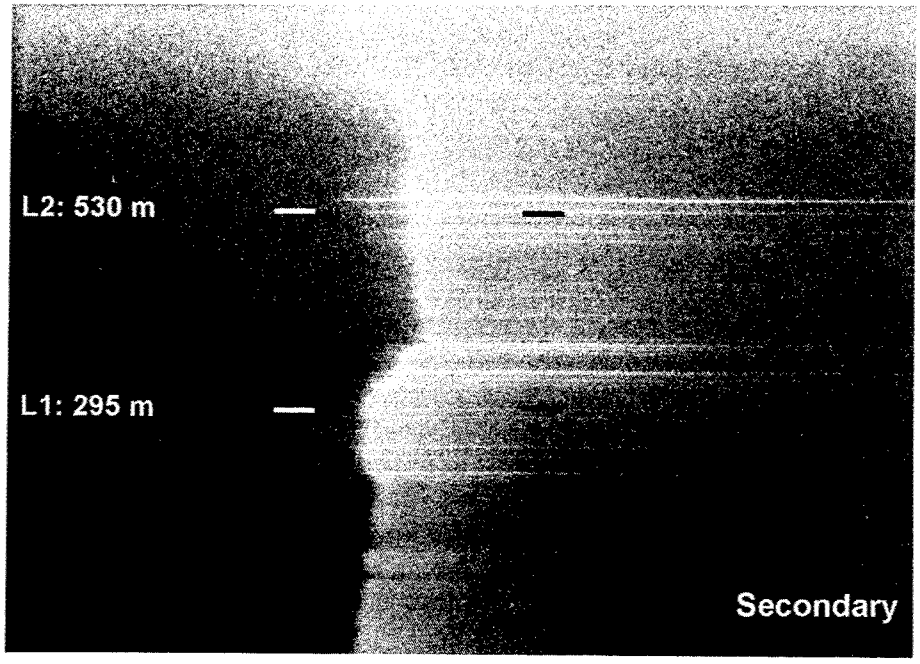


**Figure 2.** Time-resolved image of the fourth stroke (secondary) in triggered flash 9607 that occurs 1.09 ms after the primary stroke above. Time increases to the right with 140 μs (300 pixels) between the inner limits of the dashes at levels L1 and L2; level heights above ground as indicated.

the objectives of this work. The renditions of Figures 1 and 2 have been contrast enhanced to bring out the fainter image features.

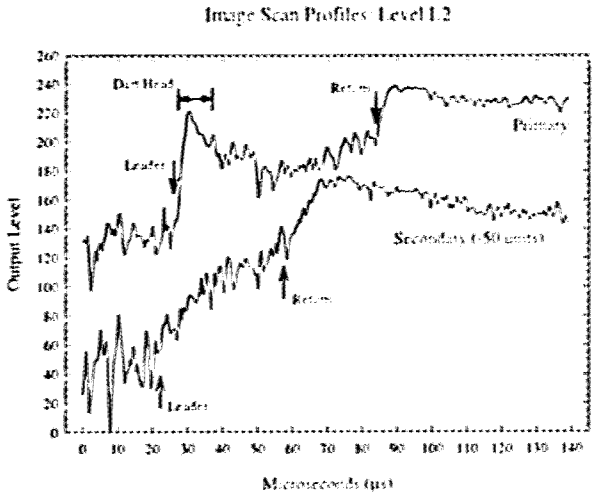


Figure 3. Image scan profiles for the primary and secondary strokes at level L2. Secondary profile displaced 50 units downward for clarity, arrows indicate leader and return phase onset.

## RESULTS

Examination of Figures 1 and 2 indicates that the primary stroke consists of a classic dart-leader return-stroke sequence. The ensuing secondary stroke clearly exhibits a downward propagating leader and an upward return stroke phase, both following the same channel as that of the primary stroke. Though evident, the leader to the secondary stroke is faint and is manifest along only certain sections of the channel, these presumably being sections inclined toward or away from the camera. A few intense streak lines, likely corresponding to acute channel kinks with near horizontal orientation of the channel, provide the strongest imaging of the generally faint leader above the high background fog of this negative. The streak line just above the 530-m level in Figures 1 and 2 is the foremost example of this.

To further examine these events, we have measured the propagation speeds of the primary and secondary leaders. To do this, we used the return-stroke image edge as representative of the true channel geometry; this is an excellent approximation, as the relative displacement of the return stroke images (assuming a return-stroke propagation speed of $10^8$ m/s or higher) would be negligible compared with that of the two leaders. The primary leader, a classic continuous dart, propagates at $0.96 \times 10^7$ m/s between level L2 of Figure 1 and ground. The secondary leader, over the same channel section, propagates at a noticeably higher speed of $1.4 \times 10^7$ m/s. These speeds are accurate to better than 10%. Note that we cannot accurately measure return stroke speeds with this record; however, had there been a significant difference in return stroke speed, the return stroke channel edges would not have been parallel. Indeed, they were very nearly parallel, implying the return stroke speeds were very nearly equal.

Since there were no current or field measurements available for these strokes, the photographic record represents the only available information on these strokes. Fortunately, the intense streak line just above level L2 provides particularly useful information. Imaging at this level persisted for 0.56 ms after initiation of the primary return stroke. As this intense streak line implies a considerable amplification of the normal channel light level on film, the cessation of imaging for 0.53 ms prior to the secondary stroke suggests that the channel was devoid of current flow for only this short period before the ensuing secondary stroke. (We cannot be absolutely certain that the lack of imaging necessarily means that no current was flowing in the channel. Even with the presumed light level amplification implied by the heavy streak line, it is possible that a small current still flowed in the channel and the net light level presented to the film remained below the image threshold. However, we think this is unlikely.)

We use the streak line just below level L2 to examine and compare qualitatively the image intensity profile across the primary and secondary stroke records. These profiles appear in Figure 3 and correspond to the image portions between the inner limits of the dashes of Figures 1 and 2. (We did not choose the intense streak line just above level L2, as the obvious significant horizontal channel section there would necessarily have yielded a convolved light profile.) Note that here we are presenting the light level in arbitrary units (output level) as seen by the Xillix camera in scanning the original film negative; this output has not been converted to true relative intensity at the source. Nonetheless, it is clear that the dart leader of the primary stroke has an abrupt rise in light level and then a fall, consistent with imaging the dart leader head; however, the leader to the secondary stroke shows no clear head structure, and the light level consistently increases (i.e., higher output levels) until the onset of the return stroke. The same type of profile is presented in Figure 4 for a lower level (L1), this being at a vertical height of 295 m and corresponding to a faint streak line. Here again, the leader to the secondary stroke shows a generally increasing light level after onset until initiation of the return stroke. In comparing the profiles of Figures 3 and 4, it is also clear that

the risetime (here, simply onset to peak) of the return stroke light level is longer by at least a factor of two or three relative to that of the secondary stroke. Finally, as is likely apparent even in Figures 1 and 2, the image profiles for levels L1 and L2 indicate that the peak light level for the secondary stroke is less than that for the primary stroke. (Note that the arrow indicators of leader and return onset are positioned in correspondence to a subjective determination of the density gradient along L1 or L2 as evaluated in examining the digitized images directly on a computer monitor.)

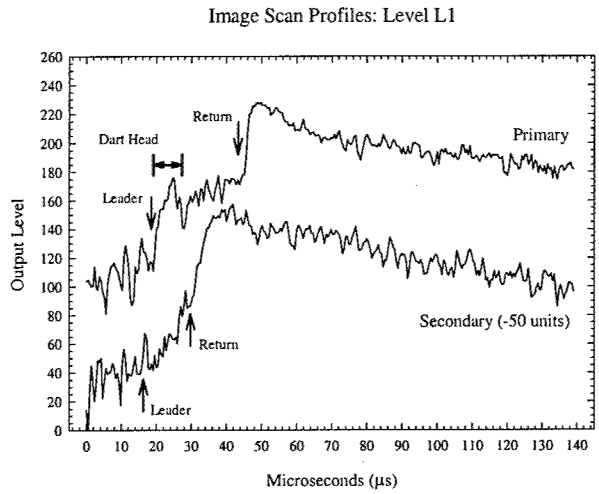


**Figure 4.** Image scan profiles for the primary and secondary strokes at level L1. Secondary profile displaced 50 units downward for clarity; arrows indicate leader and return phase onset.

## DISCUSSION

*Rakov and Uman* [1994] have noted that the previously shortest interstroke interval reported was 1.9 ms in another triggered flash [*Idone et al.*, 1984]. The stroke couplet presented here has an interstroke interval which is shorter by nearly a factor of two. Unless such short intervals are peculiar to artificially initiated flashes, given the event presented here and the previous evidence of *Rakov and Uman*, it appears almost certain that some fraction of natural lightning strokes occurs with sub-millisecond intervals.

*Rakov and Uman* [1994] also speculated that a secondary leader-return sequence would likely have different characteristics than that of the primary stroke. The observation presented here would appear to confirm their speculation with regard to a higher propagation speed for the secondary leader as well as the suggestion that such leader-return sequences might be more akin to M components than normal leader-return events. Indeed, the light profiles shown earlier show a luminous variation with time approaching what we typically see on film for strong M components. Indeed, the initial assessment of this event by the senior author was that this was a very vigorous M component – until closer examination revealed the distinct downward propagating leader.

It is unfortunate that no relevant ancillary records exist to allow estimation of the peak currents in these strokes. We may be able to estimate a ratio of peak currents based upon the optical signal, pending future detailed analyses using the film calibration curve for relative exposure. Under the assumption of a roughly linear relationship between peak current and peak luminous emission, past experience with this type of analysis suggests that the secondary stroke had a smaller peak current than the primary stroke by probably at least a factor of 1.4 to 2. A better estimate must await the actual analysis.

## CONCLUSION

We have presented unequivocal evidence for the occurrence of two complete leader-return sequences separated by only 1.09 ms, these occurring along the same channel. Documentation of this event represents effective confirmation of the hypothesis of *Rakov and Uman* [1994] that such short interstroke intervals are possible. It is likely that that some small fraction of all natural lightning strokes occurs at such short intervals. Clear differences in the optical characteristics of the primary and secondary strokes are evident in this particular set of records. Whether such differences are typical of this type of stroke couplet awaits further observations on this subset of lightning strokes.

ACKNOWLEDGEMENTS: The authors are most grateful to Dr. J. Willett for inviting us to participate in the triggered lightning campaign of 1996 at Camp Blanding and for being, as always, a most enjoyable colleague to work with. We thank Mr. S. Capuano for outstanding assistance in the field experiment and for operation of the streak camera. This work was supported under NSF grants ATM-9021909 and ATM-9627276.

## REFERENCES

Idone, V. P., R. E. Orville, P. Hubert, L. Barret, and A. Eybert-Berard, Correlated observations of three triggered lightning flashes, *J. Geophys. Res.*, 97, 9951-9957, 1984.

Rakov, V. A, and M. A. Uman, Origin of electric field signatures showing two return-stroke waveforms separated in time by a millisecond or less, *J. Geophys. Res.*, 99, 8157-8165, 1994.

# 3D Imaging of Lightning Channel and Leader Progression Velocity

Zen Kawasaki Hitoshi Isoda Sachi Yoshihashi

Department of Electrical Engineering
Faculty of Engineering, Osaka University
Yamada-Oka 2-1, Suita Osaka 565 0871, JAPAN

**Abstract.** Three dimensional imaging of lightning channels, especially for leader progression, by means of UHF interferometers has been achieved. A field campaign with two observation sites is conducted at Darwin Australia for further study. The distance between two sites is 14.2 km, and the triangulation scheme is applied to locate UHF radiation sources in three dimensions. Since the UHF radiation during the leader progression is more expected than the return stroke, images of lightning channels are given mainly for downward leaders. Velocities of downward leaders are calculated, and statistics are derived for the first and subsequent strokes. The comparison of the mean velocity of the early phase of leaders inside thundercloud with the final phase of leaders below a thundercloud is conducted. Since the optical measurement of invisible leader progression velocity inside thundercloud is impossible, the presented results are concluded to be unique and significant.

## 1 Introduction

The investigation of lightning channels has been conducted by optical observations, thunder observations, and electromagnetic wave observations. The optical observations own the advantage of high time and spatial resolution, and contribute to the intensive comprehension for leader propagation mechanism below thunderclouds. On the other hand the optical observations are not suitable to understand the development of leader inside the clouds. The thunder observations are rather easy techniques, but we can not expect the sufficient time and spatial resolution. Electromagnetic wave observations maintain the high possibility to image the lightning channel including inside the invisible clouds, and related scientists have been paying their attention. In terms of recently developed techniques TOA and Interferometer for VHF/UHF radiation are noticeable. Lighting Research Group of Osaka University has been engaged in the developing Interferometer, and has evaluated the performance of their interferometer. For this purpose the field campaigns were conducted at Darwin Australia in 1996 and 1997, and in 1996 3D imaging of lightning channels were established. In this paper 3D images of leader channels are given and the discussion on the feature of leader progression is presented.

## 2 Observations by UHF Interferometer and 3D imaging of Lightning Channels

The field campaigns were conducted during the developing stages of the monsoon for one month both in 1996 and 1997. The interferometers are operated at the center frequency of 327 MHz with 350 kHz bandwidth during the campaign. Figure 1 shows the antennas arrangement for observations, and we can see two pairs of monopole antennas, which are arranged perpendicular each other. Two pairs of antennas enable us to estimate the azimuth and elevation of radiation sources. Figure 1 includes the additionally arranged antenna pairs and those have longer baselines than the former pairs. The combination of long($9/2\lambda$) and short($\lambda$) baselines operation gives us more accurate location of radiation sources. We operated two sets of interferometers at different sites, and by applying triangulation scheme we obtain 3D image of lightning channels in terms of UHF pulse radiation sources. The systems are operated at Darwin, Northern Australia, and distance between two site is about 14.2km.

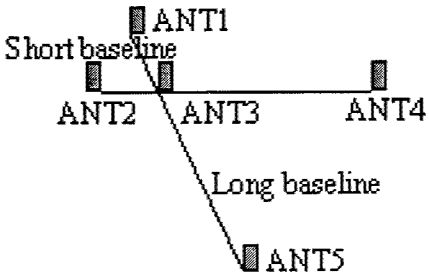


Fig.1 Antenna configuration

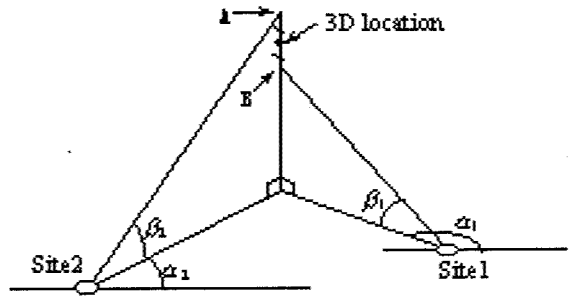


Fig.2 3D location method

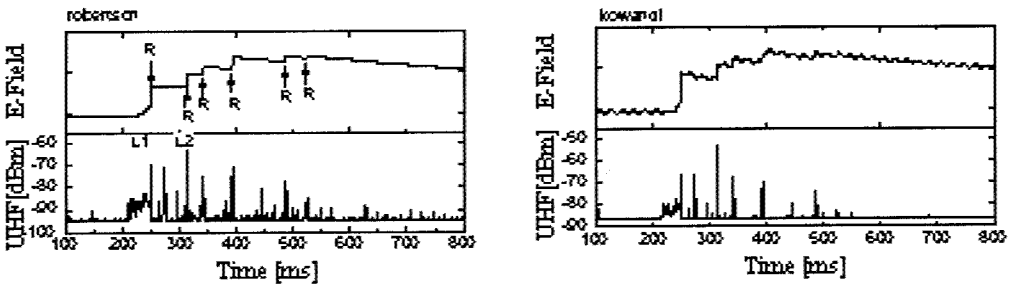


Fig.3 Electric field change and UHF radiation

Figure 2 shows an idea about applied triangulation scheme. A x-y coordinate, which is the projection of a UHF radiation source on the ground, is given as the intersection of azimuth for two sites as shown in Figure 2. This is because we know that it is nearly impossible to expect an intersection of two lines of sight of incident UHF EM pulses to two sites. If we get the X-Y coordinate, we can estimate two possible altitudes for a UHF radiation source as intersections of a perpendicular on x-y coordinate and lines of incident angles to two sites. In this paper we determine radiation source location by taking mean of these two candidate altitudes. Since we operate the slow antennas at two sites, we can discriminate the characteristics of captured lightning flashes, like CC and CG.

Figure 3 shows one of observed lightning flashes recorded at two sites simultaneously, and the electric field change and UHF radiation for one second are shown. The data were captured at 6:54'55" (UTC) on December 2, 1997. The capital letter "R"s denotes return strokes, and it is obvious that this events consists of at least six strokes of negative polarity. It is also obvious that each stroke follows the strong UHF radiation. This feature is consistent with the previously published papers, and it is believed that these radiation is due to stepped leader progressions. The leader progression marked L1 in Figure 3 is given as 3D imaging in Figure 4. Here L and R mean leaders and return strokes respectively. Figure 5 shows the time expanded signature of electric field change and UHF radiation. In Figure 4, X axis corresponds to the direction of east-to-west, and Y axis corresponds to the direction of north-to-south. Z axis is the altitude axis. The two observation sites are Robertson and Kowandi, and their coordinates are respectively origin of this Cartesian coordinate and (9.4, 10.6, 0) (km). It is noticed that this stike is initiated at (11.3, -1.1, 6.6) (km) and propagates to the ground. Figure 6 shows the 3D image of the leader progression for the second stroke marked L2 in Figure 3. Figure 7 shows the time expanded signature of the electric field change and UHF radiation for L2. It is interesting that the initiation point of the leader for the second stroke is (11.7 -1.1, 6.6) (km) and it is nearly the same for the first stroke.

## 3 Discussions

Figure 8 shows the distribution of leader propagating velocity for 16 first strokes and 25 subsequent strokes. Figure 8 shows that the most probable velocity for the first strike is in the order of $10^5$m/s with

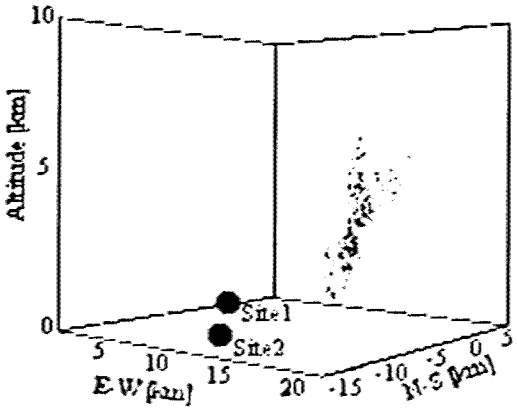


Fig.4 3D image of first CG stroke

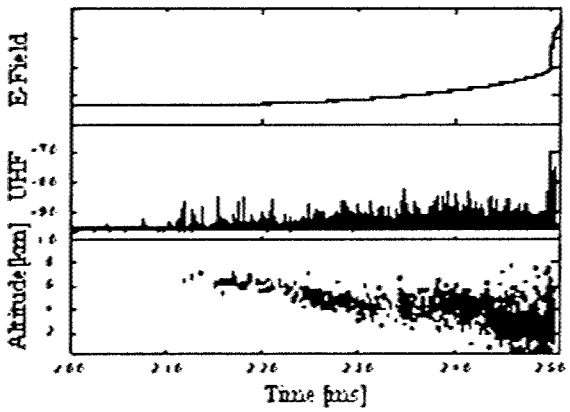


Fig.5 Detail of first CG stroke

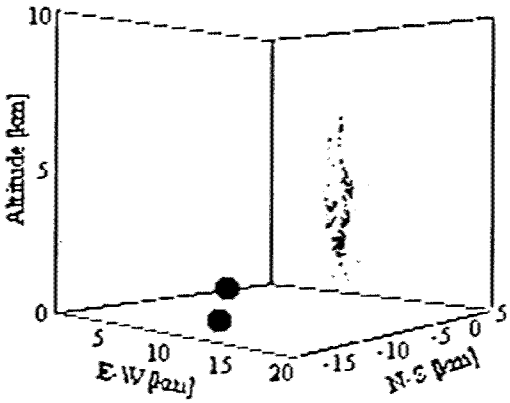


Fig.6 3D image of second CG stroke

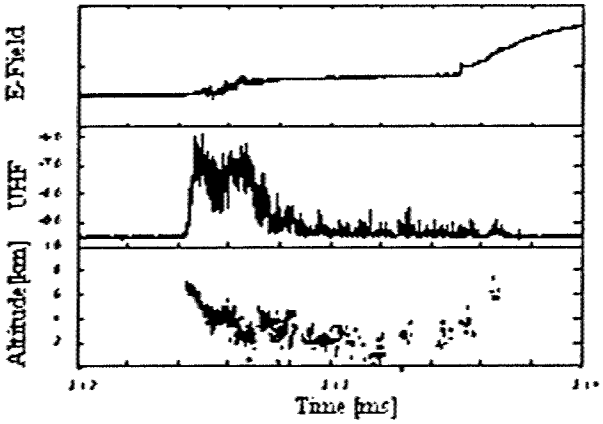


Fig.7 Detail of second CG stroke

the average of $5.3\times10^{5}$m/s. For subsequent strokes the most probable leader propagating velocity is in the range of $10^{6}$m/second and $10^{7}$m/s with the average of $2.4\times10^{7}$m/s. These results are consistent with the previous observation results optically, but it is noticed that the optcal observations baisically presented 2D velocities.

Figure 9 shows the 3D image of the leader progression for the event at 2:25'55" (UTC) on December 13. Figure 10 shows the electric field change, UHF radiation intensity, altitude of sources and propagating velocity as functions of time. It is noticed that at the very beginning of the leader it propagates eastward almost horizontally, and changes the direction at 230 milliseconds finally towards the ground. It is interesting that the averages of leader propagating velocity horizontally and vertically are respectively $2.1\times10^{5}$m/s and $2.3\times10^{5}$m/s. We can not recognize the significant defference of leader velocity between horizontal and vertical propagation.

## 4 Conclusions

This paper presented the 3D images of lightning channels, especially leader channels, in terms of observations by UHF interferometers. Observations were conducted at Darwin, Australia from the middle of November to the middle of December 1996 and 1997.The observation periods corresponds to the developing stage of the monsoon and we have frequently thunderstorm occurrence. Through the observations and data analysis we obtained the following conclusions.

1. Three dimensional imaging of leader progressions for negative cloud-to-fround flashes during summer thunderstorm were achieved by interferometers, and the capability of interferometers were shown. It is also shown that leader progression preceeding subsequent strikes of multiple

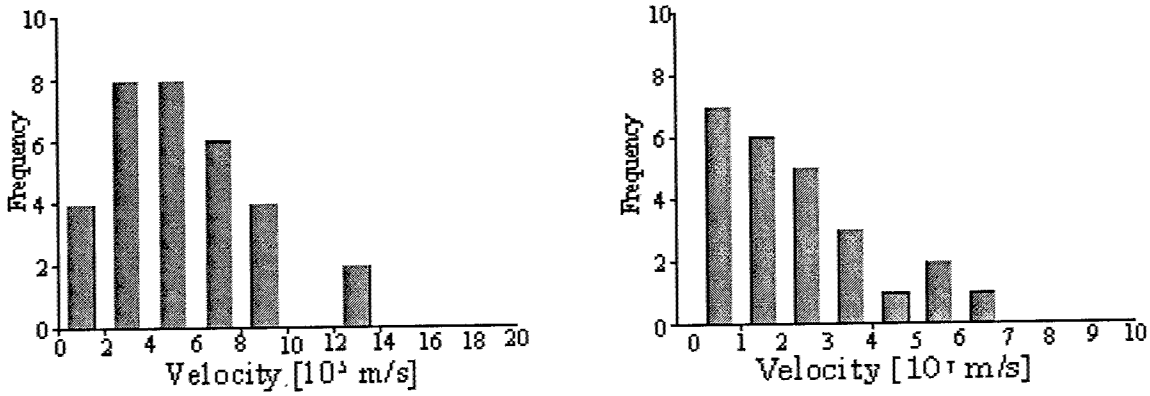


(a) first strokes (b) second strokes

Fig.8 Distribution of leader prooagating velocity

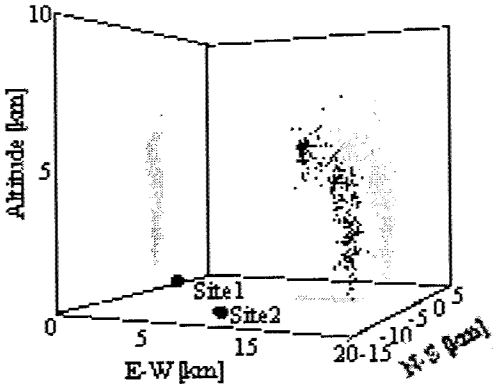


Fig.9 3D image of the leader progression

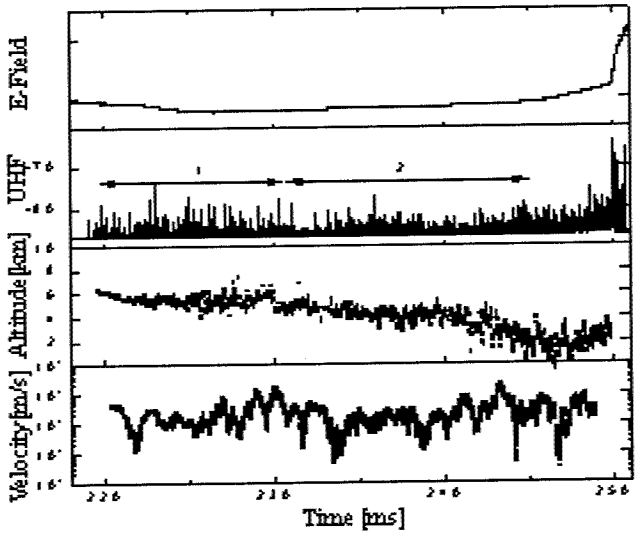


Fig.10 Detail of the leader progression

strikes took the same channel of previous strike with several hundred meters accuracy, and this evidence can contribute the confirmation of the capability of interferometer observations.

2. The leader propagation velocity of first and subsequent strikes are estimated in the order of $10^5$m/s and $10^7$m/s respectively. This results are consistent with the previously observed statistics by means of optical streak camera, This means we can confirm the interpretation of "UHF EM pulses are mainly emitted by the tip of negative leader propagation."

3. In case of negative cloud-to-ground flashes the velocity of the horizontally propagating leader inside the cloud is nearly the same of its vertically propagating leader from the aspect of interferometer observations. Interferometer enables us the observations for invisible leader progression insider the thunderclouds.

# POSITIVE LEADERS IN ROCKET-TRIGGERED LIGHTNING: PROPAGATION VELOCITY FROM MEASURED CURRENT AND AMBIENT-FIELD PROFILE

J.C. Willett[1], D.A. Davis[2], and P. Laroche[3]

[1]Air Force Research Laboratory, Hanscom AFB, Massachusetts, U.S.A.
[2]State University of New York, Albany, New York, U.S.A
[3]Office National d'Etudes et de Recherches Aérospatiales, Chatillon, France

ABSTRACT: A recent field experiment has provided ambient-field profiles a few seconds before nine rocket-triggered lightning flashes. Currents flowing in the grounded triggering wires were recorded during most of the positive leaders that initiated these flashes. We present deductions of leader velocity from the measured data for one of these events, based on three simple electrostatic models. Deduced velocities range from 1 - 5 $\times 10^4$ m/s.

## INTRODUCTION

"Classical" rocket-triggered lightning flashes allow detailed study of the very long positive leaders that initiate these discharges. Thus, the rocket-triggering technique provides a valuable opportunity to extend experimental work on long laboratory sparks to kilometer length scales. The present paper develops a method of deducing leader-propagation velocity from triggering experiments. This method is applied to leader-current and ambient-field-profile data from a recent field experiment in which direct measurements of leader velocities were not available. The method could equally well be used, however, to deduce ambient-field profiles from leader current and velocity measurements in other experiments. The details of the calculations are described here, and results are presented for one case from our experiment.

The main purposes of this work are to permit the leader-propagation velocity to be compared with the measured ambient field that is driving the discharge, and to enable more detailed comparisons between the observations and the predictions of a self-consistent, numerical model of rocket-triggered positive leaders [*e.g.*, Bondiou *et al.*, this conference]. Davis and Laroche [this conference] also compare the present results with others from the same experiment, obtained by a different method.

## EXPERIMENTAL SET-UP AND MEASUREMENTS

A major field experiment was conducted during the summer of 1996 to obtain simultaneous, collocated measurements of ambient, electrostatic-field profiles and rocket-triggered-lightning phenomenology beneath Florida thunderstorms [Willett *et al.*, in press]. First, nearly vertical profiles of the ambient electrostatic field were measured with sounding rockets very similar to those described by Marshall *et al.* [1995]. A few seconds later triggering rockets were fired, towing grounded conducting wires aloft [*e.g.*, Laroche *et al.*, 1989]. The lightning phenomenology was documented with still, video, and streak cameras, and the currents and field changes produced by the positive leaders that initiated these discharges were recorded. Unfortunately, however, neither visible nor near-ultraviolet streak photographs showed any positive leaders [V.P. Idone, personal communication], so the leader velocities were not directly measured.

Nine lightning discharges were triggered during this experiment, one of which (Flight 6) will be examined in this paper. The measured data for this flight are presented in detail by Willett *et al.* [in press].

## DEDUCTION OF LEADER-PROPAGATION VELOCITY

Building on previous work by Kasemir [1960], Heckman and Williams [1989] have presented calculations of the charge-per-unit-length, $\lambda(z)$, on thin, straight, vertical lightning channels. Strictly, their result,

$$\lambda(z) = \frac{-2\pi\varepsilon_0 V(z)}{\ln(L/R)} , \qquad (1)$$

applies only to the dependence on channel radius, and not to the absolute value, of this linear charge density. Here, $V(z)$ is the ambient electrostatic potential (relative to the uniform potential of the channel, assumed to be a conductor) at the relevant height, $z$, $R$ is the radius of the channel, including its corona sheath, and $L$ is 1/2 the channel length (or the entire length, if the channel is attached to ground). The comparable result for a thin, prolate, conducting ellipsoid in a uniform longitudinal field is

$$\lambda(z) = \frac{-2\pi\varepsilon_0 V(z)}{\ln(c/b) - 1 + \ln(2)} , \tag{2}$$

where and $b$ and $c$ are the semi-minor and semi-major axes, respectively, and $b/c << 1$. This result can be seen to have identical form and very similar magnitude to (1). Evidently, the linear charge density is predicted to be directly proportional to the channel-vs.-ambient potential difference. Either of the above formulae could be used as a relation among leader current, leader velocity, and ambient potential distribution.

We wanted to avoid the thin-conductor assumption implicit in (1) and (2), which does not apply well to a rocket-triggered leader having most of its charge distributed in a diffuse corona sheath several meters in diameter. Therefore, we have developed two simple, electrostatic models of the leader channel from which to compute the charge per unit leader extension. Our first model assumes that the corona sheath is in equilibrium with the ambient potential distribution, as follows:

Equilibrium Model

A grounded, vertical, wire/leader extends to height, $H$, above a conducting ground plane into a one-dimensional ambient-potential distribution, $U_a(z)$, prescribed by the rocket sounding. Everything is in cylindrical coordinates, $\{R, z\}$, centered on the wire/leader. We assume a potential distribution, $U_0(z)$, taken here as zero everywhere, along the wire/leader channel of radius, $R_0(z)$, taken here as a constant 1 cm. Two significant approximations yield a simplified model: 1) The field around the wire/leader is purely radial out to the boundary of the space-charge sheath at $R_1(z)$. This turns out to be a good approximation everywhere except near the leader tip because the aspect ratio of the sheath, $R_1/z$, remains small and varies slowly with height. 2) Following Goelian et al. [1997], we assume the field intensity everywhere within the corona sheath to be uniform, $E_0$, taken here as the "stability field" for positive streamers of roughly 440 kV/m [*e.g.*, Phelps and Griffiths, 1976]. The details of the "cap" on the space-charge plume around the leader tip are ignored, so the charge-per-unit-length there will not be very accurate. Another implicit assumption is that the entire wire/leader is in corona, which is not unreasonable in high ambient fields.

Uniform and radial field within the corona region implies that the linear charge density along the entire wire/leader is simply

$$\lambda_1(z) = 2\pi\varepsilon_0 E_0 R_1(z) . \tag{3}$$

Thus, there are no "conductors" in the model (except the ground plane), deviations from the ambient potential distribution being caused solely by the above linear charge density. (For purposes of calculating the potential distribution inside the corona region, this charge is taken to be distributed as $\rho(R) = \varepsilon_0 E_0/R$, plus some small surface charge on the conducting wire/leader itself that is negligible when $R_0 << R_1$.)

We can write the potential at the boundary of the corona region in terms of the assumed potential of the wire/leader as

$$U(R_1, z) = U_0 - E_0(R_1 - R_0) . \tag{4}$$

To compute the potential anywhere *outside* the corona region, it is sufficient to assume that the charge density, $\lambda_1(z)$, is concentrated at $R = 0$. Thus, we can also write,

$$U(R,z) = U_a(z) + \int_0^H \left[ \frac{\lambda_1(z')}{4\pi\varepsilon_0\sqrt{R^2 + (z-z')^2}} + \frac{-\lambda_1(z')}{4\pi\varepsilon_0\sqrt{R^2 + (z+z')^2}} \right] dz' . \tag{5}$$

Using (3) in (5) at $R = R_1$, we recognize that the only remaining unknown is $R_1(z)$. Using (4) as a matching condition between the corona plume and the environment, we find the following non-linear integral equation, to be solved for $R_1(z)$:

$$U_0(z) - E_0[R_1(z) - R_0(z)] = U_a(z) + \frac{E_0}{2}\int_0^H \left[ \frac{R_1(z')}{\sqrt{R_1^2(z) + (z-z')^2}} + \frac{-R_1(z')}{\sqrt{R_1^2(z) + (z+z')^2}} \right] dz' . \tag{6}$$

One result of this formulation is that the radius of the corona sheath decreases rapidly with decreasing height, from the leader tip to the ground (shown below in Figure 1).

Frozen-Charge Model

Our second model attempts to recognize that the corona sheath is not actually in equilibrium with the ambient potential distribution as envisioned above. Instead, we expect the corona space charge emitted from the leader tip to remain approximately fixed in space as the leader advances past it. Thus, the diameter of the corona sheath at any given height will not decrease with time as predicted by our equilibrium model (see Figure 1).

Here we use the same assumptions and formalism as above, but we freeze the charge-per-unit-length of the corona sheath at the leader tip, expressed above by $R_1(H)$ through (3), as the leader progresses. Since this space charge is no longer allowed to adjust to the potential distribution below the wire tip, we must now permit surface charge to build up on the wire/leader itself to hold it at the prescribed potential, $U_0(z)$. This is accomplished by including a second linear charge density, $\lambda_2(z)$, in the model. The only other change from above is that another term must be included in the matching equation, (4), to account for the additional potential drop between $R_0$ and $R_1$ due to $\lambda_2$. The new model equation becomes

$$U_0(z) - E_0[R_1(z) - R_0(z)] - \frac{\lambda_2(z)}{2\pi\varepsilon_0}\ln\left[\frac{R_1(z)}{R_0(z)}\right] = U_w(z) + \int_0^H \left[\frac{\frac{E_0}{2}R_1(z') + \frac{\lambda_2(z')}{4\pi\varepsilon_0}}{\sqrt{R_1^2(z) + (z-z')^2}} + \frac{-\frac{E_0}{2}R_1(z') - \frac{\lambda_2(z')}{4\pi\varepsilon_0}}{\sqrt{R_1^2(z) + (z+z')^2}}\right]dz' . \quad (7)$$

This equation is solved for $R_1$ at $z = H$, where $\lambda_2$ is set equal to zero, and it is simultaneously solved for $\lambda_2$ at all $z \ni (0, H)$. The solution must be done progressively as the leader ascends, in order to determine the function, $R_1(z)$.

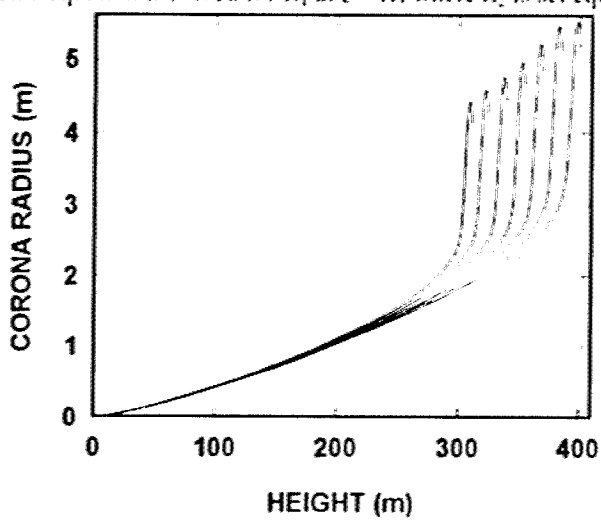


**Figure 1. $R_1$ vs. $H$ for the Equilibrium Model**

## RESULTS

The measured ambient field in Flight 6 was approximately vertical and close to 15 kV/m from just above the surface to about 400 m altitude [Willett *et al.*, in press, Figure 14]. Thus, the ambient electrostatic potential decreased almost linearly with increasing altitude from 0 at the ground to about -6 MV at 400 m. The average leader current increased irregularly from roughly 1 A to almost 3 A over the first 3 ms of propagation [Willett *et al.*, in press, Figure 10]. (Our sign convention is that negative charge aloft produces a positive vertical field, corresponding to an electrostatic potential that decreases with increasing height, and induces a positive current in the developing leader.) In this case the upward positive leader was triggered when the rocket reached an altitude of 307 m.

Figure 1 shows a family of curves of corona radius, $R_1$ (proportional to charge-per-unit-length), along the wire/leader for successive tip heights from 307 to 395 m, calculated for Flight 6 using the equilibrium model. Notice that the model assumptions are violated near the leader tip, where $R_1$ increases rapidly with height. Elsewhere, the model is validated quite well by direct computation of the potential distribution in and around the calculated space charge. Figure 2 shows $R_1$ and $\lambda_2/(2\pi\varepsilon_0 E_0)$, also in length units for direct comparison, for a tip height of 390 m, calculated for the same case with the frozen-charge model. Notice that the charge in the corona sheath increases almost linearly with height along this leader, in agreement with the Heckman-Williams model of Equation 1, but in marked contrast to the equilibrium

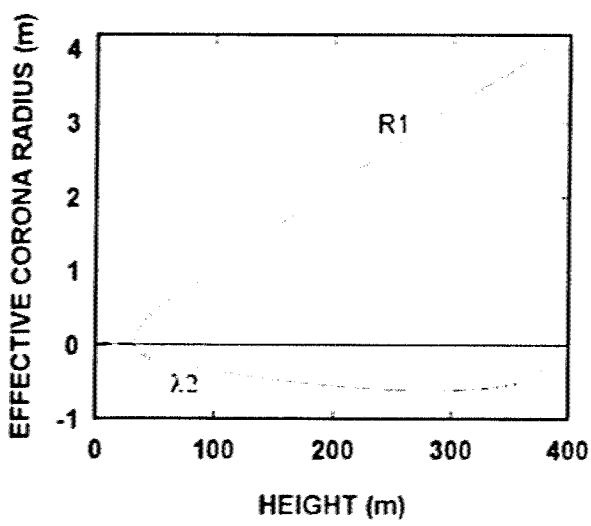


**Figure 2. $R_1$ and $\lambda_2/(2\pi\varepsilon_0 E_0)$ for Frozen-Charge Model**

model of Figure 1. Notice further that the surface charge on the wire/leader channel itself is significant. The radial field at the channel surface is computed to exceed the breakdown field (3 MV/m) by roughly an order of magnitude over most of its length. Thus, an inner layer of negative corona (not simulated here) would be expected to grow inside the positive corona sheath, starting just below the leader tip.

Figure 3 compares the leader-propagation speeds deduced for Flight 6 from the three models discussed in this paper. These velocities have been obtained by equating the integral of the measured leader current as a function of time to the net charge on the model leaders as functions of tip height. Evidently, Equation 1 and the frozen-charge model behave very much the same, whereas the equilibrium model predicts a smaller charge per unit leader extension and, hence, a somewhat higher velocity. The velocities shown in Figure 3 are comparable to those measured optically during the onset of positive leaders in other rocket-triggering experiments [*e.g.*, Kito *et al.*, 1985].

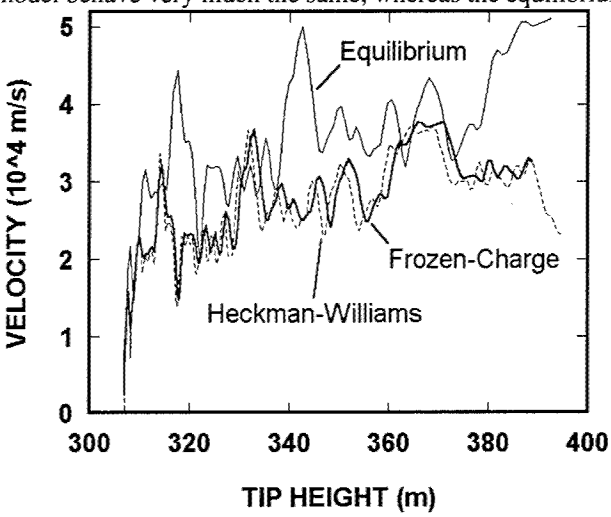


**Figure 3. Leader Velocity vs. *H* for the Three Models**

CONCLUSIONS

Leader velocities have been computed from the ambient-potential profile and the current record for one rocket-triggered lightning flash (Flight 6), using three different electrostatic leader models. The results range from 1 - 5 $\times 10^4$ m/s over the first 100 m of propagation. The equilibrium model predicts somewhat higher velocities than the other two, but the charge-per-unit-length that it manifests is probably under-estimated because of the assumption that the field intensity throughout the corona sheath is clamped at the positive-streamer stability field. On the other hand, the charge-per-unit-length predicted by the frozen-charge model is probably over-estimated because of the neglect of reverse corona behind the leader tip. The main weakness in the two new models developed here is their rather crude treatment of the space-charge distribution in the immediate vicinity of the leader tip. Nevertheless the deduced values of velocity are not greatly different among these three models and probably represent reasonable estimates of the actual leader speed.

REFERENCES

Bondiou-Clergerie, A., P. Lalande, P. Laroche, J.C. Willett, D. Davis, and I. Gallimberti, The inception phase of positive leaders in triggered lightning: comparison of modeling with experimental data, this conference.

Davis, D.A, and P. Laroche, Positive leaders in rocket-triggered lightning: propagation velocity from measured current and electric field derivative at ground, this conference.

Goelian, N., P. Lalande, A. Bondiou-Clergerie, G.L. Bacchiega, A. Gazzani, and I. Gallimberti, A simplified model for the simulation of positive-spark development in long air gaps, *J. Phys. D, 30*, 2411-2452, 1997.

Heckman, S.J., and E.R. Williams, "Corona envelopes and lightning currents ," *J. Geophys. Res., 94*, 13,287-13,294, 1989.

Kasemir, H., A contribution to the electrostatic theory of a lightning discharge, *J. Geophys. Res, 65*, 1873-1878, 1960.

Kito, Y., K. Horii, Y. Higashiyama, and K. Nakamura, Optical aspects of winter lightning discharges triggered by the rocket-wire technique in Hokuriku district of Japan, *J. Geophys. Res., 90*, 6147-6157, 1985.

Laroche, P., A. Bondiou, A. Eybert-Bérard, L. Barret, J.P. Berlandis, G. Terrier, and W. Jafferis, Lightning flashes triggered in altitude by the rocket and wire technique, presented at the *International Conference on Lightning and Static Electricity, University of Bath, UK, September 26-28*, 1989..

Marshall, T.C., W. Rison, W.D. Rust, M. Stolzenburg, J.C. Willett, and W.P. Winn, Rocket and balloon observations of electric field in two thunderstorms, *J. Geophys. Res., 100*, 20,815-20,828, 1995.

Phelps, C.T., and R.F. Griffiths, Dependence of positive corona streamer propagation on air pressure and water vapor content, *J. Appl. Phys, 47*, 2929-2934, 1976.

Willett J.C., Davis D.A., and Laroche P., "An experimental study of positive leaders initiating rocket-triggered lightning ," *Atmospheric Research*, in press.

# CLOUD-TO-GROUND LIGHTNING FLASH CHARACTERISTICS OBTAINED IN THE SOUTHEASTERN BRAZIL USING THE LPATS TECHNIQUE AND THE NEW HYBRID LIGHTNING LOCATION METHODOLOGY

Osmar Pinto Jr.[1], Iara R. C. A. Pinto[1], José H. Diniz[2], Andre M. Carvalho[2], and Armando Cazetta Filho[2].

[1] Instituto Nacional de Pesquisas Espaciais – INPE, São José dos Campos, SP, Brazil
[2] Companhia Energética de Minas Gerais – CEMIG, Belo Horizonte, MG, Brazil

ABSTRACT: Cloud-to-ground lightning flash characteristics in the southeastern Brazil were determined during two months based on data obtained by two different lightning location systems. In December 1995, the data were obtained by a lightning positioning and tracking system (LPATS), version III, and in December 1997, by a new hybrid lightning location methodology combining time-of-arrival (LPATS) and direction-finding techniques (Impact sensors). The results indicate that the flash characteristics are quite different from 1995 to 1997, mainly for positive flashes. Although limited to the small data sample, we believe that the most differences are mainly due to differences in the systems. We suggest that other independent techniques should be used in order to evaluate the performance of such systems.

## INTRODUCTION

In the last decade cloud-to-ground lightning flash characteristics have been obtained by lightning location networks in several regions throughout the world (e.g., Fournier and Pyle, 1998; Matsui et al., 1998; Pinto et al., 1998 a, b). In part, these characteristics may be a result of geographical and meteorological conditions prevailing in each region. However, they may also be a result of the characteristics of the lightning location networks, such as efficiency, location accuracy and discrimination criteria adopted. How do to distinguish between natural and technical aspects is a subject of intense research at present.

In order to investigate this problem, the lightning flash characteristics obtained in the southeastern region of Brazil in December 1995 are compared with those obtained in the same region in December 1997. In 1995, the lightning data were obtained by a 6 LPATS-III network, while in 1997 the data were obtained by a hybrid network consisting of 6 LPATS-III and 2 Impact sensors. Due to the different number of sensors and the intrinsic differences in the lightning activity in each year, only relative flash numbers are compared. The differences in the flash characteristics of positive flashes are attributed to differences in the network. Such assumption is based on our analysis of the lightning data collected between 1988 and 1995 in the same region. Besides the network reconfiguration and sensor modifications, the network in 1997 has undergone central processing modifications, from which the most relevant to this study is concern to the criteria of discrimination between cloud-to-ground flashes and intracloud flashes. In 1995, in fact, no discrimination criteria to distinguish between cloud-to-ground and intracloud flashes existed. The intracloud flashes were supposed to be no detected by the system, considering that they could not produced a radiation field above a given threshold in three sensor if they were distant by 200 km or more to each other. In 1997, in turn, the intracloud flashes were supposed to be eliminated by considering only flash-related pulses with time width larger than 11 microseconds. The possible consequences associated with these assumptions are discussed.

## RESULTS

Table 1 presents the flash characteristics for negative single and multiple flashes and positive single flashes in December 1995 and 1997.

| | 1995 | 1997 |
|---|---|---|
| Percentage Pos. Flashes (%) | 28.5 | 2.3 |
| Percentage Neg. Single Flashes (%) | 74.8 | 75.3 |
| Percentage Pos. Single Flashes (%) | 100 | 93.8 |
| Average Neg. Peak Current (kA) | 53.5 | 34.2 |
| Average Pos. Peak Current (kA) | 26.5 | 46.2 |
| Local Time Max. Flash Activity | 15-16 | 15-16 |
| Average Neg. Peak Current (Single Flashes) | 53.1 | 34.4 |
| Average Neg. Peak Current (Mult. Flashes) | 55.3 | 33.5 |

## DISCUSSION AND CONCLUSIONS

In terms of negative flashes, the results presented in Table 1 indicates that: the percentage of single flashes is almost the same in both years; the average peak current for single and multiple flashes is also almost the same; however, the average peak current for 1995 is significantly larger than that for 1997. Based on the variability of the peak current values measured between 1988 and 1995, we think that this last result is probably associated with such natural variability, being not influenced by the change in the configuration of the network.

For positive flashes, however, the results appear to be influenced by the change in the configuration of the network. In 1995, the percentage of positive flashes is significantly higher than that in 1997, whereas the average peak current is significantly lower. Both differences can be explained by assuming that in 1995 the positive cloud-to-ground flashes were contaminated by intracloud flashes. The value obtained in 1997, however, may not be representative of the region studied. Fig. 1 shows the peak current distribution of positive flashes for the whole year of 1995, compared with the NLDN distribution in the southeastern U.S. in 1994 and 1995 (Cummins et al., 1998). The data were obtained, respectively, before and after the upgrade of the NLDN network. Among other differences, in 1994 the NLDN rejected pulses below 11 microseconds width, whereas in 1995 this threshold was changed to 7.4 microseconds. Assuming that the criteria adopted by the NLDN network in 1995 (which, as far as we know, remains the same up to the present) is more realistic, the close similarity between our 1995 curve with the NLDN 1995 curve apparently indicates that the real percentage of positive flashes in southeastern Brazil is more close to the 1995 value than that in 1997 (whose configuration corresponds to the NLDN 1994 curve). Note that the differences in the NLDN curves in Fig. 1 are consistent with the differences in the average positive peak current shown in Table 1.

Clearly more data and research at different parts of the world are necessary before confident criteria to discriminate cloud-to-ground and intracloud flashes based on field waveforms can be defined. Some researchers have suggested that a peak current threshold for positive cloud-to-ground lightning should be used (Zaima et al., 1997; Zajac and Rutledge, 1998). It is even

possible that such criteria may be different at different regions, due to differences in the thunderstorm formation.

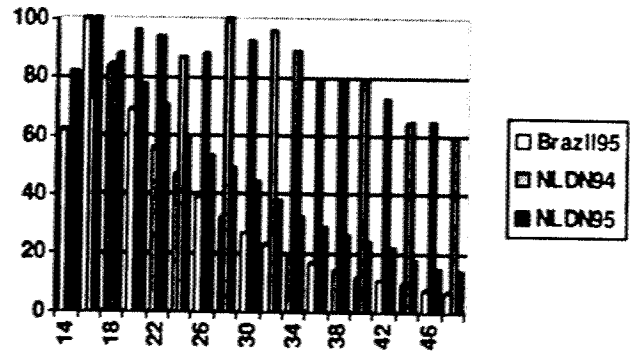


PEAK CURRENT (kA)

Fig 1- Normalized Peak current distribution of positive flashes in the southeastern Brazil in 1995 (Brazil95), and in the southeastern U.S. in 1994 (NLDN94) and in 1995 (NLDN95)

REFERENCES

Cummins, K. L., Murphy, M. J., Bardo, E. A., Hiscox, W. L., Pyle, R. B., and Pifer, A. E., A combined TOA / MDF technology upgrade of the U. S. National Lightning Detection Network, *J. Geophys. Res.*, 103, 9035-9044, 1998.

Fournier, G., and Pyle, R., The Canadian lightning Detection network, Proceedings of International Lightning Detection Conference, Arizona, 1998.

Matsui, M., Miyake, Y., and Takahashi, S., The introduction of the Japan lightning detection network, Proceedings of International Lightning Detection Conference, Arizona, 1998.

Pinto Jr., O., Pinto, I.R.C.A., Gomes, M.A.S., Vitorello, I., Padilha, A.L., Diniz, J.H., Carvalho, A.M., and Cazetta Filho, A., Cloud-to-ground lightning in the southeastern Brazil in 1993, 1. Geographical distribution. *J. Geophys. Res.*, submitted, 1999.

Pinto, I.R.C.A., Pinto Jr., O., Rocha, R.M.L., Diniz, J.H., Carvalho, A.M., and Cazetta Filho, A., Cloud-to-ground lightning in the southeastern Brazil in 1993, 2. Time variations and flash characteristics, *J. Geophys. Res.*, submitted, 1999.

Zaima, E., A. Mochizuki, N. Fukiyama, J. Hojo, and M. Ishii, Observation of lightning by means of time-of-arrival type lightning location system, *Elec. Eng. Japan*, 120(1), 1033-1038, 1997.

Zajac, B. A., and Rutledge, S. A., Climatological characteristics of cloud-to-ground lightning activity in the contiguous United States, Atmospheric Science paper 652, Colorado State Univ., 1998.

# CONDITIONS OF PLASMA CHANNELS REQUIRED FOR TRIGGERED LIGHTNING

Megumu Miki, Atsushi Wada, Hisashi Goshima and Takatoshi Shindo

Central Research Institute of Electric Power Industry, Tokyo, JAPAN

ABSTRACT: The conditions of a plasma channel required for the triggering of lightning have been estimated by comparison of observations of the actual lightning phenomenon and experiments on laser-produced plasma. The decay of the parameters of the plasma channel produced by the $CO_2$ laser was measured with microwave interferometry. From our observations on multi stroke flashes, we estimated the state of the discharge channel required to guide upward lightning discharges. Our results show that the electrical conductivity of more than 2 S/m is required for the triggering of lightning.

## INTRODUCTION

Laser-triggered lightning has been studied by many researchers. However, most of the studies have been conducted inside a laboratory. Some researchers have argued that the characteristics of actual lightning discharges are different from those of the discharges in laboratories. Recently, Kawasaki et al., succeeded in triggering the upward leader from a tower using a 2 kJ $CO_2$ laser pulse in Japan [Uchida, 1987]. However, their laser-produced plasma channel could not guide the upward negative leader from the tower for triggering lightning. In the laboratory, the negative leader could be guided by the plasma channel under any condition. Their results show that the effect of the plasma channel on the discharge is different from the effect of the plasma channel on the actual lightning discharge.

Thus, we used our observations of actual lightning discharges to estimate the conditions of the plasma channel required to guide the lightning. Based on our results, we discuss the relationship between the discharge path of the subsequent strokes, and the interval between each stroke in multiple-stroke flashes. Thereafter, based on this relationship and our experimental results on laser-produced plasma, we estimated the conditions required for the triggering of upward lightning discharges.

## OBSERVATION SYSTEM

There are lightning strokes on the 200 m-high stack on the coast of the Sea of Japan. The stations for lightning observation are located 630 m from the stack. The time variation of the lightning discharge path was observed with a high-speed video camera (Fastcam Ultima-UV, PHOTRON). The speed of the video camera was 4500 frames/s and the exposure time of the frame was 100 ns. The camera can record 3000 frames as digital data. The electric field changes accompanied with lightning discharge were measured by a plate antenna. The magnetic fields produced by the lightning current were measured by a loop antenna.

## OBSERVATION RESULTS AND DISCUSSIONS

We selected an event of multi-stroke flashes to evaluate the parameters of the plasma channel required for guiding of a lightning discharge. Figure 1 shows the observation results of the magnetic field with a loop antenna, electric field change with a plate antenna and images of the lightning discharge path with a high speed video camera. In this event, the first stroke(② in figure 1) occurred at 0.2 ms. The peak current

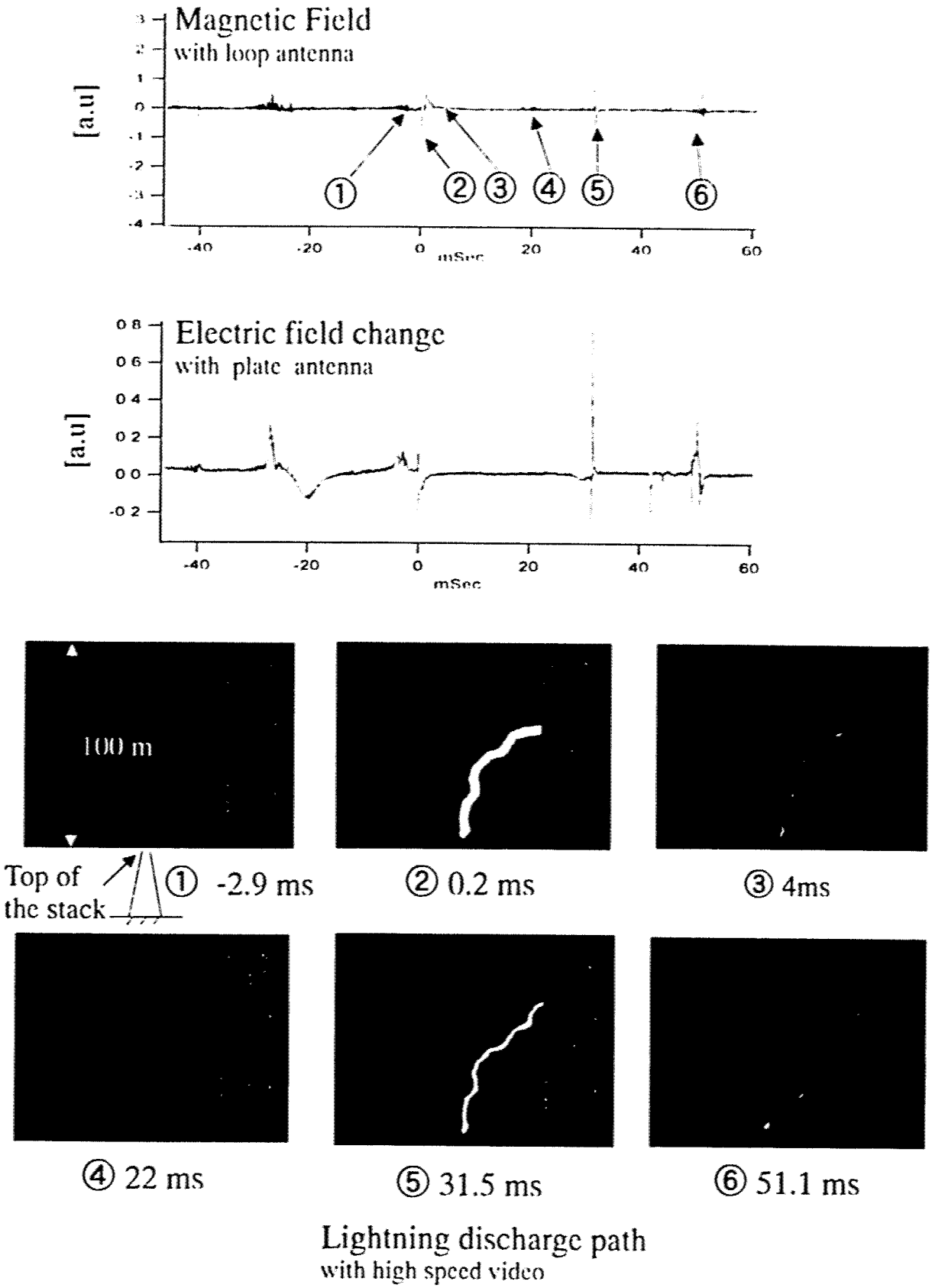


Figure 1 Observation results of multi stroke flashes

(1997. 1. 21)

of the first stroke was estimated to be about +7 kA by the peak value of the magnetic field. The second stroke on the stack occurred after the interval of about 30 ms (⑤ in figure 1). The peak current of the second stroke was about −6 kA. The discharge path of the second stroke fitted that of the first one near the stack. After the first stroke, the discharge channel continued to be luminous for more than 20 ms as shown in figure 1 ③. This suggests that the current of less than a few hundred amperes flowed continuously, along the discharge channel for more than 20 ms. The luminosity of the discharge channel disappeared after 22 ms (④ in figure 1). Thus, the interval of the light intensity from the lightning channel between the first stroke and the second stroke was about 10 ms. The third stroke appeared at 51 ms (⑥ in figure 1). The video frame shows that the third stroke did not strike the stack. The interval between the end of the second stroke and beginning of the third was about 15 ms. Although this is shorter than the interval between the first and the second strokes, the discharge path of the second stroke was different from that of the third. A possible reason is that the region of the charges corresponding to the third stroke in thunderclouds are far from the stack.

The discharge path of the subsequent stroke was the same as that of the first stroke in the event examined. The region of the charges of the first stroke are different from the region of the charges of the second stroke in thunderclouds, because the polarity of the first stroke was different from that of the second stroke. Thus, this shows that the discharge of the second stroke was guided by the rest of the discharge channel of the first stroke. The interval between the first stroke and the second stroke was estimated to be 10 ms by light intensity of the lightning channel and 30 ms by magnetic field. We considered that the actual interval was more than 10 ms and less than 30 ms. From this, the conditions of the plasma channel required for guiding lightning can be obtained by the decay of the parameters of the discharge channel.

Many researchers have reported measurements of a lightning discharge channel after a return stroke [Uman, 1986]. We used the electrical conductivity to estimate the state of the lightning discharge channel 10 ms after the return stroke. Electric conductivity of the lightning discharge can be obtained by measurement of the electron density, electron temperature and gas temperature, up to about 40 μs. Beyond 50 μs, the conductivity of the lightning discharge channel can be estimated using the gas temperature calculated by equation of thermal conductance [Uman, 1968]. These conductivities of the

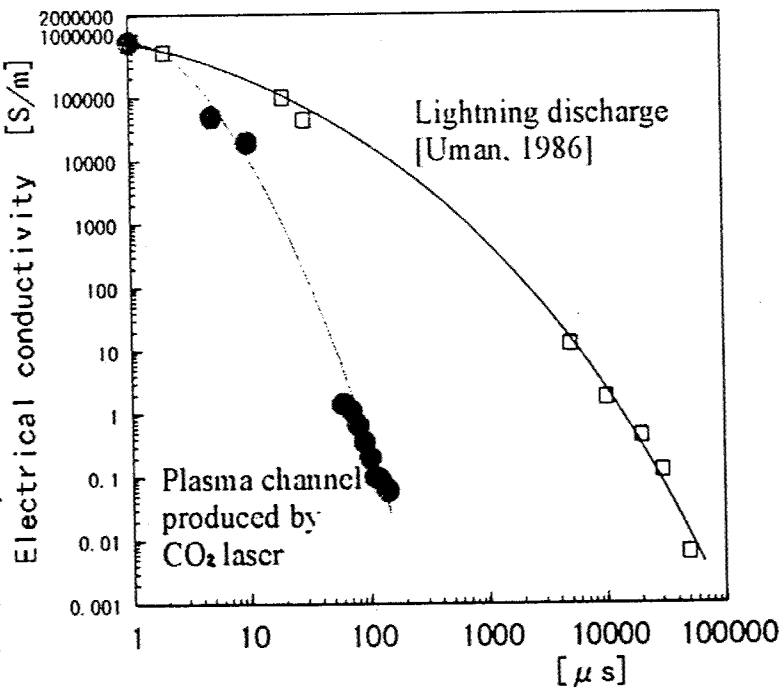


Figure 2 Electrical conductivity

lightning channel were shown in figure 2. In the evaluation of the conductivity, we assumed that the radius of the lightning channel was 2 cm. When the electrical conductivity of the lightning channel has decayed for 10 ms, it was 2 S/m. Further, the conductivity of the lightning channel which has decayed for 30 ms, was 0.1 S/m.

## EXPERIMENT OF LASER-PRODUCED PLASMA

The electrical conductivities of laser-produced plasma channels were measured with microwave interferometry (frequency = 35 GHz). A $CO_2$ laser (wave length=10.3 m) was used in the experiment Plasma channels were produced by focusing a 50J-$CO_2$ laser pulse with a concave mirror (focal length=10 m). Figure 2 shows the electrical conductivity of the plasma channels with those of the lightning channel. The conductivity decreases by 2 S/m for 50 s and by 0.1 S/m for about 100 μs. The electrical conductivities of the plasma channels up to 10 μs, were evaluated by electron density and temperature [Miki, 1996].

## SUMMARY

Based on our observations and experiments, the plasma parameters for guiding lightning were estimated. The rest of the first stroke with a peak current of more than 7 kA, could guide the subsequent strokes up to 10 ms~30 ms. From the study on the decay of the lightning discharge channel, we predicted the electrical conductivity of the rest of the first stroke. From these results, we estimated that the discharge channel which has the electrical conductivity of more than 2 S/m, can guide subsequent strokes. Our experiments show that the electrical conductivity of the plasma channel produced by the laser decreased by 0.1 S/m for 100 μs and 2 S/m for 50 μs. Thus, $CO_2$ laser-produced plasma channels could guide the lightning discharge 50 μs~ 100 μs after the generation of the plasma.

Uchiyama et al., reported that the plasma channel produced by the 2 kJ- $CO_2$ laser could not guide the lightning discharge from the tower [Uchiyama 1997]. There are two possible reasons for this result. One is that the upward leader was triggered after more than 100 μs. Another is the geometric difference between the laser-produced plasma channel and the lightning discharge channels. Although the laser-produced plasma channel is discrete, the lightning discharge channel is continuous.

In this paper, the evaluation of the conductivities and the relationships between the discharge path and the intervals between subsequent strokes are not enough to estimate the conditions of the plasma channel, accurately. We plan to pursue this objective in a future study.

## REFERENCES

Uchida, S., Y. Shimada, H. Yasuda, K. Tsubakimoto, S. Motokoshi, C. Yamanaka, Z-I. Kawasaki, T. Yamanaka, K. Matsu-ura, T. Ushio, M. Adachi, Y. Ishikubo,
Laser triggered lightning experiment in the field, 10th ICAE (Osaka), 660--663, 1996

Uman, M. A., LIGHTNING, Chapter 5.5.2 Return stroke properties and
Chapter 7.7 The lightning channels between strokes, Dover Pub. Inc., 1986

Miki, M., T. Shindo and Y. Aihara, Mechanism of guiding ability of CO2 laser-produced plasma on pulsed discharges, J. Appl. Phys., 80, 3208--3214, 1996

# CALCULATION OF ELECTRIC FIELD STRENGTH NECESSARY FOR ALTITUDE DISCHARGE ABOVE THUNDERSTORMS

V. N. Morozov

Voeikov Main Geophysical Observatory, Karbysheva, 7
St.-Petersburg, 194021, Russia

ABSTRACT: Electrical field produced by the thunderstorm lighting at high altitude atmosphere is calculated by solutions of the non-stationary equation of continuity of the electrical charge and Poisson's equation. Magnitudes and electric field strength of the electrical cloud charge necessary for high altitude atmosphere breakdown and discharges via the run away electron process are estimated.

## INTRODUCTION

High altitude discharges above thunderstorms are most mysterious phenomena in atmospheric electricity. Experimental data concerning lightning features above thunderstorms: red sprites and blue jets were considered by Winckler (1995). One of hypothesis, explaining the phenomena is related with cloud-cloud and cloud-ground discharges. The purpose of his work is to calculate the electric field, made by cloud electrical charge after thunderstorm lightning and to estimate the magnitude of the electrical field strength and electrical cloud charge necessary for high altitude atmosphere breakdown.

## THE MATHEMATICAL MODEL

The main equations, used for the theoretical calculations of the electrical field produced by cloud charge after thunderstorm lightning at high altitude atmosphere is

$$\frac{\partial \rho}{\partial t} - \nabla(\lambda \nabla \varphi) = 0, \quad \Delta\varphi = -4\pi\rho, \quad \vec{E} = -\nabla\varphi, \quad \lambda = \lambda_0 e^{\alpha z}, \quad \alpha = 0.2 km^{-1} \tag{1}$$

Where: $\varphi$ is the electrical potential, $\vec{E}$ is electrical field strength, $\lambda$ is the conductivity of the atmosphere, $\rho$ is the charge density.

Initial and boundary conditions for solution of equations (1) are:

$$\Delta\varphi|_{t=0} = -4\pi\rho_s(\vec{r}), \ \varphi|_{z=0} = 0, \ \varphi|_{|\vec{r}|\to 0} = 0, \ |\vec{r}| = \sqrt{x^2 + y^2 + z^2} \tag{2}$$

Where: $\rho_s(\vec{r})$ is the initial charge density of could, $(x, y, z)$ - Cartesian coordinates.

The initial distributions of could charge density are:

$$\rho_S = Q_{1S}\delta(z - z_0), \rho_S = \frac{Q_{2S}}{r}\delta(r)\delta(z - z_0) \tag{3, 4}$$

Where: $\delta(x)$ is Dirac's function, $(r, z)$ are cylindrical coordinates.

The equation (3) corresponds to 1-D distribution of cloud charge density and the solution of equations (1) obtained by Morozov (1995) is:

$$\varphi(z,r) = 4\pi Q_{1S} z_0 \left[ \int_0^t Ei\left(\frac{t-\tau}{\tau(z)}\right) v_1\left(\frac{\tau}{\tau_0}\right) d\tau + \frac{1}{\alpha z_0}\left[ \int_0^t \frac{1}{t-\tau}\left( e^{\frac{t-\tau}{\tau_0}} - e^{-\frac{t-\tau}{\tau(z)}} \right) d\tau \bullet \right.\right.$$
$$\left.\left. \bullet \left( \int_0^\tau Ei\left(\frac{\tau-\tau_1}{\tau(z)}\right) v_1\left(\frac{\tau_1}{\tau_0}\right) d\tau_1 \right) - \right]\right], \quad v_1\left(\frac{t}{\tau_0}\right) = \frac{1}{\tau_0} e^{-\frac{t}{\tau_0}} \int_0^\infty \frac{(t/\tau_0)^{\xi-1}}{\Gamma(\xi)} d\xi \tag{5}$$

Where: $\tau(z) = (4\pi\lambda(z))^{-1}, \tau_0 = \tau(0)$ $Ei(x) = \int_1^\infty e^{-x_n}\frac{dn}{n}$ $\Gamma(\xi)$ - gamma-function. When $t \to 0$, we find from (5) the asymptotic formula for $E_z = -\frac{\partial\varphi}{\partial z}$

$$E_z = -\frac{\partial\varphi}{\partial z} \cong 4\pi Q_{1S}\frac{z_0}{h(t)},\ h(t) = \frac{1}{\alpha}\ln\frac{\tau_0}{t},\ t \ll \tau_0 \tag{6}$$

For the initial distribution of cloud charge density (4) solution of equations (1) for time interval $0 < t < \tau_0$ is (Morozov, 1995)

$$\varphi(r,z,t) = 2Q_{2S}\int_0^\infty J_0(xr)z_0\frac{e^{-xh(t)+z}F\left(\tilde{\alpha},\tilde{\beta},\tilde{\gamma},-\frac{t}{\tau_0}e^{\alpha z}\right) - u_2 e^{xh(t)-z}F\left(\bar{\alpha},\bar{\beta},\bar{\gamma},-\frac{t}{\tau_0}e^{\alpha z}\right)}{e^{-xh(t)} - u_2 e^{xh(t)}}\bullet \tag{7}$$

$$\bullet\ \mathrm{sh}xz_0dx,\quad u_2 = \Gamma\left(1+\frac{2x}{\alpha}\right)\Gamma^{-2}(\alpha_1 - x/\alpha)\Gamma^{-1}\left(1-\frac{2x}{\alpha}\right)\Gamma^{-2}\left(\alpha_1+\frac{x}{\alpha}\right),\ z_0 < z < h(t)$$

Where $F(\alpha,\beta,\gamma,-u)$ is the hypergeometric function, $J_0(xr)$ - Bessel's function. $\tilde{\alpha} = \alpha_1 + x/\alpha$, $\tilde{\beta} = \tilde{\alpha}_1 + x/\alpha$, $\tilde{\gamma} = 1 + 2x/\alpha$; $\bar{\alpha} = \alpha_1 - x/\alpha$, $\bar{\beta} = \bar{\alpha}_1 - x/\alpha$, $\bar{\gamma} = 1 - 2x/\alpha$, $\alpha_1 = (1+\sqrt{1+4x^2/\alpha^2})/2$, $\bar{\alpha}_1 = (1-\sqrt{1+4x^2/\alpha^2})/2$.

When the conditions $\alpha z \gg 1$, $2\alpha h(t) \gg 1$ are fulfilled, we obtain for vertical component of electrical field strength $E_z$, when $r = 0$

$$E_z(0,z,t) = Q_{2S}\left[\frac{1}{(z-z_0)^2} - \frac{1}{(z+z_0)^2} + \frac{1}{4h^2(t)}\left(\sum_{n=1}^{\infty}\frac{1}{(n+u_1)^2} - \sum_{n=1}^{\infty}\frac{1}{(n+u_2)^2} - \sum_{n=0}^{\infty}\frac{1}{(1+n-u_1)^2} + \right.\right.$$

$$\left.\left. + \sum_{n=0}^{\infty}\frac{1}{(1+n-u_2)^2}\right)\right],\ h(t) = (1/\alpha)\cdot\ln\frac{\tau_0}{t} \tag{8}$$

Where $u_1 = (z-z_0)/2h(t)$, $u_2 = (z+z_0)/2h(t)$

## THE ESTIMATES OF MAGNITUDES OF ELECTRICAL FIELD STRENGTH AND CLOUD CHARGE NECESSARY FOR HIGH ALTITUDE BREAKDOWN

We estimate the magnitudes of the electrical field strength necessary for high altitude breakdown, using the relation:

$$eE_z\lambda_e = W_{ion} \tag{9}$$

Where $\lambda_e$ is the electron mean free path, $e$ is the charge of electron, $W_{ion}$ is ionization energy of molecules of nitrogen $N_2$ ($W_{ion}$=15.6 eV)

For altitude from 50 to 75 km, we have $0.79 \le \lambda_e < 7.9$ sm and magnitudes of vertical component of electrical field strength $E_z$ are

$$E_z \approx (0.2 - 2)kV/m \tag{10}$$

Using equation (6), we obtain $Q_{1S} = 0.0041 - 0.041$ for $t = 10^{-4}s, \tau_0 = 600s, h(t) = 78$ km, $z_0 = 10$ km. For the charge of cloud $\bar{Q} = Q_{1S}R^2$, where R – horizontal characteristic length of cloud, we have for R=100 km:

$$\bar{Q} = (1.36\cdot10^2 - 1.36\cdot10^3)C \tag{11}$$

For the point distribution of cloud charge (4), we estimate cloud charge after cloud-ground lightning, using equation (8). When z=50 km, $z_0$=10 km, h(t)=78 km, we find $Q = 6.4\times10^2 C$ and for z=15 km, we obtain $Q = 2.2\times10^2 C$

The condition of runaway electron breakdown is (Gurevichetal, 1992)

$$E_z > E_{zcr} = \frac{4\pi N_m Z e^3}{mV^2} ln \frac{mV^2}{ZW_{ion}} \tag{12}$$

Where: m, V are electron mass and velocity. $N_m$ is number density of neutral molecules of atmosphere. $Z = 14.5$ For $2\varepsilon = mV^2 = 2.2 \times 10^5 eV, z = 70$ km, $N_m = 9.4 \times 10^{15}$ sm$^{-3}$, $E_{zcr} = 0.1$ kV/m, i. e critical magnitude of electrical field strength for discharge via runaway process are smaller than the critical magnitude $E_z$ for atmospheric breakdown ( $E_z \approx 0.2$ kV/m), but the electron energy must be larger than ionization energy of air, i. e. Runaway electron breakdown must be produced by cosmic ray electron.

REFERENCES:

Gurevich A. V., Milikh G. M., Rousell-Dupre R. Runaway electronmechanism of air breakdown and preconditioning during at thunderstorm. Physics Letters A., 165, 463-468, 1992.

Morozov V. N. Theoretical modeling of electrical processes in low layer of the free atmosphere. A thesis on competition of a scientific degree of the doctor of physico-mathematical sciences.

Wincler J. R. Further observations of cloud-ionosphere electrical discharges above thunderstorms. J. Geophys. Res., 100, 14335-14345, 1995.

# ON THE TEMPORAL EVOLUTION OF RED SPRITES, RUNAWAY THEORY VERSUS DATA

V. Yukhimuk, R. A. Roussel-Dupré, and E. M. D. Symbalisty

Atmospheric and Climate Sciences Group, Los Alamos National Laboratory,
Los Alamos, New Mexico, USA

ABSTRACT: The results of numerical simulations of red sprite discharges, namely the temporal evolutions of optical emissions, are presented and compared with observations. The simulations are done using the recently recalculated runaway avalanche rates. The temporal evolution of these simulations is in good agreement with ground-based photometer and CCD TV camera observations of red sprites. Our model naturally explains the "hairline" of red sprites as a boundary between the region where the intensity of optical emissions associated with runaway breakdown has a maximum and the region where the intensity of optical emissions caused by conventional breakdown and ambient electron heating has a maximum. We also present for the first time simulations of red sprites with a daytime conductivity profile.

## INTRODUCTION

The ground-based and aircraft observations show that sprite duration can vary significantly. Sentman and Wescott [1993] estimated the duration of a sprite is 17 ms or less. According to Lyons [1994] the sprite duration is in the range 33 – 283 ms, and the ground-based photometer observations of red sprites [Winckler et al., 1996] show a sharp maximum of the optical emission intensity with duration of about 3 ms. In the same time the simultaneous CCD TV camera observations [Winckler et al., 1996] show that optical emissions persist for several tens of milliseconds.

The authors of the publications devoted to red sprite theories [Bell et al., 1995; Milikh et al., 1995; Taranenko and Roussel-Dupre, 1996; Pasko et al., 1996; Milikh et al., 1997; Roussel-Dupre et al., 1998; Yukhimuk et al., 1998] were mostly concerned with explaning red sprite intensity, shape, altitude and spectra. The temporal evolution of optical emissions from a red sprite was described by Pasko et al., [1996] on the basis of conventional breakdown model. In the present paper we present an explanation of the red sprite temporal evolution based on the runaway air breakdown theory. In our simulations we use the recently recalculated runaway avalanche rates [Symbalisty et al., 1998].

## SIMULATION RESULTS

We consider two cases of sprite simulations: 1) the upward discharge is driven by a quasi-electrostatic field produced by $Q_{tot}$ = -280 C of negative charge with a $\tau$ of 6 ms at an altitude, H = 9.5 km above sea level; 2) $Q_{tot}$ = -400 C, $\tau$ = 20 ms, H = 8 km. The charge Q is built on an exponential time scale:

$$Q = Q_{tot} (1 - \exp(-t / \tau))$$

We calculate the optical emissions from red sprites and their attenuation by air using the same approach and formulas as described in Yukhimuk et al. [1998], but we are now using more accurate electron – molecule collision cross sections [Trajmar et al., 1983] for our calculations of optical emissions as well as for the solution of the Boltzmann kinetic equation for a population of low energy electrons in an electric field.

The temporal evolution of the maximum intensity of optical emissions from the simulated sprite discharge for case 1,2 is shown in Figure 1(a,b) respectively. The total duration of visible optical emissions (intensity greater than about 10 kR) is about 40 ms for case 1, and about 60 ms for case 2. There is a short peak with duration of about 1 - 3 ms followed by a much longer tail for both cases. The maximum intensity of the short peak is considerably higher than that of the tail. The intensity of optical emissions calculated for the first (0 - 17 ms) and second (17 - 34 ms) camera fields for case 1 is shown in Figure 2 (a, b), and the intensities for the fields 1 – 4 for case 2 is shown in Figure 2(c-h).

The sharp maximum, in our model, results from the abrupt formation of a relativistic electron beam as soon as the electric field exceeds runaway threshold values [Roussel-Dupré and Gurevich, 1996] over a large vertical range, i. e. from the top of the cloud to the top of the main body of the sprite. This fast discharge, with duration $T_{sp}$ ≈ 1 – 3.5 ms, enhances the conductivity of the atmosphere above the cloud top

and reduces the volume of the region where the overvoltage ($\delta_0$ )> 1. The discharge produces significant ionization at altitude higher than 60 km, that leads to the local lowering of the ionosphere boundary, and, therefore to downward motion of red sprite.

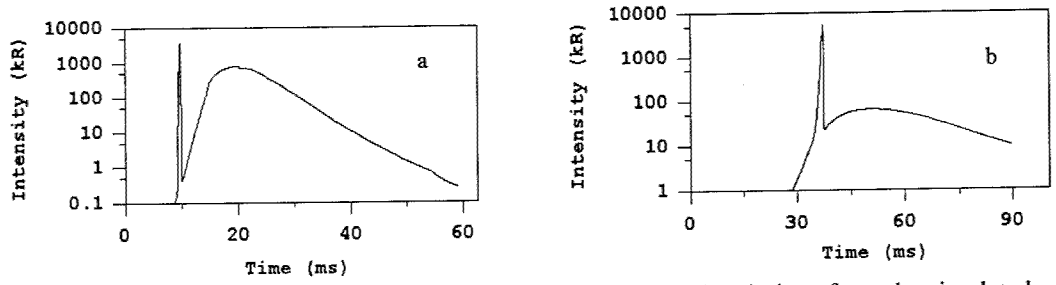


**Figure 1.** Temporal evolution of the maximum intensity of optical emissions from the simulated sprite for case 1 and 2. The time zero corresponds to the beginning of the driving CG stroke.

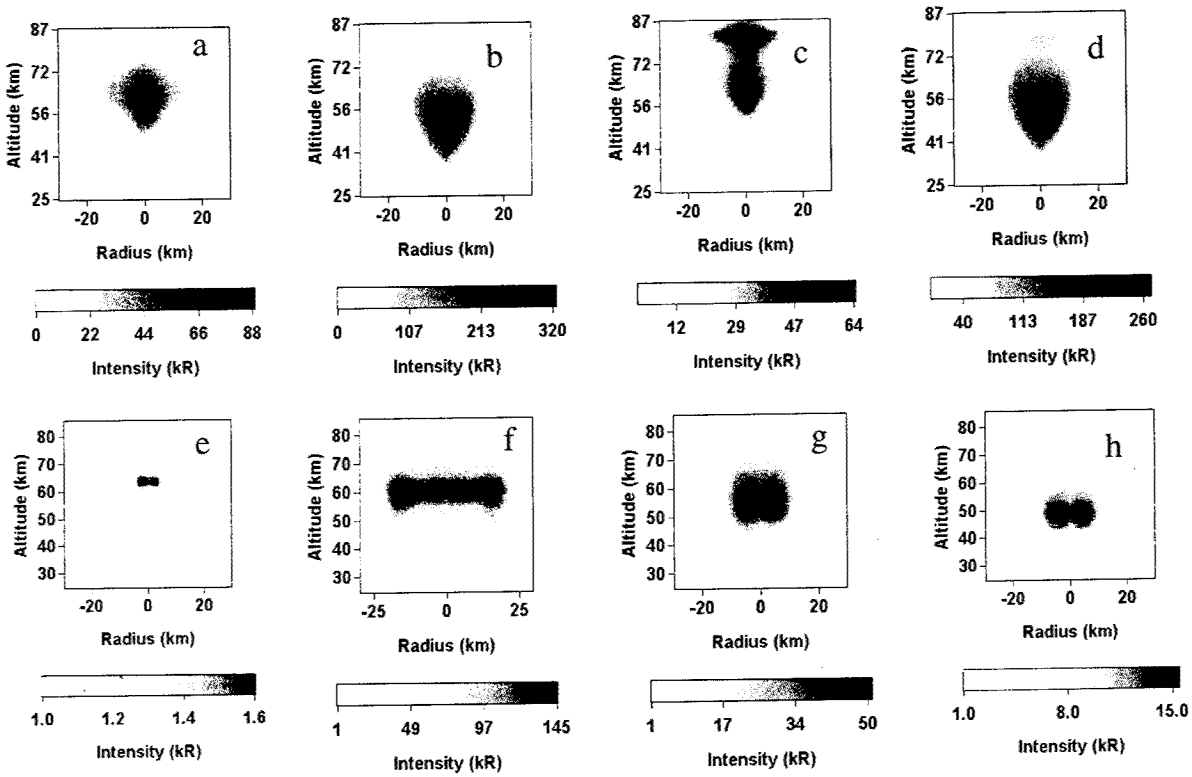


**Figure 2.** Intensity of optical emissions calculated for the first 0 - 17 ms (a,c) and second 17 - 34 ms (b,d) camera fields for the Reid (a,b) and Hale (c,d) nighttime conductivity profiles for case 1. Intensity of optical emissions for the fields 1 – 4 (e-h) for case 2 assuming the Reid nighttime conductivity profile.

The dependence of the red sprite duration and intensity on the parameters of driving CG discharge assuming nighttime conductivity profile [Reid, 1986] is shown in Table 1. Here, $H_Q$ denotes the altitude of the negative charge above sea level, Q is the charge value, $\tau$ denotes the time scale of the driving discharge, $I_{max}$ is a maximum intensity calculated for one camera field (t = 17 ms) for the first field, $T_{tot}$ is the total duration of detectable optical emissions, and $T_{sp}$ denotes the duration of the sharp peak of optical emissions. The duration of optical emissions is in broad range 10 – 60 ms for different cases, in the same time the signature of the temporal evolution is similar for all cases, a sharp peak lasting 1 to 3 ms followed by a longer tail.

TABLE 1

| Q(C) | 180 | 250 | 250 | 280 | 370 | 400 |
|---|---|---|---|---|---|---|
| $\tau$(ms) | 6 | 6 | 6 | 6 | 10 | 20 |
| $H_Q$(km) | 12 | 12 | 9.5 | 9.5 | 8 | 8 |
| $I_{max}$(kR) | 30 | 910 | 160 | 320 | 86 | 145 |
| $T_{tot}$(ms) | 19 | 10 | 28 | 40 | 46 | 60 |
| $T_{sp}$(ms) | 2.4 | 1.1 | 1.1 | 1.0 | 3.2 | 3.1 |

TABLE 2

| Conductivity profile | $I_{max}$ (kR) | $H_{top}$ (km) | $T_{tot}$ (ms) |
|---|---|---|---|
| Reid, nighttime | 320 | 77 | 40 |
| Hale, nighttime | 260 | 84 | 41 |
| Hale, daytime | 380 | 57 | 35 |

The altitude of a red sprite, its shape, and intensity of the optical emissions depend significantly on the ambient atmosphere conductivity profile. We performed sprite simulations for three different conductivity profiles. These included: (1) a nighttime conductivity profile [Reid, 1986] which corresponds to moderate ionization rates; (2) a mid-latitude nighttime conductivity profile which corresponds to low levels of ionization, [attributed to L. Hale in Holzworth, 1995], and; (3) a daytime conductivity profile [also from L. Hale in Holzworth, 1995]. We kept all other simulation parameters constant. As one can see the same CG discharge produces the brightest red sprite for the day time conductivity profile, because of the field focusing between the cloud top and the ionosphere, but the top of the sprite is at lower altitude. The results are presented in Table 2 for case 1. Figure 2 (a, b, c, d) shows the intensity of optical emissions calculated for the first 0 - 17 ms (a,c) and second 17 - 34 ms (b,d) camera fields for the Reid (a,b) and Hale (c,d) nighttime conductivity profiles for case 1. The Hale profile produces optical emissions extending to higher altitudes because its conductivity shelf is at a higher altitude than Reid's.

## COMPARISON WITH OBSERVATIONS

The ground-based photometer and CCD TV observations of red sprites [Winckler et al., 1996] show the presence of a sharp maximum of the optical emission intensity with duration of about 3 ms followed by a longer lasting but weaker tail. The tail shows appreciable luminosity for three fields (50 ms) after the initial intense field, and a decrease in luminosity of the camera fields with time. This temporal evolution is very similar to temporal evolution of the second case of simulations (Q = 400 C, $H_Q$ = 8 km, $\tau$ = 20 ms) considered in present paper. The calculated duration of the sharp maximum is 3.3 ms, and the total duration of optical emissions is 60 ms detectable for 4 camera fields, with the brightest second field ($I_{max}$ = 145 kR), and the luminosity of the camera fields decreases with time. It should be also mentioned that the simulated optical emissions for the first camera field for case 2 (Figure 2(e)) have approximately the same shape, size and altitude as the small symmetrical sprite observed by Winckler et al., (see Figure 11 in [Winckler et al., 1996]).

According to Sentman et al., [1995] the brightest region of red sprite, the "head", lies within 66 – 74 (±4) km altitude, above the head there is often a faint red glow ("hair"), separated from the bright head by a dark line ("hairline"). As one can see in Figure 2(c) for the case of low levels of ionization (Hale nighttime profile) significant optical emissions are produced at altitude 80 – 84 km as a result of conventional breakdown and heating of ambient electrons. This region is naturally separated from the region where optical emissions associated with runaway air breakdown predominate (lower than 77 km), and total optical emissions have local minimum at 77 – 80 km altitude where the hairline is usually observed [Sentman et al., 1995].

## CONCLUSIONS

The temporal evolutions of optical emissions from red sprites computed by using new ionization rates [Symbalisty et al., 1998] are in good agreement with observations. Our new results are in much better agreement with particular ground based observations [Winckler et al., 1996] than the results of our old simulations [Yukhimuk et al., 1998] which predicted a maximum duration of detectable optical emissions from a sprite to be less than one camera field. There are three major differences between our old and new simulations: (1) we use new lower ionization rates which lead to a slower discharge ; (2) we put the driving discharge at a lower altitude and start the simulations at a lower altitude, and ; (3) we use more accurate electron – molecule collision cross sections [Trajmar et al., 1983] in our new simulations. The bottom of the

computational grid, in our old simulations, was at 18 – 20 km. In our new simulations the computational grid starts at altitude 14 – 16 km, which is more consistent with the average altitude of thunderstorm cloud tops.

The cylindrically symmetric computational grid encompasses a large scale – typically Z = 14 - 90 km and R = 0 - 30 km. With existing computer resources it is virtually impossible to resolve the fine structure of red sprites, which is of the order of tens of meters, and in the same time, to perform simulations in the whole region of interest (from the cloud top to the ionosphere). In reality the region of optical emissions shown in Figures 2 (a - h) would have rich fine structure because of irregularities in the cosmic ray flux, in the ambient conductivity, and in the electric field which is a superposition of driving electrostatic fields and radiation fields from lightning.

Our model naturally explains the "hairline" in red sprites. It delineates a boundary between the region where the intensity of optical emissions associated with runaway breakdown has a maximum (50 - 76 km altitude) and the region where the intensity of optical emissions caused by conventional breakdown and ambient electron heating has a maximum (80 – 84 km altitude). Between those two region (at altitudes 76 – 80 km) the runaway electrons are collisionless and the optical emissions from ambient electrons in an electric field is weak (for reasonable values of the electric field).

ACKNOWLEDGMENTS: This work was funded by NASA under contract NRA-95-11-ITM-029.

REFERENCES

Bell, T. F., V. P. Pasko, and U. S. Inan, Runaway electrons as a source of Red Sprites in the mesosphere, *Geophys. Res. Lett*, *22*, 2127, 1995.

Gurevich, A. V., G. M. Milikh, and R. Roussel-Dupre, Runaway electron mechanism of air breakdown and preconditioning during a thunderstorm, *Phys. Lett. A 165*, 463, 1992.

R. H. Holzworth, "Quasistatic Electromagnetic Phenomena in the Atmosphere and Ionosphere," in Handbook of Atmospheric Electrodynamics, Volume I, Hans Volland ed., CRC Press, 1995, pp. 235-266.

Lyons, W. A., Characteristics of luminous structures in the stratosphere above thunderstorms as imaged by low-light video, *Geophys. Res. Lett*, *21*, 875-878, 1994.

Milikh, G.M., K. Papadopoulos, and C. L. Chang, On the Physics of High Altitude Lightning, *Geophys. Res. Lett*, 22, 85, 1995.

Milikh, G.M., J. A. Valdivia and K. Papadopoulos, Model of red sprite optical spectra, *Geophys. Res.Lett*, 24, 833, 1997.

Pasko, V.P., Inan, U.S., and Bell, T.F., Sprites as luminous columns of ionization produced by quasi-electrostatic thundercloud fields, *Geophys. Res. Lett*, 23, No. 6, 649, 1996.

Reid, G. C., Electrical structure of the middle atmosphere, in The Earth's Electrical Environment, pp. 183-194, Nat. Acad. Press, Washington, D.C., 1986.

Roussel-Dupré, R.A. and Gurevich, A.V., On runaway breakdown and upward propagating discharges, *J. Geophys. R*es. 101, No. A2, 2297, 1996.

Roussel-Dupré, R., E. Symbalisty, Y. Taranenko, and V. Yukhimuk, Simulations of high-altitude discharges initiated by runaway breakdown, *JASTP*, 60, 917 – 940, 1998.

Sentman, D. D., and E. M. Wescott, Observations of upper atmospheric optical flashes recorded from an aircraft, *Geophys. Res. Lett*,, 20, 2857-2860, 1993.

Symbalisty, E. M. D., R. Roussel-Dupré, and V. Yukhimuk, *IEEE Transactions on Plasma Science*, Vol. 26, No. 5, October 1998, pp. 1575-1582.

Taranenko, Y.N., and Roussel-Dupré, R., High-Altitude Discharges and Gamma-ray Flashes: A Manifestation of Runaway Air Breakdown, *Geophys. Res. Lett*, 23, No. 5, 571, 1996.

Trajmar, S., D.F. Register and A. Chutjian, Electron scattering by molecules II. Experimental methods and data. *Physics Reports*, 97, 5, 219-356, 1983.

Winckler, J. R., W. A. Lyons, T. E. Nelson, and R. J. Nemzek, New high-resolution ground-based studies of sprites, *J. Geophys. Res.* 101, D3, 6997-7004, 1996.

Yukhimuk, V., R. Roussel-Dupré, E. M. D. Symbalisty, and Y. Taranenko, Optical Characteristics of Red Sprites produced by runaway air breakdown, *J. Geophys. Res.*, 103, No. D10, 11473, 1998.

# ON THE NATURE OF MESOSPHERIC ELECTRIC FIELDS

A. M. Zadorozhny

Novosibirsk State University, Pirogova 2, Novosibirsk 630090, Russia

ABSTRACT: A possible mechanism for the generation of large vertical electric fields observed in the mesosphere is discussed. Simultaneous existence in the mesosphere both the negative and positive multiply charged aerosol particles of different sizes is assumed for explanation of the fields. More massive charged particles falling with larger velocities initiate a charge separation. Smaller particles carrying charges of the other sign are needed to reduce the effective conductivity of the mesospheric dusty plasma. The proposed model can explain the existence of the V/m electric fields observed both in the lower mesosphere and in the vicinity of noctilucent clouds and PMSE.

## INTRODUCTION

The first measurements of the electric fields in the mesosphere were made in the early 1970s by *Bragin et al.* [1974] and *Tyutin* [1976]. Currently, different groups using different instruments have carried out more than fifty rocket measurements of the mesospheric electric fields. In about half of them a mesospheric maximum of the vertical electric field on the order of a few V/m has been observed at about 50-70 km [see *Zadorozhny and Tyutin*, 1997]. An example of these measurements is shown in Figure 1. The large vertical electric fields were also observed by *Zadorozhny et al.*, [1993] at 82.5-84.5 km in the vicinity of noctilucent clouds (NLC) and polar mesosphere summer echoes (PMSE), but they were not detected earlier under similar conditions [*Goldberg*, 1989]. By now, some regularities have been identified concerning electric field behavior in the mesosphere [*Hale et al.*, 1881; *Maynard et al.*, 1981; *Hale*, 1984; *Goldberg*, 1989; *Goldberg and Holzworth*, 1991; *Zadorozhny et al.*, 1994; *Zadorozhny and Tyutin*, 1997, 1998]. But the nature of the fields has not yet been clarified. There is not currently an adequate theory for how such fields are produced.

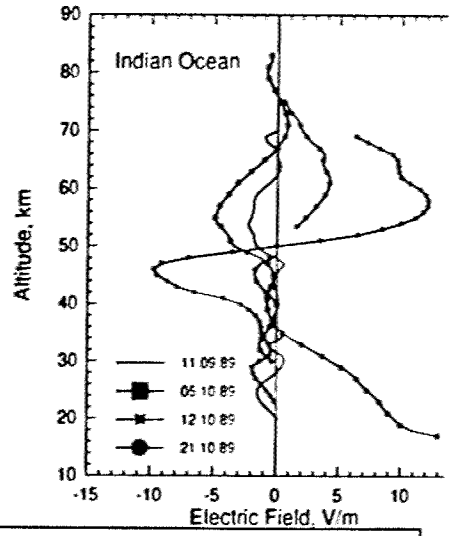


Figure 1. Altitude profiles of vertical electric field measured in the Southern Hemisphere at latitudes of 40°-60°S [*Zadorozhny et al.*, 1994].

Possible influences of aerosols on electrical properties of the mesosphere have been frequently discussed [e.g. *Bragin*, 1973; *Chesworth and Hale*, 1974; *Hale*, 1984; *Goldberg*, 1989; *Mitchell*, 1990; *Goldberg and Holzworth*, 1991; *Zadorozhny et al.*, 1994; *Mitchell et al.*, 1995]. There are direct evidences for the existence of both positively and negatively charged dust particles in the lower and upper mesosphere [*Mitchell*, 1990; *Mitchell et al.*, 1995; *Havnes et al.*, 1996; *Gelinas et al.*, 1998]. Simultaneous measurements of the electric field strength, positive ion density and aerosols [*Zadorozhny et al.*, 1994] pointed out both an ion-aerosol interaction and a connection between the mesospheric electric fields and aerosol content. The height correlation of the measured electric field disturbances with the NLC and PMSE positions indicates the importance of the aerosol particles in the generation of the vertical electric fields in the polar summer mesopause [*Goldberg*, 1989; *Zadorozhny et al.*, 1993, 1997].

In this paper a possible mechanism of the vertical electric field generation in the mesosphere due to gravitational sedimentation of multiply charged aerosol particles is discussed.

## ELECTRIC FIELD GENERATION IN MESOSPHERIC DUSTY PLASMA

A mechanism for the generation of the vertical electric fields $E_z$ caused by gravitational falling through the mesosphere of meteoric debris negatively charged in the upper D-region of the ionosphere has been analyzed by *Aikin and Maynard* [1990]. The vertical electric field generated by sedimenting aerosol particles with concentration $N_p$ is defined in *Aikin and Maynard's* [1990] model by the expression obtained from the requirement of a local current balance between a downward flux of electric charge carried by the particles and a conduction current:

$$E_z = \frac{Z_p q_e N_p V_p}{\sigma_i} \tag{1}$$

Here $q_e$ is the unit electrical charge; $Z_p$ is the number of unit charges on each particle; $V_p$ is the fall velocity of the particle; and $\sigma_i$ is the electrical conductivity of the atmosphere. The fall velocity for spherical particles is given by [*Jensen and Thomas,* 1988]:

$$V_p = \frac{\rho_p g r_p}{2p}\sqrt{\frac{\pi kT}{2m_a}} \tag{2}$$

where $\rho_p$ is the particle specific gravity; $g$ is the acceleration due to gravity; $p$ is the ambient pressure; $T$ is the atmospheric temperature; $k$ is Boltzmann's constant; and $m_a$ is the mass of a typical atmospheric molecule.

The fields calculated with the use of realistic parameters for the particles in (1) are in the range of only 10 mV/m in the lower mesosphere where the V/m fields are observed [*Aikin and Maynard,* 1990]. Calculations for NLC/PMSE conditions also show that equation (1) cannot explain the vertical electric fields observed by *Zadorozhny et al.,* [1993] if the concentration and size of the sedimenting particles as well as atmospheric conductivity are taken in accordance with the rocket data. These indicate that a more complex mechanism is required to explain the observed large vertical electric fields. The main obstacle for the formation of the large fields in this simple model is a high electrical conductivity of the atmosphere, which is defined by diffusivity of the charged particles:

$$\sigma_i = \frac{Z_i^2 n_i q_e^2}{kT} D_i \tag{3}$$

where $n_i$ is the concentration of ions or electrons; $D_i$ is the diffusion coefficient.

*Cho et al.* [1992] showed that a presence of multiply charged aerosols in the mesospheric plasma leads to a drastic decrease of an effective electron diffusivity up to a value equal to about the diffusivity of the aerosol particles. For large enough aerosols the transition to the reduced electron diffusivity occurs sharply when somewhat more than half of the charge is tied up in aerosols. The effective ion diffusivity will be obviously decreased to about the same value under the same conditions.

To explain the V/m vertical electric fields observed in the mesosphere, *Zadorozhny and Tyutin* [1998] assumed the simultaneous existence of both negative and positive multiply charged aerosol particles of different sizes. In this model, more massive charged particles falling with larger velocities initiate a charge separation. Smaller particles carrying charges of the other sign are needed to reduce the effective conductivity of the atmosphere. If both positive and negative charges carried by the particles exceed the charges carried by ions and electrons, that is, if the condition of *Cho et al.* [1992] is satisfied, the effective conductivity of the atmosphere $\sigma_{eff}$, which must be used in (1), is determined by the smaller aerosol particles.

Let us assume that the mesospheric dusty plasma consists of negatively and positively charged aerosol particles surrounded by clouds of positive ions or negative ions and electrons, respectively. We can describe the plasma as a two-component system in which the dressed aerosols are considered as single particles carrying the effective charges:

$$Z_{eff}^+ = Z_p^+ - \frac{n_i^- + n_e}{N_p^+} \quad \text{and} \quad Z_{eff}^- = Z_p^- - \frac{n_i^+}{N_p^-} \tag{4}$$

Quasi-neutrality of the plasma requires $N_p^+ Z_{eff}^+ = N_p^- Z_{eff}^-$ The flux of the negative charges caused by the falling particles must be greater than that of the positive ones in order to generate the more frequently observed positive sign of the vertical electric field. In this case the negative particles must be more massive: $m_p^- > m_p^+$ or $m_p^- > m_p^+$ if $m_p^- > m_p^+$ An expression for the positive vertical electric field generated by the proposed model can be obtained from (1) by replacing $V_p \to V_p^- - V_p^+$, $Z_p$ $N_p^-$, and $\sigma_{eff}^+$. Then using (2), (3), $m_p^\pm >> m_a$, the expression for the diffusion coefficient

$$D_p^+ = \frac{3}{8N_a(r_p^+ + r_a)^2}\sqrt{\frac{kT(m_p^+ + m_a)}{2\pi m_p^+ m_a}} \quad , \tag{5}$$

and the condition for quasi-neutrality of the plasma, the electric field can be found as

$$E_z = \frac{m_p^+ g}{Z_{eff}^+ q_e}\cdot\left(\frac{r_p^-}{r_p^+} - 1\right) = \frac{\frac{4}{3}\pi(r_p^+)^3 \rho_p g}{\left(Z_p^+ - \frac{n_i^- + n_e}{N_p^+}\right)q_e}\cdot\left(\frac{r_p^-}{r_p^+} - 1\right) \tag{6}$$

DISCUSSION AND CONCLUDING REMARKS

Electric field measurements in the vicinity of noctilucent clouds are particularly important for understanding the role of aerosols in electric field generation. During the NLC-91 rocket-radar campaign, electric field perturbations were detected in a region between the NLC and PMSE layers. The measurements were carried out with the help of the field mill mounted on the DECIMALS-B rocket payload [*Zadorozhny et al.* 1993]. The post-flight examination of the field mill in the laboratory using a supersonic ice particle beam showed that the field mill is also sensitive to ice microparticle impacts [*Zadorozhny et al.* 1997]. This means that the perturbations in the field mill signal observed in the NLC/PMSE vicinity have been caused not only by atmospheric electric fields but also by the impact of solid particles. The analysis of the rocket data on the basis of the laboratory results led to estimates of the size and concentration of these particles to be about 24 nm and 370 $cm^{-3}$ at 84 km, respectively, if the water content in the ice phase was equal to ~3 ppmv. The vertical electric field was equal to about 0.9 V/m at this altitude.

Using equation (6) we can estimate the charges which the detected ice particles must carry in order to generate the vertical electric fields observed during the NLC-91 campaign. Electron and positive ion densities were measured during the NLC-91 campaign about two hours before the DECIMALS-B flight [*Balsiger et al.*, 1993; *Friedrich et al.*, 1994; *Mitchell et al.*, 1995]. We assume $n_i^+ = n_e = 10^3$ $cm^{-3}$ at 84 km based on these measurements, so that $n_i^- = 0$. The negative particles must be more massive in order to generate the observed positive sign of the vertical electric field. We assume $r_p^-$ = 25 nm and $N_p^-$ = 300 $cm^{-3}$ [*Zadorozhny et al.* 1997]. Then the condition of *Cho et al.* [1992] requires $Z_p^- > 4$ we assume $Z_p^-$ = 5. If we use $r_p^+$ = 15 nm and $Z_p^+$ = 2, then a condition of quasi-neutrality of the plasma requires $N_p^+$ = 750 $cm^{-3}$. While the concentration of the positive particles is more than that of the negative ones, the latter cannot contribute to the field mill signal detected in the rocket experiment due to a strong dependence of the field mill response to the particle impact on their size [*Zadorozhny et al.*, 1997]. Therefore the assumed sizes and concentration of the positive particles do not contradict the field mill data obtained during the NLC-91 experiment. For the adopted parameters of the charged particles, equation (6) gives $E_z \approx 0.9$ V/m, which is in good agreement with the rocket data. The only disagreement is seen between the calculated and measured mobility of the positive aerosol particles $\kappa_p^+$ Measurements by *Mitchell et al.* [1995] during the NLC-91 campaign showed the existence near 84 km of very small mobility values $\kappa_p^+ \approx 0.6$ $m^2 \cdot V^{-1} \cdot s^{-1}$, which are thought to indicate the presence of positively charged aerosols. The calculated mobility of the assumed positive particles is ~ 0.08 $m^2 \cdot V^{-1} \cdot s^{-1}$. The calculated effective conductivity of the atmosphere, $\sigma_{eff} \approx 2.2 \cdot 10^{-12}$ S/m, is about three orders of magnitude less than the positive ion conductivity (~$3 \cdot 10^{-9}$ S/m) measured by *Mitchell et al.* [1995].

The proposed model can explain the V/m fields observed in the lower mesosphere if we assume parameters for the more massive negative particles equal to those used by *Aikin and Maynard* [1990] and parameters for the positive particles leading to the effective conductivity $\sigma_{eff}$ equal to about $10^{-12}$ S/m. This value is about two orders of magnitude less than the conductivity at 60 km which was measured simultaneously with the V/m vertical electric fields [*Hale et al.*, 1981; *Maynard et al.*, 1981; *Zadorozhny and Tyutin*, 1998]. So low effective conductivity can be produced for example by the particles with a radius of 20 nm and a concentration of $10^3$ $cm^{-3}$ if each of them carries a few unit charges.

We can see that the proposed model could explain the existence of the large vertical electric fields observed both in the lower mesosphere and in the vicinity of noctilucent clouds and PMSE in the summer polar mesopause. In both cases, the predicted effective conductivity of the atmosphere, $\sigma_{eff}$ , is about $10^{-12}$ S/m, which is about two to three orders of magnitude less than the measured ion conductivity. The difference between the estimated effective conductivity and the measured conductivity can be explained by assuming the mesospheric dusty plasma consists of negatively and positively charged aerosol particles surrounded by clouds of positive ions or negative ions and electrons, respectively. Very weak electric fields that cannot interfere with the interaction of the aerosol particles with the ions and electrons must be used to measure the effective conductivity. The electric fields usually found in conductivity probes appear to be too large and the probes cannot measure the effective conductivity. They measure only the pure ion conductivity.

It is necessary to note that the existence of the highly charged aerosols in the mesosphere, as well as the mechanisms of the particle charging, are unfortunately not well understood at present. These appear to be some of the key problems that must be resolved for a complete understanding of the nature of the V/m vertical electric fields observed in the mesosphere.

ACKNOWLEDGEMENTS: This work was supported under Grant No. 97-05-65242 of the Russian Foundation for Basic Research.

REFERENCES

Aikin, A. C., and N. C. Maynard, A Van de Graaf source mechanism for middle atmospheric vertical electric fields, *J. Atmos. Terr. Phys., 52,* 695-705, 1990.

Balsiger, F., E. Kopp, M. Friedrich, K. M. Torkar, and U. Wälchli, Small-scale structure of $O_2^+$ and proton hydrates in a noctilucent cloud and polar mesospheric summer echo of August 9/10 1991 above Kiruna, *Geophys. Res. Lett., 20,* 2315-2318, 1993.

Bragin, Yu. A., Nature of the lower D region of the ionosphere, *Nature, 245,* 450-451, 1973.

Bragin, Yu. A., A. A. Tyutin, A. A. Kocheev, and A. A. Tyutin, Direct measurement of the atmospheric vertical electric field intensity up to 80 km (in Russian), *Kosm. Issled., 12,* 306-308, 1974.

Chesworth, E. T., and L. C. Hale, Ice particulates in the mesosphere, *Geophys. Res. Lett., 1,* 347-350, 1974.

Cho, J. Y. N., T. M. Hall, and M. C. Kelley, On the role of charged aerosols in polar mesosphere summer echoes, *J. Geophys. Res., 97,* 875-886, 1992.

Friedrich, M., K. M. Torkar, E. V. Thrane, and T. A. Blix, Common features of plasma density profiles during NLC, *Adv. Space Res., 14,* 161-164, 1994.

Gelinas, L. J., K. A. Lynch, M. C. Kelley, S. Collins, S. Baker, Q. Zhou, J. S. Friedman, First observation of meteoric charged dust in the tropical mesosphere, *Geophys. Res. Lett, 25,* 4047-4050, 1998.

Goldberg, R. A., Electrodynamics of the high latitude mesosphere, *J. Geophys. Res., 94,* 14661-14672, 1989.

Goldberg, R. A., and R. H. Holzworth, Middle atmospheric electrodynamics, *Handbook for MAP, 32,* 63-84, 1991.

Hale, L. C., Middle atmosphere electrical structure, dynamics and coupling, *Adv. Space Res., 4,* 175 – 186, 1984.

Hale, L. C., C. L. Croskey, and J. D. Mitchell, Measurements of middle atmosphere electric fields and associated electrical conductivities, *Geophys. Res. Lett., 8,* 927-930, 1981.

Havnes, O., J. Troim, T. Blix, W. Mortensen, L. I. Naesheim, E. Thrane, and T. Tonnesen, First detection of charged dust particles in the Earth's mesosphere, *J. Geophys. Res., 101,* 10839-10847, 1996.

Jensen, E. J., and G. E. Thomas, Growth-sedimentation model of polar mesospheric clouds: comparison with SME Measurements, *J. Geophys. Res., 93,* 2461-2473, 1988.

Maynard, N. C., C. L. Croskey, J. D. Mitchell, and L. C. Hale, Measurement of volt/meter vertical electric fiei ds in the middle atmosphere, *Geophys. Res. Lett., 8,* 923-926, 1981.

Mitchell, J. D., Electrical properties of the middle atmosphere, *Adv. Space Res., 10,* 219-228, 1990.

Mitchell, J. D., D. J. Walter, C. L. Croskey, and R. A. Goldberg, Electrical structure and E-fields in the high-latitude mesosphere, *Proceedings 12th ESA Symposium on Rocket and Balloon Programmes & Related Research, Lillehammer, Norway, 29 May – 1 June 1995,* ESA SP-370 (September 1995), 95-100, 1995.

Tyutin, A. A., Mesospheric maximum of the electric field strength (in Russian), *Kosm. Issled., 14,* 143-144, 1976.

Zadorozhny, A. M., and A. A. Tyutin, Universal diurnal variation of mesospheric electric fields, *Adv. Space Res, 20,* 2177-2180, 1997.

Zadorozhny A. M., and A. A. Tyutin, Effects of geomagnetic activity on the mesospheric electric fields, *Ann. Geophys., 16,* 1544-1551, 1998.

Zadorozhny, A. M., A. A. Tyutin, G. Witt, N. Wilhelm, U. Wälchli, J. Y. N. Cho, W. E. Swartz, Electric field measurements in the vicinity of Noctilucent clouds and PMSE, *Geophys. Res. Lett., 20,* 2299-2302, 1993.

Zadorozhny, A. M., A. A. Tyutin, O. A. Bragin, and V. N. Kikhtenko, Recent measurements of middle atmospheric electric fields and related parameters, *J. Atmos. Terr. Phys., 56,* 321-335, 1994.

Zadorozhny, A. M., A. A. Vostrikov, G. Witt, O. A. Bragin, D. Yu. Dubov, V. G. Kazakov, V. N. Kikhtenko, and A. A. Tyutin, Laboratory and in situ evidence for the presence of ice particles in a PMSE region, *Geophys. Res. Lett., 24,* 841-844, 1997.

# SATELLITE DETECTION OF SPRITES AND OTHER MIDDLE ATMOSPHERE STORM EFFECTS

Stephen Clodman
Centre for Research in Earth and Space Science, York University, Toronto, Ontario, Canada

ABSTRACT: Satellite measurements of sprites, jets, and elves, and other middle atmosphere storm effects, would be of great scientific value. These phenomena could be found anywhere in the world that they occur. It would be possible to obtain data not available any other way. One might even be able to detect some of these phenomena in daytime. There are significant problems to overcome: signal to noise ratio limitations, false indications such as from lightning, the need to detect a sufficient number of targets, and the task of obtaining and analyzing a large quantity of data. Still, it can be done, and in several ways, each having advantages. The instrument may point straight down, or obliquely, or toward the earth's limb. The wavelengths sensed might range from ultraviolet to far infrared. Also, there are possible preliminary studies which could help prepare for a satellite mission.

## INTRODUCTION

In the last few years, ground-, and aircraft-based measurements of visible emissions, such as sprites, jets, and elves [*Boeck et al., 1998, Sentman et al., 1995, Wescott et al., 1995*], have opened up an important new area for study of atmospheric electricity of storms and of the middle atmosphere. Middle atmosphere gravity waves are a related phenomena which may in fact interact with the visible emissions. It is true that satellites have been much used to study tropospheric features of thunderstorms (including, increasingly, lightning), but they have not been systematically applied to the middle atmosphere phenomena. There have been successful short-term video tests using the space shuttle [*Boeck et al., 1998*], but these give just a hint of what is possible. This paper proposes that satellite-based measurements of these middle atmosphere storm effects are both useful and feasible, and reviews different ways such studies may be attempted.

## VALUE

Satellite detection of sprites and related emissions, combined with other data, could be scientifically valuable for the following reasons:

- Emissions could be studied anytime and anywhere in the world, not just at specific times and sites. Therefore, charts of their global climatological distribution could be prepared. It might be possible to find types of storms and lightning flashes producing these events which were not previously known to do so.
- Some information can only be obtained from satellites. This includes data at ultraviolet and infrared wavelengths which cannot be used from the ground. Also, the view from above might give knowledge about their shape not apparent from a side view. In addition, middle atmosphere gravity waves which may be related to storms could be studied by measuring the wave effect on the airglow (for brevity, this paper will not discuss this issue further).
- It might ultimately be possible to observe some of these phenomena in daylight, to determine whether their frequency or features are different then (see further discussion below).

## DIFFICULTIES

There are, however, some obstacles that must be overcome to succeed; the main ones are as follows:

- Signal to noise ratio: Despite the large distance from the event to the satellite, enough photons must be collected from each viewed pixel and time interval to achieve a signal to noise ratio sufficient for detection. Also, the sprite must be brighter than background airglow and airglow fluctuations
- Rejecting false emissions and verifying: Several types of unwanted light emissions may be mistaken for desired phenomena if not properly diagnosed. False events must be reliably rejected without eliminating too many desired events. Probably the most difficult of these problems is the light from lightning strokes. True events must be verified reliably.
- Number of detections: The number of events which will be detected is roughly proportional to the product of the field of view by the duration of operation. This number may be increased if the instrument is pointable. Given that the desired events are more or less rare, the field of view and experiment duration must be great enough for a reasonable number of events to be found.
- Data handling: A very large amount of data must be handled. A system must be devised to manage and analyze the data effectively within reasonable time and cost limits.

FIXED DOWNWARD VIEW

There are several ways of designing the instrument; I will discuss three here: fixed downward view, fixed limb view, and pointable view. All three use orbiting satellites. A geostationary satellite would be attractive if it could detect the emissions, but the received light at that altitude would be very weak and so hard to detect.

Fixed downward view – nadir to moderately oblique – is the simplest and lowest in cost. As such, it is suited to a quick initial experiment to prove the idea of satellite sprite detection, and to report on sprites in different parts of the earth. (I base this in part on the MESO satellite, a design proposal to study middle atmosphere chemistry, by Ian McDade of York University [personal communication].) This low cost satellite would be in low earth orbit (~600 km). The instrument would detect at two wavelengths, one at which sprite emissions are strong and a neighboring one at which they are weak. A pair of wavelengths could also be selected for jets. Charge coupled device (CCD) technology would be used. The pixel IFOV (instantaneous field of view) might be about 3 x 3 km, roughly the lateral dimension of a small sprite or jet, to collect the full light from the emission with minimum noise. To give a total IFOV of 700 x 700 km, the pixel array would be 250 x 250. Time resolution would be 0.3 s, a compromise intended to get adequate detection at minimum cost. A more capable experiment, at some extra cost, could be designed by decreasing the pixel IFOV and/or increasing the total IFOV and/or decreasing the time interval.

A nadir view – straight down – would give simple navigation, maximum received light from the sprite, and a direct plan view of the sprite. On the other hand, a moderately oblique view would be effective in separating sprite from lightning in the view field.

FIXED LIMB VIEW

Limb view provides certain specific advantages, but is more complicated. I base this concept on the WINDII (Wind Imaging Interferometer) instrument mounted on the UARS (Upper Air Research Satellite) [*Shepherd et al.,* 1993]. The present study began as an attempt to find sprites in WINDII data. It was found that the WINDII instrument would not detect sprites, mainly because its wavelength bands do not provide good signal to noise ratio. However, the band selection and other parameters could be changed to make a new design.

Limb view has the following advantages over downward view: Lightning and terrestrial lights would not be in the field of view. The height variation of the emission could be measured. A large area per pixel could be viewed. Daytime observations might be possible because of the dark background.

Limb view also has some disadvantages: Cost and complexity are greater. The emission is not accurately located in the radial direction. The distance to the limb is rather large, so the light received is relatively faint. The emission is being viewed from the side, which (because sprites and jets are usually vertically elongated) would cause it to appear fainter. Airglow would be brighter relative to the emission. Limb viewing has its own false indications, such as aurorae or even the moon.

POINTABLE VIEW BY SATELLITE OR SPACE SHUTTLE

If one wants to reduce the time step and the pixel size to better define the emission, one must also reduce the IFOV to keep the instrument design and data handling manageable. However, if the IFOV is too small, one would not detect enough events. Therefore, a pointable instrument would be used, with a rather narrow view angle, but able to turn under control to view optimum locations.

The sprite-finding instrument might be on a satellite already designed to detect lightning, something like the Lightning Imaging Sensor (LIS), now in operation [*Christian et al.,* 1992]. A sprite instrument could turn both autonomously or under ground command. The lightning sensor would help scout for targets; later, the lightning and sprite data could be analyzed together. The sprite finder could keep tracking a single storm, or be turned toward the site of a ground-based experiment. The main drawback of a pointable view experiment is that it would be rather expensive and complex.

An alternate, less complex and costly way of doing a pointable view experiment is to mount it on a space shuttle (or space station) mission. This would allow results to be obtained sooner than with an unmanned satellite. It could be a sort of testbed for future satellite missions.

SIGNAL TO NOISE RATIO

In general, a signal to noise ratio is on the order of one-half times the square root of the number of photons received in a pixel (after instrument losses). The MESO instrument design is predicted to receive enough light, looking straight down, for a 3 x 3 km pixel IFOV, to give a 50 to 1 signal to noise ratio [based on Ian McDade, personal communication]. This assumes that the sprite is 10 km in diameter, emits 5000 J in the visible (400-700 nm), which [*Sentman et al.,* 1995] is fairly bright, and also that a relatively strong emission band (e.g., the $N_2$ 1st positive 5-2 band at 670 nm) is used. This sprite is estimated to be $10^2$ times as bright as background airglow, for a

0.3 sec time step, provided a good sprite emission band in a weak airglow band is used. It should be possible, for some extra cost, to design an instrument which will receive more light and so have better performance.

## FALSE EVENT REJECTION AND VERIFICATION

Light from several causes might be mistaken for desired emissions. Among these, are, for downward view: lightning, artificial lights, volcanoes, fires, aurorae, moon and twilight illumination; for limb view: aurorae, the moon, dayside light, light scattered from lower altitudes. Fortunately, sprites, etc., have strongly peaked spectral signatures, so by receiving two or more bands we can compare on-peak with off-peak brightness to diagnose events not caused by sprites. This would be supplemented by examining the size, duration, and location of the unknown emission to see if they are reasonable for sprites. Handling aurora may be a little difficult, because their spectra are rather similar to those of sprites, but aurora can be rejected by other criteria.

The most serious issue is lightning. Bright lightning is a few orders of magnitude brighter than the desired emissions. Lightning has both broadband and peak emissions. Sprites, jets, and elves occur over severe lightning-producing storms. Moreover, because strong positive lightning triggers sprites and elves, a flash is generally in progress when the emission occurs. One must be able to find sprites in the presence of lightning without falsely diagnosing sprites. Because sprite spectra [*Milikh et al.*, 1998a] are peaked, it should be possible to diagnose the sprite even if the received light from the lightning is several times as strong. *Suszcynsky et al.*, [1998] discuss some ways to do this. The overlying cloud will reduce the lightning light to a limited extent.

However, other measures are needed. Using limb view will avoid the problem, or an oblique view can separate the sprite from the lightning in the field of view. Some sprites may be laterally far enough from the lightning to be visible in nadir view, but most will be obscured. One remedy for this is to use a very small timestep (<0.02 s) to try to separate the sprite in time from the initial lightning stroke. Another option is to use an infrared or ultraviolet light wavelength at which low-altitude light is absorbed.

Detecting other matching events would give further verification. Lightning can be found, either by satellite or by ground-based detectors. The triggering storm can be observed by satellite, radar, or other means. Gamma rays may be emitted by sprites; the satellite could find these with a suitable detector. ELF radiation transients are likely to coincide with sprites [*Boccippio et al.*, 1995].

## NUMBER OF EMISSIONS DETECTED

Following is an approximate calculation of the number of sprites detectable by a fixed downward-looking view. There are very roughly 500,000 sprites and 50,000 elves per year in the world (this number is open to debate, but should be the right order of magnitude). An IFOV of 700 x 700 km or 500,000 km$^2$ covers 1 part in 1000 of the earth's surface, bringing about 500 sprites and 50 elves per year in view. Assume that detection occurs only at night (~40% of flashes) and that there is a 50% probability of detection. Then 100 sprites and 10 elves per year could be actually detected, enough for a good initial experiment.

The number of jets is more uncertain. Relatively few jets are detected from the ground. However, the instruments so far used are not usually optimized for the jet emission peaks at 391 and 428 nm [*Wescott et al.*, 1995]. Moreover, the lower atmosphere significantly attenuates light of these wavelengths. Jets are usually elongated in the vertical, making them easier to see from above. Therefore, a satellite detecting at the jet peak bands should see more jets than ground or aircraft studies, and should be an effective way of estimating the number of jets.

## DATA MANAGEMENT

Even the simple downward view experiment described above would process a lot of data. The data quantity could be reduced by not operating the instrument over areas where conditions are poor for sprites. Another option is to do preliminary processing on board the satellite, deleting data that clearly show no events. The data transmitted to the ground would then be more carefully processed to reduce the data to a small set of good candidates, which would be carefully examined by hand to reach a final conclusion.

## DAYTIME MEASUREMENTS

It would be scientifically valuable to measure emissions in daytime, to see if they are different in frequency or nature from those at night. It may be possible, although difficult, to do this. One must find a way to view the emission against a reasonably dark background. If a limb view is used, the background, though brighter than night, may still allow the brighter emissions to be seen against it. In fact, aurorae have been detected in daytime this way.

A highly speculative possibility for downward view is to use a far IR band (e.g. 4.3 μ) or a far UV band to which the lower atmosphere is opaque and relatively nonreflecting, and at which solar radiation is reduced. Detailed

analysis with a short time step might identify the signal against the strong background. Although somewhat unlikely to work, this idea might be worth investigating. (See *Christian et al.*, [1992] for daytime detection of lightning.)

WAVELENGTH CHOICE

One key design decision is the selection of the main detection wavelength band. Desirable features are: strong emission at the band, transparent atmosphere between the emission and the satellite, airglow weak and relatively constant, reduced interference from lightning [*Orville and Henderson,* 1984], possibility of daytime measurements, and technical simplicity. The preliminary information here is subject to further study.

Jets emit mainly at $N_2^+$ 1st negative peaks 391 and 428 nm [*Wescott et al.,* 1995]. Lightning light is usually (not always) less at 391 nm than 428 nm. Lightning light would be slightly attenuated by the atmosphere.

Sprites have groups of main emission peaks [*Milikh et al.,* 1998a]: a number of far IR peaks, the $N_2$ 1st positive peaks in near IR 850-900 and 730-780 nm and in red 640-690 nm, and the $N_2$ 2nd positive UV peaks 280-400 nm. The peaks vary in the amount of interference from lightning light and airglow. The UV peaks would benefit from attenuation of the lightning light by the atmosphere. *Orville and Henderson* [1984] do not have data below 375 nm, but the trend of lightning brightness is decreasing with decreasing wavelength. Below 310 nm lightning is well screened by the ozone layer, but the sprite emission becomes considerably fainter.

The far IR at 4.3 μ has sprite emissions (from $CO_2$), is opaque to lower atmosphere light ($CO_2$ absorption), but has strong background emission [*Milikh et al.,* 1998b]. Another possibility may be the water vapor absorption region about 1.4 μ so lower atmosphere light is blocked. However, spectroscopy becomes more technically difficult for wavelengths above 1 μ.

PRELIMINARY STUDIES

Some studies might be done prior to launch which can make the results better. These may include:

- usability of ultraviolet bands
- usability of far infrared bands
- better assessment of jet frequency
- probability of apparent view separation between sprites and lightning for different view angles
- probability of apparent time separation between sprites and lightning for different time resolutions

ACKNOWLEDGEMENTS: The author would like to acknowledge the help of his colleagues at the Centre for Research in Earth and Space Science, including Gordon Shepherd and Ian McDade, in formulating the project and also for technical advice. Also, the author thanks Walter Lyons and Russell Armstrong for their generous and useful scientific advice.

REFERENCES

Boccippio, D.J., E.R. Williams, S.J. Heckman, W.A. Lyons, I.T. Baker, and R. Boldi, Sprites, ELF transients, and positive ground strokes. *Science,* **269,** 1088—1091, 1995.

Boeck, W.L., O.H. Vaughan, Jr., R.J. Blakeslee, B. Vonnegut, and M. Brook, The role of the space shuttle video-tapes in the discovery of sprites, jets and elves, *J. Atmos. Sol.-Terr. Phys.,* **60,** 669—677, 1998.

Christian, H.J., R.J. Blakeslee, and S.J. Goodman, Lightning Imaging Sensor (LIS) for the Earth Observing System, NASA Tech. Memo. 4350, NASA, 36 pp, 1992.

Milikh, G., J.A. Valdivia, and K. Papadopoulos, Spectrum of red sprites, *J. Atmos. Sol.-Terr. Phys.,* **60,** 907--915, 1998a.

Milikh, G.M., D.A. Usikov, and J.A. Valdivia, Model of infrared emission from sprites, *J. Atmos. Sol.-Terr. Phys.,* **60,** 895—905, 1998b.

Orville, R.E., and R.W. Henderson, Absolute spectral irradiance measurements of lightning from 375 to 880 nm. *J. Atmos. Sci.,* **41,** 3180—3187, 1984.

Sentman, D.D., E.M. Wescott, D.L. Osborne, D.L. Hampton, and M.J. Heavner, Preliminary results from the Sprites94 aircraft campaign: 1. Red sprites, *Geo. Res. Lett.,* **22,** 1205—1208, 1995.

Shepherd, G.G., et al., WINDII, the Wind Imaging Interferometer on the Upper Air Research Satellite, *J. Geo. Res.,* **98,** 10725—10750, 1993.

Suszcynsky, D.M., R. Roussel-Dupre, W.A. Lyons, and R.A. Armstrong, Blue-light imagery and photometry of sprites, *J. Atmos. Sol.-Terr. Phys.,* **60,** 801-809, 1998.

Wescott, E.M., D. Sentman, D. Osborne, D. Hampton, and M. Heavner, Preliminary results from the Sprites94 aircraft campaign: 2. Blue jets, *Geo. Res. Lett.,* **22,** 1209—1212, 1995.

# CHARACTERISTICS OF THUNDERSTORMS AND LIGHTNING FLASHES WHICH PRODUCE MESOSPHERIC TRANSIENT LUMINOUS EVENTS

W.A. Lyons[1], T.E. Nelson[1], R.A. Armstrong[2], E.R. Williams[3], D.M. Suszcynsky[4], R. Strabley[4], M. Taylor[5] and L. Gardner[5]

[1]FMA Research, 46050 Weld County Road 13, Fort Collins, Colorado 80524 USA
[2]Mission Research Corp., 1 Tara Blvd, Nashua, New Hampshire 03062 USA
[3]MIT Parsons Laboratory, MIT 48-211, Cambridge, Massachusetts 02139 USA
[4]Los Alamos National Laboratory, MS D466, Los Alamos, New Mexico 87545 USA
[5]Space Dynamics Lab, EL241, Utah State University, Logan, Utah 84322 USA

ABSTRACT: A six year record of optical observations of lightning-induced mesospheric transient luminous events (TLEs) is available from the Yucca Ridge Field Station (YRFS) near Ft. Collins, CO. Climatological analyses reveal sprites and elves occur in a variety of convective storm types, but principally mesoscale convective systems (MCSs) and squall lines. Severe supercell storms rarely produce TLEs, except during their dissipating stage. Few TLEs are observed during storms with radar echo areas <7,500 km$^2$. Above this size there is a modest correlation with radar areal coverage. A typical High Plains storm produces 45 TLEs over a 143 interval. Sprites and most elves are associated with +CGs. The probability of a TLE increases with peak current. In six storms, 5.1% of +CGs produced TLEs, the number increasing to 32% of +CGs with >75 kA and 52% of +CGs with >100 kA peak current.

## INTRODUCTION

Since the 1989 discovery of tropospheric lightning-induced TLEs in the middle atmosphere, sprites, elves and blue jets have been investigated using a variety of methods. These include RF signatures (*Boccippio et al.* 1995; *Huang et al.* 1999), broadband and multi-color photometry (*Armstrong et al.* 1998; *Suszcynsky et al.* 1998), and low-light television (LLTV) (*Lyons*, 1994). Each summer since 1993, investigators have gathered at YRFS for intensive periods of coordinated observations. A constant among these field programs has been the use of LLTV systems (primarily red sensitive Xybion ISS-255 units) which continuously image the volume above convective storms some at 100-800 km distance when conditions appeared favorable. While the summer observational periods, typically lasting 6 to 10 weeks, are not identical from summer to summer; a general climatology has begun to emerge. The peak period during which storms produce TLEs optically observable from a High Plains ground station extends from July through mid-August. Currently the dates of TLE observations range from 19 May through 12 October. To date some 132 storms have been documented to produce 1 or more TLEs. Figure 1 shows the locations of storms and the number of TLEs produced over the three most recent summers. While sprites can be imaged under ideal conditions for ranges up to 1000 km, most observation periods were constrained to storms at 700 km or less. Figure 2 shows the climatology of large peak current (>75 kA) +CGs occurring during summer months. It shows a regional concentration of powerful +CG flashes in a broad belt ranging from New Mexico into Minnesota (*Lyons et al.* 1998). It is believed that the U.S. High Plains may represent one of the highest TLE producing regions in the world. On the other hand, TLEs undoubtedly occur, albeit at lower rates, in storms worldwide.

## ANALYSES

A database was prepared of the observations from 60 storms during the 1996-1998 seasons with viewing conditions generally favorable throughout the storm's life cycle. The TLE event times were obtained from the nightly observer logs made directly from the LLTV monitors. These storm logs capture about 80% of the total events. Thus, the following statistics slightly underreport the true values. Sprites have been observed by LLTV at all times when ambient light conditions permitted their detection (about 45 minutes after sunset and before sunrise). In general, however, TLEs tend not to occur until at least an hour after darkness, perhaps in response to changes in the ionosphere after the passage of the terminator. Developing nocturnal storms also are increasing in size during this period. Figure 3 shows the temporal distribution of TLEs observed from YRFS. There is a broad maximum between 0400 and 0700 UTC (local sunset is typically around 0230 UTC). The fall off towards dawn represents the weakening of some storm systems and/or their passage beyond LLTV detection range. The number of events from storms varies from a single sprite or elve to 400 (Figure 4). The highest counts occurred during an intrusion of Mexican smoke into the central U.S. during the spring of 1998, which resulted in dramatic increases in +CG percentages and peak currents (*Lyons et al.* 1998). The mean TLE count per storm is 45. The duration of TLE production ranges from a single event to almost six hours, with a mean of 143 minutes. TLE rates vary from a few

per hour to over 2 per minute (in smoke influenced storms). A long-term mean is one TLE event every 3.2 minutes. Events often occur at rather fixed periodic intervals for an hour of more.

In addition to the LLTV images, GOES satellite imagery, NEXRAD regional radar reflectivity mosaics, and the supporting meteorological data were archived. TLEs have been observed above a variety of convective storm types. In the High Plains, years of forecasting experience have shown they are most likely above large mesoscale convective systems (MCS) exhibiting horizontally extensive stratiform precipitation regions. The greatest number of sprites and elves has been associated with the largest mesoscale convective complexes (MCCs). Linearly extensive squall lines also produce sprites. Intense, compact supercell storms, though often extremely electrically active, rarely produce many TLEs, with the exception of brief bursts of sprites during their dissipating phase when a sufficiently large stratiform convective area develops. During the 1998 campaign, 21 storms were tracked throughout most of their TLE production phase. Hourly TLE rates ranged from 1 to 168. By far the two highest hourly TLE rates were associated with storms ingesting smoke from Mexican wildfires. The areal coverage of base reflectivity (generally >15 dBZ) during the hour of peak TLE activity ranged from 10,200 $km^2$ to 140,000 $km^2$, with a mean of about 50,000 $km^2$. Only isolated instances of TLEs have been noted from storms with <10,000 $km^2$ radar area. Above a threshold value of around 7,500 $km^2$ for sprite production, the peak number of hourly TLEs is modestly correlated with echo size (Figure 5). Using data from the 1998 storms, a curve can was fit (dashed line) showing this relationship. However, the two high TLE rate outliers (associated with smoke-ingesting storms) may represent a different regime of TLE-echo size relationship. During 1998, the correlation between the peak hourly TLE rate and radar echo cover has an $R^2$ value of 0.60. The peak TLE rate was uncorrelated to the total CG flashing rate ($R^2$ = 0.12), but showed a stronger linkage to the percentage of CG flashes with positive polarity ($R^2$ = 0.39) and the total number of +CGs ($R^2$ = 0.52). The 1998 storms producing TLEs had average –CG peak currents of 21 kA and +CG peak currents of 40 kA, the latter being somewhat higher than the annual U.S. mean of 27 kA. The percent positive rates during the peak TLE hour for 1998 storms ranged form 6% to 89% with a mean of 30% during the hour of peak TLE. However, in this sample the 8 potentially smoke influenced storms averaged 63% positive polarity, versus 13% for the other storms.

Detailed analyses were conducted for six storms in which all TLEs were precisely time-tagged and correlated to their parent +CG lightning (*Lyons* 1996). The storms includes smaller MCS systems, two large MCCs and a squall line. A total of 370 TLEs were detected. During the TLE producing intervals, the NLDN recorded 67,212 –CGs and 7,242 +CGs. Thus the percent positive for active TLE producing storms (9.7%) is only marginally higher than for most (non-smoke influenced) summer convective systems in the central U.S. The rate of TLEs (roughly 90% of which are sprites) is approximately 1 event for every 200 CGs reported by the NLDN for active storms. One of every 20 +CGs produced a sprite. Sprites typically are associated with +CGs with somewhat higher (order 50%) peak currents than others in the storm. We do note several apparent sub-10 kA +CGs triggering sprites (assuming the correct attribution was made between the sprite and parent +CG). Elves are associated with the largest peak current CGs (mostly +CGs but a few –CG have been recently documented). What is clear is the percentage of +CGs producing TLEs rises monotonically with peak current (Figure 6). Only 2.5% of +CGs with peak currents <49 kA produced observable TLEs. By contrast 32% of +CGs >75 kA and 52% >100 kA had TLEs, approaching 100% above 200 kA. If this sample is representative, then Figure 2 may represent a density map of TLEs (with the contour values divided by 3).

On a global scale, we note that the regions over which TLEs have been documented from ground observatories, aircraft and the Space Shuttle very roughly correspond to the regions of high lightning frequency. Figure 7 includes recent reports of sprites above Hurricane Georges (R. Hood, G. Heymsfield, personal communication) and over the Sea of Japan snow squalls long known for producing extremely powerful +CG events (Y. Takahashi, personal communication). It is unlikely, however, given the regional variability of characteristic storm type and size and frequency of +CG flashes, that a TLE density map would correspond closely to the total lightning density maps generated from orbiting sensors (the OTD and TRMM missions). Storm types similar to TLE-bearing U.S. High Plains systems are found in limited regions, including the South American pampas, southern Africa, the Indian subcontinent, and Australia. (Tropical cyclones and winter storms represent special cases). Many tropical convective systems are not necessarily TLE producers even given very high lightning rates, due to characteristically smaller areal coverage and lower numbers of +CGs than mid-latitude MCSs. However, the recent linkage between regional

biomass smoke plumes and increased +CG percentages and peak currents compounds the difficulty in ascertaining global TLE distributions and frequency. Since massive biomass smoke palls are occurring with increasing frequency in tropical regions where deep convection is most common, it is conceivable that TLEs could episodically become very widespread throughout tropcial regions. Global-scale ELF transient monitoring may help reduce some of the uncertainties involved in developing a worldwide TLE climatology (*Huang et al.* 1999).

ACKNOWLDGEMENTS: This work was partially supported by the U.S. Department of Energy and NASA, Office of Space Science, in conjunction with the University of Houston (Gar Bering).

REFERENCES

Armstrong, R.A., J.A. Shorter, M.J. Taylor, D.M. Suszcynsky, W.A. Lyons, and L.S. Jeong, Photometric measurements in the SPRITES'95 & '96 campaigns: Nitrogen second positive and first negative emission, *J. Atmos. Terr. Phys.*, 60, 787--799, 1998.

Boccippio, D. J, E.R. Williams, S.J. Heckman, W.A. Lyons, I.T. Baker and R. Boldi, Sprites, ELF transients, and positive ground strokes, *Science*, 269, 1088--1091, 1995.

Huang, E., E. Williams, R. Boldi, S. Heckman, W.A. Lyons, M. Taylor, T. E. Nelson and C. Wong, Criteria for sprites and elves based on Schumann resonance observations. *J. Geophys. Res.* (in press).

Lyons, W.A., Characteristics of luminous structures in the stratosphere above thunderstorms as imaged by low-light video, *Geophys. Res. Lett.* 21, 875--878, 1994.

Lyons, W.A., Sprite observations above the U.S. High Plains in relation to their parent thunderstorm systems, *J. Geophys. Res.*, 101 (D23), 29641-- 29652, 1996.

Lyons, W.A., T.E. Nelson, E.R. Williams, J.A. Cramer and T.T. Turner, Enhanced positive cloud-to-ground lightning in thunderstorms ingesting smoke from fires, *Science*, 282, 77—80, 1998.

Lyons, W.A., M. Uliasz and T.E. Nelson, Large peak current cloud-to-ground lightning flashes during the summer months in the contiguous United States, *Monthly Weather Rev.*, 126, 2217--2233, 1998.

Suszcynsky, D.M., R.A. Roussel-Dupré, W.A. Lyons, R.A. Armstrong, Blue light imagery and photometry of sprites, *J. Atmos. Terr. Phys.*, 60, 801-809, 1998.

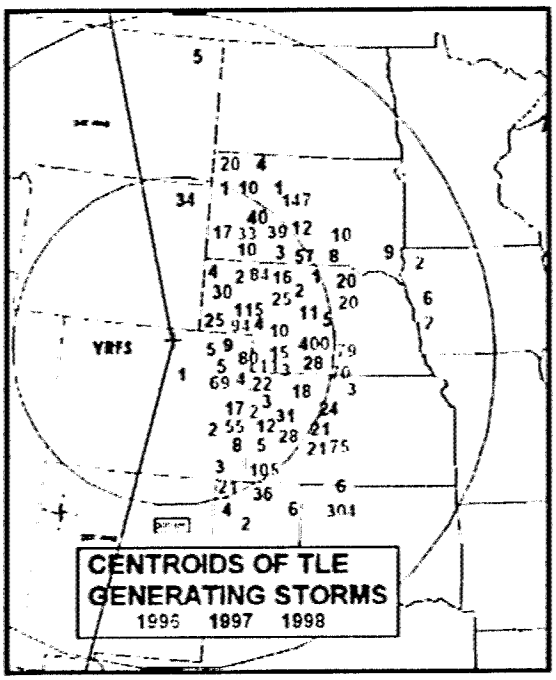


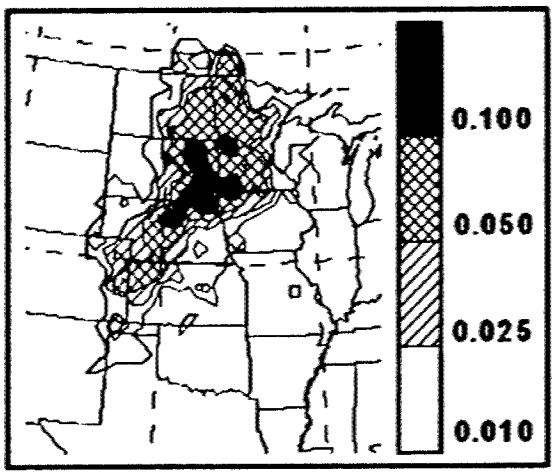


Figure 1. Locations of storms producing TLEs observed optically from the Yucca Ridge Field Station during the SPRITES'96, '97 and '98 campaigns. Figure 2. Density of +CG flashes with peak currents >75 kA, summed over 14 summer months, in flashe/ km2 (Lyons, Uliasz and Nelson, 1998).

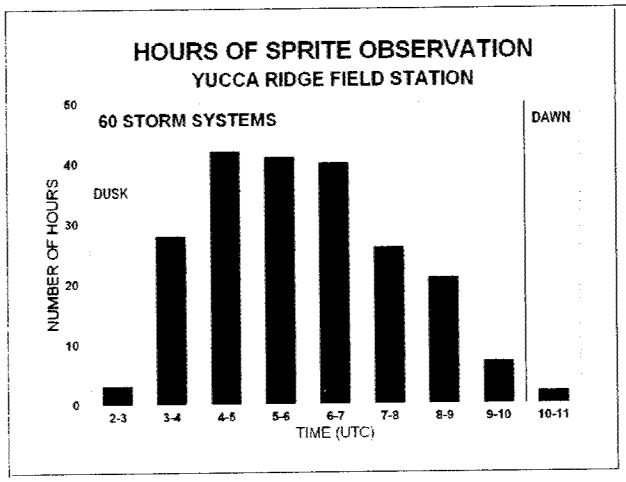


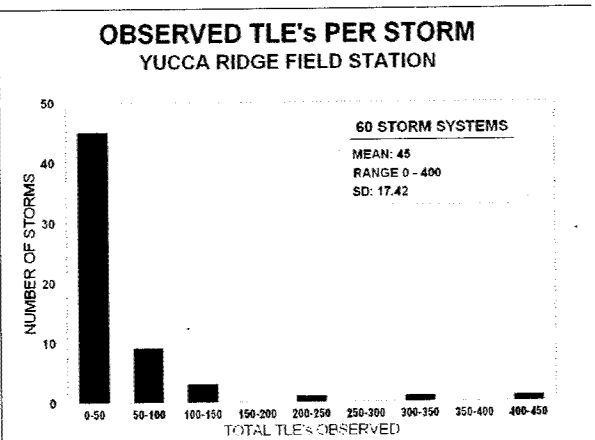


Figure 3. Hours (UTC) during which TLEs were optically observed from YRFS during the SPRITES'96,'97 and '98 campaigns. Figure 4. Distribution of the total number of TLEs optically observed from YRFS above 60 storms during the SPRITES'96, '97 and '98 campaigns.

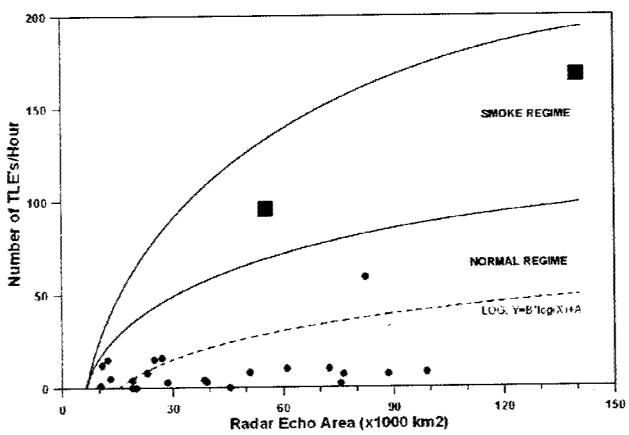


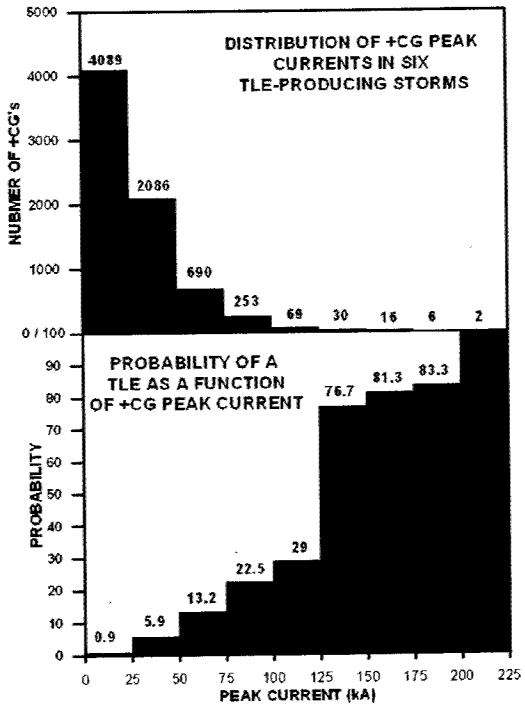


Figure 5. Distribution of radar echo area versus the highest hourly rate of TLEs for 21 storms during SPIRTES'98. The two apparent outliers are associated with storms ingesting smoke form Mexican biomass fires. Figure 6. Distribution of peak currents of all +CGs during TLE producing period in six storm systems (top) and the percentage of +CGs producing TLEs as a function of peak current (bottom).

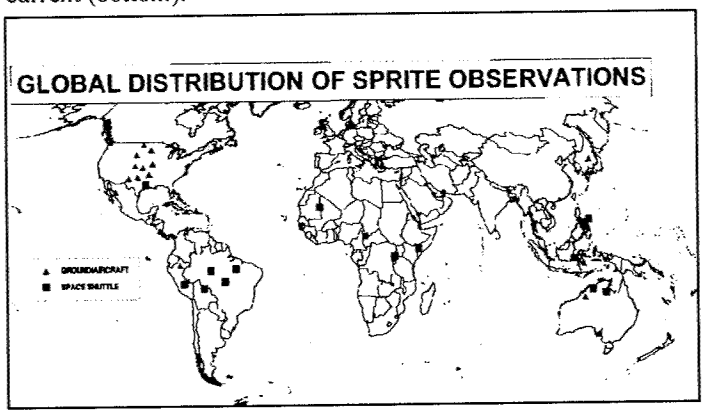


Figure 7. Global distribution of sprites confirmed by ground, aircraft and Space Shuttle observations. The distribution in the central U.S. represents a very small sample of the total events.

# PARAMETERIZATION OF SPRITES AND THEIR PARENT DISCHARGES

M. Stanley, P. Krehbiel, M. Brook, W. Rison, C. B. Moore, and R. Thomas
New Mexico Institute of Mining and Technology, Socorro, New Mexico, U.S.A.

ABSTRACT: Analysis of a close sprite-producing positive CG indicated that it had a total charge moment change of 460-740 C-km. Analysis of high speed video observations have determined that the initiation altitude of sprites is within the altitude range of 70-85 km with a mean of ≈75 km. These results are consistent with a conventional breakdown mechanism for sprite initiation. Once initiated, corona streamer characteristics are clearly visible in developing sprites.

## INTRODUCTION

In spite of measurements of current moments at ELF frequencies [*Cummer and Inan*, 1997], very little is known about the parent positive cloud-to-ground (CG) discharges which are responsible for most sprites. Basic CG parameters such as the height, horizontal extent, rate, and quantity of charge transported to ground should be determined in order to accurately address the various sprite theories. There is also a critical lack of knowledge of the initiation altitude, sequence, speed, and nature of sprite development. This paper will highlight measurements of various sprite parameters and will briefly discuss the implications for a conventional corona streamer breakdown mechanism.

## INSTRUMENTATION

In mid-May through mid-July of 1997, the NMT high-time resolution Interferometer system was operated from the Kennedy Space Center (KSC). The New Mexico Tech (NMT) Interferometer acquired 2D radio-frequency interferometry and electric field data simultaneous with 3D lightning maps obtained by KSC's Lightning Detection and Ranging (LDAR) system. Sprite-producing positive CG discharges (some within 100 km range) were observed by both systems on several nights.

During early October of 1997, a light-intensified high speed video camera system was operated from Langmuir Laboratory, NM, to observe sprite phenomena. The high speed camera was operated at frame rates of 1000, 2000, 3000, and 4000 $s^{-1}$. Image sequences of 42 sprite clusters and several elves were captured with the camera system.

## PARENT DISCHARGE OBSERVATIONS

Figure 1 shows a sprite-producing lightning discharge (1:42:57 UT, June 22nd, 1997) overlaid onto NEXRAD reflectivity contours at an altitude of 5-8 km MSL. The 20 dbZ region of the anvil is about 50 km on a side with an estimated area of 2500 $km^2$. Almost all of the discharge is confined within the 20 dbZ region, but is significantly smaller with an approximate total area of 1600 $km^2$.

The discharge began as a bi-level intracloud within a main thunderstorm cell. The upper portion of the discharge propagated up through the cell and then out through the anvil. Figure 2 shows that the upper portion of the discharge dropped several kilometers in altitude as it propagated into the anvil. A positive CG was produced about 400 ms into the discharge and is evident as an upward step in the electric field change data. The descent of the positive leader to ground is not visible in the LDAR data.

A sprite was observed in the same video frame as that of the positive CG. The total electric field change of the sprite-producing positive CG return stroke and continuing current was about 25 V/m and had a total duration of just under 20 ms with about half of the field change amplitude

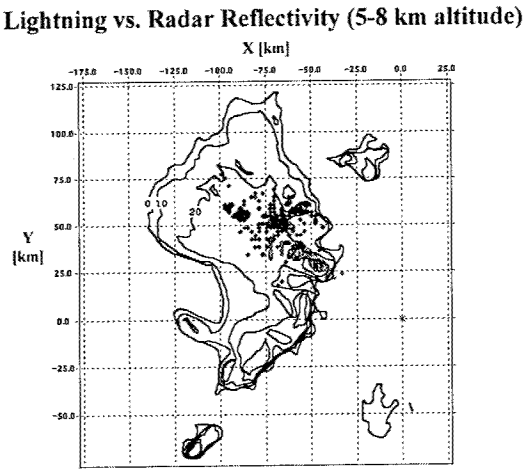


Figure 1: A sprite-producing discharge is overlaid onto NEXRAD reflectivity contours through the upper portion of the storm. The discharge is almost entirely confined within the 20 dBZ reflectivity contour.

being reached in the initial millisecond. The total field change can be used to estimate the total charge moment for the parent discharge by approximating the positive CG to a dipole:

$$\Delta E = \frac{2\,\Delta Q\,Z}{4\pi\varepsilon_o r^3}$$

where $\Delta E$ is the electric field change, $\Delta Q\,Z$ is the charge moment change, $\varepsilon_o$ is the permittivity of free space, and r is the radial distance to the dipole. Ionospheric image charges are ignored in this calculation since their contribution would be less than that due to the range uncertainty. The estimated mean radial distance to the charge source for the positive CG (and hence to the dipole) is 75±6 km. Thus, the total charge moment for the CG was 460-740 C·km. If the charge was lowered from an altitude of ≈7.5 km, as indicated by the concentration of points at that altitude in Figure 2, then the CG lowered 60-100 C of charge to ground.

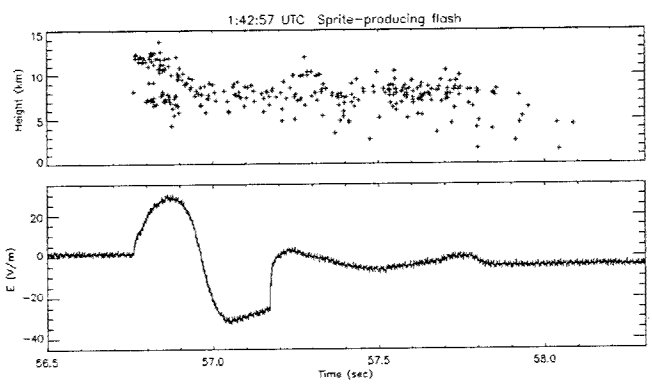


Figure 2: The time development of the 1:42:57 UT lightning discharge is shown with respect to discharge altitude (top) and electric field at the KSC observation site (bottom). The upward vertical step in electric field at 57.17 seconds was produced by a sprite-producing positive CG.

SPRITE OBSERVATIONS

Figure 3 shows a normal speed video image of a sprite cluster (8:43:57 UT, October 3rd, 1997) along with the first high speed video frame for the same region. The column visible in the first high speed video frame was at an altitude of 67-77 km and corresponded with the initial development of the carrot sprite visible in the normal speed image. The height estimate is based on the range to the associated positive CG determined by National Lightning Detection Network (NLDN) stroke-level data. The column extended primarily downwards in the second frame (not shown) and branched downwards into tendrils in the same frame. The tendrils had insignificant persistence between the 2nd and 3rd frames indicating that electrons were rapidly recombining in the region behind the downward propagating tips. This is consistent with the predictions of Pasko et al. [1998] who predicted that "corona streamers", characterized by very short persistence, are present in sprites. The tendrils were followed by upward developing structures (UDSs) which branched outwards from the main column to form the carrot shape of the sprite.

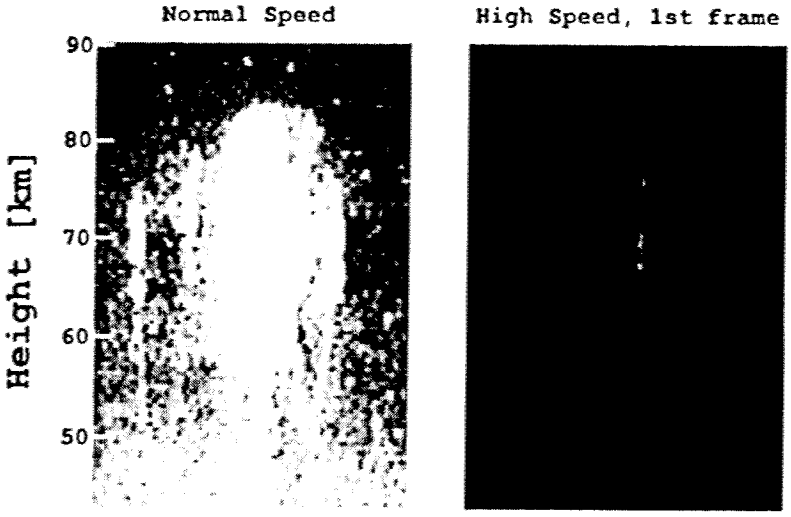


Figure 3: The image on the left was obtained at 60 fields/second while that on the right was obtained at 1000 frames/second for the same region of the sprite cluster. Both images correspond with the first one in which sprite luminosity was visible from the cluster. The carrot sprite was initiated before the columniform sprites and the carrot began as a noncontinuous column. Note that the "vertex" of the carrot sprite is below the initiation altitude region indicated in the high speed video image.

All of the sprites observed by the high speed video system started out with a columnar form (usually noncontinuous) within the first several hundred microseconds. This column appeared to extend both upwards and downwards in many cases and primarily downwards in a few others. The downward propagating portion of the column could split into 2 or more tendrils which continued to propagate downwards. The tendrils had velocities of about 0.01-0.1 c, where c is the speed of light. Based on the altitude extent of the initial column and possible bidirectional development, the initiation altitude for the sprites analyzed in this study was above ≈70 km with a mean altitude of ≈75 km.

UDSs were visible on all carrot sprites and occasionally on what was otherwise a columniform sprite. They often could be seen originating from altitudes below that of sprite initiation. These

structures propagated with velocities of 0.05-0.2 c and were followed by a short and often insignificant persistence within the upper portion of sprites. This suggests that they have corona streamer characteristics within that region. However, they could be followed by significant persistence at lower altitudes within the head region of carrot sprites. It is this persistence which is in large part responsible for the brightness of the head of carrot sprites.

## DISCUSSION

Analysis of high speed video indicates that sprites are initiated at altitudes of 70-85 km. Fernsler and Rowland [1996] calculated that a minimum charge moment change of 300 C·km would be needed for conventional breakdown to occur at 80 km altitude. This threshold is less than the observed charge moment change of the sprite-producing positive CG analyzed in this paper. Thus, the analyzed discharge should be capable of initiating a conventional breakdown process at altitudes where initial sprite development is observed. The corona streamer behavior visible in both tendrils and UDSs provides further evidence for a conventional breakdown mechanism.

Though the corona streamer nature agrees with predictions of Pasko et al. [1998], the velocities are significantly higher than theoretical predictions. Additional theoretical work is needed to address this discrepancy.

ACKNOWLEDGEMENTS: The authors would like to thank; Bill Abrahams of Speed Vision Technologies for providing the high speed camera system, Bill Kline of Eastman-KODAK Company for providing the KODAK Intensified Camera on short notice, and Ken Cummins of Global Atmospherics Inc. for providing stroke-level NLDN data.

## REFERENCES

Cummer, S. A. and U. S. Inan, Measurements of charge transfer in sprite-producing lightning using ELF radio atmospherics, *Geophys. Res. Lett., 24,* 1731, 1997.

Fernsler, R. F., and H. L. Rowland, Models of lightning-produced sprites and elves, *J. Geophys. Res., 101,* 29653-29662, 1996.

Pasko, V. P., U. S. Inan, and T. F. Bell, Spatial structure of sprites, *Geophys. Res. Lett., 25,* 2123, 1998.

# IONIZATION IN THE MIDDLE ATMOSPHERE ASSOCIATED WITH THUNDERSTORMS - MULTI-COLOR PHOTOMETRIC ANALYSIS OF SPRITE EMISSIONS

R.A. Armstrong[1], D.M. Suszcynsky[2], R. Strabley[2], W.A. Lyons[3], T.E. Nelson[3]

[1] Mission Research Corp, 1 Tara Blvd., Nashua, NH, U.S.A. 03062;
[2] Los Alamos National Laboratory, MS D466, Los Alamos, New Mexico, USA 87545;
[3] FMA Research, 46050 Weld County Rd#13, Fort Collins, CO 80524

ABSTRACT: Observations of transient luminous events (TLEs) above mesoscale convective systems (MCSs) have been a topic of much research in the last several years. Early VLF and photometric data on these events suggested the presence of substantial ionization associated with their initiation. Recent time-resolved multi-color photometric data obtained on one class of TLEs called sprites, has confirmed an impulsive ionization at the sprite initiation. Although more data is required to quantify the ionization levels and initiation mechanisms, analysis of this data suggests that for some events, ionization rates are sufficient to achieve electron densities approaching $10^5$ $cm^{-3}$ at ~65 km. Data has also been obtained which suggests that some events exhibit little, if any, ionization, indicating that more than one operative mechanism is responsible for the phenomena. We present the recent data along with the analysis supporting the level of ionization. Plans for future measurements to quantify the spatial behavior of the ionization are also presented.

INTRODUCTION AND BACKGROUND:

Although there have been many measurements of the signatures of electrodynamic events above thunderstorms (e.g., Lyons, 1996), there remains significant controversy concerning the level and persistence of ionization in these events. Mende, et al (1995) and Hampton, et al (1996) obtained the first spectral evidence that the red emission in sprites originates from electron impact excitation of the nitrogen first positive system. The "ambient" electron densities across the altitude region in which sprites occur are insufficient to excite this emission to the intensities observed, thus requiring some ionization mechanism. The first indication of ionization in sprites was obtained by Dowden, et al. using VLF measurements (Dowden, et al, 1995). In the SPRITES'95 campaign, we obtained the first photometric evidence of 427.8 nm emission from the $N_2^+$ first negative system, indicating an impulsive ionization in sprites. In SPRITES'96, in a more comprehensive experiment, we obtained a combination of blue imagery and blue photometry which again indicated significant ionization in sprites (Armstrong et al, 1998, Suszcynsky et al, 1998). However, the time resolution of these measurements was insufficient to fully characterize the blue emissions, and the bandpass of the optical filters precluded the unique assignment of the signature to nitrogen first negative emission because of the close spectral proximity of nitrogen second positive emission. In SPRITES'98, we obtained new multi-color photometry data simultaneously with blue, red and high-resolution broad-band video imagery of sprite events which confirms the presence of the nitrogen first negative radiative emission, indicating significant ionization in these events (Armstrong, et al, 1998). The associated imagery shows that the ionization is confined to well-defined channels which contain "hot-spots" of relatively high energy.

The primary objective of this investigation is to obtain simultaneous measurements of the emission time-histories of the "blue" 399.8 nm emission (nitrogen second positive), "blue" 427.8 nm and 470.9 nm emission (nitrogen first negative) and the broad-band "red" emission (nitrogen first positive). The time-evolution of the nitrogen first negative emission (391.4 nm, 427.8 nm, 470.9 nm) is a well-characterized (based on numerous auroral studies) trace of the ionization rate resulting from energy deposition into the atmosphere. The ratio of this emission to the emission from the second positive (399.8 nm) is a measure of the energy of the excitation process. The simultaneous trace of the red nitrogen first positive emission yields information on the persistence of the ionization and energy profile.

Analysis of the new results indicates that more than one mechanism can cause sprites and that the ionization level is variable among them, which partly explains the current controversy. The time-resolved emissions from the nitrogen first-positive, second positive and first negative systems suggest different time histories for their emissions. This is suggestive of at least three characteristic energy regimes. We

also find that the relative time histories are not unique from event-to-event but generally fall into two (or perhaps three) categories. The time histories can be interpreted to yield estimates of both the ionization level and the energy accommodation. We present the systematic analysis of the time-histories of the photometric emission behavior of the sprite events, correlate them with the corresponding imagery and discuss implications for the chemical and electrodynamic modeling of the phenomena.

INSTRUMENTATION:

The instrumentation used in this investigation consists primarily of an array of co-aligned photometers covering: (1) 399 nm +/- 5 nm with a 6° FOV, (2) 430 nm +/- 5 nm with both a 4° and 6° FOV, (3) 472 nm +/- 5 nm with at 6° FOV and (4) 580 nm to 900 nm with a 4° FOV. A supplemental photometer with a 10° FOV operating wide-band was used to correlate the time-base for the different data acquisition cards. A broadband photodiode detector with a ~20° FOV was used to obtain the time history of the light emission from the parent lightning stroke. In addition, a VLF receiver was employed to detect the parent lightning signature. Data was sampled at 20, 40 and 100 kHz and GPS time-stamped to within 1 microsecond by the data acquisition system.

Video images of the events were obtained with intensified Xybion video cameras (Model ISS-255), three with 12° FOV, one with a zoom lens to isolate individual regions, and one with a very wide ~50° FOV to act as a patrol camera. Three of the cameras were operated in the "white-light" mode with a spectral response in the 400 nm to 900 nm range. One camera was operated in the "red-light" mode, with an effective passband of 600 nm to 900 nm, and one was operated in the "blue-light" mode with an effective passband of 350 nm to 475 nm. Individual fields (~16.5 mS) were obtainable to maximize video time-resolution. The video was GPS time-stamped to an accuracy of 1 μS at the video field break.

OBSERVATIONS AND RESULTS:

A review of the photometry data obtained up to the SPRITES'97 campaign appears in Armstrong, et al (1998) and Suszcynsky et al (1998). Although there is a significant amount of data, this presentation concentrates on a case study event which occurred on 09August98 (day 221) at 06:12:47.749. This event exemplifies the energetics found for many sprites and is the first obtained with simultaneous 399.8 nm, 427.8 nm 470.9 nm and broad-band red emission signals. This event was observed from the Yucca Ridge Field Station, Fort Collins CO, (40.667°N, 104.94°W). The parent lightning stroke for this event (from NLDN) was 43 kA at 40.057°N, 103.402°W.

The image sequence for this event is shown in Figure 1. There is a likely connected "first stroke" giving rise to the first two, rather dim, C-sprites in the first field. The second field shows the initiation of five C-sprites in a cluster, associated with the main (second) parent stroke, which blossom into a highly structured sprite cluster by the next field. The luminosity of the event persists for at least two fields (~33 mS). The third field shown in figure 1 has a time-offset (different camera) overlapping fields two and four. This field image shows the approximate FOV of the bore-sighted 6° FOV photometers.

In figure 2, the photometric traces are shown. The first thing to note in figure 2(a) is that the sprite event is easily differentiated from the forward scatter of the parent lightning. Since the lightning is approximately a continuum in this spectral region (Orville and Henderson, 1984), the relative signals are normalized to the scattered lightning signal for analysis. In figure 2(b) the reduced data is shown for the actual (relative) line intensities of interest. The 399 nm filter, although dominated by the $N_2$ 2P(1,4) transition at 399.8 nm, has some minor contributions from other $N_2$ 2P lines. The 430 nm filter, while dominated by the 427.8 nm $N_2^+$ 1N(0,1) line when the electron energy is >10 eV, has contributions from the $N_2$ 2P(0,4 & 1,5) transitions. In fact, when the electron energy decreases to ~1 eV, the $N_2$ 2P(0,4 & 1,5) transitions totally dominate the signal in the 430 nm filter, a point that is critical to the time-resolved data analysis. The 472 nm filter, when ionization is present, is completely dominated by the 470.9 $N_2^+$ 1N(0,2) line. As the electron energy drops and ionization ceases, the signal from this filter is dominated by the N2 2P(0,5) transition, again a point critical to the time-resolved data analysis. The time evolution of the energy of the ionization process is the source of the differential photometric signal waveforms.

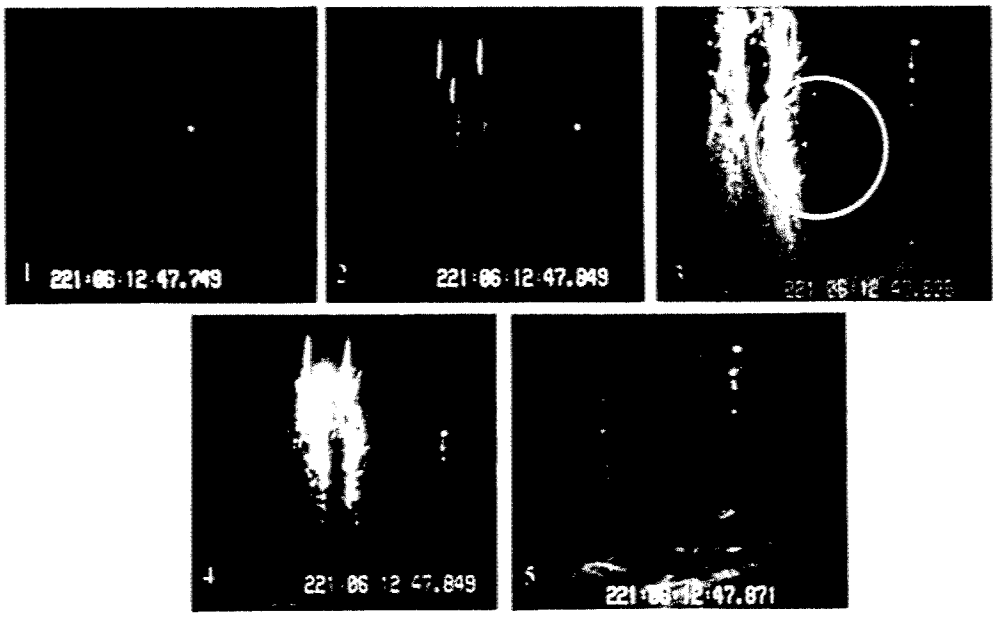


Figure 1. Sequential video images of the case study event occurring on 09August99, Yucca Ridge Field Station.

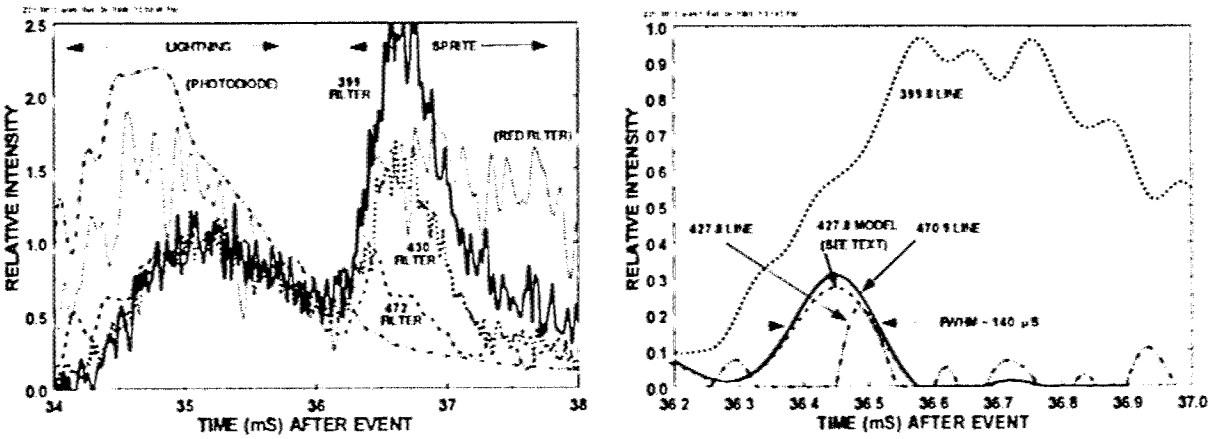


(a) (b)

Figure 2. Time trace of the photometer signals (a) lightning-normalized and (b) data-analysis-derived relative intensities of the 399.8 nm, 427.8 nm and 470.9 nm line emissions.

There are two main features to note in figure 2(a). First, the signals from the forward scatter of the lightning exhibit nearly identical waveforms for the three primary photometers – this is important for the analysis. Second, there are at least three energy regimes suggested by the relative time traces: (1) an early high-energy process where all signals rise nearly simultaneously; (2) a "sustaining" energy process of about 1 eV where the $N_2$ 2P emission continues but the $N_2^+$ 1N emission ceases; (3) a longer lasting low energy process where the $N_2$ 1P (red) emission persists but the $N_2$ 2P (blue) emission ceases.

In figure 2(b), the relative intensities of the individual lines as derived from the data analysis are shown. It is clear, from both figure 2(a) and 2(b) that the 470.9 nm line of the $N_2^+$ 1N(0,2) transition is present. It is also important to note that the FWHM of the 470.9 nm signal is ~140 µS, indicating the time duration of the ionization impulse. Since the 470.9 nm line and the 427.8 nm line originate from the same energy level, the 427.8 nm emission line must be present in the ratio of the products of the Franck-Condon factors, the atmospheric transmissions, the filter transmissions and the normalization/calibration factors. This is shown in figure 2(b) as the "427.8 model" result. However, the data-derived 427.8 signal appears to be severely truncated. The reason for this is that upon inspection of the 430 nm filter trace in

figure 2(a), one notes a noise-induced break in the signal at the critical time of ionization (~36.3 mS). This gives rise to the "bite-out" in the 427.8 nm data in figure 2(b).

The results of this case study can be used to derive an estimate of both the electron number density and the energy deposition rate. The ion pair production rate is given by

$$\text{Rate}_{IP} = \text{Intensity (kR)} \div \text{effective path} \div \text{"geometric fill factor"} \div \text{ion-pair production efficiency}$$

We know from prior investigations (Armstrong, 1998) that the total 430 nm filter signal intensity is typically 20 kR. Analysis of the data in figures 2(a) and 2(b) show that the actual 427.8 nm line is ~30% of the filter band emission during the sprite initiation, or about 6 kR. The ion-pair production efficiency is 0.07 for the 391.4 nm line (Borst and Zipf, 1970). The intensity ratio 391.4nm/427.8nm ~3. Thus the "equivalent" 391.4 nm intensity is ~18 kR. The effective path for this case, derived from detailed analysis of the image in figure 1, is ~3 km. The geometric fill factor, which accounts for the product of the fraction of the sprite optical path length that is actually emitting (~10%) and the fraction of the photometer FOV filled (~10%), is ~0.01. The ion pair production efficiency (391.4 nm) is 0.07. Thus the ion-pair production rate is $\sim 9 \times 10^7$ $s^{-1}$ $cm^{-3}$. Given this ionization rate, the energy deposition rate is estimated to be $\sim 3 \times 10^9$ eV $cm^{-3}$ $s^{-1}$. The FWHM for the ionization pulse (figure 2(b)) is 140 μS. Thus the ion-pair (electron) production is $\geq 1 \times 10^4$ $cm^{-3}$. Dowden (1995) estimates an electron density of 1-$4 \times 10^4$ $cm^{-3}$ using VLF backscatter techniques, in good agreement with our results. An electron density of this order at approximately 1 eV energy ("average" energy - Green, et al, 1996) also yields several hundred kR of nitrogen first positive emission, consistent with the results of Hampton, et al (1996).

CONCLUSIONS:

Using time-resolved filter photometer techniques, the ion-pair production in sprites can be derived. The results so obtained are consistent with independent VLF techniques. The implications of our findings are important in understanding the transient ionization and conductivity in the middle atmosphere above large thunderstorms and their importance in the global circuit.

REFERENCES:


Armstrong, R.A., J.A. Shorter, M.J. Taylor, D.M. Suszcynsky, W.A. Lyons, L.S. Jeong, Photometric measurements in the SPRITES'95 &'96 campaigns: nitrogen second positive and first negative emission, J. Atmos. Terr. Phys., 60(7-9), 787, 1998

Armstrong, R.A., D.M. Suszcynsky, R. Strabley, W.A. Lyons, T.E. Nelson, Simultaneous multi-color photometric and video recording of sprites and their parent lightning: mechanisms and energy deposition, EOS Trans., 79(45), F165, 1998.

Borst, W.L., E.C. Zipf, Cross section for electron impact excitation of the (0,0) first negative band of $N_2^+$ from threshold to 3 KeV, Phys. Rev. A., 1(3), 834, 1970.

Green, B.D., M.E. Fraser, W.T. Rawlins, L. Jeong, W.A.M. Blumberg, S.B Mende, G.R. Swenson, D.L. Hampton, E.M. Wescott, D.D. Sentman, (1996) Molecular excitation in Sprites, Geophys. Res. Lett.., **23,** 2161-2164

Dowden, R.L., J. Brundell, W.A. Lyons, T. Nelson, "Sprite structure implied by scattering of VLF transmitter signals, EOS Transactions (supplement), 76(46), F114, 1995

Hampton, D.L., M.J. Heavner, E.M. Wescott, D.D. Sentman, Optical spectral characteristics of sprites, Geophys. Res. Lett., 23, 89, 1996.

Lyons, W.A., Sprite observations above the US high plains in relation to their parent thunderstorm systems, J. Geophys. Res., 101(D23), 29641, 1996

Mende, S.B., R.L. Rairden, G.R. Swenson, W.A. Lyons, Sprite spectra: $N_2$ first positive band identification, Geophys. Res. Lett., 22,2633, 1995.

Orville, R.E., R.N. Henderson, Absolute spectral irradiance measurements of lightning from 375 to 880 nm, J. Atmos. Sci., 41(21), 3180, 1984.

Suszcynsky, D.M., R.A. Roussel-Dupré, W.A. Lyons, R.A. Armstrong, Blue light imagery and photometry of sprites, J. Atmos. Terr. Phys., 60(7-9), 801, 1998

# EM radiation associated with sprites?

T.Otsuyama Y.Hobara M.Hayakawa

Dept. of Electronic Engineering, The Univ. of Electro-Communications, Tokyo Japan

**Abstract** The mesospheric optical flashes(sprites) are associated mostly with large positive cloud-to-ground discharges (+CG). In addition, transient events in ELF range are observed often in association with sprites. Several theoretical studies including the numerical computations have been performed to explain the optical emission, but the EM(electro-magnetic) radiation during the sprites emission has not been studied intensively.

In this paper we try to derive the generation mechanism of the EM radiation during the process of the sprites in VLF/ELF range using numerical computations simulating the sprite triggering discharges. As a result, considerably large amplitude of the EM fields from the triggering discharge is obtained particularly in the ELF range, which is possibly connected with the source of the ELF transient observed for distances away from the sprites.

**Introduction** Recent observation of sprites have shown that there are still many unexplained phenomena occurring between the top of a thundercloud and the ionosphere. These phenomena have renewed the interest of scientists in electrical phenomena between the top of a thundercloud and the ionosphere.

According to observations, "sprites" mainly occur in the altitude range of 50~90km, have lateral dimensions of 20~59km, and are associated with positive cloud-to-ground(CG) stroke. The emission spectrum indicates that the $N_2$ first positive band dominates the emission spectrum. Based on a video frame analysis, the duration of a sprite is approximately 3 m-sec.

Several theories have been proposed to explain the mechanism of sprites occurrence. Pasko *et al.* explained sprites produced by quasi-electrostatic (QE) thundercloud fields. The emission intensities were shown to have peaks at altitudes between 70 and 80 km. Rowland *et al.* showed that electromagnetic pulses (EMP) driven by lightning can caused the breakdown of the neutral atmosphere in the lower D-region.

The purpose of this paper is to study the relation between a positive CG, flash, a ELF transient by means of computer simulations.

**Model Formula** For simulation, we employ an axisymmetrical two-dimensional cylindrical coordinate system. We take the z axis in the vertical direction and the r axis in the horizontal direction. The computational domain is divided into grid size of $\Delta r = \Delta z = 2800m$. For the ES code, before the discharge, we use the following equation:

$$0 = \frac{\partial \rho}{\partial t} + \frac{\rho\sigma}{\epsilon} + \nabla\sigma \cdot \mathbf{E} + \frac{\partial \rho_t}{\partial t} \tag{1}$$

For the EM code, after the discharge, we use the following equation;

$$\nabla \times \mathbf{E} = -\mu \frac{\partial \mathbf{H}}{\partial t} \tag{2}$$

$$\nabla \times \mathbf{H} = \epsilon \frac{\partial \mathbf{E}}{\partial t} + \sigma \mathbf{E} + J_s \tag{3}$$

where $J_s$ is the lightning stroke current,and $\rho_t$ is the thundercloud charge. In addition to these equations, we need the electric conductivity $\sigma$. The electric conductivity is modeled by the following equation;

$$\sigma = q\mu_e N_e + \sigma_i \tag{4}$$

where the first term on the right corresponds to the conductivity due to electrons and second term due to ions. Ionic conductivity is a function of height only, but electron density $N_e$ and electron mobility $\mu_e$ are depending on the value of electric field at each grid point.

**Results** We show the spatial variation of conductivity and number of electron density after the discharge in Fig.1. We can see a small enhancement at the lower ionosphere in each figure. This enhancement in conductivity is associated with sprites and supports the sprite current transfer to the ionosphere.

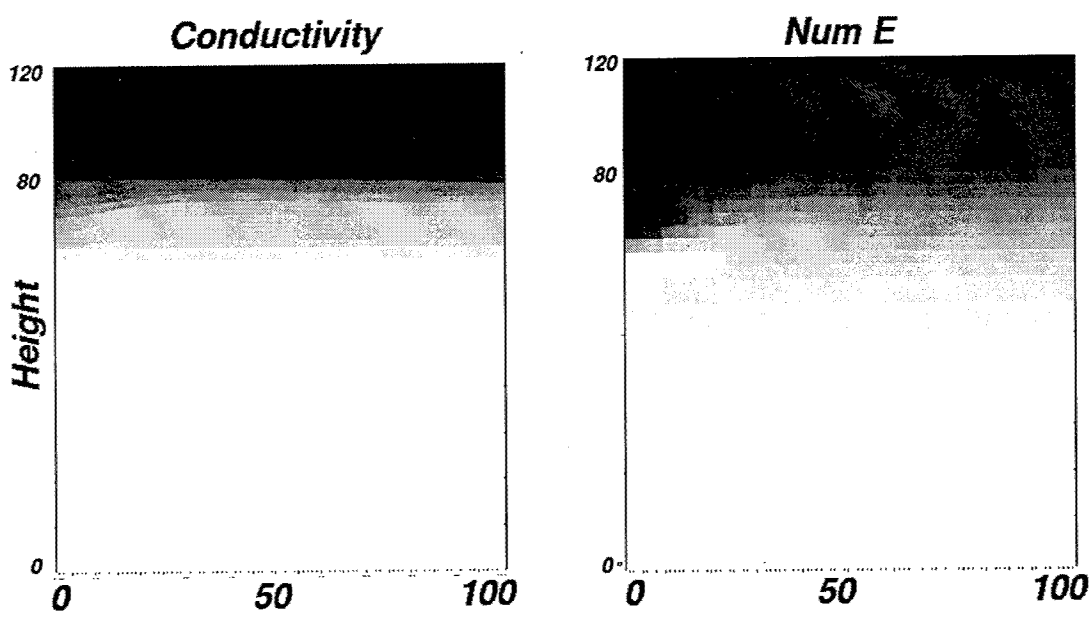


Figure 1: Spatial variation of conductivity and number of electron density after the discharge.

The EM radiation resulted from this current is possibly expected, and the actual observation has suggested the presence of EM radiation associated with sprites. We show

the temporal variation of the vertical electric field at a distance of 500 km from the source lightning in Fig.2.

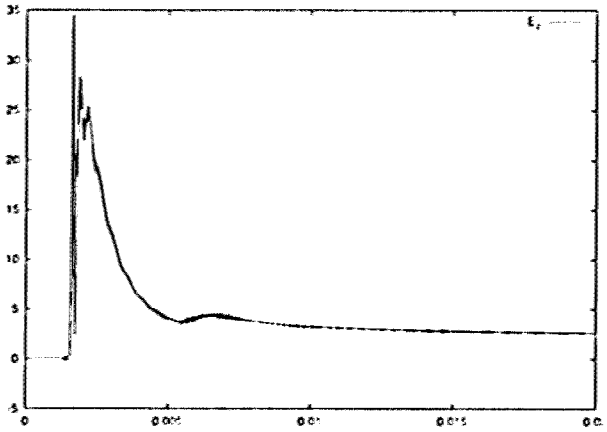

Figure 2: Temporal variation of vertical electric field at 500km

**Summary and Discussion** Recent experimental findings have elucidated the spatial structure of sprite and temporal variation of radiation field, but modeling of these structures and sprite ELF radiation is not computationally possible at present. In this paper, we show an enhancement area of conductivity and sprite ELF radiation. If the charge distribution is nonuniform, three dimensional simulations are necessary.

## REFERENCES


[1] Cho, M., Rycroft,M.J., Computer simulation of the electric field structure and optical emission from cloud-top to the ionosphere. *J. Atmos. Solar Terr. Phys.*, 60,871–888, 1998.

[2] Pasko, V.P., Inan, U.S., Bell, T.F., Taranenko, Y.N., Sprites produced by quasi-electrostatic heating and ionization in the lower ionosphere *J. Geophys. Res.*, Vol 102, 4529–4561, 1997.

[3] Powland, H.L., Fernsler, R.F., Huba, J.D., Bernardt, P.A. Lightning driven EMP in the upper atomosphere, *Geophys. Res. Lett.*, 22, 361–364, 1995.

# PROPAGATION CHARACTERISTICS OF RETURN STROKES AND M-COMPONENTS IN FLORIDA ROCKET-TRIGGERED LIGHTNING

D. Wang[1], T. Ito[1], N. Takagi[1], T. Watanabe[1], V.A. Rakov[2], M.A. Uman[2]

[1]Department of Electrical and Electronic Engineering, Gifu University, Japan
[2]Department of Electrical and Computer Engineering, University of Florida, USA

ABSTRACT: To study the propagation characteristics of return strokes and M-components, a Fourier Transform analysis has been performed on the light signals of two return strokes and two M-components recorded using a high speed digital imaging system from flashes triggered at Camp Blanding, Florida in the summer of 1997. For the two return strokes, the light signals from the higher channel sections exhibit larger phase differences relative to the signal from the channel bottom over all frequencies investigated, from below 1 kHz to more than 500 kHz. This observation suggests that all frequency waves are moving upward. The waves of different frequencies propagate at different phase velocities with higher frequency waves usually having larger phase velocities. No apparent relation has been noted between the phase velocities and the channel heights although the signals from different heights indeed show different phase velocities. The group velocities show a tendency to decrease at the higher channel sections. For the two M-components, one shows an upward propagation above 38 m, but a seemingly downward propagation at the channel bottom. The other, with a better spatial resolution, shows much more complicated phase differences at the channel bottom, so that we can not determine even the direction of its propagation.

## INTRODUCTION

The lightning channel is often modeled as a lossy transmission line. To characterize such a line, phase velocity and group velocity are commonly used. Some inferences on these two velocities for return strokes are made by Rakov (1998). This paper presents the optical measurements regarding these two velocities for both return strokes and M-components.

## RESULTS

The optical data presented in this paper were acquired using the digital imaging system ALPS (Automatic Lightning Progressing Feature Observation System) described by Wang et al. (1999a). Two return strokes and two M-components recorded from the flashes triggered in the summer of 1997 at Camp Blanding, Florida are suitable for the present study. The recording time resolution was 100 ns for the return strokes, and 2 μs for the M-components.

Figure 1a shows the light signals as a function of time at various heights for the return stroke triggered on August 2, at 21:17:15 UTC. From an expansion of this figure (not shown here), the return stroke shows an appreciable increase in rise time and a decrease in peak value when propagating from ground upward to a height of some hundred meters. A Fourier Transform analysis has been performed on the light signals in Figure 1a and the results are shown in Figures 1b to 1e. Figure 1b shows the phase differences of the signals at various heights relative to the signal at the bottom as a function of frequency. For all frequencies, from less than 1 kHz to more than 500 kHz, the higher the channel sections, the larger the phase differences, indicating that all frequency waves are moving upward, as expected for return strokes. Figure 1c shows the phase velocities as a function of frequency at different heights. As evident in this figure, higher frequency waves usually propagate with larger phase velocities, supporting the frequency dependency of the phase velocities inferred by Rakov (1998). Such frequency dependency of the phase velocities should produce a decrease in rise time at higher channel sections in the case when no amplitude attenuation is involved, being contrary to the increase in rise time observed for the return stroke. Figure 1d shows the frequency dependency of the amplitude ratios of the light waves at different heights relative to the light wave at the channel bottom. Higher frequency waves usually suffer stronger attenuation, which would yield an increase in rise time as seen in the light signals of return strokes. Thus we conclude that the degradation of the light signals of the return stroke with the increase of height is primarily caused by attenuation (Figure 1d) rather than dispersion (Figure 1c). Figure 1e presents plots of phase constant ( $\beta$ ) versus angular frequency ( $\omega = 2\pi f$) for four different channel heights. Although we could estimate the group velocity ($d\omega / d\beta$) for each narrow range of frequencies from these plots, since the phase constant and the angular frequency has a roughly linear relation in a wide range of frequency, a group velocity ($\Delta\omega / \Delta\beta$) for a relative wide range of frequencies, as defined by Kawasaki et al. (1987), is used, and its magnitude is determined by the slope of each best-fitting line with respect to the vertical axis shown in Figure 1e. The group velocities at higher channel sections tend to be lower with values around $1 \times 10^8$ m/s, similar to

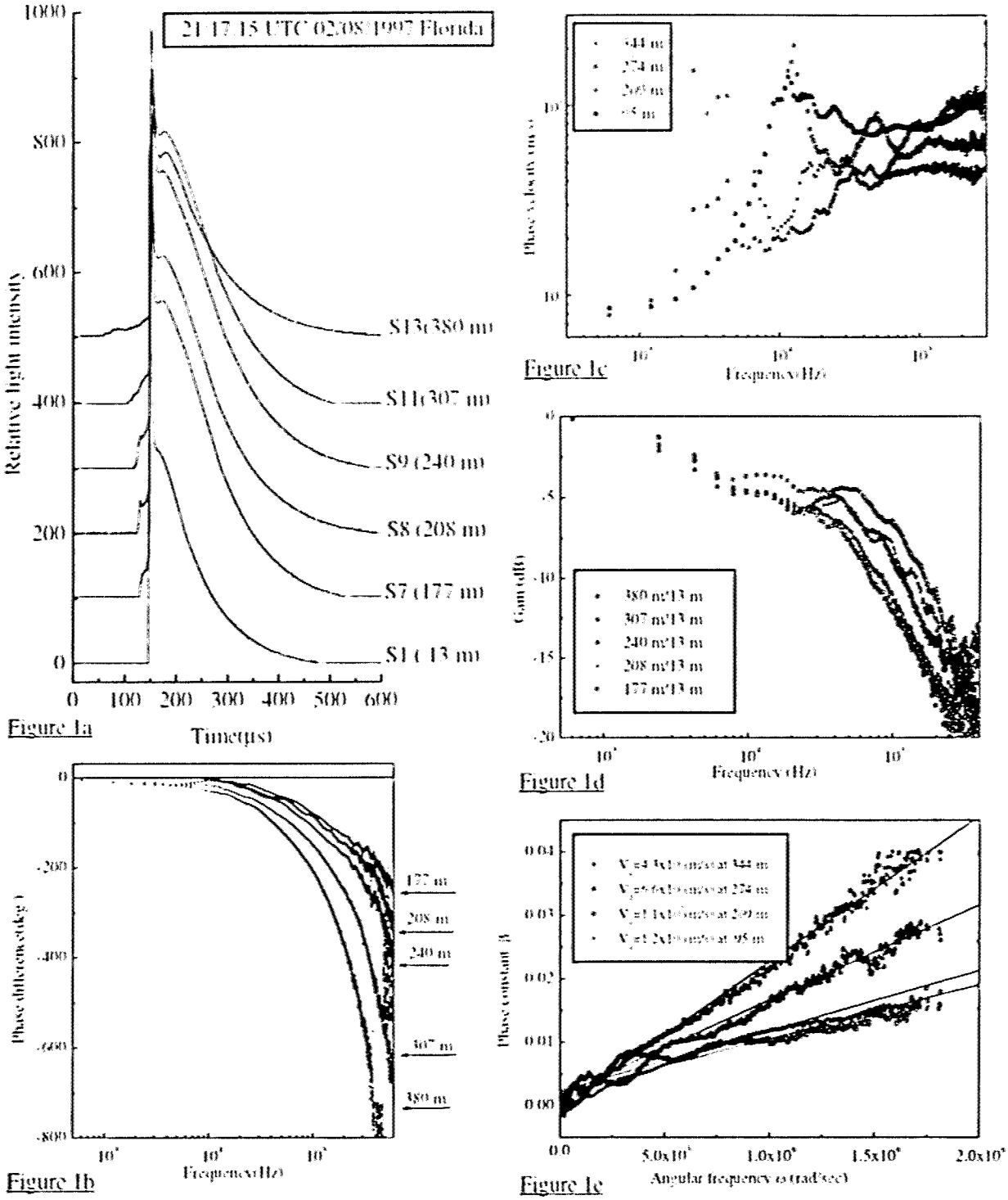


Figure 1 The results of a return stroke triggered on August 2, at 21:17:15 UTC. a) the light signals as a function of time at various heights; b) phase differences of the signals at different heights relative to that at the bottom as a function of frequency; c) phase velocities as a function of frequency at different heights; d) amplitude ratios of the light waves at different heights relative to that at the bottom as a function of frequency; e) group velocities at different heights as determined by the slopes of the fitting lines relative to the vertical axis.

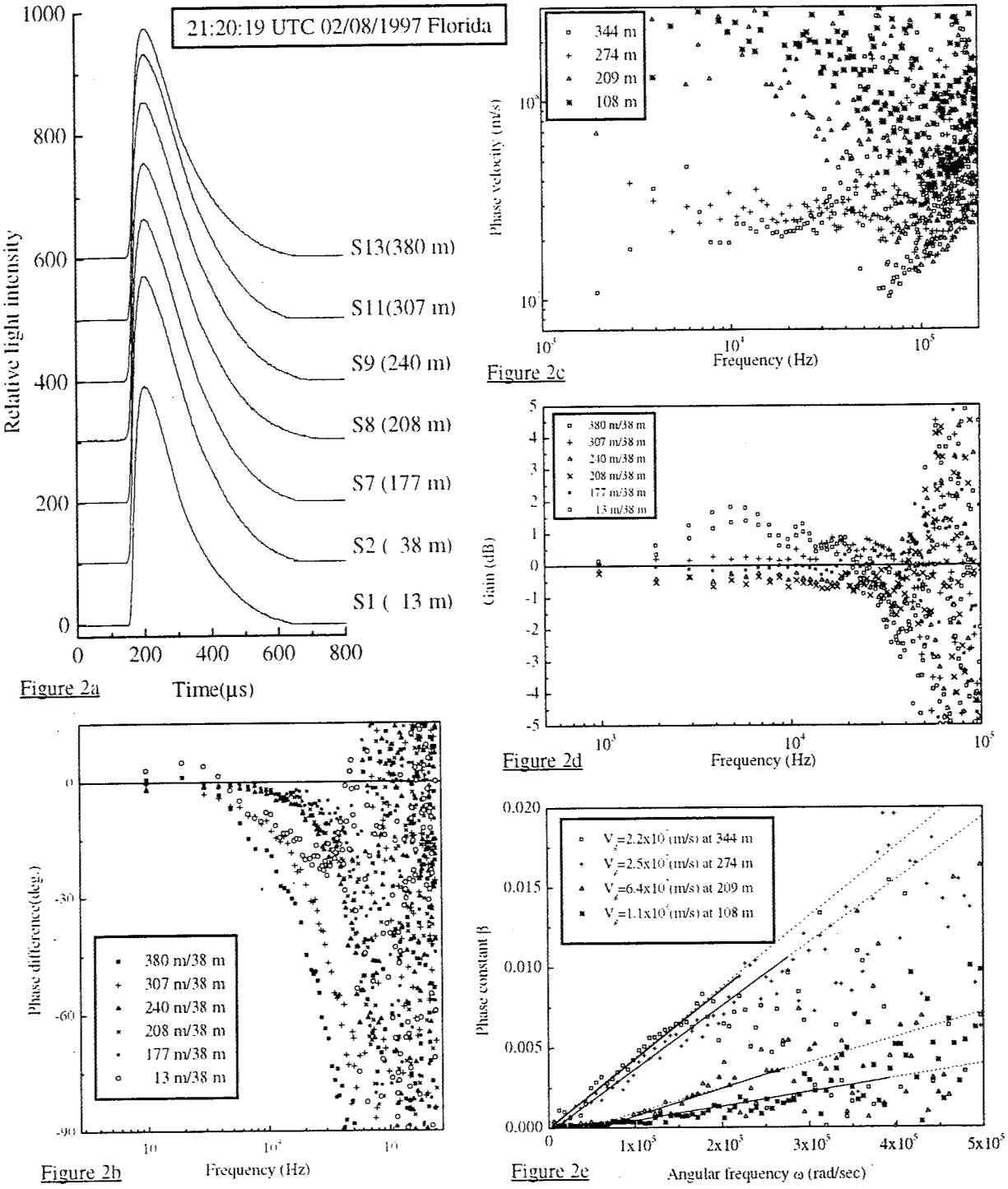


Figure 2 The results of a M-component triggered on August 2, at 21:20:19 UTC. a) the light signals as a function of time at various heights; b) phase differences of the signals at different heights relative to that from the height of 38 m as a function of frequency; c) phase velocities as a function of frequency at different heights; d) amplitude ratios of the light waves at different heights relative to that from the height of 38 m as a function of frequency; e) group velocities at different heights as determined by the slopes of the fitting lines relative to the vertical axis.

the velocity determined in the time domain by using the onset of the fast rising portion of the return stroke waves (Wang et al., 1999b). The other return stroke analyzed exhibits results similar to those shown in Figure 1 and they are not presented here due to lack of space.

Figure 2a shows the light signals as a function of time at various heights for an M-component in a lightning flash triggered on August 2, at 21:20:19 UTC. As opposed to the return stroke light signals shown in Figure 1a, the M-component light signals do not show any appreciable variation either in rise time or in peak value with height. Since the phase of the signal from the height of about 38 m is found to be the most advanced, its phase is chosen as reference for comparison. Figure 2b presents the phase differences of the signals at various heights relative to the signal at 38 m as a function of frequency for the M-component. For all frequencies from 4 kHz to nearly 40 kHz, except at the very bottom (less than 38 m) the higher the channel section, the larger the phase difference. This indicates that except for the very bottom of the channel, all frequency waves of the M-component propagate upward like a return stroke. Figure 2c shows the phase velocities as a function of frequency. As seen in this figure, the phase velocities at lower heights are very scattered and show larger values than those at higher channel sections. Unlike the return stroke shown in Figure 1, the phase velocities of the M-component do not exhibit much variation with frequency. Figure 2d shows the frequency dependency of the amplitude ratios of the light waves at different heights to the signal at 38 m. M-component waves do not suffer any attenuation while propagating several hundreds of meters along the channel. Figure 2e shows the group velocities (as explained in the discussion of Figure 1e) of the M-component at different heights. The group velocities tend to be smaller at higher channel sections.

As seen in Figure 2b, the phase at 38 m is advanced relative to that at 13 m, suggesting a downward propagation near the bottom of the M-component, if unidirectional propagation is really involved. This may be very important to understand the mechanism of M-components. As a matter of fact, data for the second M-component (not shown here) with a much better spatial resolution than the data shown in Figure 2 allow a more detailed study about the propagation of M-components near the channel bottom. For that M-component the phase difference at the channel bottom changes its polarity several times with an increase of height, implying the presence of multiple waves.

Lastly we should point out that the above analysis was based on an implicit assumption that all the light signals are produced by a single unidirectional traveling wave. For return strokes, the light signals shown in Figure 1a actually involve two waves, a downward leader wave and an upward return stroke wave. We did not separate these two waves in our analysis because the leader signal is much smaller than that of the return stroke and thus is negligible in its effect. The signals shown in Figure 2a for the M-component may also be composed of two waves, one traveling upward and one traveling downward, as inferred by Rakov et al. (1995) from correlated close electric field and channel-base current data. We could not separate these two waves in our analysis. However, we still obtained regular variation of phase differences with height for one event as shown in Figure 2b. This observation probably suggests that even if two waves are involved in an M-component, the upward wave can be dominant. At the channel bottom, the complicated phase difference profile as described above suggests that contributions from the upward wave and downward wave are comparable. From high-speed photographic records, both upward-propagating and downward-propagating M-components have been observed. These observations are interpreted, based on the two-wave M-component mechanism, by Rakov et al.(1995).

ACKNOWLEDGEMENTS: The authors would like to thank K.J. Rambo, M.V. Stapleton, D. E. Crawford, C.T. Mata and M. Bejleri for their help in carrying out the observation.

REFERENCES

Kawasaki, Z-I., M. Nakano, T. Takeuti, Group velocity of subsequent return strokes in triggered lightning, Trans. IEE of Japan, Vol.107, No.3/4, 47-53, 1987.

Rakov, V.A., R. Thottappillil, M.A. Uman, P.P. Barker, Mechanism of the lightning M-components, J. Geophys. Res., 100, 25701-25710, 1995.

Rakov, V.A., Some inferences on the propagation mechanisms of dart leaders and return strokes, J.Geophys.Res., 103, 1879-1887, 1998.

Wang, D., V.A.Rakov, M.A.Uman, N. Takagi, T.Watanabe, D. Crawford, K.J. Rambo, G.H. Schnetzer, R.J. Fisher, Z-I. Kawasaki, Attachment process in rocket-triggered lightning strokes, J.Geophys.Res., 104, 2143-2150, 1999a.

Wang, D., N. Takagi, T.Watanabe, V.A.Rakov, M.A.Uman, Observed leader and return-stroke propagation characteristics in the bottom 400 m of the rocket triggered lightning channel, J.Geophys.Res., to be published, 1999b.

# AN ANALYSIS OF NATURAL LIGHTNING DISCHARGE TO THE GROUND IN CHINESE INLAND PLATEAU

X. Qie[1], X.Liu[1], G.Zhang[1], Y.Yu[1], C. Guo[2], D.Wang[3], T. Watanabe[3], N. Takagi[3], Z. Kawasaki[4], T. Ushio[4], M. Nakano[5], K. Nakamura[6]

[1] Lanzhou Institute of Plateau Atmospheric Physics, Lanzhou Gansu 730000, P. R. China
[2] Shanghai Meteorological Institute, P. R. China,
[3] Gifu University, Gifu, Japan,
[4] Osaka University, Osaka, Japan
[5] Toyota National College of Technology, Japan
[6] Nagoya Institute of Technology, Japan

ABSTRACT: In this paper, we present some general features of natural ground lightning discharges in Chinese inland plateau by using the data from 5-station slow antenna system synchronized by GPS with 1 μs time resolution. The result shown that the altitude of the neutralized negative charge is between 2.7 ~ 5.4 km above the ground, while that of neutralized positive charge is at about 2.0 km above ground. The K-changes were initiated from negative charge region in the middle part of the cloud and propagated downward to the positive charge region at the bottom of the cloud with an average speed of $1.5 \times 10^7$ m/s.

## INTRODUCTION

The unusual characteristics of Chinese inland plateau thunderstorms have been wildly noticed in China Since 1980' s. This result was based originally upon observations made with field mill by noting the change of the field when the thunderstorm was overhead. It was deduced that a positive charge region comparable in amount to the upper positive charge region is wildly distributed in the base of northwestern thundercloud. In 1989, Liu et al. [1989] found, using the recordings of E and $\Delta E$ measured by field mills, that most of intracloud discharges often took place between the main negative charge region and the lower positive charge region instead of upper positive charge region. To better understand the charge structure of thunderstorms and the discharge features in Chinese inland plateau, scientists from China and Japan conducted jointly a multi-station simultaneous observation on natural lightning in the summer of 1996 in Zhongchuan (Log. 103° 36′ E, Lat. 36° 36′ N), Lanzhou which is located in the verge of Qinghai-Xizang Plateau. Here we present some main results of this experiment.

## EXPERIMENT AND ANALYZING METHOD

The altitude of experimental site was about 2 km high above see level. Five stations were set up during the experiment, and covered an area of $10 \times 10$ km$^2$. The data we used here were mainly from slow antenna system with a time constant of about 5s and a bandwidth of 0.2 Hz to 2 MHz. The signals of slow antenna were digitized at a sampling frequency of 1 MHz, with an amplitude resolution of 12 bits. The signals from different stations were synchronized by GPSs with 1 microsecond time resolution.

A nonlinear least-square fitting method as described by Krehbiel et al.[1979] and Krider [1989] has been employed to calculate the location of charge center for individual strokes of discharges to the ground.

## DATA AND RESULTS

The flashes were produced by a storm on August 12, 1996. 29 cloud-to-ground lightning flashes were produced by the storm during 1 hour and 17 minutes including 9 positive and 20 negative flashes.

To be analyzed here are flash 11, flash 12, flash 13 and flash 22 including three negative and one positive discharges.

Figure 1 shows an example of electric field change caused by a negative ground flash. The magnitude of the total field change ranged from 68.4 V/m at A station to 230.7 V/m at D station. The flash was consisted of three individual strokes to the ground labeled R1, R2 and R3. The positive electric field changes before the first return stroke (R1) was produced by a long-duration intracloud discharge process which lasted about 200 ms. 21 out of 29 cloud-to-ground flashes followed this kind of long-duration intracloud discharge process which usually lasted for 120 ms - 300 ms with a typical value of 189.7 ms.

Figure 2 shows an example of electric field change caused by a positive ground flash. It also followed a long-duration intracloud discharge which lasted for about 210 ms. A continuing current process which lasted more than 300 ms occurred after the return stroke.

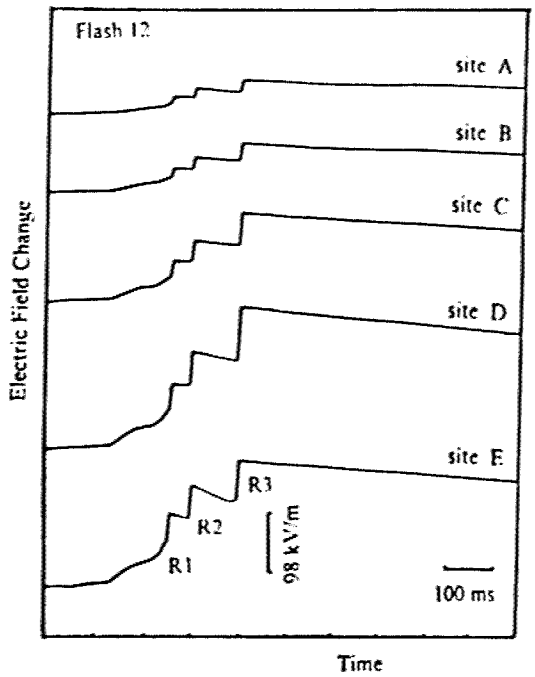


Fig. 1 Electric field change caused by a negative ground flash.

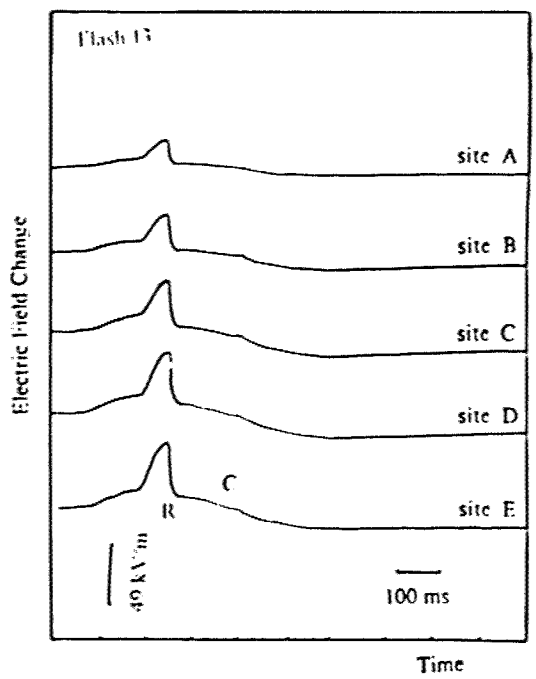


Fig. 2 Electric field change caused by a positive ground flash.

## LIGHTNING CHARGE LOCATIONS AND MAGNITUDES

Table 1 is a list of the x, y, z and Q values of 4 ground strokes. The magnitude of charge lowered to ground by discrete negative strokes ranged from a maximum of 5.44C to a minimum of 2.74C. The total charge lowered by one negative flash was no more than 11.0C. The centers of the negative charge neutralized by discrete strokes were located between 2.74 km to 5.41 km above the ground corresponding an environmental clear air temperature between -2 and -15℃.

The center of charge neutralized by the positive flash was 1.73 km above the ground corresponding an environmental clear air temperature of +5℃. '+c' in Table 1 associated with the post-stroke continuing current event. Since the continuing current flowed to the ground following the return stroke channel, it can also be fitted with a point charge model. The electric charge lowered to the ground by positive stroke was 41.67 C which is much greater than that lowered by negative one. The electric charge

transported by continuing current in 300 ms was 26.46 C, corresponding to an average current of 88.2 A.

TABLE 1 Locations and magnitudes of charges neutralized by return stroke

| Flash | Stroke number | X(km) | Y(km) | z(km) | Q(C) | $\chi^2$ |
|---|---|---|---|---|---|---|
| | | | Negative Flash | | | |
| | R1 | -23.39±0.01 | 0.62±0.07 | 2.74±0.01 | 3.83±0.01 | 0.05 |
| 12 | R2 | -21.72±0.01 | 2.02±0.02 | 3.51±0.01 | 3.11±0.01 | 0.70 |
| | R3 | -20.63±0.05 | 4.30±0.18 | 3.94±0.04 | 3.44±0.02 | 0.55 |
| | Total charge (C) | | | 10.4 | | |
| 11 | R1 | -22.25±0.01 | 0.01±0.01 | 2.96±0.001 | 5.44±0.0001 | 0.62 |
| | R2 | -23.64±0.001 | -5.27±0.02 | 2.84±0.003 | 3.15±0.001 | 1.34 |
| | Total charge (C) | | | 8.59 | | |
| 22 | -R | -17.70±0.03 | -30.61±0.01 | 5.41±0.005 | 2.74±0.001 | 4.88 |
| | | | Positive Flash | | | |
| 13 | +R | -41.91±0.01 | 4.32±0.09 | 1.73±0.01 | 41.67±0.02 | 0.36 |
| | +c | -32.84±0.01 | 8.86±0.04 | 1.60±0.01 | 26.46±0.02 | 1.59 |
| | Total charge(C) | | | 68.13 | | |

Charge sources for the individual strokes of these flashes were superimposed on the radar echoes. The comparison shows that all negative flashes were initiated in the region greater than 20 dBz or near the edge of the region with intense echo greater than 40 dBz except the first return stroke in flash 12, while the location of positive flash was in the echo region with 10 dBz.

## LOCATION OF K-TYPE BREAKDOWN PROCESSES

Figure 3 shows an example of time expanded waveforms of K-type breakdown process during the long-duration Intracloud process just before the ground flash 12 at station A. Other 3 stations recorded similar waveforms. K-type breakdown process lasted about 0.93ms. According to the sequence of pulses that can be clearly identified, we named them with a1、a2...、a10, separately. 10 pulses were identified clearly during K process, and first pulse a1 occurred about 40μs after the initiation of K process.

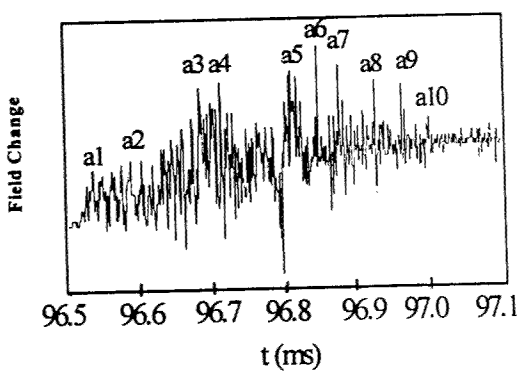


Fig.3 Time domain waveforms of K-type breakdown process.

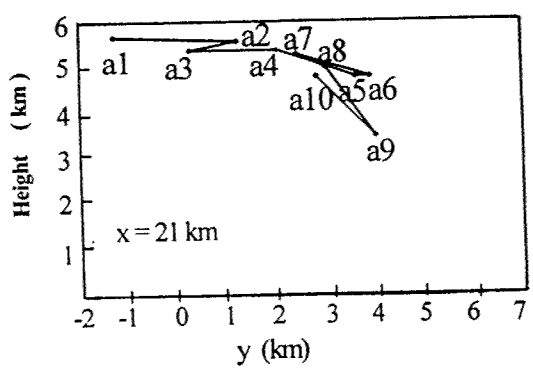


Fig. 4 Spatial development of the K-type breakdown in two-dimension.

The locations of above series of pulses have been determined by using the time difference of arriving at different station. According to above analysis, it has been found that the locations of successive strokes in the vicinity changed little in x-direction. In order to reflect the vertical development of the discharge in such a far distance, we gave x a certain value first, then fitting the discharge development in two dimensions (y, z). Figure 4 shows the best result of two-dimensional development of the K process, corresponding to x = 21 km. The first pulse a1 occurred at 5.7 km high above ground which corresponded to negative charge region in the cloud. It reached a6 quickly where was 4.8 km high above ground. a9 was the lowest point of the discharge and was 3.5km high above the ground. The discharge extended the channel downward, while the horizontal development was substantially observed. The duration was 413.3μs from a1 to a9 with an average speed of $1.4 \pm 10^7$m/s.

## CONCLUSIONS

The basic conclusions are summarized as follows:

1. The sources of charge for negative strokes of the flashes to the ground in Chinese inland plateau were confined between 2.74 to 5.41 km above the ground, and the corresponding environmental air temperature was between -2.0 to -15.0℃, while that for positive ground strokes was at about 2.0 km above the ground with the corresponding environment temperature of +5℃.

2. The magnitude of charge flowed to the ground in a negative ground flash was about -10 C, while that was 68.31 C for one positive flash.

3. Cloud-to-ground flash was usually preceded by a long-duration intracloud discharge process which lasted 120 ms to 300 ms for 85% of cloud-to-ground flashes, with a typical duration of 189.7 ms.

4. The comparison with radar echo shows that the negative discharges initiated in the region greater than 20 dBz or near the verge of the region with intense echoes greater than 40 dBz, while positive discharges initiated in a relatively weak echo region.

5. The sources of a series of pulses included in K-type breakdown are located by using time difference of arriving different station. K-type breakdown were initiated at negative charge region and propagated downward to the lower positive charge region with an average speed of $1.5 \times 10^7$ m/s.

Above results confirm again that there is a positive charge region which is large in magnitude and wild in dimension in the base of the Chinese inland plateau thunderstorms. As the reason why such a large amount of positive charges exist in the base of the cloud and why lower positive charges seems to be more effective in discharge processes really need to be answered.

ACKNOWLEDGMENTS: This work was supported by National Natural Science Foundation of China and the cooperation project between China and Japan.

## REFERENCES

Krehbiel, P. R., M. Brook and R. A. McCrog., An analysis of the charge structure of lightning discharge to the ground. J. Geophys. Res., 84, 2432-2456, 1979.

Krider, E. P., Electric field changes and cloud electric structure, J. Geophys. Res., 94, 13,145-13,149, 1989.

Liu, X., Z. Ye, X. Shao, C. Wang, M. Yan, and C. Guo, Intracloud lightning discharge in the lower part of thundercloud. Acta Meteor. Sinica, 3, 212-219, 1989.

# BROAD BAND INTERFEROMETRIC MEASUREMENT OF ROCKET TRIGGERED LIGHTNING

Wansheng Dong , Xinsheng Liu and Xiushu Qie

Lanzhou Institute of Plateau Atmospheric Physics,
Chinese Academy of Sciences, Lanzhou, Gansu 730000, P.R.C

ABSTRACT: A broad band interferometer for locating lightning radiations in two dimension has been manufactured and evaluated during the rocket triggered lightning experiment in China in 1997. We have obtained several data sets of upward leaders for both negative and positive polarity during experiments. Results showed that the altitude triggered lightning were initiated by bi-directional leaders. The onset of downward moving positive leader was prior to upward moving negative leader in a altitude triggered lightning under positive charged cloud base. A numbers of branches occurred during negative leader propagation. The waveforms of broad band electromagnetic pulses can be divided into two categories: isolated pulses and serial pulses. Isolated pulses refer to radiation whose duration were less than 35ns, serial pulses refer to radiation with longer duration. For triggered lightning, the numbers of serial pulses were dominant to isolated ones. Spectral analyses of all these pulses showed that the average energy spectral densities(ESDs) of the serial pulses were wider, in entire frequency range, the average ESDs of the isolated pulses were at lower frequencies. The time intervals between successive electromagnetic pulses were from 65us to 677us, with a mean of 106.4us. The results of broad band interferometric observations agreed well with the video observation.

## INTRODUCTION

It is well known that lightning breakdown processes produce a broad and continuous spectrum of RF radiation ranging from a few kHz through several GHz. Several techniques have been implemented for lightning location studies in VHF band. Time-of-arrival techniques have been used to locate and study lightning radiation in two and three spatial dimensions [e.g. Proctor, 1988, Rustan et al., 1980]. These techniques work best for locating isolated, impulsive radiation events, but cannot map well the continuous pulse train events, which produce images of lightning which tend to be spatially noisy and difficult to interpret. Much of energy radiated by lightning at radio frequencies occurs in continuous bursts lasting several tens or hundreds of microseconds or longer. Interferometric techniques allow the nonimpulsive radiation sources to be located as a function of time, but it cannot resolve two or many simultaneous radiation separated in space.[Rhodes, et al., 1994; Mazur et al., 1995]

Shao et al.,[1996] have illustrated the basic principle of a broad band interferometer and used this technique to investigate details of the breakdown process in dart leader. It is equivalent to many baselines with respect to a narrow band interferometer. Lower frequencies correspond to shorter baselines and higher to longer baselines. The broad band interferometry has an advantage of locating radiation at various frequencies. Since recording is done with a very high digitization rate, a radio burst can be discriminated as the train of isolated pulse. Consequently, the broad band interferometry technique enables us to location the source of each pulse in both the isolated impulsive radiation events and radiation bursts. Meantime, the spectrum of radiation from various lightning discharge process can be obtained. It is important both for scientific investigations of lightning and engineering assessments of the interference environment during thunderstorms.

In this paper, we present results of two dimensional mapping of some radiation sources from the rocket triggered discharges using the broad interferometry technique.

## EXPERIMENTS

The rocket triggering experiments were conducted at Pinliang in north-western China during the summer of 1997. The distance between the broad band VHF interferometer site and the rocket launching site was 0.8 km. The interferometer consist of three broad band (10 Mhz to 200 Mhz) flat plane antennas connected to the digital oscilloscope via a 50 meters of coaxial cables which are terminated with characteristic impedance of 50 ohms. Three antennas are aligned at three apexes of a isosceles right triangle, with right sides as orthogonal base lines of 10 meters. Such configuration of antenna array produces no phase ambiguities to the frequency of 15 MHz. The data is digitized at 500 MHz sampling rate. Having high digitization rate, a broad band interferometer is generally not able to record the entire radiation process emitted by a lightning discharge. Therefore, we introduced a method of sequential triggering for each electromagnetic pulse that allows to record as long periods of radiation as we

need. Once the electromagnetic pulse from a lightning flash is detected and its amplitude exceeds a threshold level, the triggering circuit is turned on to record waveforms.

The processing of the broad signales in this paper is similar to that described by Shao et al. [1996]. The basic idea is to extract the phase differences at different frequencies between a pair of broad band RF signals. Sometimes, different spatial radiation can arrive the antennas almost same time, we must distinguish these temporally close sources by comparing the radial signal waveform, and locate the radial sources by changing (or shifting) the DFT window width over the data series. To compute the direction of the radiation source, the Fourier transform is computed for each of the signals, which yield both power and phase spectra. The phase differences of incident electromagnetic pulses at two antennas are then obtained by subtracting the two phase spectra. Incident angles respective to the antennas base lines are computed only when the SNR exceeded a threshold. The azimuth and the elevation angles of the radiation sources are derived similar to the procedure for a narrow band interferometry.

The electrostatic field change caused by lightning flash is also recorded using a slow antenna. The traditional atmospheric electricity electric field sign convention is such that the decreased positive charge inside the cloud produces a negative (downward going ) field change in the record

## DATA AND RESULTS

Figure 1 shows the electric field change and current waveforms for a lightning flash triggered at 15:02:30 July 26, 1997, using the technique of altitude triggered lightning. The lightning current measured via a shunt resistor simultaneously with electric field change last about 14 milliseconds. The positive polarity of the current is consistent with polarity of the electric field change. Figure 2 shows the locations of radiation sources for the triggered lightning with the azimuth-elevation and projection formats. The projection view shows the sources

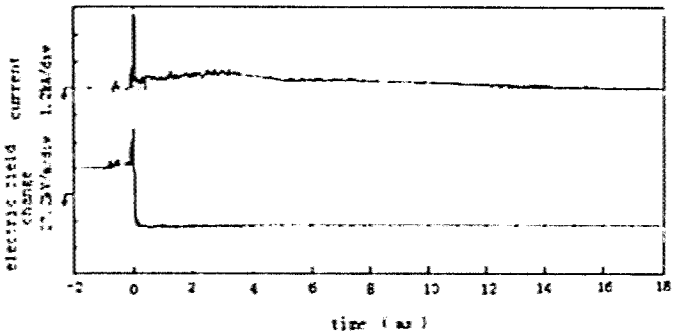


Figure 1. The current and electric field change waveforms for a altitude triggered lightning at 15:02:30 on July 26, 1997.

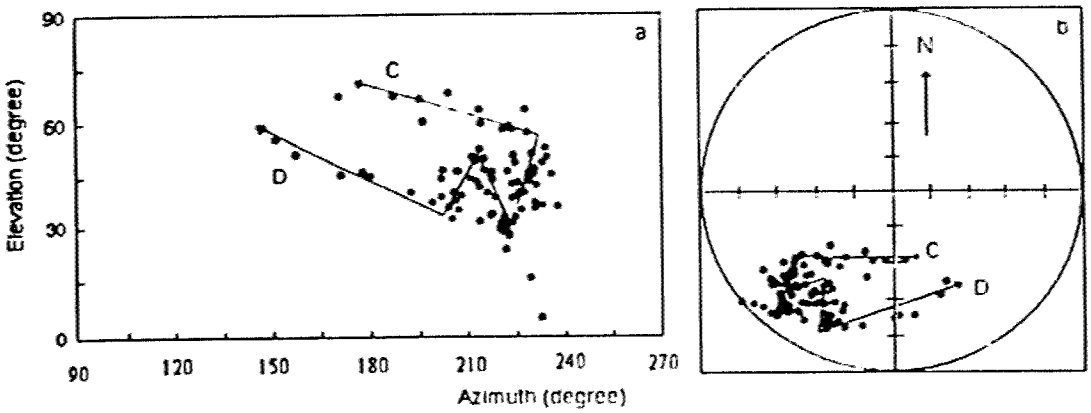


Figure 2. Radiation source locations for the altitude triggered lightning.
a) a azimuth-elevation format. b) phase projection format.

projected from a celestial sphere on the antenna array plane (detailed explanations of these two formats have been given by Rholds et al. 1994). The current waveform in the figure 1 shows two peak values(during 2-3ms and 6-10ms), according to the time of the occurring, they are related separately to the branches C and D in the figure 2. At the region of elevation of 35-40 degrees, the results of location of pulses are more scattered. This may be indicate the presence of multiple sources and branching.

During the triggered-lightning flash, 164 broad band pulses were recorded. The time intervals between these pulses range 65.0us to 677.54us, the mean time interval is 106.4us. According to their waveforms, these broad band pulses can be divided into two categories: isolated pulses and serial pulses. Isolated pulses refer to broad band radiation whose duration were less than 35ns, their waveforms are both unipolar and bipolar. Serial pulses refer to radiation with longer duration, and waveforms are bipolar. For triggered lightning, the numbers of serial pulses were dominant to isolated ones. Most of the serial pulses often occurred in initial period, but isolated pulses in final period of the flash. Spectral analyses of all these pulses showed that the average amplitude spectra of the serial pulses were wider, in entire frequency, the energy concentrated at lower frequencies for the isolated pulses. Figure 3 shows the magnitude spectra of isolated and serial pulses.

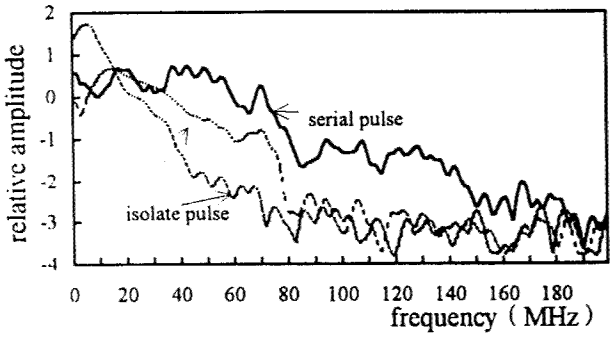


Figure 3. Average amplitude spectrum of both the isolated and serial pulses.

TABLE 1 the relative time of occurrence of pulses

| pulse | 1 | 2 | 3 | 4 | 5 | 6 | 7 | 8 | 9 | 10 |
|---|---|---|---|---|---|---|---|---|---|---|
| time(ms) | 0 | 0.121 | 0.385 | 0.643 | 0.732 | 0.797 | 0.871 | 0.947 | 1.032 | 1.098 |

Table 1 gives the occurrence times of the first 10 broad band electromagnetic pulses( defining the occurring time is 0 ms). Figure 4 shows the locations of radiation sources of these pulses with the azimuth-elevation and projection formats. The azimuth and elevation of these sources range 207 to 231 degree and 4 to 31 degree, fit well the video images of the triggered lightning. The elevation of pulse 1 is about 4 or 5 degree, corresponding to the vertical height of about 55 meters. Since the rocket and the triggering wire were isolated from the ground wire by the nonconducting Kevlar thread of 86 meters length. The two leaders of the opposite polarities are initiated both upward from the rocket and downward from the lower end of the triggering wire simultaneously. During the propagation of the downward positive leader, the electric field of near ground was intensified, and a upward leader was initiated from the top of the grounded wire. According to the altitude of the radiation source occurrence, we judges that the pulse occurred between the lower end of the altitude wire and the top of the grounded wire, Since a developing positive leader is believed not to produce detectable VHF radiation[Mazure, 1989]. The pulse would be produced by a negative breakdown proceeding of upward negative leader from the top of the grounded wire.

The azimuth of the pulse 2 is about 220 degree, the elevation is 30 degree, responding to the altitude of about 460 meters. the azimuth and elevation of the pulses 3-7 were similar to that stated above. According to their occurring altitudes, these pulses were emitted by the upward negative leader from the top of triggering wire. The azimuth of the pulse 8 is about 217 degree, the elevation is 16 degree, responding to the altitude being about 230 meters. The pulse can be related to the vaporizing of triggering wire. The location of the pulses 1- 8 lead us to conclude that a bi-directional leaders are not initiated both upward from the top of the triggering wire and down from the bottom of the triggering wire simultaneously. A positive leader is initiated from the bottom of the triggering wire and propagates toward to the ground. Its connection to the ground is produced by an upward connecting negative leader initiated from the top of the grounded wire. The connection processes enhanced the electric field at the top of the triggering wire due to the lowering of the potential of the triggering wire.

From 1.098ms to 1.48 ms, the azimuth and elevation of the radiation sources range 221 to 226 degree and 30 to 36.5 degree, the branch C of the figure 4 shows the negative leader moved to a higher elevation and to north. Then another leader initiated in a region adjacent to the former leader beginning, and produced the branch D. From 1.56 ms to 2.0 ms, the azimuth and elevation of the radiation sources range 221 to 210 degree and 30 to 45 degree. These locations of the radiation sources fit well the video images. After 2 ms, the negative leader continued propagating along the branch A (in the figure 4), and lasted approximately 3 ms (2.0 ms to 5 ms). the azimuth changed from 220 to 165 degree. elevation from 40 to 67 degree. The branch A in the figure 4 indicates that the leader developed upward and to the east. Then the another negative leader was initiated at the region (azimuth 220

degree and elevation 40 degree) adjacent to that of the first leader, and propagated along the branch D in the figure 2. This leader lasted about 6 ms (5 ms to 11 ms). The azimuth of radiation sources decreased from 220 to 145 degrees, and the elevations increased from 40 to 56 degrees. Because the interferometer can measure the direction of a radiation source (azimuth and elevation) and provides no information about distance, the negative leader propagating to lower elevation at beginning may be reflect the sources moving away from the observation site horizontally. Like the first leader, the sources located and become more scattered with the development of leader. This indicates the presence of multiple sources and branches, which is characteristic steeped negative leader

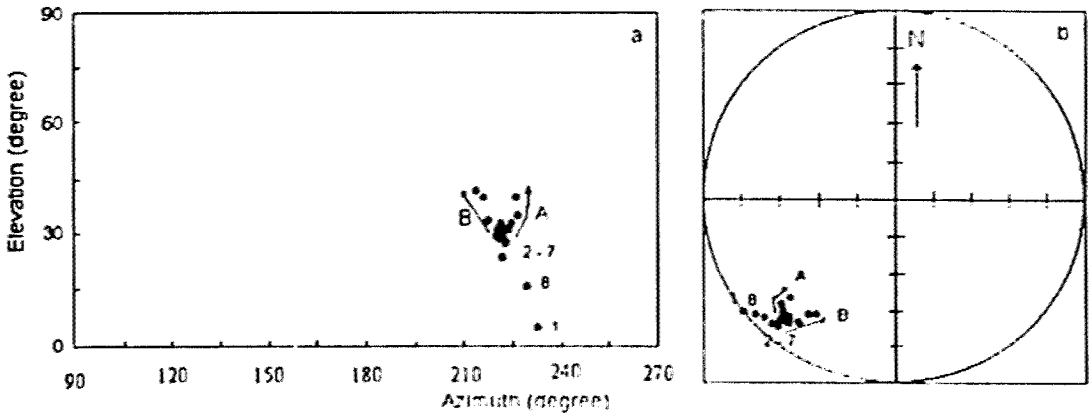


Figure 4. Radiation source locations for the altitude triggered lightning during 0 - 2 ms.
a) a azimuth-elevation format. b) phase projection format

## CONCLUSION

A broad band interferometry for two dimensional mapping of lightning progression was developed and tested during the rocket triggering lightning experiments. The results of broad band interferometric observations agreed well with the video observation. Its basic idea is to extract phase differences at different frequencies between RF signals from a pair of broad band antennas. Comparing with the narrow band interferometer, it has the flexibility of shifting and overlapping the DFT windows over the data series, which gives better time resolution to be able to distinguish temporally close sources.

Results showed that the onset of downward moving positive leader was prior to upward moving negative leader in a altitude triggered lightning under positive charged cloud base. A numbers of branches occurred during negative leader propagation. The waveforms of broad band electromagnetic pulses can be divided into the isolated pulses and the serial pulses. For triggered lightning, the numbers of serial pulses were dominant to isolated ones. Spectrum of the serial pulses were wider, the energy of the isolated pulses was at lower frequencies. The time intervals between successive electromagnetic pulses were from 65 us to 677 us, with a mean of 106.4 us.

## REFERENCES


Mazur, V., E. R. Williams, R. Boldi, L. Maier and D. E. Proctor, Comparison of lightning mapping with operational time-of-arrival and interferometric systems, Proc. International Aerospace and Groung Conference on Lightning and Static Electricity, Williamsburg, U.S.A., 1995

Proctor, D. E., R. Uytenbogaardt and B. M. Meredith, VHF radio pivtures of lightning flashes to dround, J.Geophys. Res., 93, 12683-12727, 1988

Rhodes, C., X. M. Shao, P. R. Krehbiel, R. J. Thomas, and C. O. Fayenga, Observations of lightning phenomena using radio interferometry, J.Geophys. Res., 99, 13059-13082, 1994

Rustan, P. L., M. A. Uman, D. G. Childers, W. H. Beasley, and C. L. Lennon, Lightning source locations from VHF radition data for a flash at Kennedy Space Center, J.Geophys. Res., 85, 4893-4903, 1980

Shao, X. M., D.N. Holden and C. T. Rhodes, Broadband radio interferometry for lightning observations, Geophys. Res. Lett., 23, 1917-1920, 1996.

# ABOUT THE POSITIVE LEADER PROPAGATION MECHANISM

A.V. Ivanovsky

Russian Federal Nuclear Center -VNIIEF
Sarov, Nizhny Novgorod Region, 607190, pr. Mira, 37, Russia

ABSTRACT: The model of the leader breakdown of air in which the channel is formed by warming-up of the streamer track in the streamer zone field is discussed. The previous streamer model is expanded for the description of the charged particle recombination. The mathematical model of the streamer track heating is created. It is obtained that only the streamers with specific charge and corresponding propagation velocity create the channel. The velocity of these streamers determines the velocity of the leader discharge in steady-state conditions. The cloud potential dependence of the leader velocity is determined.

## INTRODUCTION

Two spatial regions namely streamer zone and channel characterize the leader stage of the lightning (Bazelyan and Raizer, 1997). The channel is the high-temperature formation that ensures the transport of charge from the cloud to the leader head. The leader head velocity is $\vartheta_h = 10^6$-$10^8$cm/s. The channel length reaches some kilometers but its diameter is about parts of millimeter. The streamer zone represents great number of the streamers starting from the leader head. The streamer's velocities $\vartheta_{st}$ may be much more than the $\vartheta_h$. The streamer zone length is tens of meters. The channel current provides the charge transport, propagation, streamer zone formation. However the streamer zone processes determine the channel parameters. Therefore the streamer zone is important for the leader formation. In spite of ascertained character of the process development the physics model of the leader stage of lightning relating of the propagation velocity, the channel and the streamer zone parameters to cloud potential $\mathbf{V_{cl}}$ is absent.

## BASIC ASSUMPTION

By analogy with the arc discharge the electric field strength in the channel is about ~1 kV/m when the current is greater than ~10A. The potential drop on the channel may be neglected and consider the steady-state propagation with the velocity $\vartheta_h$ corresponding the potential of the leader head **V** equals $\mathbf{V_{cl}}$ when megavolt potential applies on the base of hundreds of meters. The channel transfers potential $\mathbf{V_{cl}}$ from the cloud to the streamer zone base only.

In constructing a model we consider the electric field $\mathbf{E_{st}}$ is constant along the streamer zone. The charge introducing by all streamers starting from the leader head into the streamer zone creates and maintains the field $\mathbf{E_{st}}$. Streamer is the plasma core with charge $\mathbf{q_{st}}$. The attachment and recombination determine the plasma core length. The field in the streamer head increases as a result of polarization. Ionization in the increased field compensates the electron decrease because of the attachment and the recombination and provides the propagation. The charge $\mathbf{q_{st}}$ uniquely determines the streamer velocity $\vartheta_{st}$, radius $\mathbf{a_{st}}$ and electron concentration $\mathbf{n_{st}}$ at fixed $\mathbf{E_{st}}$ (Ivanovsky,1996).

The heating of the streamer track in the field $\mathbf{E_{st}}$ by the currents of ion and of electrons appearing as a result of both the attachment and ionization forms the channel. The interaction between negative ions and electron excited molecules determines the detachment. What is the streamer of the streamer zone that forms the channel? When heating time $\mathbf{t_{st}}$ is constant the channel formation potential $\mathbf{V_{st}} \cong \mathbf{E_{st}} \cdot \vartheta_{st} \cdot \mathbf{t_{st}}$ increases with increase of the $\vartheta_{st}$ or of the $\mathbf{q_{st}}$. The streamer radius $\mathbf{a_{st}}$ decreases when the velocity $\vartheta_{st}$ decreases and thermal conduction leads to the increase of $\mathbf{t_{st}}$. The increase of the $\mathbf{t_{st}}$ leads to $\mathbf{V_{st}}$ increase. In that way we expect that at fixed $\mathbf{E_{st}}$ the dependence $\mathbf{V_{st}}(\vartheta_{st})$ has the minimum $\mathbf{V_m}$ and corresponding to it both the streamer velocity $\vartheta_m$. and charge $\mathbf{q_m}$. In steady-state conditions the minimum $\mathbf{V_m}$ determines both the leader potential $\mathbf{V}=\mathbf{V_m}$ and the propagation velocity $\vartheta_h = \vartheta_m$. So, from the great number of the streamers only that with charge $\mathbf{q_m}$ form the channel. The others create and maintain the field $\mathbf{E_{st}}$.

The cloud potential $\mathbf{V_{cl}}$ determines the leader current $\mathbf{J}=\mathbf{c_0} \cdot \vartheta_h \cdot \mathbf{V_{cl}}$ ($\mathbf{c_0}$-is the capacitance per unit length). In one's turn the leader current **J** determines the steady-state channel parameters in accordance with arc discharge theory.

## STREAMER DISCHARGE

We shall describe the charge distribution along the streamer length by the head $\mathbf{q_1}$ and the track $\mathbf{q_0}\lambda$ charges

$$\mathbf{q(z)} = \mathbf{q_0} \cdot \begin{cases} 0, & z \geq z_f \\ \exp\left(\dfrac{z - z_f}{\lambda}\right), & z < z_f \end{cases} + \mathbf{q_1} \cdot \delta(z - z_f), \quad \mathbf{q_{st}} = \int_{-\infty}^{+\infty} \mathbf{q(z)} \cdot dz = \mathbf{q_0} \cdot \lambda + \mathbf{q_1}, \tag{1}$$

where the attachment and recombination determine the scale $\lambda$: $z_f$ is the front coordinate.

When $\lambda/a_{st}>>1$ the electric field E along the streamer axis is obtained by solving equations (Ivanovsky, 1996)

$$\begin{cases} \dfrac{dE}{dx} - \dfrac{a_{st}}{\vartheta_{st}} \cdot \dfrac{\sigma}{\varepsilon_0} \cdot E = -E_{st} \cdot \dfrac{q_0}{2\pi\varepsilon_0 a_{st} E_{st}} \cdot \left\{ 1 - \dfrac{x - x_f}{\sqrt{(x-x_f)^2+1}} + \dfrac{1}{\left(\sqrt{(x-x_f)^2+1}\right)^3} \right\}, & x \ge x_f \\ \pi \cdot \dfrac{a_{st}}{\vartheta_{st}} \cdot \dfrac{d}{dx}(\sigma \cdot E) + C_0 \cdot E = C_0 \cdot E_{st} \cdot \left\{ 1 + \dfrac{q_0}{2\pi\varepsilon_0 a_{st} E_{st}} \cdot \left( E_1(\lambda / a_{st}, x) + E_2(x) \right) \right\}, & x < x_f \end{cases} \quad (2)$$

where $x = z/a_{st}$; $E_1$, $E_2$ are the functions of x: $C_0 = 2\pi\varepsilon_0/\ln(2\lambda/a_{st} - \gamma + 0.5)$ is the capacitance per unit length; $q_f = a_{st} \cdot q_0$.

The conductivity $\sigma = e \cdot \mu_e \cdot n_e$ ( $\mu_e(E)$ is the electron mobility ) is determined from the equations for the electron $n_e$, positive $n_+$ and negative ion $n_-$ concentrations. For quasi-neutral plasma these equations have the form

$$\begin{cases} \dfrac{dn_e}{dx} = \dfrac{a_{st}}{\vartheta_{st}} \cdot (\nu_{att} - \nu_{ion}) \cdot n_e + \alpha_r \cdot n_e \cdot n_+ \\ \dfrac{dn_+}{dx} = \dfrac{a_{st}}{\vartheta_{st}} \cdot \alpha_r \cdot n_+^2 \end{cases} \quad (3)$$

where $\nu_{ion}(E)$, $\nu_{att}(E)$ are the frequencies of the ionization and attachment. We have taken the coefficient of the ion-ion recombination equal to that of the electron-ion recombination $\alpha_r(E)$ because the difference of degree is small.

By the fixing $E_{st}$ the conditions of the maximum of the charge per unit length q(x) and of the continuity of the field E(x) at the streamer head ( $x = x_f$ ) determine correspondingly the parameters $q_0/(2\pi\,\varepsilon_0 a_{st} E_{st})$ and $\tau = a_{st}/\vartheta_{st}$. The condition of the equality of the total streamer charge to $q_{st}$ determines the parameter $\lambda/a_{st}$ (Ivanovsky, 1996).

Figures 1, 2 show the results of a numerical simulation of equations (2), (3). When streamer with charge $q_{st}$ propagates at the field $E_{st}$ the dimensionless charge $Q = q_{st}/(2\pi\,\varepsilon_0 a_{st}^2 E_{st})$ determines the streamer radius $a_{st}$. The radius $a_{st}$ and dimensionless time $\tau(E_{st})$ determine the velocity $\vartheta_{st}$ (Fig. 1). Fig. 2 shows the electron concentration $n_e$ behind the streamer head versus the field $E_{st}$ ($n_0 = 10^{14}$ 1/cm$^3$). The streamer discharge exists when the electric field greater than threshold field coinciding with the field in which the attachment is minimum (curve 2, $\nu_0 = 10^8$ 1/c).

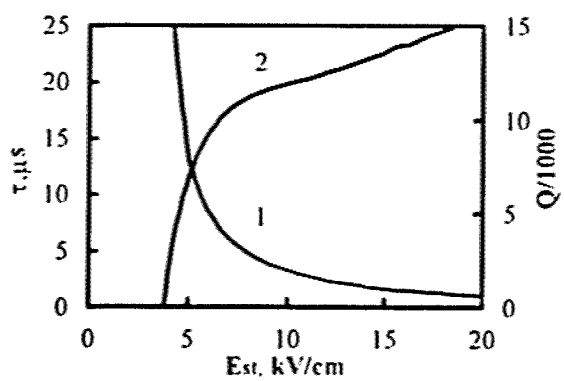


Fig. 1. The Est dependence of the (1) time τ and (2) charge Q.

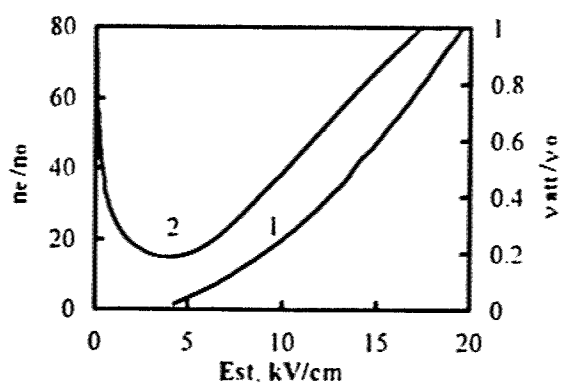


Fig. 2. The Est dependence of the (1) electron concentration $n_e$ and (2) attachment frequency $\nu_{att}$.

## LEADER DISCHARGE FORMATION

Let us assume the channel is formed at atmospheric pressure $P_0$. The concentration N and the temperature T of the neutral molecular component determine the $P_0$ when dissociation and ionization are small. The equations for determination of the N, T, on neglecting kinetic energy and longitudinal heat flow and velocity, has the form

$$\begin{cases} N c_p \left( \dfrac{\partial T}{\partial \tau} + u \dfrac{\partial T}{\partial r} \right) = \dfrac{1}{r} \dfrac{\partial}{\partial r} \left( r \lambda \dfrac{\partial (kT)}{\partial r} \right) + q_t, \\ T \dfrac{1}{r} \dfrac{\partial}{\partial r}(r u) = \dfrac{\partial T}{\partial \tau} + u \dfrac{\partial T}{\partial r}, \quad P_0 = N k T. \end{cases} \quad (4)$$

In Eqs. (4): $\tau = t - z/\vartheta_{st}$; $\lambda$ is the heat-transfer coefficient; $c_p = 7/2kT$ is the specific heat at constant pressure. The elastic

electron $q_{en}$ and ion $q_{in}$ collisions, the rotational excitation $q_r$ ($T_r$=T), the acts of the electron-ion $q_{ei}$ and ion-ion $q_{ii}$ recombination and the dissociative attachment $q_{att}$ determine the air heating $q_t$. We neglect the air heating owing to the energy relaxation of the vibrational and electronic excitation of the molecules.

The value of $q_t$ depends on the charge particle concentrations which are given by the solution of the equations

$$\begin{cases} \frac{\partial}{\partial \tau}[n_e \cdot (1-\vartheta_{dr}/\vartheta_{st})] + \frac{1}{r}\frac{\partial}{\partial r}(r n_e \vartheta_e) = (\nu_{ion} - \nu_{att}) \cdot n_e - \alpha_{ei} \cdot n_e \cdot n_+ + \nu_{det} \cdot n_-, \\ \frac{\partial n_-}{\partial \tau} + \frac{1}{r}\frac{\partial}{\partial r}(r n_- \vartheta_-) = \nu_{att} \cdot n_e - \alpha_{ii} \cdot n_- \cdot n_+ - \nu_{det} \cdot n_-, \quad n_+ = n_- + n_e. \end{cases} \tag{5}$$

In the quasi-neutral plasma the medium movement and ambipolar diffusion determine the radial particles flow $n_e\vartheta_e$, $n_-\vartheta_-$. The electron drift along the field is negligible when $\vartheta_{st} >> |\vartheta_{dr}|$ ( $\vartheta_{dr} < 0$, for positive leader ).

The electron temperature $T_e$ determining the specific reaction rate ($\nu_{ion}$, $\nu_{att}$, $\alpha_{ei}$), the radial charge particles flow and the electron drift velocity may be obtained solving the next equation

$$\frac{\partial}{\partial \tau}(\frac{3}{2} n_e k T_e) + u \frac{\partial}{\partial r}(\frac{3}{2} n_e k T_e) + \frac{5}{2} n_e k T_e \frac{1}{r}\frac{\partial}{\partial r}(ru) = \frac{e^2 n_e}{m_e \nu_m} E_{st}^2 - q_e + \frac{1}{r}\frac{\partial}{\partial r}\left(r \lambda_e \frac{\partial (kT_e)}{\partial r}\right), \tag{6}$$

where $\nu_m$ ($T_e$,N) is the elastic collision electron frequency; $q_e=q_{en}+q_r+q_v+q_{ex}+q_i$; $q_v$, $q_{ex}$, $q_i$ are the electrons energy losses in the acts of the vibrational, electronic excitation and ionization; $\lambda_e=5/2 \cdot n_e k T_e/m_e \nu_m$ is the electronic heat-transfer coefficient.

The detachment frequency is $\nu_{det}=\alpha^* \cdot N^*$, where the electronic excitation molecules concentration $N^*$ is determined from the equation ($\nu_{ex}$ ($T_e$,N) is the electronic excitation frequency, $\alpha^*$ is the specific reaction rate)

$$\frac{\partial N^*}{\partial t} + \frac{1}{r} \cdot \frac{\partial}{\partial r}(r u N^*) = \nu_{ex} \cdot n_e - \alpha^* N^* \cdot n_-. \tag{7}$$

The numerical simulation of equations (4)-(7) with initial condition determined using the Fig. 1,2 shows the sharp air density decrease (rise of the medium T and electron $T_e$ temperature) on the channel formation stage. The rise of the corresponding air conductivity unavoidably leads to the electric field $E_{st}$ drop. This allows to lead the time $t_{st}$ and the channel formation potential $V_{st} \cong E_{st} \cdot \vartheta_{st} \cdot t_{st}$. The $\vartheta_{st}$ ($q_{st}$) dependence of the potential $V_{st}$ for the field

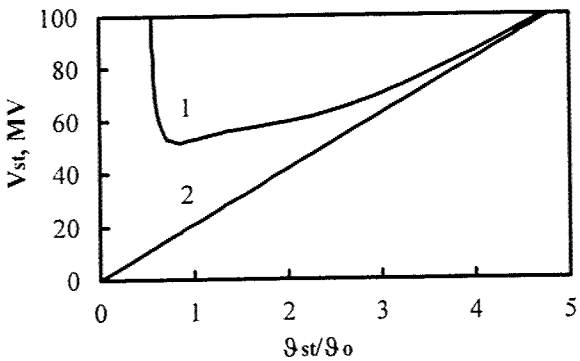


Fig. 3. The $\vartheta_{st}$ dependence of the Vst: 1 - with transport processes; 2 - without transport processes.

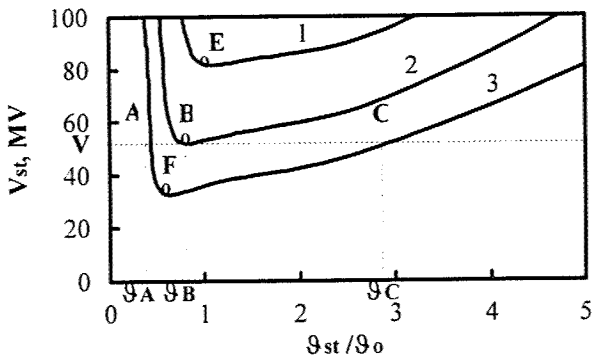


Fig. 4. The $\vartheta_{st}$ dependence of the Vst: 1 - $E_{st} = E_1$; 2 - $E_{st} = E_2$; 3 - $E_{st} = E_3$.

$E_{st}$=12.7kV/cm and $\alpha^*=10^{-8}$cm$^3$/s is shown in Fig. 3 ($\vartheta_0=10^8$cm/s). When the velocity $\vartheta_{st}$ is small the influence of the transport processes (basically of thermal conduction) increases because the streamer radius decreases. This leads to the potential $V_{st}$ increase (the curve 2 is obtained with $\vartheta_e=\vartheta_-=u$, $\lambda_e=\lambda=0$). The streamer velocity $\vartheta_{st}$ dependence of the potential $V_{st}$ for three values of $E_{st}$ is shown in Fig. 4 ($E_1$=12.4kV/cm, $E_2$=12.4kV/cm, $E_3$=12.4kV/cm). Let the cloud potential equals V. In steady-state regime we must to require the truth both $V=V_{st}$ and $\vartheta_h=\vartheta_{st}$. It is impossible the leader propagation when $E_{st}<E_2$. For $E_{st}>E_2$, for example $E_{st}=E_3$, there are two streamer groups that satisfies mentioned above conditions. For $E_{st} = E_3$ these are the streamers propagating with velocities $\vartheta_A$ and $\vartheta_C$. The existence of two leader velocities is possible. The stable propagation with $\vartheta_h = \vartheta_A$ is impossible, since the potential of the channel formation by the streamers with velocities $\vartheta_A<\vartheta_{st}<\vartheta_C$ greater than $\vartheta_h$ is smaller. The steady-state propagation with $\vartheta_C$ is also instability, because the streamers with $\vartheta_{st}>\vartheta_C$ moving in front of the leader decrease the field $E_{st}$. One may assume that the stable leader propagation is possible when $E_{st}=E_2$ and $\vartheta_h = \vartheta_{st}=\vartheta_B$ (the point B).

The cloud potential dependence of the leader propagation velocity (the points F, B, E of Fig.4) for varies value

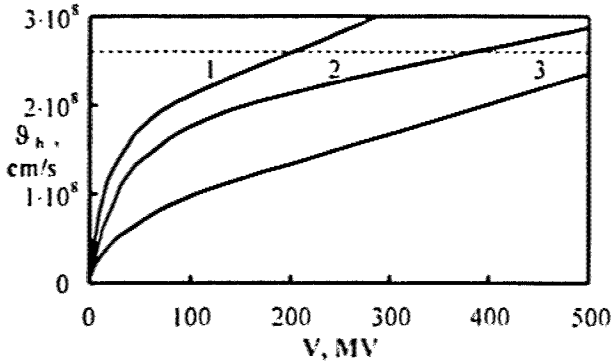


Fig. 5. The V dependence of the leader velocity $\vartheta_h$ : 1 -$\alpha^*$=2.5·10$^{-9}$cm$^3$/s; 2 -$\alpha^*$=5·10$^{-9}$cm$^3$/s; 3-$\alpha^*$=10$^{-8}$cm$^3$/s.

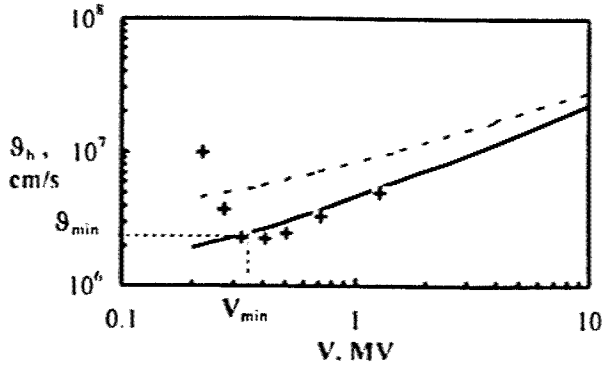


Fig. 6. The V dependence of the leader velocity $\vartheta_h$ : --- -$\vartheta_{dr}$=0, $C_0$=∞; — -$\vartheta_{dr}$≠0, $C_0$=∞; +++ -$\vartheta_{dr}$≠0, $C_0$≠∞.

of $\alpha^*$ is shown in Fig. 5. For natural lightning the maximum velocity is about 2.6·10$^8$cm/s, the maximum total charge is about 20 coul (Uman, 1987). Estimating the leader capacitance by the value of 4·10$^{-8}$ f one can obtain the maximum potential is about 500 MV. The similar value is obtained when $\alpha^*$=(0.5-1)·10$^{-8}$ cm$^3$/s (Fig. 5).

The electron drift along the longitudinal field essentially influences on the leader parameters when the drift and leader velocities are compared (the curves — and --- of Fig. 6). Taking into account the streamer zone capacitance (the diameter takes to equal 1/3 of length) one can obtain the minimum of the leader velocity $\vartheta_{min}$ and corresponding to it potential $V_{min}$ (the curves — and +++ of Fig. 6). The minimum velocity observed in experiments is about 2·10$^6$ cm/s, corresponding to it potential is about 300-400 kV (Bazelyan and Raizer, 1997).

For estimation of the maximum leader length $L_m$ we represent the cloud potential $V_{cl}$ as a sum of the potentials of streamer zone V and channel $V_c$=$E_c$·L. The field $E_c$ we estimate by the arc value $E_c$ (V/m)≅10$^4$·J$^{0.5}$ (Krinberg, 1968), where J(A)=$c_0$·$\vartheta_h V_{cl}$ is the leader current, $c_0$≅6.5·10$^{-12}$ f/m, $\vartheta_h$(m/s) ≅4.5·V$^{2/3}$ (the data interpolation of curve 3, Fig. 5). As a result the maximum velocity is $\vartheta_m$ ≅4.5·$V_{cl}^{2/3}$, the maximum length is reached when V=2/11·$V_{cl}$ and it's value equals $L_m$≅20·$V_{cl}^{11/6}$. Specifically the steady-state propagation is possible if the leader length L<<$L_m$($V_{cl}$).

For maximum potentials of the artificial lightning (3-5) MV: $L_m$≅(150-380)m; $\vartheta_m$≅(0.94-1.3)·10$^5$m/s. Observed values are L ≅(100-200)m, $\vartheta$ ≅10$^5$m/c (Bazelyan and Raizer, 1997). For minimum length of the natural lightning $L_m$ ≅ 1000m: $V_{cl}$ ≅ 8 MV; $\vartheta_m$ ≅ 1.8·10$^5$m/s. Observed value is $\vartheta$ ≅10$^5$m/s (Uman, 1987). For titanic lightning ($V_{cl}$ ≅500MV): $L_m$ ≅ 2000 km; $\vartheta_m$ ≅ 2.8·10$^6$ m/s.

The electron energy losses in acts of the electronic excitation rise sharply when the field exceeds about 10 kV/cm (Fig.7). One can say the sharp rise of the electronic excitation determines the threshold of the leader air discharge. It should be noted that generally supposed $E_{st}$ ~5 kV/cm (Bazelyan and Raizer, 1997) that is above the threshold of the streamer discharge (curve 2 of Fig. 2).

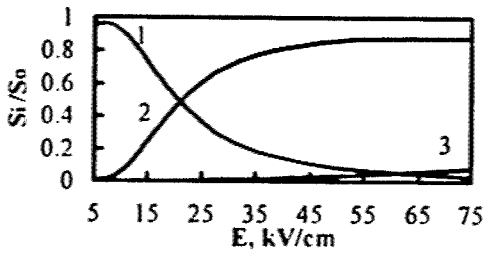


Fig.7. The E dependence of the partial energy loss of electrons: 1-vibrational excitation; 2 - electronic excitation; 3 - air ionization.

In the fields ~10kV/cm the basic excited electronic levels are $N_2(A^3\Sigma_u^+)$, $N_2(B^3\Pi g)$. The corresponding value of $\alpha^*$ is about 2.5·10$^{-9}$cm$^3$/s. The better coincidence between calculated and observed data takes place when $\alpha^*$ larger in 2-4 times. It may be explained additional detachment by interaction both with the molecules at high-lying electronic levels of excitation (such particles ~10%) and with the resonance radiation or detachment by electron impact in the regions with high electron concentration, for example, near the streamer head.

It is impossible to construct the similar breakdown regime for negative leader because of the electron drift velocity $\vartheta_{dr}$ at the channel formation stage always greater than streamer velocity $\vartheta_{st}$ (look (5)).

REFERENCES

Bazelyan E. M., Raizer Yu.P. Spark Discharge. CRC Press, Boca Ration, Florida, 1997.

Ivanovsky A.V. About the Streamer Breakdown of the Air and the Mechanism of Lightning Initiation by Runaway Electrons// Proceeedings 10th ICAE, Osaka, Japan, 1996, pp. 252-257.

Uman M. The Lightning Discharge. Academic Press, 1987.

Krinberg I.A. On the Theory of the Electric Arc Column in Free Convection. Sov. Journal of Technical Physics, v.38,N10,1968, pp.1705-1713.

# PROPERTIES OF LEADER DEVELOPMENT IN ALTITUDE-TRIGGERED LIGHTNING

M. Chen[1], T. Watanabe[1], N. Takagi[1], D. Wang[1], X. Liu[2], Y. Zhang[2], L. Zhou[3], and D. Zhong[3]

[1]Department of Electrical and Electronic Engineering, Gifu University, Gifu City, JAPAN
[2]Lanzhou Institute of Plateau Atmospheric Physics, Lanzhou City, CHINA
[3]Guangzhou Institute of Electrical Power Test, Guangzhou City, CHINA

ABSTRACT: Simultaneous measurements of two-station electric fields and space- and time-resolved light signals (sampling time 0.1 $\mu$ s) made for 5 negative altitude-triggered lightning flashes, in Guangzhou, China, during the summer of 1998, are analyzed. Results show that these 5 flashes have similar main chronological sequence of events, including a bidirectional leader initiated from extremities of the floating wire with the onset of the upper positive leader prior to that of the lower negative stepped leader by just 20-30 $\mu$ s, followed by a mini-return stroke occurring several milliseconds later. The mini-return stroke (speed $1\text{-}2\times10^{8}$ m/s) rapidly weakens down when it reaches the lower end of the wire, and a few microseconds later a bright discharge process (speed $1.5\text{-}5.4\times10^{7}$ m/s) appears from the upper end of the wire which becomes optically undetectable after extending forward (upward) several hundred meters. Just after the upper bright discharge process weakens down, another bidirectional leader starts from the lower end of the wire with the upward speed being $3\text{-}10\times10^{5}$ m/s and downward one $2\text{-}2.6\times10^{5}$ m/s.

## INTRODUCTION

The "altitude-triggering lightning technique" has been proved to be a valuable tool to study the physical mechanism of leader development, as it allows to do measurements in very close distance [Lalande et al., 1998; Chen et al. 1999]. In this paper we report the results of a triggering lightning experiment carried out during July 13 to August 24 of 1998, in Guangzhou, Southern China.

## INSTRUMENTATION

Figure 1 shows the "altitude-triggering lightning technique" and the site setup of this experiment. After ignition, the rocket first spools out 100 m of nylon cable from the bobbin attached to the rocket tail, and then a steel wire is unreeled. The nylon cable is tied to a 4 m high grounded lightning rod. The lightning triggered by using this technique involves a bidirectional leader from extremities of the floating wire (leaders A and B in Figure 1) and an upward connecting leader from an object grounded (leader C in Figure 1), followed by a so-called "mini-return stroke" process. The two observation sites, 1 and 2, were located at 60 m and 1.3 km, respectively, from the triggering site. Electric fields were measured by using a flat-plate slow antenna system ( band-width 4 Hz -1.5 MHz, sampling rate 12.5 MHz, resolution 12 bit, recording length 2 M words ) at both sites. A high speed digital 16×16 photodiode array system (ALPS) operating at a time resolution of 0.1 $\mu$ s with internal trigger was also used to photograph the lightning channel. The ALPS can record up to 16,000 frames for each event with up to 100% pre-trigger frames. The output of the trigger signal from the ALPS was used as

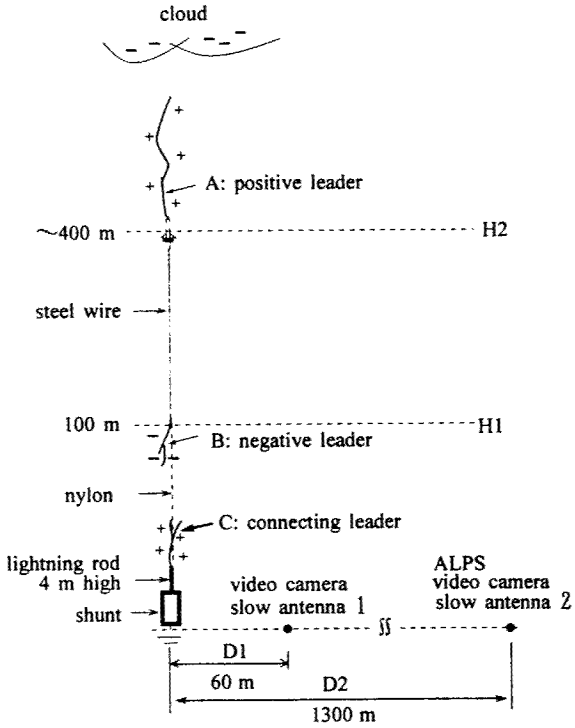


Figure 1. Illustration of altitude-triggering lightning technique and the site setup.

the external trigger signal of the slow antenna at site 2 to synchronise the time of these two measurements.

RESULTS

During the experiment, 5 altitude-triggered negative lightning flashes, CHN9801, CHN9802, CHN9803, CHN9804 and CHN9805, were obtained on Aug. 22. The main chronological sequence of events, as inferred from the measurements of electric fields and light signals recorded by the ALPS, is similar for these 5 flashes. As an example, Figure 2 shows the electric field measurements and Figure 3 the light signal recorded by ALPS for CHN9805. For analysis, the peaks of the electric waveform produced by the mini-return stroke at both sites are set to time 0 with an accuracy greater than 1 $\mu$ s.

As shown in Figure 2a, from time t1 (t= -3.4 ms), the electric field at 60 m begin to decrease first step-wisely (step number 11, step magnitude -50 to -75 V/m each, and step interval 20 to 30 $\mu$ s) then continuously (mean slope -3530 kV $m^{-1}S^{-1}$). The field step, 50-75 V/m, is consistent with a charge Q of -88 to -132 $\mu$ C placed at the lower end of the floating wire (100 m above ground). The following slope, -3530 kV $m^{-1}S^{-1}$, is in consistency with a charging current of about 6.2A to the lower end of the wire. Based on the laboratory experimental results [Bondiou-Clergerie et al., 1996], these suggest the inception of a negative stepped leader from the lower end of floating wire.

Also from t1, the electric field at 1300 m begins to increase slowly with several bipolar pulses superimposed on the beginning of the rising slope ( the mean slope: 26 kV $m^{-1}S^{-1}$) (Figure 2b). Both the pulse number and interval are as same as that of the field steps occurring around time t1 at site 1. This is consistent with a positive leader extending forward from the upper end of the floating wire.

In the following 3 ms (from time t1 to t2), the field step/pulse train appear and disappears 4 times (indicated by the pulse train at t1, -1.6 ms, -1.0 ms, and t2 in Figure 2) while the field at site 2 keeps increasing continuously, indicating that the upper positive leader exhibits a continuous upward development, while the negative stepped leader starts and stops a few times.

The light signal records (Figure 3) of ALPS (available for time from -1.1 to 0.5 ms ) show that the section around 111 m above ground of the channel begins to light at least from time -1.1ms with light pulses (unresolved in Figure 3) appearing around the time -1.0 ms and -348 $\mu$ s, due to the negative stepped leader from the lower end of the wire. It also show that the upper positive leader in this stage, if any, is undetectable by the ALPS.

From time t2 (t= -348 $\mu$ s), at site 2, the electric pulse resumes with a much bigger amplitude than that occurring before t2 and the field slope increases to 460 kV $m^{-1}S^{-1}$, indicating that both the upper positive and the lower negative leaders accelerate from this time (Figure 2). The step interval of the lower negative leader is about 20 $\mu$ s (Figure 4).

The connection between the lower negative stepped leader and the positive connecting leader from ground is derived to be finished around time t3 (t= -1.6 $\mu$ s), as the light signals at the segments 0-55 m and 55-111 m above ground begin to increase continuously from this time (Figure 5a). This connecting process temporally corresponds to a big sharp pulse at site 1 (pulse a in Figure 5b) and a slow front change of the electric filed at site 2 (Figure 5c).

Following this is a so-called mini-return stroke process which produces intensive light emission only at the part between ground and the lower end of the floating wire (time 0 in Figures 3 and 5a). The upward speed of the mini-return stroke, v1, as estimated from the onset of the fast transition of the light signal at various height (the onset is defined as the point the relative light intensity first excesses 50), is about $1.8\times10^{8}$ m/s.

About 3 $\mu$ s after the mini-return stroke, at t5 (t= 3 $\mu$ s), a bright upward discharge process appears from the top of the wire ( Figure 3). This upper bright discharge process becomes unvisible to the ALPS after extending forward about 275 m with a speed, v2, of $5.4\times10^{7}$ m/s.

Just after the upper bright discharge process weakened down, at t6 (t= 40 $\mu$ s), a bright bidirectional leader (named lower bi-directional leader in Figure 3, for CHN9801, CHN9802, and CHN9803, only the upward positive leader is observed ) starts from the lower end of the wire. The upward one (upward positive leader 2 in Figure 3) of this bidirectional leader has a speed, v3, of $5.5\times10^{5}$ m/s while the downward one (downward negative leader 2 in Figure 3) a speed, v4, of $2.6\times10^{5}$ m/s.

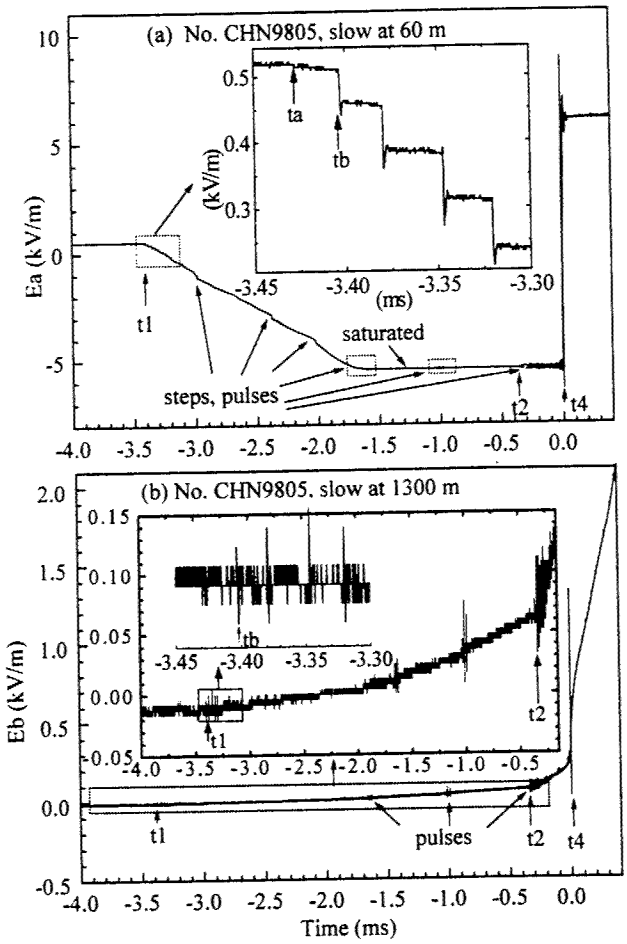


Figure 2. Measurements of electric field changes at 60m (a) and 1300m (b) from the launcher for flash CHN9805. Peaks of electric waveforms of the mini-return stroke are set to time 0.

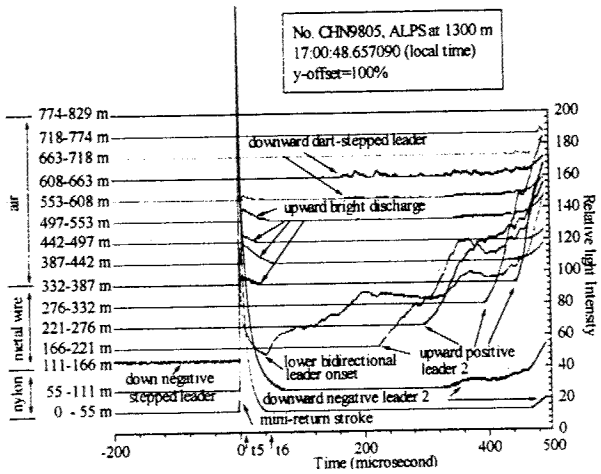


Figure 3. Light signal versus height and time observed by using the ALPS at 1300 m far from the launcher, for flash CHN9805.

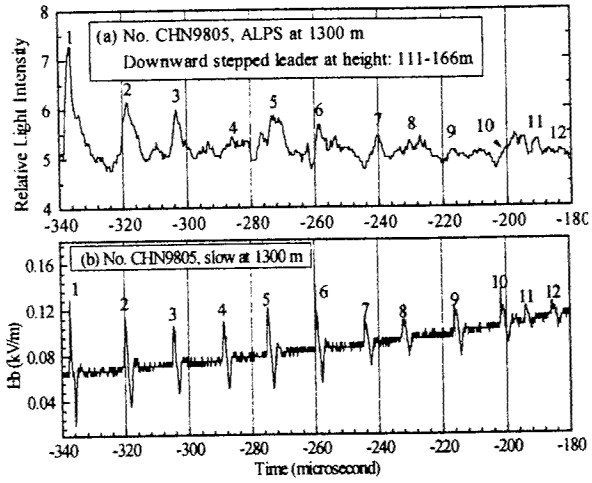


Figure 4. Light pulses of ALPS (a) and electric field pulses at site 2 (b), produced by the downward negative stepped leader of flash CHN9805.

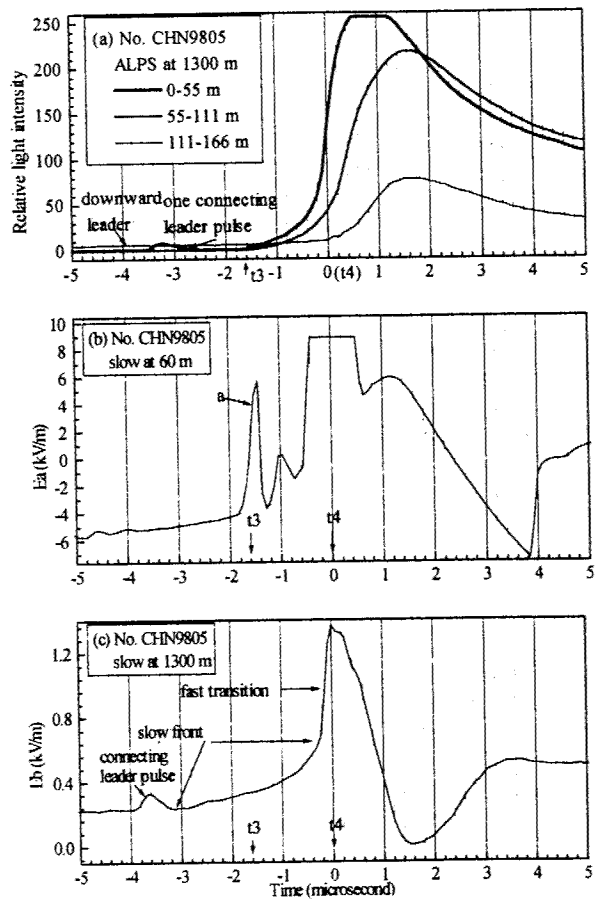


Figure 5. Waveforms of light signals (a) and electric fields at sites 1 (b) and 2 (c), due to the mini-return stroke of flash CHN9805.

The analysis results for other cases are summarized in Table 1. As shown in the table, the parameters for the same event in different flashes is similar in values.

TABLE 1. Summary of Statistics on the 5 Altitude-triggered Lightning Flashes

| Flash No. | Triggering time | Triggering height (m) | Bidirectional leader t1(ms) | Bidirectional leader t2($\mu$ s) | Mini-return stroke v1 ($10^8$m/s) | Upper bright discharge v2 ($10^7$m/s) | Lower bidirectional leader ($10^5$m/s) v3 (up) | Lower bidirectional leader ($10^5$m/s) v4 (down) |
|---|---|---|---|---|---|---|---|---|
| 9801 | 16:41:48.97 | 276 | -4.7 | -290 | 1.1 | 1.5 | 4.0 | -- |
| 9802 | 16:45:55.87 | 553 | -8.5 | -208 | 1.4 | 3.1 | 10.9 | -- |
| 9803 | 16:52:22.51 | 387 | -5.5 | -350 | 1.4 | 4.6 | 3.2 | -- |
| 9804 | 16:55:25.13 | 276 | -3.4 | -315 | 1.9 | 4.4 | 6.1 | 2.1 |
| 9805 | 16:00:48.66 | 442 | -3.4 | -348 | 1.8 | 5.4 | 5.5 | 2.6 |

## DISCUSSION AND SUMMARY

Electric field measurement at 60 m allows us to discuss the exact onset time of the bidirectional leader. As shown Figure 2a, there is a slow decrease slope starting at time ta with a mean slope of -400 kV $m^{-1}$ $S^{-1}$, which is consistent with a downward negative charging current of about 0.7A at the lower end of the wire. Such a current apparently due to a positive streamer-leader from the upper end of the wire, not a kind of corona discharge. The first field step that is believed as the onset of the negative leader from the lower end of the wire occurs at tb, only 25 $\mu$ s after ta. Other 4 cases also show a time delay (tb-ta) of 20 to 30 $\mu$ s, quite shorter than that reported by Lalande et al. [1998].

As a summary, the main chronological sequence of events involved in these 5 altitude-triggered flashes is illustrated in Figure 6.

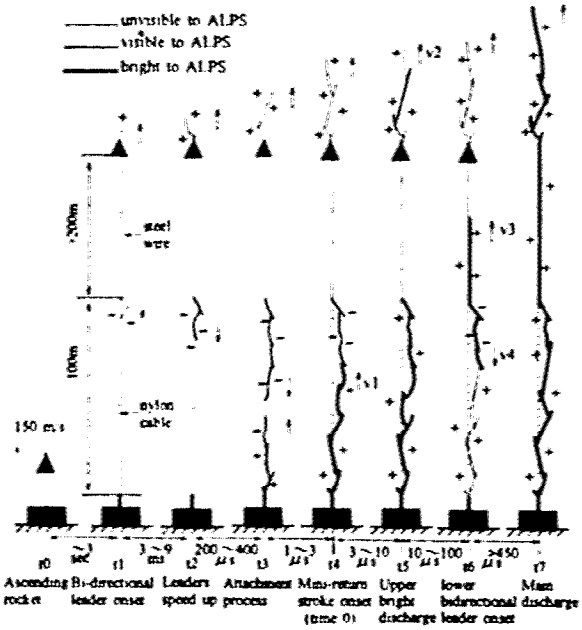


Figure 2. Chronological sequence of events involving in the altitude-triggered lightning flash inferred from electric field measurements and the optical observations by the ALPS.

## REFERENCES


Chen, C. et al., Leader properties and attachment process in positive triggered lightning flashes, J. Atmos. Electr., 19, No.1, 1999.

Lalande, P. et al., Leader properties determined with triggered lightning techniques, JGR, 103, 14109-14115, 1998.

Bondiou-Clergerie A. et al., Experimental and theoretical study of the bi-leader process, Part I: Experimental investigation, Presented on proceeding of 10th ICAE, Osaka, Japan,1996.

# PEAK RADIATION FIELDS OF LIGHTNING RETURN STROKES OVER FINITELY CONDUCTING GROUND

Vernon Cooray
Institute of High Voltage Research
University of Uppsala, Sweden

ABSTRACT: This paper elucidates the propagation effects on the lightning generated electric fields. A simple procedure that can be used to predict the propagation effects is outlined together with its experimental confirmation. This procedure is used to analyse the propagation effects on the radiation fields of negative first return strokes, positive first return strokes and subsequent return strokes in triggered lightning flashes. From the results empirical equations that can be used to correct for the propagation effects are extracted. The results show that the propagation effects may differ in negative and positive return strokes and that the data from triggered lightning flashes should be applied with caution in correcting for the propagation effects of natural lightning flashes.

## INTRODUCTION

As the electromagnetic fields propagate over finitely conducting ground, different frequencies are attenuated by different amounts. As a result, the signatures of broad-band electromagnetic radiation fields generated by lightning flashes change as they propagate over such ground. These effects are known in the scientific literature as propagation effects. The knowledge on propagation effects is important both in characterising the interaction of lightning electromagnetic fields with structures and in the remote sensing of lightning current parameters from the electromagnetic fields.

In this paper we evaluate the propagation effects on the radiation fields of negative first return strokes, positive first return strokes and subsequent return strokes of triggered lightning flashes as they propagate over finitely conducting and homogeneous ground. The results given here are valid for propagation distances less than about 300 km because in deriving these results, the curvature of the earth and the ionospheric effects have been neglected. The results given here replace some of the results obtained previously by Cooray [1987].

## THEORY AND ITS EXPERIMENTAL CONFIRMATION

The radiation field generated by a return stroke, $E_{z,\sigma}(t,D)$, at a distance $D$ over finitely conducting ground is given by [Cooray, 1987]

$$E_{z,\sigma}(t,D)=\int_0^t E_z(t-\tau,D)\,S(0,\tau)\,d\tau \qquad (1)$$

where $E_z(t, D)$ is the radiation field present at the same distance over perfectly conducting ground, $t$ is the time and $S(0,t)$ is given by

$$S(0,t)=\frac{d}{dt}\left\{1-\exp\left(-\frac{t^2}{4\zeta^2}\right)+2\beta(\varepsilon+1)\frac{J(t/2\zeta)}{t}\right\} \qquad (2)$$

where $J(x) = x^2(1-x^2)exp(-x^2)$, $\beta = 1/\mu_o\sigma c^2$, $\zeta^2 = D/2\mu_o\sigma c^3$, $\varepsilon$ is the relative dielectric constant and $\sigma$ is the conductivity of the ground. It is important to point out that in equation 2 the third term inside the bracket takes into account the effects of displacement current in the ground. Calculations done by Cooray [1987] show that, as far as the risetimes and the attenuation of the waveforms are concerned, the contribution from this term is small. Consequently, the propagation effects are mainly governed by the parameter $D/\sigma$ and the results can be normalised against this parameter.

In an attempt to validate the above equation, Cooray et al. [1998] conducted an experiment in Denmark. In the experiment electric fields of lightning return strokes striking the sea were measured simultaneously at two stations; one located at the coast and the other situated 250 km inland. The antenna system used in the measurements could record electromagnetic fields to a resolution better than 5 ns and the total decay time constant of the antenna system was 20 ms; which is much longer than the duration of the electromagnetic fields of interest. The signals coming out

from the antenna system were recorded with 10 ns resolution in a transient recorder working in pre-trigger record mode. The path of propagation of the electromagnetic fields from the strike point to the coastal station was over salt water. Thus, the electric fields measured at this station can be assumed to represent the undistorted electric fields generated by return strokes (i.e. $E_z(t,D)$). During the experiment more than 25 waveforms were measured simultaneously at the two stations. For each waveform measured at the coastal station, the electric field that would be present at inland station was calculated using the equation (1) with $D$ = 250 km and $\sigma$ = 0.01 S/m, the latter being the average conductivity of the path of propagation. The shapes of the calculated and the measured waveforms at the inland station was compared by normalising their amplitudes to unity. In all the cases we found the agreement between the calculation and measurement to be remarkable. One example of this comparison is given in Figure 1. The reader might wonder why we have not compared the exact amplitudes of the measured and calculated waveforms at the distant station. The reason for this is that the amplitude calibration of the inland station was not accurate enough to make a comparison of amplitudes. However, the decrease in amplitude due to propagation is directly connected with the attenuation of the high frequencies which also dictates the shape of the electric field at the distant station. Thus the change in the shape of the radiation fields due to propagation will also uniquely determine the change in the amplitude of the waveform. Thus, a comparison of the shapes alone is sufficient to test the validity of the propagation equation and the results show that the equation (1) can be used to predict the propagation effects to a high degree of accuracy.

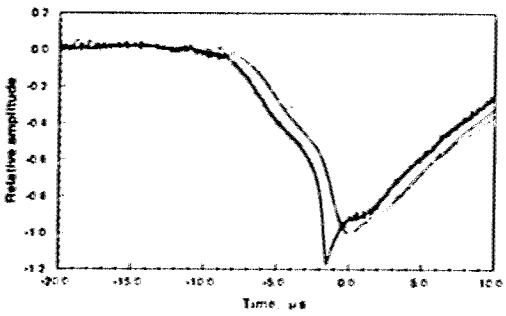


Figure 1. Comparison between theory and experiment. (1) The radiation field measured at the coastal station, (2) the radiation field measured at the inland station (rugged line) and (3) the calculated radiation field at the inland station (smooth line) using equation (1).

## RESULTS

The first step in analysing the propagation effects is to gather a sample of electric radiation fields from return strokes recorded in such a way so that the propagation effects are minimal. This can be done by recording the electromagnetic fields from lightning flashes striking the sea at a coastal station. Both data samples used here to analyse the propagation effects of negative and positive return strokes were recorded in this manner. The data sample of negative return strokes was recorded with a resolution of 0.1 μs by Bailey and Willett [1989] and Izumi and Willett [1991] and the data sample of positive return strokes was recorded with a resolution of 10 ns by Cooray et al. [1998]. The distances to the respective lightning flashes are known in both samples. In analysing the propagation effects, these electric field waveforms were used in equation (1) to calculate the signature of radiation fields at different distances over finitely conducting ground. By comparing these signatures with the original undistorted ones, the effects of propagation were evaluated. As mentioned previously, propagation effects are mainly determined by the ratio $\sigma/D$ where $\sigma$ is the conductivity and $D$ is the distance of propagation. Thus one can normalise the results as a function of $\sigma/D$ which is denoted here by $\gamma$.

In order to make the presentation easier, let us define the coefficient of attenuation, $A$, as $E_p / E_\infty$ where, $E_p$ is the peak of the radiation field corresponding to a certain value of $\gamma$ and $E_\infty$ is the radiation field at the corresponding distance over perfectly conducting ground. With this definition, the quantity $1-A$ gives the amount of attenuation of the radiation field peak due to propagation over finitely conducting ground. The results show that there is a slight tendency for the attenuation of the initial peak, $1-A$, to decrease with increasing initial peak, $E_\infty$, of both negative and positive return strokes. The linear correlation coefficient between the two variables for different values of $\gamma$ lies in the range of -0.58 to -0.6. This observation indicates that the width of the initial peak of the negative and positive radiation fields increases with increasing peak value.

Our calculations show that the average value of the attenuation coefficient, $A$, as a function of $\gamma$ can be represented by the equations

$$A_e = 0.24\exp\left[\frac{-\gamma}{10^7}\right] + 0.24\exp\left[\frac{-\gamma}{50x10^7}\right] + 0.525 \qquad \text{for negative} \qquad (3)$$

$$A_e = 0.134\exp\left[\frac{-\gamma}{1.5x10^7}\right] + 0.312\exp\left[\frac{-\gamma}{55x10^7}\right] + 0.555 \qquad \text{for positive} \qquad (4)$$

It is important to note that these equations are valid for $10^6$ m$^2$/S < $\gamma$ < 2x$10^9$ m$^2$/S, and 5 km< $D$ < 300 km. The reason why $D$ should not be allowed to exceed 300 km is that the equations used to estimate the propagation effects were derived by neglecting the curvature of the earth and this assumption could lead to significant errors for distances larger than about 300 km. We would like to point out that the mean attenuation coefficients at different values of $\gamma$, as given out by the equation (3) are slightly different to the values previously published by Cooray [1987]. The reason for this is the following; in that study the electric fields used as inputs to the equation (1) were recorded by an antenna located 200 - 300m inland from the coast line. The propagation across this strip of land may have caused some distortion of the initial peaks of the radiation fields leading to slightly different results.

The observation that $A$ is a function of $E_\infty$ motivated us to evaluate how $E_\sigma$ vary as a function of $E_\infty$. To achieve this goal, we have calculated how these two parameters are related to each other by fitting a straight line of the form $E_\infty = a\ E_\sigma + b$ for data obtained for different values of $\gamma$. The results obtained can be combined into the following general equation:

$$E_\infty = F_1(\gamma)\ E_\sigma + F_2(\gamma) \qquad (5)$$

where

$$F_1(\gamma) = a_o + a_1 x + a_2 x^2 + a_3 x^3 \qquad (6)$$

$$F_2(\gamma) = b_o + b_1 x + b_2 x^2 + b_3 x^3 \qquad (7)$$

with $x = \log[\gamma/10^7]$. The values of the coefficients are tabulated in Table 1. Again note that the equations are valid for $10^6 < \gamma < 2 \times 10^9$ m$^2$/S. These equations can be used to correct for the attenuation effects if the peak field over finitely conducting ground is known. For example assume that the peak radiation field measured at a distance of $D_X$ over finitely conducting ground of conductivity $\sigma_x$ is $E_x$. Then the value of $\gamma = \frac{D_x}{\sigma_x}$. Let us denote this by $\gamma_x$. The value of the measured electric field normalised to 100 km, $E_{nx}$ is given by $E_{nx} = D_x * E_x / 10^5$. Substitution of $\gamma_x$ and $E_{nx}$ for $\gamma$ and $E_\sigma$ respectively in the above equations will give the value of $E_\infty$ which is the undistorted field normalised to 100 km. The absolute value of the undistorted field can then be obtained by the transformation $E_\infty * 10^5 / D_x$.

The vast amount of lightning direction finders deployed at different geographical locations measure the initial peak of the magnetic field in un-calibrated units sometimes referred to as LLP units. One of the important problems in lightning directing finding is to evaluate the connection between these LLP unites and the return stroke peak current. Thus, the calibration of the direction finders were attempted using the data from triggered lightning flashes (Orville, 1991). As in the case of natural return strokes, the triggered lightning fields also attenuate as they propagate over finitely conducting ground and one cannot assume a priory that the propagation effects are the same for both natural and triggered lightning fields. In any calibration procedure of the sort mentioned above, it is necessary to know how the fields from triggered lightning flashes are attenuated as they propagate over finitely conducting ground. In order to gain some knowledge concerning this point we have evaluated the propagation effects on triggered lightning electric radiation fields using a sample of 28 waveforms measured by Willett et al. [1989] in a

study conducted in Florida. The location of the measuring system used by these authors was such that the path of propagation of the fields were over brackish water except for the last few hundred meters. We consider, these waveforms to represent the undistorted electric fields generated by triggered lightning flashes. Employing equation (1) as before we have studied the propagation effects on these waveforms. As in the case of natural lightning, we observed that $1-A$ decreases with increasing peak value. The average value of $A$ as a function of $\gamma$ for triggered return strokes are shown together with the corresponding values for natural return strokes in Figure 2. Note that the attenuation of triggered lightning fields is more pronounced than that of the natural return strokes. This shows that the results pertinent to the attenuation of electric fields extracted from triggered lightning flashes should be applied with caution in correcting for the propagation effects of natural return strokes.

TABLE 1. Values of coefficients of equations 6 and 7

| | Negative return strokes | Positive return strokes |
|---|---|---|
| $a_0$ | 1.039 | 1.014 |
| $a_1$ | $1.375\times10^{-2}$ | $7.619\times10^{-3}$ |
| $a_2$ | $1.909\times10^{-3}$ | $4.894\times10^{-3}$ |
| $a_3$ | $8.056\times10^{-4}$ | $1.952\times10^{-3}$ |
| $b_0$ | $9.275\times10^{-1}$ | $7.906\times10^{-1}$ |
| $b_1$ | $3.258\times10^{-1}$ | $2.848\times10^{-1}$ |
| $b_2$ | $1.621\times10^{-2}$ | $1.553\times10^{-2}$ |
| $b_3$ | $-3.953\times10^{-3}$ | $-3.44\times10^{-3}$ |

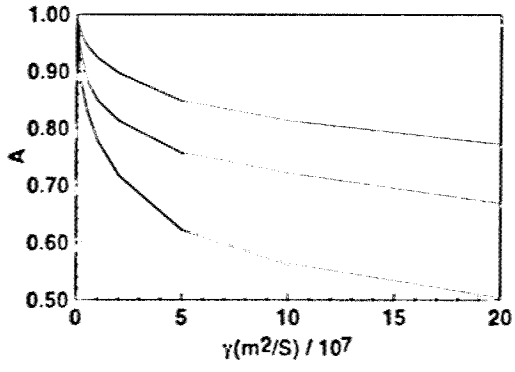


Figure 2. The mean value of the attenuation oefficient, $A$, as a function of $\gamma$. (1) Positive return strokes. (2) Negative return strokes. (3) Triggered return strokes. Note that $A = c\,E_r / E_\infty$ where, $E_r$ is the peak of the radiation field corresponding to a certain value of $\gamma$ and $E_\infty$ is the radiation field at the corresponding distance over perfectly conducting ground. $\gamma = D/\sigma$.

ACKNOWLEDGEMENTS: Author thanks John Willett for providing the records of electric fields used in the analysis.

REFERENCES

Bailey, J. C. and J. C. Willett, Catalog of absolutely calibrated, range normalised, wideband, electric field waveforms from located lightning flashes in Florida, NRL memorandum Report 6497, Naval Research Laboratory, Washington, DC, USA, 1989.

Cooray, V., Effects of propagation on the return stroke radiation fields, Radio Sci., vol. 22, 757-768, 1987.

Cooray, V., M. Fernando, V. Scuka, T. Sorenssen, A. Pedersen, The fine structure of positive return stroke radiation fields - A collaborative study between researchers from Sweden and Denmark, Proceedings of the International Conference on Lightning Protection, Birmingham, England, 1998.

Izumi, Y. And J. C. Willett, Catalog of absolutely calibrated, range normalised, wideband, electric field waveforms from located lightning flashes in Florida: Vol II: 8 and 10 August 1985 data, Phillips Laboratory, Hanscom AFB, Massachusetts, 1991.

Orville, R. E., Calibration of a magnetic direction finding network using measured triggered lightning return stroke peak currents, J. Geophys. Res., 96, pp. 17135 – 17142, 1991.

Willett, J. C., J. C. Bailey, V. P. Idone, R. E. Orville, A. Eybert-Berard, L. Barret and E. P. Krider, Submicrosecond intercomparison of radiation fields and currents in triggered lightning return strokes based on the transmission line model, J. Geophys. Res., vol. 94, 13275 - 13286, 1989.

# RETURN-STROKE CURRENT MODELING OF LIGHTNING STRIKING A TALL TOWER ACCOUNTING FOR REFLECTIONS WITHIN THE GROWING CHANNEL AND FOR UPWARD-CONNECTING DISCHARGES

V. Shostak[1], W. Janischewskyj[2], A.M. Hussein[2], J.-S. Chang[3], and B. Kordi[2*]

[1] Department of High Voltage Engineering and Electrophysics, Kyiv Polytechnical Institute, Kyiv, Ukraine
[2] Department of Electrical and Computer Engineering, University of Toronto, Toronto, Ontario, Canada
[3] Department of Engineering Physics, McMaster University, Hamilton, Ontario, Canada

ABSTRACT Results of return stroke (RS) current simulation in case of lightning strikes to a tall tower are presented. Calculations are performed on the basis of the new extended version of the modified transmission line (MTL) model which takes into account: (1) reflections that occur within the continuously growing RS channel, and (2) the situation of RS channel initiation above the top of the tower (when an upward-connecting discharge is present). The results of modeling are compared to those obtained using the previously developed MTL model for strikes to elevated objects, and to experimental observations made at the 553-m tall CN Tower in Toronto.

## 1. INTRODUCTION

In recent studies of electromagnetic radiation emanating from a lightning strike to an elevated strike object (ESO), efforts have been concentrated upon close modeling of current in the lightning path during the return stroke (RS) phase [*Diendorfer, 1991; Thottappillil et al., 1991; Rachidi et al., 1992; Beierl, 1992; Motoyama et al., 1996; Guerrieri et al., 1996; Rusan et al., 1996; Janischewskyj et al., 1996*]. Developed models took into account reflections of the RS current pulse within the ESO but did not consider reflections from the front of the advancing RS stroke channel nor the possibility of the existence of an upward-connecting discharge. Since some significant details of RS current waveforms were not reproduced, perhaps, it was one of the reasons why the use of these current models in field simulation resulted in a noticeable discrepancy with observations [*Zundl, 1994; Motoyama et al., 1996; Guerrieri et al., 1996; Rachidi et al., 1998*]. Also, while the need to account for the presence of an upward-connecting discharge has been raised [*Leitenturier et al., 1990; Guerrieri et al., 1996; Janischewskyj et al., 1998; Rachidi et al., 1998*], the problem remains unsolved.

In their latest work, *Janischewskyj et al.* [1998] have initiated an extension of the existing modified transmission line (MTL) model by taking current reflections within the lightning return stroke (RS) channel into account. Their eventual plan has been to fully model the complete RS current path, including the channel and also the ESO with its internal discontinuities. In the present simulation, however, within the ESO only the reflections at its bottom and top are considered.

The goal of the present work is to further extend the approach, initiated in [*Janischewskyj et al.*, 1998], to the more general case which includes the existence of an upward-connecting discharge. All calculations and observations are related to the specific ESO, the 553-m CN Tower. In the paper, measured current waves are compared to those computed by the use of the conventional MTL model for the ESO and also to the results of computations performed by the proposed Extended Modified Transmission Line (EMTL) model.

## 2. EXPERIMENTAL RECORDS OF CURRENT

The experimental setup on the CN Tower is described in [*Hussein et al., 1995*]. In 1997 a second Rogowski Coil was added. The Second Rogowski Coil (SRC) fully surrounds the steel structure of the CN Tower, rather than only one fifth of the structure as is the case with the First Rogowski Coil (FRC), and is located at the 509m level, 35m above the FRC. Both coils are connected to a 10-bit, 10-ns digitizer. The connection uses an optical fiber link, rather than a triax cable as is the case for the FRC. For that reason the SRC records have a much better signal-to-noise ratio than those of the FRC.

Examples of typical RS current waveforms for two events are presented in Figs. 1 and 2. Both flashes are negative but the waveforms, for convenience, are shown with inverted polarity. A rather complex shape of current waveforms is observed. The presence of reflections from all discontinuities within the lightning current path (CN Tower and RS channel) may be detected, especially for cases of strokes with steep wavefronts (subsequent strokes). In order to facilitate the comparison between the outputs of the two coils, the waveforms in Figs. 1b and 2b are plotted in relative units with the first main peaks taken as the bases. The influence of different coil locations and the much reduced level of noise in SRC records cannot be missed.

---

* B. Kordi is on leave from The Electrical Engineering Department of Amirkabir University, Tehran, Iran.

## 3. RESULTS OF CURRENT SIMULATION USING THE EXISTING MTL MODEL

Time variation of the RS current and its spatial distribution are first computed on the basis of the existing MTL model [*Guerrieri et al., 1996, Rusan et al., 1996, Rachidi et al., 1998*]. Results are presented in Figs. 3a,b and 3c,d for the current in the tower and in the RS channel, respectively. Waveforms are presented in relative units using the injected current peak at the tower's top as the basis and the parameter $z$ is used to denote the observation point above ground.

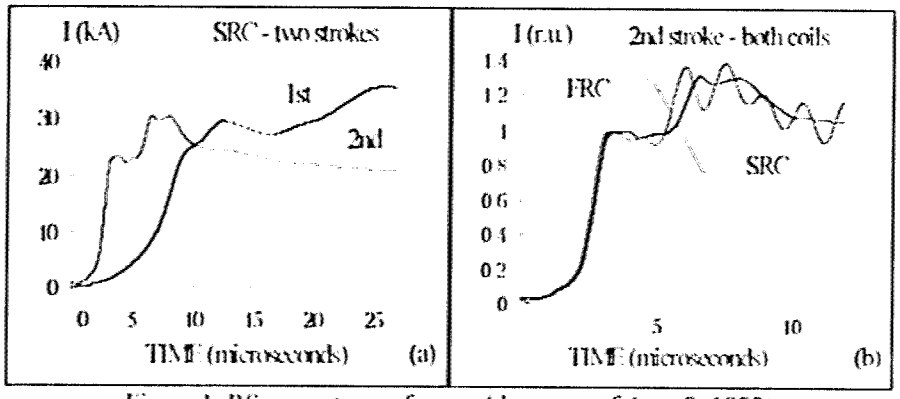


Figure 1. RS current waveforms (the event of Aug. 9, 1998)

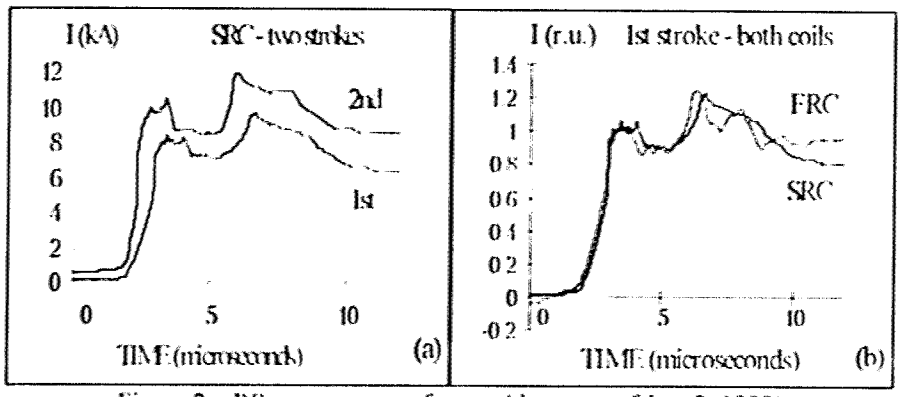


Figure 2. RS current waveforms (the event of Jan. 2, 1999)

The tower is represented as an ideal single-section transmission line, and the model accounts only for reflections at its bottom and its top. The reflection coefficients and the attenuation factor $\lambda_1$ are described in section 4. Two current pulses, one moving downwards through the tower and the other moving upwards along the channel, are simulated using one of the known double exponential approximations [*Kravtchenko*, 1991]:

$$I_0(t) = \frac{I_1}{\eta_1}[\exp(-a_1 T(t)) - \exp(-a_2 (T(t))^2)] \qquad (1)$$

where: $I_1$ is the current peak, t is the time, $T(t) = a_1 / a_2 + t$, $\eta_1$=0.973, $a_1$=0.005·$10^6$ $s^{-1}$, $a_2$ = (0.3064 or 10.64)·$10^6$ $s^{-2}$ (which correspond to front time of about 3 or 0.55 μs, respectively).

Comparison with experimental observations indicates that the MTL model does reproduce the ground reflection (the major second peak), however, a closer scrutiny of Figs. 2a and 3b reveals absence of an important "depression", between first and second peak, in the calculated wave. This points to a need of looking for a better approach to RS current simulation.

## 4. EXTENSIONS OF THE MTL RETURN STROKE CURRENT MODEL

In the proposed new EMTL model the following factors are taken into account: (1) the reflections of RS current pulses that take place within the continuously growing RS channel, (2) the possibility of RS initiation above the tower's top in the presence of an upward-connecting discharge, and (3) the attenuation of reflected current pulses within the channel.

From the point of RS initiation, where the downward- and upward-directed leaders meet each other, two RS fronts are moving in opposite directions with the speeds of $v_u$ (upward) and $v_d$ (downward). The last one, after reaching the tower's top, is partially reflected (with the reflection coefficient $\rho_{cb}$) and partially penetrates into the tower, where it continues to move with the speed of light $c$. After reaching the ground the pulse is reflected ($\rho_g$) and returns to the tower's top. Here it is partially reflected ($\rho_{tt} = -\rho_{cb}$) and partially penetrates into the channel. (It is assumed that the pulses reflected from the channel's front and tower's extremities are moving within the tower and the channel with the speed of light). After reaching the RS front, at the channel's top, the pulses are reflected ($\rho_{ct}$) and come back to the tower, etc. The model takes into account the possibility of an exponential attenuation: (a) of the initial RS current pulse during its upward propagation (with the decay factor $\lambda_1$ [*Rachidi et al.*, 1992]), and (b) of all other pulses during their propagation within the existing RS channel (with a decay factor $\lambda_2$).

The results of simulation (in relative units based on the injected current at the tower's top) are presented in Figs. 4 and 5, within the tower and the channel, respectively. Note, that the initial pulse within the channel is smaller than the injected current. The values of the RS front velocities, of the reflection coefficients, of the upward-connecting leader length $L_O$ , and of the attenuation factors are derived from [*Rachidi et al.*, 1992] ($\lambda_1$) and from previous experimental observations at the CN Tower [*Wang et al.*, 1995; *Janischewskyj et al.*, 1996, 1998]: $v_d$=0.30c; $v_u$=0.15c; $\rho_{tt}$ = –0.365, $\rho_{tb}$ = 0.395, $\rho_{ct}$ = –0.5 and –0.9; $L_O$=90m; $\lambda_1$=2000m; $\lambda_2$= 3000m. Additional parameters are listed in Figs. 4 and 5. In calculations, the heights of the CN Tower, of the SRC and FRC levels are taken, correspondingly: h=555m, $h_{SRC}$=510m, $h_{FRC}$=475m.

The main features of the waveforms obtained with the use of the EMTL model show a good agreement with recorded waveforms. In particular, the "depression" seen in Fig. 2a is quite faithfully reproduced in Fig. 4b. Furthermore, the influence of the reflection factor at the RS front ($\rho_{ct}$) is clearly visible by comparison with Figs. 4b,c. Current waveforms existing at different levels of the complete RS current path may be followed in Figs. 4d and 5b. It is expected that small spikes in measurement records that are not reproduced by calculations, may be caused by reflections from intermediate discontinuities in the Tower.

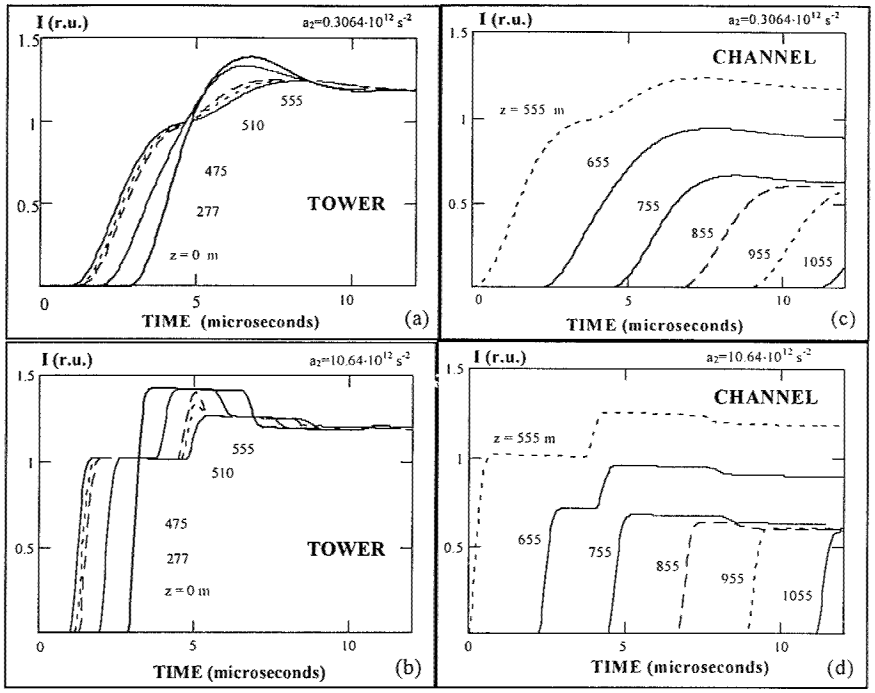


Figure 3. RS current distribution neglecting reflections within the channel, using the MTL model: $v_u$=0.15c, $\lambda_1$=2000 m; z - height

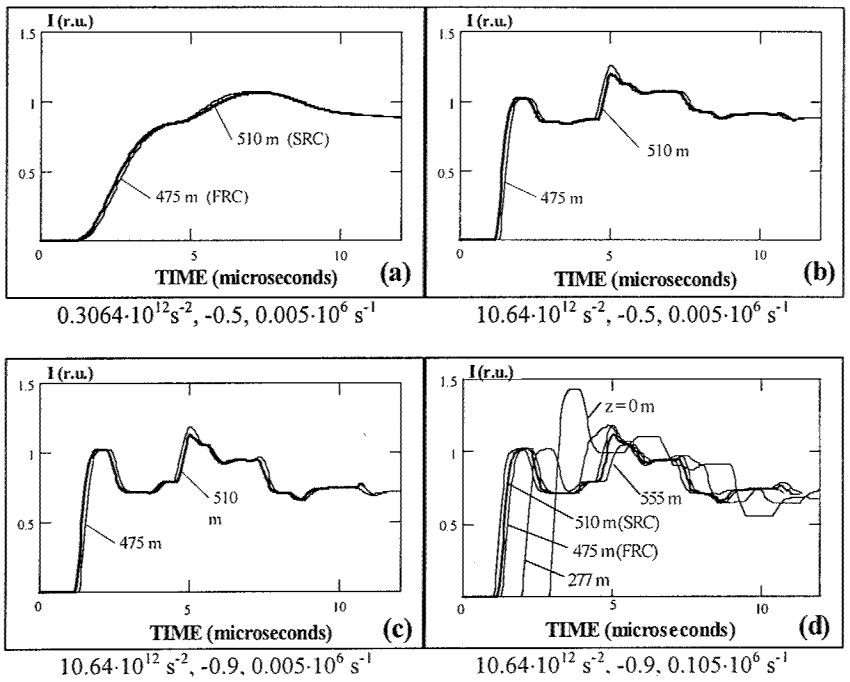


Figure 4. RS current within the Tower according to the EMTL model: $L_0$=90m, $v_d$=0.30c, $v_u$= 0.15c, $\lambda_1$=2000m, $\lambda_2$=3000m; numbers below each plot mean: $a_2$, $\rho_{ct}$, $a_1$

## 5. CONCLUSIONS

The results of return stroke (RS) current simulation obtained using the proposed Extended Modified Transmission Line (EMTL) model display significant additional features that are not reproduced by previously developed models, and provide a better agreement with the observed data. Consequently, the new model is recommended for the determination of the RS current waveshape: (a) with multiple reflections of current pulses both within the elevated strike object (ESO) and within the growing RS channel, and (b) with the possible presence of an upward-connecting discharge. So determined current waveshapes may be applied: (1) to retrieve the signature of the current pulse injected at the ESO's top, and (2) to compute the electromagnetic field surrounding the ESO.

For further improvements of simulation it may be suggested to use: (a) a more sophisticated model of the ESO's structure (for example, see corresponding approaches in [*Rusan et al.*, 1996]), (b) more accurate values of reflection coefficients [*Janischewskyj et al.*1996], and (c) time variation dependencies of RS front velocities [*Thottappillil et al.*, 1991; *Rachidi et al.*, *1992*].

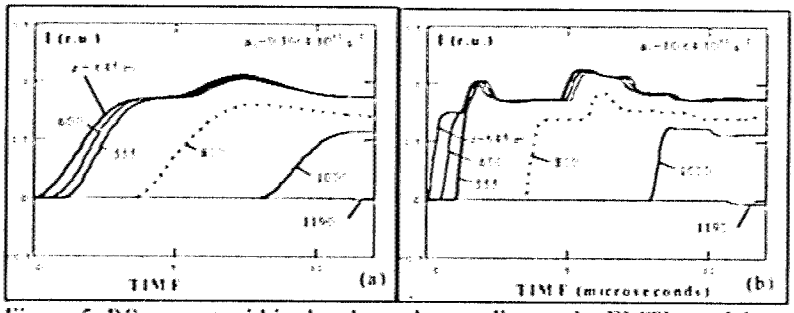


Figure 5. RS current within the channel according to the EMTL model: $L_0$=90m, $v_d$=0.30c, $v_u$=0.15c; $\rho_{ct}$=-0.5, $\lambda_1$=2000m, $\lambda_2$=3000m; $a_1$=0.005·$10^6$ $s^{-1}$

## REFERENCES


Beierl, O., Front shape parameters of negative subsequent strokes measured at the Peissenberg Tower, *Proc 21st Int Conf on Lightning Protection (ICLP'92), Paper 1.04*, 19-24, Berlin, Germany, Sept. 21-25, 1992.

Diendorfer, G., Effect of an elevated strike object on the lightning electromagnetic fields, *Proc of the Int Symp on Electromagnetic Compatibility (EMC'91)*, 235-238, Zurich, March 1991.

Guerrieri, S., F. Heidler, C.A. Nucci, F. Rachidi, M. Rubinshtein, Extension of two return stroke models to consider the influence of elevated strike objects on the lightning return stroke current and the radiated electric field: comparison with experimental results, *Proc Int Conf Electromagnetic Compatibility (Rome EMC'96)*, Rome, 1996.

Hussein, A.M., W. Janischewskyj, J.-S. Chang, V. Shostak, W.A. Chisholm, P. Dzurevich, and Z.-I. Kawasaki, Simultaneous measurement of lightning parameters for strokes to the Toronto Canadian National Tower, *JGR-Atmosphere*, 100, 5, 8853-8861, May 1995.

Janischewskyj, W., V. Shostak, J. Barratt, and A.M. Hussein, Collection and use of lightning return stroke parameters taking into account characteristics of the struck object, *Proc 23rd Int Conf on Lightning Protection (ICLP'96)*, Florence, Italy, Sept. 23-27, 1996.

Janischewskyj, W., V. Shostak, and A.M. Hussein, Comparison of lightning electromagnetic field characteristics of first and subsequent return strokes to a tall tower: 1. Magnetic Field, *Proc 24th Int Conf on Lightning Protection (ICLP'98)*, Birmingham, United Kingdom, Sept. 14-18, 1998.

Kravtchenko, V.I., Lightning protection of radio electronic devices (in Russian), Radio and Communications Pub. Co., Moscow, 264 p., 1991.

Motoyama, H., W. Janischewskyj, A.M. Hussein, R. Rusan, W.A. Chisholm, and J.-S. Chang, Electromagnetic field radiation model for lightning strokes to tall structures, *IEEE Trans on Power Delivery*, 11, 1624-1632, 1996.

Leteinturier, C., C. Weidman, and J. Hamelin, Current and electric field derivatives in triggered lightning return strokes, *J Geophys Res.*, 95, D1, 811-828, 1990.

Rachidi, F., M. Ianoz, C.A. Nucci, C. Mazzetti, Modified transmission line model for LEMP calculations. Effect of the return stroke velocity decreasing and elevated strike objects in close fields, *Proc of the Int Conf on Atmospheric Electricity (ICAE'92)*, 664-667, St. Petersburg, Russia, June 1992.

Rachidi, F., W. Janischewskyj, A.M. Hussein, C.A. Nucci, S. Guerrieri, and J.-S. Chang, Electromagnetic fields radiated by lightning return strokes to high towers, *Proc 24th Int Conf on Lightning Protection (ICLP'98)*, Birmingham, United Kingdom, Sept. 14-18, 1998.

Rusan, R., W. Janischewskyj, A.M. Hussein, and J.-S. Chang, Comparison of measured and computed electromagnetic fields radiated from lightning strokes to the Toronto CN Tower, *Proc 23rd Int Conf on Lightning Protection (ICLP'96)*, Florence, Italy, Sept. 23-27, 1996.

Thottappillil, R., D.K. McLain, M.A. Uman, and G. Diendorfer, Extension of the Diendorfer-Uman lightning return stroke model to the case of a variable upward return speed and a variable downward discharge current speed, *J Geophys Res*, 96, 17143-17150, 1991.

Wang, D., Z.-I. Kawasaki, K. Yamamoto, K. Matsura, J.-S. Chang, and W. Janischewskyj, Luminous propagation of lightning attachment to the CN Tower, *JGR-Atmosphere*, 100, 6, 11661-11667, June 1995.

Zundl, Th., Lightning current and the LEMP calculations compared to measurements gained at the Peissenberg Tower, *Proc 22nd Int Conf Lightning Protection (ICLP'94), R1c-08*, 1-6, Budapest, Hungary, Sept. 1994.

MAGNETIC FIELD OF A BRANCHING DISCHARGE

V.V.Borisov[1] and A.B.Utkin[2]

[1] Research Institute of Physics, St.Petersburg University, St.Petersburg, Russia
[2] Institute for Laser Physics, Sci. Center "S.I.Vavilov State Optic Institute", St.Petersburg, Russia

ABSTRACT: We consider space-time representation to the magnetic field produced by a right-angle branching discharge. Current pulse starts and propagates to the T-branching point. Then one discharge segment carries a part of the initial current in the original direction to the first (cloud) terminal point. The rest of the current pulse propagates in the vertical direction to the other (ground) terminal point. This scheme can serve as a rough model of complicated cloud-to-cloud discharge that partially branches to the ground. The report was stimulated by observation of corresponding natural phenomenon in July 1996 at the Ladoga Lake.

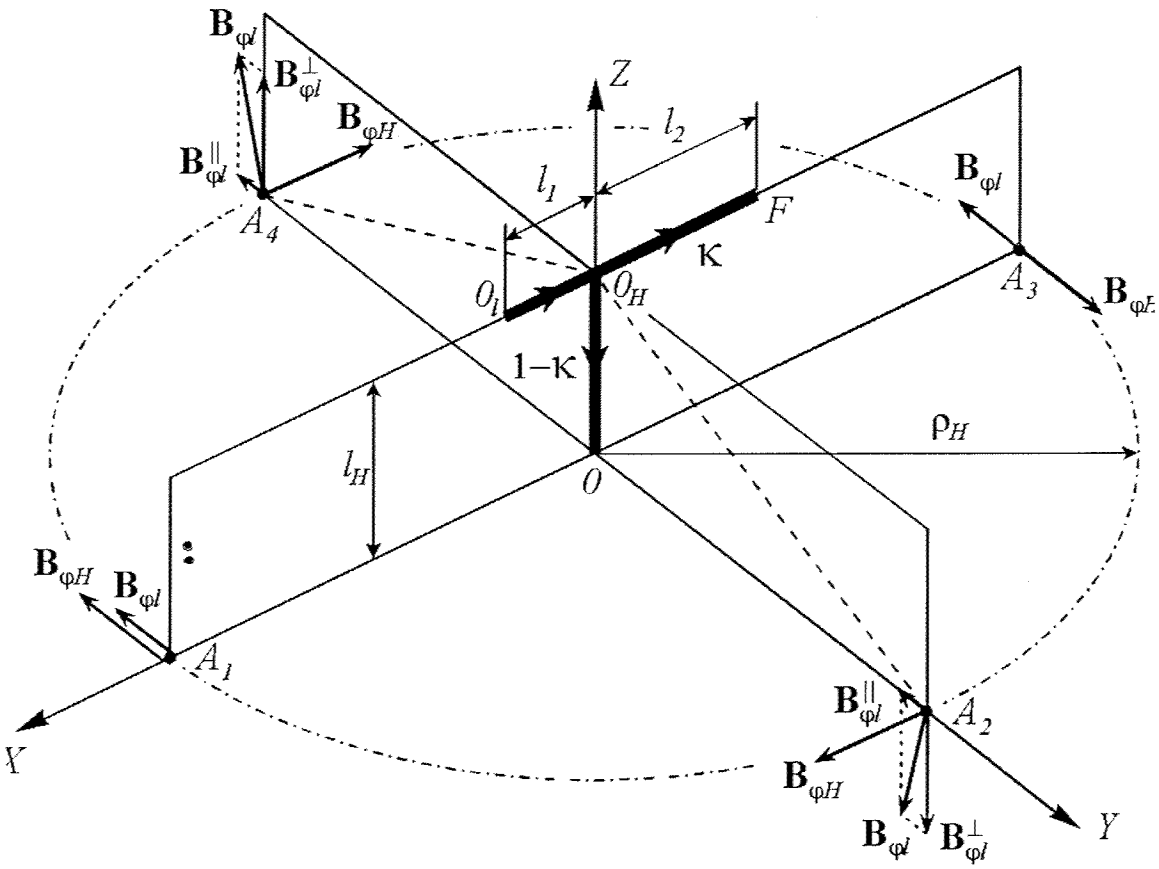


**Figure 1.** Structure of the discharge and field components.

The discharge structure is shown in Figure 1. The current pulse starts at the point $O_l$ and propagates to the T-junction point $O_H$ at which it branches. One segment carries the part $\kappa$ of the initial current to the terminal point $F$. The rest of the current $1-\kappa$ is directed at a right angle to the terminal point $O$. According to the superposition principle, the total field produced by a discharge of this shape is a sum of three partial fields of radiating segments $O_lO_H$, $O_HF$, and $O_HO$. To find these fields we consider some segment $z\in[0, l]$ carrying current density

$$\mathbf{j} = j\mathbf{e}_z, \quad j = \frac{1}{2\pi}\frac{\delta(\rho)}{\rho} h(\tau)h(z)h(l-z)h(\beta\tau - z)h\big(z-\beta(\tau-T)\big)I(z,\tau) \tag{1}$$

which is a pulse of duration $T$ starting at the point $z=0$ at the moment $\tau=0$ ($\tau=ct$ is the time variable measured in the units of length, $c$ is the velocity of light) and propagating along the $z$ axes to the terminal point $z=l$ with the velocity $c\beta$. The term $I(z, \tau)$ is the continuous part of the current. We use the cylindric coordinate system $\rho$, $\varphi$, $z$. As it is shown in [*Borisov and Utkin*, 1995], the magnetic induction $\boldsymbol{B} = B_\varphi(z, \rho, \tau, l)\,\boldsymbol{e}_\varphi$ can be found with the help of the Bromwich-Borgnis potential $u$ as

$$
\begin{aligned}
&B_\varphi(z,\rho,\tau,l) = 0 \qquad \text{for} \quad \tau < r \quad \text{and} \quad \tau > T + \frac{l}{\beta} + r_l \\
&B_\varphi(z,\rho,\tau,l) = -\frac{\partial}{\partial\rho}\left(\frac{\partial u}{\partial\tau}(z,\rho,\tau,l)\right) \quad \text{for} \quad r < \tau < T + \frac{l}{\beta} + r_l, \\
&\frac{\partial u}{\partial\tau}(z,\rho,\tau,l) = \frac{1}{c}\int_{\Phi_1(z,\rho,\tau,l)}^{\Phi_2(z,\rho,\tau,l)} dz' \frac{1}{\sqrt{\rho^2 + (z-z')^2}} I\left(z', \tau - \sqrt{\rho^2 + (z-z')^2}\right)
\end{aligned}
\tag{2}
$$

The integral limits for different interrelations between $z$, $\rho$, and $\tau$ are given in the table below:

| Condition | $\Phi_1$ | $\Phi_2$ |
|---|---|---|
| $r < \tau < \min\left(T + r, \frac{l}{\beta} + r_l\right)$ | $0$ | $\frac{\beta}{\sqrt{1-\beta^2}}(\tau_\beta - r_\beta)$ |
| $T + r < \tau < \frac{l}{\beta} + r_l$ | $\frac{\beta}{\sqrt{1-\beta^2}}(\tau_l - r_l)$ | $\frac{\beta}{\sqrt{1-\beta^2}}(\tau_\beta - r_\beta)$ |
| $\frac{l}{\beta} + r_l < \tau < T + r$ | $0$ | $l$ |
| $\max\left(T + r, \frac{l}{\beta} + r_l\right) < \tau < T + \frac{l}{\beta} + r_l$ | $\frac{\beta}{\sqrt{1-\beta^2}}(\tau_l - r_l)$ | $l$ |

Here we use the Gaussian units, $r = \sqrt{\rho^2 + z^2}$, $z_\beta = \frac{z - \beta\tau}{\sqrt{1-\beta^2}}$, $r_\beta = \sqrt{\rho^2 + z_\beta^2}$, $\tau_\beta = \frac{\tau - \beta z}{\sqrt{1-\beta^2}}$,

$$
z_l = \frac{z - \beta(\tau - T)}{\sqrt{1-\beta^2}}, \quad r_l = \sqrt{\rho^2 + z_l^2}, \quad \tau_l = \frac{\tau - T - \beta z}{\sqrt{1-\beta^2}}, \quad z_l = z - l, \text{ and } \quad r_l = \sqrt{\rho^2 + z_l^2}.
$$

Let us investigate the magnetic induction in four equidistant observation points $A_1$-$A_4$ located as shown in Figure 1 at the distance $\rho_H$ from the terminal point $O$ on the plane perpendicular to $O_H O$. It can be found geometrically that the induction components in the Cartesian coordinates $XYZ$ of Figure 1 may be expressed via general function $B_\varphi(z, \rho, \tau, l)$ of equation (2) as follows:

$$
\begin{aligned}
&B_{\varphi,1}(A_1) = -B_\varphi(-\rho_H + l_1, l_H, \tau, l_1) - \kappa B_\varphi(-\rho_H, l_H, \tau - l_1/\beta, l_2) - (1-\kappa) B_\varphi(-\rho_H, l_H, \tau - l_1/\beta, l_H) \\
&B_{\varphi,1}(A_2) = (1-\kappa) B_\varphi(-\rho_H, l_H, \tau - l_1/\beta, l_H) \\
&B_{\varphi,2}(A_2) = -\frac{l_H}{\sqrt{\rho_H^2 + l_H^2}}\left(B_\varphi(l_1, \sqrt{\rho_H^2 + l_H^2}, \tau, l_1) + \kappa B_\varphi(0, \sqrt{\rho_H^2 + l_H^2}, \tau - l_1/\beta, l_2)\right) \\
&B_{\varphi,3}(A_2) = -\frac{\rho_H}{\sqrt{\rho_H^2 + l_H^2}}\left(B_\varphi(l_1, \sqrt{\rho_H^2 + l_H^2}, \tau, l_1) + \kappa B_\varphi(0, \sqrt{\rho_H^2 + l_H^2}, \tau - l_1/\beta, l_2)\right) \\
&B_{\varphi,1}(A_3) = -B_\varphi(-\rho_H + l_1, l_H, \tau, l_1) - \kappa B_\varphi(-\rho_H, l_H, \tau - l_1/\beta, l_2) + (1-\kappa) B_\varphi(-\rho_H, l_H, \tau - l_1/\beta, l_H) \\
&B_{\varphi,1}(A_4) = B_{\varphi,2}(A_4) = B_{\varphi,3}(A_3) = B_{\varphi,3}(A_3) = 0 \\
&B_{\varphi,1}(A_4) = -B_{\varphi,1}(A_2), \quad B_{\varphi,2}(A_4) = B_{\varphi,2}(A_2), \quad B_{\varphi,3}(A_4) = -B_{\varphi,3}(A_2)
\end{aligned}
\tag{3}
$$

Time dependencies of the magnetic induction components for the case of $l_1=5$ *km*, $l_2=15$ *km*, $l_H=5$ *km*, $T=30$ *km*, $\beta=0.8$, three values of the branching current share $\kappa=0.25$, $0.75$, and $1$ (pure cloud-to-cloud discharge), and two distances of the observation point $\rho_H=15$ *km* and $50$ *km* are shown in Figure 2. $B_\varphi$ is represented on the plots by the dimensionless parameter $B=c\rho_H B_\varphi$. For the sake of simplicity we take the triangle current pulse $I(z,\tau)=1-\frac{1}{\beta T}(\beta\tau - z)$ that allow analytical representation of the field [*Borisov and Kononov*, 1996]. However, one can use relations (2) and (3) for the current pulse of arbitrary shape.

The results obtained for the magnetic field in free space can be readily extended to another limiting case: ideally conducting earth's surface. Here the normal component is zero while the tangential components are increased two-fold

$$B_{\varphi z}\to 0,\ B_{\varphi x}\to 2B_{\varphi x},\ B_{\varphi y}\to 2B_{\varphi y}.$$

Generalization of the discussed scheme to the case of several branches and arbitrary location of the observation point $A$ is also possible. However, it results in much more complicated expressions. It should be noted that the horizontal part of the branching current can be represented as a sum of the pulse $\kappa I(z,\tau)$ propagating along the path $l_0= l_1+l_2$ and the pulse $(1-\kappa)I(z,\tau)$ propagating along $l_1$. Total induction due to the horizontal current can be obtained with the help of function

$$\frac{\partial u}{\partial \tau}=\frac{\kappa}{c}\int_{\Phi_1(z,\rho,\tau,l_0)}^{\Phi_2(z,\rho,\tau,l_0)} dz'\frac{1}{\sqrt{\rho^2+(z-z')^2}}I\left(z',\tau-\sqrt{\rho^2+(z-z')^2}\right)$$
$$+\frac{1-\kappa}{c}\int_{\Phi_1(z,\rho,\tau,l_1)}^{\Phi_2(z,\rho,\tau,l_1)} dz'\frac{1}{\sqrt{\rho^2+(z-z')^2}}I\left(z',\tau-\sqrt{\rho^2+(z-z')^2}\right)$$

which is easier to extend to the case of several branches than the ordinary relation resulting from consideration of pulses $I(z,\tau)$ and $\kappa I(z,\tau-l_1/\beta)$ propagating along the segments $l_1$ and $l_2$.

Note that calculation of the magnetic induction component allows defining the electric strength component of the discharge field in the far zone.

REFERENCES

Borisov, V.V., and I.I. Kononov, Variations of lightning waveforms being conditioned by lightning channel geometry, *Proc. of 23-rd Int. Conf. on Lightning Protection*, 1, 374, 1996.

Borisov, V.V., and A.B. Utkin, Transient field produced by a moving pulse of line current, *J. Phys. D*, 28, 614--622, 1995.

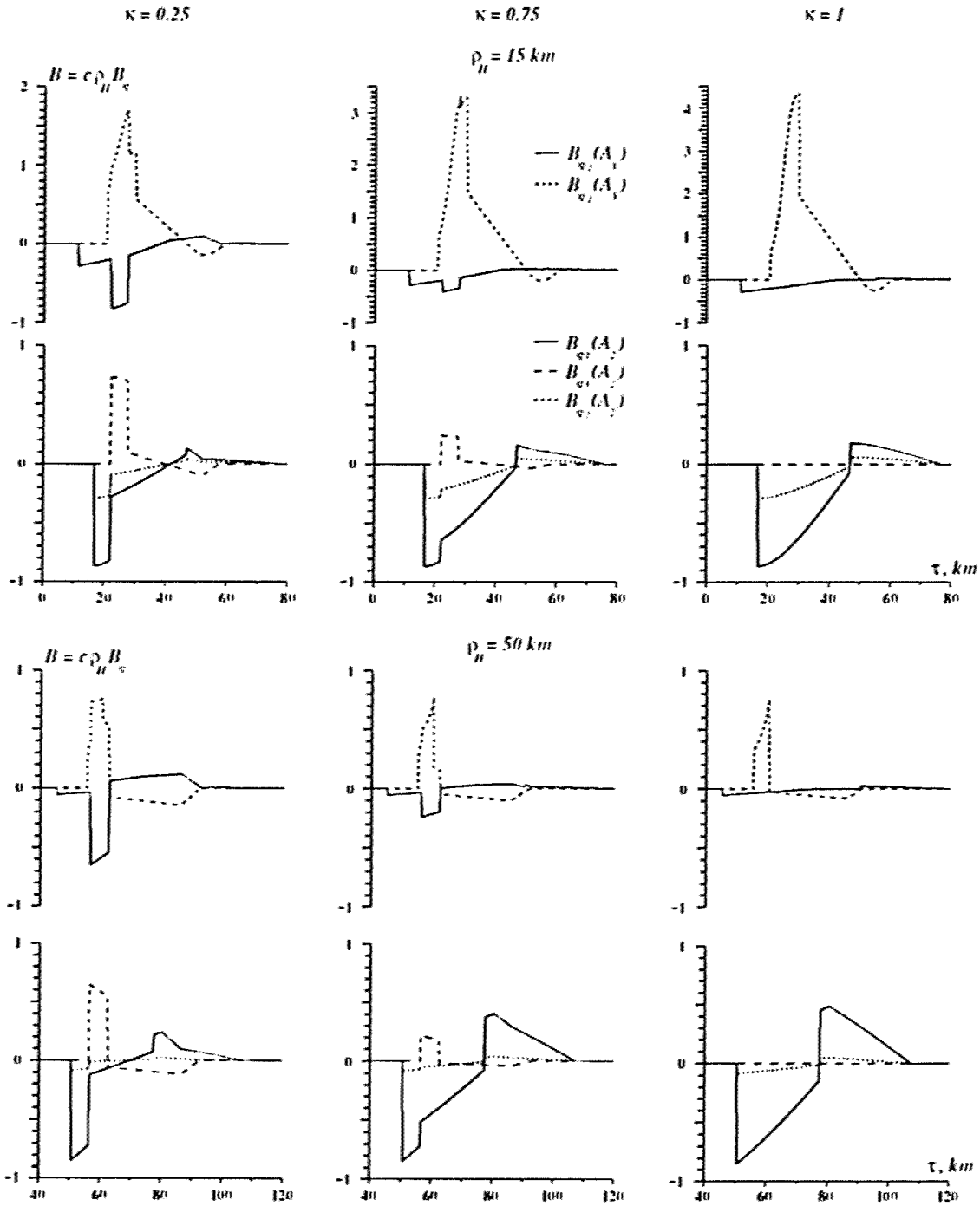


**Figure 2.** Calculated lightning magnetic induction components illustrating variation of the waveforms for different observation points and values of the branching parameter $\kappa$ ; $l_1$=5 km, $l_2$=15 km, $l_H$=5 km, $T$=30 km, and $\beta$=0.8.

# THIN STRUCTURE OF ATMOSPHERICS

Y. A. Krasnitsky

Aviation University of Riga, Riga, Latvia

ABSTRACT. A convolutional model has been developed for spherics waveform radiated from a lightning channel. Any spherics is supposed to be a result of convolution of the channel base current with channel radiation pulse function (CRPF) mapping channel structural inhomogeneities into the spherics. The relations of the CRPF with essential types of channel inhomogeneities are considered. Estimation of CPRF from real spherics data by digital processing methods are briefly described.

## 1. INTRODUCTION

Matematically, the spherics waveform

$$e(t) = L\,[i(0,t)] \tag{1}$$

generated by the lightning channel is the result of action of the operator $L$ on the base current pulse $i(0,t) = i(z,t)\,|_{z=0}$. Value $z$ is the length reading along the channel filament. Thus, $L$ contains all information about structural features of the channel. Both modeling of channel radiation (or direct problem) and finding of channel characteristics from the spherics waveform (or inverse problem) demands the knowledge of $L$ or its evaluation based on experimental data.

Solutions of these problems should minimize a discrepancy among modeled and observed spherics. However, well-known models of the channel radiation recently reviewed by *Rakov* [1997] ignore any inhomogeneities of a channel structure. Thereby, the direct problem solutions create oversmoothened waveforms and do not predict the fast waveform variations which are inherent in any real spherics record. More realistic models should include effects of inhomogeneities. Some from them have been considered at least qualitatively (see, e. g., *LeVine and Meneghini* [1978]), but complete analysis of relations of channel structure with radiation field has not been yet performed.

This paper consists of two parts. At first, convolutional form of Eq.(1) is discussed. In place of $L$ the channel radiation pulse function (CRPF) is introduced for mapping of inhomogeneities into the spherics. Features of CRPF are examined using the scattering matrix approach. Then the inverse problem of evaluating of CRPF from real spherics data is considered. Examples of extracting of CRPF based on Fourier transformation as well as on linear prediction methods are presented.

## 2. STRUCTURE OF CHANNEL RADIATION PULSE FUNCTION

Ignoring any nonlinearities that perhaps are feasible in the course of generation of spherics one can consider (1) as the convolutional equation. In shorthand form

$$e(t) = i(0,t) * h_c(t) * h_t(t) \tag{2}$$

where $h_c(t)$ is CRPF [*Krasnitsky,* 1994], $h_t(t)$ is a trace pulse function. Asterisks are the symbols of convolution. If distance from lightning is about 100 km or less, and ground is a good conductor for spherics record frequency band, then, $h_t(t) \approx 2$. Thus, it is the CRPF that is mainly responsible in (2) for mapping of channel features into spherics waveform. Mathematically, $h_c(t)$ is the spherics (2) generating by the same channel provided $i(0,t) = \delta(t)$ where $\delta(t)$ is Dirac's delta function.

The $e(t)$ in (2) is equivalent to pulse radiating by travelling wave antenna with current $i(0,t)$ as the input. Smoothened models for $e(t)$ are based on some assumptions: 1) the antenna is formed by plurality of contiguous radiating elements, 2) current wave velocity $v$ is a constant or monotonously alters along the channel, and 3) all the channel elements create rather equal contributions into $e(t)$.

However, real contributions from different channel parts are not equal. They increase when velocity gradients $dv/dz$ are greater. Great velocity gradients are accompanied by abrupt changes of current values. Therefore the major contributions are created by just those channel parts where local inhomogeneities of channel structure are placed.

It is seen that evaluating of the $h_c(t)$ from real data modeled by (2) are allied to the inverse problem of antenna synthesis. Solution should give such spatial and exciting current distributions for elementary radiators represented by main inhomogeneities of channel, which create the same (in a certain sense) spherics as it was observed from the real lightning. Thus, the channel is rather modeled by discrete antenna array than contiguous one, and it will be better to rewrite $h_c(t)$ in (2) as

$$h_c(t) = \sum_{m=1}^{M} A_m\,\delta(t-\tau_m). \tag{3}$$

One can see that every element of the array is mapped into (3) by pair $(A_m, \tau_m)$ where $A_m$ is excitation factor, $\tau_m$ is current pulse delay for the $m$-th member of that array.

The inhomogeneities are to play double role in channel radiation process. Firstly, they are the local radiating centers, or some "brigthing points", forming discrete antenna array. Then, reflected waves are brought about as travelling current wave meets any inhomogeneities. In turn, being repeated many times these reflected waves initiate brigthing points excitation recurrently. That is why the value of M in (3) should be greater than number of inhomogeneities expected to account.

Because of plurality and irregular positions of inhomogeneities placed along a channel, one would think the CRPF (3) should be construct as a rather random sequence. However, sharp inhomogeneities and reflections from them give rise to the nearly quasi-periodical part of CRPF. This part includes the members commonly displayed in (3) over weaker background pulses.

Mainly, the sharp inhomogeneities are channel and branches ends, bends and tortuosities, and branching points. As antenna array elements, they are excited by abrupt changes of current caused by great sizes of current wave velocity gradients. Every current step, and, then, value of $A_m$ in (3), both depend on the reflection coefficient of the inhomogeneity [*Krasnitsky*, 1998]. Evaluation of these coefficients will be done below, but determining of $\tau_m$ in (3) deviate from the frames of this paper.

The simplest case arise as inhomogeneity is channel (or branch) end point. Suitable reflection coefficient is -1, as it is seen from boundary conditions. More generally, any inhomogeneity should be considered as a linear passive multiport network incorporated into transmission line conforming to main lightning channel. Similar network is described by the scattering $N \times N$ matrix [*Chen, 1976*]

$$[S] = \begin{vmatrix} R_{11} & T_{12} & \dots & T_{1N} \\ T_{21} & R_{22} & \dots & T_{2N} \\ \dots & \dots & \dots & \dots \\ T_{N1} & T_{N2} & \dots & R_{NN} \end{vmatrix} \tag{4}$$

which relates the reflected, incident and transmitted currents occured in the network branches and designated accordingly as $i_{kr}$, $i_{ki}$ and $i_{kt}$. Main diagonal elements are current reflection coefficients $R_{kk} = -i_{kr}/i_{ki}$ for the $k$-th branch provided the other branches are matched. The rest elements in (4) are $T_{lk} = i_{kt}/i_{ki}$, or current transmittion coefficients from the branch $l$ to the branch $k$.

Used (4), main types of channel structure inhomogeneities have been considered [*Krasnitsky*, 1995]. Briefly, the results are as follow.

1. The isolated bend of a channel (or a branch) is described by $2 \times 2$ matrix. If angle among bended parts is obtuse the reflection coefficient for upgoing current wave is $R_{11} \approx -0.1$. Its relation to the angle values is weak. For downgoing wave reflected from channel top, $R_{22} = -R_{11}$. The signs of corresponding values of $A_m$ in (3) should not depend from direction of the wave. Inversion of sign, as $R_{11}$ is changed by $R_{22}$, put off by one more inversion due to reflection from channel or branch end.

2. Tortuosities, or multiple contiguous small bends, play double role in forming of CRPF (3). Firstly, they give raise to channel spatial modulation. Thus, one ought to consider a channel as a delaying structure. Excited wave propagation velocity along the axis of spiral-like channel is perhaps lower than being read along the channel filament. Optically resoluted periods of tortuosities are 60 - 100 m but thunder acoustic spectra analysis gives periods about 3 m [*Ribner and Roy*, 1982].

Secondly, reflections from plural tortuosities should be considered statistically. From this standpoint, tortuosities should give raise in CRPF (3) for noncorrelated sets of pulses with low magnitudes. It should create nearly regular background for more strong isolated pulses generated by more powerful local centers of radiation. In addition, being oriented towards the observation point, some parts of tortuous channel have not to contribute into radiation field and, thus, into CRPF.

3. The branching point is 6-th port network with $3 \times 3$ matrix. Main diagonal elements are

$$R_{11} = \frac{1 + w_3/w_2 - w_3/w_1}{1 + w_3/w_2 + w_3/w_1}, \quad R_{22} = \frac{1 + w_3/w_1 - w_3/w_2}{1 + w_3/w_1 + w_3/w_2}, \quad R_{33} = \frac{1 + w_2/w_1 - w_2/w_3}{1 + w_2/w_1 + w_2/w_3}, \tag{5}$$

$w_1$ is channel characteristic resistance under that point, and $w_2, w_3$ are these resistances for branches over. Mapping of that point into (3) is defined by $R_{11}$, if current wave runs up to branch tops, and both $R_{22}$ and $R_{33}$, as the wave being reflected by these tops. The sign of $R_{11}$ is important. When

$$w_3/w_1 > 1 + w_3/w_2, \tag{6}$$

the branching point should generate the negative pulse in (3). The same signs have pulses from channel or branch ends. This coincidence can impede as channel geometry is evaluated from CRPF.

From physical standpoint, the (6) represents perhaps the most likely case as main channel is forked into two more thin branches. If radii of these are equal, i.e., $W_2 = W_3$, one can derive from (5)

$$R_{11} = (2 - w_3/w_1)/(2 + w_3/w_1), \qquad R_{22} = R_{33} = (w_3/w_1)/(2 + w_3/w_1), \tag{7}$$

and unequality (6) is reduced to $w_3/w_1 > 2$. Contrary to described case, as radius of main channel is unchanged before and after branching point, then, $W_1 = W_2$. One obtains from (5)

$$R_{11} = R_{22} = 1/(1 + 2w_3/w_1), \qquad R_{33} = (2w_3/w_1 - 1)/(2 + w_3/w_1). \tag{8}$$

It is seen that the unequality (6) is not valid for this case. If the primary current wave is upgoing, the branch point radiation would be mapped into the positive pulse in CRPF (3).

## 3. EVALUATING OF CRPF FROM SPHERICS RECORD

Before processing, anyone from convolutional components in (2) is not yet known. Those can be resolved due to appreciably distinct behaviour. Really, being responsible for interference of fields radiated by different channel inhomogeneities, CRPF is to be the fast function relative to channel base current (or, more exactly, to the result of convolution of the current with trace pulse function).

Being modeled by Bruce-Golde's current form, slow component should be sought by spectral minimization procedure [*Krasnitsky*, 1994]. Then, CRPF is found as inverse Fourier transformation (FT) from the quotient of direct FT of the spherics (2) by the spectrum of the slow component.

The predictive deconvolution method [*Hayes*, 1996] is suitable to evaluate the fast component, i.e., the CRPF, without profound knowledge of inherent properties for convolved terms in (2). One can suppose that linear $p$-order estimator for discrete-time representation of (2) is

$$\hat{e}(n) = \sum_{k=1}^{p} a_p(k)\, e(n-k). \tag{9}$$

Finding the coefficients $a_p(k)$ is equivalent to minimizing the sum of squares of prediction errors, i.e. the differencies $\hat{e}(n) - e(n)$. It is possible to demonstrate that discrete-time form of CRPF in (2) is presented by set of these errors.

Sofware to realize these procedures has been developed [*Krasnitsky*, 1998]. The examples are presented in figure. Plot (*a*) shows the spherics registered from distance 32 km to observer. CRPFs were sought by both methods: fast FT (*b*), and linear prediction (9) for $p=2$ (*c*). Plot(*d*) is modified CRPF derived by remaining in (*b*) those samples only which are the local extrema.

As it is seen CRPF sought from spherics data has really the features exposed in Part 2. One can assume that the pulse signed *E* in (*d*) is mapping of channel top excited by primary outgoing current wave. The pulse E' should perchaps resulted from channel bottom being excited by reflected downgoing wave. The pulse BE is branch end radiation, and so on. CRPF's found by different methods are similar.

## 4. CONCLUSIONS

Analysis of the CRPF (3) allows not only to detect that the channel has heterogeneous structure, but also to resolve more fine details determining the inhomogeneities of specific kinds. For example, branching point position is estimated from the delay of the appropriate pulse in CRPF, and the kind of branching is identified from the sign of this pulse using Eqns. (5-8).

Being recovered by different methods fundamental features of CRPF are similar, but usage of linear prediction method (9) does not require estimation of the base current form previously.

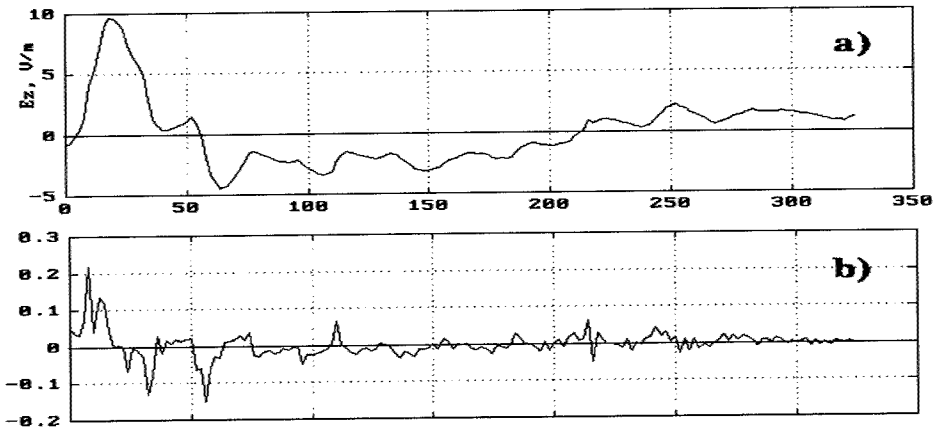

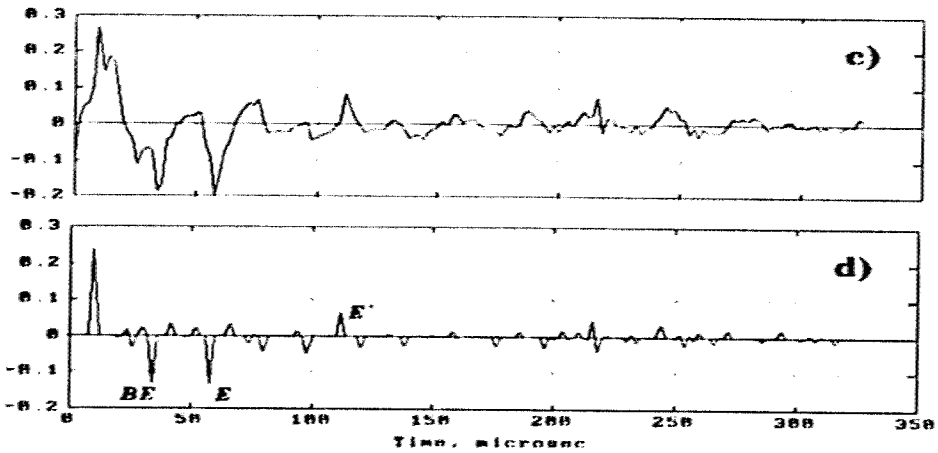


REFERENCES

W.K.Chen, *Theory and design of broadband matching networks*, Pergamon Press, 1976 (Russian translation, 287 pp., Moscow, Sviaz, 1979)

M.H.Hayes, *Statistical digital signal processing and modeling*, John Wiley & Sons,Inc., 1996, 608 pp.

Y.A Krasnitsky, Evaluation of lightning current pulse parameters from spherics waveforms, *Journ. of Geophys. Res.*, 99, No.D5, 10723-10725, 1994

Y.A. Krasnitsky, Some features of the radiation pulse characteristics of complex radiating structures, *RAU Proc.*, Riga, 1995, pp.12-16 (in Russian)

Y.A. Krasnitsky, Radiation from travelling wave antenna: Influence of sructural inhomogeneities, 1998 (be published)

LeVine D.M., and R.Meneghini, Simulation of radiation from lightning return strokes: The effect of tortuosity, *Radio Sci.*, 13, No.5, 801-809, 1978

V.A.Rakov, Lightning electromagnetic fields: modeling and measurements, 12th Int. Zurich Symp. and Techn. Exhibit. on Electromagn. Compat., 59-64, 1997

Ribner H.S., and Roy D., Acoustic of thunder: A quasilinear model for tortuous lightning, *J.Acoust.Soc.Am.*, 72, No.6, 1911-1925, 1982

# INVESTIGATION OF A FREQUENCY SPECTRUM OF DISCHARGES GENERATED BY A CHARGED AEROSOL CLOUD

A.V. Orlov and A.G. Temnikov

Moscow Power Engineering Institute
High Voltage Engineering Department
Krasnokazarmennaya st., 14
Moscow, 111250, RUSSIA.

ABSTRACT: Charged aerosol clouds allow to create strong electric fields which generate discharges. A character of appearance and development of the discharges is similar to thundercloud processes. That is why the charged aerosol clouds are used for experiments on studying of discharges in air. Experimental data on electromagnetic fields investigation produced by discharges between charged cloud and ground are considered.

## INTRODUCTION

Lightning parameters are studied for a long time. Electromagnetic fields is one of them which is studied for noise level estimation and for lightning location. Lightning is a unique phenomena connected with atmospheric activity. Attempts to create lightning in the laboratory led to high voltage pulse generation invention. They are able to create a long spark in air gaps. But the discharge is generated between two metallic electrodes thanks to the power stored in capacitors. A generator of charged aerosol forms charged aerosol clouds in a small volume in comparison with natural thunderstorm clouds. Charged aerosol clouds induce strong electric fields and create conditions which are very close to natural. It makes possible to study processes of lightning generation and electromagnetic fields produced by discharge.

## PROBLEM

Charged aerosol generation allows to simulate thunder clouds and investigate discharges in an air gap between the cloud and the grounded electrode. We can consider the discharges as lightning taking into account a certain approximation. Discharges arise electric field changes of the cloud and generate electromagnetic fields. The problem is to estimate a frequency spectrum of electromagnetic field of the discharge.

Analysis of a frequency spectrum of CG lightning shows that it has a broad band. In practice lightning location instruments have a band from 10 to 500 kHz [*Vereshchagin et al, Anzupov et al, Baru et al.* ]. *Pierce* [1971] found that maximal amplitudes have frequency of 10 kHz. Experimental data show that distant thunderstorms have maximum at 8 kHz, close thunderstorms have maximum at 10 - 12 kHz.

Discharges generated by charged aerosol clouds have their lengths about 1.5 m. If we consider these discharges as antennas so we can suppose that the resonance frequency can be higher than lightning has.

## EXPERIMENT

Charged aerosol generators are described completely in [*Kononov et al., Pierce, Uman et al.*]. They are used for charged aerosol formations which generate discharges striking into grounded

electrodes. Fig 1 shows an experimental set-up. The charged aerosol cloud of 1 cubic meter is formed above grounded plane on 0.7 - 0.8 m height by the charged aerosol generator. A field meter was installed under the grounded plane surface with a hole. Field strength exceed 10 kV/cm. Jet outlet current of 150 μA provided space charge density of $10^3$ C/$m^3$ and charged cloud potential of 0.9 - 1.2 MV.

Electromagnetic field was measured by a dipole antenna at a distance of 4 m from discharges. The dipole antenna was constructed of two copper hemispheres of 2.0 cm diameter which were placed on a teflon insulator at a distance of 7 cm. The dipole antenna was connected with a differential input of an oscilloscope by a screened circuit pair.

## EXPERIMENTAL RESULTS

Experimental set-up is given in Fig.1 [*Vereshchagin et al, Anzupov et al, Baru et al.* ]. The vertical component of electric field of vertical oriented discharge was measured by the described antenna. The upper hemisphere of antenna was connected to a positive input and the lower hemisphere - to negative input. The typical form of a signal is given in Fig. 2. Impulse parameters are the following: duration of the pulse was from 20 to 40 μs, front of the pulse was 2.0 μs, amplitude was from 20 to 40 mV. Parameters of pulses was computed after experiments and were taken the Fourier transformation of the pulses. The frequency spectrums were obtained and one of them is presented in Fig. 3.

## CONCLUSION

Analysis of the computed data showed that the maximum amplitudes correspond to 50 kHz. Amplitudes of upper harmonics have a sharp decay - Fig. 3. It allows to make a conclusion that the frequency spectrum of discharges generated by charged aerosol clouds are practically corresponds to frequency spectrums of lightning. Hence, frequency spectrums depend on ionization processes in discharge channels, but not from the discharge length.

Obtained results show that the physical processes in discharges generated by electric field of the charged aerosol cloud are similar to thundercloud processes.

## REFERENCES

Vereshchagin I.P., Koshelev M.A et al. Elektricheskyi razryad v zaryazhennom aerosole. Izv. AN SSSR. Energetika i transport, 4, 100 - 106, 1989.

Antzupov K.V., Vereshchagin I.P. et al., Metody polucheniya zaryazhennykh aerozolnykh obrazovanyi i ikh ispolzovanie. Izv> AN SSSR, 5, 78 - 92, 1990.

Baru N.V., Kononov I.I., Solomonik M.E. Radiopelengatory-dalnomery blizhnikh groz.L.Gosmeteoizdat, 1976.

Kononov I.I., Petrenko I.A. and Snegurov V.S. Radiotekhnicheskie metody mestoopredeleniya grozovykh ochagov. L. Gosmeteoizdat, 1986.

Pierce E.T. Atmospherics - their characteristics at source and propagation. Introductory Review Paper.XV-th Journal Assembly of USSJ. Munhen 1971.

Uman M.A., McLane B.K., Krider E.P. The electromagnetic radiation from a finite antenna. A.J.P. Vol. 98, D12, 22903 - 22914, December 20, 1993.

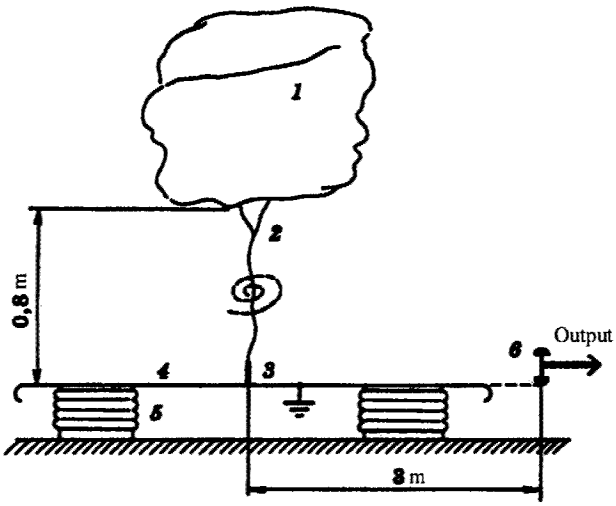


Fig. 1. Experimental set-up
1 – charged aerosol cloud; 2 – discharge; 3 – electrode; 4 – grounded plate; 5 – insulator; 6 – differential antenna

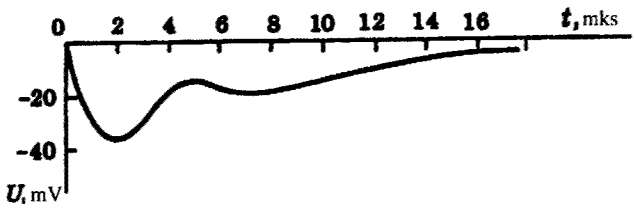


Fig. 2. Signal wave form

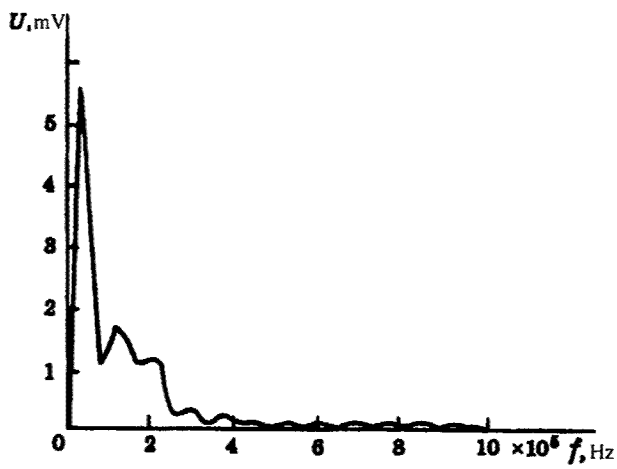


Fig. 3. Frequency spectrum

# FORMATION OF PLASMA SPACE STEMS IN CHARGED AEROSOL CLOUDS: EXPERIMENTAL RESULTS AND THEORETICAL EXPLANATION

A.G. Temnikov, A.V. Orlov and V.S. Syssoev

Moscow Power Engineering Institute
High Voltage Engineering Department
Krasnokazarmennaya st., 14
Moscow, 111250, RUSSIA.

ABSTRACT: Experimental investigations of plasma space stem formation in the charged water aerosol clouds allowed to describe the phenomenology and suggest the possible mechanism of their appearance. These space stems can appear on the charged flow boundary where the external electric field strength becomes enough for intensive ionization when the weak streamer arrives there. Rarity and accidental nature of the space stem appearance are explained.

## INTRODUCTION

Investigation of the discharge phenomena in the charged water aerosols plays an important role for the understanding of the electrical processes in atmosphere, especially for the lightning physics studying and for simulation of lightning development stages.

Experimental investigations of discharges in the artificially charged aerosol clouds [Antsupov et al., 1990; Temnikov et al., 1993] showed that sometimes the luminous plasma formations (called us «space stems») appear on the boundaries of the turbulent charged aerosol flows. This phenomenon is rare and occasional. Frequency of appearance of such plasma formations is by the orders less than the appearance of spark discharges in the charged aerosol cloud and near it. Visual beginning sizes of the appeared space stems are in the range of millimeters.

## PHENOMENOLOGY OF PLASMA SPACE STEM APPEARANCE IN THE CHARGED AEROSOL CLOUDS

Observations of the discharge development in the artificially charged aerosol clouds showed that the space stem appearance is preceded by the corona discharge development near the charged aerosol formations. Moreover, these corona discharges represent the weakly branched long filaments of the tube of diffusive discharge (probably the weakly current streamers). Development of the bright powerful streamer discharges near the charged aerosol cloud was not accompanied by the plasma space stem appearance.

It was found that for charge aerosol clouds of vertical orientation space stems mainly appear under the positive polarity of charged aerosol, and for aerosol flows of the negative polarity stems occur more often for horizontal orientation. Application in experiments of the artificially strong charged flow of horizontal orientation allowed to study detailed the process of the plasma space stem formation.

Charged aerosol generator of the condensate type was used. It had the outlet currents up to 150 μA and allowed to create the charged aerosol clouds with potentials up to 1,5 MV. Scheme of experimental installation is shown in Fig. 1.

It was found that space stem appearance was preceded by the appearance of the mentioned above diffusive discharge tubes from the inhomogeneities (drops, rough parts) on the situated closely grounded screens. Such tubes occurred in the different places and ended on the boundary of the charged aerosol jet. However, plasma space stem appearance on the jet boundary was the sufficiently more rare and occasional phenomenon, and region of their appearance was localized on the distance 0,3 - 1,1 m from the jet outflow plate. Thus, the diffusive discharge tubes ending on the charged flow boundaries outside of that zone did not lead to the space stem appearance.

We can derive the parameters of the charged aerosol jet accompanying the space stem appearance. Space stem appeared only under the outlet currents of the charged aerosol generator more than 100 μA when the cloud potential was more than 1 MV and the electric field strength on the jet boundary not less than 13-15 kV/cm were provided.

After appearance of space stem, the future discharge development could go in two directions: (a) discharge process ended on this stage; (b) sometimes the space stem could developed into the space leader discharge and then the leader discharge from the grounded objects.

POSSIBLE MECHANISM OF THE PLASMA SPACE STEM APPEARANCE

Let's present possible mechanism of the space stem appearance. Luminescence of the space stem shows about intensive ionization processes in that region of medium. We can assume that it is necessary that average electric field strength in the space of the possible space stem appearance (more than some hundreds microns) has exceeded the critical one for air (30 kV/cm). Maximal value of the electric field strength on the charged aerosol jet boundary is achieved in the region 0.2 - 1.0 m from the jet outflow plane [Orlov A.V., Temnikov A.G.]. Because of the turbulent character of jet and action of own electric field of the charged flow on the charged aerosol particles, real boundary of the charged aerosol jet will have not regular, constantly changing in time and in some space range character which can be determined as fluctuation zone (Fig. 2).

Let's consider situation when «weak streamer» of the diffusive discharge tube approaches to the charged aerosol jet boundary (Fig. 3). As in experiments, we consider the negative aerosol jet and the approaching positive streamer. Head of streamer with the charge $Q_t$ and the radius $R_t$ has approached on the distance Y to one of the fluctuation projections of the charged flow boundary. Average electric field in the gap Y will be added from the external field of the charged aerosol jet $E_{ZAO}$ and from the field of the excess charge of the streamer head:

$$E_{Yav} = E_{ZAO} + \frac{Q_t}{4\pi\varepsilon_0 R_t (Y + R_t)} \qquad (1)$$

Proceeding from the required for the possible appearance in the region Y of the space stem $E_{yav} \geq 30$ kV/cm and calculating the electric field on the charged flow boundary, we can estimate the required distance of the head streamer approach Y to the fluctuation of the jet boundary:

$$Y = \frac{Q_t}{4\pi\varepsilon_0 R_t (E_{Yav} - E_{ZAO})} - R_t \qquad (2)$$

Calculations fulfilled for typical parameters of the streamer head and the charged aerosol cloud showed that there is the possibility of appearance in the space on the boundary of the turbulent charged aerosol jet the areas with length of some mm where electric field strength exceeds 30 kV/cm and the space stem can appear. Length of the appearing space stems increases with the rise of the streamer head charge and with the rise of the electric field strength on the charged flow boundary, and it decreases with the rise of the streamer head radius and with the rise of the required for the space stem appearance average field strength. Calculated sizes of space stem lie in the range 0.5 - 8 mm and well correlate with the beginning sizes of the space stems observed under experiments.

Polarity and accidental nature of space stem appearance are connected with the following: (1) hit of the weak streamers of the diffusive discharge tube to the region of maximal field strength on the jet boundary is the rare case; (2) time is required for space stem formation, so only streamers with the limited range of their parameters (they should be enough slow, but have enough excess charge of the head) can lead to the space stem appearance; (3) if the humidity of air will be low, that leads to

evaporation of water aerosol particles and to appearance near the charged aerosol jet boundary of ion zone where approaching streamer can move rapidly and with less charge of head; (4) streamer often approaches not to the fluctuation projection of the charged aerosol jet boundary, but to the fluctuation hole where the external electric field $E_{ZAO}$ is less.

Thus, the most favourable case for the space stem appearance is the meeting of the streamer of the diffusive discharge tube with the powerful fluctuation projection of the charged aerosol flow boundary. Future development of the appearing space stem and its possibility of transition to space leader will depend on the electric field in the region of the appeared space stem (it should be enough for the streamer corona initiation from the ends of space stem).

## CONCLUSION

On the base of experimental data, the phenomenology and possible mechanism of the space stem appearance are presented. Calculation results well correlate with the experimental observations. Investigations of the space stem appearance in the charged water aerosols require the future continuation because probably appearance of such space stems near the inhomogeneity zones of the space charge of thunderstorm cells is necessary condition fir the start of the lightning discharge in thunderstorm cloud.

## REFERENCES


Antsupov K.V. and oth. Investigation of spark discharges from cloud of charged aerosol particles. *Izvestia AN USSR. Energetika i transport*, 4, 1990 (in Russian).

Temnikov A.G., Antsupov K.V., Makalsky L.M., Koshelev M.A. Appearance of electric discharges in charged aerosols. *Proc. of Russian aerosol conference*, Moscow, 1993 (in Russian).

Orlov A.V., Temnikov A.G. Determination of electric field of turbulent flow of charged aerosol. *Electrichestvo*, 8, 1996 (in Russian).


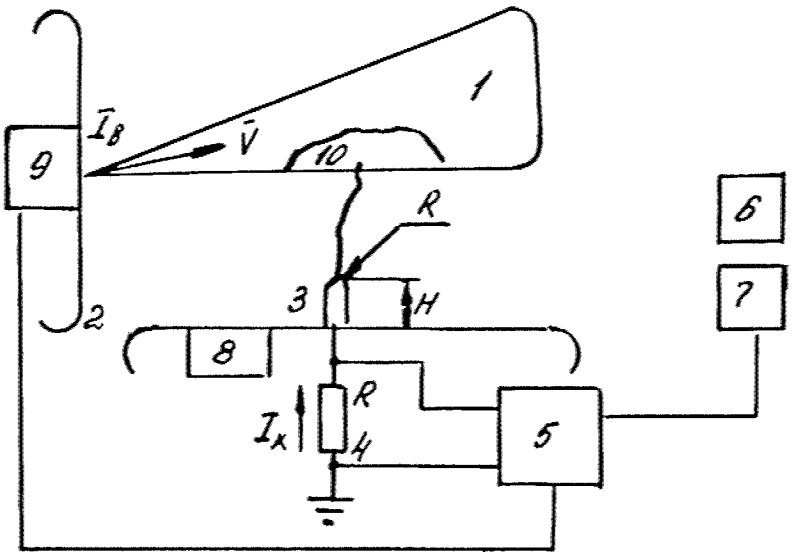


Fig. 1. Scheme of experimental installation.

1- artificially charged aerosol cloud; 2 - electrostatic screens; 3 - electrode; 4 - shunt; 5 - oscilloscope; 6 - discharge counter; 7 - photoelectron multiplier; 8 - electric field strength meter; 9 - charged aerosol generator; 10 - zone of space stem appearance

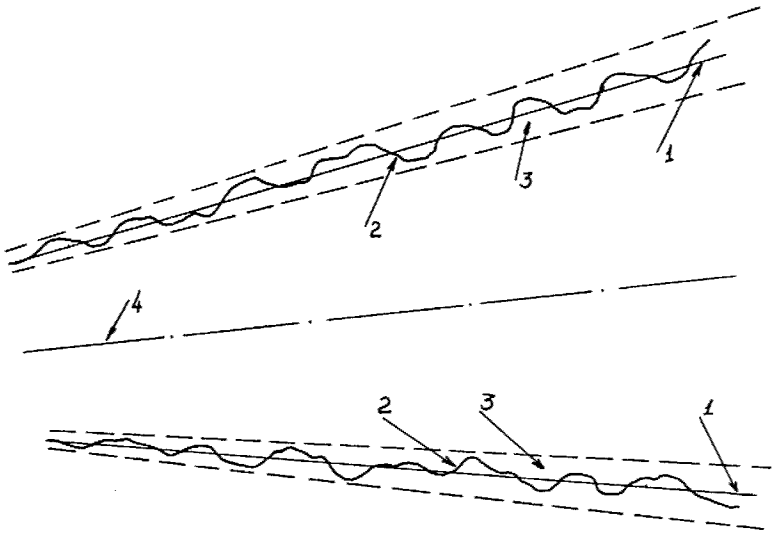


Figure 2. Structure of charged aerosol flow boundary.

1- approximation flow boundary; 2 - real location of charged aerosol in that time moment; 3 - fluctuation zone; 4 - jet axis

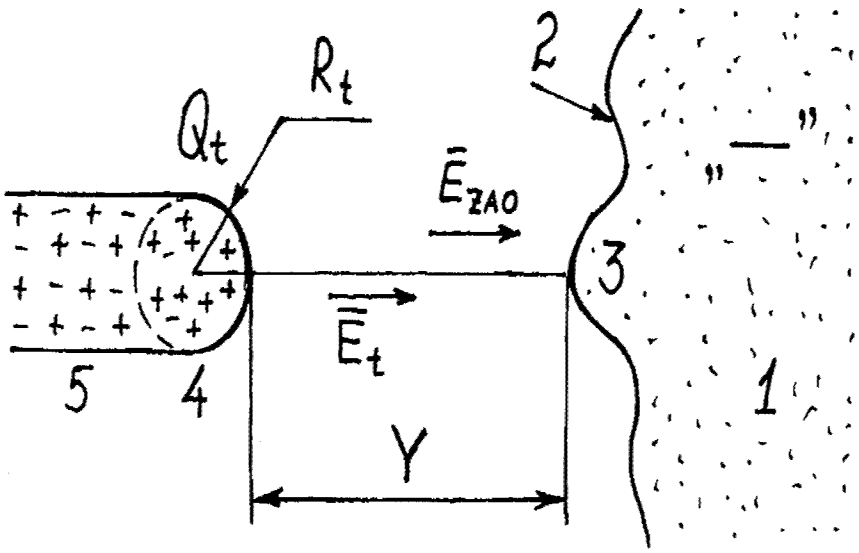


Figure 3. Possible mechanism of space stem appearance.

1 - charged aerosol jet; 2 - jet boundary; 3 - fluctuation rejection of flow boundary; 4 - head of approaching streamer; 5 - streamer channel

# STATISTICAL ANALYSIS AND POLYMER-COMPOSITE STRUCTURE OF BALL LIGHTNING

A. Kh. Amirov, Vladimir L. Bychkov

Institute for High Temperatures Russian Academy of Science, Izhorskaya 13/19
Moscow 127412 Russia

ABSTRACT: The work is devoted to the statistical analysis of events of observation Ball Lightning (BL) collected in the Stakhanov-Keul-Bychkov (SKB) computer data bank on BL. This data bank provided data for analysis of BL properties using a personal computer and modern statistical software such as analysis of variance, ANOVA, for revelation of significant factors and methods of non - parametric regression. The properties of BL as a high energy storing and an object with the framework are analyzed. The model of BL as a highly charged polymer-composite dielectric structure is described. All obtained results show that BL can be heterogeneous (polymer or composite) formation, with movable framework and glowing surface. At least one type of BL can be the object with the material structure or the framework.

## INTRODUCTION

Problem of Ball Lightning (BL) – long-lived glowing spherical object, that appears mainly in summer during thunderstorms (in the Northern Hemisphere) and exists autonomously from evident external sources of energy attracts constant attention of scientists for a long time. It is connected with difficulties of determination of the experimental direction of researches. Nowadays in the BL problem appeared four directions of the investigation. The first is collection of observational data and the primary analysis of it. The second direction is the computer analysis of the observational data with determination of properties inherent in BL. The third is development of theoretical models of the object that can describe main observational BL properties and allows develop the fourth direction of investigations - experiments on the creation of laboratory BL analogues. In last ten years there were achieved considerable progress in all these directions. In frames of this report is impossible to give the review of the subject, so we consider some results of our own investigations.

New facts allow look at one type of BL as the object with the structure or the framework. It usually appears in summer when take place both thunderstorms and highest release of organic particles of different forms of green vegetation origin (pollens of grass, oak, pine, spores of mushrooms, etc. and destruction of leaves, wood, grass, etc. under the action of atmospheric electricity) into the atmosphere. It can have polymer organic or composite (organic macromolecules and particles of sand, dust and soot) structure. This work is devoted to statistical and theoretical analysis of this concept.

## STATISTICAL ANALYSIS

Ball lightning (BL) observation data were collected in the Stakhanov-Keul-Bychkov (SKB) personal computer data bank on BL (about1900 events). It includes information of collections of Prof. I.P. Stakhanov (1503 events in USSR), A.G. Keul (150 events in Austria) and Bychkov V.L. (about 100 events in Russia). It allows evaluate the internal energy store of BL in range 5-100 J/cm$^3$, and even more <470 J/cm$^3$. In SKB there are 268 observations that show BL to have a complex structure. 81 BLs had tails or rays or branches. Outgoing sparks or glowing particles were observed from 52 BLs. Stripes, layers and rings were observed on surfaces of 5 BLs. There were observed 5 double or triple structures; 9 BLs had a form of tangles with definite interknitted structure; 34 BLs had galo or nucleus. We also want to mention that BL can have a form different from a spherical one. Out of 1397 cases of SKB 61 were ellipse like, 21 - pear, 21 - irregular, 16 - sphere-tape (form changed from sphere to tape, or from tape to sphere during BL lifetime), 25 - sphere - ellipse, 5 ellipse-tape, 5 - ring and 3 - disk.

Created SKB allowed continue to investigate BL properties with the aid of personal computer and to use not only the correlation analysis for it. By means of ANOVA (analysis of variance) there was made revelation of the significance factors BL color and way of disappearance (explosion, extinction, decay) for parameters BL diameter and lifetime. The factor BL color turned out to be insignificant for the parameters BL lifetime and diameter while the factor BL way of disappearance was significant for them. Dependence logarithm of radiation losses - logarithm of BL volume obtained with a help of non parametric treatment turned out to be different according to BL ways of disappearance.

ANOVA analysis showed that the factor of the BL location (indoors or outdoors) proves to be significant for such BL parameters as diameter, lifetime and the radiation power (in comparison with the power of incandescent lamp). The distribution of BL over colors does not depend on its location.

The correlation analysis of BL distribution over colors has been made. 18 factors, which could affect the observers' perception, were analyzed for six main colors of BL. The correlation coefficients for all the factors but four turned out to be in the 95% confidence interval from 0.903 to 1 of correlation coefficients for random samplings. Four factors falling out of this range are: observation in September, during night time and before thunderstorms and disappearance of BL through decay.

The rank correlation method was applied to investigate the influence of atmospheric thunderstorm conditions on the observation time of BL. For the analysis a ranking of BL over sizes has been made and a ranking of atmospheric conditions of the BL observations in respect to electric field strength of the atmosphere ground layer has been made. Statistical analysis reveals that both the increase of the humidity and of electric field strength decreases the BL observation time, and the effect of electric field strength is the secondary in comparison with the role of humidity.

Methods for non-parametric regression have been applied for pair lifetime and diameter of BLs that disappear through explosion, extinction and decay. BL lifetime increases in case of BL, that disappear through extinction and decay in range of diameters 0.5-100 cm. Lifetime of BLs, that disappear through explosion, increases at diameters smaller than 60 cm and decreases for greater diameters. For all types of BLs observed during thunderstorms the statistical dependence of natural logarithm of BL lifetime (sec) in respect to natural logarithm of its diameter (cm) is represented in the figure.

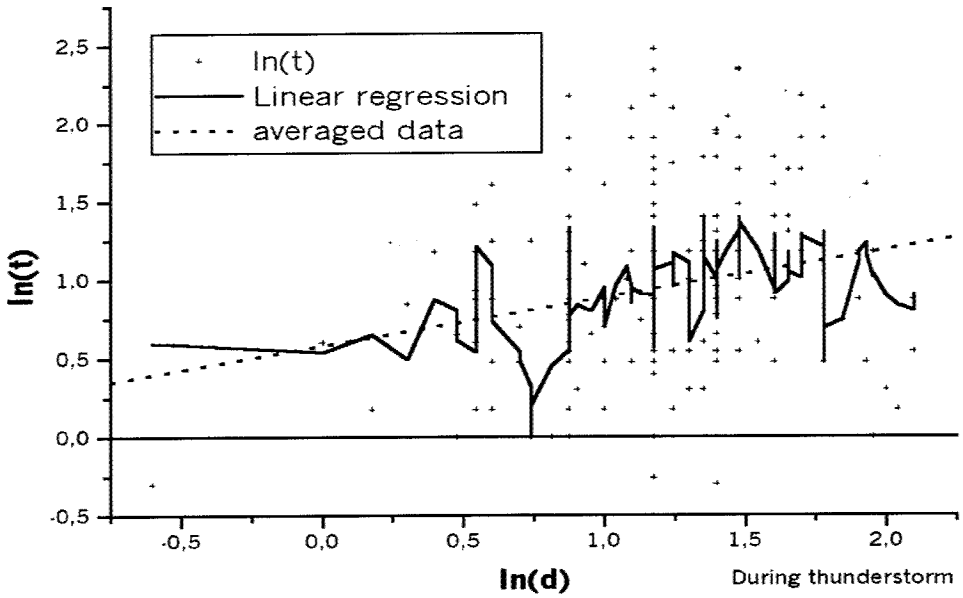


During analysis it was shown that the distribution function of BL parameters like diameter, lifetime, radiation power, and the shortest distance to the BL can not be described by a log-normal distribution function, though earlier some authors used it to describe BL properties.

These works gave possibility to make some conclusions, namely. BL color can be determined by photo or chemical processes near BL surface (with the participation of surface gas discharges) and/or by reflection or refraction of light by the surface material. Exploding BLs have the most specific energy and the least radiation ability. BLs those disappear through extinction have the most radiation ability and the least specific energy. BLs those disappear through decay represent the intermediate case.

BLs those appear indoors are secondary phenomena in correspondence to the outdoor BLs, or they are the result of the formation of less amount of BLs material in comparison with outdoor BLs.

Analysis of the most probable action of the humidity on BL lifetime on the basis of theoretical models revealed that plasma, electric field, cluster and fractal models can not explain the obtained statistical results. These models also can not explain the observed dependence lifetime-diameter. According to plasma and cluster models BL lifetime is dependent on concentration of plasma particles and is independent of its size and it contradicts to the statistical results. Dependence of BL as the vortex or of overcooled plasma transition significantly differs from the statistical one. Close to the observed dependence was obtained on the basis of polymer BL theory [*Amirov et al.*, 1998]. All obtained statistical results show that BL can be heterogeneous (polymer or composite with air filled pores) formation, with movable framework and glowing surface.

POLYMER-COMPOSITE BL THEORY

Taking into the account successful gas discharge experiments on generation of artificial fireballs in discharges with the polymer additions and polymerizing components in a gas mixtures in [*Bychkov* 1994, *Bychkov et al.* 1996]. There was represented a theory of BL and fireballs in discharge plasmas. The framework of this object is the polymer structure or composite of polymer organic macromolecules, soot, silicon and other dielectric particles that exist in atmosphere. Such BL can be formed at the destruction of polymer isolation during shorting in high power electric devises or at the injection of streamers of linear lightning into subjects made of the polymer materials, for example bark of trees, grass, leaves etc. If the origin of BL is connected with organic components then the appearance of BL in radio, TV sets, in telephones and other electronic devices with polymer isolation parts and possibility of realization of local high electric fields and currents inside the device can be explained. Mass $m$ of such polymer BL is determined as mass of fractal structure of radius $R_{sp}$

$$m = m_0 \cdot \left( \frac{2 \cdot R_{sp}}{r_0} \right)^D \qquad (1)$$

where $m_0$ and $r_0$ are the monomer mass and radius, respectively, $N_i$ is the number of monomers. $D$ is the fractal dimension, in case of the polymer structures $D \approx 2.5 \pm 0.3$. According to (1) the mass of BL framework of radius 10 cm made of molecules like $CH_4$ is ~0.85 g and of cellulose ~0.15 g. At the same time the mass of the same sphere of air is ~5.1 g, it shows that such BL (framework and pores filled by air) is slightly heavier than the sphere of air, so it can be moved by air flow. The surface $S$ of such structure, if we consider, for the sake of simplicity that the fractal BL consists of equal spheres of radius $r_0$ and density $\rho_0$, is

$$S = \frac{3m}{\rho_0 r} = \frac{6m_0 \left( \frac{2R_{sp}}{r_0} \right)^D}{r_0 \rho_0} \qquad (2)$$

Because of great surface the fractal BL during the aggregation and charging can accumulate on its surface and structure a high amount of charges from the environment. Iin stationary conditions in respect to charging it is possible to estimate the excess of charges, $q$, on its surface when ions are captured by molecules of the structure

$$q = \frac{r_0 \cdot T}{2e} \cdot \log_e \left( \frac{M_-}{M_+} \right) \cdot N_i \qquad (3)$$

where $M_-$ and $M_+$ -are reduced masses of negative and positive air ions, $e$ –is the electron charge, $T$ is a gas temperature. According to (3) BL is charged negatively at usual atmospheric conditions. BL of $R_{sp}$ = 10 cm consisting of molecules like $CH_4$ can obtain negative charge $q \sim 8 \cdot 10^{-5}$ C and of cellulose $q \sim 1.4 \cdot 10^{-4}$ C. BLs with such characteristics can levitate at height 3-10 m at local electric fields in range 100-500 V/m during thunderstorm conditions if we take into the account their weight and mirror attraction to the earth.

It is well known that dielectric structures usually are charged mosaic like, and the distance between charges greater than regions of charge locations. In case of the dielectric polymer-composite material of BL it can be also charged mosaic like by negative and positive ions. On the basis of Gauss equation the dependence of energy, E, of the sphere charged mosaically was obtained

$$E = (Q_0 \cdot m)^2 \cdot \left(1 + \varepsilon_2 / (\varepsilon_1 (2D - 1))\right) / (2 \cdot R \cdot \varepsilon_2)$$

where $Q_0 \approx 10^{-2}$ C/g, typical for dielectrics coefficient of charging. In figure 2 dependence (4) BL energy –diameter is represented for structures made of molecules like $CH_4$, lines 1 and 2, and of cellulose, lines 3 and 4. Lines 1, 3 correspond to $D = 2.5$, and lines 2,4 to $D = 2.3$. In Figure 2 is represented also the data on the energy of BL obtained from observations. Comparison shows good agreement between theoretical and statistical results.

Conducted analysis showed that the accumulation of charges by the BL leads to the appearance of high electric fields near it and to the generation of gas discharge conditions near its surface. These discharges heat the surface and change the conductivity of BL material. Increase of temperature of surface up to 600 K leads to changing of conductivity of polymer films by several orders of magnitude. Conducted calculations for typical conditions of corona discharges near the sphere showed that the BL lifetime is rather long and comparable with the observed one, lifetime range of BL of radius 1 cm is 2÷5 s, of 10 cm is 20-50 s, and of 30 cm is 40-150 s.

The appearance of discharges on the surface explains its ability to shine. Since BL it is the polymer structure then it's optimal form in a flow is a sphere, but without a flow it can have any different form from a sphere. Because of the fact

that the own volume of the elastic framework of polymer BL is much smaller than its effective volume BL has ability to penetrate through little holes. The BL appearance from "nowhere" can be described as the transition of polymer structure to the stressed state with convenient conditions of discharge appearance on the surface [*Bychkov* 1994, *Bychkov et al.* 1996]. This theory is also applicable for explanation of appearance of fireballs in discharges with polymer additives and gives time of their formation comparable with the experimental ones.

Using the idea of BL aggregation and charging in experiments [*Emelin, S.E., et al.*, 1997.] little particles of carbon or cotton wool (~10 units) were located in the channel 1-2 mm wide made of organic glass (PMMA).

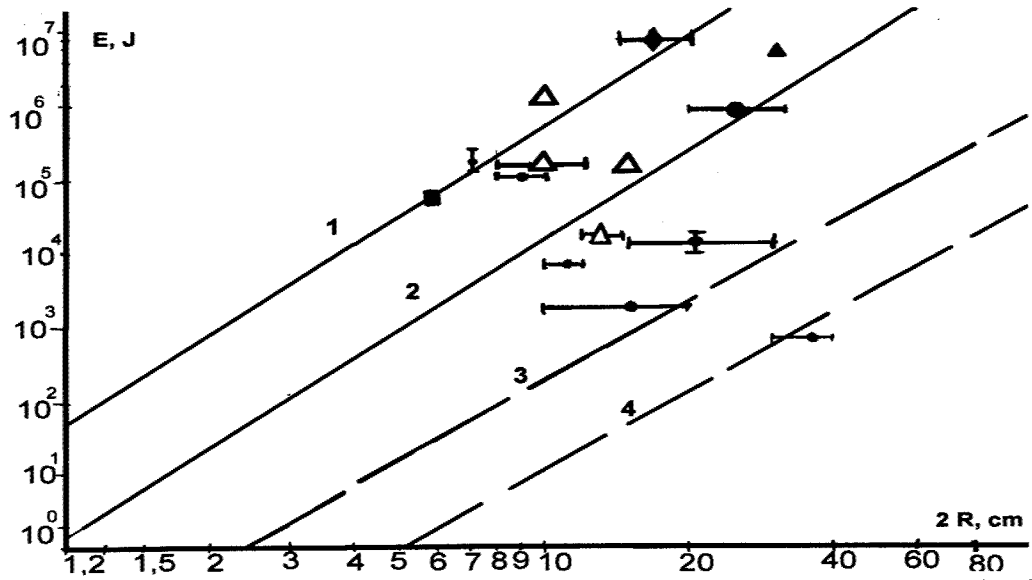


Discharge of input energy ~ 1÷3 kJ lead to the appearance of one or several autonomous formations. They flew high up to 0.5÷1.5 m and fell down like snowflakes. They shone red color, had irregular form and size 5÷7 mm that was greater than the channel's size. The time of glow was 5÷6 s. Remains of these objects, had white-yellow highly porous structure, sometimes it consisted of bunches of fibers, or separate long filaments. Density of their material was $5 \cdot 10^{-2}$ g/cm$^3$. After the sufficient deformation-compression and tension the object restores its form, what represents high elasticity of material. Electronic microscopy showed that the framework of the object consists of modified PMMA.

Results of experiments qualitatively validate the polymer structure of Ball Lightnings. They show that one of types of BLs can be charged excited polymer formations that consist of porous material or fiber like structures.

## CONCLUSIONS

All obtained results show that BL can be heterogeneous (polymer or composite) formation, with movable framework and glowing surface. Represented material on statistics, theory and experimental approaches to BL show that one type of BL can have polymer-composite structure

## REFERENCES


Amirov, A.Kh., S.E. Bobkov, V.L. Bychkov, On the Dependence Lifetime-diameter for Ball Lightnings, *Physica Scripta*, 58, 56-60, 1998.

Bychkov, V.L., Polymer Ball Lightning Model, *Physica Scripta*, 50, 591-599, 1994.

Bychkov, V.L., A.V. Bychkov, S.A. Stadnik, Polymer Fire Balls in Discharge Plasma, *Physica Scripta*, 53, 749-759, 1994.

Emelin, S.E., V.S. Semenov, V.L. Bychkov, et al., Some objects formed in the interaction of electrical discharges with metals and polymers, *Tech. Phys.*, 42, 269-277, 1997.

# CURRENT MEASUREMENTS OF UPWARD NEGAITVE LEADERS IN ROCKET TRIGGERED LIGHTNING

M. Nakano [1], S. Sumi [2], and K. Nakamura [3]

[1] Toyota National College of Technology, Toyota, Japan
[2] Department of Electrical Engineering, Chubu University, Kasugai, Japan
[3] Department of System Management Eng., Nagoya Institute of Technology, Nagoya, Japan

ABSTRACT: Negative upward leader currents in rocket triggered lightning are measured with high and low sensitive measuring systems. The upward developing leader from the ground show different two stages, that is, the initial stage in which the mean current amplitude of the leader pulses is 129 A, and the following developing stage of large current pulses. The mean current amplitude is 9kA. The current amplitude of the initial stage is similar to a leader current which is reported in natural negative ground flash. The mean time interval between leader pulses are 30us in the initial stage and 77us in the following developing stage, which are in the same range as those of a negative leader in natural lightning and lightning to a tower. The transition from the initial stage to the developing stage is very clear, and this suggests that two different discharge processes exist when the leader develops upward to cloud charge center.

## INTRODUCTION

The experiments of triggered lightning in Japan have been made at the top of a moutain in the winter season since 1987. The height of the moutain top is 890m above the sea level and the height of cloud base is normally from 500m to 1000m. Then the experiment site is often in clouds, and lightning discharges in clouds are observed at very close distance. A test transmission line tower of 60m height is close to the rocket launchers, and if a rocket with an nylon string near the ground instead of a steel wire is used, lightning strike to the tower through virgin air, which is called as altitude lightning.

Main objectives of the experiments are: (1) measurements of lightning parameters at close distance with high time and spatial resolutions, (2) lightning to a transmission line tower and measurements of the current and voltage at the transmission line tower, (3) insulation test of electric equipments for lightning, (4) evaluation of a lightning conductor, (5) production of a fulgurite.

During winter thunderstorms in Japan, a positive ground flash is often observed. Even in rocket triggered lightning experiments, the positve ground flash is often triggered. The positive ground flash is usually initiated with an upward negative leader from the tip of a rocket with a grounded steel wire.

The electric current is measured with a shunt and a Rogowski coil along the current path. High and low gain systems are used, and current pulses with small amplitude of a few hundred amperes are found before the large current pulses of several kiloamperes. In this paper the current characteristics of the negative upward leader of positive ground flash are reported.

## DATA

Direct current measurements of the leader developing upward as well as the main stroke current are made. In positive lightning, a distinct return stroke is often not detected. Fig. 1 shows an example of typical current waveforms of a positive ground flash. Fig.1(a) is measured with a low gain system. Fig.1(b) is time expansion of a few millisecond from the bigining of large current pulses. Fig.1(c) is the current measured with high gain system. The peak currents of leader pulses are in the range of several kiloamperes which are seen in Fig.1(b). On the other hand, current pulses of a few hundred amperes are observed in the initial stage shown in Fig.1(c). The current data of eleven flashes are used for present analyses.

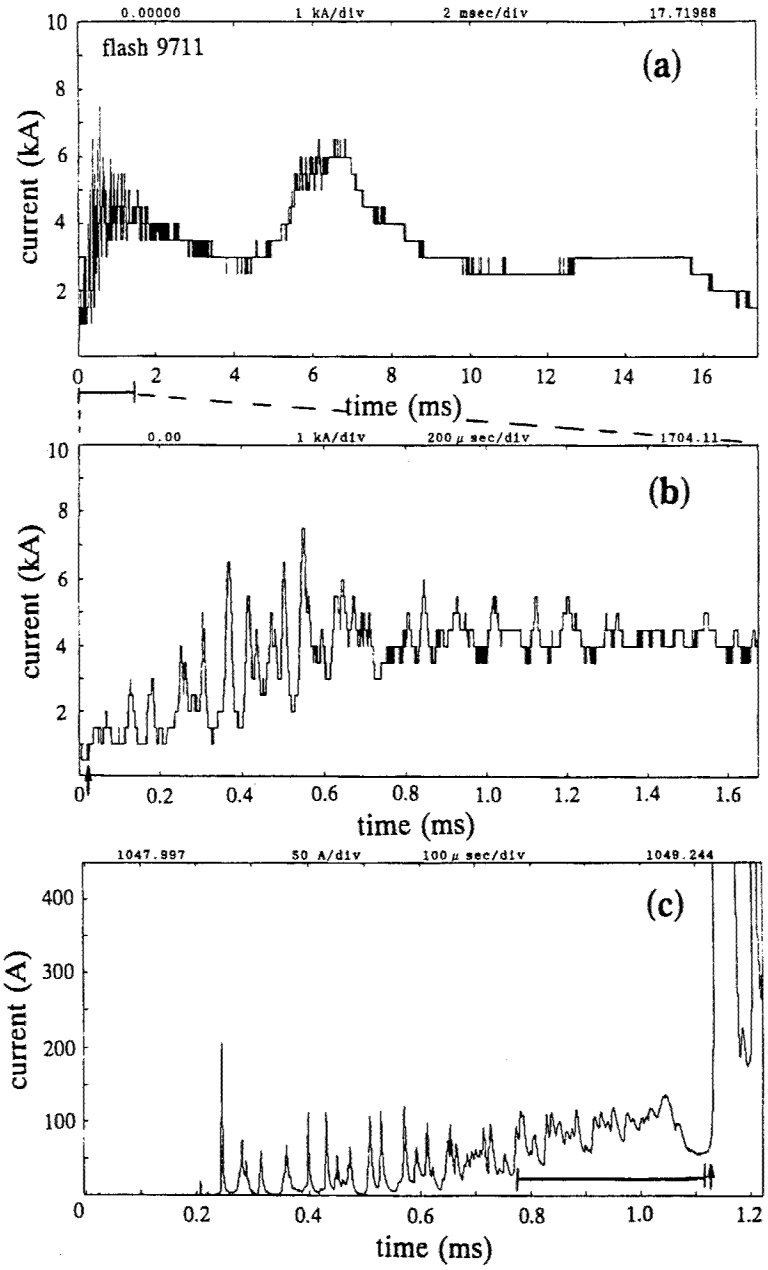


Fig.1 An example of the current waveforms, (b) is time expansion of the initial part of (a), and (c) is high gain output. The time pointed by arrows in (b) and (c) indicates the corresponding time.

## NEGATIVE UPWARD LEADER

Fig.1 shows a current waveform of typical negative upward leader from the ground. During about 1ms from the begining of the leader, the waveform of the current pulse is changed, the rise time of pulse is about several microseconds in a half millisecond from the begining, then the rise time of the current pulse is changed to 10 microseconds in a next half millisecond.

## PEAK AMPLITUDE OF LEADER CURRENT PULSES

Fig.2(a) and Fig.2(b) show the distribution of leader current amplitudes with low and high gain measurements respectively. The current amplitude in the initial stage within a first 1ms from the begining of the leader is in a range of a few hundred amperes, and the mean value is 130A. On the

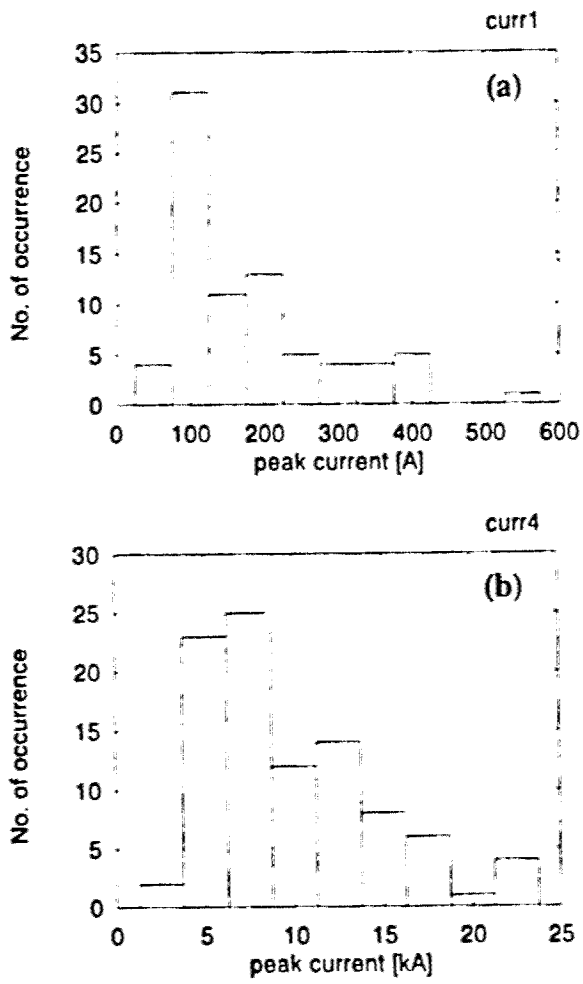


Fig.2 Histgram of peak current,(a):initial stage, (b):developing stage.

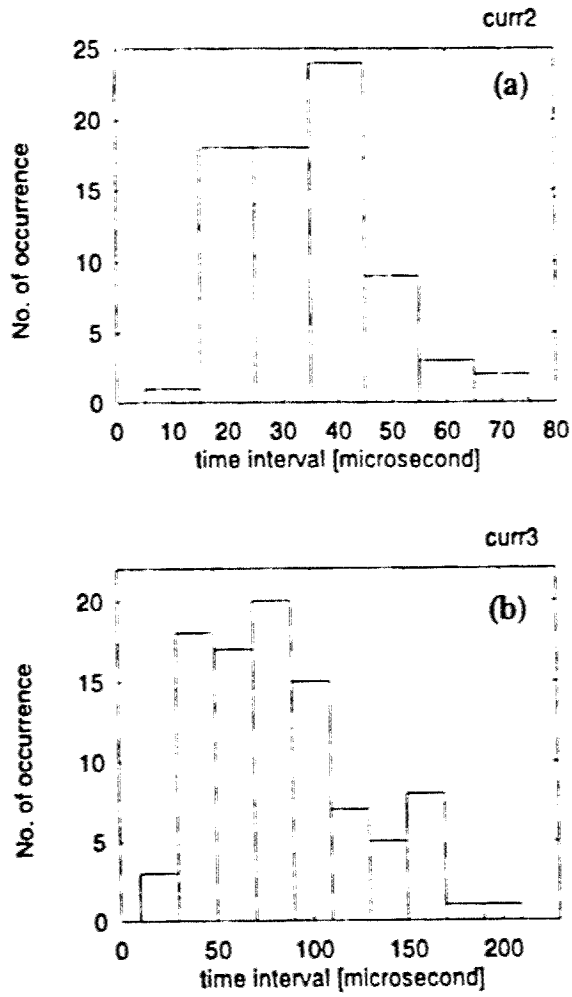


Fig.3 Histgram of time interval between current pulses, (a):initial stage, (b):developing stage.

other hand, the current amplitude after about 1ms from the begining is in a range from 5kA to 20kA, and the mean value is 9kA.

## TIME INTERVAL BETWEEN LEADER CURRENT PUSLSES

Fig.3(a) and Fig.3(b) show the time interval between current pulses. (a) is in the initial stage of leader in a half millisecond from the onset of leader. The data are distributed from 20us to 50us, and the mean is 30us which is in the same range as those of a natural lightning. (b) is in the developing stage after a half millisecond from the onset. The data are distributed widely and the mean is 77us which is longer than those of a natural lightning.

## DISCUSSIONS

The current pulses of several kiloamperes are often observed in a negative upward leader in winter.

Those are the same order of magnitude as a return stroke current. In this study, it is found that small current pulses of order of 100A within 1ms exist in the initial stage, and these current pulses are followed by large current pulses of order of 10kA in a few millisecond. The transition to developing stage may be related to the evaporation of the steel wire. The steel wire evaporates by about 20As and the evaporation of wire is supposed to be occured within about 1ms from the onset of discharge. If the conductivity of the channel is increased by a large current after the evaporation, the large current flows to the ground succesively, acording to upward progress of leader into the cloud. Fig.4(a) and Fig.4(b) show other examples of initial part of negtive leader currents. The waveform of current pulses change at about 0.5ms from the onset, as well as shown in Fig.1(c). These changes may correspond to the begining of the evaporation of wire. The conductivity of the channel decreases temporarily by the evaporation of wire, and this reduces the current and increases the rise time of current pulse, as shown in Fig.4. In Fig.4 estimated preriod of evaporation is also shown by horizontal bars. The height of channel tip is 100m to 200m above the ground after 1ms. When the tip of channel penetrate into the cloud, large currents flow into the main channel from many branches. This increases the current amplitude and also the channel conductivity. The mechanism of large current pulses is strongly related to the charge distribution of the storm clouds. The sounding of the charge distribution of winter storm clouds is important for further study.

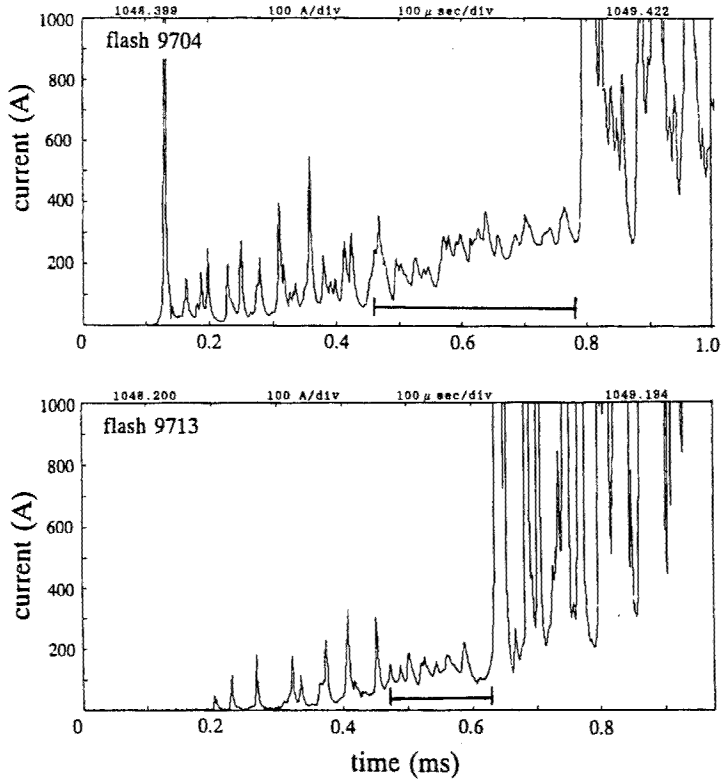


Fig.4 Current waveforms of initial stage (high gain outputs).

The authors would like to thanks to many colleagues joining the experiments. Thanks are also due to Hokuriku Electric Power Co. for the support of the experiments.

# LIGHTNING, THE GLOBAL CIRCUIT, AND THE MIDDLE ATMOSPHERE

Leslie C. Hale
Communications and Space Sciences Laboratory
Department of Electrical Engineering, Penn State University
University Park, Pennsylvania, USA

**ABSTRACT**: A capacitive discharge model of a thundercloud can be used to explain AC (ELF and below) and DC current and energy coupling to the middle atmosphere and global circuit (GC). It is found that the DC GC current can approach the basic "meteorological" charge separation generator for thunderclouds with only CE lightning but is reduced by IC lightning. Point discharge and precipitation currents reduce the cloud and cloud-to-earth capacitance charging and hence the lightning rate. The waveshape and hence frequency spectrum of the current pulses to the GC are controlled by the middle atmosphere conductivity profile, which is extremely variable. The low conductivity of the nighttime mesosphere is probably due to "invisible" aerosol. The acceleration by the ELF pulse of free electrons photo-detached from the aerosol particles by lightning may explain the VHF pulses observed in connection with "red sprites" and other lightning.

## CAPACITIVE MODEL OF THUNDERCLOUD IN GLOBAL CIRCUIT

The energy at ELF frequency and below coupled to the mesosphere and global circuit by lightning is much larger than had been predicted by early models, which used invalid free space (or half space, with images) "dipole moment" expansions. Data show that the real nature of both the DC and the ELF and below AC currents to the ionosphere and global circuit (I+GC) are better explained by a lumped circuit "capacitor discharge" model of a thundercloud.

The "Maxwell current" density (curl H) has been measured at high altitudes above thunderstorms and found to contain both "DC" and transient components [Figure 1]. (Maxwell current, is useful, because it is divergenceless, and solenoidal, and can be followed through a complete circuit, taking on the role of displacement current in low conductivity regions and "real" current in high conductivity parts of the circuit.

Kasemir [1971] suggested using a capacitor to model a thundercloud and Berger [1977] found cloud-to-earth capacitance necessary to explain underground blasting explosions due to lightning. Hale [1983] combined two capacitors with the cloudtop-to-ionosphere and global circuit impedances, as shown in Figure 2. A meteorological generator Im and a generator Ip (consisting of point discharge Ipd and precipitation current Ipr) are considered. Im-Ip provide the current charging Cc and Ce in parallel, hence Ip may reduce the lightning rate.. When one capacitor discharges due to lightning, the <u>other</u> capacitor "dumps" energy through the I+GC to approximately equalize the voltages, and most of this energy, which is comparable to the lightning energy, is deposited in the mesosphere, for reasons described below. The results of this process are very strong ELF "slow tail" pulses which are coupled to the global circuit as propagating "zero mode" (TEM) wavelets. These wavelets are unipolar, and together with ULF pulses resulting from the decay of "Wilson monopoles" created by lightning flashes, contribute to the "DC" current to the "global electrical circuit." The waveshape and frequency spectrum of the ELF pulses is largely controlled by the conductivity profile of the mesosphere, a process discussed below.

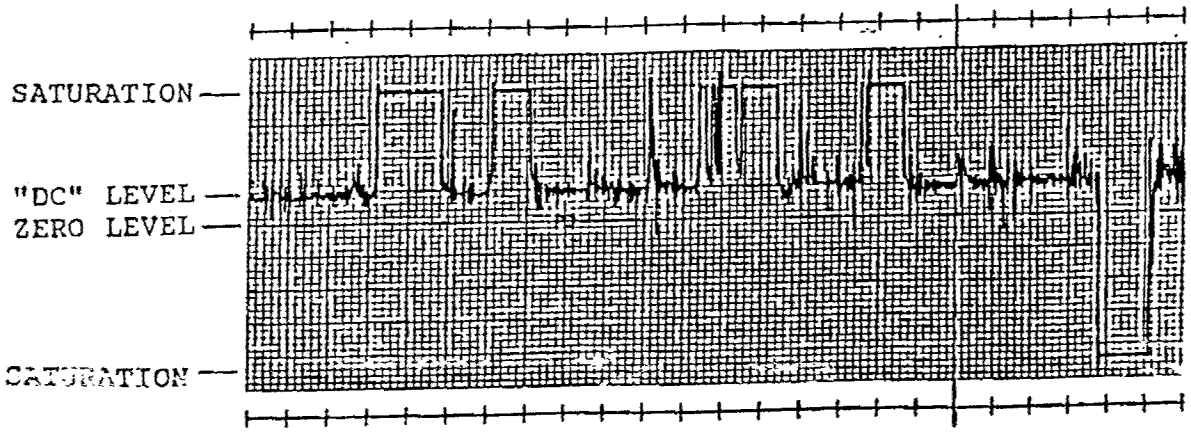


Figure 1. Data of vertical Maxwell current density measured above thunderstorm. The data were taken above an offshore thunderstorm at Wallops Island, VA by a rocket-launched parachute-borne split-cylinder sensor at ~40 km at ~2330UT on July 26, 1987. This data segment is about 12 seconds (2 timing marks/s). This storm was characterized by a preponderance of CE lightning as indicated by the transients which add to the upwards "DC" current, which was about $10^{-10}$A/m$^2$. Note that the single IC flash to the right contributed a current in the opposite direction of the "DC" current.

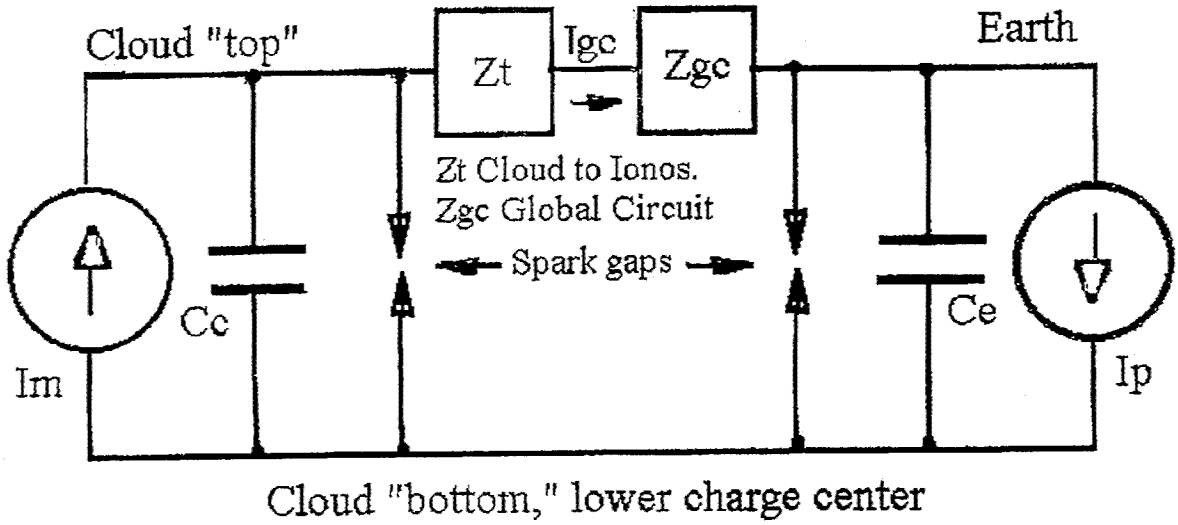


Figure 2. Lumped parameter equivalent circuit to explain data of Figure 1. A "meteorological" generator Im charges a cloud capacitor Cc, and also in parallel a cloud-to-earth capacitor Ce through the cloud-top-to-ionosphere impedance Zt and the global circuit impedance Zgc. Point discharge current Ipr adds to precipitation current Ipd to form a generator Ip which directly charges the cloud-to-earth capacitor Ce and, through Zgc and Zt, charges Cc. The total charging current is Im reduced by Ip, which may reduce the lightning rate. The "DC" global circuit current approaches Im if all the lighting is cloud-to-earth (CE) and Ip if only intra-cloud (IC) lightning occurs.

## WAVESHAPES OF THE PULSES TO THE MIDDLE ATMOSPHERE AND GLOBAL CIRCUIT

Although the capacitive model of Figure 2 explains the basic energy relationships, the waveshape of the individual current pulses to the ionosphere is determined by the path connecting the two capacitors, involving the cloudtop-to-ionosphere impedance Zt and the global circuit, whose impedance Zgc changes character with frequency, going from a few hundred ohms at DC to a few farads (frequency dependent) capacitor at low ULF frequencies, a lossy cavity resonator in the "Schumann resonance" region of 7 to 35 Hz, and the input to a "transmission line," the earth-ionosphere waveguide, at higher ELF frequencies. However, this impedance is always very low compared to the cloudtop-to-ionosphere impedance Zt, which is the principal factor controlling the waveshape.

Zt is a very complex impedance, and is also quite variable in the mesosphere (Figure 3a). It is not possible to represent with a simple lumped model, and it is necessary to return to solving the complete Maxwell's equations in order to determine the current waveform. This is generally done by injecting "Wilson [1920] monopoles" produced by the lightning discharge into the atmosphere and solving for the resulting transient. This is most easily done for simple CE lightning (with an equal and opposite charge placed simultaneously on the earth). An early calculation by C. and P. Greifinger [1976] used this technique to calculate the ULF waveform, which is controlled by the electrical conductivity profile in the stratosphere and mesosphere (Figure 3b). They also suggested a physical model which has stood the test of time and provides considerable insight to the problem. They postulated that the role of the local relaxation time ($\tau_r = \epsilon/\sigma$) was to determine the time scale on which a material acts as a conductor ($t>\tau_r$) and a dielectric ($t<\tau_r$). This gives rise to a downward moving boundary defined by $t=\tau_r$. This physical model was translated into an algebraic formula by Hale and compared with an exact computer solution by Baginski [Hale and Baginski, 1987]. It was found that the analytic (A) and computer (C) solutions were in exact agreement on a time scale of milliseconds to seconds but the computer solution indicated a much stronger pulse on the millisecond time scale (Figure 3b). The reason for this pulse was later interpreted by Hale [1987]. After a CE stroke an initial "electrostatic" solution is set up involving the Wilson monopole and the earth in a time scale of order $10^{-4}$ second (determined by the speed of the return stroke and speed of light). The existence of the "ionosphere" in the problem comes into play in about a millisecond ($10^{-3}$s), determined by the round trip propagation delay from the lightning to the height of the ionosphere, which is generally above 80 km at night, typically about 60 km in the daytime, and as low as 40 km or below under "disturbed" high latitude conditions. The transition to the final electrostatic solution launches the millisecond "slow tail" wavelet, which does not require "continuing currents."

## DEPOSITION OF ELF ENERGY IN THE MESOSPHERE

In the global circuit the solenoidal and divergenceless "Maxwell current" of the pulses satisfies continuity. In the highly conducting earth and ionosphere, and in the lower atmosphere where it is primarily a displacement current, relatively little energy is deposited. Thus most of the pulse energy is deposited in the middle atmosphere, with the ULF energy in the stratosphere and the ELF in the mesosphere. This latter energy is important since it is relatively large compared to the internal energy of the medium, and may be responsible for spectacular phenomena such as "red sprites." Free electrons photo-detached by lightning may be accelerated by the ELF pulses to produce observed millisecond VHF pulses. Conductivity changes due to these free electrons may vastly alter the energy deposition, and perhaps contribute to the stratification of the observed optical emissions.

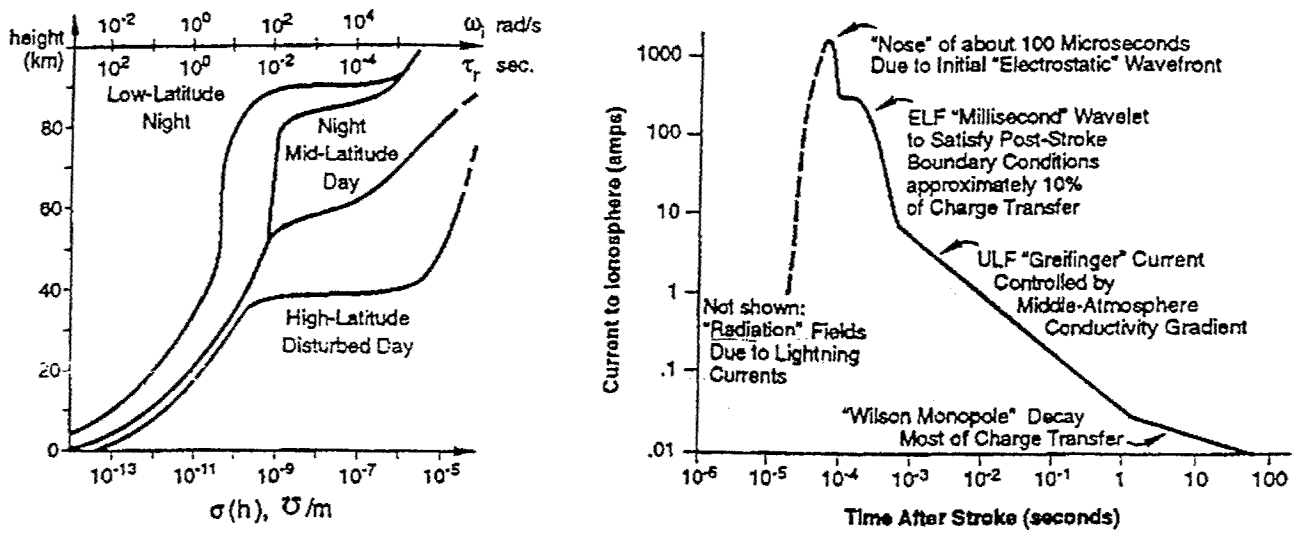


(a) (b)

Figure 3. (a) Showing wide range of middle-atmosphere conductivity profiles under different geophysical conditions. The low conductivity nighttime mesosphere allows the penetration of ELF energy to the "ledge" at about 80 km, but in order to deposit the maximum energy between 50 and 80 km some enhancement may be required, which may be provided by photo-detachment of electrons from aerosol particles. (b) Showing the calculated pulse of Maxwell current to the ionosphere and global circuit (I+GC) for the mid-latitude "quiet" night case. The current waveform is for a one coulomb Wilson monopole deposited at about 7 km. The time scale is in "retarded" time.

REFERENCES


Berger, K., Protection of underground blasting operations, in Golde, R.H. (ed), *Lightning,* Vol. 2, Academic Press, 1977.

Greifinger, C., and P. Greifinger, Transient ULF electric and magnetic fields following a lightning discharge, *J. Geophys. Res.*, 81, 2237, 1976.

Hale, L. C., Experimentally determined factors influencing electrical coupling mechanisms, *Weather and Climate Responses to Solar Variations*, Colorado Associated Univ. Press, 14, 1983.

Hale, L.C., The coupling of ELF/ULF energy from lightning and MeV particles to the middle atmosphere, ionosphere, and global circuit, *J. Geophys. Res.*, 99, 21089, 1994.

Hale, L.C., On the coupling of energy in parallel plane waveguides, *IEEE Trans. on EMC*, 38, 513, 1996.

Hale, L. C., and M. E. Baginski, Current to the ionosphere following a lightning stroke, *Nature*, 329, 814-816, 1987.

Kasemir, H.W., The Thundercloud, *Pure and Applied Geophysics* 84, 64, 1971.

Wilson, C.T.R., Investigation on lightning discharges and on the electric field of thunderstorms, *Phil. Trans, A.* 221, 73, 1920.

# MULTIPLE-STATION MEASUREMENTS OF TRIGGERED-LIGHTNING ELECTRIC AND MAGNETIC FIELDS

D. E. Crawford, V. A. Rakov, M. A. Uman, G. H. Schnetzer, K. J. Rambo, and M. V. Stapleton
University of Florida, Gainesville, USA

ABSTRACT: We have measured electric and magnetic fields produced by 12 strokes in five lightning flashes triggered using the rocket-and-wire technique in 1997 at Camp Blanding, Florida. The measurements have been made at seven distances from the triggered-lightning channel ranging from 5 to 500 m, although not every measuring station acquired valid data for every event. Additionally, for each lightning stroke we measured channel-base current and obtained photographic and video images of the channel. In this paper, we present selected results of the ongoing analysis of the acquired data including (1) electric field waveforms due to leader/return-stroke sequences as a function of distance, (2) the magnitude of leader electric field change as a function of distance, and (3) the magnitude of M-component electric field change as a function of distance. We compare these results with our previous findings and, for the case of M-components, with the predictions of the two-wave mechanism of this lightning process.

## 1. INTRODUCTION AND LITERATURE REVIEW

*Rubinstein et al.* [1995] found that, at tens to hundreds of meters from the lightning channel, leader/return-stroke vertical electric field waveforms appear as asymmetrical V-shaped pulses. The bottom of the V is associated with the transition from the leader (the leading edge of the pulse) to the return stroke (the trailing edge of the pulse). The first multiple-station electric field measurements within a few hundred meters of the triggered-lightning channel have been performed in 1993 at Camp Blanding, Florida [*Uman et al.*, 1994] and at Fort McClellan, Alabama [*Fisher et al.*, 1994]. A detailed analysis of these data have been presented by *Rakov et al.* [1998]. The results of *Rakov et al.* [1998] for distances, r, 30, 50, and 110 m are shown in Table 1, where $I_P$, $\Delta E_L$, and $T_{HPW}$ are the channel base current peak, net electric field change due to leader, and half-peak width of the V-shaped pulse, respectively.

Table 1 – Electric field measurements for 1993 triggered lightning flashes made at 30, 50, and 110 m from the launcher. In the rightmost column, r is in meters and $\Delta E_L$ is in kV/m.

| Flash | Event | $I_P$ (kA) | $\Delta E_{L30}$ (kV/m) | $T_{HPW30}$ (μs) | $\Delta E_{L50}$ (kV/m) | $T_{HPW50}$ (μs) | $\Delta E_{L110}$ (kV/m) | $T_{HPW110}$ (μs) | $\Delta E_L = f(r)$ |
|---|---|---|---|---|---|---|---|---|---|
| 9313 | RS2 | 9.7 | 23 | 2.6 | 20 | 4.3 | 15.9 | 9.1 | $\Delta E_L(r) = 60.7r^{-0.28}$ |
| 9313 | RS3 | 11.4 | 25 | 2.2 | 20.8 | 4 | 16.8 | 7.5 | $\Delta E_L(r) = 69.3r^{-0.30}$ |
| 9313 | RS4 | 12.9 | 27 | 2.2 | 23.1 | 3.5 | 18.2 | 7.3 | $\Delta E_L(r) = 75.8r^{-0.30}$ |
| 9313 | RS5 | 10.9 | 23 | 3.5 | 20.6 | 5.1 | 16.5 | 9.1 | $\Delta E_L(r) = 55.7r^{-0.25}$ |
| 9320 | RS1 | 9.6 | 30 | 8.5 | 23.7 | 14 | 15.5 | 29 | $\Delta E_L(r) = 172r^{-0.51}$ |
| 9320 | RS2 | 8.4 | 24 | 8.4 | 20 | 15 | 13.9 | 29.7 | $\Delta E_L(r) = 102r^{-0.42}$ |

As seen in the last column of Table 1, the variation of the close dart leader electric field change with distance is slower than inverse proportionality ($r^{-1}$), the latter being predicted by the uniformly charged leader model (e.g., *Rubinstein et al.*, 1995). The variation of $\Delta E_L$ with distance slower then $r^{-1}$ is corroborated by independent Fort McClellan measurements at 10 and 20 m [*Fisher et al.*, 1994].

From a comparison of electric fields at 30 m from the triggered-lightning channel and corresponding channel-base currents of lightning M-components and from associated modeling, *Rakov et al.* [1995] have proposed a two-wave mechanism for this lightning process. The two-wave mechanism predicts that M-component electric field magnitude is relatively insensitive (compared to leader electric field magnitude) to variation in distance, ranging from tens to hundreds of meters, from the lightning channel.

## 2. INSTRUMENTATION AND DATA

The experiments were conducted in summer of 1997 at the International Center for Lightning Research and Testing (ICLRT) at Camp Blanding, Florida. The total height of the rocket launcher used for this experiment was

about 5 m. The launcher was grounded, with the measured DC ground resistance being about 220 Ω. Electric fields were measured using flat-plate antennas connected via passive integrators and fiber-optic links to either 12-bit Nicolet or 8-bit LeCroy digitizers. The Nicolet digitizers were operated at 10 MHz sampling rate (100 ns sampling interval) with the total record length being 51.2 ms. Only one trigger per flash was possible so that generally only one leader/return-stroke sequence per flash (plus M-components, if any) could be recorded. The fiber-optic links used with Nicolet digitizers had an upper frequency bandwidth of about 15 MHz. The LeCroy digitizers, which were also used to record channel-base currents, were operated at 25 MHz sampling rate (40 ns sampling interval) with the total record length being 100 μs. Multiple triggers per flash were possible on the LeCroy units. The fiber-optic links used with LeCroy digitizers had an upper frequency bandwidth of 10 MHz. Electric field data presented in this paper were acquired with the Nicolet digitizers and current data with LeCroy digitizers.

Field measuring stations were located at distances 5, 10, 20, 30, 50, 110, and 500 m from the rocket launcher. Most of the data obtained at 5 m appeared to be corrupted, possibly due to ground surface arcs developing radially from the base of the launcher (e.g., *Rakov et al.*, 1998) and are not considered in this paper.

## 3. ANALYSIS AND DISCUSSION

### 3.1 ELECTRIC FIELD WAVEFORMS DUE TO LEADER/RETURN-STROKE SEQUENCES

Leader/return-stroke electric field waveforms in one flash (S9721) simultaneously measured at 10, 20, 30, 50, 110, and 500 m are shown in Fig. 1. The evolution of the leader/return-stroke electric field waveform as distance increases is consistent with previous measurements (Rubinstein et al. 1995; Rakov et al. 1998) and reflects an increasing contribution to the field from progressively higher channel sections.

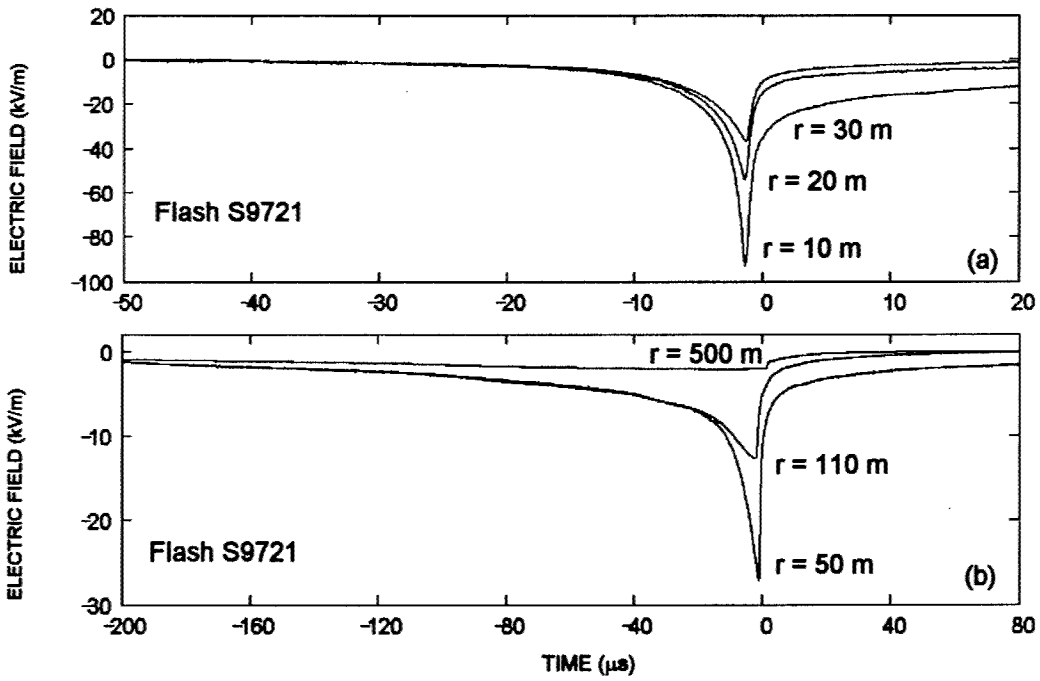


Fig. 1 – Electric field waveforms of the first leader/return-stroke sequence of flash S9721 as recorded at distances (a) 10, 20 and 30 m and (b) 50, 110, 500 m at Camp Blanding, Florida.

### 3.2 MAGNITUDE OF LEADER ELECTRIC FIELD CHANGE AS A FUNCTION OF DISTANCE

As stated in the Introduction, previous multiple-station electric field measurements suggest a variation with distance slower than the inverse proportionality (see Table 1). These data were obtained at distances 30, 50, and 110 m. To facilitate direct comparison between the previous and new data, we present the new data for the same three distances (three leader/return-stroke events out of a total of 12) in Table 2.

Table 2 – Electric field measurements for 1997 triggered flashes made at 30, 50, and 110 m from the launcher. In the rightmost column, r is in meters and $\Delta E_L$ is in kV/m.

| Flash | Stroke | $I_P$ (kA) | $\Delta E_{L30}$ (kV/m) | $T_{HPW30}$ (μs) | $\Delta E_{L50}$ (kV/m) | $T_{HPW50}$ (μs) | $\Delta E_{L110}$ (kV/m) | $T_{HPW110}$ (μs) | $\Delta E_L = f(r)$ |
|---|---|---|---|---|---|---|---|---|---|
| S9718 | RS1 | 11.8 | 43.2 | 1.9 | 27.0 | 3.2 | 11.8 | 7.5 | $\Delta E_L(r) = 1413.5r^{-1.02}$ |
| S9720 | RS1 | 20.5 | 56.2 | 1.7 | 35.6 | 2.7 | 15.8 | 6.4 | $\Delta E_L(r) = 1701.1r^{-0.99}$ |
| S9721 | RS1 | 11.4 | 40.4 | 4.1 | 26.9 | 7.2 | 12.3 | 23.2 | $\Delta E_L(r) = 944.1r^{-0.93}$ |

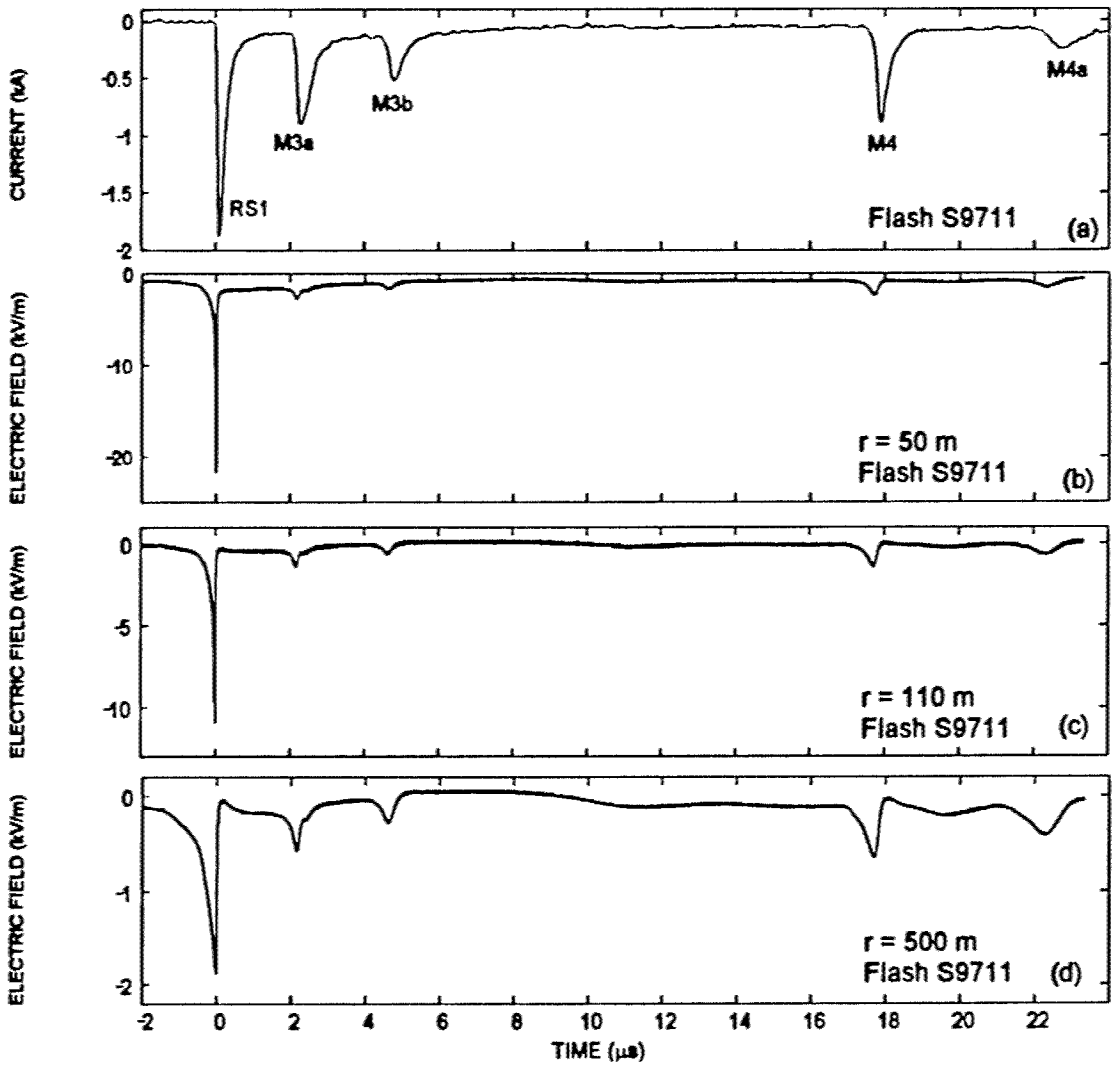


Fig. 2 – A leader/return-stroke (RS1) sequence followed by four pronounced M components (M3a, M3b, M4, and M4a) in flash S9711 initiated using the rocket-and-wire technique at Camp Blanding, Florida: (a) current (intentionally clipped at approximately –1.8 kA), (b) electric field at 50 m, (c) electric field at 110 m, (d) electric field at 500 m. Note that the magnitude of the M component electric field pulses relative to the magnitude of the leader/return-stroke electric field pulse increases with distance, as predicted by the two-wave M-component mechanism. See text for details.

As seen in the last column of Table 2, the leader electric field change varies approximately inversely proportional ($r^{-1}$) to distance from the lightning channel. This trend holds for all the 1997 events for distances ranging from 10 to 500 m (not only for the three distances represented in Table 2), except for one event (S9712) for which the field varied approximately as $r^{-0.5}$ between 10 and 30 m from the channel. Variation of $\Delta E_L$ with distance as $r^{-1}$ is consistent with a more or less uniform distribution of charge along the bottom portion of the fully formed leader channel and is in contrast with the 1993 data presented in Table 1. A variation of $\Delta E_L$ with distance slower than $r^{-1}$ implies a decrease of leader charge density with decreasing height. It is worth noting that the 1997 data are biased in that only first strokes in triggered flashes were recorded, whereas the 1993 data include strokes of different order. The 1993 data show some tendency for the exponent of the relation $\Delta E_L = f(r)$ to decrease with stroke order. On the other hand, the 1993 data came from only two flashes which may be not representative of the majority of triggered lightning flashes.

### 3.3 MAGNITUDE OF M-COMPONENT ELECTRIC FIELD CHANGE AS A FUNCTION OF DISTANCE

As stated in the Introduction, the magnitude of M-component electric field change is expected, based on the two-wave mechanism of this lightning process, to vary with distance appreciably slower than the leader electric field change [*Rakov et al.*, 1995]. The multiple-station electric field measurements beyond 30 m (five events) from the lightning channel confirm this theoretical prediction, as illustrated in Fig. 2. Also shown in Fig. 2 is the corresponding current record (Fig. 2a). In Figs. 2b, c, and d, the magnitude of each of the four M-component electric field pulses, labeled M3a, M3b, M4, and M4a, relative to the magnitude of the leader/return-stroke pulse, labeled RS1, increases as distance increases from 50 m to 110 m and then to 500 m. Within 30 m (two events), M-components exhibited a relatively rapid electric field increase with decreasing distance (not illustrated in this paper), inconsistent with the two-wave mechanism. For one of the latter two events, electric fields were also measured beyond 30 m, with the field variation with distance being as predicted by the two-wave mechanism.

## REFERENCES


Fisher, R. J., G. H. Schnetzer, and M. E. Morris, Measured fields and earth potentials at 10 and 20 meters from the base of triggered-lightning channels, paper presented at the 22nd International Conference on Lightning Protection, Technical Univ. of Budapest, Budapest, Hungary, September 19-23, 1994.

Rakov, V. A., R. Thottappillil, M. A. Uman, and P. P. Barker, Mechanism of the lightning M-component, *J. Geophys. Res.*, 100, 25, 701-25, 710, 1995.

Rakov, V. A., M. A. Uman, K. J. Rambo, M. I. Fernandez, R. J. Fisher, G. H. Schnetzer, R. Thottappillil, A. Eybert-Berard, J. P. Berlandis, P. Lalande, A. Bonamy, P. Laroche, and A. Bondiou-Clergerie, New insights into lightning processes gained from triggered-lightning experiments in Florida and Alabama, *J. Geophys. Res.*, 103, 14, 117-14, 130, 1998.

Rubinstein, M., F. Rachidi, M. A. Uman, R. Thottappillil, V. A. Rakov, and C. A. Nucci, Characterization of vertical electric fields 500 m and 30 m from triggered-lightning, *J. Geophys. Res.*, 100, 8863-8872, 1995.

Uman, M. A., V. A. Rakov, J. A. Versaggi, R. Thottappillil, A. Eybert-Berard, L. Barret, J. P. Berlandis, B. Bador, P. P. Barker, S. P. Hnat, J. P. Oravsky, T. A. Short, C. A. Warren, and R. Bernstein, Electric fields close to triggered-lightning, in *Proc. of the Int. Symp. on Electromagnetic Compatibility*, pp. 33-37, Univ. of Rome "La Sapienza," Rome, Italy, September 13-16, 1994.

# POSITIVE LEADERS IN ROCKET-TRIGGERED LIGHTNING: PROPAGATION VELOCITY FROM MEASURED CURRENT AND ELECTRIC FIELD DERIVATIVE AT GROUND

D.A. Davis[1], and P. Laroche[2]

[1]University at Albany, Albany, NY, U.S.A
[2]Onera, Chatillon, France

ABSTRACT: In 1996, current and surface electric field change recordings were obtained coincident with the inception of positive leaders initiating rocket-and-wire triggered lightning flashes [Willett *et al.*, in press]. The current records show initially isolated (~10 ms separation), and later occasionally grouped (~20-30 μs separation), intermittent current pulses (~10's of Amperes). The onset of the main positive leader follows with a sequence of ~10-15 similar grouped pulses, whose amplitudes decline into a continuous current of a fraction to a few amperes. The assertion that pulses prior to the main leader onset are associated with positive leader development arrested after a few meters of propagation [Lalande *et. al.* 1998, p.14113] is investigated by comparison, between the main leader and prior grouped multiple-pulsed events, of crude velocity and line charge density estimates. These estimates, deduced from the current and surface field change records, range from 1.6-2.5x $10^5$ m/s and 0-150 μC/m for the main leader velocity and line charge density, respectively, whereas the same parameters deduced for prior grouped multiple-pulsed events range from 0.13-2.8x $10^5$ m/s and 4-92 μC/m.

## 1. LEADER VELOCITY AND LINE CHARGE DENSITY FROM CURRENT PULSE ANALYSIS

Fig. 1 shows the current recording vs. time for flight 15 of the experiment described in [Willett *et al.*, in press]. Also shown is the triggering rocket altitude vs. time, as inferred from a composite trajectory by J.C. Willett that incorporated data from all flights. This trajectory data included video of the rocket ascents analyzed by S. Capuano, triggering wire heights deduced by V. Idone from still photographs, and timing of the rocket ascent and main leader onset times. The main leader onset is recognized by the continuous rise in current at 0.35 s, whereas the impulsive events prior to this time are either isolated or grouped current pulses.

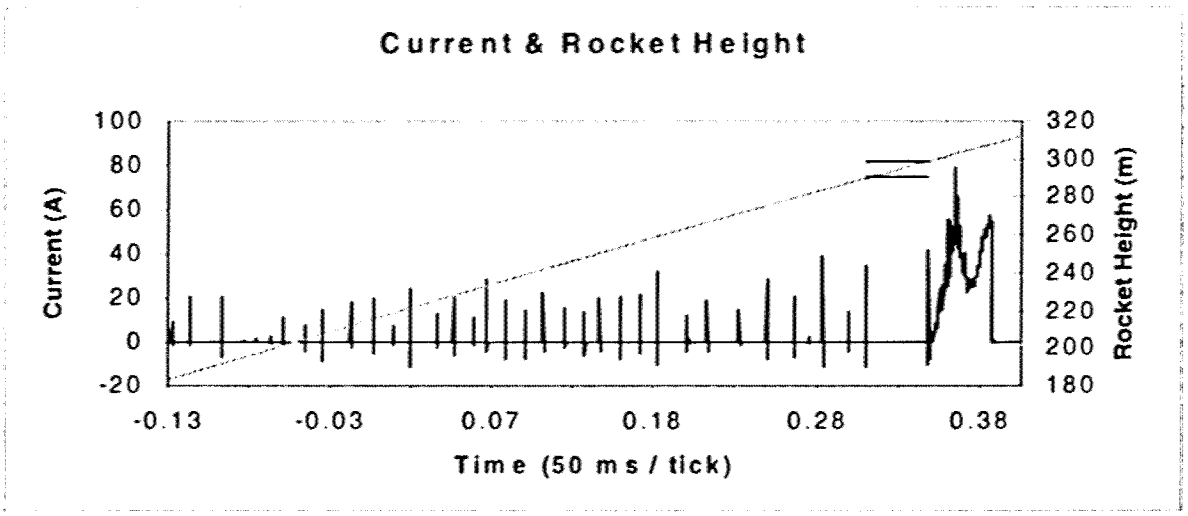


Fig.1 – Current and rocket/wire tip height for flight 15 of the experiment described in [Willett *et al.*, in press]

Following the ideas of Lalande et. al. [1998,p112-4], it is assumed the initiation of a current pulse requires sufficient field conditions at the conductor tip, dependent upon the ambient electric field, conductor length, and the presence of space charge. Concurrent with each pulse is the deposition of space charge about the tip, reducing the field there and inhibiting subsequent pulse initiation until the tip field is restored through conductor extension. The change in conductor length required for subsequent pulse initiation may then be evaluated using knowledge of the conductor velocity and time between pulses. For example, an approximate mean conductor extension per pulse may

be found by taking the product of the time between impulsive events of ~10ms, (these events including grouped, but being predominantly isolated pulses), and the rocket velocity of ~200m/s for an extension per pulse of ~2m.

However, some extension of the above ideas is required upon consideration of grouped pulsed events, such as the one occurring at ~0.31s in Fig.1, and shown on an expanded time scale in Fig. 2, where the current pulses are separated by (~20-30 μs) rather than ~10ms. In such cases, the growth of a conductive leader channel between pulses is postulated as being necessary to provide the field restoration required for subsequent pulses to occur in a time too short to be provided by wire extension. This assumes the leader channel behaves essentially as an extension of the wire, the reduced inter-pulse time being due to, among other processes, the quicker tip field restoration of a proportionately more rapid 'conductor' (i.e. leader) extension. An approximate leader velocity may be estimated by dividing the mean conductor extension per pulse above of ~2m by the inter-pulse time for grouped pulses of ~20μs, giving a velocity of ~1e5 m/s.

Under the further assumption that leader arrest occurs just short of subsequent pulse initiation, an (over-estimated) leader length may be found on a per-case basis from the distance the wire travels between one impulsive event and the next, (a grouped set of pulses counting as a single event). To illustrate this, two horizontal bars, with length corresponding to the time between the last impulsive event and main leader onset (39ms), have been superimposed on the rocket trajectory in Fig.1, showing the wire tip height at these times. Between these times, the wire tip traversed a distance of 8.6m, giving an estimate for the arrested leader length of this last event.

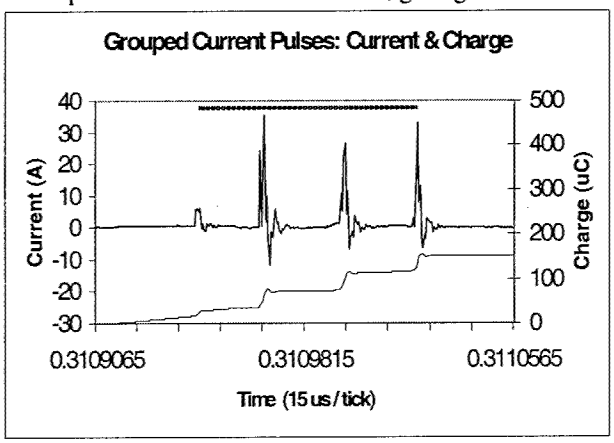


Fig. 2 – Current & charge of event at ~0.31s in Fig. 1

A reasonable estimate for the leader duration in grouped multiple-pulsed events may be taken as the time between first and last pulse peaks. For the event shown in Fig. 2, this duration is 78 μs, as illustrated by the heavy bar at the top of the figure. Also shown is the charge obtained through integration of the current record, 133 μC being transferred in this time. Leader velocity is obtained by dividing the estimated length by duration, 8.6m/78μs = $1.1 \times 10^5$ m/s, and line charge density by taking the ratio of charge to length, 133μC/8.6m = 15.5μC/m. Table 1 shows the sample size, average, standard deviation, max and min values of deduced leader length, velocity and line charge density for all grouped multiple-pulsed events occurring in three triggered flashes.

| Flight | # events | $\Delta H_{ag}$ m | $\sigma\Delta H$ m | $\Delta H_{mx}$ m | $\Delta H_{mn}$ m | $V_{ag}$ m/s | $\sigma V$ m/s | $V_{mx}$ m/s | $V_{mn}$ m/s | $\lambda_{ag}$ μC/m | $\sigma\lambda$ μC/m | $\lambda_{mx}$ μC/m | $\lambda_{mn}$ μC/m |
|---|---|---|---|---|---|---|---|---|---|---|---|---|---|
| 12 | 21 | 3.1 | 1.8 | 8.4 | 0.6 | 8.0E+04 | 4.1E+04 | 1.8E+05 | 2.0E+04 | 26.1 | 18.0 | 78.1 | 5.6 |
| 14 | 16 | 2.7 | 1.7 | 7.2 | 0.7 | 6.5E+04 | 4.3E+04 | 1.6E+05 | 1.3E+04 | 31.3 | 20.8 | 91.8 | 7.0 |
| 15 | 9 | 4.1 | 1.8 | 8.6 | 2.5 | 1.7E+05 | 7.8E+04 | 2.8E+05 | 6.4E+04 | 11.0 | 5.2 | 19.5 | 3.8 |

Table 1- leader length, velocity, and line charge density values inferred from current pulse analysis

Because the estimated relative error of the composite rocket trajectory is only 6%, while the measured durations are accurate to ~1μs, error in leader length and duration is likely dominated by the accuracy of the assumptions. Regarding charge and line charge density, however, estimated uncertainties of 28% in the current scale, due to an unknown change, and 35% in the charge due to under-sampling, lead to a net measurement uncertainty of 45%, independent of the validity of any assumptions.

## 2.LEADER VELOCITY & LINE CHARGE DENSITY FROM CURRENT AND FIELD DERIVATIVE

For analysis of the main leader, the assumption is made that the current flowing through the channel coincides with charge deposition only at the advancing tip, the line charge density behind the tip remaining unaltered. The plausibility of this assumption has been demonstrated by Ruhnke [1988,p.381], who obtained electrical estimates of positive leader velocities consistent in both magnitude and trend with other optical measurements by Idone [1992]. The discharge tip height as a function of time may then be estimated from the ratio of current to field derivative using electrostatics. Consider the situation depicted in Fig. 3. A charge 'dq', resulting from the measured current 'I(t)' at ground within an interval 'dt', is deposited at the tip of the wire/leader conductor a height 'z' above ground.

A distance 'r' away from the wire base, the vertical component of the change in surface electric field 'dEz' is measured, with equal contributions from 'dq' as well as its image '-dq' within the ground plane.

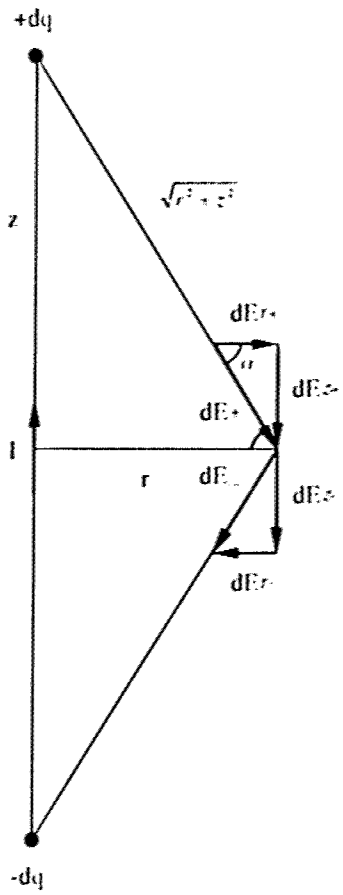


Fig. 3 – Schematic for electrostatic inference of leader tip height.

Application of Coulomb's law yields (eq. 1):

$$1)\qquad \frac{dE_z(t)}{dt} = \frac{I(t)}{2\pi\varepsilon_o}\cdot\frac{z}{[z^2+r^2]^{\frac{3}{2}}}$$

Neglecting r = 24m as being much less than even the minimum observed triggering altitude zmin = 230 m. [Willett *et.al.*, in press], and solving for z (eq.2):

$$2)\qquad z(t) \cong \left[\frac{I(t)}{2\pi\varepsilon_o\cdot\frac{dE_z(t)}{dt}}\right]^{\frac{1}{2}}$$

Taking the derivative of eq. 1 and applying the same approximation used in eq. 2 gives (eq. 3):

$$3)\qquad v_z(t) = \frac{1}{2}\cdot z(t)\cdot\left[\frac{1}{I(t)}\frac{dI(t)}{dt} - \frac{1}{\frac{dE_z(t)}{dt}}\frac{d^2E_z(t)}{dt^2}\right]$$

Equation 3 may be justifiably simplified by examining Fig. 4, the measured surface electric field change E(t). This signal was obtained by 'de-drooping', (i.e. correcting for the exponential decay), the output of a capacitive antannae with 460 ms time constant digitized at 25 kHz. The surface field change records for flights 12,14, and 15 all show the surface electric field to vary essentially linearly with time (eq. 4):

$$4)\qquad E_z(t) \cong E_o + k_E\cdot t$$

The coefficient kE was determined through linear a least-sqaures fit of E(t), the value of which is listed in Table 2. For such a linear dependence of E(t) with t, a constant first and vanishing second time derivative result, eliminating the second bracketed term in eq. 3. Further simplification is made plausible in examining Fig. 5, the current record digitized at 2 MHz, for which a roughly quadratic dependence of current with time (eq. 5) was observed for the cases analyzed. The quadratic fit coefficient kI was determined through least-squares regression, forced through zero at leader onset. The kI value for each case is also included in Table 2.

$$5)\qquad I(t) \cong k_I\cdot t^2$$

With linear dependence of E(t) and quadratic dependence of I(t), the leader velocity is constant, being determined by the fit coefficient values (eq. 6). The velocities thus obtained are listed in Table 2.

$$6)\qquad v_z = \sqrt{\frac{k_I}{2\pi\varepsilon_o k_E}}$$

With constant leader velocity, the leader height obviously increases linearly with time, its estimated altitude 10 ms after leader onset is also included in Table 2.

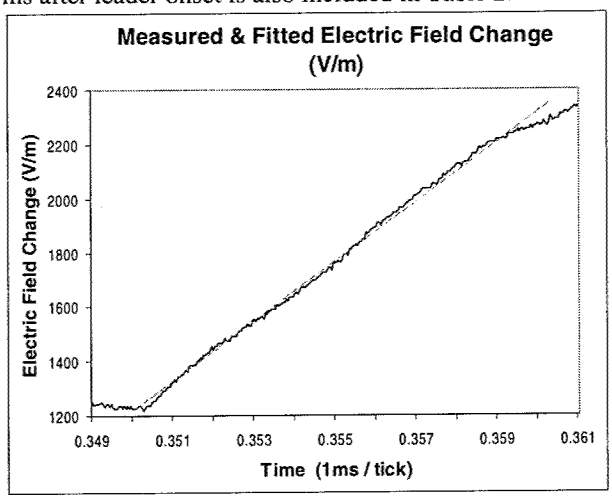


Fig. 4 – Measured surface electric field change and linear least- squares fit.

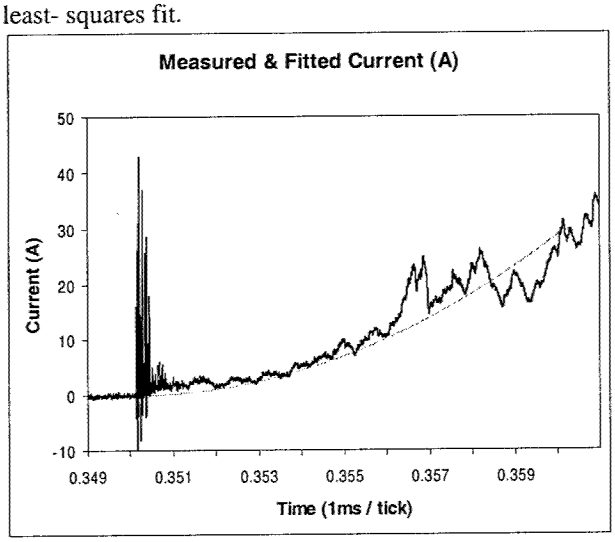


Fig. 5 – Measured current and quadratic least-squares fit forced through zero.

The inferred leader line charge density is found from the ratio of the fitted current (eq. 5) to inferred velocity (eq. 6). For the chosen fit dependencies of E(t) and I(t), it varies, as does the fitted current, quadratically with time (eq. 7), the value of the coefficient kλ being listed in Table 2.

$$\lambda = \frac{I(t)}{v_z} = \frac{k_I}{v_z} \cdot t^2 = k_\lambda \cdot t^2 \qquad 7)$$

Also listed in Table 2 is the estimated line charge density determined 10ms after leader onset.

## 3.CONCLUSIONS

Note that for the analysis of section 2, the constant leader velocities in Table 2 are a result of the chosen fit dependencies, and thus may not be indicative of the actual leader velocity temporal dependence. Also note that for a roughly constant surface field derivative, the leader tip height varies as the square root of the current, so that any peaks occurring in the current record would demand an unphysical leader tip height that would not monotonically increase with time. Further, due to the assumptions used in the analysis of section 1, the leader lengths and velocities of Table 1are over-estimated, whereas the line charge densities are under-estimated. Therefore, although comparison of Tables 1 & 2 seemingly indicate comparable velocity and line charge density for leaders 10's and 100's of meters in length, the crudeness of the analyses and limitations of the required assumptions leave open the possibility that this similitude may be coincidental rather than physical.

| Flight | tdur (ms) | Zmx (m) | $k_E$ (V/m)/ms | $k_I$ (A/ms$^2$) | Velocity (m/s) | $k_\lambda$ (μC/m)/ms$^2$ | λmx (μC/m) |
|---|---|---|---|---|---|---|---|
| 12 | 10 | 1599 | 85.2 | 0.1213 | 1.60E+05 | 0.7579 | 75.8 |
| 14 | 10 | 2485 | 106.34 | 0.3652 | 2.49E+05 | 1.4695 | 147 |
| 15 | 10 | 2196 | 110.02 | 0.295 | 2.20E+05 | 1.3435 | 134.3 |

Table 2 – time interval from leader onset used for fit application, maximum leader length, linear E and quadratic I least-squares fit coefficients, estimated leader velocity, quadratic line charge density coefficient, and maximum line charge density.

REFERENCES


Willett J.C., Davis D.A., and Laroche P., "An experimental study of positive leaders initiating rocket-triggered lightning", *Atmospheric Research*, in press – submitted July, 1998

Lalande,P., et. al., "Leader properties determined with triggered lightning techniques", *Journal of Geophysical Research*, Vol. 103, No. D12, p.14,109-14,115, June 27, 1998

Ruhnke, L.H., Kasemir, H.W., "Electrostatic Fields of Ground Triggered Lightning", *1988 Proceedings International Conference on Atmospheric Electricity*, June 13-16, 1988, Uppsala, Sweden

Idone, V.P., "The Luminous Development of Florida Triggered Lightning", *Research Letters Atmospheric Electricity*, Vol. 12, p.23-28, 1992

# SIGNAL STRENGTH OF RETURN STROKES OCCURRING OVER THE SEA AND OVER LAND: A SENSITIVITY ANALYSIS

Arturo Galván, Vernon Cooray, Thomas Götschl and Viktor Scuka

Institute of High Voltage Research
Uppsala University, 752 28 Uppsala, Sweden

## ABSTRACT

This paper attempts to answer the following question: Is the initial peak of radiation fields generated by lightning return strokes striking the sea higher than that of return strokes occurring over the land? To answer this question, a sensitivity analysis was conducted using the information collected by the Swedish Lightning Location System from 1990 to 1997. After correcting for the propagation effects and the limited bandwidth of the direction finding system, the results show that there is no significant difference in the peak radiation fields of the two categories of lightning flashes.

## INTRODUCTION

The results to be presented in this paper are based on the data collected since 1990 by a network of nine Direction Finders (DF) that make use of magnetic direction finding system. The data were analyzed to investigate whether there is a significant difference in the peak amplitude of the radiation fields of lightning return strokes striking the sea and the land. In order to avoid any errors caused by the differences in the antenna gain of DFs, data pertinent to a single DF were used in the analysis. The lightning flashes analyzed were confined to well defined sectors, each of area 2000 km$^2$, and were located both over land and over sea at distances of 100 to 200 km from the selected DF station. Moreover, in comparing the signal strengths of positive and negative return strokes, only the lightning flashes striking a given sector were used. The results were corrected for propagation effects and for amplitude errors caused by the limited bandwidth of the DF system.

## INITIAL PEAK OF RADIATION FIELDS

The analysis procedure was as follows: a) sample area was divided into twelve squares each with an area of 2000 km$^2$; b) a search for was conducted to identify and retrieve the information stored on all lightning flashes within the squares selected from the 1990 to 1997; c) the squares were located at distances of 100, 150 and 200 km from the Hudiksvall DF station and 100, 140 and 150 km away from the Vitemöla DF station (the distance is defined from the DF station to the middle of the square), d) all lightning flashes recorded in the base line between the DF station used to estimate the initial field peak and any other DF station involved in the localization of the lightning flash were rejected, e) only those lightning flashes in which the DF station under consideration was involved in the calculation of the signal strength were taken into account, and f) in the analyses, the average signal strength was calculated for each square.

Fernando et al. [3] analyzed the behavior of several thunderstorms over Swedish territory that

took place in 1997. They showed that the average signal strength of negative lightning flashes occurring over the land was considerably less than that of those occurring over the sea and the average signal strength of positive lightning flashes occurring over the land was comparable to that of those occurring over the sea. However, we conducted a detailed analysis which indicated that the sensitivity of the DF station used to estimate the signal strength played an important role. In their study, several DF stations were used to evaluate the average value of the signal strength in a particular thunderstorm, which can generate important deviations due to the differing sensitivities of the different DF stations. Because of that, we avoided using different DF stations when each square was analyzed. Tables 1 and 2 show the average signal strength for the area located different distances from the DF station when positive and negative lightning flashes over the sea and over the land were analyzed. In these tables, *NC* refers to uncorrected signals and *C* means corrected signals.

## DISCUSSION

In order to perform a reasonable analysis, the average signal strengths obtained for each square should be corrected by the correction factor due to propagation effects and the correction factor calculated for the antenna system.

Let us first consider the attenuation caused by propagation. All lightning flashes occurring over land were corrected in accordance with the propagation factors given by Cooray [4,5] as the signal propagates over finite soil. For the Vitemöla DF station, the average value of the soil resistivity estimated in the zone [6] was 1550 Ω-m and for the Hudiksvall DF station it was 5000 Ω-m for the distances of interest. Second, the bandwidth of the sensor system is in the range of 1 to 350 kHz. The behavior of the sensor system can be simulated by a RC equivalent circuit in series. In this case, the 350 kHz corresponds to the cut-off frequency at -3 dB. Signals representative of negative and positive lightning flashes occurring over the sea were applied to the equivalent circuit. The attenuation produced by the limited bandwidth of the antenna system was particularly important for signals propagating over the sea because of its high frequency content. For signals propagating over the land, the propagation effect was the most important attenuation factor. The factors obtained by applying the procedure referred to above are summarized in Tables 3 and 4. Finally, we observed that the sensitivity of the DF stations varied from station to station. Thus we used one particular station to estimate lightning flashes occurring over the land and over the sea to avoid mixing different sensitivities in the same average signal strength calculation.

It can be observed, from Tables 1 and 2, that the average signal strength of lightning flashes occurring over land and over sea, once the correction factors have been applied is of the same order of magnitude. That means that, at least in principle, the physics behind a lightning flash occurring over the sea and another occurring over the land could be the same. In addition, the signal strength is higher for positive flashes than for negative flashes by about 60-75%, which is in agreement with the percentages published in [1] and [2].

## CONCLUSIONS

At first, using the information given by the lightning location system, lightning flashes occurring over the sea seemed to have higher signal strength than those occurring over the land. However,

once correction factors had been applied to compensate for propagation effects (for lightning flashes over land) and the limited bandwidth of the antenna system (for lightning flashes over the sea), the average signal strengths became similar. The direct consequence or interpretation of this is that the physics behind the return stroke is likely to be similar whether the lightning flash occurs over the land or over the sea.

The limited bandwidth of the antenna system (1-350 kHz) produces significant attenuation of signals propagating over the sea because of the higher frequency content in comparison to those signals propagating over land. As the signals propagating over the land have already been attenuated when they reach the antenna system of the DF station, the effect of the limited bandwidth on lightning flashes occurring over the land is negligible.

Finally, it is important to note that, when analysis using lightning location systems is carried out, caution have to be taken when parameters calculated by different DF stations are to be determined. For a single flash, the normalized signal strength, for instance, can vary from station to station, producing an important deviation in the calculations.

**Table 1. Average signal strength at different distances from the *Vitemöla* DF station.**

| | Average Signal Strength (DF units) | | | | | | | |
|---|---|---|---|---|---|---|---|---|
| | Negative Flashes | | | | Positive Flashes | | | |
| Distance | Land | | Sea | | Land | | Sea | |
| | NC | C | NC | C | NC | C | NC | C |
| 100 km | -1249 | -1805 | -1470 | -1763 | 2238 | 2862 | 2628 | 2888 |
| 140 km | -1181 | -1749 | -1415 | -1697 | 2276 | 2991 | 2623 | 2883 |
| 150 km | -1085 | -1614 | -1317 | -1580 | 2042 | 2697 | 2403 | 2640 |

**Table 2. Average signal strength at different distances from the *Hudiksvall* DF station.**

| | Average Signal Strength (DF units) | | | | | | | |
|---|---|---|---|---|---|---|---|---|
| | Negative Flashes | | | | Positive Flashes | | | |
| Distance | Land | | Sea | | Land | | Sea | |
| | NC | C | NC | C | NC | C | NC | C |
| 100 km | -897 | -1444 | -1261 | -1512 | 1449 | 2106 | 2052 | 2255 |
| 150 km | -851 | -1423 | -1115 | -1337 | 1271 | 1937 | 1949 | 2142 |
| 200 km | -886 | -1527 | -1266 | -1518 | 1297 | 2058 | 1902 | 2090 |

**Table 3. Correction factors used in making the estimations presented in Table 1 for the *Vitemöla DF* station. Average soil resistivity: 1550 Ω-m**

| | Correction Factors | | | |
|---|---|---|---|---|
| | Negative Flashes | | Positive Flashes | |
| Distance | Land (Propagation effects) | Sea (antenna system) | Land (Propagation effects) | Sea (antenna system) |
| 100 km | 1/0.692 | 1/0.8336 | 1/0.782 | 1/0.91 |

| | Correction Factors | | | |
|---|---|---|---|---|
| | Negative Flashes | | Positive Flashes | |
| Distance | Land (Propagation effects) | Sea (antenna system) | Land (Propagation effects) | Sea (antenna system) |
| 140 km | 1/0.675 | 1/0.8336 | 1/0.761 | 1/0.91 |
| 150 km | 1/0.672 | 1/0.8336 | 1/0.757 | 1/0.91 |

**Table 4. Correction factors used in making the estimations presented in Table 2 for the *Hudiksvall DF* station. Average soil resistivity: 5000 Ω-m**

| | Correction factors | | | |
|---|---|---|---|---|
| | Negative Flashes | | Positive Flashes | |
| Distance | Land (Propagation effects) | Sea (antenna system) | Land (Propagation effects) | Sea (antenna system) |
| 100 km | 1/0.621 | 1/0.8336 | 1/0.688 | 1/0.91 |
| 150 km | 1/0.598 | 1/0.8336 | 1/0.656 | 1/0.91 |
| 200 km | 1/0.580 | 1/0.8336 | 1/0.630 | 1/0.91 |

ACKNOWLEDGMENTS

Arturo Galván thanks to Conacyt and Instituto de Investigaciones Investigaciones Eléctricas for their financial support. The authors' thanks go to Dr. Troel Sorensen for his fruitful comments about the antenna system of the DF stations. We also thank John Willett for providing the electric fields used in the propagation analysis.

REFERENCES

[1] Cooray V. and Lundquist S., "On the characteristics of some radiated fields from lightning and their possible origin in positive ground flashes", Journal of Geophysical Research, Vol. 87, 1982, pp. 11203-11214.

[2] Orville R.E., Weisman R.A., Ronald B.P., Henderson W. and Orville E.O. Jr., "Cloud-to-ground lightning flash characteristics from June 1984 through May 1985", Journal of Geophysical Research, Vol. 92, No. D5, 1987, pp. 5640-5644.

[3] Fernando M., Galván A., Götschl T., Cooray V. and Scuka V., "Analysis of Swedish lightning using LLP data", 24th. International Conference on Lightning Protection ICLP, Birmingham, UK, Sept., 1998, pp. 150-155

[4] Cooray V., "Effects of propagation on the return stroke radiation fields", Radio Science, Vol. 22, pp. 757-768, 1987.

[5] Cooray V., "Propagation of lightning generated electromagnetic fields over finitely conducting ground", ICAE-99 (The proceedings of this conference).

[6] Pettersson G.A., "Electrical resistivity of Swedish soil" (in Swedish), Royal Academy of Engineering Science, Series Paper 183, Stockholm, 1975.

# AN INTERCOMPARISON OF GROUND, AIRBORNE, AND SPACE INSTRUMENTATION DEFINITIONS OF THE LIGHTNING ELEMENT

Douglas Mach[1], William Boeck[2], and Hugh Christian[3]

[1]University of Alabama in Huntsville, Huntsville, Alabama, U.S.A.
[2]Niagara University, Niagara University, New York, U.S.A.
[3]Marshall Space Flight Center, Huntsville, Alabama, U.S.A.

ABSTRACT: For the past century, scientists have made quantitative measurements of lightning discharges. In the process, they refined the definition of a lightning unit, or basic quantum of lightning, in order to base it on observable parameters. In this paper, we will use cluster analysis to derive a basic spatial and temporal definition or scale length for the unit of lightning. We will use data from three different systems that detected pulses from the same storm complex over Central Oklahoma during June, 1998. Since the different instruments detect lightning in different ways with different resolutions, there may not be a single definition of the unit of lightning that can be applied to all three systems. However, common components can be found since all instrumentation are detecting aspects of the same phenomenon.

## INTRODUCTION

For the past century, scientists have made quantitative measurements of lightning discharges. In the process, they refined the definition of a lightning unit, or basic quantum of lightning, based on observable parameters. Although many components of a lightning discharge have been identified, lightning usually occur in groups of discharges or pulses that, although complex, have been organized into units of flashes. This unit definition is based mainly on measurements of lightning from electric field, video, and ground flash lightning locating networks. More recent instrumentation with various combinations of high sensitivity, high temporal, or high spatial resolution often measure signals produced by lightning that do not cleanly divide into flashes. The data from these systems indicate the need for a more fundamental unit for lightning. Without a common lightning unit definition, intercomparisons are difficult.

For an example, the Lightning Detection And Ranging system (LDAR) at Kennedy Space Center (KSC) have detected "flash" rates as high as 600 per minute while analysis based on the Advanced Ground Based Field Mill network (AGBFM) detect only 33 "flashes" per minute in the same area and time periods. The satellite based Optical Transient Detector (OTD) and Lightning Imaging Sensor (LIS) sometimes see single "flashes" that last longer than 10 seconds. Such long duration flashes are not found in electric field records or ground strike location system data sets.

For this study, we will examine the ground strike data from the National Lightning Detection Network (NLDN) [*Orville and Silver*, 1997], the pulse data from the Lightning Detection And Ranging (LDAR) system, and the group data from the Lightning Imaging Sensor (LIS) for a storm complex where all three systems were operating. The chosen storm complex was in Central Oklahoma on June 11, 1998.

## DATA SETS

The NLDN data set consisted of 46 flashes over the region of interest (Figure 1). Although the NLDN data base includes many other flashes, the temporal and spatial limits were set to overlap both the LDAR and LIS data set temporal and spatial limits. The LDAR data set consists of almost 64,000 pulses over the region of interest (Figure 2). The temporal limits of the data were set to correspond to the LIS overpass. The LIS data set consists of over 3000 groups within the region of interest (Figure 3). The LIS data was spatially limited to match the range of the LDAR system data.

## SPATIAL/TEMPORAL CLUSTERING

There is a physical basis to the expectation that lightning will form clusters in space and time. Lightning is a process that dissipates some of the electrical energy stored in a volume of cloud. Once the breakdown electric field threshold is exceeded, a charge transfer occurs between regions of opposite charge. The macroscopic electric field is reduced below the field strength necessary for sustained current flow. A pause follows the lightning "unit" while the macroscopic field rebuilds. These volumes of charged cloud are not larger than the size of the physical cloud and are often the size of a convective cell. We then expect the radio frequency and optical pulses from a single "unit" to be confined to a region the size of one or two cells and occur over a time period followed by a distinct pause. In a mesoscale convective complex we will expect some discharges to progress through several cells and to continue for a longer than average duration. However, even in these cases, there should be a time and space interval over which pulses are occurring followed by a pause. This pattern of spatial and temporal activity followed by inactivity will form clusters in time and space. It is these basic clusters, or units, of lightning that we are attempting to find.

One way to detect the lightning clusters in the three systems is to group the data in time and space and see where the natural breaks in the data occur. To accomplish this, we will use the Nearest Neighbor Clustering Analysis (NNCA) [e.g., *Cover and Hart*, 1967]. The NNCA works by calculating the three (x, y, t) or four (x, y, z, t) dimensional distance between each data point and then clustering the closest two points. This is called the Nearest Neighbor Distance (NND). The algorithm then measures the three or four-dimensional distance between the centroid of the first cluster and all the other points. The closest two points (either two points or the first cluster and another point) are then grouped together. This continues until all points are in a single cluster. The NND table is then plotted and examined for slope changes. If there is a natural division in the clustering distance, it will show as a change in the NND slope. If the basic unit of lightning in the datasets can be measured, the clustering analysis should show slope changes at the boundaries between the lightning units.

One problem is how to fold the time dimension into the "distance" calculations. Obviously, different time conversion factors can greatly affect the definition of the nearest neighbor. A legitimate estimate of the conversion factor is the speed at which the initial lightning streamers

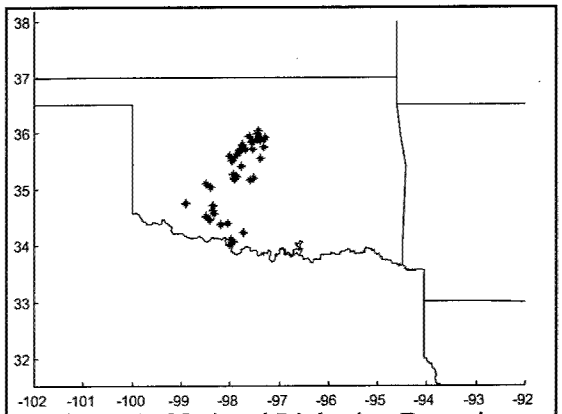


Figure 1. National Lightning Detection Network (NLDN) data for this study. There were 46 flashes during the time of the LIS overpass within the range of the LDAR system.

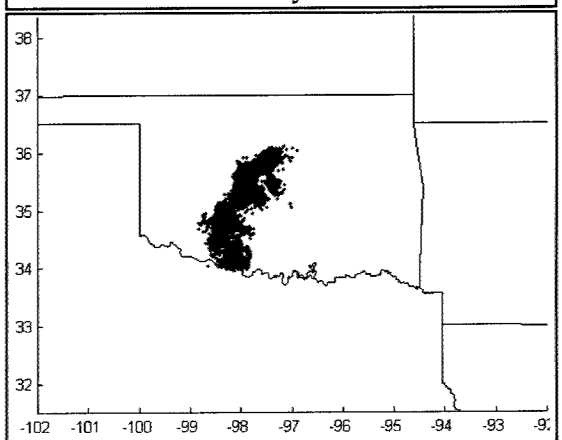


Figure 2. Lightning Detection And Ranging (LDAR) data for this study. There were almost 64,000 pulses during the LIS overpass.

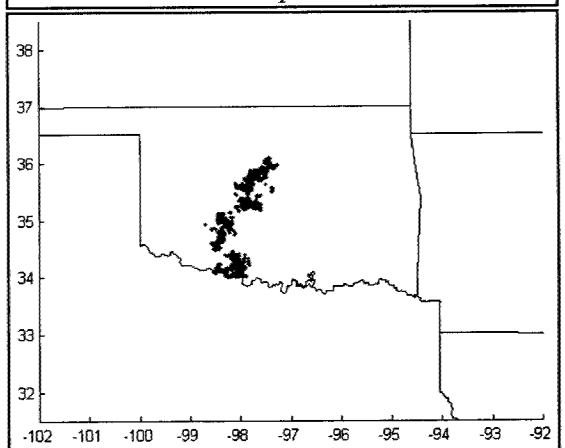


Figure 3. Lightning Imaging Sensor (LIS) data for this study. There were over 3000 groups within the range of the LDAR system for this overpass.

propagate within the cloud. For this analysis, we have chosen a range of speeds from 2.2 x$10^4$ $ms^{-1}$ to 2.2 x $10^5$ m $s^{-1}$. These speeds cover the average speed of horizontal lightning propagation found by *Proctor et al.* [1988] to the typical values for initial streamers [e.g., *Proctor*, 1981; and *Mazur and Rust*, 1983]. With these values, we can convert the time difference between pulses into equivalent "distances".

RESULTS

The first results are shown in Figure 4. The first difficulty in comparing the data sets is the vast differences in data volume and pulse rates. The LDAR dataset can have over 2000 pulses in a single second while the NLDN data set will have at most 2 flashes per second. The LIS dataset falls in between the LDAR and NLDN pulse counts. This will make it difficult to find a common lightning unit between the three systems.

We will calculate the NND plots for each of the three systems using three time conversion values, 2.2 x $10^4$ m $s^{-1}$, 7.0 x $10^5$ m $s^{-1}$, and 2.2 x $10^5$ m $s^{-1}$. These three values cover the range of possible horizontal lightning propagation speeds. The plots for the different time conversion factors will illustrate the time dependence of the lightning unit.

The plot of LDAR NND is shown in Figure 5. The major feature is the almost constant slope in the central part of the NND curve and the almost vertical slopes at the two ends. The lower drop-off is due to dataset granularity while the upper part is the indication of the lightning unit size of around 3-5 km. The time equivalent for the 3-5 km distance is in a range from 22 ms to 150 ms.

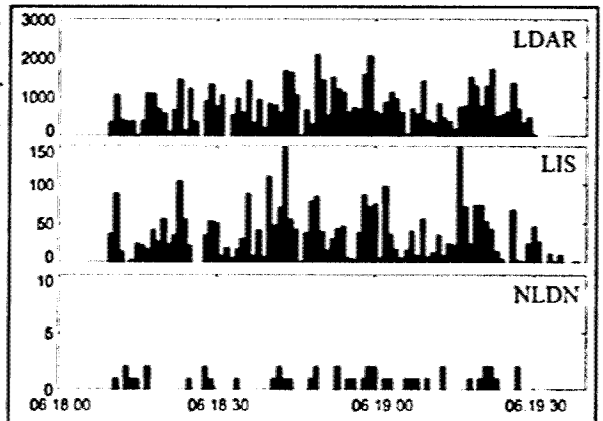


Figure 4. Time series of the LDAR, LIS, and NLDN data for this study. Note the differences in the scales (3000 for LDAR, 150 for LIS, and 10 for NLDN) of the plots.

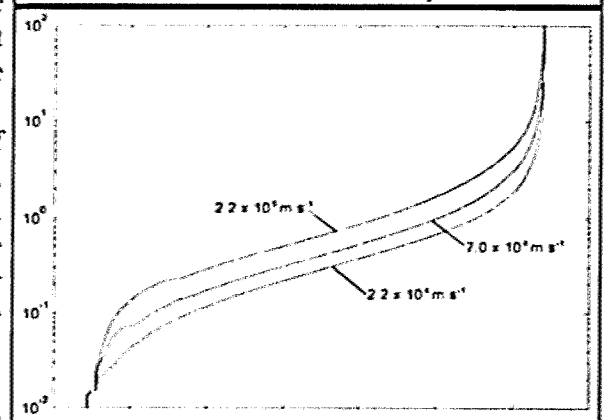


Figure 5. Nearest Neighbor Distance (NND) plot for the LDAR data using three different time to distance scale factors. The vertical scale is in km while the horizontal axis is counts. The top/leftmost curve was developed using 2.2 x $10^5$ m $s^{-1}$ as the conversion while the center curve was developed using 7.0 x $10^5$ m $s^{-1}$ as the time conversion factor. The bottom/rightmost curve was developed using 2.2 x $10^4$ m $s^{-1}$ as the time conversion.

The plot of the NLDN NND is shown in Figure 6. The difficulty in interpreting this plot is the lack of data. Since only flashes were analyzed, the resulting data is too coarse to effectively determine a lightning unit for the NLDN data (other than the flash). Note that there were no NNDs of less than 10 km (0.3 s) for the NLDN dataset.

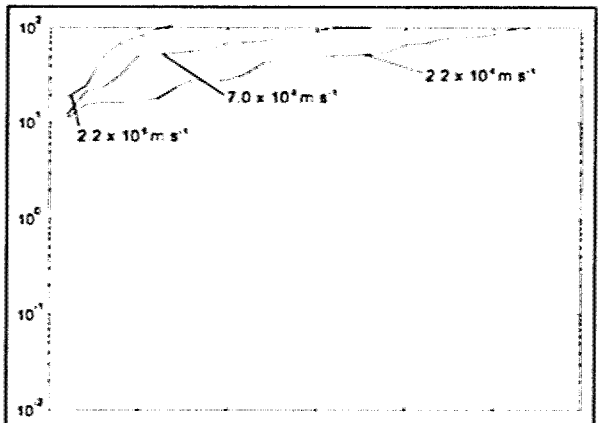


Figure 6. NND plot for the NLDN data using the same three different time to distance scale factors as in Figure 5. The vertical scale is in km while the horizontal axis is counts.

The plot of LIS NND is shown in Figure 7. The major feature again is the almost constant slope in the central part of the NND curve and the almost vertical slopes at the two ends. The lower drop-off is

due to the LIS dataset granularity while the upper part is the indication of the lightning unit size of around 7-12 km. The time equivalent for the 7-12 km distance is from 55 ms to 320 ms.

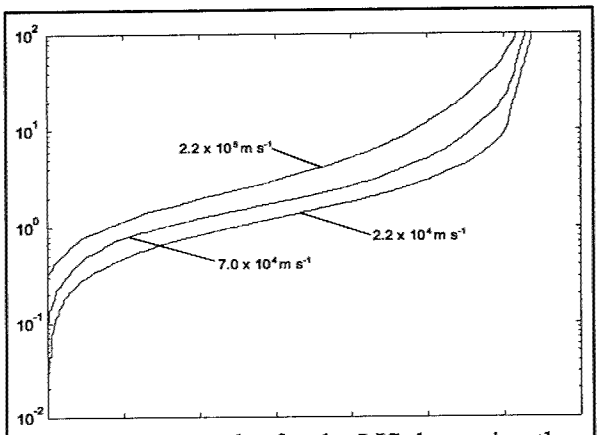


Figure 7. NND plot for the LIS data using the same three time to distance scale factors as Figures 5 and 6. The vertical scale is in km while the horizontal axis is counts.

## CONCLUSIONS

The three NND curves for the slowest time to distance conversion speed are plotted together in Figure 8. The NLDN does not indicate any clustering, however, the resolution of the NLDN dataset used for this study may be too coarse to indicate the lightning unit. This conclusion is supported by the results of the LDAR and LIS analysis. Both the LDAR and the LIS datasets, however, do show a break in the clustering around 3-7 km. This cluster would correspond to a lightning unit scale size of 3-7 km with a time scale of 150-330 ms. The LIS data may be limited by the pixel dimension of ~5 km indicating that the lightning unit scale size may be nearer the 3 km value found in the LDAR dataset. Since neither system's time resolution is close to the time scale found in this analysis, setting the time scale of the lightning unit to 150-330 ms would seem appropriate.

From this analysis, a typical unit of lightning extends spatially around 3-7 km and temporally around 150-320 ms. Others have found similar lightning time scales [e.g., *Malan*, 1956]. The spatial scales can be used in the analysis of lightning pulses detected by systems such as the LDAR and LIS.

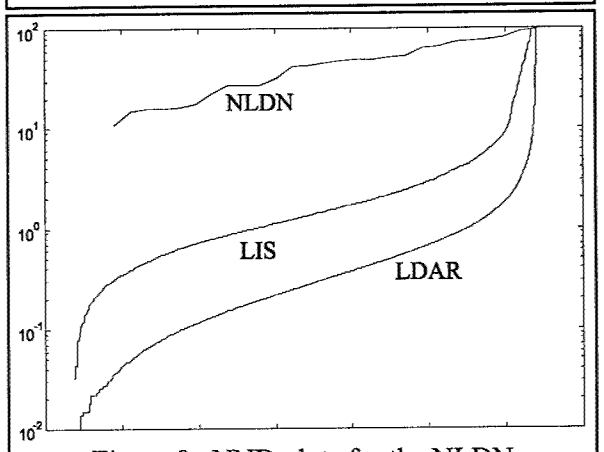


Figure 8. NND plots for the NLDN (top/leftmost), LIS (center), and LDAR (bottom/rightmost) data using the lowest time to distance scale factor of 2.2 x $10^4$ m $s^{-1}$. The vertical scale is in km while the horizontal axis is counts.

## REFERENCES


Cover, T. M., and P. E. Hart, Nearest neighbor pattern classification, *IEEE Trans. Information Theory*, **IT-13**, 21--27, 1967.

Malan, D. J., The relation between the number of strokes, stroke intervals, and the total durations of lightning discharges, *Geofis. Pura Appl.*, **34**, 224-230, 1956.

Mazur, V., and W. D. Rust, Lightning propagation and flash density in squall lines as determined with radar, *J. Geophys. Res.*, **88**, 1495--1502, 1983.

Orville, R. E., and A. C. Silver, Lightning ground flash density in the contiguous United States: 1992--95, *Mon. Weather Rev.*, **125**, 631--638, 1997.

Proctor, D. E., VHF radio pictures of cloud flashes, *J. Geophys. Res.*, **86**, 4041-4071, 1981.

Proctor, D. E., R. Uytenbogaard, and B. M. Meredith, VHF radio pictures of lightning flashes to ground, *J. Geophys. Res.*, **93**, 12683--12727, 1988.

# Session III:

# Lightning Detection and Protection

# COMPARISON OF GROUND-BASED 3-DIMENSIONAL LIGHTNING MAPPING OBSERVATIONS WITH SATELLITE-BASED LIS OBSERVATIONS IN OKLAHOMA

Ronald J. Thomas, Paul R. Krehbiel, William Rison, Timothy Hamlin
New Mexico Institute of Mining and Technology, Socorro, New Mexico, U.S.A.

Dennis Boccipio, Steve Goodman, Hugh Christian
Global Hydrology and Climate Center, Huntsville, Alabama, U.S.A.

ABSTRACT: 3-dimensional lightning mapping observations obtained during the MEaPRS program in central Oklahoma during June, 1998 have been compared with observations of the discharges from space, obtained by NASA's Lightning Imaging Sensor (LIS) on the TRMM satellite. Excellent spatial and temporal correlations are observed between the two sets of observations. Most of the detected optical events were associated with intracloud discharges that developed into the upper part of the storm. Cloud-to-ground discharges that were confined to mid- and lower-altitudes tended not to be detected by LIS. Extensive illumination tended to occur in impulsive bursts toward the end or part way through intracloud flashes and appeared to be produced by energetic K-changes that typically occur at these times.

## INTRODUCTION

A deployable, 3-dimensional Lightning Mapping System (LMS) developed at New Mexico Tech was initially operated in central Oklahoma during June, 1998 as part of the MEaPRS program [Krehbiel et al., 1998]. A number of interesting storms were observed, including several supercell storms, a tornadic storm, and storms along convective lines. One storm on June 11 was observed by NASA's Lightning Imaging Sensor (LIS) on board the TRMM spacecraft [Christian et al., 1992]. The overpass was at 06:18 UTC, about an hour after local midnight as a convective line passed by the southeastern edge of the LMS network. Simultaneous observations were obtained over a 90 second period of the spatial and temporal development of lightning discharges inside the storm and of the illumination of the upper part of the storm cloud by the lightning.

## OBSERVATIONS

Figure 1 shows an overview of the lightning activity detected by the LMS during a 30 second time interval while the satellite was passing directly overhead. A number of lightning discharges were occurring every second within the extensive storm system. The LMS detects impulsive RF events during successive 100 $\mu$s time intervals and is typically able to locate several hundred to 2000 events or more per flash. Over 37,000 events were located during the time interval of Figure 1. The rectangular contours show the outline of detected luminosity by the LIS during the same time interval. The LIS images are obtained every 2 ms, with individual pixels of the CCD corresponding to an area 4-7 km on a side at the ground. A total of 7500 pixel illuminations occurred during the 30 second period, which fully covered the electrically active part of the storm.

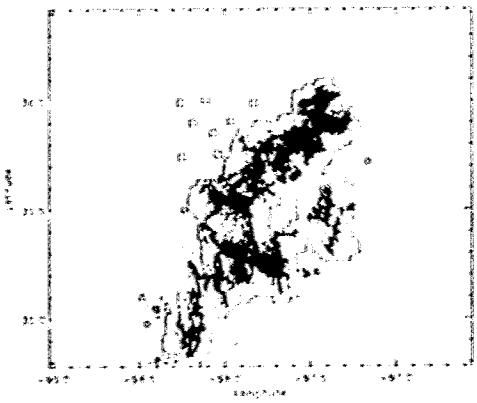

Figure 1: Overview of the storm, showing the correlation between LMS-detected lightning activity (dots) and the outline of the LIS-detected cloud illumination (rectangular contour lines). Individual LMS stations are denoted by squares and covered an area about 60 km in diameter. The map covers an area about 200 km on a side; Oklahoma City is in the center right of the map.

Figure 2 shows an expanded view of the observations during a 4 second time interval containing a total of six intracloud and cloud-to-ground lightning discharges. Optical illumination is detected above the intracloud (IC) lightning flashes, whose sources and channels extended up 11-12 km altitude MSL, but little or no luminosity is detected from the cloud-to-ground (CG) discharges whose sources were typically confined below 7 km altitude. This is illustrated in the plan view of panel 2*e* (see for example the CG discharges in the lower left of the plan view), and in the vertical cross-sections of panels 2*c* and 2*f* and in the height vs. time plot of panel 2*b*. In the latter panels the occurrence of detected luminosity is indicated by + symbols.

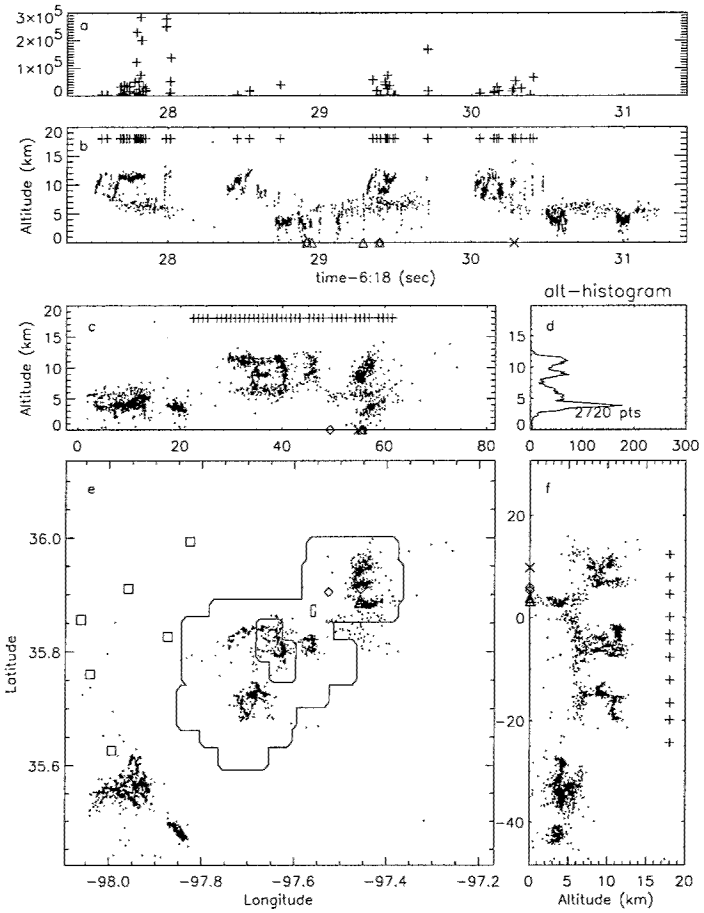


Figure 2: An expanded view of four seconds of observations, illustrating how the satellite-detected luminosity is associated primarily with intracloud lightning discharges that develop into the upper part of the storm and much less or not at all with cloud-to-ground discharges. The interior rectangular contour in panel *e* is twice the intensity of the outer contour and is centered above a classic bilevel IC discharge. Panels *c* and *f* show vertical projections as viewed from the south and west, respectively; these panels also show the horizontal scale in km. Detected LIS events are denoted by + symbols above the top of the lightning activity. Shown along the abscissa are the locations and times of negative (△) and positive (×) strokes to ground located by the National Lightning Detection Network (NLDN). Panel *d* shows a histogram of the radiation source heights and the total number of located points. Panel *a* shows the integrated light intensity observed by LIS.

Figure 3 shows detailed views of the bilevel discharge of Figure 2. As is typical of such discharges, detected breakdown began at about 8 km altitude and quickly progressed up to 11–12 km altitude along a nearly vertical channel, then developed horizontally at along the upper and lower levels. This agrees well with the observations of Shao and Krehbiel [1996], who correlated the lower and upper levels with the main negative and upper positive storm regions, respectively. The first detected luminosity occurred at the end of the initial upward development and then again immediately following brief renewed activity at the top of the channel. Virtually all of the subsequent luminosity was associated with further development of the upper

level channels but not with the continued activity in the lower level. The strongest integrated light emissions occurred during the last half of the flash, when the LIS observations showed many pixels to be impulsively illuminated over the entire cloud region. These events were undoubtedly associated with K-changes that are known to occur along the entire extent of the channels in the later stages of IC flashes [e.g., Shao and Krehbiel, 1996]. Similar (but weaker) K-events probably terminated the initial upward development sequence and produced the early luminosity pulses.

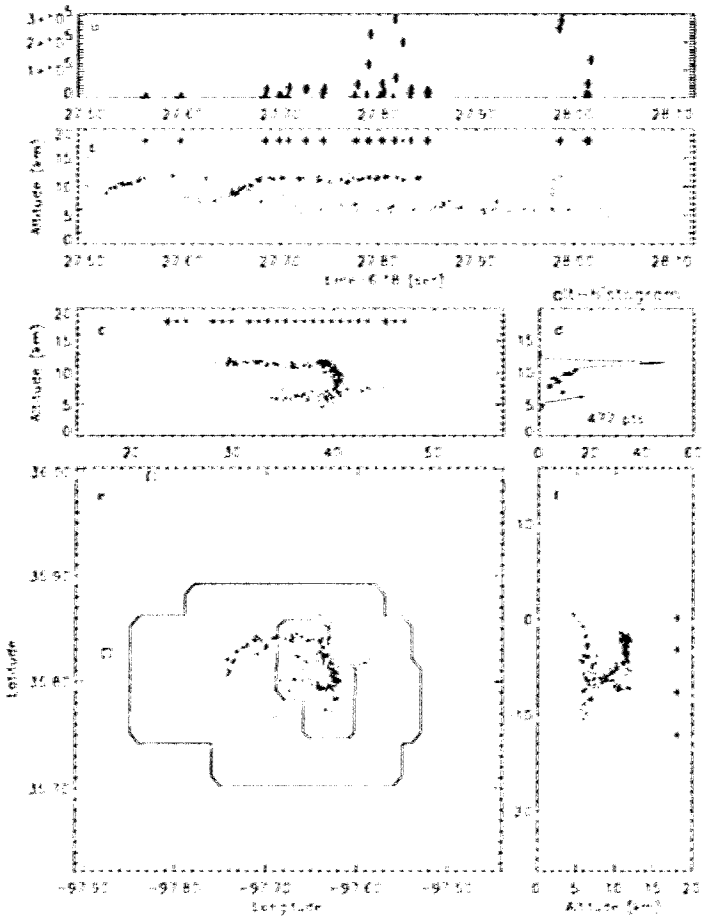

Figure 3: Detailed observations for the classic bilevel intracloud discharge of Figure 2, further showing the association of satellite-detected luminosity with upper level activity. At the time of the overpass the satellite was traveling almost directly from west to east, causing the illuminated pixels to be displaced in that direction (panel *c*) but to lie on top of each other in the north-south vertical cross-section (panel *f*).

Figure 4 shows observations for a more complex, hybrid flash. The flash began as a normal CG discharge, producing a sequence of negative polarity strokes to ground. This activity continued for 0.7 second but was confined below 7 km altitude and sufficient luminosity was not produced at the top of the cloud to be detected by LIS (panel *b*). At 49.2 seconds an upward-developing IC component began that was immediately detected by the LIS. The optical activity intensified during more intense upward breakdown around 49.5 seconds and then became impulsive in nature, associated with final, impulsive upward breakdown events. The last optical event was by far the most energetic, and simultaneously illuminated a number of the LIS CCD pixels out to the edges of the discharge region. It was undoubtedly caused by a similarly energetic, final K-change. Although the low-level activity continued for another 0.4 seconds, no additional luminosity was detected. (Also seen in the vertical cross-sections and histogram is a third level of activity at about 4 km altitude just below the negative charge. The LMS data show this tri-level structure in numerous discharges both in Oklahoma and New Mexico; the third level appears to be associated with lower positive charge in the storm.)

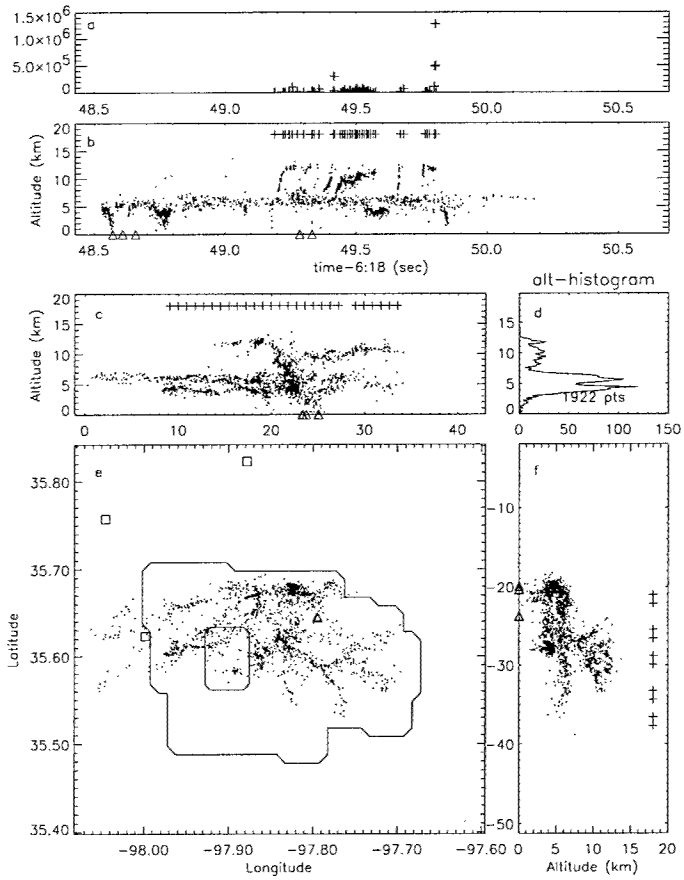


Figure 4: Same as Figure 3, except for a horizontally extensive, hybrid cloud-to-ground and intracloud discharge.

## SUMMARY AND DISCUSSION

The results of this study show that space-borne optical observations of lightning from directly above clouds will primarily or predominantly detect intracloud discharges into the upper part of the cloud. The occurrence of such discharges is indicative of deep convection in the atmosphere and the areal and temporally integrated light intensity would provide a good measure of the convection. At the same time, the luminous events are indicative of high-temperature, impulsive processes that will be important sources of odd nitrogen compounds at high altitudes in the atmosphere, which in turn are very important to the ozone chemistry [Coppens et al., 1998]. The combination of satellite- and ground-based lightning observations valuably complement each other and give a complete picture of the lightning and storm activity.

## REFERENCES


Christian, H.J., R.J. Blakeslee, and S.J. Goodman. "Lightning imaging sensor (LIS) for the earth observing system", *NASA TM-4350*, Available from Center for Aerospace Information, P.O. Box 8757, Baltimore Washington International Airport, Baltimore, MD 21240, 44 pp, 1992.

Coppens, F., A. Bondiou-Clergerie, and I. Gallimberti, Theoretical estimate of NOX production in lightning corona, *J. Geophys. Res.*, 103, 10769-10785, 1998.

Krehbiel, P., R. Thomas, W. Rison, T. Hamlin, J. Harlin, and M. Davis, Lightning mapping observations during MEaPRS in central Oklahoma, Fall Ann. Mtg. Amer. Geophys. Union, 1998.

Shao, X.M., and P.R. Krehbiel, The spatial and temporal development of intracloud lightning, *J. Geophys. Res.*, 101, 26641–26668, 1996.

# TRMM/LIS observations of Lightning Activity

Zen Kawasaki Sachi Yoshihashi

Department of Electrical Engineering
Graduate School of Engineering, Osaka University
Yamada-Oka 2-1, Suita Osaka 565 0871, JAPAN

**Abstract.** Lightning Imaging Sensor (LIS) which is equipped on Tropical Rainfall Measuring Mission satellite (TRMM) is introduced in the report. It is noticed that LIS consists of an optical detection system with telescope lens and CCD matrix, and a data processing unit. The specification of LIS is given from the aspects of both hard ware and software. The preliminary observation results are presented and discussions from meteorological aspects are shown. The comparison with ground base measurement for the evaluation of LIS function is also shown.

## 1 Introduction

Lightning discharge is a phenomenon of neutralization of stored electric charges inside thundercloud. Neutralization occasionally occurs between a thundercloud and the ground, and we call it cloud to ground lightning. The other type neutralization between thundercloud and thundercloud or inside one thundercloud may often happens, and we call it cloud lightning. In both cases neutralizations are achieved by long distance electric breakdown over several kilometers. Once we have electric breakdown, or we can call it electric discharges, we have strong optical emission called lightning, terrible sound called thunder, and electromagnetic radiation.

The history of the investigation of lightning discharges is originated to B. Franklin, who carried out the experiment of a kite nearly 250 years ago. The real scientific investigation may start after the well known discussion between Simpson and Wilson on "Charge distribution inside the thundercloud" during 1930's. There are many reports and papers form aspects of optical signal observations, thunder observations, and electromagnetic observations.

We know the fair weather electric field intensity (100Volt/m) which may depend on the potential difference between the ionosphere and the ground. Wilson believed that the electric potential of the ionosphere to the ground is contributed by lightning activity distribution and global circuit . Brooks estimated 100 flashes per second are required to sustain the ionospheric potential. Recently the problem of global warming becomes one of our current topics, and related scientists are interested in revealing the global lightning activity and its distribution, because it can be one of indicators of the global warming. For these background LIS is designed and equipped on TRMM.

In this paper we introduce LIS and preliminary results of its observations. We also present comparison LIS and ground base measurement to evaluate the LIS function.

## 2 Specification of LIS

LIS has been designed by a team of H. Christian (NASA) to achieve optical observations of lightning activity from space. It is equipped on TRMM satellite, and it has been operated since November 1997 when TRMM satellite was launched successfully. LIS consists of two main, and one of main systems is CCD matrix with telescope lens. The other is the real time data processing unit on board.

The history of lightning observations from space itself is rather long, and in early 60's when human beings obtained the capability of a spacecraft the project named OSO-2 was conducted. The optical observations and electromagnetic wave observations are well known. The former owns the disadvantage of the difficulty to detect lightning activity in the daytime hemisphere because the intensity of solar

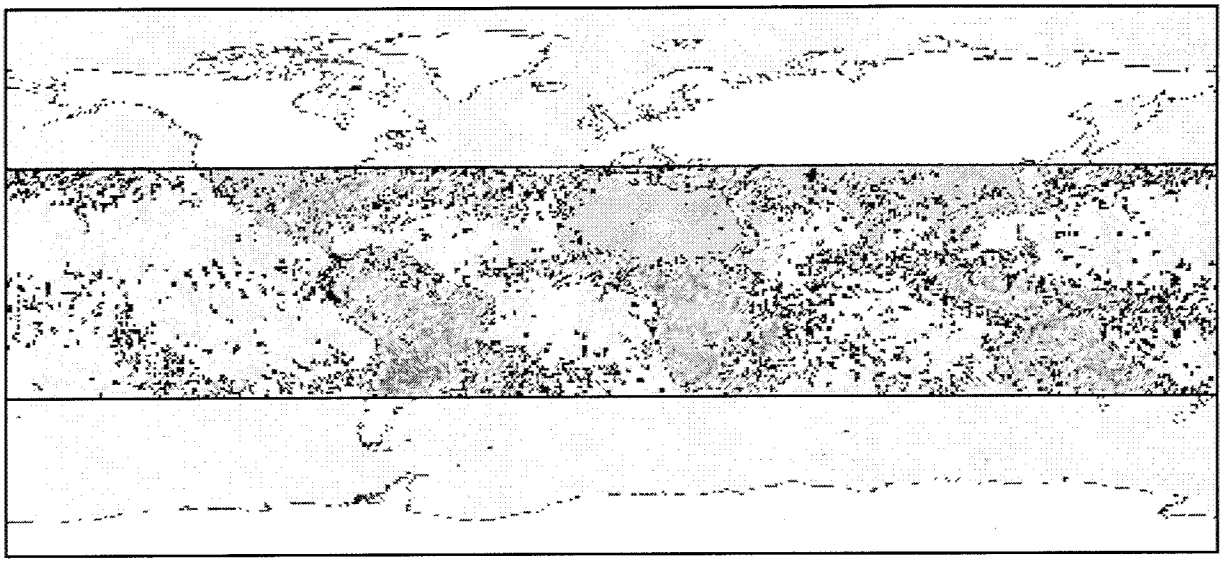

Fig. 1 LIS Observations(From December 1997 to February 1998)Color scale is relative and absolute calibration is on going. (by courtesy of Hugh Christian)

optical emission is much stronger than that of lightning. On the other hand the disadvantage of the latter is the lower spatial resolution than the former.

The requirement to reveal the global distribution of lightning activity, seasonal variations and diurnal variations is increasing year by year, and that is why we are forced to have observations of lightning activity for both day and night.

It is known that the temperatures of lightning channels are normally between 20000K and 30000k. That means the lightning channel is believed to be plasma, and we have many atomic line optical emissions. We know lines of H$\alpha$(656.3nm), OI(1)(777.4nm) and NI(1)(868.3nm) among various atomic line emissions are intense. Hugh and his staff pay their attention on OI(1) line and designed LIS. To detect the emission by lightning discharges in extremely intense back ground signals due to solar emission, LIS is carefully designed with optical filter of its band width 1 nm. LIS owns the 8.5km spatial resolution and 2mseconds time resolution with 128 by 128 CCD matrix and telescope lens. The threshold level for lightning discharge detection is given as 4.7J/m/m/sr by H. Christian and S. Goodman, and they expect 90 % of detection efficiency.

## 3 Comparison LIS observations with ground base measurements

Figure 1 shows the summary of LIS observations for first three month. Since three months lightning flashes are integrated, it may be considered to be the statistically siginificant lighting activity of southern hemisphere summer seasons. We can recognize more lightning activities in southern hemisphere than northern hemisphere. We recognize more lightning activities on lands than those over the ocean. Hugh concludes that "Lightning likes lands more than water." and this feature is consistent with the previously obtained characteristics by former satellite observations, like DMSP.

Figure 1 implies an additionally interesting feature. We can discriminate the line like lightning activity at middle latitude. In other words the lightning activity at middle latitude, where we have occasionally lightning activities during winter, seems to cross the ocean. If we think about the thunderstorm near Japan, we know that the local low pressure system which is formed on the sea of Japan develops rapidly during traveling to north east with thunderstorm activity. It has decaying stage when it reaches north east Pacific Ocean. Since our knowledge about a local low pressure system and its thunderstorm activity is limited near Japan, the LIS observations presents us a new discovery.

Figure 2 shows a comparison of one of LIS observations with SAFIR observation. SAFIR is an interferometric lightning monitoring system, and it has been operated since 1991 as a cooperation between Kansai Electric Power Company (KEPCO) and Osaka University. The data in Figure 2 are

captured at 4:14'15" (UTC) on February 12, 1998. The location of a flash captured by SAFIR and locations of LIS events are coincident well. If we compare the location of a flash which are derived by SAFIR and LIS, we find the exact coincident form the aspect of location. The activity during winter thunderstorm is relatively intermittent, and results in Figure 2 make us confirm the capability of LIS for intermittent lightning activity.

Figure 4 shows a comparison between LIS and SAFIR for a summer thunderstorm. The data are obtained on August 12, 1998, and those are the integration for 105 seconds. We can conclude both show the good correspondence qualitatively. To have further scientific discussions in terms of meteorology and climatorogy we need the further observations.

## 4 Conclusions

We showed the interpretation of first three months observations from the aspects of climatorogy. We also showed the comparison of LIS observations with ground base measurement to evaluate LIS capability. The LIS function can be confirmed from the aspects of the case study. Though fourteen months have passed after TRMM satellite launching, and quality controlled data have been released to the related scientists, we need more data accumulation to get the scientifically significant conclusions from the view points of meteorology and climatorogy. We also need further evaluation and improvement of LIS function for coming possible project. The great success of LIS may sugest us the geostatinary LIS operation to realize the operational system.

Followings are the tentative conclusion for 14 months observations. "Lightning likes land more than water" and "Winter thunderstorm activity may cross the ocean."

## References

C.E.P. Brooks, The Distribution of Thunderstorm over the Globe, Geophys. Mem. No.24, Air Ministry, Meteorological Office, London 147 ,1925.

H.J. Christian, R. J. Blakeslee and S. J. Goodman, Lightning Imaging Sensor (LIS) for the Earth Observing System, NASA Technical Memorandum 4350 , 1992.

J. A. Vorpahl and J. G. Sparrow, Satellite Observations of Lightning, Science, 169, 860-862 ,1970.

M. A. Uman, Lightning, Lightning Spectroscopy, 138-180, McGraw-Hill ,1968.

H.J. Christian, and S. J. Goodman, Optical Observations of Lightning from a high altitude Airplane, J. Atmos. Ocean. Tech., 4, 701 ,1987.

URL http://thunder.msfc.nasa.gov/lis.html

Z-I. Kawasaki, Lightning Activity in Darwin and LIS Observations, 32nd Scientific Assembly of COSPAR, Nagoya, July 12-19 ,1998.

Z-I. Kawasaki, K. Yamamoto, K. Matsu-ura, P. Richard, T. Matsui, Y. Sonoi and N. Shimokura, SAFIR operation and evaluation of it's performance, Geophysical Research Letters, 21, 12, 1133-1136 ,1994.

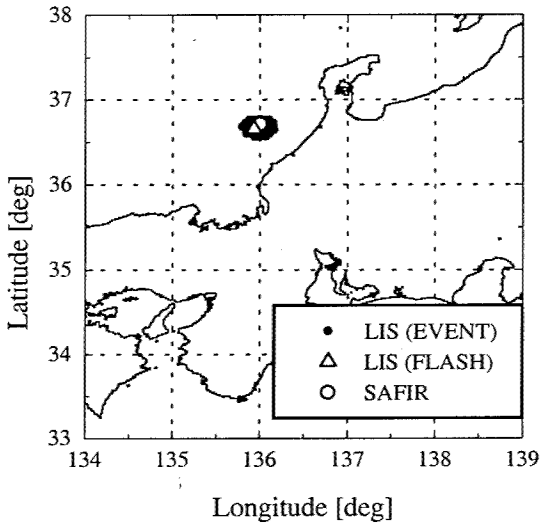


Fig. 2 Comparison of one of LIS observations with SAFIR observation. (February 12, 1998. 4:14715" (UTC))

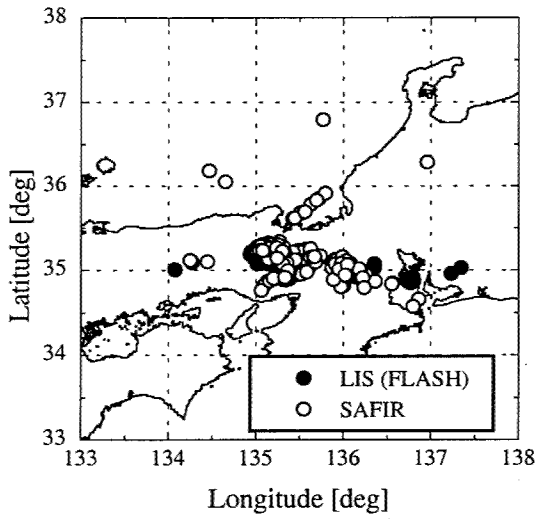


Fig. 3 Comparison of one of LIS observations with SAFIR observation. (August 12, 1998.)

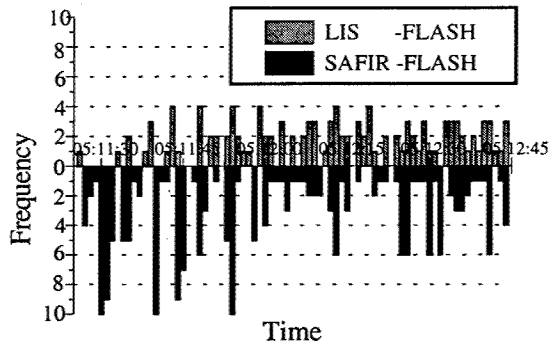


Fig. 4 Time sequence of flashes of flashes detected by LIS and SAFIR

# TOWERS, LIGHTNING AND HUMAN AFFAIRS

L.G. Byerley III[1], W.A. Brooks[2], R.C. Noggle[2], K.L. Cummins[2]

[1]Lightning Protection Technology, Tucson Arizona, U.S.A.
[2]Global Atmospherics, Inc., Tucson, Arizona, U.S.A.

ABSTRACT: The number of tower structures to support cellular-telephone and wireless communications in North America has grown dramatically in the last ten years. In addition to cell-phone antenna towers, there are hundreds of thousands of towers with heights between thirty and two hundred meters. These towers include ham radio towers, water towers, microwave repeater and VHF communication towers. Tall towers are in some cases erected in residential and industrial areas. Some municipalities now lease public spaces for tower sites. Measurements of lightning strikes to towers between 30 and 200 m in height have shown that such towers increase the incidence of lightning at the tower location and that the probability of lightning to a tower increases roughly as the square of the tower height. Recent work has characterized the multiple ground attachments of natural, negative discharges and the electromagnetic environment near the ground strike point. We review the tower/lightning problem in light of these findings and relate a recent case of multiple lightning incidents at a water tower in which it appears that the tall structure is a land-use-nuisance to people nearby. We use lightning ground flash density data to show the skew of lightning incidence near towers of 300 m or more in height. We review mitigation measures for some lightning effects at towers.

## INTRODUCTION

It is common knowledge that people seeking shelter near isolated trees increase their risk of lightning death or injury. By the same token, lightning strikes isolated towers more frequently than it strikes undisturbed ground in the same area. For this reason, towers have provided productive sites for lightning laboratories during the past century. For example, *Idone, et al.*, [1998] report that a radio tower was struck by five flashes in a single storm, an occurrence that would be extraordinarily unlikely in the same small area without the tower. Studies of lightning to instrumented towers of various heights in Europe by *Muller-Hillebrand* [1960], *Szpor et al.*, [1964], and *Popolansky* [1965] show that the probability of lightning striking towers of moderate height increases roughly as the tower height squared. *Golde* [1975] refers to the steep increase in probability of lightning strikes with tower height as "law."

Here we are mainly concerned with the increase in lightning strike frequency associated with towers of moderate height (10 - 200 m) and the attendant increase in risk such towers pose to human activities nearby. An anecdote from rural North Carolina is instructive. In the Fall of 1998 near Murfreesboro, NC, a 42 m tall water tower was erected about 45 m from a farmhouse situated on a one acre plot in a large open area of rolling farmland. The farmhouse had been occupied by the same family for over ten years during which time no lightning damage was experienced. After the tower was erected, five separate discharges near the house occurred over a period of five months causing the deaths of two trees, a fire in electrical equipment, complete destruction of all phone wiring, and damage to electrical fixtures. The central thesis of this paper is that a tower of moderate height may serve to concentrate lightning and lightning damage nearby.

## LIGHTNING TO TOWERS

Tower measurements summarized by *Mousa* [1986] show that the majority of discharges to towers of moderate height on flat terrain at low altitude are normal with a downward stepped leader followed by an upward positive connecting streamer and return stroke. When a tower is situated at higher altitude, or on a ridge or hilltop, the number of flashes initiated by long positive streamers from the tower increases, and therefore the total number of lightning strikes to the tower increases. The towers on Mt. San Salvatore with a height of 70 m above the mountain top [*Berger*, 1967], initiated the majority of discharges that

occurred to them as did the Empire State Building (410 m) at sea level [*McEachron*, 1939].

The mechanism(s) responsible for increasing the incidence of lightning strikes to tall towers is not fully understood. *Standler* [1975] showed how tall, conducting objects enhance the electric field and make it easier for an upward-propagating streamer to meet the downward-propagating stepped leader. *Uman* [1987] discussed measurements of striking distances, showing about an order of magnitude separating the shortest and longest final jumps. *Golde* [1978] suggested that positive space charge generated by the high electric field at a tower and carried away from the tower may facilitate lightning attachment from greater distances. While we do not have consensus regarding the magnitude of, and mechanisms for, increased incidence of lightning to towers, it is an indisputable fact, known to lightning researchers for more than 50 years, that towers suffer more lightning strikes than the undisturbed ground. Further, no measurements exist to refute the basis for Golde's *law*.

## THE TOWER LIGHTNING ENVIRONMENT

Because human activities take place near many towers of moderate height, it is important to understand the tower lightning environment and the electrical effects that accompany lightning discharges to towers. Most discharges to towers of moderate height in typical metropolitan settings are normal; therefore, the discharge processes and lightning effects which occur close to the ground strike points of natural and triggered lightning, occur at towers also.

Even if a tower receives all of the direct lightning current, nearby objects can be significantly impacted by the strike as follows. Near a tower of moderate height we expect first return strokes to be preceded by streamers launched upwards from nearby grounded objects such as trees, buildings and even people. [*Golde*, 1947]. Within a few tens of meters of a tower struck by lightning, we expect electrostatic field changes of 100,000 V/m and greater, with magnetic field changes of 300 A/m and greater [*Fisher and Schnetzer*, 1994]. We expect the time scale for strong radiation to be on the order of a fraction of a microsecond [*Willett, et al.*, 1998]. Long, high-current ground surface arcs sometimes emanate from the bases of towers struck by lightning [*Fisher and Schnetzer*, 1994]. Injection of lightning current into the ground at a tower base causes potential differences to appear in the soil around the tower, driving surge currents in buried conductors, and causing voltage differences to appear between physically separate or poorly bonded metal objects.

As with other natural negative flashes, we expect multiple ground strike points to occur in some fraction of flashes to towers of moderate height [*Thottappillil, et al.*, 1992] thereby increasing the lightning stroke density around the tower. Near a struck tower, electromagnetic interference effects may increase because return stroke current velocity is near the speed of light in a metal tower. Therefore, the lower portion of a discharge to a tower radiates more strongly than would the same section of discharge channel in air. Finally, we expect some combination of these nearly simultaneous effects to increase in frequency near a tower relative to the frequency on undisturbed ground.

## LIGHTNING LOCATION DATA FOR TOWERS OF MODERATE AND TALL HEIGHT

Following *Diendorfer and Schulz* [1998], who used lightning location data to find towers of moderate height on mountaintops in Austria, we searched for approximately twenty towers of moderate height situated on relatively flat terrain in southern Arizona and central New Mexico using five-year averaged NLDN flash density data. For each tower studied, we obtained a GPS location. We failed to find these towers as local increases in ground flash density. Our failure to find higher lightning incidence at towers of moderate height in southern Arizona and central New Mexico may be due to the moderate to low ground flash density around the towers, and the selection of towers on flat terrain. In addition, the larger than average location errors in the "border" region of the NLDN (median accuracy of 0.5 - 1.0 km) may scatter measured lightning locations, thus obscuring any flash density enhancement.

The failure to locate towers of moderate height in the archived NLDN data, spurred us to look for taller towers in a region of the NLDN where the average location errors are on the order of a tower height. For numerous tall towers near Tulsa and Oklahoma City, we obtained GPS fixes or locations registered with

the FCC. At these towers we found increases in flash density, even though it is unlikely that the NLDN detected the tower-initiated first strokes.

Again following *Diendorfer and Schulz* [1998], who analyzed the signal strengths of discharges near mountaintop towers of moderate height in Austria, we also found that discharges nearest tall towers have larger than average peak field strengths compared to discharges fixed farther away. Greater peak field strengths from lightning to towers can be produced by higher return stroke velocity in the metal structures, by higher peak current, or by both. This fact suggests that towers of moderate height may be subjected to higher than normal peak current discharges with the attendant indirect effects. Neither the NLDN nor the Austrian network are capable of measuring the effect of faster current propagation in towers of moderate height because the radiation enhancement occurs on a time scale shorter than the minimum response time of the sensors. Figure 1 is an example of the increase in measured *stroke* density at a pair of tall (311 m) TV towers near Tulsa, Oklahoma. Figure 2 shows the decrease of flash density with distance around the same pair of towers.

## HISTORIC TOWER STRIKE FREQUENCIES AND MEASURED GROUND FLASH DENSITY

As a way of showing the increase in lightning risk near towers of moderate height, we compare tower strike frequency measurements from *McCann* [1944] and *Idone, et al.* [1998] with measured lightning ground flash density. In Table 1, N is the measured five-year ground flash density for the region around each tower, multiplied by four to account for the average number of strokes per flash and for the limited detection efficiency of the NLDN. For each N, we calculate the probability of a *stroke* falling in an area of 1000 $m^2$ and compare this to measured striking rates. The column "risk" is the ratio of measured striking rate to expected strikes per 1000 $m^2$. We assume that the corrected ground flash density measurements are roughly representative of recent history for each tower location. Even if large errors affect the comparison, these towers are clearly places of higher lightning risk.

| tower | h (m) | N (st/km$^2$/yr) | strokes/yr (McCann) | risk × |
|---|---|---|---|---|
| SUB-STATION PHILADELPHIA, PA | 24 | 10 | .2 | 20 |
| WHK CLEVELAND, OH | 91 | 10 | 1 | 100 |
| WADC AKRON, OH | 110 | 13 | 2.6 | 200 |
| WWSW PITTSBURGH, PA | 30 | 13 | .33 | 25 |
| LEXINGTON BLDG. BALTIMORE, MD | 107 | 10 | .38 | 38 |
| STACK GREAT FALLS, MT | 166 | 2 | 1.5 | 750 |
| CATHEDRAL PITTSBURGH, PA | 178 | 13 | 2.6 | 200 |
| RADIO TOWER (Idone, et al) ALBANY, NY | 210 | 8 | >10 (Idone) | 1250 |

(from McCann, 1944)

Table 1.

| | | | | | | |
|---|---|---|---|---|---|---|
| 3 | 9 | 5 | 12 | 5 | 20 | 11 |
| 7 | 9 | 12 | 13 | 9 | 8 | 19 |
| 17 | 11 | 5 | 29 | 8 | 9 | 5 |
| 12 | 9 | 13 | 24 | 22 | 5 | 17 |
| 13 | 7 | 8 | 15 | 9 | 12 | 13 |
| 9 | 12 | 8 | 8 | 11 | 3 | 16 |
| 8 | 4 | 5 | 5 | 5 | 5 | 4 |

KJRH KOTV N

Figure 1. Three year averaged stroke density around a pair of 311 m tall towers near Tulsa, OK. Grid is .5 km$^2$.

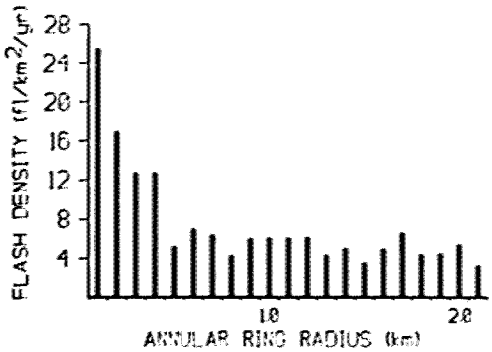


Figure 2. Five year averaged flash density in 0.1 km wide annular rings from midpoint between towers in Fig. 1.

## MITIGATION

Measures can be taken to reduce ground surface arcs and potential differences that arise in the soil around the base of a tower struck by lightning. *Schnetzer, et al.* [1995] showed that surface arcing at the ground terminus of triggered lightning discharges can be controlled with long horizontal ground electrodes. Equipotential grounding methods used for power substations can lessen shock hazards near the base of a tower.

Minimizing tower height and maximizing the distance between towers and people are two certain ways to reduce the effects of lightning at towers on people nearby.

CONCLUSIONS

Since it is certain that the lightning risk increases near towers of moderate height, this fact ought to be considered in the planning process for tower siting and construction, particularly in areas where lightning ground flash density and population density are high. We assert that people near towers of moderate height in regions of high flash density may be in places of higher lightning risk. Since local ground flash density varies across the United States by almost two orders of magnitude, so will the lightning risk posed by towers. Mitigation measures can be taken to reduce earth conduction effects near a tower. NLDN data provide useful analysis of lightning incidence to tall towers, but have limited utility for towers of moderate height on flat ground. The lightning environment near towers of moderate height is no less severe than that characterized near natural- and triggered-lightning flashes.

ACKNOWLEDGEMENTS: We are grateful for the editorial and research assistance of Yvette Banegas, and for the changes to the paper suggested by Ronald Standler.

REFERENCES

Berger, K., Novel Observations of lightning discharges: results of research on Mt. San Salvatore. *J. Franklin Institute*. **283**, 478--525, 1967.

Diendorfer, G., W. Schulz, Lightning incidence to elevated objects on mountains. *Proceedings of the 24th International Conference on Lightning Protection*, Birmingham, U.K., 173--175, 14-18 Sept. 1998.

Fisher, R.J., G.H. Schnetzer, M.E. Morris, Measured fields and earth potentials at 10 and 20 meters from the base of triggered lightning channels. Paper presented at the 22nd Int. Conf. on Lightning Protection, Budapest, 1994.

Golde, R.H., Occurrence of upward streamers in lightning discharges. *Nature*, **160**, 395--396, 1947.

Golde, R.H., *Lightning Protection*, Chemical Publishing Company, Inc., 42, 1975.

Golde, R.H., Lightning and tall structures. *Proc. Institution of Electrical Engineers*, **125**, 347--351, 1978.

Idone, V.P., D.A. Davis, P.K. Moore, Y. Wang, R.W. Henderson, M. Ries, P.F. Jamason, Performance evaluation of the U.S. National Lightning Detection Network in Eastern New York, *JGR*, **103**, 9057--9069, 1998.

Mousa, A., A study of the engineering model of lightning strokes and its application to unshielded transmission lines. Ph.D. Thesis, University of British Columbia, Vancouver, Canada, 1986.

McCann, G.D., The Measurement of lightning currents in direct strokes. *Trans. AIEE*, **63**, 1157-1164, 1944.

McEachron, K.B. Lightning to the Empire State Building. *J. Franklin Institute*, **227**, No. 2, 149-217, Feb. 1939.

Muller-Hillebrand, D., On the frequency of lightning flashes to high objects, A study on the Gulf of Bothnia. *Tellus*, **XII**, 444-449, 1960.

Popolansky, F., Study of lightning strokes to high objects in Czechoslovakia. English translation, *ERA Trans./IB 2291*, 1965.

Schnetzer, G.H., R.J. Fisher, R.J. Magnotti, 1995 Triggered lightning program: Temporary lightning protection experiments. *Report 96-01*, U.S. Army Armament Research Development and Engineering Center, Picatinny Arsenal, New Jersey, 1995.

Standler, R.B., The Response of Elevated Conductors to Lightning. Master's Thesis, New Mexico Institute of Mining and Technology, 1975.

Szpor, S., E. Wasilenko, J. Samula, E. Dytkowski, J. Suchocki, B. Zaborowski, Results of lightning stroke registrations in Poland. *CIGRE Rep. 319*, 1964.

Thottappillil, R., V.A. Rakov, M.A. Uman, W.H. Beasley, M.J. Master, D.V. Shelukhin, Lightning subsequent-stroke electric field peak greater than the first stroke peak and multiple ground terminations. *JGR*, **97**, 7503--7509, 1992.

Uman, M.A., *The Lightning Discharge*, Academic Press, -101, 1987.

Willett, J.C., E.P. Krider, C. Leteinturier, Submicrosecond field variations during the onset of first return strokes in cloud-to-ground lightning. *JGR*, **103**, 9027--9034, 1998.

# « ORAGES » : A PROJECT FOR SPACE-BORNE DETECTION OF LIGHTNING FLASHES USING INTERFEROMETRY IN THE VHF-UHF BAND

A. Bondiou-Clergerie[1], P. Blanchet[1], C. Théry[1], A. Delannoy[1],
J.Y. Lojou[2], A. Soulage[2], P. Richard , F. Roux[3], S. Chauzy[3]
[1]ONERA, Châtilllon, France
[2]DIMENSIONS, Meyreuil, France
[3]Laboratoire d'Aérologie, Toulouse, France

ABSTRACT: Recent successful experiments have demonstrated the high scientific interest for the detection of lightning from space. The main objectives of these projects are the analysis, at large geographic and temporal scales, of the relationships between electrical activity and other thundercloud parameters. Within the frame of increasing the knowledge of the behavior of convective systems, the objectives of the« ORAGES » project is to locate the lightning flashes within the inter-tropical region from a low orbit microsatellite. The « ORAGES » instrument will determine the location of lightning discharges at the Earth's surface through interferometric analysis of VHF-UHF sources associated with intracloud and cloud-to-ground flashes. This project has been selected by the French Space Agency (CNES) with an expected launch date around the year 2004.

## 1. INTRODUCTION

Theoretical and experimental studies show that the inception and development of atmospheric discharges are closely related to the updraft activity and microphysical processes within the cloud. The detection of total lightning activity then appears to be a valuable tool to understand the structure and evolution of convective systems. Lightning detection from space enables us to study the correlation between lightning activity and storms characteristics over a wide variety of convective systems. This was demonstrated successfully by previous spaceborne missions which were designed to detect and locate lightning flashes using optical sensors from low orbits satellites (OTD/Microlab and LIS/TRMM missions). The « ORAGES » project consists of spaceborne detection and location of lightning flashes by VHF interferometry; it has been selected by the French Space Agency in 1998 within its microsatellite program of Earth Observation. The VHF sensor will be implemented on a low orbit (700 km) microsatellite, with an expected launch date in 2004. This paper is giving the main features of the project including a description of the proposed sensor currently under study.

## 2. PROJECT SCIENTIFIC OBJECTIVES

The correlation between lightning and meteorological data given by satellite and ground measurements will be investigated in order to analyze :

- the variability of lightning activity with season and geographical location
- the correlation between lightning flash rates and precipitations at ground, altitude of cloud top, etc..
- the behavior of mesoscale convective systems (for instance, intensification of convective activity in hurricanes)

The ORAGES lightning data are also expected to be compared with that obtained with optical detection method in previous and future missions in order to increase the existing database.

The mission parameters have been chosen to perform a lightning detection within the inter-tropical area where more than 60% of total earth lightning activity is located. With a 13° inclination orbit (optimum angle to fit the specific constraints of microsatellite launch by Ariane V), it is expected to get a space-time sampling of the observed area consistent with our objectives (see section 4). Furthermore, this orbit offers the opportunity of getting complementary data from the « TROPIQUES » mission scheduled by the French Space Agency around the same date, and devoted to the study of the convective systems that affect the intertropical zone, and the associated water vapor and liquid water distributions .

## 3. SENSOR DESCRIPTION AND EXPECTED PERFORMANCES

### 3.1. Basic principles

Lightning electromagnetic radiation has been widely studied by numerous authors (R.L. Gardner, 1990) and it has been shown that the radiation in the VHF-UHF band is associated to a very large set of intra-cloud and cloud-to-

ground lightning processes as stepped leaders, dart leaders, recoil-streamers,etc. In the past 20 years, several laboratories have developed location systems working in this frequency range, part of them using interferometric technique. Interferometry in radio-frequency relies on differential phase measurements over an antennas array to provide the direction of arrival of the electromagnetic wave (see figure 1). This interferometric technique in the VHF-UHF range has been widely tested and validated in France and USA, within the scope of research programs and operational applications (Richard et al, 1986; Shao and Krehbiel, 1996; Laroche et al, 1994).

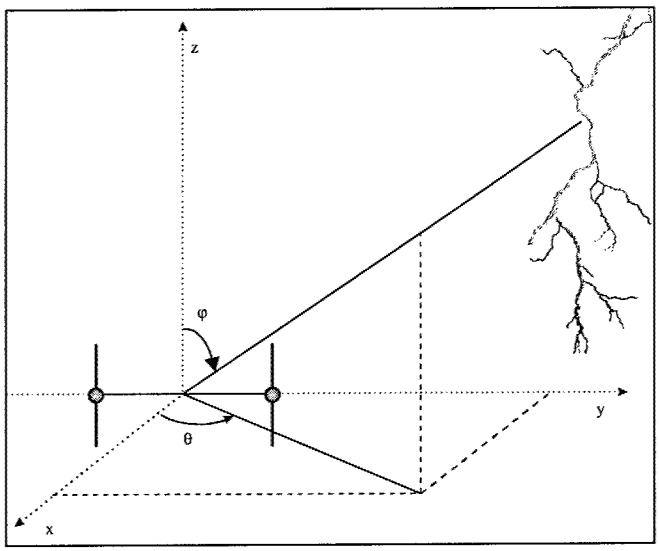


Figure 1 : Principle of interferometric measurement. The phase difference $\Delta\Phi$ over a couple of antennas is

$$\Delta\Phi = \frac{2\pi D}{\lambda}\sin\varphi\,\sin\theta$$

D : distance between antennas
$\lambda$ : receiving wavelength

Each array of antennas gives a measurement of the source azimuth and elevation. The combination of data provided by several stations provides either a 2D location in XY (combining the azimuths given by 2 or more stations) or a 3D location in XYZ (combining both elevations and azimuths). The time resolution of these systems is generally in the range 1-100 µs according to specified accuracy requirements.

3.2. Space-borne system

*Expected performances*

The space-borne interferometer will be designed to provide 2D location of the flashes on Earth, through the measurement of the azimuth and elevation of each detected source. The system's angular accuracy has to been sufficient to provide a detection within pixels of average size of 10x10 $km^2$ within an observation area of 1000km diameter. The time resolution will be probably around 100µs to allow the detection of most of the flash components. From the temporal structure of the flash radiation, it is expected to get additional information such as :

- the cumulated radiation duration (which can give an indication of the flash extension)
- the distinction between intra-cloud and cloud-to- ground flashes

Data processing will finally provide the location (averaged over the different associated sources) and the characteristics of each flash with a final time resolution of one second.

*Selection of receiving frequency*

The choice of the receiving frequency is a compromise between the following factors :

- the signal to noise ratio which varies approximately as the inverse of frequency
- the system size which increases with the wavelength
- the avoidance of anthropogenic noise radiation from Earth

It turns out that the receiving frequency has to be below 200 MHz to keep an acceptable S/N ratio and above 100 MHz to limit the size of the array of antennas. Within this range, it is possible to find some receiving frequencies where the disturbances by anthropogenic noise are at an acceptable level. However, a noise rejection system, similar to the ones existing on ground interferometric systems, will be implemented to identify and avoid narrow band emissions.

*Description of the system*

The general scheme of the system functions is given figure 2. The antennas array will be made of 4 to 5 antennas to be deployed in space. The maximum size of the antenna array will be around 2m. Numerical simulations have been performed to estimate the system accuracy. It is shown that an antenna array with D=2m (D : distance between a couple of antennas), at a receiving frequency f=150 MHz, enables a non-ambiguous location of flashes with a space resolution of 4km in the vertical direction and 7km at the limit of the detection area.
The shape of each antenna is still under investigation to get the better optimization between lobe shape, gain and size. The operations of filtering and amplification will be done in 4 to 5 receivers. The combination of the output signals gives the phases differences between each antennas couple (see figure 3) .

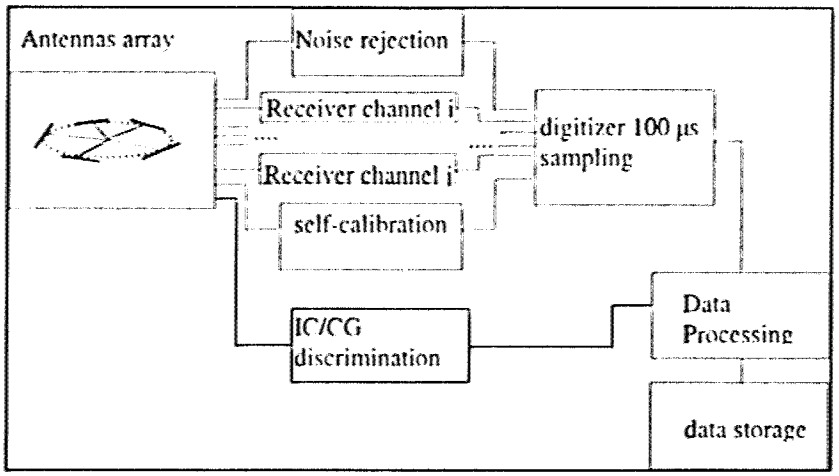


Figure 2 : General scheme of the system functions

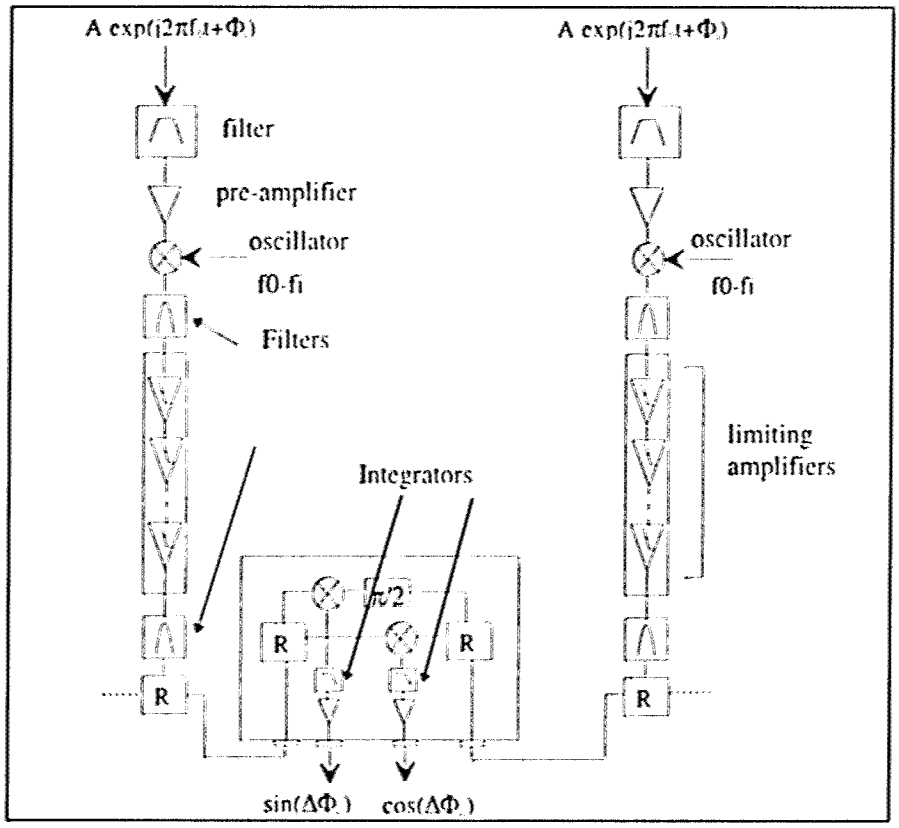


Figure 3 : Principles of phase difference measurements

The total weight of the payload will not exceed 15kg, with a volume of $10dm^3$ (excluding the array of antennas). The power requirement is 1 to 2 A and 12 Volt for continuous operation.

## 4. MISSION PARAMETERS AND SIMULATION

The altitude of the microsatellite will be around 700km. The activity detected by the satellite sensor with an orbit inclination of 13° has been numerically simulated. Figure 4 gives the data sampled by the satellite sensor for a storm located at 0° latitude - 0° longitude, that occurs every days at the same time, with 3 hours duration. The time shape of the total activity of the storm has been deduced from previous measurements at ground. This simulation indicates the re-visiting period is around 20 days; with this orbit, an individual storm of sufficient duration may be observed at different times of its evolution. These first simulations then indicate that the choice of a low inclination orbit leads to very promising sampling capabilities.

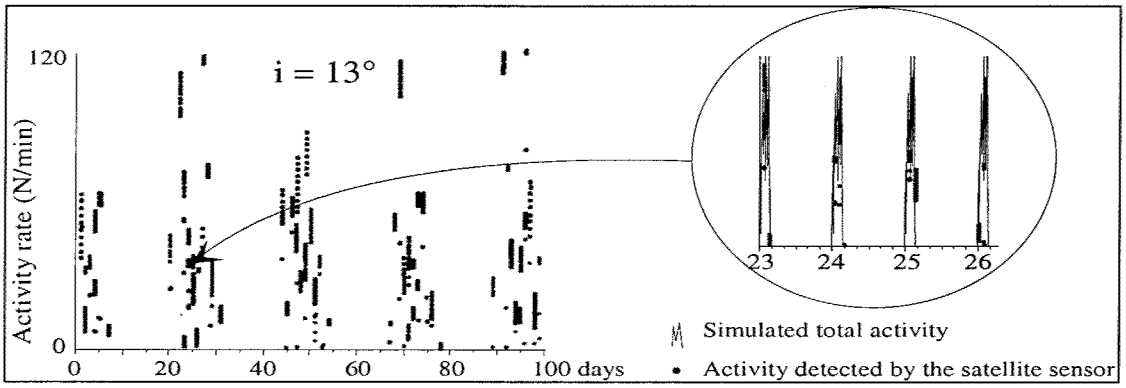


Figure 4 : 13° inclination orbit. Simulation of the activity detected by the satellite sensor for a 0°lat-0°long storm of 3 hours duration

## 5. CONCLUSION

The ORAGES project is now entering the main phase of sensor development. A first sensor model will be tested on a stratospheric balloon during summer 2000 or 2001. This validation experiment is expected to provide the system location accuracy, its detection efficiency and its capability of noise rejection. In parallel to the payload development, ONERA and the Laboratoire d'Aérologie are opening a specific research program to investigate the correlations between lightning activity and storm convective properties ; this program includes the extension of existing numerical models and the analysis of ground data.

## REFERENCES

R.L. Gardner « Lightning electromagnetics », Hemisphere Publishing Corporation, 1990

Laroche P., A. Bondiou, P. Blanchet, J. Pigère, M. Weber and B. Boldi, 3D mapping of lightning discharges within storms, Int. Aerospace and Ground Conf. on Lightning and Static Electricity, Mannheim (Germany), 24-25 May 1994

Richard P., A. Delannoy, G. Labaune and P. Laroche, Results of spatial and temporal characterization of the VHF-UHF radiation of lightning. *J. Geophys. Res.* , **91(D1)** , 1,248-1,260, 1986.

Shao, X.M. and P.R. Krehbiel, The spatial and temporal development of intracloud lightning. *J. Geophys. Res.* , **101(D21)** , 26,641-26,668, 1996.

# LIGHTNING FIRST PULSES USED IN THE "LASI" (TIME-OF-ARRIVAL) AND "ATLAS" (SINGLE STATION) TOTAL LIGHTNING MAPPING SYSTEMS

Ralph Markson and Lothar Ruhnke

Airborne Research Associates, Weston, Massachusetts, U.S.A.

**Abstract**: The first RF pulse from "total lightning" discharges (cloud and ground flashes) has been used in different ways to locate the origin of flashes in two new types of lightning detection systems. The multisensor LASI time-of-arrival (TOA) system uses GPS timing of the first pulse. The ATLAS single sensor system uses the amplitude of the first pulse, which is invariant in magnitude and polarization for all lightning discharges, to determine distance from the sensor. It is significantly more accuracy than past single sensor lightning mapping systems. The polarity of the first pulse generally identifies lightning type (IC or CG). Both systems utilize only the first pulse which makes signal processing much simpler than with previous lightning locating systems. Knowing the position where lightning begins (maximum electric fields, mixed phase hydrometeors and updrafts) is valuable for identifying convective cells producing the hazardous meteorological conditions caused by thunderstorms. It is also important for research studying thunderstorm electrification and associated microphysical problems.

## A. "First Pulse" Principles

Every lightning flash has an initial discharge at its onset. This electrical breakdown is controlled primarily by electric field intensity and the shape of ice particles and liquid filaments, as well as to a lesser extent by pressure, temperature and the dielectric constant of air. These factors control the onset of corona from the sharp tips of ice particles and/or liquid filaments [*Blyth et al.*, 1998]. The corona leads to the first pulse breakdown of thousands or more which follow through the life of the lightning flash as it grows with all its tortuous branches extending through much of the cloud volume.

The first pulse serves as a well defined signal in time and space. We believe it has a dimension of one to several meters and leads to the subsequent cloud scale lightning flash with all its channels and branching having dimensions on the order of 10 km or more. It has a rise time on the order of 50-100 nsec and a subsequent relaxation to baseline on the order of 200 nsec. Then there is a dead time with no radiation for about 100 usec before the second pulse. So the first pulse stands alone and can be identified. It propagates into virgin air and has no branching. Thus the location of the first pulse of a lightning flash -- near the updraft region where mixed phase hydrometeors exist and interact, charge is being separated, and electric fields maximize -- can be used to locate convective cells. This is harder to do with systems that detect the multitude of radiation pulses which occur along the numerous channels.. Many of the subsequent pulses from separated channels overlap in time making them difficult to identify. Also, the subsequent pulses in the channels generally are not vertical and move toward or away from the sensor. These lead to polarization errors in the magnitude measurement and variable polarity. These problems are avoided by only detecting first pulses and not accepting any signals not preceded by at least one second of quite time where no radiation is detected.

The first pulse is vertical following the electric field lines from the typical horizontally stratified space charge layers in clouds. Its polarity is a function of whether it will grow into a cloud-to-ground (CG) discharge or an intracloud (IC) discharge. We find most CGs start at 3 to 6 km and are positive while most ICs start at 4 to 9 km and are negative. This is consistent with a tripole model of charge distribution in updraft regions with a horizontal layer of negative charge between about 5 and 8 km which we used in agreement with the findings of *Stolzenburg et al.* [1998]. This characteristic allows identification of the flash type and approximate height of the first pulse. It also allows the vertical electric field sensing antenna to be in the same plane as the propagating electric field wave eliminating polarization errors in measuring the amplitude of the first pulse. A schematic model of charge distribution, height, and polarity of first pulses for each type of lightning in a convective cell is illustrated in Fig. 1.

Because the primary factors controlling the initial breakdown (E field intensity and point sharpness) are always about the same for all lightning, regardless of type, size, or intensity, the amplitude of the first pulse is approximately invariant for all flashes. Therefore, since signal amplitude decreases linearly with distance, it is possible to make a relatively accurate estimate of the distance to the radiation source by a simple measurement of pulse magnitude. This has not been possible in the past with the single sensor ELF/VLF lightning mapping systems that have been used.

## B. Application of "First Pulse" Lightning Detection and Advantages

LASI (Lightning and Storm Intensity), and ATLAS (Aircraft Total Lightning Advisory System), new types of total lightning mapping systems, have been developed with particular application toward location and quantification of convective cells. They are different than previous systems in that they only detect and provide the location of the "first pulse" of all lightning flashes which are assumed to occur near regions of intense convection. Updraft location and intensity are important for forecasting hazardous conditions associated with convective weather -- regions of particularly concern in aviation operations. All dangerous thunderstorm conditions are created in the updraft; these include severe turbulence, supercooled water (airframe icing), hail, heavy rain and lightning. In addition, the updraft leads to the downdraft/microburst and its subsequent windshear near the ground. Thus, identification of the updraft through increase in local total lightning rate in a cellular region can provide advanced warning of windshear. Since lightning rate is proportional to the fifth power of updraft velocity, it can be used to quantify storm severity and for prediction of severe weather such as high winds and tornadoes.

There are several advantages in detecting and depicting only the first pulse of lightning:

1) A single dot is shown for each flash rather than the multitude of radiation pulse positions along the numerous lightning channels and branches that fill the cloud as depicted on past total lightning mapping systems. This declutters the screen and allows convective cells to be seen;
2) By having to detect and process only one pulse per flash the signal processing is greatly simplified;
3) Having to communicate only information from a single event eliminates for a TOA system the need for expensive high data rate telemetry and phone lines can be used;
4) The invariant amplitude of first pulses allows accurate single station estimation of distance. This is particularly valuable for an aircraft lightning mapping system.
5) Whether the lightning is IC or CG generally can be determined from the polarity of the first pulse.

## C. LASI: A SIMPLE "FIRST PULSE" TIME-OF-ARRIVAL TOTAL LIGHTNING MAPPING SYSTEM

LASI is a TOA system utilizing a minimum off 4 remote sensors in an array for 3-D positioning. Communication can be by phone line or other means. GPS provides timing. Five 4-station solutions can be derived from 5-station arrays, their mean is the best estimate of position. LASI was tested at Orlando during summer 1997 using a 9-sensor array in a 24 km diameter circle. Comparisons were made with the KSC LDAR total lightning data and National Lightning Detection Network CG data (Fig. 2). Most differences between LASI and LDAR were 1-4 km and between LASI and NLDN they were 1-6 km. Some of the discrepancy between LASI and LDAR is because LASI locates the first pulse while the centroid of many points is listed for the LDAR position. Also, LDAR loses accuracy at the 65 km distance from KSC to Orlando. The CG data depict where lightning comes to earth, typically many km away from the initial breakdown location. Comparing solutions from different 5-station arrays (from the 9 sensors around Orlando), the maximum in the difference distribution was within 100 meters and the mean was 200 meters. Thus LASI had an accuracy on the order of 100 m both in geographic position and height.

Figure 3 shows the distribution of LASI derived first pulse heights. For CG the maximum is in the 4-6 km range and for IC it is in the 6-8 km range similar to the findings of *Proctor* [1991].

The LASI system should be valuable both for forecasting and diagnosing convective weather and predicting microbursts near airports as well as for thunderstorm research.

## D. ATLAS: A "FIRST PULSE" SINGLE-SENSOR TOTAL LIGHTNING MAPPING SYSTEM

ATLAS determines the distance to total lightning using the amplitude of first pulses and direction from magnetic crossed loops which also sense only the first pulse. Previous single-sensor systems are ELF/VLF and thus mostly detect CG return strokes. Since these vary in intensity by one or more orders of magnitude, determining the distance from return strokes leads to large errors. For example, we find "radial spread", a characteristic line of dots that often appears at various distances along a radial line from the center of ELF/VLF system displays, is due to the different intensities of the multiple return strokes in a flash. Also, ELF/VLF systems generally do not detect IC flashes, which emit much of their radiation at higher frequencies. By not detecting IC lightning (which generally makes up most of total lightning) such systems can not provide a measure of convective intensity.

ATLAS positions total lightning relatively accurately as a dot at a single location. A single point is shown on the display which allows convective cells to be defined -- the screen is not cluttered with dots. ATLAS can determine if the flash is CG or IC from the polarity of the first pulse and thus estimate its height. The aerial density of the dots is a measure of the convective velocity in updraft regions.

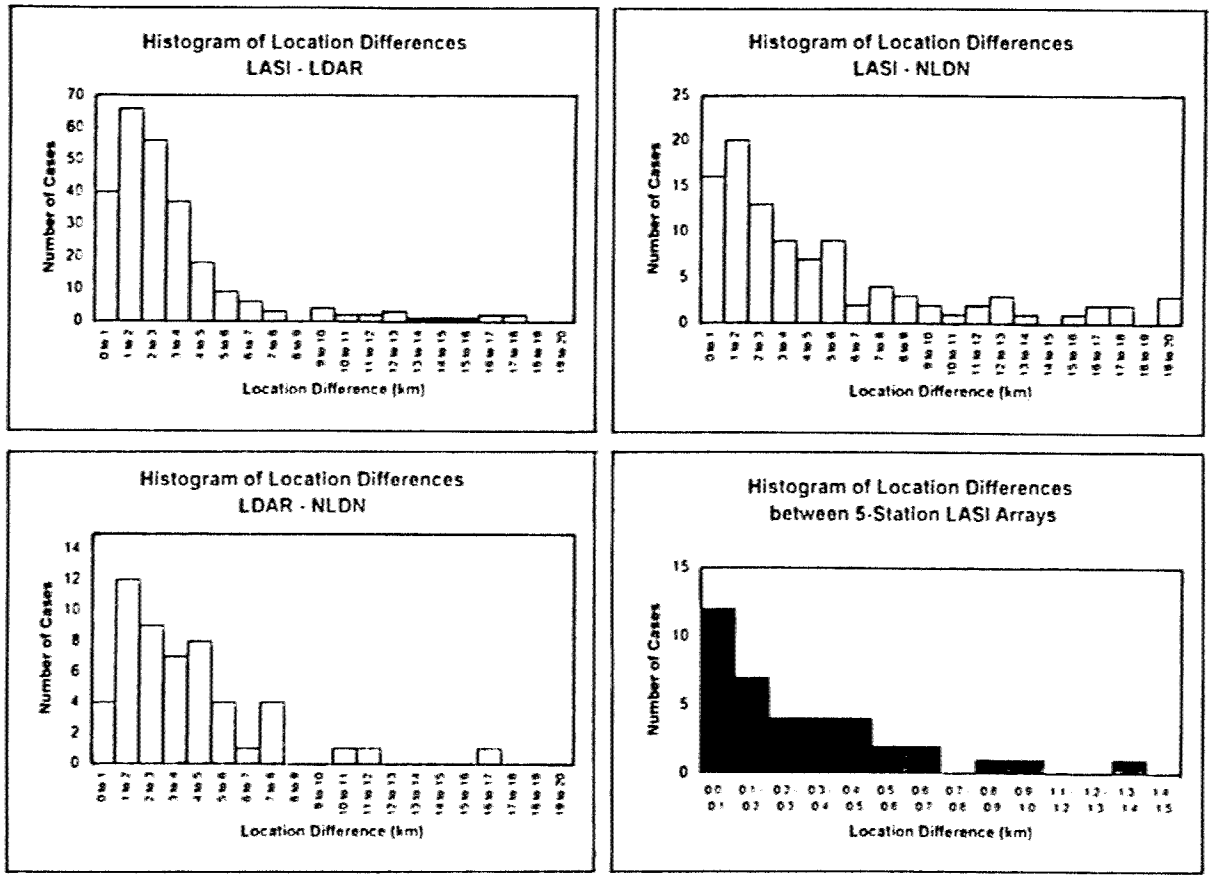


Fig. 2 Comparison between ATLAS and other lightning mapping systems for same flashes. Note the scale in the comparison between different sets of LASI sensors (lower right box) is 100s of meters.

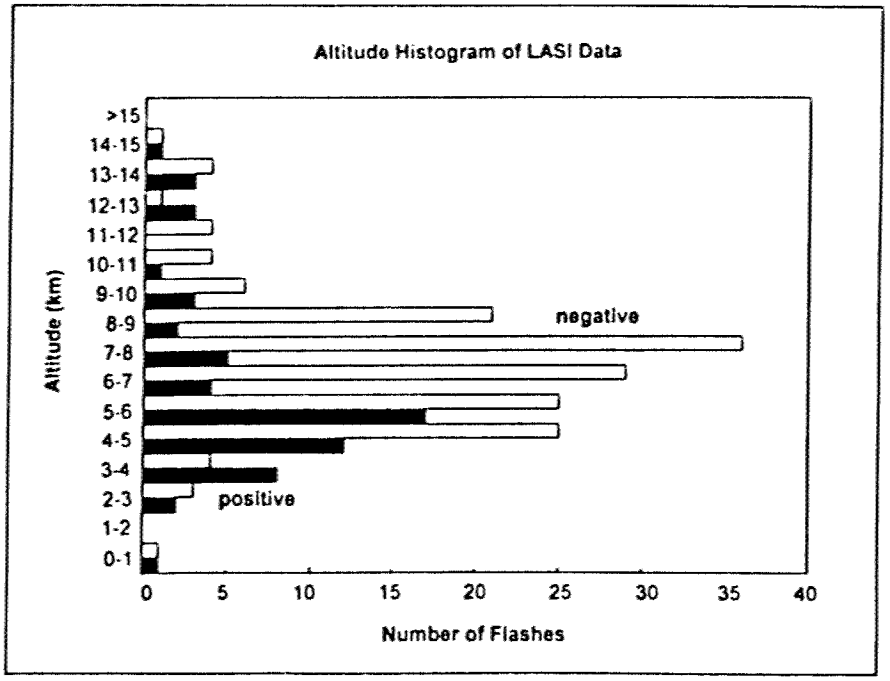


Fig. 3 Distribution of first pulse heights for positive (CG) and negative (IC) flashes (summer Florida).

Contouring lightning rate will provide a map of "convective intensity" much as contours of reflectivity provide a map of rain rate on a radar display. The primary objective of the ATLAS program is to provide a convective activity map to pilots.

The instrument is in its final development and testing phase. Current results with a ground based system indicate an accuracy in direction of +/- 4° and in distance on the order of +/- 10%. The apparent range of the system is greater than 200 km. Airborne testing is scheduled for this summer.

ATLAS was developed for use on aircraft where range estimates must be made from a single sensor without the benefit of cross-bearing or time-of-arrival networks which can be used on the ground. However, with minor modification it can be used as a ground station capable of obtaining the position of total lightning without the need of a network of sensors and the associated communications.

## E. Conclusions

The use of first pulse detection to locate total lightning offers economic and powerful methods for locating and quantifying convective cells in thunderstorms with ground based and airborne systems. It makes possible the first reliable single sensor lightning mapping system and could provide convective activity mapping for small aircraft which do not have radar. Such information may be more valuable than radar. Light rain sometimes exists in hazardous regions and heavy rain sometimes is in non-hazardous regions. Lightning always comes from regions with intense convective activity. Besides pilots, potential uses include interfacing to AWOS/ASOS automatic weather observing systems, providing information to air traffic controllers, the National Weather Service and weather research.


## Acknowledgments/Notes

LASI system development was supported in part by NASA / NAS1-20594. ATLAS system development was supported in part by NASA / NAS1-97039 and the NASA AGATE Program to revitalize General Aviation. The first pulse detection techniques used in both systems have been patented.


## References


Blyth, A.M., H.J. Christian and J. Latham, Corona emission thresholds for three types of hydrometeor interaction in thunderclouds, *J. Geophys. Res.*, 103, 13975-13977, 1998.

Proctor, D., Regions where lightning flashes begin, *J. Geophys. Res.*, 96, 5099-5112, 1991.

Stolzenburg, M., W.D. Rust and T.C. Marshall, Electrical structure in thunderstorm convective regions, 3. Synthesis, *J. Geophys. Res.*, 103, 14097-14108, 1998.


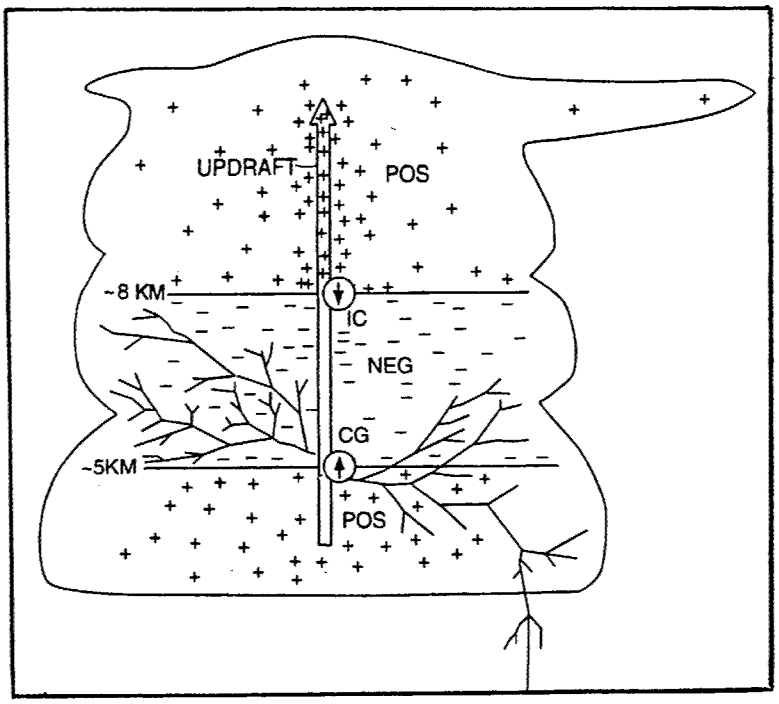


Fig. 1 Schematic representation of a thundercloud with a tripole charge distribution. The maximum electric fields are at the top and bottom of the central negative charge layer. Charge is separated in the updraft. Vertical negative first pulses for IC flashes originate near 8 km while vertical positive first pulses for CG flashes originate near 5 km. A CG flash is shown.

# A SPHERICAL EARTH SOLUTION FOR TOA LIGHTNING LOCATION RETRIEVAL

W. J. Koshak[1], R. J. Solakiewicz[2]

[1]Global Hydrology and Climate Center, NASA-MSFC, Huntsville, Alabama, U.S.A.
[2]Department of Mathematics & Computer Science, Chicago State University, Chicago, Illinois, U.S.A.

ABSTRACT: The problem of retrieving lightning ground-strike location on a spherical Earth surface using a network of 4 or more time-of-arrival (TOA) sensors is considered. It is shown that this problem has an analytic solution and therefore does not require the use of nonlinear estimation theory (e.g., $\chi^2$ minimization). The mathematical robustness of the analytic solution is tested using computer-generated lightning sources and simulated TOA measurement errors. A summary of a quasi-analytic extension of the spherical Earth solution to an oblate spheroid Earth geometry is also provided.

## INTRODUCTION

With the advent of high-speed digital computers, the method of $\chi^2$ minimization is a highly practical means for analyzing a wide variety of (otherwise intractable) nonlinear inversion problems in applied mathematical physics. A minimal amount of effort is required to apply the $\chi^2$ method to obtain quick and reasonable estimates of a solution, and the method offers a means to assess retrieval errors. Because the $\chi^2$ method is simple and practical it is sometimes applied to problems that, in reality, can be solved by formal analytic or quasi-analytic means.

Presently, Global Atmospherics Inc. (GAI) finds the minimum of a $\chi^2$ function to analyze time-of-arrival (TOA) *and magnetic bearing data* derived from the National Lightning Detection Network (NLDN): Earth curvature is taken into account [Cummins et al., 1998]. An analytic solution to this problem has not yet been attained, but by considering and solving less general problem statements a solution might eventually be found. In this work, an analytic solution is found for the case of a spherical Earth, when only TOA measurements are considered.

## ANALYTIC SOLUTION

It is assumed that four or more ($n \geq 4$) TOA sensors are available and that the experimenter is interested in accounting for the effects of Earth curvature. To solve this problem, a spherical coordinate system as shown in Figure 1 is used. By definition, the Prime Meridian is associated with $\lambda = 0$ and the

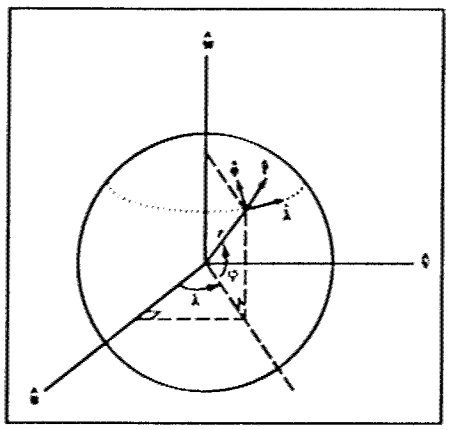

Figure 1. Spherical coordinate system used to obtain a solution

Equator with $\varphi = 0$. The spherical Earth radius is denoted by the variable $r$. If $\mathbf{r} = r\hat{\mathbf{r}}$ is the lightning source location and $\mathbf{r}_i = r\hat{\mathbf{r}}_i$ is the location of the $i^{th}$ sensor, one can write the unit vectors as:

$$\hat{\mathbf{r}}_i = \cos\varphi_i \cos\lambda_i \hat{\mathbf{u}} + \cos\varphi_i \sin\lambda_i \hat{\mathbf{v}} + \sin\varphi_i \hat{\mathbf{w}}$$
$$\hat{\mathbf{r}} = \cos\varphi \cos\lambda \hat{\mathbf{u}} + \cos\varphi \sin\lambda \hat{\mathbf{v}} + \sin\varphi \hat{\mathbf{w}} \ . \tag{1}$$

So the spherical form of the arrival time equation becomes

$$t_i = t + \frac{1}{c} r\xi_i \ , \tag{2}$$

where $t$ is the time of occurrence of the lightning at $\mathbf{r}$, $t_i$ is the arrival time measurement at $\mathbf{r}_i$, and the angle, $\xi_i$, between the unit vectors in (1) is given by

$$\xi_i = \cos^{-1}(\kappa_i \cos\varphi \cos\lambda + \mu_i \cos\varphi \sin\lambda + \eta_i \sin\varphi) \ , \tag{3}$$

where $\kappa_i = \cos\varphi_i \cos\lambda_i$, $\mu_i = \cos\varphi_i \sin\lambda_i$, and $\eta_i = \sin\varphi_i$. Note that the product $r\xi_i$ in (2) is simply the great circle distance between the lightning source and the $i^{th}$ sensor. Using (3) and a standard trigonometric identity, the arrival time equation in (2) can be written as

$$\cos\frac{c}{r}t_i \cos\frac{c}{r}t + \sin\frac{c}{r}t_i \sin\frac{c}{r}t = \kappa_i \cos\varphi \cos\lambda + \mu_i \cos\varphi \sin\lambda + \eta_i \sin\varphi \ . \tag{4}$$

The form in (4) is invariant under coordinate system rotations. If one rotates the coordinate system $(\hat{\mathbf{u}}, \hat{\mathbf{v}}, \hat{\mathbf{w}})$ into $(\hat{\mathbf{u}}', \hat{\mathbf{v}}', \hat{\mathbf{w}}')$ by an (Euler) angle $\lambda_1$ about $\hat{\mathbf{w}}$ and then $(\hat{\mathbf{u}}', \hat{\mathbf{v}}', \hat{\mathbf{w}}')$ is rotated into $(\hat{\mathbf{u}}^*, \hat{\mathbf{v}}^*, \hat{\mathbf{w}}^*)$ by an Euler angle $\varphi_1$ about $-\hat{\mathbf{v}}'$, (4) maintains the same form in the starred system

$$\cos\frac{c}{r}t_i \cos\frac{c}{r}t + \sin\frac{c}{r}t_i \sin\frac{c}{r}t = \kappa_i^* \cos\varphi^* \cos\lambda^* + \mu_i^* \cos\varphi^* \sin\lambda^* + \eta_i^* \sin\varphi^* . \tag{5}$$

Here, $(\kappa_i^*, \mu_i^*, \eta_i^*)$ are identical to the expressions for $(\kappa_i, \mu_i, \eta_i)$ given in (3), but with $(\lambda_i, \varphi_i)$ replaced with $(\lambda_i^*, \varphi_i^*)$. In (4), all latitudes and longitudes are referenced to the Prime Meridian and Equator, but in (5) all locations are expressed relative to site 1. This fact will help simplify the mathematics since $(\lambda_1^* \equiv 0, \varphi_1^* \equiv 0)$. If one now invokes the convention that site 1 excites at $t_1 \equiv 0$ the transit equation in (5) evaluated at $i = 1$ is

$$\cos\frac{c}{r}t = \cos\varphi^* \cos\lambda^* \ . \tag{6}$$

Since $t_1 \equiv 0$ and $t \le t_1$, one must have $t \le 0$. Hence, $\sin\frac{c}{r}t = -\left|\sin\frac{c}{r}t\right| = -(\sin^2\frac{c}{r}t)^{1/2}$, or

$$\sin\frac{c}{r}t = -(1 - \cos^2\frac{c}{r}t)^{1/2} \ . \tag{7}$$

Substituting (7) into (5) and using (6) allows one to write the remaining scalar arrival time equations as

$$a_{i-1} = S_{i-1,1}h_1 + S_{i-1,2}h_2 + S_{i-1,3}h_3 \ ; \qquad i = 2,3,\ldots,n \ , \tag{8}$$

where:

$$
\begin{aligned}
a_{i-1} &= -\sin\frac{c}{r}t_i \\
S_{i-1,1} &= \cos\varphi_i^* \cos\lambda_i^* - \cos\frac{c}{r}t_i \\
S_{i-1,2} &= \cos\varphi_i^* \sin\lambda_i^* \\
S_{i-1,3} &= \sin\varphi_i^* \\
h_1 &= \cos\varphi^* \cos\lambda^* [1-\cos^2\varphi^* \cos^2\lambda^*]^{-1/2} \\
h_2 &= \cos\varphi^* \sin\lambda^* [1-\cos^2\varphi^* \cos^2\lambda^*]^{-1/2} \\
h_3 &= \sin\varphi^* [1-\cos^2\varphi^* \cos^2\lambda^*]^{-1/2} \quad .
\end{aligned}
\tag{9}
$$

In matrix/vector form one has

$$\mathbf{a} = \mathbf{S}\mathbf{h} \ . \tag{10}$$

Hence, for $n = 4$ sensors the vector $\mathbf{h}$ is

$$\mathbf{h} = \mathbf{S}^{-1}\mathbf{a} \ . \tag{11}$$

For $n > 4$ sensors the (over-determined) solution for $\mathbf{h}$ is

$$\mathbf{h} = (\tilde{\mathbf{S}}\mathbf{S})^{-1}\tilde{\mathbf{S}}\mathbf{a} \ . \tag{12}$$

The location information is extracted from the components of $\mathbf{h}$ as:

$$
\begin{aligned}
\lambda^* &= \tan^{-1}(h_2/h_1) \\
\varphi^* &= \tan^{-1}\left(\frac{h_3}{h_1}\cos\lambda^*\right) \quad .
\end{aligned}
\tag{13}
$$

By inspecting the standard Euler angle transformations between the coordinate system $(\hat{\mathbf{u}},\hat{\mathbf{v}},\hat{\mathbf{w}})$ and $(\hat{\mathbf{u}}^*,\hat{\mathbf{v}}^*,\hat{\mathbf{w}}^*)$ the source location $(\lambda,\varphi)$ relative to the Prime Meridian and Equator can be written in terms of $(\lambda^*,\varphi^*)$. With the aid of (6), the final solution is:

$$
\begin{aligned}
\lambda &= \tan^{-1}\left(\frac{\mu_1 \cos\varphi^* \cos\lambda^* + \cos\lambda_1 \cos\varphi^* \sin\lambda^* - \eta_1 \sin\lambda_1 \sin\varphi^*}{\kappa_1 \cos\varphi^* \cos\lambda^* - \sin\lambda_1 \cos\varphi^* \sin\lambda^* - \eta_1 \cos\lambda_1 \sin\varphi^*}\right) \\
\varphi &= \sin^{-1}\left(\eta_1 \cos\varphi^* \cos\lambda^* + \cos\varphi_1 \sin\varphi^*\right) \\
T &= T_1 - \frac{r}{c}\cos^{-1}(\cos\varphi^* \cos\lambda^*) \quad ,
\end{aligned}
\tag{14}
$$

where $T_1$ is the absolute time (e.g., in GPS seconds) that site 1 is excited by the RF ground wave. Note that the principal values of the inverse cosine function are used, i.e., $0 \le \cos^{-1}(\cos\varphi^* \cos\lambda^*) \le \pi$, $-\pi/2 < \lambda^* < \pi/2$, $-\pi/2 < \varphi^* < \pi/2$, and $T$ is the absolute time-of-occurrence of the lightning ground-wave emission, where $T < T_1$.

In summary, all the arrival time measurements and sensor location data is buried in the vector **a** and matrix **S**. The matrix equation in (10) is inverted via (11) or (12) to determine the vector **h**. Certain ratios of the components of **h** provide the lightning source location in the starred coordinate system. A standard Euler angle transformation is employed to obtain the lightning location in the absolute (Prime Meridian and Equator) reference frame as provided in (14).

## SIMULATED TESTS

To test the mathematical validity and stability of the solution in (14), several known lightning sources were computer-generated across the Maritime Continent Thunderstorm Experiment (MCTEX) analysis region in Darwin, Australia [Keenan et al., 1996]; the region considered was about 660 km on a side and was centered on the central site of the four station TOA network. The analytic solution described above was used to analyze the arrival times produced from the known sources, and retrieval error was determined. When no errors were added to the simulated arrival time measurements, the retrieval error was below 10 meters across the entire analysis region; almost 50% of the region had retrieval errors below 1 meter. When an error selected from an uniform random distribution with limits: [-100 to 100 ns] and [-300 to 300 ns] was added to the simulated arrival times, the respective retrieval errors were under 0.5 km and 1 km for more than about 70% of the region.

## OBLATE GEOMETRY

One can extend the results to an oblate spheroidal Earth geometry. Eq. (2) can be modified to $c(t_i - t) = S_i(\varphi, \lambda; \varphi_i, \lambda_i)$, where the distance $S_i$ from source to station is measured along a geodesic. Eq. (14) can be used as the starting point in a perturbation procedure. Expanding the modified version of (2) in a Taylor series leads to $c(t_i - t) - S_i \approx (\partial S_i / \partial \varphi)\Delta\varphi + (\partial S_i / \partial \lambda)\Delta\lambda + c\Delta t$ from which corrections can be calculated. Both $S_i$ and its derivatives can be expressed in terms of elliptic integrals. These quantities are evaluated at $(\varphi, \lambda; \varphi_i, \lambda_i)$ as given by (14). This process can be applied repeatedly to yield a Newton-type approximation procedure. An improvement in accuracy is expected particularly for distant sources.

## CONCLUSIONS

The incorporation of magnetic bearing information into these analytic solutions would lead to a general and elegant analytic retrieval scheme that could at some point replace the $\chi^2$ estimation theory currently employed by Global Atmospherics Inc. (GAI). Explicit analytic or quasi-analytic solutions to complicated inversion problems lead to improved physical insights, particularly with respect to the effect of measurement errors on final solution retrieval error [Koshak et al., 1999].

ACKNOWLEDGEMENTS: The authors would like to thank Prof. E. Philip Krider for his helpful comments in the early phase of this work, and Janine Roskowski for her help in preparing the figure.

## REFERENCES

Cummins, K. L., M. J. Murphy, E. A. Bardo, W. L. Hiscox, R. B. Pyle, and A. E. Pifer, A combined TOA/MDF technology upgrade of the U.S. National Lightning Detection Network, *J. Geophys. Res.*, Vol. 103, NO. D8, 9035 – 9044, 1998.

Keenan, T., R. Carbone, S. Rutledge, J. Wilson, G. Holland, and P. May, The Maritime Continent Thunderstorm Experiment (MCTEX): Overview and initial results, Seventh Conference on Mesoscale Process, Reading, UK, By AMS, Boston, MA, pp. 26-328, September 9-13, 1996.

Koshak, W. J., R. J. Blakeslee, and J. C. Bailey, ALDF data retrieval algorithms for validating the Optical Transient Detector (OTD) and the Lightning Imaging Sensor (LIS), submitted to *J. Tech.*, 1999.

# PERFORMANCE OF THE NEW LLP-IMPACT SYSTEM IN FINLAND

Tapio J. Tuomi

Finnish Meteorological Institute, P.O. Box 503, FIN-00101 Helsinki, Finland

ABSTRACT: In 1984-1997, the southern half of Finland was covered by an LLP lightning location system based on four model DF-80-02 direction finders. In August 1997, it was replaced by a system consisting of five IMPACT sensors, with coverage extended further to the north. Parallel operation of the two systems in August and September 1997 showed a substantial increase in both the location accuracy and the detection efficiency, although the declining thunderstorm season provided only limited data. The improvements are due to better-chosen sites and the inclusion of time-of-arrival techniques, and to the higher sensitivity to detect weak strokes. The full season in 1998 provided enough data for intrinsic analysis of the new system (the old system was closed down in October 1997). The angular errors, given automatically by the system, show typical double-period sine curves with ± 5° maximum errors. The initial typical error of 2-3 km was improved to the 1-km level. The improving accuracy has remedied some bad locations and even some non-intersecting cases, hence also improving the detection efficiency. A case study suggests that a maximum flash detection efficiency > 80 % estimated by the manufacturer is reached in the central region of the network.

## INTRODUCTION

Figure 1 shows the map of Finland with the lightning location sensor sites of the previous and present systems. The four sensors of the old system covered the southern part, which has a temperate climate, up to the 65-degree latitude. The short summer of the subarctic northern Finland (Lapland) occasionally produces quite a lot of lightning, and the new IMPACT-based LLP location system was extended to cover at least the southern half of Lapland, up to the 68-degree latitude.

The two systems were run parallel in August and September 1997, but due to the declining season, little data for comparison were obtained. Yet it was established that the old system failed to detect weak lightning: most of the strokes below 20 kA remained undetected. Consequently, the new system detected 3.5 times as many flashes as the old one, but this factor was not constant. Full evaluation of the new system had to wait until the 1998 season, based on its own results because the old system was closed down.

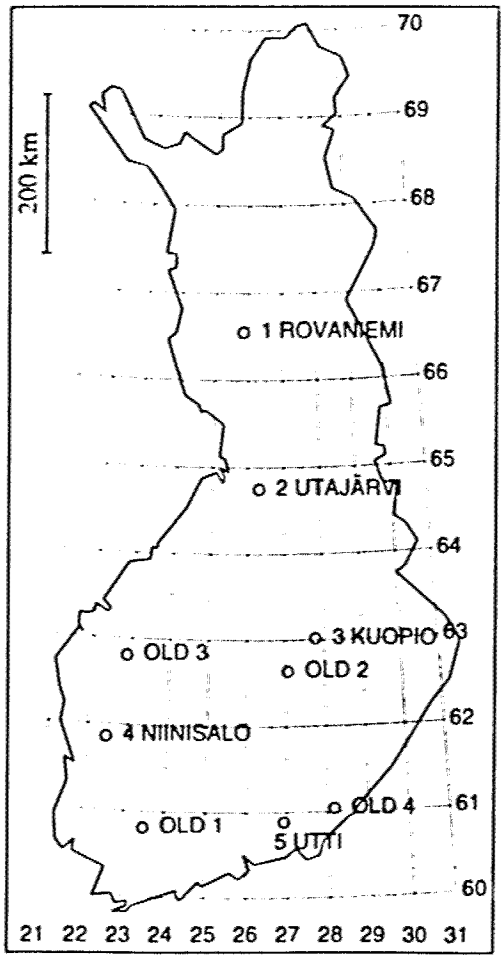


Figure 1. Sites of the old and new sensors.

## LOCATION ERRORS

The five-sensor Impact network was designed to have as much coverage as possible, leading to a less than ideal configuration with respect to accuracy. Due to the shape of the country, the northern sensors form a chain rather than a triangle. The south-western part, which is the most active thunderstorm region, is slightly outside the best detection area, but this confuration was expected to give satisfactory performance because of the high sensitivity and the double location techniques (triangulation and time-of-arrival).

All five sensor sites were carefully selected for openness and low noise. However, two sensors had to be realigned by a few degrees during the 1998 season, and the incoherent data did not allow the best possible determination of the site errors, which will await the next season. The site errors for each stroke are estimated by the system itself and can be simply collected for analysis (the central unit is the basic one, without tools for automatic analysis). Two sensors had very small site errors while the three others showed the

typical double-sine behavior with an amplitude of about 5 degrees. When the uncorrected locations are optimized by combining the triangulation and time-of-arrival methods, 55 % of the estimated errors are below 4 km and 17 % below 2 km; some exceed 20 km (in the optimal detection area). After corrections, 55 % of the errors are below 3 km and 42 % below 2 km; some large errors still remain. As an example, Figure 2 shows the located flashes (first strokes) of the most active day of 1998, June 16, when a warm and a cold front traversed from southeast to northwest. A dot is negative flash, a cross is positive flash. The total number is about 23,500 flashes.

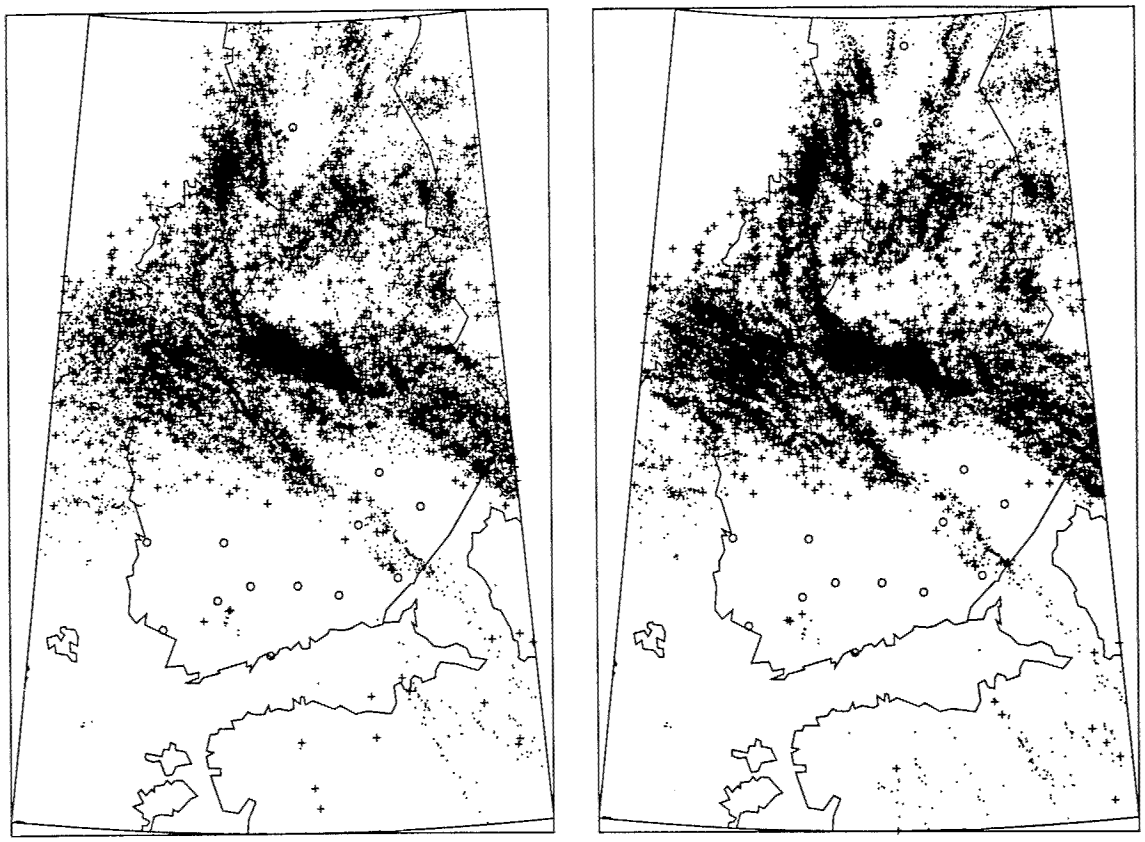

Figure 2. Uncorrected (left) and corrected (right) flash locations on 19980616.

Even when the typical correction is of the order of two kilometers, the increase of the solidity of the dense flash patterns is clearly visible. This is especially true for the large cluster reaching over the western sea. It is conceivable that the estimated error (semimajor axis of the 50 % probability ellipse) is not always the best descriptor of the error. Two-sensor locations seem to be optimistic about the accuracy, while three-sensor cases may give an accurate location (with two accurate bearings) with large error estimate (due to an inaccuracy of the third bearing). In some cases, bearing errors tend to result in ambiguities of which strokes belong to the same flash. In Figure 2, the improvement in the lightning pattern formation seems better than could be told by the increase of the estimated accuracy. In other words, bearing corrections improve not only the estimated accuracy but also the consistency of the data.

## DETECTION EFFICIENCY

Figure 1 shows that the best detection area of the new location system is in the central part of southern Finland, between latitudes 61 - 64 and longitudes 23 - 29, close to four of the five sensors. The typical distance between sensors is 200 km which, together with the sensitivity threshold of the sensors, sets a limit to the weakest locatable (by at least two sensors) strokes. The threshold appears to be near 10 LLP units (the strength reported by a sensor), which is reflected in the lower limit of located-stroke strength, about 2.5 kA. In fact, this limit appears also in the data for uncorrelated strokes (detected by only one sensor). For strokes in the central region, at a distance of 100 -

150 km from four sensors, a case study gives the following rough statistics: for strength below 20 LLP units (5 kA), a stroke is detected by 1 or 2 sensors; between 20 - 30 LLP (5 - 7 kA), by 3 sensors; between 30 - 40 LLP (7 - 9 kA), by 4 sensors. Because of the high fraction of weak strokes, the mean strength in the best detection area remains slightly below 10 kA. For the whole useful area (the whole country excluding northern Lapland) the mean strength is 16 kA because of the larger distances included.

When the numbers of strokes are considered irrespective of the strength, a case study from the central area gives following results: uncorrelated strokes 1182, 2-sensor strokes 556, 3-sensor strokes 773, 4-sensor strokes 1771 and 5-sensor strokes 460. Thus 75 % of all detected strokes were located.

As another example, Figure 3 depicts the region around the two northernmost sensors. A thunderstorm proceeded between them, producing 1303 located strokes. In addition to these, each sensor detected a lot of strokes for which there were no coincident reports from the other (the three other sensors in the south detected hardly any uncorrelated strokes while they participated in many of the located cases). The uncorrelated reports are grouped into 10-degree sectors; the longest lines correspond to about 90 strokes per 10 degrees. The uncorrelated signals are clearly coming from that thunderstorm. Together they represent about another 1300 unlocated strokes. This sets an upper limit of 50 % for the detection efficiency in this region; there are probably also some strokes that were detected by neither sensor. The manufacturer's preliminary estimate (without using actual data) for the flash detection efficiency in this region is 70 %, which would correspond to a stroke detection efficiency of 54 % for the observed multiplicity distribution (50 % single-stroke, 25 % two-stroke, 12.5 % three-stroke flashes etc.).

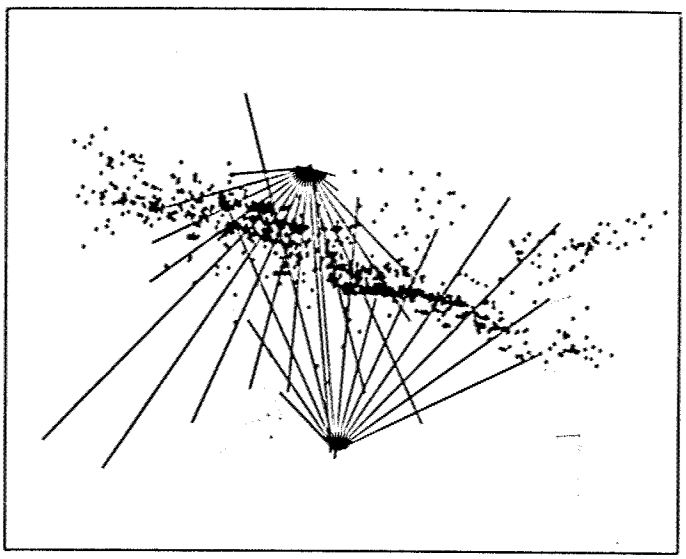

Figure 3. Located strokes and unlocated bearings on 19980826.
Lines: 50 mm = 89 strokes per 10 degrees.
Points: 1303 located strokes.

This particular case clearly demonstrates that the detection of a close enough stroke is not only a matter of its signal strength but is also subject to probabilistic factors.

The data from the 1998 season, 144,000 strokes or 83,000 flashes in the useful area, is still too sparse and regionally inhomogeneous to allow a full analysis of the detection efficiency.

## FORKED LIGHTNING

It is evident from numerous photographs that a large fraction of cloud-to-ground lightning are forked, *i.e.* the separate strokes of a multiple flash strike two or more points on the ground. According to a study by *Rakov et al.* [1994], half of all flashes, including single flashes, are forked, and the strike-point separation varies between 0.3 and 7.3 km. The study is based on 76 negative flashes only, observed in Florida, and the conditions in Finland, say, are different enough for a possibility to give different results.

The improved accuracy allows some conclusions to be drawn about forked lightning, even though separations below 1 km necessarily remain uncertain. A case study is again based on June 16, 1998, selecting a tight cluster of flashes between 63 - 64 degrees latitude, 23 - 24 degrees longitude. The fraction of multiple flashes is about 50 %. Of these, flashes were chosen for which the estimated error (semimajor axis of the error ellipse) remained below a set limit, which was varied at 0.7, 1.0 and 2.0 km. The result was relatively independent of this limit, and it can be said that the result with the lowest limit is fairly applicable to strike-point separations down to 1 km. The procedure was to seek temporally adjacent strokes of a flash and see if at least one pair had a separation exceeding the limit. The possibility of more than two strike points was ignored in this study.

The numbers of all multiple flashes (including non-forked ones) were 1523 (error limit 0.7 km), 4024 (1.0 km) and 9360 (2.0 km). Figure 4 shows an average distribution based on the three cases. 42 % of all multiple flashes has a strike-point separation exceeding 2 km. If the interval 1 - 2 km is reliable, the fraction with separation exceeding 1

km is 60 %. The fraction of strike-point separation below 1 km remains uncertain in this study. In any case it can be said safely that *at least* one half of multiple flashes (one fourth of all negative flashes) are forked. Very few separations exceed 5 km, and the limit between 7 and 8 km is in accord with the result cited above.

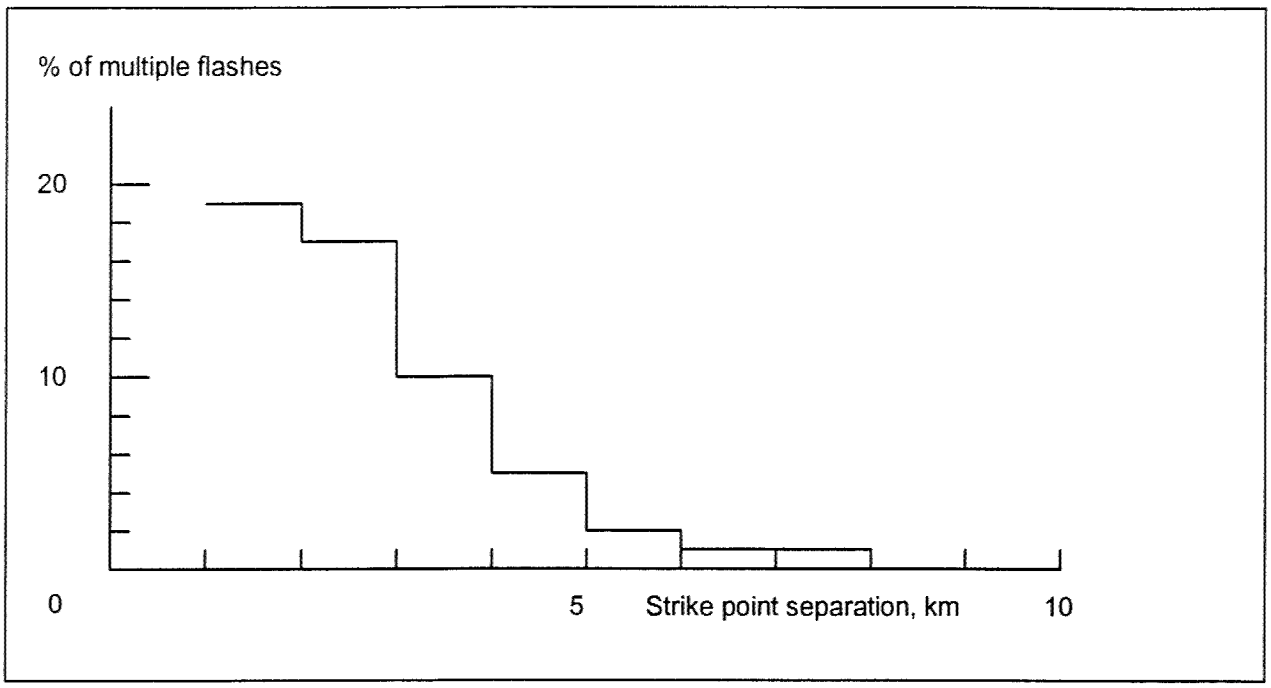


Figure 4. Percentages of forked flashes of all multiple flashes per 1-km strike-point separation intervals.

The advent of the combined triangulation and time-of-arrival techniques has replaced the flash by the stroke as a natural "unit" of located lightning, necessitated by the very principle of the time-of-arrival method. The high occurrence of forked flashes is another factor which stresses the importance of the stroke concept, *e.g.* in studying lightning damages to power lines and other structures. Yet the flash concept also remains important because the strokes share a common upper section of the channel and are part of the same well-defined process. Lightning databases should include all strokes with their individual properties, but also indicate their grouping into flashes.

## DISCUSSION AND CONCLUSIONS

Lightning location technology has reached a stage which allows the combination of rather wide coverage with acceptable accuracy and detection efficiency at a reasonable cost. After initial installation, the improvement of the accuracy to the 1-km level is straightforward, at least within the network core area (the maximal polygon defined by the sensor sites). The accuracy is partly compatible with the typical separation distance of forked lightning. Also, the accuracy will allow new kinds of routine studies, for example of the effect of topography, including*e.g.* the ever-increasing mobile-phone masts, on lightning occurrence.

The detection efficiency remains a parameter which calls for improvements. While VHF interferometry is capable of detecting virtually all electrical activity of a thundercloud, it is often too expensive for wide coverage, and for many purposes produces too much data. Parallel study of VHF and Impact-type systems could perhaps help to find means of identifying cloud-to-ground strokes from the signals and illuminate the "probabilistic" side of detection efficiency.

## REFERENCES

Rakov, V.A., M.A. Uman, and R. Thottappillil, Review of lightning properties from electric and TV observations, *J. Geophys. Res.*, 99, D5, 10,745—10,750, 1994.

# DEMOGRAPHICS OF U.S. LIGHTNING CASUALTIES AND DAMAGES FROM 1959-1994

Ronald L. Holle and Raúl E. López
National Severe Storms Laboratory, NOAA, Norman, Oklahoma

E. Brian Curran
National Weather Service, NOAA, Fort Worth, Texas

The NOAA Publication *Storm Data* has 3,239 deaths, 9,818 injuries, and 19,814 property-damage reports due to lightning from 1959-1994 in the U.S. Spatial and temporal variations that are identifiable with this dataset will be described by state, region, year, month, and hour of the day. The number of lightning casualty and damage events is less variable from year to year than nearly all other weather causes. Therefore, lightning is a constant and widespread threat to people and property during the thunderstorm season.

Florida leads the nation in deaths and injuries, while the largest number of damage reports comes from Pennsylvania. When population is taken into account, New Mexico and Wyoming lead the nation in death, injury, and casualty rates per million people. Highest rates of damage reports weighted by population are on the plains.

All types of lightning reports in *Storm Data* reach maxima during July. Damage reports are spread more evenly through the year than casualties. In northern states, casualties and damages have narrower distributions centered on summer than southern regions. There are more damage reports during the night in the plains and midwest states than elsewhere. Most incidents involve one person. Locations of casualties in *Storm Data* are not well identified. Comparison with other datasets shows that *Storm Data* entries tend to include more expensive widely-known events and to exclude most of the small losses.

## INTRODUCTION

This paper summarizes casualties and damages due to lightning in the U.S. based on the NOAA publication *Storm Data*. Curran et al. (1997) has expanded versions of these results.

Table 1 shows the number of deaths, injuries, and costs of property damage from convective weather based on *Storm Data*. When all weather deaths are examined, only flash floods and river floods rank higher than lightning.

Knowledge of medical issues concerning lightning victims has grown in recent years (e.g., Andrews et al. 1992; Cherington 1995; Cooper and Andrews 1995; Primeau et al. 1995). Improved understanding of medical profiles and demographic distributions of victims has resulted in a multidisciplinary effort concentrating on safety and education (Vavrek et al. 1999). A significant emphasis is being placed on sports and recreation (Bennett 1997; Walsh et al. 1997).

## LIGHTNING CASUALTY AND DAMAGES

Reports of damaging weather phenomena are compiled monthly at National Weather Service offices for the NOAA publication *Storm Data*. Reports are sent to the National Climatic Data Center where *Storm Data* is assembled. This publication has been compiled with similar procedures since 1959. *Storm Data* from 1959 to 1994 had 3,239 deaths, 9,818 injuries, and 19,814 damage reports from lightning. Each report contains year, month, day, time, state, and county, as well as number, gender, and location of fatalities and injuries, and costs of damages.

Lightning-caused casualties and damages are often less spectacular and more widely dispersed in time and space than tornadoes and hurricanes. Therefore, lightning deaths are underreported by 28 to 33% (Mogil et al. 1977; López et al. 1993). The number of *Storm Data* damage events was underreported by 367:1 in a review of insured property (Holle et al. 1996). So lightning-caused damages are similar to, or exceed costs of other phenomena in Table 1. Nevertheless, *Storm Data* is the only consistent data source for several decades, and its information was used without modification.

*TABLE 1. Annual convective-weather deaths, injuries, and property damage, 1992-1994 (National Weather Service, Office of Meteorology). Order is by number of deaths.*

| Convective weather type | Fatalities | Injuries | Damages ($million) |
|---|---|---|---|
| Lightning | 51 | 345 | 32 |
| Tornadoes | 47 | 1,114 | 551 |
| Thunderstorm wind | 18 | 352 | 295 |
| Hail | 0 | 43 | 345 |

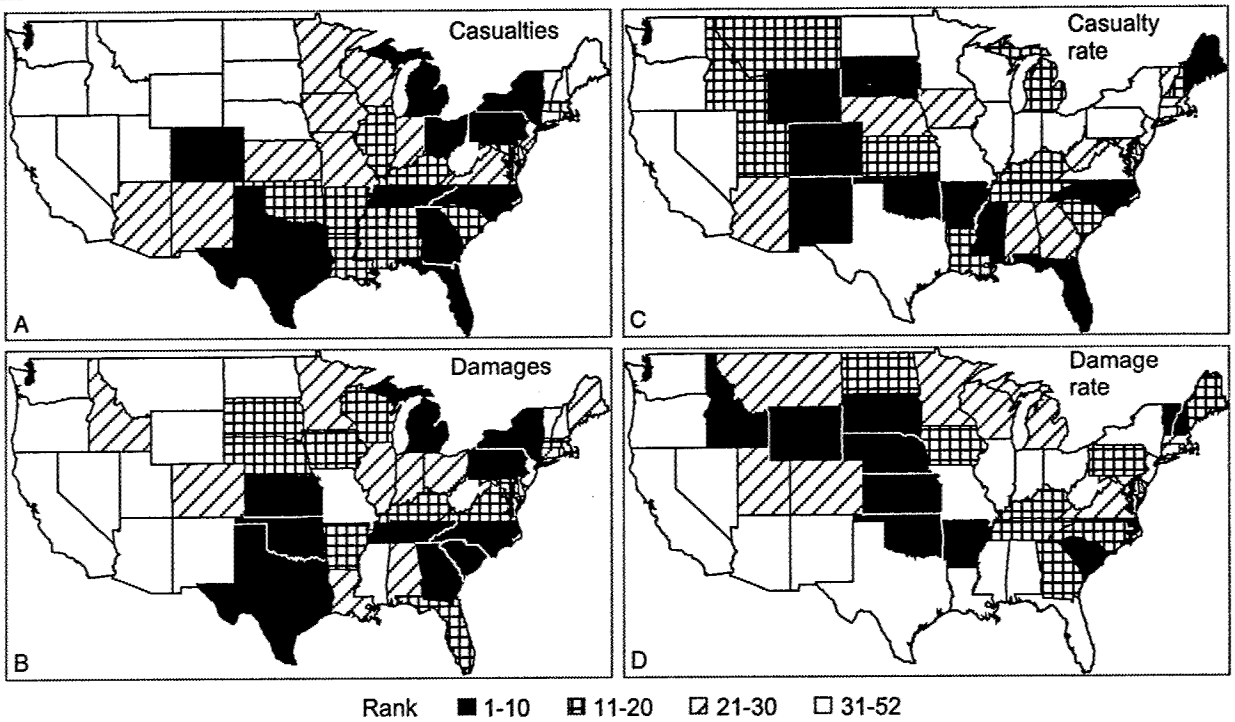


FIGURE 1. Rank of each state in lightning impacts from 1959 - 1994. A) Number of casualties. B) Number of damage reports. C) Casualty rate per million people. D) Damage report rate per million people.

## VARIATIONS BY STATE IN REPORTS

Figure 1A shows the rank of each state in lightning-caused casualties (deaths and injuries combined). Florida has twice as many casualties as any other state. Fewest casualties are in Alaska, Hawaii, D. C, northwest states, Puerto Rico, and small eastern states.

Previous studies of U. S. lightning fatalities by Duclos and Sanderson (1990), Mogil et al. (1977) and Zegel (1967) had similar results for smaller samples. Deaths by Canadian province were compiled by Hornstein (1962), and fatalities were plotted on a map of Singapore by Pakiam et al. (1981). Deaths divided by political boundaries were shown by Coates et al. (1993) for Australia and Gourbière et al. (1997) for France. Deaths by county in U. S. states are in publications listed by Curran et al. (1997).

The distribution of damage reports by state (Figure 1B) shows a concentration on the plains from South Dakota to Texas. The largest number is from Pennsylvania, where less than half as many casualties were reported as in Florida. Six of the 10 states with the highest damage counts are on the top-ten lists for casualties, deaths, or injuries.

## VARIATIONS BY STATE PER POPULATION

When population is taken into account, the maxima shift from populous eastern states to Rocky Mountain and plains states (Figure 1C). The top two rates are in Wyoming and New Mexico; these states were 35th and 21st in number of casualties. Wyoming had most of its casualties in the 1960s and 1970s. Southeast states often have high rankings in both Figures 1A and 1C. The only states in the top 10 of both casualties and casualty rate are Florida, Colorado, and North Carolina.

A swath of high rates of damage reports is located from Idaho to the Dakotas, Oklahoma, and Arkansas (Figure 1D). The plains also had high numbers of damage reports (Figure 1B) with two exceptions. North Dakota did not have many actual reports, but this less populous state becomes sixth in damage rate. Texas had numerous reports, but its damage rate became small due to it being so populous. Recall that *Storm Data* damage reports are greatly underreported (Holle et al. 1996).

## YEAR-TO-YEAR VARIATIONS

The number of lightning deaths decreased from 1959 to 1994, while injuries increased (Figure 2). As a result, the ratio of injuries to deaths increased. After population growth was taken into account (normalization), several major trends were identified by López and Holle (1996, 1998). A 30% decrease was attributed to improved forecasts and warnings, better light-

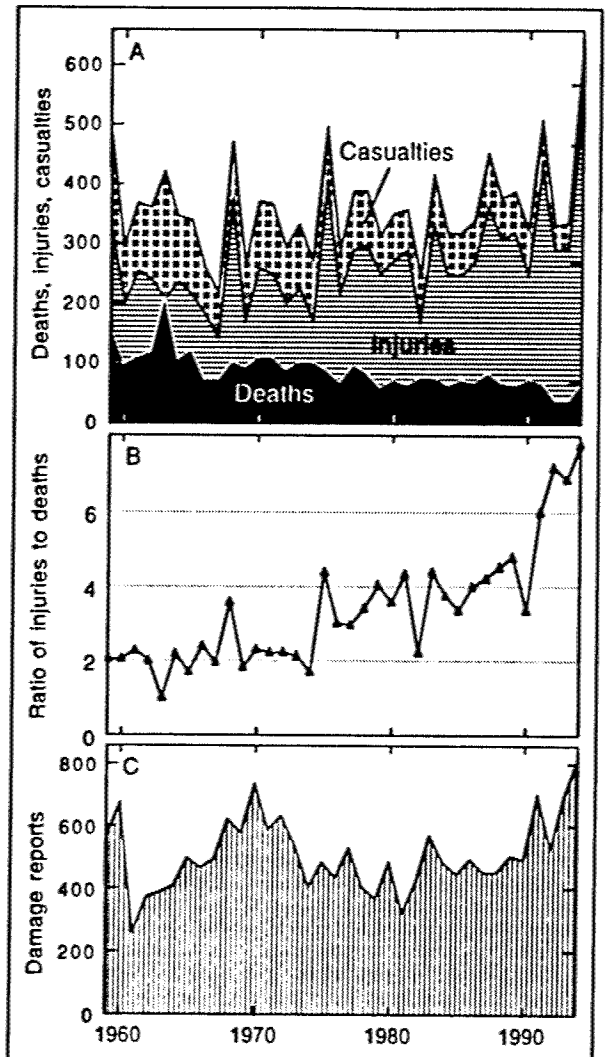


FIGURE 2. A: Number of casualties, deaths, and injuries. B: Ratio of injuries to deaths. C: Number of damage reports by year.

ning awareness, more substantial buildings, and/or socioeconomic changes. An additional 40% reduction may be due to improved medical care and communications. The injury rate decreased only 8% because of the transfer of some deaths to injuries. Additional fluctuations on the scale of one or two decades parallel national changes in thunder-days, cyclones, and temperature. An increase in damage reports (Figure 2C) could be due to population growth.

Decreases in deaths were also documented with long-term datasets in England and Wales (Elsom 1993), Australia (Golde and Lee 1976), and Singapore (Pakiam et al. 1981). Australian deaths increased from 1825 to 1918, then decreased to 1991 (Coates et al. 1993).

## MONTHLY AND SEASONAL VARIATIONS

Lightning casualties and damages peak during July. Monthly percentages increase gradually before, then decline more quickly after July. Cloud-to-ground flashes also show these features (Orville and Silver 1997). Casualties reach a higher July maximum than damage reports. Prior *Storm Data* studies also found a July maximum, a slower increase before and a faster decrease after July (Zegel 1967; Mogil et al. 1977; Curran et al. 1997).

Seasonal maps in Curran et al. (1997) show that summer casualties and damage reports follow annual maps. During other seasons, lightning cases are more frequent in southern states. Frequencies in the northeast are low except during the summer, while they are high on the West Coast during autumn and winter. The largest number of Australian fatalities were in January due to the reversal of seasons from the U.S. (Coates et al. 1993). Singapore fatality maxima in November and April (Pakiam et al. 1981) are similar to those found in the annual cycle of local thunderstorms.

## TIME OF DAY VARIATIONS

Most lightning casualty and damage reports occur in the afternoon (Curran et al. 1997). They show a steady increase toward a maximum at 1600 LST, followed by a slightly slower decrease after the maximum. Damage reports are more broadly distributed in time. Narrower distributions are apparent in the Rockies, southeast, and northeast. The broad time series in the plains and midwest are due to nocturnal thunderstorm complexes. Similar maxima in lightning casualties and/or damages were found elsewhere (Curran et al. 1997)

## OTHER INFORMATION IN *STORM DATA*

Males account for 84% of the lightning fatalities, 82% of injuries, and 83% of casualties (Curran et al. 1997). Similar results were found in the U.S. (Duclos and Sanderson 1990), Singapore (Pakiam et al. 1981), and England and Wales (Elsom 1993).

The most common situation is for one victim in a lightning incident. For death incidents only, 91% had one fatality; another 8% had two people killed in an incident.

Location categories in *Storm Data* are not very useful. "Not reported" and "at various other and unknown locations" account for 40% of the entries. It is important to go beyond the *Storm Data* digital record to find a victim's activity, which tells more of the situation.

Sunday has 24% more deaths than other days; a slight tendency for more deaths is also evident on Wednesday (Curran et al. 1997).

Nearly half of all lightning damages in *Storm Data* are between $5,000 and $50,000 (Curran et al. 1997). Holle et al. (1996) found that over a third of insurance losses were between $251 and $1,000, and only a few were over $5,000. Therefore, *Storm Data* damage report losses are much larger than the insured lightning losses.

## SUMMARY AND CONCLUSIONS

Florida led the nation in actual deaths and injuries. The largest number of damage reports came from Pennsylvania. When population was taken into account, Wyoming and New Mexico led the nation in death, injury, and casualty rates. The highest rate of damage reports was on the plains from North Dakota to Oklahoma.

Casualties had a strong July maximum, while damage reports were spread more evenly through the year. Casualties and damages in northern states had narrower distributions centered on summer than states to the south.

Two-thirds of casualties occurred between 1200 and 1600 LST. Damage reports lagged casualties by two to three hours. There were relatively frequent damage reports at night in the plains and midwest states.

For incidents involving deaths (injuries) only, 91% (68%) of the cases had one fatality (injury). The dominance of single-person events shows the need for lightning safety education so that people take personal responsibility for protection from lightning.

Half of all lightning-caused damages were between $5,000 and $50,000 according to *Storm Data*, but comparison with other datasets shows these entries to include more widely known events and fewer small losses.

## REFERENCES


Andrews, C.J., M.A. Cooper, M. Darveniza, and D. Mackerras, 1992: *Lightning injuries: Electrical, medical, and legal aspects.* CRC Press, Boca Raton, FL, 195 pp.

Bennett, B.L., 1997: A model lightning safety policy for athletics. *J. Athletic Training*, **32**, 251-253.

Cherington, M., 1995: Central nervous system complications of lightning and electrical injuries. *Sem. Neurology*, **15**, 233-240.

Coates, L., R. Blong, and F. Siciliano, 1993: Lightning fatalities in Australia, 1824-1991. *Natural Hazards*, **8**, 217-233.

Cooper, M.A., and C.J. Andrews, 1995: Lightning injuries. In *Wilderness Medicine*, P. Auerbach, ed., 3rd Edition, St. Louis, MO, C.V. Mosby, 261-289.

Curran, E.B., R.L. Holle, and R.E. López, 1997: Lightning fatalities, injuries, and damage reports in the United States from 1959-1994. NOAA Tech. Memo. NWS SR-193, 64 pp.

Duclos, P.J., and L.M. Sanderson, 1990: An epidemiological description of lightning-related deaths in the United States. *Intl. J. Epidemiology*, **19**, 673-679.

Elsom, D.M., 1993: Deaths caused by lightning in England and Wales, 1852-1990. *Weather*, **48**, 83-90.

Golde, R.H., and W.R. Lee, 1976: Death by lightning. *Proc., Inst. Electrical Engineers*, **123**, 1163-1180.

Gourbière, E., J. Lambrozo, C. Virenque, P. Menthonnex, and J. Cabane, 1997: "Lightning injured people in France" the first French national inquiry with regard to the striking of people – objectives, methods, first results. *Proc., Conf. on Lightning and Mountains '97*, Chamonix Mont Blanc, France, M71-M83.

Holle, R.L., R.E. López, L.J. Arnold, and J. Endres, 1996: Insured lightning-caused property damage in three western states. *J. Appl. Meteor.*, **35**, 1344-1351.

Hornstein, R.A., 1962: Canadian lightning deaths and damage. Meteorological Branch, Dept. of Transport, Canada, CIR-3719, TEC-423, 11 Sept. 1962, 5 pp.

López, R.E., and R.L. Holle, 1996: Fluctuations of lightning casualties in the United States: 1959-1990. *J. Climate*, **9**, 608-615.

—, and —, 1998: Changes in the number of lightning deaths in the United States during the twentieth century. *J. Climate*, **11**, 2070-2077.

—, —, T.A. Heitkamp, M. Boyson, M. Cherington, and K. Langford, 1993: The underreporting of lightning injuries and deaths in Colorado. *Bull. Amer. Meteor. Soc.*, **74**, 2171-2178.

Mogil, H.M., M. Rush, and M. Kutka, 1977: Lightning---An update. Preprints, *10th Conf. on Severe Local Storms*, Omaha, NE, Amer. Meteor. Soc., 226-230.

Orville, R.E., and A.C. Silver, 1997: Lightning ground flash density in the contiguous United States: 1992-95. *Mon. Wea. Rev.*, **125**, 631-638.

Pakiam, J.E., T.C. Chao, and J. Chia, 1981: Lightning fatalities in Singapore. *The Meteor. Mag.*, **110**, 175-187.

Primeau, M., G.H. Engelstatter, and K.K. Bares, 1995: Behavioral consequences of lightning and electrical injury. *Sem. Neurology*, **15**, 279-285.

Vavrek, R.J., R.L. Holle, and R.E. López, 1999: Updated lightning safety recommendations. Preprints, *8th Symp. Education*, Dallas, TX, Amer. Meteor. Soc.

Walsh, K.M., M.J. Hanley, S.J. Graner, D. Beam, and J. Bazluki, 1997: A survey of lightning policy in selected Division I colleges. *J. Athletic Training*, **32**, 206-210.

Zegel, F.H., 1967: Lightning deaths in the United States: A seven-year survey from 1959 to 1965. *Weatherwise*, **20**, 169-173, 179.

# RESULTS OF INVESTIGATIONS INTO ANNUAL USA LIGHTNING COSTS AND LOSSES.

R. Kithil

National Lightning Safety Institute, Louisville Colorado USA

ABSTRACT: Researchers who attempt to describe the economic impact of lightning in the USA are confronted with contradictory data. National Weather Service (NWS) figures place the most recent yearly losses at some $35 million. Such a severe understatement of costs from an official source tends to inhibit attentions focused at lightning problems. In general, lightning safety issues are not taken seriously by individuals, by business, or by government. If actual dollar losses were understood more fully, then awareness and mitigation measures might be raised to a higher priority.

## INTRODUCTION

*Storm Data* is the NWS reporting vehicle for collecting and describing severe weather information. Each NWS field office has an appointed Warning Coordinating Meteorologist or other staff person responsible for collecting local news to be forwarded to *Storm Data*. Newspaper accounts are a frequent source of this information. If an incident does not appear in the newspapers, or is overlooked by the reviewer, it may not get into the *Storm Data* statistical base.

## RECENT CONFIRMED ECONOMIC CONSEQUENCES

1. Source: St. Paul Insurance Company, St. Paul MN. During the 5 year period 1992 through 1996 some $USD 1.7 billion was paid out in lightning-related claims. All claims were commercial in nature. Lightning accounted for 8.7% of the total number of claims and 3.8% of the property dollar losses. The average annual paid claims for this period equaled $ 340 million.

2. Source: Anonymous Large Insuror (Holle, et al: *Insured Property Damage Due to Lightning in Three Western States*, Proc. IAGCLSE, Williamsburg VA, Sept. 1995). Lightning losses to residential and commercial property in Colorado, Utah, and Wyoming were sampled over a six year period. Most claims (90%) were individual homeowners. When extrapolated into national averages, 307,000 annual claims totaled some $ 332 million each year.

3. Source: The National Fire Protection Association (NFPA), Quincy, MA. NFPA publishes *Annual Averages of Fires and Losses Reported to U.S. Fire Departments Caused by Lightning*. Information is collated by property classification and by source of origin. In the most recent reporting period 1991-1995, each year lightning was the cause of 30,190 fires accounting for annual losses of $ 175.2 million.

4. Source: Insurance Information Institute (III), NY NY. A press release from III in 1989 reported that 5% of all insurance claims were lightning related, amounting to more than $USD 1 billion per year. In 1997 and 1998, press releases from III said that "lightning strikes are responsible for over $ 250 million per year."

5. Source: Clausen Miller PC, Chicago IL During July 23, 1997 a lightning-induced fire broke out at 5120 Race Court, Denver, Colorado to the CS Integrated refrigerated warehouse. There was a total loss to building and contents of some $ 72 million. This is believed to be the largest structural loss due to lightning on record.

6. Source: Project Report NOAA – 18 (Weber et al, *An Assessment of the Operational Utility of a GOES Lightning Mapping Sensor*, MIT Lincoln Laboratory, 13 February 1998. "The FAA currently estimates that thunderstorms cost the airlines and the U.S. public approximately $2 billion per year in operating costs and passenger delay."

7. Source: Electric Power Research Institute (EPRI), Palo Alto, CA, Ralph Bernstein; Diehls, et al(1997). Some thirty percent of all power outages are lightning-related on annual average, with total costs approaching $ 1 billion.

8. Source: The Ohio Insurance Institute, Colombus OH reports that 18% of all lumberyard fires are originated by lightning. Further, they state that 30% of all church fires are started by lightning.

9. Source: Journal of Hazardous Materials 40 (1995) 43-54. Lightning accounts for 61% of all accidents in storage and processing activities where natural events were the root cause. In North America, 16 out of 20 accidents involving petroleum products storage tanks were due to lightning strikes.

10. Source: National Park Service, Gary Hasty, Risk Management. "We have determined that about half the wildfires in the western USA are lightning-related. About 10,000 such fires cost about $ 100 million annually. In 1996 the National Park Service experienced 517 lightning-induced fires which cost $ 19,576,128. In 1997, the Boise National Forest fire cost $ 47 million and took 45 days to bring under control."

11. Source: National Lightning Safety Institute, Richard Hasbrouck, Director of Engineering. "Low voltage electronic equipments are especially vulnerable to lightning upset. Such insults include explosions, fires, burn marks, and mechanical distortion. Data corruption and slow degradation of circuit boards are time-delayed, serious hidden problems. No one knows the dollar cost or magnitude of damage here."

12. Source: Department of Energy (DOE), Occurrence Reporting & Processing System (ORPS), period from September 1990 to September 1998. ORPS-reported lightning incidents at DOE sites for the 8 year period totaled 461 incidents, or 57.6 accidents per year on average. Types of losses, but no costs, were identified. An examination of the incidents can be summarized:

a. ORPS reporting frequency is not related to localized lightning frequency. Hanford Site, for example, located in a low lightning area was second in numbers of reported incidents. Savannah River site was the leader in reported lightning problems.

b. Lightning-caused incidents included failure of protective devices, equipment malfunctions, standby generator failures, grass and range fires, power pole destruction, and injury to personnel.

c. Voltage surges accounted for about 80% of the physical damage reported. Affected equipment in this category included: transient limiters (arrestors, fuses, switches); telephones, pumps & motors, and generator systems.

d. Alarm systems suffered the most damage. Areas affected included perimeter security intrusion alarms, fire and radiation alarms (both failures and activations were reported),

as well as communications systems equipment (pagers, public announcement speakers, telephone and radio communications).

## CONCLUSION

Accurate lightning cost and loss reports are elusive. There is not good agreement between sources. The NWS *Storm Data* reporting system appears to be flawed, since there is evidence that annual lightning losses are in excess of the "official" $ 35 million figure. Further investigation is needed to provide better statistical data. It seems a reasonable estimate that there may be $ 4-5 billion in lightning costs and losses each year in the USA.

ACKNOWLEGEMENTS: The author would like to thank Dennis Kubicki (DOE-Fire Safety), Ron Holle (NOAA-NSSL), Bruce Lunning (St. Paul Fire & Marine Insurance Co.), Linda Kremkau (NWS – Office of Meteorology) and Stan Grzybowski (Mississippi State Univ.) for their help and suggestions.

## REFERENCES

Kithil, R., *A Risk Management Approach to Lightning Safety*, IAGCLSE, Williamsburg VA, 1995.

AUTHOR'S ADDRESS: National Lightning Safety Institute, 891 N. Hoover Ave., Louisville CO 80027. Email: *rkithil@ix.netcom.com*

# THE TWO IMPORTANT CHARACTERISTICS OF GROUND FLASHES FOR THE HUMAN SAFETY

N. Kitagawa[1], A. Sugita[2], and S. Takahashi[2]

[1]Central Lightning Protection Inc., Urawa-shi, Japan
[2]Franklin Japan, Yokohama-shi, Japan

ABSTRACT: For the safety of human beings against lightning, it is essential to keep away form direct strikes. A person in the outdoors has to move into the safe space against the lightning incidence. To provide proper guides to avoid lightning strikes, the following two factors have to be disclosed:
① Time intervals between subsequent flashes that strike the ground within a small area
② The distances between struck points of subsequent ground flashes.
The authors analyzed the data obtained by the lightning location system, covering Kanto District, Japan for two years and obtained the statistical distributions of the above two factors.

## INTRODUCTION

Based on the clinical investigations of lightning injuries and the laboratory simulation experiments, Kitagawa et al. [1985] studied the nature of lightning discharges on human bodies. It was revealed that the internal organization of the human body functions as an effective conductor and attracts the lightning incidence in the outdoors. When a person stays close to tall objects, such as trees, poles, chimneys, etc., he is apt to be struck by secondary discharges from tall objects struck by lightning and be severely injured. Therefore, when thunderstorms are active overhead, a person has to move into the safe space, namely inside of buildings, cars, buses, trains, etc. to avoid the lightning incidence. The time interval between subsequent flashes, that strike the ground within small area, is an important factor for a person to take refuge in a safe space.

When thunderstorms are approaching, a person has to take refuge in a safe space beforehand. The distance between struck points of subsequent ground flashes, namely, skip distance of subsequent ground flashes is another important factor for him to judge when he should start to take refuge.

For the skip distances of subsequent lightning discharges, Hatakeyama [1959] provided a statistics, based on his multi-point electric field measurements. However, except Hatakeyama's work no detailed data have ever been analyzed regarding the above two factors. Nowadays, lightning location systems are widely operated and numerous data have been accumulated concerning times and positions of ground flashes. The authors statistically analyzed the data for two years and obtained the reliable results as to the above two factors.

## LIGHTNING LOCATION SYSTEM, INVESTIGATED AREA AND PERIOD

Figure 1 shows the positions of sensors of the lightning location system that provided data for the present work. The system uses 6 IMPACT sensors to cover Kanto District, Japan. IMPACT is an abbreviation for "Improved Accuracy from Combined Technology." The system combines the direction finding method and the arrival time difference measurement, and locates the ground flashes with higher accuracy than the system using a single method. The time accuracy of the system is 1.5 μs and the location accuracy for Kanto District is 500 m.

The authors dealt with data for two years in 1996 and 1997 and the area covering the latitude from 35.2° to 37.1° and the longitude from 138.6° to 140.6° as shown in Figure 1.

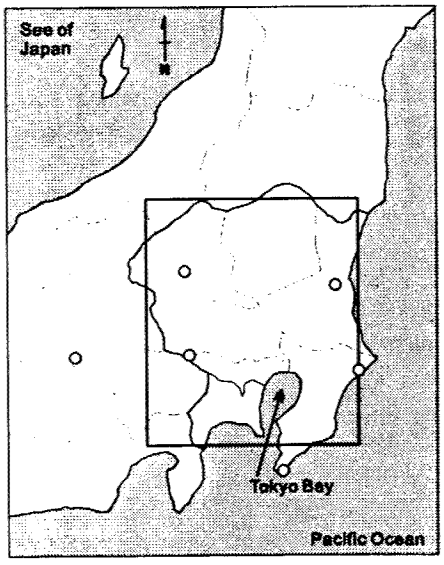


Figure 1. Positions of 6 IMPACT sensors (circles) and investigated area (square). Bold line represents the border of Kanto District.

## TIME INTERVALS BETWEEN SUBSEQUENT FLASHES THAT STRIKE THE GROUND IN A SMALL AREA

For the safety of human beings, the time intervals between subsequent flashes that strike the ground within a small area of a circle of 500 m radius seem important. The area where a person moves around in one minute, is confined within such an area. When he is in the outdoors under severe thunderstorms, he has to refuge into a safe space. If he knows the time intervals of such nearby ground flashes correctly, he can

judge whether he should move or stay while keeping his posture low.

Based on the data obtained by the lightning location system, the authors statistically investigated the time intervals between subsequent flashes that struck the ground within a circle of 500 m radius. The time intervals are divided into 0 to 10 s, 10 to 20 s, 20 to 30 s and likewise up to 600 s. The occurrence numbers of individual time intervals are represented by the column diagram. The tops of the columns thus plotted indicate the statistical occurrence distribution of the time intervals. Figure 2 and 3 show the results of data in 1996 and 1997 respectively, where the time intervals longer than 600 s are abbreviated. The numbers of the data dealt are approximately 25,000 for each year. Since the numbers are not large enough, the tops of the columns exhibit somewhat irregular distributions, but the smoothed curves of the column tops would represent the statistical distribution of the intervals.

As no essential difference is noticed between the column diagrams in Figures 2 and 3, it is interpreted that the year to year variation does not exist in the distribution of occurrence numbers. As shown in Figure 4, the authors plotted the data in 1996 and 1997 together in one diagram and drew the smoothed curve for the column tops. The curve in Figure 4 represents the best statistical distribution of the time intervals treated in this section.

Since 500 m is the limit of the location accuracy of the system, the reliability of the above statistics should be checked in some way. Based on the same data, the authors statistically investigated the time intervals of subsequent ground flashes that struck the ground within a circle of 1 km radius. In this case, the location accuracy is high enough for the statistical analysis. The authors made the column diagrams for the data obtained in 1996 and 1997 respectively, ascertained no year to year variation and composed them in one diagram. Figure 5 shows this diagram where the smoothed curve of the column tops is drawn. Comparing Figure 4 and 5, they show essentially the same statistical characteristics; the difference is that the most frequent interval is approximately 40 s in Figure 4, while the one approximately 30 s in Figure 5. It is apparent that statistics in Figure 4 is equally reliable as one in Figure 5.

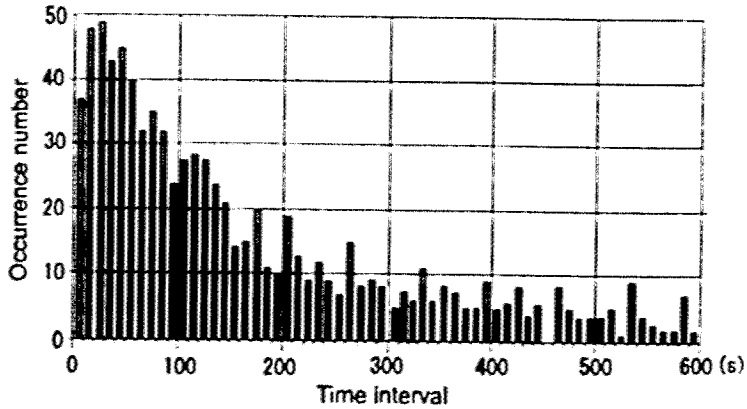


Figure 2. The occurrence number of time intervals between subsequent flashes that struck the ground in a circle of 500 m radius, based on data in 1996

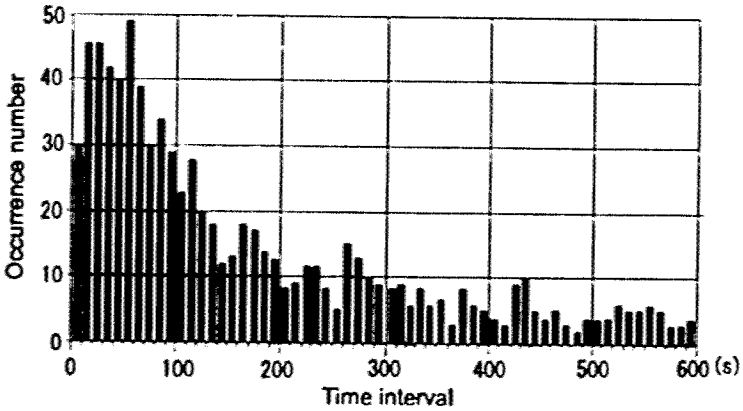


Figure 3. The occurrence number of time intervals between subsequent flashes that struck the ground in a circle of 500 m radius, based on data in 1997

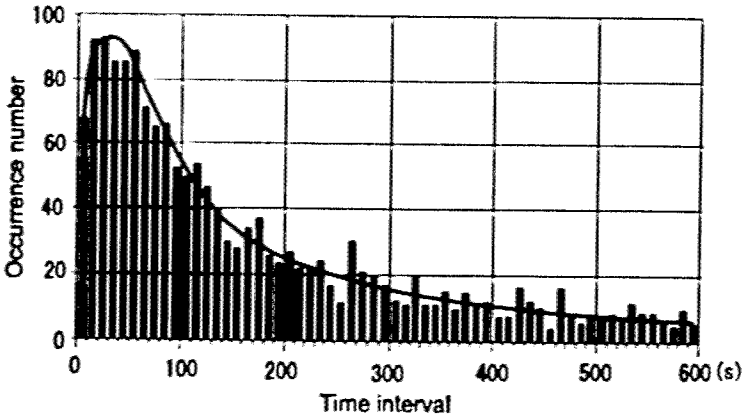


Figure 4. The occurrence number of time intervals between subsequent flashes that struck the ground in a circle of 500 m radius, based on data in 1996 and 1997

The authors anticipated that the time intervals between subsequent flashes that strike the ground within a circle of 500 m radius would be longer than 60 s. However, the results of the statistical investigation reveal that most of the intervals range from 0 to 600 s, having the maximum frequency at around 40 s. When a ground flash strikes open field under active thunderclouds, it is most likely that the next flash strikes the ground 40 s later after the first strike within a circle of 500 m. Under such condition, it is very dangerous that a person keeps walking or running with high posture. When safe spaces, such as buildings, cars, buses, trains, etc. exist nearby, he should enter into the nearest one. When tall objects, such as trees, poles, chimneys, etc. exist nearby, he should keep away from them as far as possible, at least, more than 2 m from all projected points of the objects. Essentially a person is advised to lower his posture as low as possible.

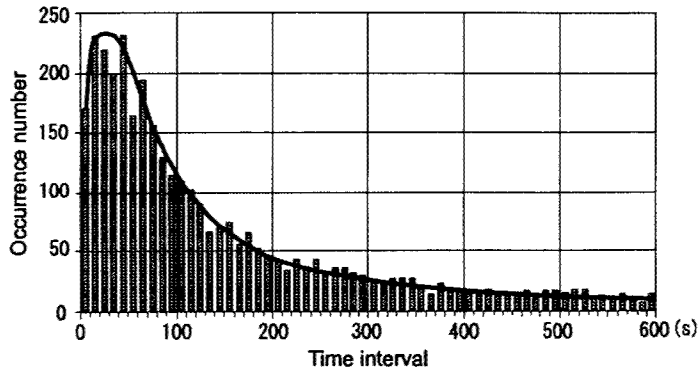


Figure 5. The occurrence number of time intervals between subsequent flashes that struck the ground in a circle of 500 m radius, based on data in 1996 and 1997

## SKIP DISTANCES OF SUBSEQUENT GROUND FLASHES

In Japan, an extensive thunderstorm research project was executed in the summer from 1940 to 1944, in Northen Kanto District. In the project, Hatakeyama [1958] operated 5 electric field measuring stations scattering with mutual distances from 5 to 10 km. Analyzing the data obtained, he calculated the charge neutralized by individual cloud flashes and plotted their positions on the map, postulating the positive dipole model. He presented the statistics of the occurrence distribution of the skip distances between subsequent cloud flashes as shown in Figure 6. The statistics indicate that most of the skip distances lie between 2 and 6 km and they range from 0 to 10 km. The statistics contain important information to judge when a person should start to take refuge, when thunderstorms are approaching. For the safety of human beings, the information concerning the skip distances of ground flashes are essentially needed.

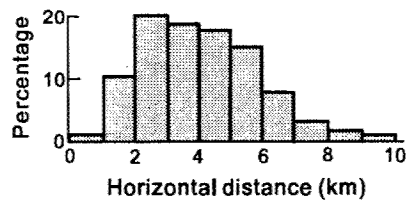


Figure 6. Occurrence percentage of skip distances of subsequent cloud flashes

Figure 7 shows the distribution of one large group of struck points, obtained by the lightning location system from

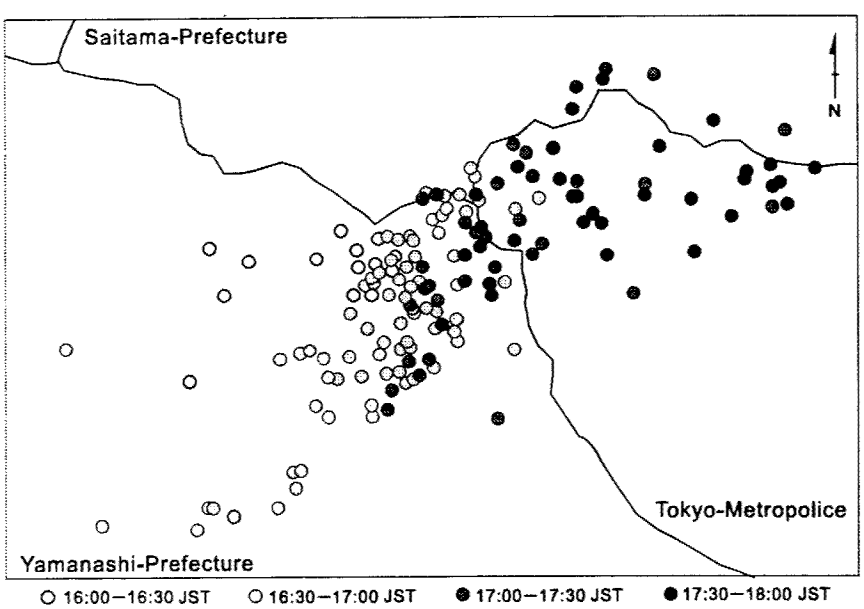


Figure 7. A large group of struck points

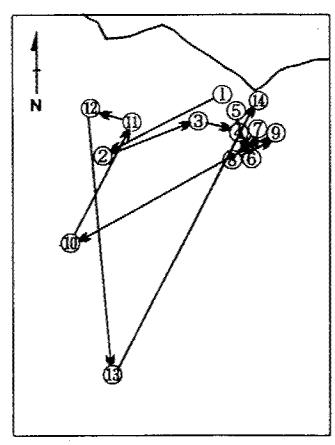


Figure 8. Movement of individual struck points from 16:00 to 16:30 JST

16:00 to 18:00 JST, August 3, 1997 over the southwestern border of Kanto District. The circles that indicate the positions of struck points are classified into the following four groups:

Plain circles: indicate the positions of struck points occurred from 16:00 to16:30 JST

Light-gray circles: indicate the positions of struck points occurred from 16:30 to17:00 JST

Dark-gray circles: indicate the positions of struck points occurred from 17:00 to17:30 JST

Black circles: indicate the positions of struck points occurred from 17:30 to 18:00 JST.

Figure 8 shows the movement of each struck point from 16:00 to 16:30 JST, putting the order number on it. When Figures 7 and 8 are combined, they indicate that the whole lightning activity moved toward east-north-east direction while the individual struck points exhibited a so-called "random walk."

The authors found 7 similar large groups of struck points in the data obtained in 1997. They measured all skip distances and counted the occurrence numbers for each range of 0~1 km, 1~2 km, 2~3 km and likewise up to 30 km. The occurrence numbers of individual time intervals are represented by the column diagram. Approximately 3,100 data are analyzed and the results are shown in the column diagram in Figure 9, where the left ordinate indicates the occurrence number and the right one indicates the occurrence percentage. The statistical characteristics of the skip distances thus obtained turned out to be almost the same as that Hatakeyama had found for the cloud flashes in 1958.

Figure 9 indicates that though most of the skip distances lie between 2 and 6 km, the occurrence percentage is still 2% for the skip distance of 12~13 km. Since the audible distance of thunder is usually 14 km, this result is very notable. When a person hears thunder, he is already within the range where a next ground flash will occur with the probability of 2%. Therefore, he should immediately take refuge into the safe space. The audible distance of thunder sometimes extends up to 20 km under the favorable condition, and the occurrence percentage of 20 km skip distance is 1%. Therefore, a person also should start to take refuge in this case. The corresponding flash-to-bang time is 41 s.

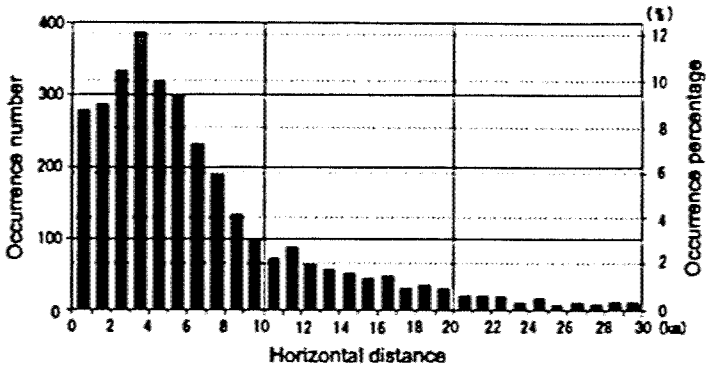


Figure 9. The occurrence number and the occurrence percentage of skip distance of subsequent ground flashes

## SUMMARY

As to the time intervals between subsequent ground flashes that strike the ground within a circle of 500 m radius, the reliable statistics have been obtained. Most of the intervals range from 0 to 600 s, having the maxim frequency at around 40 s. It is concluded that there exists no safe time interval during which a human being is free from direct strikes.

When a person takes refuge from thunderstorms in the outdoors, he should behave, taking the above statistics in account. When safe spaces such as buildings, cars, buses, trains, etc. exist nearby, he should enter the nearest one. When tall objects such as trees, poles, chimneys, etc. exist nearby, he should move away as far as possible, at least, 2 m away from all projected points of the objects. In case no safe space exists nearby, he should lower himself; wait till the lightning activity diminishes and then start to take refuge toward safe spaces.

As to the skip distances of subsequent ground flashes, the reliable statistics have been obtained. Though most of the skip distances lie between 2 and 6 km, the occurrence percentage of 12~13 km is 2%. This is a very notable result, because 14 km is usually the audible limit of the thunder. When a person hears thunder, he is already within the range where a next ground flash will occur with the probability of 2%. For the safety, a person should start to take refuge, when he hears even faint thunder.

## REFERENCES

Hatakeyama, H., The distribution of the sudden change of electric field on the earth's surface due to lightning discharge, Recent Advances in Atmospheric Electricity, Pergamon Press, London, 289--298, 1958.

Kitagawa, N., S.Turumi, T. Ishikawa, and M.Ohashi, The nature of lightning discharges on human bodies and the basis for the safety and protection, Conference Proceedings of 18th International Conference on Lightning Protection, 435--438, 1985.

# COMMENTS ON THE E.S.E. AIR TERMINALS

C. Guo
Shanghai Institute of Meteorology, Shanghai, P.R.CHINA

ABSTRACT: Based on analyzing the "E.S.E. lightning conductor assessment procedure" provided by the French Standard NF C 17-102, it is inferred that if the product is manufactured following this assessment procedure, the declared improvement or performance could not be insured, mainly due to imperfect simulation of natural condition. In turn, the products manufactured under such a Standard cannot be considered with enough experimental evidence as having declared performance.

Some suggestions are provided to improve such a situation.

## INTRODUCTION

The Early Streamer Emission (E.S.E.) air terminals or E.S.E. lightning conductors have been introduced into and sold in China for years. The device differs from a conventional air terminal , lightning rod or lightning conductor in that it is equipped with a device that supposedly initiates an upward streamer earlier than the conventional one does under the same background field and its change, thus resulting in earlier connecting with the downward leaders. In turn, it supposedly could offer a longer striking distance and wider protection zone than the conventional one could.

Careful laboratory experiments, field experiments, long term data collection and analyzing and theoretical work are all needed to obtain a completely accepted and fully convinced assessment, in order to answer if it is a real improvement and an invention.

Here, some comments are provided for assessing the laboratory experiment following the French Standard (NF C17-102, 1995)(hereafter, the **Standard**), which probably offers the only existing criteria available for manufacturing and performance assessment.

The main point we have to make or accept is that the manufactured E.S.E. air terminal could perform early streamer emission under such an experimental condition.

## DISCUSSION

First, the small distance (**C2** and **d** of **Fig.C1**) (around 1m or so) between the test plate and the rod, and the restriction of the size of the plate, provides a condition that whenever there is a small discharge, it will be very easy to have a spark over between electrodes, since the background field would increase appreciably for small gap, instead of keeping roughly constant as in the natural condition.

Requirement for a full size laboratory experiment, size of the rod and especially the limited capacity of the experimental high voltage device cause such a hard-to-overcome shortage. Under such a condition, since the E.S.E. air terminal would emit earlier than the single rod would, it will provide more chance for E.S.E. air terminal operating, otherwise at least some of the small discharges would stop developing and extinguish.

Second, in **C1.1 ground field simulation of NF C17-102**, it says, " **The natural ground field existing before a lightning stroke affects the conditions of corona formation and of space charges. The natural ground field should therefore be simulated: its value ranges from 10kV/m to 25 kV/m.**" The statement of simulating natural ground field is, of course, correct. But the set range of field is not practical, since the natural ground field is always lower than 10 kV/m. This simulation will usually cause corona around the rod, which would prevent from initiating leader by space charge effect. For E.S.E. air terminal, it will absorb more energy and to be more prepared for streamer of emission.

To make sure if this effect really exists, simple experiment with different background fields could be easily made or just simply define a smaller ground field.

Third, the **standard** defines a waveform slope range of **0.2 to 2 kV/m/μs (C1.2)**.Let us look at the natural condition. It has been estimated that the voltage of the stepped leader channel to ground is around $10^7$ V or higher, and the downward speed of the leader, when close to the ground, is $10^6$ m/s or higher. And if the striking distance is around 100 m, then the lower limit of the waveform slope should around 1 kV/m/μs,

which is at the upper end set by the **Standard.** It tells that usually, the natural condition provides faster field change than that the test ,set by the **Standard**, does. It is quite possible that within certain range, the faster the field change, the shorter the triggering advance will have. The test result, due to slower slope range set by the **Standard,** could exaggerate the triggering advance.

Fourth, the **Standard** defines a reference waveform with rise time of **650μs (C4.2 and Fig.C2)** for normalization and a rise time range of **100μs to 1,000μs (C1.2)** . The way of normalization infers that it accepts that faster slope waveform will result in shorter triggering advance, as also pointed out in our last paragraph. And in turn, some questions should be raised. If we accept this idea, then there won't be any fixed triggering advance, for different lightning , there are different rise times, then there should be different triggering advances. How can we use such an E.S.E. air terminal to improve lightning protection ?.Especially, a stronger lightning might have shorter triggering advance, which would diminish the expected improvement.

Talking about the simulation of the natural condition, it should also be pointed out that when the downward negative leader is approaching, the ground field will increase faster and faster, the slope of which will become steeper and steeper, instead of become slower, which would make the triggering advance longer. This is another difference from the natural condition.

Fifth, if we consider the stepped leader process further into its fast change, it will be found that the pulses with about one microsecond width superimposed on the relatively slow field change are indicators of the existence of stepped leader. The triggering of the upward leader is mostly possible, when the last downward step starts to emit a last pulse, the field of which is quite large due to the short distance in between. Hence, the real triggering advance could be less than one microsecond, no matter what kind of E.S.E. air terminal is used.

Test set by the **Standard** does not simulate this field impulse, which could be essential for the real initiation of the upward leader from any ground object including any lightning conductor.

## CONCLUSIONS AND SUGGESTIONS:

It seems that the assessment procedure set by the French **Standard NF C17-102** is inadequate to simulate natural condition for assessing the real triggering advance, and cannot provide comparable and consistent results. Under certain conditions, it could provide a better environment for E.S.E. device to trigger discharge. At present, it is probably hard to use laboratory experiment to get a convinced result.

As partly improving the experiment, a rod to rod setup might be a better simulation than that of the **Standard** the background field should be set lower than 10 kV/m, and a fixed field peak and rise time waveform, similar to that occurs under thunderstorm, should be decided. Since the trick for the triggering advance depends possibly on a relatively slow slope, it is probable that a successful triggering advance would need an waveform and field peak that do not exist in most natural condition.

The analysis gives an impression that the slower slope of the waveform set by the **Standard** will make it possible to carry out appreciable triggering advance by the E.S.E. air terminal, otherwise a negligible advance will appear and means no real improvement.

Since lightning striking a fixed place is a very, very low probability event, a full scale comparison using artificially triggered lightning might be a choice for some people to have a better understanding of the real performance of all the existing E.S.E. lightning conductors. It should be emphasized that only real striking to the E.S.E. air terminal can be some kind of proof.

ACKNOWLEDGMENTS: The author would like to thank Dr. R. Cohen of Panamax for providing useful papers.

## REFERENCES

Van Brunt, R. J., et al., E. S. E. Air Terminals Lightning Protection Systems,–Literatures Review and Technical Analysis, NIST, *National Fire Protection Research Foundation*, 1995

French Standard NF C17-107, Lightning Protection, Protection of Structures and Open Areas Against Lightning Using Early Streamer Emission Air Terminals, June 1995.

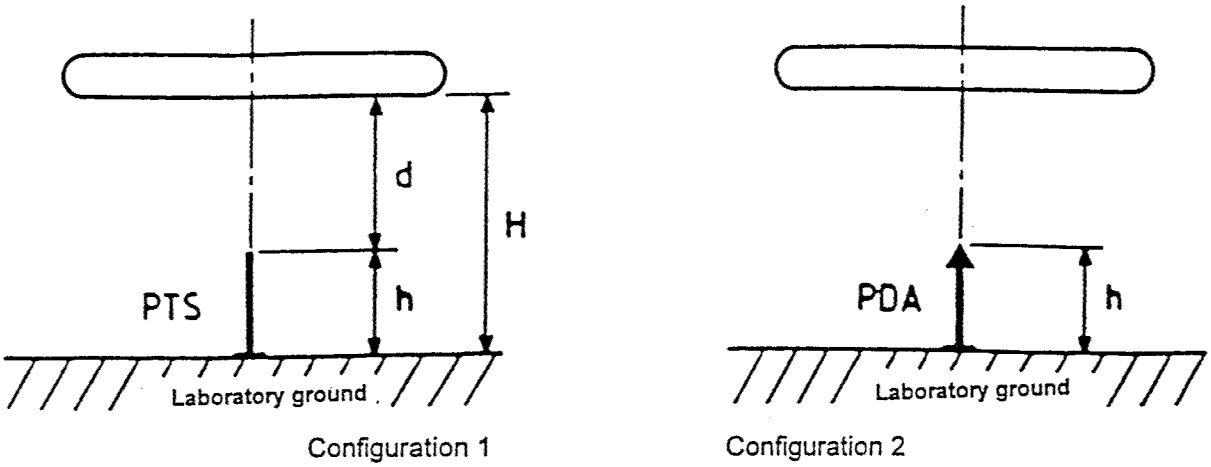


Figure C1

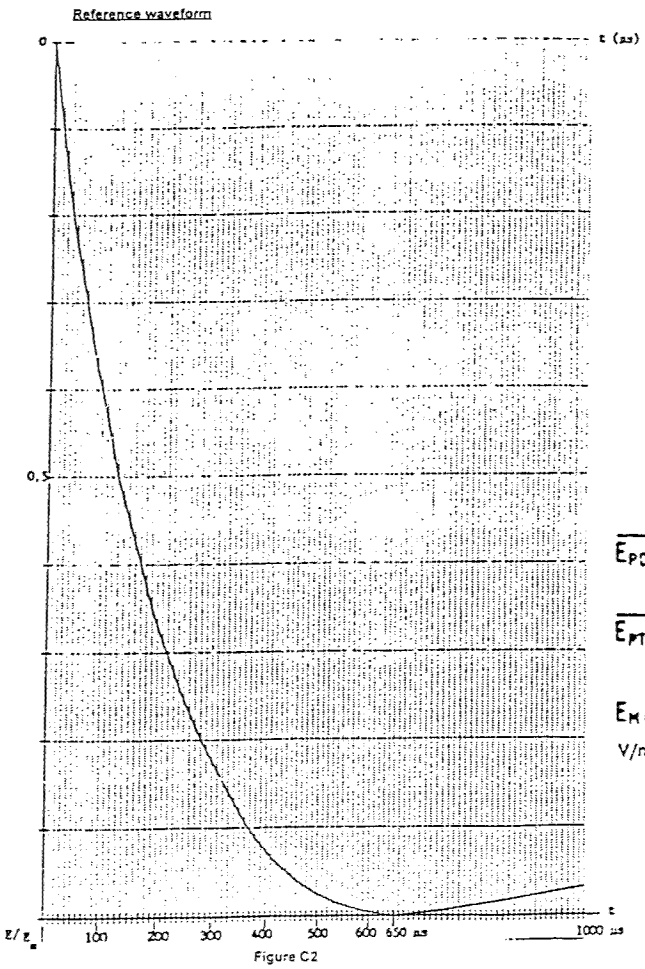


Figure C2

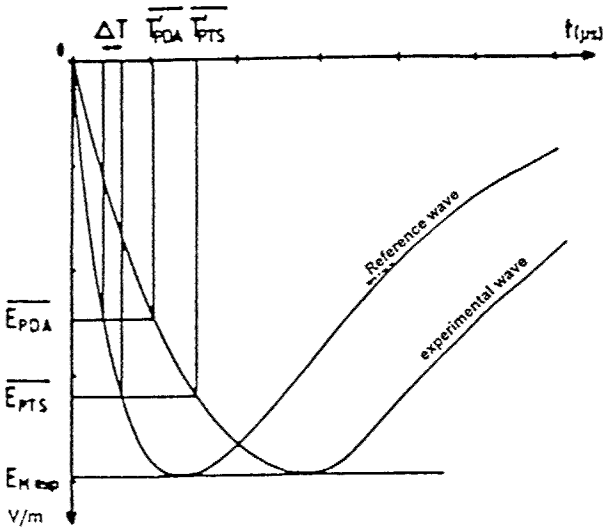


Figure C3

# LIGHTNING INJURIES TO HUMANS IN FRANCE

## STATISTICAL, PATHOPHYSIOLOGICAL, AND CLINICAL CHARACTERISTICS OF LIGHTNING INJURIES RESEARCH ACTIONS AND PLANS, ESPECIALLY IN THE FIELD OF INDIVIDUAL PROTECTION

Elisabeth Gourbière, MD (Electropathology & keraunopathology)
ELECTRICITE DE FRANCE, Service des Etudes Médicales, 30 avenue de Wagram, 75382 PARIS Cedex 08, FRANCE
Tel. +33-1-47 64 73 25 - Fax +33-1-47 64 73 15 -E.mail: elisabeth.gourbiere@edfgdf.fr

ABSTRACT: The pathology of lightning, or keraunopathology is known only to a few specialists. In an average year in France, lightning kills ten people and injures another 60, often with serious sequelae. Because of the seriousness of the lightning accidents, increased promotion of awareness among the entire population is essential and not necessarily expensive.

## INTRODUCTION

In France, few doctors except those specializing in emergency care are familiar with the specific effects of lightning accidents on humans. Consequently, public awareness about these effects is nearly nonexistent. This injury is defined by the passage of lightning current through the body of a person struck, directly or indirectly, by lightning. It is a particular type of high tension electrical accident.

There is a widespread belief that anyone struck by lightning is killed. It has long been known, however, that this belief is wrong. *Pliny the Elder* wrote : « Man is the one creature that is not always killed when struck--all others are killed on the spot ; nature doubtless bestows this honour on man because so many animal surpass him in strength ».

One explanation of why mortality from being struck by lightning probably does not exceed 20% is the phenomenon known as the external flashover: in most cases, only a small part of the current passes through the body, while most of it spreads out over the body's surface. The other reason is the extreme brevity of the current's duration.

## STATISTICAL DATA

The climate in France is, on the whole, temperate. Its keraunic level (number of days/year that thunder is heard) is roughly 20. The ground flash density is, according to Météorage, 1.2 impacts/km²/year, on average, for the entire country. It can exceed 2 or even 3 in the South, especially the Southeast. Similarly, lightning injuries (or, more specifically, deaths) occur most often in the South (the regions Provence-Alpes-Côte-d'Azur, Auvergne, Rhône-Alpes, Aquitaine and Midi-Pyrénées). During the 1979-1996 period, the mean number of lightning deaths per year was 10 (minimum 5, maximum 19) [French National Cause-of-Death Statistics, *Inserm*]. Eighty per cent of the victims were male. The distribution by age class showed that 61% (110/180) of the victims were between 15 and 44 years old.

The mean annual frequency of lightning deaths has diminished substantially in France over the 20th century, falling, according to our estimations, from 1.80 cases per million inhabitants around 1900 to 0.17 today. This reduction is largely due to the urbanization of the population and the improvements in emergency medical care [*Gourbière*, ICLP 1998]. A similar trend has been observed in the US and has been studied in detail by *López and Holle [1998]*.

Our principal sources of information about the circumstances of lightning injuries are newspapers, physicians (especially *SAMU* Mobile Emergency Medical Services teams), and some survivors. Despite our efforts, we have not been able to obtain detailed information except for a few cases, generally the most serious (deaths, permanent disabilities) [*Gourbière et al.*, 1997, *Gourbière*, 1998].

Accidents most often occur outside, during the two months of summer vacation (July and, especially, August). They primarily involve those who, alone or in small groups, are involved in sports or other recreational activities - walks, hiking, biking or boating excursions, etc. - or during such everyday activities as crossing open spaces. Occupational accidents are rare. We know of cases that have occurred inside homes, especially in rural areas where the electrical lines are overhead; these cases are associated with use of the telephone or various electric devices. Outdoor accidents always involve at-risk situations: the victim did not check the short-range weather forecasts, or did not pay attention to the deterioration, which can be rapid, in meteorological conditions. In some cases, the victims, moving on foot or by bicycle, were targets, isolated and projecting upwards into space; in other cases, they held objects above their shoulder or head, instruments (golf clubs, fishing rods), tools (hayforks, saws), or, simply, umbrellas. Many victims thought they were finding a safe shelter under a tree, high and relatively isolated, along the road or at the edge of a forest; others have sought shelter in telephone booths or inside a shed. Multiple accidents (groups of children and teens, hiking or camping) can become medical disasters, especially when they occur in the mountains, in areas difficult for rescue teams to reach.

PATHOPHYSIOLOGICAL AND CLINICAL DATA

The pathology of « classic » electric shocks, most often due to current at industrial frequencies, is much better known than that of lightning injuries. There are, of course, similarities between these two categories of electrical trauma: the primary likeness is that the victim's body is accidentally and transiently included in an electric circuit. It is crucial, however, to know the differences, which are essentially related to the physical characteristics of the lightning current and the mechanisms of the lightning injury. There are four principal mechanisms by which lightning strikes a person: a direct lightning bolt, a side flash, contact voltage and step voltage. Because previous reports analyse them in detail, such a description is not necessary here [*Gourbière et al.*, 1995, *Leikin and Cooper*, 1997, *Andrews and Cooper* 1992]. Table 1 below outlines the pathophysiological and clinical differences between lightning injuries and electrical injury from high-voltage alternating current.

TABLE I.- Comparison of the characteristics of injuries from lightning and from high-voltage industrial current (taking into account the most common voltages and frequencies used in France) [*Gourbière*, 1998, *Lee*, 1997, *Leikin and Cooper*, 1997, *Ten Duis*, 1998]

| Accident characteristics | « Industrial » current (Repair of electric installations / Work on construction sites near overhead power lines. Feet are supposed to be at the ground potential). | Lightning current (Direct hit - Victim standing, feet in contact with the ground - Sports or other recreational activities, more rarely occupational) |
|---|---|---|
| Source | - Electric installation (transmission line, transformer substation) | - Natural atmospheric discharge |
| Type of current | - Alternating sinusoidal 60 Hz | - Impulse followed by a continuing current |
| Contact voltage | - Typically 20 or 63 kV | - Approximately 300 kV (peak current) |
| Points of contact | - Typically located on the upper limbs (hands, wrists) | - Prominent parts of the body Head (skull, face), neck, shoulders |
| Duration of current passage through the body | - Up to 500 ms (rarely more because the victim is often thrown far from the live conductor) | - Several µs or ms<br>- Most of the current passes over the surface of the body (external flashover) |
| Burn injuries | - Deep, sometimes extensive, electrical burns, at the points of contact<br>- Possible deep tissues destruction along the entire current path | - Small cutaneous deep burns, at the entry and exit points<br>- Other cutaneous burns, most often superficial |
| Blunt injuries | - Falls - Being thrown | - Blast explosive effects - Falls |
| Leading cause of immediate death | - Cardiopulmonary arrest by ventricular fibrillation (VF) | - Cardiac arrest (asystole) that may be transient, but persisting apnoa may lead to a secondary cardiopulmonary arrest (VF) due to hypoxia |
| Consequences of burns | - Myoglobinuria - Kidney failure - Infection ...<br>- Fasciotomies - Amputations | - Exceptionally life-threatening.<br>- Diagnostic and forensic interest |

Lightning injuries are varied and take many different forms. The most dangerous (and possibly fatal) immediate complications are cardiovascular and neurologic. It must be kept in mind that only immediate and effective cardiorespiratory resuscitation (started by rescuers), followed as soon as possible by emergency medical treatment, can save victims who are in cardiopulmonary arrest, or avert the serious consequences of cerebral hypoxia. Some victims remain in a coma despite intensive resuscitation and die of secondary causes including hemorrhages and multiple lesions (encephalic, cardiac, pulmonary, intra-abdominal).

Table 2, below, outlines the many complications of lightning injuries. Of the sequelae that subsist among roughly 70% of survivors, the most common are neuropsychiatric and sensory (vision, audition). Early testing should be systematic, because these can develop insidiously, becoming apparent only much later. The harmful effects on family and social life, school, and work can be substantial.

TABLE 2. Causes of lightning deaths, and the most typical disorders reported in the literature and in the author's experience [*Gourbière et al., 1995, Gourbière,* 1998, *Leikin and Cooper,* 1997, *Ten Duis,* 1998, *Andrews and Cooper et al.,* 1992, *Cherington et al.,* 1995]

| | |
|---|---|
| Lightning deaths<br>( ~ 20% ) | - Asystole / Ventricular fibrillation<br>- Inhibition of brainstem respiratory centers<br>- Multi-system failure (delayed death) |
| Cardio-pulmonary injuries | - Arrhythmias - Arterial pressure changes<br>- Electrocardiographic changes<br>- Myocardial damages (infarction)<br>- Cardiac dysfunction<br>- Pulmonary edema - Respiratory distress syndrome |
| Neurologic / psychiatric injuries (Patients with sequelae must be referred to specialists and support groups) | - Loss of consciousness / coma<br>- Amnesia / Anxiety / Confusion / Aphasia / Seizures /<br>- Electroencephalographic abnormalities<br>- Brain / Cerebellum damages<br>- Numbness / Weakness in limbs / Impossibility to move / or typical complete but transient paralysis (called keraunoparalysis)<br>- Neuropathy / Pain syndromes / Paralysis /<br>- Spinal cord injury / Parkinsonism /<br>- Sleep and memory disorders / Concentration disturbances / Irritability / Depression / Various disturbances, including headaches, tiring easily, lightning storm phobia, etc.<br>- Posttraumatic Stress Disorder |
| Burns and<br>Cutaneous marking | - Small, deep entry/exit points (typical)<br>- Contact, metal chain heating (typical)<br>- Superficial linear<br>- Flash<br>- Lichtenberg figures (arborescent, fernlike marking): pathognomonic (on trunk, arms, shoulders) |
| Clothing, shoes | - Exploded off, torn out, shredded, singed... |
| Blunt trauma (explosion) | - Contusion, internal hemorrhage (brain, lungs, liver, intestine...)<br>- Rarely: fractures (skull, cervical spinal column, extremities...) |
| Auditory and ocular injuries | - Tympanic membrane rupture: typical<br>- Deafness / Tinnitus / Vertigo<br>- Transient blindness / Photophobia-Conjunctivitis - Corneal damage<br>- Retinal abnormalities (macular hole) - Optic neuritis<br>- Cataract |

## INDIVIDUAL PROTECTIVE MEASURES - PROSPECTS AND CONCLUSIONS

Insufficient information is available to the French public about the risks of lightning. Various groups of experts, such as those from the *Association Protection Foudre*, have published recommendations for individual caution, similar to those of American experts [*Vavrek et al.*,1999], but they have received only limited diffusion. We also participate in the work of the *International Electrotechnical Commission* on the effects of lightning on humans (Technical Committee 64, Lightning Ad Hoc subgroup of the Working Group 4). The tendency – or rather, the temptation – to work only among specialists often predominates, to the detriment of multi- and interdisciplinary collaboration. One advantage of the latter is that it maximizes the number of population groups to whom information is furnished. State-of-the-art techniques include nowcasting, used for the French Tennis Open (Rolland-Garros), aviation, and urban hydrology [*Météo-France*, 1997], as well as early streamer emission air terminals used for the Grand Stade de France (80,000 seats). Little use is made, however, of some elementary and relatively inexpensive

means of informing the public and promoting general awareness. These could include short information sessions in schools, in small sports associations and groups, and in occupational settings. The speaker could integrate consideration of the electric risks of residential current and of lightning, the means of avoiding them, and, of course, steps to take for survival and to provide first aid when accidents occur.

ACKNOWLEDGEMENTS: The author expresses her thanks to all those who support and encourage her work on electric risks and lightning, both in France and internationally, in particular: J. Lambrozo, MD, her director; R. Kithil, president & CEO of the NLSI and M. Cherington, MD, president of the LDC, who have named her to their scientific committees; M.A. Cooper, MD (Lightning Injury research program), and R.E. López and R.L.Holle, Research Meteorologists for the NSSL (NOAA).

REFERENCES (see note below)

Pliny the Elder (Gaius Plinus Secundus, AD 23-79), (lv, Catholica fulgurum), Liber II, De fulminibus, *Naturalis historia / Natural history I (Books 1-2)*, The Loeb Classical Library (original Latin text, with English translation by Rackham H.), Harvard University Press, Cambridge, Massachusetts, 280--283, 1997.

Inserm, Institut National de la Santé et de la Recherche Médicale, *Personal communication*, Sept. 1998.

Gourbière, E., Lambrozo, J., Folliot, D. and C. Gary, Complications and sequelae of accidents due to lightning, (paper in French, with English abstract), *Reanimation, Soins Intensifs, MEDECINE D'URGENCE*, 11(3), 138--161, 1995.

Gourbière, E., Lambrozo, J., Koch, F.-X., Menthonnex, Ph., Cabane, J. and Ch. Virenque, Draft ' Lightning-injured people in France' : the first national French survey about lightning to persons, (paper in French, with English abstract), Proceedings of the *2nd International Conference Lightning & Mountains'97*, *Medical symposium*, M71--M83 - Chamonix (France), June 1997.

Gourbière, E., Lightning injury to human beings in France, *24th International Conference on Lightning Protection*, 2 (8a.2), 814--819 - Birmingham (UK), Sept. 14-18, 1998.

Gourbière, E., Lightning injuries features - Pathophysiological aspects, *10th Congress of the ISBI, International Society for Burn Injuries*, Electrical burns (part 2), Abstracts, 68 - Jerusalem, Israel, Nov. 1-5, 1998.

Lee, R.C., Injury by electrical forces : Pathophysiology, Manifestations, and Therapy, *Current Problems in Surgery, (Mosby)*, 34(9), 677-765, Sept. 1997.

Leikin, J.B., Aks, S.E., Andrews, S., Auerbach, P.S., and M.A. Cooper, Lightning injuries, In Environmental Injuries, *Disease-a-Month*, 43(12), 871--892, Dec. 1997.

Ten Duis, H.J., Lightning strikes : danger overhead, *British Journal of Sports Medicine*, 32(4), 276--278, 1998.

Meteofrance, -La prévision immédiate à Rolland-Garros, Service gagnant-, *La Météorologie (Société Météorologique de France)*, 8 (18), 70--71, 1997.

Vavrek, R.J., Eggers, H.W., Holle, R.L. and R.E. López, Updated lightning safety recommendations, *Eighth Symposium on Education, sponsored by American Meteorological Society*, 58--61 - Dallas Texas, 10-15 Jan.1999.

López, R.E. and R.L. Holle, Changes in the number of lightning deaths in the United States during the twentieth century, *Journal of Climate*, 11, 2070--2077, 1998.

Cherington, M., Yarnell Ph.R. and S.F. London, Neurologic complications of lightning injuries, *The Western Journal of Medicine*, 162 (5), 413--417, 1995.

Andrews, C., Cooper, M.A., Darveniza, M. and D. Mackerras, Lightning injuries : electrical, medical and legal aspects, 195 p., *Boca Raton Fla, CRC Press, Inc.*, 1992.

- Note: Because we cannot be exhaustive here, we note here the existence of many other excellent publications, international lists of which are kept up to date for keraunopathology, by, among others C. Andrews, M, Cherington, M.A. Cooper, and for electropathology and keraunopathology, by E. Gourbière.

Several Internet sites focus on keraunopathology and individual protection:
- Service des Etudes Médicales d'Electricité de France/Gaz de France: French/English site, in the first trimester of 2000.
- Lightning Data Center, directed by M. Cherington (Denver, Co): *http://www.centura.org/services/lightning_data_center/lightning_data_center.htm*
- Lightning Injury Research Center, directed by M.A. Cooper (Chicago, Il): *http://www.uic.edu/~macooper/cindex.htm*
- National Lightning Safety Institute, directed by R. Kithil (Louisville, Co): *http://www.lightningsafety.com/*

# AN INTEGRATED NORTH AMERICAN LIGHTNING DETECTION NETWORK

K.L. Cummins[1], R.B. Pyle[1], G. Fournier[2]

[1]Global Atmospherics, Inc., Tucson, Arizona, U.S.A
[2]Environment Canada, CANADA

ABSTRACT: The U.S. National Lightning Detection Network (NLDN) and the recently-completed Canadian Lightning Detection Network (CLDN) are operated as an integrated North American Lightning Detection Network (NALDN), employing 187 sensors covering nearly 20 Million square kilometers. This large network provides a unique opportunity to study lightning characteristics over a wide range of climate and terrain. In this paper we briefly discuss the NLDN and CLDN and their performance characteristics. The first measured continental-scale (U.S./Canada) annual ground flash density is presented. Taking advantage of the vast range in latitude covered by the NALDN, we also provide evidence for a latitude and regional dependence for cloud-to-ground flash parameters. An example "storm day" with over 200,000 cloud-to-ground flashes is shown to cover large portions of the U.S., Canada, and Mexico.

## INTRODUCTION

In February 1997 Atmospheric Environment Service (AES) of Canada contracted with Global Atmospherics to provide a Canadian National Lightning Detection Network (CLDN). AES has the ongoing objective to enhance its predictive capability by the year 2003, especially with regard to its Severe Weather Program. The implementation of CLDN is one of the cornerstones of this modernization. The CLDN system was designed to provide 90% cloud-to-ground (CG) flash detection efficiency with a median location accuracy of 500 meters throughout most of Canada. Integration with the existing U.S. National Lightning Detection Network (NLDN) at the sensor level was also a requirement for the CLDN, resulting in two key benefits. Sharing of sensors across the Canada-USA border assures uniform detection performance along the border. In addition, a single network control center can operate as the primary processing, monitoring, and distribution facility, thereby minimizing operating costs. This integration is accomplished by employing a satellite-based communications system for both sensor and user-related communications.

The NLDN is described in detail in *Cummins et al.* [1998]. The NLDN is comprised of 59 LPATS-III Time-of-arrival (TOA) sensors and 47 IMPACT sensors that provide both TOA and direction-finding information. These ground-based sensors transmit lightning data to a Network Control Center (NCC) in Tucson, Arizona, via a two-way satellite communication system. Data from the remote sensors are recorded and then processed in the NCC to provide the time, location, an estimate of the peak current, and other waveform and data-quality parameters for each detected cloud-to-ground lightning return stroke. The real-time solutions are then recorded in an on-line database and then transmitted via satellite to real-time users. All this takes place within 30-40 seconds of each lightning flash. All recorded data are reprocessed off-line within a few days of acquisition and then stored in a permanent database that can be accessed by users who do not require real-time information. The median location accuracy provided by the NLDN is 500 meters, and the estimated flash detection efficiency varies between 80 and 90 percent for peak currents greater then 5 kA. Performance of the NLDN in the New York area has been evaluated in detail by *Idone et al.* [1998a,b].

In the following section, we provide a brief description of the CLDN and its estimated performance. This is followed by some lightning observations made possible by combining the NLDN and CLDN into an integrated North American Lightning Detection Network (NALDN). The first measured continental-scale (U.S./Canada) annual ground flash density is presented. Taking advantage of the vast range in latitude covered by the NALDN, we also provide evidence for a latitude and regional dependence for CG flash parameters. An example "storm day" with over 220,000 CG flashes is shown to cover a large portion of the U.S., Canada and Mexico.

## THE CANADIAN LIGHTNING DETECTION NETWORK

The CLDN is an 81-sensor lightning detection network covering more than 9 Million square kilometers of Canada. The design utilizes a heterogeneous mix of 26 IMPACT/ES sensors and 55 LPATS-IV sensors. These sensors are the next-generation beyond those employed in the NLDN. By utilizing the LPATS-IV sensors, the CLDN is also able to detect and locate inter- and intra-cloud discharge. Because these sensors are separated by 300-500 km, only a small percentage of cloud discharges are located by the network. Even with this low detection efficiency, preliminary studies indicate that cloud discharge detection by the CLDN may provide excellent early warning of impending CG lightning. A study of 7 storms distributed throughout Canada yielded advance-warning times ranging between one and 60 minutes, with a median of about 5 minutes. This is comparable to the lead-times provided by the LDAR 3D total-lightning system at NASA's Kennedy Space Center [*Maier et al., 1995*].

CLDN Network performance has been characterized using location accuracy and detection efficiency (DE) models developed by Global Atmospherics. A description of these models is provided in the appendix in *Cummins et al.* [1998]. These models were verified in a two-year study by the State University of New York in Albany, carried out on behalf of the Electric Power Research Institute [*Idone et. al. 1998a,b*]. The estimated CG flash DE for peak currents larger than 5 kA ranges between 80 and 90 percent throughout Canada, and is 90 percent in most areas. This projected performance relied upon successful integration of the U.S. based sensors with the new Canadian owned equipment.

Location accuracy is characterized by the median expected location error for a CG discharge (first or subsequent stroke). By utilizing a network combining Time-of-Arrival technology (LPATS-IV) and IMPACT ES sensors, the CLDN is expected to provide a median location accuracy of better then 500 meters throughout most of Canada. As with DE, this level of performance across the southern border of Canada can only be achieved if the US NLDN sensors are included.

In order to accommodate the significant increase in the number or sensors and related data, a new central processing system was developed for the NALDN. The system utilizes streamlined dual redundant processing paths with dual communications systems in an on-line/backup configuration. The new system is composed of the newest APA2000 suite of central processing software running on four multi-processor Sun Microsystems SPARC computers. The system is configured to handle the load of both the US and Canadian network datasets and provides user access to the data via satellite broadcast and dial-up phone lines. A large DA2000 was configured with Redundant Arrays of Independent Disks (RAID) technology which forms the databases backbone for user-access to lightning data. This system is capable of processing over 200,000 discharges per hour, and storing 5-years of data for on-line use. See *Pyle and Fournier* [1998] for a detailed discussion of the CLDN network and related project logistics.

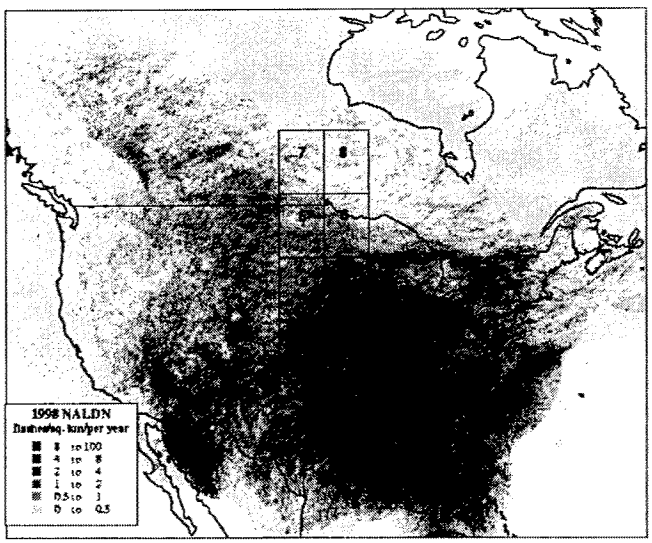


Figure 1. 1998 Ground Flash Density for the NALDN

## CONTINENTAL-SCALE OBSERVATIONS

There are a number of unique lightning-related observations that are made possible by the creation of this single homogeneous network covering nearly 20 Million square kilometers, with latitudes ranging from 25 to 60 degrees North. Figure 1 shows the measured ground flash density (GFD) from the first year of operation of the NALDN, depicted in a gray-scale with 10-km grids. The GFD ranges from over 16 flashes/km$^2$ in central Florida to a fraction of a flash/km$^2$ in the Northwestern U.S. and Canada. The eight rectangular regions depicted in this figure were evaluated in terms of CG flash peak current and number of strokes in a flash (multiplicity), as discussed later in this paper.

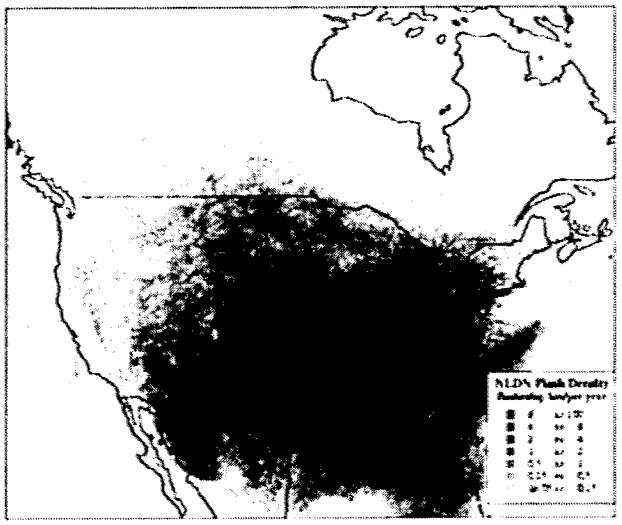


Figure 2. 1996 Ground Flash Density for the NLDN.

A particularly striking feature in Canada is the dramatic increase in GFD that occurs along the eastern edge of the Canadian Rockies. This "boundary" appears as a Southeast to Northwest "line" in Western Canada, separating a western area with 0.25-0.5 flashes/km$^2$ from an eastern area with 2-4 flashes/km$^2$. Comparison of this 1998 GFD to the U.S. NLDN 1996 GFD (see Figure 2) illustrates the effect of degrading DE along the Canadian border prior to integration with the CLDN. It also clearly shows a dramatic increase in the detectability of lightning in Maine (Northeastern U.S.) when the CLDN is included.

The limitation of these figures to single-year and gray-scale images does not illustrate the compelling relationship between lightning GFD and terrain. Accumulating GFD data over many years provides a much clearer picture of the large-scale lightning climatology and its relation to terrain, but the information can only be properly conveyed using color mapping.

The large North-south extent of the NALDN provides an opportunity to evaluate CG flash characteristics as a function of latitude. Using flash data for the month of August, 1998, negative first stroke peak current distributions and flash multiplicity were studied in the eight 5-degree-by-5 degree regions shown in Figure 1. Table 1 summarizes the mean multiplicity and mean peak current for each of these regions, and provides the number of flashes used to obtain these statistics. The multiplicity values range from 1.7 to 2.5. As discussed in *Cummins et al.* [1998], these values are smaller than the generally accepted values of 3-4, partially due to limited detection efficiency of subsequent strokes (50-60% in the NLDN). The results shown in Table 1 do not indicate any relationship between latitude and multiplicity. Note from the table that average multiplicity varies more between regions at the same latitude than it does between regions at different latitudes. The results shown in Table 1 do indicate a significant and stable reduction in the mean peak current in regions 5-8, relative to regions 1-4. The latitude boundary between these areas is 45 degrees North. It is not likely that this 15-20% reduction is a result of relative performance of the network in these regions, for the following reasons. Regions 5 and 6 "straddle" the boundary between NLDN and CLDN sensors, and are predominantly in the NLDN. In addition, if low DE were the reason for a high median peak current in Regions 1-4, then one would also expect a lower average multiplicity in these regions. As shown in Table 1, this is not the case.

Table 1. Flash Statistics for Selected NALDN Regions

| Region | 1 | 2 | 3 | 4 | 5 | 6 | 7 | 8 |
|---|---|---|---|---|---|---|---|---|
| Flash Count (Thousands) | 225 | 268 | 113 | 94 | 74 | 35 | 43 | 22 |
| Ave Multiplicity | 2.3 | 2.5 | 1.9 | 2.1 | 2.2 | 1.7 | 2.4 | 1.7 |
| Ave. Peak Current | 23.4 | 23.7 | 22.8 | 22.8 | 19.7 | 19.5 | 19.1 | 19.9 |

As part of this study of the peak current and multiplicity, the relationship between first stroke peak current and multiplicity was also evaluated. All eight regions exhibited a very strong relationship between estimated first stroke peak current for negative flashes and the number of strokes in the flash. Figure 3 depicts the relationship between mean multiplicity and first stroke peak current for Region 1, aggregated in 10-kA bins. The bin for 50 kA includes all events with peak currents above 50 kA. This same relationship existed in all eight regions, and is consistent with previous unpublished studies involving three different regions in the U.S. NLDN. It is likely that these observations are somewhat contaminated by "threshold effects" resulting from imperfect detection efficiency. However, it is unlikely that the factor-of-two effect shown in Figure 3 is strictly due to instrumentation. Similar results have been obtained in Austria, where CG flash and stroke detection efficiency are quite high [Diendorfer and Schulz, personal

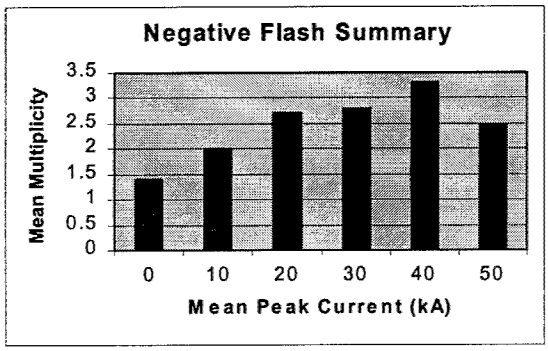


Figure 3. Mean Multiplicity as a function of Peak current, aggregated in 10-kA bins.

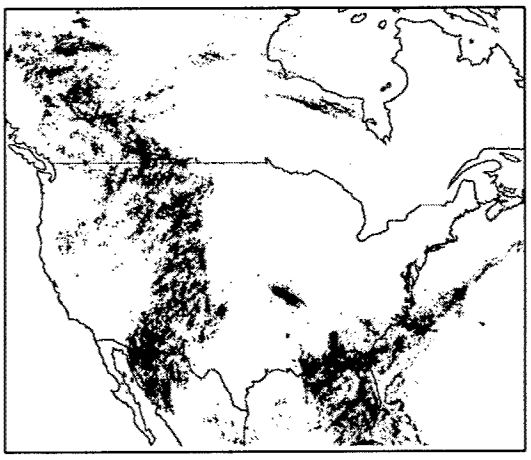

Figure 4. Thunderstorms on August 1, 1998.

communication]. These findings might indicate that key factors that determine the charge in the lower portion of the lightning channel are also related to the total charge available for producing a flash.

As an illustration of the spatial scope of thunderstorms in North America, Figure 4 shows lightning for the 24-hour period commencing at 00z on August 1, 1998. In this case, there is a continuous line of thunderstorms from central Mexico to Northern Canada, isolated storms in Missouri and Northern Ontario, and a large storm system in the Southeastern U.S. that continued off the East coast and into the Gulf Stream. More than 220,000 CG flashes occurred during the 24-hour period. Of these flashes, 1.5 percent had peak currents in excess of 200 kA. The largest flashes were just over 300 kA, and were located using information from 8-12 sensors. Interestingly, CG discharges with estimated peak current in the range of 100-200 kA were invariably located using 30-40 sensors. When lightning peak currents are this big, it is not unusual for nearby sensors (within 200-300 km) to saturate and thereby not participate in determining the location or parameters of the discharge. Also, such big discharges usually remove charge from large regions of the cloud, resulting in very complex and long-duration discharges, thereby complicating detection. Based on preliminary evaluations of these hi-current discharges, there is reason to believe that lightning detection networks with a small number of sensors may not be able to properly detect these events.

REFERENCES

Cummins, K., Murphy, M., Bardo, E., Hiscox, W., Pyle, R., Pifer, A., A combined TOA/ MDF Technology Upgrade of the U.S. National Lightning Detection Network. *Journal of Geophysical Research*, 103: 9035-9044 1998.

Fournier, G. and R. B. Pyle, The Canadian National Lightning Network, presented at the 1998 International Lightning Detection Conference, Tucson, AZ Nov 17-18 1998.

Idone, V., Davis, D., Moore, P., Wang, Y., Henderson, R., Ries, M., Jamason, P., Performance evaluation of the U.S. National Lightning Detection Network in eastern New York 2. Location Accuracy. *Journal of Geophysical Research*, 103: 9057-9069 1998

Idone, V., Davis, D., Moore, P., Wang, Y., Henderson, R., Ries, M., Jamason, P., Performance evaluation of the U.S. National Lightning Detection Network in eastern New York 1. Detection Efficiency. *Journal of Geophysical Research*, 103: 1998

Maier, L., L. Lennon, T. Britt, Lightning Detection and Ranging (LDAR) system performance analysis, *Proceedings, 6th Conference on Aviation Weather Systems,* AMS Society Meeting, Dallas, Texas, 1995.

# ELECTRIC-FIELD CHANGES OF LIGHTNING OBSERVED WITH BALLOON-BORNE SLOW ANTENNAS

William H. Beasley[1], Kenneth B. Eack[2], Heidi E. Morris[2,3], W. David Rust[4], Donald R. MacGorman[4]

[1] School of Meteorology, University of Oklahoma, Norman, OK 73019
[2] Los Alamos National Laboratory, Los Alamos, NM 87545
[3] Department of Physics and Astronomy, University of Oklahoma, Norman, 73019
[4] National Severe Storms Laboratory, Norman, OK 73069

## ABSTRACT

During the Summer and Fall of 1998 we launched five balloon-borne slow antennas into thunderstorms to observe the changes in electric field caused by lightning. Four of these were for measurement of field change only. The fifth was part of a larger package that included an x-ray detector and a GPS receiver on board. We have processed electric-field-change data from two of these flights. Interpretation of the field-change waveforms has not been as straight-forward as we had hoped. Several appear to be coincident in time with cloud-to-ground lightning flashes that were recorded by the National Lightning Detection Network (NLDN). We discuss examples of field changes observed at altitude and compare them with data from the NLDN. Limits on time resolution and timing accuracy prevent us from making unambiguous identification of the lightning processes that caused the field changes. It appears that the field changes we have observed may have been caused by charge movements relatively near the instruments as compared with the ground-strike location of coincident flashes, but nonetheless possibly related in some way to the ground flashes.

## INTRODUCTION

As reported in Eack et al.(1996), x-ray pulses have been observed above a mesoscale convective system at an altitude of about 15 km msl with no significant steady electric field present. This raises the question of whether lightning flashes might be a cause of changes in electric field at those altitudes that are of duration too short to be recorded by the standard electric-field meters (EFM) of the type used for studies of the charge structure of storms (Winn and Byerley (1975), Marshall et al. (1995)), but perhaps of sufficient magnitude and duration to cause production of bremstrahlung x rays such as those observed. Furthermore, if the cause of such field changes were cloud-to-ground lightning flashes, it might be the same field changes that, according to some hypotheses (Taranenko and Roussel-Dupre (1996), Pasko et al. (1996), Bell et al. (1995)) may be causing, or at least related to the causes of, high-altitude discharge phenomena such as sprites and blue jets. Therefore, in order to attempt to observe such field changes directly, we undertook to design an instrument of the type commonly called a "slow antenna" that could be deployed on a free balloon and flown along with with an EFM and conventional sonde.

## INSTRUMENT DESIGN

An example of the primary configuration of the instrument we used to observe electric-field changes at altitude is shown in Figure 1. A CD-ROM is shown in the figure for size comparison. The principle of operation and basic electronic design are similar to that of "slow" and "fast" antennas discussed in MacGorman and Rust (1998). The terms "slow" and "fast" refer to the character of the response of a system to a step-function input. For a typical "slow" antenna the response to a step input decays to zero in a few seconds, more or less. In our instruments we set the 1/e decay time at 30 ms, or about 150 ms to zero. We chose this relatively short decay time because we knew that the instrument would be going

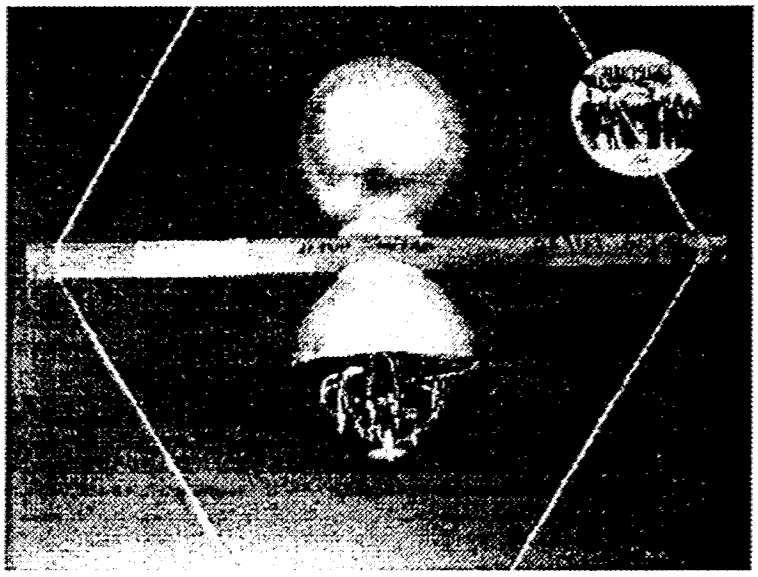

**Figure 1.** Electric-Field-Change Antenna for Balloon Deployment. The bottom hemispherical shell has been removed to expose the electronics. CD-ROM shown for size comparison.

through regions of storms that could produce slowly varying fields that might saturate the electronics if the decay time were too long. Since 30 ms is long enough that we can expect to see field changes caused by individual strokes of a cloud-to-ground lightning flash that is within range, we have chosen to call our instruments "slow antennas". The term "slow" does not necessarily mean that the bandwidth of the system is limited severely at the high-frequency end. In our case, the high-frequency limit was dictated by the trade-off between bandwidth and telemetry capabilities. In the case of the instruments that measure field change only, the 3 dB rolloff was set at 15 kHz for an A/D rate of 32 kHz. In the case of the instrument flown with an x-ray detector in the same package, the A/D rate was limited to 15 kHz, so we set the 3 dB rolloff at 7.5 kHz. Though the basic design of the sensor is conventional, its application in instruments to be launched on balloons into thunderstorms presented a few challenges. We deliberately chose the same well known and well characterized configuration for sensing elements as that which has been used for balloon-borne electric-field meters (EFM) for at least a decade: two six-inch alumninum spheres mounted on a fiberglass rod. As in the EFM design, we enclose the electronics within the spheres, one of which serves as the "ground" reference and the other of which serves as both the sensor plate and the telemetry antenna. We used lithium batteries to power the sensor electronics, a microprocessor, A/D converter, and telemetry transmitter. The batteries typically last for at least two hours. This instrument does not need to rotate in either the vertical or horizontal plane, so there is no motor and there are no styrofoam vanes as on an EFM. All of the electronics and the batteries are in the lower sphere. The total mass of a complete instrument, including batteries, is about 1 kg. The weight is sufficient to keep the spheres aligned within a reasonable angle from the vertical, at least for these preliminary observations.

DEPLOYMENT and OBSERVATIONS

We have processed and analyzed data from two flights. The larger single-sphere package, with x-ray detector in addition to the field-change antenna, was launched at 0010 UTC on June 19,1998 from latitude 34.58°N, longitude 97.41°W into a storm in the vicinity of Elmore City, Oklahoma. The instrument reached a peak altitude of 22.6 km at 0105 UT, at which time its position was at latitude 34.60°N, longitude 97.00°W. This instrument had rough GPS timing to the nearest second on board. The flight path is depicted in vertical and horizontal planes as a function of longitude in Figure 2. The numbers along the flight path denote the order of successive trigger times. In Figure 3 we show the waveforms recorded for triggers 9 and 21. In the case of event 9, there were two field changes separated by 60 ms when the instrument was at about 12 km altitude, latitude 34.59°N, longitude 97.12°W. The first of these field changes was about 160 V/m +/- 30 V/m. The second field change was about 70V/m +/- 30 V/m. At the same time also separated by 60 ms in time, there were two positive cloud-to-ground flashes recorded by the NLDN. The first was at latitude 34.32°N, longitude 97.57°W, which is 50.8 km along the ground from the sub-balloon point and and 52.2 km from the balloon itself. The second was at latitude 34.24°N, longitude 97.58°W, which is 50.2 km along the ground from the sub-balloon point and and 51.6 km from the balloon itself. Both of these had peak currents, according to the NLDN estimate, of about 60 kA. In the case of trigger 21, the instrument

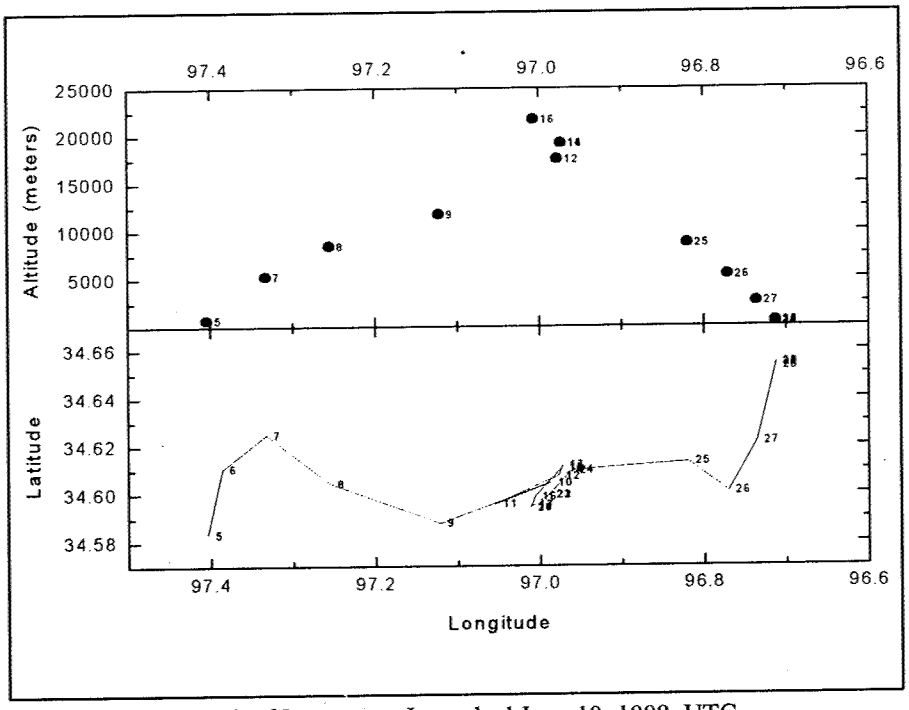


**Figure 2**. Flight Path of Instrument Launched June 19, 1998, UTC.

was at an altitude of approximately 14.5 km, at latitude 34.59°N, longitude 97.01°W. The field change was approximately 235 V/m +/- 30 V/m. There was a positive cloud-to-ground flash located by the NLDN (2 s earlier, within our timing uncertainty) at latitude 34.21°N, longitude 97.67°W, which is 73.4 km along the ground from the sub-balloon point and and 74.8 km from the balloon itself. The peak current, estimated by the NLDN, was approximately 130 kA. We have also examined data obtained with a field-change-only instrument (the one shown in Figure 1) launched at 0319 UTC, September 22, 1998, from latitude 35.38°N, longitude 97.27°W, east of Oklahoma City. The next day, we recovered the instrument from a location near Prague, Oklahoma, latitude 35.65°N, longitude 96.68°W, about 62 km, from the launch point. One of the 9 events recorded had four field changes of about 100 V/m each with time between them of about 150 ms. At the same time, within the +/- two-second time uncertainty, and within about a 50 km radius, there were 15 NLDN located flashes, some with multiplicities of 3, 4, and 5, and all but one were negative. However, we feel that there are too many ambiguities that cannot be resolved in order to attribute the at-altitude field-changes to a particular flash.

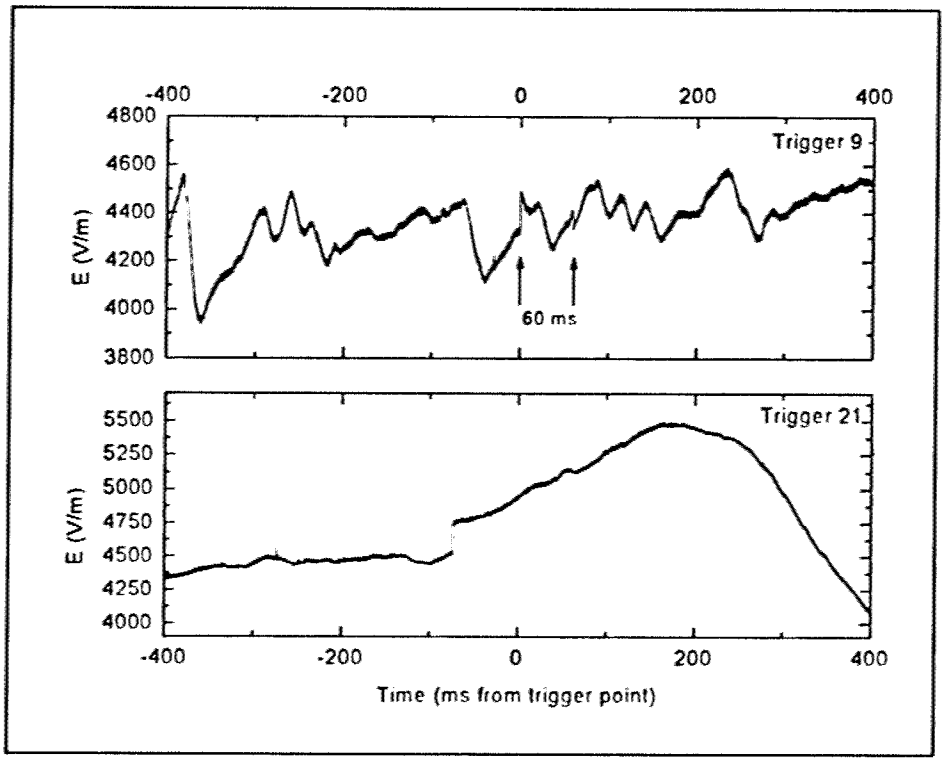


**Figure 3**. Field Changes Observed 6/19/98, UTC.

DISCUSSION

The waveforms of field changes presented here are not as easy to interpret in terms of lightning as we had hoped. For the cases on June 19, there were relatively few cloud-to-ground lightning flashes, so that coincidences in time at least invite our further attention. For example, in the case of trigger 9, Figure 3, there were two field changes with 60 ms interval between them, two cloud-to-ground flashes separated by 60 ms at the same time as the field changes, and no other cloud-to-ground flashes within reasonable range at that time. However, the time resolution of the waveforms is insufficient for us to identify them with any particular process in a cloud-to-ground flash. Furthermore, we note that the NLDN reported the flashes that were coincident with the field changes as positive and at about the same distance, with about the same peak currents, yet the two field changes at the balloon were of opposite polarity and differed in magnitude by a factor of 2. Indeed, we cannot rule out the possibility that the field changes we observed could have been caused by an undetected cloud-to-ground flash or an intracloud discharge that might or might not have been related to the NLDN located ground flashes but relatively near our instrument at 12 km altitude. In the case of trigger 21, Figure 3, our measured field change was larger, the distance from instrument to NLDN located flash farther, and the NLDN peak current estimate larger thanin the case of trigger 9. If we assume that the field change of trigger 21 is the result of the charge transfer that occurs during the return-stroke, a process that appears to be completed in about 1 ms or so (Beasley et al., 1982), we can estimate the amount of charge transfer it would take at a distance of 74 km to cause the observed field change of 235 V/m at the balloon. It turns out to be 400 C, which seems unrealistically large even for a positive return stroke. By comparison, creation of a positive charge of 0.03 C at a distance of 1 km directly below the instrument would cause a field change of about the magnitude observed. This increases our suspicion that the field change we recorded was caused by motion of charge closer to the balloon than the NLDN

located ground strike point of the coincident flash. Another feature of interest of trigger 21 is the ramp following the fast field change. It might at first appear to be evidence for a continuing current, but, noting that the decay time constant of the system is 30 ms, the actual field change would have been much larger than the observed 700 V/m over a period of about 235 ms. If the field change were a result of a flow of charge in the channel of the NLDN located flash to ground, 74 km distant, it would have taken unrealistically large amounts of charge. This again suggests that the field changes, both fast and slow, in Figure 3, are the result of charge motion relatively close to the balloon, possibly, but not necessarily associated in some way with the distant ground flashes, and, in these cases at least, near the top of the cloud.

## CONCLUSIONS

We succeeded in observing electric-field changes of lightning at altitudes in and above thunderstorms. However, we cannot unambiguously identify the process responsible for the field changes because of limitations of our time resolution and timing accuracy. Our tentative conclusion is that the field changes we saw were more likely a result of charge motion relatively near the instrument as compared with the distances of 50 km to 75 km to time-coincident ground flashes. Clearly we will need better timing accuracy and time resolution in the future to be able to identify the processes responsible for the field changes observed at altitude.

## ACKNOWLEDGEMENTS

We gratefully acknowledge the support of the AFOSR, grant No.F49620-96-1-0430 (Maj. J. Kroll and Maj. P. Bellaire, Program Managers) and the Physical Meteorology Program of the NSF, Grant No. ATM98-07179 (R. Rogers, Program Director). We wish to thank D.M Jordan, University of West Florida, for his invaluable help with design of the field-change circuit. We thank Dennis Nealson and Leslie Cain for their dedicated and meticulous maintenance of the mobile laboratories in top shape, ready for deployment. We thank K.L. Cummins of Global Atmospherics, Inc. for help with interpretation of NLDN data. Many thanks to M.A. Uman for helpful discussions of the field-change waveforms. Special thanks to D. M. Suszcynsky for his support in general and his participation during the field programs. The balloons could not have been launched without the many students who served on balloon crews, including Aaron Bansemer, Christina Hannon, Montra Lockwood, Ted Mansell, Jim O'Brien, and Ivy Winger.

## REFERENCES

Beasley, W.H., M.A. Uman, P.L. Rustan, Electric fields preceding cloud-to-ground lightning flashes, *J. Geophys. Res.*, **87**, No. C7, 4883-4902, 1982.

Bell, T.F., V.P. Pasko, U.S. Inan, Runaway electrons as a source of red sprites in the mesosphere, *Geophys. Res. Lett.*, **22**, 2127-2130, 1995.

Eack, K.B., W.H. Beasley, W. D. Rust, T.C. Mar5shall, M. Stolzenburg, X-ray pulses observed above a mesoscale convective system, *Geophys. Res. Lett.*, **23**, 2915-2918, 1996.

Pasko V. P., U. S. Inan, and T. F. Bell, Blue jets produced by quasi-electrostatic pre-discharge thundercloud fields, *Geophys. Res. Lett.*, **23**, 301, 1996a.

Taranenko, Y., and R. Roussel-Dupre, High-altitude discharges and gamma-ray flashes: A manifestation of runaway air breakdown, *Geophys. Res. Lett.*, **23**, 571-574, 1996.

Winn, W.P. and L. G. Byerley ,III, Electric field growth in thunderclouds, *Q.J. Roy. Meteor. Soc.*, **101**, 979-994, 1975.

Marshall, T.C., W. Rison, W.D. Rust, M. Stolzenburg, J. C. Willett, W.P. Winn, Rocket and balloon observations of electric field in two thunderstorms, *J. Geophys. Res.*, **100**, 20,815-20,828, 1995.

# A NEW, HIGH VOLTAGE, ARBITRARY WAVEFORM GENERATOR FOR SIMULATING PRE-RETURN STROKE C-G LIGHTNING ELECTRIC FIELDS

F. D'Alessandro, J.R. Gumley

ERICO Lightning Technologies, Hobart, AUSTRALIA.

ABSTRACT: In this paper we describe the main features of a new prototype high voltage impulse generator designed to produce a variable, programmable wavefront up to a 150 kV peak voltage. This generator is capable of precisely simulating the range of rapidly escalating electric fields due to a lightning downward leader as it approaches an attachment point near or on the ground. It utilises a computer-controlled interface that drives a unique set of series-stacked flyback transformers. The resulting output is any desired, monotonically increasing waveform or "wavefront", downloaded from the computer.

## INTRODUCTION

Research into direct-strike lightning protection design and, specifically, comparative air terminal performance, is usually conducted by one of three means: (i) "natural" field experiments where air terminals are placed in locations of high lightning incidence [*Gumley*, 1990, 1994], (ii) "artificial" field experiments where air terminals are exposed to lightning triggered by rockets [*Rison et al* 1998, *Uman et al* 1996], and (iii) laboratory experiments using high voltage impulse generators [*Gary et al* 1989, *Berger* 1994, 1995].

The last of these is an attractive option because testing of air terminals on demand can provide results much more quickly than having to rely on the vagaries of field testing. However, progress in the laboratory has been limited for a number of reasons. One problem relates to the scaling of results from the laboratory to the field, although some aspects of this limitation can be overcome by performing a large number of systematic experiments. A more difficult problem stems from the fact that the Marx-style impulse generator [*Marx* 1923, *Kuffel & Zaengl* 1984], which is used in most high voltage laboratories around the world, produces an RC-type wavefront. Hence, these generators are unable to simulate the temporal electric field wavefronts evident in natural lightning phenomena prior to the return stroke.

In simple terms, the natural, pre-return stroke electric field at ground level has two components: a "permanent" (or DC) and an "impulse" component. The latter component is a rapidly escalating wavefront for a nearby lightning strike [*Beasley et al* 1982] which cannot be reproduced by the present generators. Figure 1 illustrates the difference between the two basic waveforms.

Researchers have attempted to circumvent this problem by using switching impulses and a peak voltage for a given terminal-plate air gap such that the field risetimes are similar to those observed in nature, typically of the order of 1 kV/m/μs [*Gary et al*, 1989]. However, this practice disregards the importance of the build-up to breakdown and the role it plays in air terminal performance. Furthermore, it disregards the fundamental difference in driving voltage between the two wavefronts. As the gap between the upward discharge and the overhead electrode decreases, the natural wavefront voltage drives the discharge in an ever-increasing manner whereas the Marx-style wavefront voltage has reached its peak or may actually be decreasing. For example, a laboratory leader discharge travelling at 2 cm/μs would take 500 μs to transit a 10 metre gap, by which time a 250/2500 μs switching impulse is well beyond its peak value.

The remainder of this paper describes the main features of a new prototype, high voltage, arbitrary waveform generator (HVAWG). This prototype was developed in order to demonstrate that the aforementioned problems can be overcome by generating wavefronts that more accurately reflect those observed in natural conditions.

## GENERATOR DESIGN

The generator is comprised of a 10-stage, series connected stack of 15 - 20 kV high voltage output modules, giving a maximum output voltage of ~ 150 kV. The key to the whole concept lies in the combined effect of series stacking a number of specially tailored transformers. A personal computer installed with a high speed digital I/O card is used to output a 10-bit data word which is a pulse width modulated (PWM) representation of the rate of rise of a point on the desired waveform. Typically, the PWM frequency is 100 kHz and the data rate is 2 MHz. This enables a PWM resolution of 5 %. Consequently, delays can be inserted between each bit in the data stream in 5 % steps, creating a ripple effect. A simple example of this "interleaving" principle is illustrated in Figure 2.

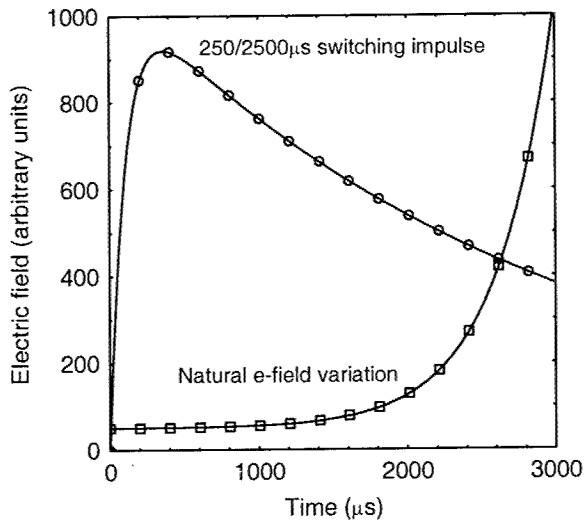


Figure 1. Comparison of waveform obtained from Marx-style generator with that observed in nature from a progressing lightning downward leader.

Each delayed bit of the output data is passed into one of ten opto-driven cables as shown in Figure 3. Each of these fibre optic signals is then passed into an isolated switched-mode power supply (SMPS) with its own floating DC power supply. The fibre optic signals are converted back to electrical form inside the SMPS's.

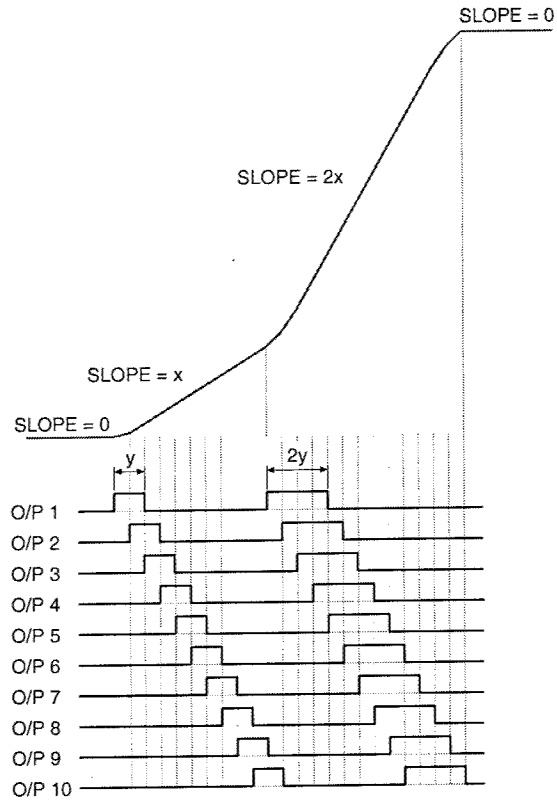


Figure 2. Simplified example of the "interleaving" principle of the generator. The waveform slope is approximately proportional to the duty cycle.

The output stage of the generator uses transformers configured in a flyback topology to eliminate the need for output inductors. When the transformer primary winding switches are activated by the amplified SMPS outputs, the primary side of each transformer acts as an inductor due to the blocking action of the output diode. When the switches are deactivated, the voltage reverses and the inductive energy stored in the primary is released through the secondary winding. The output diode then conducts so that a negative voltage appears on each output capacitor, as shown in Figure 3.

Hence, the computer sends pulses to each generator module which produces an output voltage step. The overall generator output voltage *magnitude* and *rate of rise* depends on the number of modules fired in series, pulse width, amount of pulse width interleaving (by relative delay of bits in the output data stream), pulse repetition rate and the total number of pulses. Therefore, the more modules that are used, the higher the degree of interleaving and the smoother the output wavefront.

Risetimes > 1 kV/μs are achievable with this system. A further advantage of series-stacking the modules comprising the generator is that each module only needs to be able to output a voltage of $V_{out}/n$ and, more importantly, output it at a rate of only $1/n$ of the required slew rate, where $n$ is the number of modules.

Each module can maintain a constant voltage output, thus allowing the waveform to rise from a predetermined static level. No attempt has been made to simulate the common return stroke current waveforms produced by conventional Marx generators. This prototype has been designed to simulate only a millisecond or so immediately prior to the return stroke of a lightning discharge and hence is a voltage generator rather than a current generator.

Other advantages of this new generator system include: (i) the test waveform can be changed from one waveshape to another in a relatively short period of time (~ seconds) so that empirical corrections for variations in temperature, pressure and humidity are not needed; (ii) computer control means that the waveshapes can be stored and recalled at a later time to repeat a test under identical conditions.

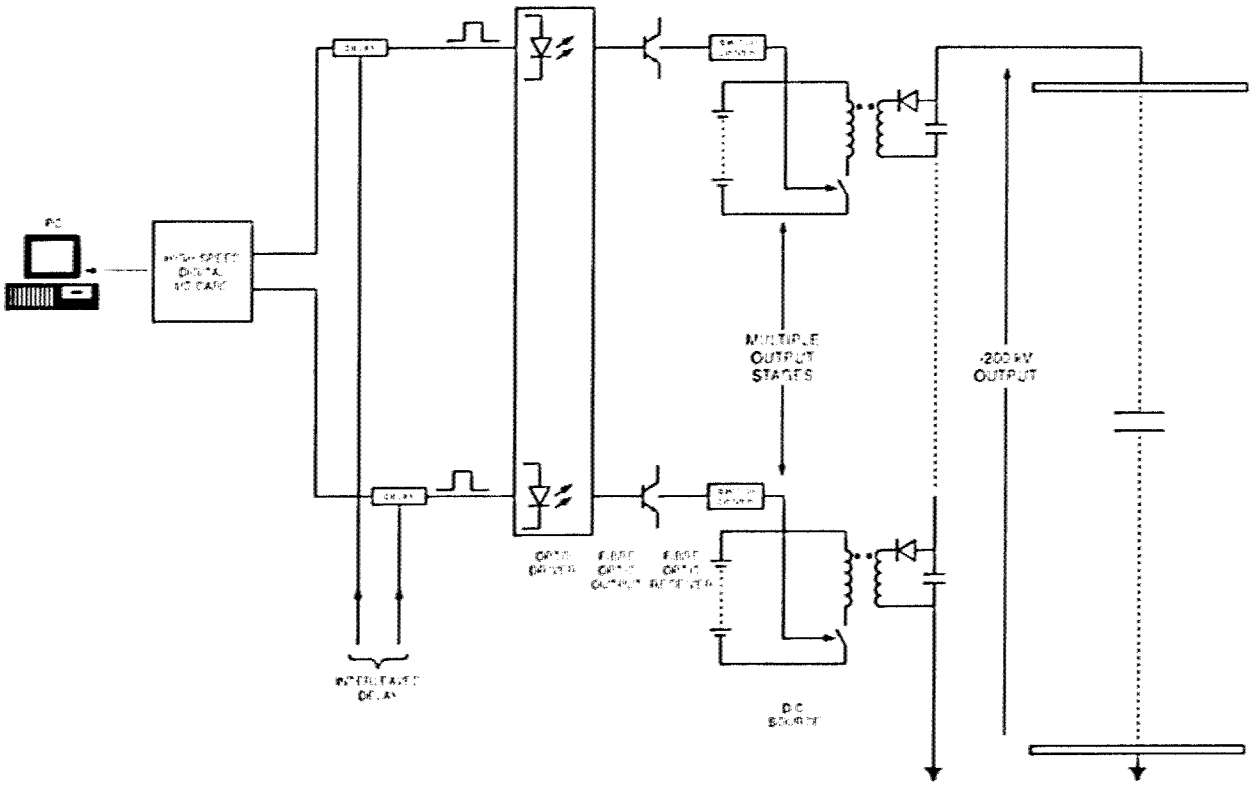


Figure 3. Schematic diagram of the prototype, 200 kV, high voltage, arbitrary waveform generator.

PRELIMINARY TESTS

The prototype generator described in this paper had a design objective of producing a variable, programmable wavefront with a 150 kV peak voltage. Tests conducted so far show that this objective has been met, within the practical constraints of such a new development. Test results characterising the generator and its capabilities can be summarised as follows:

- Pulse widths to 5 μs and data rates up to 4 MHz.
- Risetimes of ~1 and ~ 0.5 kV/μs for a Marx and natural wavefront respectively.
- Peak voltage of 150 kV using 10 modules.
- Breakdown of air gaps up to ~ 200 mm.
- Drive current capability of 300 A.
- Negligible loading of the voltage waveform as the discharge is created and progresses to breakdown.
- Maximum allowable capacitive loading of ~ 50 pF.
- Superior speed of testing and recording: existing generators ~ 20 shots per hour, whereas the new HVAWG is capable of ~ 100 shots per hour (only limited by space charge clearance time)
- Ability to generate multiple impulses with delays that match those of natural lightning (10 – 200 ms).
- Generation of any monotonically increasing waveshape, such as:
  - wavefront due to vertically descending, stepped downleader
  - "angled" lightning (e-field waveform depends on the lateral distance between object and downleader - this is calculable and can be downloaded from the computer)
  - any other waveform with a sufficiently long front time

The main results obtained from air terminal testing using the generator are:

- geometric shape has a significant effect on the length of the air gap that can be broken down
- geometric shape has a significant effect on the time to breakdown and the breakdown voltage

- the scatter in breakdown times can be drastically reduced if the time to breakdown is controlled and optimised.

The above results are only preliminary and cannot be generalised because the discharge from the air terminal cannot enter the "leader regime" over such short inter-electrode distances. We believe that a true streamer-to-leader transition will not be observed with a generator producing much less than 1 MV. Of course, the voltage required to observe this transition is not known with any certainty. All past testing with Marx-type generators has a progressively reducing rate of rise of electric field from t = 0 to the wavefront peak. At the time the generator has reached the general area of the critical breakdown voltage, the dV/dt is considerably reduced. On the other hand, this generator can produce the typical waveforms observed in nature and, hence, provides a streamer with the electric field conditions that can initiate and sustain upward leader propagation when the rate of rise of electric field is rapidly increasing.

## CONCLUSIONS

This paper has described a completely new design of high voltage impulse generator which is capable of producing a waveform that faithfully replicates the type of lightning electric field waveforms observed in nature. Tests with the generator are still in progress and form one component of a broad program of lightning protection research which also involves computer modelling and field testing.

The ability to generate any monotonically increasing waveform has implications for the broader application of the generator. For example, with the addition of a waveshaping "bleed resistor" and the ability to generate bipolar output voltages, it is conceivable that the HVAWG could be used for switching impulse testing of insulators, fundamental tests concerning the insulation strength of long air gaps, etc.

It is our intention to increase the capacity of the generator to ≥ 1 MV. If this is achievable, it will revolutionise high voltage laboratory experiments in general and, specifically, comparative testing of lightning air terminals.

## REFERENCES


Beasley, W.H., et al, Electric fields preceding cloud-to-ground lightning flashes, *J. Geophys. Res.*, 87, 4883-4902, 1982.

Berger, G., Formation of the positive leader of long air sparks for various types of rod conductor, *22nd ICLP*, Budapest, Hungary, Paper R 2-01, 1994.

Berger, G., Inception electric field of the lightning upward leader initiated from a Franklin rod in laboratory, *11th Int. Conf. Gas Disch. Appl.*, Tokyo, Japan, 1995.

Gary, C., Hutzler, B., Cristescu, D., Dragan, G., Enache, R. & Popa, B, Laboratory aspects regarding the upward positive discharge due to negative lightning, *Rev. Roum. Sci. Techn. - Electrotechn. et Energ.*, 34, 363-377, 1989.

Gumley, J.R., Lightning interception techniques, *20th ICLP*, Interlaken, Switzerland, Paper 2.8, 1990.

Gumley, J.R., Lightning interception and the upleader, *22nd ICLP*, Budapest, Hungary, paper R 2-11, 1994.

Kuffel, E. & Zaengl, W.S., High Voltage Engineering, Pergamon Press, Oxford, 1984.

Marx, E.: Deutsches Reichspatent no. 455933, 1923.

Rison, W., Moore, C.B., Mathis, J. & Aulich, G.D., Comparative tests of sharp and blunt lightning rods, *Proceedings of ICLP*, Birmingham, pp. 436-441, 1998.

Uman, M.A., et al, Triggered Lightning Experiment in Florida, *10th ICAE*, Osaka, Japan, pp. 644-647, 1996.

# A PRELIMINARY ASSESSMENT OF THE LONG-TERM PERFORMANCE IN THE FIELD OF AN ENHANCED AIR TERMINAL AND THE LIGHTNING PROTECTION DESIGN METHOD

F. D'Alessandro

ERICO Lightning Technologies, Hobart, AUSTRALIA

ABSTRACT: The aim of this study was to assess the performance of an enhanced air terminal installed on a wide range of structures in Hong Kong using a design method based on an improved electrogeometric model. Lightning strike statistics for 161 suitable installations over the period 1988-1996 have been collated. Analysis of these data shows that there is a highly significant positive correlation between the *actual* and *expected* annual strike frequency to the air terminals. The result provides strong evidence that the air terminal, and the lightning protection design principle, is performing according to its specifications.

## INTRODUCTION

Lightning is an extremely variable phenomenon which necessarily involves the use of statistics. For example, the probability $P(n)$ that a given area will be struck by lightning exactly 0, 1, 2, 3 ..... $n$ times over a given period of time may be expressed by the Poisson relation,

$$P(n) = e^{-\mu} \mu^n / n! \tag{1}$$

where $\mu$ is the average number of strikes to the area. The same can be said about lightning protection and risk assessment where, for example, one is interested in the probability of a strike to a particular building or other structure. In general, two factors determine the probability of a strike to a structure, namely the local ground flash density, GFD (strikes/km$^2$/yr), and the attractive (or exposure) area of the structure, $A_{eq}$ (km$^2$). If these two parameters are known, then the average strike frequency (ASF, strikes per annum) can be computed using

$$\text{ASF} = \text{GFD} \times A_{eq} \tag{2}$$

The average GFD for a particular region can be obtained over a period of time (usually years) using lightning flash counters or lightning detection and location systems such as LPATS. In many countries, this information is not available and only the number of thunderstorm days per year (TSD) is known. The latter is called the *keraunic level* of the region and the corresponding contour line plot of TSD is called an *isokeraunic map*. Many empirical relationships have been derived between TSD and GFD over the last twenty years or so [*Uman*, 1987]. One of the most quoted ones is from *Anderson & Eriksson* [1980] who, using CIGRE 10 kHz flash counters, obtained the relationship GFD = 0.023 (TSD)$^{1.3}$. *Popolansky* [1992] recently obtained a relationship using lightning flash counter data from 14 countries spanning 4 continents, and obtained the relationship GFD = 0.0086 (TSD)$^{1.45}$.

On perfectly flat ground with uniform properties, lightning will strike each square kilometre with equal probability. However, an object that is taller than the surrounding area has an "equivalent attractive area" greater than the ground area it occupies. Hence, the attractive area of a structure is defined as the equivalent area on flat ground which would be struck with the same frequency. It depends on the structure height, the charge on the lightning downward leader (which, in turn, is related to the return stroke peak current) and to a lesser extent the ground surface area occupied by the structure.

Invariably, the attractive area is computed using the equivalent attractive *radius*, $R_{eq}$, of the structure. For free-standing structures, the area is approximated by $A_{eq} = \pi R_{eq}^2$ whilst for structures of significant extent such as power lines the area is given by $A_{eq} = L\,(b + 2R_{eq})$, where $L$ is the line length and $b$ is the line effective width. In the present study, only the former equation is needed.

A number of expressions have been derived for $R_{eq}$, using electrogeometrical [*Mousa & Srivastava*, 1989], statistical [*Bazelian et al*, 1978] and other models such as those based on the streamer zone method [*Rakov & Lutz*, 1990]. Electrogeometric models are based on the concept of "striking distance", $R_s$, defined as the distance between the object to be struck and the tip of the downward-moving leader at the instant that the connecting (upward) leader is initiated from the object [*Uman*, 1987]. The striking distance depends on the charge on the downleader and hence return stroke current. Some workers have extended this concept to include a dependence on structure height and atmospheric conditions [*Petrov & Waters*, 1995]. As a very crude approximation, the striking distance can be used in place of the attractive radius although readers should note that $R_s$ is an *overestimate* of $R_{eq}$. Some of the more common attractive radius or striking distance models in past and present usage include:

| | | |
|---|---|---|
| *Golde* [1977]: | $R_s = 2\,h$ | (3) |
| *Anderson & Eriksson* [1980]: | $R_s = 16.3\,h^{0.61}$ | (4) |
| *Eriksson* [1987]: | $R_{eq} = 0.84\,I_p^{0.74}\,h^{0.6}$ | (5) |
| *Rakov & Lutz* [1990]: | $R_{eq} = [h^*(h^* + 206]^{0.5}$, where $h^*=h+16\ln(h)-31$ | (6) |
| *Rizk* [1994]: | $R_{eq} = 27.1\,h^{0.4}$ | (7) |
| *Petrov & Waters* [1995]: | $R_s = 0.8\,[(h + 15).\,I_p]^{2/3}$ | (8) |

where $h$ is the height of the structure in metres and $I_p$ is the return stroke peak current in kA.

In Equations (3), (4), (6) and (7), the dependence on $I_p$ is in-built whereas in (5) & (8) it is explicit. The latter make the computation of $R_{eq}$ more involved because the lightning peak current varies from 0 to 150 kA or more. There are variations in the reported current distributions (relative percentages of each) because there are differences between the three main measurement techniques used - shunts or Rogowski coils on tall structures, magnetic induction on chimneys and power line towers, and those deduced from remote electric and magnetic field recordings, predominantly of strikes to ground. The median peak current resulting from each technique is 32, 26 and 23 kA respectively [*Popolansky*, 1992]. There is also evidence that the distribution is latitude dependent [*Torres et al*, 1996].

Standards committees have adopted an "average" distribution taken from a number of sources and ~ 32 kA is often taken as the median peak current. The computational implications are clear - for a structure of given height, there is a spectrum of attractive radii according to the current distribution. A rough but sufficient method of obtaining a single representative value of $R_{eq}$ for a particular structure using Equation (5) or (8) involves a piecewise integration of a tabulated distribution.

## LIGHTNING PROTECTION SYSTEM

The remainder of this paper describes the correlation analysis performed on the lightning strike data obtained from air terminal installations in the Hong Kong region. This region was chosen as the case study because of the high level of lightning activity (~ 80 TSD per year), large number of installations with registered maintenance contracts which validate the counter readings / data, and large range of structure types, heights and locations.

Lightning strike data taken from the field under natural lightning conditions is arguably the most valid way of assessing the performance of air terminals and the particular design method used to optimise their placement on structures. The particular air terminal assessed in this analysis is essentially an "enhanced Franklin rod", comprising a central grounded conductive rod surrounded by a conductive but electrically isolated sphere. The sphere couples capacitively to changes in the ambient electric field and hence rises in voltage as the downward leader descends toward ground. When a critical potential is reached, a triggering spark is produced from the sphere to the central rod, creating a sudden change in the electric field above the air terminal which assists the production of an upward streamer. This configuration satisfies two key criteria: (i) prevention of early corona emission and (ii) by producing a triggering spark at the optimum time, a streamer is launched at a time when the electric field conditions can sustain upward leader propagation.

A lightning event counter placed around the lightning current downconductor cable was used to register strikes to the air terminals. One or more of these air terminals are installed on each of a large number and variety of structures in Hong Kong. The placement of air terminals on structures is often performed by implementing the Rolling Sphere Method, which is based on the electrogeometric model (EGM). The EGM states that the striking distance is a function of the prospective peak stroke current. However, this model disregards the physical basis of the spark discharge initiation and the importance of the structure height or the geometry of the launching point, e.g., air terminal. The modified EGM allows for the electric field intensification of the structure or air terminal. The theory is described in Eriksson (1979, 1980, 1987), is commonly known as the "collection volume method" (CVM) and is synthesised in part by Equation (5). The placement of the above air terminals was optimised using the collection volume method as the basis of the overall lightning protection design.

## ANALYSIS

Data spanning the period 1988-1996 were selected using the following criteria: (i) known length of downconductor, and (ii) existence of a registered maintenance contract with certified counter readings. The primary information extracted from this exercise was the structure height, estimated from the length of downconductor in the installation and ranging from 14 to 430 metres, and the counter readings at the start and end reading dates, giving the actual number of strikes over the time interval. This information was then used to compute the structure attractive area using Equations (3)-(8) and hence the expected number of strikes to the structure per annum. A sample size of 161

valid air terminal installations was available after the application of the above criteria. Approximately one third of these had non-zero annual strikes. The retention of the remaining two thirds of zero-strike data is important, because it is characteristic of the statistical nature of lightning.

In this preliminary analysis, it was necessary to make a number of assumptions, namely the: (i) GFD for Hong Kong is in the range 5 – 6.8 strikes/km$^2$/yr, using the relationships described earlier; (ii) probability weighted median peak current is 32 kA; (iii) building height is 10, 15 and 20 % *less* than the downconductor length for lengths 0-99, 100-299, and 300+ metres (this allows for the extra cabling needed for taller structures); (iv) counters recorded all genuine strike events; and finally (v) no discrimination between downward and upward flashes.

The main statistic used to assess the performance of the air terminal and the design method was the degree and significance of correlation between the *expected* and *actual* strikes per annum to the lightning protection systems. The most common estimator is Pearson's linear correlation coefficient, $r$. Unfortunately, this is a rather poor statistic for deciding whether an observed correlation is *statistically significant* because it is ignorant of the individual distributions of the two variables being correlated. Hence, tests such as the complementary error function, Student's t-distribution, or Fisher's z-transformation, [e.g., see *Press et al* 1989 or *Neave* 1979] must be used to return the probability that the correlation is not statistically significant. However, nonparametric correlation methods are far more robust techniques because they do not assume the data set has a bivariate normal distribution. Rank correlation methods are examples of such a method, returning the Spearman ($r_s$) or Kendall ($\tau$) correlation coefficients. The correlation based on rank results in a slight loss of information (it desensitizes the correlation) but this is a small price to pay for a major advantage - when a correlation is demonstrated nonparametrically, it is real.

In the present analysis, the correlation coefficients were computed using both methods, along with their respective probabilities. Also, a series of experiments were performed in order to assess the effect on the correlation coefficients of: (i) using building heights derived from the length of downconductor according to the 10, 15 and 20% rule of thumb, (ii) using different models for the equivalent attractive radius, (iii) combining counts from installations that are close together, (iv) changing the GFD figure used, and (v) changing the median peak current used.

The only parameter that could not be included in the correlation tests is the specific region-to-region GFD within Hong Kong, where geographical features can result in departures from the average strike density. This detailed information was not available at the time of writing. Using a constant GFD will average out the underestimates and overestimates of the expected strikes. This can easily reduce the degree of correlation found in the data because the expected strikes in regions where there were large numbers of zero-strike (actual) data would have been *lower* than those computed using a constant GFD, and hence *closer* to the actual data. Therefore, the correlation coefficients shown in the next section are considered to be lower limits.

The primary information used in the analysis can be summarised as follows: sample size of 161 air terminal installations in service for a total of 640 years, with 246 strikes captured. Figure 1(a) shows the distribution of structure heights and Figure 1(b) shows the number of strikes captured as a function of structure height, where the heights were binned in 50 - 200 m ranges.

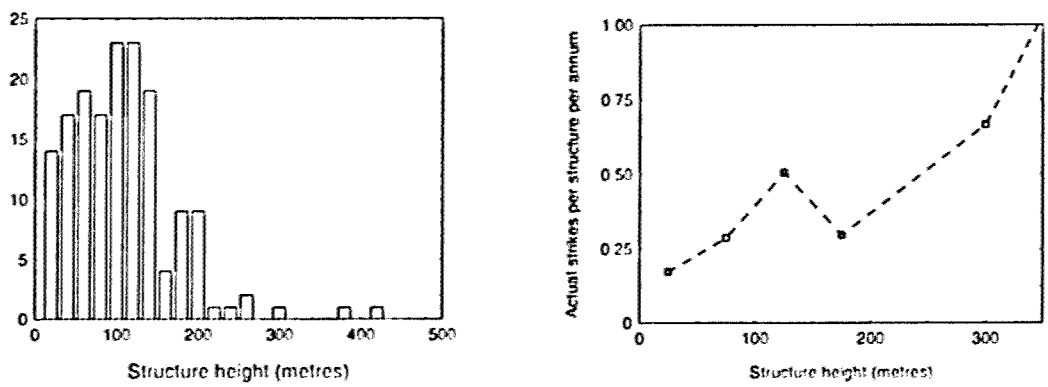


Figure 1: Summary of the primary data used in the analysis. (a) Histogram of structure heights. (b) Recorded strike data as a function of structure height.

RESULTS

A simple, broad-brush indicator of performance is the ratio of actual to expected strikes per annum across the whole sample of structure installations. Taking an average of all the attractive radius models (Eqns 3–8) and GFD's

in the range 5 – 6.8 $km^{-2}$ $yr^{-1}$, this ratio is in the range 0.8 – 1.1, whilst use of *Eriksson's* [1987] model alone (Eqn. 5), on which placement of air terminals is based, results in a ratio of 0.9 – 1.2.

In the main analysis, both the linear and rank correlation coefficients were computed along with their respective probabilities. These are shown in Table 1. The percentage quoted in the table represents the probability that the correlation coefficient is exceeded if the two variables are *uncorrelated*, i.e., a *small* probability indicates the correlation is *highly significant*. The Kendall rank method gave a similar probability to that obtained using the Spearman method.

Table 1: Coefficients and probabilities obtained from the correlation analysis of expected vs actual strikes per annum. Both linear (Pearson) and rank (Spearman) correlation techniques were used.

| *Technique* | *Correl. coeff.* | *Probability* |
|---|---|---|
| Pearson linear, $r$ | 0.43 | < 0.1 % |
| Spearman rank, $r_s$ | 0.65 | 0.3 % |

The results quoted in Table 1 were based on the attractive radius model computed with Equation (5). A final check on the robustness of the correlation found in the raw data was undertaken in the form a series of realistic changes to the variables that could bias the result, such as the method of calculation of building height, attractive radius model, GFD estimate, median current, etc. The results shown in Table 1 were found to be remarkably insensitive to these changes, with only minor variations in the coefficients and probabilities. The linear correlation coefficient was always in the range 0.39 – 0.55 and, importantly, always with a no-correlation probability of < 1%.

## CONCLUSIONS

The preliminary statistical analysis described in this paper has shown that there is a highly significant positive correlation between the measured annual lightning strike frequency to air terminals installed on structures in Hong Kong and the rate expected using a range of empirical and theoretical models for the capture area of the structures in the absence of the lightning protection system. In other words, the design principle of the air terminal and the reliability and efficiency of the design method used to optimise their location on the structures (the Collection Volume Method) has been validated. This conclusion is further strengthened if one considers that there are no documented cases of bypasses (zero "shielding failure rate") of these installations in Hong Kong.

More specifically, the manufacturer of the air terminals, ERICO Lightning Technologies, claim that the lightning protection design packages offer a protection level between 85% and 98%, depending on the level requested by the customer. It can be readily seen from the Results section that the ratio of actual to expected strikes is entirely consistent with these general claims.

A more rigorous analysis of the data is presently being carried out in order to account for some of the second order effects listed in the assumptions and the results will be published as soon as they become available.

## REFERENCES


Anderson, R.B. & Eriksson, A.J., Lightning parameters for engineering application", *Electra*, 69, 65-102, 1980.

Bazelian, E., Gorin, B. & Levitov, V., Physical and engineering foundations of protection against lightning, Leningrad, 1978.

Eriksson, A.J., The lightning ground flash - an engineering study, *PhD thesis*, University of Natal, Pretoria, Sth Africa, 1979.

Eriksson, A.J., Lightning striking distances - an analytical study, *6th Int.Conf. Gas Disch. Appl.*, Edinburgh, 143-146, 1980.

Eriksson, A.J., The incidence of lightning strikes to power lines, *IEEE Trans. Pow. Del.*, PWRD-2, 859-870, 1987.

Golde, R.H. (editor), Lightning, Academic Press, London, 1977.

Mousa, A.M. & Srivastava, K.D., The implications of the electrogeometrical model regarding the effect of height of structure on the median amplitude of collected lightning strokes, *IEEE Trans. Pow. Del.*, 4, 1450-1460, 1989.

Neave, H.R., Elementary Statistical Tables, George Allen & Unwin, London, 1979.

Popolansky, F., Relationship between the number of thunderstorm days and the lightning flash density registered by LFC in the world scale, *21st ICLP*, Berlin, Paper 6.10, 1992.

Press, W.H., Flannery, B.P., Teukolsky, S.A. & Vetterling, W.T., Numerical Recipes, Cambridge Uni. Press, U.K., 1989.

Petrov, N.I. & Waters, R.T., Determination of the striking distance of lightning to earthed structures, *Proc. R. Soc. Lond. A*, 450, 589-601, 1995.

Rakov, V.A. & Lutz, A.O., A new technique for estimating equivalent attractive radius for downward lightning flashes, *20th ICLP*, Switzerland, Paper 2.2, 1990.

Rizk, F.A.M., Modelling of lightning incidence to tall structures. Part I: Theory / Part II: Application, *IEEE Trans. Pow. Del.*, 9, 162-193, 1994.

Torres, H., Rondon, D., Briceno, W. & Barreto, L., Lightning peak current estimation analysis from field measurements in tropical zones, *23rd ICLP*, Florence, 181-185, 1996.

Uman, M.A., The Lightning Discharge, Academic Press, Inc., New York, 1987.

# OPERATIONAL LPATS NETWORK IN AUSTRALIA

A.J.Sharp
Bureau of Meteorology, Melbourne, Australia

ABSTRACT: In a collaborative agreement, the Bureau of Meteorology has arranged for the company Global Position and Tracking Systems Pty Ltd (GPATS) to install a lightning detection network in Australia based on Lightning Position and Tracking System (LPATS) technology. This involved the use of Bureau of Meteorology observing sites and communications networks. An initial network of five sensors existed covering parts of New South Wales and Queensland. A network expansion was commenced in 1997 with the first phase covering the Eastern half of Australia and a second phase to cover the remainder of the country. Lightning stroke rates of over 20,000 per hour have been observed over Australia and adjacent waters. Demand for this new data is already high. Within the Bureau of Meteorology, forecasters are already finding the data invaluable, particularly over large areas of the country that are not adequately covered by weather watch radar. The availability of data within seconds of the event means that developing storms can be detected well before satellite imagery is available. Significant uses include forecasting for aviation, fire weather and severe thunderstorms. After a small number of years of operation, it is anticipated that a high quality climatological database on lightning frequencies will be available for the whole of Australia.

## INTRODUCTION

Australia has vast areas of sparsely inhabited land for which the only source of meteorological information is satellite imagery. Even over farming land, observations can be scarce, most stations reporting once or twice a day. Weather watch radar provides coverage for most coastal regions and some inland areas and satellite images can be inconclusive for locating thunderstorm activity, particularly where there are mid-level cloud bands. There is also a 20-30 minute delay in receiving satellite imagery. A network of local sensors has existed for some time, but these have limited range and no capabilities to locate strokes. There was a need for lightning data coverage over Australia that can be observed in real time.

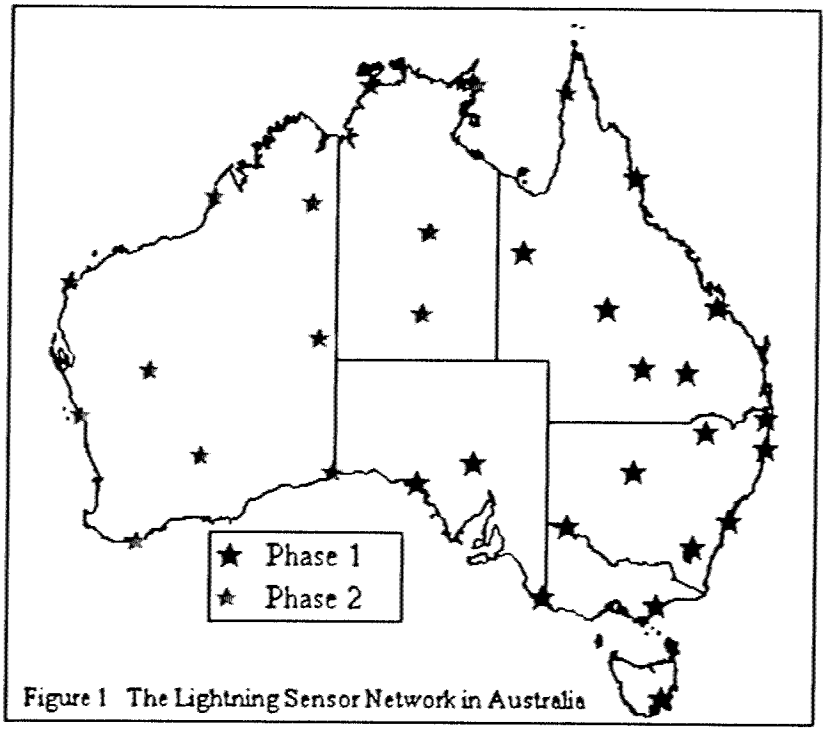


Figure 1 The Lightning Sensor Network in Australia

In the 1980s, three small detection networks using direction finding technology were established around Melbourne, Sydney and Brisbane, but these were only moderately successful. In the mid 1990s, a private company (Kattron Pty Ltd) set up a small LPATS network of six sensors in Southeast Australia through an arrangement with the Bureau of Meteorology. In late 1997, the GPATS company commenced developing a network in collaboration with the Bureau of Meteorology based on GPS time of arrival technology. The network of lightning sensors is being installed in two phases. The first phase covers the eastern half

of Australia shown in figure 1. The second phase extends coverage to the whole of the country. Most of the sensors are to be located at Bureau of Meteorology observing stations. This allows the GPATS company to use the Bureau's communications network to receive the raw data from the sensors. Large parts of inland Australia are desert and sparsely populated. This means that some large gaps in the network with less than optimal detection efficiency and accuracy are unavoidable.

LIGHTNING DATA

During the first half of 1998, the first phase of the network was progressively implemented, starting from an existing five sensor network in November 1997. During this period, the Bureau has worked with GPATS to improve data quality. GPATS has tuned the sensors to obtain a balance in sensitivity that maximises stroke detection rates while minimising the amount of erroneous data. Strokes have been detected up to 10,000 km from the network, albeit at a markedly reduced detection efficiency and reduced spatial accuracy. Only strokes recorded in and close to Australia are used.

In February 1998, with just 12 initial sensors active, the network recorded 17,000 strokes per hour on one occasion. On 1st February 1999, stroke rates of up to 21,500 strokes per hour were recorded for Australia and adjacent waters, using the eastern network. The stroke rates for the UTC day, measured over 12 minute intervals, are illustrated in Figure 2 (0000 UTC is 11:00am local summer time for eastern Australia). Note that between 0300 and 0340UTC and between 0630 and 0705UTC up to 30% of data was lost due to an intermittent software fault.

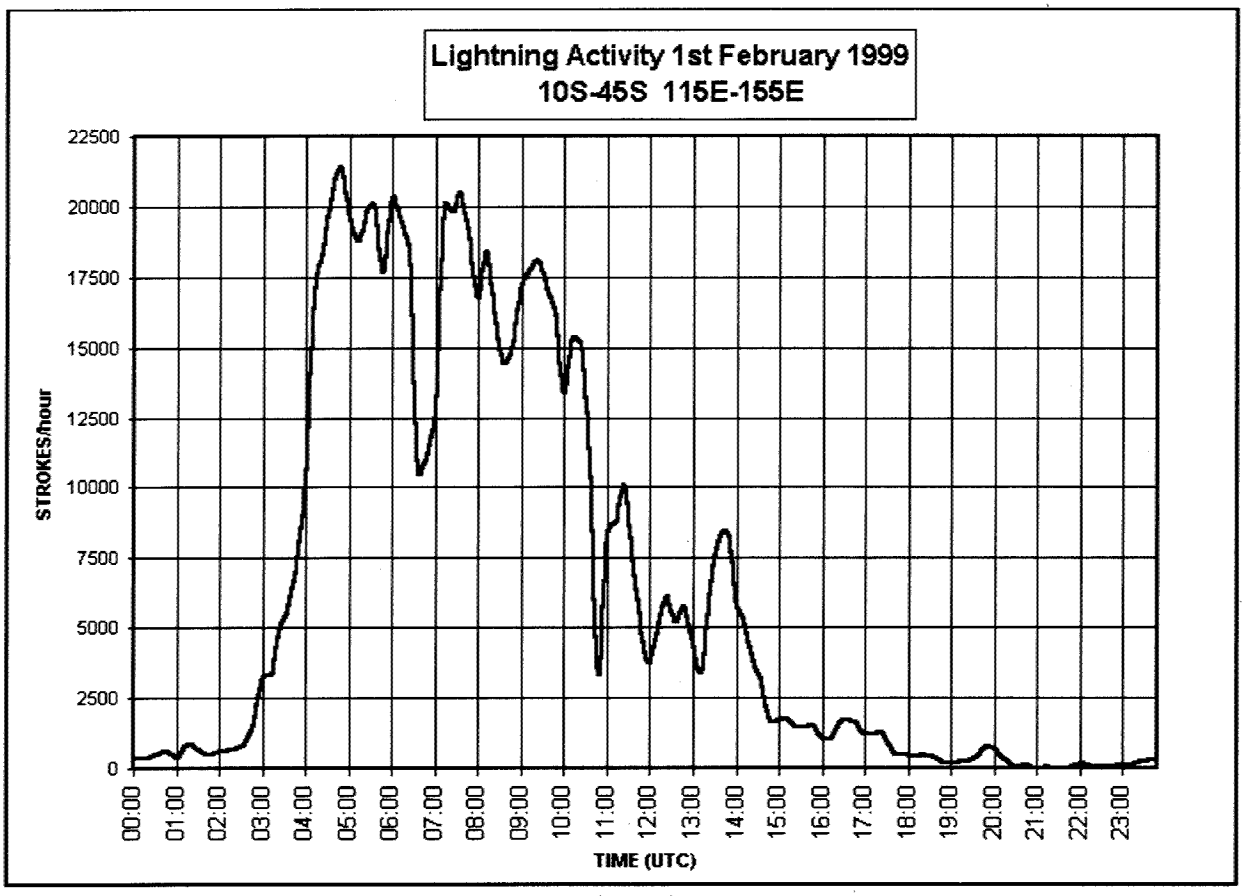


Figure 2

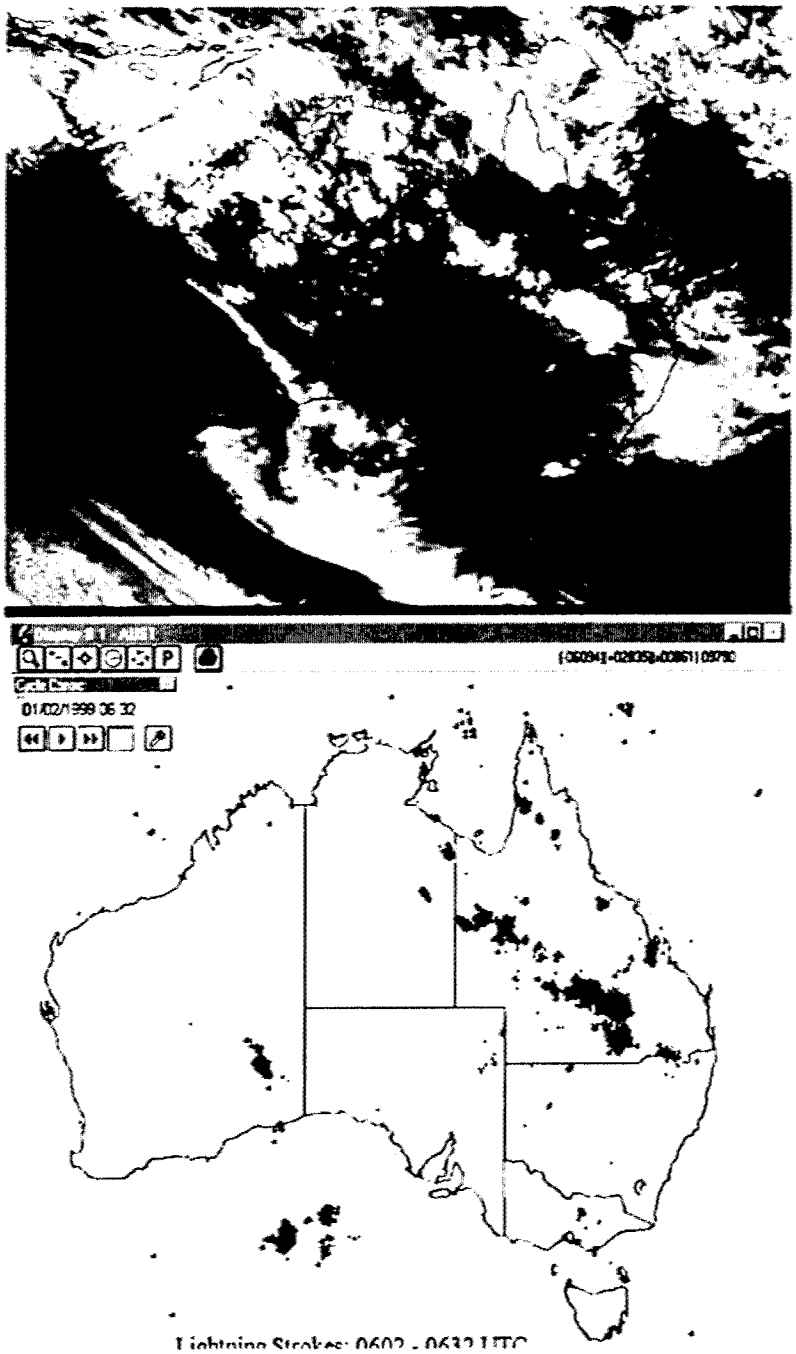


Figures 3 & 4. Satellite and Lightning Data 0630 UTC 1/2/99

Figures 3 and 4 show the data at about 0630UTC (1730 EDST). The satellite data is taken from the operational data display system as received hourly from the GMS5 geostationary satellite. There were 9790 strokes recorded over the illustrated area during the 30 minute period indicated. The satellite image also shows thunderstorm activity over northwest Australia and the adjacent Timor Sea, outside the current sensor network, some of which would most likely have been recorded had the nationwide network been in used. It has been observed that sensitivity beyond the bounds of the network declines rapidly when lightning activity within the network is high.

Several isolated erroneous lightning strokes are evident on the lightning map. In a situation of 9790 recorded strokes, this error rate is low and is not expected to cause false alarms amongst competent users of the data.

The data is displayed with a '+' for positive cloud to ground discharges, '.' for negative cloud to ground discharges and 'x' for cloud to cloud discharges. The system is selectively tuned to detect cloud to ground strokes, hence there are few cloud to cloud strokes detected. Signals from lightning detected far from the network are likely to have reflected off the ionosphere at least once hence the polarity of the stroke would be uncertain

## LIGHTNING DATA USEAGE

The lightning data provided by the new Australian network is being used for a number of purposes. The raw data is useful for lightning stroke verification, although provision of such a service to customers outside the Bureau of Meteorology is restricted as this is the major source of revenue for the GPATS company. For forecasters within the Bureau, the GPATS lightning data is often the first evidence of thunderstorm activity received. Weather watch radar coverage is limited and when available, storms embedded in rain-bands are often hard to detect. Individual storms will often display lightning

activity before they are detected by another observing system, which assists the determination of potentially dangerous weather conditions.

Satellite imagery is usually too late for the provision of an effective nowcasting service and storm clouds are often difficult to detect in mid level cloud bands. Developing storms can cause much havoc before detection on satellite images. The images are received just hourly, with a further 20 minute delay between the image being recorded and it being available to the bench forecaster. Storms are difficult to detect in mature storm systems where new cells are often masked by the cirrus out flow from older storms.

Bureau forecasting services that are being enhanced using the data include fire weather warning services, severe storm warning services, aviation services both in flight and terminal area forecasts and also lightning stroke forecasting for ground operations at major aerodromes. NSW has established a state-wide thunderstorm warning service based primarily on lightning data. As reliable data has only been available for less than 2 years, forecasters have not yet fully embraced the potential of the new data source. However, as is evident from the overview of lightning detection systems and their uses by *Holle and Lopez* [1993] as long as six years ago, there is plenty of research already done that can be of use, now that the technology is in place.

Ultimately the data will be used for climatological purposes, however the developing nature of the network means that data collected so far will not be suitable. When the network is finished and then two to three years of comparable data becomes available, climatological analysis may begin. This will include the updating of lightning and thunderstorm frequency maps that are biased by the limited network of observers and are already known to be not very effective after observing the data received so far.

## SUMMARY

The Bureau of Meteorology has taken advantage of a cooperative arrangement with a private company to obtain lightning data. The network, using LPATS technology to provide lightning data is proving to be invaluable. The number of uses for this data is steadily increasing as forecasters and other Bureau staff become used to using the data. While it is too early to use the data for climatological studies, it is already evident that there is a need to redefine the thunderstorm climatology of Australia.

## AWKNOWLEDGEMENT

The author thanks the GPATS company for lightning data.

## REFERENCES

Holle R.L. and Lopez R.E., Overview of Real-Time Lightning Detection Systems and Their Meteorological Uses, *NOAA Technical Memorandum ERL NSSL-102,* 1993.

# LIGHTNING LAUNCH COMMIT CRITERIA FOR AMERICA'S SPACE PROGRAM

W. P. Roeder, J. E. Sardonia, S. C. Jacobs, M. S. Hinson, D. E. Harms, J. T. Madura[1], S. P. DeSordi[2]
45th Weather Squadron — [1] KSC Weather Office — [2] 30th Weather Squadron
Patrick Air Force Base, FL — Kennedy Space Center, FL — Vandenberg AFB, CA

ABSTRACT: The danger of natural and triggered lightning significantly impacts space launch operations supported by the USAF. The lightning Launch Commit Criteria (LCC) are used by the USAF to avoid these lightning threats to space launches. This paper presents a brief overview of the LCC. More detailed discussions of the LCC are available at Roeder, et al. (1999a), Roeder, et al. (1999b), and Krider, et al. (1999).

## INTRODUCTION

The LCC are a set of 11 rules used to avoid the threat of natural and triggered lightning threat to launches from the US Air Force's Eastern Range (ER) and Western Range (WR), and NASA's Kennedy Space Center (KSC). The LCCs are evaluated and forecast operationally by the USAF's 45th Weather Squadron (45 WS) for the ER and KSC, and by the 30th Weather Squadron (30 WS) for the WR. If a LCC is violated during the launch window, the launch is delayed or scrubbed, depending on time remaining in the launch window. The cost of a scrub varies from $150,000 to over $1,000,000 depending on launch vehicle. Launch scrubs can also delay future launch schedules. Launch customers include the DoD, NASA, and commercial customers for over 55 launches per year of Titan, Atlas, Delta, Athena, Pegasus, Taurus, and Space Shuttle space launch vehicles; and Trident, Minuteman, and Peacekeeper ballistic missiles.

Triggered lightning, as opposed to natural lightning, dominates the LCC. Ten of the eleven LCC are for triggered lightning. Even the one natural lightning rule is partially for triggered lightning, due to charge deposition from the natural lightning near the rocket flight path. Triggered lightning is an electrical discharge caused by the rocket and electrically conductive exhaust plume passing through a sufficiently strong pre-existing electric field. The exhaust plume is conductive primarily due to its high temperature. The triggered lightning process can be viewed as a compression of the ambient electric field until the breakdown potential voltage of air is reached or exceeded, resulting in a triggered lightning strike. Due to this compression, the ambient electric fields required for triggered lightning are two orders of magnitude less than those required for natural lightning. Several atmospheric phenomena other than thunderstorms, as listed in the LCC, can generate electric fields sufficiently strong to threaten rocket triggered lightning. Some phenomena can generate higher electric fields that occur over a shallow depth near the ground and are not a triggered lightning threat, examples include: fog, surf, raindrop fracturing, 'Sunrise Effect' (Marshall, et al., 1999a) (Marshall, et al., 1999b), and powerlines. The LCC protect primarily against electric charge generated in the mixed solid-liquid phase of water, either directly at the charge generation site or advected elsewhere after charge generation, e.g. via anvil or debris clouds. However, two LCC are for charge generation from sources others than mixed phase of water: smoke plume and triboelectrification.

The importance of triggered versus natural lightning is also shown by the scrub rates between ER/KSC and Western Range (WR). The ER/KSC space launch complex is located on the central Florida Atlantic coast, near the area of the nation's maximum thunderstorm activity. The WR launch complex is on the central California coast, near the nation's minimum of thunderstorm activity. Despite this wide difference in thunderstorm (natural lightning) climatology, WR has a LCC scrub rate of 5.4% (DeSordi, 1999), nearly identical to the ER/KSC scrub rate of 4.7% (Maier, 1999).

## CURRENT LCC

The current LCC rules are complex and very atypical within operational meteorology. The Launch Weather Team must have clear and convincing evidence that LCC are not violated. If a LCC is violated during the launch window, then the launch is delayed or scrubbed, depending on time remaining in the launch window. The same LCC are used for all space launch vehicles from ER, KSC, and WR.

The delay and scrub rates for the LCC before 1998 are discussed by Maier (1999). The new 1998 LCC have not been used long enough to reliably estimate their scrub and delay rates. However, the 45 WS subjectively estimates an overall decrease in scrub rate of about 25% due to the new LCC. The most significant changes for improved safe launch availability in the 1998 LCC include: allowing incrementally closer approach to anvil cloud over time, increased surface electric field threshold under more atmospheric conditions, increased use of cloud transparency to exempt the LCC, increased use of surface electric field mills to reduce thresholds, added non-convective cold (T ≤ -

15 °C) cirrus as a non-threat, added a threat for long distance lightning into clear air, and added the first-ever cut-off distance for connections to thick cloud. In addition, the 1998 LCC were restructured and reworded for improved operational usability and easier training.

The new LCC are described below. Even though the LCC are the same for ER, KSC, and WR, they cannot be used operationally the same, due to instrumentation differences. Most significantly, the WR can not use the parts of the LCC requiring surface electric fields since they do not have those sensors.

*(Natural) Lightning LCC*: Do not launch for 30 minutes after any type of lightning occurs in a thunderstorm if the flight path will carry the vehicle within 10 NM of that thunderstorm. Do not launch for 30 minutes after any type of lightning occurs within 10 NM of the flight path, unless: the cloud that produced the lightning is not within 10 NM of the flight path; and there is at least one working field mill within 5 NM of each such lightning flash; and the absolute values of all electric field measurements at the surface within 5 NM of the flight path and at the mill(s) within 5 NM of the lightning flashes have been less than 1,000 V/m for 15 minutes. Notes: Anvil clouds are covered in the third LCC; if a cumulus cloud remains 30 minutes after the last lightning occurs in a thunderstorm, then the second LCC applies.

*Cumulus Clouds LCC*: Do not launch if the flight path will carry the vehicle within 10 NM of any cumulus cloud with its cloud top higher than the -20 °C level. Do not launch if the flight path will carry the vehicle within 5 NM of any cumulus cloud with its cloud top higher than the -10 °C level. Do not launch if the flight path will carry the vehicle or through any cumulus cloud with its cloud top higher than the -5 °C level. Do not launch if the flight path will carry the vehicle through any cumulus cloud with its cloud top between the +5 °C and -5 °C levels unless: the cloud is not producing precipitation; and the horizontal distance from the center of the cloud top to at least one working field mill is less than 2 NM; and all electric field measurements at the surface within 5 NM of the flight path and at the specified mill(s) have been between -100 V/m and +500 V/m for 15 minutes. Note: these cumulus clouds do not include altocumulus, cirrocumulus, or stratocumulus.

*Anvil Clouds LCC*: The anvil cloud LCC has two main sections: attached and detached anvil. The attached anvil and detached anvil are handled differently within this LCC.

*1) Attached Anvil LCC*: Do not launch if the flight path will carry the vehicle through nontransparent parts of attached anvil clouds. Do not launch if the flight path will carry the vehicle within 5 NM of nontransparent parts of attached anvil clouds for the first three hours after the time of the last lightning discharge that occurs in the parent cloud or anvil cloud. Do not launch if the flight path will carry the vehicle within 10 NM of nontransparent parts of attached anvil clouds for the first 30 minutes after the time of the last lightning discharge that occurs in the parent cloud or anvil cloud.

*2) Detached Anvil LCC*: Do not launch if the flight path will carry the vehicle through nontransparent parts of a detached anvil cloud for the first 3 hours after the time that the anvil cloud is observed to have detached from the parent cloud. Do not launch if the flight path will carry the vehicle through nontransparent parts of a detached anvil cloud for the first 4 hours after the time of the last lightning discharge that occurs in the detached anvil cloud. Do not launch if the flight path will carry the vehicle within 5 NM of nontransparent parts of a detached anvil cloud for the first 3 hours after the time of the last lightning discharge that occurs in the parent cloud or anvil cloud before detachment or in the detached anvil cloud after detachment, unless: there is at least one working field mill within 5 NM of the detached anvil cloud; and the absolute values of all electric field mill measurements at the surface within 5 NM of the flight path and at the specified mill(s) have been less than 1,000 V/m for 15 minutes; and the maximum radar return from any part of the detached anvil cloud within 5 NM of the flight path has been less than 10 dBZ for 15 minutes. Do not launch if the flight path will carry the vehicle within 10 NM of nontransparent parts of a detached anvil cloud for the first 30 minutes after the time of the last lightning discharge that occurs in the parent cloud or anvil cloud before detachment or in the detached anvil cloud after detachment. Note: detached anvil clouds are never considered debris clouds, and are not handled by the debris clouds LCC.

*Debris Clouds LCC* : Do not launch if the flight path will carry the vehicle through any nontransparent parts of a debris cloud during the 3-hour period defined below. Do not launch if the flight path will carry the vehicle within 5 NM of any nontransparent parts of a debris cloud during the 3-hour period, unless: there is at least one working field mill within 5 NM of the debris cloud; and the absolute values of all electric field measurements at the surface within 5 NM of the flight path and at the specified mill(s) have been less than 1,000 V/m for 15 minutes; and the maximum radar returns from any part of the debris cloud within 5 NM of the flight path has been less than 10 dBZ for 15 minutes. The 3-hour period required above begins at the time when the debris cloud is observed to have detached from the parent cloud or when the debris cloud is observed to have formed from the decay of the parent cloud top below the altitude of the -10 °C level. The 3-hour period begins anew at the time of any lightning discharge that occurs in the debris cloud.

*Disturbed Weather LCC*: Do not launch if the flight path will carry the vehicle through any nontransparent clouds that are associated with a weather disturbance having clouds that extend to altitudes at or above the 0 °C level and contain moderate or greater precipitation or a radar bright band or other evidence of melting precipitation within 5 NM of the flight path.

*Thick Cloud Layers LCC*: Do not launch if the flight path will carry the vehicle through nontransparent parts of a cloud layer that is greater than 4,500 Ft thick and any part of the cloud layer along the flight path is located between the 0 °C and the -20 °C levels; or connected to a cloud layer that, within 5 NM of the flight path, is greater than 4,500 Ft thick and has any part located between the 0 °C and the -20 °C levels, unless: the cloud layer is a cirriform cloud that has never been associated with convective clouds; and is located entirely at temperatures of -15 °C or colder; and shows no evidence of containing liquid water, e.g. aircraft icing.

*Smoke Plumes LCC*: Do not launch if the flight path will carry the vehicle through any cumulus cloud that has developed from a smoke plume while the cloud is attached to the smoke plume, or for the first 60 minutes after the cumulus cloud is observed to have detached from the smoke plume. Note: cumulus clouds that have formed above a fire but have been detached from the smoke plume for more than 60 minutes are considered cumulus clouds and are handled in the second LCC.

*Surface Electric Fields LCC*: Do not launch for 15 minutes after the absolute value of any electric field measurement at the surface within 5 NM of the flight path has been greater than 1,500 V/m. Do not launch for 15 minutes after the absolute value of any electric field measurement at the surface within 5 NM of the flight path has been greater than 1,000 V/m, unless: all clouds within 10 NM of the flight path are transparent; or all nontransparent clouds within 10 NM of the flight path have cloud tops below the +5 °C level and have not been part of convective clouds with cloud tops above the -10 °C level within the last 3 hours. Notes: the electric field measurements at the surface are used to increase safety by detecting electric fields due to unforeseen or unrecognized hazards; for confirmed failure of one or more field mill sensors, the countdown and launch may continue.

*Electric Fields Aloft LCC*: The first seven LCC ('Lightning' through 'Smoke Plumes' LCC) and the second part of the eighth LCC ('Surface Electric Fields') need not be applied if, during the 15 minutes prior to launch time, the instantaneous electric field aloft, throughout the volume of air expected to be along the flight path, does not exceed $E_c$, where $E_c$ is provided as a function of altitude ($E_c$ not provided here). This LCC is not currently in use due to lack of available electric field profile sensors.

*Triboelectrification LCC*: Do not launch if a vehicle has not been treated for surface electrification and the flight path will go through any clouds above the -10 °C level up to the altitude at which the vehicle's velocity exceeds 3,000 Ft/sec. A vehicle is considered treated for surface electrification if all surfaces of the vehicle susceptible to precipitation particle impact have been treated to assure that the surface resistivity is less than $10^9$ ohms/square, and all conductors on surfaces (including dielectric surfaces that have been treated with conductive coatings) are bonded to the vehicle by a resistance that is less than $10^5$ ohms; or it has been shown by test or analysis that electrostatic discharges on the surface of the vehicle caused by triboelectrification by precipitation particle impact will not be hazardous to the launch vehicle or the mission.

*"Good Sense" Rule*: Even when these criteria are not violated, if any other hazardous conditions exists, the Launch Weather Team will report the threat to the Launch Decision Authority. The Launch Decision Authority may 'HOLD' at any time based on the instability of the weather.

## WEATHER SYSTEMS USED TO EVALUATE LCC

The 45 WS uses many weather systems to evaluate the LCC operationally for the ER and KSC (Harms, et al., 1997). The Lightning Detection And Ranging system has a 7 time-of-arrival radio antenna, which provides a three-dimensional depiction of the lightning, including in-cloud, cloud-to-cloud, cloud-to-air, and cloud-to-ground lightning. The Cloud to Ground Lightning Surveillance System is a short-baseline 6-antenna magnetic direction-finding/time-of-arrival (Improved Accuracy from Combined Technology) system. The Launch Pad Lightning Warning System is a network of 31 surface electric field mills. Other systems used include: National Lightning Detection Network, two weather radars, weather reconnaissance aircraft, a local radiosonde, and others (Harms, et al., 1998).

The 30 WS has a different suite of weather systems to evaluate the LCC at the WR. The Lightning Location and Positioning System is a cloud-to-ground lightning detection system. Other systems used include WSR-88D radar, weather reconnaissance aircraft, two local radiosondes, and others. An important difference from the ER and KSC is an absence of surface electric field mills.

## LCC CHANGE PROCESS

The LCC change process begins with a proposal to, or from, the Lightning Advisory Panel (LAP). The LAP is a group of atmospheric electricity experts from universities, national laboratories, and industry. The LAP is intentionally independent of launch operations, to ensure objectivity. The LAP members are Dr. Krider/University of Arizona, Dr. Koons and Dr. Walterscheid of Aerospace Corporation, Dr. Rust/National Severe Storms Laboratory, Dr. Willet/Air Force Research Laboratory, and Dr. Christian/NASA Marshall Space Flight Center. Proposed LCC changes are discussed extensively, in coordination with the operational range weather community. An extensive coordination process is required before implementing the new LCC (Roeder, et al., 1999b).

## DESIRED OPERATIONAL RESEARCH

The USAF and NASA have two main goals for future LCC changes: 1) continue increasing safe launch availability, and 2) improve operational usability and training. Some of the more pressing LCC questions are listed below. The USAF and NASA are always open to suggestions or proposals for better LCC.

The current 'Anvil Clouds' LCC prevents launch through attached anvil, regardless of the time or distance since the anvil emerged from the thunderstorm. Indeed, launches have been scrubbed for attached anvil even when the parent thunderstorm was hundreds of miles away over the Gulf Of Mexico. While this LCC may be justified, since anvil clouds are known to be able to carry large electric charge, better measurements of how fast charge can relax in anvil are needed. Several field experiments in Florida during Aug-Sep 98 collected some data on electric fields in and near anvil cloud. In addition, KSC is considering a new airborne field mill study. Numerical modeling sensitivity studies, and dual-polarization radar experiments, may also be useful in analyzing the anvil question.

The 45 WS and KSC have solicited operationally-viable, cost-effective ways to measure profiles of electric fields, so the 'Electric Fields Aloft' LCC can start being used. This may require innovative technology, since local analysis shows airborne field mills may not be cost-effective and have other operational limitations.

Finally, an operational sensor/technique for objective measurement of transparency is desired. The new 1998 LCC greatly expanded the use of cloud transparency to safely relax the LCC. The guidelines to operationally evaluate cloud transparency were also significantly improved. But cloud transparency is still evaluated subjectively.

## SUMMARY

The threat of natural and triggered lightning has significant impact on space launch. Approximately 35% of launches are delayed, and 5% scrubbed due to the lightning LCC. The LCC are a set of eleven rules which provide protection against the lightning threat. These rules are complex and very atypical of operational meteorology, as are some of the weather sensors used to evaluate the LCC. The importance of triggered lightning, and the distinction from natural lightning, cannot be overemphasized. The LCC undergo continuous incremental improvement. The USAF and NASA are always open to suggestions and proposals for improved LCC.

ACKNOWLEDGMENTS: The authors express their deepest gratitude to the LAP for their dedication to scientific accuracy in the LCC. Without their selflessness, the LCC would not have achieved their current level of excellence. This paper was reviewed by the following 45 WS personnel: Col David Urbanski and Mr. Billie Boyd.

## REFERENCES

DeSordi, S. P., 1999: Weather Impacts To Launch Operations At Vandenberg AFB CA, *8th Conference On Aviation, Range, And Aerospace Meteorology*, 10-15 Jan 99, 573-577

Harms, D. E., B. F. Boyd, R. M. Lucci, and M. W. Maier, 1998: Weather Systems Supporting Launch Operations at the Eastern Range, *AIAA 36th Aerospace Sciences Meeting and Exhibit*, Reno, NV, 12-15 Jan 98, Paper 98-0744

Harms, D. E., B. F. Boyd, R. M. Lucci, M. S. Hinson, and M. W. Maier, 1997: Systems Used To Evaluate The Natural And Triggered Lightning Threat To The Eastern Range And Kennedy Space Center, *28th Conference on Radar Meteorology*, 240-241

Krider, E. P., H. C. Koons, R. L. Walterscheid, W. D. Rust, and J. C Willet, 1999: Natural And Triggered Lightning Launch Commit Criteria (LCC), Aerospace Report No. TR-99(1413)-1, *The Aerospace Corporation*, 15 Jan 99, pp 15

Maier, M. W., 1999: Weather Impacts On Space Launch Operations At The United States Eastern Range, *8th Conference On Aviation, Range, And Aerospace Meteorology*, 10-15 Jan 99, *(manuscript not submitted)*

Marshall, T. C., W. D. Rust, M. Stolzenberg, W. P. Roeder, and P. R. Krehbiel, 1999a: Enhanced Fair-Weather Electric Fields After Sunrise, *11th International Conference on Atmospheric Science*, pgs TBD

Marshall, T. C., W. D. Rust, M. Stolzenberg, W. P. Roeder, and P. R. Krehbiel, 1999b: A Study of Enhanced Fair-Weather Electric Fields Occurring Soon After Sunrise, submitted to *Journal Geophysical Research*

Roeder, W. P., J. E. Sardonia, S. C. Jacobs, M. S. Hinson, A. A. Guiffrida, J. T. Madura, 1999a: Avoiding Triggered Lightning Threat To Space Launch From The Eastern Range/Kennedy Space Center, *8th Conference on Aviation, Range, and Aerospace Meteorology*, 10-15 Jan 99, 120-124

Roeder, W. P., J. E. Sardonia, S. C. Jacobs, M. S. Hinson, A. A. Guiffrida, J. T. Madura, 1999b: Lightning Launch Commit Criteria At The Eastern Range/Kennedy Space Center, *37th AIAA Aerospace Sciences Meeting and Exhibit*, 10-15 Jan 99, Paper 99-0890, pp 9

# NEW MECHANISM OF THUNDERCLOUD ELECTRICITY AND LIGHTNING PRODUCTION

V.I. Ermakov[1] and Y.I. Stozhkov[2]

[1]Central Aerological Observatory, Roskomgidromet, 141700 Dolgoprudny, Pervomayskaya str., Moscow region, Russia

[2]Lebedev Physical Institute, Russian Academy of Sciences, Leninsky Prospect, 53, Moscow, 117924, Russia

ABSTRACT: A new mechanism of thundercloud electricity and lightning production is given. The essential role in this mechanism belongs to cosmic rays. Cosmic rays ionize atoms of air. When in the low atmosphere there are powerful ascending wet air masses thunderclouds are produced. Near the Earth's surface in the low atmosphere positive and negative heavy ions are present. When air masses are rising to the altitude of several km they are cooled and the process of the condensation of water vapor on nucleation centers begins. On negative charged nuclei the condensation is going on faster than on positive ones. Upward air fluxes produce the large-scaled spatial separation of negative and positive charges and in turn it gives an electric field within a cloud. As soon as the electric field goes up to about 3 kV/cm the cloud becomes electric active and begins to work as a generator of new electric charges. Intracloud and cloud-to-ground discharges arise when extensive air showers of charged particles in the cloud are produced by high energy cosmic particles. These discharges propagate along the ionized tracks of particles of these showers. The mechanism proposed allows to estimate electric characteristics of thundercloud and describes lightning parameters known from the observations.

## INTRODUCTION

The thundercloud electricity production includes two different processes: unlike electric charge production and its large-scale spatial separation. Many mechanisms were proposed to explain these processes. The mechanism commonly accepted includes the electric charge production through freezing and subsequent splitting into small splinters of supercooled water drops. The spatial separation of light negative splinters from heavy positive ones occurs as a result of the difference speeds of these pieces in the gravitational field of the Earth [Baker, Dash, 1994]. However, till now there are not conclusive experimental facts to proof of this hypotheses.

Below the new mechanism of thundercloud electricity and lightning production is given. This mechanism includes lightning as a main generator of thundercloud electricity. In the numerous channels of lightning an abundance of unlike electricity charges is produced. The condensation of moisture prevails on the condensation nuclei having negative charge in comparison with positive ones and upward air fluxes produce the large-scale spatial separation of unlike electric charges inside of the cloud. The primary electric charges are produced by cosmic ray fluxes and natural radioactivity of air. When charge separation occurs the electric field inside of the cloud increases and new discharges are propagated along the ionized tracks of particles of extensive air showers (the bunches of charged particles with number of them $>10^5$ - $10^6$). High energy cosmic ray particles generate extensive air showers inside of the cloud.

## INITIAL PHASE OF THUNDERCLOUD PRODUCTION

The thundercloud formation takes place when powerful ascending fluxes of air are produced. It occurs when cold air mass meets with warm one (dynamic convection) or as the result of nonuniform heating of air mass by the irregular surface of the Earth (thermal convection). There are three phases of the thundercloud development. The first one is the growth phase characterized by the presence of a rising air fluxes in a cloud. In the next phase (the phase of mature) there are ascending and descending airflows and electric discharges arise. In the third phase (the phase of thundercloud decay) a vertical air motion is damped out and precipitation are observed.

The main reason of a cloud (and thundercloud) production is the process of supersaturation water vapor condensation in the atmosphere when the air masses are quickly cooled during their ascending. As the result of this process water drops arise. The supersaturation of water vapor occurs in the course of the arising and cooling of wet air mass. Aerosol particles (solid or liquid) are the germs of water drops. Because the ionization of air by cosmic rays and natural radioactivity some part of aerosols is charged (negatively or positively). The measurements show that in

the lower part of the atmosphere the concentration of heavy ions of both signs equals several thousands of particles in $cm^3$ and the concentration of all aerosols may be as much as several hundred thousands of ones in $cm^3$.

The energies to form the small water drops on the charged and neutral centers of condensations are different. As was shown by Rusanov [1978] this energy is minimal for negative charged aerosols and maximal for positive charged ones. At the supersaturation about 1% this difference equals $\sim 10^4$ times. It means that in upward air mass the process of water vapor condensation takes place mainly on the negative heavy ions. The water drop production and their coagulation decrease their upward motion. In turn, the positive charged heavy ions continue their motion with upward air because the more high value of water vapor supersaturation (which is observed at higher altitudes) is required to begin the condensation process. As a consequence the large-scale separation of charges and the spatial charge formation take place. The negative charge is clustered in the low part of a cloud and the positive one is clustered in the upper part of a cloud. The latent heat liberated in the condensation process enhances the upward air fluxes and the separation of unlike charges. The formed spatial negative charge reinforces also spatial separation of ions with unlike charges. Together with the growth of the spatial negative charge the electric field $E$ inside of the cloud grows also.

As soon as the value $E$ exceeds (2-3) kV/cm intracloud discharges arise. It happens in ~10 min. from the moment of the charge separation onset. By which time each the spatial charge is ~35 C and the positive charge rises at the altitude ~3.5 km relative to the negative charged water drops. The existence of free electrons in a cloud is an obligatory condition of any electric discharge occurrence. These electrons produce avalanches. For all time in the atmosphere there are free electrons produced by cosmic rays. However the maximal concentrations of such particles are observed when an extensive air shower formed by a high energy cosmic ray particle (energy $\varepsilon > 10^{14}$ eV) develops in a cloud. In this case the free electron concentration exceeds the value of background one more than 100 times. Since the high energy cosmic particle produces the extensive air shower all ionized tracks of shower particles are coupled together. The total number of electrons in the tracks exceeds $\sim 10^{12}$. At the altitudes where the thunderclouds are observed the number of electrons in track is (50-100) electrons/cm and the total length of ionized tracks is more than $\sim 10^5$ km. Under the strong electric field ($E$>(2-3) kV/cm) the electron avalanches inside of the ionized tracks are produced. Owing to it the growth of the ionization and the conductivity takes place. The ionized tracks link with each other and form "conducting tree". Predominantly the intracloud discharges run along the "branches" of this tree [Ermakov, 1992]. One such discharge neutralizes unlike charges in the cloud volume corresponding to the cylinder with the height ~3 km and with the diameter ~200 m. The growth rate of electric field inside of the cloud defines the frequency of intracloud discharges. In practice this frequency does not depend on the extensive air shower flux which equals ~1300 events/s for the clouds with the base ~13 $km^2$.

## CLOUD MATURITY PHASE

Since intracloud discharges arise the thundercloud is in the phase of maturity. It becomes the generator of unlike charges and produces their large-scale separation (see Fig. 1a). In the numerous channels of intracloud discharges more than $\sim 10^{20}$ electron-ion pairs are produced and the total charge (positive or negative) exceeds 100 C. Most of ion pairs is lost in the base of recombination and the rest being captured by aerosol particles of a cloud gives new heavy ions with unlike charges. These ions take part in the above process of a large-scale separation of charges. The concentration of drop germs is substantially enhanced, the process of moisture condensation and the release of latent heat is enhanced also. All gives additional growth of upward air fluxes in the cloud. The large water drops begin to fall down as the result of their coagulation.

In response to the spatial positive charge the current of light negative ions flows from the ionosphere to the top of the cloud (see Fig. 1b). Also the current of positive light ions flows from the atmosphere to the base of the cloud. The current of negative ions is more than the current of positive one by factor of $\geq 10$ because the mobilities and the concentrations of ions in the upper atmosphere are higher than these values in the low atmosphere. The negative ion current compensates partially spatial positive charge at the cloud top. As the result of it the electric dipole of the cloud becomes non-symmetrical one with the excess of negative charge in the base of the cloud. It increases the electric field between the cloud and the Earth's surface. It is favorable to emergence of cloud-to-ground lightning which transfer the negative charge to the Earth's surface (see Fig. 1b). These lightning propagate along the ionized tracks of extensive air shower particles produced by cosmic ray particles with the energy $E \geq 10^{15}$ eV. The flux of these high energy cosmic ray particles on the cloud surface ~13 $km^2$ is ~13 particles/s.

As a rule cloud-to-ground lightning consist of several discharges. The first discharge propagates along the tracks of extensive air shower particles produced by particle with the $E \geq 10^{15}$ eV. The other discharges pass along

non-cooled channels of the first discharge and new channels of small extensive air showers produced by particles with the energy $E \geq 10^{14}$ eV in the nearby region of the first discharge. As the geometrical size of a large extensive air shower exceeds the sizes of small showers the current of the first cloud-to-ground discharge is more than the current in the following ones.

The phase of maturity persists about 20-30 min. During this period ~50-100 cloud-to-ground discharges can occur. The intracloud discharges originate in 5-10 times more. Thus the total number of discharges during the cloud maturity phase equals several hundreds. The total electric charge of both sign ions produced in the lightning channels is more than $10^4$ C. The main part of these charges is lost in the process of their recombination. The small part of negative charges is transferred to the Earth' surface and some part of positive ones goes to the ionosphere. In such a manner thundercloud feeds the global electric circuit.

## CLOUD DECAY

During the first and second phases in the thundercloud a continuous growth of water drops takes place as the result of the condensation, sublimation, and coagulation processes. The water drops become heavy and begin to fall down under gravity. The upward air fluxes die out and precipitation arise. The cloud enters into the decay phase. With the precipitation the spatial negative charges from the bottom part of the cloud fall dawn also and the positive charges in the top part of the cloud replace negative ones. In the consequence of this the direction of electric field between the cloud and the Earth's surface is reversed and ground-to-cloud lightning transfer negative charges from the Earth to the cloud (see Fig. 1c). These discharges as the cloud-to ground ones propagate along the tracks of extensive air shower particles produced by high energy primary particle with $E \geq 10^{15}$ eV. In this phase upward air fluxes are absent and the generation of new charges does not take place. Because of this ground-to-cloud lightning undo only part of positive charges inside of the cloud. The rest of positive charges goes down with precipitation and is scattered in ambient air. In connection with a small value of positive charges (about 100 C) the number of ground-to-cloud lightning is many times less than cloud-to-ground ones. For this reason the total charge transferring to the Earth's surface by cloud-to-ground and ground-to-cloud lightning is the negative one.

## CONCLUSION

A put forward mechanism of thunderstorm electricity and lightning production in comparison with other known ones has the following special features: 1. The lightning are the main generator of unlike charges which are necessary to produce the strong electric field in the cloud and later lightning. In the numerous channels of lightning take place of the ionization of air and a large amount of unlike charges is produced. A primary charges to produce the first intracloud lightning are made by cosmic rays and radioactivity of the Earth; 2. In the process of a cloud formation when there are upward wet air fluxes the large-scale separation of unlike charges takes place because of moisture condensation predominantly on the negative charged ions. The latent heat released in the condensation process enhances upward air fluxes and the cloud formation process; 3. The extensive air showers produced by high energy cosmic ray particles initiate lightning discharges. In these showers the free electron concentration (free electrons are primary element in the mechanism of any air puncture) is higher than background one as much as 100 times; 4. The proposed mechanism gives the explanation the charging of the Earth's surface by negative electricity.

Acknowledgments. This work was supported by the Presidium of the Russian Academy of Sciences and in part by Russian Foundation for Basic Research (grant no. 98-02-16420).

## REFERENCES

Baker, M.V., H.G. Dash, Mechanism of charge transfer between colliding ice particles in thunderstorms, *Journ. Geophys. Res.*, *99*, N D5, 10,621-10,626,1994

Byers, H.R., Thunderstorms, *in Compendium of Meteorology, American Meteorological Society*, Boston, Mass., 681, 1951

Ermakov, V.I., Lightning initiation by galactic cosmic rays, *Proc. 9th Intern. confer. on atmospheric electricity*, St-Petersburg, 2, 485-488, 1992

Ermakov, V.I., G.A. Bazilevskaya, P.E. Pokrevsky, and Y.I. Stozhkov, Ion balance equation in the aymosphere, *Journ. Geophys. Res.*, *102*, N D19, 23,413-23,419, 1997

Rusanov, A.I., To thermodynamics of nucleation on charged centers, *Doklady Academii Nauk*, USSR, *238*, ' 4, 831-834, 1978 (in Russian)

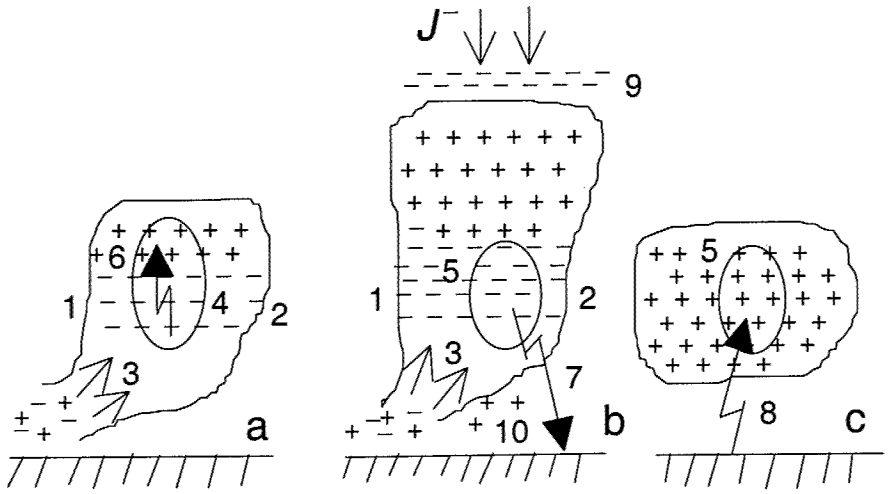


Fig. 1. The phases of the thundercloud formation: a-initial phase; b-maturity; c-decay. Notations: 1-the region of the warm front of air; 2-the region of the cold front air; 3-ascending fluxes of wet ionized air; 4 and 5-extensive air showers produced by primaries with the energies $\varepsilon \geq 10^{14}$ eV and $\varepsilon \geq 10^{15}$ eV; 6- intracloud lightning; 7- cloud-to-ground lightning; 8-ground-to-cloud lightning; $J^-$-the current of negative ions from the ionosphere to the top of the cloud; 9-the negative screen layer; 10-the positive charge in the cloud base.

# PRELIMINARY FAA INVESTIGATIONS INTO USING TOTAL LIGHTNING TO IMPROVE CONVECTIVE FORECASTING FOR AVIATION

A. Nierow[1], R.C. Showalter[2], and C.G. Souders[3]

[1]FAA, 800 Independence Avenue, SW, Washington, DC, 20591 USA
[2]CTA Inc., Portals Building, 1250 Maryland Ave., SW, Washington, DC, 20024 USA
[3]SAIC, Portals Building, 1250 Maryland Ave., SW, Washington, DC, 20024 USA

ABSTRACT: The Federal Aviation Administration (FAA) is investigating the use of total lightning (Cloud-to-Ground (CG), Intra-Cloud (IC), and Cloud-to-Cloud (CC) strokes) to supplement existing weather data sets in order to meet current requirements for convective forecasting, enhance aviation safety, and increase capacity. Total lightning could significantly enhance the ability to provide information on rapidly developing hazardous weather to both en route and terminal air traffic control personnel. The FAA is also evaluating the use of lightning data over oceanic regions.

## 1. INTRODUCTION

The FAA is responsible for meeting the safety and efficiency needs of a wide range of aviation users throughout the National Airspace System (NAS). According to FAA studies, aviation activity is expected to increase by 18%-24% over the next twelve years. The Nall Report (1997) states that 68% of all weather-related, general aviation accidents resulted in fatalities. The FAA Aviation Capacity Enhancement (ACE) Plan (1997) reveals that from 1992 to 1996 adverse weather was a major factor affecting NAS capacity, accounting for 72% of system delays greater than 15 minutes. Aviation weather systems will play a crucial role in reducing these statistics and attaining modernization of the NAS.

In order to mitigate weather-related delays, timely and accurate forecasts of convective weather must be available throughout the NAS to support an increased number of aircraft operations. Several FAA weather systems will be implemented the near term that will aid aviation forecasting. However, they do not enhance the capability for short term forecasting (30 minutes to 3 hours) until system upgrades are realized (around 2003). The technology to provide supplemental data sets such as total lightning data is available and could be obtained to provide that capability. Initially used as an interim measure, total lightning data could later be integrated into the algorithm-development effort associated with the system upgrades. Consequently, the FAA will be conducting preliminary investigations into the use of total lightning to improve its ability to meet convective weather forecasting requirements (FAA Order 7032.15).

## 2. CURRENT LIGHTNING CAPABILITIES

The current National Lightning Detection Network (NLDN) system provides lightning data over the Contiguous US (CONUS) and offshore waters. Both the National Weather Service (NWS) and the FAA use these data operationally. Although the NLDN only measures CG lightning, it has excellent spatial and temporal resolution (1 km and 1 minute respectively). However, it doesn't support convective weather forecasting requirements as there is minimal correlation between this type of lightning and the severity of the storms.

Operational lightning data is not currently available over the oceanic regions. The only weather data sets available to the meteorologist at the Center Weather Service Unit (CWSU) and the Traffic Flow Manager (TFM) at the Air Route Traffic Control Centers (ARTCCs) are satellite imagery (e.g., visible, water vapor, and infrared). While satellite imagery depicts the tops of clouds, it does not delineate the difference between cirrus clouds (comprised of ice crystals) and those associated with convective storms. Consequently, satellite imagery is often inadequate for relating storm severity and routing aircraft.

## 3. POTENTIAL IMPROVEMENTS TO CAPABILITIES

Recent advances in technology have improved the capabilities to measure total lightning. Studies have shown that IC/CC lightning activity provides a reliable precursor to storms with a lead-time of 5–20 minutes. Severe storms are defined as thunderstorms having hail greater than ¾ inch, winds in excess of 50 knots, or tornadoes. According to Weber et al. (1998) for severe storms (especially in the developing

stage), the total lightning flash rate is extraordinarily high and the lightning activity is overwhelmingly dominated by CC/IC lightning versus CG lightning. By definition a thunderstorm implies icing and turbulence, both of which have a significant impact on aviation. Therefore, this capability significantly increases the lead-time in determining which storms are rapidly developing (becoming increasingly dangerous) will improve decision-making, thereby enhancing safety and increasing fuel savings.

Systems are now available which provide the capability to measure lightning over oceanic regions. In particular, a ground-based "sferics" detection and localization system has been developed for the oceanic regions. The sferics system detects lightning-generated, Very Low Frequency radio noise between 5 and 15 kHz, which can propagate several thousand kilometers. Integrating sferics data with satellite imagery and making it available to oceanic ARTCC meteorologists, traffic managers, and airline dispatchers (possibly in the cockpit as well) could increase situational awareness and contribute to improved trans-oceanic capacity. This capability combined with improved communications would allow for the reduction in separation between aircraft without degrading safety.

The FAA will determine the viability of using total lightning and sferics technology to improve convective forecasting capabilities via Demonstrations Validations (DEMVALs).

## 4. DEMONSTRATION PROJECTS

In the CONUS, the FAA is investigating the utility of conducting a DEMVAL to determine the benefits of employing total lightning data for the en-route and terminal airspace. Implementation of total lightning data systems would be tested at the Jacksonville and Ft. Worth ARTCCs, as well as airports such as Dallas-Ft. Worth and Orlando. Furthermore, the FAA is also investigating via a DEMVAL the possibility of utilizing lightning data for the oceanic regions.

### 4.1 CONUS (En route and Terminal Airspace)

In the ARTCC, the CWSU meteorologist would use the Weather and Radar Processor (WARP) to integrate total lightning data with other data including Doppler Next Generation Weather Radar (NEXRAD), computer model output, and surface observations. This would allow them to provide better assistance to traffic management personnel involved in routing aircraft around rapidly developing storms. Additionally en route controllers could provide more in-depth advisory information to pilots.

For the airport terminal, total lightning data would be incorporated into the Integrated Terminal Weather System (ITWS) prototype. ITWS would integrate the total lightning data with other data sets to aid tower/Terminal Radar Approach Control (TRACON) personnel in determining which cells are rapidly developing, and therefore pose a significant hazard to arriving/departing air traffic. Unlike the ARTCC in the en route domain, no meteorologist is present at airport terminals to interpret the data. Therefore, ITWS is designed to display weather information (not data) which readily conveys the impact of severe weather on terminal operations (ground and air) to air traffic personnel.

An additional benefit of lightning data to terminal operations is that by knowing the potential severity of a thunderstorm in advance, traffic managers can optimize runway usage for wind shifts and gust front passage. This helps mitigate the impact of passing storms on airport capacity and allows airport traffic personnel to configure runway usage accordingly and sequence arriving/departing aircraft in an optimal pattern. In addition, the Storm Growth and Decay algorithm, currently being perfected for ITWS, would utilize these data, thereby enhancing its accuracy. This work is being funded by the FAA's Aviation Weather Research program.

### 4.2 OCEANIC AIRSPACE

The FAA is also investigating the possibility of utilizing lightning data in a region beyond the CONUS. This would include the western Atlantic Ocean and the Caribbean. No lightning data is currently available operationally over this great expanse, but a ground-based, cost-beneficial lightning detection system is needed nonetheless to improve aircraft routing by accounting for oceanic convective activity. Oceanic air traffic control is more strategic than that over CONUS as the aircraft aren't on radar for most of the transit, and much greater separation is required because of poor quality and infrequent High

Frequency (HF) voice position reports from the aircraft. Improved awareness of hazardous weather would allow for an earlier track adjustment with minimal deviation thereby enhancing fuel savings. In addition, more time would be available for coordination with controllers or dispatchers given the difficulty of oceanic communications.

One proposal the FAA is investigating is a sferics detection and localization system developed by a commercial vendor, Resolution Displays Inc. (RDI). The sferics are produced by vertical lightning discharges within clouds or cloud-to-ground discharges. The sferics system is more sensitive to CG discharges (or strokes) than to IC/CC discharges; however, it will report more IC/CC than CG due to the preponderance of IC/CC discharges.

RDI and the National Aeronautics and Space Administration (NASA) developed a network consisting of 5 receivers, located in MA, VA, AL, FL, and PR during 1997. Data were collected for a period of time, however, the contract expired and the flow of data was turned off in 1999. The network of receivers, however, is still in place. Weinman et al. (1999) states the errors in locating lightning from the East Coast network range from 5 km to 50 km increasing with distance from the receiver network. (Note–lightning has been detected with this system in Europe and Africa). The system response time is under 2 minutes.

Lightning Fills NEXRAD Holes

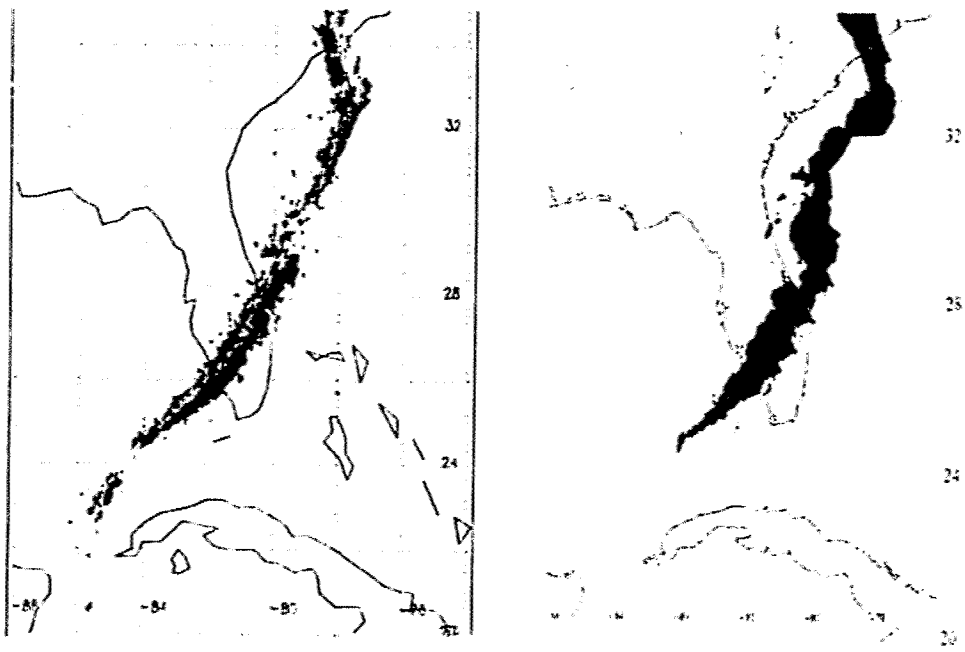

**Figure 1 Comparison of Lightning and NEXRAD coverage**

In Figure 1, from Weinman et al. (1999), the left side depicts lightning discharges between 0800 and 0900 UTC March 9, 1998 over the Florida peninsula. The right side shows a line of thunderstorms as viewed by the NEXRAD. Note that the lightning or sferics system fills in the "holes" within the radar coverage (between 29°N and 32°N) and captures the southern extension of the front missed by NEXRAD off the coast of Cuba.

Since the oceanic TFMs only have access to satellite data and pilot reports, the sferics system will aid them in determining where are the oceanic thunderstorms are. This will allow the meteorologists/TFM personnel to differentiate between showers, cloud cover, ice crystals and significant weather (i.e. thunderstorms). This is important since, for oceanic flights, improved weather data and communications could allow the separation standards to be reduced from 100 nmi to 50 nmi lateral separation.

## 4.3 DEMVAL EXPECTATIONS

For the near to mid term, the CONUS DEMVALS would essentially be a 'proof of concept'. If successful, they could lead to the utilization of total lightning data at all ARTCCs and major airports for both the en route and terminal airspace. If the oceanic DEMVAL is successful, it could lead to the acquisition of lightning data over the Pacific Ocean by the FAA, Department of Defense (DoD), and various airlines leading to a decrease in non-coordinated diverts and enhance safety. In the long term, much improved detection probabilities and spatial localization of the lightning activity could be accomplished using a geostationary-satellite based Lightning Mapper Sensor (LMS) under development by NASA and the National Oceanic and Atmospheric Administration (NOAA). However, advocacy from other agencies (FAA, DoD, etc.,) is needed if this type of system is ever to be realized.

## 5. FUTURE CAPABILITIES

Interagency efforts have begun to investigate the need to field a LMS that will provide continuous lightning measurements over the Western Hemisphere during the next decade. Christian (1998) stated that NASA is investigating putting a LMS system on the next Geostationary Operational Environmental Satellite (GOES) planned to be operational in late 2003 or early 2004. This will cover most of the Atlantic and eastern Pacific. In 2004 and beyond, use of the LMS system will improve detection probabilities of total lightning and spatial localization of oceanic lightning activity. There is some concern as to whether the 10-km spatial resolution of the LMS is sufficient for CONUS use.

## 6. SUMMARY

The FAA will determine the benefits versus the costs of employing total lightning data. A favorable cost benefits analysis is a crucial first step in implementing total lightning prototype systems. The addition of total lighting to the NAS weather architecture will enable the FAA to further mitigate the deleterious effect of convective weather on NAS safety and capacity in CONUS. Over the oceanic regions, lightning would help increase capacity by enabling the FAA to decrease oceanic separation without degrading safety and by reducing non-coordinated deviations through greater situational awareness. However, since the likelihood of a satellite-borne system appears to be at least 4 years away, the FAA is investigating currently available solutions as a possible interim measure until the LMS is operational

## 7. REFERENCES


"Aviation Weather Services, A Call for Federal Leadership and Action," National Academy Press, Washington, D.C., p. 10, 1995.

Christian, H.J., NASA Marshall Space Flight Center, Personal communication, 1998.

FAA Architecture 4.0, Chapter 25, 1999.

FAA Aviation Capacity Enhancement Plan, Table 1-2, p. 1-23, 1997.

FAA Order 7032.15, Air Traffic Weather Needs & Requirements, 1994.

"Nall Report, Accident Trends and Factors for 1996," The Aircraft Owners and Pilots Association Air Safety Foundation, p. 8, 1997.

Weber, M.E., E.R. Williams, M.M. Wolfson, S.J. Goodman, *An Assessment of the Operational Utility of a GOES Lightning Mapping Sensor,* Lincoln Laboratory Project Report NOAA-18, 1998.

Weinman, J.A., C.A. Morales, J.S. Kriz, S.J. Goodman, Long Range Thunderstorm Distribution Continuously Observed by Means of Ground Based Sferics Measurements. *Preprints, 8th Conference on Aviation, Range, and Aerospace Meteorology*, Dallas, TX., American Meteorology Society, p. 304-307, 1999.

# LONG-RANGE AND TRANS-OCEANIC LIGHTNING DETECTION

J. A. Cramer and K. L. Cummins

Global Atmospherics, Inc., Tucson, Arizona, U.S.A

ABSTRACT: Lightning observations over the oceans provide valuable information for identifying regions of severe weather and the related threat of turbulence. Global Atmospherics, Inc. has provided real-time lightning observations over the oceans for use by the U.S. National Weather Service Aviation Weather Center since 1996. This paper discusses the features and limitations of this information, and summarizes recent experiments that quantify the performance of an integrated system composed of widely-separated networks of sensors.

## INTRODUCTION

Global Atmospherics, Inc. (GAI) currently provides the U.S. National Weather Service (NWS) with long-range lightning information obtained from ionospherically reflected electromagnetic waves. This information, coupled with IR satellite imagery, is used by the Aviation Weather Center to produce periodic severe weather warnings in both the Atlantic and Pacific Oceans. This lightning information includes time and location of a subset of cloud-to-ground lightning discharges within 2000-4000 km of the U.S., covering portions of the Pacific and Atlantic Oceans, as far south as Panama.

The first practical configuration of this "Long Range" or "Maritime" network was brought on-line in 1996. Physically, this network was comprised of all sensors in the U.S. National Lightning Detection Network (NLDN) [*Cummins et al., 1998*], reprocessed in a manner that identifies and employs signals from ionospherically-reflected electromagnetic waves produced by distant lightning, rather than the "normal" ground-wave propagated signals. As with the NLDN, the source location method uses a combination of Time-of-Arrival (TOA) and direction finding (DF) methods. An overview of radio location methods is provided by *Norinder* [1953]. Lee [1989] describes a more-recent VLF "sferics" locating method based on arrival-time differences.

Early experience with GAI's Long-Range network demonstrated two key limitations. Location accuracy in the 2000-4000 km range was limited to about 16-32 km, due to the geometry of the network. Detection efficiency was also poor at these long distances, and was quite variable due to the diurnal variations in ionospheric propagation associated with VLF signals. In 1997, GAI began to explore ways to overcome some of these limitations. The most practical way was to add sensors outside of the current network. The first improvements came about in 1998 with the addition of sensor information from the Canadian Lightning Detection Network (CLDN) [*Cummins et al., this Proceedings*]. This led to a significant increase in coverage of the North Atlantic and Pacific oceans, improving both detection efficiency and location accuracy.

Due to geographic limitations, further improvements in the North Pacific or Atlantic would mean that new equipment would have to be located thousands of kilometers from the existing North American networks, thereby locating lightning that occurred *between* widely-spaced networks. Given this fact, we initiated a quantitative investigation aimed at evaluating the performance of such a configuration. This paper describes the results of these experiments and illustrates the practicality of trans-oceanic lightning detection.

## METHOD

To evaluate the viability of long-range lightning detection using widely separated sets of sensors, a pair of subnetworks was created using sensors from the East and West coasts of the United States. Locations of cloud-to-ground lightning were then re-computed using the long-range algorithm and sensor data from these subnetworks. These "transcontinental" locations were then compared to the locations obtained from the standard NLDN configuration. This allowed estimates of network detection efficiency and location accuracy, relative to the NLDN, to be made.

The two subnetworks were composed of two groups of 9 sensors , as shown in Figure 1. The region of interest is shown in the center of the map, in Kansas and Oklahoma. This configuration results in propagation paths of 1200-1600 km. A mix of sensor types was used. In Figure 1, IMPACT sensors are indicated by a star symbol, and LPATS III sensors are represented by a square symbol. No CLDN LPATS IV sensors were available for evaluation during the experiment. The individual sensor data were then reprocessed, and solutions inside the region of interest were compared to corresponding data from the complete NLDN network.

Given the positive results from this transcontinental network experiment (discussed below), the feasibility of using groups of sensors separated by oceans was then considered. Since no land based lightning network existed to be used as "ground truth" in such a comparison, verification was limited to comparing lightning positions to cloud temperature data obtained from GOES IR satellite data provided by the Aviation Weather Center. Such information is used routinely by forecasters at the Aviation Weather Center. This transoceanic experiment was carried out using data from sensors in the Météo-France network operated by Météorage, in conjunction with an East-coast subset of sensors from the NLDN.

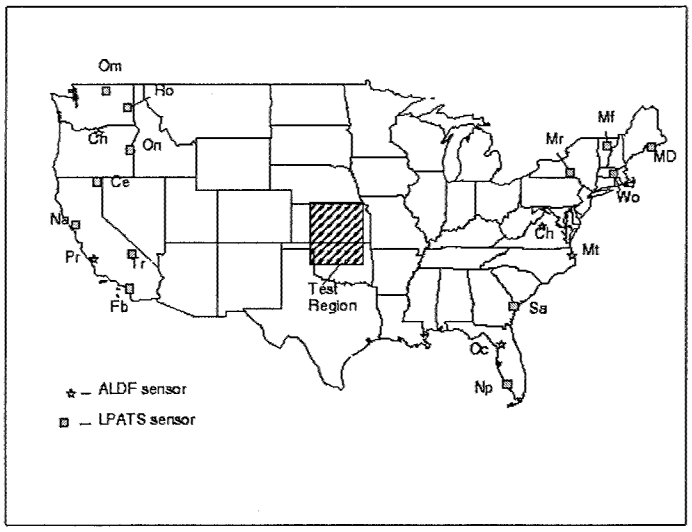


**Figure 1. Transcontinental Test Configuration**

RESULTS

Since it was anticipated that there would be strong diurnal variations in the transcontinental data, the contributions from each set of sensors were analyzed at different times during the day. For one time period it was dark along the whole path of propagation; a second period was associated with an all-day propagation path. Third and fourth periods examined times when a day-night boundary was between the groups of sensors. The aggregate contribution of individual sensors is shown in Table 1. For the East and West sensors, the number of times they contributed to a transcontinental solution is enumerated for each of the four time periods: Day, East Dark, All Dark, and West Dark. During Day time, West and East coast sensors performed equally poorly. During the afternoon period (East Dark), when western sensors were still in daylight, there was a distinct favoring of eastern sensors. This was also the case during the All Dark condition. In the early morning (West Dark), there was a slight favoring of western sensors. This result suggests a slight favoring of west to east propagation, which is consistent with previous reports in the literature. [*Wait, 1996*].

**TABLE 1. Contributions By Sensor**

| Condition | West Count | East Count |
|---|---|---|
| Daytime | 451 | 571 |
| East Dark | 97 | 2649 |
| All Dark | 24186 | 49676 |
| West Dark | 3573 | 2554 |

Transcontinental data were also computed continuously for several days, and compared to the NLDN. A comparison of detection efficiency is provided in Figure 2, where counts of lightning discharges located by the transcontinental network are compared to counts produced by the standard NLDN. This figure indicates a peak detection efficiency of 10-25% during the night and only a few percent during the day. Although these results

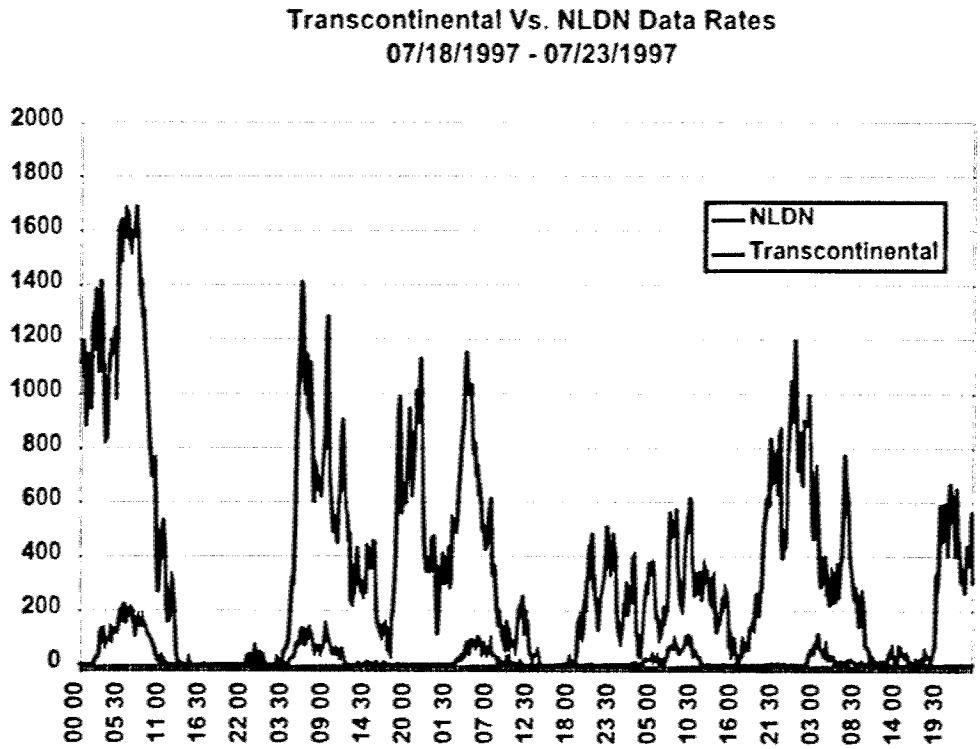


**Figure 2. Lightning Counts in 10-minute Intervals in the Test Region.**

illustrate the fact that using widely spaced sensors extends the daily time duration for VLF detection, it is clear that the detection efficiency has a strong diurnal variation.

In an effort to further characterize the detection efficiency of the transcontinental network, the distribution of peak currents for NLDN events that were time-correlated with events detected by the transcontinental network was examined. This distribution was compared to the peak current distribution of the complete set of NLDN data. Figure

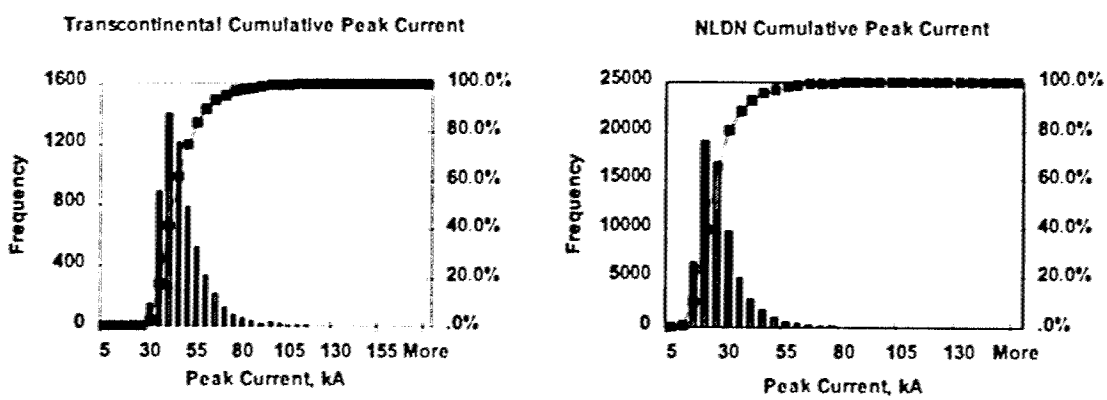


**Figure 3. Peak Current Distributions**

3 shows these peak current histograms and the distributions for a typical 24-hour period. The mean for the NLDN data is about 24 kA, and the mean for the transcontinental network is about 45 kA. Note that there are very few transcontinental events with peak currents less then 30 kA. Above 45 kA, the detection efficiency of the transcontinental network approaches 50%.

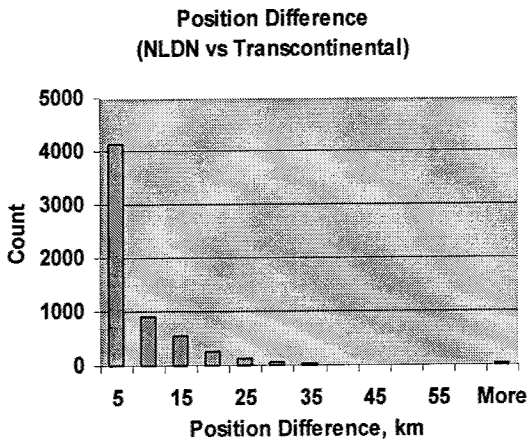


**Figure 4. Position Difference Between NLDN and Transcontinental Networks**

Location accuracy of the transcontinental was also evaluated. Position differences between the NLDN and transcontinental data were determined for events having times that matched to +/- 1 millisecond. As shown in Figure 4, more then 50 percent of the data had position differences of less than 5 km. There were 6103 events in this assessment; the 95 percentile is at 15-20 km. This location accuracy is clearly better than can be obtained when all sensors are located on one side of the storm.

## CONCLUSIONS AND FUTURE STUDIES

These investigations indicate that 1) only larger peak current (>30 kA) events are seen by GAI's long-range network employing ionospherically-propagated VLF lightning signals; 2) detection efficiency is still strongly dependent on the time of day, but this can be reduced by placing sensors several thousand kilometers to the East and West of a region of interest; and 3) median location accuracy for this long-range network employing a combination of direction finding and time-of-arrival location methods is approximately 5 km when lightning is located between subsets of sensors. As this investigation was conducted with propagation paths of around 1200-1600 km, it would be useful to investigate longer propagation paths to determine if they yield similar results.

Further analysis of trans-oceanic network performance is required. During the Spring and Summer of 1999, a multi-country experiment will be carried out, lead by researchers from GAI, the U.S. NWS Aviation Weather Center, and Météo-France. In addition, GAI will be conducting a more detailed investigation of the existing North American Long-Range network, including repeating the transcontinental experiment described above in Canada, where propagation paths are longer. Future investigations may also include a study of seasonal variations and a more theoretical examination of the propagation characteristics. The techniques used in these networks are applicable to any large network that employs broadband VLF/LF sensors, and they enable researchers and commercial users to track lightning over the oceans.

## REFERENCES


Cummins, K.L., E.P. Krider, M.D. Malone, The U.S. national lightning detection network and applications of cloud-to-ground lightning data by electric power utilities, *IEEE Trans. Elec. Comp.*, 40, 465-480, 1998.

Cummins K.L., R.B. Pyle, and G. Fournier, An integrated North American lightning detection network, *ICAE'99*, Guntersville, Alabama, USA, 1999.

Lee, A.C.L, Ground truth confirmation and theoretical limits of an experimental CLF arrival time difference lightning flash locating system, *Quart. J. R. Met. Soc.*, 115, 1147-1166, 1989.

Norinder, H., Long-distance location of thunderstorms, Chapter 14 in *Thunderstorm Electricity*, by H.R. Byers, U. Chicago Press, 276-327, 1953.

Wait, J.R, *Electromagnetic Waves in Stratified Media*, Oxford University Press, Inc. 1996 .

# A diagnostic analysis of the Kennedy Space Center LDAR network

**D.J. Boccippio, S. Heckman, S.J. Goodman**

**Global Hydrology and Climate Center**
**Huntsville, AL 35812**

**Abstract.** The performance characteristics of the Kennedy Space Center Lightning Detection and Ranging (LDAR) network are investigated at medium-far range (50-300 km). A 19 month noise-filtered sample of LDAR observations is examined, from which it is determined that the "climatological" VHF source density as observed by LDAR falls off approximately 10 dB every 71 km of ground range from the network centroid. The underlying vertical distribution of LDAR sources is approximately normally distributed with a mean of 9 km and a standard deviation of 2.7 km, implying that loss of below-horizon sources has a negligible effect on column-integrated source densities within 200 km ground range. At medium to far ranges, location errors are primarily radial and have a slightly asymmetric distribution whose first moment increases as $r^2$. A range calibration derived from these results is used to normalize source density maps on monthly, daily and hourly time scales and yields significant improvements in correlation with NLDN ground strike densities.

## 1. Introduction

The Lightning Detection and Ranging (LDAR) network installed at Kennedy Space Center is a sensor capable of locating the impulsive 66 MHz (VHF) radiation emitted from total (intracloud and cloud-to-ground) lightning channel processes, using a time-of-arrival (TOA) technique. Recent pilot studies by MIT/Lincoln Laboratories, the Marshall Space Flight Center and the Melbourne National Weather Service Forecast Office have sought to quantitatively use KSC LDAR flash (source cluster) counts operationally to improve local severe storm forecasts (the LISDAD experiment; *(Williams* et al., *1999)*), building on early applications research by *(Forbes & Hoffert, 1995)*. Global Atmospherics, Inc. was recently award a contract to upgrade and improve the KSC LDAR *(Starr* et al., *1998)*; this may eventually lead to more widespread deployment of commercial TOA systems. Total lightning mappers such as the LDAR also provide one of the best tools for validating spaceborne total lightning sensors, such as the Optical Transient Detector (OTD) and Lightning Imaging Sensor (LIS).

One of the significant drawbacks of TOA total lightning networks is their limited (and as yet poorly quantified) useful range, owing to VHF signal attenuation, loss of below-horizon VHF sources (VHF radiation not being ducted by the ionosphere) and increasing location errors at far ground range. *(Mazur* et al., *1997)* undertook a preliminary examination of LDAR performance using TOA and interferometric data from three storms at varying ranges from the sensors. This study will expand that analysis to include an empirical assessment using a very large (19 month) sample of noise-filtered LDAR data.

## 2. Methodology

The basic observable of the LDAR system is the occurrence and location of VHF impulsive sources. The LDAR reports these sources in a Cartesian coordinate system with the $z = 0$ plane tangent to the earth surface at the network centroid. It will be more convenient in this study to work in a coordinate system of $(r_g, \theta, z)$, where $r_g$ is the ground range to a point on the Earth's surface directly below a VHF source, $\theta$ the azimuth to this point, and $z$ the source altitude above the local earth surface. While the parameter of most physical relevance in this study is likely the true source range $r$, the differences between the true range and ground range are small for most of the analysis domain used in this study ($r \gtrsim 30$ km).

Nineteen months of LDAR source data (March 1997 - September 1998) are used to determine the "climatological" volumetric and areal source densities $S_3(r_g, \theta, z)$, $\overline{S_3}(r_g, z)$, $S_2(r_g, \theta)$ and $\overline{S_2}(r_g)$ at various time scales and spatial resolutions. The raw source data is obtained in hourly "packet files"; a single source location solution for each source is reported in these files, the result of a "voting" algorithm integrated into the LDAR processing system designed to select robust locations from various combinations of multi-antenna solutions. Characteristic source amplitudes are not reported in the packet files. These data are publicly available through the Global Hydrology Resource Center (http://thunder.msfc.nasa.gov). Approximately 11,200 hourly files comprise the 19 month dataset. Noise from a nearby calibration signal was automatically filtered from the data and noise from nearby aircraft (common in the data set) was removed manually from all affected files. Analyses performed here which are height-independent use the entire 19-month dataset;

analyses which involve vertical structure information use only data from May-Sep 1997,1998 to ensure "free convective" rather than frontal storm behavior and a comparatively constant vertical temperature profile.

## 3. "Climatological" distributions

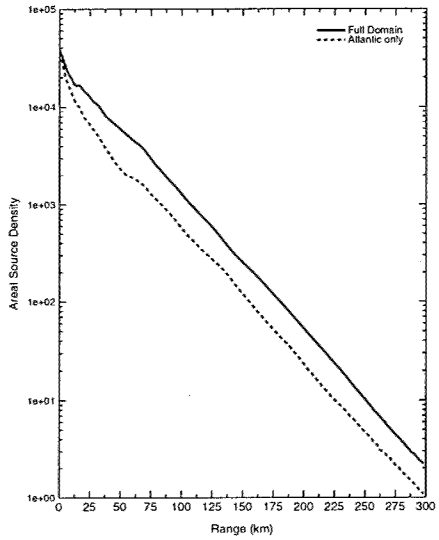


Figure 1: *LDAR areal source density vs. range.*

Fig. 1 shows the total (azimuth-integrated) areal source density over 19 months for the entire 300 km domain around the LDAR and for the oceanic azimuths only. More than $10^8$ sources were used to construct this composite. Observed areal source density follows a nearly perfect exponential decline with ground range (totalling 40 dB over 300 km, or a 31 km $e$-folding scale), and only differs in magnitude over the oceanic azimuths. Inspections of this data in an $(r_g, \theta)$ composite grid (not shown) suggested that the 19 month sample was long enough to proxy some underlying geographic uniformity in the true VHF source distribution, at least over the peninsular and oceanic subregions around KSC. The rapid decline is not unexpected given the attenuation of VHF radiation with range (following a conventional $1/r$ decline in amplitude); however, the precise shape of the falloff (exponential) provides important information about the underlying true amplitude distribution. A complete discussion of inferences about this amplitude distribution is beyond the scope of this paper but will be discussed at the ICAE. The 31 km $e$-folding scale should be noted: it indicates a fundamental limiting scale for quantitative use of LDAR source densities; beyond the range where LDAR location errors exceed this scale, nominal source densities from mislocated sources will begin to dwarf the true lightning signal. This will be discussed in more detail below.

Fig 2 shows the azimuth integrated volumetric source densities as a function of height for the 1997 and 1998 convective seasons only, and the corresponding *relative* vertical distribution of sources (i.e., each volumetric source density is normalized by the azimuth- integrated column total of each range bin). Several features are notable in these plots: *(1)* At ranges close to the LDAR, the vertical distributions peak at about 9-10 km AGL, suggesting that the majority of sources arise from the upper branches of intracloud (IC) channels. This is consistent with the findings of *(Mazur* et al., *1997). (2)* Comparatively few sources are observed from CG channels, far fewer than would be expected if ICs and CGs radiated similarly, and given typical IC:CG ratios of 3:1 or 4:1. The total source density is thus dominated by IC flashes, even at far ranges. *(3)* Loss of below-horizon sources is clearly evident at far ranges, with most of the troposphere missed by 300 km range. The effective "minimum elevation angle" derived from these results appears to be about 0.5 degrees. *(4)* A significant number of sources are located at altituds which are probably spurious (higher than about 18 km AGL), and the fraction of "too-high" sources increases with range. The true 9-10 km maximum level appears to be "pushed up" at increasing range with something like an $r^2$ dependence.

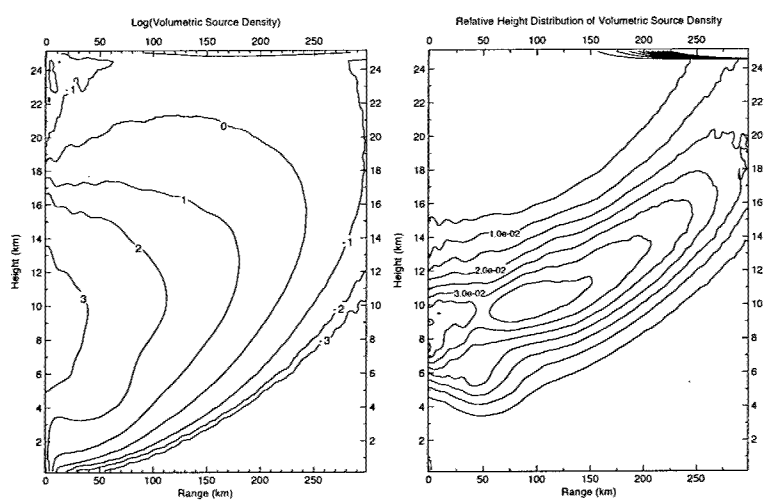


Figure 2: *LDAR total and relative volumetric source density.*

## 4. Loss of below-horizon sources

From Fig 2 it is apparent that altitudes of sources within about 50 km ground range from the sensor are reasonably stable and correct. Compositing all data within 50 km, we may estimate the "true" underlying climatological vertical distribution of VHF sources; this is shown in Fig 3, along with a Gaussian fit with a mean of 9 km and a standard deviation of 2.7 km. We may combine this analytic approximation with the minimum observable altitude $z_0$ at a given range to estimate the fraction of true sources lost below the LDAR effective horizon. $z_0$ is given directly by:

$$z_0(r) = \sqrt{R_e^2 + r^2 + 2R_e r sin(\Phi_{min})} - R_e \qquad (1)$$

and hence the fraction of lost sources, $\delta$ is given by:

$$\begin{aligned}\delta(r_g) &= \int_0^{z_0(r_g,\Phi_{min})} \frac{1}{\sqrt{2\pi}\sigma} e^{-\frac{(z-\mu)^2}{\sigma^2}} dz \\ &= \frac{1}{2}(Erf(\frac{\mu}{\sqrt{2}\sigma}) + Erf(\frac{z_0(r_g,\Phi_{min}) - \mu}{\sqrt{2}\sigma}))\end{aligned} \qquad (2)$$

The fraction of retained sources, $1 - \delta(r_g)$, is shown in Fig 5 for $\Phi_{min}$ of 0 and 0.5 degrees.

Clearly, even though the horizon rises to modest altitudes (about 4 km at 200 km ground range), the high bias of the actual source distribution buffers the horizon effect, and relatively few sources are lost from the column total. This loss increases rapidly from 200 to 300 km, although even at 300 km the loss is still only about a factor of two (40-60%). Note that this is a convective season result; during winter when lightning occurs at lower altitudes the horizon lossess will of course be more severe.

## 5. Location errors

The relative vertical profiles shown in Fig 2 strongly suggest that radial location errors at medium-far ranges in the LDAR dataset are nontrivial, and indeed, likely larger than the e-folding scale of amplitude decay of LDAR sources. This is evident in the upward deflection of the vertical source distribution with range: sources which contain large positive range (radial) errors will be "overlocated" in altitude, while sources with large negative radial errors will be "underlocated". However, the rapid amplitude decay with range implies that overlocated sources from a given range may dwarf the climatological signal at farther ranges, and that is indeed what we observe in the vertical profiles. Fig 5 summarizes the best available estimates of various TOA network radial errors. The best error estimates (filled squares) are analytically derived for a network recently designed and deployed by Krehbiel, Rison and Thomas (this issue), and are small in magnitude in part because of the large antenna spacing of this network. Analytic estimates by *(Koshak & Solakiewicz, 1996)* (filled circles) for a generic network are also on the low end of values. Empirical estimates of the KSC LDAR accuracy by *(Maier* et al., *1995)* using aircraft-borne spark generators (open squares) and *(Pochler,*

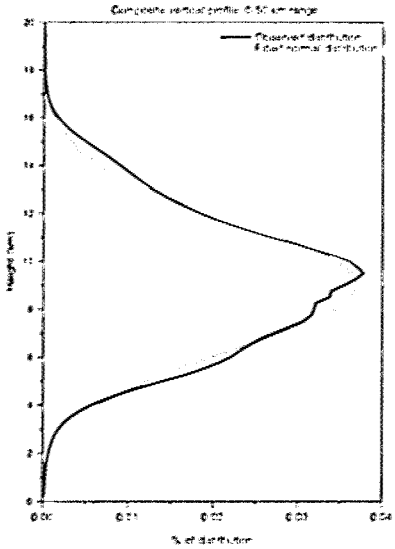

Figure 3: *Best estimate of true vertical VHF source distribution.*

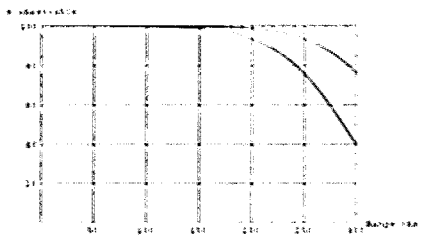

Figure 4: *Percent of VHF sources above the LDAR effective horizon.*

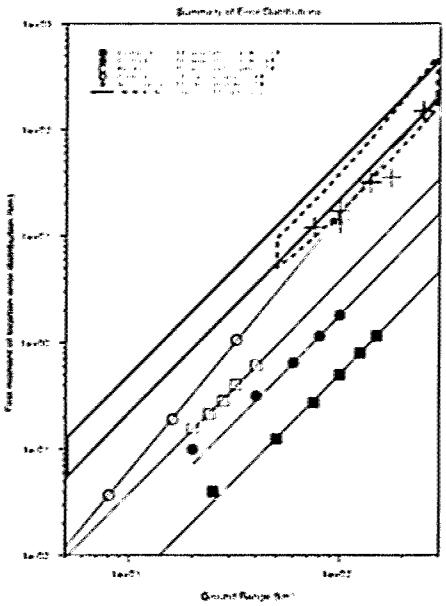

Figure 5: *Summary of TOA network errors.*

*1977)* (open circles) using calibration signals fall somewhat higher. Bootstrapped estimates of errors in 8 storms observed in the present dataset, based upon the actual source count histograms in range, are overlaid (crosses) and fall even higher. Finally, Monte Carlo simulations performed by the author (upper polygons) in which the underlying amplitude distribution slope and error magnitude were varied required the largest error moments to match the observed and simulated distributions. In all cases, predicted, observed or inferred error moments increase approximately with $r^2$.

### 6. Range normalization

The observed near-exponential decline in column-integrated source density with range (Fig 1) suggests that a range normalization factor might exist which would allow LDAR areal source densities to be quantitatively intercompared across ranges. A simple normalization of the form:

$$N(r) = e^{\frac{r_g}{r_{scl}}} \tag{3}$$

$$S_{2,norm}(r_g, \theta) = S_{2,obs}(r_g, \theta) N(r_g) \tag{4}$$

was investigated using various values of $r_{scl}$. The normaliztion was tested using NLDN ground flash counts as a "poor man's truth", and performance estimated by testing the correlation of corrected LDAR densities with NLDN densities over 20 km grids at climatological (19 month), monthly, daily and hourly time scales.

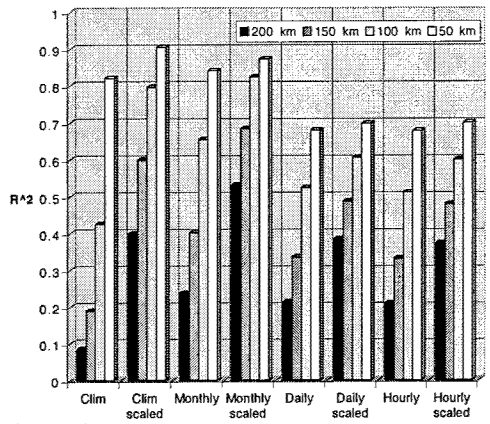


Figure 6: *LDAR range normalization improvements (correlation with NLDN CG density).*

$R^2$ values were computed for data within 50, 100, 150 and 200 km from the LDAR centroid. For each test the value of $r_{scl}$ was found which maximizes $R^2$; these values range from 39-50 km. The $R^2$ values are shown in Fig 6 for raw and optimally scaled LDAR data. The range normalization produces significant improvements for data beyond 50 km range, with the greatest improvements being at the farthest ranges. The fact that $r_{scl}$ exceeds the intrinsic $e$-folding decay scale of the raw data (31 km) is explainable by the presence of radial location errors: the optimal normalization underweights "overlocated" sources which partially contaminate the true signal at far range. The true skill improvement is likely higher than shown here, as we only expect the true source densities to loosely correlate with the imperfect truth of NLDN.

# References


Forbes, G.S., & Hoffert, S.G. 1995. *Lightning forecasting studes using LDAR, LLP, field mill, surface mesonet and Doppler radar data.* Tech. rept. CR-199891. NASA.

Koshak, W.J., & Solakiewicz, R.J. 1996. On the retrieval of lightning radio sources from time-of-arrival data. *J. Geophys. Res.*, **101**(D21), 26631–26639.

Maier, L., Lennon, C., & Britt, T. 1995. Lightning detection and ranging (LDAR) system performance analysis. *In: Proceedings, 6th Conf. on Aviation Weather Systems.* American Meteorological Society, Dallas, TX.

Mazur, V., Williams, E., Boldi, R., Maier, L., & Proctor, D.E. 1997. Initial comparison of lightning mapping with operational Time-Of-Arrival and Interferometric systems. *J. Geophys. Res.*, **102**, 11071–11085.

Poehler, H.A. 1977. *An accuracy analysis of the LDAR system.* Tech. rept. CR-154631. NASA.

Starr, S., Sharp, D., Merceret, F., & Murphy, M. 1998 (Apr.). *LDAR, a Three-Dimensional Lightning Warning System: Its Development and Use by the Government, and Transition to Public Availability.* Tech. rept. KSC 00325. NASA Kennedy Space Center.

Wiliams, E.R., Boldi, B., Matlin, A., Weber, M., Hodanish, S., Sharp, D., Goodman, S., Raghavan, R., & Buechler, D. 1999. The behavior of total lightning activity in severe Florida thunderstorms. *Atmos. Res.* in press.

# Session IV:

# Storm Electrification

# AIRCRAFT MEASUREMENTS OF PARTICLE IMAGE AND CHARGE INSIDE A NEW MEXICO THUNDERCLOUD

W. Clifton Murray[1], W. P. Winn[1], Ronald J. Thomas[1], Arnold E. Ebneter[1], Peter R. Fleischhacker[1], R. Paul Lawson[2], Kim A. Weaver[2], Roy Stewart[3], and Chris Wieland[4]

[1]Langmuir Laboratory for Atmospheric Research, New Mexico Tech, Socorro, New Mexico, U.S.A.
[2]SPEC, Inc., 5401 Western, Boulder, Colorado, U.S.A.
[3]Tesseract Design & Instrument, 5401 Western, Boulder, Colorado, U.S.A.
[4]Della Enterprises, Inc., 3425 North County Road 3, Loveland, Colorado, U.S.A.

ABSTRACT: The popular hypothesis for how thunderclouds become electrified invokes collisions between graupel (or hail) and small ice crystals. While there has been considerable laboratory investigation of this ice-ice mechanism, in-situ testing of it by particle observations consists only of a few instrumented balloon and aircraft flights into actual thunderclouds [*Marshall and Winn*, 1982; *Vali et al.*, 1984; *Weinheimer et al.*, 1991; *Bateman et al.*, 1999]. Some of the results of these in-cloud measurements are puzzling because the larger charges are not especially associated with the larger particles.

To better understand this puzzling result, Langmuir Laboratory's airplane SPTVAR (Special Purpose Test Vehicle for Atmospheric Research) was equipped with an instrument for imaging particles and measuring their charge. On August 19, 1998, the airplane was able to fly into a growing cloud a few minutes before its first lightning flash. In this case the particle data are limited to the edge of the region of strong electric field, possibly because icing obscured the laser beam used to image the particles. Analysis of the data reveals that many of the larger charges were carried by the smaller particles.

## INSTRUMENTATION

The particle-imaging instrument carried by SPTVAR (Figure 1) was a High Volume Precipitation Spectrometer (HVPS) manufactured by SPEC, Inc. The instrument directs a plane of laser light onto a line of photodetectors, so that when a particle intercepts the plane of light, some of the photodetectors (pixels) are shadowed. The 1-channel HVPS used here operates under the same principle as the 4-channel HVPS described in *Lawson et al.*, 1998. The main difference is that whereas the 4-channel device used four identical channels with 128 photodiodes and 400 $\mu$m resolution, the 1-channel HVPS has 256 photodiodes and 200 $\mu$m resolution. The 1-channel HVPS can image particles ranging from 200 $\mu$m to about 4 cm in diameter.

Charge-sensing capability was added to the HVPS. The sensors consist of two arrays of four electrodes each, with the arrays facing each other in parallel-plate fashion. They were installed to match the imaging area as closely as possible, in order to minimize the chances of an unimaged particle entering the charge-sampling space. Figure 2 is a sketch of the 1-channel HVPS with the charge detector addition. Particle image and charge data were stored on an on-board disk drive.

In addition to the particle-detection instrument, SPTVAR also carried recently-designed electric field meters [*Mo et al.*, 1998], a King probe (for measuring liquid water content), and a reverse-flow temperature probe. The data from these instruments, along with pressure, position (from the Global Positioning System), and other information, were telemetered to a ground receiving station.

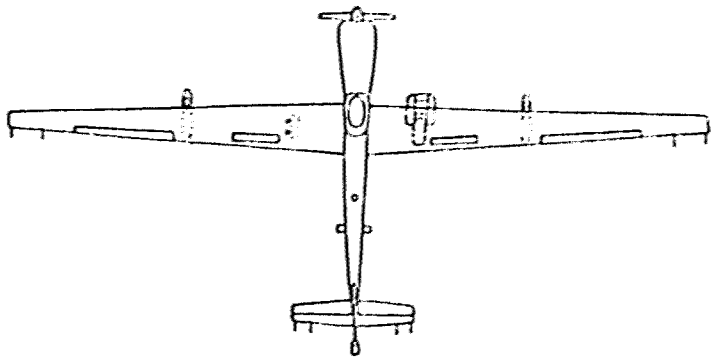

Figure 1.

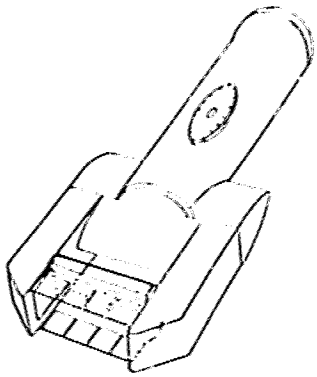

Figure 2.

## OVERVIEW OF FLIGHT

On August 19, 1998, SPTVAR penetrated a growing cloud over the Magdalena Mountains in central New Mexico at an altitude of 7 km above sea level, where the temperature was −13 °C. As the airplane approached the cloud, the pilot estimated he was 450 m below cloud top. SPTVAR entered the cloud about 18:18:00 UTC. Inside, the pilot reports included (in order) "Something on windscreen, probably ice," "Fair amount of turbulence," "Big particles," and "Updraft." SPTVAR exited the cloud about 18:20:00 UTC, and the pilot reported that the aircraft had accumulated 1/4 in. of ice. The second pass was delayed to give the cloud time to electrify.

At about 18:25:40 UTC, SPTVAR re-entered the cloud for a second pass at 7 km altitude. The pilot reports included, in order, "Heavy particles," "Large particles, turbulence," "Lot of big particles," "Smooth," "Big drops of some sort," "Updraft," "Losing altitude," and "In and out of cloud." He emerged fully into the clear about 18:28:50 UTC, and reported that SPTVAR had accumulated additional ice. The airplane encountered significant electric fields during this second pass.

Due to the icing, SPTVAR descended to study the cloud at a lower altitude.

## OBSERVATIONS

Figures 3a and 3b show overhead and west-looking views, respectively, of the aircraft path during the second pass. The part of the path shown as a solid line is where the electric field magnitude was greater than 37 kV/m. Shortly after SPTVAR emerged from the second penetration, the cloud produced lightning, at 18:29:09 UTC. The radiation sources for this discharge, courtesy of New Mexico Tech's Lightning Mapping System [*Rison et al.*, 1998], are super-imposed onto the airplane path. These sources, represented as dots, are regions of positive charge into which the main channel or its branches extend; the five circled sources are those occurring first in time. This agrees with the observation that during the second pass through the cloud the electric vector pointed downward most of the time (Figures 4a and 4b), indicating positive charge overhead and/or negative charge below.

Figure 4c shows the particle charge density, calculated over one-second "bins," for both passes. Comparing the two passes, we see the charge density had increased considerably toward the negative by the time of pass 2. We are undecided as to the significance of the rather abrupt ends to the presence of particles in Figure 4c. It may be that the HVPS stopped taking data (for about a minute, in the case of pass 2), due perhaps to ice blocking the image beam. Although the sapphire windows through which the laser beam passes are heated, they may not have been able to keep up with the high icing rate, and so might not have cleared the ice until the airplane was outside the region of high liquid water content.

The particles' diameters ranged from 200 $\mu$m (1 pixel) to nearly 3/4 cm, for both passes. Images for particles with diameters of a few mm often appear irregular in shape, while larger-particle images typically show a granular outline and often have a roughly conical shape.

Figure 5 is a plot of particle charge versus equivalent diameter (the diameter assuming a spherical particle), for several bins spanning the largest (most negative) charge-density region of Figure 4c. The interesting association of several of the larger charges with the smaller particles is characteristic of most bins, positive or negative, in both passes.

## CONCLUSIONS

The magnitude of the negative particle charge density in pass 2 suggests that the observed particles carried at least part of the charge of electrification.

The particles greater than about 1 mm in diameter appear to be ice in the form of snow pellets or hail. Because the smallest particles' images are near the instrument's resolution limit (200 $\mu$m), we cannot discern their shape, and so cannot say from the images alone whether they are ice or liquid. However, other studies in comparable cloud conditions, including a flight through a New Mexico summer thunderstorm with a higher-resolution probe, found that particles larger than 300 $\mu$m were graupel [*Weinheimer et al.*, 1991].

Most of the larger charges measured in this study, whether negative or positive, were not attached to the larger particles.

Many of the larger charges measured in this study appear to have been carried by graupel in the size range from 400 $\mu$m to 1.0 mm.

Assuming each graupel-crystal collision event transfers a typical laboratory value of several fC [*Jayaratne*, 1983], a graupel pellet would need to have experienced about 1000 collisions in order to accumulate a several-

pC charge. Even if we suppose an optimistic transfer of 500 fC per event [*Jayaratne and Saunders*, 1985], we still need at least 20 collisions to build up a graupel charge of only 10 pC. Given, then, that the magnitude of graupel charge depends on the number of collisions experienced, which in turn should depend on particle diameter, it is puzzling that we found most of the larger charges on our smaller size-range of particles.

ACKNOWLEDGEMENTS: We thank Dr. Ronald Taylor for support of this work with funding from NSF Grant ATM-9318887.

REFERENCES

Bateman, M.G., T.C. Marshall, M. Stolzenburg and W.D. Rust, Precipitation charge and size measurements inside a New Mexico mountain thunderstorm, *J. Geophys. Res.*, in press, 1999.

Jayaratne, E.R., C.P.R. Saunders and J. Hallett, Laboratory studies of the charging of soft-hail during ice crystal interactions, *J. R. Met. Soc.*, *109*, 609–630, 1983.

Jayaratne, E.R. and C.P.R. Saunders, Reply, *J. Geophys. Res.*, *90*, 10755, 1985.

Lawson, R. Paul, R.E. Stewart and L.J. Angus, Observations and numerical simulations of the origin and development of very large snowflakes, *J. Atmos. Sci.*, *55*, 3209–3229, 1998.

Marshall, T.C. and W.P. Winn, Measurements of charged precipitation in a New Mexico thunderstorm: Lower positive charge centers, *J. Geophys. Res.*, *87*, 7141–7147, 1982.

Mo, Q., A.E. Ebneter, P. Fleischhacker and W. P. Winn, Electric field measurements with an airplane: A solution to problems caused by emitted charge, *J. Geophys. Res.*, *103*, 17163–17173, 1998.

Rison, W., P.R. Krehbiel, R.J. Thomas, M. Davis, T. Hamlin, J. Harlin, T. Barber and M. Jones, A deployable 3-dimensional lightning mapping system, *Trans. Supp., Am. Geophys. Union 1998 Fall Meeting*, *79*, *F127*, November 10, 1998.

Vali, G., J. Cupal, C.P.R. Saunders and W.P. Winn, Airborne measurements of the electrical charges of hydrometeors, paper presented at 9th International Cloud Physics Conference, Tallinn, U.S.S.R., 1984.

Weinheimer, A.J., J.E. Dye, D.W. Breed, M.P. Spowart, J.L. Parrish, T.L. Hoglin and T.C. Marshall, Simultaneous measurements of the charge, size, and shape of hydrometeors in an electrified cloud, *J. Geophys. Res.*, *96*, 20809–10829, 1991.

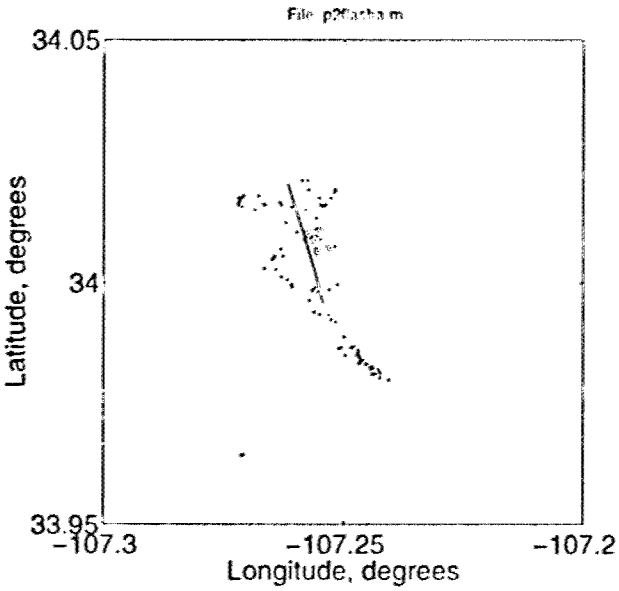


Figure 3a.

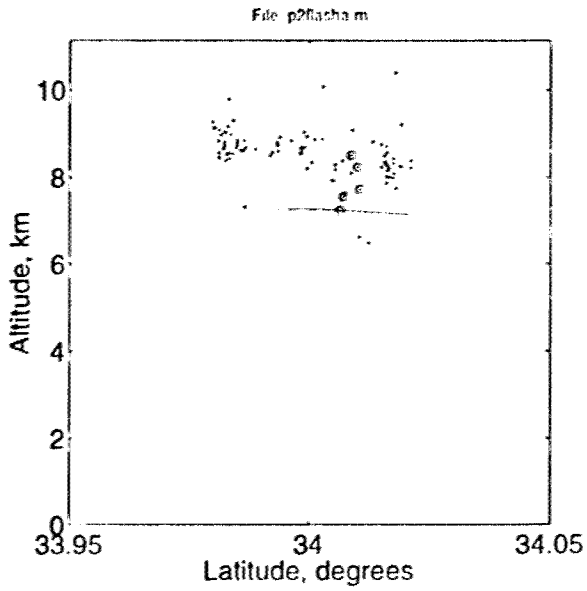


Figure 3b.

Figure 4a.

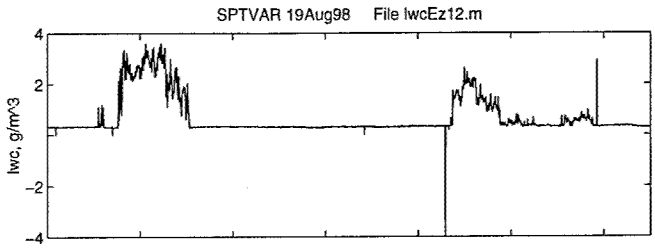


Figure 4b.

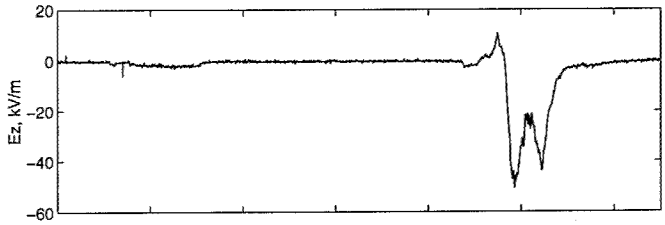


Figure 4c.

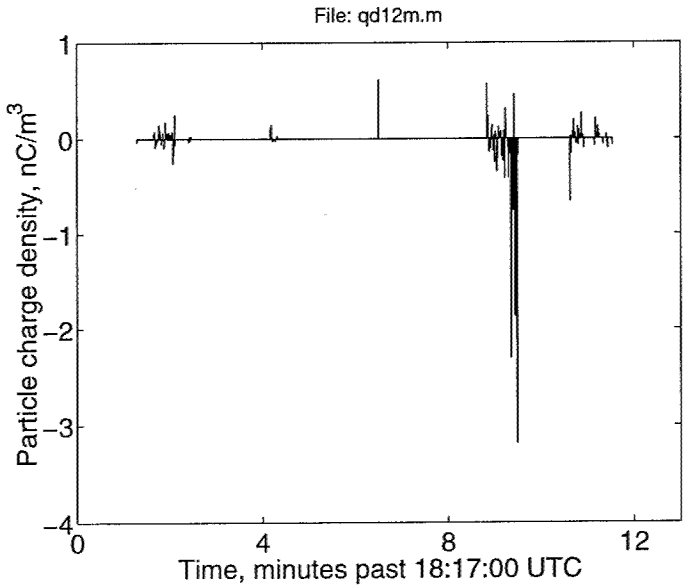


Figure 5.

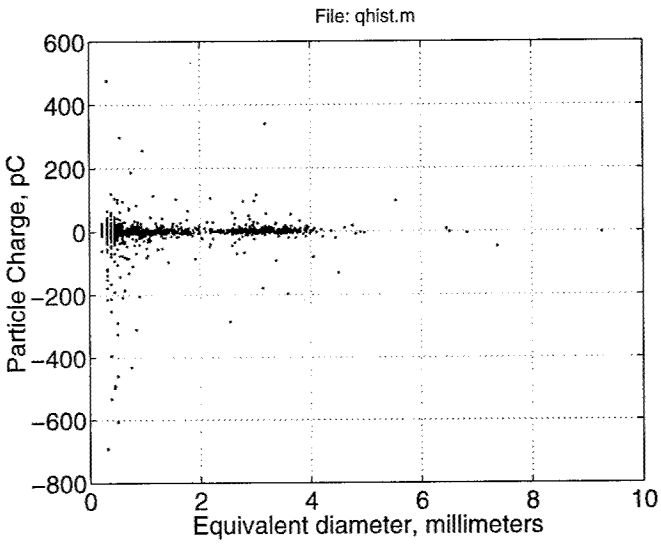

# AN EXPERIMENTAL STUDY OF CHARGE AND MASS TRANSFER DURING ICE CONTACT INTERACTIONS.

B. L. Mason[1], J. G. Dash[2]

[1]North Carolina State University, Raleigh, NC, U.S.A.
[2]University of Washington, Seattle, WA, U.S.A.

ABSTRACT: An experiment to test the prediction of Baker and Dash (1989, 1994) that charge transfer in ice contact interactions is associated with the transfer of microscopic quantities of surface melted liquid has been performed. The results, while presenting a new challenge to the model, have clearly illustrated one important phenomenon. Earlier researchers have indicated that charge transfer may be related to the growth state of the ice particles involved, rather than temperature effects. The present work, by presenting charge and mass contact transfer data with respect to the measured growth rate of the ice surfaces, confirms this observation.

## INTRODUCTION

The theory proposed by BD predicts that charge transfer between colliding ice particles in a thunderstorm is mediated by the transfer of microscopic quantities of surface melted layers. The existence of liquid-like layers on the surface of ice at temperatures below the bulk melting temperature has been observed using a variety of experimental techniques and is reviewed by Dash, et al. (1995). The present experiment was designed to observe ice-ice contact events and has measured both charge transfer, using an electrometer, and mass transfer, using quartz crystal microbalances (QCM). The results conflict with the quantitative predictions of the Baker-Dash theory; however, charge and mass transfers do appear to be correlated, suggesting that the theory must be reexamined.

## EXPERIMENT

The experimental design and assembly have been described in detail by Mason (1998) and preliminary results have been presented by Mason and Dash (1999). Briefly, the apparatus consists of a copper chamber housing two 1 MHz QCMs on which ice samples are prepared. The QCMs monitor the ice mass with a sensitivity of about $5\times10^{-4}\mu g$. If the contacting area is $10^{-4}cm^2$, this corresponds to about 150 monolayers of ice thickness. The orientation of the QCMs is such that the two ice surfaces face each other, and brief contact between the two layers is achieved by pulsing a simple audio speaker, on which one the QCMs is mounted. In a separate but similar experiment charge transfer is monitored during contact events using an electrometer in voltage mode: Transferred charge drains away through a grounded shunt resistance after the corresponding potential shift of one of the ice samples has been recorded. For both mass the charge transfer experiments, a large number of individual events were recorded, analyzed and compared with respect to average temperature, temperature difference between the samples, and impact strength.

## RESULTS

Charge and mass transfer data were collected for three ambient temperatures (-16, -11 & -6°C) as a function of the relative growth rate between the two ice layers. Data for the temperature –6°C are shown in Figure 1. The data are presented with two horizontal axes; growth rate and temperature difference. The latter was calculated from the former, given assumptions about the geometry of the layers. When the data for all three temperatures are compared it is clear that the slope of the charge data (Figure 1[a]) near the origin does not vary

with ambient temperature when the *growth rate scale* is used as the abscissa. This suggests that charge transfer is more closely associated with growth rate of the ice, rather than temperature difference between the layers. The direction of mass transfer corresponds to the direction of positive charge, indicating that the transferred liquid is positively charged.

The magnitude of the mass transfer (Figure 1[b]) is larger than predicted. However, the BD model assumes liquid layer thicknesses corresponding to equilibrium surface melting, which, given the conditions of the impacting surfaces, cannot be realistic.

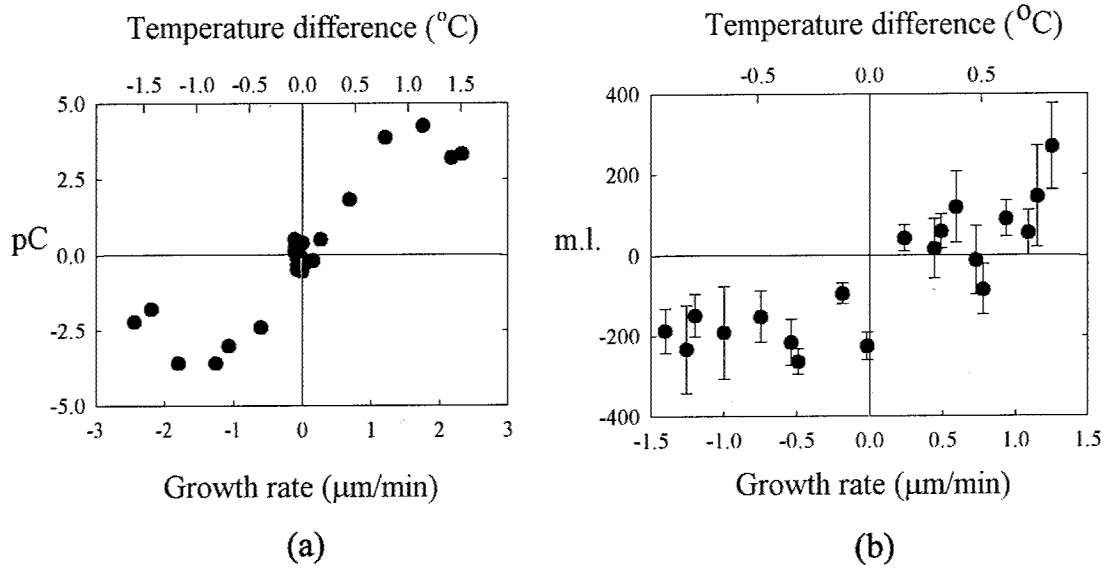


*Figure 1. Charge transfer (a) and mass transfer (b) to the upper QCM ice layer versus temperature difference between the layers (top scale) and versus growth rate of the upper ice layer (bottom scale).*

Figure 2 shows the dependence of charge and mass transfer on impact strength. The two series of data were collected in separate experiments. Care was taken to ensure that the threshold of impact, indicated by the charge data of Figure 2(a) to correspond to a speaker voltage of 8.05V, was the same for both series. Both charge and mass transfer increase with increasing impact strength.

These results confirm earlier observations (Buser and Aufdemaur [1977], Gaskell and Illingworth [1980], Baker, et al. [1987], Jayaratne [1993]) that charge transfer resulting from ice-ice contacts is more closely related to the growth state of the ice, and is difficult to account for in terms of temperature differences between particles or temperature gradients within the ice. The present results clearly illustrate this effect by showing the growth rate dependence of charge transfer. Specifically, when the slope of the data shown in figure 1(a) is estimated versus temperature difference and compared to those for the other two values of ambient temperature, the variation is about 90% of the average value. However, when the slope is estimated using *growth rate* as the abscissa, the variation is only 10% of the average value. This suggests that growth rate is more fundamentally related to the details of charge transfer than temperature difference.

Although there is disagreement with details of the BD theory of charge transfer, it appears that there is mass transfer associated with charge transfer. Currently, the model is being reexamined in the light of these results.

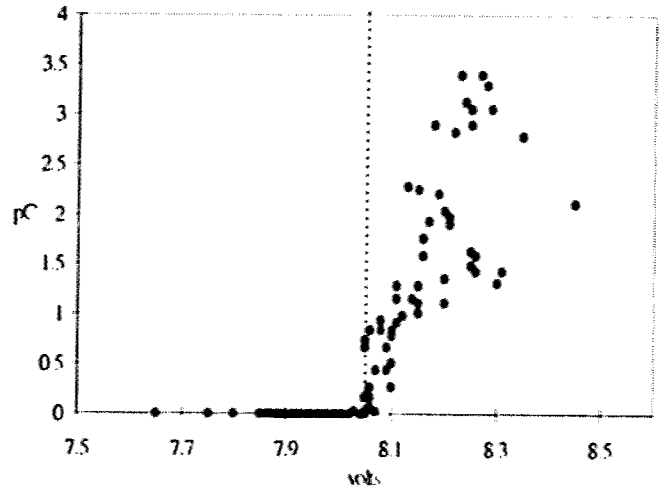


(a)

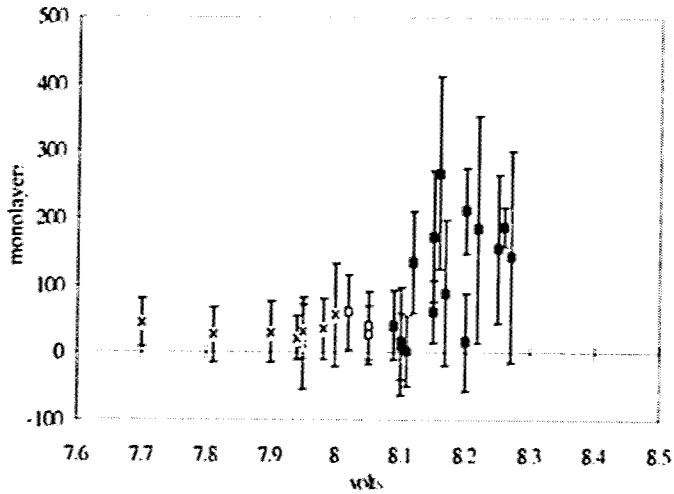


(b)

*Figure 2. Charge transfer (a) and mass transfer (b) versus impact strength, or speaker pulse voltage.*

ACKNOWLEDGEMENTS: This work was generously supported by the Leonard X. Bosack and Bette M. Kruger Foundation, and the Seattle Chapter of the ARCS Foundation.

REFERENCES

Baker, B., M.B. Baker, E.R. Jayaratne, J. Latham, and C.P.R. Saunders, 1987. The influence of diffusional growth rates on the charge transfer accompanying rebounding collisions between ice crystals and soft hailstones. Q.J.R. Meteorol. Soc. **113,**1193-1215.

Baker, M. B., and J. G. Dash, 1989. Charge transfer in thunderstorms and the surface melting of ice. J. Crystal Growth **97,** 770-776.

Baker, M.B., and J.G. Dash, 1994. Mechanism of charge transfer between colliding ice particles in thunderstorms. J. Geophys. Res. **99**,10621-10626.

Buser, O., and A.N. Aufdermaur, 1977. Electrification by collisions of ice particles on ice or metal targets. *Electrical Processes in Atmospheres*, ed. H. Dolezalek and R. Reiter, Steinkopff, Darmstadt, 294-301.

Dash, J. G., Haiying Fu, and J. S. Wettlaufer, 1995. The premelting of ice and its environmental consequences. Rep. Prog. Phys.**58**, 115-167.

Dash, J. G., 1999. Private conversation.

Gaskell, W., and A. J. Illingworth, 1980. Charge transfer accompanying individual collisions between ice particles and its role in thunderstorm electrification. Q.J.R. Meteorol. Soc. **106**, 841-854.

Jayaratne, E. R., 1993. Temperature gradients in ice as a charge generation process in thunderstorms. Atm. Res.**29**, 247-260.

Mason, B.L. 1998. Thesis, University of Washington, unpublished.

Mason, B.L. and J.G.Dash 1999. *Ice Physics and the Natural Environment*, eds. J.S.Wettlaufer, J.G.Dash and N.Untersteiner, NATO ASI Series I, Vol.56, 321-324.

# VAPOR AND HEAT SUPPLY TO RIMING GRAUPEL: EFFECT ON CHARGING

C. P. R. Saunders[1], E. E. Avila[2], S. L. Peck[1], N. E. Castellano[2], and G. G. Aguirre Varela[2]

[1]Physics Department, UMIST, Manchester, M60 1QD, UK
[2]FaMaF Universidad Nacional de Cordoba, Argentina

ABSTRACT. Graupel charging in thunderstorms may involve collisions with ice crystals. Laboratory studies of this process have shown that the charge transfer depends on many variables including the surface states of the interacting particles. This work shows the importance of the supply of heat and vapor to the riming graupel in influencing the sign of the charge transferred. The effects of rimer heating and cloud droplet size are considered.

## INTRODUCTION

Laboratory studies of charge transfer during the collision of ice crystals with a riming target representing graupel pellets falling in thunderstorms, have shown that the charge sign and magnitude is a sensitive function of the droplet accretion rate, the cloud temperature, the terminal velocity of the graupel, the particle sizes and the impurity concentration of the riming droplets (Reynolds, Brook and Gourley, 1957; Takahashi, 1978; Jayaratne et al., 1983; Jayaratne and Saunders, 1985; Saunders et al., 1991; Avila and Caranti, 1994; Avila et al., 1998). Essentially, ice crystals rebounding from a graupel pellet riming with pure droplets, charge the pellet positively in high accretion rates and high temperatures, while at low temperatures and low accretion rates the rimer charges negatively. This observation of sign reversal was used by Jayaratne et al., (1983) to account for the charge structure in thunderstorms having a negative charge center around the -15°C level with positive crystals aloft; in the higher temperature region below the negative charge center, reversed charge transfer accounts for the observations of a lower positive charge center. These laboratory results, obtained at rimer/crystal velocities in the range 4 to 11 m $s^{-1}$ are summarised in Figure 1 (Saunders and Peck, 1998) who determined the rime accretion rate, RAR, required to reverse the graupel charge transfer sign as a function of cloud temperature. Brooks et al., (1987) had pointed out the usefulness of plotting these figures in terms of RAR which permits comparisons between data collected over a range of velocities. The observations of Saunders and Peck of negative charging of graupel at temperatures as high as -2°C extended considerably the temperature range over which negative charge had been reported. Also of note is the result that both signs of charge transfer are observed while the latent heat from accretion is insufficient to cause sublimation.

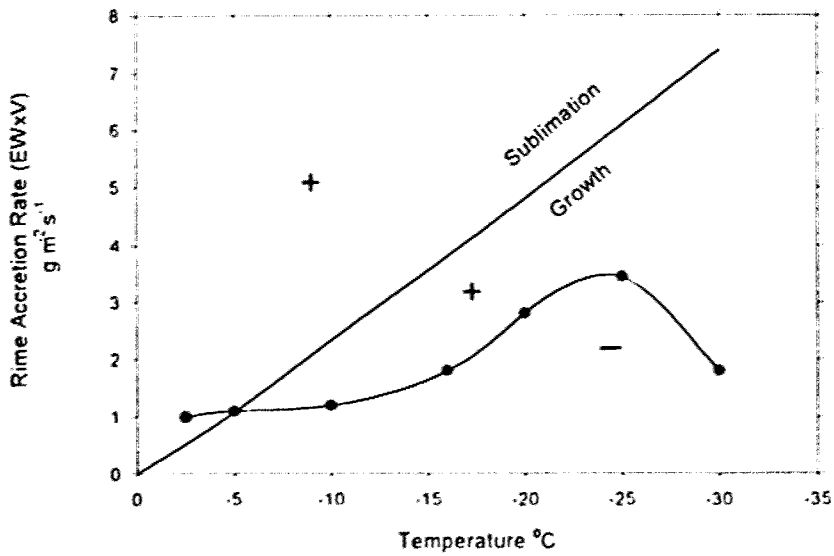


Figure 1 Charge sign reversal points and the rimer growth/sublimation line associated with natural rime heating.

A theory that is consistent with elements of the observations was first proposed by Baker et al. (1987) and involved the material transfer of charged layers between the colliding surfaces, such that the surface with the thicker layer charges negatively. A theory of relative diffusional growth rates, with the interacting surface growing fastest by vapor

diffusion charging positively, is consistent with the region of negative graupel charge in Figure 1 in which the rime is heated sufficiently to reduce its vapor diffusion rate below that of the ice crystals. However at higher accretion rates it would be expected that rime heating would continue to be sufficient to reduce the vapor diffusional growth rate of the rimer below that of the ice crystals, but this is not consistent with the positive charges observed; in fact negative charge would be expected to extend to wet growth. The positive charge regime shown in Figure 1 extends with increase in accretion all the way up to wet growth where charging falls to zero when the ice crystals stop rebounding (Saunders and Brooks, 1992).

## OBSERVATIONS AND DISCUSSION

### 1) Rime heating

In order to check on this question of the effect of high accretion rates on rimer temperature influencing the diffusional growth rate and hence the charge sign, experiments were conducted in UMIST in which the riming target was heated internally in order to separate the influence on riming of heat transfer to the target from that of vapor arrival from the local environment and from droplets freezing on the surface. Figure 2 shows how experiments in which a riming target charges positively in the absence of the provision of extra heat, can have its charge sign reversed when heat is provided through the rime substrate by a heater. Given sufficient heat the charge sign reverses to negative and at higher accretion rates, provided by increasing the cloud liquid water content (measured here in terms of EW, the effective liquid water that can be captured by the rimer), more heat input is required for reversal. The point here, with respect to the natural situation, is that during crystal collisions, the rimer charges negatively when heated sufficiently to reduce its diffusional growth rate below that of the ice crystals, but that the presence of rime on the surface at higher accretion rates, can easily overcome this heating effect. Even a rime surface heated sufficiently to sublimate is able to charge positively because of the provision of water molecules on its surface from the accreted droplets freezing at 0°C which continue to provide vapor to the local rimer surface.

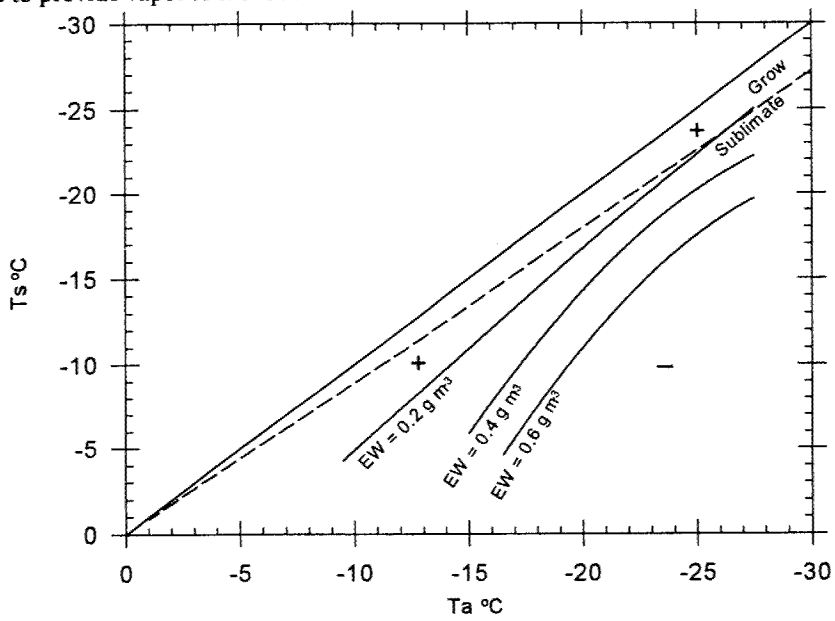


Figure 2 Values of EW for charge sign reversal with a heated rimer. Rime and air temperatures, Ts and Ta.

### 2) Studies with small water droplets

The experiments leading to the results shown in Figure 1 were obtained with a droplet spectrum having a mean droplet volume diameter of 19 μm and extending to 33 μm. In order to determine the effect of a cloud of smaller droplets, such as that used by Takahashi (1978), (see Williams and Zhang, 1996 and Brooks and Saunders, 1995), experiments were performed with a droplet cloud extending to 15 μm, peaking at 7 μm diameter. This droplet spectrum was achieved by replacing the boiler droplet source with atomisers. Because the effect of reducing the

droplet size is to reduce the collision efficiency of the rimer for droplets, which would itself reduce accretion and favor negative charging according to Figure 1, the experiments were conducted so that the Rime Accretion Rate, RAR, for charge sign reversal was determined, where RAR = EW x Velocity. The experiments were conducted in the velocity range 6.2 to 7.6 m $s^{-1}$ and gave rise to the results shown in Figure 3 (Peck, 1997).

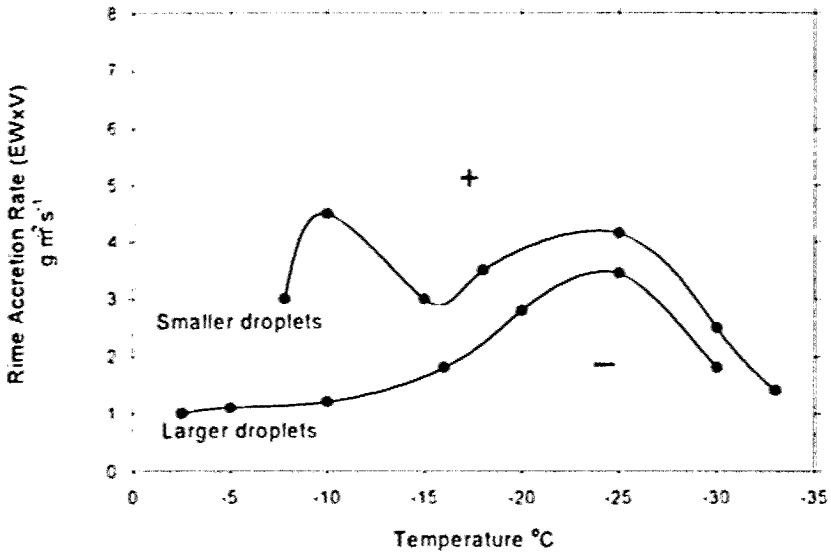


Figure 3 A comparison between charge reversal points with two droplet spectra.

There is a significant shift in the reversal line indicating an increase in the RAR/T region associated with negative graupel charging. Because RAR is plotted here, there are no differences in natural riming heat supply in the cases represented by Figures 1 and 2 to help account for the different results. A possible explanation for such an effect, in terms of the relative growth rate hypothesis discussed above, is that the ice crystal growth rate is enhanced in the presence of a higher concentration of smaller droplets helped by the higher LWC required to provide the same accretion rate. Marshall and Langleben (1954) showed how crystal growth rate is increased when the diffusion field can no longer be assumed to be infinite; increase in LWC and the concentration of smaller droplets permits the mean droplet/graupel distance to be reduced and so enhances the crystal growth rate. For this mechanism to apply, the increase in surface roughness associated with the riming of smaller droplets must be insufficient to overcome the enhanced ventilation/cooling effect which would be expected to favor positive charge transfer to the graupel.

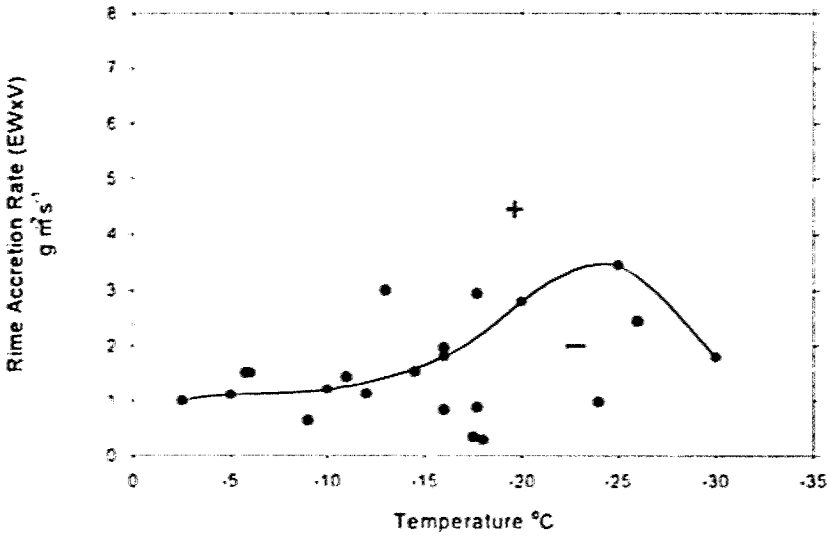


Figure 4 Rimer negative charging with a spectrum of large droplets.

3) Studies with larger water droplets

The effect on charge transfer of larger droplets was investigated, as described by Avila et al., (1998). A spray of droplets with diameters extending beyond 60 μm was used as the cloud source and the accretion rate was noted together with the charge sign. Figure 4 shows how the charge sign reversal line is moved to higher accretion rates in the presence of larger droplets. Here the process is possibly associated with the smoother rime surface and associated decrease in ventilation, which permits the rimer to retain its heat leading to stronger negative charging.

## CONCLUSION

The experiments described here emphasise the importance of vapor and heat supply to the surfaces of interacting ice particles involved in charge transfer processes. Negative rime charging is associated with heating reducing the rimer diffusional growth rate below that of the ice crystals; on the other hand, sufficient riming provides a very powerful positive charging influence which is able to overcome the net sublimation of a heated rimer surface by the provision of vapor from recently accreted, freezing droplets. The presence of small droplets (7 μm diameter) favors negative rimers by providing enhanced vapor supply to the ice crystals, while larger droplets (up to 60 μm) also favor negative charging by permitting the retention of heat in a smoother rimer surface. These effects are consistent with the concept that the interacting surface with the thicker surface layer charges positively during crystal/graupel interactions. The conclusion is clear, further laboratory studies are required in order to clarify these apparently conflicting requirements on droplet size. Most importantly, field experiments are needed in the active charging regions of thunderstorms so that the laboratory studies may be made as representative as possible.

## REFERENCES


Avila, Eldo E., and Giorgio M. Caranti, A laboratory study of static charging by fracture in ice growing by riming, *J. Geophys. Res.*, 99, 10,611--10,620, 1994.

Avila, Eldo E., Giorgio Caranti, and Nesvit Castellano, Laboratory studies of the influence of cloud droplet size on charge transfer during crystal-graupel collisions, *J. Geophys. Res.*, 103, 8985--8996, 1998.

Baker, B., M. B. Baker, E. R. Jayaratne, J. Latham, and C. P. R. Saunders, The influence of diffusional growth rates on the charge transfer accompanying rebounding collisions between ice crystals and soft hailstones, *Q. J. R. Meteorol. Soc.*, 113, 1193--1215, 1987.

Baker, M. B., and J. G. Dash, Mechanism of charge transfer between colliding ice particles in thunderstorms, *J. Geophys. Res.*, 99, 10,621--10,626, 1994.

Brooks, I. M., and C. P. R. Saunders, Thunderstorm charging:laboratory experiments clarified, *Atmos. Res.*, 39, 263--273, 1995.

Brooks, I. M., C. P. R. Saunders, R. P. Mitzeva and S. L. Peck, The Effect on Thunderstorm Charging of the Rate of Rime Accretion by Graupel, *J. Atmos. Res.*, 43, 277--295, 1997.

Jayaratne, E.R., C. P. R. Saunders and J. Hallett, Laboratory studies of the charging of soft-hail during ice crystal interactions, *Q. J. R. Meteorol. Soc.*, 109, 609--630, 1983.

Jayaratne, E. R., and C. P. R. Saunders, Thunderstorm Electrification: The Effect of Cloud Droplets, *J. Geophys. Res.*, 90, 13,063--13,066, 1985.

Marshall, J. S., and M. P. Langleben, A Theory of Snow-Crystal Habit and Growth, *J. Met.*, 11, 104--120, 1954.

Reynolds, S. E., M. Brook and M. F. Gourley, Thunderstorm Charge Separation, *J. Met.*, 14, 426--436, 1957.

Saunders, C. P. R., and I.M. Brooks, The Effects of High Liquid Water Content on Thunderstorm Charging, *J. Geophys. Res.*, 97, 14,671--14,676, 1992.

Saunders, C. P. R., and S. L. Peck, Laboratory studies of the influence of the rime accretion rate on charge transfer during crystal/graupel collisions, *J. Geophys. Res.*, 103, 13949--13956, 1998.

Takahashi, T., Riming electrification as a charge generation mechanism in thunderstorms, J. Atmos. Sci., 35, 1536--1548, 1978.

Williams, Earle R., and Renyi Zhang, Density of rime in laboratory simulations of thunderstorm microphysics and electrification, *J. Geophys. Res.*, 101, 29715--29719, 1996.

# TURBULENT ELECTRIC DYNAMO IN THUNDERSTORM CLOUDS

E.A Mareev

Institute of Applied Physics, Rus. Acad. Sci., 603600 Nizhny Novgorod, Russia

ABSTRACT: Electric dynamo due to random motion of a medium is of particular interest with respect to numerous applications especially to thunderstorm clouds. In the present paper we focus on the theory of turbulent electric dynamo in a multi-component multi-flow system and its applications to the thunderstorm electrification problem. The mean field formation in weakly ionized aerosol medium has been investigated, taking into account charging of aerosols due to their collisions when turbulent mixing. The effect of the mean field growth has been found, caused by induction charging of aerosol particles. This phenomenon takes place for the turbulence intensive enough when the air conductivity is sufficiently small.

## INTRODUCTION

The problem of large-scale quasi-stationary electric field and space charge generation in the moving weakly ionized medium (electric dynamo) is of fundamental significance for atmospheric electricity (see e.g. [*Mareev and Trakhtengerts*, [1996]), as well as for dusty plasmas. Electric dynamo due to random motion of a medium is of particular interest with respect to numerous applications especially to thunderstorm clouds. General criteria for large-scale electric field formation in a continuous conducting medium have been formulated by *Mareev*, [1996]. In the present paper we focus on the theory of turbulent electric dynamo in a multi-component multi-flow system and its applications to the thunderstorm electrification problem.

Our theory is based on the calculation of turbulent convective current (assuming small-scale random fluctuations) and its further account in the large scale evolution equations. The first, we formulate the diffusion equation for the mean electric field in the medium. Then we go to the key problem of turbulent current calculation in two flow aerosol system with charge transfer via aerosol collisions. Particles accumulate charge still charging current is greater than leakage one. Velocity difference arises due to air velocity fluctuations. Inductive and non-inductive charging mechanisms are taken into account, but it is turned out that just for inductive mechanism quasi-stationary aerodynamic turbulence might support large scale charge separation.

Note that the problem of appearance of large - scale structures in gyrotropic hydrodynamic turbulence in the framework of the two scale approach (developed firstly within the theory of turbulent magnetic dynamo, see e.g. [*Krause and Radler*, 1980]) was considered for the first time by *Moiseev et al.*, [1983]. Basing on the formalism developed in this work, *Kikuchi* [1991] demonstrated the possibility to form large scale vortices of the velocity field by using energy of helical turbulence in a weakly conducting medium. This paper studies another problem: formation of large-scale structures of the electric field and space charge in the background of present turbulent motion of the medium.

## BASIC EQUATIONS

In the simplest case of one-fluid description of a weakly conducting medium *Mareev* [1996] developed an approach based on the continuity equation for the mean field of space charge density and account of the turbulent convective current $\mathbf{J} = \langle \rho' \mathbf{v}' \rangle$ in this averaged equation. When solving many other problems it is rather more convenient to use instead of the equation for charge continuity, the equation for the mean electric field. For example, it may be used when in the volume occupied by the turbulence the large scale field is generated due to accumulation of charges at the boundaries of this volume (a "plane capacitor"). A simplest example of such a problem is the unidimensional model of a distributed (owing to the diffusion) plane capacitor, the field of which obeys the following equation:

$$\frac{\partial E_0}{\partial t} = \sum_i j_i = 4\pi(J - j_{cd} - j_{dif}) \qquad (1)$$

The equation for the mean field includes the turbulent convective current $J$, competing with the currents of conductivity, $j_{cd}$, and diffusion, $j_{dif}$. Usually (in the framework of the so-called closure models [*Willett*, 1979]) the turbulent convective current is reduced to the turbulent diffusion current

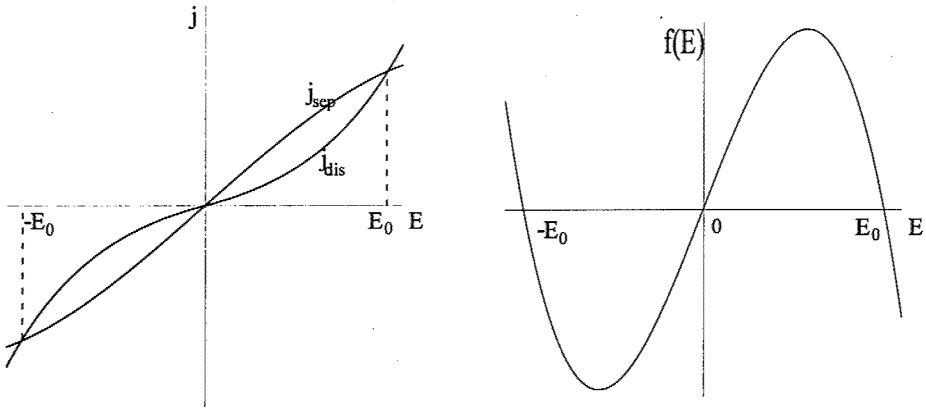


Figure 1: Equilibrium states of the distributed thunderstorm generator

so that $j_{dif} = -D_T \rho'_{0z} = -D_T E''_{0zz}/4\pi$, where $D_T$ is the coefficient of turbulent diffusion of the charge. Influence of the turbulence then is reduced completely to blurring of the mean charge density and electric field. On the other hand, when we are interested in the effect of generation of a large-scale field and charge, we have to calculate the vector $< \rho' \mathbf{v}' >$ from the first principles.

Knowing the dependence of the currents $J$ and $j_{cd}$ on the mean electric field, one can find the equlibrium states of the Eq.(1) (see Fig.1) and draw the phase plane for this equation. Qualitative dynamic theory, based on the diffusion equation, could serve as a powerful mean of electric field evolution analysis in thunderstorm clouds; it will be developed in detail elsewhere.

TURBULENT DYNAMO IN AEROSOL MEDIA

The most vivid manifestations of electric dynamo are to be expected in a weakly conducting medium that contains aerosols, which can exchange their charges during collisions. As is known, these are the conditions, under which the strongest fields are formed in the atmosphere. From the viewpoint of this study the main question here is whether the turbulence plays only a "destructive" role and compensates partially the charging current, or, under certain conditions, the turbulent convective current can provide maintenance of the large-scale structure of the electric field. As will be seen from an example of the simplified model of a "plane capacitor" filled with turbulence, at least in one important case the answer to the question set proves to be positive.

Let us use Eq. (1) for the mean field, in which we must choose adequate parameterization of the expression for the charging current. The literature studies many mechanisms for charge separation, which have specific microphysics (see e.g. [*Beard and Ochs*, 1986]). They depend on a great number of factors, specifically, on distribution of temperature, phase composition and spectrum of dimensions of aerosol particles. We will not be interested here in details of microphysics: of basic importance for this problem is the dependence of the value of a charge $\delta q$ transferred in one collision, on the electric field. According to this parameter all mechanisms are traditionally classified as induction and non-induction mechanisms. For the first class of mechanisms the value of $\delta q = \delta q_i$ depends on the value and direction of the external electric field, $\mathbf{E}$, and is connected with polarization of interacting particles. In the case of spherical particles with their dimensions $R \gg r$ (where $R$ and $r$ are radii of large and small particles, respectively) in the unidimensional problem for $\delta q_i$ one can use generally the following expression: $\delta q_i = \xi \cdot r^2 E \mathrm{sign} U$, where $\xi$ is a constant and function $\mathrm{sign} U$ determines the sign of the transmitted charge when the direction of the velocity difference vector for aerosol particles $\mathbf{U} = \mathbf{u} - \mathbf{v}$ relative to the direction of the external electric field.

In storm clouds a great role is played also by non-induction charging, which does not depend explicitly on intensity of the electric field. For example, charge $\delta q = \delta q_s$ transmitted to an ice crystal during one collision with a more massive hailstone can be represented as $\delta q_s = |\mathbf{U}/U_0|^p \cdot A_s(r, R, T)$, where $p \approx 2 \div 3$, $U_0 \simeq 3m/s$, $A_s(r, R, T)$ is empiric function that reflects dependence of $\delta q_s$ on characteristic dimensions of aerosols and air temperature. This separation of charging mechanisms by their induction or induction-free character, though based on the different physical nature of

these processes, at strong external electric fields becomes somewhat factitious, since the relative velocity of the particles carrying the charges begins to depend on the electric field itself. In this paper we will limit ourselves to the account for induction charging of aerosol particles.

When charged particles collide, the value of the transferred charge is limited by the resulting electric field at the point of the contact of particles. This field, in its turn, depends on their charge, and the expression for the value of the total charge transferred by the collision can be written down as

$$\delta q = \delta q_i + \eta(-q + r^2 Q/R^2), \tag{2}$$

where $q$ and $Q$ are charges of small and large particles, and coefficient $\eta \simeq (0.5 \div 5)\xi$.

Let us assume that in the volume of the "plane capacitor" filled with turbulent gas there are aerosol particles of two types. Then, by each collision of the particles charge $\delta q_i$ is divided in accord with the above formulas. Within the hydrodynamic approximation evolution of the charge on heavy or light aerosol particles is described in the general case by rather complicated equations of the following form:

$$\partial_t Q + u\partial_z Q = -\delta q_i \nu_Q - (\nu_{iQ} + \eta\frac{r^2}{R^2}\nu_Q)Q + \eta\nu_Q q; \tag{3}$$

$$\partial_t q + v\partial_z q = \delta q_i \nu_q - (\nu_{iq} + \eta\nu_q)q + \eta\frac{r^2}{R^2}\nu_q Q, \tag{4}$$

where $q$ and $Q$ are charges of aerosol particles, $n$ and $N$ are their densities, $\nu_q = SUN$ and $\nu_Q = SUn$ are the mean rates of collisions, $\pi(R+r)^2$ is cross-section of the collision; $\nu_{iQ}$ and $\nu_{iq}$ are the coefficients of ion adhesion to aerosol particles, which for the sake of simplicity can be assumed equal: $\nu_{iQ} = \nu_{iq} = \nu_i$. Diffusion of aerosols is not taken into account.

The problem becomes simpler in the case of intensive charging, when the characteristic scale, on which velocity of turbulent gas changes in space and time, is large as compared to the scales, on which stationary values of the charge, $Q = -\delta q_i \nu_Q/\nu_r$ and $q = \delta q_i \nu_q/\nu_r$, where $\nu_r = \nu_i + 4SU\eta(N + \frac{r^2}{R^2}n)$, get stabilized. Then one can assume that charges of particles $Q$ and $q$ change "instantaneously" with the difference of velocities $\mathbf{U}$ induced by turbulent vortices changing at each point. In the simplest case the difference of velocities can be found using the following formulae:

$$\mathbf{U} = i\mathbf{v}_T \frac{\Omega_2/\nu_2 - \Omega_1/\nu_1}{(1 - i\Omega_2/\nu_2)(1 - i\Omega_1/\nu_1)}, \tag{5}$$

where $\Omega_1 = \omega - k_z V_{d1}$, $\Omega_2 = \omega - k_z V_{d2}$. Certainly, turbulence plays here the very important role: it mixes aerosol particles permanently thus providing the difference in velocities of the two sorts of aerosols that have different mass and, consequently, different inertia.

Writing the expression for the charging current down, one should bear in mind that in a real aerosol system the induction mechanism starts functioning beginning with some finite value of the electric field. Under the atmospheric conditions, e.g., the usual vertical fair-weather field can serve as such a field. It is direction of this field that determines the geometry of the formed "plane capacitor", in which the dynamics of the mean field obeys Eq. (1). Choosing the z-axis along the axis of symmetry of this capacitor we will be searching for the projection of the charging current to this axis. Taking into account the expression for $\nu_Q$ we obtain:

$$J_z = QNU_z = \xi\frac{r^2 Sn}{\nu_r}E_0 U_z \cdot NU_z. \tag{6}$$

Thus, we can see that at induction charging, whichever is the sign of relative motion velocity of heavy and light aerosol particles, their contribution to the current of large-scale separation of charges proves to be positive. This non-trivial circumstance agrees with the fact that the external field introduced to the system of two inter-penetrating aerosol flows gains in strength due to induction charging of particles at any orientation of this field. This can lead, in particular, to stratification of this system with formation of areas with different signs of the field [*Marcev et al.*, 1999].

In the simplest case one can assume that saturation of the charge of aerosol particles is determined by attachment of small ions to them, therefore $\nu_r = \nu_i$. Within the assumption that the

turbulence is homogeneous and stationary averaging of the z-component of the current is elementary and yield the following expression:

$$J_{sz} = A_0 E_0 \int\int A_v \frac{G_V \omega^2}{(1+\omega^2/\nu_1^2)(1+\omega^2/\nu_2^2)} d\omega d\mathbf{k}, \tag{7}$$

where $A_0 = \xi r^2 SNn/\nu_i$, $A_v = (R-r)^2(R+r)^2(2\rho/9\eta)^2$, and $G_V$ is the amplitude of the correlator of the vertical component of turbulent velocity. Using the traditional representation for the correlator of velocities in the Kolmogorov turbulence, we will write $J_z$ down as a double integral:

$$J_z = AE_0 \int_{-\infty}^{\infty} d\omega \int_0^{\infty} dk \frac{\omega^2 \exp(-3\omega^2/2k^2\sigma_v^2)}{(1+\omega^2/\nu_1^2)(1+\omega^2/\nu_2^2)} \cdot \frac{4\pi k^2 \exp(-k^2/k_m^2)}{k\sigma_v(k^2+k_0^2)^{11/6}}, \tag{8}$$

where $A = 0.061 C^2 \varepsilon^{2/3} (3/2\pi)^{1/2} A_0 A_v$. The integral obtained can be estimated easily. The integral over $\omega$ depends on the ratio of parameters $\nu_1$, $\nu_2$ and $k_0\sigma_v$. For the most characteristic case of $\nu_1 \gg k_0\sigma_v \gg \nu_2$, the integration over $\omega$ yields in the first approximation on $\nu_2/k_0\sigma_v$:

$$J_z = \frac{1}{2} AE_0 \nu_2^2 \sqrt{\frac{2\pi}{3}} \int_0^{\infty} dk \frac{4\pi k^2 \exp(-k^2/k_m^2)}{(k^2+k_0^2)^{11/6}} \tag{9}$$

After integration over $k$ we obtain the final expression:

$$J_z = \alpha E_0 = AE_0 \pi \sqrt{\frac{2\pi}{3}} \pi B\left(\frac{3}{2}, \frac{1}{3}\right) k_0^{-2/3} = aE_0 \xi \varepsilon^{2/3} r^2 R^2 nN \nu_i^{-1} k_0^{-2/3}, \tag{10}$$

where $B(\frac{3}{2}, \frac{1}{3})$ is beta-function, and $a \simeq 0.5$ is a number of the order of unity. Realization of the dynamo requires $\alpha > 4\pi\sigma$, i.e. in the simplest case $\alpha > \nu_i$. In order to estimate $\alpha$, let us take values of parameters characteristic for an intense storm cloud: $\xi = 10^{-1}$, $\nu_i = 10^{-1}\mathrm{s}^{-1}$, $r = 10^{-2}$cm, $R = 10^{-1}$cm, $n = 10^2\mathrm{cm}^{-3}$, $N = 5 \cdot 10^{-3}\mathrm{cm}^{-3}$, $L_0 = 10^2$m, $\varepsilon = 10^{22}/\mathrm{s}^3$. Therefrom we find $\alpha \simeq 2 \cdot 10^2\mathrm{s}^{-1}$, i.e. the field can be maintained by the turbulence. As seen from Eq. (10), growth of particle dimensions and increase in their density, along with the increase in the external scale of the turbulence and decrease of conductivity favor the growth of the mean electric field.

## CONCLUSION

The study of the problem of electric dynamo in a turbulent weakly conducting medium results in the conclusion that under certain conditions turbulence can maintain a large-scale electric field. Estimations have been performed for a thunderstorm cloud conditions when Kolmogorov spectrum for turbulence is valid. These results could be drawn for the explanation of abnormally high electric field strength in thunderstorm cells with high level of turbulence. In our opinion, the problem of turbulent electric dynamo deserves further detailed study.

## REFERENCES


Beard, K.V., and H.T. Ochs, Charging mechanisms in clouds and thunderstorms, in: *The Earth's Electrical Environment* ed. by E.P.Krider and R.G.Roble, Washington, D.C.: National Academy Press, 1986. P.114-129.

Kikuchi, H., Electromagnetohydrodynamic vortices and corn circles, in: *Environmental and Space Electromagnetics*, ed. by H.Kikuchi, Tokyo: Springer-Verlag, 1991. P. 585-595.

Krause, F., and K.-H. Radler, *Mean-Feald Magnetohydrodynamics and Dynamo Theory*, Academie-Verlag, Berlin, 314 pp., 1980.

Mareev, E.A., and V.Yu. Trakhtengerts, On the problem of electric dynamo, Radiophysics and Quantum Electronics, 39, 797-814, 1996.

Mareev, E.A., On the theory of turbulent electric dynamo, *Proc. X Int. Conf. on Atmospheric Electricity*, Osaka, 1996, p. 504-507.

Mareev, E.A., A.E. Sorokin and V.Yu. Trakhtengerts, Effects of collective charging in a multiflow aerosol system, *Plasma Phys. Rep.*, 25, 261-272, 1999.

Moiseev, S.S., R.Z. Sagdeev et al., Theory of large-scale structures appearance in the hydrodynamic turbulence, Sov. Phys. *JETP*, 85, 1979-1987, 1983.

Willett, J.C., Fair weather electric charge transfer by convection in an unstable planetary boundary layer, *J.Geophys.Res.*, 84, 703-718, 1979.

# INFERRING SELECTED CLOUD PROPERTIES FROM SATELLITE LIGHTNING DATA

Vicki Schroeder and M.B.Baker

Geophysics Program, University of Washington, Seattle, U.S.A.

ABSTRACT: The recent advent of satellite lightning detection programs has introduced a new potential for obtaining global information about other (hard to measure) cloud properties. We have made use of observations together with numerical model studies to show that positive correlations exist between (i) lightning flashrate (F) and vertical velocity (w), and (ii) flashrate (F) and the amount of condensate (water and ice) lofted through the -10C isotherm ($C_u$). The lightning flashrate appears to be very sensitive to the magnitude of the updraft velocity, with F increasing rapidly with w above a threshold of w ~ 5 - 10 m/s. By contrast, we have found that the flashrate/condensate relationship appears to be approximately linear. We are currently refining the F-updraft and F-condensate relationships with further model studies before applying them to lightning data from the Optical Transient Detector (OTD) and the Lightning Imaging Sensor (LIS). We hope, with this method, to provide estimates of the large scale vertical water transport by continental convective systems over seasonal timescales.

## INTRODUCTION

Water in the upper troposphere is supplied largely by vertical advection in convective systems. The convective water flux is a source for stratiform anvils with horizontal advection of condensate from convective cells accounting for 60-75% of the stratiform condensate [*Gamache & Houze*,1983]. The climatology of convective water flux is poorly known and is difficult to monitor directly. A combination of physical reasoning, numerical modeling and in situ observations suggest that correlations between updraft velocity, the amount of condensate (ice and liquid water) lofted by convective thunderstorms and the lightning flashrate exist, particularly in continental locations [*Baker et al* 1995, *Solomon & Baker* 1998].

The physical basis for the relationship between updraft velocity, condensate and lightning flashrate results from the charging process which takes place within the thundercloud. Rimed ice particles rise and grow within convective updrafts. As they grow larger, the fall speeds of many of these particles exceeds the updraft velocity and they begin to settle. A number of these rimed ice particles collide with smaller ice particles rising in the updraft and laboratory studies show that charge is transferred during such collisions. The region in which the charge transfer takes place is typically delineated by the -10°C and -20°C isotherms - and is referred to as the charging zone. If the E-field exceeds a threshold value, in the range E ~ 100 - 300 kV/m, lightning is initiated. There is still much uncertainty about the exact mechanism(s) for lightning initiation. However, several laboratory and modelling studies have indicated that a microphysical initiation mechanism is quantitatively possible [*Schroeder et al.* 1999].

## MODEL AND DATASETS

We make use of a 1.5 dimensional numerical thundercloud model which includes cloud dynamics, a simple representation of turbulent mixing and entrainment, explicit microphysics, electrification and a lightning parameterization [*Solomon & Baker* 1998].

We utilize data collected at the New Mexico and Convective and Precipitation Electrification (CaPE) field projects. Both the New Mexico and CaPE data include soundings, radar reflectivity data, mass flux estimates from radar data, E-field data from field mills and lightning flash records. In addition the CaPE data includes dual Doppler radar measurements from which vertical velocities were derived. The sounding data along with observations of cell size and duration are used to initialize our numerical model while the radar, mass flux, E-field and lightning data are used to verify the model output.

Global lightning data are being acquired by both the Optical Transient Detector (OTD) aboard the Microlab-1 satellite as well as the Lightning Imaging Sensor (LIS) on the Tropical Rainfall Measuring Mission (TRMM) observatory. The OTD was launched in 1995 and was the first optical detector with the ability to detect lightning during daylight hours. The newer LIS instrument, in a tropical orbit, has reduced coverage (30N to 30S) but offers improved detection efficiency (~90%). Both detectors record the duration for which a particular location is viewed and it is thus possible to determine the flashrate at that location.

## RESULTS

### A) Flashrate and convective cell updraft velocity:

*Zipser* [1994] suggested that there is a threshold value for updraft velocities in convective storms, below which cloud electrification is too weak to produce lightning. He estimated that the threshold value for peak updraft velocity was ~ 10 m/s, based on the fall speeds of water and ice particles and the need for these particles to reach the charging zone. Detailed lightning flashrate and vertical velocity data were not available in the GATE dataset.

The idea of a threshold is further supported by a dimensional analysis study by *Baker et al* [1995] which found that there was a high order dependence of flashrate (F) on updraft velocity (w) - $F \propto w^6$ - which gives an onset of lightning at roughly w ~ 7-9 m/s.

*Price & Rind* [1992] compiled data from a wide variety of sources to establish a relationship between cloud height and the peak updraft velocities ($w_{peak}$) measured in continental storms. This relationship, together with previous data relating cloud height and total lightning flashrate, gave Price & Rind the following high order relationship between total flashrate and peak updraft velocity: $F \propto w_{peak}^{4.5}$ . This relationship again suggests that a threshold value of $5 < w_{peak} < 10$ m/s exists, above which the lightning flashrate increases rapidly.

Following the studies cited above, we used the more direct observations of updraft velocity (from dual Doppler analysis) and lightning flashrates (from magnetic direction finders) made during the CaPE field campaign in Florida 1991 (○ and ❑ in Fig 1). The observational data is augmented with results from our numerical thunderstorm model (Fig 1, ▲), based on a case study of a storm during the TOGA COARE project [*Solomon et al* 1996]. The cloud-to-ground (CG) flashrate [#/min] is an average over a 5 minute period with the corresponding updraft velocity measured at the start of that period.

The CG flashrates shows a high order dependence on updraft velocity (similar to the Price & Rind relationship) and seem to concur with Zipser's hypothesis of a threshold value in updraft velocity below which no, or very little, lightning is produced. The lack of high flashrate data and the observations (○) that have high updraft velocities but for which the CG flashrates are low are probably a result of the fact that we observed only CG flashes. These cells may have had many intra-cloud (IC) flashes and thus looking at the total flashrate would give a more accurate picture.

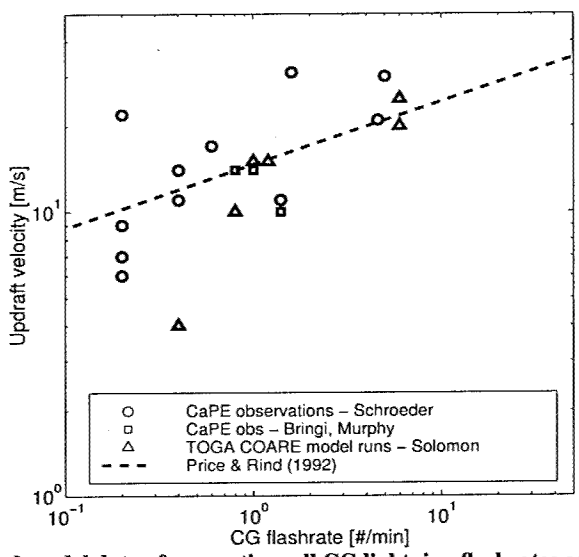


**FIGURE 1. Observational and model data of convective cell CG lightning flashrates as a function of updraft velocity at the charging zone boundary (-10 °C). The dashed line, from Price & Rind (1992), shows the variation in total (IC+CG) flashrate with updraft velocity.**

Much of the available lightning data, however, is only for CG lightning whereas the satellites sample both IC and CG lightning. To study the relationship between total lightning (CG + IC) and updraft velocity we analyzed model data from our New Mexico case studies. We began by considered the time difference between large updraft velocities in the cloud and the occurrence of lightning. When we considered the peak updraft velocity and the lightning flashrate during the same 5 min time bin there did not appear to be a very strong correlation between these two

quantities. We found, for this particular dataset, that a 10 minute lag between large updrafts in clouds and the high lightning flashrates gave the best correlation. This lag likely corresponds to the amount of time it takes for the charged ice particles to be separated within the cloud.

In Fig 2 the peak updraft velocities during the duration of a number of modelled storms (New Mexico and CaPE datasets) are shown as a function of the peak lightning flashrates. The flashrates [#/min] were calculated by averaging over 5 minute time bins. Again, as in Fig 1 for CG lightning, the data suggest a high order dependence of F on updraft velocity. A best fit of this data gave $F \propto w^{3.3}$. This gives an updraft threshold of 7-8 m/s for lightning.

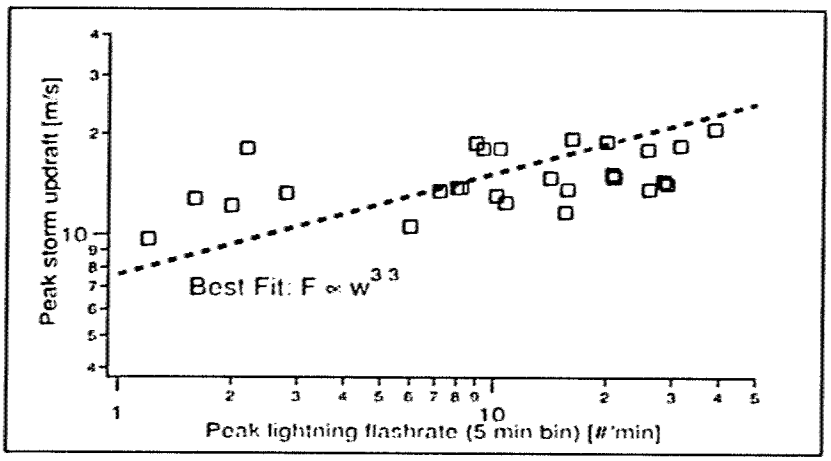


**FIGURE 2. Peak updraft velocity [m/s] during modeled storms as a function of the peak lightning flashrate [#/min].**

## B)Flashrate and water transport

As described in the introducion the updraft velocity is only one of the important cloud properties governing the growth of the electric field. *Solomon & Baker* [1998] found that a threshold value in the peak liquid water flux entering the charging zone of ~ 10 g $m^{-2}s^{-1}$ was required in order to produce lightning. They also found that the ice crystal concentration appeared to have a strong influence on the lightning flashrate which remained low (< 10 $min^{-1}$) until the ice concentration entered the range ~ 10 -100 $l^{-1}$, after which it rose rapidly. These early results appear to be physically reasonable. Based on this evidence we have proceeded with more detailed studies of the relationship between the lightning flashrate and water and ice masses lofted into the charging zone.

We define the total mass of condensate lofted into the charging zone (i.e. through the -10°C isotherm) of a convective cell as:

$$C_u = \int w \ \pi R^2 \ q_{(water+ice)} \ \rho_{air} \, dt \qquad \text{(EQ 1)}$$

where w is the average updraft velocity during each 100s time step in our model, R is the cell radius and $q_{(water+ice)}$ is the combined mixing ratio of ice and water at the -10°C level. The integration is over the lifetime of the storm. We have found, from model studies, that the vast majority of condensate is lofted shortly prior to (beginning ~ 5min before) and during lightning activity. This is consistent with polarimetric radar observations by *Lopez & Aubagnac* [1997]. They estimated the mass of water, graupel and small hail between -10 °C and -20 °C (charging zone) and found that these masses peaked before or early on in the period of lightning activity with the early and late stages of the cell contributing negligible amounts.

The model results (for New Mexico storms) of condensate lofted through the -10 °C isotherm in Fig 3 indicate that, at a minimum, a positive correlation exists between $C_u$ and F. In addition, there appears to be an approximately linear increase in $C_u$ with storm average flashrate. For storms in which no lightning occurred, $C_u$ varied between $30 \times 10^6$ and $100 \times 10^6$ kg while values of $C_u > 100 \times 10^6$ kg only occurred in storms with non-zero flashrates.

The monthly mean high cloud fractions from the International Satellite Cloud Climatology Project (ISCCP) dataset provided an additional way with which we could broadly compare water transport with lightning activity. When seasonal maps of lightning flashrate density compiled from Optical Lightning Detector (OTD) data recorded in

1995/96 were compared with the ISCCP maps of monthly mean high cloud fractions we did indeed noticed that continental regions with a large fraction of high cloud cover also corresponded with regions of high lightning flashrates.

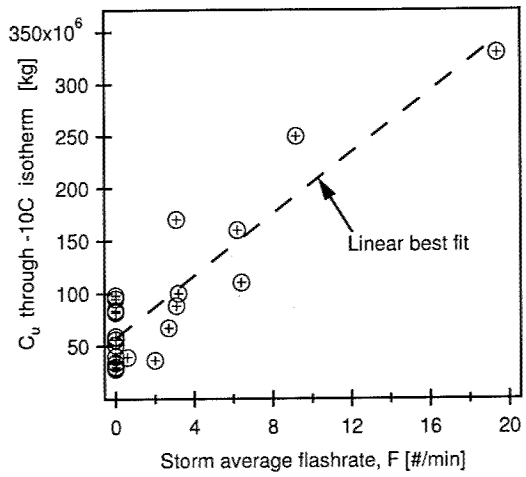


**FIGURE 3. Condensate (water + ice) lofted by modeled storms as a function of the storm averaged lightning flashrate [#/min]. The mass of condensate lofted through the -10°C isotherm, $C_u$, tends to increase with increasing average storm flashrate. In the absence of lightning $C_u$ varied between $30x10^6$ and $100x10^6$ kg while values of $C_u > 100x10^6$ kg were only observed for F > 0.**

## FUTURE WORK

We plan to augment both the updraft velocity and water transport studies with measured data and additional model runs from other field projects where such data was available. Notably at this time we plan to expand this study to include more data from CaPE (Florida), as well as the DUNDEE and MCTEX field projects which conducted in Northern Australia and Tiwi Islands respectively. We hope to obtain threshold values for updraft velocities and water transport based on the lightning flashrates and apply these relationships to satellite lightning data in order to obtain global, large scale estimates of these quantities.

## ACKNOWLEDGMENTS

This work was supported NASA Grant NAG8-1150 and GEWEX Grant NAG8-1512.

## REFERENCES

Baker, M B, H Christian and J Latham, 1995: A One-Dimensional Model of Lightning from Convective Clouds., *Quart J Roy Met Soc.*, **121**, 1525-1548.

Gamache, J.F. and R. A. Houze 1983:, Water Budget of a Mesoscale Convective System in the Tropics, *J Atmos Sci*, **40**, 1835-50.

Lopez, R.E. and J-P Aubagnac, The lightning activity of a hailstorm as a function of changes in its microphysical characteristics inferred from polarimetric radar observations, *J Geophys Res,* **102**, 16799-813.

Price, Colin and David Rind, 1992: A Simple Lightning Parameterization for Calculating Global Lightning Distributions. *J Geophys Res*, **97**, 9919-9933.

Schroeder, Vicki, M.B.Baker and J. Latham, 1999: A model study of corona emissions from hydrometeors, *Q J R Met Soc,* to be published.

Solomon, Robert and Marcia Baker, 1996: A One-Dimensional Lightning Parameterization., *J Geophys Res*, **101**, 14,983-90.

Solomon, R and Marcia Baker, 1998: Lightning Flash Rate and Type in Convective Storms., *J Geophys Res.*, **103**, 14041-57

Zipser, Edward J 1994: Deep Cumulonimbus Cloud Systems in the Tropics with and without Lightning., *Mon Wea Rev*, **122**, 1837-1851.

# CONTACT TIME IN ICE - ICE COLLISIONS

Giorgio M.Caranti, Guillermo G. Aguirre Varela and Rodolfo G. Pereyra

FaMAF Universidad Nacional de Córdoba
Ciudad Universitaria 5000 Córdoba, Argentina

ABSTRACT: There is strong indication that the interactions among ice particles in clouds are the main cause for their electrification. Therefore a characterization of the collisions themselves is of great importance. In this work we present measurements of contact time in metal - metal, ice - metal and ice - ice collisions by a simple electrical method. The method assumes that the ice is conductive enough to allow a measurable current to flow during contact. The experiments were carried out in a cold room under controlled ambient conditions. Temperatures between -3 to -25 °C and impact velocities 0.5 to 2.5 m/s were used for particles formed from tri-distilled water. Preliminary measurements suggest times much longer than theory predicts for ice and for elastic collisions. One cm spheres at the above velocities give times between 200 and 600μs when they collide with a plane ice surface. These times are more compatible to plastic deformation than to elastic interactions. Variability is also very large, successive collisions of the same sphere can give very different contact times. It was possible to observe that on some occasions fracture developed after the first impact which affected the following one resulting in larger contact times, some times, by a factor greater than 2. The yield for the beginning of cracking or plastic flow whichever come first could be estimated as about 7 bars assuming constant stress during the deformation at -10°C. Implications for the mechanisms of charge separation in ice -ice collision are discussed.

## INTRODUCTION

The time two colliding particles remain in contact is of great interest for several physical processes. For example adhesion and charge transfer. About the former, one can infer that given sufficient time more molecular bonds may be established between the interacting particles while for the latter the time can be a limiting factor.

If the interacting bodies have very low relative kinetic energy the contact time will be given by processes occurring in the close proximity of the impacting zones and assuming that the interaction is elastic, one can use the hertzian formulation to calculate the contact time (Tabor, 1951). Then the contact time when a sphere collides with a plane surface is

$$t_c = \frac{2.94 Z_o}{V}, \text{ and replacing } \mathbf{Z_o} \text{ we get: } t_c = \frac{2.74 m^{\frac{2}{5}}}{V^{\frac{1}{5}} r^{\frac{1}{5}}}\left(\frac{1}{E_1} + \frac{1}{E_2}\right)$$

where **V** the impact velocity, $\mathbf{Z_o}$ is the indentation depth, $\mathbf{E_1}$ and $\mathbf{E_2}$ are the elasticity coefficients of both materials, **m** is the mass and **r** the size of the spherical particle. As it is possible to see the dependence of the $\mathbf{t_c}$ with the velocity it is very weak.

If at any time during the collision the elastic limit is surpassed there will be permanent deformation in the material. In this case the formulation must be changed to include this plastic flow. In particular when the deformation of the sphere can be neglected the contact time will be a function of the yield pressure P (assumed constant) and the contact area Ac

$$PA_c = -ma \quad \text{with} \quad A_c = 2\pi r x$$

Where a is the acceleration, x the penetration length at any given time.

The differential equation will be

$$\frac{d^2x}{dt^2} + \frac{2\pi \, \mathrm{Pr}}{m} x = 0, \text{ and finally the time is a quarter of a period: } t = \frac{\pi}{2}\sqrt{\frac{m}{2\pi \, \mathrm{Pr}}}$$

note that this is actually the time needed to get a full stop of the impacting particle which probably is of the same order of the contact time.

In this approximation the contact time becomes independent of the impact velocity. When ice is involved apart from the mere mechanical deformation some of its peculiar properties can also intervene.

In this work we present measurements of contact times between a spherical particle and a flat surface. Three cases were considered: ice – ice, metal – ice and metal – metal. For the cases involving ice the contact time were investigated as function of ambient temperature and velocity.

## EXPERIMENTAL ARRANGEMENT

The time was measured electrically. At the moment of contact a circuit was closed and the current was detected the duration of which was assumed equal to the contact time. For ice, the current was quite low and required an amplifier. Its duration was recorded with a digital oscilloscope. Figure 1 shows the apparatus.

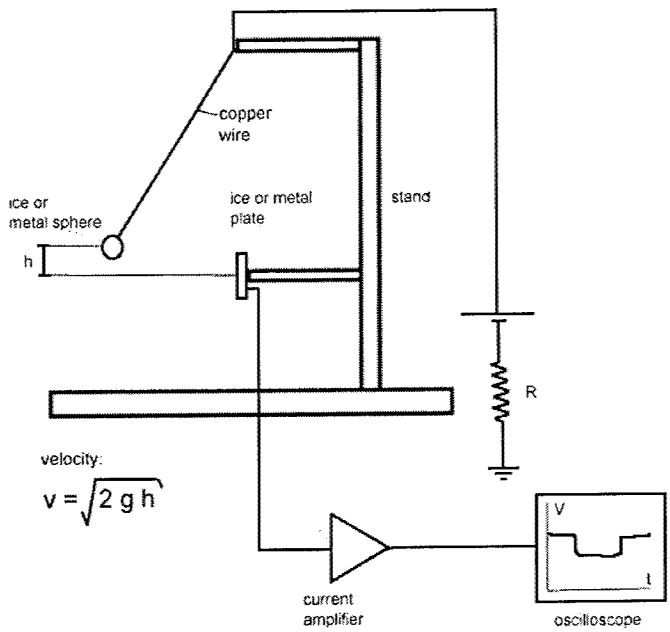


Figure 1: Experimental device

The impact velocities were achieved by letting the pendulum fall from specified heights.

For the metal-metal collisions a steel ball 4.5 mm in diameter collided with the flat end of a cylindrical bar of 7 mm in diameter and 14 mm in length also made of steel. This experiments were carried out at room temperature. The set of measurements of ice –ice collisions were carried out in a cold room varying the temperature between -3 to -25 °C. The ice plates were 8 to 12 mm width by 20 x 30 $mm^2$ stuck on the same steel cylinder. The ice pendulum was made with a spherical bob 9 to 11 mm in diameter and a connecting wire hanged from a metal ring. Both the plate and sphere were made out of tri-distilled water. And finally the measurements for ice – metal the ice plate design was kept but an steel sphere 4.5 mm in diameter was used instead.

## RESULTS

### Ice-ice

Figure 2 shows the measured times at different temperatures and velocities. Also shown are the maximum and minimum values observed together with the mean of the first few collisions. The latter meaning collisions in a fresh region (not previously impacted) of the plate or after annealing of the surfaces. As seen in this figure the minimum values of the time are close to 200μs almost independent of temperature and speed. At higher velocities the contact time had less fluctuations.

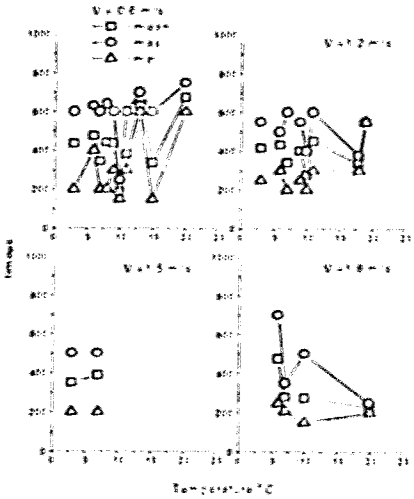

Figure 2 Ice-ice results varying the impact velocity

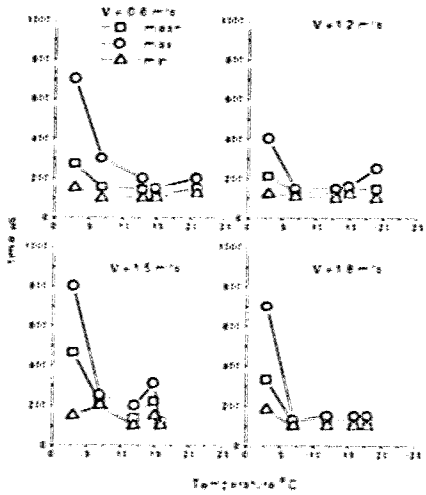

Figure 3 Ice -metal results

The contact times increased dramatically in some cases up to 2000μs when the collision were repeated in the same spot in the plate. The same happened when some cracks were observed in either the plate or the sphere. When the speed exceeded 1.2 m/s the majority of impacts left marks in either of the interacting bodies.

**Ice - steel**

Figure 3 shows results for this kind of collisions. Clearly, the minimum times observed were in general independent of temperature and velocity. The time ranged from 110 to 140 μs. It is important to note the completely different behavior that maximum times present which are remarkably longer at higher temperatures.

**Steel-steel**

The results with the steel ball impacting on the cylinder are shown in Figure 4. As mentioned above the temperature used was the room temperature about 25 °C. Interestingly, there is a tendency to lower times at higher velocities. Also the dispersion is noticeably less than the other measurements.

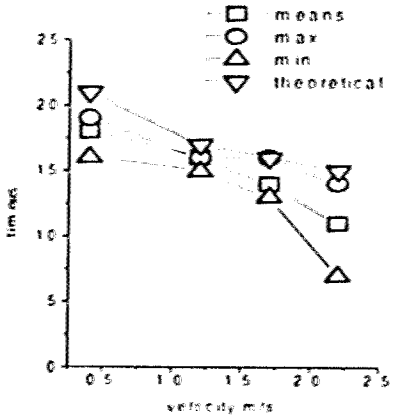


Figure 4 Metal - metal results

## DISCUSSION

For the sake of comparison the theoretical contact times for elastic collisions were calculated and Figure 4 shows this results superimposed to the experimental ones for steel - steel. The agreement is quite acceptable suggesting that, as expected, steel – steel collisions in this range of relative speeds behave elastically. It is quite noticeable from the figure that every experimental value is lower than the theoretical. This may be due to the use of ball bearings steels that are superficially treated both thermally and mechanically while in our calculations we used the Young modulus for a typical steel. Another interesting aspect is that at higher velocities the measured contact times decrease faster than the theoretical ones maybe due to the same argument. We do not have as yet a complete explanation for this phenomenon.

We will turn now to the ice - ice collisions and try to give a justification for having kept the three characteristic times instead of just the average as in any standard measurement one would do. We will assign real meaning to these times. In fact, no two collisions have the same mechanics and even taking precautions in repeating the processes as faithfully as possible slight changes in the collision spot, unwanted rotations, etc. can result in a spreading of times. Since processes such as the latter result in longer times, we will take the minimum time as more representative of the actual contact.

On the other hand in Figure 2 and in spite of a large spreading of values no clear velocity dependence can be inferred. As mentioned in the introduction this can be attributed to plastic deformation (another cause for time spreading) and therefore the yield pressure can be calculated. Using 0.5g and 0.5cm for the mass and radius of the ice sphere respectively, 250μs of stopping time (which we take here as equal to the contact time) a yield pressure of $P=6.8\ 10^6$ dyn/cm$^2$ is obtained. Although a direct comparison with published yield pressures (Hobbs, 1974) is rather difficult, because of the very different techniques involved in their measurements, this value is in reasonable accord. As we will see below the actual yield is probably larger since the stopping time is only a part of the total contact time.

Other kind of plastic deformations were also observed. Cracks and other marks were noted suggesting the release of impact energy through the generation of new surfaces. These mechanisms are probably more probabilistic than the simple yield flow resulting in wider range of contact times. More work in this respect is under way.

When the results of ice –steel collision (Figure 3) are examined it is immediately observed that the time is controlled by the ice component since the minimum times are of the same order of the ice -ice and much longer than steel - steel case. There is one aspect different in the ice-steel case from the ice-ice case: the width of the time distribution which in the former is quite narrow especially at low temperatures and higher velocities. Before giving an explanation of this phenomenon lets look at another aspect. At temperatures near the melting point there is a sudden increase in contact time. As prevalent theories suggest at these high temperatures a quasi-liquid layer may exist on the surface of ice leading to an increase in another force which the adhesion force. This force acts in both ice-ice and ice –metal cases in the direction of producing longer contacts. This adhesion ends quickly in ice – steel contacts as we lower the temperature and so does the variability in ice-steel collision. But this is not the case for ice-ice collisions, the adhesion in ice –ice contact could be the cause of the large dispersion. As we are using polycrystalline ice, different collisions put into contact different crystal orientations and therefore a large variety of adhesion forces.

ACKNOWLEDGEMENTS: We thank the support of CONICET, CONICOR and SeCyT UNC for their respective grants. Also, we are very grateful to José Barcelona for his technical assistance.

## REFERENCES

Hobbs P.V. Ice Physics. Clarendon Press - Oxford, 1974.

Tabor D. The Hardness of Metals. Clarendon Press - Oxford, 1951.

Pruppacher H. R. Klett J. D. Microphysics of Clouds and Precipitation. D. Reidel Publishing Company - Holland, 1980.

# ELECTRICAL STRUCTURE OF CLOUDS AND THUNDERCLOUD ELECTRIFICATION

Peter H. Handel
Department of Physics and Astronomy, University of Missouri St. Louis, St. Louis, MO 63121, USA

ABSTRACT: The electrification processes in clouds and thunderclouds determine to a large extent their electrical structure. Therefore, the observed electrical structure can be compared with the structure calculated on the basis of various electrification models. The models used include charge transfer between ice crystals and riming graupel pellets, the inductive mechanism, a combination of these two models, and also the polarization catastrophe model (Handel, 1985). Both the electric field profile and the charge density profile are calculated.

For the polarization catastrophe model, the free energy of the cloud is calculated as a function of the order parameter and is minimized in two stages. First the free energy is minimized for a homogeneous cloud, and then large-scale inhomogeneities are considered. The free energy is finally minimized in the presence of arbitrary inhomogeneities. This later step leads in certain conditions to the generation of a structure which is characterized by thick horizontal sheets of alternating polarization direction and by thin horizontal space charge regions of polarization charges and masking charges separating them. Finally, both the characteristic times governing the transition from an arbitrary non-equilibrium state to the polarized state, and the stratification times during which a stratified structure is obtained, are estimated theoretically.

Considering these four electrification models, the theoretical field and charge distributions are compared with the experimental field and charge distributions in nimbostratus, cumulonimbus, in stratus clouds and in mesoscale convective system (MCS) stratus formations (Rutledge and MacGorman, 1988). In particular, the observed altitude dependence of the length scale of the field-reversals in the upper regions of MCS stratus formations (Rust et. al. 1996, Marshall et al. 1996) is compared with the altitude dependence of the theoretical field-reversal length scales obtained from the four models considered. Furthermore, the measured charge densities are compared with the theoretical charge densities in the corresponding horizontal layers. The observed and calculated characteristic times are also compared. Finally, the position and timing of the expected flashes is roughly estimated for the four models and compared with the airborne observations of Christian et al. (1980). These observations included thunder reconstruction which located the sources of the first flash of a thunderstorm cell and of the subsequent flashes from progressively lower levels in the cloud. The acoustic sources were correlated with regions of high radar reflectivity. The coincident timing and localization of the reflectivity maxima and earliest sound sources provides a particularly sensitive discrimination of the four models considered.

## INTRODUCTION

The polarization catastrophe approach (Handel 1980, 1984, 1985) to cloud and thundercloud electrification is based on the hypothesis of internal spontaneous ferroelectric polarization of small, heterogeneously nucleated, $H_2O$ aggregates. According to this hypothesis, each of the small $H_2O$ aggregates which have scaled the free-energy barrier is created with a large spontaneous electric dipole moment corresponding to polarization of all hydrogen bonds close to saturation. While the aggregate continues to grow, this large spontaneous

dipole moment is expected to persist up to a maximal aggregate size, $\nu_{max}(T)$, which decreases with the temperature. On the basis of this hypothesis, the above mentioned papers have proven the inevitability of a transition of the whole cloud into a polarization catastrophe (PC), for all aggregate concentrations $N=n/\nu$ exceeding the modest requirements of the universal **PC criterion**

$$\langle\nu^2 N\rangle > \mathbf{2.5\ 10^{21} cm^{-3}};\ \text{in general},\ \int_0^{\nu_{max}} \nu^2 N_\nu d\nu = \int_0^{\nu_{max}} \nu n_\nu d\nu > 2.5\ 10^{21} cm^{-3}[T/260^oK]. \quad (1)$$

With <> denoting the local cloud average, this is the simplified form of the (Handel 1980, 1985) PC criterion $\mathbf{n\nu\mu^2/9\varepsilon_0 kT_1}$. In the non-rationalized Gaussian system of units this criterion becomes $4\pi n\nu\mu^2/9kT_1$. We wrote n for the total number of $H_2O$ molecules bound in ferroelectric aggregates per unit volume of air, $\nu$ for the average number of $H_2O$ molecules in a single small aggregate, $\mu$ for the dipole moment of a $H_2O$ molecule in the aggregate, $\varepsilon_0$ for the vacuum permitivity, k for Boltzmann's constant, and T for the absolute temperature. Finally, $n_\nu=\nu N_\nu$ relates the spectral densities of the concentration of molecules $n_\nu$ and of aggregates $N_\nu$ in terms of the number of molecules $\nu$ in an aggregate, with $(dn)_\nu = n_\nu d\nu$ and $(dN)_\nu = N_\nu d\nu$. The criterion is fulfilled whenever the denominator in the expression of the polarization

$$P = \frac{\chi}{1 - \chi/3} E \quad (2)$$

becomes zero or negative, with $\chi$ _ $\mathbf{n\nu\mu^2/3\varepsilon_0 kT}$.

The presence of the factor $\langle n\nu\rangle = \langle N\nu^2\rangle$ restricts the PC to cold clouds and allows it in less cold clouds only if N is large enough to compensate for the smallness of the maximal $\nu$ value, $\nu_{max}(T)$, compatible with spontaneous ferroelectric polarization at the relatively high temperatures of not so cold clouds. Let us consider, for instance, a condensed phases content of $9g/m^3$, which corresponds to the presence of $n = 3\ 10^{17}\ cm^{-3}$ molecules of $H_2O$ in the condensed phases. The same molecular concentration is found also in saturated vapor at 10.8°C which may have been advected from the ground and raised up into the cloud, where it condenses on impurities and ice nuclei. Assuming at $T=260^oK$ a maximal size of 10 μm for the ferroelectric aggregates, with $3\ 10^4$ molecules in any direction, we obtain $\nu_{max}(T)= 2.7\ 10^{13}$ and $\nu^2 = 7.3\ 10^{26}$ for -13°C. The $\langle\nu^2 N\rangle > \mathbf{2.5\ 10^{21} cm^{-3}}$ PC criterion is thus satisfied for $N>3.4\ 10^{-6} cm^{-3}$ and $n>10^8 cm^{-3}$. This is much smaller than the molecular concentration of $10^{17}\ cm^{-3}$ corresponding to the solid phase content of $9g/m^3$, considered by us. The PC criterion is over-satisfied by a factor of $10^9$. We notice that even for $9\ 10^{-9} g/m^3$ in crystallites we would still get a PC.

In warm clouds with maximum ferroelectric aggregate sizes of 0.3 μm, $\nu_{max}(T)= 10^9$, assuming only a small-size condensed phases content of $0.0009g/m^3$, which corresponds to the presence of $n = 3\ 10^{13}\ cm^{-3}$ molecules of $H_2O$ in the condensed phases with $\nu < \nu_{max}$, the PC criterion is over-satisfied by a factor of 10. Nevertheless, the main PC will occur only for a short time while the nucleated aggregates undergo growth before stabilizing as small cloud particles or droplets with $\nu > \nu_{max}$. The PC is then weak, but noticeable in warm clouds. It is localized to a pair of close horizontal sheets of polarization charge in this case. These sheets or thin layers are stationary and located on the column of rising moist air at the condensation level. A small level of polarization is usually extending higher into the cloud, with the PC

criterion barely satisfied, and with a polarization level several times lower than between the layers mentioned. Most of the cloud mass is not involved, having $\nu > \nu_{max}$.

Most cumulus and stratus clouds extend to altitudes above the 0°C isotherm, where $\nu_{max}$ is much larger, of the order of $10^{12}$-$10^{14}$. Therefore, in general, the PC approach introduces large "fictitious" polarization charges into atmospheric electricity as precursors and roughly equal counterparts of the "real" cloud and thundercloud charges. Without the PC it is hard to understand: **1)**The very early charge buildup in swelling cumulus clouds with neither precipitation, nor radar reflections which would detect precipitation which did not reach the ground; **2)**The charging during the early stages of formation of almost-precipitation-sized particles observed through the first high-resolution radar echoes; **3)**The occasional observation of early lightning simultaneous with the first radar echo, i.e., before precipitation had time to fall an appreciable distance (Moore and Vonnegut 1977); **4)**The measured speed of negative charging in the base of growing non-precipitating cumuli, which exceeds the ion accumulation rate by more than an order of magnitude (Reiter 1974, 1992); **5)**The frequently observed presence of lightning in clouds with very low precipitation rates (Moore and Vonnegut 1977); **6)**The sharp "benchmark" localization of the cloud charges in multiple thin horizontal layers in the lower part of the stratus cloud or thundercloud and to a lesser degree throughout the bulk (Rust et. al. 1996, Marshall et.al. 1996); **7)**The mutual compensation of the charges present in several thin horizontal pairs of charge layers present in the bulk of most clouds (Rust et. al. 1996, Marshall et.al. 1996); **8)**The early and continuous presence of large currents flowing to the cloud from the conductive air masses around the cloud (Vonnegut 1994); **9)**The general existence of a localized superimposed electric field opposed to the fair-weather field at the condensation level even in rapidly rising non-turbulent column of moist air (Reiter 1974, 1992); **10)**The total alignment, and the rapid (0.1 s) reorientation of small ice crystals in clouds and thunderclouds occurring often even in the absence of lightning, in spite of wind and considerable turbulence, observed in cross-polarization measurements on radio link paths (Bostian and Allnut, 1979, Cox and Arnold, 1979) as well as in radar and optical polarization studies (Mendez 1969, Vonnegut 1965; Greenler 1980 in cirrostratus clouds); **11)**The frequency and the speed of cloud and thundercloud polarization -depolarization -repolarization cycles in the strong turbulence conditions of violent thunderstorms; **12)**The presence of lightning and spokes in the B-ring of Saturn (Handel and James 1983). Some of these points were mentioned in a different context in Vonnegut's (1994) critical discussion of the atmospheric electricity paradigm.

The PC provides the initial electric field in which other gravitation based electrification processes, such as the ice-hail charge mechanism, the convective mechanism and the inductive mechanisms have to be considered. On the other hand, the direction of the polarization vector of the PC will often be determined by the other electrification processes acting locally in the cloud, thundercloud, or mesoscale convective system. The PC theory also allows to distinguish growing clouds formed in the fair weather field due to their weak positive lower PC limit charge and negative upper PC limit charge. Dissipating clouds are recognized due to their negative lower PC limit masking charge excess, and upper positive masking charge excess, released by the decreasing or vanishing PC. This is in close agreement with the observation by Imyanitov and Chubarina (1969) of reverse polarity over growing (lower)

clouds, and regular polarity over mature (taller) nimbostratus clouds, and thunderclouds. Here "regular polarity" corresponds to a positive charge at cloud top and negative charge in the lower part of the cloud.

FREE ENERGY CONSIDERATIONS

The free energy density of a cloud is given by

$$F = (P/2\varepsilon_0\chi)(1 - \chi/3) + \mathbf{E}\cdot\mathbf{D}/2 \qquad (3)$$

If the PC criterion is satisfied, F<0 and the PC is present in equilibrium. **E·D** is zero both for a thin slab with PC in it (D=0) and for a closed ring with PC in it (E=0). The creation of suitably arranged ferroelectric domains with different directions of polarization can reduce the free energy (free enthalpy, stricly speaking). In particular, if horizontal sheets in which the PC criterion is satisfied alternate with sheets in which it is not satisfied, in the growing phase of the cloud we notice a sequence of uncompensated polarization charges which start with a positive charge at the bottom and continue with alternatively negative and positive charges, ending with a negative polarization charge on top. [This also corresponds to the convective region of mesoscale convective storms (MCS) and at higher altitudes also to the transition zone and beginning of the stratiform region.] In the dissipating phase, which in the case of MCSs corresponds to the trailing stratified part of the storm, the PC has been reduced in intensity in all the layers where it was present, and we notice a sequence with opposite polarity, starting with a negative excess of uncompensated real charge on the bottom, and ending with a positive uncompensated excess of real charge on top. The width of the charge regions is small, of the order of 50-100m. However, the higher we go, the larger this width becomes, due to.increasing electrical conductivity. Also the width of the space charge region at the bottom is increased due to large-sized rapidly falling precipitation and due to contribution from the melting electrification mechanism (Drake, 1968). This is in good agreement with the results of balloon soundings by Shepherd, Rust and Marshall (1996) and with the conceptual model of MCS electrical structure by Stolzenburg (1996) and Rust, Marshall, Stolzenburg, Bateman, Shepherd and Smull (1966).

**REFERENCES**


Bateman, M.G., W.D. Rust, T.C. Marshall, and B.F. Smull, 1995: Precipitation charge and size measurements in the stratiform region of two mesoscale convective systems. *J. Geophys. Res.,* 100, 16,341-16,356.

Drake, J.C., 1968: Electrification accompanying the melting of ice particles. *Q. J. Roy. Meteor. Soc.,* 94, 176-91.

Handel, P.H., Polarization catastrophe theory of cloud electricity, 1995: *J. Geophys, Res.* **90**, 5857-5863.

Marshall, T.C., and W.D. Rust, 1993: Two types of vertical electrical structures in stratiform precipitation regions of mesoscale convective systems. *Bull. Amer. Meteor. Soc.,* 74, 2159-2170.

Marshall, T.C., Stolzenburg, M. and Rust, D.V., 1996: electric field measurements above mesoscale convective systems" *J. Geophys. Res.* **101**, 6979-6996.

Rust, W.D., Rust, T.C. Marshall, M. Stolzenburg, M.G. Bateman, T.R. Shepherd and B.F. Smull, 1966:, Observations of electrical structure of midlatitude mesoscale convective systems: review and update, *Proc. 10th Int. Conf. on Atm. Electricity,* Osaka 1996, p. 108-111.

Schuur, T.J. and S.A. Rutledge, A modeling study of MCS electrification, 1996:*Proc. 10th Int. Conf. on Atm. Electricity,* Osaka 1996, p. 120-123

Shepherd, T.R., W.D. Rust, and T.C. Marshall, 1996: Electric fields and charges near 0° C in stratiform clouds, *Monthly Weather Review* 124, 919-937.

Stolzenburg, M., 1966: An observational study of the electrical structure in the convective region of mesoscale convective systems. Ph.D. dissertation, Oklahoma Univ. Norman.

Christian, H., H., C.R. Holmes, J.W. Bullock, W. Gaskell, A.J. Illingworth & J. Latham, 1980 Airborne and ground based studies of thunderstorms in the vicinity of Langmuir Laboratory,.*Qurt.J. Royal Met. Soc.* **106**, 159.

# AN EXAMINATION OF THE CONVECTIVE CHARGING HYPOTHESIS

J. H. Helsdon, S. Gattaleeradapan, and R. D. Farley

Institute of Atmospheric Sciences, SD School of Mines & Technology, Rapid City, SD, USA

ABSTRACT: An examination of the convective charging hypothesis is undertaken using the 3D Storm Electrification Model (SEM). Elements of the model relevant to the convective hypothesis are the full treatment of polar small ions including attachment to hydrometeors, the inclusion of point discharge from the surface depending on the electric field strength, the 3D motion field associated with storm development, and the components of the Maxwell current. Simulations for both a small storm and a large storm were run to test the efficacy of convective charging in two very different dynamic frameworks. Each storm was also simulated using a noninductive charging mechanism to compare the magnitude and development of the attendant electrification. The simulations show that, while the Maxwell current distributions for conduction and convection are as envisaged by Vonnegut, the magnitude is not great enough to provide any significant electrification to these storms during their life cycles. Use of a noninductive charging mechanism leads to significant electrification for both storms.

## INTRODUCTION

The search for a satisfactory understanding of thunderstorm electrification is a continuing process. Vonnegut (1994) pointed out that despite the major effort that has been devoted to studies of precipitation-based charge separation processes, it is a worthwhile exercise to occasionally take stock of the potential anomalies accumulated over the years that might eventually lead to a change of the paradigm.

One of the proposed areas of investigation is to construct realistic computer models based on the convective theory of electrification and compare the results with those using precipitation-based electrification mechanisms. Saunders (1993, 1995) also suggested the use of numerical models to test the time taken for advection of charged volumes to operate in the convective process. The purpose of this study is, then, to examine the convective charging hypothesis using the 3D SEM developed by the researchers at the Institute of Atmospheric Science, South Dakota School of Mines and Technology.

Two well-documented storms were simulated using the model for comparative purposes. A small convective storm was simulated - the 19 July 1981 storm from the Cooperative Convective Precipitation Experiment (CCOPE) described by Helsdon and Farley (1987). The other was the large hailstorm of 1 July 1993 from the North Dakota Tracer Experiment (NDTE).

## THE MODEL

The numerical model used in this study is a modified version of the Clark-Farley three-dimensional, time-dependent, bulk-water model originally developed by Clark (1977, 1979) and Clark and Farley (1984). Modifications to the model include the coupling of the electrical processes with the model dynamics and microphysics. Electrical processes include a full treatment of small ions with attachment to 5 classes of hydrometeors (the convective mechanism), equations for the conservation of charge associated with the 5 hydrometeor classes, the ability to simulate charge transfer by inductive and/or noninductive mechanisms, the lightning discharge, and point discharge from the surface dependent on the electric field strength. Wojcik (1994) described in more detail the use of the noninductive charging mechanism of Takahashi (1978) in his study of the same CCOPE case using the 2D version of the SEM.

The model domain for the CCOPE simulation is 20 x 20 km in the X and Y directions and 16 km in the Z direction with a 250-m grid interval. For the NDTE storm, the model domain used is increased to 40 x 40 km in the X and Y directions and 20 km in the Z direction with the same 250-m grid interval. The increase in model domain size is to resolve the greater size of the NDTE storm. Convection is initiated by perturbations of the environmental temperature and humidity at the initiation of the model run. The perturbation bubble is placed horizontally in the center of the model domain, and decreases with the square of the distance from the center.

Four simulations were run. For each cloud a run was made with only convective processes (ion attachment) active. Then an identical simulation was run with the parameterization of Takahashi'snoninductive mechanism. Results are compared as to the strength and structure of the charge distribution within the simulated clouds.

## MODEL RESULTS

19 July 1981 CCOPE Case

The simulation of this cloud resulted in a rather short-lived storm, in agreement with the observations. Dissipation of the storm began by 30 min and the simulation was terminated after 32 min. Figure 1 shows cross sections of the storm's evolution at Y = 11.5 km at 20, 24, 28, and 32 min (see figure caption for details). For convective-only charging we see pockets of charge density develop in response to the convection pattern and the ambient electric field. In particular, Fig. 1(b) at 24 min shows the lower cloud shelf with a negatively charged underside with positive charge above (negative ions drift up, positive ions down in the fair weather field). Some elements of the way Vonnegut envisioned the process working are visible on the right side of the cloud at 20 min. However, for the most part, the charge structure is disorganized with no definite structure emerging. Electric fields only show minor perturbations from the fair weather field and the maximum charge densities do not exceed $\pm 5 \times 10^{-3}$ nC m$^{-3}$. In contrast the simulation employing the noninductive process shown in Fig. 1(c) develops a strong positive charge dipole with maximum charged reaching around $\pm 4$ nC m$^{-3}$ and a maximum negative vertical electric field of -229 kV/m. Clearly, for this simulation, convective charging does not suport strong electrification, whereas the use of a noninductive mechanism does.

1 July 1993 NDTE Case

Figure 2 shows the simulation of this severe storm, which produced damaging hail and copious lightning near Bismarck, ND, at 16, 32, and 48 min. Recall that the horizontal domain for this simulation has been doubled to 40 km. Results through 48 min are shown considering that this should allow ample time for the convective process to operate, if it is to be effective in generating significant electrification. Examination of the total charge density in Fig. 2 shows the same tendency as in the CCOPE case. The charge structure that develops by ion attachment and convection is weak and disorganized throughout the simulation. While the charging is somewhat stronger in this case, the maximum charges do not exceed $\pm 9 \times 10^{-3}$ nC m$^{-3}$ and the electric fields, again, are only perturbed from their fair weather values. The simulation of this storm using noninductive charging (not shown) had a positive charge dipole structure and significant fields by 16 min. Lightning potential was reached a short time later.

CONCLUSION

Although the convective charging mechanism is not to be neglected, the results from these 3D SEM simulations indicate that, at least for these two cases, it does not produce significant electrification. Both storms were observed to produce lightning, an indication that they were strongly electrified. The use of a small, weak storm and a larger, strong storm in the simulations is an attempt to cover the range of storm conditions over which the convective mechanism might be expected to have to produce significant electrification. The use of a noninductive mechanism more realistically simulated each storm's electrical development. The treatment of small ions and their attachment to hydrometeors remains an important aspect in the modeling of thunderstorm electrical behavior because it accounts for the formation of screening layers. However, it appears that the convective hypothesis is not a viable mechanism for the generation of strong electrification in thunderstorms.

ACKNOWLEDGMENTS: This work was supported by the Physical Meteorology Program of the U. S. National Science Foundation under grants ATM-9200698 and ATM-9613679.

REFERENCES

Clark, T. L., 1977: A small-scale dynamic model using a terrain-following coordinate transformation, *J.Compt. Phys.*, **24**, 186-215.

Clark, T. L., 1979: Numerical simulations with a three-dimensional cloud model: lateral boundary condition experiments and multicellular severe storm simulations, *J. Atmos. Sci.*, **36**, 2191-2215.

Clark, T. L., and R. D. Farley, 1984: Severe downslope windstorm calculations in two and three spatial dimensions using anelastic interactive grid nesting: a possible mechanism for gustiness, *J. Atmos. Sci.*, **41**, 329-350.

Helsdon, J. H., Jr., and R. D. Farley, 1987: A numerical modeling study of a Montana thunderstorm, 1, Model results versus observations involving electrical aspects, *J. Geophys. Res.*, **92**, 5645-5659.

Saunders, C. P. R., 1993: A review of thunderstorm electrification processes, *J. Appl. Meteor.*, **32**, 642-655.

Saunders, C. P. R., Thunderstorm electrification, in *Handbook of Atmospheric Electrodynamics, Vol. 1*, ed. H. Volland, CRC Press, Boca Raton, FL, 61-92, 1995.

Wojcik, W. A., 1994: An examination of thunderstorm charging mechanisms using the IAS 2D storm electrification model, *M. S. Thesis*, 113 pp., Department of Meteorology, SD School of Mines and Technology, Rapid City, SD.

Vonnegut, B., 1994: The atmospheric electricity paradigm, *Bull. Amer. Meteor. Soc.*, **75**, 53-61.

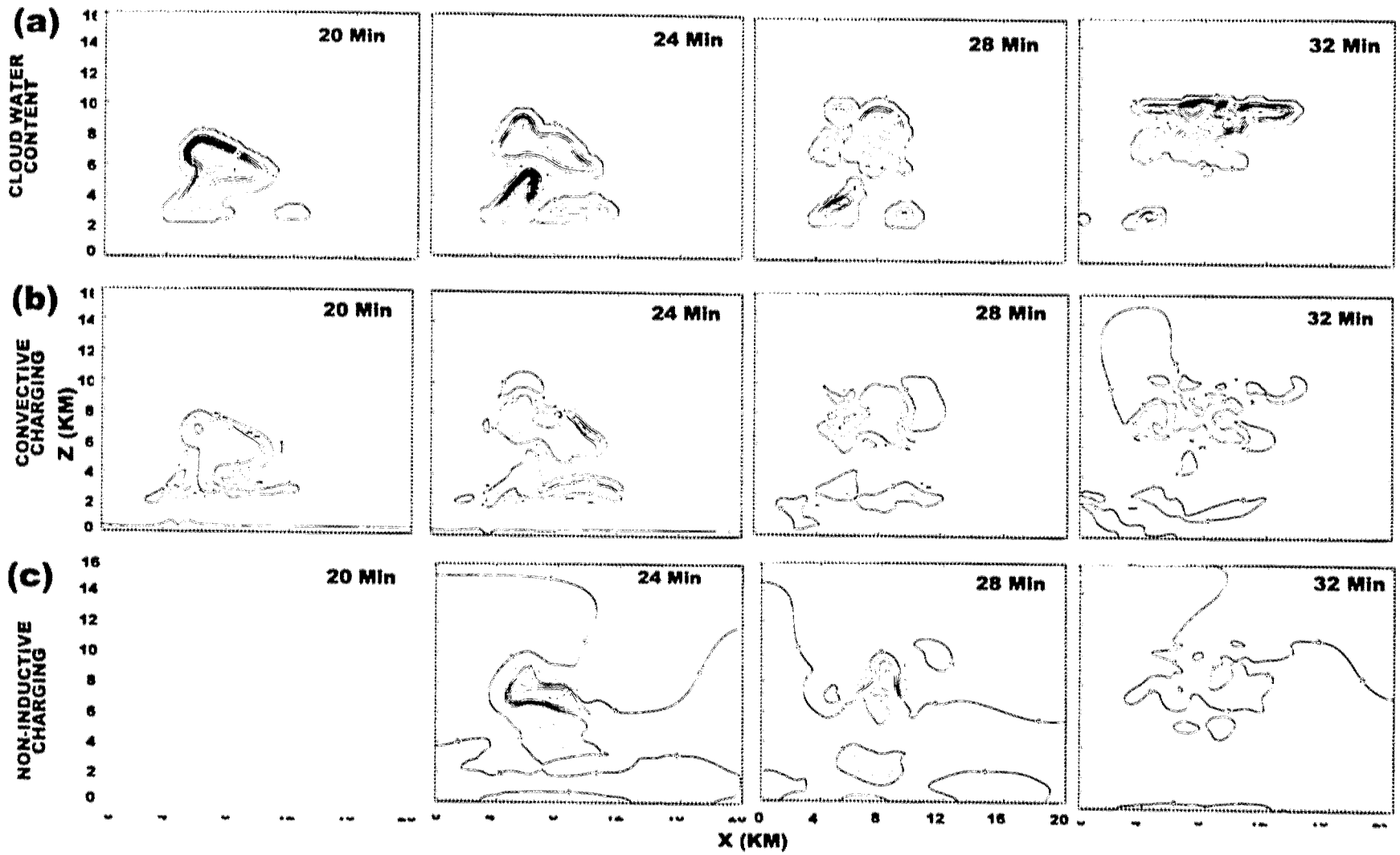


Figure 1: (a) total cloud field, (b) total charge density for convective-only charging, (c) total charge density for noninductive charging at 20, 24, 28, and 32 min for the CCOPE simulation. Contour intervals are: (a) 0.5, 0.25, 0.25, and 0.125 g/kg; (c) 0.125, 0.5, 0.5, and 0.5 nC $m^{-3}$, (b) 0.0005, 0.0005, 0.001, and 0.001 nC $m^{-3}$, respectively.

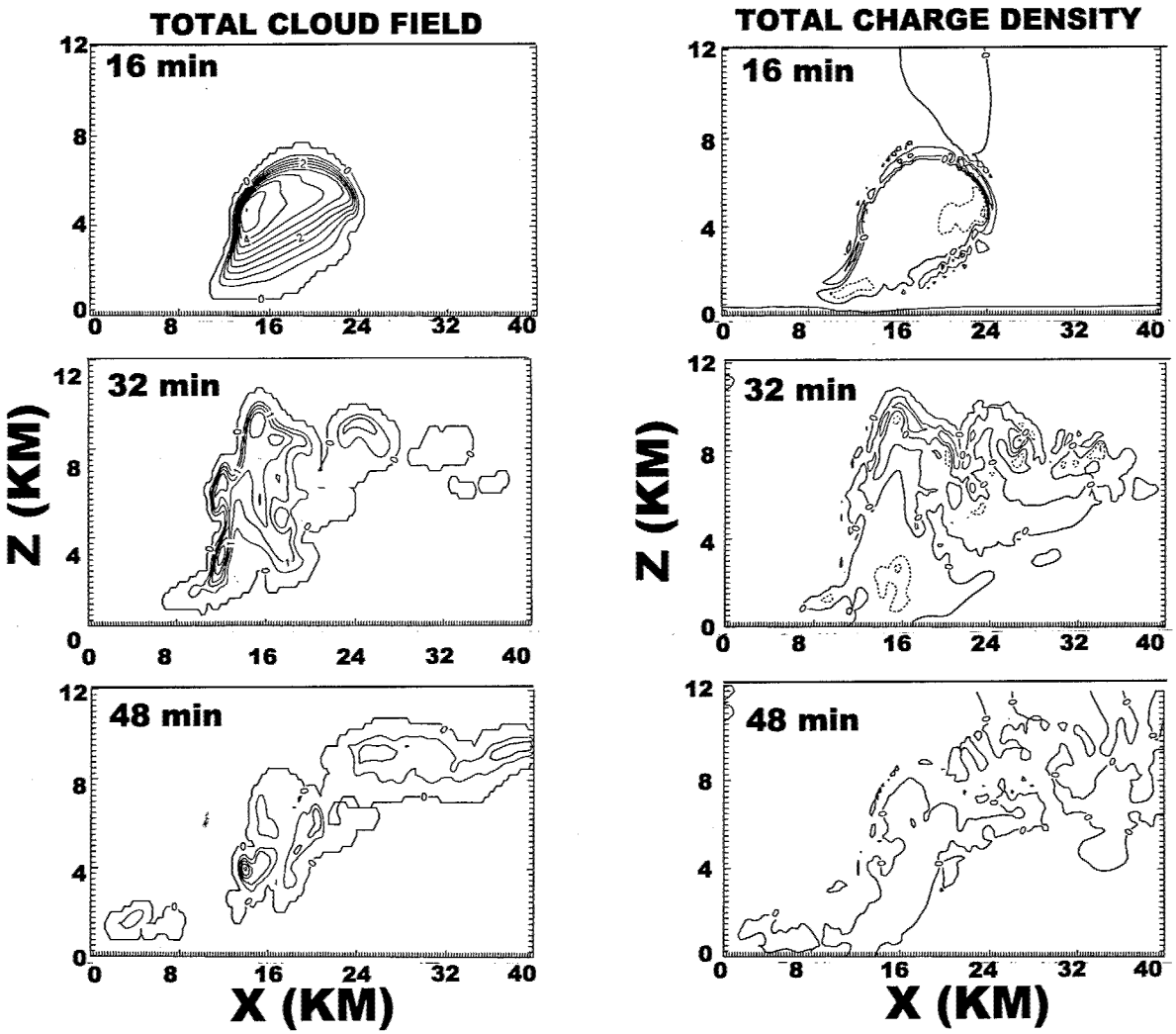


Figure 2: Total cloud field (left column) and total charge density for convective-only charging at 16, 32, and 48 min for the NDTE simulation. Contour intervals are: total cloud field - 0.5 g/kg for all panels and charge density - 0.0005, 0.001, and 0.002 nC $m^{-3}$, respectively.

# THE EFFECT OF THE CLOUD DROPLET SPECTRUM ON ELECTRICAL CHARGE TRANSFER DURING INDIVIDUAL ICE-ICE COLLISIONS

Rodolfo Pereyra, Eldo E. Avila, Giorgio M. Caranti and Guillermo G. Aguirre Varela.

Facultad de Matemática Astronomía y Física,
Universidad Nacional de Córdoba
Ciudad Universitaria, 5000 Córdoba, Argentina

ABSTRACT: New experiments were performed with a wind tunnel in a cold room in order to investigate the influence of the cloud droplet spectrum on the charges transferred during ice-ice collisions. A fixed artificial graupel growing by riming, placed inside a wind tunnel, is collided by ice spheres. The experiments were performed using two different cloud droplet spectrum; the ice spheres used were of about 100 μm in diameter; the impact velocity around 4 m $s^{-1}$. The ambient temperature ($T_a$) was varied in the range -10 to -30 °C. The effective water content EW, was between 0.2 and 1.1 g $m^{-3}$. The results show that the predominant sign of the charge transfer for a set of given conditions is dependent on the cloud droplet spectrum which means that the charge sign reversal temperature is also a function of the spectrum. In particular, using smaller droplets, the reversal sign occurs below -25°C, while for larger droplets the reversal sign is produced at -18°C. These results show that the droplet spectrum is an important parameter to keep under control when natural cloud conditions are being simulated.

## INTRODUCTION

There is extensive field evidence showing that the development of electric fields within thunderstorms is the result of charge separation during collisions between ice particles. In attempts to understand the physical mechanisms that operate in charge separation process, many laboratory experiments have been performed (Takahashi, 1978; Gaskell and Illingworth, 1980; Jayaratne et al., 1983; Saunders et al., 1991; Avila and Caranti, 1994).

These experiments indicated that the electrification process could be parametrizaded by temperature (T) and liquid water concentrations (LWC). Thus, these variables are generally used as a pair of variables describing the sign of the charge transferred in ice particle collisions. However, some of the previous mentioned work, performed under supposedly similar conditions, have given results not in complete accord; it suggests that there are others variables involved in the process.

Jayaratne and Saunders (1985) showed that the size distribution of the droplets is an important parameter in the electric charge transfer when ice crystals collide and then separate from an ice target. They used two different cloud droplet spectra. One (Big), had droplets between 5 and 30 mm in diameter; while the other one (Small) had droplets between 5 and 14 mm in diameter. These authors, using a particle replicator, found that when the target was charging positively, droplets greater than 4 mm were present on the replicator film and there were no droplets greater than 4 mm present (small spectrum) when the current was negative. However, it is important to note that during the experiments the cloud droplet concentration, the cloud droplet spectrum and the crystal size spectrum were continuously changing since the crystals grew at the expense of the cloud droplets. Furthermore, both rime accretion rate and cloud droplets spectrum were measured before seeding the cloud of droplets in order to produce ice crystals.

On the other hand, Avila et al. (1998) observed a different effects of the cloud droplet size on charge transfer during collisions between ice crystals and a simulated spherical graupel. They found that broadening the cloud droplet spectrum leads to negative graupel charging at higher values of EW than has been reported in previous laboratory studies. These results are not in complete accord with the previous results of Jayaratne and Saunders (1985)

In this work we performed experiments in order to investigate the influence of the cloud droplet spectrum on the charge separation process of ice-ice collisions. The ranges of ambient temperatures, liquid water

concentration, impact velocities and droplet spectra used in this work are representative of those corresponding to thunderstorms.

Both the liquid water content and the cloud droplet spectrum remained fairly constant during each experiment, so the conditions for charge generation remained unchanged. We work with two different CDS and measured the charge transfer during individual collisions between small spheres of ice and an ice target growing by riming. We examine the dependence of the sign of the charging with both CDS for different ambient temperatures and show that small changes in droplet size result in important changes in charging. In particular, our results could be applied to graupel-graupel interactions if we assume that the ice spheres are considered as small graupel.

## EXPERIMENTAL DEVICE AND MEASUREMENTS

The experimental device designed to study the electrical charge transfer during ice-ice collisions involved the same apparatus and procedures as described by Avila and Caranti (1994) and Avila et al. (1995), (1996). Thus for a detailed description of the technique of the present laboratory experiments we refer the reader to the cited papers.

The cloud was generated outside the cold room by condensation of vapour originated in a stainless steel boiler and was conducted to the wind tunnel by several metallic tubes in order to ensure that the temperature of the cloud droplets achieves the ambient temperature. The effective liquid water concentration (EW) was determined by weighing the mass of water collected by the target during a given time.

In order to produce different CDSs, the technique described in Mossop (1984) was used. Accordingly, nozzles of diameter 15 and 80 mm were used to obtain two CDSs.

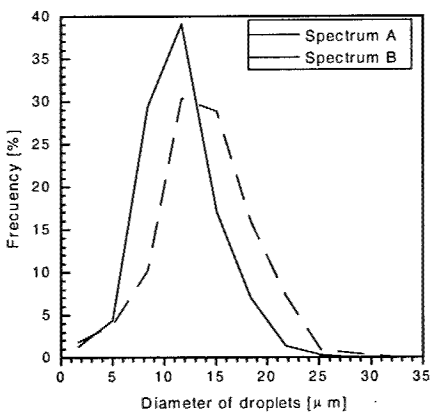


**Figure 1: Cloud droplets spectra A and B**

The measurements of the clouds spectra were made with a glass cylinder, similar to target, covered with a film of formvar solution. Figure 1 shows the normalized droplet size distributions for the clouds generated; the spectrum A was obtained with the larger nozzle and the spectrum B was obtained with the smaller nozzle.

It is possible to observe that CDS B has a higher proportion of larger droplets than the CDS A.

The experiments of charge transferred, with the spectra A and B, were performed with ice spheres of 100 μm in diameter (D). The impact velocity (V) was 4 m $s^{-1}$. The ambient temperature (Ta) was varied in the range -10 to -30 °C. The effective water content EW was between 0.2 and 1.1 g $m^{-3}$.

## DISCUSSION AND RESULTS

Figure 2 shows an EW-Ta diagram of the sign of the charge transferred to the target using the A and B spectra. It is important to note that when spectrum A was used the main sign of the charge transfer is positive for a wide range of temperature; it was necessary to decrease the temperature below -25°C to get negative charging. While when spectrum B was used, it was possible to obtain negative charge transfer by cooling to below -18°C.

The temperature at which the sign of the charge transferred reverses from positive to negative depends on the cloud droplet spectrum used for the accretion, for example with CDS A the reversal sign occurs around -25°C, while for CDS B the reversal sign occurs at about -18°C. This is important in thunderstorm electrification since it could help to understand the location of the main charge centre.

The present results are in agreement with Avila et al. (1998). These authors suggested that the results could be compatible with a mechanism proposed by Baker et al. (1987); the particles with the surface growing faster by vapour diffusion charges positively during crystal-graupel interaction.

Thus different kind of droplets, freezing over the graupel surface, can provide vapour to the surface in different way. Then, different regions on the graupel surface could have different diffusional growth rates and then different charging.

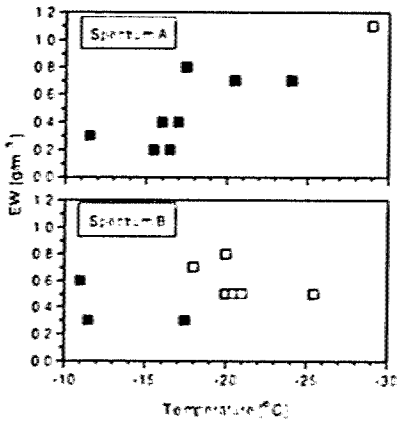


**Figure 2: Sign of the charge transfered to the target for two different cloud droplet spectrum. Solid square: positive; Open square: negative.**

In principle, the mechanism proposed by Baker et al. (1987) concerning with the relative diffusional growth rate of the interacting particles could be applied to the present results in which ice spheres were used instead of ice crystals and the previous discussion is still valid for individual collisions between ice spheres and a cylindrical target growing by riming.

On the other hand, the latent heat released by riming increases the graupel temperature and it will induce sublimation of the surface. Moreover, Avila et al. (1999) found that for a given EW, velocity, and ambient temperature, the rime temperature depends on the cloud droplet spectrum used for the accretion. The warming produced by large droplets is greater than the warming produced by small droplets. Thus, large droplets could lead to negative rimers by reducing the vapour diffusional growth rate to the rime below that to the crystals. This effect could be caused because larger droplets have a smaller total surface area than the smaller droplets.

## CONCLUSIONS

The results show that the predominant sign of the charge transfer for a set of given conditions is dependent on the cloud droplet spectrum which means that the charge sign reversal temperature is also a function of the spectrum. In particular, using CDS A, the reversal sign occurs below -25°C, while for CDS B the reversal sign is produced at -18°C.

As it was suggested before, the collisions between ice spheres and a rime target could be ascribed to the graupel-graupel kind of interactions. Thus the present results together with those of Avila et al. (1998) indicate that larger cloud droplets lead to negative charging for graupel and hailstones as consequence of impacts with ice crystals and other smaller graupel. The present results show that the droplet spectrum is a very important parameter to keep under control when cloud conditions are being simulated, since it can determine the sign of the charge transferred in collisions between ice particles.

These results are relevant to our understanding of the electrification processes inside thunderclouds. But, more detailed experiments and theoretical studies should be conducted to understand this mechanism.

ACKNOWLEDGEMENTS: This work was supported by the Consejo Nacional de Investigaciones Científicas y Técnicas, the Consejo de Investigaciones Científicas de la Provincia de Córdoba, and Secretaría de Ciencia y Técnica de la Universidad Nacional de Córdoba, Argentina. We want to thank Jose Barcelona for his technical assistance in this work.

## REFERENCES

Avila, E.E., and G.M. Caranti, A laboratory study of static charging by fracture in ice growing by riming. J. Geophys. Res., 99, 10611-10620, 1994.

Avila, E.E., G.G. Aguirre Varela, and G.M. Caranti, Temperature dependence of static charging in ice growing by riming . J. Atmos. Sci. 52, 4515-4522, 1995.

Avila, E.E., G.G. Aguirre Varela, and G.M. Caranti, Charging in ice-ice collisions as a function of the ambient temperature and the larger particle average temperature. J. Geophys. Res., 101, 29609-29614, 1996.

Avila, E.E., G.M. Caranti, N.E. Castellano and C.P.R. Saunders, Laboratory studies of the influence of cloud droplet size on charge transfer during crystal-graupel collisions. J. Geophys. Res., 103, 8985-8996, 1998.

Avila, E. E., N. E. Castellano, and C.P.R. Saunders, Relationship between rime surface temperature and cloud droplet spectra and their influence on the charge transfer process in ice-ice collisions. This issue. 1999.

Baker, B., M. B. Baker, E. R. Jayaratne, J. Latham, C. P. R. Saunders, The influence of diffusional growth rates on the charge transfer accompanying rebounding collisions between ice crystals and soft hailstones, Q. J. R. Meteorol. Soc., 113, 1193-1215, 1987.

Brooks I.M. and C.P.R. Saunders, Thunderstorms charging: Laboratory experiments clarified. Atm. Res. 39, 263--273, 1995.

Caranti, G. M., Avila E. E., and M. A. Re, Charge transfer during individual collisions in ice growing from vapour deposition. J. Geophys. Res., 96, 15363-15375, 1991.

Gaskell W. and A.J. Illingworth, Charge transfer accompanying individual collisions between ice particles and its role in thunderstorm electrification. Q. J. R. Meteorol. Soc. 106, 841--854, 1980.

Hobbs P.V. and Rangno A.L., Ice particle concentrations in clouds. J. Atmos. Sci. 42, 2523--2549, 1985.

Jayaratne E.R. and C.P.R. Saunders, Thunderstorm electrification: the effect of cloud droplets. J. Gheophys. Res. 90, 13063--13066, 1985.

Jayaratne E.R., C.P.R. Saunders and J. Hallett, Laboratory studies of the charging of soft hail during ice crystals interactions. Q. J R. Metereol. Soc. 109, 609--630, 1983.

Mossop, S. C., Production of laboratory clouds. Q. J. R. Meteorol. Soc. 110, 275--279, 1984.

Saunders, C.P.R., W.D. Keith and R. P. Mitzeva, The effect of liquid water on thunderstorm charging. J. Gheophys. Res. 96, 11007--11017, 1991.

Takahashi T., Riming electrification as a charge generation mechanism in thunderstorms. J. Atmos. Sci. 35, 1536--1548, 1978.

Williams E. R., 1989: The tripole structure of thunderstorm J. Geophys. Res., 94, 13151-13167.

# CHARGE TRANSFER PROCESS DURING COLLISION OF RIMING GRAUPEL PELLET WITH SMALL ICE CRYSTALS WITHIN A THUNDERCLOUD

Saswati Datta[1], Utpal K. De[2], K. Goswami[2] and Linwood Jones[1]

[1]Department of Electrical and Computer Eng., University of Central Florida, Florida, U.S.A
[2]Physics Department, Jadavpur University, Calcutta, India

ABSTRACT: A charge transfer process during the collision of a riming graupel pellet and an ice-crystal at low temperature is proposed. During riming, the surface structure of graupel deviates from perfect crystalline structure. A concept of quasi-solid layer (QSL) formation on the surface is introduced. This QSL contains defects formed during riming. In absence of impurities, positively charged X-defect abundance is considered in the outer layer. These defects are assumed to be the charge carriers during the charge transfer process. Some part of the QSL is stripped off by the colliding ice crystals, which thereby gain some positive charge, leaving the graupel pellet negatively charged. With the proposed model, fC to pC of charge transfer is observed per collision. A transition temperature between –10 C to –15 C is also noted beyond which the QSL concept does not hold. This transition temperature is dependent on the bulk liquid water content of the cloud.

INTRODUCTION:

The principal means of macroscopic charge separation in thunderclouds appears to be differential particle motion under gravity. The fact that thunderstorms world wide have charge centers in similar and well defined temperature bands below 0 Celsius indicates that the presence of ice phase is a prime requirement of thundercloud electrification. An examination of thunderstorm properties reveals that active charge separation occurs when the growth of graupel/soft hail, by the accretion of super cooled water droplets, is the dominant process during the storm's life cycle. Substantial charges are transferred when ice-crystals hit and rebound from riming graupel pellets (*Saunders*, 1994).

Many researchers have theories concerning the charging microphysics. Most of these are qualitative, and none satisfactorily describes the actual situation. For example, Baker and Dash [1994] proposed a charge transfer model during the interaction of ice-crystals with graupel pellets based on the concept of surface melted quasi-liquid layer (QLL) over the ice surface. Their estimate of charge transfer was found to be consistent with laboratory observations; however, in thunderstorms, appreciable charge transfer is observed at –35 C where surface melting cannot occur. Thus, at lower temperatures there must be some different mechanism, other than the surface melted QLL approach, to explain the collisional charging. In the present work a charge transfer mechanism is proposed based on surface defects formed during riming.

QUASI SOLID LAYER (QSL) CONCEPT:

Due to the random impact and rapid freezing of droplets during riming over the ice particle, various defects are formed in the surface structure of ice. As this process continues, the surface structure of ice deviates from its perfect crystalline nature. This type of disordered surface layer during riming is known as quasi-solid layer (QSL). The density of this QSL is much less than that of the crystalline ice, and the charged defects formed here during riming are the charge carriers in the proposed charge transfer model.

*Types of defects :* In the temperature region characteristic of the troposphere, generally hexagonal ice crystals are formed (*Shimaoka*, 1960). Only the oxygen atoms are crystallographically arranged in the ice lattice with the protons relatively randomly distributed following two Bernal & Fowler rules (*Glen*, 1968). Any breach of these rules gives rise to the formation of structural defects in ice.

In absence of any contaminants, the equilibrium concentration of ionic defects is generally very low compared to that of orientational defects (*Eisenberg and Kauzman*, 1969). The well known orientational defects as proposed by Bjerrum are L and D pair, but the electrostatic repulsion between two collinear protons in the D-defect makes it more metastable. Instead Dunitz [1963] proposed another type of orientational defect in which the two protons are not exactly collinear, termed as X-defects. These X-defects appear in pair with L-defects and are positively charged. These X-defects are also less active and more stable compared to its conjugate L-defects. In this model these L-X pairs are assumed to be the most abundant defects in ice structure.

Further, the mechanical stress due to the impact of droplets on the ice substrate may activate the self diffusion mechanism. Self diffusion is believed to occur due to the migration of entire water molecule within the lattice, creating vacancies at certain lattice positions (*Granicher*, 1969a). Onsager and Runnels (1963) proposed that during self diffusion the water molecule traverses several lattice distances through the lattice position. They have also shown

that the migration of diffusing molecules is faster than the migration of the orientational defects by one order of magnitude.

Now, during its journey through the interstitial space, the diffusing molecule may encounters an L-defect. The lone pair electrons in the L- will show an affinity to form hydrogen bonds with this interstitial molecule. Thus, an interstitial associate (LI associate ) will form (*Haas*, 1962) thereby immobilizing the diffusing molecule and leaving a vacancy. This creates a relatively inactive positive X-defect. Vacancies so formed in the riming process will provide more space for air inclusions within the structure and, thus, will appreciably reduce the density of rime ice (*Granicher*, 1969b). In fact, the density of rimed ice is found to be much less than the density of ordinary crystalline ice depending upon other environmental conditions (*Macklin*, 1962).

In this model, it is further assumed that there are no free negative ions available in the lattice to surround the positive charge so as to neutralize it. Thus, these inactive positive X-defects will remain near the surface of the ice particle and will act as charge carriers in the mass transfer process during collision. The number density of available positive charge carriers will be equal to the number density of LI associates formed. As the riming process continues, successive layers with positive defects will be deposited leading to the formation of the quasi-solid layer (QSL).

*Number density of defects formed:* As the riming process proceeds, the surface temperature of the particle becomes warmer because of the latent heat release. This will reduce the freezing rate that in turn reduces the number density of defects formed. Thus, a concentration gradient of defects across the depth of the rimed layer will be created. This gradient is assumed to be exponential

$$n(h) = n_s \exp(-h/h_m)$$

Where, $n_s$ is the concentration of defects at a layer adjacent to the core of the crystal substrate, n(h) is the concentration at a distance h from that adjacent layer and the scaling factor $h_m$ is the maximum possible depth of rimed mass over an ice particle for a specific condition. The scaling factor $h_m$ is estimated from a relative growth rate calculation ( *Datta et. al*, 1996).

Again, since the defects are considered to form by riming, the number of defects is a function of rate of accretion. For maximum possible rate of accretion $\alpha_m$ , the number of defect formed will be maximum ($n_m$). This $\alpha_m$ is given by

$$\alpha_m = W_m U_m R_m^2$$

where, $R_m$ is the maximum possible size of ice particle, $W_m$ is the maximum possible water content of a cloud and $U_m$ is the maximum possible fall velocity of ice particles.

It is assumed that no defects will form without accretion, i.e, when the rate of accretion $\alpha=0$, $n_s=0$. Keeping this view in mind a relation between accretion rate $\alpha$ and $n_s$ is written as

$$n_s = n_m\{1 - \beta_1 \exp(\alpha/\alpha_m)\}$$

where, $\alpha=W_1UR^2$ and $\beta_1 = 1- \alpha/\alpha_m$. The maximum number density of defects is the equilibrium concentration of defects (*Haas*, 1962) given by

$$n_m = N \exp(-Q_{LI}/kT_{av})$$

where, N is the number of molecules per unit volume, $Q_{LI}$ is the formation energy of LI associates, k is the Boltzman constant and $T_{av}=(T+T_s)/2$, when $T_s$ is the surface temperature of the riming particle.

*Charge transfer process:* It is assumed that during collision, the soft QSL part containing positive defect is shared by the two colliding bodies across the contact interface resulting in a transfer of charge after separation. During riming, the conductivity of ice particle increases (Saunders, 1993); thus, there is sufficient time for the transferred charge to be redistributed over the colliding rimed particle surface. As a result, large field cannot be developed during separation to initiate return flow of charge by corona as proposed by Keith and Saunders (1988).

The particle with thicker QSL will loose mass and the other, with thinner QSL, will gain mass. The former particle will thereby acquire a negative charge and the latter a positive charge. The sign of charge transfer will then be a function of relative growth rate that is consistent with the proposition of Baker et al. (1987). The magnitude of charge transfer will depend on the depth of QSL containing defects and the area of the contact interface. The equilibrium depth of QSL containing defects can be estimated from a free energy consideration.

## THE MODEL

*Assumptions:* (1) All particles are spherical in shape. (2) The distribution of cloud liquid water is uniform. (3) Due to the formation of vacancies and interstitials, there will be a redistribution of the layer charge. This gives rise to some electrostatic interaction; but only dipole interaction is considered, and the higher order terms are neglected. (4) Since elastic constant of rime is not available, the estimated elastic moduli of crystalline ice are equally applicable to rime ice. (5) The larger particles are falling with a characteristic fall velocity but the smaller ice crystals and super cooled liquid droplets are carried by the up or down draft within the cloud.

*Equations:* At a depth h the free energy of formation of LI associates is

$$(\Delta F_f)_h = \{n_s \exp(-\frac{h}{h_m})Q_{LI} - 2n_s kT_{ov} \exp(-\frac{h}{h_m})[\ln N - \ln n_s + \frac{h}{h_m}] - kT_{ov}[\ln 2 + \ln N] - Q_L$$

The dipole moment due to a single defect formation is

$$\mu = e_d x/\sqrt{2}$$

where x is the interstitial spacing and $e_d$ is the charge on a single defect. The net dipole moment is given by

$$M_e = n(h)\mu$$

and the associated electric field is given by

$$E_{di} = 4\pi M_e / \chi .$$

where $\chi$ is the dielectric constant which is again a function of temperature (*Eisenberg and Kauzman*, 1969). The total free energy change at depth h is therefore, $(\Delta F)_h = (\Delta F_f)_h + M_e E_{di}$. Thus, the net free energy change due to the whole layer of depth $h_T$ is

$$\Delta F = \int_0^{h_T} (\Delta F)_h dh$$

The equilibrium depth of QSL ($h_{QSL}$) is estimated minimizing $\Delta F$ with respect to $h_T$. The charge transfer during collision of two particles is then calculated as

$$\Delta q = \bar{n} e_d (h_{QSL2} - h_{QSL1}) \pi a_c^2$$

and

$$\bar{n} = \frac{n_1 + n_2}{2}$$

where, $n_i$ is the average number density of defects for particle I and $h_{QSLI}$ is the $h_{QSL}$ for particle I and $a_c$ is the radius of the contact area. The contact area is calculated using Hertz theory of impact (*Love*, 1944).

RESULTS

Table 1 : $\Delta q$ for graupel of radius 5.0 mm at T= -10 C and $W_l$=1.0 $gm^{-3}$

| Ice Crystal Radius $R_l$ (μm) | Draft speed $U_d$ ($ms^{-1}$) | $\Delta q$ in fC U: 5.0 m/s | 7.0 m/s | 9.0 m/s |
|---|---|---|---|---|
| 50 | 3.0 | 0.021 | 0.142 | 0.408 |
| | 5.0 | 0.000 | -0.049 | 0.022 |
| | 7.0 | -0.183 | 0.000 | -0.151 |
| | 9.0 | -0.531 | -0.347 | 0.000 |
| 100 | 3.0 | 0.070 | 0.425 | 1.190 |
| | 5.0 | 0.000 | -0.091 | 0.141 |
| | 7.0 | -1.404 | 0.000 | -0.290 |
| | 9.0 | -1.140 | -1.730 | 0.000 |
| 250 | 3.0 | 0.348 | 1.890 | 5.140 |
| | 5.0 | 0.000 | -0.157 | 0.995 |
| | 7.0 | -1.320 | 0.000 | -0.728 |
| | 9.0 | -3.610 | -2.230 | 0.000 |

Table 2: $\Delta q$ for graupel of radius 5.0 mm at T= -10 C and $U_d$=3.0 $ms^{-1}$

| $W_l$ In $Gm^{-3}$ | Impact speed $v_{imp}$ $ms^{-1}$ | $\Delta q$ in fC R1: 50 μm | 100 μm | 250 μm |
|---|---|---|---|---|
| 1.0 | 2.0 | 0.021 | 0.070 | 0.348 |
| | 4.0 | 0.142 | 0.425 | 1.890 |
| | 6.0 | 0.408 | 1.190 | 5.140 |
| 3.0 | 2.0 | 0.222 | 0.659 | 3.130 |
| | 4.0 | 1.350 | 3.590 | 15.000 |
| | 6.0 | 3.850 | 9.940 | 40.100 |
| 5.0 | 2.0 | 2.170 | 4.990 | 19.100 |
| | 4.0 | 11.800 | 24.200 | 82.400 |
| | 6.0 | 34.600 | 68.400 | 222.000 |

The results of the model are presented in Table 1 and Table 2. They show that the magnitude of charge transfer increases with increasing interacting particle size. This is quite obvious since the contact area in that case increases which in turn increases the amount of mass transfer. In the calculations presented here, the effective water accreted is directly proportional to the respective fall speed of the particle. Since the depth of QSL is actually dependent on the effective liquid water collected, the associated charge transfer also shows the dependence on the fall speed of the particle. $\Delta q$ is also found to increase with increasing liquid water content.

It is to be noted that the calculated order of magnitude of $\Delta q$ ($10^{-15}$ to $10^{-12}$ coulombs) agrees approximately with the experimental observations. Appreciable charge transfer is observed with this model down to -35 C.

The concept of QSL is not suitable above around -10 C depending upon the liquid water content of the cloud. Above that transition temperature the particle grows in wet growth regime which modifies the surface property of ice. The proposed charge transfer mechanism will be applicable only to the temperature region below this transition

temperature depending upon specific atmospheric conditions. Above this transition temperature the QLL hypothesis of charge transfer by Baker and Dash (1994) may apply. It should be noted that in case of QLL formalism, the sign of charge transfer is of opposite polarity to that considered in this work. So the transition temperature noted in this model may carry some implication to the well know charge sign reversal temperature observed in laboratory experiments.

ACKNOWLEDGEMENT : Part of the present work is carried out under a research fellowship grant by the Council of Scientific and Industrial Research (CSIR), India. Authors (SD and LJ) are also indebted to the NASA Tropical Rainfall Measuring Mission project of the Goddard Space Flight Center for supporting the continuation of this work.

REFERENCES

Baker B., Baker M.B., Jayaratne E.R., Latham J. and Saunders C.P.R., The influence of diffusional growth rates on the charge transfer accompanying rebounding collisions between ice crystals and soft hailstones, *Q.J.R.Meteorol.Soc.*,113, pp. 1193, 1987.

Baker M.B. and Dash J.G., Mechanism of charge transfer between colliding ice particles in thunderstorms, *J. Geophys.Res.*,99(D4), pp 10621, 1994.

Datta S., Goswami K., and De U.K, Depth of surface layer over ice during riming in super cooled atmosphere.,*Ind.J.Radio & Space Phys.*,25(2),pp 79,1996.

Dunitz J.D.,Nature of orientational defects in ice,*Nature*, 197(4870),pp.860, 1963.
Eisenberg D.and Kauzmann W.,*The Structure and Properties of Water*, Oxford University Press, Oxford, 1968.

Glen J.W., The effect of hydrogen disorder on dislocation movement and plastic deformation of ice, *Phys.kondens. Mat.*,7, pp.43, 1968.

Granicher H.,Review on problems of the physics of ice, *Physics of Ice*, (eds.) N. Reihl, B. Bullemer, H. Engelhardt, Plenum Press, New York, pp.1,1969a.

Granicher H.,On the interpretation of the pressure dependence of properties controlled by lattice defects. , *Physics of Ice*, (eds.) N. reihl, B. Bullemer, H. Engelhardt, Plenum Press, New York, pp.534,1969b.

Haas C., On diffusion relaxation and defects in ice, *Phys.Lett.*,3(3), pp.126, 1962.

Keith W.D. and Saunders C.P.R.,Light emision from colliding ice particles, *Nature*, 336, pp.362.1988.

Love, A.E.H., *A treatise on mathematical theory of elasticity,* Dover Pub. New York, 1944.

Macklin, W.C., The density and structure of ice formed by accretion, *Q.J.R. Meteorol. Soc.*, 88, pp.30,1962.

Onsager, L, and Runnels, L.K., mechanism for self diffusion in ice, *Proc. Natn. Acad. Sci,* 50, p. 208, 1963.

Saunders, C.P.R, A review of thunderstorm electrification processes, *J. Appl. Met.*, 32(4), pp. 642, 1993.

Saunders, C.P.R., Thunderstorm electrification laboratory experiments and charging mechanisms, *J. geophys. Res.*, 99(D5), pp. 10773, 1994.

Shimaoka, K., Electron diffraction study of ice, *J. Phys. Soc. Japan*, 15(1), pp. 106, 1960.

# ELECTRIC CHARGE ON RAINDROPS DURING THUNDERSTORM PRECIPITATIONS

P. Barański

Institute of Geophysics, Polish Academy of Sciences, Warsaw, Poland

ABSTRACT: The ground-based measurements of electric charge on the raindrops (or other precipitation particles) that was brought to the earth surface during thunderstorm were carried out in Warsaw thunderstorms throughout summer seasons of 1996, 1997 and 1998. The examination of the obtained data, together with the data from simultaneous measurements of the electric field and the Maxwell current (total and convective component), allowed us to distniguish different types of observed storms. The electrical parameters used to characterize the charge transport during the period of the considered rainfalls are as follows: numbers of positive ($N^+$) and negative ($N^-$) drops counted in the given time interval ($\Delta t$); total positive ($I_p^+$) and negative ($I_p^-$) precipitation current for $\Delta t$; total positive ($Q^+$) and negative ($Q^-$) electric charge of drops for $\Delta t$; average positive charge $<q^+>$ of a single drop for $\Delta t$; average negative charge $<q^->$ of a single drop for $\Delta t$; and precipitation charge density $D=(Q^++Q^-)/S$, where S is the entrance area of the measuring device. In spite of various difficulties discussed, ground based measurements of the electrical properties of thundercloud precipitation seem to be able to bring some valuable information concerning electrical structure and electrification processes acting in the observed cloud and below it.

## INTRODUCTION

Although the thundercloud electrification processes are strongly interrelated with the formation and the growth of precipitation particles, these relations of large significance are still not well understood by cloud physicists [*MacGorman et al.*, 1996]. For these and other reasons, any information that could enlarge our knowledge about electrical behaviour of precipitation particles from thunderstorms of various kind and their different development stages is still very desirable, including measurements made at the earth surface.

Observations of electrical properties of precipitation are worth attention not only in relation to problems of thunderstorm electrification. They concern also not sufficiently explained problems of lightning initiation, its occurrence and development. High correlation between the number of lightning flashes per minute and rainfall intensity was observed [*Piepgrass et al.*, 1982]. Initiation and development of lightning discharge is significantly influenced by the growth of smaller precipitation particles and the degree of their effectiveness is closely related to charge carried by drops [*Nguyen and Michnowski*, 1996]. On the other hand, *Nisbet* [1985] has pointed out that the role of precipitation current can be significant for the electric budget of thunderstorm generator and for the estimation of efficiency of this generator from current measurements performed at the earth surface. These measurements are involved also in investigation of the origin of small charge centers localized at the cloud base [*Williams*, 1989]. The precipitation transfer of charge from these centers is expected to be associated with positive electric field excursion observed with rain gushes at the earth surface [*Moore and Vonnegut*, 1977]. Sometimes, this highly localized transient event occurs in a negative electric field region beneath a thundercloud [*Marshall and Winn*, 1982; *Barański and Michnowski*, 1987) and then the precipitation current can enhance the electrical energy of an acting thundercloud generator. Another need of experimental determination of electric charges of precipitation particles and the current transported by them to the earth concerns the estimation of the precipitation contribution to the global electric balance of the earth surface [*Magono*, 1980].

## MEASUREMENTS AND THE SETUP OF THE MEASURING EQUIPMENT

Simultaneous measurements of the total Maxwell current, the convective component of this current, the space charge density, the electric field and meteorological parameters have been carried out on the flat roof of the detached building of the Institute of Geophysics in Warsaw during summer thunderstorms. The details of that site and its measuring equipment were described previously [*Barański*, 1996]. In summer of 1996, these measurements were extended to include the determination of the sign and magnitude of the electric charge on precipitation particles arriving to the earth surface. The new instrument designed for this purpose [*Warzecha*, 1996] was based on the principle of recording of the voltage induced during passage of each charged particle through an induction ring [*Gunn*, 1947].

The preamplifier and the AC-picoamperometer joined to the conducting ring measures the current induced on it. The measured magnitude of this current does not directly determine the total charge ($Q_o$) of falling drop but allows to get the charge (Q) induced on the ring which is strongly related to $Q_o$. The calibration procedure has to be done to obtain the value of calibration ratio $k=Q/Q_o$. By comparing the signal amplitude measured by the AC-picoamperometer at passage of precipitation particle through the ring with the amplitude of controlled calibrating current of 10 pA that was imposed through the ring, we obtained the calibration ratio, k, of 0.1. This value corresponds to the frequency band from 20 Hz to 200 Hz of calibrating current variations which simulates the changes of falling drop velocities from 1 m/s to 10 m/s. The accuracy of the obtained measurement corresponds to the error of 2% for frequency current changes greater than 20 Hz.

The charge calibration characteristics (pC) versus precipitation current (pA) for positively and negatively charged drops have been achieved using a simple charged drop generator with a metal syringe needle connected to a voltage generator and fed with water from a small tank.

The sign of the electric field and current is taken as positive, if there are positive charges aloft and if they move downwards the earth surface.

## RESULTS AND DISCUSSION

The first example of 30 August, 1996, concerns the intense rainfall, with the maximum rain intensity of 31.2 mm/h (19:35÷19:40 LT), in measuring site placed then within the reversal distance from the approaching thunderstorm. The values of the electrical parameters used to characterize the charge transport during the period of studied rainfall in thunderstorm of 30 August, 1996, are listed in Table 1. In the last four columns, there are also presented the averaged, over $\Delta t$, values of: the electric field intensity $\langle E_{EXT}\rangle$, the total Maxwell current $\langle I_{AOC}\rangle$, the convective component of Maxwell current $\langle I_{AIC}\rangle$, and the space charge density $\langle\rho\rangle$. The time intervals in the first column of Table 1 are chosen as those laying between the largest jumps of the electric field caused by lightning discharges. This allows us to reduce the interference of lightning transient into averaging of simultaneous records of analyzed courses by graphical integration.

The results of Table 1 clearly show that the thunderstorm rainfall of 30 August, 1996, is characterized by dominant negative raindrop charge transport with a density of the order of (-0.30±0.95) $\mu C/m^2$ . Although the total recorded numbers $N^+$ and $N^-$ are similar, i. e., the ratio $N^+/N^-=0.94$, the negative balance of charge transport in the whole precipitation period ($Q^++Q^-$) is evident and equals -1025 pC. In the considered case, the mean charge of positively charged drops is (14.7±4.9) pC, while the mean charge of negatively charged ones is somewhat grater and equals (-18.6±11.5) pC. These results are consistent with the values obtained by *Chauzy and Despiau* [1980] in a temperate region of France. However, there is a significant difference between our data and the French results, which follows from the opposite charge polarity of the resultant raindrop charge transport to the earth surface. It may be caused by a different electrical structure of the thunderclouds.

In our case, we believe that the observed thundercloud has been a typical dipole with the main negative charge center at the bottom and that the precipitation particles which have arrived to the earth surface originated from that cloud region. This conclusion is supported by additional measurements of $E_{EXT}$ , $I_{AOC}$, $I_{AIC}$ and $\rho$ during that rainfall (see the four last columns in Table 1). The negative deflections of $E_{EXT}$ and $I_{AOC}$ together with negative value of $\rho$ and positive convective component of Maxwell current, $I_{AIC}$, are due to the fact that all of them have been connected to the dominant negative charge transport to the earth surface by raindrops.

The second case examined is that of the rainfall from thunderstorm on 24 July, 1997, with the maximum rain intensity of 34.5 mm/h in time interval 15:02÷15:06 LT. Its main electrical structure is given in Table 2, in a similar form as for the former case. But because of the short duration of the intense rain period in thunderstorm on 24 July, 1997, we arbitrarily divided it into 1-minute intervals to calculate the values of the electrical parameters indicated in Table 2.

Here we have another situation. The raindrop charge transport to the earth surface during that rainfall is distinctly positive and gives the density of the order of (0.65±0.63) $\mu C/m^2$. Thus, $N^+$ is much grater than $N^-$ and the ratio $N^+/N^-=3.4$. Also the positive balance of charge transport in the whole period of intense rain (in that case only 10 minutes), i. e., ($Q^++Q^-$), is clearly seen and equals 1538 pC. However, the individual charge linked to a single drop during this rainfall is lower than in the previous case. Its mean value is (7.0±3.8) pC for positively charged drops and (-5.8±3.7) pC for negatively charged ones. These small values are still in accordance with the results obtained by *Chauzy and Despiau* [1980] for some cases of thundershowers.

We attribute the dominant positive charge transport to the earth surface observed during the intense 24 July, 1997, thunderstorm rainfall to a probable removal of the lower positive charge center (LPCC) from the thundercloud caused by a downdraft appearing during heavy precipitation [*Holden et al.*, 1983]. This interpretation is confirmed by great positive deflections of $E_{EXT}$ and $I_{AOC}$ (see Table 2). Unfortunately, this polarity of a long lasted change has not appeared in the course of $I_{AIC}$. This may be explained by strong and frequently variable air turbulence impact on the resultant convective component of Maxwell current in time when downdraft flow reaches the earth surface.

TABLE 1. Values of electrical parameters characterizing the raindrop charge transport to the earth surface and measured during intense rainfall from the 30 August, 1996, thunderstorm in Warsaw. LT denotes local time

| Time interval (LT) | $N^+$ | $I_p^+$ [pA] | $Q^+$ [pC] | $N^-$ | $I_p^-$ [pA] | $Q^-$ [pC] | $Q^+ + Q^-$ [pC] | $<q^+>$ [pC] | $<q^->$ [pC] | D [μC/m²] | $<E_{EXT}>$ [kV/m] | $<I_{AOC}>$ [nA] | <ρ> [nC/m³] | $<I_{AIC}>$ [nA] |
|---|---|---|---|---|---|---|---|---|---|---|---|---|---|---|
| 19 24 40-19 25 28 | 20 | 443 | 221 | 3 | -138 | -65 | 156 | 11 1 | -21 7 | 0 50 | 8 6 | 15 | -2.3 | 0 6 |
| 19 25 28-19 26 44 | 36 | 916 | 457 | 13 | -422 | -195 | 262 | 12 7 | -15 | 0 83 | 3 5 | 12 | -3 | 0 6 |
| 19 26 44-19 28 19 | 13 | 352 | 175 | 43 | -2048 | -943 | -768 | 13 5 | -21 9 | -2 45 | -10 5 | -21 | -0 4 | 1 2 |
| 19 28 19-19 30 03 | 12 | 554 | 276 | 37 | -1564 | -720 | -444 | 23 | -19 5 | -1 41 | -7 | -10 5 | -0 7 | 0 8 |
| 19 30 03-19 32 13 | 16 | 460 | 229 | 34 | -750 | -346 | -117 | 14 3 | -10 2 | -0 37 | -14 | -7 5 | -1 2 | 0 7 |
| 19 32 13-19 34 28 | 58 | 2272 | 1135 | 22 | -2248 | -1035 | 100 | 19 6 | -47 | 0 32 | 14 | 9 | -2 3 | 0 3 |
| 19 34 28-19 36 28 | 33 | 1470 | 734 | 26 | -1608 | -741 | -7 | 22 2 | -28 5 | -0 02 | -1 8 | 6 | -2 1 | 0 4 |
| 19 36 28-19 38 21 | 8 | 192 | 95 | 13 | -336 | -156 | -61 | 11 9 | -12 | -0 19 | -7 | -3 | -1 2 | 0 5 |
| 19 38 21-19 39 57 | 8 | 184 | 91 | 14 | -228 | -106 | -15 | 11 4 | -7 6 | -0 05 | -5 3 | -3 | -0 8 | 0 5 |
| 19 39 57-19 42 16 | 17 | 490 | 244 | 16 | -290 | -135 | 109 | 14 4 | -8 4 | 0 35 | -3 5 | -3 | -1 | 0 5 |
| 19 42 16-19 45 24 | 10 | 156 | 77 | 25 | -686 | -317 | -240 | 7 7 | -12 7 | -0 76 | -7 | -4 5 | -1 | 0 5 |
| Σ | 231 | | 3734 | 246 | | -4759 | -1025 | | | | | | | |

TABLE 2. The same as for Table 1, except that in 24 July, 1997

| Time interval (LT) | $N^+$ | $I_p^+$ [pA] | $Q^+$ [pC] | $N^-$ | $I_p^-$ [pA] | $Q^-$ [pC] | $Q^+ + Q^-$ [pC] | $<q^+>$ [pC] | $<q^->$ [pC] | D [μC/m²] | $<E_{EXT}>$ [kV/m] | $<I_{AOC}>$ [nA] | $<I_{AIC}>$ [nA] |
|---|---|---|---|---|---|---|---|---|---|---|---|---|---|
| 14 57-14 58 | 6 | 27 6 | 13 | 2 | -10 4 | -5 9 | 7 1 | 2 2 | -3 0 | 0 02 | 4 8 | -1 2 | 0 02 |
| 14 58-14 59 | 38 | 404 8 | 201 6 | 5 | -43 2 | -21 0 | 180 6 | 5 3 | -4 2 | 1 15 | 10 4 | 9 6 | -0 27 |
| 14 59-15 00 | 32 | 280 | 139 2 | 6 | -44 8 | -21 7 | 117 5 | 4 4 | -3 6 | 0 75 | 5 6 | 2.4 | -0 13 |
| 15 00-15 01 | 14 | 103 2 | 50 8 | 16 | -93 6 | -44 2 | 6 6 | 3.6 | -2 8 | 0 02 | -1 6 | -1 2 | 0 16 |
| 15 01-15 02 | 35 | 832 8 | 415 6 | 17 | -310 8 | -144 1 | 271 5 | 11 9 | -8 5 | 0 86 | 12 0 | 26 4 | -0 24 |
| 15 02-15 03 | 45 | 870 | 434 2 | 4 | -36 | -17 7 | 416 5 | 9 6 | -4 4 | 1 33 | 7 2 | 16 8 | -3 2 |
| 15 03-15 04 | 43 | 1002 | 500 2 | 5 | -30 | -14 9 | 485 3 | 11 6 | -3 0 | 1 55 | 9 6 | 26 4 | -2 4 |
| 15 04-15 05 | 20 | 408 | 203 2 | 9 | -207 | -96 3 | 106 9 | 10 2 | -10 7 | 0 34 | 0 | 12 0 | -0 4 |
| 15 05-15 06 | 2 | 18 | 8 2 | 5 | -132 | -61 8 | -53 6 | 4 1 | -12 4 | -0 17 | -10 4 | -2 4 | 0 4 |
| Σ | 235 | | 1966 | 69 | | -428 | 1538 4 | | | | | | |

The obtained averaged value of D (see Table 2) makes it possible to estimate how large is the LPCC connected with a tripole electrical structure of the observed thundercloud. If we assume that the intense rain shaft during the 24 July, 1997, thunderstorm rainfall obeys the 2×2 km area, then the estimation of the amount of the LPCC will give a value of (2.6÷2.4) C. This is in a good agreement with the observations reported by *Jacobson and Krider* [1976].

Table 3. Rain intensity and values of electrical parameters characterizing the precipitation charge transport to the earth surface during two summer thunderstorms in 1998, in Warsaw

| Date<br>Time interval (LT) | Rain intensity [mm/h]<br>(duration LT) | $N^+$ | $N^-$ | $N^+/N^-$ | $(I_p^+ + I_p^-)$ [pA] | $(Q^+ + Q^-)$ [pC] | $<q^+>$ [pC] | $<q^->$ [pC] | <D> [μC/m²] |
|---|---|---|---|---|---|---|---|---|---|
| 22 May<br>15:42÷15:52 | 1.2<br>(15:42÷15:52) | 42 | 49 | 0.86 | -348 | -150 | 4.5±5.1 | -6.2±1.7 | -0.05±0.13 |
| 14 August<br>13:56:47÷14:03:58 | 9.0<br>(14:00÷14:02) | 46 | 15 | 3.1 | 174 | 82 | 4.6±2.8 | -4.1±2.7 | 0.044±0.03 |

Results of summer 1998 measurements are summerized in Table 3. The total values of $(I_p^+ + I_p^-)$, $(Q^+ + Q^-)$, $<q^+>$, $<q^->$ and <D> listed in that table are obtained from their 1-minute means for the case of 22 May, 1998. For

the second case of 14 August, 1998, the time interval between close lightning discharges (approximatively also 1-minute period) was used to evaluate these individual means of the considered electrical parameters. Especially interesting is the thunderstorm of 14 August, 1998, when, because of the observed negative polarity of all close lightning discharges from the single thundercell, we can assume that this thundercell may be represented by a rare negative dipole with positive charge layer in the cloud base. On the other hand, the thunderstorm of 22 May, 1998, in accordance with the obtained field mill and Maxwell current recordings at that time, can be connected with a positive dipole far away from our measuring site and having an extended negative charge layer in the cloud base.

Measurement data such as those presented above are not sufficient to describe quantitative relationships between precipitation charge transport and variations of the electric field and currents at the earth surface and their relations to the intracloud processes. A much more complicated cause-effect chain exists between them to be studied by measurements limited to one observation site. Nevertheless, the determination of the sign and amount of the electric charge arrived to the earth surface with raindrops during thunderstorm rainfalls allows us to verify some hypotheses concerning the important role played by charged precipitation particles in the development of a thundercloud electrical activity.

## REFERENCES


Barański, P., and S. Michnowski, Variations of the electric field and precipitation measured under thunderclouds in Warsaw, *Publ. Inst. Geophys. Pol. Acad. Sc.*, D-26 (198), 59--74, 1987.

Barański, P., Electric charge transport to the earth surface by precipitation accompanying downdrafts from nearby thunderstorms, *Acta Geoph. Pol.*, XLIV, No. 4, 383--389, 1996.

Chauzy, S., and S. Despiau, Rainfall rate and electric charge and size of raindrops of six spring showers, *J. Atmos. Sci.*, 37, 1619--1627, 1980.

Gunn, R., The electrical charge on precipitation at various altitudes and its relation to thunderstorms, *Phys. Rev.*, 71, 181--186, 1947.

Holden, D. N., C. R. Holmes, C. B. Moore, W. P. Winn, J. W. Cobb, J. E. Griswold, and D. M. Lytle, Local charge concentrations in thunderclouds, *In: „Proceedings in Atmospheric Electricity" eds. Ruhnke L. H., and J. Latham*, A. Deepak Publishing, Hampton, Virginia, 179--183, 1983.

Jacobson, E. A., and E. P. Krider, Electrostatic field changes produced by Florida lightning, *J. Atmos. Sci.*, 33, 103--117, 1976.

MacGorman, D. R., C. L. Ziegler, and J. M. Straka J, Considering the complexity of thunderstorm electrification, *Proc. of the X-th ICAE, June 10-14, Osaka, Japan*, 128--131, 1996.

Magono, C., Thunderstorms, Elsevier Scientific Publishing Company, Amsterdam, Oxford, New York, 43--76, 1980.

Marshall, T. C., and W. P. Winn, Measurements of charged precipitation in a New Mexico thunderstorm: Lower positive charge centers, *J. Geophys. Res.*, 87, 7141--7157, 1982.

Moore, C. B., and B. Vonnegut, The thundercloud, *In: Golde R. H. (ed.), „Lightning"*, vol.1, 51--98, Academic Press, New York, 1977.

Nguyen, M. D., and S. Michnowski, On the initiation of lightning discharge in a cloud, 1, The lightning initiation on precipitation particles, 2, *J. Geophys. Res.*, 101, 26675--26680, 1996.

Nisbet, J. S., Thundercloud current determination from measurements at the earth's surface, *J. Geophys. Res.*, 90, 5840--5856, 1985.

Piepgrass M. V., E. P. Krider, and C. B. Moore, Lightning and surface rainfall during Florida thunderstorms, *J. Geophys. Res.*, 87, 11193--11201, 1982.

Warzecha S., AC-picoamperometer, *Technical report, Archives of Atmos. Electricity Lab. of Inst. Geophys. Pol. Acad. Sci.*, Warsaw, 1996.

Williams, E. R., Tripole structure of thunderstorms, *J. Geophys. Res.*, 94, 13151--13167, 1989.

Reversal of the Sign of the Charge on Graupel during Riming Electrification: Measurements in Hokuriku Winter Clouds and in a Wind Tunnel

Tsutomu Takahashi
School of International Studies, Obirin University, Machida, Tokyo, Japan

ABSTRACT: Riming electrification was examined in a wind tunnel in which semi-hemispherical ice particles were floated in updrafts of either 3 or 9 $ms^{-1}$. Cloud drops and ice crystals were then introduced into the tunnel and the ice particles were subsequently forced to fall through an induction ring. The experiments were conducted in three different critical regimes: water content at 1 gm $m^{-3}$ at −15 °C; water content at 0.2 gm $m^{-3}$ and −15 °C; and water content at 1 gm $m^{-3}$ and −5 °C. The results of the experiments showed the ice particles to be highly charged when both cloud drops and ice crystals were supplied and the charge sign reversal to occur at the temperature and cloud water content previously reported by Takahashi (1978).

## INTRODUCTION

There is now general agreement that the major charge separation process in thunderstorms occurs during collisions between graupel and ice crystals. Both the magnitude and the sign of the separated charge greatly depend upon cloud temperature and cloud water content (Takahashi 1978; Jayaratne et al. 1983). Results from a numerical thunderstorm model reported by Takahashi (1984) showed that the electric charge sign reversal is essential in building the tri-pole structure as well as intensifying the negative charge in the storm. However, the temperature at which the charge sign reversal occurs differ significantly in the reports by Saunder's group and by Takahashi. The reason for the differences have been extensively examined by Williams and Zhang (1993) without any firm conclusions having been reached. The present author and his colleagues have attempted to examine this problem from two directions: wind tunnel experiments and evidence from natural clouds.

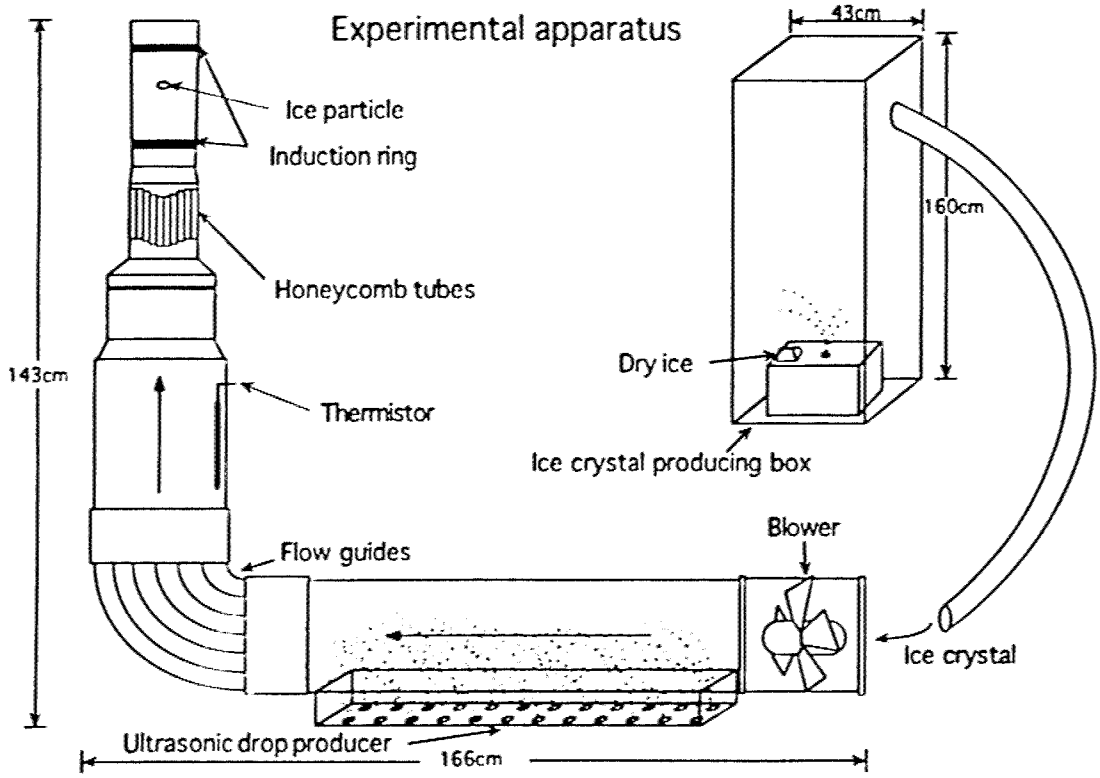


Fig. 1. Experimental apparatus.

WIND TUNNEL EXPERIMENT

An L-shaped wind tunnel was constructed inside of a cold room (Fig. 1). A parabolic, vertical wind profile with a minimum at the center was obtained by adjusting the configuration of the honeycombed tubes in the tunnel. Concave hemispheres of ice, 18 mm diameter, could then be suspended in the airflow. Induction rings were installed at the upper and lower ends of the tunnel, 15 cm apart and the hemispheres floated between the rings. The electric charge on the ice was measured by reducing the wind speed and thus forcing the hemispheres to fall through the lower ring.

Cloud droplets, with a modal diameter of 7 $\mu$m, were produced by an ultrasonic humidifier. The cloud water content was estimated by measuring the mass of rimed ice on a thin wire exposed in the airflow. Ice crystals with a modal diameter of 11 $\mu$m, were formed in a separate box, using dry ice as a nucleator. The experiments were conducted in air flows of 3 and 9 $ms^{-1}$ and only the sign of the charge was examined.

The experimental procedure was as follows: the ice hemisphere was first suspended in the airflow, following which the cloud droplets were introduced followed by the ice crystals. The speed of the airflow was then reduced and the hemisphere fell through the lower induction ring. Before the experiments were run, a series of tests were conducted using only droplets or ice crystals to insure that they produced no substantial charges.

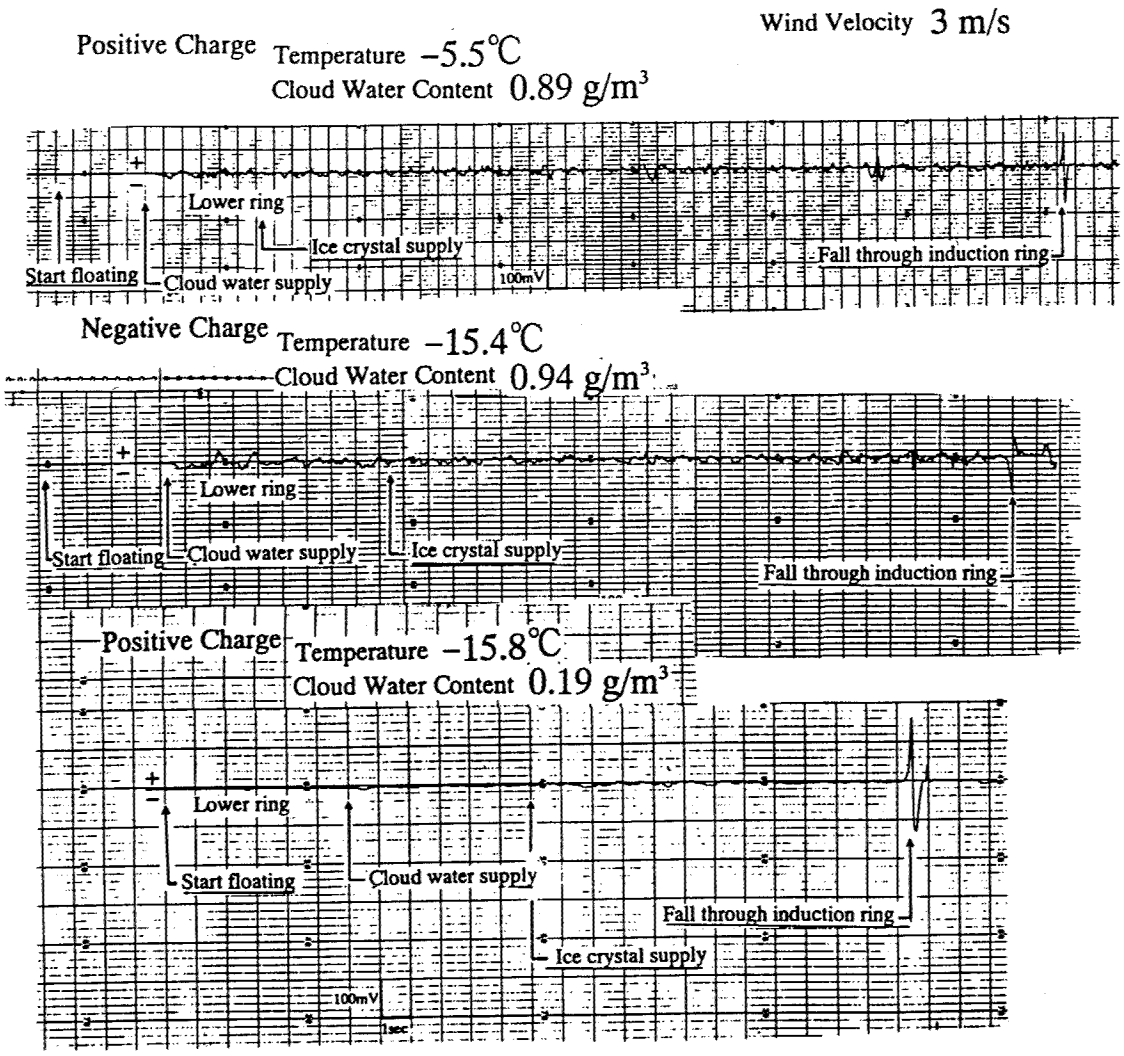


Fig. 2. Examples of experiment.

Three critical combinations of temperatures and cloud water contents were used in the experiments: ~ -15°C and 0.2 gm$^{-3}$; ~ -15°C and 1 gm$^{-3}$; and ~ - 6°C and 1 gm$^{-3}$. In the first set of conditions Takahashi (1978) found positively charged graupel and Jayaratne et al. (1983) reported that graupel were negatively charged. In the second set, Takahashi found negatively charged graupel and Jayaratne et al. reported positive charge. In the third set of conditions, Takahashi found the graupel to be positively charged.

The experimental results showed the ice hemispheres to be positively charged at ~ -15°C and 0.2 gm$^{-3}$; negatively charged at ~ -15°C and 1 gm$^{-3}$; and positively charged at ~ -6°C and 1 gm$^{-3}$ (Fig. 2). The charge sign reversal was independent of the airflow velocity (Fig. 3). These results appear to support Takahashi's 1978 report.

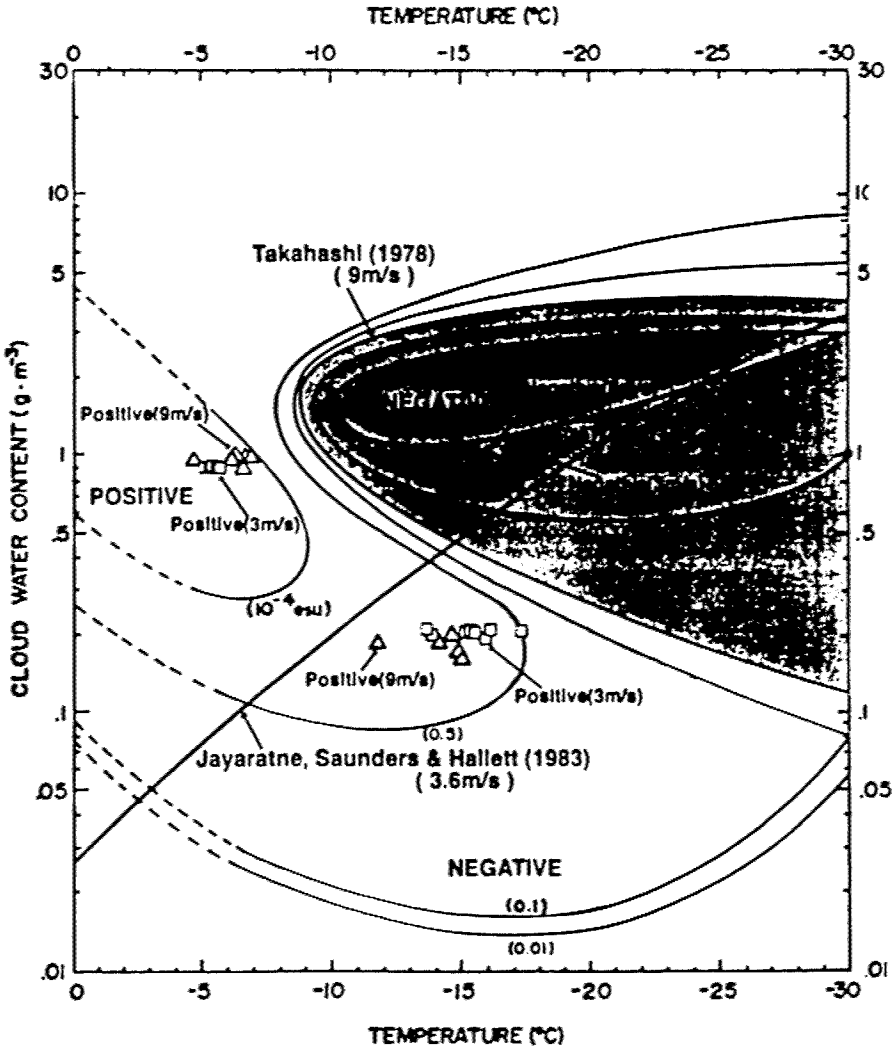


Fig. 3. Experimental results on charge sign with respect to cloud water content and temperature.

HOKURIKU WINTER CLOUDS

During the winter season in Hokuriku, Japan, it is not unusual to observe lightning from snow clouds, even in clouds no deeper than five kilometers. During 1993 to 1995, 19 videosondes were launched into winter clouds from Joetsu and Tsunekami, Hokuriku. The shapes of precipitation particles and the charge on them are determined from videosonde data in which particles larger than 0.5 mm diameter interrupt an infrared light beam, triggering a flash and a videocamera that captures the particle image. The charge is measured by an induction ring and the data is transmitted to a receiving station on the ground over a 1680 MHz carrier wave.

In four cases that contained sufficient information, the number of positively charged graupel clearly increased below about -10°C in the cloud (Fig. 4, Takahashi et al., 1999). In one case in which the updraft was about 5 $ms^{-1}$, indicating the cloud to be in a developing stage, many negatively charged graupel existed just above about -10°C. The cloud water content in such a developing cloud has been reported to be approximately 1$gm^{-3}$ and the observations given above appear to support Takahashi's laboratory work.

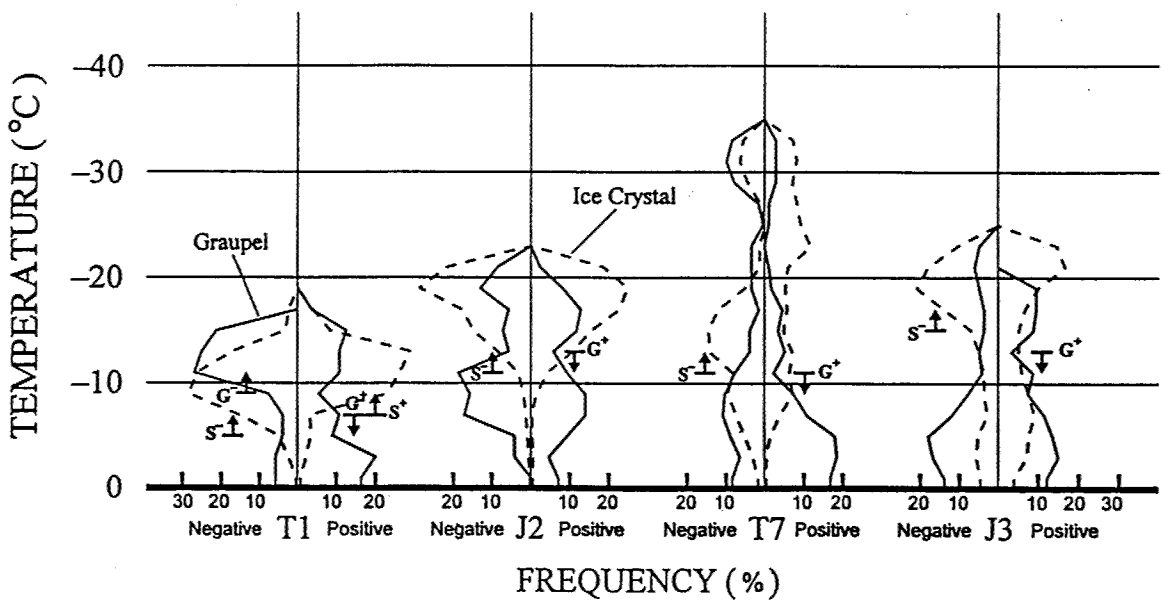


Fig. 4. Frequency of charge sign of graupel (solid line) and ice crystals (dashed line) in Hokuriku winter cloud.

RERERENCES


Jayaratne, E.R., C.P.R. Saunders and J. Hallett, Laboratory studies of the charging of soft hail during ice crystal interactions, *Q. J. R. Meteorol. Soc.*, 109, 609-630, 1983.

Takahashi, T., Riming electrification as a charge generation mechanism in thunderstorms, *J. Atmos. Sci.*, 35, 1536-1548, 1978.

Takahashi, T., T. Tajiri and Y. Sonoi, Charges on graupel and snow crystals and the electrical structure of winter thunderstorms, in press, *J. Atmos. Sci.*, 1999.

Williams, E., and R. Zhang, Comment on "The effect of liquid water on thunderstorm charging" by C.P.R Saunders et al., *J. Geophys. Res.*, 98, 10819-10821, 1993.

# SEPARATION OF CHARGE DURING REBOUNDING COLLISIONS BETWEEN GRAUPEL AS A POSSIBLE MECHANISM OF THUNDERSTORM ELECTRIFICATION

E. Rohan Jayaratne

Dept of Physics, University of Botswana

ABSTRACT: A laboratory study was conducted in a large chest freezer to determine the sign and magnitude of the electric charge separated during rebounding collisions between graupel. A cloud of supercooled droplets was drawn through a tube to form a deposit of soft rime on a wire mesh. A rimed metal rod simulating a graupel pellet was mounted downwind of the mesh. The rod could be heated or cooled by means of a Peltier element. With the air flow on, tiny fragments of rime were gently dislodged from the mesh and allowed to impact on the graupel target. The charge separated on impact was measured at an air temperature of -15°C. The graupel charged negatively when it was warmer than the fragments of rime and positively when its temperature was more than about 2°C colder. The introduction of droplets into the airstream shifted the charge reversal temperature to warmer values. In nature, owing to the latent heat released by the accretion of supercooled droplets, larger graupel pellets are generally warmer and fall faster than the smaller pellets. Resulting interactions between these particles followed by subsequent gravitational separation may thus lead to a dipolar charge structure with the smaller positively charged graupel above the larger negatively charged pellets. It is suggested that this process may form the basis of a viable charge generation mechanism in thunderstorms which may explain the reported existence of graupel pellets carrying charges larger than that can be expected by interactions with vapor-grown ice crystals alone.

## INTRODUCTION

Ice crystals, once they have grown to a size of a few hundred micrometers, begin to accrete supercooled droplets. The onset of riming depends on the shape of the crystals and may range from about 150 μm for hexagonal plates to about 800 μm for dendrites. The resulting graupel or soft-hail have bulk densities of 0.05 to 0.89 g $m^{-3}$ (Pruppacher and Klett, 1997). Updrafts of 10-20 m $s^{-1}$ can support graupel pellets as large as 10 mm and are found in concentrations up to 10 $L^{-1}$ in the active parts of thunderstorms (Dye et al. 1986; Weinheimer et al. 1991). These carry individual charges of up to a few hundred pC giving charge densities of about 10C $km^{-3}$ in the high-field regions within thunderstorms. Gardiner et al (1985) made particle size and charge measurements in a Montana summer thunderstorm at a level where the temperature was -5°C and found that only about 10% of the particles carried a charge greater than ±5 pC. Of these, no more than 10% had a charge greater than 25 pC. Weinheimer et al found 2-4 mm graupel carrying charges of 10-100 pC in a New Mexico thundercloud but noted that only a few of the graupel pellets were charged. They also noted the absence of pristine large ice crystals (>500 μm) in the highly charged regions and suggested that the charge separation may be a consequence of rebounding collisions between graupel pellets.

Laboratory experiments so far have concentrated on the charge separation during rebounding collisions between vapor-grown ice crystals and riming graupel (Takahashi, 1978; Jayaratne et al. 1983). No work has been done on the charging during graupel-graupel interactions. The charge acquired by a graupel pellet per crystal collision increases sharply with crystal size up to about 450 μm and remains fairly constant thereafter. The maximum charge that has been measured in the laboratory is about +220 fC with dendritic crystals of size 800 μm while plate crystals of the maximum size of 300 μm gave a charge of only 90 fC (Keith and Saunders, 1990). Typically, crystals of size 100 μm separate charges of the order of 10-100 fC. Baker et al (1987) have suggested that the sign of the charge separated is controlled by the relative growth rates of the two interacting surfaces such that the particle with the faster-growing surface acquires the positive charge. Avila and Caranti (1994) showed that 100 μm ice spheres impacting on a riming graupel at a speed of 5 m $s^{-1}$ knocked off charged rime and frost fragments. Jayaratne et al (1996) showed that grains of sand of size 200-500 μm produced many ice fragments while particles of the order of a few tens of micrometers did not. Takahashi et

al (1995) showed that many ice fragments were produced when two rimed graupel pellets were impacted together. However, they did not carry out any measurements of the charge separated.

## EXPERIMENTAL DETAILS

The experiments were performed in a large chest freezer in which a cloud of supercooled droplets were produced by passing steam from a boiler. The cloud could be sucked out through a tube of internal diameter 3 cm at controllable speeds. A stainless steel rod of diameter 5 mm and length 1.5 cm was mounted within the tube, at a distance of 4 cm from its opening, to simulate the target graupel pellet. The rod was attached to a Peltier element so that it could be heated or cooled with respect to the airstream. The target and air temperatures were measured with thermocouples. A sensitive electrometer was connected to the rod to measure any charge acquired. The smallest detectable charge was 0.2 pC. A flat circular wire grid made of thin steel wire spaced 3.5 mm apart was fitted over the opening of the tube.

## RESULTS

The steam supply rate was controlled to obtain a cloud water content (CWC) of 0.5 g $m^{-3}$ at an air temperature of -15 °C. The air flow was set to 5 m $s^{-1}$ until both the mesh and the rod were covered with about 2 mm of soft rime. The steam supply was removed to allow the cloud to dissipate completely. The Peltier element current was switched on to cool the target rime by about 4 °C. The flow was reintroduced at 10 m $s^{-1}$ and tiny fragments of rime were gently dislodged from the wire mesh. Each time one of these fragments impacted with the target rime, a charge transfer was recorded. Charges up to about 10 pC were recorded. The Peltier current was switched off and readings were taken as the target temperature approached -15 °C. Then the current was reversed to allow the rime to slowly warm up to about -10 °C while continuing to record the charge transfer values. One such run is shown in Fig 1.Each point is a single charging event. Note that the charge transferred by the rime fragment to the target rime was more likely to be positive when the target was

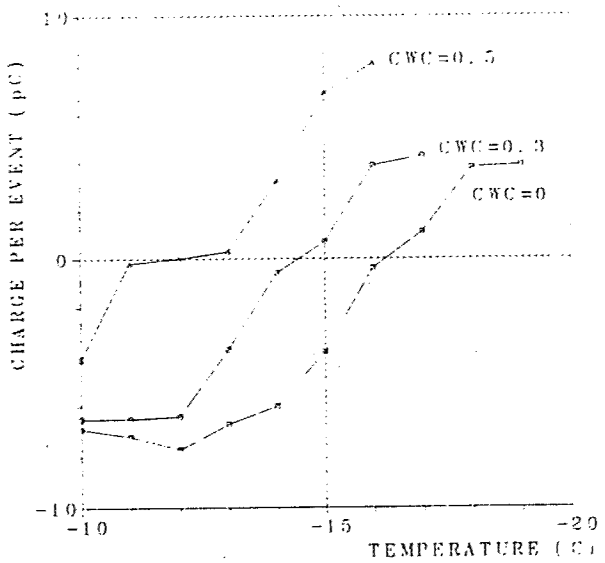


**Fig 1**

A typical experimental run showing the charges transferred to the rimed target by each rebounding rime fragment as the target rime temperature was varied. CWC=0. Air temperature = -15 °C. Impact speed = 10 m $s^{-1}$.

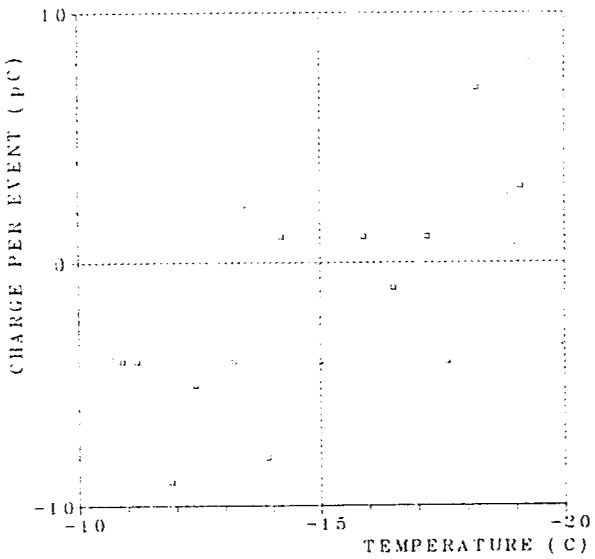


**Fig 2**

Mean values of charge transfer measured in all runs at each of three values of CWC. Each point is the mean of all readings obtained within 0.5 °C of each target rime temperature. Air temperature = 15 °C. Impact speed = 10 m $s^{-1}$.

colder than the fragments and negative when it was warmer. Several such runs were carried out. In some of the runs, the target was first heated and allowed to cool in the air stream. The average of all the charge values obtained within ±0.5°C of each degree of temperature was calculated for each temperature and this curve is shown in Fig 2 as "CWC=0". The experiment was repeated at CWC's of 0.3 and 0.5 g m$^{-3}$ and the results also appear in Fig 2. Note that the charge sign reversal temperature shifted to higher values as the CWC was increased.

## DISCUSSION OF RESULTS

The results show that charges of a few pC are separated when graupel pellets rebound off each other. Positive charge appears to flow from the graupel that is evaporating to the graupel that is growing. At zero CWC, the rime target charged negatively even when it was slightly cooler than the airstream. However, as the temperature increased, it is likely that the target rime began to evaporate in the undersaturated airstream even before its temperature attained the ambient air temperature. With droplets present in the airstream, the target continued to charge positively even after the rime temperature exceeded the air temperature of -15°C. Supercooled droplets produce vapor while freezing and this vapor supply makes the area surrounding the droplet grow. Overall, a greater percentage of the target rime surface would be in a state of growth, thus explaining the enhanced positive charging with increasing CWC. It follows that a riming graupel pellet charges more positively at higher CWC's whether the impacting particle be a rime fragment (this study), a vapor-grown ice crystal (Jayaratne et al. 1983; Baker et al. 1987) or a grain of sand (Jayaratne 1991).

Jayaratne et al (1996) argued that vapor-grown ice crystals are not able to fracture rime branches on graupel at typical impact speeds. However, it is clear that particles with greater momentum such as 100 μm frozen droplets (Avila and Caranti, 1994) and 200 μm grains of sand (Jayaratne et al. 1996) do give rise to rime or frost fragments during impacts with riming graupel. Although we know that graupel-graupel collisions give rise to fragmentation of ice (Takahashi et al. 1995), it is not yet clear whether the separation of charge is a consequence of this fracture mechanism.

## APPLICATION TO THUNDERSTORMS

The presence of charged graupel in high field regions of thunderstorms in the absence of pristine ice crystals raises the possibility of a graupel-graupel charge separation mechanism in addition to the well studied ice crystal-graupel mechanism. Laboratory experiments have shown that the magnitude of the charge separated increases dramatically with particle size and impact velocity (Jayaratne et al. 1983; Keith and Saunders, 1990). Theoretical models have stressed the importance of the larger ice particles in contributing to the charge densities in thunderstorms (Scavuzzo et al. 1998). The observation of only a few ice particles carrying the bulk of the charge in thunderstorms suggests that the charge separation must occur due to a few large charge transfer events rather than many small charge transfer collisions such as would be expected when graupel fall through a cloud of ice crystals. No charge transfer is possible when two identical surfaces touch; there needs to be an assymetry to drive the charge in a preferred direction between the two particle surfaces. Temperature differences, or to be more precise differences in growth (and evaporation) rates, appear to provide this assymetry in the case of graupel.

Graupel are generally warmer than the ambient air owing to the latent heat provided by freezing droplets. Heat balance equations have shown that, at a given CWC and cloud temperature, the larger the graupel, the warmer its surface will be (Macklin and Payne, 1967). The present results suggest that, during collisions between graupel pellets, larger graupel are more likely to acquire a negative charge while the smaller pellets are expected to charge positively. Differential fall velocities would then give a dipolar charge structure with the positive charge above. This does not quite agree with the classical dipolar and tripolar charge structures that have been observed in thunderstorms but, together with the competing mechanism of ice crystal-graupel charging, may offer an explanation for the more complex charge structures that are now being observed (Stolzenburg et al. 1998).

REFERENCES


Avila, E.E. and G.M. Caranti, A laboratory study of static charging by fracture in ice growing by riming, *J. Geophys. Res.*, 99, 10611-10620, 1994.

Baker, B., M.B. Baker, E.R. Jayaratne, J. Latham and C.P.R. Saunders, The influence of diffusional growth rate on the charge transfer accompanying rebounding collisions between ice crystals and hailstones, *Quart. J. R. Meteorol. Soc.*, 113, 1193-1295, 1987.

Dye, J.E., J.J. Jones, W.P. Winn, T.A. Cerni, B. Gardiner, D. Lamb, R.L. Pitter, J. Hallett and C.P.R. Saunders, Early electrification and precipitation development in a small isolated Montana cumulonimbus, *J. Geophys. Res.*,91, 1231-1247, 1986.

Gardiner, B., D. Lamb, R.L. Pitter, J. Hallett and C.P.R.Saunders, Measurement of initial potential gradient and particle charges in a Montana summer thunderstorm, *J. Geophys. Res.*,91, 1231-1247, 1986.

Jayaratne, E.R., Charge separation during the impact of sand on ice and its relevance to theories of thunderstorm electrification, *Atmos. Res.*, 26, 407-424, 1991.

Jayaratne, E.R., C.P.R. Saunders and J. Hallett, Laboratory studies of the charging of soft-hail during ice crystal interactions, *Quart. J. R. Meteorol. Soc.*,109, 609-630, 1983.

Jayaratne, E.R., Peck, S.L. and C.P.R. Saunders, Comments on "A laboratory study of static charging by fracture in ice growing by riming by Avila and Caranti", *J. Geophys. Res.*, 122, 9533-9536, 1996.

Keith, W.D. and C.P.R. Saunders, Further laboratory studies of the charging of graupel during ice crystal interactions, *J. Atmos. Sci.*, 25, 445-464, 1990.

Macklin, W.C. and Payne, G.S., A theoretical study of the ice accretion process, *Quart. J. R. Meteorol. Soc.*, 93, 195-213, 1967.

Pruppacher, H.R. and Klett, J.D., *Microphysics of clouds and precipitaion*, Kluwer Academic Publ, Dordrecht, The Netherlands, 1997.

Scavuzzo, C.M., S. Masuelli, G.M. Caranti and E.R. Williams, A numerical study of thundercloud electrification by graupel-crystal collisions, *J. Geophys. Res.*, 103, 13963-13973, 1998.

Stolzenburg, M., W.D. Rust and T.C. Marshall, Electrical structure in thunderstorm convective regions 3. Synthesis, *J. Geophys. Res.*, 103, 14097-14108, 1998.

Takahashi, T., Riming electricity as a charge generation mechanism in thunderstorms, *J. Atmos. Sci.*,35, 1536-1548, 1978.

Takahashi, T., Nagao, Y. and Kushiyama, Y., Possible high ice particle production during graupel-graupel collisions, *J. Atmos. Sci.*,52, 4523-4527, 1995.

Weinheimer, A.J., J.E. Dye, D.W. Breed, M.P. Spowart, J.L. Parrish and T.L. Hoglin, Simultaneous measurements of the charge, size and shape of hydrometeors in an electrified cloud, *J. Geophys. Res.*, 96, 20809-20829, 1991.

# THUNDERSTORM ELECTRIFICATION: THE EFFECT OF CHEMICAL IMPURITIES IN CLOUD WATER

E. Rohan Jayaratne

Dept of Physics, University of Botswana

ABSTRACT: It is known that trace chemical impurities in cloud water may control the sign and magnitude of the electric charge separated when vapor-grown ice crystals rebound off riming graupel - a mechanism thought to be responsible for the electrification of thunderstorms. In a series of laboratory experiments, ice crystals interacting with a simulated graupel pellet charged the graupel negatively when the riming cloud droplets contained traces of sodium chloride. Ammonium salts in the droplets had the opposite effect of charging the graupel positively. A very similar result was observed when particles of sand were made to rebound off a steel target coated with slightly contaminated ice. In all cases, the magnitude of the charge separated increased sharply as the temperature decreased. The results of the two sets of experiments are compared in an attempt to understand the physical mechanism controlling the charge transfer. The results also have important bearing on the location of charge centers in thunderstorms forming over different geographical regimes such as deep continental interiors and in maritime environments.

## INTRODUCTION

The non-inductive ice-ice mechanism is widely believed to be responsible for the generation of electric charge in thunderstorms. Jayaratne et al (1983) conducted a series of laboratory experiments where a simulated graupel pellet was moved through a cloud of vapor-grown ice crystals and supercooled droplets produced by an ultrasonic droplet generator (atomiser). At an impact speed of 3 m $s^{-1}$, a crystal size of about 50 μm and a cloud water content of 1.0 g $m^{-3}$, the graupel charged positively at all temperatures greater than about -17°C and negatively at temperatures below, as shown by the upper curve in Figure 1 below. When slight traces of

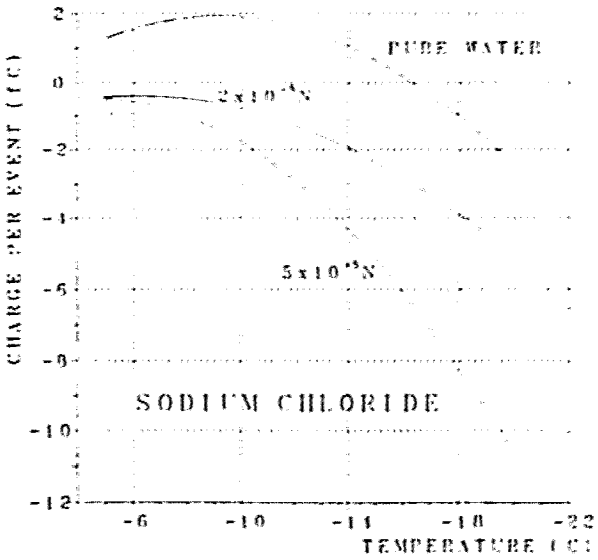


**Fig 1**
Ice crystals interacting with graupel made of pure water and NaCl solutions (from Jayaratne, 1981 and Jayaratne et al. 1983)

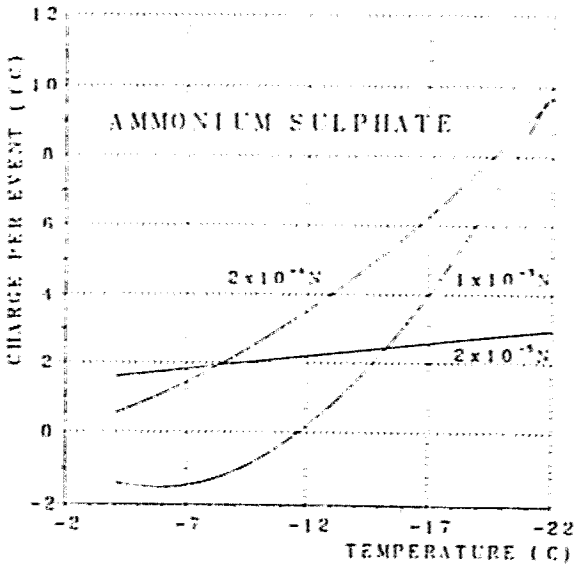


**Fig 2**
Ice crystals interacting with graupel made of solutions of ammonium sulphate (from Jayaratne, 1981 and Jayaratne et al. 1983)

impurities were added to the water, the charging pattern changed significantly. With a weak solution of sodium chloride (NaCl) of $2x10^{-5}$ N, the graupel charged negatively at all temperatures with the magnitude of charge separated per crystal collision increasing sharply as the temperature was decreased. At a higher concentration of $5x10^{-5}$ N the charging was even greater, approaching -10fC at -20°C (Fig 1). With ammonium salts, the charging was more complicated. Figure 2 shows the results obtained with ammonium sulphate ($(NH_4)_2SO_4$). At higher temperatures, for example -5°C, the tendency was for the graupel to charge less positively and eventually more negatively as the salt concentration was increased. At lower temperatures, for example -22°C, the same procedure resulted in increased positive charging. Both ammonium hydroxide ($NH_4OH$) and ammonium chloride ($NH_4Cl$) showed a similar effect but with a greater tendency for negative charging at higher temperatures (Figs 3 and 4). Although, briefly reported in Jayaratne et al (1983), these two figures have not been published, and are taken from Jayaratne (1981).

In a separate set of experiments conducted in a large chest freezer, Jayaratne (1991) bounced fine grains of sand off an ice coated target and found that the ice acquired a positive charge that increased in magnitude as the temperature decreased (see Fig 5, top curve). In this paper, we report on experiments where grains of sand interacted with an ice target contaminated with NaCl and $NH_4$ salts.

## PRESENT RESULTS

The experimental apparatus was similar to that reported in Jayaratne (1991). A stainless steel sphere of diameter 16 mm was coated with a layer of ice. The ice was formed from dilute solutions of NaCl, $(NH_4)_2SO_4$ and $NH_4OH$. Each experimental run was performed with a carefully measured mass of 0.50 g of clean dry sand dropped on to the sphere at an impact speed of 1 m $s^{-1}$. The grain size was 300±50 μm. The charge acquired by the ice was measured with a sensitive electrometer and the charge per grain calculated. The experiments were conducted at four temperatures, -5°C, -10°C, -15°C and -20°C. Figs 5, 6 and 7 show the results. Each point shown is the average of several runs carried out at that particular temperature. The experiment with NaCl was performed with three different concentrations as shown in Fig 5.

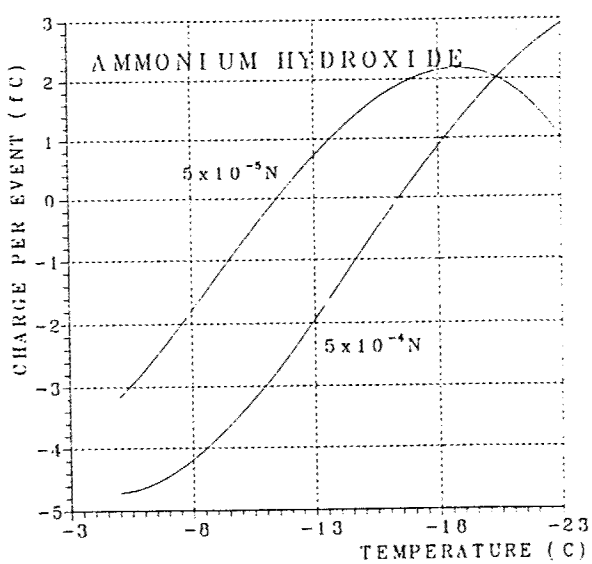


**Fig 3**
Ice crystals interacting with graupel made of solutions of ammonium hydroxide.
(from Jayaratne, 1981)

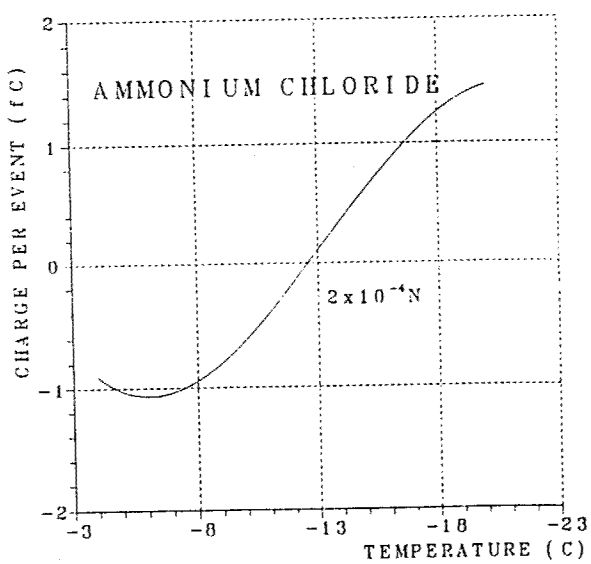


**Fig 4**
Ice crystals interacting with graupel made of a $2x10^{-4}$N solution of ammonium chloride.
(from Jayaratne, 1981)

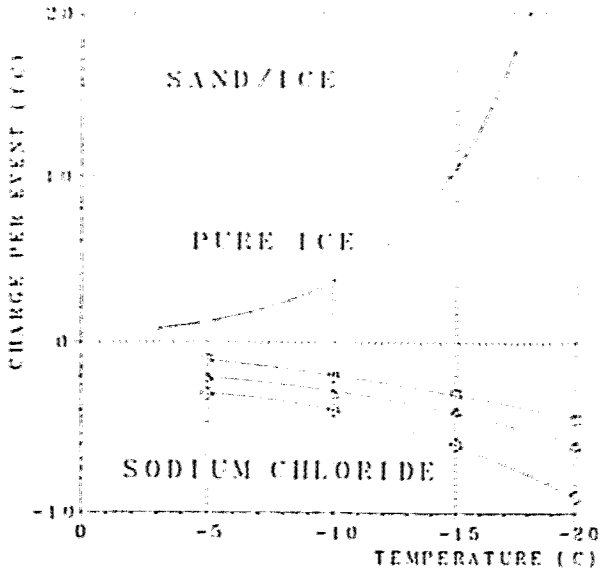


**Fig 5**

The charge transferred by a rebounding grain of sand to ice made of pure ice (from Jayaratne, 1991) and solutions of sodium chloride (this study). □: $10^{-5}$ N; Δ: $10^{-4}$ N; ○: $10^{-3}$ N.

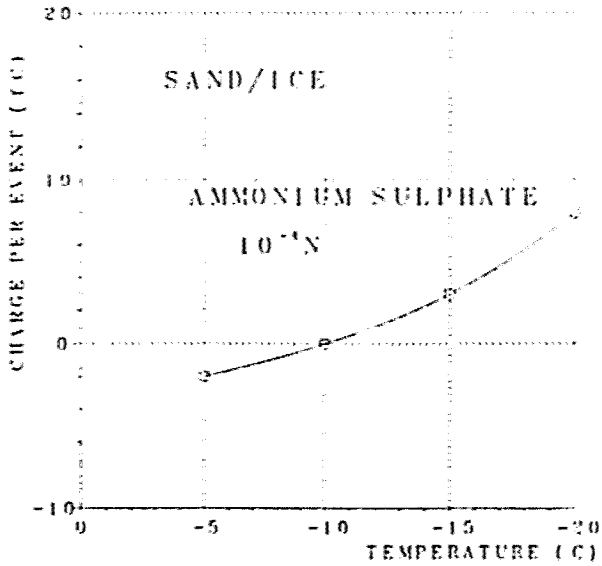


**Fig 6**

Grains of sand interacting with ice made of a $10^{-4}$N solution of ammonium sulphate.

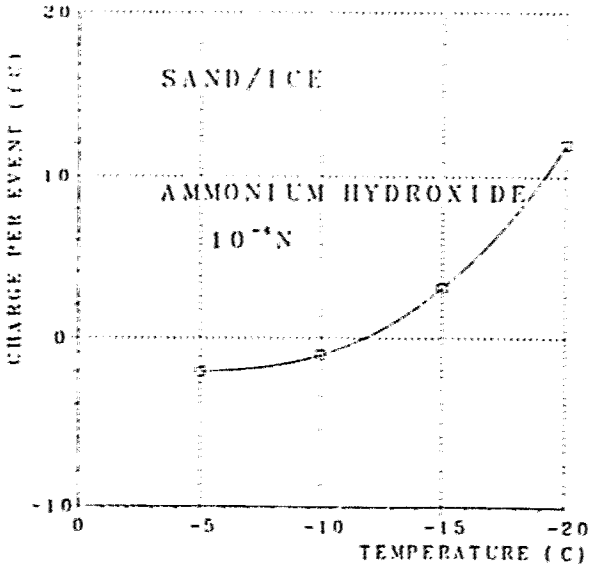


**Fig 7**

Grains of sand interacting with ice made of a $10^{-4}$N solution of ammonium hydroxide.

## DISCUSSION AND CONCLUSIONS

Comparison of the ice-ice results with the sand-ice results shows several interesting points which may yield useful insights into the physical mechanism of the charge transfer. Before doing this, we should keep in mind that the sign and magnitude of the charge separated is controlled by *both* the interacting particles. In one case the rebounding particle is an ice crystal growing from the vapor provided by the supercooled droplets in

the cloud. In the other case, it is an inert sand grain.

(a) Uncontaminated Ice: There was a marked difference between the charge versus temperature curves when ice crystals interacted with rime formed from pure, uncontaminated water droplets ( Fig 1) and when grains of sand bounced off clean ice (Fig 5). This behavior may be attributed to the nature of the impacting particle. Evidence has been presented to show that during the interaction between two ice particles, the particle growing faster from the vapor would acquire the positive charge (Baker et al, 1987). It was argued that, during the interaction of ice crystals with a riming graupel pellet, the graupel would be growing faster at higher temperatures while the ice crystal would grow faster at colder temperatures, thus explaining the shape of the pure water curve in Fig 1. In Fig 5, the grain of sand was not growing at all. This may explain why the ice charged positively at all temperatures.

(b) Sodium Chloride: When the target ice contained NaCl in a concentration as low as $10^{-5}$N, the ice charged negatively at all temperatures irrespective of the nature of the impacting particle (Figs 1 and 5). The magnitude of the charging increased with increasing concentration and with decreasing temperature. The suggestion here is that the impurity ions in the target ice is controlling the direction of charge transfer. During freezing, there is selective incorporation of ions into the ice. With NaCl, the $Cl^-$ ion is more readily accepted by the ice than the $Na^+$ ion (Gross et al., 1977). The electrical balance is restored by $H^+$ ions. This would leave a surplus of positive ions near the surface for the interacting particle, whatever its nature, to remove during rebounding events, charging the ice target negatively. Higher concentrations of NaCl would give more $Na^+$ ions close to the surface unable to be incorporated into the bulk ice, resulting in greater negative charge transfer to the ice target when particles rebounded off. The temperature dependence of the charging may be a consequence of the different mobilities of the ions in the ice.

(c) Ammonium Salts: With ammonium salts, the charging was more complicated. The $NH_4^+$ ion is readily incorporated into ice during freezing. By the same argument as with NaCl, we would now expect the target ice to acquire the positive charge, with its magnitude increasing as the temperature is decreased. This tendency is apparent in all the experiments with ammonium salts. However, the negative charging of the ice at temperatures close to -5 °C is difficult to explain. As in the experiments with NaCl, an important observation is that the effect of trace ammonium salts in the target ice on the temperature dependence of the charging sign was independent of the nature of the impacting particle, being very similar in both the ice-ice and sand-ice cases. Note also that the charge sign reversal temperature with $(NH_4)_2SO_4$ is higher than that with $NH_4OH$ in both cases. An ice target containing traces of $NH_4OH$ is generally more reluctant to charge positively than one containing $(NH_4)_2SO_4$, probably due to the $OH^-$ ion which must affect the concentration of $H^+$ ions on the ice.

(d) Application to thunderstorms: Analysis of cloud and rain water samples have shown trace impurities such as chlorides, sulphates and ammonium salts in concentrations of the order of $10^{-5}$N to $10^{-4}$N. Naturally, the NaCl concentrations generally dominate clouds in maritime environments. Does this mean that maritime and coastal thunderstorms are likely to have more negatively charged graupel and hence stronger lower negative charge centers than continental thunderstorms? There is not much field evidence to support this prediction. The charge structure in thunderstorms forming over various conditions and terrains appear remarkably similar.

## REFERENCES


Baker, B., M.B. Baker, E.R. Jayaratne, J. Latham and C.P.R. Saunders, The influence of diffusional growth rate on the charge transfer accompanying rebounding collisions between ice crystals and hailstones, *Quart. J. R. Meteorol. Soc.*, 113, 1193-1295, 1987.

Gross, G.W., P.M. Wong and K. Humes, Concentration dependent solute redistribution at the ice-water phase boundary, *J. Chem. Phy.*, 67, 5264-5274, 1977.

Jayaratne, E.R., Laboratory studies of thunderstorm electrification, PhD Thesis, Univ Manchester, 1981.

Jayaratne, E.R., Charge separation during the impact of sand on ice and its relevance to theories of thunderstorm electrification, *Atmos. Res.*, 26, 407-424, 1991.

Jayaratne, E.R., C.P.R. Saunders and J. Hallett, Laboratory studies of the charging of soft-hail during ice crystal interactions, *Quart. J. R. Meteorol. Soc.*, 109, 609-630, 1983.

# ESTIMATION OF THE TOTAL CORONA CHARGE TRANSFER FROM THE SURFACE TO THE THUNDERCLOUD

Serge Chauzy and Serge Soula

Laboratoire d'Aérologie, UMR 5560, CNRS/Université Paul Sabatier,
OMP, 14 avenue Edouard Belin, 31400 Toulouse, France

ABSTRACT: The present work estimates the efficiency of the convective charging mechanism, by computing the amount of ground corona charge which is expected to reach cloud base by conduction and convection processes during the lifetime of a thunderstorm. This estimate is made using the numerical model PICASSO, previously designed to characterize the evolution of the ground corona space charge, and initiated by the surface electric field evolution measured during six events. The overall charge amount roughly estimated for the considered events suggests that the convective charging mechanism is unlikely to account for one of the major electrification processes of the thundercloud. However, it could be consider as a relevant mechanism contributing to the lower positive charge center of the thundercloud.

## INTRODUCTION

According to the convective charging process proposed by Bernard Vonnegut [*Vonnegut*, 1953; *Vonnegut*, 1963], the positively charged upper pole of the cloud system receives its electric charge from the positive space charge produced by corona discharges from the ground irregularities under high surface field conditions. *Standler and Winn* [1979], *Chauzy and Raizonville* [1982], and others provided experimental evidences of such a generation which strongly depends on the ground structure. It is therefore important to investigate on the eventual evolution, in relation to the cloud, of the corona space charge generated from the ground. In order to estimate the amount of corona charge transferred from ground level up to cloud base, we use the numerical model PICASSO [*Chauzy and Rennela*, 1985] forced by experimental data.

## THE PICASSO MODEL

The 1D model used in this study is the improved version of a model originally presented in *Chauzy and Rennela* [1985] and adapted to experimental use by *Soula* [1994] and *Qie et al.* [1994]. The latter paper describes in detail the structure and basic equations of the updated model. The basic microphysical mechanisms involved in the computation include ion production from ground irregularities, attachment of small ions on aerosol particles, recombinations of small ions of opposite polarities, capture of small ions by charged aerosol particles. The dynamics of the system is described by the conduction current due to the electric field, the convection current produced by the upward air motion, and the eddy diffusion process.

The convective transport is introduced by considering a linear profile of vertical velocity between the surface and the top of the 1000-m layer, where the velocity reaches a maximum intensity of 5 m $s^{-1}$. The time and height evolutions of the space charge layer are computed within the boundary layer, using a step by step method. Time and space resolutions are respectively 0.1 s and 10 m. The initial and boundary conditions are set up according to the location and to the initial electrical situation.

Each run of the model is forced by the surface electric field actually measured during a field experiment. Finally, the model is able to provide the variation of the whole set of electrical parameters describing the evolution of the space charge during the lifetime of the studied event.

## THE FIELD EXPERIMENTS

The six events selected for the present study come from four different summer experiments, two in Florida (1989, 1995), and two in Southern France (1994, 1996). The surface electric field, and

sometimes the field aloft were measured by a system especially designed and described in *Chauzy et al.* [1991].

The joint triggered lightning experiments taking place in Florida were organized at NASA Kennedy Space Center during the summer of 1989 [*Soula and Chauzy*, 1991], and at Camp Blanding near Gainesville by the University of Florida, during the summer of 1995 [*Uman et al.*, 1996]. A detailed previous study [*Qie et al.*, 1994] provides the most relevant initial conditions for the model runs corresponding to the studied events (August 10, 1989, and July 20, 1995).

In 1994 and 1996, the field experiments took place at the Laboratoire d'Aérologie field site, the « Centre de Recherches Atmosphériques » at Lannemezan, located at the foothill of the Pyrénées range. We present here the results concerning one event from the 1994 experiment (July 31), and three events from the 1996 experiment (July 26, July 27, and August 7). The initial and boundary conditions are also defined in a specific way for each experimental site and each event.

## MODELING THE VERTICAL CHARGE TRANSFER

All model runs performed in this study are initiated by the surface electric field measured during each event. The ground corona current density is formulated by the expression:

$$J_C = c_1(E - E_0)^3 + c_2(E - E_0)^2 + c_3(E - E_0)$$

where $J_C$ is the corona current density, E the surface ambient electric field, $E_0$ the field onset (i. e. the field value above which the corona effect takes place), and $c_1$, $c_2$, and $c_3$ three constants related to the structure of the terrain. The evolutions of the following set of parameters are displayed: (i) the electric field aloft, at a height which allows the comparison with the corresponding experimental evolution (in order to validate the computation); (ii) the cumulated positive electric charge generated by unit area of the ground from the beginning of the event, along with the total amount of charge that reaches the top of the 1000-m layer.

Figures 1, 2, and 3 display, as an example, the results obtained during the thunderstorm of July 31, 1994 in Southwestern France. From the measured evolution of the surface field (fig. 1a), the model retrives the field evolution at 40 m (fig. 2) which can be compared to that actually measured at 44 m (fig. 1b). Figure 3 shows the evolution of the charge density generated from the ground (A) and those reaching the upper level by conduction only (B), and by conduction and convection (C). The fraction of the generated charge reaching the top ranges about 74 % at the end of the run. The same process is applied to the whole set of data for the five other events, and the corresponding results are summarized in Table 1.

In order to roughly estimate an upper limit of the total charge amount which actually reaches the base of a given thundercloud, we assume that the present mechanism covers a surface area of 10 km by 10 km. The charge density calculated by the model can therefore be integrated over this area. Under this assumption, and except for the case of July 26, 1996 which provides a very high charge amount, the total charge reaching cloud base ranges roughly from around 40 to 80 C.

## CONCLUSION

From a storm to another, the fraction of the corona charge reaching cloud base varies within a wide range and is largely affected by the influence of the convection process. Except for the case of July 26, 1996 which provides a very high charge amount, the maximum total charge reaching cloud base ranges roughly from around 40 to 80 C. If we consider that the charge amount neutralized by a single flash often reaches values of the same order of magnitude, we can hardly consider that this convective/conductive mechanism is responsible for the overall electrification of the thunderclouds considered here. However, as it was early proposed by *Malan* [1952] this process might be essential to the formation of the LPCC (lower positive charge center). Although several other processes can account for the formation of such a pole, the present investigation provides a serious candidate with a reasonable estimation of the amount of charge compatible with the observations.

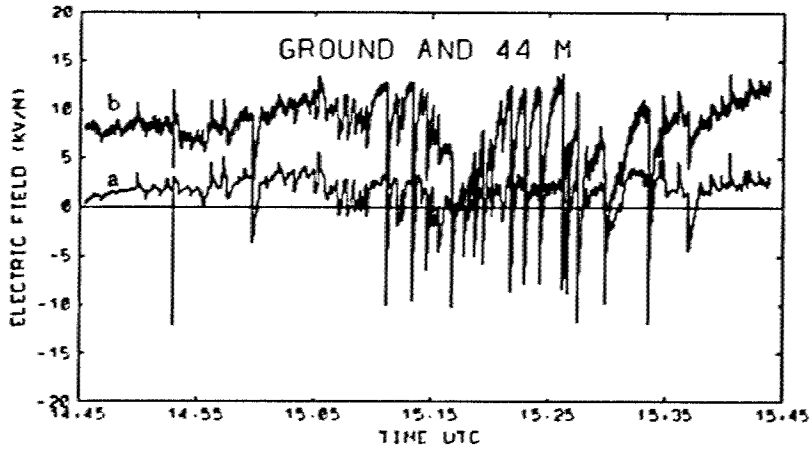


Figure 1: Electric field evolution measured at the ground (a) and at 44 m (b) on July 31, 1994.

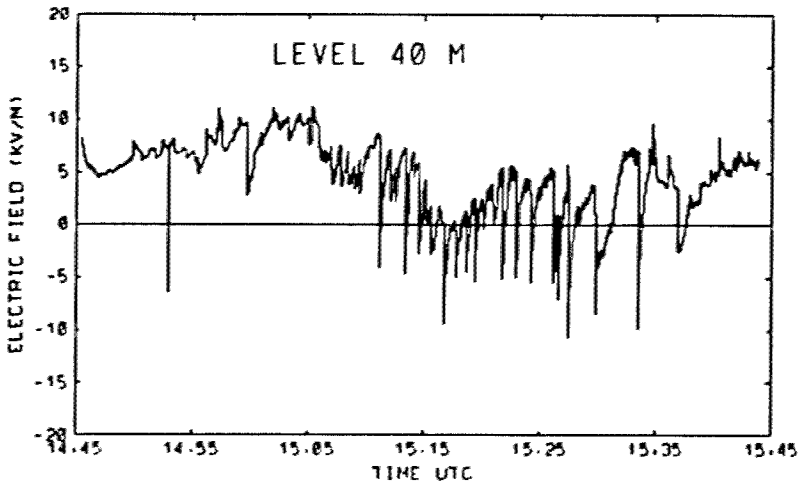


Figure 2: Electric field evolution at 40 m computed by PICASSO model for the same event.

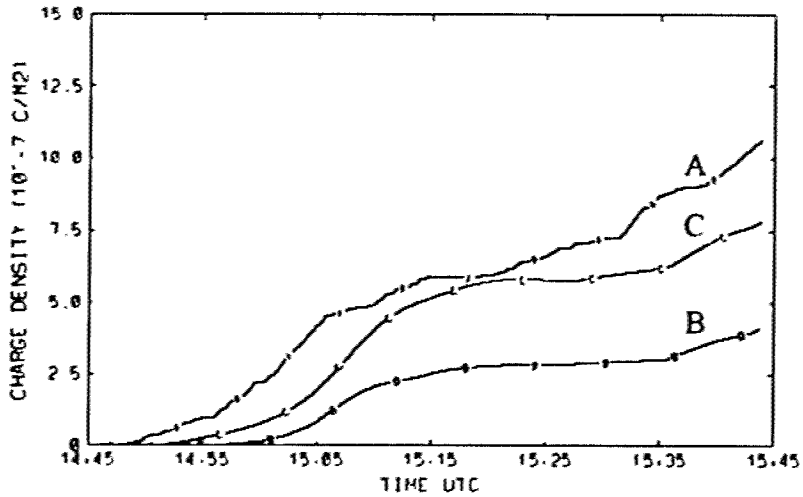


Figure 3: Evolution of the corona charge density produced at the ground (A), transferred to the cloud by conduction (B), and by conduction and convection (C), computed by PICASSO model for the same event.

| Event | Generated corona charge density (C $m^{-2}$) Charge over 100 $km^2$ (C) | Conduction charge density (C $m^{-2}$), (rate, %) Charge over 100 $km^2$ (C) | Cond. + conv. charge density (C $m^{-2}$), (rate, %) Charge over 100 $km^2$ (C) |
|---|---|---|---|
| August 10, 1989 Florida | $1.0 \times 10^{-6}$ 100 C | $0.51 \times 10^{-6}$, (51 %) 51 C | $0.90 \times 10^{-6}$, (89 %) 90 C |
| August 20, 1995 Florida | $1.2 \times 10^{-6}$ 120 C | $0.25 \times 10^{-6}$, (22 %) 25 C | $0.50 \times 10^{-6}$, (43 %) 50 C |
| July 31, 1994 South Western France | $1.1 \times 10^{-6}$ 110 C | $0.42 \times 10^{-6}$, (39 %) 42 C | $0.78 \times 10^{-6}$, (74 %) 78 C |
| July 26, 1996 South Western France | $3.6 \times 10^{-6}$ 360 C | $2.7 \times 10^{-6}$, (75 %) 270 C | $3.1 \times 10^{-6}$, (86 %) 310 C |
| July 27, 1996 South Western France | $1.4 \times 10^{-6}$ 140 C | $0.25 \times 10^{-6}$, (18 %) 25 C | $0.63 \times 10^{-6}$, (44%) 63 C |
| August 7, 1996 South Western France | $2.4 \times 10^{-6}$ 240 C | $0.50 \times 10^{-6}$, (21 %) 50 C | $0.63 \times 10^{-6}$, (26 %) 63 C |

TABLE I

ACKNOWLEDGMENTS: The authors thank the Direction des Recherches, Etudes et Techniques, and the Programme Atmosphère et Océan à Moyenne Echelle of the Institut National des Sciences de l'Univers for their financial and scientific supports. They are grateful to Bill Jafferis (NASA) and Martin Uman (University of Florida), for their respective organization of the 1989 and 1995 experiments in Florida.

REFERENCES

Chauzy, S., and Raizonville P., Space charge layer created by coronae at ground level below thunderclouds: measurements and modeling, *J. Geophys. Res.* 87, 3143-3148, 1982.

Chauzy, S., and Rennela, C., Computed response of the space charge layer created by corona at ground level to external electric field variations beneath a thundercloud, *J. Geophys. Res.* 90, 6051-6057, 1985.

Chauzy, S., Médale, J.-C., Prieur, and S., Soula, S, Multilevel measurement of the lectric field underneath a thundercloud, 1. A new system and the associated data processing, *J. Geophys. Res.* 96, 22319-22326, 1991.

Malan, D. J., Les décharges dans l'air et la charge inférieure positive d'un nuage orageux, *Ann. Geophys.*, 8, 385-401, 1952.

Qie, X., Soula, S., and Chauzy, S., Influence of ion attachment on the vertical distribution of the electric field and charge density below a thunderstorm, *Ann. Geophysicae* 12, 1218-1228, 1994.

Soula, S., and Chauzy, S., Multilevel measurement of the electric field underneath a thundercloud, 2. Dynamical evolution of a ground space charge layer, *J. Geophys. Res.* 96, 22327-22336, 1991.

Soula, S., Transfer of electric space charge from corona between ground and thundercloud: measurements and modeling, *J. Geophys. Res.* 99, 10759-10765, 1994.

Standler, R. B., and Winn, W. P., Effects of coronae on electric fields beneath thunderstorms, *Q. J. R. Meteorol. Soc.* 105, 285-302, 1979.

Uman, M. A., Rakov, V. A., Rambo, K. J., Vaught, T. W., Fernandez, M. I., Bach, J. A., Su, Y., Eybert-Bérard, A., Berlandis, J.-P., Bador, B., Lalande, P., Bonamy, A., Audran, F., Morillon, F., Laroche, P., Bondiou-Clergerie, A., Chauzy, S., Soula, S., Weidman, C. D., Rachidi, F., Rubinstein, M., Nucci, C. A., Guerrieri, S., Hoidalen, H. K., and Cooray, V., 1995 Triggered Lightning Experiment in Florida. Proc. 10th International Conference on Atmospheric Electricity, Osaka, Japan, 644-647, 1996.

Vonnegut, B., Possible mechanism for the formation of thunderstorm electricity, *Bull. Am. Met. Soc.* 57, 1220-1224, 1953.

Vonnegut, B., Some facts and speculations concerning the origin and role of thunderstorm electricity, *Meteorol. Monogr.* 27, 224-241, 1963.

# DISCHARGE INITIATION BY UNCHARGED RAINDROPS FALLING AT TERMINAL VELOCITY IN A HORIZONTAL ELECTRIC FIELD

S. Coquillat, S. Chauzy, J. F. Georgis, B. Combal, and X. Silvani

Laboratoire d'Aérologie, UMR CNRS/UPS 5560, Observatoire Midi-Pyrénées, Toulouse, France

ABSTRACT: The behavior of uncharged raindrops falling at terminal velocity in still air and submitted to a horizontal electric field is analyzed by means of a laboratory experiment and by modeling. In the former, the disruption field is measured and compared to previous results. Moreover, the electrical circuit is designed to detect the bi-directional discharge using a 2-channel digital oscilloscope. The amount of charge involved in the discharge process is therefore evaluated. In the latter, the previous model by *Coquillat and Chauzy* [1993] is adapted to the horizontal field configuration and the disruption field, the change in fall speed, and the corona occurrence altitude are computed. As expected, the corona emission from raindrops is more easily triggered in a horizontal than in a vertical ambient field.

## INTRODUCTION

In order to characterize the microphysical and electrical conditions favorable to natural triggering of lightning, several mechanisms likely to produce corona discharges from raindrops have been studied over the 30 past years. In particular, *Blyth et al.* [1998] showed that glancing collisions can produce long liquid filaments at the tips of which corona is easily emitted in electric fields lower than 400 kV/m. All theses studies involve a vertical electric field. However, given that horizontal propagating flashes are commonly observed and that the electric field can be horizontally directed in regions surrounding the negative pole of thunderclouds, we wonder if a raindrop in such a field configuration would be a suitable source of corona. Since the horizontal stretching it undergoes reinforces the aerodynamic distortion due to its fall, corona emission would certainly be facilitated. It can be pointed out from the experimental work by *Dawson* [1969] that corona emission from water drop surfaces is favored by an intense surface electric field and by a large radius of curvature. Previous modeling of raindrop behavior in a vertical ambient field downward directed [*Coquillat and Chauzy*, 1993; 1994] showed that corona is most often emitted from the bottom of the drop where the surface field is rather low and the radius of curvature large. In a horizontal ambient field, the combination of electric and aerodynamic distortions leads to a corona emission from the equator of the drop characterized by a high surface field but a small radius of curvature. However, we still do not know which field configuration is the most favorable to corona triggering. As an answer to this question, the characteristics of a discharge triggering under horizontal electric field conditions has been established by conducting a twofold study. (i) First we performed a laboratory experiment in order to determine the onset field necessary to cause a discharge from an uncharged raindrop falling at its terminal velocity and to measure, at ground pressure, the structure of the bi-directional corona produced. (ii) Second we realized a numerical modeling of the raindrop behavior in such a horizontal electric field configuration, taking into account the influence of drop distortion and pressure dependence. The eventual study of charged drop behavior will be considered. The modeling allows us to overcome the practical constraints of the laboratory experiment, almost impossible to conduct with charged drops and variable pressure, and also to determine which field configuration (vertical or horizontal) produces corona emission at the lowest altitude.

## EXPERIMENTAL PROCEDURE

The present laboratory experiment involves the same system as that described by *Georgis et al.* [1997] but a change of site allowed us to set up a vertical tunnel 17 m height which ensures all the drops to reach 100 % of their terminal velocity in still air. The generated drops of radius equal to 1.9 mm, 2.3 mm, and 2.8 mm (accuracy about 0.2 mm) enter the electric field region fully aerodynamically distorted. Their time of residence in the horizontal field being about 40 ms, it is long enough for the drops to be electrically distorted and to undergo disruption according to *Brazier-Smith and Latham* [1969]. We used distilled water whose measured conductivity was equal to 260 μS/m. The whole electrical circuit is displayed in Figure 1. The horizontal field is created between two polished and chromed copper plates 40 cm high and 30 cm wide with rounded edges, and separated by a distance of 10 cm. Each plate is connected to a high voltage DC power supply of 0 to ±100 kV via a resistor R = 100 MΩ which limits the discharge current intensity into the generators. The apparatus is designed to detect the negative and positive corona currents emitted from both sides of the drop. Both discharge signals are analyzed through a resistor r = 50 Ω by a digital oscilloscope LeCroy 9370L (50 Ω input impedance, 1 Ghz bandwidth). Most of the measurements are

performed with a sample rate of 50 MS/s (20 ns/pt) which ensures a total length of the signal equal to 40 ms since the memory available is 2M points. At last, two capacitors C = 60 nF are used to avoid any direct connection of the oscilloscope to the high voltage circuit. In the present experiment, the maximum electric charge carried by a whole discharge does not exceed 70 nC which is markedly lower than the global charge accumulated in each capacitor C which reaches 1.8 mC for an average voltage equal to 30 kV. Therefore, we can state that the electric field is not affected by the discharge process.

The horizontal disruption field versus the drop radius is plotted in solid line in Figure 2 and compared to results from previous studies. As noted by *Georgis et al.* [1997], the relatively high value of the disruption field measured by *Macky* [1931] and *Ausman and Brook* [1967], is a consequence of the fall velocity of the drop which was substantially less than the terminal speed, so that the drops did not undergo their maximum aerodynamic distortion. The comparison with the results by *Georgis et al.* [1997] shows that the change in the height of the fall distance does not affect significantly the onset field all the more as the absolute uncertainty on its measurement is about 10 kV/m. This confirms that the drops were nearly at their terminal velocity in *Georgis et al.* experiment. On the other hand, the results by *Kamra et al.* [1993] seem so different from the whole set of measurements that one can consider the part played by the wind tunnel in generating turbulence which could be responsible for a disruption field lowering.

A typical signal corresponding to the bi-directional discharge triggered by a drop of radius R = 1.9 mm in its disruption field E = 800 kV/m is displayed in Figure 3. It features the potential difference $U_r$ across the resistance r versus time. The positive and negative signatures are very similar and symmetrical, no time lag has been detected even with a sampling rate of 5 ns/pt. This signal is characterized by a succession of pulses with an average rate of about 1700 Hz corresponding to a period of 590 μs, an average pulse duration of about 0.93 μs with a rising time typically equal to 100 ns, and a total duration of about 10 ms. The end of the signal probably corresponds to the moment when the drop leaves the field region between the plates. As far as the current intensity defined by $I = 2\ U_r/r$ is concerned (the oscilloscope impedance must be taken into account), the average peak intensity is about 42 mA for the positive signal and -39 mA for the negative one corresponding to an average charge of about 3.9 nC and -3.6 nC per pulse respectively. The total charge carried in this case reaches 62 nC and -58 nC on both sides of the drop. Most of these parameters are not clearly drop size dependent, this is the case for the temporal variables. On the contrary, the average charge per pulse (together with the average maximum peak current) whose size dependence is displayed in Figure 4, decreases with increasing radius. This is probably due to the fact that the larger the drop the lower the ambient electric field that causes the discharge to occur. And in lower fields, the pulses display lower intensities. Nevertheless, whatever the drop radius is, the positive charge is systematically larger than the negative charge. When the whole current signature is considered, the final charge of the drops is about 4 nC, 2.6 nC, and 1.5 nC for radii 1.9 mm, 2.3 mm, and 2.8 mm respectively. Therefore the drops become positively charged like for weaker ambient fields at high altitudes where only pure corona emission happens according to *Dawson* [1969].

## MODELING

Present modeling is an adjustment of previous work by *Coquillat and Chauzy* [1993] to the horizontal field configuration. In this case, the drop shape does not exhibit any axial symmetry. It is assumed to be constituted of two half ellipsoids (top and bottom) having two common horizontal axes, the longer of which is along the field direction, and two different vertical semi axes. The method is based on the local pressure balance involving the internal overpressure, the pressure due to surface tension, and the hydrostatic, aerodynamic and electrostatic pressures. The equilibrium shape determination arises from a step by step method, by adjusting the length of the various axes in order to make the internal overpressure uniform at four test points of the drop surface. For each value of the ambient field, the stable shape is determined and the corona occurrence altitude is deduced from the experimental data of *Dawson* [1969]. The disruption field is reached when no convergent process is possible. The lack of axial symmetry induces two main problems: first, the computation of the surface electric field and second, the determination of the aerodynamic pressure distribution necessary to calculate the terminal velocity. The former was solved by developing an integral method based on a sampling of the surface charge density. The latter was overcome by using the semi empirical method by *Beard and Chuang* [1987] which adjusts a known pressure distribution for a sphere to the distorted shape of the drop. In the unseparated flow (bottom), the adjustment is that found in the case of a potential flow when comparing the pressure distribution for a sphere to that for the distorted drop (computed by developing the velocity potential as a series of spherical harmonics), meanwhile in the separated flow region (top), the correction is made from the balance between the drag and the weight of the drop. At last, the fall velocity is calculated by an iterative method based on the conservation of the total drag expressed in terms of the Reynolds number and of the pressure drag coefficient which is deduced from the aerodynamic pressure distribution.

The computed disruption field is displayed in Figure 2 and the comparison with experimental results seems rather good. However, the present modeling is not fully satisfactory since for R = 2 mm the aerodynamic pressure had to be artificially corrected in the separated flow for ambient fields greater than 400 kV/m, otherwise the disruption field would have been substantially underestimated. This problem, raised in the case where R = 2.5 mm for which no equilibrium shape would have been found even in a zero field, probably originates from the simplified geometry which would not be suitable for the larger drops. Nevertheless, keeping in mind this bias for the larger drops, we calculated the critical field which is the horizontal ambient field that causes either disruption at lower altitudes or pure corona emission at higher altitudes. Its vertical profile is displayed in solid line in Figure 5 where the profile of the vertical critical field is also plotted in dashed line. The comparison between both kinds of profiles clearly shows that the horizontal field configuration allows corona triggering at lower altitudes than does the vertical one. Furthermore, the larger the drop, the more important the lowering of the corona occurrence altitude. On the other hand, we performed the calculation of the terminal velocity. The results are displayed in Figure 6 in relative unity by dividing the terminal velocity by the velocity in a zero field. It clearly appears that the terminal velocity is much less affected by the horizontal ambient field than it is in the vertical configuration. This can be interpreted in terms of drag force which is weaker in a vertical field since the electric distortion counteracts the aerodynamic flattening, giving to the drop a more aerodynamic shape.

## CONCLUSION

The computed critical fields show that the ambient field intensities or the corresponding altitudes are not realistic of intra cloud initiation conditions. Thus, the aim of the present experiment and calculations is not to demonstrate that an uncharged drop can trigger a cloud discharge, but rather to show that corona is favored by the horizontal field configuration as compared to the vertical one. The modeling results are in agreement with the experimental observations corresponding to the fall of raindrops in still air without any influence of turbulent airflow. However, the geometry used in this modeling is probably not totally adapted to largest drops. Providing a change in the geometrical definition of the drop shape, the following step of this work will be to evaluate the influence of a net charge which is known to clearly reduce the critical field [*Coquillat and Chauzy*, 1994]. Thus the probability for a stable drop to trigger a cloud discharge should be enhanced by the presence of a net charge. Since pure corona emission is more easily triggered from positively charged raindrops, such drops submitted to a horizontal electric field would be fairly efficient sources of corona emission, and the low positive charge center of a thundercloud should be a propitious site for natural triggering of lightning. Of course the interaction between drops [*Georgis et al.*, 1997] should reduce again the triggering onset fields. On the other hand, the laboratory experiment showed that the bi-directional discharge process initiated from the drop leaves a residual positive net charge on this drop. The corresponding remaining charge reaches a few nanocoulombs.

## REFERENCES


Ausman, E. L., and M. Brook, Distortion and disintegration of water drops in strong electric fields, *J. Geophys. Res.*, 72, 6131--6135, 1967.

Beard, K.V. and C. Chuang, A new model for the equilibrium shape of raindrops, *J. Atmos. Sci.*, 44, 1509--1524, 1987.

Blyth, A. M., H. J. Christian, and J. Latham, Corona emission thresholds for three types of hydrometeor interaction in thunderclouds, *J. Geophys. Res.*, 103, 13975--13977, 1998.

Brazier-Smith, P. R., and J. Latham, Numerical computations of the dynamics of the disintegration of a drop situated in an electric field, Proc. Roy. Soc., Ser. A, 312, 277--289, 1969.

Coquillat, S., and S. Chauzy, Behavior of precipitating water drops under the influence of electrical and aerodynamical forces, *J. Geophys. Res.*, 98, 10319--10329, 1993.

Coquillat, S., and S. Chauzy, Computed conditions of corona emission from raindrops, *J. Geophys. Res.*, 99, 16897--16905, 1994.

Dawson, G. A., Pressure dependence of water-drop corona onset and its atmospheric importance, *J. Geophys. Res.*, 74, 6859--6868, 1969.

Georgis, J. F., S. Coquillat, and S. Chauzy, Onset of instability inprecipitating water drops submitted to horizontal electric fields, *J. Geophys. Res.*, 102, 16793--16798, 1997.

Kamra, A. K., R. V. Bhalwankar, and A. B. Sathe, The onset of disintegration and corona in water drops falling at terminal velocity in horizontal electric fields, J. Geophys. Res., 98, 12901--12912, 1993.

Macky, W. A., Some investigations on the deformation and breaking of water drops in strong electric fields, Proc. Roy. Soc. London, Ser. A, 133, 565--587, 1931.

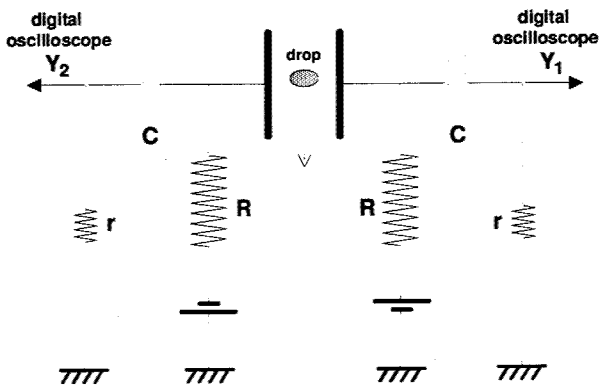


Figure 1.

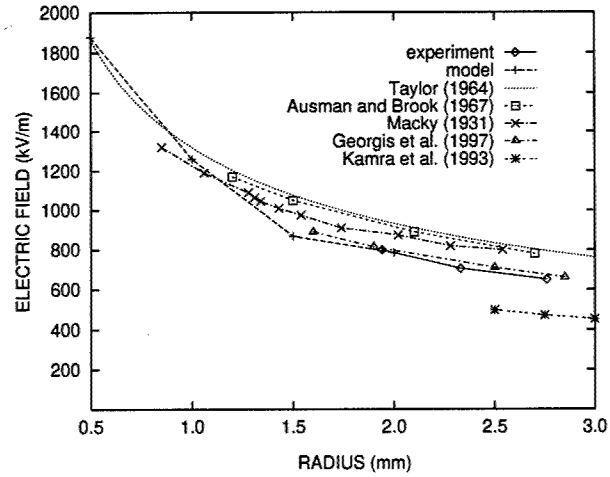


Figure 2.

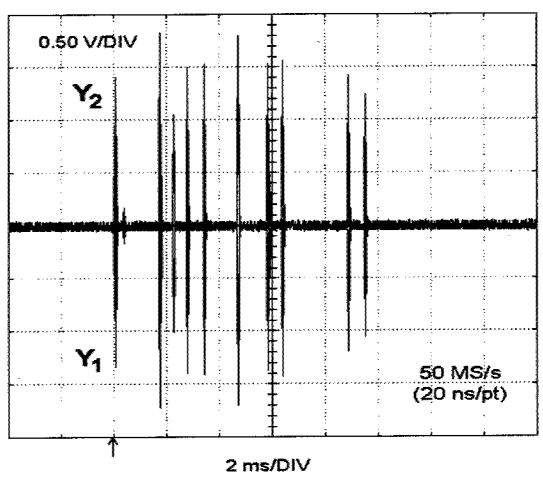


Figure 3.

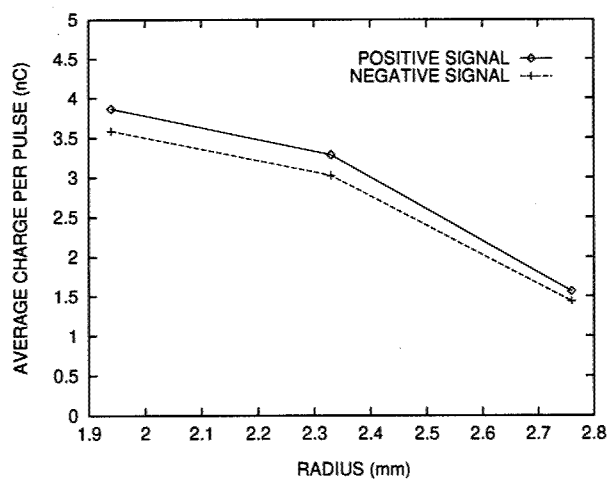


Figure 4.

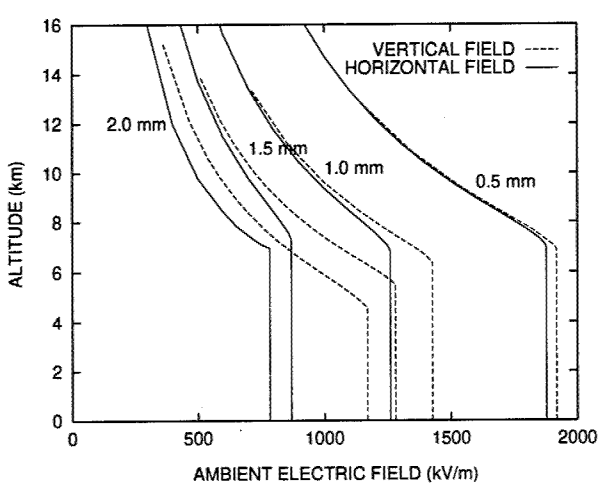


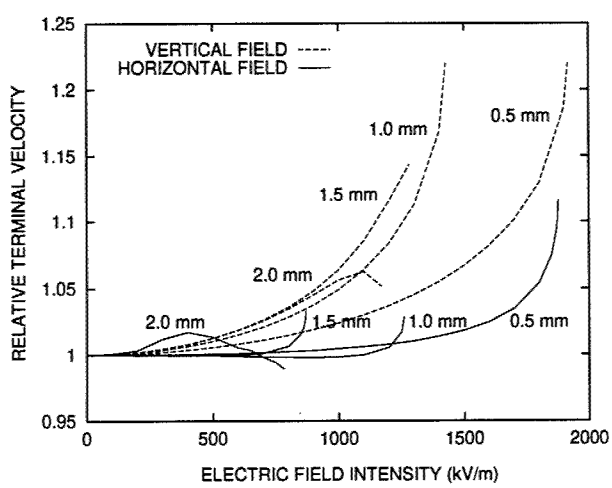

# EFFECT OF DROPLET SIZE ON GRAUPEL SURFACE PROPERTIES IN CONNECTION WITH NONINDUCTIVE CHARGE TRANSFER

Rumjana Mitzeva[1], Tzveta Kassabova[1] and Clive Saunders[2]

[1] Faculty of Physics, University of Sofia Sofia-1164, Bulgaria
[2] Dept of Physics, UMIST, Manchester- M60 1QD, UK

**ABSTRACT:** Results from a numerical study concerning the effect of droplet size on graupel surface properties (surface temperature, growth rate of graupel size, sublimation/deposition) are presented. The calculations are based on the published equations for graupel surface temperature and growth rate by vapor diffusion. To account for the fact that graupel surface temperature depends on droplet size the results from laboratory experiments in UMIST concerning the heat balance and ventilation coefficient of riming graupel as a function of the droplet spectrum were used. The results demonstrate the significant effect of cloud droplet size on graupel surface properties, hence on the sign of the noninductive charge transferred.

## INTRODUCTION

Many efforts during the past 15 years were devoted to establishing the parameters which determine the sign and magnitude of the charge transferred during rebounding collisions between ice crystals and riming graupel. Despite the lack of a unified theory to explain the reason for the sign reversal, it is unanimously accepted that the sign and magnitude of the charge depends on the surface conditions of the graupel.

This work examines the impact of cloud droplet size on the surface conditions of riming graupel at various effective liquid water contents and cloud temperatures. The analysis of the results is directed to non-inductive charge transfer based on the two most discussed in the literature hypotheses for the charge sign reversal:

**Relative growth rate hypothesis** (Baker et al., 1987) (RGR)- the faster growing ice particle by vapor diffusion acquires positive charge.

**Sublimation/deposition hypothesis** (Williams et al., 1991) ($S/D$)- the sublimating graupel is charged negatively while the graupel undergoing deposition is charged positively. The charge of the ice crystal is always opposite to that of graupel.

## THEORETICAL BACKGROUND

To formulate mathematically the above hypotheses the growth rate of the size of the interacting ice particles by vapor diffusion has to be considered.

It is reasonable to assume that the air in a laboratory cloud is saturated with respect to water, so it is supersaturated with respect to ice if the ice surface temperature is equal to cloud temperature. The ice crystal's surface temperature is close to the cloud temperature and their growth rate can be roughly calculated by:

$$\left(\frac{dr_c}{dt}\right)_c = \frac{D\,F_c\,(\rho_w(T_c) - \rho_i(T_c))}{\sigma_c\, r_c} \tag{1}$$

where: $T_c$ - cloud temperature, $\rho_w$, $\rho_i$ - density of water vapour with respect to the water and ice surface, $D$ - surface coefficient of molecular diffusion of water vapour in the air, $d_c$ - size of the ice crystal, $F_c$ - ventilation coefficient for ice crystal.

Riming graupel grows by vapor due to the diffusion of vapor from the surrounding air ( so called far-field -FF) and by vapor transferred by the local field (LF) which exists around each freezing droplet on the graupel surface. The growth rate of graupel size from the far field can be calculated by

$$\left(\frac{dR_g}{dt}\right)_f = \frac{D\,F_g\,(\rho_w(T_c) - \rho_i(T_g))}{\sigma_g\, R_g} \tag{2}$$

where: $T_g$ - mean surface temperature of the grauple, $R_g$ - radius of the graupel, $\sigma_c, \sigma_g$ - density of the ice crystal and grapel, $F_g$ - ventilation coefficient for the graupel.

Using the approximation for the vapor flux from a single freezing drop suggested in Baker et al., 1987, we obtained the following equation for the growth rate of graupel size by the local vapor field:

$$\left(\frac{dR_g}{dt}\right)_l = \frac{2^{1/3}\,9}{4}\,\frac{D\,F_l\,EW\,V\,\tau_f\,(\rho_w(0) - \rho_(T_g))}{\sigma_g\,\sigma_w\,a^2} \tag{3}$$

where: $EW$ - effective liquid water content $EW = E_c\,LWC$, $\tau_f$ - freezing time of the droplets, $V$ - air speed or speed of the grapel, $F_l$ - 'local' ventilation coefficient for the graupel.

To account for the fact that bulk graupel density $sigma_g$ depends on the growth conditions Macklin's (1962) empirical formula for the bulk density of graupel as a function of the droplet size $a$, graupel surface temperature $T_g$ and velocity $V$ was used

$$\sigma_g = 110\left(-\frac{a\,V}{T_g}\right)^{0.76} \tag{4}$$

Eq (2) and eq.(3) show that for the estimation of the growth rate of graupel size the freezing time of cloud droplets and graupel surface temperature has to be known. The freezing time of the droplets was calculated by an equation suggested by Marshall, 1967 (see Prupacher and Klett, 1996)

The temperature of an ice deposit (graupel) growing by the accretion of supercooled droplets is raised above that of its environment because of the release of heat of fusion. Following Macklin and Payne,196? we used a simple relation from which the mean surface temperature of a cylindrical deposit can be calculated

$$\frac{EW\,V\,(L_f + c_w\,(T_c - T_0) + c_i\,(T_0 - T_g))}{\pi} =$$

$$\frac{\pi\,\chi\,R_e^{0.6}(P_r^{1/3}\,k_a\,(T_g - T_c) + S_c^{1/3}\,L_v\,D\,(p_w(T_c) - p_i(T_g))}{2R_g} \tag{5}$$

where: $P_r$ - Prandtl number, $Re$ - Reynolds number, $S_c$ - Schmidt number, $\chi$ - numerical factor in the heat transfer coefficient.

According to this equation $T_g$ depends on the size of the cloud droplets via the dependence of $EW$ on $E_c$. However, if $EW$ is kept constant by adjusting $LWC$ appropriately, then there is no dependence of $T_g$ on the cloud droplet spectrum used. But in nature as well as in the laboratory experiments the shape and surface roughness of the accreted rime does depend on the size of the droplets. Therefore, the ventilation factor and hence $T_g$ should be affected by the droplet size.

Laboratory experiments conducted in UMIST (Avila et al., 1999) showed that the surface temperature is not increased as much by smaller droplets as by larger ones for a fixed rate of accretion. This fact was taken into account in our calculations using the suggestion in Avila et al., 1999 empirical equation for a numerical factor chi in eq.5 as a function of graupel velocity and droplet diameter.

$$\chi = 0.308 + 0.253\,exp\,(-1.104\,10^{-6}\,k) \qquad k = a^4\,V \tag{6}$$

## NUMERICAL EXPERIMENTS AND RESULTS

The numerical experiments were carried out for effective liquid water content in the range $0.1 \div 3.5gm^{-3}$, cloud temperature in the range $-5 \div -35°C$ and droplet sizes in the range $5 \div 35\mu m$. These ranges are consistent with observations in real clouds and with usual laboratory conditions.

The empirical equation for the numerical factor $\chi$ has been obtained for a target with diameter $2.8mm$ and that is why all numerical experiments have been made for graupel with this size. In all numerical experiments the velocities of the graupel and the size of the ice crystals were constant $V = 3ms^{-1}$ and $d_c = 10^{-4}m$. It was also assumed that $F_c = 1, F_g = \chi\,D\,P_r^{1/3}$ . The calculations were carried out using different value for in the range $F_l = 1 \div 10$.

Some of the results concerning growth rate of graupel size were rather complicated and not obvious. The reason for this is the fact that droplet size affects the graupel surface conditions directly by the local vapor field and indirectly, via the numerical factor $\chi$, i.e. via the graupel surface temperature, by the bulk density of the graupel $\sigma_g$ and the freezing time of the droplets $\tau_f$. The results can be summed up as follows:

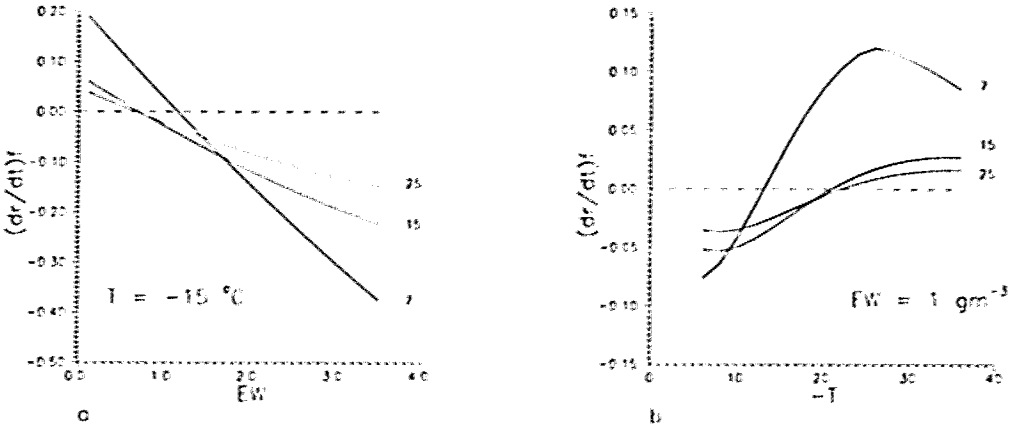


Figure 1: Growth rate of graupel size by the far field for droplet sizes $a = 7, 15, 25\mu m$

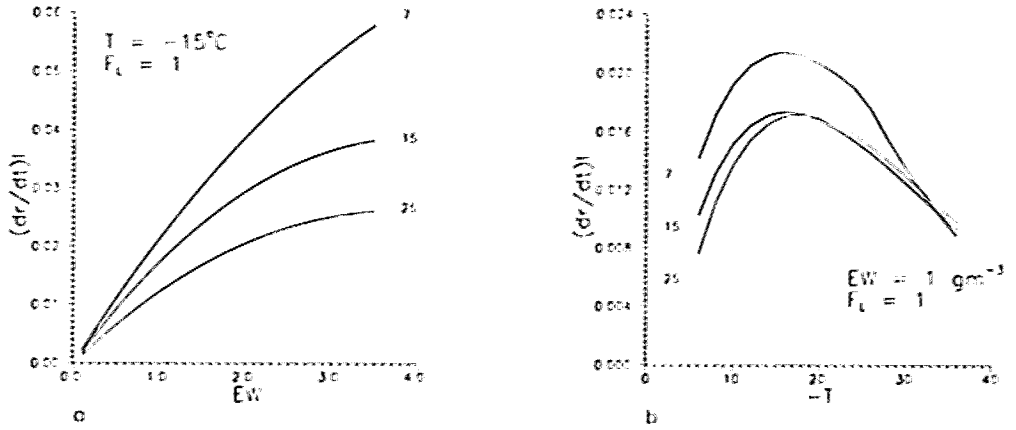


Figure 2: Growth rate of graupel size by the local field for droplet sizes $a = 7, 15, 25\mu m$

- the surface temperature of graupel is higher when the size of the droplets is larger and when effective liquid water contents are higher

- the growth rate of graupel size due to the vapor from the far field increases when droplets have smaller sizes and at lower effective liquid water content because larger droplets warm the graupel surface more (Fig.1b); at a fixed EW vapour from the far field is deposited on the graupel surface at low temperature (Fig.1a)

- the impact of the local field on the growth rate of graupel by vapor diffusion is stronger when droplets are smaller and when the effective liquid water content is higher (Fig.2b) and depends on cloud temperature (Fig.2a).

From Fig.3 a, b one can see whether the graupel is growing or sublimating and which particle is growing faster by vapor diffusion. The results show the importance of the use of an adequate value for $F_l$. Whith $F_l = 1$ the graupel grows faster than the ice crystals when the freezing droplets are small ($a = 7\mu m$) at a low value of EW, and the graupel sublimates at high EW . Accordingly, it follows from the RGR and S/D hypotheses that the graupel will charge positively at low EW and negatively at high EW, which does not agree with the laboratory measurements in Saunders et al.,1991. With $F_l = 10$, the graupel grows faster than the ice crystals for all EW when freezing drops are small ($a = 7\mu m$); the graupel grows slower than the ice crystals when $a = 25\mu m$ and at $a = 15\mu m$ the graupel grows faster than the ice crystals for higher values of EW. On the basis of RGR, at a fixed cloud temperature higher values of EW and smaller droplets are conducive to positive charging of the graupel. This result is in agreement with the laboratory measurements in Saunders et al., 1991 and in Avila et al.,1998. Fig.3 b shows that at $F_l = 10$ the graupel surface grows by

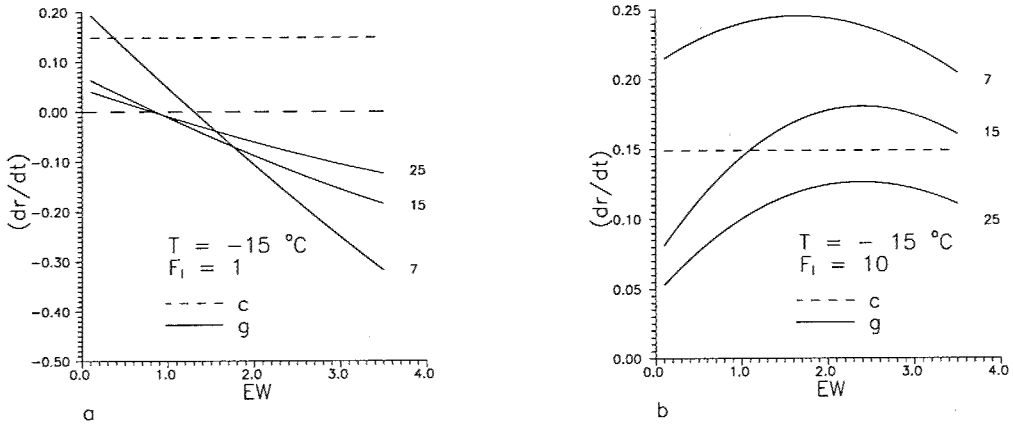


Figure 3: Fig.3 Growth rate of crystal (short dashed line) and of graupel size (solid line)

vapor deposition for small and high values of EW, i.e. the S/D hypothesis does not explain the charge sign measured.

## CONCLUSIONS

The results presented in this work demonstrate the significant impact of the size of freezing droplets on graupel surface temperature and growth rate. Since it is believed that the sign of noninductive charge transfer in rebounding collisions between ice crystals and riming graupel depends on the graupel surface properties, it follows that some discrepancies between the results from different laboratory experiments may be due to the different spectra of cloud droplets. The results from calculations also point out the importance of adequate representation of ventilation around freezing drops, hence laboratory experiments in this direction are needed. Although the results for the effect of the local vapor field as a function of EW is in qualitative agreement with some papers, the analysis of the results shows that more precise calculations of the contribution of the local vapor field on growth rate of graupel is necessary.

**ACKNOWLEDGEMENTS:** This work is supported by the Royal Society, the National Science Foundation in Bulgaria ( grant NZ-624/96) and the Science Foundation of Sofia University (grant 330/98)

## REFERENCES

Avila E., N. Castellano and C. Saunders Effects of cloud droplet spectra on the average surface temperature of ice accrated on fixed cylindrical collectors , accepted by *Q.J.R.Meteorol.Soc.*, 1998

Avila E., G. Caranti, and N. Castellano, Laboratory studies of the influence of cloud droplet size on charge transfer during crystal-graupel collisions,*J. Geophys. Res.*, **103**, 1998, 8985-8996

Baker B., M. Baker, E. Jayaratne, J. Latham and C.P.R.Saunders, The influence of diffusional growth rates on the charge transfer accompanying rebounding collisions between ice crystals and soft hailstones *Q.J.R.Meteorol.Soc*, **113**, 1193- 1215, 1987

Macklin W. and G. Payne, A theoretical study of the ice accretion process *Q.J.R.Meteorol.Soc*, **95**, 1969

Pruppacher H. and J. Klett , Microphysics of clouds and precipitation **Reidel Publishing Company**, 1996

Saunders C. , W. Keith and R. Mitzeva, The effect of liquid water on thunderstorm charging, *Journal of Geophysical Research*, **96**, 11007-11017, 1991

Williams E., R. Zhang and J. Rydoc, Mixed phase microphysics and cloud electrification, *J.Atmosph. Sci*, **48**, 2195 -2203, 1991

# ON CHARGEING PHENOMENA IN SNOWSTORM

Hisashi Shio
Department of Physics, Hokkaido University of Education
Iwamizawa Campus JAPAN

ABSTRACT:

Charging phenomena of snowstorms were investigated at ASAHI-Hill (Height: 1970 m). results obtained as follows: i) In a case of snowstorm with precipitations, snowflakes drifting in lower layer (height 2 m) were positively charged, while those drifting in higher layer (height 2 m) were negatively charged. During all periods in the snowstorms, total of charge of snowflakes collected in Faraday Cage is electrical neutral, namely to be near zero mV. those results come to Conclusion that a snow crystal is separated into two kinds of snowflakes charged positively and negatively by the destroying of the snow crystal. ii) In a case of snowstorms consisting irregularly formed ice particles generated by peeling of hardened snowfield hardened by powerful wind pressures, a charge polarity was controlled by crystallographic characteristics of particularly windward area of hardened snow field where the ice particles were generated by peeling off and the ice particles became to be charged by saltating of them.

## INTRODUCTION

The charge polarity of snow particles was dependent on a vertical distance above the snow field due to an electrostatic potential gradient in snow storms without the precipitation at Mt. Teine (height: 1023 m) (Magono et al 1963). latham (1967) investigated that the vertical electric field strength near snow cornices on Bridge Ridge (2590 m), and suggested that the main cause of the development of cornices is due to the electrostatic force generated between the snowfield and the charged snow particles under comparatively low velocities of drifting snow particles and a dependence of temperature gradient effect (Latham et al 1965) on the charging phenomena of snow storms. Shio et al (1969, 1978) and Shio (1983) pointed out a shortcomings of the temperature gradient effect on triboelectrification of ice, and paied attention to dependance of crystallograpic characteristics on the charging phenomena. In order to investigate how kind of facters have influence on charging phenomena of snow storms, the charge of snow flakes and ice particles were measured using Faraday Cage and checked out the crystallographic orientation of surfaces of snowfield by the making etch-pit on these surface.

## METHODS OF MEASUREMENTS

Charge of snow flakes and ice particles were measured using Faraday Cage, which is held in a cylindrical snow hole with 3 m diameter, 2 m

depth under the snow field. The snow flakes and ice particles become to be fall through a metallic cylinder with two small conically shaped mouths at height 0.3 m (lower layer) and 2 m (higher layer) from snow field. The etch-pits were observed using polarizing microscope.

## RESULTS AND DISCUSSIONS

Due to the results of observation the charging phenomena may be divided into two kinds of groups, whether the precipitation was or not in snowstorms.

### i) Snowstorms with precipitation

An example of these conditions is shown in Figure 1. Charge of fractured snowflakes drifting at a higher are (height: 2 m) and a lower area (height: 0.3 m) too in snowstorm. In this figure the former is a period from 12h48m to 12h56m, the latter is a period from 12h56m 56m to 13h04m15s. Faraday Cage was grounded at 12h48m, 12h53m10s, 12h55m50s, 12h57m40s, and 13h04m20s as shown a sign E. A charging curve suddenly reversed from negative to positive at a point as shown signs A, B and C in the higher area. While at the lower area the charging curve reversed from positive to negative at a point as shown by sign D, F and G. Figure 2 shows a trajectory of the fractured snowflakes drawing unnaturally in Faraday Cage. At these times the charging curve were suddenly reversed in electric sign. Namely these phenomena shows that large charged snowflake was absorbed into Faraday Cage by the pulling of stronger electrostatic forces induced by the negative charged snowflakes accumulated in Faraday Cage. From these results the charging phenomina was dependent upon the vertical distances from the snowfield except in a few periods. on the otherhand Magono et al (1963) pointed out the dependence of the charge of particles on their sizes to explicate the above phenomena. In order to determine how the charge polarity was depended on the size of particles, the dependence of the sign of the charge upon particle sizes was investigated using Wells and Gerke method (Wells et al. 1919). Figure 3 shows that charge of snowflakes against their diameters were distributed uniformly between positive area and negative area. In this case sizes of the snowflakes fixed by Replica method on slide glass are shown by

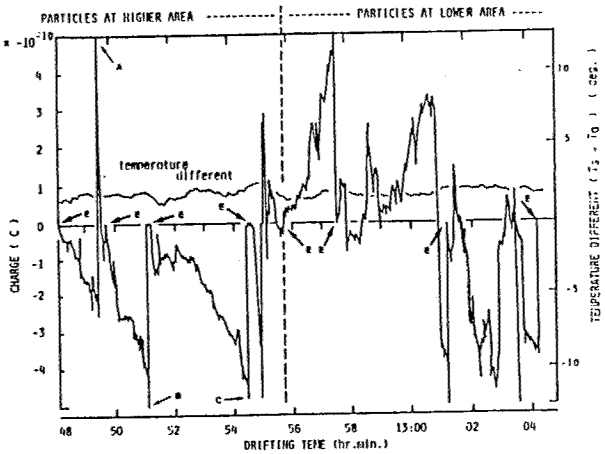


Fig.1. Charge against drifting time. Higher area:12h 48min to 12h 55min. Lower area:12h 55min 30sec to 13h 4min 10sec. Arrows A, B and C show the points where the stored charge is over the regions measured possibly using the electrometer, then, it was earthed as shown by arrow E.

Fig.2. Trajectory of particles moving unnaturally into Faraday Cage.

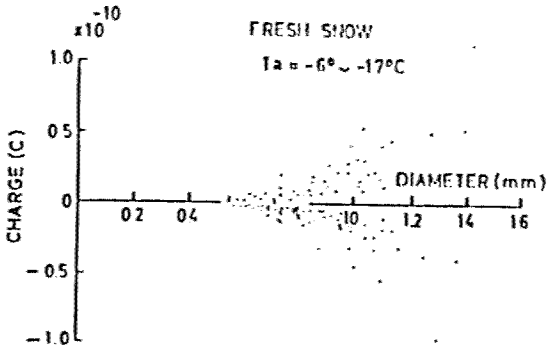


Fig. 3 Charge of the destroyed particle against its size.

green diameters. Latham et al (1967) reported that a negative charge per a snowflake was $-4 \times 10^{-13}$ C. Magono et al (1963) obtained a result as an average charge per snowflakes $-3 \times 10^{-15}$ C. On comparing the above two results our result become to be greater than the other on quantity of the charge per the snowflake.

ii) Snowstorms with irregular ice particles generated by peeling of hardened surface of snowfields without precipitations

In the daytime the particles always acquired negative charge regardless of height. While after sundown a direction of wind was suddenly changed from windward to leeward. and then the charge was changed from negative to positive regardless of height.

In oder to investigate whether the inverting phenomena on the charging are depended upon the change of wind direction or not, crystallographic orientations of ice plate made of snowlumps collected from a various snowfields at the windward and leeward were observed using polarimicroscope. results are shown in Fig. 4. As a result the hardened snowfield with a similarcrystallographic orientation were centered on a specific area. To investigate whether the charge polarity on ice particles is depended upon an anisotropy of snowfield or not, the charges of ice particles generated by peeling snow lumps collected on the hardened snow field at windward area and leeward area using a compressor were measured. As a result snow particles peeling snow lumps with crystallographic orientation of an angle 0°~ 30° against the C-axis got to be negative charge and with 60° to 90° angle against the C-axis got to be positive charge at below ambient temperatures -7°C. Above ambient temperatures -7°C the particles with both groups were electrified positively too.

Fig. 4 Crystal orientation of hardened snow field determined by pits. The upper photo, is surface of hardened snow field oriented nearly with prism plane, collected at windward. The lower photo, shows its surface with nearly basal plane, collected at leeward.

## CONCLUDING REMARKS

The results are summarized as follows:

i) In snowflakes with precipitations

The charge polarity of snowflakes were depended upon destroying phenomena of snowflakes and the charge of fractured snowflakes indicated

electric polarity.

ii) In ice particles without precipitations

The charge of ice particles was dependent upon an crystallograpic anisotropy of a surface on the hardened snowfield below -7°C. While above -7°C the ice particles were positively charged regardless of an anisotropy of these surface.

References

Latham, J., and B. J. Mason, Pro. Roy. Soc. London., A, 260, 523-530, 1961

---------, and C. D. Stow, Quar. J. R. Meteor. Soc., Vol. 93 No. 9395,

Magono, C., and K. Sakurai, J. Meteor. Soc., Japan. 41. 211-217, 1963

Shio, H and C. Magono, Planetary Electrodynamics., Vol. 93, 55-61, 196

----------, J. Meteor. Soc. Japan Vol. 56 489-48, 1978

Shio, H, Pro. Atmosphic Electricity., 229-233, 1983

Wells, P. V., and R. H. Gerke, J. Amer. Chem. Soc., 312-320, 1919

# THE ELECTRIC CHARGE'S SEPARATION DURING BREAK – UP OF THE ELECTROLYTE SOLUTIONS

A.V. Kolpakov, L.V. Maliarova and E.I. Titova

The Odessa State University, The Laboratory of Physics of Aerodisperse Systems, Odessa, Ukraine.

ABSTRACT. The electric charges of cloud drops containing NaCl solutions of different low concentrations were measured. The drops were created during break – up of the liquid in the generator of monodisperse drops of "vibrating needle" type.

Such a characteristic as monodispersion doesn't determinate unambiguously the physical and chemical properties of the drop's arising during break – up of the liquid of same compositions.

The identity of mechanical process of formation for separate drop is of very importance. Only in such a case the properties of the drops of the same dimensions ($d_k$) will be identity. Such drops may be called monoparametric.

For monoparametric drops of different dimensions we have obtained the depedences the value of electric charges ($q$) with the concentration of the solution ($c$). The charge ($q$) arises during the process of break – up by the separating of the double electric layer.

The curves of the function $q=f(c)$ for solution of NaCl ($d=const$) have typical minimum at the same concentration of the NaCl solution for drops of different dimensions. It shows the complex character of the process of separation of electric charges.

## INTRODUCTION

It is known Kolpakov et al [1983] that during partial coalescence in the process of coagulation of cloud and rain drops the separation of charges take place. This phenomenon may be considered as a primary, elementary act of the global charge's separation which leads to the storm discharge. The mechanism of appearing of electric charge during partial coalescence of cloud drops or break – up of the rain drops is not clear till now. The different scientists use available modeling conceptions based on the indirect experiments.

The most famous two models of electrization of liquid during break – up. The first model is based on the idea of existing a potential difference along the dispersed surface (the equilibrium value of surface potential on the section of an "old" surface and unequilibrium value on the section of a "new", fresh – formed during of the deformation surface) [Lopatenko and Maliarova, 1985]. The other model supposes the mechanical displacement the double electric layer (DEL) plates relative to one another at the expense of the outer forces applied to the surface.

In [Kolpakov, 1991] was proposed one more model of the drop electrization process during break – up to a certain extent uniting both previous models. It is based on the phenomenon [Kochurova and Rusanov, 1981] when between the section of an "old" and a "new" surface the gradient of surface tension arises. Just at the expense of this gradient the displacement of outer plate of DEL takes place. This model in contrast to the previous two models is not based on the speculative propositions but deals with the values measuring experimentally. We really can measure experimentally the values of the surface tensions of an equilibrium ("old") and an unequilibrium ("new") surface of liquid [Kochurova and Rusanov, 1981].

As the forces determining the results depend on the properties of the liquid we may propose that the charge separating during the break – up of the liquid doesn't depend on outer forces. Specifically it expresses in the fact that the glide plane will place just in DEL on independent of outer forces distance. At the same time it is known that the structure of DEL may be changed at the expense of the introduction of admixtures into the liquid [Fridrichsberg, 1974].

In particular, it is known that the introduction of NaCl leads to the compression of diffuse plate of DEL and therefore more antiions of diffuse plate of DEL occur higher then glide plane. It will lead to reduction of the drop's charge separating during the break – up.

## EXPERIMENTAL METHOD

For modelling the process of break – up of rain drops was used the experimental set – up Kolpakov et al. [1989]. It cousists from three main units:

1) the generator of monoparametric drops of "vibrating needle" type;
2) the optic – lighting system on the base of impulse lamp and long – focus microscope;
3) the electromeasuring system based on the electrometer.

The system of the break – up of the liquid allowed to get the drops parameters of which (the value, the velocity, the trajectors, the charge, the chemical composition) differ within the limits of 1% - 2%. The optic – lighting system allowed to control both the process of separation of the drop inself and its further movement. Moreover the scheme of "time machine" was realized because the set – up gave the possibility to watch by sight the process of break – up in any its phase and in any moment. "Freezing" the process in the phase of interest we arrange the measurements of geometrical parameters of the separating element of liquid without help of photographing.

The electromeasuring system allowed to catch the drop into the trap (the Faraday's cylinder) and to fix the drop's charge both in accumulating and current regime. The value of current corresponded to electrometer range of $\sim 10^{-12}$ A.

The experiments were carried with the NaCl solution in the distille water. Besides the drop's charge was also determined with other parameters, particularly with the electric capacitance of the liquid element at the moment of its separating. It leads to the necessity of measuring the geometric parameters of liquid element and calculating its capacitance.

Since the liquid element is "spindle" like form at the moment of separating its capacitance is [Sommerfeld, 1949]

$$C_c = \frac{2\pi l \varepsilon \varepsilon_0}{\ln\left(\frac{l}{d_n}\right)}$$

were $d_n$ is the diameter of the middle part of the element; $l$ is its length, $\varepsilon$ and $\varepsilon_0$ - are dielectric permeability and relative electric constant in $SI$, correspondingly $\varepsilon_0 = 8.85 \cdot 10^{-12} Cl^2 / N\,m^2$. It was carried a great number of measurements both with the solutions of different concentrations and with liquid elements of different geometric parameters. It allowed reliably determine the dependence between the drop's charge and the concentration of NaCl solution.

The variation $q = f(C)$ for different fixed significanes of capacitance of separating liquid element $C_c$ is represented on fig. 1

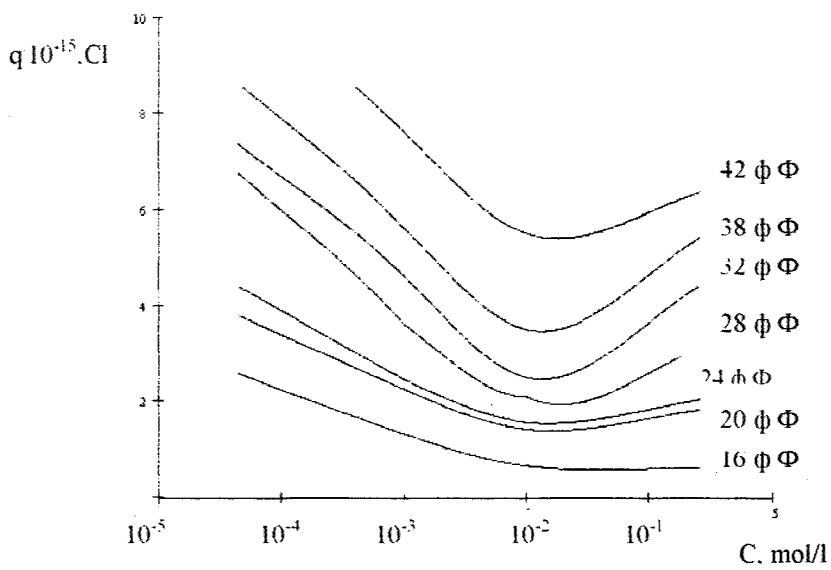


Fig.1. The variation of the electric charge ($q$) with concentration of NaCl solution ($c$) for different values of capacitance of separating liquid element.

All variations have the characteristic minimum. It corresponds to the concentration of solution of $10^{-2}$ mol/l. It is clear that capacitance of the spherical drop differs from the capacitance of liquid element from which the drop appears making several oscillations with mode n=2. And the drops of same dimensions may arise from the liquid elements of different geometric dimensions and, consequently, capacitance.

We can't compare our results with the same researchers of other scientists because they were oriented on the dimension of the drop. But there is one [Lopatenko and Maliarova, 1985] where it was determined an existence

of minimum on the curve of variation of drop's charge with the solution concentration. Ascending branch of the curve $g=f(c)$ from the point $C=10^{-2}$ mol/l is connected with the structure of DEL.

The capacitance $C_e$ was measured independent that allows to determine its functional connection with the value of the electric charge (fig. 2)

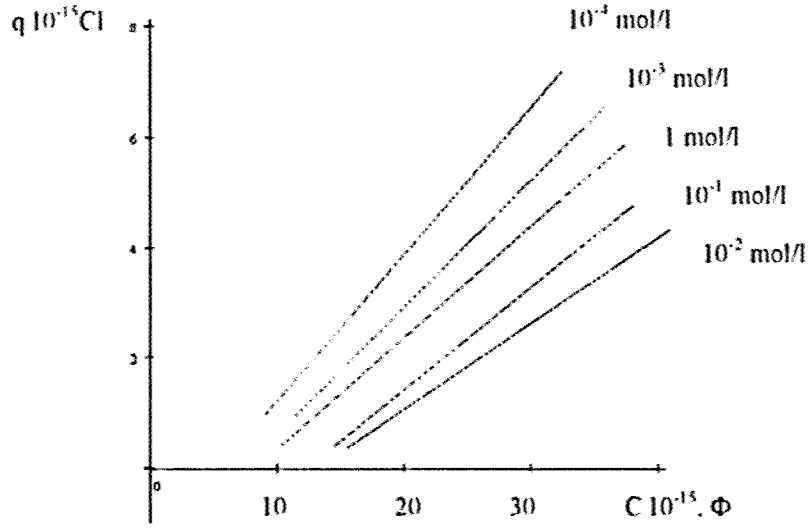


Fig. 2. The variation of electric charge ($q$) with the capacitance of separating liquid element ($C_e$) for different solution concentration.

As it has been expected the variation $q(C_e)_{c=const}$ is linear.

The next logic step is to introduce such a value as an electric potential $\zeta \sim \frac{q}{C_e}$

Calculating $\zeta$ from fig. 2 for concentration $C=10^{-2}$ mol/l we'll get minimum.

At the same time independent measuring of surface potential at different concentrations of solutions [Jarvis, 1972] shows that this depentence is linear and no extremums could be determined.

Therefore the value of $\zeta$ could not be interpreted as a surface potential of liquid. The arising of minimum of function $g=f(c)$ is determined on the one hand by the process of structure reconstruction of DEL – the compession of inside diffusive layer and on the other hand by increasing of charge carrier in outer layer. The growth of surface potential is indicative of this process.

REFERENCES


Kolpakov A.V., Kontush S.M., Dmitrieva E.M., Izmerenie elektrizacii kapel vodi pri chastichnom sliyanii. Meteorologiya i gidrologiya, 1983, № 7, p. 120 – 122

Lopatenko S.V., Maliarova L.V., K voprosu optimizacii procesa zaryadki jidkosti pri dispergirovanii. Coll J. 1985, v. 47, №4, p.809-812

Kolpakov A.V., Mechanizm elektrizacii jidkosti pri droblenii. J. Phys. Chem., 1991, v.65 №4, p.1095-1096

Kochurova N.I., Rusanov A.I., Svoistva neravnovesnoy poverchnosti vodi i vodnich rastvorov. Coll. I. 1981, v. 43, №1, p.36-42

Fridrichsberg D.A., Kurs colloidnoy chimii. Chimiya, 1974, p.351

Kolpakov A.V., Salov V.A., Dmitrieva E.M., Metodika i ustanovka dlya issledovaniya zaryadki kapel pri soudarenii. Phys. aerodisp.syst., v.32, 1989, p.6-9

Sommrefeld A., Elektrodynamik Leipzig, 1949

Jarvis N.L., Effect of Various Salts on the Surface Potential of the Water – Air Interface. J. Of Geophysical Resach. September 20, 1972 v.77, № 27, p.5177-5182

**Thunderstorm and Lightning Development : Modeling and Observations**

Robert Solomon, Claire Thery, Eric Defer, Anne Bondiou-Clergerie
ONERA, BP 72, 92322 Chatillon Cedex, France

Abstract

We use results of a numerical model of convective clouds with a lightning parameterization to examine thunderstorm development and the location of lightning initiation in a Florida storm. These results are compared with radar observations and interferometric measurements of VHF emissions from both intra-cloud (IC) and cloud-to-ground (CG) lightning flashes. Observed rate and mean duration of flashes are analyzed through model results, and we comment altitudes of VHF sources given by the ONERA 3D interferometric system.

## 1. Introduction

Until recently, numerical models of thunderstorms described only the earliest period of storm development, to the time of initiation of the first lightning channel. We use a 1.5 dimensional cloud model which includes an electrification of cloud particles and lightning parameterization (Solomon and Baker 1998, Thery et al, 1998), in order to examine the temporal development of lightning flashes type and frequency, and their vertical extension within the cloud. We compare this to observations made with the ONERA 3D VHF interferometric system and MIT/Lincoln Laboratory radar data.

Initial results of the model prove promising in relating lightning flash rate and type (IC and CG) for a range of differing environments. However, the lightning parameterization under predicts the number of CG lightning events typically observed in thunderstorms (Solomon and Baker 1998) suggesting that some mechanism not currently accounted for may be responsible for initiation of CG lightning, specifically the effect of large droplets and/or ice (Coquillat et al, 1995; Schroeder et al 1998, Cooray et al, 1998). Solomon and Baker (1998) comment on the importance of altitude of lightning initiation point in determining if a lightning channel remains within cloud or can propagate to ground. All altitudes are given here above mean sea level.

## 2. Methods of Analysis

### 2.1 The thunderstorm model

The thunderstorm model (Solomon and Baker, 1998) consists of three communicating coaxial cylinders: inner and outer cloudy regions and an unsaturated environment. We assume only one charge separation mechanism : the non-inductive charge transfer accompanying collisions of ice crystals and soft hail particles observed and documented in a range of laboratory conditions (Saunders et al, 1991). The instantaneous charge separation rate depends on the liquid water content, temperature and numbers and sizes of ice crystals and hail particles in the charging zone (between -5 °C and -20 °C).

The thunderstorm model includes a lightning parameterization which consists in extending in up and down direction an electrostatic conductor from the point where the electric field exceeds a prescribed value (here 100 $kVm^{-1}$). Charge induced on the channel with its final length modifies the charge distribution in the cloud through redistribution onto hydrometeors. The lightning parameterization closely follows that of Solomon and Baker (1996) with the addition of an internal field within the parameterized lightning channel and a slightly different propagation criterion (Thery et al, 1998).

### 2.2 Data set : Florida 14 August 1992 (Orlando)

Observations consist in environmental soundings, radar 3D pictures and interferometric observations of the VHF emissions from lightning flashes. On 14 August, the CAPE was 2 kJ/kg and the observed cloud base was at 1200 m. Thunderclouds developed during the afternoon and last for three hours. We focus our studies on cells that formed between 1900 and 2030 UT.

Three Doppler radars were installed on the summit of a triangle around the Orlando airport. Measurements have been used by the MIT Lincoln Laboratory to obtain a three-dimensional picture of the radar reflectivity and wind field every three minutes and having a 200 m spatial resolutions.

The ONERA high resolution VHF 3D interferomenter was also installed in this region to obtain detailed descriptions of the three dimensional structure of the lightning activity of storms around the Orlando airport. This system was developed by the DIMENSIONS company. The system consists in two independent angular localization stations 40 km apart. One station gives the angular elevation of VHF sources, while both report the azimuth of sources, with a temporal resolution of 23 μs (Laroche et al, 1994).

## 3. Results

### 3.1 Radar observations

The figure below shows the total flash rate after 19:00 UTC around the Orlando airport, from the ONERA measurements. Two very active cells developed in a multicell storm, their contribution to the flash rate are shown by two different greys. These two cells were also recognized on radar data, and we extracted the times of maximum updraft and maximum altitude of their top, indicated by arrows on figure.

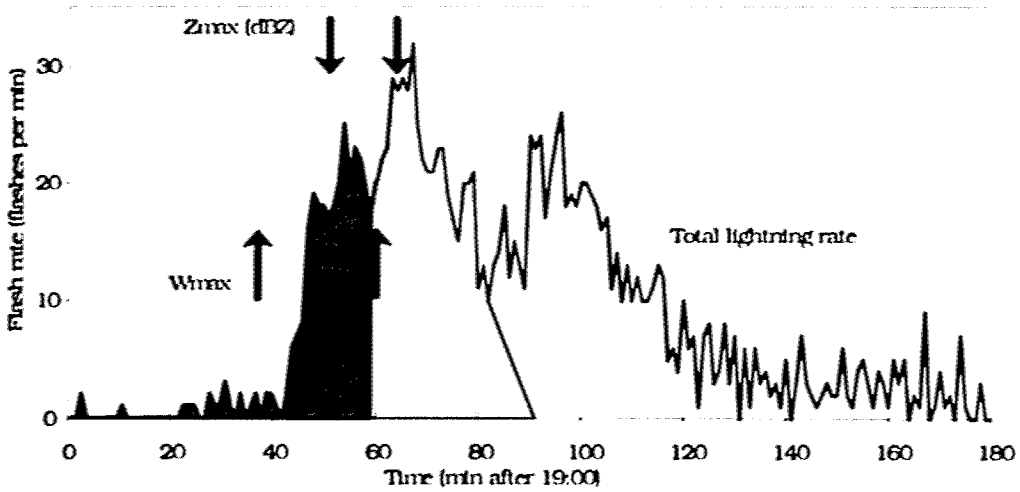


In these two cells, the maximum updraft occurred just before the sharp increase of the total flash rate, and this rate was maximum when the top of the cell was at its highest altitude.

### 3.2 Interferometric observations

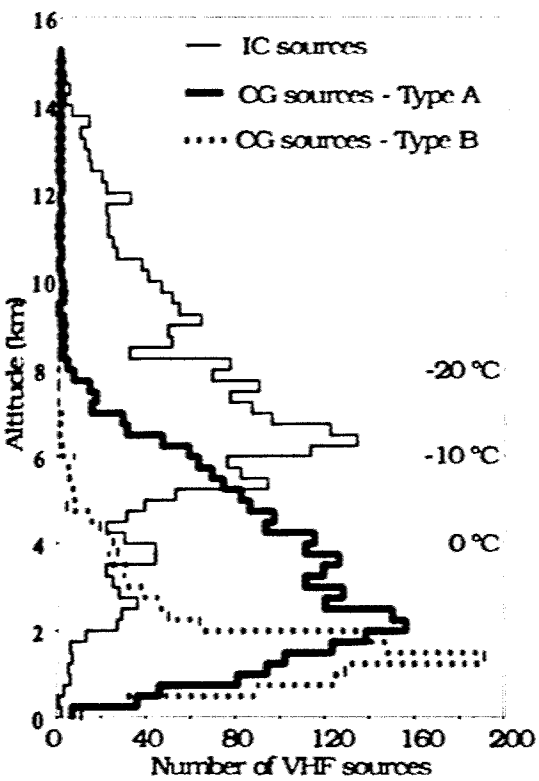


We present here an histogram of altitudes (increment of 250 m) of all VHF sources between 1930 and 2000 UTC for an isolated section of the 14 August 1992 storm (including the first cell cited above). The thick dashed line represents all VHF sources associated with events (bursts) with a duration greater than 800 µs inside negative CG flashes, indicative of negative leaders /return stroke processes. The thick line is for sources associated with events shorter than 800 µs of negative CG lightning (recoil streamers and dart leaders). The thin line is for all sources associated with IC lightning. One can see that sources from negative CG have a maximum density just below 3 km. The initial leader of negative CG lightning and subsequent dart leaders start at low altitude (below 3 km) and go to the ground, and associated recoil processes extending higher into the cloud. Density of sources from IC flashes reaches a maximum near 6 km. These two zones (below and above 6 km) probably correspond to the respectively negative and positive main charge centers of the storm. This bi-modal distribution of VHF sources is similar to that observed by others (Ray et al, 1987). The interferometric system cannot give reliable elevations below 5 °, so low altitude sources are recorded but they are reconstructed at a higher altitude (~ 1.5 km).

The following figure gives the total lightning flash rate determined from the interferometric system in a small isolated cell with a peak flash rate of 18 per minute around 1948 UTC. Also shown is the mean lightning duration (ms) averaged over a one minute interval. This kind of cell, quite isolated from the rest of the multicell storm, can be better compared to the results of our numerical model. During the period of highest flash rate, the mean flash duration is under 100 ms indicating many short lightning events. With continued storm development, the lightning flash rate decreases, however, the mean duration of lightning is several hundred ms, indicating fewer lightning events with a much larger spatial extent within the cloud and long lasting negative CG.

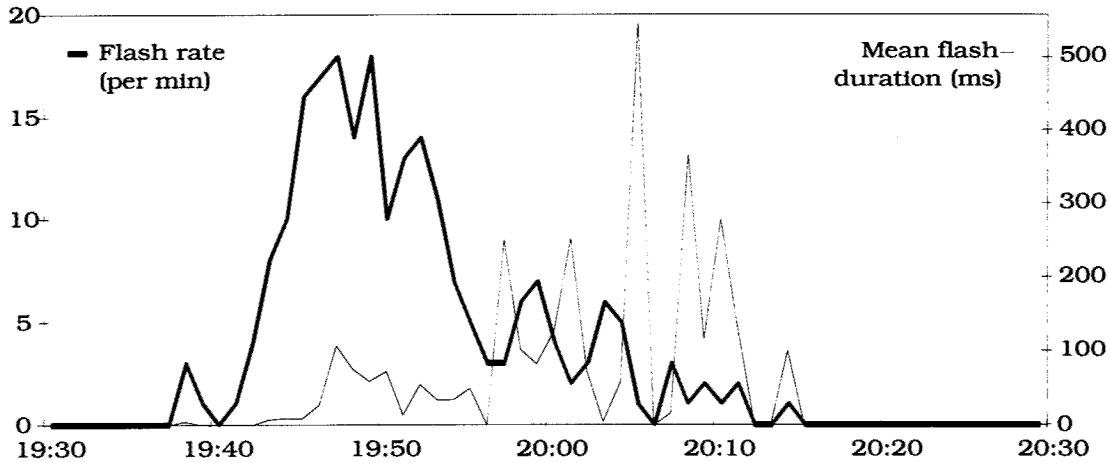


3.3 Modeling

We show below the time evolutions of the axial electric field (negative value of the field in light greys, positive ones in dark greys) given by the thunderstorm model, along with the lightning flash rate, the vertical extent of each lightning channel (vertical lines) and the altitude of lightning initiation (black dots).

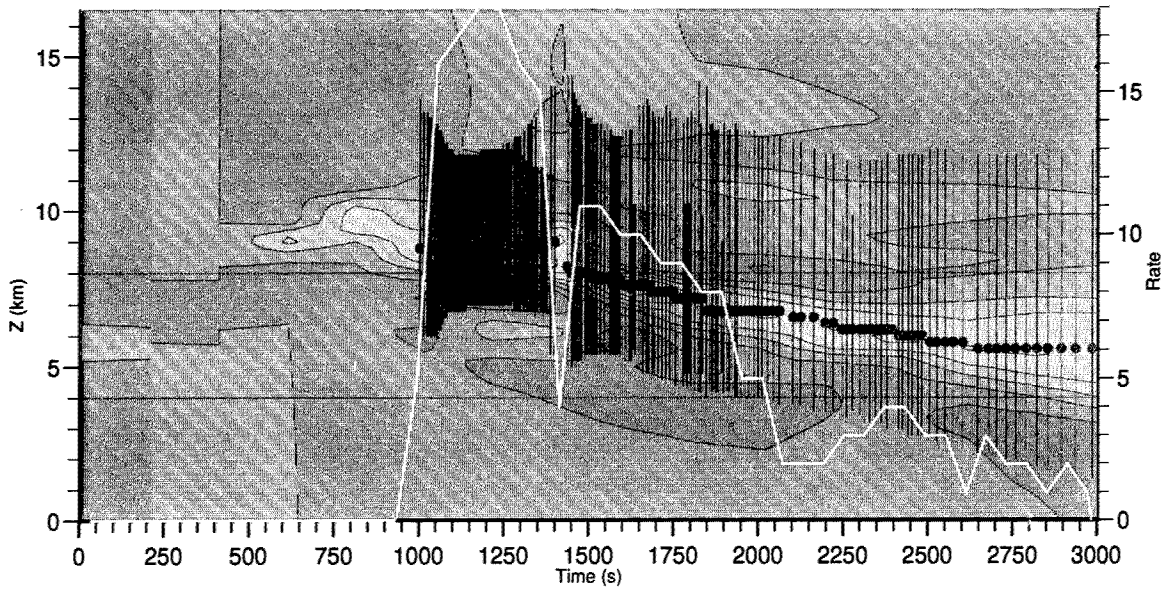


The early history of the storm is characterized by very rapid electrical development and a high initial lightning flash rate that reaches a maximum of 18 per minute, few minutes after the peak in mid-level updraft and near the time of the maximum altitude of the calculated reflectivity. The high flash rate can be related to the past high updraft (maximum updraft was 25 $ms^{-1}$), a large flux of liquid water and a large amount of ice particles with a wide spectrum of sizes into the charging zone (-5 °C to -20 °C). During this active electrical period of the storm, lightning channels tended to remain relatively short in vertical extent, typically less than 5 km.

Subsequent storm development shows a decrease in high altitude updraft and of the available liquid water in the active charging zone of the cloud. The large riming graupel are not sustained anymore, they fall from the charging zone and effectively decreases the separation rate of charges. This is due in part to the strong size dependence of charge separation and the strong dependence on available liquid water (Saunders et al 1991, Solomon and Baker, 1998). Lightning becomes less frequent and have a much larger vertical extent than the previous stage of the cloud's development with channels reaching 10 km in length. During the high charge rate period, the initiation electrical field is reached before charged ice particles can spread over a large vertical extent. When the charging rate is lower, lightning flashes develop in more diffuse and spread charge centers, so they can be longer. All lightning channels were initiated above 5 km and we never observed CG lightning in this particular model evaluation of this storm.

## 4. Summary

In the numerical simulation, during the initial period of thunderstorm development, the conditions for charge generation (coexistence of riming graupel, ice and supercooled liquid water in the charging zone) have not been met. When such conditions do exist, there is a very rapid build up of charge and the magnitude of the electric field quickly reaches the value preset for initiation of lightning. This period of the thunderstorm is characterized by continued charge generation via ice-ice collisions with a constant supply of liquid water from below. Lightning flash rate can be quite high and the channels themselves tend to be short in vertical extent. With time, the updraft decays, there is less large ice suspended within the charging zone and the supply of liquid water into the charging zone is no longer sufficient to maintain the high charging rate of the previous period. The negative charge region is seen to descend and intra-cloud lightning can be quite long in vertical extent.

These model reconstructions are in good agreement with the radar and interferometric observations with the exception of lack of cloud-to-ground lightning within the model : the first lightning activity appears after the end of the main updraft, quickly reaches its maximum value, when the top of the cloud exhibits its maximum altitude. Then the flashes become longer and less numerous in a second phase.

Altitude coverages of observed lightning flashes vary with the type of flash and the type of process inside the flash : in negative CG, negative leaders and subsequent dart leaders spread between 0 and 3-4 km, and associated recoil streamers between 2 and 8 km. In IC flashes, we mostly observed recoil streamers, with a first group of altitudes between 4 and 15 km, and a second smaller group between 2 and 5 km.

These interferometric data suggests that it is necessary to initiate cloud-to-ground lightning at a lower altitude, specifically, below the altitude of the peak negative charge density. This result is similar to Solomon and Baker (1996 & 1998). However, the electric field at lower altitudes (less than approx. 5 km) is never sufficient within the model to initiate lightning there. Continuing work is being done to investigate the ability of large drops to locally increase the electric field at these altitudes in order to more easily initiate lightning at low altitudes.

## Acknowledgments

RS was partially supported by USRA Cooperative Agreement NCC8-142. We thank the MIT Lincoln Laboratory for giving us the 3D radar pictures.

## References

Cooray, V., M. Akyus, M. Berg, M. Zitnik, A. Larrson, V. Scuka, 1998: Initiation of ground flashes : some microscopic electrical processes associated with precipitation particles. *Proceedings of the 24th International Conference on Lightning Protection, Birmingham, UK*, 128-133.

Ray, P. S., D. R. MacGorman, W. D. Rust, W. L Taylor and L. Walters Rasmussen, 1987 : Lightning location relative to storm structure in a supercell storm and a multicell storm., *J. Geophys. Res.*, **92**, 5713-24.

Schroeder, V., M. B. Baker, J. Latham, 1998 : A model study of corona emission from hydrometeors. *Accepted by Q J R Meteorol Soc.*

Thery, C., E. Defer, R. Solomon, 1998 : Numerical modelisation of storm dynamics, precipitation and electrisation. *Abstract for the 23rd General Ass. Of the EGS*, Nice, France.

Coquillat S., S. Chauzy and J.C. Medale, 1995 : Microdischarges between Ice Particles,. *J. Geophys. Res.*, **100**, 14327-14334.

Laroche P., A. Bondiou, P. Blanchet and, J. Pigère, 3D VHF mapping of lightning discharge within a storm, *Proceedings SEE "lightning and mountains", Chamonix, France*, 1994.

Saunders C. P. R., W. D. Keith and P. P. Mitzeva, 1991, The Effect of Liquid Water on Thunderstorm Charging, *J. Geophys. Res.*, **96**, 11007-11017.

Solomon R., and M. Baker, 1996, A one-dimensional lightning parametrization, *J. Geophys. Res.*, **101**, 14983-14990.

Solomon R., and M. Baker, 1998, Lightning flash rate and type in convective storms, *J. Geophys. Res.*, **103**, 14041-14057.

# SIMULATION STUDY OF NON-INDUCTIVE CHARGING AND DISCHARGE PROCESSES IN THE THUNDERSTORM

Yijun Zhang Muhong Yan Xinsheng Liu

(Lanzhou Institute of Plateau Atmospheric Physics, Chinese Academy of Sciences)

ABSTRACT: An axisymmetric, time-dependent numerical cloud model has been applied to study non-inductive charging and discharge characteristics in thunderstorm. The affect of environmental stratification factors, convection, rainfall and ice crystal size distribution on charging process and the relationships among convection, precipitation and lightning are discussed.

## INTRODUCTION

The non-inductive charging mechanism collided between graupel and ice crystals is a main charging process for formation the charge and electrical field structure in the thunderstorm(Noville et al., 1991, Ziegler et al., 1991). Meanwhile, convection, precipitation and lightning are three main physical processes in thunderstorm. However, many researchers have only paid attention to description of characteristics about convection, precipitation and lightning, related physical mechanisms among them have been rarely studied. In this paper, an axisymmetric, time-dependent numerical cloud model has been applied to study non-inductive charging. Based on the work of Helsdon, et al.,(1992), discharge process is introduced into thunderstorm electrification model by means of parameterized method. The coherence between lightning activities and dynamic, precipitation is discussed by using this model.

## MODEL

The model structures are described by Yan Muhong et al.(1997). An electric force term is introduced into the equation of motion to simulate a direct electric influence on the air motion. The reverse temperature is -10 ℃ for non-inductive charging.

## RESULTS

(1).The influence of environmental stratification factors

We use seven sounding stratification data to simulate the electric action in cloud. The thermal and kinetic forcing of air around the cloud base ($E_{kin}$(J/kg)=$W_b^2/2$ ) is introduced into the equation, where $W_b$ is updraft velocity around the cloud base at $t_{cb}$ when the downdraft just appears around the cloud base. So, $(E_{kin})_{tcb}$ at $t_{cb}$ show last updraft energy of the simulated cloud. It depends on stratification condition. Figure 1 show maximum of cloud-top-height $Z_p$, updraft velocity W and space charge concentration $\rho_c$ for different cloud region as a function of $(E_{kin})t_{cb}$ at $t_{cb}$. The lateral coordinate is value of $(E_{kin})t_{cb}$ to indicate sounding date. It is indicated from figure 1 that the simulated cloud still develop after $t_{cb}$ for each sounding time and $Z_p$, W and $\rho_c$ reach the maximum after 5-10 min.

Figure 1 also show that $Z_p$ and $\rho_c$ increase with increase of $(E_{kin})t_{cb}$. But after $(E_{kin})t_{cb}$ reach a certain value, with the magnitude of 0.8-0.9 J/kg, $Z_p$ and $\rho_c$ decrease with increase of $(E_{kin})t_{cb}$ (case on 30 August is a reverse example due to affect of frontal weather). When $(E_{kin})t_{cb}$ is large than 1J/kg , $\rho_c$ rapidly decrease with increase of $(E_{kin})t_{cb}$. That is that the maximum of $Z_p$, W and $\rho_c$ appear when $(E_{kin})t_{cb}$ is middle value, with the magnitude of 0.8-0.9J/kg in this paper (correspondingly updraft velocity around cloud base is 1.3m/s). At this time, $Z_p$ already develop above 10km and $\rho_c$ also reach maximum, for example, $\rho_-$ (negative charge concentration) is 2-3 $\times$ $10^{-8}$ c/m$^3$, $c_+^H$ (positive charge concentration of upper cloud region ) 0.4 $\times$ $10^{-8}$c/m$^3$ and $\rho_+^L$ (low cloud region) is 1-2 $\times$ $10^{-8}$ c/m$^3$ .

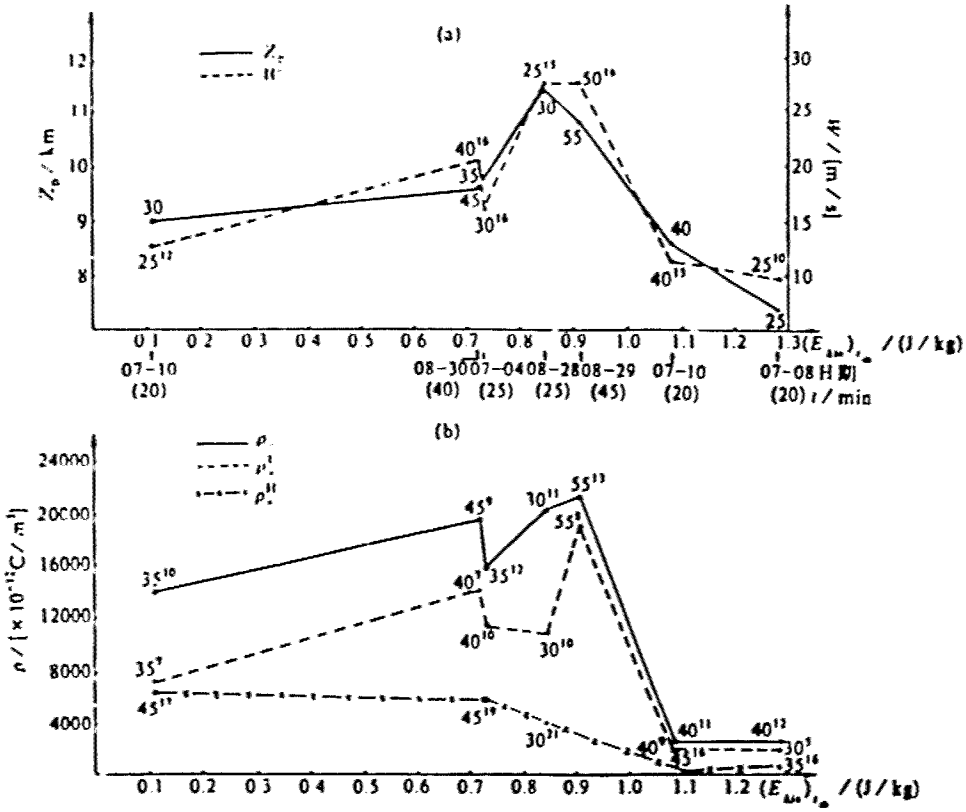


Fig.1. Model-computed maximum of cloud-top height(a) and space charge concentration(b) as a function of $E_{kin}$ at $t_{cb}$. $\rho_-$, $\rho_+^L$ and $\rho_+^H$ represent negative charge, positive charge of the lower part and the upper part of the cloud respectively. The numbers represent time at these values( × 0.4km). Arrow indicates calculating stratification date, the number in parenthese represents the time at this $E_{kin}$ value (min).

Therefore $(E_{kin})t_{cb}$ is more useful than CAPE (convective available potential energy )as a parameter which represents intensive or weak dynamic and electric action in the clouds. The thermal and kinetic forcing of air at temperature layer of -10 ℃, -20 ℃ can well exhibit intensity of electric actions in the cloud, and also have optimum threshold of 60-70J/kg and 20J/km, respectively. The $Z_p$ also is a correlative factor, the optimum threshold value is 9.0km for plateau clouds in China.

(2). Influence of cloud parameters

The electrification in cloud depends on not only environmental stratification but also dynamics and microphysics processes in cloud. Five size distributions of ice crystal and graupel are considered in this model. The results show that electrification rate obviously depends on the updraft. There are intensive charging in cloud when intensive updraft center passes -20 ℃ temperature layer. The intensive charging occurs during the stage in which maximum updraft velocity just begins to decrease. The charge center regions are not coincident with the updraft regions, it commonly appears near lower boundary of the updraft region and downdraft region. The precipitation is an important condition of separating different polar charge. But it is obviously weaker than the convection. The size distribution of ice crystal has a little affect on the air current field. But it can change the temporal and space distribution of ice particle,

especially the vertical distribution. Therefore, it can change the temporal and space distribution of the non-inductive charging rate. The height of main negative charge center and carriers of charge also change correspondingly.

Simulated positive charge concentration in lower part of the cloud is larger and coincident with main negative charge. But its lasting time is shorter and the region is also smaller. The intensive updraft only last 5-10 min after the maximum. If the intensive updraft can last longer time, the lasting time of lower positive charge center also can increase. For thunderstorms in North China, the positive charge center in lower part of cloud has usually been observed because the intensive updraft have longer lasting time. For thunderstorms in South China, it has not been observed due to heavy precipitation and intensive downdraft.

(3).Characteristics of discharge

The calculated results show that the discharges mainly occur between 4.4-4.8km and 6.4-6.8km(corresponding to -10°C and -25°C). They locate between lower positive charge area and middle negative charge area, and between upper positive charge area and middle negative charge area respectively. Discharge out of 90% occurs in lower of thunderstorm.

(4).Discharge, updraft velocity and precipitation on the ground

Figure 2 shows simulated variation of discharge number and maximum updraft velocity with time. There are 116 discharges (dashed line) which mainly occur at the time between 32min and 43min. The peak of discharges with the number of 21 occurs at 38min. The updraft velocity reaches maximum value at 34min, with the magnitude of 22.1m/s. Thereafter, the updraft velocity decreases with time, being 1.2m/s at 60min. Before 31min, there are no discharge due to no precipitation, even though updraft velocity is larger(see figure 3). There are discharges at 32min and maximum updraft velocity is larger than 20m/s. After that time, discharge number increases with increase of maximum updraft velocity. When maximum updraft velocity decreases after its peak, discharge number also decreases in about 1min. But it increases again and reaches peak at 38min.(This may be caused by increase of precipitation, see analysis later). The maximum updraft velocity is 13m/s at that time. Soon afterwards, discharge number decreases rapidly. The maximum updraft velocity with magnitude of 10m/s seems to be a threshold of discharge. The formation of intense electric field in thunderstorm mainly depends on updraft. The peak of discharge number lags the peak of maximum updraft velocity.

Figure 3 shows the simulated variation of precipitation with time on the ground. By comparison with figure 2, it is found that discharge occurs when precipitation rate is more than 5mm/h on the ground. The discharge number increases rapidly with increase of precipitation. The precipitation rate on the ground is 30mm/h when the discharge number reaches peak at 38min. The maximum value of precipitation rate on the ground appears at 44min, being 114mm/h. The peak of precipitation rate on the ground lags the peak of discharge number by a period of about 6 minutes. These calculated results are consistent with the results obtained by Williams et al.(1989). The discharge processes need stronger updraft velocity. The peak of discharge lags the peak of updraft velocity. The discharge number decreases during the stage in which updraft velocity begins to decrease (in figure 2 at 33 -34min). After that time, discharge number increases with increase of precipitation (in figure 2 at 34-38min). This shows that besides updraft velocity, discharge also needs hydrometer particles with a specified concentration and size. These hydrometer particles increase through collision processes and cause the increase of precipitation on the ground. It can be seen from figure 2 and 3 that discharge number decreases rapidly after 38min even though the increase of precipitation is fast. This is caused by decease of updraft velocity. So, lightning activity may be an important factor for monitoring and warning thunderstorm. The heavy rain of thunderstorm can be forecasted by using lightning data.

CONCLUSIONS

(1). The kinetic forcing of the air around the cloud base $(E_{kin})t_{cb}$ is more useful than CAPE as a parameter of representing intensive or weak dynamic and electric action in clouds. The thermal and kinetic forcing of air at temperature larger of -10 ℃, -20 ℃ can well exhibit intention of electric actions in the cloud.

(2). In simulated thunderstorm with tripole electric structures, 90 percent of discharges occur between lower positive charge area and middle negative charge area during precipitation and intensive updraft and propagate downwards.

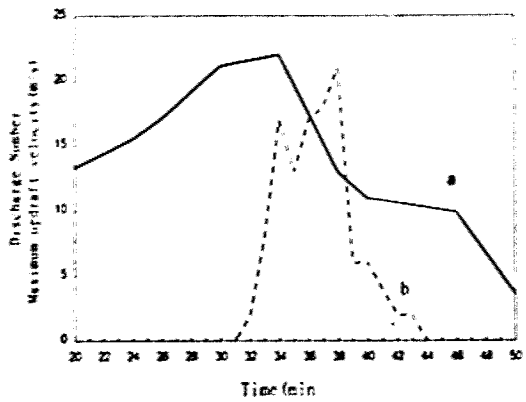


Fig.3. Simulated variation with time of discharge number and maximum updraft velocity

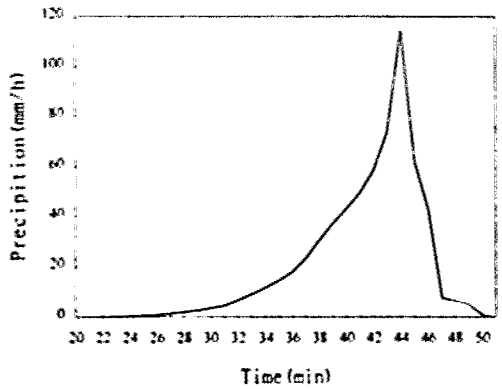


Fig.4. Simulated variation with time of precipitation on the ground

ACKNOWLEDGMENTS: This research was supported by Chinese Academy of Sciences(KZ951-B1-405) and the National Natural Science Foundation of China(49775254).

REFERENCES

Noville, K., M.Baker, A numerical study of thunderstorm electrification: model development and case study, J.Geophys.Res., 96(D4), 7463-7481, 1991.

Ziegler, C. L., D. R. MacGorman, A model evaluation of non-inductive graupel-ice charging in the early electrification of mountain thunderstorm, J.Geophys.Res., 96(D7), 12833-12855, 1991.

Helsdon, J.H., G.Wu, R.D.Farley, An intracloud lightning parameterization scheme for a storm electrification model, J. Geophys. Res., 97, 5865-5884, 1992.

Yan Muhong, Guo Changming, and Ge Zhengmo, Numerical study of cloud dynamical-electrification in an aximmetric, time-dependent cloud model. 1. Theory and model, ACTA Geophysica sinica, vol.39 supplement(in Chinese), 52-64, 1996.

Williams E.R., M.E.Weber, R.E.Orville, The relationship between lightning type and convective state of thunderclouds, J. Geophys. Res., 94, 13213-13220, 1989.

# RATE OF EVAPORATION OF THE CHARGED AND UNCHARGED WATER DROPS SUSPENDED IN THE AIR STREAM OF A WIND TUNNEL

A. K. Kamra, Rohini V. Bhalwankar and A. B. Sathe

Indian Institute of Tropical Meteorology, Pune, India

ABSTRACT: A laboratory simulation experiment has been performed to study the effect of ventilation on the rate of evaporation of millimeter-sized charged and uncharged water drops falling at terminal velocity in air. Water drops range in size from $1.91 > D > 4.10$ mm and carry a charge of $10^{-10}$ C. The mean ventilation coefficients computed for each size of the drop have been plotted against $(N_{Sc})^{1/3}(N_{Re})^{1/2}$ where $N_{Sc}$ is the Schmidt number and $N_{Re}$ is the Reynold's number. Our results for the uncharged drops are in conformity with those of Pruppacher and Rasmussen (1979). However, these results show that charged drops evaporate at a rate slower than that of uncharged drops. Moreover, the effect of ventilation is stronger on the evaporation of uncharged drops than that of charged drops. The results are interpreted in terms of the changes in terminal velocity, distortion and oscillation of the water drops when these are charged. The distance which is required for a water drop to fall from cloud base through a NACA Standard Atmosphere of various relative humidites in order to reach the earth's surface with a given size has been computed. The calculations show that at the cloud base, a charged water drop is required to be smaller in size as compared to an uncharged drop in order to reach the earth's surface with the same size.

## INTRODUCTION

For a complete understanding of the life cycle of a water drop in a cloud, it is essential to know various processes which govern the growth and evaporation of the drop within the cloud and during its fall from the cloud base to the ground. Several investigators have theoretically and experimentally studied the rate of evaporation of water drops (e.g. Froessling, 1938; Kinzer and Gunn, 1951; Ranz and Marshall, 1952a, b; Lee and Ryley, 1968; Woo and Hamielec, 1971; Beard and Pruppacher, 1971). Pruppacher and Rasmussen (1979) have studied the effect of ventilation on the evaporation of millimeter-size water drops suspended in a vertical wind tunnel. However, in all these studies, water drops have been assumed as electrically neutral. On the other hand, nearly all water drops in clouds are observed to carry charge of either polarity. The magnitude of charge on some drops in thunderstorms may approach Rayleigh's limit (Gaskell et al., 1978). Here, we report the results of a laboratory simulation experiment to study the effect of ventilation on the rates of evaporation of the charged and uncharged water drops suspended in a vertical wind tunnel.

## EXPERIMENTAL SETUP

Kamra et al. (1986, 91, 93) describe the details of the wind tunnel used in this experiment. It consists of a blower, a divergent section, a reservoir, a section having a honeycomb and three wire-mesh screens, a contraction section having a cross-wired screen at its downstream end and a test-section. A back-pressure plate is placed about 22 cm above the test section. Millimeter size water drops can be floated above the test section for as long as 30 minutes.

Water drops formed out of triply distilled water are introduced with a calibrated pippet, in the test section of the tunnel where turbulence level in the air stream is less than 0.8% (Kamra et al., 1991). The drops are photographed at 1-minute interval with a Nikon 35 mm still camera using a close-up lens No. 2 and ASA-400 black and white film. The drop volume and therefrom the drop's equivalent radius $a_0$ is determined from these photographs. In our experiment, the equivalent radii of the drops ranged between 0.955 and 2.05 mm. The wind tunnel is located inside an air-conditioned room and the temperature and relative humidity of the air-stream are between 28 and 31°C and 30 and 40%, respectively. The temperature is measured with a mercury thermometer to an accuracy of 0.1°C and the relative humidity with a dew-point hygrometer. The atmospheric pressure of the air in the laboratory is about 950 mb.

## DATA ANALYSIS

We will follow the procedure described by Pruppacher and Rasmussen (1979) to analyze our data. If (dm/dt) and $(dm/dt)_0$ are the rates of evaporation of a water drop falling at its terminal velocity in air and at rest, respectively, then the mean ventilation coefficient is defined by

$$\frac{dm}{dt} = \bar{f}_v \left(\frac{dm}{dt}\right)_0 \tag{1}$$

Following Beard and Pruppacher (1971), (1) can be written as

$$\bar{f}_v = \frac{dm/dt}{\dfrac{4\pi a_0 D_{v,a} M_w}{R}\left(\dfrac{e_\infty}{T_f} - \dfrac{e_a}{T_f}\right)} \tag{2}$$

when $e/p << 1$ where p is the total air pressure. In (2), $T_f = (T_\infty + T_a)/2$ where $T_a$ is the temperature at the drop surface, $T_\infty$ the temperature of the air stream, $M_w$ molecular weight of the water, R the universal gas constant, $e_\infty$ = RH x $e_{sat}(T_\infty)$ the water vapour pressure of the air, $D_{v,a}$ is the diffusivity of water vapour in air at the drop surface temperature $T_a$, $e_a = e_{sat}(T_a)$.

The values of dm/dt and $a_0$ are determined from our photograph of the drop and $e_\infty$ from the dew point of the air. $D_{v,a}$ is given by Hall and Pruppacher (1976) as

$$D_{v,a} = 0.2111\left(\frac{T_a}{T_0}\right)^{1.94}\left(\frac{p_0}{p}\right) \tag{3}$$

The drop surface temperature $T_a$ is determined from

$$\Delta T = T_\infty - T_a = \frac{L_e D_{v,a} M_w (e_\infty - e_a)\bar{f}_v}{kRT_f \bar{f}_h} \tag{4}$$

where $L_e$ and k are the latent heat of evaporation and thermal conductivity of the air at the drop's surface temperature respectively. $\bar{f}_h$ is a measure for the effect of ventilation on the transfer of heat to the drop. Equation (4) has been numerically solved following Beard and Pruppacher (1971). The values of thermal conductivity of moist air and the latent heat of evaporation are computed from the equations given by Pruppacher and Rasmussen (1979).

## RESULTS

Fig.1a shows the variation of the mean ventilation coefficient with $N_{Sc\,v}^{1/3} N_{Re}^{1/2}$ = X for the uncharged drops as determined from (2).

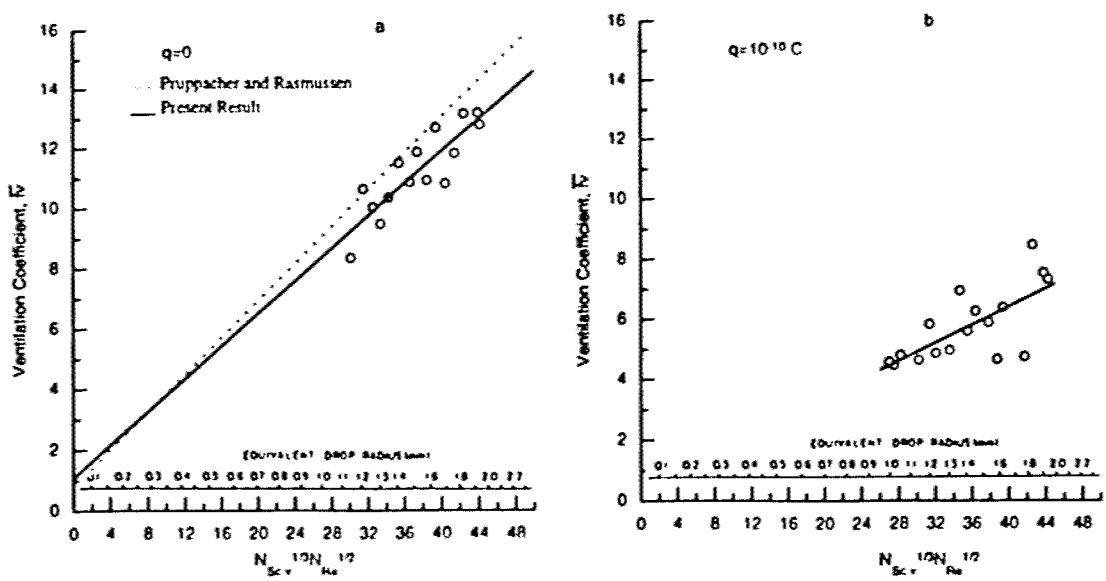


Fig 1 Variation of ventilation coefficient with $N_{Sc\,v}^{1/3} N_{Re}^{1/2}$ for (a) uncharged drops (b) charged drops

The line of best-fit found from least-square method can be expressed by

$$\bar{f}_v = 1.087 + 0.271X \tag{5}$$

From a total of 90 raw data points obtained in the 30-40% relative humidity, 15 average data points were calculated and are plotted in Fig.1a. Our results for uncharged drops are in reasonably good agreement with those of Pruppacher and Rasmussen (1979). For example, a water drop of $a_0 = 2$ mm freely falling at its terminal velocity will evaporate at a rate 15 or 13.6 times faster than a water drops of the same size at rest according to the results of Pruppacher and Rasmussen (1979) and ours, respectively.

Fig 1b shows the variation of the mean ventilation coefficient with $N_{Sc,v}^{1/3} N_{Re}^{1/2} = X$ and $a_0$ for the charged drops carrying a charge of $10^{-10}$ C. In the case of charged drops, the line of best-fit is given by

$$\bar{f}_v = 0.428 + 0.150X \tag{6}$$

In this case a total of 60 raw data points obtained in the same range of relative humidity were used to claculate 17 average data points. The line of best-fit in Fig. 1b is extended only upto $a_0 = 0.92$ mm since the charge of $10^{-10}$ C will be larger than the Rayleigh's limit for smaller drops. Our results show that the rate of evaporation of charged drops is lesser than that of uncharged drop. For example, the rates of evaporation of a charged drop of $a_0 = 2$ mm falling at its terminal velocity is only 7.2 times faster than that of the charged drop as compared to being 13.6 times faster in the case of uncharged drops of the same size at rest.

These results can be applied to learn about the evaporation of raindrops falling from clouds through the subsaturated subcloud air of various relative humidities in a NACA standard atmosphere. We have computed the size of drops by an iterative method falling below the cloud in air of various humidities and reaching the ground with a radius of 1 mm. Our results for uncharged drops shown in Fig. 2a are in good agreement with those of Pruppacher and Rasmussen (1979) i.e. the lower the relative humidity of the subcloud air the larger the drop has to be to reach the ground with a given size.

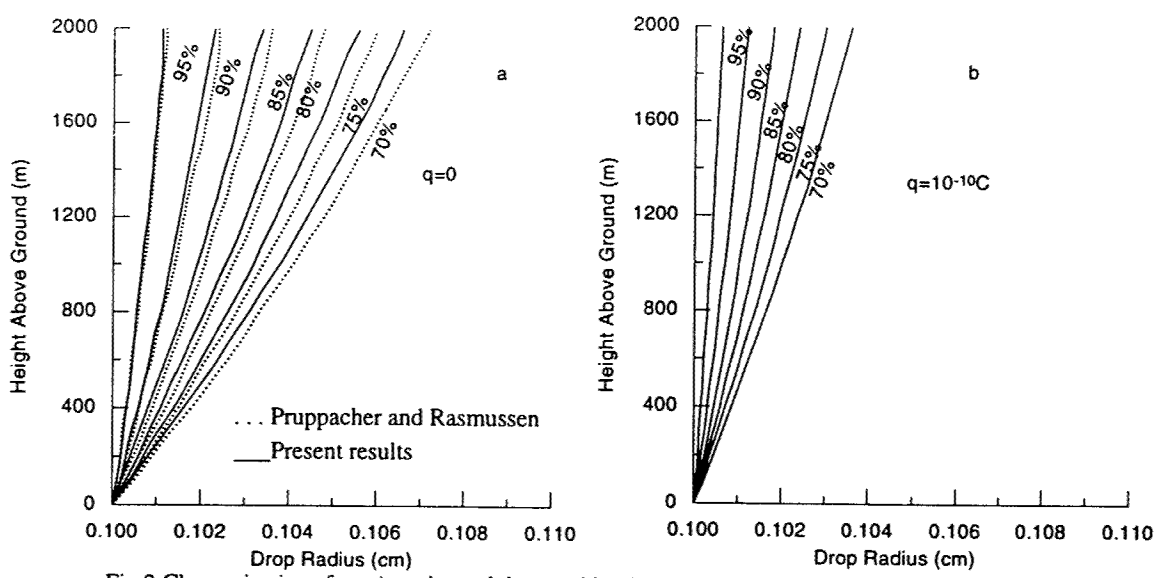


Fig.2 Change in size of an a) uncharged drop and b) charged drop falling below a cloud through the subsaturated air of various relative humidities in NACA Standard Atmosphere to arrive at the ground with the radius of 1 mm.

Fig. 2b shows similar curves for the charged drops carrying a charge of $10^{-10}$ C. The size of the charged drops leaving the cloud has to be smaller than the uncharged drops to reach the ground with the same size.

## DISCUSSION

Water drops >140 μ, freely falling in air, distort from their spherical shape and oscillate between the prolate and oblate spheroidal shapes. Pruppacher and Rasmussen (1979) conclude from their experimental results that the distortion, oscillation and internal circulation of large drops have no effect on the effect of ventilation on the evaporation of uncharged drops. Our results for uncharged drops confirm their results. Pruppacher and Rasmussen justify their conclusion on the basis that the larger effect of ventilation for a prolate spheroid than for a sphere is approximately compensated by the smaller effect of ventilation for an oblate spheroid than for a sphere. Kamra et al. (1991) have shown that the effect of drop's charge on its shape is to enhance its oblateness i.e. to increase the mean value of drop's major axis around which it oscillates between the prolate and oblate spheroidal shapes. Consequently, the terminal velocity of a charged drop will decrease as compared to the uncharged drop. Therefore, the effect of ventilation on the evaporation of a charged drop will be less than that of an uncharged drop. The results of our experiment confirm this. Thus, the raindrops falling from an electrified thunderstorm may evaporate at a lesser rate than those falling from a weakly electrified cloud.

In our experiment , water drops of all sizes uniformly carry a charge of $10^{-10}$C. So the smaller drops will have larger surface charge density than the larger drops. The fact that the scatter of data points in Fig. 1b increases with increase in drop size indicates that the contribution of electrical forces on the effect of ventilation on the rate of evaporation increases with the increase in the surface density of charge on drops.

## REFERENCES


Beard, K.V., and H. R. Pruppacher, A wind tunnel investigation of the rate of evaporation of small water drops falling at terminal velocity in air, J. Atmos. Sci., 28, 1455-1464, 1971.

Froessling, N., Ueber die Verdunstung fallender Tropfen. Gerlands Beitr. Z. Geophys., 52, 17,216, 1938.

Gaskell, W., A. J. Illingworth, J. Latham, and C. B. Moore, Airborne studies of electric fields and the charge and size of precipitation elements in thunderstorms, Q. J. R. Meteorol. Soc., 104, 447-460, 1978.

Hall, W. D., and H. R. Pruppacher, The survival of ice particles falling from cirrus clouds in subsaturated air, J. Atmos. Sci., 32, 1995-2006, 1976.

Kamra, A. K., R. V. Bhalwankar and A. B. Sathe, Spontaneous breakup of charged and uncharged water drops freely suspended in a wind tunnel, J. Geophys. Res., 96, 17,159-17,168, 1991.

Kamra, A. K., Rohini V. Bhalwankar, and A. B. Sathe, The onset of disintegration and corona in water drops falling at terminal velocity in horizontal electric fields, J. Geophys. Res., 98, 12,901-12,912, 1993

Kamra, A. K., A. B. Sathe and D. V. Ahire, A vertical wind tunnel for water drop studies, Mausam, 37, 210-222, 1986.

Kinzer, G. D., and R. Gunn, The evaporation temperature and thermal relaxation time of freely falling water drops, J. Meteor., 8, 71-83, 1951.

Lee, K., and D. J. Ryley, The evaporation of water drops in supersaturated steam, J. Heat Transfer, 90, 445-451, 1968.

Pruppacher, H. R., and R. Rasmussen, A wind tunnel investigation of the rate of evaporation of large water drops falling at terminal velocity in air, J. Atmos. Sci.,1255-1260, 1979.

Ranz, W. E., and W. R. Marshall, Evaporation from drops, Chem. Eng. Progr. 48, 141-146, 1952a.

Ranz, W. E., and W. R. Marshall, Evaporation from drops, Chem. Eng. Progr. 48, 173-180, 1952b.

Woo, S. W., and A. E. Hamielec, A numerical method of determining the rate of evaporation of small drops falling at terminal velocity in air, J. Atmos. Sci., 28, 1448-1454, 1971.

# A STUDY OF THE ION ATTACHMENT BY DROPLETS IN CLOUD CONDITIONS: IMPLICATION FOR POLLUTANT TRANSPORT

G. M. Caranti and S. Masuelli

FaMAF, UNC, Córdoba, ARGENTINA

ABSTRACT: In this work, we study the ion attachment by droplets for a wide range of ambient conditions. By means of a numerical model we simulate the ion trajectories in the fields (air flow and electrical) determined by a spherical charged conductor immerse in uniform ambient electric and air velocity field. From these trajectories we calculated the capture cross section and the ion current. This cross section depends on many variables: droplet radius, ambient electric field, droplet charge, droplet terminal velocity, ion mobility, air viscosity, etc. It is important to note that, when the electric field is not vertically oriented, this problem becomes a three dimensional and a much more complex one. We studied various different situations depending of what force was predominant the electrical (due to droplet charge or due to ambient electric field) or the aerodynamical. Both ion mobilities and ambient parameters varied over the range encountered in storms with the former including small and large ions.

## INTRODUCTION

The collision efficiency of small particles by cloud droplets depends on many variables, such as temperature, pressure, electric field, respective charges, recombination coefficients, radius, mobility, etc. (Prodi and Tampieri, 1982). Recent cloud models with detailed microphysical processes only take into account Brownian diffusion and the nucleation and avoid taking into consideration the electrical force in the scavenging of aerosols by cloud droplets (Zhang et al 1998, Wang and Chang 1993). Older laboratory and numerical works (Schlamps 1976, 1979) pointed out that for typical cloud conditions the collision efficiency between droplets could be greatly enhanced when they are charged. This suggests that the same could happens in the case of aerosols by droplets. Therefore, one can only speculate that the electrical parameters were not considered because of the difficult integration of all the dynamical, microphysical, chemical and electrical parameters in the same model. In fact, the magnitude of the electrical interaction is comparable or even greater than the other processes in pollution models.

The studies so far published about capture of little particles by charged droplets and in electric fields similar to thunderclouds are insufficient to develop a complete parameterization. This is why in this work we need to carry out first a numerical simulations of the collision efficiency between ions and droplets using detailed trajectories calculated in a variety of conditions. With all this information a global parameterization for the ion current by electric forces is proposed whenever this current exceeds the Brownian diffusion.

The thermodynamical, electrical, and geometrical parameters for this simulation were chosen as representative of cloud conditions. T=5 °C, P=800mb, $\rho$=1kg/m$^3$, $\eta$=1.742 $10^5$ kg/m, r=10μm, $\lambda$=0.078 μm. E-fields are $|E| \leq 100$ kV/m and charges are $Q \leq 1$ fC. The size spectrum of large ions to be studied is 0.01 to 1 μm characteristic of CCNs and the corresponding mobilities 5 $10^{-7}$ and 5 $10^{-10}$ m$^2$/(V s).

## NUMERICAL MODEL

The model considers the droplet as a charged conducting sphere moving with a velocity resulting from the balance of gravity, electric force, and aerodynamical drag. From the electric point of view an ion is acted by the superposition of stresses from the ambient field, the polarization of the sphere and the image charge. And the strong hypothesis here is that the ion moves relative to the air with a velocity only dependent of the total field. On the other hand, the flow around the droplet will be represented by the Proudman and Pearson approximation which is valid for Reynolds numbers smaller than 0.01. Therefore, the motion equation used is:

$$\frac{d\vec{r}}{dt} = \vec{v}_a + \left(\vec{E}_e + \vec{E}_p + \vec{E}_i\right)\mu \,, \qquad (1)$$

where **r** is the position, $\mathbf{v_a}$ is the air velocity, $\mathbf{E_e}$ is the external electric field, $\mathbf{E_p}$ is the electric field due to polarization and $\mathbf{E_i}$ is the image charge electric field. Equation 1 is solved using centered finite differences and with a time step adjustable according with the ion speed.

## RESULTS

First of all the collision efficiencies for vertical electric field were calculated varying E, Q and r in what it could be considered quite wide ranges: 1 V/m ≤ E ≤ 100 kV/m, $10^{-18}$ C ≤ |Q| ≤ $10^{-15}$ C y r=0.01, 0.1 and 1 μm,

giving a grand total of 1008 different situations with five or more trajectories each, as the algorithm converges. One example of efficiencies obtained for positive ion capture as a function of the droplet charge are shown in Figure 1a.

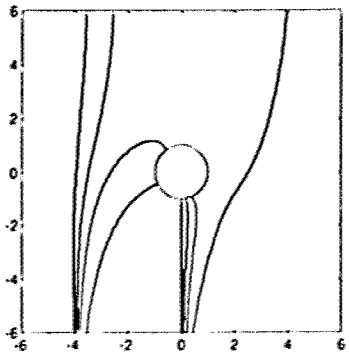


Figure 1: Ion trajectories coming from below for E=50 V y Q=-.001 fC and two impact parameters α, varies from 0°, to 135°. Leftmost trajectory are in both cases 0°, and progressing to the right are 45°, 90° and 135°.

Curves are parameterized with the external E-field in V/m and the solid and dashed lines are for negative and positive droplets respectively. Figure 1b shows the corresponding normalized ion current. Clearly the electrical parameters cannot be overlooked since they can produce variations of several orders of magnitude. To the left of these figures the E-field dominates while to the right the droplet charge is the important parameter. In the latter region, something that could be expected since the droplet is trapping positive ions, positive droplets decrease to the point of vanishing their cross section and the negative ones increase it becoming almost independent of the external field. The shape of these curves resemble somewhat the small ion behavior at strong fields.

After all the calculations a set of fitting functions are proposed for the capture cross section and the ion current for strong E-fields:

$$S = A\left(1+\frac{Q}{B}\right) \qquad (2)$$

$$\begin{cases} A = \exp\left(a + b(Log(E) - c)^2\right) \\ B = f + g\exp\left((Log(E) - 3)/h\right) \end{cases}$$

$$I = G\left(1+\frac{Q}{H}\right)^2 \qquad (3)$$

On the other hand, when the force from the droplet charge is the dominant one the appropriate fitting is:

$$S = C\,Q^D \qquad (4)$$

Where A, B, C, D, G, H, a, b, c, d, g, h are the fittings parameters. Note that these formulas are functionally similar to the traditionally used for small ion attachment (Chiu 1978). A sample of these fittings are in Figure 3.

For sake brevity we only show the parameterization obtained for $r = 0.1\mu m$. The expressions corresponding to $r = 1\mu m$ and $r = 0.01\mu m$ are similar but with different parameters and validity ranges. The units in the following expressions are in MKS, except the droplet charge Q that is in aC.

-If $E \le 20kV/m$

We use (2) with $a = -2.1$, $b = 0.29$ and $c = 2.53$. In addition, if $Log(E) \le c$ then $b = 0$.

For $Q > 0$; $f = -143$, $g = -16$, $h = 0.33$.

For $Q < 0$; $f = -62$, $g = -24$, $h = 0.39$.

-If $E \le 5kV/m$ and $Q < 0$ or $E \ge 5kV/m$ and $-Q > -B$.

We use (4) with $C = 5.62\ 10^{-4}$ and $D = 0.92$

-If $E \leq 20kV/m$ and $Q > -B$.

$$I_E = 0$$

-If $E > 20kV/m$

We use (3) with: $\begin{cases} G = -3.64\,10^{-3}(1 - E/50000) + 1.85\,10^{-3}(2 - E/50000) \\ H = 2285(1 - E/50000) - 1500(2 - E/50000) \end{cases}$

If $|\mu\vec{E}| \leq \vec{v}_{tg}$ and $|F_{Ez}| \geq |F_{Gz}|$ and $Q > 0$, then $I_E = 0$.

Of course the vertical electric field is an idealization, in general a droplet will see fields with varying angles. To what extent the angle must be taken into account will depend on the relative magnitudes of the forces. If the charge on the sphere is very large the flow of ions will be almost spherically symmetric. Another extreme case is the very strong ambient electric field arbitrarily oriented in which the axis of symmetry is given by the field itself and so the ion flow is almost axial then the angle is immaterial. So, it is for intermediate cases that the angle matters. Being the S as a function of angle so complicated (see Figure 4) it is found easier to fit the current instead.

If $|\vec{F}_E| < |\vec{F}_G|$ and $|\mu E| < |\vec{v}_{tg}|$ and $-Q_{pol} < Q < 0$ and $\alpha > 120^o$, then: $I_E(\alpha) = I_E(0)\cos(1.5(\alpha - 120^o))$

If $|\vec{F}_E| < |\vec{F}_G|$ and $|\mu E| < |\vec{v}_{tg}|$ and $-Q_{pol} > Q > 0$ and $\alpha > 60^o$, then: $I_E(\alpha) = I_E(0)\cos(0.75(\alpha - 60^o))$

DISCUSION

The model was also used to calculate the attachment cross section of small ions by droplets. When diffusion can be neglected we found that the theoretical expression by Whipple and Chalmers (1944) fits perfectly our data.

Just to show the kind of complexities involved in this modeling let us take a case with strong fields, the two top curves shown in Figure 2 (r=0.1μm). The E=100 kV/m and Q > 0 curve first increases and then drops to zero while the curve for Q<0 decreases contrarily to intuition. The explanation can be found in a different phenomenon: the variation of the terminal velocity by the E-force which in the present case reverses and the droplet is actually lifted up exchanging the role of the hemispheres in the sweeping of ions.

In spite of the problem complexity we found that for the majority of cases the ion current is almost independent of the E-field angles.

In order to check the goodness of our parameterization we calculated the ion attachment cross section again but for a large random set of variables (E, Q and α) in wide ranges and for each ion size. We can conclude that our fittings are quite accurate and in pathological cases they ensure at least the order of the magnitude.

REFERENCES:


Chiu, C . S., Numerical study of cloud electrification in an axisymmetric, time-dependent cloud model. *J. Geophys. Res.*, 83, 5025--5049, 1978.

Prodi, F and F. Tampieri, The removal of particulate matter from the atmosphere: The physical mechanisms. *Pageoph*, 120, 286--325, 1982.

Schlamps, R. J., S. N. Grover, and H. R. Pruppacher, A numerical investigation of the effect of electric charges and vertical external electric fields on the collision efficiencies of cloud drops. *J. Atmos. Sci.*, 33, 1747--1755, 1976.

Schlamps, R. J., S. N. Grover, H. R. Pruppacher and A. E. H amielec, A numerical investigation of the effect of electric charges and vertical external electric fields on the collision efficiencies of cloud drops: Part II. *J. Atmos. Sci.*, 36, 339-349, 1979.

Wang, C and J . S. Chang, A three-dimensional numerical model of cloud dynamics, microphysics, and chemistry. 1. Concepts and formulation. *J. Geophys. Res.*, 98, 14827—14844,1993

Whipple, F.J.W. and J. A. Chalmers, On Wilson's theory of collection of charge by falling drops. *Quart. J. R. Met. Soc.* 70, 103—120, 1944.

Zhang, Y. , S Kreidenweis and G .R. Taylor, The effects of cloud on aerosol and chemical species production and distribution. Part III: Aerosol model description and sensitivity analysis. *J. Atmos. Sci.*, 55, 921--939, 1998.

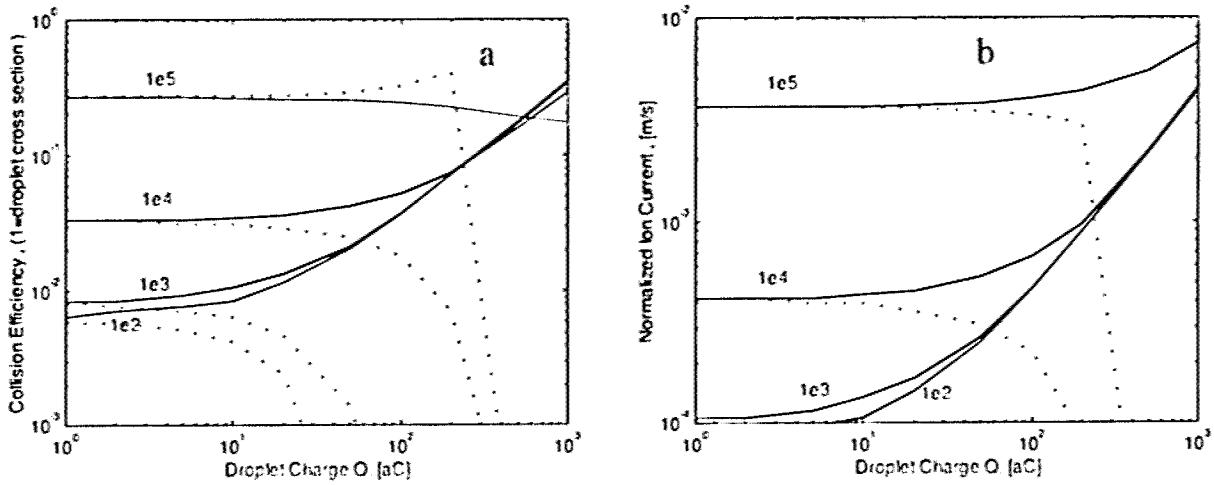


Figure2: a) Collision efficiency vs. Droplet charge. Curves are labeled in V/m and dashed positive droplets, solid negative. b) Ion current normalized with the droplet geometrical cross section.

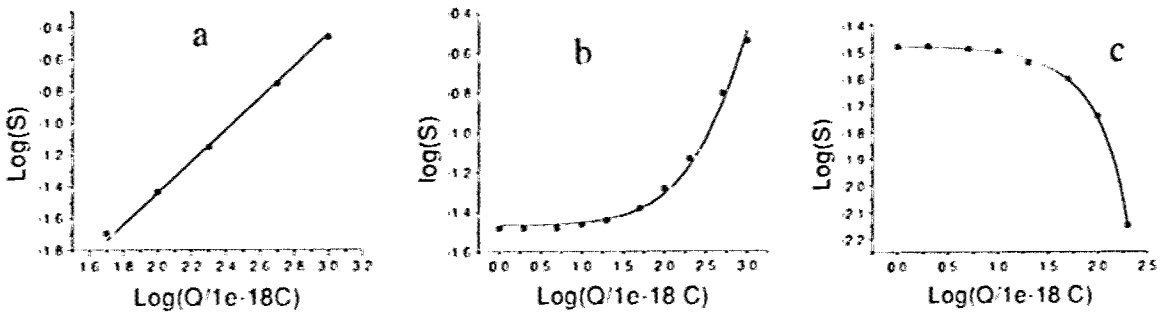


Figure3: Collision efficiency S vs. Q. The dots are from the modeled trajectories and the lines are the fittings. a) E=500 V/m, r=0.1μm, Q<0. b) E=10 kV/m, r=0.1μm, Q<0. c) same as b) but for Q>0.

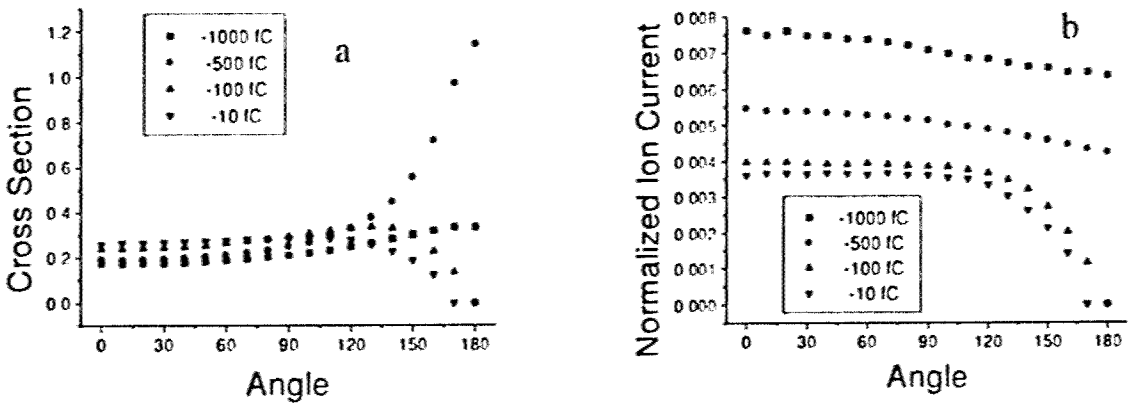


Figure 4: S (a) and I (b) vs. the angle of the external E-field measured from the upward direction. r=0.1μm, E=100kV/m.

# TO SELECTIVE ION CHARGING OF WATER DROPS IN THUNDERSTORMS

Andrew E. Sorokin

Institute of Applied Physics RAS,Nizhny Novgorod, Russia

ABSTRACT: The interaction between cloud droplet and moving ionized air has been investigated in the uniform Electric Field (EF). The attachment coefficients of air ions were obtained , tacking into consideration the track assumption. It has been shown that droplet charging regimes are strongly connected with the parameter $\xi_\pm$ - ratio of drift ions velocity to air flow velocity far away from droplet. The classical Wilson effect, that was shown, lies in the limit $|\xi_l| < |\xi_d| < \xi_{up} \simeq 1$. The upper limit $\xi_{up}$ is determined by the diffusive and volume ionization current influence to space charge distribution around droplet. The lower limit $\xi_l$ depends on ions diffusivity coefficient $D_i$. On the basis of attachment coefficient obtained, the electrohydrodynamic 1D model for the collective of charging drops has been designed. The homogeneous stationary state for certain cloud conditions is examined. And it is shown that high EF, like $1\,kV/cm$, can change ions concentration trough droplets-ions interactions. Also it is obtained that the system can be unstable to the wide spectra fluctuations of space charge and EF.

## INTRODUCTION

First, the idea of selective ion capture, SIC, mechanism of particles charging falling in air in the ambient electric field was concurred by Wilson. The simplest case is the following: one droplet fall down on the ionized air in the electric field. Succeeding Wilson the picture be is follows: ions of one sign are attached by the droplet surface, but ions of opposite sign are flowing around droplet. Thus droplet acquires charge determined by sign of first ions, [*Wilson*, 1929]. Thus system "droplet+ions+air flow" works as distributed EHD generator. The SIC effect differs from symmetrical charging in EF, $|\xi| \gg 1$, which is investigated in details, [*Drukaev*, 1946]. In this case droplet charges if only ions conductivities are different: $\sigma_+/\sigma_- \neq 1$. The main goal of this paper is to clarify - when SIC or symmetrical charging takes place in clouds, one determines criteria of SIC validity and find charges on droplets with respect to ions space charge.

## IONS ATTACHMENTS COEFFICIENTS. TRACKS APPROACH

To deduce the expression for current of ions, at least system of two continuity equations must be analyzed. In the system connected with droplet, it is stationary:

$$div(n_\pm \mathbf{V}_\pm - \gamma_\pm \nabla n_\pm) = \beta(1 - n_+ n_-),\ \gamma_\pm = \frac{D_\pm}{RV_0},,\ \beta = \frac{R}{V_0}\sqrt{I\lambda} \tag{1}$$

where $n_\pm$-normalized ions density, $V_0$ - magnitude of fall velocity, $I$ - volume ionization constant, $\lambda$- recombination constant, $R$ - droplet's radii, $D_\pm$-ions diffusivity coefficient. and $\mathbf{V}_\pm$ - normalized ions velocity is determined by expressions:

$$V_r = cos\theta\frac{\Psi}{r^2} + \frac{\eta_\pm}{r^2},\ V_\theta = -sin\theta\frac{\Psi'_r}{2r},\ \eta\mp = \frac{qB_\pm}{R^2V_0} \tag{2}$$

On the first step of calculation it is neglected of diffusivity and ionization effects: $\gamma \to 0$ and $\beta \to 0$. The equation can be written in the simple form $\mathbf{V}_\pm \nabla n_\pm = 0$, $div\mathbf{V}_\pm = 0$. It means concentration is a constant along each track and is determined of its magnitude on start point of each track (boundary conditions). An expression for ions tracks near by spherical droplet in case $\eta \neq 0$ and $\mathbf{EV} = \pm EV$ can be found from the equation:

$$\frac{dr}{d\theta} = -2\frac{\Psi cos\theta + \eta}{\Psi'_r sin\theta},\ \Psi = \Psi_0 + \Psi_i,\ \Psi_i = \xi(r^2 + \frac{2}{r}) \tag{3}$$

$$\Psi_0 = r^2(1 - \frac{3}{2r} + \frac{1}{2r^3}),\ Re \ll 1\ \Psi_0 = r^2 - \frac{1}{r},\ Re \gg 1,\ Re = \frac{2RV}{\mu} \tag{4}$$

where $\mu$ - dynamic viscosity, for air on sea level $\mu \approx 0.15, cm^2/s$. The solution of (3) with respect of infinity conditions: $rsin\theta_{\theta\to\pi,\, r\to\infty} \to h$ can be written as

$$\Psi = \frac{2\eta(cos\theta + 1) + h^2(1 + \xi)}{sin^2\theta} \tag{5}$$

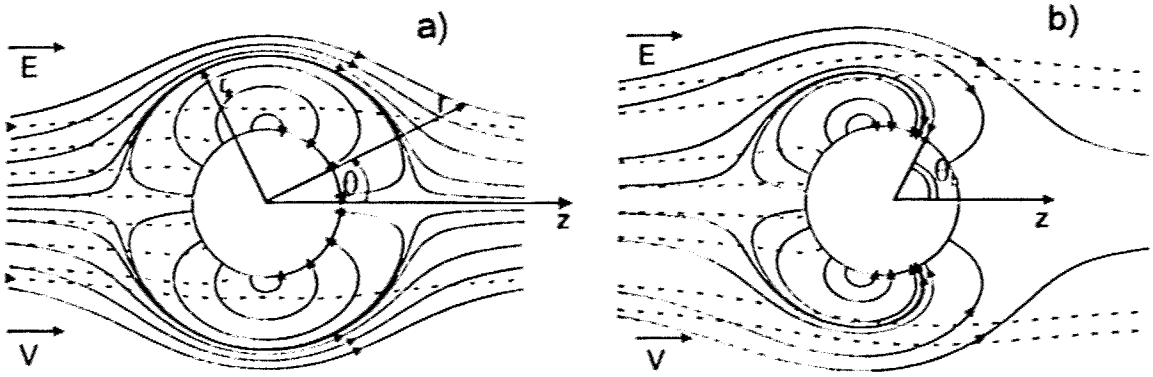


Figure 1: Ions tracks ($Re \ll 1$) nearby droplet in the EF. Solid lines - negative ions, dashed - positive. a) $\xi_- = -0.25$, $\eta_- = 0$, b) $\xi_- = -0.25$, $\eta_- = -0.2$

To find cross section one choose those ions from the flow which are collected by droplet, e.g. set $r = 1$, $\Psi(1) = 3\xi$. So we obtain an expression which connects an attachment angle $\theta_a$ with shoot parameter $h$:

$$cos\theta_a = -\frac{\eta}{3\xi} \pm \sqrt{(1 - \frac{\eta}{3\xi})^2 - h^2\frac{1+\xi}{3\xi}} \tag{6}$$

where sign + is for direct current and − for backward one. To find direct current set $cos\theta_a = -\eta/\xi$ and we have for $h$ and direct ions current $J_d$:

$$h^2 = \frac{3\xi}{1+\xi}(1 - \frac{\eta}{3\xi})^2,\ J_d = en_i(1+\xi)\pi R^2 h^2 = \frac{1}{4}\nu_i 3ER^2(1 - \frac{q}{3ER^2})^2 \tag{7}$$

where $\nu_i = 4\pi\sigma_i = 4\pi e n_i B_i$ - reverse time relaxation for ions. Droplet charging of ions of the opposite sign is realized through backward current. As shown in Fig.2, ions with $h = 0$ attach droplet with angle $\theta_b$, ($cos\theta_b = 1 - 2\eta/3\xi$ follows from equation (6)) and crossection $h$ and current $J$ is determined by the tracks with attachment angle is equal to zero ($\theta_a = 0$):

$$h^2 = -4\frac{\eta}{1+\xi},\ J_b = en_i(1+\xi)\pi R^2 h^2 = -q\nu_i \tag{8}$$

This formula is valid if $|\xi| < 1$, in the opposite case $|\xi| > 1$ it is simply to obtain from (3) with new limit conditions, ($rsin\theta_{\xi\to 0,\ r\to\infty} \to h$) new expression for current:

$$J_{b+} = \frac{1}{4}\nu_i 3ER^2(1 + \frac{q}{3ER^2})^2 \tag{9}$$

It is obviously that in such a case there are no effects of EHD screening and charge division near droplet, and no selection of ions flow. So the upper limit of SIC is $|\xi_{up}| = 1$.It is important that $J_b$ does not depend on $E$, and this is the result that we are neglecting the inner tracks add to current - tracks which start and end points lie on the droplet surface.

## RANGE OF VALIDITY TRACKS APPROACH

Let us consider the initial charging stage: $|\xi| \gg |\eta|$. And return again to Fig. 1.a). The negative ions concentration inside sphere ($r < r_*$) is assumed to be much smaller than the positive one, and also $n_-(r < r_*) \ll n_-(r > r_*)$. The sphere radius $r_*$ is determined by the expression $V_r = 0$.

$$r_*^3 = \frac{1-2\xi}{1+\xi},\ if\ Re \gg 1,\ r_* = \frac{3}{2(1+\xi)},\ |\xi| > .25,\ and\ r_* = 1 + \sqrt{2\xi},\ |\xi| \ll 1,\ if\ Re \ll 1 \tag{10}$$

But it is necessary to estimate at least two factors which can reduce SIC EHD charging effects: diffusivity and volume ionization. The average depth of boundary diffusive layer (where the diffusive current is greater

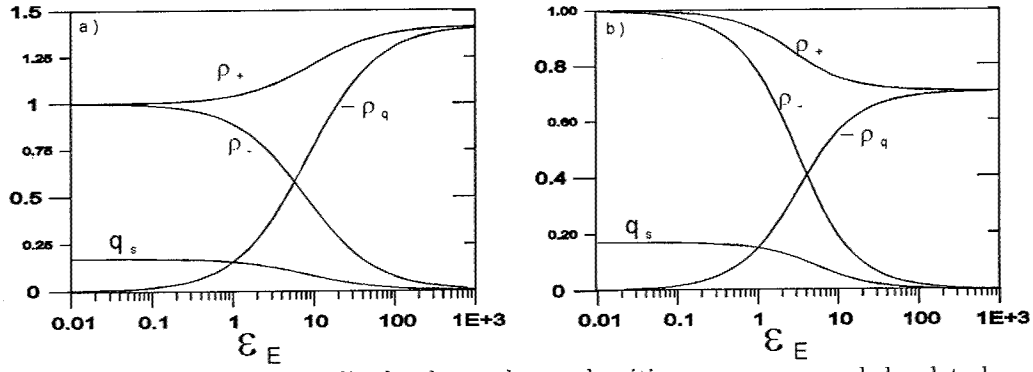


Figure 2: Stationary normalized volume charge densities $\rho_+$, $\rho_-$, $\rho_q$ and droplet charge $q_s$ versus control parameter $\varepsilon_E$, p=1. a) $\varepsilon_1 = 0.5$ , b) $\varepsilon_1 = 2$

than the drift one) $\delta_{D1} = r - 1 = \gamma/\xi$, where $\gamma = D_i/VR = 2Di/Re\mu$ - dimensionless parameter. The depth of such a layer around the sphere $r = r_*$ can be found from continuity equation assuming $\beta = 0$ , $\delta = r - r_*$, $V_r = s\delta$ near the point $r_*$ for radial current we have equation: $-\gamma dn/d\delta + n\delta s = 0$. From what it is following $\delta = \delta_{D2} = \sqrt{\gamma/s}$, and $s$ can be trivially found from the equations (10). So, to realize such charge derivation, as shown in Fig.1.a), the size of spherical layer $1 < r < r_*$ must exceed sum $\delta_{D1} + \delta_{D2}$. So the following criteria can be written:

$$|\xi| \ll 1: \quad |3\xi| \gg \frac{\gamma}{\xi} + \sqrt{\frac{\gamma}{3}},\ Re \gg 1\ and \sqrt{|2\xi|} \gg \frac{\gamma}{\xi} + \sqrt{\frac{\gamma}{3}},\ Re \ll 1 \tag{11}$$

$$|\xi| \sim 1, \quad \gamma \ll (1+\xi)^{2/3}(1-2\xi)^{1/3},\ Re \gg 1,\ and \gamma \ll 1,\ Re \ll 1. \tag{12}$$

Analyzing criteria (11), (12) the new minimal SIC criterium for any EF ($\xi$) can be found: $\gamma \ll 1$. It is comfy to rewrite it through Reynolds number: $Re \gg 2D_i/\mu$. For low heights $\mu \sim 0.15 cm^2/s$ and $D_i \sim .05\, cm^2/s$ for light ions, so critical $Re$ is about 0.67. Thus, only large $r > 40\mu$ particles can be charged by SIC, shurely for given $E$ the criterion (11) or (12) must be satisfied. To take into account volume ionization current, one integrates (1) on spherical layer $1 < r < r_*$ (assuming $\gamma = 0$ and that all ions (negative) inside it attach drop surface) and maximum estimation for ionization current gives:

$$J_i = \frac{4\pi}{3} r_*^3 \beta = \frac{4\pi}{3} R^3 r_*^3 eI, \quad \frac{J_i}{J_d} = 9\frac{\beta}{\xi} r_*^3 \tag{13}$$

it is assumed that $r_* \gg 1$ in the opposite case $r_* \sim 1$ $J_i/J_d = 9\beta$. For atmospheric conditions recombination time $1/\sqrt{I\lambda}$ lies in the range $1 - 400$ seconds, and effective span time $R/V$ is about $2 \cdot 10^{-4}$s for $R = 50\mu$ and $2.8 \cdot 10^{-4}$s for $R = 2mm$. So, the maximum value of $\beta$ is about $10^{-4}$. Thus, volume ionization current, $J_i$, gathering around the droplet could not bring reasonable add in total current $J_b$. But the situation can be changed if we take into account the corona discharge current, which take place on droplet in high EF. As preliminary estimations are shown, it can rise $\beta$ up to the 1.

## COLLECTIVE SIC EFFECTS

The real cloud contains the droplets and ice crystals set in ionized gas. And droplets themselves can effect to charge of separate one and to ions concentration. Thus, to understand, cloud characteristics: droplet charge, ions concentration the complete system of EHD equations must be analyzed. The 1D model is assumed and $z$ axis, **E** and **V** are directed along **g** - free fall acceleration. The EHD system of equations in the nonmovement set be as follows:

$$\partial_t q + v\partial_z q = -q\nu_{i+} - \frac{3}{4}\nu_{i-} ER^2 (1 - \frac{q}{3ER^2})^2; \quad \partial_t N + v\partial_z N + N\partial_z v = 0; \tag{14}$$

$$\partial_t v + v\partial_z v + \alpha_q v^2 = g + \frac{Eq}{m}; \ \partial_z E = 4\pi(Nq + en_+ - en_-); \tag{15}$$

$$\partial_t n_+ + V_+\partial_z n_+ + n_+\partial_z V_+ = I + 4\pi q N n_+ B_+ - \lambda n_+ n_-; \tag{16}$$

$$\partial_t n_- + V_-\partial_z n_- + n_-\partial_z V_- = I - \frac{3}{4}\nu_- ER^2(1 - \frac{q}{3ER^2})^2 - \lambda n_+ n_-, \qquad (17)$$

where $q$, $N$, $v$ - droplets charge, concentration, fall velocity; $n_\pm$, $V_\pm$ - ions concentrations and drift velocities, $B_\pm$ - their movebilities. At first, let us investigate the droplet charge and ions concentration as a function of external field and ions initial set $n_0 = \sqrt{I/\lambda}$.

STATIONARY DROPLET CHARGE

Assuming $\partial/\partial z = 0$, and $\partial/\partial t = 0$ the following system describing droplet charge and ions concentration can be found:

$$\rho_+ - \rho_- + \rho_q = 0, \quad 1 - \rho_+\rho_- + \rho_q\varepsilon_1\rho_+ = 0, \quad 4p\frac{\rho_+}{\rho_-}\frac{\rho_q}{\varepsilon_E} + (1 + \frac{\rho_q}{\varepsilon_E})^2 = 0 \qquad (18)$$

$$\rho_\pm = \frac{n_\pm}{n_0}, \ \rho_q = \frac{Nq}{n_0 e}, \ \varepsilon_1 = \frac{4\pi e B_+}{\lambda}, \ p = \frac{B_+}{B_-}, \ \varepsilon_E = \frac{N}{n_0}\frac{3ER^2}{e}, \ q_s = \frac{\rho_q}{\varepsilon_E} \qquad (19)$$

$q_s$ - charge, normalized on $3ER^2$. The value $\varepsilon_E$ plays role of a control parameter and determines the degree of ions perturbation. The general decision of (18) is possible only numerically and presented on Fig. 2 a),b). Let us estimate $\varepsilon_E$ for development cloud stage: $E = 0.01\,kV/cm$, $R = 100\,\mu$, $N = 0.05\,cm^{-3}$, $n_0 = 5\cdot 10^3\,cm^{-3}$, and we have $3ER^2/e \sim 2\cdot 10^4$, $N/n_0 = 10^{-5}$ so $\varepsilon_E = 0.2$. For thunderstage set $E = 1\,kV/cm$, $R = 1\,mm$, $N = 0.03\,cm^{-3}$, $n_0 = 3\cdot 10^4\,cm^{-3}$, and we have $3ER^2/e \sim 2\cdot 10^8$, $N/n_0 = 10^{-6}$ so $\varepsilon_E = 200$. Analytical decision the system (18) can be obtained in two important cases 1) $\varepsilon_E \ll 1$ and 2) $\varepsilon_E \gg 1$:

$$1)\ q_s = \frac{1}{1 + 4p\varepsilon_E}(-1 - 2p + \sqrt{(2p+1)^2 - 1}), \ \rho_+ = 1 + \frac{1}{2}\varepsilon_E q_s(1 - \varepsilon_1), \ \rho_- = 1 - \frac{1}{2}\varepsilon_E q_s(1 + \varepsilon_1). \qquad (20)$$

$$2)\ \varepsilon_E q_s = \rho_q = -\frac{1}{\sqrt{\varepsilon_1}} + \frac{2p(1+\varepsilon_1)}{\varepsilon_1^2\varepsilon_E}, \ \rho_+ = \frac{1}{\sqrt{\varepsilon_1}} + \frac{2p(1-\varepsilon_1)}{\varepsilon_1^2\varepsilon_E}, \ \rho_- = \frac{4p}{\varepsilon_1\varepsilon_E} \qquad (21)$$

In small EF the maximum droplet charge provided by SIC is about (it is assumed $p = 1$) $q_s = 3 - 2\sqrt{2} = 0.17$ and much less than charge is acquainted in unipolar ionized air, $q_s = 1$. For large field and particles net charge is determined by a simple expression: $q_s = en_0/N\sqrt{\varepsilon 1}$. Negative ions concentration is order of $1/\varepsilon_E$ and much less than 1. It is interesting to examine the collective charging effects in SIC media, see [*Mareev et al*, 1999]. Numerical analysis of linearized system (14) - (17) has shown, that stationary state, described above, makes unstable under the condition $bVR^2N > 2\nu_i$, $b = .1 - 4$-dimensionless constant depending on $\varepsilon_E$. There are wide spectra of electrostatic waves is excited but maximum increment is only for long waves: $\gamma^2_{max} = VR^2N\nu_i$. It is a pity, but analysis in details of collective SIC effects is a theme of separate paper and there is no place to put it here.

CONCLUSIONS: So, it is found SIC mechanism takes place in limited range of parameters. For clouds it is valid only for large droplets $R > 40\mu$. But size of droplet is limited by condition $|\xi| < 1$, and thus it is rigidly connected with EF magnitude. For light ions $B_i \approx 0.15cm^2/Vs$ and EF $E = 1kv/cm$ the drift velocity is $V_i = 1.5\,m/s$ and it lies in the range of fall velocities of raindrops in cloud So that in thunderstorm cloud $|\xi| \ll 1$ and estimate the criteria (11). For $R = 3mm$ we have $V = 8.85m/s$, $\gamma = 1.5\cdot 10^{-5}$, $\xi = 0.17$ and condition (11) is fulfilled. Charge of drop is determined by the expression (21) since control parameter $\varepsilon_E = 214$ ($N = 10^3\,m^{-3}$, $n_0 = 10^4\,cm^{-3}$). In real cloud there are size spectrum of particles exists and SIC "choose" from such media drops of appropriate size $R > R_c$. The SIC mechanism of particles charging can play the principal role to amplifying EF in clouds up to breakdown magnitudes. Because particles charge depends of EF direction, as shown estimation, it can be important to form unstable space charge and electric field structures in clouds. For $R = 3mm$, $N = .001cm^{-3}$ and $\nu_i = .01s^{-1}$ the development time of EF is about 10 seconds. Of course, on nonlinear stage development time reduces. Thus, SIC mechanism can have wide spectra of application to clouds electrodynamics and plays the principal role of particles charging in thunderclouds precipitation regions.

REFERENCES

C.T.R. Wilson, J.Franklin Inst., 1929, 208, 12.

G.F.Drukaev, Charges of raindrops, *Izv USSR Acad. Sc.*, v.8, No 6, pp. 330-336, 1946 (in Russian).

Mareev E.A., A.E.Sorokin and V.Yu.Trakhtengerts, Effects of collective charging in a multiflow aerosol plasma, *Plasma Physics Reports*, Vol. 25., No. 3, pp. 261-272.

# Charge Generation with and without Secondary Ice Production

John Hallett

Desert Research Institute, 2215 Raggio Parkway, Reno NV 89512

ABSTRACT: Aircraft observation and laboratory experiment demonstrate that separation of electric charge is associated with the simultaneous presence of graupel growing from supercooled cloud droplets, together with vapor grown ice crystals. Laboratory measurements suggest that charge is separated during collision and bounce of the vapor grown crystals, with magnitude and sign of the separated charge depending on temperature, liquid water content and the droplet size distribution. The conditions necessary for the optimum mix of particles in the atmosphere relates to the shear of horizontal wind with height in the environment of the convective cloud. This determines not only the input of graupel from aloft to the developing water cloud below but also the turbulent transport of ice/water at the sloping interface between the ascending upshear supercooled water cloud and the descending downshear ice cloud. Conditions for the occurrence of secondary ice are present for a deep, warm base temperature cloud (>20C) and are necessary for beginning electrification; inhibition of secondary ice for a cool cloud base temperature (<0C) leads to efficient transport of supercooled cloud to low temperatures aloft and ultimately a much higher separation rate of charge, with positive charge aloft.

## INTRODUCTION

Laboratory studies of charge separation under simulated atmospheric clouds typically utilize a cold chamber with cloud droplets produced by condensation of moist air or an ultrasonic nebuliser. Simulated graupel is moved relative to the cloud and charge acquired by the graupel measured. Ice crystals are nucleated by dry ice or a $LN_2$ cooled probe (Reynolds et al,1957; Takahashi, 1978; Jayratne et al 1983). The graupel carries a positive charge at temperatures above -5C to -10C and negative charge below, depending on both liquid water content and temperature; droplet size distribution, impact velocity and impurity also have significant effects.There is some disagreement amongst authors. The necessity of the presence of growing graupel was demonstrated in the mountain top studies of Kuettner 1982; the onset of electrification has been linked closely to the onset of the ice phase in aircraft studies., Dye et al 1986; Willis et al,1994. The purpose of this discussion is to relate the onset of the charging process to the situations giving rise to the optimum particle mix under atmospheric conditions, bearing in mind that secondary ice particles also occur during the growth of graupel under specific conditions (Hallett and Mossop, 1973; Mossop 1985 a,b; Hobbs and Rangno,1990; Mason 1996.) Limitations of application of laboratory studies may be limited in as far as particles may mix into the cloud water and graupel environment in a way not necessarily well represented by the laboratory simulation; the time constant of the surface build up may differ depending on the scale of the ice/water mix (Dong and Hallett,1992).

## DEPENDENCY ON CLOUD COMPOSITION

The concept of a mixed cloud in the atmosphere is ill defined and needs appraisal since electrical as well as secondary ice processes may vary. At one extreme a mixed cloud implies mixing *uniformly* down to the separation distance of individual particles such that any measurement gives uniformity consistent with a spatial distribution to be described by the

random distribution of Poisson statistics. Accretion and impaction in such a cloud is therefore subject to the same laws. An alternative concept could be defined where regions of all ice are interspersed with regions of all water on prescribed or a variety of scales- one example is the sheared cumulus cloud described above on a scale of at least several hundred meters. A 'swiss roll' spiral resulting from a Kelvin-Helmholtz instability provides another scenario. The result is that the particle grows and evolves - or the aircraft ices - in a way quite different in each case. Aircraft measurement to characterize such scales are difficult in as far as different instruments have different sample volumes, and are not collocated on the aircraft. A mixed region in an evolving cumulus may be only 100/200 meters wide, (Willis et al 1994), be traversed by an aircraft in a second or so, yet contain the right microphysical mix for secondary ice production and/or charge separation. Thus to characterize varying particles and distributions, a time resolution of a fraction of a second may be necessary. The problem is shown schematically in Figure 1 of a cross section through such a cloud. Upshear the cloud has strong updraft, possibly with cloud liquid water content approaching adiabatic values. As the cloud grows vertically, environmental mixing occurs on the upshear side, leading to a sharp cloud edge, and mixing at the upper levels of the cloud penetration to give local cooling to $T_W$ (where ice nucleation is most likely) and eventual negative buoyancy and descent downshear. Between the two lies the mixed region where water and ice coexist together with appropriate complex microphysical processes. Measurements show that indeed there is a gradation of microphysical properties from the upshear to the downshear. It is necessary to return to older technology to find this out in detail, as uncertainties in comparison of non-collocated instruments on aircraft leads to difficult problems of intercomparison. The formvar replicator can be operated at a film velocity of 60 cm/s, adequate for a spatial resolution of about 1 meter and is capable of collecting particles from a few microns to greater than a mm *at the same location*. Observation shows that on occasion all particles are mixed on this scale (Figure 2). A simplistic interpretation of such observations is that not only the magnitude but also the sign of any separated charge varies along the horizontal in the direction of the shear under appropriate circumstances (Black and Hallett,1998;1999). The situation is in reality much more complex than is indicated here as the cloud droplet size distribution (influencing both secondary ice production and also charge separation) depend on the CCN spectrum of the cloud droplets activated at cloud base and their subsequent evolution. Thus a tropical maritime cloud, a summertime convective cloud in Texas, a Montana convective cloud and a summertime high level mountain convection in Nevada cover a range of cloud base temperatures - from +20 to <0C - and cover a wide range of CCN spectra leading to quite different cloud droplet spectra. This in turn influences liquid phase coalescence and precipitation for higher temperature cloud base.

CHARGE SEPARATION.

The concept of charge separation devolves to hypothesizing where the most appropriate mix of particles might occur in the different scenarios. Conditions for secondary ice formation relate to the presence of droplets bigger than 23μm and smaller than 13μm; the former is more likely for a maritime aerosol origin, the latter for an aerosol of continental origin. The cloud base temperature and updraft similarly influence the activation of the CCN and the subsequent droplet spectra (Mossop and Hallett 1974). Similar considerations apply to the role of drop size distribution in charge separation at the appropriate temperatures (Saunders and Peck 1998). In situations where secondary ice is inhibited and where the shear is weak, the possibility exists of lofting of supercooled cloud and liquid phase precipitation to high levels, so that when the down draft really begins, microphysical interactions leading to charge separation occur at temperatures down to below -30C and may lead to high generation rates. Such a situation may lead to positive strokes to ground, a possible result of high CCN input from

combustion (Lyons et al 1998, 282 Science,77-80). Thus extreme cases my dominate for ice inhibition, leading to higher level effects, as weaker electrical cases may be dominated be rapid ice evolution earlier in the cloud evolution. In order to sort this out it will be necessary to have CCN and cloud base temperature information together with a knowledge of the ice and water particle evolution to high levels. This may seem a tall order, requiring both polarized radar and aircraft penetration under critical conditions. Yet if indeed such scenarios are extreme, selected analysis from a number of smaller individual projects could give a clue to the driving microphysical and dynamical process.

CONCLUSIONS: Information is needed on the occurrence of both liquid phase precipitation, on the spatial evolution of the ice phase precipitation and also a knowledge of the nuclei to drive the supercooled cloud properties. Numerical models of these scenarios are probably not adequate to predict the overall outcome unless CCN have a well defined seasonal and spatial predictability. It is clear that 1D models have limited utility in the case of the (usually) sheared environment; their use lies in the rare case with updraft slopes less than a few degrees. Extreme shear - greater than say 50 degrees -may separate graupel almost completely from the supercooled cloud below and inhibit electrical effects for a quite different reason. Regions for production of the 'best' microphysical mix may be determined by *enhancement* of secondary ice production as in the lower levels of a developing convective cloud by reduced CCN - or by *inhibition* of secondary ice by enhanced CCN or cool cloud bases enabling supercooled cloud to be lofted in strong updrafts to provide ice - growing graupel interactions at temperature lower than about -25C. A flow field set in a microphysical context is necessary to provide further insight into this problem.

Figure 1.

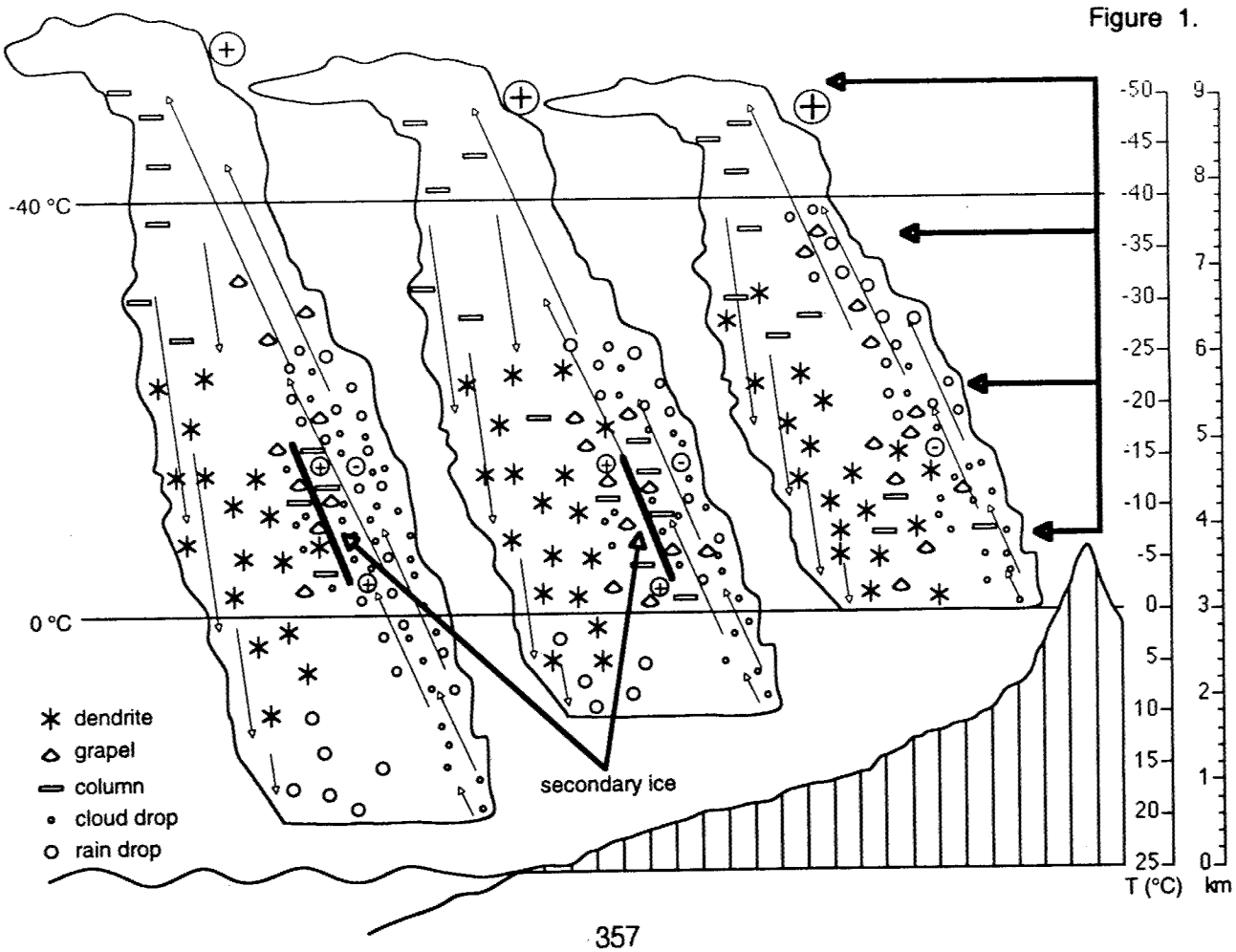

Figure 1. Schematic of evolution of convective cloud having different cloud base temperatures leading to different droplet size distributions. Cloud base CCN and vertical velocity, together with the subsequent evolution of liquid phase precipitation predicate the droplet size distribution for graupel growth and the rate of secondary ice particle production. In general warmer cloud bases and low CCN are favorable whereas cooler cloud bases and high CCN are unfavorable. Production of secondary ice leads to the right mix for charge separation at higher temperatures (-5 to -15C), whereas inhibition of secondary ice leads to lofting of supercooled clouds to low temperatures (< -20C ) and rapid charge separation above these levels. (For details see Black and Hallett, 1998 American Scientist **8 6** 526 -534 and J.Atmos. Sci 1999 in Press)

Figure 2. Formvar replica of particles collected in the mixing zone between all water updraft and all ice downdraft. Penetration by NOAA P-3 in a convective cloud along a sea breeze front near Orlando,FL. The columns have dimension about 100μm; small graupel 350μm and cloud droplets,10 - 40μm can be seen in the same frame, collected from a parcel of air from about 2m of flight path. ( For details see Willis et al, 1994, Atmospheric Research **3 3** 1-24)

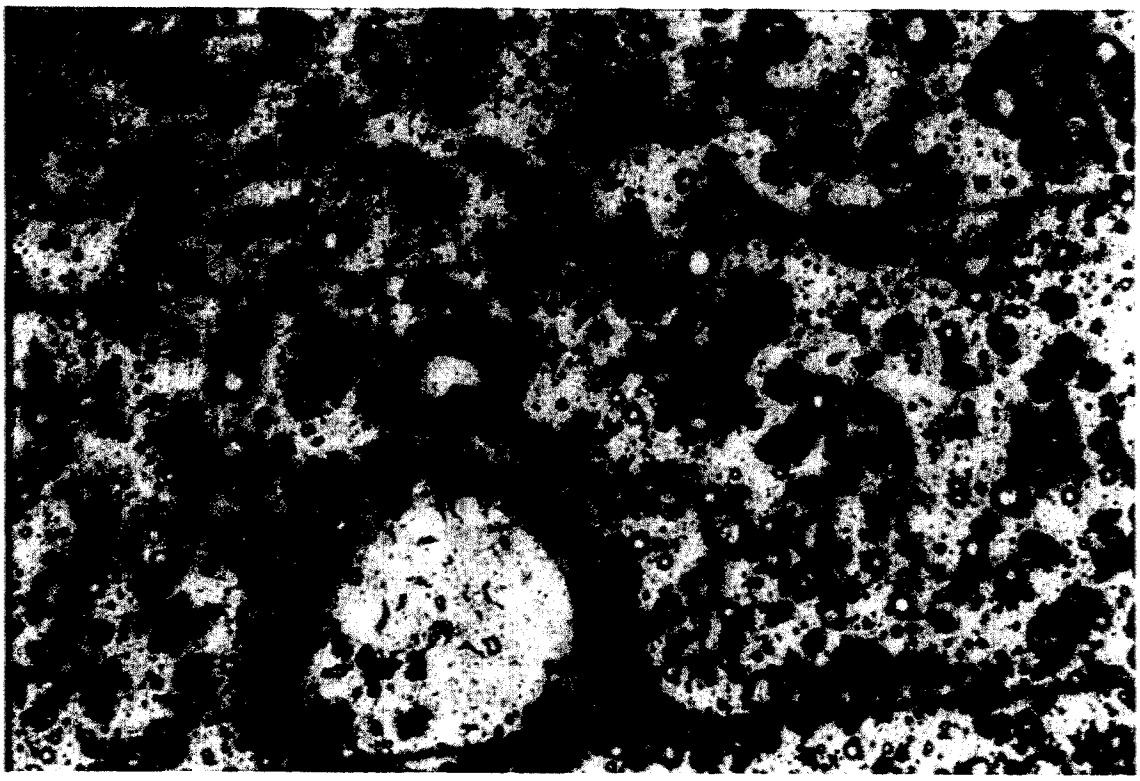

REFERENCES: General and historical references are given in the papers by Black and Hallett, see caption figure 1.

ACKNOWLEDGEMENT: Support is acknowledged from the Physical Meteorology Program, Grant ATM-9413437, National Science Foundation, Arlington,VA.

# SIMULATION OF EARLY ELECTRIFICATION IN A THREE-DIMENSIONAL DYNAMIC CLOUD MODEL

C. L. Ziegler[1], J. M. Straka[2], and D. R. MacGorman[1]

[1]National Severe Storms Laboratory, Norman, Oklahoma, U.S.A.
[2]School of Meteorology, University of Oklahoma, Norman, Oklahoma, U.S.A.

ABSTRACT: This paper highlights the results of our efforts to incorporate parameterized expressions for non-inductive and inductive charging, lightning discharges, and formation of screening layers into a three-dimensional dynamic cloud model (ie. "cloud model"). The cloud model is time dependent and involves simultaneous solution of the equations of atmospheric motion with equations for mass, heat, and water substance continuity. Electrification is modeled by solving additional continuity equations for liquid and ice hydrometeor space charge densities and a Poisson equation for scalar electric potential. The present dynamical cloud simulation approach extends earlier kinematic modeling studies of tornadic supercell and New Mexico mountain thunderstorms. At present we are engaged in efforts to validate the preliminary simulations versus observations of morphologically similar storms and also to investigate the impact of the storm environment on the simulated electrical and lightning morphology.

## INTRODUCTION

In recent modeling studies, we have evaluated the role of non-inductive graupel-ice charging in the early electrification of a mountain thunderstorm (Ziegler et al. 1991) and have explored the relationships between space charge, electric fields, and lightning morphology in a tornadic storm (Ziegler and MacGorman 1994). These studies employed a kinematic model with parameterized expressions for non-inductive and inductive charging, lightning discharges, and formation of screening layers. However, large or rapidly moving storms and storm systems are not usually observed with Doppler radars to the extent required by the time-varying kinematic model. Hence, it is desirable to develop a capability to simulate electrifying storms to complement the kinematic modeling method.

In the present study, we report results of our efforts to incorporate these electrification mechanisms into a time dependent, three-dimensional dynamic cloud model. To demonstrate the new model's capabilities, we simulate the development of a supercell thunderstorm, terminating the cloud model integration after the first few simulated intra-cloud lightning discharges to focus on the early storm electrification phase.

## MODEL FRAMEWORK

### a. Airflow dynamics

The numerical simulations are made using a non-hydrostatic, fully compressible, three-dimensional dynamic cloud model (Straka and Anderson 1993). Prognostic equations are included for three momentum components, pressure, potential temperature, and turbulent kinetic energy. There are also conservation equations for the number concentrations (when required) and mixing ratios of aerosols, water vapor, and hydrometeors.

The advection and diffusion numerics in the simulation model all include a conservation principle. For momentum advection, the model uses a time-centered, quadratic-conserving differencing scheme or a sixth-order local spectral scheme (Straka and Anderson 1993). Choices for scalar advection include a forward in time, sixth-order, flux divergence-corrected, Crowley scheme, and a time-centered, second-order flux scheme. The diffusion parameterization is based on K-theory, with the mixing coefficient derived from the variable turbulent kinetic energy.

### b. Microphysics

The model employs a general microphysical package that was designed for cloud and mesoscale models in which new information about microphysical processes could be added without rewriting significant portions of the source code. Optional features include: (1) prediction of N habits and size categories of hydrometeor, aerosol, and chemical species, including more than 12 distinct ice crystal habits; (2) prediction of microphysical processes with either a number of parameterizations or with explicit microphysics, the latter incorporating logarithmically spaced mass categories to represent the size distribution; (3) hybrid applications with some species using parameterizations and some using explicit microphysics. The options desired for a particular simulation are easily chosen via namelist parameters input to the model during compilation.

In its present configuration, the model solves prognostic equations for the following hydrometeor habits: liquid drops (cloud and rain), frozen raindrops (900 kg $m^{-3}$), bullets, solid and hollow columns, needles, sheaths, thick and thin plates, planar and spatial dendrites, sectors, stellars, columns with plates, plates with dendrites, snow aggregates, three density categories of graupel (ie. 200 kg $m^{-3}$, 450 kg $m^{-3}$, 700 kg $m^{-3}$), and two size categories of (high density) hail (ie. 5-20 mm, > 20 mm, respectively). Hydrometeor formation and growth rates include the nucleation of water drops, primary and secondary ice nucleation, vapor diffusion, stochastic coalescence, continuous collection of cloud droplets, wet and dry growth of graupel and hail, melting and freezing, breakup of large drops and aggregates, conversions from one hydrometeor specie to another, variable hail and graupel particle density, ice particle temperature, and sedimentation.

c. Electrification

The formulation of electrification processes is essentially identical to that described by Ziegler et al. (1991), though generalized to incorporate optional treatments of charging. Prognostic equations are integrated for space charge on cloud ice, cloud droplets, rain, snow, graupel, and hail. The vector electric field is derived from the scalar electric potential, which in turn is derived by inverting a Poisson equation forced by net space charge density.

The space charge continuity equation for hydrometeors is given by

$$\frac{\partial \rho_l}{\partial t} = -\frac{1}{\rho_a}\frac{\partial(u_i \rho_a \rho_l)}{\partial x_i} + \frac{\rho_l}{\rho_a}\frac{\partial(u_i \rho_a)}{\partial x_i} + \frac{\partial}{\partial x_i}\left(\frac{K_h}{\rho_a}\frac{\partial(\rho_a \rho_l)}{\partial x_i}\right) + \frac{1}{\rho_a}\frac{\partial(V_{tl}\rho_a \rho_l)}{\partial t} + S_l \qquad (1)$$

where $\rho_l$ is the space charge (C $m^{-3}$) of hydrometeor habit l, $V_{tl}$ is terminal velocity ($ms^{-1}$) for habit l, $S_l$ is sources and sinks of space charge density (C $m^{-3}$ $s^{-1}$) for habit l, $\rho_a$ is air density (Kg $m^{-3}$), $x_i$ are the Cartesian coordinates (m), $u_i$ are the Cartesian wind components ($ms^{-1}$), and $K_h$ is the sub-grid eddy mixing coefficient ($m^2$ $s^{-1}$). The equations for the source and sink terms for the space charge that are included are non-inductive charging, inductive charging, screening layer charging, and mass transfer. The definitions for total space charge, potential, and electric field components are

$$\rho_t = \sum_{l=1} \rho_l \qquad (2)$$

$$\frac{\partial^2 \phi}{\partial x_i^2} = -\frac{\rho_t}{\varepsilon_o} \qquad (3)$$

$$E_i = -\frac{\partial \phi}{\partial x_i} \qquad (4)$$

where $\rho_t$ is the total charge density on hydrometeors (C $m^{-3}$), $\phi$ is scalar electric potential (V), and $\varepsilon_o$ = $8.8592 \times 10^{-12}$ $N^{-1}$ $m^{-2}$ $C^2$ is the electrical permittivity of air.

d. Charge source terms

Four options for the non-inductive charging rates per collision are available in the model: 1) Helsdon and Farley (1987), wherein various levels of fixed separated charge are assumed per rebounding collision between graupel/hail and snow particles; 2) Ziegler et al. (1991), wherein collisional charging is a function of size of the graupel/hail and snow particles; 3) Saunders et al. (1991), utilizing a lookup table approach to specify charge per collision as a function of particle size, cloud liquid water content, temperature, and other parameters (total charging determined by quadrature over modeled particle size distribution); 4) Saunders and Peck (1998), which follows the Saunders et al. (1991) method, with functional replacement of liquid water content by rime accretion rate. Since neither observations nor laboratory experiments explicitly provide information to accommodate charging versus ice crystal habit, the same parameterizations are used for all crystal types in the model. Depending on what option is employed, the model evaluates the parameterization either analytically or by quadrature from look-up tables, and can consider partial and complete distributions.

The model also includes expressions for inductive charging, screening layer formation, and charge transfers accociated with (microphysical) mass transfer (Ziegler et al. 1991). A new lightning parameterization, which can simulate either IC or CG flashes, has recently been added to the model (MacGorman et al. 1998) and is activated in the present run. An option to include explicit ion processes following Helsdon and Farley (1987) is under development. The model also does not treat inductive charging owing to any ice – ice, ice – drizzle or ice – rain rebounding collisions; from any liquid – liquid rebounding collisions; or from shedding of cloud, drizzle, or rain owing to melting or wet growth.

RESULTS

The simulated supercell is initialized in a horizontally homogeneous base state environment with 2200 J $kg^{-1}$ of convective available potential energy and a 1/2 circle hodograph with an arc of 50 m $s^{-1}$ (ie.

0-5 km shear = 31.8 m $s^{-1}$). Vertical motion is initiated by introducing a warm thermal bubble with an amplitude of 1 °C, horizontal and vertical radii of 10 and 1.4 km respectively, and an elevation of 1.4 km AGL. For this test, electrification mechanisms are treated as by Ziegler et al. (1991). A reversal temperature of –10 °C for non-inductive graupel-ice charging is assumed. the model is integrated for a period of 35 min.

Early supercell electrification displays a distinctly exponential character (Fig. 1). As also shown by Ziegler et al. (1991) for a New Mexican mountain thunderstorm, the exponential character of the early electrification is caused by graupel-ice collision rates and mean separated charge per collision increasing exponentially. After the storm achieves a maximum field of breakdown intensity (~ 150 kV $m^{-1}$; see MacGorman et al. 1998) just after 31 min, IC discharges commence at a rate of 2-3 flashes $min^{-1}$ (Fig. 1, inset). The later, mature stage of electrification, including the individual interflash recoveries, is more linear in character due to a relatively slowly varying microphysical charging current in the storm after ice contents become established.

The simulated supercell morphology (Fig. 2) bears many similarities to earlier kinematic model results for the Binger, Oklahoma tornadic storm (Ziegler and MacGorman 1994). Just prior to the first IC flash, the storm has achieved an altitude of 14 km and a maximum updraft of 40 m $s^{-1}$. The net space charge density ranges from roughly –1 to 1 nC $m^{-3}$, and the corresponding maximum electric field magnitude is 135 kV $m^{-1}$. The intense convection elevates the main charge region in the updraft, and sloping main negative and upper positive charge regions gradually separate with downstream distance into the anvil due to the differing fallspeeds of cloud ice, snow particles, graupel, and hail.

## CONCLUSIONS

We have developed a versatile cloud model which may be used to investigate a wide range of questions concerning storm electrification. The model may be configured to simulate both isolated storms, such as illustrated here, and larger Mesoscale Convective Systems (MCSs). In addition to studying early electrification, we are presently using the new model to investigate lightning parameterizations and the variations of supercell electrical and lightning morphology across a spectrum of convective instability and wind shear values representing typical storm environments.

ACKNOWLEDGEMENTS: Model runs were performed by JMS on the CRAY J-90 computer at the University of Oklahoma through sponsorship of the OU Graduate College and NSF Grant EAR-9512145. Additional support for this project was provided under NSF Grants ATM-9311911, ATM-9120009, ATM-9617318, and EAR-9512145.

## REFERENCES

Helsdon, J. H., and R. D. Farley, 1987: A numerical study of a Montana thunderstorm: 2. Model results versus observations involving electrical aspects. *J. Geophys. Res.*, **92**, 5661-5675.

Saunders, C. P. R., W. D. Keith, and R. P. Mitzeva, 1991: The effect of liquid water on thunderstorm charging. *J. Geophys. Res.*, **96**, 11,007-11,017.

Saunders, C. P. R., and S. L. Peck, 1998: Laboratory studies of the influence of the rime accretion rate on charge transfer during crystal/graupel collisions. *J. Geophys. Res.*, **103**, 13,949-13,956.

Straka, J. M., and J. R. Anderson, 1993: Numerical simulations of microburst-producing storms: Some results from storms observed during COHMEX. *J. Atmos. Sci.*, **50**, 1329-1348.

MacGorman, D. R., J. M. Straka, and C. L. Ziegler, 1998: A lightning parameterization for numerical cloud models. Preprints, 19th Conference on Severe Local Storms, AMS, pp. 348-351.

Ziegler, C. L., D. R. MacGorman, J. E. Dye, and P. S. Ray, 1991: A model evaluation of non-inductive graupel-ice charging in the early electrification of a mountain thunderstorm. *J. Geophys. Res.*, **96**, 12,833-12,855.

Ziegler, C. L., and D. R. MacGorman, 1994: Observed lightning morphology relative to modeled space charge and electric field distributions in a tornadic storm. *J. Atmos. Sci.*, **51**, 833-851.

Fig. 1 (right panel). Semi-logarithmic plot of the maximum electric field magnitude (kV $m^{-1}$) in the control simulation versus time (min). Inset depicts last 5 min of field evolution on a linear vertical scale. Lightning flash is located by vertical arrow at end of time step containing discharge.

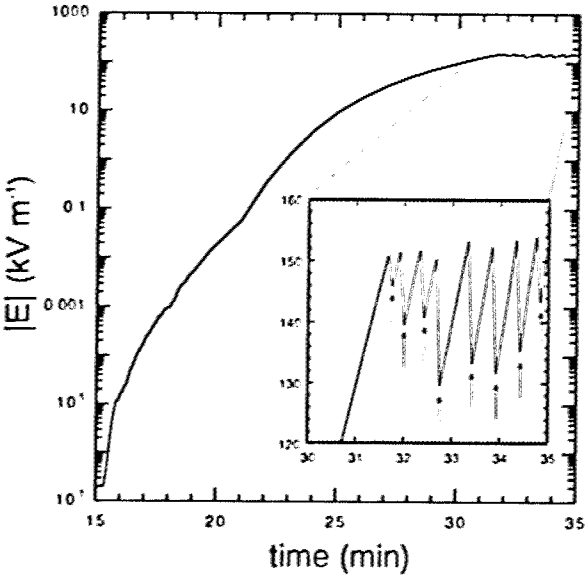


Fig. 2 (bottom panels). Vertical west-east cross-sections through the maximum storm updraft at y = 24 km and 31.4 minutes into the control simulation. a) vertical velocity; b) net charge density; c) electric field magnitude; d) location of bidirectional leader and branching volumes of 1st IC discharge (see MacGorman et al. 1998); e) cloud water (solid) and cloud ice (dashed) mixing ratios; f) total cloud charge density; g) snow aggregate mixing ratio; h) snow aggregate charge; i) total graupel/hail mixing ratio; j) total graupel/hail charge density.

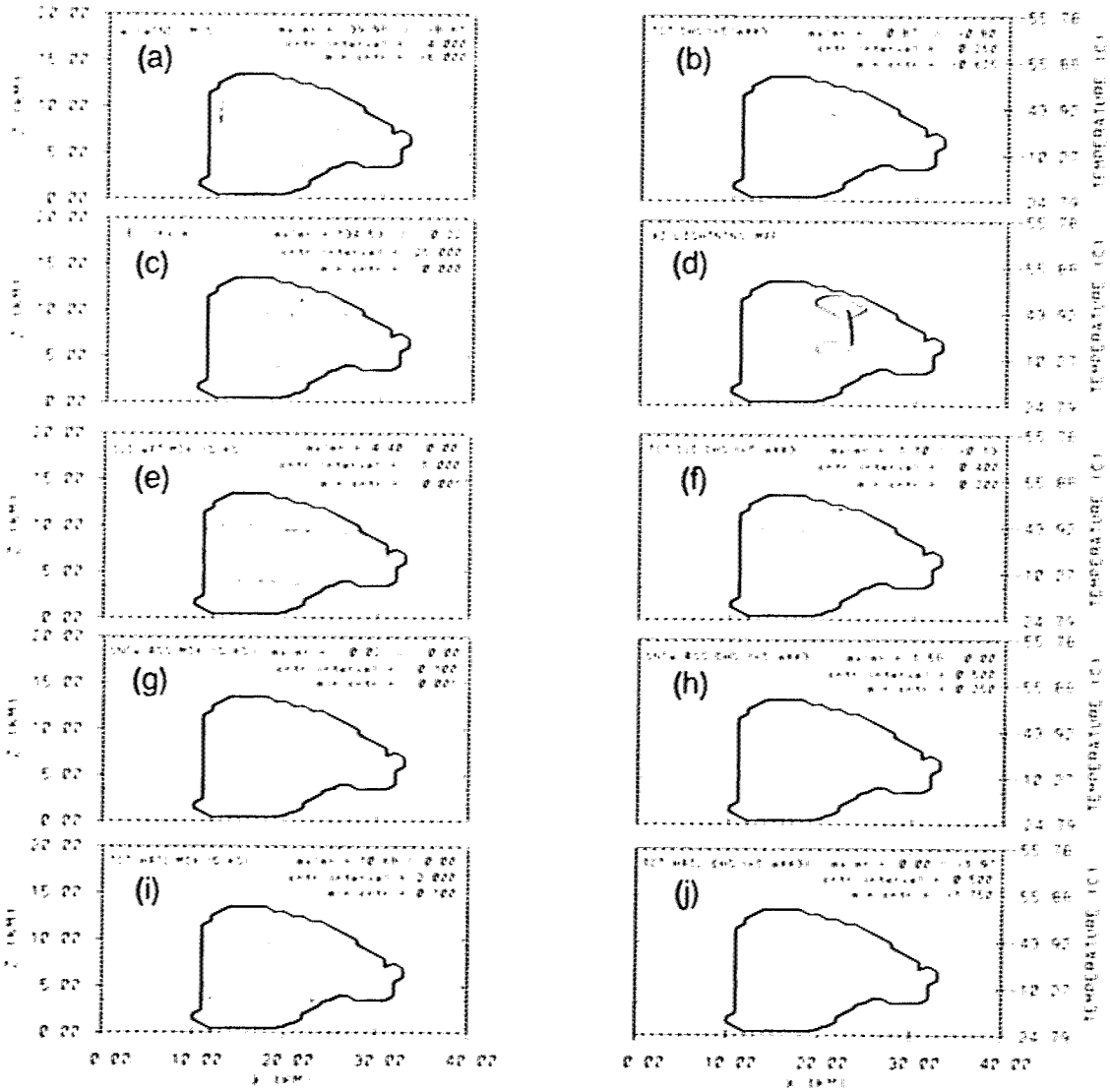

# DETERMINATION OF THUNDERSTORM ANVIL ICE CONTENTS AND OTHER CLOUD PROPERTIES FROM SATELLITE OBSERVATIONS OF LIGHTNING

Alan M. Blyth[1], Hugh J. Christian Jr[2], and John Latham[3]

[1]Physics Dept, NMIMT, Socorro, New Mexico 87801
[2]ES43, NASA/MSFC, Huntsville, Alabama 35812
[3]MMM Division, NCAR, PO BOX 3000, Boulder, CO 80307-3000

ABSTRACT: The lightning frequency model developed by Baker, Christian and Latham (1995) has been refined and extended, in an effort to provide a more realistic framework from which to examine computationally the relationships that might exist between lightning frequency f (which is now being routinely measured from satellites, using NASA/MSFC devices) and a variety of cloud physical parameters, including precipitation rate, updraught speed and non-precipitating ice content.

Model results indicate the existence of a simple relationship between lightning frequency f and the upward flux of ice crystals into the thunderstorm anvil. It follows that, for a particular situation, one can assign a specific mass of non-precipitating ice to an individual lightning stroke. Therefore it may prove possible - using satellite measurements of global lightning - to estimate the atmospheric loading of ice crystals in thunderstorm anvils: a parameter of climatological importance.

Early results from this work are presented, together with further studies of the relationships between f and other thundercloud parameters.

## INTRODUCTION

As a first step in the possible exploitation of satellite-borne lightning measurements (Christian and Goodman (1992), Christian, Blakesee and Goodman (1992)) made with NASA/MSFC devices, Baker, Christian and Latham (1995) developed a crude model of multiple lightning activity in thunderclouds, with a view to examining the hypothesis (supported by the research of Chauzy et al. (1985), Goodman, Buechler and Wright (1988), Goodman and Buechler (1990), Orville (1990), Williams et al. (1990) and others) that quantitatively definable relationships exist between lightning frequency f and thundercloud parameters such as precipitation rate (P), updraught speed (w), radar reflectivity (Z), cloud-width (W) etc. If such relationships are established, then measurements made with the OTD (Optical Transient Detector) or its successor, the LIS (Lightning Imaging Sensor), can be used to derive values of P, w, Z and other parameters; and the instrument could thus have significant forecasting or nowcasting importance.

This preliminary work yielded the conclusion that over a wide range of conditions f was roughly proportional to the first power of the parameters Z and W (and also the ice crystal and

graupel pellet concentrations); and, in some circumstances, to around the sixth power of w. The relationship between f and P depended critically on the extent to which the value of w determined the location of the "balance level" in the thundercloud, i.e. the altitude at which the precipitation started to fall towards ground.

We reiterate here a point stressed by Baker et al., that their "model" cannot be regarded as a quantitatively adequate thunderstorm electrification model, but as rather a vehicle enabling sensitivity tests to be conducted into the possible relationships between f (which models have not computed hitherto, because of the complexity and unknown features of thunderstorm characteristics following the first lightning stroke) and the cloud parameters defined earlier. In these sensitivity tests each parameter was varied in turn - the others being held constant - thus making no concession to the fact that strong interdependencies exist between some of them. These workers considered that our current limited understanding of multiple lightning activity rendered premature the utilisation of a more comprehensive model; and indeed, that the simplicity of this first model (in which explicit cloud microphysics is retained) is helpful in identifying the separate sensitivities of f to the individual cloud parameters.

## RELATIONSHIPS BETWEEN LIGHTNING ACTIVITY AND CLOUD ICE CONTENT

In this section we present some preliminary results concerned with possible relationships between lightning frequency f and total ice content I: and in particular the possibility that measurements of f might yield information on the ice crystal concentrations in the anvils of thunderclouds, a parameter of considerable climatological importance.

It is well established that thunderstorms - more specifically thunderstorm anvils - are an important source of ice particles in the upper atmosphere, and that such particles exercise a considerable influence on the radiative balance of the atmosphere.

A simple non-dimensional analysis indicates that f might be roughly proportional to thunderstorm non-precipitating ice content, I. This analysis, of course, is not identifiably associated with a particular region of a thundercloud, although it is most likely, in reality, to relate closely to the highest levels of the charging zone, since this is where the great preponderance of the charging occurs. Accordingly, it was decided to use a recently refined version of our model to examine the relationships between f and I at three separate locations: (1), the top of the charging zone; (2), throughout the charging zone, the lower level of which is at either 0C or -3C, according to whether ice is assumed to be created by either the primary nucleation mechanism or the Hallett-Mossop process; (3), the ice crystal anvil.

In the case of (1), our preliminary results indicate that for both glaciation mechanisms mentioned earlier f increases roughly linearly with I, as predicted by the dimensional analysis, and illustrated in Table 1. Such a dependence is not

surprising, since the charging (resulting from rebounding collisions between ice crystals and growing graupel pellets) is principally concentrated near the balance level, and the charging rate per unit volume (which will determine the rate at which breakdown fields can regenerate after a lightning flash) depends on the numbers and sizes of ice crystals in this region.

Virtually identical results were obtained in the case of (2), which is as expected, since both the ice content and the charging rate in the charging zone increase rapidly as the altitude increases towards the highest region (the balance level).

In the case of (3), the value of I increased steadily with time, whereas the value of f tended to be roughly time-independent. This result is not surprising since, on our simple model, in which the dimensions of the anvil are fixed, its ice content increases linearly ly ly with time, whereas - once the cloud is fully developed - that in the charging zone remains roughly constant throughout much of the active period of lightning production.

Plots of f against J, the upward flux of ice crystals through the top of the charging zone into the ice crystal anvil of the model thundercloud indicate a relationship between these two parameters which is close to linear.

It follows from the above considerations that a fixed mass $M_i$ of ice (in the form of non-precipitating crystals) can be associated with a single lightning stroke; and the preliminary computational work conducted to date suggests that a characteristic value for $M_i$ is around $10^6$ kg. This figure, emanating from a simplistic model and with no direct observational evidence against which to test it, cannot be regarded as accurate. The same statement must be applied to the crude calculations that follow. Our primary conconcern at this stage is simply to illustrate how it is possible, in principle, to derive characteristics of ice crystal anvils from satellite measurements of lightning. Detailed global-scale measurements of anvil characteristics are urgently required.

Taking the above-mentioned value for Mi, and assuming a figure of 40/s (as determined from OTD measurements) for the global lightning frequency $f_{glob}$, we deduce that the global flux $J_{glob}$ of ice crystals upwards into thunderstorm anvils is approximately $4.10^7$ kg/s.

An estimate of the global ice crystal content $M_{glob}$ present in thunderstorm anvils can be determined by noting that the rate of creation of cirrus crystals by thunderstorm activity (the product $M_i.f_{glob}$) must be equal to $M_{glob}/t_{anv}$, where $t_{anv}$ is a characteristic time defining anvil dissipation. Taking $t_{anv}=10^4$ s, and the above-mentioned values of $M_i$ and $f_{glob}$, we obtain a global ice crystal thunderstorm anvil content $M_{glob}$ of $4.10^{11}$ kg.

For an individual thunderstorm or a thunderstorm complex, the amount of ice (as crystals) introduced into the anvils is given simply by the product $M_i.N_{tot}$, where $N_{tot}$ is the satellite-derived number of lightning strokes associated with the storm.

Much more data acquisition and analysis, together with

computational improvement, are required in order to obtain more definitive and quantitative information on the question of the extent to which satellite measurements of lightning can provide estimates of large-scale and global upper level atmospheric ice crystal contents resulting from thundercloud activity. These first results, however, are encouraging, and if confirmed should be of climatological importance.

ACKNOWLEDGEMENTS

This work was supported by NASA/USRA.

REFERENCES

Baker, M.B., H.J.Christian and J.Latham (1995) "A computational study of the relationships linking lightning frequency and other thundercloud parameters" Quart J Roy Met Soc., 121, 1525-1548

Chauzy, S., Chong, M., Delannoy, A. and Despiau, S. (1985) The June 22 tropical squall line observed during COPT 81 experiment: Electrical signature associated with dynamincal structure and precipitation. J. Geophys. Res. 90, 6091-6098.

Christian, H.J. and Goodman, S. (1992) "Global observations of lightning from space". Proc. 9th Internat. Conf. on Atmospheric Electricity, St. Petersburg, pp316-321.

Christian, H.J., R.J.Blakesee and S.J.Goodman (1992) Lightning imaging sensor for the earth observing system. NASA Tech. Memorandum 4350.

Goodman S.J., D.E.Beuchler and P.D.Wright (1988) Lightning and precipitation history of a microburst-producing storm. Geophys. Res. Letters, 15, 1185-1188.

Goodman S.J. and D.E.Buechler (1990) Lightning-rainfall relationships. Proc. AMS Conf. on Operational Precipitation Estimation and Prediction, Anaheim, California, 1990.

Orville, R.E. (1990) Winter lightning along the East Coast. Geophys. Res. Lett., 17, 713-715.

Williams, E.R., S.G.Geotis, N.Renno, S.A.Rutledge, E.Rasmussen, T.Rickenback. "Hot Towers" in the tropics. Proc AMS Conf on Atmos. Elect., Alta, Canada, 1990.

# Sessions V and VI:

# Thunderstorm Characteristics

# Lightning and Radar Characteristics of the Bow Echo Event of May 24-25, 1998

**Natalie D. Murray and Richard E. Orville**
**Cooperative Institute for Applied Meteorological Studies and the Department of Meteorology**
**Texas A&M University**
**College Station, Texas 77843-3150**

**Abstract.** The mesoscale convective system of May 24-25, 1998 in Kansas and northern Oklahoma produced numerous regions of intense convection associated with bow echoes. Data collected by the National Lightning Detection Network (NLDN) have been analyzed for this storm which had a duration of twenty-six hours. Overall, 42% of the 50,000 cloud-to-ground flashes lowered positive charge. The maximum percent positive reached 75% per half-hour interval and occurred during the first quarter of the storm's lifetime. Our analysis has been narrowed to small time intervals of twenty minutes, which complement the available NOWRAD MOSAIC images for this date. Percent positives range between 60 and 70%. Locations of cloud-to-ground lightning flashes occurring in each interval are overlaid on the corresponding radar image. Further analysis provides information about the electrical structure of the intense convection.

## 1. Introduction

Bowing convective line segments, called bow echoes, are often associated with swaths of damaging downburst winds and are sometimes accompanied by tornadoes that may reach intensities of F4 or higher (Przybylinski 1995). Bow echoes may be as small as 20 km or extend to 100 km with a broad bowing segment. The features of the bow echo, summarized by Jorgensen and Smull (1993), include a pronounced bulge or "bow" in the convective line (convex toward the storm's direction of propagation), a strong descending rear inflow jet whose axis is aligned with the apex of the bow, and a cyclonic vortex (most pronounced at heights of 2-3 km) situated in the trailing stratiform region lateral to the axis of strongest rear inflow. Marshall and Rust (1993) first studied the electrical structure of bow-echo MCSs. They report vertical charge structures with four main charge regions. In their electrical field soundings, they reported a substantial region of charge and a large electric field at or near the zero degree C level.

In this paper we report on the cloud-to-ground lightning characteristics in a line of long-lived bow echoes that propagated on the evening of May 24 along the Oklahoma-Kansas border into the early morning hours of May 25. The National Lightning Detection Network detected and recorded the cloud-to-ground lightning data. The operational characteristics of the NLDN have been reported recently by Cummins et al. (1998), Idone et al. (1998a, b) and Wacker and Orville (1999a, b). A series of electric field soundings into these storms were obtained by D. Rust, D. MacGorman, T. Marshall, and M. Stolzenburg and their results are reported in a separate paper in these conference proceedings.

## 2. Methods

The storm system of May 24-25 is one of several that occurred in May and June of 1998 during the Mesoscale Electrification and Polarimetric Radar Study (MEaPRS) field program. The composite NOWRAD MOSAIC images used in our study are research products of MEaPRS, obtained via the World Wide Web. The main development of the observed intense convection was south of the Kansas-Oklahoma border, while stratiform elements remained northward in Kansas. In later stages, the storm system moved eastward into Missouri and northern Arkansas. Radar images are available at 0, 4, 5, 6, and 8 UTC on May 25, 1998. Lightning data from the NLDN were restricted to twenty-minute intervals centered on the beginning time of the radar scan. Overlaying the lightning data onto the radar image can provide us with an assessment of the lightning characteristics and their relation to the corresponding radar image. Another method of analysis, which we found useful, is to restrict the region

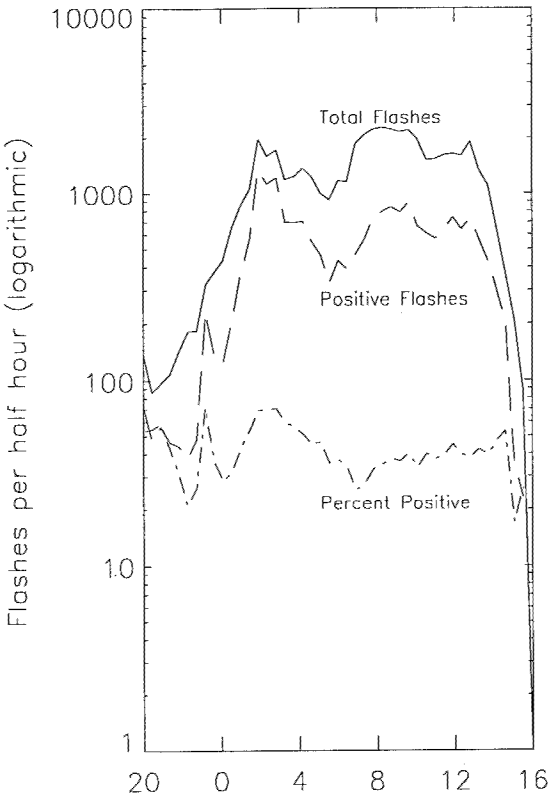


Fig 1. Flashes per half hour are plotted for the period from 20 UTC on 24 May to 16 UTC on 25 May 1998. The percent of positive flashes is also plotted for this period.

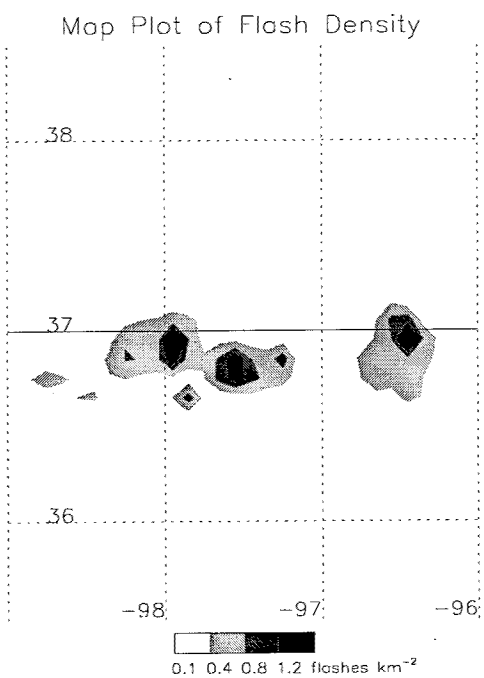


Fig. 2. Flash density plots for 20 UTC May 24 to 08 UTC May 25 over the area 36-38 N to 96-98 W.

under study to one-degree longitude and two- degrees latitude. This allows for a more detailed view of a cell of intense convection and the lightning associated with it.

## 3. Observations

Lightning analysis, using the NLDN database, for the storm system's full duration of twenty-six hours reveals a maximum flash rate of 4800 per hour. The percentage of positive flashes was 42% for the entire period of study. Figure 1 is a time series of flashes per half-hour for the storm's duration. The solid line shows total flashes and the dashed line denotes positive flashes. Percent positive are shown by the dotted line. All are on the logarithmic scale. From the time series the maximum flash rate is found at 02 UTC and 08 UTC for positive flashes. The values for percent positives have a substantial peak at both 23 UTC and 02 UTC.

A flash density plot is shown in Figure 2. For this figure, we are only concerned with densities associated with the available radar images. This restricts our time from 20 UTC on May 24 to 08 UTC on May 25, 1998. Flash density is calculated with a resolution of 10 km. Maximum density values of 0.8 flashes/km$^2$ are seen in three distinct areas, which correspond to the regions affected by the system's intense convection. The maximum positive flash density occurs in the first half of the storm's lifetime when it was in northern Oklahoma and southern Kansas.

The second part of our study is to examine strike location with respect to radar reflectivity. Radar images were imported and contoured for values of 10, 30, and 50 dBZ. At times, the maximum reflectivity reached 65 dBZ. The available radar coverage extends from 93 to 105 west longitude and from 33 to 42 north latitude. The regions of intense convection can be isolated. This is shown in Figures 3 and 4 on the following page. Figure 3 is for 04 UTC with the corresponding lightning data from 0350-0410 UTC. All CG flashes are plotted. The main concentration of flashes occurs in the area of high reflectivity. Located just below latitude 37 and positioned in the center of the convection the strikes show a clear easterly movement. For the larger region at this time interval, the lightning exhibits 61% positive flashes of the total 740. Flashes are concentrated in regions of high reflectivity with fewer in the northern stratiform region. Strikes are also concentrated along the leading edge of the intense convention.

Figure 4 shows the radar contours for 05 UTC and the plotted lightning locations, again restricted to a twenty-minute interval. Negative and positive flashes are

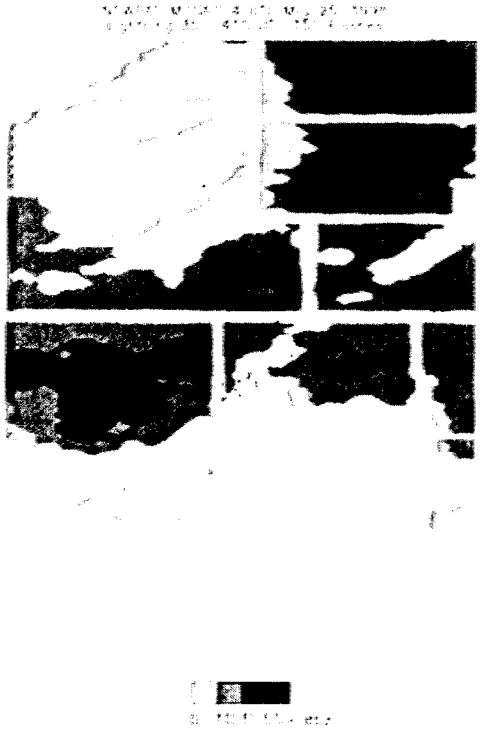

Fig. 3. Radar and lightning overlays for 04 UTC.

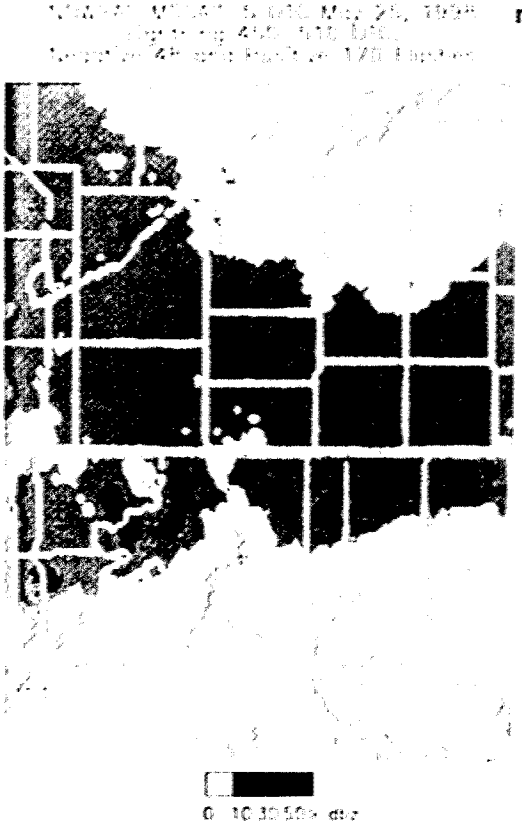

Fig. 4. Radar contour and lightning for 05 UTC.

plotted separately. Negative flashes, denoted by a square, are scattered throughout the region. Primarily they are found in the stratiform region. Positive flashes are denoted by a plus sign. The percent positive for this small region is 78% and the flashes occur in the high dBZ region. Note, however, that not all convective regions have CG lightning associated with them.

## 4. Conclusions

Positive flashes have high concentrations in regions of dBZ values of 50 and greater. They are also observed in stratiform regions (>30 dBZ) on the northeastern edges and are generally not observed in regions with less than 30 dBZ. Negative flashes occur less than positive flashes in all time intervals examined. The percentage of positive flashes ranges from 60 to 70% for the entire region covered by the radar in this study. Low flash concentrations are observed in convective regions and are also scattered in the stratiform. The exception to these observations is the leading edge of the storm. The northeastern edge line of convection is almost completely dominated by negative flashes. These flashes occur mainly on the north edge of the convection. This phenomenon is observed for all of the available radar images.

Our analysis will continue by using composite 88D radar images with lightning overlays. Peak currents for positive and negative flashes will be considered. Location of flashes over their median values (28 kA for positives and 15 kA negatives) will be determined.

This particular storm exhibits many qualities that have also been observed in other storms in spring and early summer of 1998 in the central United States. Further examination of this storm will provide useful information concerning the effect of aerosol particles, such as the smoke from the Central American fires (Lyons et al. 1998).

**Acknowledgment.** The lightning data were obtained from Global Atmospherics, Inc., Tucson, Arizona. The interest and assistance of Ken Cummins are greatly appreciated. We thank D. Rust, D. MacGorman, W. Beasley, T. Marshall, and M. Stolzenburg for the opportunity to participate in the MEaPRS program. Data handling at Texas A&M University is under the direction of Jerry Guynes and we thank him for his assistance. The assistance of Gary Huffines is gratefully acknowledged in the preparation of this manuscript. Our research is part of a lightning program supported by the National Science Foundation (ATM-9806189) and the National Oceanic and Atmospheric Administration (NA87WA0063).

**References**


Cummins, K. L., M. J. Murphy, E. A. Bardo, W. L. Hiscox, R. B. Pyle, A. E. Pifer, 1998: A combined TOA/MDF technology upgrade of the U.S. National Lightning Detection Network, *J. Geophys. Res.,* **103**, D8, 9035-9044.

Idone, V. P., D. A. Davis, P. K. Moore, Y. Wang, R. W. Henderson, M. Ries, and P. F. Jamason, 1998a: Performance evaluation of the U.S. National Lightning Detection Network in eastern New York; Part I: Detection efficiency, *J. Geophys. Res.,* **103**, D8, 9045-9055.

Idone, V. P., D. A. Davis, P. K. Moore, Y. Wang, R. W. Henderson, M. Ries, and P. F. Jamason, 1998b: Performance evaluation of the U.S. National Lightning Detection Network in eastern New York; Part II: Location accuracy, *J. Geophys. Res.,* **103**, D8, 9057-9069.

Jorgensen, D. P. and B. F. Smull, 1993: Mesovortex circulations seen by airborne Doppler radar within a bow-echo mesoscale convective system, *Bull. Amer. Meteor. Soc.*, **74**, (11), 2146-2157.

Lyons, W. A., T. E. Nelson, E. R. Williams, J. Cramer, and T. Turner, 1998: Enhanced positive cloud-to-ground lightning in thunderstorms ingesting smoke from fires, *Science*, **282**, 77-81.

Marshall, T. C. and W. D. Rust, 1993: Two types of vertical electrical structures in stratiform precipitation regions of mesoscale convective systems, *Bull. Amer. Meteor. Soc.,* **74**, (11), 2159-2170.

Przybylinski, R. W., 1995: The bow echo - observations, numerical simulations, and severe weather detection methods, *Wea. Forecasting*, **10**, (2), 203-218.

Wacker, R. S. and R. E. Orville, 1999a: Changes in Measured Lightning Flash Count and Return Stroke Peak Current after the 1994 U. S. National Lightning Detection Network Upgrade, Part I: Observations, *J. Geophys. Res.,* **104**, D2, 2159-2162.

Wacker, R. S. and R. E. Orville, 1999b: Changes in Measured Lightning Flash Count and Return Stroke Peak Current after the 1994 U. S. National Lightning Detection Network Upgrade, Part II: Theory, *J. Geophys. Res.,* **104**, D2, 2151-2162.

# COMBINED MICROWAVE AND SFERICS MEASUREMENTS AS A CONTINUOUS PROXY FOR LATENT HEATING IN MESOSCALE MODEL PREDICTIONS

D. -E. Chang[1], C. A. Morales[2], J. A. Weinman[3], W. S. Olson[4]

[1]Universities Space Research Association, NASA Goddard Space Flight Center, Greenbelt, MD 20771
[2]CnPQ Brazil and University of Maryland, College Park, MD 20742
[3]Microwave Sensors Branch, NASA Goddard Space Flight Center, Greenbelt, MD 20771
[4]Joint Center for Earth Systems Technology, University of Maryland-Baltimore County, Baltimore, MD 21250

**ABSTRACT**: Planar rainfall distributions were retrieved from data provided by the Tropical Rainfall Measuring Mission (TRMM) Microwave Imager (TMI) and Special Sensor Microwave/Imager (SSM/I) radiometers. Lightning generates Very Low Frequency (VLF) radio noise pulses called sferics. Those pulses propagate over large distances so that they can be continuously monitored with a network of ground based radio receivers. An empirical relationship between the sferics rate and the convective rainfall permitted maps of convective latent heating profiles to be derived continuously from the sferics distributions. Those inferred latent heating rates were assimilated into the Penn State/NCAR Mesoscale Model (MM5) that depicted an intense winter cyclone that passed over Florida on 2 February 1998. When compared to a 14 hour MM5 rainfall forecast using conventional data, the use of lightning data improved the forecast.

## BACKGROUND

Convective clouds pose a threat to aviation because of severe turbulence, icing and lightning produced in their proximity. Although NOAA operational radars provide severe weather warnings over much of the continental United States, coverage over adjacent maritime regions has been inadequate. Spaceborne infrared imagery from operational geostationary weather satellites provides some limited guidance regarding the distribution of the heights of convective cloud tops. Lightning measurements can serve as indicators of strong convection that impact aviation operations [*Weber et al.*, 1998]. Because charge separation in cumulus clouds requires updrafts sufficiently intense to suspend graupel or hail [*Baker et al.*, 1995], lightning flash rates have been related to cloud top height, the radar reflectivity above the freezing level that exceeds 40 dBZ and the Vertically Integrated Liquid (VIL) water. This study combines continuous lightning observations with spaceborne microwave radiometric measurements to furnish input for a mesoscale model short term forecast.

Lightning generates VLF radio noise, between 5 and 15 kHz, called sferics. Because sferics propagate several thousands of km in the Earth-ionosphere waveguide [*Lee*, 1986], sferics receivers can be widely separated so that a sparse network can observe oceanic regions at a reasonable cost. Sferics are mainly produced by vertical discharges that may occur within clouds or more probably as cloud-ground discharges. A Sferics Timing And Ranging NETwork (STARNET) was developed by Resolution Displays Inc. under NASA Small Business Innovative Research (SBIR) grant NAS5-32825. STARNET consists of five receivers, located in MA, VA, AL, FL and PR. Morales (private communication) showed that random errors in locating lightning range between 5 and 30 km over much of the continental US, increasing with the distance from the STARNET receivers. That resolution is compatible with that of spaceborne microwave radiometric retrievals of convective precipitation obtained intermittently from the SSM/I [*Hollinger et al.*, 1990] and the TRMM Microwave Imager (TMI). The TRMM satellite also carries a 14 GHz PR, the first weather radar in space and a Lightning Imaging Sensor (LIS) [*Kummerow et al.*, 1998].

## METHOD

The present study addresses the genesis of a cyclone over the Gulf of Mexico that led to the 1998 Ground-hog day storm in Florida [*Rippey*, 1998]. That storm damaged 235 aircraft, produced seven tornadoes and developed wind gusts of 104 mph around Miami. Convective rainfall rates were determined from SSM/I and TMI microwave radiometric measurements using the Goddard PROFiling (GPROF) algorithm [*Kummerow et al.*, 1996]. Although lightning flash rates are proportional to convective rainfall, direct relationship between lightning flash rate and convective rainfall rate is not easy to define due to the location error of sferics observation. To eliminate this problems, number of sferics measured within a fifteen minute interval around the satellite overpasses is counted over a 0.5° × 0.5° grid box. The number of sferics is then compared to averaged convective rainfall rate in the

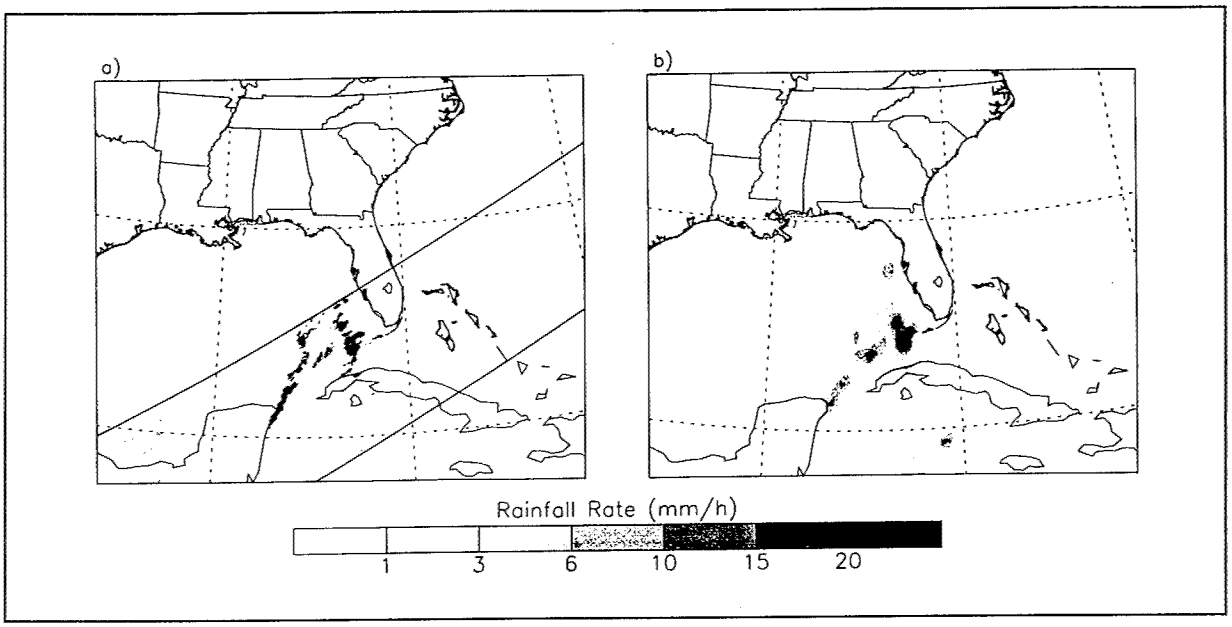


*Fig.1 (a) The distribution of surface rainfall on 2 February 1998 at 1959 UTC obtained from TMI by means of GPROF. The parallel lines depict the TMI swath boundaries. (b) Surface rainfall derived from the empirical relationship between microwave and sferics measurements between 1945 and 2000 UTC.*

corresponding grid box by means of the probability matching technique [*Calhieros and Zawadski*, 1987]. That permitted the continuously measured sferics to be transformed into convective rainfall rate distributions.

Rainfall rates inferred from combined sferics and microwave data were assimilated into the Penn State/NCAR Mesoscale Model (MM5) Version 2 [*Grell et al.*, 1994]. The assimilation scheme follows those of *Manobianco et al.* [1994] and *Alexander et al.* [1999] which is based on scaling the model predicted latent heating profiles by observed and model produced precipitation rate. The model run was initiated at 1200 UTC on 2 February 1998 and integrated forward 24 hours. Assimilation of rainfall rates was performed for the first 12 hours integration. The model physics for this study include Kuo-Anthes cumulus parameterization and Blackadar high resolution planetary boundary layer model. The model domain contains 100×120 horizontal grid points with 40 km resolution and 23 vertical layers.

**RESULTS**

In order to illustrate the validity of deriving convective rainfall from sferics measurements, Fig.1a shows the distribution of the surface convective rainfall on 2 February 1998 at 1959 UTC derived from the TMI by means of GPROF along a 790 km wide swath. Fig.1b shows the coincident convective rainfall at the surface derived from the empirical relationship between microwave and sferics measurements. Rainfall rates inferred from sferics observation show very good agreement in terms of horizontal distribution and amounts as well. Data such as those shown in Fig.1b were used to continuously provide latent heating distributions for the MM5 model.

The MM5 model predictions of surface rainfall are compared to the rainfall distribution archived from the NWS radar network data. Fig. 2a presents the rainfall distribution at 0200 UTC on 3 February 1998 derived from the radars. Note that all rain that fell south of northern Cuba was beyond the range of the radars. Radar observation shows maximum rainfall rate of 35 mm/h over southern tip of Florida and a squall line southwestward. Fig. 2b shows the corresponding 14 hours prediction of surface rainfall using only conventional data and Fig. 2c shows the corresponding prediction of surface rainfall after latent heating rates derived from sferics-microwave data were continuously assimilated into the MM5 model for 12 hours. The assimilation experiment produced two times greater maximum rainfall over southern Florida compared to the experiment without assimilation, and the squall line orientation was more realistic.

Although space does not permit a presentation of the results, the present study showed that the surface pressure fields derived by the MM5 model were in satisfactory agreement with the analysis even if latent heating was not

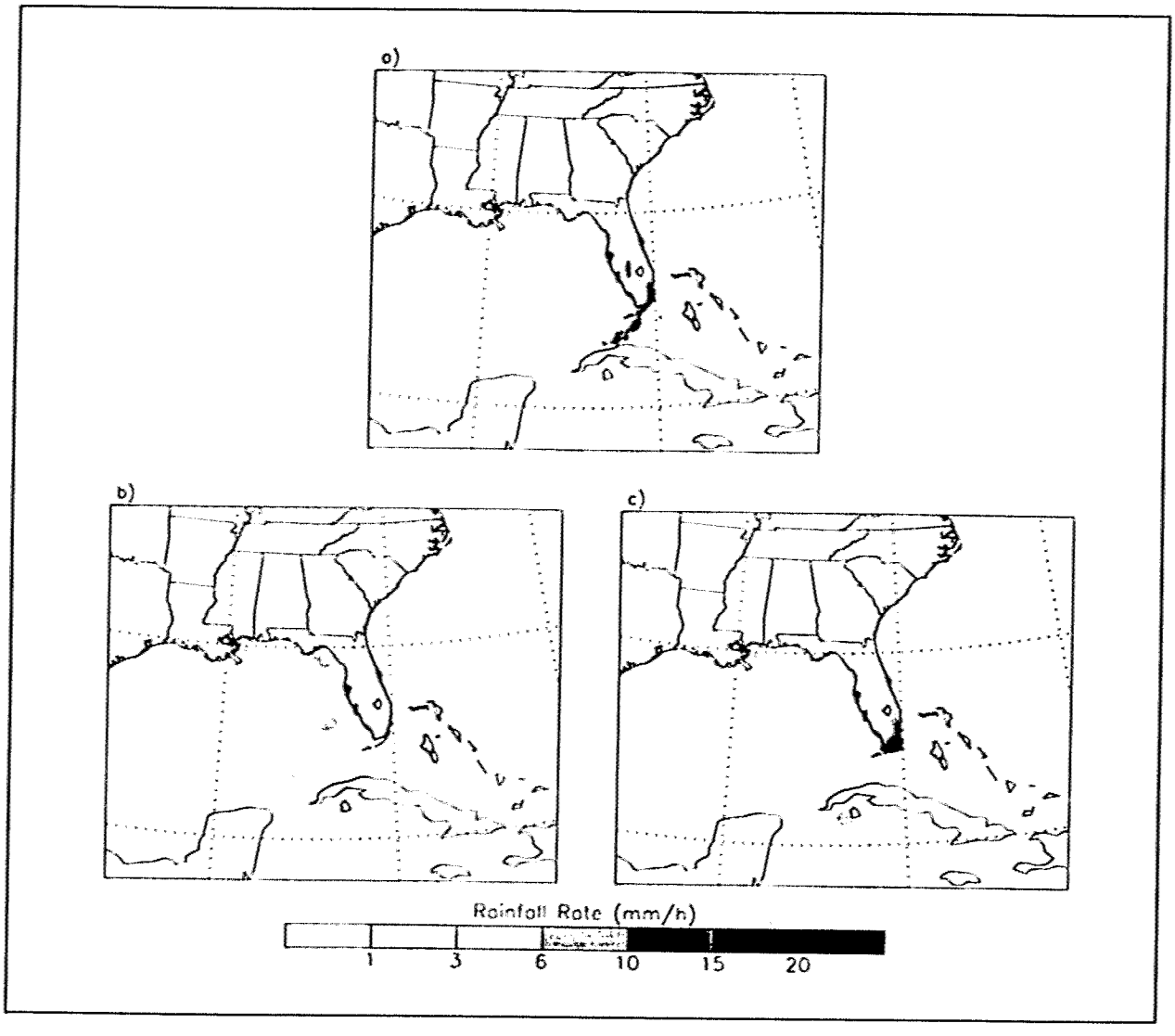


*Fig. 2 (a) The surface rainfall distribution at 0200 UTC on 3 February 1998 derived from NWS radars. The maximum radar range extends to the northern Cuban coast. (b) The 14 hour prediction of surface rainfall using only conventional data in the MM5. (c) The corresponding prediction of surface rainfall after latent heating rates derived from sferics-microwave data were continuously assimilated into the MM5 model for 12 hours.*

assimilated from external data. However predictions of integrated water vapor as well as surface rainfall distributions were significantly improved by assimilating latent heating from combined microwave and sferics data.

## DISCUSSION

The present study showed that lightning occurs frequently over the Gulf of Mexico along winter cold fronts. Sferics, suitably tuned with intermittent spaceborne microwave radiometer data, can be assimilated as latent heating into a mesoscale weather prediction model. Such assimilated heating rates improve predictions of hydrologic parameters such as integrated water vapor and surface rainfall. A geostationary Lightning Mapping Sensor (LMS) has been proposed to provide continuous lightning measurements over the Western Hemisphere [*Christian et al.*, 1989]. The present analysis suggests how continuous data from LMS might improve weather forecasts. A global sferics monitoring network could provide weather hazard warnings until the time when geostationary satellites of all countries will carry LMS sensors.

**ACKNOWLEDGMENTS**: This work was supported by NASA grant NAS5-32484 to promote TRMM applications. We wish to thank Dr. Ramesh Kakar of the NASA Earth System Science Office for his helpfulness.

**REFERENCES**

Alexander, G. D., J. A. Weinman, V. M. Karyampudi, W. S. Olson, and A. C. L. Lee (1999) The Impact of the Assimilation of Rain Rates from Satellites and Lightning on Forecasts of the 1993 Superstorm, Accepted for Publication in *Mon. Wea. Rev.*

Baker, M. B., H. J. Christian, and J. Latham (1995) A Computational Study of the Relationships Linking Lightning Frequency and Other Thunderstorm Parameters, *Q. J, Roy. Met. Soc.*, **121**, 1525-1548.

Calhieros, R. V., and I. Zawadski (1987) Reflectivity-Rain Rate Relationships for Radar Hydrology in Brazil, *J. Cli. and Appl. Met.*, **26**, 118-132.

Christian, H. J., R. J. Blakeslee, and S. J. Goodman (1989) The Detection of Lightning from Geostationary Orbit, *J. Geophys. Res.*, **94**, 13329-13337.

Grell, G. A., J. Dudhia, and D. R. Stauffer (1994) *A Description of the Fifth Generation Penn State/NCAR Mesoscale Model.* NCAR Tech Note NCAR/TN-398+STR, 138 pp.

Hollinger, J. P., J. L. Pierce, and G. A. Poe (1990) SSM/I Instrument Evaluation, *IEEE Trans. on Geosci. and Remote Sensing*, **28**, 781-790.

Kummerow, C., W. Barnes, J. Shiue, and J. Simpson (1998) The Tropical Rainfall Measuring Mission (TRMM) Sensor Package, *J. Atmos. and Ocean Tech.*, **15**, 809-817.

Kummerow, C., W. S. Olson, and L. Giglio (1996) A Simplified Scheme for Obtaining Precipitation and Vertical Hydrometeor Profiles from Passive Microwave Sensors, *IEEE Trans. On Geosci. And Remote Sensing*, **34**, 1213-1232.

Lee, A. C. L. (1986) An Operational System for the Remote Location of Lightning Flashes using a VLF Arrival Time Difference Technique, *J. Atmos. and Ocean Tech.*, **3**, 630-642.

Manobianco, J., S. E. Koch, V. M. Karyampudi, and A. J. Negri (1994) The Impact of Assimilating Satellite-derived Precipitation Rates on Numerical Simulation of the ERICA IOP 4 Cyclone, *Mon. Wea. Rev.*, **122**, 341-365.

Rippey, B. (1998) Weatherwatch-January, February 1998, *Weatherwise*, **51-3**, 52.

Weber, M. E., E. R. Williams, M. M. Wolfson, and S. J. Goodman (1998) *An Assessment of the Operational Utility of a GOES Lightning Mapping Sensor*, Lincoln Laboratory Project Report NOAA-18.

# THREE-DIMENSIONAL LIGHTNING MAPPING OBSERVATIONS DURING MEAPRS IN CENTRAL OKLAHOMA

P.R. Krehbiel, R.J. Thomas, W. Rison, T. Hamlin, J. Harlin, M. Davis
New Mexico Institute of Mining and Technology, Socorro, New Mexico, U.S.A.

ABSTRACT: 3-dimensional observations of lightning have been obtained for different kinds of storms in central Oklahoma, including several supercell storms, a tornadic storm, and storms having a large fraction of positive cloud-to-ground (+CG) lightning. A number of interesting results continue to emerge from the observations. Among these are a) the occurrence of inverted polarity intracloud discharges in storms, b) the observation of a new regime of lightning at very high altitudes in storms (15-20 km MSL), apparently in overshooting convective tops, and c) the result that lightning in supercell storms is essentially continuous and volume-filling, and sometimes contains 'holes' that appear to be associated with strong updraft regions.

## INTRODUCTION

A deployable, 3-dimensional Lightning Mapping System (LMS) developed by New Mexico Tech with NSF support was initially operated in central Oklahoma during June, 1998 in conjunction with the MEaPRS program [Thomas et al. and Rison et al.; this conference]. A network of ten measurement stations were deployed over a countywide area 60 km in diameter; each station used GPS signals to accurately measure the time of arrival of lightning radiation events in the frequency band 60-66 MHz. Accurate 3-dimensional source locations were obtained over an area about 100 km in diameter above and around the network; 2-dimensional observations of decreasing accuracy were obtained out to 200 km km distance or more.

## RESULTS

Figure 1 shows one minute of lightning activity in a line of convective storms that moved rapidly over the edge of the network from the southwest after local midnight on June 10-11. The small squares indicate individual stations of the network and the coordinate origin is at the center of the network. Lightning was detected as far away as the Oklahoma-Texas border, 200 km south of the network. At such distances, lightning activity below the local horizon is not detected, as seen in the vertical cross-section on the lower right of the figure. Figure 2 shows an extensive, hybrid cloud-to-ground (CG) and intracloud (IC) flash that

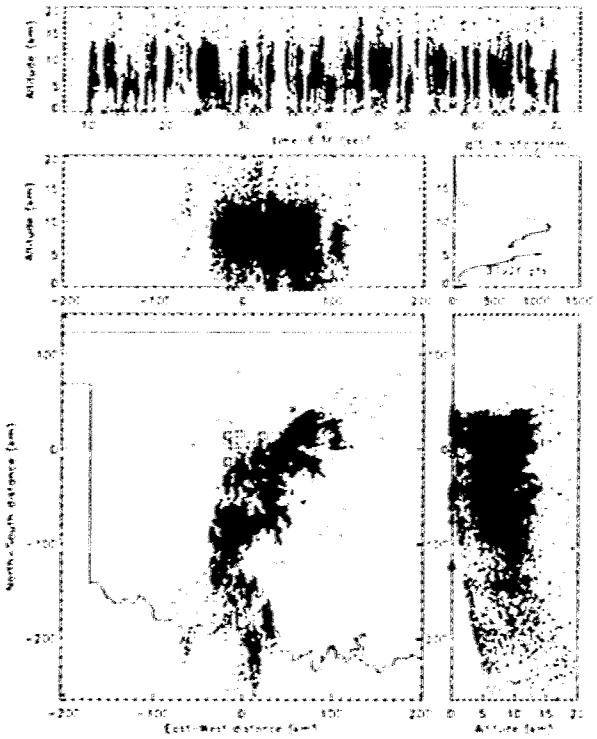

Figure 1. One minute of lightning in a convective line after local midnight on June 10-11.

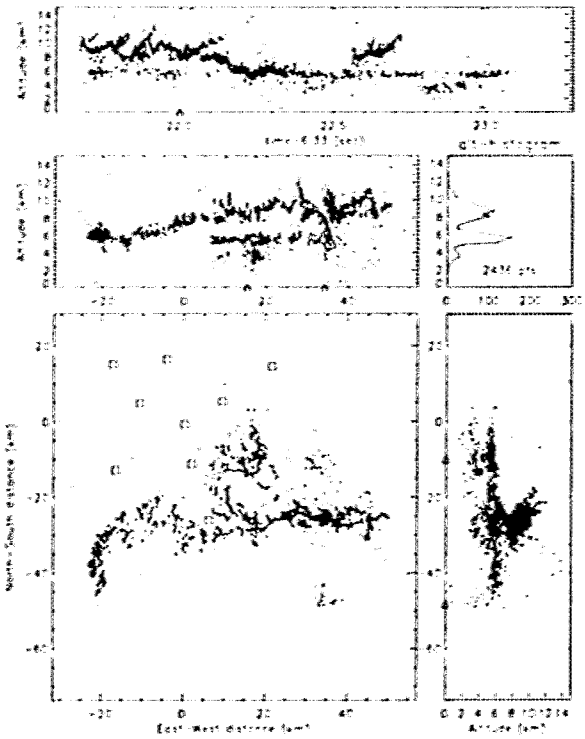

Figure 2. An extensive, hybrid IC-CG discharge a few minutes earlier in the storm.

occurred at 063322 UTC, a few minutes before the observations of Figure 1. The discharge began as a bi-level intracloud flash between the main negative charge (5–6 km altitude) and upper positive charge (8–10 km) regions of the storm. The upper level channels progressed away from the main part of the storm into an apparent stratiform region to the west and decreased in altitude as they did so, indicating that the upper positive charge region similarly decreased in altitude. A third level of activity (at 3–4 km altitude) was above the negative CG strike point (△) and appeared to be associated with lower positive charge in that part of the storm. Similar trilevel structures are commonly seen in the overall lightning data for normal convective storms both in Oklahoma and New Mexico.

Figures 3 and 4 show comparative examples of normal- and inverted-polarity IC discharges. The two normal-polarity discharges of Figure 3 occurred five seconds apart in time in separate regions of a storm on June 19. Each discharge had a classic bilevel structure and was initiated by upward-propagating breakdown typical of normal polarity ICs [Shao and Krehbiel, 1996]. Relatively few radiation events were located in the lower, main negative charge level, in comparison to the upper, positive charge level. This is a typical feature both of time-of-arrival and interferometer observations of lightning RF radiation, and indicates that breakdown in the positive charge region, which is due to negative-polarity streamers, radiates more strongly at VHF than the positive-polarity breakdown in negative charge regions.

Inverted polarity IC discharges (Figure 4) also have a bilevel structure, but exhibit downward rather than upward initial development and have many more radiation sources in the lower than in the upper level. In addition, late-stage K streamers in the flashes are sometimes slow enough for their motion to be resolved, and progress from the top to the bottom level rather than from bottom to top (as in normal polarity discharges), further confirming the inverted nature of the discharges.

The observations of Figures 3 and 4 are from storms on successive days, both of which produced a high proportion of positive CG lightning, as determined from NLDN data. Inverted polarity IC discharges were commonly observed in both storms. As might be expected, some inverted IC flashes produced +CG discharges. An unexpected result is that some normal polarity IC flashes also appeared to produce +CG discharges. The question of how the storms develop an inverted polarity is an important one that is not at all understood.

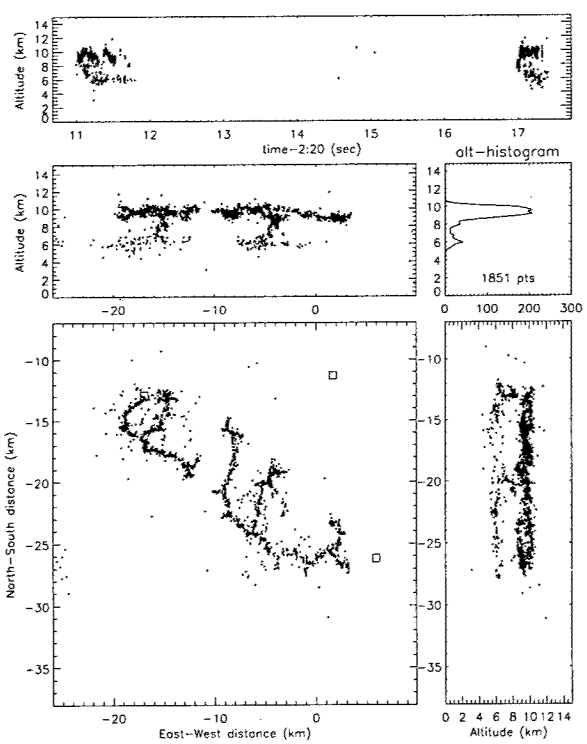


Figure 3. Two normal-polarity IC discharges in the storm of June 19.

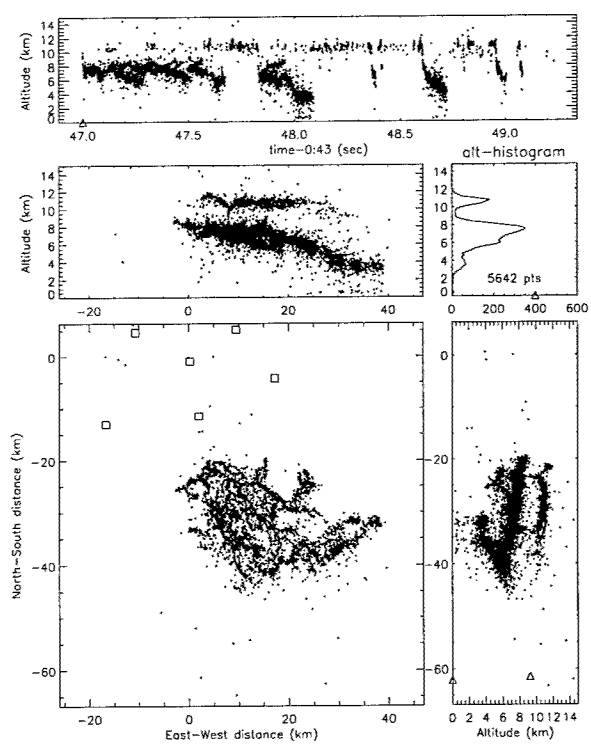


Figure 4. An inverted polarity IC discharge in the storm of June 20.

Figures 5 and 6 show lightning in the first of several supercell storms on June 8. Figure 5 shows 30 seconds of activity as the developing storm moved over the southwestern edge of the network. Figure 6 shows the activity 3 minutes later, during a 60 second interval. The time-height panels in the figures shows that the lightning was essentially continuous. Time-animated plots of the observations show that a number of discharges occurred every second at a variety of locations within the supercell. Unlike lightning in 'normal' storms, which has a relatively well defined structure, the discharge channels in the supercell storm had no characteristic structure but appeared random and amorphous. Visual observations of the lightning in the upper part of a second, similar supercell just after sunset were spectacular.

The accumulated effect of the supercell lightning was to fill a bowl-shaped volume over the diameter of the storm (60 km) up to a height of about 12 km MSL. A relatively small number of CG discharges of both negative (△) and positive (×) polarity occurred in the lowest part of the bowl. A significant feature of the otherwise volume-filling activity is the presence of lightning-free 'holes' in the plan views. The holes were about 5 km in diameter and were undoubtedly associated with some dynamical and/or microphysical feature of the storm, such as a hailshaft or strong updraft. Also, the holes were ephemeral on the time scale of several minutes. Lightning holes were also observed in the tornadic storm discussed later.

Another feature of the supercell observations is the occurrence of radiation at high altitude (15–16 km) above the south central part of the storm. Similar activity has been seen in a variety of storms from the Oklahoma study and represents an entirely new lightning regime. The lightning occurs between 15 and 20 km altitude, is localized and sometimes intense in nature, and occurs continuously and independently of lightning in the lower part of the storm. Its sources are observed to rise up out of the maximum altitude of the other lightning and to subsequently die out, indicating that the discharges occur within (or possibly above) overshooting convective tops that penetrate the base of the stratosphere. In the Figure 6 instance, the high altitude sources are located directly above the lightning hole, indicating that the holes are associated with strong updrafts.

In hindsight the amorphous nature of the supercell lightning is not surprising given the high discharge rate. The essentially continuous redistribution of charge by the discharges would tend to dominate the electrical structure of the storm and is the likely reason the lightning has a random structure. It would follow that the lightning activity almost certainly enhances the electrification rather than reducing it.

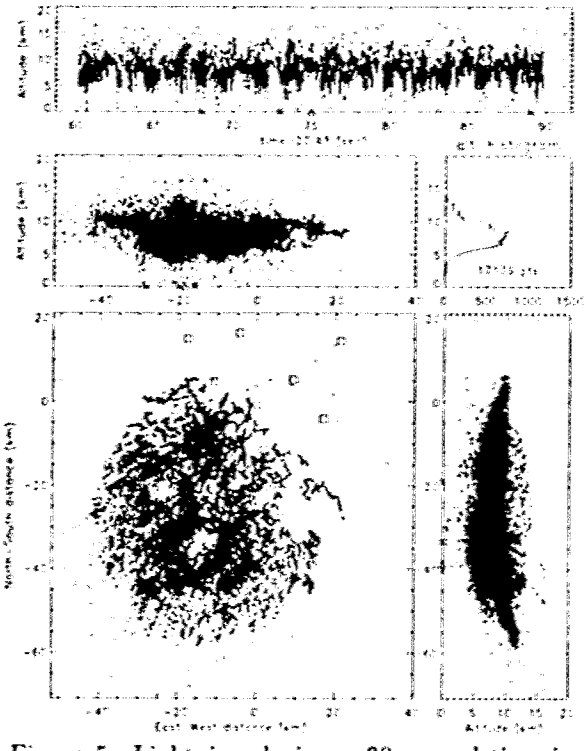

Figure 5. Lightning during a 30 second time interval in the first supercell storm of June 8.

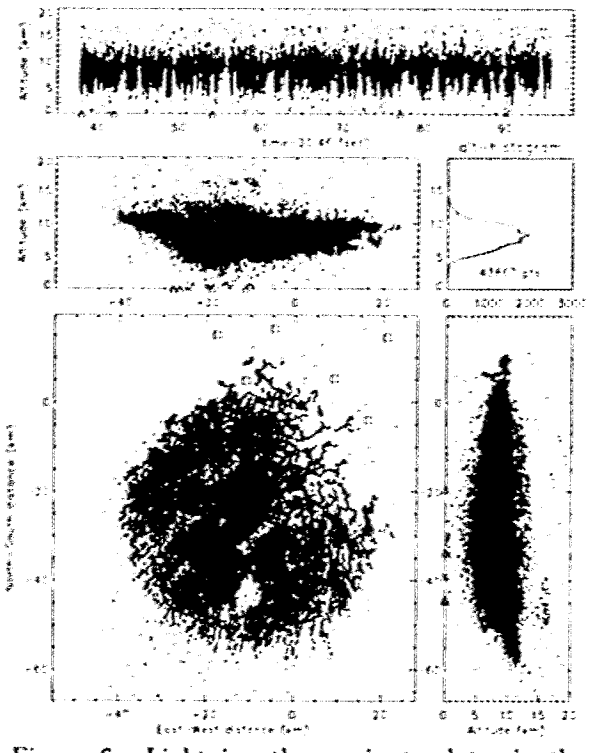

Figure 6. Lightning three minutes later in the storm, over a 60 second time interval.

Figures 7 and 8 show observations for the evening storm of June 13 that produced four F1 and F2 tornadoes over northern Oklahoma City. Figure 7 shows 30 seconds of lightning activity an hour earlier in the storm (00:11 UTC), a few minutes prior to touchdown of an initial F0 tornado. Amazingly, the lightning exhibits a counterclockwise hook-like structure on the west side of the storm, similar to hook echoes observed by radar in tornadic storms. The hook encloses an irregularly shaped lightning-free region, or hole, and the tornado occurred immediately below this region (rectangular bar). The lightning hole presumably corresponded to the updraft and associated weak echo region of the storm. The lightning at low altitude (3–4 km) below the northwest part of the hook was presumably associated with the wall cloud of the storm. Overall, the lightning consisted of more or less continuous discharges at high altitude in the storm (11–14 km), punctuated by discrete discharges at lower altitudes, including several into the wall cloud structure. Interestingly, the NLDN data indicated no discharges to ground.

Figure 8 shows the storm about an hour later (01:07 UTC) and 50–60 km to the east, at the time of the F1 and F2 tornadoes. The first three tornadoes (small bars) occurred around a tighter hook and lightning-free structure on the very southwest corner of the storm, between 01:02 and 01:11. The final, more long-lived tornado (01:12 to 01:23) began four minutes after the Figure 8 interval at the edge of the lightning hole and stayed on the ground for several miles, passing through an amusement park.

From 01:01 to 01:08, immediately prior to and during the first three tornadoes, the lightning exhibited rapid upward growth from 14 to 19 km altitude above the western flank of the storm. This activity is seen in its fully developed state in Figure 8 and was undoubtedly associated with a strong convective burst and overshooting top. CG discharges during this time were confined to the east-central and southern parts of the storm, well ahead of the tornadoes. Between 01:00 and 01:05, the CG discharges were predominantly negative and few in number; at 01:05 the discharges abruptly reversed sign to consist entirely of positive CGs, and the discharge rate increased. Similar variations in tornadic storm CG activity have been reported by MacGorman and Burgess [1996]. The lightning structure above the +CG region resembled that of inverted polarity IC discharges, consistent with the polarity reversal.

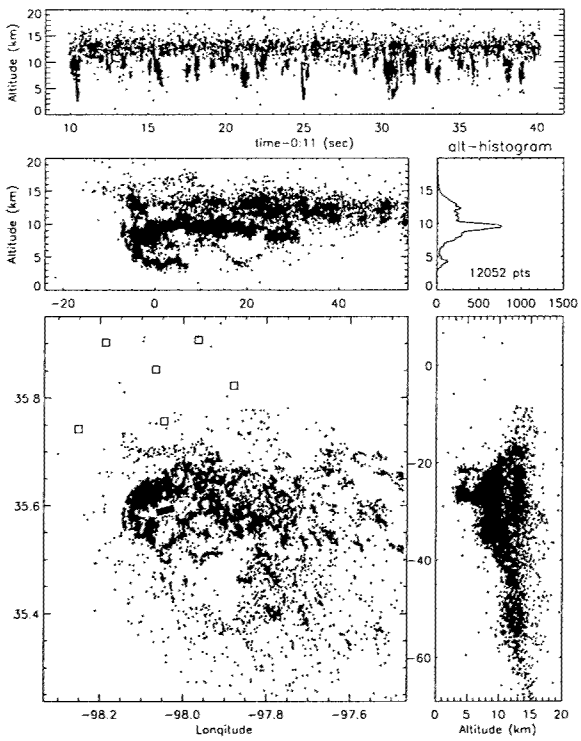


Figure 7. Initial part of the tornadic storm.

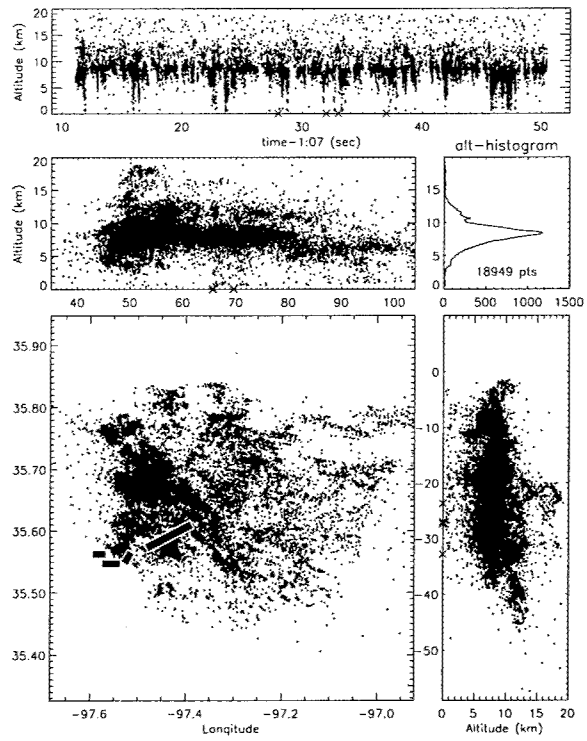


Figure 8. Later part of the tornadic storm.

REFERENCES

MacGorman, D.R., and D.W. Burgess, Positive cloud-to-ground lightning in tornadic storms and hailstorms. Mon. Weath. Rev., 122, 1671-1697, 1994.

Shao, X., and P. Krehbiel, The spatial and temporal development of intracloud lightning, J. Geophys. Res., 101, 26641-26668, 1996.

# CHARACTERISTICS OF "SUPERBOLT" RELATED WINTER THUNDERCLOUDS OVER THE JAPAN SEA

T. Shimura[1], F.Kobayashi[1], Takatoshi Shindo[2], A. Wada[2], and T. Sakai[3]

[1]National Defense Academy, Yokosuka, Kanagawa, Japan
[2]Central Research Institute of Electric Power Industry, Komae, Tokyo, Japan
[3]Hokuriku Electric Power Company, Toyama, Toyama, Japan

**ABSTRACT**: One of the typical features of winter thunderclouds in the Hokuriku district of Japan is positive lightning strikes with large lightning currents or huge charges neutralized by lightning. "Superbolt" thunderclouds which generated large current lightning strikes twice in succession to the 200m-high stack were observed using a Doppler radar on December 21, 1995. Both of the peak currents observed by shunt register were over 250kA. On that day, meso-$\alpha$-scale low pressure system formed over the Japan sea and a band-shaped radar echo about 100km long, developed near the coastline within only about 1 hour. The results of the Doppler radar observation show that the first lightning strike occurred at the leading edge of the echo band whose intensity was weak (less than 16dBZ or no echo), and the second one occurred at the core of those whose intensity was strong (greater than 30dBZ). "Superbolt" occurred after a long time charge accumulation in the southern part of the band echo system.

## INTRODUCTION

Winter thunderclouds in the Hokuriku district of Japan, can cause serious damage to society, because of lightning with large currents so-called "Superbolt". Using optical emission recorded by satellite, *Turman* [1977] found lightning flashes with high peak power ($10^{11}$-$10^{13}$W) as compared to the typical value ($10^{9}$W) and called this phenomena on "Superbolt". *Brook et al.* [1982] observed lightning flashes in which over 300C positive charges were neutralized. Some electrical observation about "Superbolt" has been presented in case studies. However, there has been no meteorological observation using weather radar to discuss the structure of "Superbolt" related winter thunderclouds. In this study, we succeeded to observe with Doppler radar, thunderclouds which generated large current lightning strikes twice in succession to 200m-high stack on 21 January 1995. In this paper, we define strikes with large current (over 200kA) as "Superbolts".

In addition, winter thunderclouds were classified into three types : frontal thunderclouds, winter monsoon thunderclouds and cold airmass thunderclouds [*Kobayashi et. al.*, 1996]. In this paper, we discuss about the subsynoptic weather conditions and the structure of radar echo which caused large current lightning strikes.

## OBSERVATION

The winter thunderstorm observation program was carried out from December 1995 to February 1996. An X-band Doppler radar (Maximum range 64km) and a C-band conventional radar were set up at Komatsu Air Base in the Hokuriku district, and a Doppler sodar (acoustic radar) and weather stations (automatic meteorological data observation system) were installed at Mikuni, close to a 200m-high stack about 30km from Komatsu (Figure 1). A shunt register

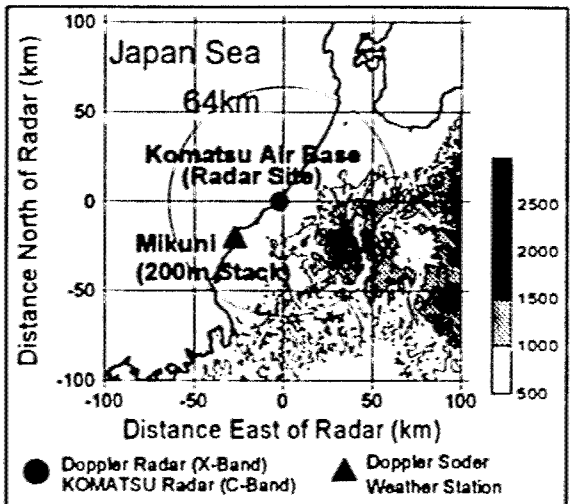


Figure1. Observation area

was installed at the top of the 200m-high stack to measure the lightning current.

## METEOROLOGICAL BACKGROUND OF "SUPERBOLTS"

The distribution of flash density is highly dependent on the type of meteorological disturbances. When a cold front passes over the Japan Sea, the flash density maximum exists over sea accompanied by advance of the frontal echo band. During the northwesterly winter monsoon period, it occur in the northwestern side of the mountainous region because thunderclouds move to the foot of the mountains and develop near the mountain upslope region. On the other hand, during the cold airmass period, lightning is generally inactive. But lightning is active and flashes concentrate in the coastal area when a cold vortex associated with meso- $\alpha$ -scale low pressure system in the cold airmass, passes. Figure 2 shows the CG (cloud-to-ground) flash density detected by LLP system for 3 winter seasons during the cold vortex period. The cold vortex accompany the spiral or band shaped radar echo system and cause heavy snow, gust wind and lightning [*Ninomiya et al.*, 1990]. Moreover radar echoes sometimes develop near the coastline because of the convergence of the lower atmospheric currents and CG flashes concentrate at this area [*Kobayashi et. al*, 1994].

"Superbolt" thunderclouds were observed in association with the meso- $\alpha$ -scale low pressure system over Japan sea during the cold airmass period (Figure 3). The radar echo structure is discussed in next section in detail.

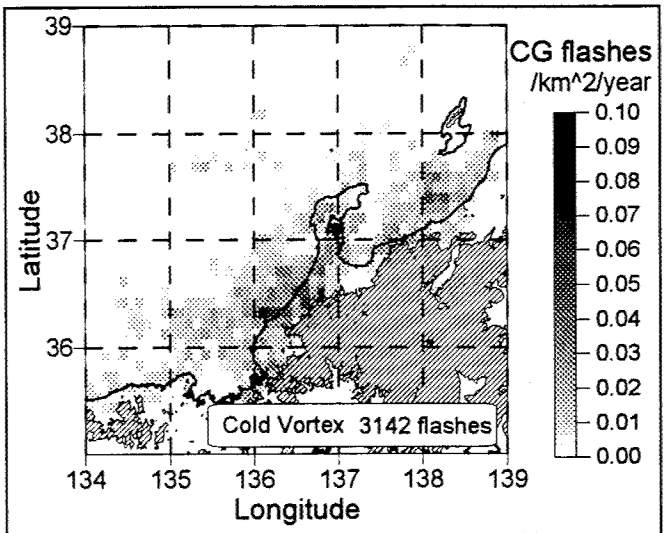


Figure 2. CG flash density during the cold vortex period detected by LLP system for 3 winter seasons. The elevation of the hatched area is over 500 m.

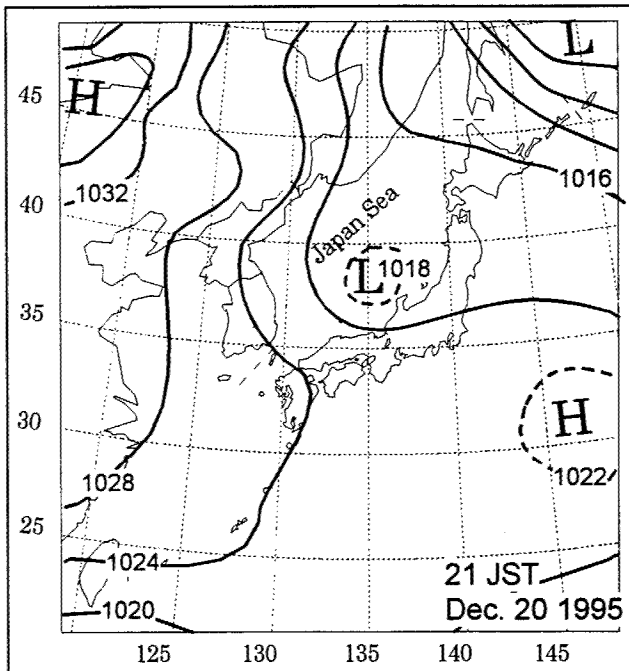


Figure 3 Synoptic weather chart at 21 JST on December 20, 1995

## DEVELOPMENT OF RADAR ECHO AND CHANGE OF ECHO VOLUME

During the cold vortex passage, thunderclouds develop rapidly near the coastline. Figure 4 shows the development process of radar echoes observed by C-band conventional radar at Komatsu. The cell groups A and B appeared about 40km northwest of Mikuni at 01:30 JST (Japan Standard Time ; UTC + 9hour). Another cell group C (weak) appeared at 01:41 JST. Group A developed with the generation of new echo cells on the southwest of the echo system, and Group B developed with the generation of new echo cells on northeast side. At 01:51, a band-shaped echo system formed with a length of about 80km, and the first CG flash occurred in cell groups A and B at this time. From 02:02 to 02:12 JST, Group B developed and caused many CG flashes. Subsequently, the cells of Group B dissipated after landing. However, there was no CG flash in Group A after 02:02 JST. At 02:23 JST, Group A developed near the

coastline and a first "Superbolt" occurred at 02:23:59 JST. This reason is discussed in the next section. Therefore, the first "Superbolt" occurred in the leading edge of the band-shaped echo (intensity below 20dBZ or no echo). After this time, Cell Group A moved over the stack, and second "Superbolt" occurred in the core of Cell Group A (intensity over 30dBZ) at 02:34:35 JST.

The electrical structure of winter thunderclouds in Hokuriku District, is regarded as having a tripole structure : a positive charge region consisting of ice crystal at the roughly -30℃ altitude, a negative one of graupel from the -10 to the -20℃ altitude and a pocket positive one of graupel at the over -10 ℃ altitude [*Takahashi*, 1984]. So we assumed that the positive region had an area radar echo intensity below 32 dBZ at the level with a temperature below -20℃, the negative region, one of over 32dBZ at the altitude between -10 to -20℃ and the pocket positive region, one of over 32dBZ at the altitude above -10℃. Figure 5 indicates calculations of the radar echo volume of each charge region in each group (A and B). In both groups A and B, first CG flashes occurred during the maximum of positive charge region. Although were no CG flashes in Group A for 30 minutes after, many CG flashes occurred in Group B. "Superbolts" occurred in Group A, when the pocket positive region increased. Group B contained region of much more high intensity. In addition, the volume of pocket positive was almost equal to negative region, and the lightning frequency was high compared to A.

Figure 6 shows the radar echo intensity and wind vector derived by the VVP (Volume Velocity Processing) method using the Doppler radar data. There was a convergence zone near the coastline at Mikuni (about 30km southwest of the radar), between the northwest monsoon wind and northeast wind. This convergence zone triggered the rapid development of Cell Group A near the coastline and the pocket positive charge region increased.

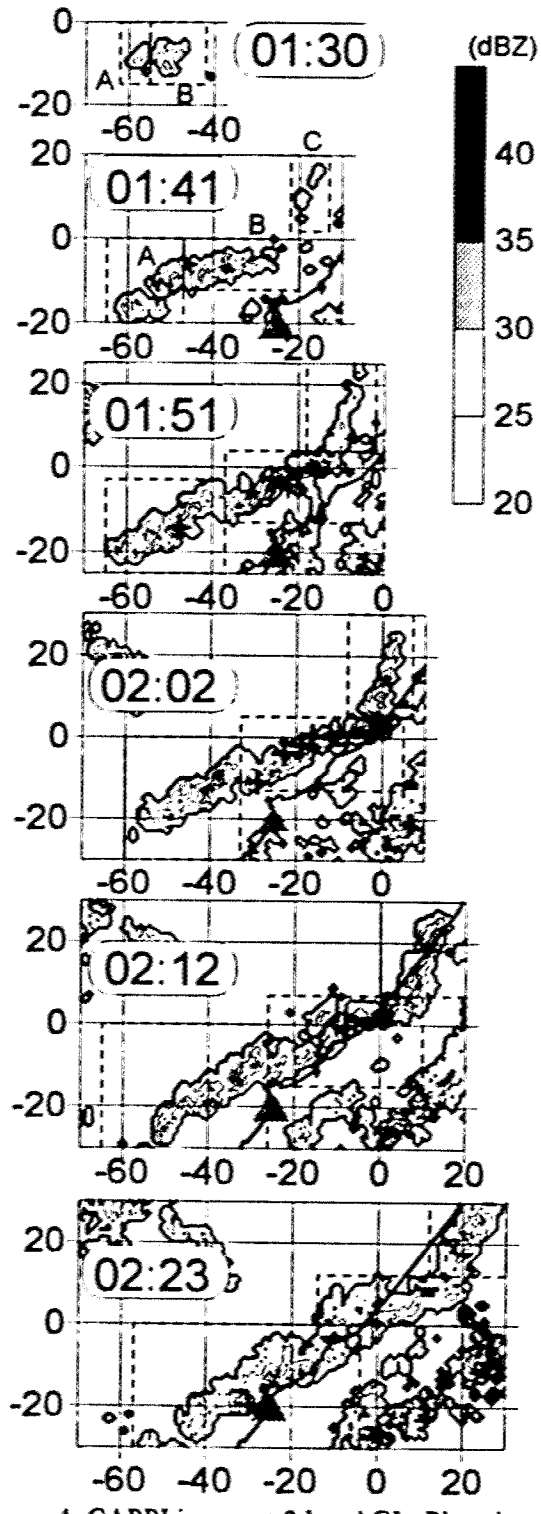


Figure 4. CAPPI image at 2 km AGL. Plus signs indicate positive CG flashes and minus signs, negative CG flashes. Broken line boxes show the boundary of each cell group. The triangle shows the location of Mikuni.

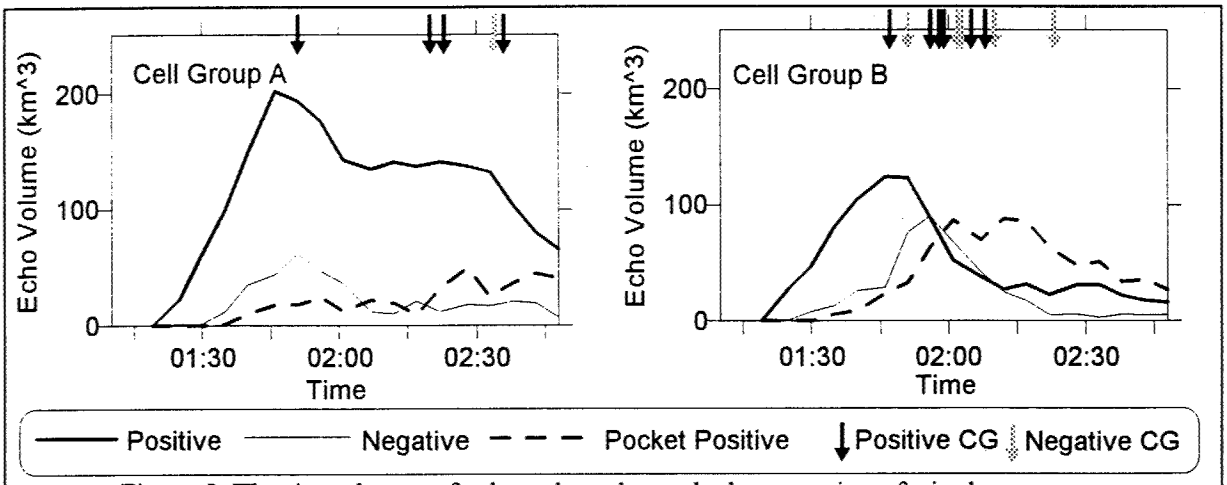


Figure 5. The time change of echo volume by each charge region of tripole structure.

## CONCLUSION

Two successive "Superbolts" were generated during the cold vortex thundercloud period. The lifecycle of the band-shaped echo was only about 1 hour near the coastline and CG flashes were concentrated at this area. Lightning frequency in the part of this echo system which generated "Superbolts" (Cell Group A), was low compared to the other part (Cell Group B). Cell Group B consisted of active echo cells which contained high intensity regions, and charges accumulated in the clouds were neutralized by active CG flashes. By contrast, Cell Group A had a relatively weak intensity and larger echo volume, especially in the upper part of the radar echo (positive charge region), compared to B, and no lightning was observed before landing. But convergence near the coastline triggered the rapid development of echo cells and a "Superbolt" occurred at the stack. Therefore, long term charge accumulation in Cell Group A may be regarded as the main cause of the "Superbolts".

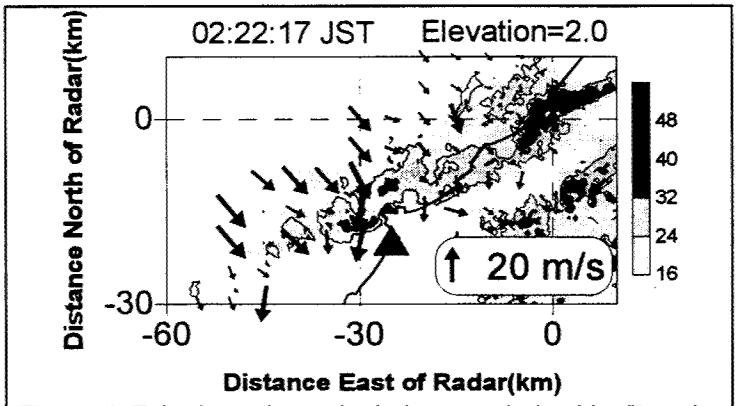


Figure 6. Echo intensity and wind vector derived by Doppler radar data. The triangle shows the location of Mikuni.

## REFERENCES


Brook M., M. Nakano, P. Krehbiel, and T. Takeuti, The electrical structure of Hokuriku winter thunderstorm, *J. Geophys. Res.*, **87**, 1202-1215, 1982

Kobayashi, F., G. Naito, T. Wakai and T. Shindo, The role of the lower atmospheric condition to development of winter thunderclouds in the Japan Sea coast, *J. Atmos. Electr.*, **14**, 31-40, 1994

Kobayashi, F., T. Shimura, A. Wada and T. Sakai, Lightning activities of winter thundercloud systems around the Hokuriku coast of Japan, *Proc. 10th ICAE*, 560-563, 1996

Ninomiya, K., K. Hoshino, and K. Kurihara, Evolution process and multi-scale structure of a polar low developed over the Japan sea on 11-12 December 1985. Part I : Evolution process and Meso-$\alpha$-scale structure, *J. Meteor. Soc. Japan*, **68**, 293-306, 1990

Takahashi, T., Thunderstorm electrification - a numerical study, *J. Atmos. Sci.*, **41**, 2541-2558, 1984

Turman, B.N., Detection of lightning superbolts, *J. Geophys. Res.*, **82**, 2566-2568, 1977

# SOME ASPECTS OF CORRELATION BETWEEN LIGHTNING ACTIVITY AND RAINFALL IN THUNDERSTORMS

S. Soula, G. Molinié, S. Defoy, S. Chauzy, and N. Simond

Laboratoire d'Aérologie, UMR 5560, CNRS Université Paul Sabatier, OMP, Toulouse, France

ABSTRACT: The correlations between cloud-to-ground (CG) lightning flash and rain activities have been widely studied during the past ten years. They are usually estimated in terms of location, of rates evolution and of water volume per flash. This work presents some results obtained from this kind of study with data issued from French networks. The CG lightning flash activity is detected by the Météorage network and the rain is estimated from the radar observations. We studied 21 thundercells or systems from 4 days most of them occurring over the French territory. The water volume per flash ranges from $6.2 \times 10^3$ to $75 \times 10^3$ $m^3$ with an average value of $26 \times 10^3$ $m^3$. The time lag between the peaks of both activities depends on the detection height of the rain by the radar and the flash maximum preceds by a few minutes the rain detection at low altitude. The flash density maximum is tightly related to the location of the heavy rainfall, specially in the case of a flash flood caused by a thunderstorm in Northern Spain.

## INTRODUCTION

The first value of the water volume per flash was proposed by *Battan* [1965], who found, with little sophisticated observation means, $30 \times 10^3$ $m^3$ per CG lightning flash. Then, with the development of the lightning flash location technology, several works have been performed and the values for this volume were close to the first estimation [*Kinzer*, 1974 ; *Piepgrass et al.*, 1982 ; *Sheridan et al.*, 1997 ; *Tapia et al.*, 1998]. Another important observation has been made by *Piepgrass et al.* [1982] when they noted an advance of a few minutes of the lightning peak rate as compared to that of the rain peak at the ground. So, the CG flash activity can precede the arrival of the heavy rain at the ground [*Williams et al.*, 1989]. The location of both activities is also a discussed question. The CG lightning location usually corresponds to the strong radar reflectivities and therefore to the high rain rates [*Kuettner*, 1950 ; *Tapia et al.*, 1998]. Some authors observe that lightning tends to avoid the region of highest reflectivities to occur just outside of it [*Dye et al.*, 1986]. So, the lightning flash activity of a thunderstorm could be used in local short term forecasting of strong rain or in rain estimation for areas uncovered by radar detection. We have investigated this topic with data from the French networks of meteorological radars (Météo-France) and of lightning flash location provided by the Météorage network.

## DATA DESCRIPTION

We have used data from the Météorage LLP network which detects the spatial and temporal location of the positive and negative CG flashes. This network is composed of 16 magnetic direction-finders [*Tourte et al.*, 1988]. The detection efficiency is better than 90 % over the whole French territory and the localization accuracy is better than 4 km for 50 % of all flashes. We consider in this study the flash density and the flash rate according to the parameter of rain to be compared with.

The rain estimations are issued from the meteorological radars of the French network of Météo-France. The cm-radars automatically scan at low elevation angle, typically 0.6°, and directly provide the dBZ reflectivity. The rain rate is usually estimated by using the standard Z-R laws, especially that for convective rainfalls proposed by *Austin* [1987] viz. $Z = 400\ R^{1.3}$, where Z is the reflectivity in $mm^6\ m^{-3}$ and R the rain rate in $mm\ h^{-1}$.

## RESULTS

The results presented in this study concern 21 different cells or systems, according to the ability of separating the activity zones. Thus, the individual cells are not always separated and we call a system when several cells are gathered together. Table 1 shows the synthesis of the calculated parameters for each one of these cases. Four days of activity are considered, two in Southwestern France on August 20 and 30, 1994, with 16 cells, one in Northern Spain on August 7, 1996 with only one cell, and one in Paris area on July 11, 1997 with 4 systems. It namely indicates the CG flash number with the number of positive ones. The maximum CG flash number is 1534 for the cell which occurred in Biescas causing a flash flood in a camp-ground, causing severe casualities. This case studied by *Soula et al.* [1998] presented exceptional duration and stationarity. The number of positive flash is low in each case since its maximum proportion is 7 %. First, the water volume per CG flash has been calculated for each case. It ranges from 6,200 to 75,000 $m^3$ and the average value is 26,000 $m^3$. These values are rather common as compared with other results and the variation does not seem to be due to the daily conditions since it appears also

within the same day. No correlation appear between this volume and the activity intensity on one hand, and the positive flash proportion on the other hand.

In order to compare the evolution of both activities, we calculated the flash rate and the rain rate and we display them in a same graph as it is shown in figure 1. This case of figure 1 corresponds to a cell very close to the radar and therefore, the rain is detected very low, close to 1,000 m. The lightning maximum preceds by 25 minutes in this case. We have considered this time lag between both maxima for each one of the 21 cases and we plot it versus the detection height by the radar beam in figure 2. The time lag is positive if the flash maximum comes first. The time lag clearly tends to decrease when the detection altitude increases. When this altitude is low, the time lag is generally positive which indicates that the flash maximum precedes the arrival of the heaviest rain. Sometimes it can precede by several tens of minutes. The plots do not tightly undergo a mathematic law and therefore display a substantial dispersion. It is important to note that the time lag is calculated between maxima and it can be partly the result of different shapes for both evolutions. Furthermore, in some cases, the global activity is not due to a single cell but to a small system and both maxima can be the results of various cells.

From the evolution of both rates for each case, we make a quantitative correlation study by curve fitting from the distribution of values pairs of rain and flash rates. In order to take into account the different heights of rain detection, we apply the time lag discussed before to associate both rates. We try to find a linear relationship between rain rate and flash rate. In Table 1, the results of this fitting are summarized for each case according the following law : $V = a L + b$, where V and L are respectively the rain volume and the flash rate over 5 minute periods. The values of the constants a and b are indicated in the table as well as the determination coefficient r of the curve fitting. The coefficient r is most of the time clearly larger than 0.5 which indicates a good correlation between both evolutions. The parameter a ranges from $2.34 \times 10^3$ to $31.3 \times 10^3$ $m^3$ $flash^{-1}$ and it is close to the water volume per flash when r is high. The parameter a is lower compared to the water volume per flash because the curve fitting do not consider the period with rain and without lightning flash, specially at the end of the thunderstorm lifetime.

The location of the CG flashes is also compared to the rain location. The strong activities of both types generally correspond. The case presented here is that of the cell over Biescas in Northern Spain on August 7, 1996. Figure 3 displays the distributions of the rain height (a) and of the flash density (b) in a zone of 60 x 60 $km^2$ around Biescas as the iso-density surfaces with a resolution of 2 x 2 $km^2$. The white corresponds to the lowest iso-density values between 0 and 0.5 $km^{-2}$ for the flash density and between 0 and 25 mm for the rain. The black corresponds to the largest ones between 3 and 3.5 $km^{-2}$ for the flash density and between 200 and 225 mm for the rain. Two cores appear within the cell in each graph. Their locations correspond very well. The rain appears more concentrated, the horizontal gradient of its height being larger. It signifies that part of the flashes strikes out of the strong rain area. The highest rain values larger than 200 mm are very comparable to that indicated by *Sénési et al.* [1996] for a flash flood in Vaison-La-Romaine (France), i.e. 220 mm for a similar period of 3 hours. The total water volume estimated is $47 \times 10^6$ $m^3$ over the surface of about 3600 $km^2$. The total flash number for the same area is 1534, including 40 positive ; the proportion of positive flashes is therefore weak. Thus, the average water volume per CG flash is $30.6 \times 10^3$ $m^3$. The flash density from this graph reaches 3 $km^{-2}$, with the 2 x 2 $km^2$ resolution, which is a very large value as compared, for example, to the yearly maxima over the US territory roughly estimated at 12 $km^{-2}$ [*Orville and Silver,* 1997]. This thunderstorm was exceptional for its duration and its stationary characteristics, which leads to very large densities of CG lightning flash. It shows a good correlation between the rain and the CG lightning activity locations.

## CONCLUSION

The aspects of rain and lightning activities approached in this study show several correlations. For the water volume per flash, our values agree well with previous results. We observe an advance for the CG flash maximum as compared to the heaviest rain at the ground. Both rates of activity seem to be tightly proportional for most of the cases. In the case of storm causing a flash flood, large values of the CG flash rate are detected before large radar reflectivities appear close to the ground. Therefore the CG flashes could be a good indicator of the rainfall. Furthermore the location of both intense activities correpond very well.

ACKNOWLEDGEMENTS: The authors thank the Météorage Company for the lightning data and the French meteorological institution Météo-France for the radar data.

## REFERENCES

Austin, P. M., Relation between measured radar reflectivity and surface rainfall, Mon. *Weather Rev.*, 115, 1053-1070, 1987.

Battan, L. J., Some factors governing precipitation and lightning from convective clouds, *J. Atmos. Sci.*, 22, 79-84, 1965.

Dye, J. E., Early electrification and precipitation development in a small, isolated Montana cumulonimbus. J. Geophys. Res., 91, 1231-1247, 1986.

Kinzer, G., D., Cloud-to-ground lightning versus radar reflectivity in Oklahoma thunderstorms. J. Atmos. Sci., 31, 787-799, 1974.

Orville, R. E. and A. C. Silver, Lightning ground flash density in the contiguous United States: 1992-1995, *Mon. Weather Rev.*, 125, 631-638, 1997.

Piepgrass, M. V., E. P. Krider, and C. B. Moore, Lightning and surface rainfall during Florida thunderstorms, *J. Geophys. Res.*, 87, C13, 11193-11201, 1982.

Sénési, S., P. Bougeault, J.L. Chèze, P. Cosentino, and R. M. Thepenier, The Vaison-La-Romaine flash flood, mesoscale analysis and predictability issues, *Weather Forecasting*, 11, 417-442, 1996.

Sheridan S. C., J. H. Griffits and R. E. Orville, Warm season cloud-to-ground lightning-precipitation relationships in the South-Central united States, *Weather Forecasting*, 12, 449-458, 1997.

Soula S., H. Sauvageot, G. Molinié, F.. Mesnard, and S. Chauzy, The CG lightning activity of a storm causing a flash-flood, *Geophys. Res. Lett.*, 25(8), 1181-1184, 1998.

Tapia, A., J. A. Smith, and M. Dixon, Estimation of convective rainfall from lightning observations, J. Appl. Meteorol., 37, 1497-1509, 1998.

Tourte, J.L., F. Helloco, M. Le Boulch, and J. Hamelin, First results obtained with the Météorage thunderstorm monitoring system, in *Proceedings of the 8th Conference on Atmospheric Electricity*, pp 697-702, Institute of High Voltage Research, Uppsala, 1988.

Williams, E.R., M. E. Weber, R. E. Orville, The relationship between lightning type and convective state of thunderclouds. *J. Geophys. Res.*, 94, 13,213-13,220, 1989.

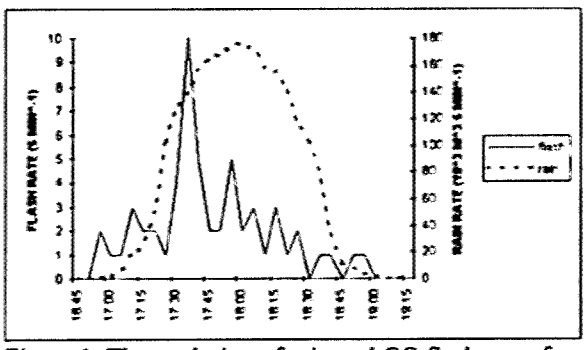

Figure 1. The evolution of rain and CG flash rates for one cell of August 30th, 1994.

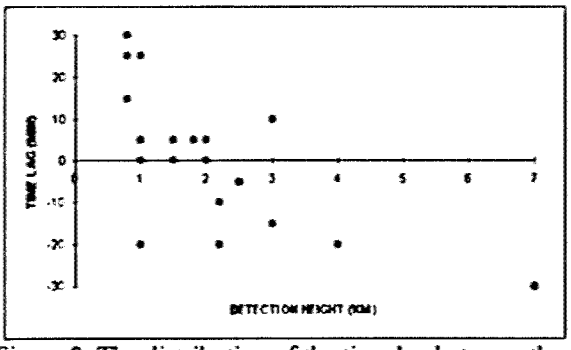

Figure 2. The distribution of the time lag between the maxima of rain and CG flash rates versus detection height of the rain

Table 1. Caracteristics for 21 cases studied

| Date and location | a $10^3$ $m^3$ $flash^{-1}$ | b $10^3$ $m^3$ | r | vol / flash $10^3$ $m^3$ | flash total - positive |
|---|---|---|---|---|---|
| | 9.65 | 28.17 | 0.86 | 16.75 | 102 - 4 |
| Southwestern | 6.35 | 18.67 | 0.92 | 8.8 | 235 - 0 |
| France | 5.47 | 45.03 | 0.63 | 20.6 | 76 - 0 |
| August | 8.41 | 32.24 | 0.74 | 11.26 | 588 - 7 |
| 20th, 1994 | 13.05 | 30.98 | 0.93 | 18.26 | 224 - 2 |
| | 2.34 | 14.21 | 0.65 | 6.2 | 39 - 0 |
| | 22.60 | 55.08 | 0.79 | 26.94 | 407 - 20 |
| | 9.91 | 83.94 | 0.66 | 21.49 | 175 - 6 |
| | 6.14 | 62.27 | 0.79 | 11.20 | 263 - 0 |
| Southwestern | 5.08 | 26.94 | 0.80 | 7.21 | 388 - 0 |
| France | 4.37 | 15.27 | 0.73 | 7.64 | 71 - 0 |
| August | 2.52 | 20.16 | 0.51 | 7.86 | 65 - 4 |
| 30th, 1994 | 10.48 | 41 | 0.75 | 16.57 | 155 - 11 |
| | 7.44 | 118.67 | 0.5 | 40.75 | 57 - 0 |
| | 6.95 | 29 | 0.68 | 16 | 74 - 1 |
| | 4.34 | 37.46 | 0.79 | 8.35 | 198 - 4 |
| Biescas | 16 | 41.8 | 0.57 | 30 | 1534 - 40 |
| Paris area | 13.45 | 194 | 0.44 | 75 | 99 - 2 |
| July, 11th | 17 | 141 | 0.75 | 36 | 241 - 2 |
| 1997 | 31.28 | 118.26 | 0.85 | 41 | 561 - 7 |
| | 10 | 208 | 0.69 | 29 | 335 - 4 |

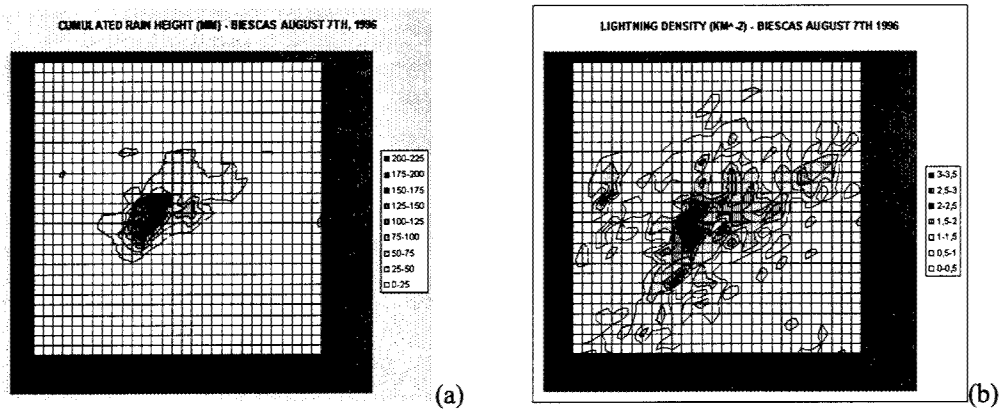


Figure 3. Distribution of the rain height (a) and of the CG flash density (b) for the case of Biescas, on August 7th, in Northern Spain.

# An Investigation of the Horizontal Extent of Charge Regions in One Thunderstorm

T. C. Marshall[1], M. Stolzenburg[1], D. L. Bartels[2], and W. D. Rust[3]

[1] Department of Physics and Astronomy, University of Mississippi, University
[2] NOAA/ERL/National Severe Storms Laboratory, Boulder, CO
[3] NOAA/ERL/National Severe Storms Laboratory, Norman, OK

## Introduction

On June 10, 1998, we flew two balloons, each carrying an electric field meter and a radiosonde, into a small thunderstorm in central Oklahoma. The balloons were launched about six minutes apart from the same location (near Tupelo, OK) as the storm passed overhead; both were launched ahead of the main convective precipitation region of the storm. In this presentation we compare electric fields and lightning field changes observed with the two balloons to get an idea of the horizontal extent of the main charge structure and of the localization of charge affected by the lightning flashes.

## Data and Discussion

Figure 1 shows the electric field data as a function of time from both balloons. The first sounding, Tupelo1, was launched at 0528:44 UT, and the electric field data ended abruptly below cloud top at 0611:13 UT. The second sounding, Tupelo2, was launched at 0534:52 UT and exited through cloud top at about 0610 UT. The thermodynamic data and ascent rate curves for each balloon are also included Figure 1. Ten lightning-related field changes (*a* - *k*) are indicated in the electric field sounding in which each field change is most evident.

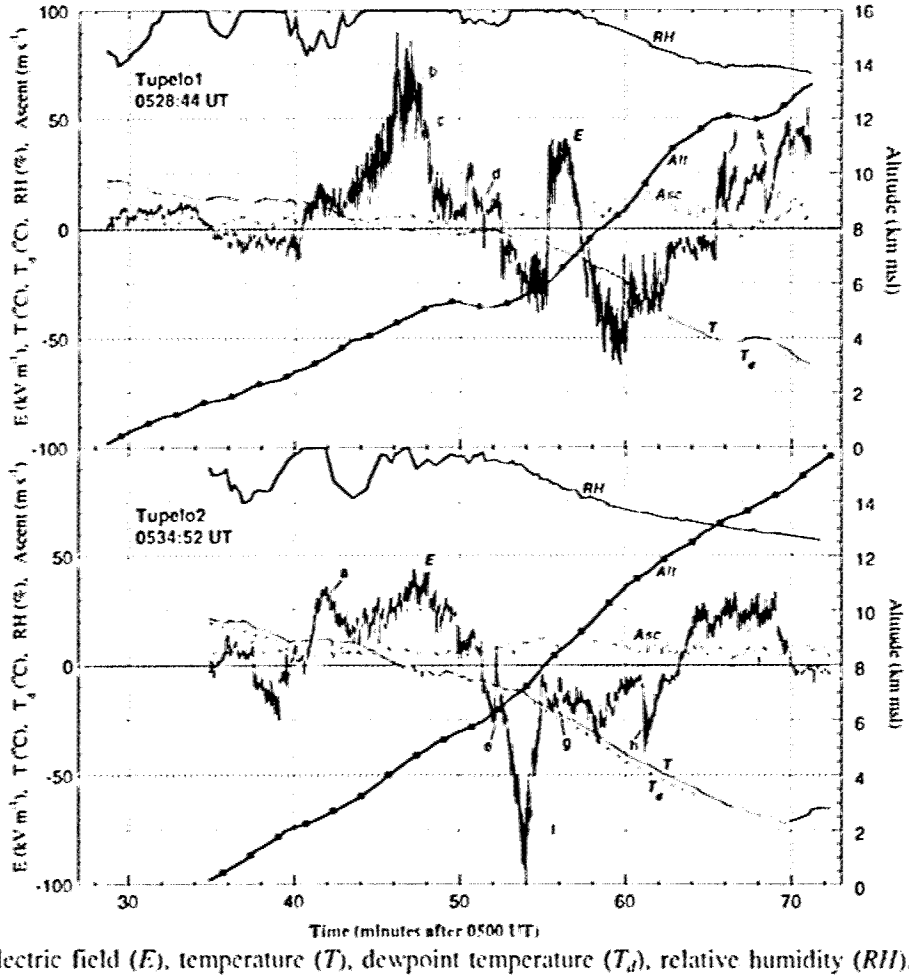


**Figure 1.** Electric field (*E*), temperature (*T*), dewpoint temperature ($T_d$), relative humidity (*RH*), balloon ascent rate (*Asc*) and altitude (*Alt*, along right axes) all as functions of time for two balloon soundings from June 10, 1998.

Figure 2 shows the locations, both absolute and relative to one another, of the two balloons. In the upper panel of Figure 2 the horizontal tracks of the balloons are seen to be quite similar: both were in westerly flow from just above the surface to cloud base (1.8 km), then they were in south-southwesterly flow through the cloud. Several times are marked along both balloon tracks, including those times when the balloons were closest in horizontal location and in altitude. At 0548:38 UT the Tupelo2 balloon passed through the altitude of the Tupelo1 balloon, which had a slower ascent rate up to 6 km than the second balloon. Figure 2 also shows the vertical and horizontal separation of the two balloons as a function of time, along with the altitudes of the balloons. The most important information in Figure 2 for this paper is that the balloons were separated horizontally by 3-8 km and separated vertically by 0-2 km. The vertical proximity of the balloons allows us to use lightning-related field changes in the electric field data from the two balloons to look for the horizontal extent of the in-cloud effects of lightning.

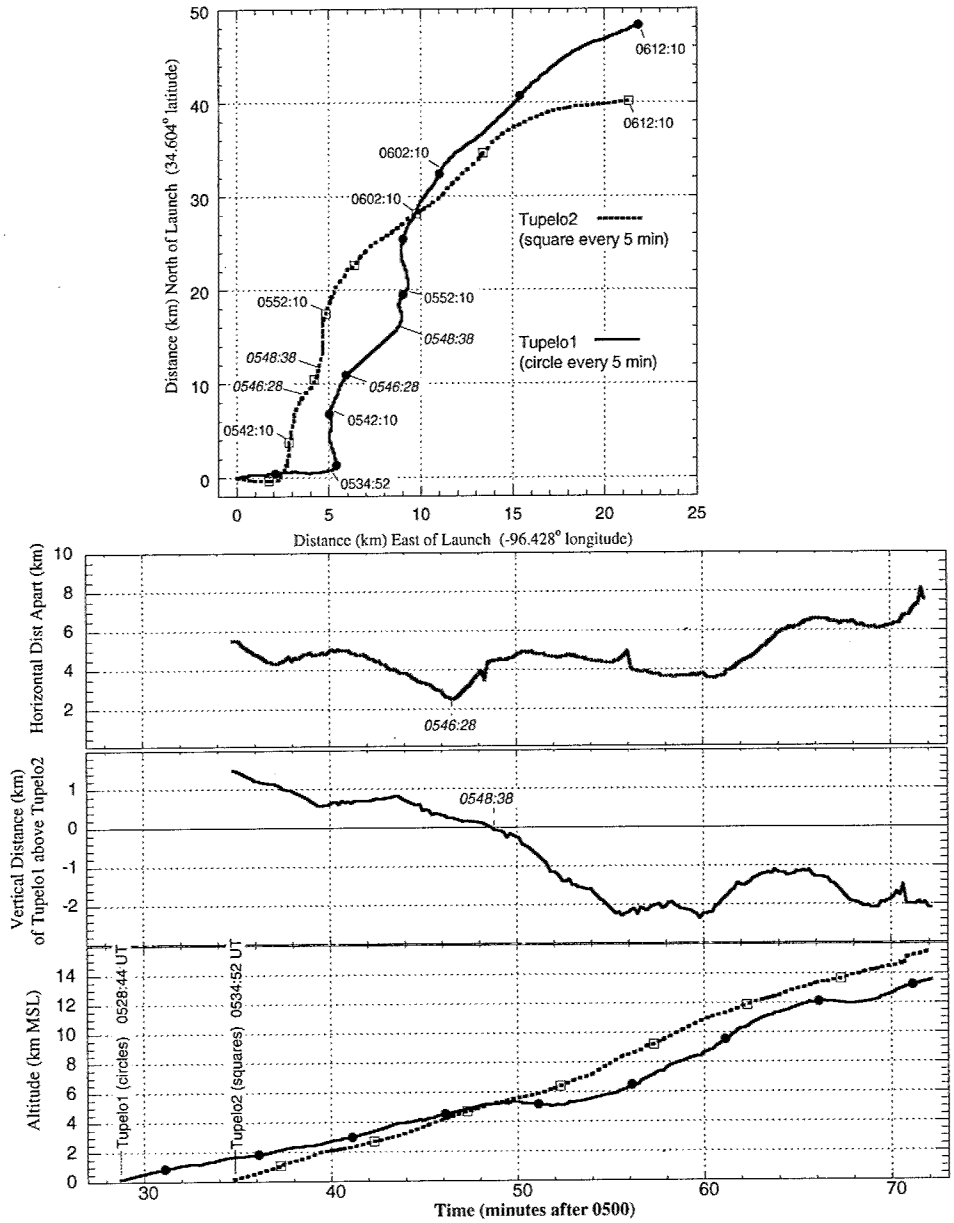


**Figure 2. Top panel** shows ground-relative balloon tracks for the two balloons on June 10, 1998. Several times are marked along both tracks, including the times when the balloons were closest together in the horizontal or vertical (altitude) direction. Note that the north-south distance scale is half that of the west-east scale in this plot. **Middle panels** are the horizontal and vertical displacement between the two balloons as a function of time. The curves start at the launch time of the second balloon. **Bottom panel** shows altitude vs. time for the two balloons.

Corresponding lightning-related field changes in the two balloon soundings are indicated by the vertical dashed lines in Figure 3, which shows three ten-minute periods of the electric field data from Figure 1 with expanded time axes. (We have not marked all of the lightning-related field changes in Figure 3 or in Figure 1.) Note that our balloon-borne electric field data are at roughly 1 Hz rate, so we can only see the quasi-static (or slow) electric field change due to lightning. That is, only the "steady" electric field before and after the flash are time resolved; the fast field changes during the flash are not.

Some of the field changes in Figure 3 are similar in both soundings, while others are very different. The lightning field change labeled *a* is similar in both soundings; the field is reduced in magnitude by about 10 kV $m^{-1}$ in both records. At the time of *a* (0542:15 UT) the balloons are about 5.0 km apart horizontally and separated by about 0.7 km vertically. The field change marked *d* reverses the electric field polarity in both records, with field changes of similar magnitudes. In contrast, field change *b* has a magnitude of about 17 kV $m^{-1}$ in Tupelo1 and less than 5 kV $m^{-1}$ in Tupelo2. The field change marked *c* is visible in both soundings, with magnitude of 25 kV $m^{-1}$ in Tupelo1 and 17 kV $m^{-1}$ in Tupelo2. In spite of their different appearance in the two soundings, field changes *b* and *c* both occurred when the balloons were at nearly the same altitude. One simple explanation for the difference seen in *b* between the two soundings is that the lightning flash effectively removed charge that was nearer the Tupelo1 balloon. Field changes *e*, *h*, *j*, and *k* are further examples of pairs of field changes with very dissimilar magnitudes between one sounding and the other. This discrepancy is especially noticeable in field change *e*, which has a magnitude of about 33 kV $m^{-1}$ in Tupelo2 but less than 5 kV $m^{-1}$ in Tupelo1, while the horizontal distance between the two balloons was only about 5 km. Assuming point-charge geometry for the discharge, the difference between field change magnitudes for *e* suggests the charge transferred by this flash was between 6 and 26 C.

We can also get an indication of where the lightning-effected charge was relative to the two balloons from the horizontal component of the electric field. Between 0544 and 0547:40 UT (the time of flash *b*) the Tupelo1 electric field data show a much larger horizontal component than the Tupelo2 electric field data. (The magnitude of the horizontal component of the electric field is directly related to the amplitude of the higher frequency oscillations in the electric field curve.) This horizontal component is substantially reduced after flash *b*. The data indicate that the charge affected in this flash was relatively near to but horizontally displaced from the Tupelo1 balloon—"near to" because the field change is large here but not at the other balloon; "horizontally displaced from" because both the horizontal field and the vertical field are reduced by the flash. Two additional examples of abruptly changing magnitude of horizontal field can be seen in Tupelo1 at flashes *f* and *g*. The horizontal component of the electric field increases after flash *f* and is substantially reduced at the time of flash *g*. For both these flashes, the field change at the Tupelo2 balloon is primarily a reduced vertical electric field, while the field change at the Tupelo1 balloon is primarily a change in horizontal field. During this time period, the Tupelo1 balloon is about 2 km below and about 4 km northeast of the Tupelo2 balloon.

Another aspect of the expanded electric field records (Figure 3) is the general similarity between the measurements made at the two balloons in spite of their relative horizontal displacement ranging from 3 to 8 km. In particular, during the 0540-0550 UT period the Tupelo1 balloon is within 0.8 km of the altitude of the Tupelo2 balloon (which passes it in this period). The similarities in electric field at the two balloons are maintained even though there are numerous lightning field changes in both soundings and suggest that the gross charge structure is similar over horizontal scales of 3-8 km or more.

## Conclusions

In summary, the electric field and field change data from two horizontally and vertically displaced balloons provide a new way of looking at the relationship between lightning and the overall storm charge structure. Some flashes affect the electric field at one balloon location much more than at the other, suggesting that areal extent of the charge associated with these field changes is relatively small in extent. Also, it is apparent from these measurements that the effect of lightning on the overall charge structure is small in magnitude and area and lasts for only a short time. Comparison of the two electric field soundings as functions of height and examination of the available radar data from this small thunderstorm should yield additional insight for this study.

***Acknowledgments:*** These data were collected during the MCS Electrification and Polarimetric Radar Studies hosted by NSSL; we greatly appreciate the help of the many people involved in planning, preparing equipment, collecting radar, aircraft, and balloon data, and guiding our storm intercepts during this program. We especially thank Dave Jorgensen for his multifarious efforts. This work was funded in part by NSF Grant ATM-9626542.

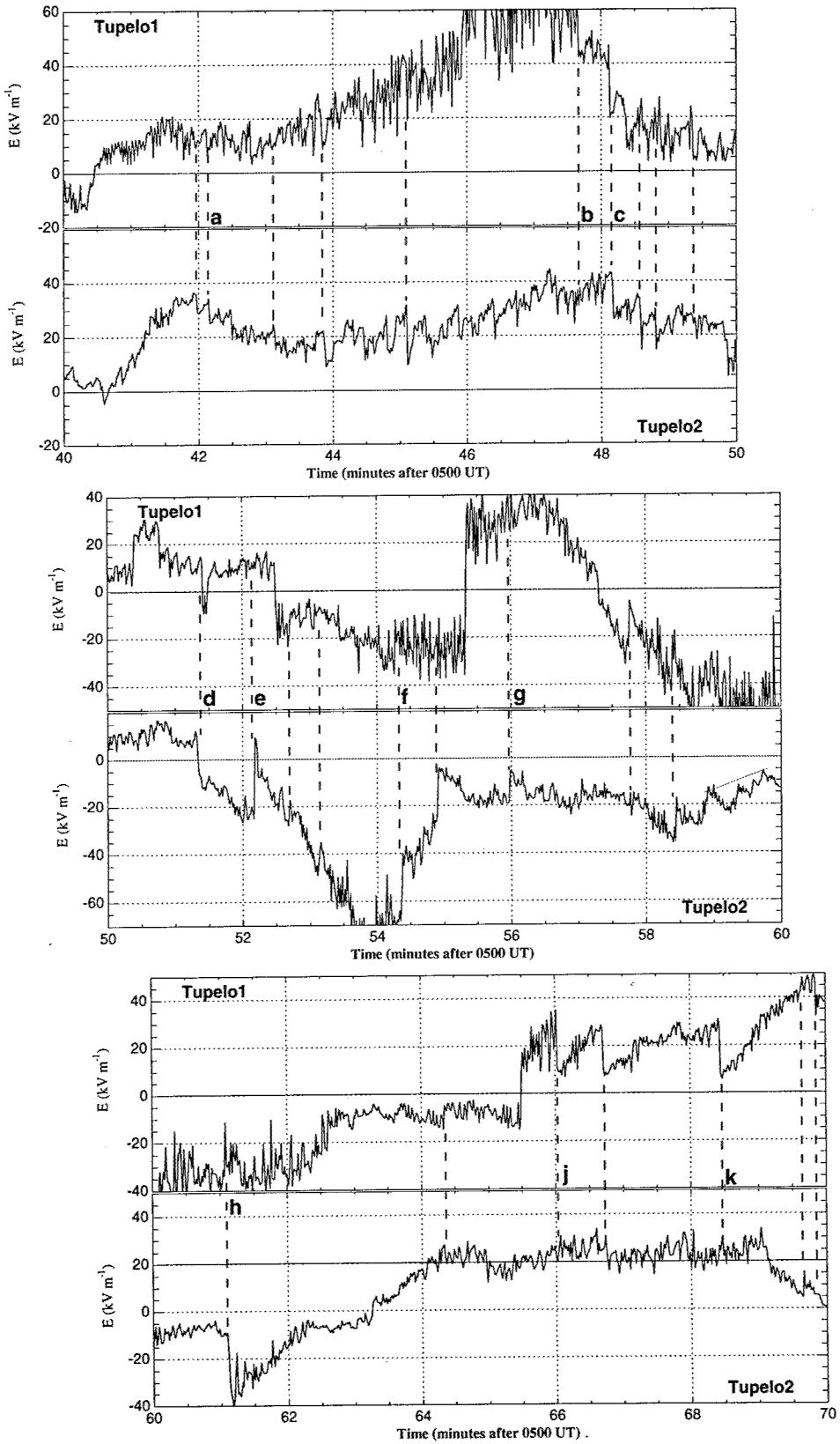


**Figure 3.** Expanded plots of electric field vs. time from two balloons for three ten-minute time periods. Pairs of lightning-related field changes are marked with vertical dashed lines, marked *a* through *k* for reference.

# LIGHTNING CHARACTERISTICS IN THE 1992-1996 PERIOD IN THE BASQUE COUNTRY AREA: LIGHTNING-PRECIPITATION RELATIONSHIPS.

J. Areitio, I. Herrero, A.Ezcurra
Dpto. Fisica Aplicada I. EUITI e ITT. Unv. Pais Vasco
C/Nieves Cano 12, 01006 Vitoria. Spain

## ABSTRACT

This study is focused in the Spanish Basque Country in the north of the Iberian Peninsula. Lightning data bases has been provided by the INM (Instituto Nacional de Meteorologia) direction finder network (DF) and the Time of Arrival (TOA) network of the Iberdrola power supply company. The number of lightning flashes recorded in the 1992 –1996 period was 92212. Positive lightning fraction ranges between 4% in July and 39% in January. Mean intensity for negative and positive lightning is 27 kA and 55KA respectively. Negative lightning single strokes vary between 80% in winter and 40% in summer while positive lightning single strokes are approximately the 90% throughout the year. The annual flash density maximum (3 lightning / km$^2$) was observed over Bilbao, the greatest city of the area. Relationships between lightning density and precipitation are unclear. Three storm events present different correlation coefficients between lightning density and several precipitation parameters. In this way two flash floods with few lightning were observed.

## INTRODUCTION

Spanish Basque Country is located in South-western Europe, conforming the south-eastern corner of the Biscay Gulf, in the Iberian Peninsula. The orografy is characterised by a very complex terrain that presents a mean height of 1000m. The Basque Mountains, close to the Cantabric Sea, separate two climatic areas. Oceanic at north and Mediterranean, at south of them. Storm annual mean number is between 20 and 30, mostly in Summer, later Spring or early Autumn in both climatic areas. This climatical and geographical factors implies that flash floods are no rares in this area. This paper is divided in two sections: The first is a study of lightning phenomenology in the Basque Country and the second is a preliminary study about the lightning–rainfall relationships in the same area.

## DATA

Lightning database have been provided by the Spanish National Meteorological Institute (INM) direction finder (DF) network and by the Iberdrola power supply company, Time of Arrival (TOA) system network. Precipitation data have been provided by the Basque Service of Meteorology (SVM).The principles and characteristics of DF and TOA systems are described by several authors (Krider *et al.* 1976; Orville *et al.* 1987; Hojo *et al.* 1989; Jansen 1989). The detection efficiency of the INM DF network system in the Basque Country, has been estimates approximately in a 55% and the accuracy between 2 km and 4 km ( Pérez F. 1997).

## LIGHTNING FENOMENOLOGY

### Results

#### a. Ground flash counts.

The INM lightning location network recorded a total number of 92212 ground flashes in the 1992- 1996 period, over an area of 20800 km$^2$ centered over the Basque country and located between the coordenates 42° 24'N – 43° 36'N and 3° 36'W – 1° 24'W. Table 1 presents the monthly ground flash counts and the percentage of positive flashes for the years analysed. The 77% of total flashes were recorded in June, July and August. Positive lightning were the 7% of total lightning, but in 1993 a 11% was observed. The annual flash number vary from 14001 in 1995 to 28026 in 1993 and for a certain month the lightning number and positive percentage also varies, specially in Winter, Spring and Autumn. Such variations in the flash number and percentage of positive flashes has been also observed by Orville (1997) in the United States. The percentage of total positive lightning is highest in Winter and varies from 39% in January to 5% in July, this fact is commonly observed by several authors as Orville *et al.* (1997) and Hojo *et al.* (1989).

Table1 Monthly ground flash counts and the percentage of positive lightning in brackets

| | 1992 | | 1993 | | 1994 | | 1995 | | 1996 | | Total | |
|---|---|---|---|---|---|---|---|---|---|---|---|---|
| **January** | | | | | 194 | (39) | 123 | (44) | 35 | (26) | 352 | (39) |
| **February** | 66 | (58) | 300 | (28) | 58 | (22) | 134 | (10) | 131 | (53) | 689 | (31) |
| **March** | 1383 | (21) | 74 | (57) | 17 | (59) | 59 | (68) | 60 | (13) | 1593 | (24) |
| **April** | 83 | (24) | 1681 | (16) | 192 | (49) | 51 | (47) | 371 | (17) | 2378 | (19) |
| **May** | 3445 | (12) | 3016 | (5) | 648 | (11) | 1040 | (8) | 654 | (11) | 8803 | (9) |
| **June** | 3376 | (9) | 10398 | (6) | 1183 | (3) | 1190 | (7) | 4351 | (5) | 20498 | (6) |
| **July** | 5175 | (7) | 6463 | (2) | 11429 | (4) | 6337 | (6) | No data | | 29404 | (5) |
| **August** | 3086 | (11) | 4137 | (9) | 7551 | (4) | 3078 | (2) | 3369 | (3) | 21221 | (6) |
| **September** | 1202 | (5) | 1415 | (12) | 423 | (11) | 415 | (9) | 630 | (10) | 4085 | (9) |
| **October** | 208 | (30) | 532 | (15) | 291 | (22) | 964 | (4) | 125 | (43) | 2120 | (14) |
| **November** | 4 | (100) | 1 | (100) | 67 | (60) | 511 | (6) | 189 | (32) | 772 | (18) |
| **December** | 145 | (37) | 9 | ( 89) | 19 | (84) | 99 | (1) | 25 | (8) | 297 | (27) |
| **Total** | 18173 | (11) | 28026 | (7) | 22072 | (6) | 14001 | (6) | 9940 | (7) | 92212 | (7) |

**b. Lightning intensity.**

The mean intensity of negative lightning is 26kA and the median is 22kA while positive lightning mean intensity is 55kA and the median 42kA. Fig1 shows that most intense negative lightning are in winter (79kA) and positive in autumn (100kA).

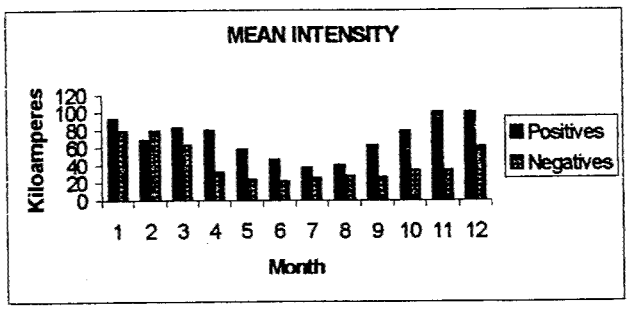


Fig.1 Monthly distribution of mean flash intensity

Fig.2 shows the negative and positive lightning intensity distribution for the Oceanic and Mediterranean areas. The histogram of negative lightning is similar in form in both areas, but tilted towards the highest intensities in the oceanic area. However the positive lightning histogram is different for the two areas, in this way the histogram of Mediterranean area presents a bimodal form with a large peak in the 5kA-10kA interval and a secondary peak in 45kA – 50KA while the oceanic histogram only presents a broad peak in the 30 kA –55kA interval.

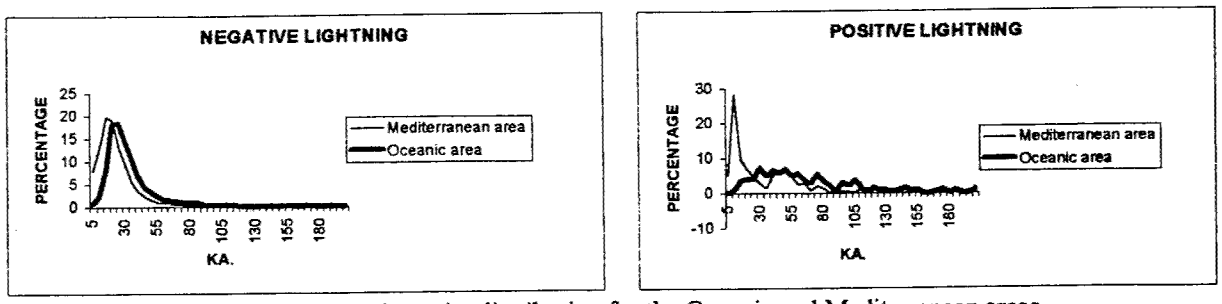


Fig 2. Lightning intensity distribution for the Oceanic and Mediterranean areas

**c. Multiplicity.**
Positive single stroke flashes are approximately the 90% throughout the year while negative single strokes are the 80% in Winter and 45% in Summer, similarly to the data reported by Orville (1987) in EEUU. The maximum multiplicity value observed was 15 for negative lightning and 5 for positive lightning.

**d. Flash density.**
Figure 3 shows the flash density for the 1992 - 1996 period, computed for a pixel of 5km x 5km. The flash density values must be multiplied by a 1.8 factor if the detection efficiency is considered. The maximum annual lightning density (3 lightning / $km^2$) is observed over Bilbao city. The increase of lightning activity over urban areas has been also reported by Westcot (1993, 1995).

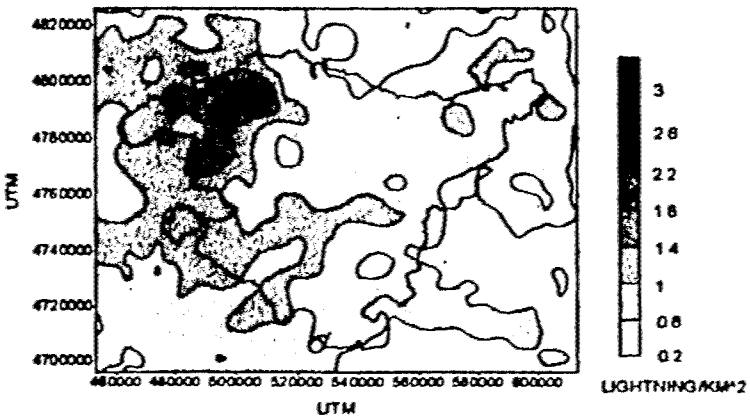


Fig 3. Annual flash density

## LIGHTNING PRECIPITATION RELATIONSHIPS

**a. Relation between rainfall and lightning.**
In order to study possible relation between lightning density and precipitation, a preliminary study over three storms events has be carried out
a) 7/8/92 event: Low or not precipitation was register in the stroke areas (dry storm) and 280 flashes were recorded.
b) 8/9/92 event: Total Precipitation registered in two hours were 10mm-20mm and 190 flashes were recorded
c) 4/10/92 event: Precipitation total amounts registered in 24 hours range from 40mm to 100mm and only 43 flashes were recorded over the region in the same period.
Three correlation coefficients $R_1$, $R_2$, $R_3$, has been computed: $R_1$ represents the correlation coefficient between lightning number in a pixel of 20km x 20km centred in the raingauge and total precipitation. $R_2$ is the correlation coefficient between the same lightning number and maximum intensity of precipitation in 10 minutes and $R_3$ is the correlation coefficient between that lightning number and precipitation recorded during the period of lightning activity in the pixel. The results are summarised in table3.

Table3. Correlation coefficients and Synoptic characteristics for the storms events.

| Date | 500Hpa wind | Surface wind | Synoptic features | $R_1$ | $R_2$ | $R_3$ |
|---|---|---|---|---|---|---|
| 7/8/92 | SW | SW | Weak low to W. | 0.15 | 0.07 | 0.25 |
| 8/9/92 | SW | Local winds | Thermic low. Short wave at 500HPa | 0.35 | 0.88 | 0.78 |
| 4/10/92 | N-NE | N | Deep low to E. | 0.21 | 0.37 | 0.49 |

Only in the 8/9/92 event has been possible to establish a good correlation between lightning density and the precipitation parameters: precipitation intensity and precipitation during lightning activity. Lightning density and total precipitation are related in any case.

**b. Flash flood events.**
Three flash flood events with similar synoptic features has been studied. Surface charts show a weak low over the Iberian Peninsula. The 500Hpa charts presents a cool air mass associated to a depression. Table 4 resume main

characteristics of the flood events; Rainfall total amounts, maximum intensity of precipitation in ten minutes, number of ground flashes in an area of 100 $km^2$ centered in the raingauge, percentage of positive lightning and mean intensity of negative and positive lightning are studied.

Table4. Summary of the main characteristics of floods events

| Date | Location | Rainfall | Max.Intensity (10') | Flashes | % (+) | Mean intensity kA |
|---|---|---|---|---|---|---|
| 23/6/92 | S. Sebastian (Sea) | 144mm | 18.9mm | 1 | 0 | (-18) |
| 31/5/97 | Vitoria (continental) | 69mm | 16.8mm | 137 | 17.5 | (-33.4) (+12.4) |
| 1/6/97 | S. Sebastian (Sea) | 193mm | 27.6mm | 10 | 50 | (-63) (+94) |

The observed fact that oceanic flash floods are associated to few lightning, comparing with continental flood, is in agreement with the reported by Zipser (1994) who hypothesised that oceanic storms have a updraft weaker than a possible threshold value, below witch electrification is not sufficient to lead the lightning. It must be remarked that in the 1/6/97 oceanic flash flood, the lightning were more intense that in the 31/5/97 continental flash flood, especially the positive lightning.

## CONCLUSIONS

We have presented the first results of lightning phenomenology in the Spanish Basque Country during the 1992/1996 period. Possible relations between lightning and precipitation has been studied.

1.Lightning number and positive percentage show an annual and a monthly variation.
2. Positive lightning are the 7% of total lightning and this value varies between 39% in January and 5% in July
3. The 77% of lightning occurs in June, July and August.
4. Positive lightning mean intensity is twice the negative lightning mean intensity .
5. Winter and Autumn lightning are most intense that summer lightning
6. A regional difference in lightning intensity distribution is observed.
7. Multiplicity of positive flashes are single strokes in approximately 90% throughout the year while negative lightning varies from 85% in winter to 45% in summer.
8. Annual flash density maximum (3 lightning / $km^2$ ) was observed over Bilbao the greatest urban area.
9. Lightning precipitation relationships are unclear. Only in certain cases lightning density will be correlationed with precipitation.
10.The existence of flash floods with few lightning in the oceanic area, in agreement with Zipser (1994), support his idea that oceanic storms updrafts, not reach a possible threshold value that possibilities sufficient electrification to lead the lightning.

## Bibliography


Hojo J., Ishi M., Kawamura T. and Suzuki F. 1989: Seasonal variation of cloud to ground lightning flash characteristics in the coastal area of the Sea of Japan. *J.Geophys. Res.* V 94, NO D11, 13207-13212

Janssen, M. 1989: The LPATS III system in the Netherlands. Critical evaluation of the results. Proc., 1989 Int.Conf.on Lightning and Static Electricity. Bath , England. Ministry of Defense Procurement Executive,12A.2.1- 12ª.2.7

Kridder E.P., Noogle R.C. and Uman M.A. 1976: A gated, wideband magnetic direction finder for lightning return strokes. *J. Appl. Meteor.*, **15**, 301- 306

Orville R.C. and Silver A.C. 1997: Lightning ground flash density in the contiguous United States. *Mon. Wea. Rev.*, **125**, 631-637

Orville,R.E., Weisman,R.A., Pyle R.B., Henderson, W. and Orville, R. E. Jr , 1987: Cloud to ground lightning flash characteristics from June 1984 through May 1985. *J.Geophys. Res.* V 92, NO D5, 5640-5644.

Pérez F.,1997: Riesgo eléctrico natural en España. Inner document from Teledetection Service of INM. Madrid.

Westcott, N.E.1993: Preliminary examination of urban/rural differences in cloud to ground lightning frequency for 19 central United States cities. Conf on Atmosf. Elect. 4-8 October1993, St Louis, MO, Amer. Met.soc., 752-755.

Zipser E.J. 1994: Deep cumulonimbus cloud systems in the tropics with and without lightning. *Mon. Wea. Rev.*, **122**, 1837-1851.

# FIRST MEASUREMENTS OF THE ATMOSPHERIC ELECTRIC FIELD IN THE SPANISH BASQUE COUNTRY.

I. HERRERO , J. AREITIO, A. EZCURRA
Dpto. Fisica Aplicada I , EUITI y ITT, Unv. País Vasco
C/Nieves Cano 12 , 01006 Vitoria, Spain

## ABSTRACT

First measurements of atmospheric electricity field in the Spanish Basque Country were made during the summer of 1997 with an electric field mill located inside of an automatic meteorological closure. Data from the field mill was afterwards compared with those of the meteorological station. Data from the INM lightning detection system in order to compare the lightning stroke and the field signal were also considered. The aim of this paper is to determine characteristic behaviors of the electric field under different meteorological conditions, and to focus on those situations that originate severe thunderstorms, and severe precipitation. Under thunderstorm conditions, the behavior described by many authors is observed in our study: sign inversion, strong oscillations and high values. When considering the lightning stroke, the value of the intensity and the distance to the measuring point appears to play an important roll affecting the signal structure. Finally, a FFT analysis of signal shows waves with a day and half a day of periodicity, probably connected to the diurnal and semidiurnal variation of the global fair weather electric field. Nevertheless, some shorter periodicities are also detected, that could correspond with precipitation-related phenomena.

## INTRODUCTION

The electric field produced by charges in the atmosphere tells us about its electrical properties. This parameter can be measured by means of the induced charges in a conductor exposed to the field. Under fair weather conditions, the electric field is more or less stable. When disturbed weather occurs, spatial and temporary variations of this parameter are related with the electrical activity of the clouds. Different studies show the existence of a relationship between the electric field variations and cloud electrification or electrical discharge (Marshal *et al.*, 1995; Schuur *et al.*, 1991). Chauzy *et al.* (1991) suggests the possibility of using the electric field parameter for the estimation of the risk of thunderstorm. Changes in this parameter related with precipitation have been observed by Marshal *et al.* (1982), Chauzy *et al.* (1985) et Marshal *et al.* (1991). Reiter's book, "Phenomena in atmospheric and environmental electricity" (1992), show typical variations of the electric under different kinds of precipitation. Those variations have been studied *qualitatively*, but the author notes a lack of quantitative analysis, fact that opens a new field of research. The use of the electric field in this sense requires obtaining representative date in the site where they are to be used, due to the existence of different climates and to the influence of the topography, that can modify the measured electrical parameters.

This work is centered in the study of the first measurements of the atmospheric electric field in the Spanish Basque Country and the possible relationship with lightning and precipitation. With that aim, a measuring system has been developed based on a field mill. The analogic data obtained by the device are transformed to digital using a multimeter controlled by a computer, that means approximately 90 instantaneous values of the electric field every minute.

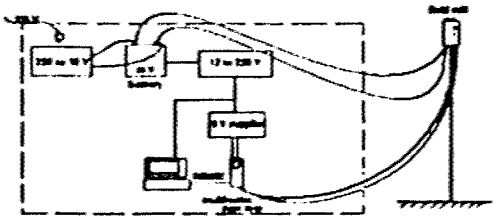

Figure 1. Data acquisition system.

## FIRST RESULTS OF THE MEASURED ELECTRIC FIELD IN THE SPANISH BASQUE COUNTRY

The data were obtained all long the summer, from mid-august to october of 1997. The measuring was made inside the closure of an automatic weather station.

Output from the field mill (V) was transformed to V/m by means of calibrations, applying a known field between two aluminum plates to the field mill. To avoid the screening of the closure, simultaneous data were taken with another calibrated field mill, brought by Dr. Serge Chauzy from the Aerology Laboratory in the Paul Sabatier University of Toulouse. The regression line from the two sets of data permitted to obtain V/m of free atmosphere.

Statistical description of the results

The mean in the measuring period was 113 V/m. Almost 40% of the cases correspond to fair weather conditions. Cases below fair weather are approximately 30%. Negative values represent the 15 % of the cases. Maximum and minima values were 3098 V/m and –999 V/m respectively (both reached during a nighttime storm in august).

The data show a tilted frequency distribution towards the positive values (figure 2).

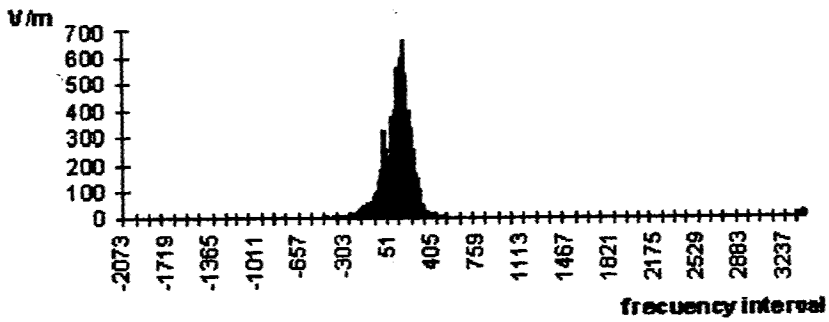


Figure 2. Frequency distribution of the electric field (V/m free atmosphere).

In view to interpret data it is of interest to know that strong electrical storm activity was observed during the first two months of the measuring period (august and september, specially during the first one). In october, the electrical activity decreased.

It is of interest to observe the behavior of the atmospheric electric field parameter during different times of the day. For this purpose, we have chosen four periods of six hours, all referred to solar time. Table 2 resumes the results:

Table 2. Some statistical values of the electric field during different daytimes.

| Day-time | 00:00-05:59 | 06:00-11:59 | 12:00-17:59 | 18:00-23:59 |
|---|---|---|---|---|
| Data number.. | 25200 | 25566 | 26105 | 25920 |
| Mean..... | 110 | 117 | 119 | 110 |
| Maximum..... | 2518 | 3098 | 2930 | 2259 |
| Minimum..... | -294 | -974 | -999 | -971 |

As can be seen, the mean are similar in the different periods of the day, and shows a slight increasing tendency from daylight to dawn, and returns to the same value during the nighttime. Higher maxima are found during the morning, and lower minima during the second half of the day.

Frequency distribution spectrum

With the aim of determining the existence of a diurnal variation curve of the electric field (Carnegie curve), a Fourier analysis has been made, taking a period of 8 days (11552 data). The Fourier transform of the electric signal, after correction of the lineal tendency, showed frequency peaks in the periods of 24 and 12 hours, that probably correspond to a diurnal and semidiurnal oscillation of this parameter.

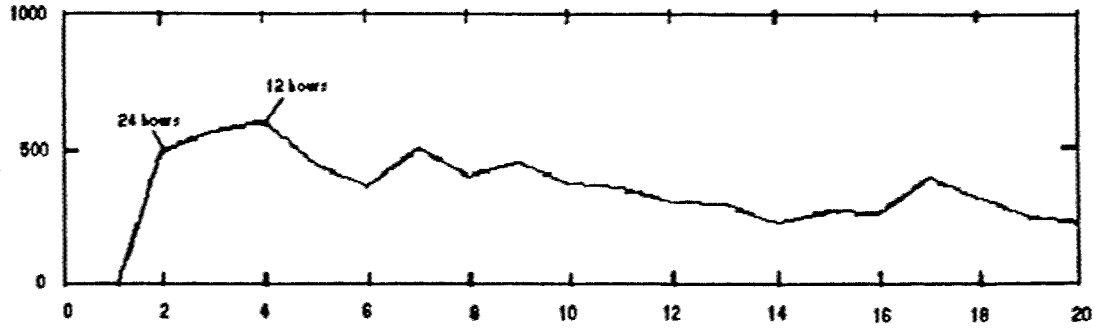


Figure 3. Spectrum of frequencies for an 8 day period during summer of 1998.

## ANALISIS OF A THUNDERSTORM CASE

During the night from 14th to 15th of august 1997 a storm with high electrical activity occurred over the measuring station. Precipitation was registered in the morning of the 15th. Comparing the electric field signal with electric discharges and meteorological parameters given by the automatic station follows (figure 4).

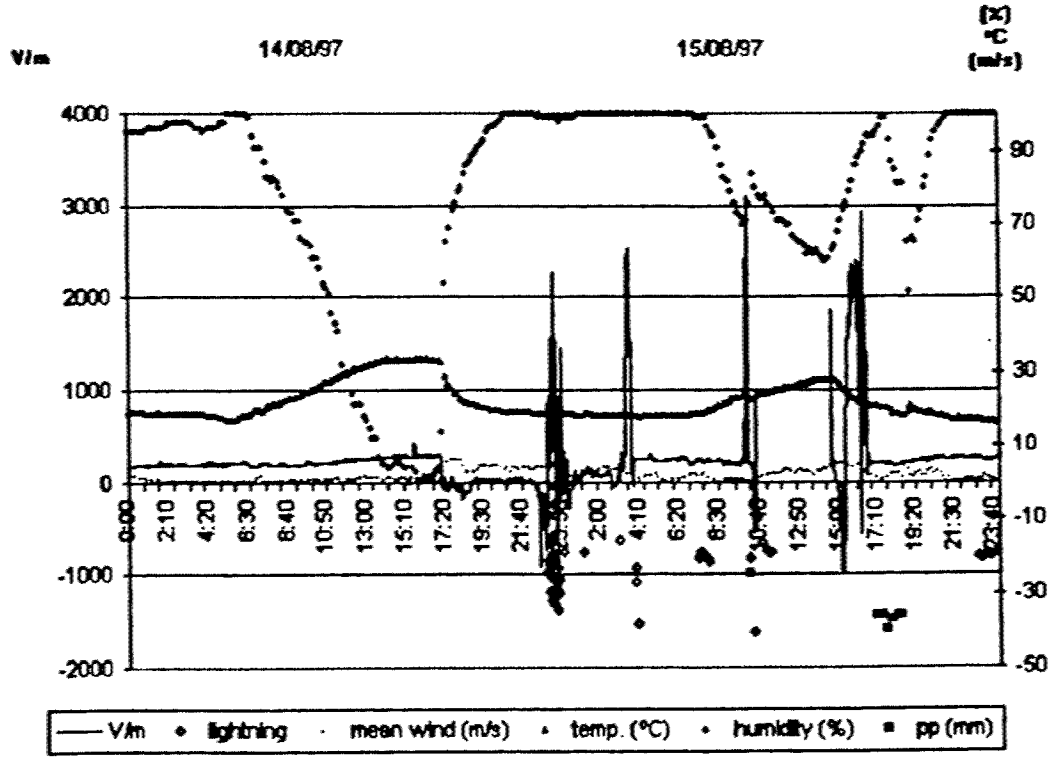


Figure 4. Comparing electric signal from field mill with meteorological parameters and lightning, during 14th to 15th of august 1997.

- A very stable signal was registered during the night, with constant temperature and humidity, close to or reaching saturation.
- There is a slight decrease in the electric field just immediately after sunrise, when increasing irradiation and temperature suggest breaking of the boundary layer.

- The field acquires negative values and then shows oscillations around zero when meteorological parameters show the approaching of the storm cells: wind speed increases over 4 m/s, there is a strong increase in the relative humidity and temperature decrease.
- Electric field oscillates strongly when discharges of high intensity are registered near of the measurement point. The values registered are between 3098 and –999 V/m.
- The field becomes positive and fluctuates around fair weather values when the intensity and frequency of the electrical discharges decreases, announcing that the storm is dissipating.
- No direct relationship is reflected between electric field and precipitation.

## CONCLUSIONS

That is the first time that the atmospheric electric field has been measured in the Spanish Basque Country. The characteristic climatology of this area influences the measuring of this parameter. Specially during august, they were many days of strong electrical activity, and in many cases, even without electrical activity, clouds were present under anticyclonic situations (stacked clouds against Cantabric mountains), which were sufficient to disturb field behavior. Electric field appears to correspond to charge in the clouds.

A preliminary study comparing meteorological and electrical parameters under storm conditions shows behaviors already related by other authors (strong oscillations and high values).

Electrical discharge alters the electric field behavior in some cases, when the intensity of the discharge is high and it strikes close to the measuring point. From this, the value of the intensity and the distance to the measuring point appears to play an important roll affecting the signal structure, but a closer study should be carried out before giving any conclusion.

The first FFT analysis has shown a diurnal and semidiurnal periodicity. Nevertheless, minor frequencies are also present, which we consider of interest for future studies, due to a possible relationship with precipitation. In this sense, measuring precipitation with some precision system at the same measuring site of the electric field would be of higher interest.

## Bibliography


Chauzy, S., Chong, M., Delannoy, A., Despiau, S. The June 22 tropical squall line observed during COPT 81 experiment: electrical signature associated with dynamical structure and precipitation. *J.Geophys.Res.*, 90 (D4): 6091-6098, 1985.

Chauzy, S., Médale, J-C., Prieur, S., Soula, S. Multilevel measurement of the electric field underneath a thundercloud, 1. A new system and the associated data processing. *J.Geophys.Res.*, 96(D12), 22,319-22,326, 1991.

Marshall, T.C., Rust, W.D. Electric field sounding through thunderstorms. *J.Geophys.Res.*, 96(D12): 22,297-22,306, 1991.

Marshall, T.C., McCarthy, M.P., Rust, W.D. Electric field magnitudes and lightning initiation in thunderstorms. *J.Geophys.Res.*, 100(D4): 7097-7103, 1995.

Reiter, R. (1992). Phenomena in atmospheric and environmental electricity. De. Elsevier.

Schuur. T.J., Smull, B.F., Rust, W.D., and Marshall, T.C. Electrical and kinematic structure of the stratiform precipitacion region trailing an Oklahoma squall line. *Journal of the atmospheric sciences*, vol. 48, n.6, 825-842, 1991.

# LIGHTNING IN THE HURRICANE CORE: DISTRIBUTION AND SIGNIFICANCE

John E. Molinari[1], Michael Black[2], Peter Black[2], and Vincent Idone[1]

[1]Department of Earth and Atmospheric Sciences
University at Albany, State University of New York
1400 Washington Avenue
Albany, NY 12222

[2]Hurricane Research Division/AOML/NOAA Miami, FL 33149 USA

ABSTRACT: Observations of lightning in hurricanes have been made using the National Lightning Detection Network (NLDN). This presentation will focus on the ground flashes detected in the vicinity of the eyewall of Hurricane Elena (1985). NLDN-based lightning locations are combined with high-frequency ground-based PPI radar images, infrared satellite images, airborne vertically pointing Doppler radar, and airborne flight-level wind data. The evidence shows that on-and-off periods of lightning in the hurricane core are related to whether or not elevated reflectivity occurs in the mixed-phase region, as has been found by many others. It is proposed that increases in vertical velocity and presumably buoyancy associated with elevated high reflectivity occur simultaneously with a shear instability in the eyewall. The results suggest that inner core lightning can serve as an early warning signal for significant impending changes in eyewall structure and hurricane intensity.

## INTRODUCTION

The radial distribution of lightning in hurricanes displays a maximum in ground flash density in and near the eyewall, a strong minimum over the region 80-100 km outside the eyewall, and a second maximum centered on average at the 240 km radius, in the vicinity of the outer rainbands [*Molinari et al.*, 1994, 1999]. The same papers found that outbreaks of lightning in the vicinity of the eyewall frequently foreshadow a significant change of intensity of the storm. Curiously, this change can represent the onset of rapid deepening or the imminent end of a period of rapid deepening. In this paper we will focus on the events that occurred in Hurricane Elena on 1 September 1985 during the last 8 hours of an extended period of deepening of the storm. Of interest are the relationship between flash locations, the vertical and horizontal structure of radar reflectivity, and flight-level wind variation. Ground-based PPI images are available during this period, often with 1 or 2-minute resolution, and vertically pointing Doppler is available during each eyewall pass.

Figure 1 (following page) shows a radius-time profile of NLDN-detected ground flash occurrences on 1 September. No flashes were detected within 150 km of the center until about 1430 UTC. During the following 4 1/2 hours, 15 flashes were recorded near the core (not all can be easily made out in the figure because they occurred close together in space and time). This storm occurred during the very early years of the NLDN, when no magnetic direction finders (DFs) were located west of Mississippi. Thus, although updated site corrections have been incorporated into the ground flash locations, it is quite possible that only a fraction of ground flashes are being detected. Nevertheless, it seems clear that a long period of very low activity in the storm core was followed by a short period of much greater activity, then another extended period of low activity. We are interested in what factors were responsible for the outbreak of flashes near the core, and what significance the lightning has in the evolution of the hurricane.

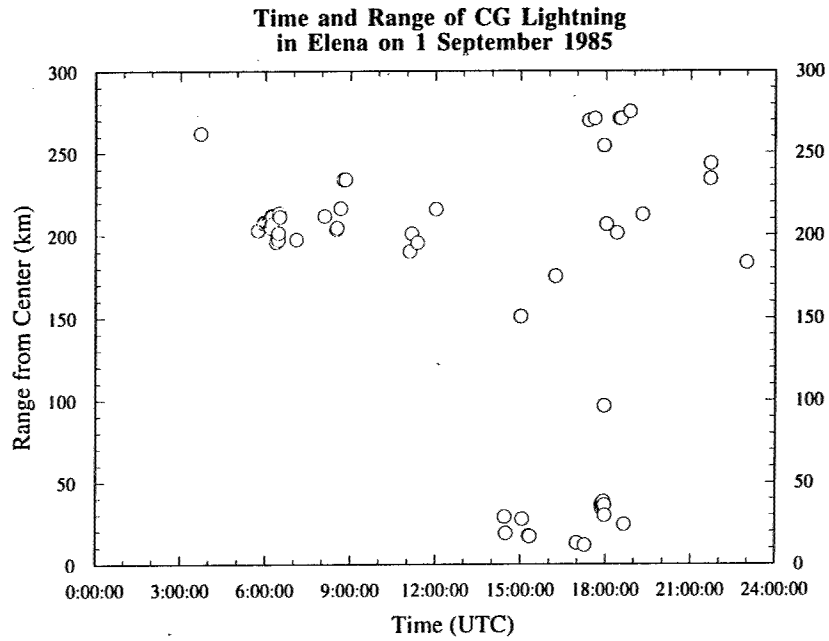


Figure 1. Radius-time series of ground flash locations (circles) in Hurricane Elena on 1 September 1985.

RESULTS

We have found three "lightning proximity eyewall crossings". These are defined to be times when airborne vertically pointing Doppler radar data was collected within 30 minutes and 40° azimuth (roughly 25-30 km at the eyewall radius) of a ground flash. The three occurred at 1452 UTC (east of the center, just upwind of and 8 minutes before the ground flash), 1545 UTC (NNE of the center, nearly colocated with the ground flash but 25 minutes later) and 1715 UTC (west of the center, simultaneous with but 20 km downwind of the flash location). The vertical profiles of vertical velocity and radar reflectivity for the lightning proximity profiles are compared to non-lightning profiles. Because the eyewall does not experience ground flashes the vast majority of the time [e.g., *Molinari et al.*, 1999], we chose non-lightning profiles in which the maximum reflectivity in the core exceeded 40 dBZ for comparison with the others.

The lightning proximity profiles (not shown; these will be shown at the conference) all displayed elevated regions of high reflectivity, as would be expected [e.g., *Williams et al.*, 1992]. The 25 dBZ contour was above the 11 km level at 1452 and 1545 UTC, and reached 9 km at 1715 UTC. At 1415 UTC, vertical velocity exceeded 10 $ms^{-1}$ between 9 and 11 km, with greater than 7 $ms^{-1}$ downdrafts radially outward from the updraft. These values are quite large for mature storms like Hurricane Elena [e.g., *Black et al.*, 1996]. At 1545 UTC, magnitudes of the updraft-downdraft couplet exceeded 4 $ms^{-1}$. At 1715 UTC, downdrafts occurred in the high-reflectivity region; this is perhaps not surprising because the Doppler data was collected downstream of the ground flash, where precipitation drag might be generating downdrafts.

The 1311 UTC non-lightning sounding had a maximum reflectivity of more than 40 dbZ below the 5 km level; the 25 dBZ contour in the core remained entirely below 6 km. Thus reflectivity within the mixed phase region was not large. The 1840 UTC profile exceeded 40 dBZ between 4 and 5 km, and contained subsiding air between 4 and 9 km. Overall, the structure of the lightning proximity and non-lightning profiles was consistent with the findings of others on the importance of high reflectivity and relatively strong localized updrafts in the mixed phase region to achieving meaningful charge separation [*Saunders,* 1993; *Williams et al.*, 1992; *Zipser and Lutz*, 1994].

Next the ground-based PPI images will be considered. Updrafts in hurricanes are helical in nature. This occurs because orbital periods for horizontal flow are the same order of magnitude as the time it takes a parcel to rise from the lower troposphere to the tropopause at typical hurricane vertical velocities. For instance, a 4 $ms^{-1}$ updraft requires about 40 min to reach the tropopause; that time is about half the orbital period for air moving at 50 $ms^{-1}$ at the 35 km radius, numbers representative of Hurricane Elena.

In addition, updrafts tend to initiate downshear in hurricanes. Recently, *Corbosiero* (1999) showed a strong tendency for the largest ground flash density to occur to the left of the downshear direction in the hurricane core. This is consistent with the updraft initiating straight downshear, rising helically past the -10°C level where charge separation is greatest (and thus where ground flashes would be expected), and continuing to rise helically to a broad reflectivity maximum further downwind where precipitation is falling. By this reasoning, if updraft strength is not too intense, lightning should occur somewhere between the azimuth of updraft initiation and that of maximum reflectivity; the latter typically occurs at about a 180° azimuth from straight downshear.

Vertical shear was from the northwest in Hurricane Elena on 1 September, and thus updraft initiation would be expected to the southeast. Figure 2 (below) shows the reflectivity in Hurricane Elena at 1500 UTC, within one minute of a ground flash northeast of the center. The ground flash location fits the idea of a helical updraft passing the -10°C level between its initiation and the maximum reflectivity downstream.

Also of interest in this figure is the notch in the eyewall adjacent to the strongest convection. This structure bears some resemblance to eye mesovortices described by *Black and Marks* (1991). Such features may represent the response to a shear instability in the eyewall (*Schubert and Montgomery*, 1999).

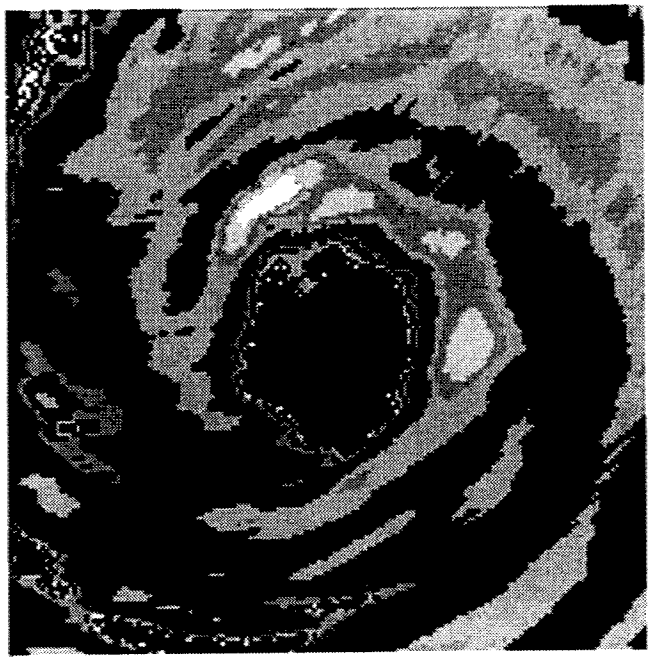

Figure 2. PPI image of radar reflectivity from ground-based radar in Hurricane Elena at 1500 UTC 1 September 1985. Light shading represents higher reflectivity; darker shading represents lower values. The white region has reflectivity greater than 45 dBZ. The minimum contoured value is 10 dBZ.

The evidence from the above figures, as well as those for other times during the lifetime of Hurricane Elena (not shown), suggests that lightning locations with respect to azimuth are closely

related to the direction of the vertical wind shear vector. The on-and-off nature of cloud-to-ground lightning in the core appears related to the vertical profile of reflectivity, as has been suggested by many others. The key question then becomes why it is that elevated reflectivity maxima (i.e., localized upward motion maxima) occur only episodically in the hurricane and not continuously. We hypothesize that this relates to the development of eyewall shear instabilities (*Schubert and Montgomery*, 1999) during strong localized convection. Prior to the lightning outbreak, the radial profile of vorticity (not shown) satisfies the condition for instability determined by *Schubert and Montgomery*. Only as this instability is realized in the form of mesovortices in the eye and polygonal eyewalls does lightning occur in the storm core. Once the eye returns to a nearly circular shape late on 1 September, the mesovortices and polygonal eyewalls vanish and the lightning stops. It appears that the existence of lightning can be an indicator of such instabilities, and thus an indicator of large changes in eyewall structure and hurricane intensity.

Acknowledgments. We are indebted to Global Atmospherics, Inc. for providing the revised site corrections used to process the NLDN data. This work was supported by National Science Foundation Grant ATM9423229.

REFERENCES

Black, M.L., R.W. Burpee, and F.D. Marks, Jr., Vertical motion characteristics of tropical cyclones determined with airborne Doppler radial velocities, *J. Atmos. Sci.*, **53**, 1887-1909, 1996.

Black, P.G., and F.D. Marks, Jr., The structure of an eyewall mesovortex in Hurricane Hugo (1989), *19th Conference on Hurr. and Trop. Meteor.*, American Meteorological Society, Miami, Fl., 6-10 May, 579-582, 1991.

Corbosiero, K., Lightning in hurricanes, *23rd Conference on Hurr. and Trop. Meteor.*, American Meteorological Society, Dallas, TX., 10-15 January, 66-67, 1999.

Molinari, J., P.K. Moore, V.P. Idone, R.W. Henderson, and A.B. Saljoughy, Cloud-to-ground lightning in Hurricane Andrew, *J. Geophys. Res.*, **99**, 16,665-16,676, 1994.

Molinari, J., P. Moore, and V. Idone, Convective structure of hurricanes as revealed by lightning locations, *Monthly Weather Review*, 520-534, 1999.

Saunders, C.P.R., A review of thunderstorm electrification processes, *J. Appl. Meteor.*, **32**, 642-655, 1993.

Schubert, W.H., M.T. Montgomery, R.K. Taft, T.A. Guinn, S.R. Fulton, J.P. Kossin, and J.P. Edwards, Polygonal eyewalls, asymmetric eye contraction, and potential vorticity mixing in hurricanes, *J. Atmos. Sci.,* in press, 1999.

Williams, E.R., S.A. Rutledge, S.G. Geotis, N. Renno, E. Rasmussen, and T. Rickenbach, A radar and electrical study of tropical "hot towers", *J. Atmos. Sci.*, **49**, 1386-1395, 1992.

Zipser, E.J., and K.R. Lutz, The vertical profile of radar reflectivity of convective cells: A strong indicator of storm intensity and lightning probability?, *Mon. Wea. Rev.*, **122**, 1751-1759, 1994.

# A Multi-Platform Study of the February 10, 1998 Squall Line Event and TRMM Overpass of Southeast Texas

David B. Wolff[1], Richard E. Orville[2] and Edward L. Zipser[2]

[1]*Joint Center for Earth Systems Technology (JCET)/*
*University of Maryland, Baltimore *(UMBC)*
*NASA/GSFC, Code 910.1, Greenbelt, MD 20771*

[2]*Texas A&M University, College Station, Texas 77843-3150*

Abstract

*A vigorous Mesoscale Convective System (MCS) propagated over southeast Texas in the morning and early afternoon hours of February 10, 1998. This was one of the first significant precipitation events that coincided with a Tropical Rainfall Measuring Mission (TRMM) overpass of the Houston WSR-88D radar/TRMM Ground Validation site. The first part of this study investigates the relation between vertical structure of reflectivity and National Lightning Detection Network (NLDN) cloud-to-ground lightning data for this event. Using standard TRMM products, including three-dimensional reflectivity (2A-55) and stratiform-convective rain type maps (2A-54), vertical profiles of reflectivity were constructed in areas where lightning occurred. The profiles were classified as either "convective" or "stratiform", and as being associated with either "positive" or "negative" flashes. The resultant profiles are consistent with previous studies showing a well-defined bright band in the stratiform region, and significantly more intense and deeper echoes in the convective region. This study also investigates the relation between the TRMM Microwave Imager (TMI) measurements and lightning peak current and polarity. The TMI 85.5 GHz brightness temperatures show that approximately 42% of negative flashes occur in regions of depressed 85.5 GHz Polarization Corrected Temperature (PCT) < 200 K, while only half as many (21%) of the positive flashes were associated with PCT less than 200 K.*

## I. INTRODUCTION

A vigorous Mesoscale Convective System (MCS) formed over central Texas during the early morning hours of February 10, 1998, in response to a negatively tilted 500 mb trough axis located in west Texas. The associated squall line propagated through the I-35 corridor (e.g., Austin, San Antonio) around 1330 UTC, reaching the Houston metropolitan area by 1930 UTC. The aftermath of the storm included reports of a 60 m $s^{-1}$ wind gust at Lake Livingston Dam in east Texas, and reports of 6 tornadoes near the Houston area around 1830 UTC, at the time of the TRMM satellite overpass time. There were also extensive reports of hail over southeast Texas K (Cecil et al. 1998)

## II. DATA

The data used in this study includes ground-based radar reflectivity measurements made by the League City, Texas WSR-88D radar, hereafter referred to as KHGX; lightning data obtained from the National Lightning Detection Network (NLDN); and, TRMM Microwave Imager 85.5 GHz Polarization Corrected Temperatures (PCT) (Spencer et al, 1989).

### *II.a. Lightning data*

Data from the National Lightning Detection Network (NLDN) was obtained from Global Atmospherics, Inc. of Tucson, Arizona. Each file consists of a single day of data and contains, date, time, latitude, longitude, multiplicity and peak current of the first stroke in each flash. The location for each flash is accurate to within 500 m (Orville, 1998, *personal communication*). A summary of the instrumentation and specifications of the direction finders is given in Orville (1994).

### *II.b. Ground validation radar data*

Through an agreement with the National Weather Service and the WSR-88D Operational Support Facility (OSF), NASA has established southeast Texas as a Direct Data (DD) Ground Validation site. The WSR-88D Archive II data is recorded and then copied by the National Weather Service office in Houston and sent directly to the Joint Center for Earth Systems Technology (JCET) at NASA Goddard Space Flight Center (GSFC). The data are quality controlled using an automated technique (Kulie et al., 1999), which is designed to remove non-precipitating echo such as ground clutter, anomalous propagation and other non-meteorological targets. The polar volume scan data was interpolated to a three dimensional grid at 2

km by 2 km horizontal resolution and 1.5 km vertical resolution from 1.5 km to 19.5 km height. The horizontal grid extends to a distance of 150 km from the radar.

*II.c Stratiform/convective rain classification*

The two dominant modes of tropical precipitation are convective and stratiform. Convective rain falls from cumulus and cumulonimbus clouds, with updrafts exceeding the terminal velocity of ice crystals and snow (1-3 m $s^{-1}$). Tropical stratiform precipitation typically occurs as a result of convective processes, which pump a rich supply of hydrometeors and water vapor aloft, giving rise to expansive areas of upper level cloud in which the vertical air velocity is less than the terminal velocity of ice crystals and snow. The growth of ice crystals in the upper portion of stratiform clouds is primarily due to water vapor deposition, where vertical air motion does not exceed a few tens of centimeters per second. The ice crystal growth processes of aggregation and riming can start to occur when the ice particles descend to within about 2.5 km of the 273 K isotherm. Identification of stratiform and convective rainfall is important in observational, modeling and remote sensing studies because the micro-physical processes described above affect radar- and microwave-rainfall estimation algorithms and cloud modeling parameterizations via the raindrop size distribution (DSD). However, observations of vertical velocities and hydrometeor fall speeds within clouds are rare, therefore identification of convective or stratiform rain is usually accomplished by indirect methods. In this study, the TSDIS 2A-54 stratiform/convective rain type product, which follows the algorithm of Steiner et al., (1995) was used to identify areas of "convective" and "stratiform" precipitation.

III. VERTICAL PROFILES OF REFLECTIVITY

Mean vertical profiles of reflectivity were computed from the reflectivity column over areas where lightning occurred. This area is defined as area bounded by the closest 2 km x 2 km radar grid box in which lightning occurred within +/- 3 minutes of a given volume scan. The profiles were further classified as either "convective" or "stratiform", and as being associated with either "positive" or "negative" flashes. Figure 1a illustrates the resultant mean vertical reflectivity profiles for the February 10, 1998 MCS event over southeast Texas. The overall mean profile is dominated by convective structure, as evidenced by the fact that the convective profiles so closely mimics the overall profile, with mean low-level (1.5 km) reflectivity values on the order of 48-50 dBZ, steadily decreasing to near 40 dBZ at 5 km, 20 dBZ at 10 km and leveling off at about –2 dBZ above 13 km.

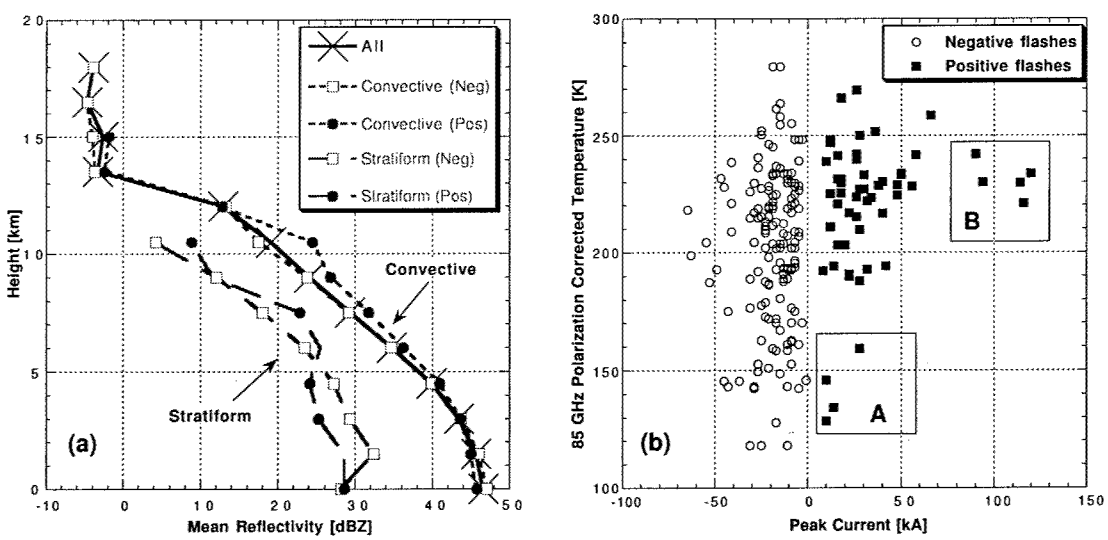


*Figure 1: a) Vertical Profiles of reflectivity in "convective", "stratiform" and "all" areas where "positive" or "negative" flashes occurred within +/- 3 minutes of the beginning of a given radar volume scan. Solid circles represent the reflectivity profiles for "positive" flashes and the open squares represent the "negative" flashes. The large crosses represent the overall mean reflectivity profile; b) scatter plot of 85.5 GHz PCT versus associated NLDN peak current. The open circles represent the negative flashes and the solid squares represent positive flashes. Note that in order to derive more robust statistics, the significantly larger area bounded by the TMI FOV during the period 1828 - 1832 UTC was used to derive these statistics.*

On the other hand, the mean stratiform profiles are distinctly different than their convective counterparts with mean low-level reflectivity values of only 28-30 dBZ and a maximum depth of about 10.5 km. Also evident is a radar "bright band" associated with the stratiform/negative profile, which is not present in the stratiform/positive profile. A common, and not yet understood characteristic of both the stratiform and convective profiles is that the positive flashes appear to be associated with *increased reflectivities aloft*, and somewhat *decreased reflectivities* in the *low-* and *mid-levels*.

## IV. TMI/NLDN COMPARISONS

The TMI measures upwelling microwave radiation at 10.7, 19.4, 21.3, 37.0 and 85.5 GHz. The instrument views 49° off nadir, with a 758.5-km swath width. Footprint size varies inversely with frequency, ranging from about 4 km at 85.5 GHz to approximately 50 km for the 10.7 GHz channel (Kumerrow et al. 1998). The low frequency channels are primarily sensitive to emissions by liquid water and water vapor, while the higher frequencies are more sensitive to scattering by ice crystals. Thus, one would expect that the lowest brightness temperatures at 85.5 GHz would be associated with abundant icing (and hence strong vertical velocities).

Several charge separation theories have been proposed. One of the more popular theories suggests that rapid cloud electrification can occur when large and small ice particles collide in the presence of super-cooled cloud liquid water in the mixed phase region of the cloud (253-273 K) (Reynolds et al. 1957). Since both lightning activity and 85.5 GHz ice scattering signatures are related to ice microphysics, comparison of these two data sets may further our understanding of storm structure and intensity.

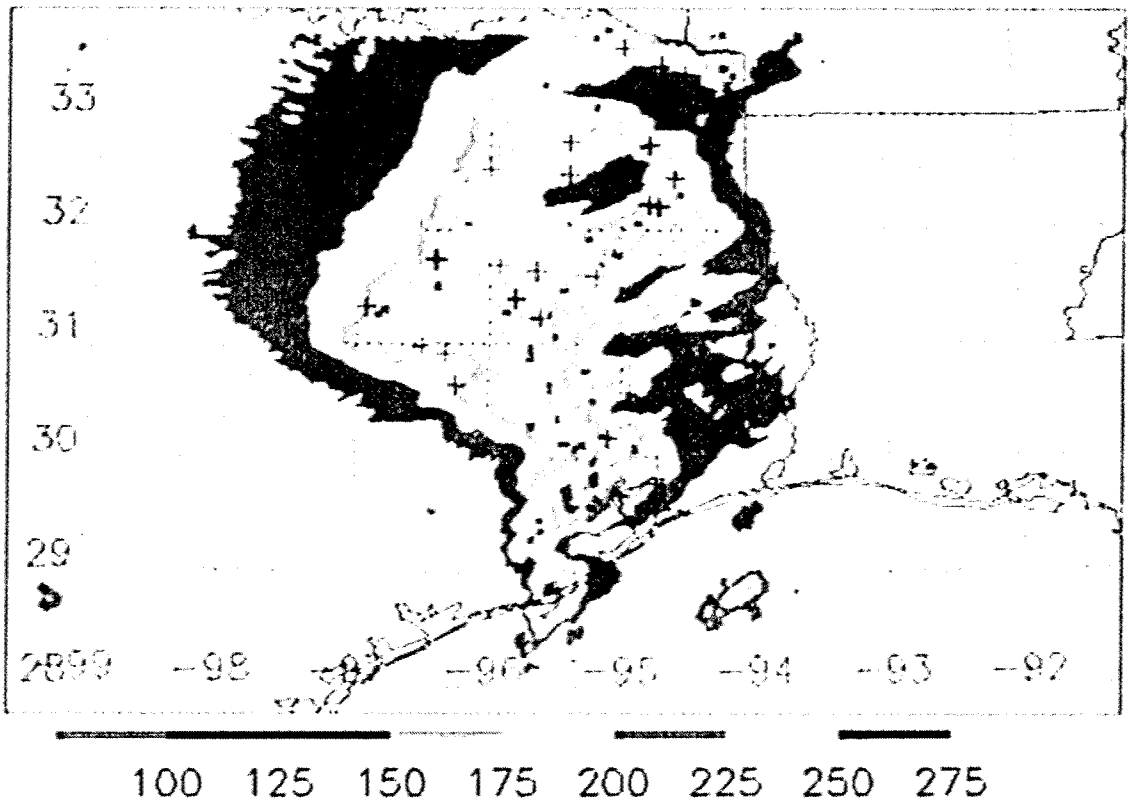


*Figure 2: TRMM Microwave Imager (TMI) 85.5 GHz Polarization Corrected Temperature (PCT) for the February 10, 1998 1828-1832 TRMM overpass. Locations of positive (plus signs) and negative (dots) flash locations are overlaid.*

Figure 1b is a scatter plot of co-located peak current (kA) and 85 GHz PCT values. While a large number of the negative flashes were associated with PCT > 200 K (about 58.6%), the bulk (~ 78%) of the positive flashes were associated with the relatively warm PCT values greater than 200 K. The two boxes in Fig. 1b denote areas of special interest. The box marked "A" represents flashes that occurred in areas that were

classified in the 2A-54 product (not shown) as stratiform precipitation, although the PCT < 160K would usually be considered to be associated with convection. The box marked "B" represent intense positive flashes ( > 75 kA) that occurred in the northern, more mature portion of the storm. Figure 2 provides an illustration of the 85.5 GHz PCT field over eastern Texas with the locations of positive flashes (plusses) and negative flashes (dots) overlaid. It is apparent that the many of the negative lightning flashes tended to occur in the convective cores, while the bulk of the positive flashes tended to occur in the older more mature stratiform portions of the storm. Table 1 provides a synopsis of the lightning/TMI characteristics.

*Table 1: NLDN Lightning/TMI statistics.*

| Category | Negative Flashes | Positive Flashes |
|---|---|---|
| Total Flashes (TMI FOV) | 157 | 54 |
| Minimum 85.5 GHz PCT | 118.0 | 128.3 |
| Maximum 85.5 GHz PCT | 279.5 | 269.4 |
| Median 85.5 GHz PCT | 207.3 | 227.0 |
| Mean 85.5 GHz PCT | 202.6 | 219.7 |
| % of PCT < 200 K | 65/157 (41.4%) | 12/54 (22%) |

V. ACKNOWLEDGEMENTS
The lightning data was obtained from Global Atmospherics, Inc., of Tucson, Arizona. Many thanks to Major Gary Huffines (USAF) for his expertise in working with and interpreting the lightning data. Brad Ferrier, Mark Kulie and Mike Robinson of the Joint Center for Environmental Technology (JCET)/NASA provided the GV radar data. The TRMM satellite data and interpretation was greatly aided by Daniel Cecil, Rick Toracinta and Stephen Nesbitt of Texas A&M University.

VI. REFERENCES

Cecil, D., D. B. Wolff, E. R. Toracinta and S. M. Nesbitt: 1998: Multi-sensor comparison of TRMM satellite and ground validation products from Texas and Florida squall line events. *19th Conference on Severe Local Storms*, Minneapolis, Minnesota, 14–18 September 1998.

Kulie, M. S., M. Robinson, D. A. Marks, B. S. Ferrier, D. Rosenfeld and D. B. Wolff, 1999: Operational processing of ground validation data for the Tropical Rainfall Measuring Mission. *29th Int. Conference on Radar Meteorology*, Montreal, QC, Canada, Jul. 12-16, 1999,.

Mohr, K. I., E. R. Toracinta, E. J. Zipser, and R. E. Orville, 1996: A comparison of WSR-88D reflectivities , SSM/I brightness temperatures, and lightning for mesoscale convective systems in Texas. Part II: SSM/I Brightness temperatures and lightning. Jou. Appl. Met., 35, 919-931.

Orville, R. E., 1994: Lightning ground flash density in the contiguous United States: 1989-1991. J. Geophys. Res., 99, 10 833-10 841.

Reynolds, S. E., 1953: Thunderstorm-precipitation growth and electrical-charge separation. Bull. Amer. Meteor. Soc., 34, 117-123.

Kumerrow, C, W. Barnes, T. Kozu, J. Shiue, and J. Simpson, 1998: The Tropical Rainfall Measuring Mission sensor package. Notes and Correspondence: *J. Atmos. Oceanic Technol.*, **15**, 809-817.

Steiner, M., R. A. Houze Jr., and S. E. Yuter, 1995: Climatological characterization of three-dimensional storm structure from operational radar and rain gauge data. J. Appl. Meteor., 34, 1978-2007.

Spencer, R. W., H. M. Goodman, and R. E. Hood, 1989: Precipitation retrieval over land and ocean with the SM/I: Identification and characteristics of the scattering signal. Jou. Atmos. Ocean Tech., 6, 254-273.

# CLOUD-TO-GROUND LIGHTNING ACTIVITY IN MESOSCALE CONVECTIVE COMPLEXES IN SOUTHEASTERN BRAZIL IN 1993-94

Iara R. C. A. Pinto[1], Osmar Pinto Jr.[1], Jorge C. Conforte[1], José H. Diniz[2], Andre M. Carvalho[2], and Armando Cazetta Filho[2].

[1] Instituto Nacional de Pesquisas Espaciais – INPE, São José dos Campos, SP, Brazil
[2] Companhia Energética de Minas Gerais – CEMIG, Belo Horizonte, MG, Brazil

ABSTRACT: The characteristics of cloud-to-ground lightning flashes in association with Mesoscale Convective Complexes (MCC) which occurred in the southeastern Brazil in the years of 1993 and 1994 were investigated. During this period 4 MCCs were identified. However, only 1 of 4 MCCs occurring in 1993-94 spent their entire life cycle within the 50 % detection efficiency region. It had a duration of 15 hours and at time of maximum extent its area was approximately 110,000 km$^2$. The characteristics of cloud-to-ground flashes during their major life-cycle phases were studied in terms of the hourly flash rate, polarity, multiplicity and average peak current intensity.

## INTRODUCTION

Mesoscale Convective Complexes (MCC) are large mesoscale convective systems defined in terms of their circular appearence, duration and size of the weather system cloud shield in GOES infrared satellite images (Maddox, 1980). In the United States, MCC generally occur over the central region in the spring and summer months (McAnelly and Cotton, 1989) and are associated with severe weather (Maddox, 1980). In South America, Velasco and Fritsch (1987) and Conforte (1997) have found that MCC occur in almost all months between September and May. Although more frequently in the north part of Argentine, south of Brazil, Paraguay and Bolivia, they occur in almost all regions of South America from the equator to 40 degrees south.

The cloud-to-ground lightning activity in MCC, in turn, has not been studied in details, in part due to the difficulties to detect all events in space and time. At present, the more complete study and the first to provide a characterization of the lightning activity throughout the MCC life cycle was reported by Goodman and MacGorman, 1986 (hereafter referred to as GM, 1986). They studied the lightning activity in 10 MCC, which occurred in Oklahoma between 1981 and 1983. However, only in three of the ten cases the entire MCC life cycle take place in the region covered by the local lightning detection network (NSSL). Nevertheless, their results were sufficient to infer some lightning activity properties of MCC: flash rates in excess of 1000 h$^{-1}$ can be sustained on average for more than nine consecutive hours; the development and mature phases constitute the most electrically active period; the most electrically active period also corresponds to the period of large flash multiplicity, while the fewest multiple flashes occur during the first hour of the MCC development. GM (1986) also found that the lightning flash activity appears to be independent of the size of the local storm system cloud shield at maximum extent and MCC life cycle duration. However, in their study, flash polarity discrimination as well as peak current intensity were not available.

In this paper, the first results about the cloud-to-ground lightning activity in tropical MCC are reported. The characteristics of cloud-to-ground flashes during the major MCC life cycle

phases were studied in terms of the hourly flash rate, polarity, multiplicity and average peak current intensity. The results are compared with those obtained by GM (1986) for middle latitudes MCC in the United States.

RESULTS

The characteristics of cloud-to-ground lightning flashes in association with Mesoscale Convective Complexes (MCC) which occurred in the southeastern Brazil in the years of 1993 and 1994 were investigated using a LPATS lightning detection network. During this period 4 MCCs were identified. However, only one of these cases spent their entire life cycle within the 50 % detection efficiency region. The first storms begun to develop on 28 October 1994 at 21:00 UT (cloud top area with temperatures < – 52°C equal to 10,000 $km^2$). The MCC initiated (cloud top area with temperatures < – 52°C equal to 50,000 $km^2$) on 29 October 1994 at 02:00 UT, had its maximum extent at 06:00 UT, and terminated (cloud top area with temperatures < – 52°C equal to 10,000 $km^2$) on the same day at 12:30 UT. It had a duration of 15.5 hours and at time of maximum extent its area was approximately 110,000 $km^2$. Fig. 1 shows an infrared GOES image of the MCC on October 28-29, 1994 at the instant of maximum extent. Near its center, the cloud top reached the tropopause at about 16 km. During its life time about 5500 cloud-to-ground lightning flashes were recorded, assuming an average lightning detection efficiency of about 50 % in the region of the MCC and considering only positive flashes above 15 kA.

About 12.2 % of the flashes were positive. The average peak current along the whole life cycle was 33.2 kA for negative flashes and 33.5 kA for positive flashes. It was found that the peak currents of both polarities tended to increase after the MCC initiation. Table 1 shows a comparison between the lightning flash characteristics of the MCC on October 28-29, 1994 with the average values obtained by GM (1986). The instants of first storm development, initiation, maximum extent and termination are represented, respectively, by the letters F, I, M and T.

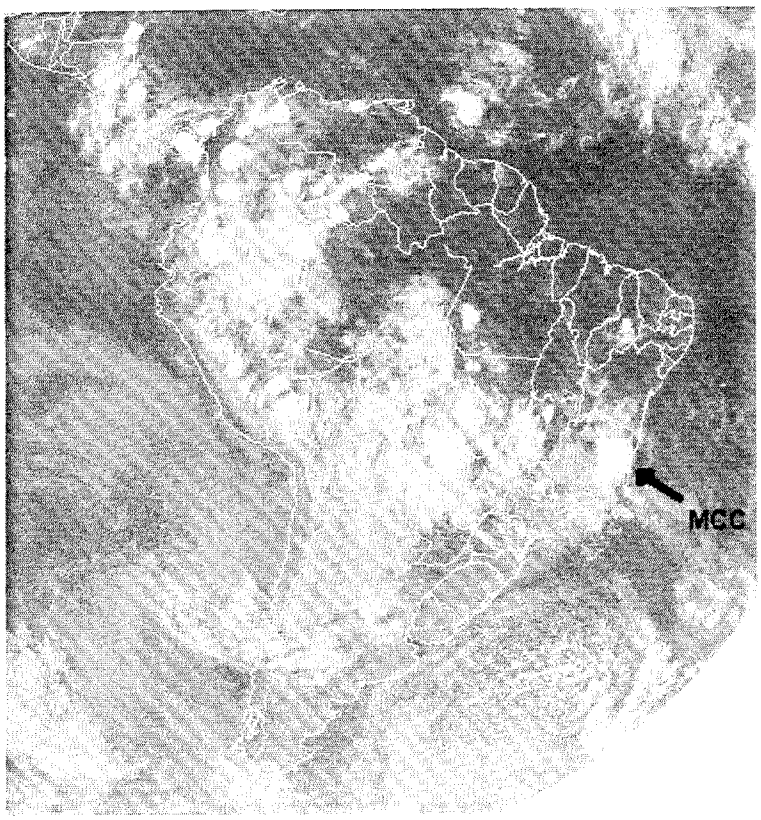

| | Duration (h) | Cloud top area <52°C at maximum extent ($km^2$) | Peak flash rate ($h^{-1}$) | Characteristics at different phases | F-I | I-M | M-T |
|---|---|---|---|---|---|---|---|
| Goodman and MacGorman (1986) | 14.3 | 160 | 2679 | Total Flashes | 7538 33.8% | 16878 41.9% | 5438 24.4% |
| 1994 MCC | 15.5 | 110 | 1020 | Total Flashes | 2860 51.9% | 1980 36% | 666 12.1% |
| | | | | Neg. | 2480 | 1780 | 574 |
| | | | | Pos. | 380 | 200 | 92 |
| | | | | % Pos. | 13.3 | 10.1 | 13.8 |
| | | | | % Neg. S. | 66 | 67 | 53 |
| | | | | % Pos. S | 100 | 100 | 100 |

Table 1

DISCUSSION AND CONCLUSIONS

From the analysis of Table 1, several interesting points are worth mentioning:

- most lightning activity in the 1994 MCC occurred in the same periods as reported by GM, that is, between the F and M;
- the lightning activity in the 1994 MCC was very low compared with the middle latitude MCCs reported by GM.
- the percentage of positive flashes presented only small variations along the life cycle of the 1994 MCC.
- the percentage of negative single flashes decreased in the M-T period of the 1994 MCC, in agreement with the results of GM (1986).
- the percentage of positive single flashes was constant along the life cycle of the 1994 MCC.

The lower activity of the 1994 MCC may indicate that tropical MCCs produced less flashes than middle latitude MCCs or, perhaps, less cloud-to-ground flashes. The MCC with lower activity in the ten cases reported by GM (1986) had two times the number of flashes of the 1994 MCC. More data, however, is necessary to confirm such a difference.

ACKNOWLEDGMENTS: The authors would like to thank the Fundação de Amparo à Pesquisa do Estado de São Paulo (FAPESP) for supporting the research through the projects 1995/5266-9 and 1996/2239-3.

REFERENCES

Confort, J. C., A study about mesoscale convective complexes over and near South America, PhD Thesis, Brazilian Institute of Space Research (INPE), 1997.

Maddox, R. A., Mesoscale convective complexes, Bull. Amer. Meteor. Soc., 61, 1374-1387, 1980.

McAnelly, R. L., and W. R. Cotton, The precipitation life cycle of meso-scale convective complexes over the central United States, *Mon. Weather Rev.*, 117, 784-808, 1989.

Pinto Jr., O., Pinto, I.R.C.A., Gomes, M.A.S., Vitorello, I., Padilha, A.L., Diniz, J.H., Carvalho, A.M., and Cazetta Filho, A., Cloud-to-ground lightning in the Southeastern Brazil in 1993, 1. Geographical distribution, *J. Geophys. Res.*, submitted, 1999.

Pinto, I.R.C.A., Pinto Jr., O., Rocha, R.M.L., Diniz, J.H., Carvalho, A.M., and Cazetta Filho, A., Cloud-to-ground lightning in the southeastern Brazil in 1993, 2. Time Distribution and flash characteristics, *J. Geophys. Res.*, submitted, 1999.

Goodman, S. J., and MacGorman, D. R., Cloud-to-ground lightning activity in mesoscale convective complexes, *Mon. Wea. Rev.*, 114, 2320, 1986.

Velasco, I., and Fritsch, J., Mesoscale convective complexes in the Americas, *J. Geophys. Res.*, 92, 9591-9613, 1987.

# Lightning Ground Flash Measurements over the Contiguous United States: A Ten-Year Summary 1989-1998

**Richard E. Orville and Gary R. Huffines**
**Department of Meteorology**
**Texas A&M University**
**College Station, Texas 77843-3150**

**Abstract.** The National Lightning Detection Network (NLDN) has recorded cloud-to-ground lightning characteristics for ten years over the contiguous United States producing a database of 216 million flashes. What have we learned? Results are a combination of natural observations free of instrumentation effects and biased observations affected by the characteristics of the network. The valid natural observations appear to be 1) maximum cloud-to-ground negative flash densities in central Florida in most years, but moving to the upper Midwest during high precipitation years, 2) maximum cloud-to-ground positive flash densities in the Midwest, 3) maximum percentage positive lighting in the upper Midwest and along the West Coast, 4) highest median negative currents in the Southeast, 5) highest median positive currents in the upper Midwest and the lowest in Louisiana and Florida. The biased observations include, apparently, 1) low median negative and positive peak currents in the western Carolinas resulting from close (<100 km) spacing of the sensors and 2) high flash negative multiplicity in the same region for the same reason.

## 1. Introduction

Beginning with the invention of the modern lightning direction finder (Krider et al., 1976), lightning direction finder networks were established in the United States for operations (Krider et al. 1980) and research field programs (Orville et al. 1983; MacGorman et al. 1989). These networks operated by the Bureau of Land Management, the National Severe Storms Laboratory, and the State University of New York at Albany (Orville et al. 1987, Orville 1991) were combined in 1987 and expanded by 1989 to form the National Lightning Detection Network (NLDN) covering the continental United States. Since that year, annual summaries of these data have been published (Orville 1991,1994; Orville and Silver 1997; Orville and Huffines 1999). In this paper we present cumulative results from the continuous operation of the NLDN over the first decade of its operation, 1989 through 1998. These results include the cloud-to-ground lightning characteristics for both negative and positive lightning including their flash densities, peak currents, multiplicity (number of strokes per flash), and the percentage of total lightning that lowers positive charge to ground.

## 2. Data

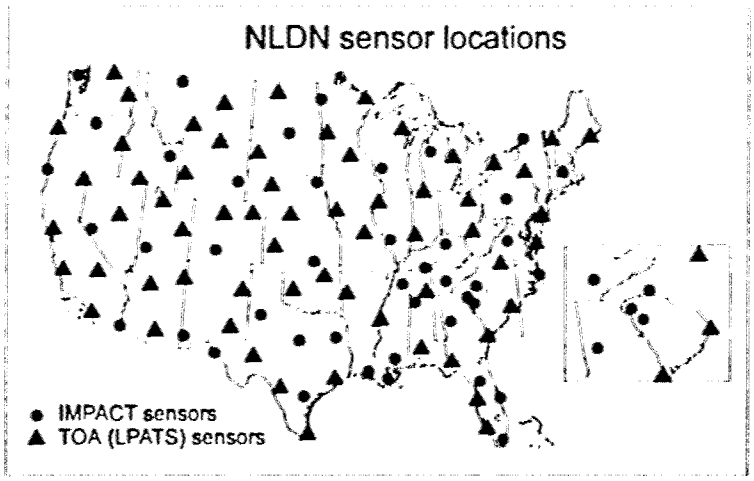


Figure 1. The locations of sensors in the National Lightning Detection Network are shown for 1998. Note the call-out that shows the clustering of IMPACT sensors in the western Carolinas.

The NLDN, Figure 1, operated by Global Atmospherics, Inc., has recorded over 216 million cloud-to-ground lightning flashes in the ten-year period, 1989-1998. Changes in the NLDN have occurred throughout this period. Location accuracies, initially evaluated to be on the order of 5-10 km (NSSL, Maier work), have decreased to approximately 0.5 km (Idone et al. 1998a). Detection efficiencies, initially estimated to be on the order of 70% (Orville 1991), have improved to 80-90% (Idone et al.

1998b). In the analyses presented in this paper, we make no corrections for the detection efficiency. Thus, all graphs and contoured maps present the measured results with no corrections.

**3. Results**

The cloud-to-ground lightning data for the continental United States are summarized for the ten-year period in the Table 1. Two sets of data are provided for the ten-year period. The left half of the table shows the information associated with all the measured flashes. These include flashes detected within approximately 600 km of the closest sensors, which therefore contain distant flashes over the oceans. The right half of the Table contains the information on the flashes that occur only over the 48 contiguous states. Thus, flashes over the oceans, Mexico, and the Great Lakes are eliminated in this count.

Table 1. Cloud-to-Ground (CG) lightning summaries for 1989 through 1998.

| All Measured Flashes | | | | | US Boundary Only | | | |
|---|---|---|---|---|---|---|---|---|
| | | | Median peak current (kA) | | | | Median peak current (kA) | |
| Year | Flashes (x $10^6$) | % Positive | Positive | Negative | Flashes (x $10^6$) | % Positive | Positive | Negative |
| 1989 | 13.422 | 3.07 | 54.3 | -29.7 | 10.957 | 3.22 | 52.1 | -28.0 |
| 1990 | 15.929 | 3.83 | 44.0 | -30.1 | 12.601 | 4.21 | 42.4 | -27.9 |
| 1991 | 16.903 | 3.98 | 43.8 | -29.2 | 13.206 | 4.31 | 41.8 | -27.3 |
| 1992 | 16.260 | 4.18 | 40.3 | -27.8 | 13.203 | 4.37 | 38.2 | -26.4 |
| 1993 | 24.234 | 4.56 | 37.2 | -27.8 | 20.191 | 4.80 | 34.6 | -26.3 |
| 1994 | 24.218 | 4.93 | 32.9 | -26.4 | 19.884 | 5.24 | 31.0 | -25.0 |
| 1995 | 22.721 | 7.66 | 23.9 | -22.7 | 17.474 | 7.94 | 22.2 | -21.0 |
| 1996 | 26.217 | 8.05 | 22.2 | -21.5 | 19.683 | 8.52 | 20.9 | -19.8 |
| 1997 | 26.943 | 7.72 | 21.4 | -21.6 | 18.697 | 8.35 | 20.4 | -19.4 |
| 1998 | 29.123 | 8.60 | 22.1 | -20.0 | 20.210 | 9.05 | 21.4 | -18.3 |

The total number of all measured flashes for the ten years is 216 million of which 166 million flashes occurred within the US borders. The efficiency of the network increased slightly from 1989 to 1992 as improvements were made in the network processing of data. In 1993-94 the NLDN went through an upgrade in the instrumentation (Cummins et al. 1998) that increased the detection efficiency and resulted in higher flash counts (Idone et al. 1998a, b; Wacker and Orville 1999a, b). The higher values in 1993 before the upgrade, however, may be largely the result of the high number of thunderstorms in the Midwest that produced extensive flooding in the Midwest. The maximum lightning flash density in 1993 was in the Midwest as opposed to Florida, which usually has the highest density (Orville and Silver 1997).

Figure 2 summarizes the results for contouring the ten years' of lightning data for the period 1989 through 1998. In Figure 2a, we plot the measured mean annual flash density and display it in six gray shades, from less than 0.1 to over 9 flashes/km$^2$/yr. The highest values are in Florida, along the Gulf Coast and in the Midwest. The lowest flash densities occur along the West Coast. Note the lower flash densities over the Appalachian Mountains in Virginia and West Virginia and higher flash densities all around this geographical feature.

In Figure 2b we see the distribution of the percentage of positive flashes for the ten-year period. The most significant feature of this distribution is the high values in the upper Midwest, from Colorado to Minnesota and the Canadian border. Values exceed 20% through much of this area. We note that this is the area in which "sprites" were first discovered by Winckler et al. (1993) and subsequently studied in detail by Sentman and Westcott (1993) and Lyons (1994, 1996). Areas with a high percentage of positive lightning appear to be a favored region for the observation of sprites.

Median peak positive current for cloud-to-ground flashes are contoured and displayed in Figure 2c. The highest peak currents, over 35 kA, occur in the upper Midwest, along the West Coast from the states of California to Washington, and over the Appalachian Mountains in West Virginia and Virginia. The lowest values, in contrast, are observed in Florida and in general in the southeastern part of the United States.

Figure 2d is a summary of the ten-years of median peak negative current for the continental United States. We see high values, exceeding 25 kA, along the Gulf Coast from Texas to Florida. Regions of high peak negative current also occur over the Appalachian Mountains and along the West Coast. The lowest peak negative currents are observed in the western Carolinas and are probably caused by the higher detection efficiency of the close IMPACT sensors shown in the call-out in Figure 1.

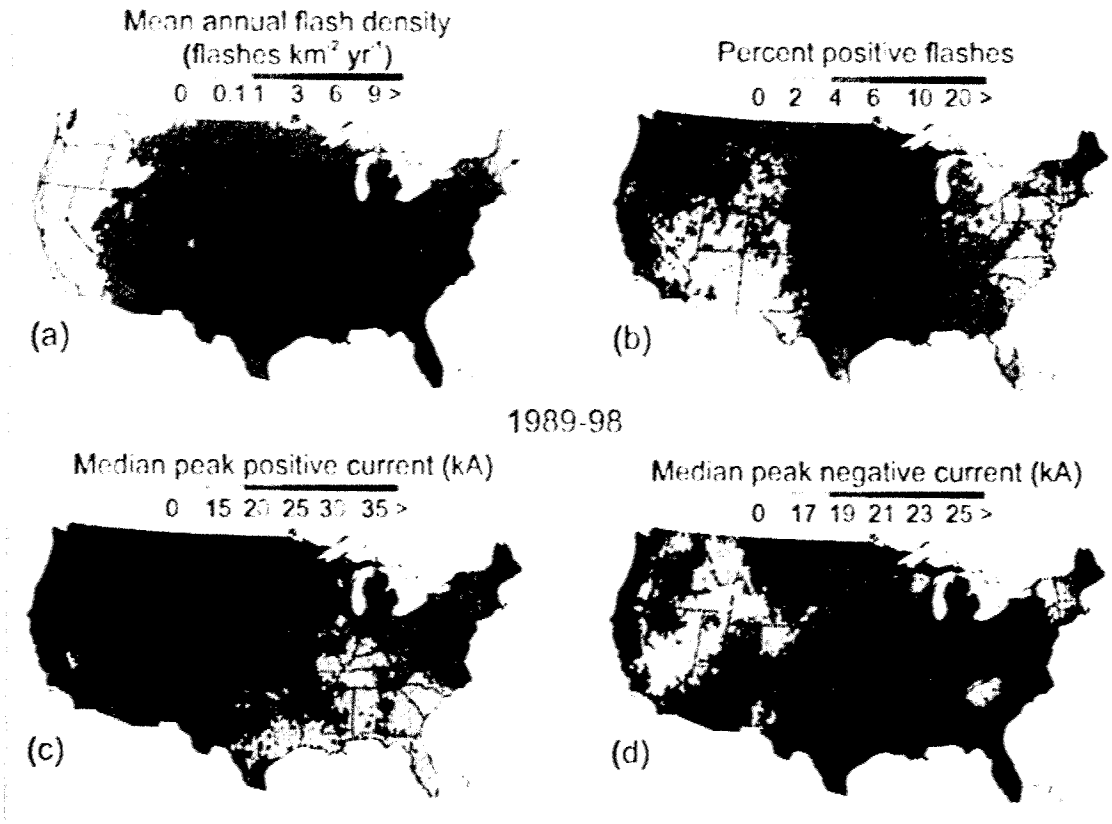


Figure 2. Summary of CG lightning characteristics for the ten years from 1989 through 1998. The mean annual flash density (a) indicates a consistent minimum in CG flashes over the Appalachian Mountains and a maximum over Florida. The percentages of all flashes that are positive (b) have a maximum over the Plains and minimum values in the Southeast and Southwest. This maximum in percent positive flashes matches with the maximum of median peak positive current, (c), in the Plains. The maximum median peak negative current, (d), can be found along the Gulf Coast, Florida and along the East Coast. All calculations use a grid size of 0.2 degrees latitude and longitude.

## 4.Conclusions

We have presented the results of ten-years of observations of cloud-to-ground lightning in the continental United States representing an area of approximately 7.6 million km$^2$. The variations within the year and from year to year have been masked by this large summary of an entire decade. Nevertheless, the persistent variations are apparent. These include (1) the high flash densities along the Gulf Coast, (2) the high percentage of positive flashes in the upper Midwest, (3) the high peak positive

currents in the upper Midwest and the lowest values in the Southeast, and (4) high peak negative currents along the Gulf Coast and in Florida. A geographical effect on lightning appears to occur in association with the Appalachian Mountains in that, there is a lower flash density, a higher percent positive flash density, a higher peak positive current. Detailed studies of these observations in association with the meteorological conditions may provide clues to the causes and these studies are in progress.

**Acknowledgment**

The lightning data were obtained from the Global Atmospherics, Inc., Tucson, Arizona. The interest and assistance of Ken Cummins are greatly appreciated. Data handling at Texas A&M University is under the direction of Jerry Guynes and we thank him for his assistance. This research is part of a lightning program supported by the National Science Foundation (ATM-9806189) and the National Oceanic and Atmospheric Administration (cooperative agreement NA87WA0063).

**References**

Cummins, K. L., M. J. Murphy, E. A. Bardo, W. L. Hiscox, R. B. Pyle, A. E. Pifer, 1998: A combined TOA/MDF technology upgrade of the U.S. National Lightning Detection Network, *J. Geophys. Res.*, **103**, D8, 9035-9044.

Idone, V. P., D. A. Davis, P. K. Moore, Y. Wang, R. W. Henderson, M. Ries, and P. F. Jamason, 1998a: Performance evaluation of the U.S. National Lightning Detection Network in eastern New York; Part I: Detection efficiency, *J. Geophys. Res.*, **103**, D8, 9045-9055.

Idone, V. P., D. A. Davis, P. K. Moore, Y. Wang, R. W. Henderson, M. Ries, and P. F. Jamason, 1998b: Performance evaluation of the U.S. National Lightning Detection Network in eastern New York; Part II: Location accuracy, *J. Geophys. Res.*, **103**, D8, 9057-9069.

Lyons, W. A., 1994: Low-light video observations of frequent luminous structures in the stratosphere above thunderstorms, *Mon. Wea. Rev*, **122**, 8, 1940-1946.

Lyons, W. A., 1996: Sprite observations above the U. S. High Plains in relation to their parent thunderstorm systems, *J. Geophys. Res.*, **101,** D23, 29641-29652.

MacGorman, D. R., Burgess, D. W., Mazur, V. Rust, W. D., Taylor, W. L., Johnson, B. C., 1989: Lightning rates relative to tornadic storm evolution of 22 May 1981, *J. Atmos. Sci.*, **46**, (2), 221-250.

Orville, R. E.: 1991: Lightning ground flash density in the contiguous United States-1989, *Mon. Wea. Rev*, **119**, 573-577.

Orville, R. E. 1994, Cloud-to-ground lightning flash characteristics in the contiguous United States: 1989-1991, *J. Geophys. Res.* **99**(D5), 10833-10841.

Orville, R. E. and A. C. Silver: 1997: Lightning ground flash density in the contiguous United States: 1992-1995, *Mon. Wea. Rev.*, **124**, 4, 631-638.

Orville, R. E. and G. R. Huffines, 1999: "Lightning ground flash measurements over the contiguous United States: 1995-1997, *Mon. Wea. Rev,* **127**, In Press.

Sentman, D. D. and Westcott, E. M., 1993: Observations of upper atmospheric optical flashes recorded from an aircraft, **20**, (24), 2857-2860.

Wacker, R. S. and R. E. Orville, 1999a: Changes in Measured Lightning Flash Count and Return Stroke Peak Current after the 1994 U. S. National Lightning Detection Network Upgrade, Part I: Observations, *J. Geophys. Res.*, **104**, D2, 2159-2162.

Wacker, R. S. and R. E. Orville, 1999b: Changes in Measured Lightning Flash Count and Return Stroke Peak Current after the 1994 U. S. National Lightning Detection Network Upgrade, Part II: Theory, *J. Geophys. Res.*, **104**, D2, 2151-2162.

Winckler, J. R., R. C. Franz, and R. J. Nemzek, 1993: Fast low-level light pulses from the night sky observed with the SKYFLASH program, *J. Geophys. Res.*, **98**, D5, 8775-8783.

# VERTICAL PROFILE OF SPACE CHARGE NEAR GROUND SURFACE ESTIMATED WITH CORONA CURRENT

K. Narita[1], Y. Goto[2], N. Takeuchi[3], N. Honma[4] and N. Suzuki[4]

[1] Miyagi Polytechnic College, Tsukidate, Miyagi, 987-2223, JAPAN
[2] Tohokugakuin University, Tagajyo, 985-0873, JAPAN
[3] Tohoku University, Sendai, 980-8579, JAPAN
[4] Tohoku Electric Power Co., Inc., Sendai, 981-0952, JAPAN

ABSTRACT: To investigate a winter thunderstorm, we have been acquiring data on the corona currents through the needle point electrodes from the 1972 winter season at the west coast of Japan. We prepare three needle electrodes, and they are installed at the different altitudes of 4.5m, 8.5m and 21m. The corona current signals are terminated at the pen-recorder which is controlled by the personal computer, and collected in the Hard Disk Unit. The corona currents at lower altitude are changed mainly within the same minus polarity, on the other hand, that current at 21m height are oscillated to both polarities. That's reason will be contributed by the space charge near the ground surface.

## INTRODUCTION

In winter season, the charge regions in the thundercloud are observed at very low altitude along the west coast of Japan. It leads to high electric field under thunderclouds, in spite of no lightning discharges (*Uyeda, et al., 1996, Michimoto and Shimura, 1996*).

The corona currents could be used to estimate the electric field under thunderclouds. While the space charges affect seriously corona measurement. However, its effect can be reduced by mounting the needle at 20 meters above ground (*Markson and Anderson, 1988*). Moreover, its effects were also calculated in detail (*Chauzy and Rennela, 1985, Markson, Anderson, Govaert and Fairall, 1989*).

We have observed a winter lightning at the west coast of Japan. Among the measurements of winter lightning, which hit the tower for acquiring meteorological elements, there are the images of lightning channels. In order to take efficiently the images of accidental lightning, automatically driven video camera system has been used since the winter of 1984. The recording of this system is initiated with the lightning sensor as a needle corona electrode. It starts automatically when the corona current exceeds a certain level and is operated to record for a preset period (*Goto and Narita, 1989*). From the beginning, the system uses a couple of needles at 21meters. We are planning to replace the tall needle with the lower needle, because of difficult maintenance of this tall needles. Then the corona currents through three needles have been measured concurrently.

## OBSERVATION SITE

The corona currents are measured at Maki in Niigata Prefecture as shown in Figure 1. This site is located about 100m inland from the coast of Japan Sea, and its altitude is 10m above sea level. The area around this site is surrounded with tall bamboo grasses, which are 1 or more meters high. Consequently, they produce many space charges.

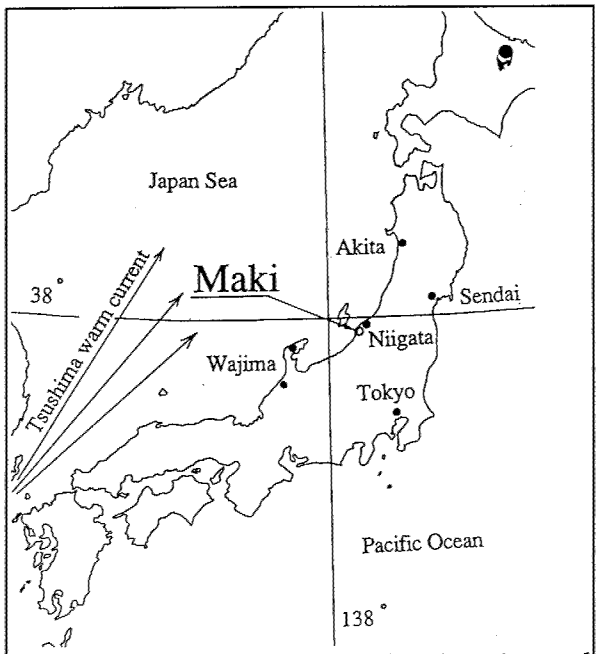


Figure 1. Map showing the location of observation site.

## NEEDLE ELECTRODE

Two kinds of needle are used. One is made from copper, 6mm in diameter and the tip is sharpened. Another one is made 3mmϕ stainless steel rod. Therefore each time constant are 6ms. Three needles are installed at the different altitudes of 4.5 meters, 8.5 meters and 21 meters. Figure 2 shows the profiles of each needle. The corona currents are estimated with the potential drop along the 150kΩ resistance, connected parallel with a 40μF capacitance avoiding small oscillations. The corona current signals are terminated to the pen-recorder which is controlled by the personal computer, and recorded in the Hard Disk Device. Data are collected every one seconds.

## RESULTS

Figure 3 shows time series of corona current variations derived from needle electrodes. The corona current at 21m heights is divided in half to one needle because of using a couple of needles. In order to each line is drawn separately, the current at 21m is added 1μA. On the other hand, the current at 4.5m is subtracted 1μA. The upper line is the corona current derived from the needle at heights of 21 meters, the middle line is the current at 8.5 meters and lower line is at 4.5m.

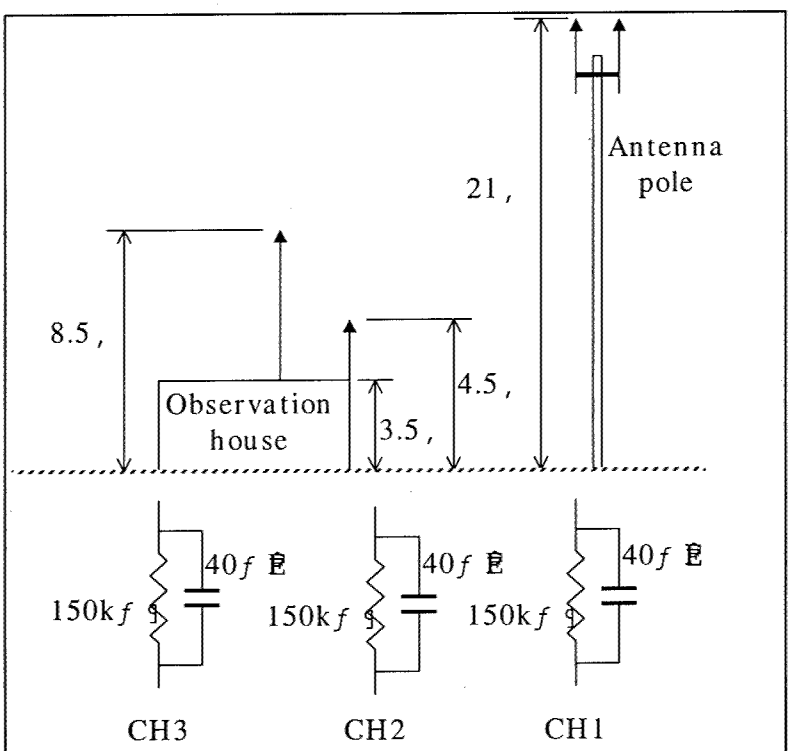


Figure 2. Schematic configuration of needle electrodes.

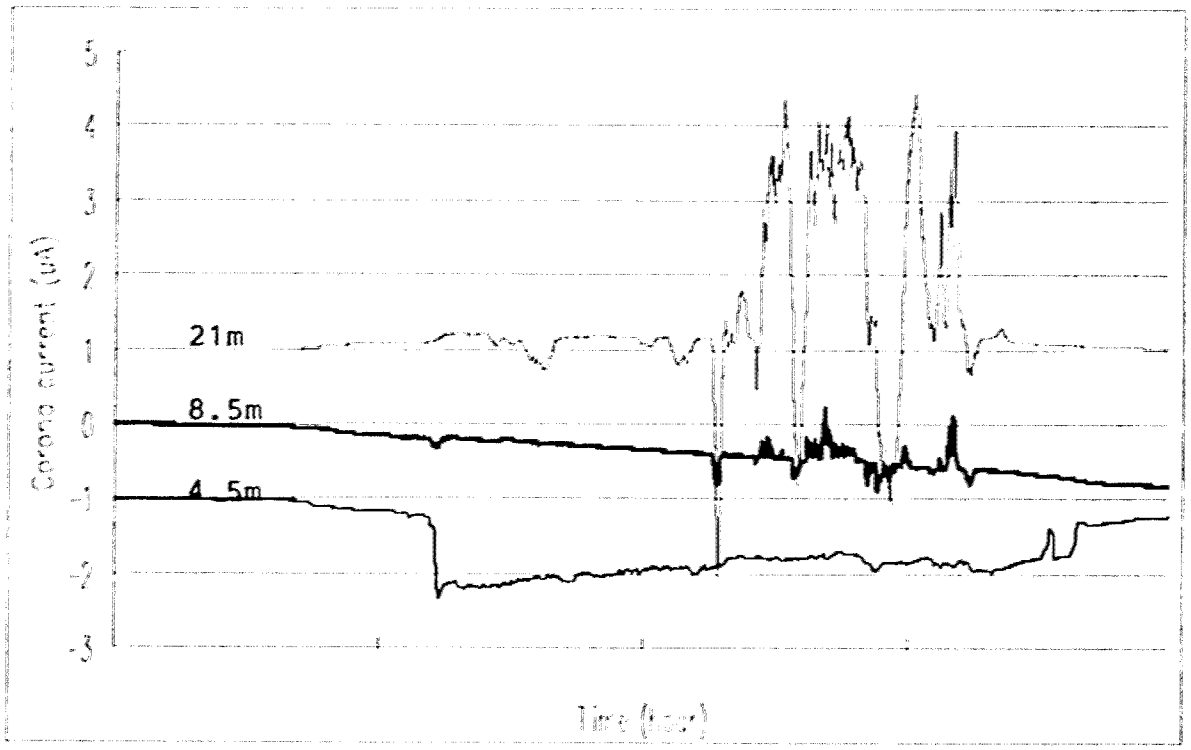


Figure 3. Corona currents from needle electrodes at heights of 21m, 8.5m, and 4.5m. The 21m data are added 1μA and the 4.5m data are subtracted 1μA for indicating each lines separately on the graph. (January 25, 1999, from 0:00 to 4:00 JST)

## DISCUSSION

As shown in figure 3, it seems that the corona current derived from the lower needle is biased to a negative region. Ordinary, a space charge near the ground suppresses or enhances surface electric fields. However, the obtained corona current from lower needle is dissimilar to the current from the tall needle.

At this stage, we can not imagine how many the space charge affects the corona current through the needle overspread by space charges and how many the wind affects it. According to make clear, another electrode has been installed at 6.5m altitude on January, 1999. Moreover, an anemometer has been added to the measurement.

## REFERENCES

Markson, R. and B. Anderson, New electric field in instrumentation and the effects of space charge at Kennedy Space Center, *Proc. 1988 Conf. on Lightning and Static Elect.*, Oklahoma City, 1988.

Markson, R., B. Anderson, J. Govaert and C. W. Fairall, Cparison between field mill and corona point instrumentation at Kennedy Space Center: use of these data with a model to

determine cloudbase electric fields, *Proc. 1989 Conf. on Lightning and Static Elect.*, University of Bath, UK, 1988.

Chuzy S. and C. Rennela, Computed response of the space charge layers created by corona at ground level to external electric field variations beneath a thundercloud, *J. Geophys. Res.*, 90, 6051--6057, 1985.

Goto Y. and K. Narita, The characteristics of winter lightning strokes to an isolated tower observed with automatically driven video camera system, *Res. Lett. Atmos. Electr.*, 9, 73--80, 1989.

Michimoto K. and T. Shimura, Relation between lightning activity of thunderclouds and surface electric field variation in the Hokuriku district, Japan, *Proc. 10th Int. Conf. on Atmospheric Electricity*, Osaka, Japan, 580-583, 1996.

Uyeda H., T. Otsu, H. Kagaya, Y. Asuma, K. Kikuchi, Z-I. Kawasaki and Y. Sonoi, Characteristics of winter thunder clouds observed by a dual-polarization doppler radar around Wakasa bay, west coast of Japan, *Proc. 10th Int. Conf. on Atmospheric Electricity*, Osaka, Japan, 568-571, 1996.

# OPTICAL OBSERVATIONS OF LIGHTNING IN NORTHERN INDIA, HIMALAYAN MOUNTAIN COUNTRIES AND TIBET

W. L. Boeck[1], D. Mach[2], S. J. Goodman[2], H. J. Christian, Jr[2]

[1] Niagara University, Niagara University, NY
[2] Global Hydrology and Climate Center, Huntsville, AL

ABSTRACT: This study summarizes the results of an analysis of data from the LIS instrument on the TRMM platform. The data for the Indian summer monsoon season is examined to study the seasonal patterns of the geographic and diurnal distribution of lightning storms. The storms on the Tibetan plateau show a single large diurnal peak at about 1400 local solar time. A region of Northern Pakistan has two storm peaks at 0200 and 1400 local solar time. The morning peak is half the magnitude of the afternoon peak. The region south of the Himalayan Mountains has a combined diurnal cycle in location and time of storm occurrence.

## THE DATA BASE

The focus of the study is an area of Asia bounded by 20° to 37.5° North and 65° to 100° East (Figure 1). This region includes portions of India, Pakistan, Afghanistan, Tibet, China, Bangladesh and Burma. Within this region is an arc of mountains, the Himalayan chain, including the Hindu Kush and Karkoram range. The regional weather pattern is dominated by the southwest Monsoon season. The span of dates chosen for this study are from June 16, 1998 to September 30, 1998. The dates were set to begin the study at the time the monsoon moisture reached the Himalayan Mountain range in Nepal. Storms were observed on all days between day 167 and day 273 with few exceptions.

The data set from LIS includes the UTC time, the latitude and longitude of the centroid of a storm area, the elevation of that location and summary measurements of the storm properties during the brief time it was within the

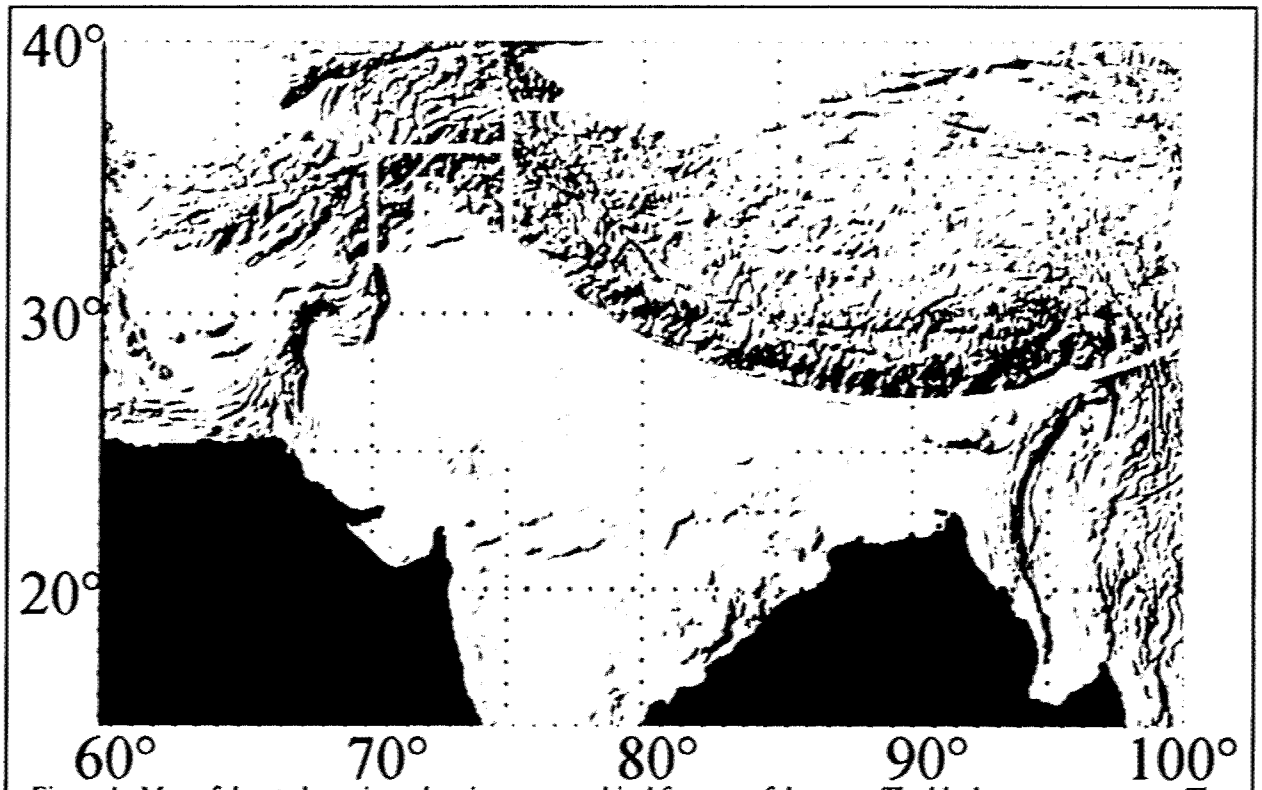


Figure 1. Map of the study regions showing topographical features of the area. The black areas are oceans. The Pakistan region is labeled "P" and is 32° to 36° North and 70° to 75° East. The Tibet region is labeled "T" and is an arc containing most of the Himalayan mountain chain. The India region is labeled "I" and contains the area from 25° to 36° North and 75° to 85° East not in the Tibet region.

LIS field of view. The optically measured storm area properties are the total radiance of all lightning, the duration of lightning activity, the number of flashes and a flash rate derived by dividing the flash count by the view time of an individual area. The lightning data set was partitioned both geographically and temporally.

The geographical regions are shown in Figure 1. Although there can be several countries in a section, each range is given a single label. The large arc region that includes most of the Himalayan mountain range is defined as Tibet. The Himalayan mountain chain is an arc that can be approximated by a circle centered on 40° North, 90° East (40N90E). The box region from 32° to 36° North and 70° to 75° East is defined as Pakistan while the box region from 25° to 36° North and 75° to 85° East not in the Tibet region is defined as India. All 24 hours of data are contained in each of the three subsets.

A second partitioning by local solar hour provides 4 data subsets, one for each 6-hour interval. The divisions are 0000 to 0600, 0600 to 1200, 1200 to 1800, 1800 to 2400. Local solar time was chosen to determine any solar heating patterns in the lightning data. Each temporal subset contains data from all three geographic regions.

RESULTS

Figures 2 and 3 present map plots of the locations of observed storms in the monsoon season of 1998. Figure 2 shows the LIS detected storms during the 0600 to 1200 local solar time. Solar heating is beginning to force convection as the afternoon approaches. There is very little storm activity in a band south of the mountains in Nepal

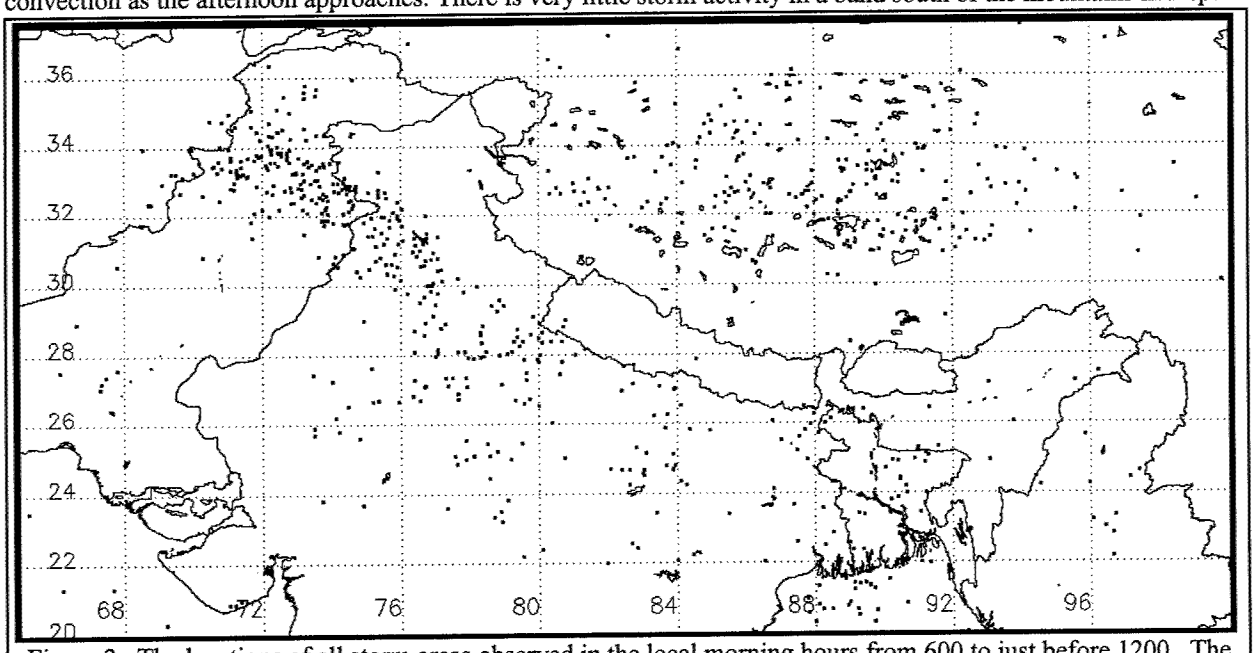


Figure 2. The locations of all storm areas observed in the local morning hours from 600 to just before 1200. The points are the LIS areas while the lines show the local political boundaries. The numbers along the left side of the plot are the North latitude values and the numbers along the bottom are the East longitude values.

and Northern India. The most active locations for storms are in Pakistan near 33° North, 73° East.

Figure 3 plots the locations of all storm areas observed during the local hours of 1200 to 1800. The plot shows the development of thunderstorms during the local afternoon. Note there are several areas with very few storms. These low storm areas include the oceans, deserts and high mountains. The lower left corner from 24° North, 65° East to 20° North, 70° East is the Arabian Sea. A portion of the Bay of Bengal is found near 20° North, 90° East. There is an obvious lack of storms in the arc of the Himalayan Mountain chain extending from 36° North, 75° East to 29° North, 98° East. There are relatively fewer storms in several desert regions including the Great Indian Desert from 27° North, 68° East to 30° North, 72° East and a portion of Afghanistan near 32° North, 68° East.

The storm diurnal cycle for the Tibet region is shown in Figure 4. There is a strong afternoon peak from 1400 to 1700 local time. The peak storm counts are more than 30 times greater than storm counts during the early morning. The data set is from days 167 to 273.

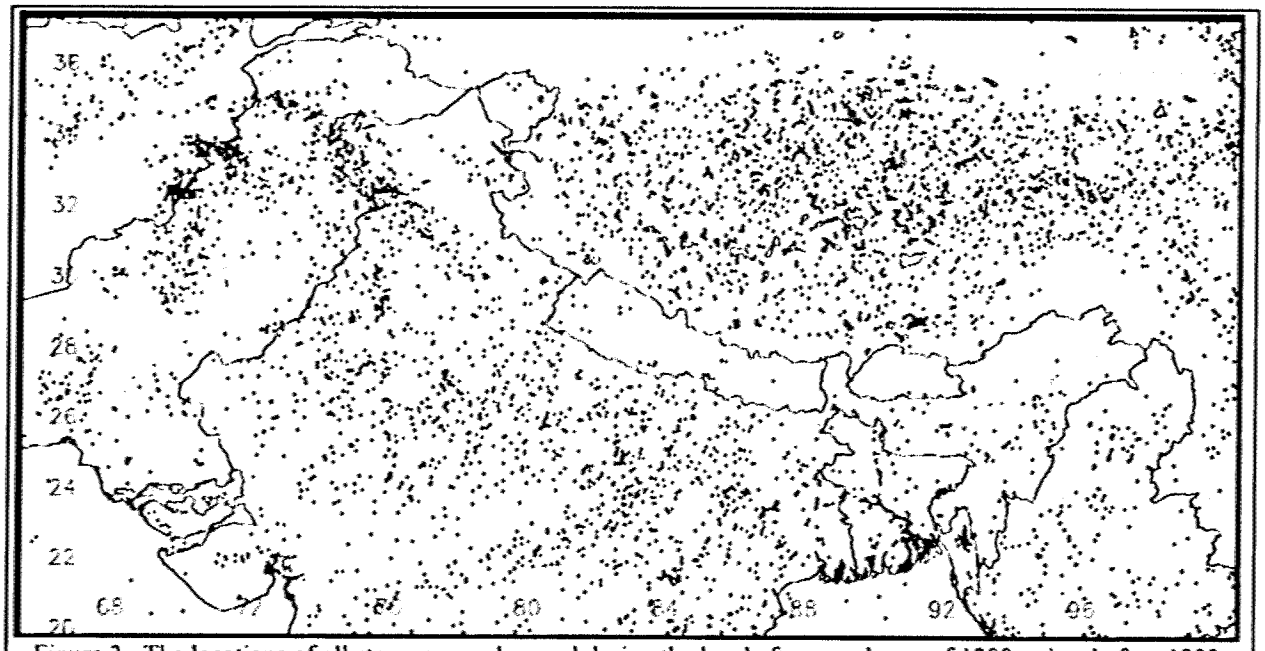


Figure 3. The locations of all storm areas observed during the local afternoon hours of 1200 to just before 1800. The points are the LIS areas while the lines show the local political boundaries. The numbers along the left side of the plot are the North latitude values and the numbers along the bottom are the East longitude values.

The storm diurnal cycle in the Pakistan region is very different from that of Tibet. Figure 5 shows a secondary peak at 300 to 400 local hours that is about 1/2 size of the afternoon peak. Because the orbital period of TRMM is about 90 minutes, data displayed in hourly bins will contain some aliasing. However, the two peaks are nevertheless real and the data represents most features of the diurnal cycle for this location from 32° North to 36° North and 70° East to 75° East.

The diurnal cycle of storms in the India region is more complex. Figure 6 is a scatter plot of terrain elevation beneath the storm vs. local solar time for each storm in the India region. There are no observed storms in the mountain regions with terrain elevation from about 5000 m to the mountain peaks above 8000 m. During the afternoon hours, however, some storms can be found in mountainous areas with elevations of up to 5000 meters. During the morning hours from 800 to 1200 there are very few storms at any elevation above 500 meters. This plot suggests there is a diurnal variation of the preferred location for storm in this geographical area.

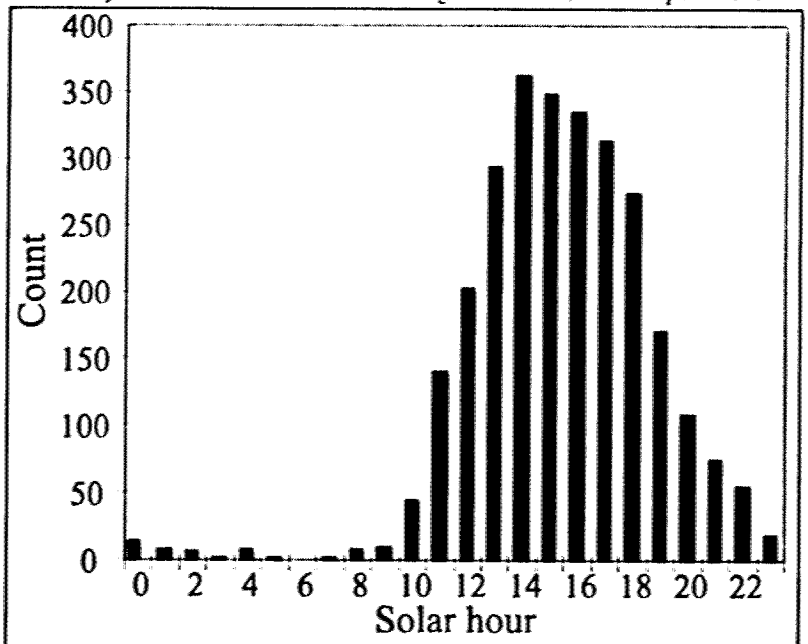


Figure 4. The storm diurnal cycle for the Tibet region.

Figure 7 is a contour plot of storm counts as a function of solar hour and distance from the edge of the India/Tibet regions boundary within the India region. There seems to a boundary of storm activity that moves upward in elevation toward the mountains (smaller values of range) during afternoon hours and recedes after dark for a total daily geographic variation of perhaps 100 km. The peak thunderstorm activity at all hours is found at a range of about 150 km from the front range peaks of the Himalayan mountain chain.

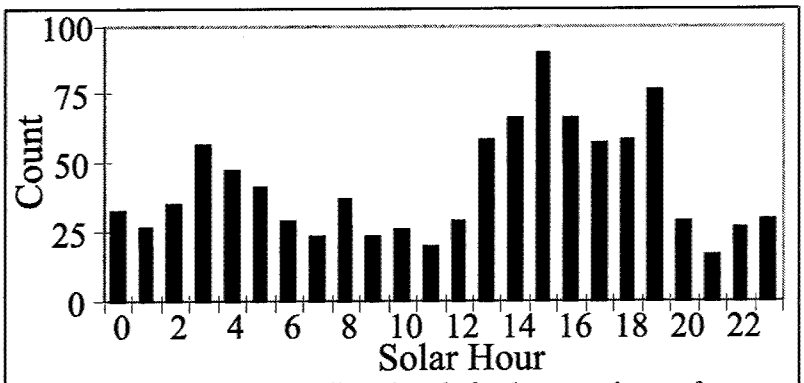


Figure 5. The storm diurnal cycle for the general area of Northern Pakistan.

stan at all hours. There is the expected afternoon peak and a significant second peak twelve hours later in the pre-dawn hours. There is dynamic support for convection many hours after sunset in addition to solar driven convection.

The storm patterns south of the Himalayan mountains near Nepal suggest the existence a mountain breeze front that moves upslope and toward the mountains during the afternoon and recedes to locations away from the mountains in a diurnal cycle.

This study illustrates the use of satellite data to identify preferred storm locations in mountainous regions that would be otherwise difficult to study. The TRMM orbit provides an 80 s snapshot of the lightning activity of a location about once a day. Although 80 s is not long enough to completely track the development of individual storms, over time, repeated measurements can be used to derive storm patterns. A search engine that will map LIS lightning flash data is available on the Internet. The data can be selected by geographic location, calendar month and daytime vs. nighttime. The URL is found at http://thunder.msfc.nasa.gov/query/STDsearchHTML.html.

SUMMARY

The time frame for this study was chosen to coincide with the southwest monsoon season and to exceed the 110 days necessary for repeat ground track coverage. Because the orbital period is about one and one half-hours caution is needed when interpreting storm counts in one-hour bins.

The storm observations on the Tibetan plateau are consistent with strong solar heating in the afternoon and a rapid cool down after sunset. Thunderstorms are found in northern Paki-

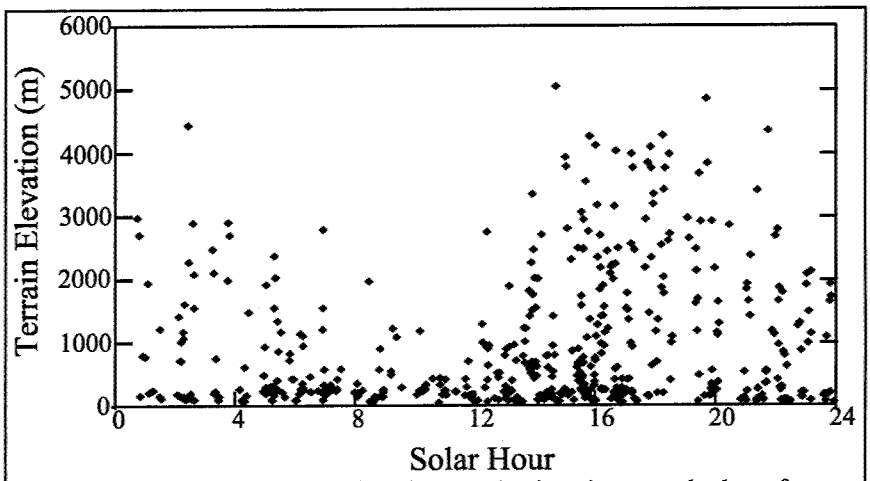


Figure 6. Scatter plot of storm location terrain elevation vs. solar hour for an area near the Himalayan Mountains.

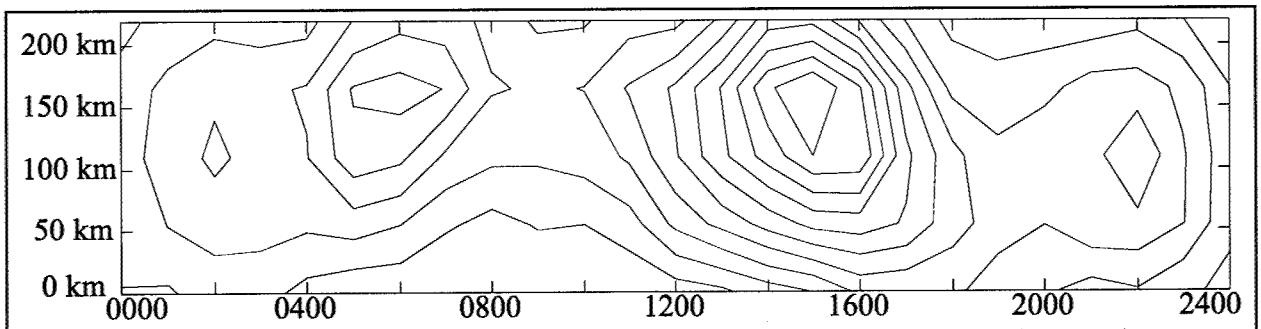


Figure 7. A contour plot of storm counts vs. range and solar hour for an area near the Himalayans. The range measurement is along the great circle line from the "center" of the Himalayan mountain chain, 40N90E. The 0 km distance is at the peaks of the Himalayan front range mountains. It is also the boundary between the India and Tibet regions discussed in the text.

# THUNDERSTORM DEVELOPMENT IN CONVECTIVE CLOUDS

A.Kh. Adzhiev[1], R.Kh. Kalov[1], S.M. Sizhazhev[1], M.B. Agzagova[1], and Kh.K. Kumykov[1]

[1] High-Mountain Geophysical Institute, Nalchik, KBR, RUSSIAN FEDERATION

ABSTRACT: The thunderstorm development in convective clouds is the important part in the thunder cloud theory. That's why it is necessary to make the complex investigation of the development of all electrical and non-electrical parameters of convective cloud. In this work we used the active-passive radiolocation of thunderstorms in $cm^{-1}$, dm-bands of wavelengths allowing us to receive the qualitatively new information on electrical state of cloud during its development. The received data allow to follow the change character of pulse-time characteristics of thunder activity in convective clouds at the natural development and seeding. It is shown that the reception of the non-thermal radio-emission from convective clouds in USW-bands of wavelengths allows to warn of the thunderstorm approaching long before the appearance of thunder discharges. Our studies showed that at the certain stage of development of convective cloud, when its upper boundary reaches the level of natural crystallization of cloud droplets, the pre-thunder electromagnetic radio-emission (EME) appears in it spontaneously.

When the convective cloud approaches to the upper boundary of radar echo at the -18...-35°C level and radar reflectivity of $6 \cdot 10^{-8}$ $cm^{-1}$ at 3,2 cm wavelength the transition of the cloud from pre-thunder stale into the slate of thunder activity occurs. The detailed investigation of change tendency of amplitude-frequency characteristics of ERE in the intervals between the lightning discharges was made. This investigation showed that the pulse duration of radio-emission increases with the approaching of the next lightning discharge. It was shown that the thunderstorm development in convective clouds has the gradual character. The increase of EME packets of lightning discharges, the frequency of appearance and time of existence of signals reflected from the ionized channels at the lightning discharge are the evidence of it.

## INTRODUCTION

The study of thunder-discharge events in clouds are carried out intensively for a long time, due to scientific and applied value of problem. At the present time there is a large volume of the data about the electrical events in clouds, in particular, about processes causing a beginning, intensity and duration of thunder-storms [1, 4, 6]. However there is no satisfactory agreement between experimental and theoretical results especially for processes of separation of electrical charges and discharge events. It is, apparently, because of absence of the reliable experimental data of complex researches of the discharge events in clouds.

The data obtained by methods of an active and passive radar-location of thunder centers in medium- and short-wave frequency bands satisfy to the greatest degree to modern requirements in a research study of thunderstorm electricity of clouds in combination to usual observations of clouds with the help of weather radars.

THE MAIN RESULTS

The fulfilled researches [2, 3] have shown, that on the definite stage of development of convective cloud, when its upper boundary achieves a level of natural crystallization of water drops, in it spontaneously appears the pre-thunder electromagnetic emission (EME). In our opinion, the EME on this stage results from the development of the avalanche and avalanche-streamer processes between zones of electrical inhomogeneities. The researches of a moment of transition from pre-thunder stage into a stage of thunder activity, as a function of its thermodynamics, show, that the most informative parameter is the ratio of the supercoolled part of cloud to its warm part.

$$K = \frac{H_b - H_o}{H_o - H_k},$$

where $H_b$ is the height of upper boundary of cloud,

$H_o$ is the height of null isotherm,

$H_k$ is the height of condensation level.

So, for example, if this ratio is less 1.2, and maximum reflectivity ($\eta$) of cloud at 3.2 cm wavelength does not exceed $4 \cdot 10^{-8}$ $cm^{-1}$, than with probability 80 % in convective cloud the electrical discharges are absent capable to create the concentration of free electrons and ions with an effective reflecting surface, sufficient for achieving the reflected signal at the input of the receiver of radar with decimeter range, the sensitivity of which is $2.8 \cdot 10^{-14}$ W.

In 85 % of cases the transition of convective cloud from pre-thunder stage into the stage of thunder activity occurs if the ratio of width of the supercoolled part to width of warm part makes 1.2...1.5. At $K > 1.5$ and $\eta > 4 \cdot 10^{-8}$ $cm^{-1}$ in clouds, as a rule, the intensive lightning discharges take place.

In an initial stage of development of thunder events, when the sizes and density of volume discharges in inhomogeneous electrical structure of cloud are very small, the intra-cloud discharges have small-scale character. The duration of the pulse packet of radio-emission at this stage is of 10-15 ms with characteristic frequency of occurrence of 3-4 pulses per minute. In accordance with development of convective cloud the gradual growth of density of volume charges and intensification of thunder activity takes place. In particular, the intensity and duration of radio-emission is increased, the gradual transition of convective cloud into thunder state occurs. By researches of 1984-1995 is established, that the duration of pre-thunder state on time can achieve 16 min., with average value of 8 min. In 75 % of cases the duration of pre-thunder state of cloud is in the interval from 3 to 10 minutes. If for 14-16 minutes the cloud has not reached the thunder state, it dissipates as a rule.

In accordance with further development of convective cloud, when the upper boundary of radar echo reaches the temperature level of -18 ...-35°C and radar reflectivity at the wavelength of 3.2 cm obtains the value $6 \cdot 10^{-8}$ $cm^{-1}$ the cloud transit from pre-thunder state into state of

thunder activity takes place, i.e. the lightning discharges occur, fixed with the help of radar and in some cases visually.

We also carried out studies of modification of parameters of separate lightning discharges with the development of convective cloud. These studies showed, that during the cloud growth there is a modification of amplitude of the signal reflected from the ionized channel of lightning discharge and time of its existence, as well as the time, during which the ionized channel, after the lightning discharge, is an ideal reflecting surface for the electromagnetic wave of radar with decimeter range of wavelength. The latter characterizes the power of lightning discharge and amount of return strokes in it [5].

In the beginning of thunderstorm the durations of existence of the reflected signals from the ionized channel of lightning discharge makes 0.1...0.3 s. During the development of cloud there is a growth of its thunder activity and in mature stage the thunder discharges occur with the greater amplitude and duration of existence of the reflected signal (0.4...0.6 s), than in the beginning of the development. At this time from separate discharges appear the reflected signals with time of existence up to 0.8 s.

During the development of cloud the increase not only average time of existence of the reflected signal from the ionized channel of lightning discharge, but also the intensity of discharges occurs. The number of thunder discharges in unit of time, have reached the maximum in a middle of development of thunderstorm, gradually decreased. And the average time of existence of the reflected signal from the channel of lightning discharge is gradually increased and reaches the maximum in a stage of cloud dissipation.

## CONCLUSIONS

The characteristic feature of development of thunderstorm in convective clouds is the gradual increase of linear size of electrical charges. The increase of pulse packets of radio-emission of lightning discharges, the frequency of their appearance in cloud and the existence time of signals, reflected from lightning channels, can serve as evidences. As a result of change of cloud microstructure and turbulent pulsings the electrical discharges of different linear size appear, which are responsible for radio-emission with appropriate duration of pulse packets. The discharge intervals are gradually increased as the next discharge approached.

## REFERENCES

Adzhiev A. Kh., and E.M. Bogatchenko, Pulse-time characteristics of an electromagnetic emission of thunder clouds in decimeter range, *Physics of Atmosphere and Ocean*, 24, 9, 973-979, 1983.

Adzhiev A. Kh., Bogatchenko E.M. et al. A radar technical complex for study of thunder processes in clouds. - *Proc. VI Conference on Radiometeorology*, L, Hydrometeoizdat, 146-148, 1984.

Adzhiev A. Kh., Definition of intensity of thunder activity by radio engineering tools, *Electricity*, 11, 60-62, 1986.

Imyanitov I.M., Chubarina E.V., and Ya.M. Shvarts, An electricity of clouds, L, Hydrometeoizdat, 93, 1971.

Kachurin L.G., Divinski L.I. et al. An active-passive radar-location of thunder and thunder-dangerous centers in clouds, L, Hydrometeoizdat, 216, 1992.

Medaliev Kh.Kh., Sizhazhev S.M., and Kh.B. Kyarov, A research of some conditions of origin of thunder discharges in clouds, *Proc. VGI*, 24, 76-81, 1973.

# THE CHARACTERISTICS OF POSITIVE GROUND DISCHARGES OF TROPICAL THUNDERSTORMS AT IBADAN, NIGERIA.

Oladiran[1], E. O.; U. E. Akpan[2]; E.F. Numphas[3] and S. Israelsson[4].

1. Physics Department, University of Ibadan, Ibadan, Nigeria.
2. Physics Department, University of Uyo, Uyo, Nigeria.
3. Physics Department, Federal University of Agriculture, Abeokuta, Nigeria.
4. Department of Meteorology, Uppsala University, Uppsala, Sweden.

Topic: Lightning - Natural and Artificial.

## ABSTRACT

Positive ground lightning discharges were continuously recorded over a period of three years at Ibadan to supplement earlier composite records from 1987 by adapting the earlier design of Oladiran, et al. (1988a) using the shape of the radiation field signatures and the frequency components of positive discharges (Oladiran and Israelsson, 1990). We recorded a 92% discrimination between negative and positive ground flashes. The positive ground flashes were recorded at vlf and 17.3 kHz, 3dB attenuation and yielded an average 13 and 11.6% ratios for (+CG)/(-CG) respectively. Compared to our results of 1988, the flash-rate characteristics for positive ground flashes is not significantly different from those of negative ground flashes and it does not show any seasonal preference. This leads to the conclusion that the occurrence of positive and negative ground flashes depends only on the cloud charge structure, its dynamics and the ground conditions.

## 1. Introduction

The ground discharges, (CG) have been classified into two groups - (a) those that brings negative charges to the ground (-CG); and (b) those bringing positive charges to the ground (+CG). The physical and electrical manifestations of these two types of flashes are very distinct, vide (i) the radiation fields contain maximum energies at different peak frequencies (9.7kHz and 17.3kHz for (-CG) and (+CG) respectively at 3dB attenuation (Cooray, 1984; Oladiran et al 1988a). (ii) When the leader is followed by return strokes, the number of return strokes accompanying (-CG) is usually more than those accompanying (+CG), Bruce and Golde, 1942). (iii) The shape of the radiation fields for the two types of discharges are of different forms in shape, rise time, duration and frequency component (Kitagawa and Brook, 1960). (iv) The (+CG) carry a larger magnitude of charge to earth than the (-CG) (Rust, et al 1981). Consistent studies of the two types of CG's started at Ibadan in 1986 and consists of:

(a) (-CG) flashes as earlier reported in 1988 (Oladiran, et al, 1988b) using a new lightning flash counter and calibration circuit with improved discrimination of cloud and ground discharges to within 92% (Oladiran, et al 1988a). There are no contradicting evidences to the characteristics of (-CG) as earlier reported, though finer determinations of empirical constants can now be made. Weibull distribution is further confirmed as a strong mathematical tool for characterizing thunderstorm parameters.

(b) The spectral characterization as reported by Oladiran and Israelsson (1990): The highlight of the results are (1) the weather characterization of the tropical thunderstorms as shown in Table 1

TABLE 1: WEATHER CHARACTERIZATION OF LIGHTING SIGNALS

| Storm durat. hr | Max. & Mean rain rate mm.hr | Peak frq. range & Mean kHz | Aver. disch. per storm (ground) | No. of Sign Studies | % distn. of dur. | Peak field kv/m |
|---|---|---|---|---|---|---|
| 0 - 0.5 | max = 186<br>Av. = 92 | 8.4-14.2<br>Av. = 12.4 | 36 | 46 | 8 | 16 |
| 0.5 - 1.0 | max = 138<br>Av. = 67 | 6.8-20.6<br>Av. = 8.9 | 148 | 18<br>3 | 26 | 10<br>8 |
| 1 - 1.5 | max = 105<br>Av. = 52 | 10-15.3<br>Av. = 13.6 | 302 | 19<br>8 | 31 | 63 |
| 1.5 - 2.0 | max = 156<br>Av. = 43 | 9.3-21.8<br>Av. = 10.3 | 185 | 10<br>4 | 22 | 38 |
| > 2.0 | max = 122<br>Av. = 22 | 6.5-22.7<br>Av. = 7.8 | 87 | 83 | 13 | 13 |

(2) The fraction of (-CG) to cloud discharge was obtained as 14.2.
(3) For all signals monitored, only 2.3% of the flashes from thunderstorms were (+CG).

In this report further characterization of the (+CG) by direct measurement of ground flash density and the waveform characteristics of the accompanying spherics is made. A simple electrical circuit implementation for (+CG) counts is presented. The results are based on three years of continuous comparative recordings of counts and signal form of (+CG), (-CG) and the spharic signals.

## 2. EXPERIMENTAL ARRANGEMENTS:

Pisler and Oladiran (1985) have designed and constructed an instrument for time registration of flashes which stores 2000 flash events by date and time to the nearest 10ms interval. The flash count was also simultaneously made mechanically via a modified flash counter (Oladiran et al 1988a).

Spheric signals from a horizontal wire antenna elevated at 10m above the ground and 26m in length were simultaneously monitored and recorded on a channel of a transient storage oscilloscope. A coupling network as described by Oladiran and Israelsson (1990) was used to divide the signal from a plate antenna into two components to simultaneously activate the flash counter for mechanical counting and electronic occurrence time storage and also be recorded on the other channel of the transient storage oscilloscope, so that visual signal comparison of the various signals can be made. The digitized data is being prepared for rigorous computer-aided data comparison.

## 3. RESULTS AND DISCUSSIONS

Using results obtained from spheric signals at various frequencies, Table 2 shows the percentage distributions of (-CG) and (+CG). Table 2 is a low frequency characterization of discharges to the ground and the results can be summarized as follows:

(i) The percentage distributions are strongly dependent on the frequency at which one is monitoring the signal;
(ii) There is no significant weather dependence observed when flashes are monitored at low frequencies;
(iii) The average (+CG) to -CG) ratio was found to be 0.13.

Table 2: Groundflash characterization from Spheric Signals.

| Frequency Hz | Number of Flashes | Type of Flashes | |
|---|---|---|---|
| | | -CG | +CG |
| 1000 | 160 | 146 | 14 |
| 500 | 190 | 179 | 11 |
| 200 | 185 | 145 | 40 |
| 100 | 107 | 90 | 17 |

For measurements with lightning flash counters using the plate antenna and with a circuit peak frequency response at 17.3kHz and 3dB attenuation the following results were obtained:

(a) The rise time of the monitored radiation field lies within the range 0.4 - 20μs with a model frequency response range of 110 - 13.8 kHz and mean values of 2.4μs rise time and 17.3 kHz peak frequency response at 3dB attenuation respectively.

(b) No multiple recordings were observed from the counter as verified by the transient signal recording at a circuit response time of 0.26s.

(c) The diurnal variation of (+CG) showed a maximum at between 2100 LT and 2200 LT, while the minimum was situated between the local time range of 1400 LT and 1500 LT and a fractional distribution of 36% during the day and 64% during the night. The highest count rate of (+CG) was 105/hour between the hours of 2000 and 2200 LT.

(d) The number of thunderstorm days on which (+CG) occurred is 36 days on an annual average over a period of three years (1996 - 1998) with an annual count rate of 458/year as compared to an annual average of 24,850/year for (-CG) resulting in +CG/-CG ratio of 0.018 ≈ 2%. This is shown in Table 3. For each storm in which (+CG) occurred, the ratio,+CG/-CG, averages 11.6%

Table 3: Monthly Distribution of Annual Positive Ground Flashes

| | Jan | Feb | Mar | April | May | June | July | Aug | Sept | Oct | Nov | Dec |
|---|---|---|---|---|---|---|---|---|---|---|---|---|
| No. of thunder storms in days | 1 | 1 | 2 | 3 | 2 | 5 | 8 | 0 | 6 | 7 | 1 | 0 |
| No. of (+CG) | 1 | 2 | 14 | 10 | 21 | 58 | 79 | 0 | 108 | 165 | 3 | 0 |
| % Distribution | 0.2 | 0.4 | 3.1 | 2.2 | 4.6 | 12.7 | 17.3 | 0 | 23.6 | 35.4 | 0.7 | 0 |

We note that the annual average of the updated (-CG is not significantly different from our earlier report (Oladiran, et al 1988b) and that the effect of the august break as earlier observed by many workers (Oshodi, 1971; Osagbaede, 1987) is a consistent phenomenon of this region.

It is probable that the short rise times monitored for (+CG) (0.4μs to 6μs) would be directly related to the rise time of the accompanying currents. If this were so, then the degree of protection of properties offered by lightning protectors may not be adequate for (+CG) (Geophysics study Committee, et al 1986).

**ACKNOWLEDGEMENTS**

This research was supported by equipment grants from the International Science Programs, Uppsala University, Sweden through a cooperative research link with the Department of Physics, University of Ibadan, Ibadan, Nigeria.

**REFERENCES**

1. Oladiran, E. O.; E. Pisler and S. Israelsson (1988a). New lightning flash counter and calibration circuit with improved discrimination of cloud and ground discharges., IEE Proceedings, Vol. 135 ptA, 22-28.
2. Oladiran, E. O. and S. Israelsson (199). Spectral analysis of the lightning discharges at Ibadan, Proc. 1st All-Africa International Symposium on Lightning, Harare, Zimbabwe 30 April, - 4th May, 1990 pp6, Published by Zimbabwe Institute of Engineers.
3. Oladiran, E. O.; J. I. Aina and S. Israelsson (1988(b)). Lightning Flash-rate characteristics of the tropical thunderclouds, Proc. 8th ICAE, Uppsala, Sweden.
4. Coorary, V. (1984) Further characteristics of positive radiation fields from lightning in Sweden, J. Geophysics. Res. 89. p. 11807.
5. Nymphas, E. F. (1995). Very low freqnency atmospherics from distant sources, M.Sc. Dissertation, University of Ibadan, Ibadan, Nigeria.
6. Geophysics Study Committee; Geophysics Research Forum; Commission for Physical Sciences, Mathematics and Resources and the National Research Council (1986) National Academy Press, Washington D.C. pp 1 - 45.
7. Pisler, E. and E. O. Oladiran (1985). Time registration of event occurrence using SDK-85 Kit, University of Uppsala Institute of High Voltage Research, Sweden, UURIE 175 - 85.
8. Berger, K. (1967) Novel observation on lightning discharges, J. Frnaklin Institute, London, 283, 478-525.
9. Oshodi, R. F. (1971) A study of pentane normals of rainfall in Nigeria, Quart. Meterorol. Magazine, 1(4), 44-66.
10. Osagbaede, S.E. (1987). The effect of the tropospheric winds on the "little dry season", M.Sc., Dissertation, University of Ibadan, Ibadan, Nigeria.

# 3-DIMENSIONAL LIGHTNING AND DUAL-POLARIZATION OBSERVATIONS OF THUNDERSTORMS IN CENTRAL NEW MEXICO

W. Rison, R. Scott, R.J. Thomas, P.R. Krehbiel, T. Hamlin and J. Harlin

New Mexico Institute of Mining and Technology, Socorro, New Mexico, U.S.A.

ABSTRACT: Following its initial operation in Oklahoma, Tech's 3-dimensional Lightning Mapping System (LMS) was set up in August of 1998 over a 60-km diameter area around Langmuir Laboratory and the New Mexico Tech campus in central New Mexico. Preliminary results show that lightning activity in New Mexico storms has a simpler structure and smaller extent than in the larger Great Plains storms. Lightning discharges are also much less frequent in a storm, compared to the nearly continuous activity observed in Oklahoma. Intracloud (IC) lightning often has only a vertical channel but in more developed storms shows a clear bilevel structure, undoubtedly associated with the main negative and upper positive charge regions of the storm. These results agree with previous observations both in New Mexico and Florida.

Cloud-to-ground (CG) discharges often show considerable activity in a third region below the negative charge level, presumably associated with lower positive charge. The overall lightning activity exhibits a clear trilevel structure, consistent with the tripole model of storm electrification, and appears to map out the basic charge structure of the storm. Similar structures have been observed in the more complex Oklahoma storms. A few negative CG discharges originate in the main negative charge region, propagate up through the upper positive charge region, and then horizontally out of the upper positive region before going to ground.

Narrow positive bipolar (+BP) events, located by a Los Alamos sferics network (Smith et al., this conference) were also detected by the LMS. All the +BP events detected were the first RF events in an otherwise ordinary IC discharge. The RF power of the +BP events were 20 to 30 dB stronger than the RF power from any other part of a lightning discharge.

A few isolated events (RF radiation lasting less than 100 $\mu$s) were observed.

## INTRODUCTION

New Mexico Tech has developed a deployable instrument for mapping the total lightning activity of a storm in three spatial dimensions and time. The instrument, called the Lightning Mapping System (LMS), is based on the Lightning Detection and Ranging (LDAR) system developed and used at NASA's Kennedy Space Center. Tech's Lightning Mapping System consists of 10 stations deployed over an area about 60 km in diameter. Each of the remote stations detects and accurately times the peak intensity of RF radiation in a 6 MHz bandwidth centered at 63 MHz. The time and magnitude of the peak value of RF radiation events which exceed a noise threshold is recorded during every 100 $\mu$s time interval. RF radiation events that have a well-defined peak and are strong enough to be detected by at least six remote stations are located in three spatial dimensions and time.

Figure 1 shows received power vs. time for an event detected by the LMS. The vertical grid shows the 100 $\mu$s windows used by the LMS. The noise threshold is about -85 dBm. Using a 20 MHz digitizer phase-locked to GPS time, the time of the peak of the VHF radiation above the noise threshold is determined with an accuracy better than 100 ns. In the 1 ms of data shown, station C, for example, detected VHF radiation above threshold in two of the ten 100 $\mu$s windows. Between 995.9 ms and 996.2 ms each of the nine operational LMS stations detected VHF radiation from an impulsive event. From the data the time and location of the event can be determined. The vertical dashed line in Figure 1 shows the calculated time of the event. The $\chi^2$ calculated from the least-squares data analysis indicates that the timing errors of the analysis are less than 100 ns. The timing errors are a combination of system timing errors, source extent and source duration. Thus, most RF breakdown events come from source regions smaller than 30 m and with a duration of less than 100 ns.

A typical lightning discharge produces from 100 to 3,000 events locatable by the LMS. The system obtains accurate three-dimensional images of discharges (with location errors of about 50 m) over an area about 100 km in diameter and images of decreasing accuracy at further distances, with the latter images being primarily two-dimensional. Because negative streamers radiate more strongly than positive streamers, the system preferentially locates negative streamers propagating into positive charge regions, and the images produced tend to highlight the regions of positive charge in a cloud. A typical intracloud discharge imaged by the system is shown in Figure 2. The lower left plot of Figure 2 shows a plan view of the discharge. (The origin of the coordinate system is Langmuir Laboratory.) The two squares in the plan view show the

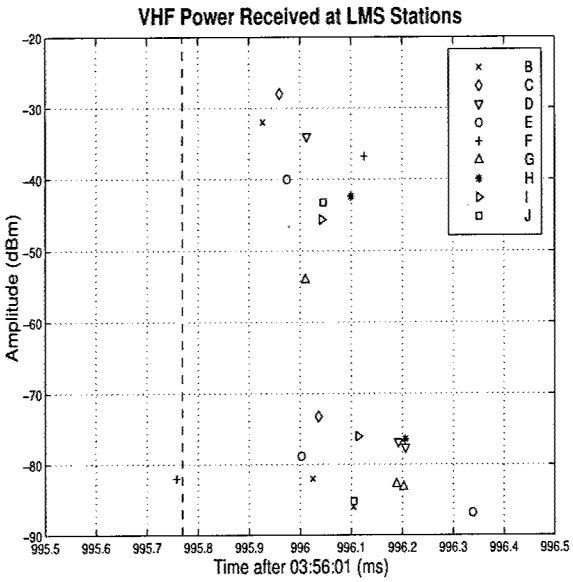


Figure 1. Power of VHF signal and time received at nine LMS stations. The dashed line is the actual time of the event which produced the VHF radiation.

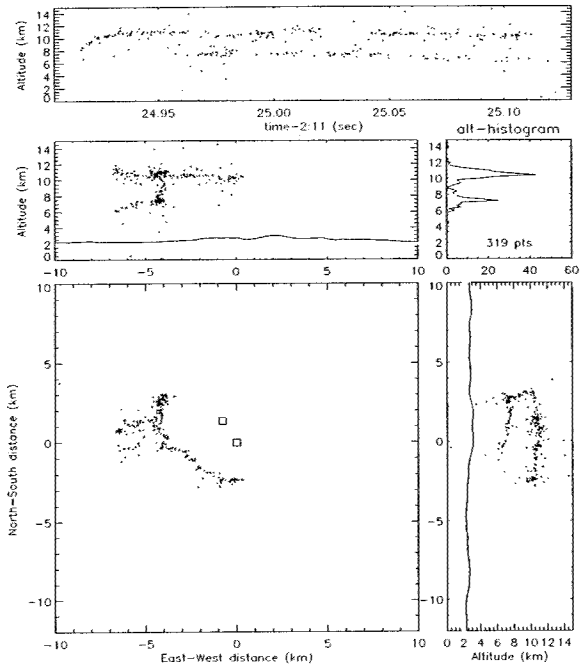


Figure 2. Isolated intracloud discharge imaged by the Lightning Mapping System. The squares show the location of two of the LMS stations.

locations of two LMS stations. The plots immediately above and to the left of the plan view show vertical cross sections of the discharge. The solid lines at about 2 km altitude in the cross sections show the local topography. The top plot of Figure 2 shows the time-evolution of the discharge with altitude. From this plot one can see that the initial negative streamer started at about 8 km and propagated up to about 11 km. This initial streamer was followed by streamers propagating horizontally in both the main negative and upper positive charge regions. The histogram shows the number of located points a function of altitude. This particular discharge had 319 locatable points. The located points clearly map out the main negative charge region of the cloud (between 6 and 8 km), and the upper positive charge region (between 10 and 12 km).

## INITIAL RESULTS

There are three particularly interesting results from early analysis of LMS data in New Mexico.

**1) Cloud-to-Ground Discharges.** Figure 3 shows a typical negative CG discharge observed by the LMS. The initial negative streamer started at 9 km and propagated downward. The LMS shows most locatable sources in the discharge in the 3 to 6 km altitude level, below the main negative charge region. These sources map an apparent lower positive charge region. The National Lightning Detection Network (NLDN) reported this as being a negative CG with 3 return strokes. The LMS clearly shows a negative leader at 03:50:39.52, and a second leader at 03:30:39.78. The three points at about 03:50:39.87 may represent a third leader to ground.

In addition to the typical CG's such as that shown in Figure 3, we observe negative CG discharges in which the lightning appears to propagate out of the upper positive charge region and progress to ground outside the cloud. Figure 4 shows such a discharge. This CG occurred in the same cell as and about 2 minutes after the discharge shown in Figure 3. (An IC discharge occurred in this cell between these two CG's.) The discharge shown in Figure 4 began about the same plan location as the CG in Figure 3 (5 km west and 32 km north of Langmuir Lab), with a leader propagating upward from the main negative charge region towards the upper positive charge region. The initial part of the discharge appears very similar to the IC discharge shown in Figure 2. However, rather than simply neutralizing positive charge in the upper region, a negative streamer came out of the upper part of the cloud, propagated horizontally towards the southwest, and continued on to ground about 5 km southwest of the part of the cloud where the discharge began. The NLDN reported a single-stroke negative CG at a location consistent with the LMS image.

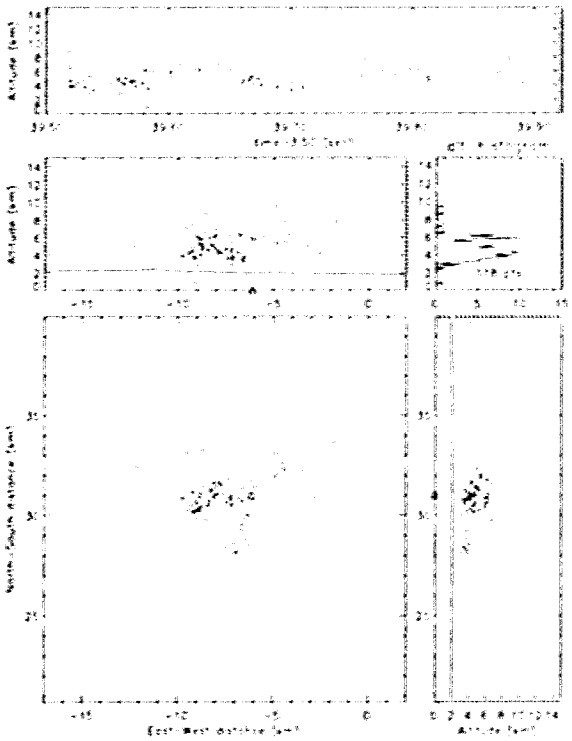

Figure 3. Normal cloud-to-ground discharge detected by the LMS. The Δ shows the location of the CG as detected by the NLDN.

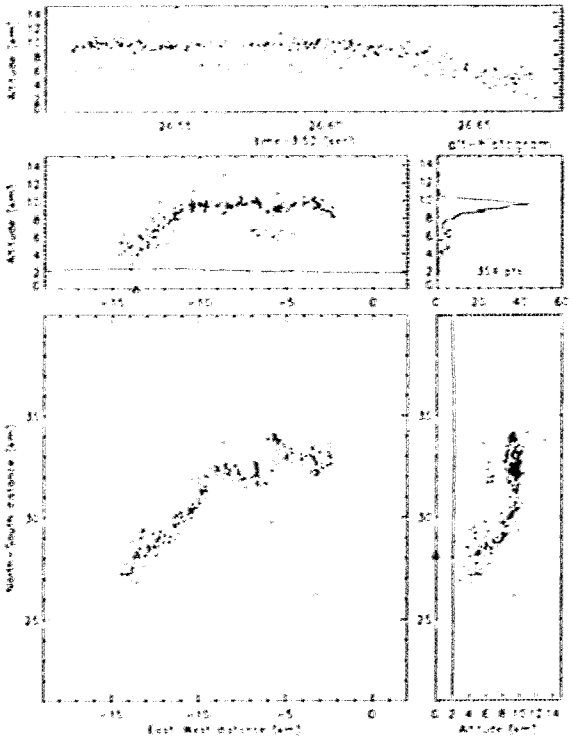

Figure 4. CG discharge with leader coming from upper region of cloud.The Δ shows the location of the CG as detected by the NLDN.

**2) Positive bipolar events** During the summer of 1998 Los Alamos National Laboratory operated a four-station sferics detection network in New Mexico, as discussed by Smith et al. elsewhere at this conference. From the four-station measurements, Smith et al. determined the time and location of +BP events. These events, first discussed by LeVine [1980] and Willett et al. [1989], consist of very large field changes of very short duration, and very strong RF radiation. The LANL sferics network detected several bipolar events in the vicinity of the LMS during a storm on 29-30 September 1998. Figure 6 shows the detected power as a function of time at the nine operating LMS stations. The LMS imaged lightning discharges associated with these nearby bipolar events. Figure 5 shows an LMS image of a lightning discharge which had a +BP as the initial located point. The LMS found several interesting characteristics for these +BP's:

- The VHF power in the +BP is 20 to 30 dB stronger than any other RF-producing event we have observed in a lightning discharge (Figure 6).
- For the storm on 29-30 September 1998, the LANL sferics network located 13 +BP events within 100 km of the center of the LMS network. For all of these events, the +BP's were the first RF radiation in otherwise ordinary IC discharges. Before the +BP the received RF at all LMS stations was at the noise level. After the BP, the next next locatable event follows in about two to six milliseconds.
- The data analysis shows that the +BP events are larger and/or longer than other impulsive events in lightning. Least-squares fit of the data from the nine or ten operational stations indicate that source region of the +BP events is on the order of a few hundred meters, and the +BP events have a duration of several hundred nanoseconds.

The IC discharges initiated by +BP events were preceded and followed by ordinary IC discharges in the same thunderstorm cell. Apparently, a +BP event is associated with electric fields much stronger than are present when an ordinary IC discharge is initiated. Whatever process initiates a lightning discharge is delayed, allowing the field strengths to increase. When a breakdown finally does occur, the fields are so strong that the breakdown involves a source volume a thousand or more times larger than the source volumes associated with ordinary RF-producing breakdown events. These larger source volumes probably consist of smaller breakdown regions, so the end result is incoherent RF radiation thousands of times stronger than the radiation from other events.

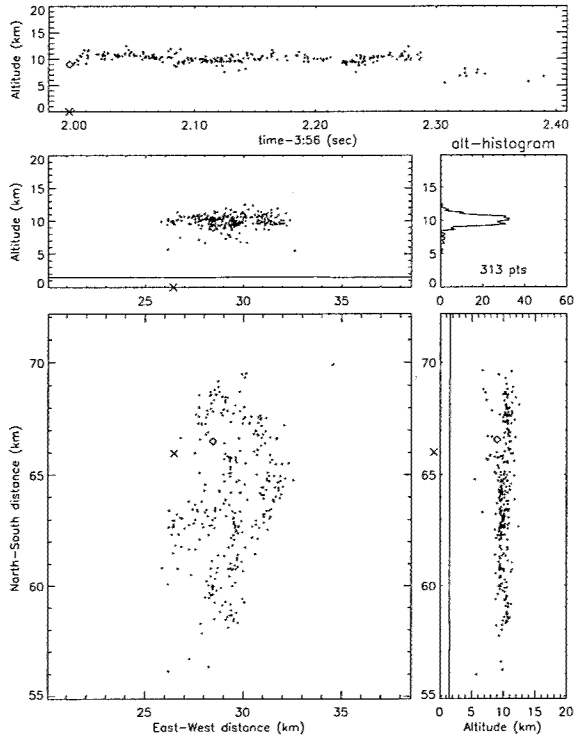


Figure 5. IC discharge initiated by a +BP event. The ◇ shows the location of the +BP as determined by the LMS. The × shows the location as determined by the LANL sferics array.

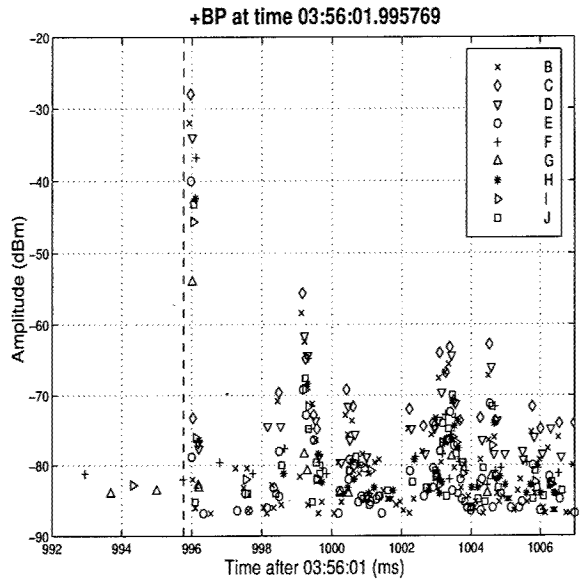


Figure 6. Raw LMS data for IC of Figure 5, showing difference in amplitude between +BP event and subsequent RF-producing breakdown events.

Brook [1992] observed that most IC discharges in winter storms in Albany, New York, were initiated by +BP events. These +BP events were often smaller in amplitude than field changes in the subsequent IC discharge, but often were much larger than any subsequent field changes. He also found leader durations of CG discharges were shorter than leader durations during summer thunderstorms, and suggested that the electric fields in these winter storms were exceptionally high. Our LMS results on bipolar discharges suggest that such exceptionally high fields can, on occasion, occur in summer thunderstorms, and give rise to the +BP events.

**3)** Isolated Breakdown. A few isolated points are observed in active thunderstorm cells. With the LMS, a single isolated point is due to RF radiation with a source duration of less than 100 $\mu$s. In all cases we have observed, each isolated point was followed in tens of seconds by an ordinary IC discharge originating at the location of the isolated point. Apparently the fields had built up to a strength which could initiate but not sustain a breakdown. After an attempted discharge, the fields continued to build until a full discharge could be sustained.

## RADAR COMPARISONS

For two storms we have good data from both the LMS and New Mexico Tech's dual-polarization radar. In addition to showing the reflectivity structure, the radar detects the presence of electrically aligned ice crystals and thereby remotely senses both the electric fields and the locations of significant ice crystal concentrations in storms. Work is in progress to compare the LMS data with 3-dimensional radar observations of storm structure.

## REFERENCES


Brook, M., "Breakdown Electric Fields in Winter Storms", *Res. Lett. Atmos. Electr.*, **12**, pp. 47-52, 1992.

LeVine, D.M., Sources of the strongest RF radiation from lightning, *J. Geophys. Res.*, **85**, 4091-4095, 1980.

Willett, J.C., J.C. Bailey, and E.P. Krider, A class of unusual lightning electric field waveforms with very strong high-frequency radiation, *J. Geophys. Res.*, **94**, 16,255-16,267, 1989.

# Characteristics of Cloud-to-Ground Lightning in the Contiguous U.S. from 1995-1997

Bard A. Zajac, Steven A. Rutledge* and Lawrence A. Carey

Department of Atmospheric Science
Colorado State University
Ft. Collins, CO 80523

*Corresponding Author and Presenting Author
Dr. Steven A. Rutledge
Rutledge@olympic.atmos.colostate.edu
970-491-8283
970-491-8449 (FAX)

## 1. Introduction

Convective storms play an important role in our society. In addition to producing beneficial rainfall, convective storms can also produce flooding, severe weather (e.g., tornadoes, hail, strong winds), and deadly lightning. Knowledge of the distribution of these weather phenomena in space and time can be used to 1) plan for the beneficial and destructive effects of convective storms, 2) understand what physical processes control the frequency of occurrence of convective storms, 3) forecast for convective storms, and 4) verify output from numerical models which resolve the effects of convective storms. For these reasons, climatologies of precipitation, flash floods, tornadoes, hail and strong winds, cloud-to-ground lightning, and thunder have been developed. These climatologies have documented significant spatial, annual, and diurnal variations in convective activity over the contiguous U.S. Interestingly, the diurnal variations in cloud-to-ground (CG) lightning activity have not been documented over the contiguous U.S. For this reason, the first goal of this study is to extend the national climatology of cloud-to-ground lightning and document the spatial, annual, *and diurnal variations* in CG lightning activity over the contiguous U.S. This study of CG lightning activity in the contiguous U.S. from 1995–97 compliments climatologies of convective activity in the contiguous U.S. and helps refine our knowledge of convective storms. The second goal of this study is to document the spatial, annual, and diurnal variations of positive cloud-to-ground lightning activity in the contiguous U.S. The documentation of these variations from 1995–97 provides a large-scale context for storm-scale studies of positive CG lightning. Case studies of convective storms have shown that positive CG lightning tends to be produced by: 1) dissipating non-severe thunderstorms, 2) dissipating severe storms, 3) convective and stratiform regions of mesoscale convective systems, and 4) positive strike dominated storms. The production of positive cloud-to-ground lightning is examined in greater detail over two case study areas located in the north-central U.S. (Sioux Falls, SD; KFSD) and along the Gulf Coast (Ft. Rucker, AL; KEOX). These two case study areas were chosen for specific reasons. The KFSD area was chosen because it is located within a region characterized by a high percentage of positive polarity lightning and by high positive peak current values. The KEOX area was chosen because it is located within a region where diurnally-forced convection tends to occur during the warm

season and synoptically-forced convection tends to occur during the cold season. Positive CG lightning activity over the KEOX area is compared between the warm and cold seasons. In both case studies, annual and diurnal variations in positive CG lightning activity are documented from 1995–97. Morphological and electrical characteristics of convective events which produce positive CG lightning over the two case study areas during 1996 are identified by comparing maps of low-level radar reflectivity with maps of CG strike locations.

## 2. Data and Method

The cloud-to-ground lightning data analyzed in this study was collected by the National Lightning Detection Network (NLDN). The NLDN is a lightning location network which comprises a network of 105 electromagnetic sensors, a satellite communications system, and a central processor. The NLDN records the time, location, polarity, peak signal strength, and multiplicity (number of return strokes per CG flash) of CG flashes detected over the contiguous U.S. Peak signal strength was converted to peak current using the following equation published in Orville et al. (1991):

$$I_{cur} = 0.2 \bullet I_{sig} \qquad (1)$$

where $I_{cur}$ is peak current in kiloamps (kA) and $I_{sig}$ is peak signal strength in LLP units. Data from 1995–97 were analyzed as a part of the national and case study analyses; data from June–August 1994–96 were analyzed as part of the national analysis of diurnal variations.

Radar data used in this study are national radar summaries produced by the WSI Corporation (a NOWrad™ product). Summaries are composites of low-level reflectivity scans collected by National Weather Service radars operational in the contiguous U.S. (e.g., 10–cm WSR-88D and WSR-57S radars and 5–cm WSR-74C radars). WSI maintains the quality of national radar summaries by using algorithms to remove ground clutter and other spurious reflectivity echoes. Summaries are produced every 15 minutes and have 8 km x 8 km spatial resolution. National radar summaries from 1996 were examined as part of the case study analysis.

## 3. Findings

The main findings of this study are:

1) Surface features such as elevated and depressed terrain, coastlines, and the Gulf Stream appear to control the location, amount, daily frequency, and timing of CG lightning activity. Maps of annual CG flash density, annual positive CG flash density, annual CG lightning days, and the normalized amplitude and phase of the diurnal cycle frequently show maximum located over elevated terrain in the western U.S. and over the Florida peninsula, the Gulf Coast, and the Gulf Stream.
2) Cumulative frequency distributions of daily CG flash count show a similar degree of skewness throughout the contiguous U.S.; 50% of cloud-to-ground lightning is produced on less than 15% of the days with cloud-to-ground lightning.

3) The majority of cloud-to-ground lightning is produced during summer over most areas in the contiguous U.S. with the exceptions of the south-central U.S. and the Pacific Coast.
4) Summertime cloud-to-ground lightning activity over the western and eastern U.S. is modulated by the diurnal cycle with an afternoon or early evening maximum.
5) Summertime cloud-to-ground lightning activity over the central U.S. is complex with significant longitudinal variations in daily activity. Daily CG lightning activity transitions from an afternoon regime over the western Great Plains to an afternoon-nocturnal regime over the eastern Great Plains and back to an afternoon regime over the lower Midwest and Mississippi Valley.
6) The percentage of positive polarity lightning reaches a minimum during summer over most areas in the contiguous U.S. with the exceptions of the northwestern and north-central U.S.
7) Three regional-scale signals are collocated over the north-central U.S.: a maximum in the percentage of positive polarity lightning, a maximum in mean positive peak current, and a region of negative time lag (i.e. negative CG lightning activity *lagging* positive CG lightning activity).
8) The production of positive cloud-to-ground lightning over the north-central U.S. is dominated by convective events which occur during summer and during late afternoon and evening. These events comprise thunderstorms, some of which produce predominantly positive CG lightning and are likely severe (i.e., positive strike dominated storms).
9) Positive strike dominated storms (PSD's) exhibit unique lightning characteristics including high percent positive polarity values, high mean positive peak current values, and low mean negative multiplicity values.
10) Positive cloud-to-ground lighting is produced throughout the year over the Gulf Coast, by diurnally-forced convection during the warm season and by MCSs with areally-extensive stratiform regions during the cold season.
11) MCSs and diurnally-forced convection exhibit different lightning characteristics along the Gulf Coast; MCSs (diurnally-forced convection) exhibit high (low) percent positive polarity values and high (low) mean positive peak current values.
12) A large population of low peak current positive CG flashes is observed over localized areas in the southeastern U.S. It is not known whether these flashes are real or false detections of intracloud lightning.

The most significant result of this study is the finding that positive strike dominated storms (PSD's) — which are usually severe — produced a significant portion of the positive cloud-to-ground lightning observed over the KFSD area during 1996. The implication of this result is that the three signals observed over the north-central Plains, these being the maximum in the percentage of positive polarity lightning, the region of negative time lag, and the maximum in mean positive peak current, may be associated with PSD storms. Results from the KFSD case study suggest that these signals 1) are related to the climatological lifecycle of convective activity over the north-central U.S. and 2) represent areas over which PSD storms dominate positive lightning production. More research on cloud-to-ground lightning activity over the north-central U.S. is needed in order to verify or refute this contention.

The identification of positive strike dominated storms in real-time using cloud-to-ground lighting data should be explored as a method for aiding the nowcasting of severe weather. Scientific evidence is building that most PSD storms produce severe weather and that PSD storms produce a significant portion of severe weather over certain regions in the United States. Carey et al. (1997) found that 37 and 45% of large hail and tornado reports in the central and northern Great Plains, respectively, are accompanied by greater than 50% positive polarity cloud-to-ground lightning. Also, the association of PSD storms with severe weather outbreak conditions (MacGorman and Burgess 1994), long-track tornadoes (Perez et al. 1997), and F5 tornadoes (Seimon 1993) should provide further motivation.

Acknowledgements: This research is supported by the Division of Atmospheric Science at the National Science Foundation. NLDN data were obtained from NASA/Marshall Space Flight Center.

References

Carey, L. A., S. A. Rutledge, and B. A. Zajac, 1997: An investigation of the relationship between severe storm reports and positive cloud-to-ground lightning. *Eos, Trans., AGU*, **78**, Fall Meeting Suppl., No. 46.

MacGorman, D. R., and D. W. Burgess, 1994: Positive cloud-to-ground lightning in tornadic storms and hailstorms. *Mon. Wea. Rev.*, **122**, 1671–1697

Orville, R. E., R. W. Henderson, and L. F. Bosart, 1991: Calibration of a magnetic direction finding network using measured triggered lightning return stroke peak currents. *J. Geophys. Res.*, **96**, 17,135–17,142.

Perez, A. H., L. J. Wicker, and R. E. Orville, 1997: Characteristics of cloud-to-ground lightning associated with violent tornadoes. *Wea. Forecasting*, **12**, 428–437.

Seimon, A., 1993: Anomalous cloud-to-ground lightning in an F5 tornado-producing supercell thunderstorm on 28 August 1990. *Bull. Amer. Meteor. Soc.*, **74**, 189–203.

# Lightning and 85-GHz MCSs in the Global Tropics

E. Richard Toracinta[1] and E. J. Zipser[2]
[1]Department of Meteorology, Texas A&M University
[2]Meteorology Department, University of Utah

## 1. Introduction

Numerous observations of tropical convection show that tropical continental mesoscale convective systems (MCSs) are much more prolific lightning producers than their oceanic counterparts (Williams et al. 1992; Zipser 1994; and others). Satellite-based climatologies using 85-GHz passive microwave ice-scattering signatures from the Special Sensor Microwave/Imager (SSM/I) indicate that MCSs of various size and intensity are found throughout the global tropics (Mohr and Zipser 1996; Zolman et al. 1998). In contrast, global lightning distributions show a strong land bias with an order of magnitude difference between land and ocean lightning (Goodman and Christian 1993). This is somewhat puzzling, since 85-GHz ice-scattering and the charge separation processes that lead to lightning are both thought to depend upon the existence of large graupel particles.

The fact that low 85-GHz brightness temperatures are observed in tropical oceanic MCSs containing virtually no lightning leads to the postulate that tropical oceanic and tropical continental MCSs have fundamentally different hydrometeor profiles through the mixed phase region of the cloud ($0^{\circ}C \leq T \leq -20^{\circ}C$). Until recently, validation of this postulate has not been practicable on a global scale. Recent deployment of the Tropical Rainfall Measuring Mission (TRMM) satellite presents a unique opportunity for MCS studies. The multi-sensor instrument ensemble aboard TRMM (Kummerow et al. 1998), including a multi-channel microwave radiometer, the Lightning Imaging Sensor (LIS), and the first space-borne radar, facilitates high-resolution case studies of MCS structure throughout the global tropics. An important precursor, however, is to better understand the distribution of MCSs and lightning in the tropics. With that objective in mind, this research undertakes a systematic comparison of 85-GHz-defined MCSs and lightning over the global tropics for a full year, as an initial step toward quantifying differences between land and ocean convective systems.

## 2. Data and Methods

The lightning flash data for this study are from the Optical Transient Detector (OTD) (Buechler et al. 1996) from June 1995 through May 1996. The OTD is mounted aboard the polar orbiting Microlab-1 satellite. The 70° inclination and altitude of approximately 735-km allow the OTD to sample the diurnal cycle every 55 days. The instrument swath width is 1300-km x 1300-km and the average ground-pixel resolution is 11 km. The OTD detects radiance centered at the 777.4-nm oxygen emission line. Radiance events exceeding a threshold value are lightning candidates. The OTD detects total lightning (intracloud and cloud-to-ground), without distinguishing polarity, and has a nominal detection efficiency around 60% (Boccippio et al. 1999). In the current study, no detection efficiency correction has been applied to the lightning data.

Using a simple algorithm, based on the LIS Algorithm Theoretical Basis Document (ATBD) (Christian et al. 1998), the OTD lightning flashes are grouped into lightning clusters, an MCS analog, using a 30-km distance criterion. One or more flashes meeting the distance criterion during the view time of the OTD are considered a cluster. A systematic comparison using several distance thresholds revealed that 30-km was adequate to preserve MCS-scale lightning features and minimize erroneous clustering of isolated lightning occurrences. The lightning flashes and lightning clusters are tallied over three-month periods for 18 global regions of varying size, following Mohr and Zipser (1996), between 35°N and 35°S (Table 1). The three-month periods are June-July-August (JJA), September-October-November (SON), December-January-February (DJF), and March-April-May (MAM). The approximate area of each region is used to normalize the flash and cluster counts.

The OTD experiences excessive radiation noise over a region bounded approximately by 0°W – 90°W and 10°S – 50°S known as the South Atlantic Anomaly (SAA). Although a filtering algorithm (Boccippio 1998, personal communication) has been applied to remove most of the noise from the data set, the net impact of the

[1] *Corresponding author address:* E. Richard Toracinta, Texas A&M Univ., Dept. of Meteorology, College Station, TX 77843-3150.
email: etoraci@ariel.met.tamu.edu

SAA is a data undersampling. Data undersampling also occurs over the eastern and southeastern United States due to satellite reset and corresponding downtime of the OTD. Boccippio (1997) estimates viewtime reductions as much as 80% over the SAA and 30% over North America. In the current study, these viewtime losses primarily affect Tropical and Subtropical South America, the Tropical and Subtropical Atlantic, and North America. No sampling corrections have been applied to these regions at this time.

Table 1. Global land and ocean geographic divisions and approximate areas.

| Land | | Ocean | |
|---|---|---|---|
| Region | Area ($x10^6$ $km^2$) | Region | Area ($x10^6$ $km^2$) |
| Tropical Africa | 27 | South Pacific | 30 |
| North America | 23 | East Pacific | 24 |
| India & East Asia | 21 | Maritime Continent | 22 |
| Tropical S. America | 11 | Central Pacific | 20 |
| Australia | 10 | North Pacific | 19 |
| Subtropical S. America | 7 | Tropical Indian | 16 |
| Subtropical Africa | 6 | South Indian | 14 |
| Central America | 2.8 | Tropical Atlantic | 14 |
| Madagascar | 2.3 | South Atlantic | 12 |

Using SSM/I 85-GHz polarization corrected temperature (PCT) (Spencer et al. 1989) data, Mohr and Zipser (1996) define MCSs as a 250-K PCT area of at least 2000 $km^2$ and having at least one 225-K PCT pixel. In order to quantitatively compare the 1995-96 OTD lightning distributions with the SSM/I 85-GHz MCSs compiled by Zolman et al. (1998), ratios of lightning flashes to MCSs have been computed for each global region. Although lightning flashes undoubtedly originate from convective systems not meeting the 85-GHz MCS definition, the ratios are a suitable means to compare relative regional and seasonal differences in the lightning and MCS distributions.

## 3. Results and Discussion

### *a. Lightning distributions*

Table 2 lists the OTD lightning flash counts for the land and ocean regions summed over three-month periods, normalized by the respective areas, and sorted in descending order by the total annual flash density (not shown). Tropical Africa has the highest flash density of all the geographic regions in each of the four periods, and is also the most seasonally consistent. The flash densities in most land regions are approximately an order of magnitude higher than those in ocean regions. This is consistent with previous observations of order-of-magnitude differences in land versus ocean lightning occurrence (Williams et al 1992; Goodman and Christian 1993). A notable exception is the Maritime Continent, with flash densities comparable to those in North America.

Table 2. Three-month land and ocean region lightning flash density (x $10^{-5}$ flashes/$km^2$).

| Land | | | | | Ocean | | | | |
|---|---|---|---|---|---|---|---|---|---|
| | JJA | SON | DJF | MAM | | JJA | SON | DJF | MAM |
| Trop. Africa | 369 | 411 | 400 | 363 | Maritime Cont. | 62 | 73 | 75 | 108 |
| Trop. S. America | 102 | 253 | 134 | 102 | South Pacific | 18 | 15 | 34 | 21 |
| Central America | 242 | 147 | 46 | 96 | South Indian | 2 | 25 | 8 | 27 |
| Madagascar | 0 | 54 | 253 | 64 | Trop. Indian | 16 | 10 | 7 | 28 |
| Australia | 2 | 141 | 205 | 20 | Trop. Atlantic | 10 | 15 | 9 | 6 |
| India & East Asia | 139 | 51 | 11 | 114 | East Pacific | 7 | 4 | 6 | 11 |
| North America | 144 | 73 | 28 | 44 | North Pacific | 3 | 8 | 12 | 3 |
| Subtrop. S. America | 8 | 41 | 60 | 31 | South Atlantic | 6 | 8 | 6 | 4 |
| Subtrop. Africa | 6 | 27 | 44 | 14 | Central Pacific | 5 | 3 | 8 | 6 |
| **Total Land** | 121 | 128 | 111 | 97 | **Total Ocean** | 15 | 17 | 18 | 23 |

In order to assess and compare land and ocean lightning cluster characteristics, the cumulative distribution functions (CDFs) of OTD lightning clusters and lightning flashes for all land and ocean regions have been constructed as a function of the cluster flash count for each three-month period. The JJA flash and cluster CDFs in Figures 1a and 1b show that nearly 43% of the JJA clusters in land regions contain only one flash, and these constitute about 6% of the JJA land flash total. Land clusters with three or more flashes represent 42% of the land cluster population and contain 89% of the JJA land flashes. By comparison, 52% of the ocean clusters have one flash, accounting for 13% of the flash total, while clusters with three or more flashes constitute 30% of the ocean cluster population and contain approximately 77% of the JJA ocean flashes. The distribution of lightning flashes is similar for the remaining three-month periods. In general, although low flash count clusters dominate the population, they account for less than 25% of the lightning flash total over land and ocean regions.

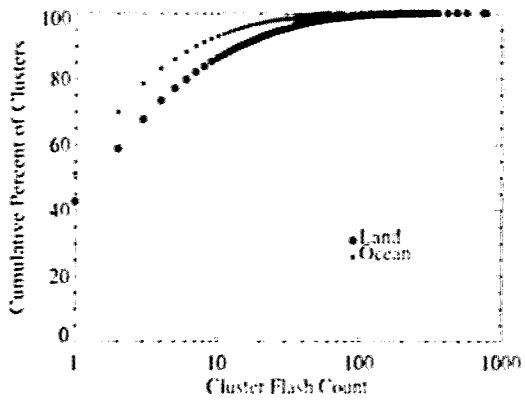


Figure 1a JJA 1995 cumulative distribution function of OTD lightning clusters as a function of cluster flash count

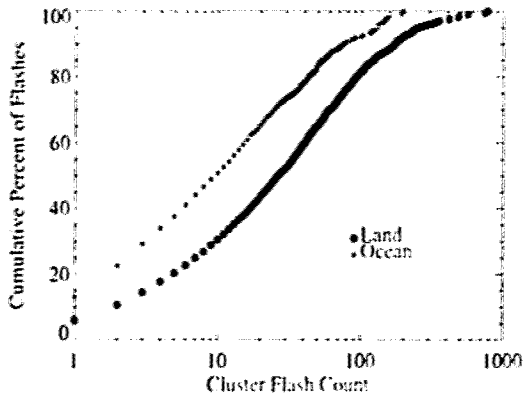


Figure 1b JJA 1995 cumulative distribution function of OTD lightning flashes as a function of cluster flash count

*b. Lightning and 85-GHz MCS distributions*

The ratios of OTD lightning flashes to SSM/I 85-GHz MCSs for each of the land and ocean regions are listed in Table 3, sorted in descending order by the total flash-per-MCS ratio for the 12-month period (not shown). While the land flash-per-MCS ratios are as much as an order of magnitude greater than the ocean ratios, the median flash-per-MCS ratio is 3, and for land regions the median is 17. Australia, Madagascar, and South Indian, show order-of-magnitude increases in the flash-per-MCS ratio from JJA to SON. In the first two cases, the increased flash-to-MCS ratio reflects an increase both in lightning flashes and 85-GHz MCSs. For South Indian, the increased flash-to-MCS ratio results from an increase in lightning and a *decrease* in the total number of MCSs. One or more factors could explain this. There may be a shift in the mode of convection in the South Indian to fewer, more electrically active MCSs. Another possibility is that the increased lightning might originate from convective-scale systems that are too small to meet the Mohr and Zipser (1996) 85-GHz MCS definition, but occur much more frequently than MCS.

Table 3. 1995-96 OTD lightning flash to 85-GHz MCS ratios.

| Land | | | | | Ocean | | | | |
|---|---|---|---|---|---|---|---|---|---|
| | JJA | SON | DJF | MAM | | JJA | SON | DJF | MAM |
| Australia | 3 | 74 | 41 | 12 | Maritime Cont. | 7 | 7 | 6 | 13 |
| Trop. Africa | 30 | 33 | 38 | 27 | South Indian | 2 | 30 | 2 | 8 |
| Subtrop. Africa | 75 | 44 | 34 | 24 | Trop. Atlantic | 3 | 7 | 6 | 2 |
| India/East Asia | 15 | 10 | 31 | 35 | North Pacific | 2 | 4 | 5 | 3 |
| North America | 23 | 14 | 14 | 24 | South Pacific | 5 | 4 | 4 | 3 |
| Trop. S. Amer. | 18 | 30 | 12 | 10 | South Atlantic | 7 | 7 | 3 | 2 |
| Central Amer. | 16 | 11 | 8 | 14 | Trop. Indian | 3 | 2 | 1 | 6 |

| Land | | | | | Ocean | | | | |
|---|---|---|---|---|---|---|---|---|---|
| Madagascar | 1 | 46 | 18 | 10 | East Pacific | 2 | 1 | 4 | 4 |
| Subtrop. S. Amer. | 8 | 8 | 6 | 7 | Central Pacific | 1 | 1 | 1 | 1 |

A third possibility to explain the increase in lightning and decrease in MCS occurrence is sampling. The OTD and SSM/I operate aboard satellites with different orbital modes. When the OTD sampling is significantly out-of-phase with the sun-synchronous SSM/I, the lightning-per-MCS statistic is misleading, especially in this case with relatively few MCSs (50) in the South Indian region during SON. Work in progress using simultaneous microwave and lightning observations from the TRMM satellite will ameliorate this sampling problem and facilitate investigation of the relative contribution to total lightning by convective-scale systems as well as MCSs.

## 4. Summary

A systematic analysis of the distribution of OTD lightning flashes and lightning clusters has been conducted over three-month periods from June 1995 through May 1996 for nine land and nine ocean regions between 35°N and 35°S. Although clusters with fewer than three flashes dominate the population, they represent about 25% of the total flash count. A comparison of OTD lightning flashes with 85-GHz MCSs over the same temporal and spatial domain reveals that the median flash-per-MCS ratio for land regions is 17. For ocean regions, the ratios are often an order of magnitude less, and the median flash-per-MCS ratio is 3. Several regions exhibited significant seasonal changes in the flash-per-MCS ratios, which may suggest a shift in the convective regime. Sampling using data from satellites with different orbital modes may bias the statistics; especially where the sample size is small as it typically is over ocean regions. The next steps are to seek an understanding, using data from the TRMM satellite, of the specific microphysical properties that permit substantial ice-scattering at 85-GHz in an oceanic MCS, but with little or no lightning.

## 5. Acknowledgements

The OTD data and software were provided by the Global Hydrology Resource Center in Huntsville, AL. Thanks also to Jody Zolman and Daniel Cecil, Steven Nesbitt, David Wolff, and Chris West. This research is supported by the National Aeronautics and Space Agency (NAG5-4699).

## 6. References

Boccippio, D. J., 1997: Summary of OTD data/viewtime losses. Tech. Rep., Global Hydrology and Climate Center, 11 pp. [Available from Global Hydrology and Climate Center, 977 Explorer Boulevard, Huntsville, AL, 35806.]

Boccippio, D. J., K. Driscoll, W. Koshak, R. Blakeslee, W. Boeck, D. Mach, H. J. Christian, and S. J. Goodman, 1999: Cross-sensor validation of the Optical Transient Detector (OTD). *J. Atmos. Oceanic Tech.* (submitted).

Buechler, D. E., R. J. Blakeslee, H. J. Christian, R. Creasey, K. Driscoll, S. J. Goodman, and D. M. Mach, 1996:Lightning activity in a tornadic storm observed by the Optical Transient Detector (OTD). Preprints, *18th Conf. on Severe Local Storms*, San Francisco, CA, Amer. Meteor. Soc., 494-498.

Christian, H. J., R. J. Blakeslee, S. J. Goodman, and D. M. Mach, cited 1998: Algorithm theoretical basis document for the Lightning Imaging Sensor. [Available on-line from **Error! Bookmark not defined.**]

Goodman, S. J., and H. J. Christian, 1993: Global observations of lightning. *Atlas of satellite observations related to global change.* R. J. Gurney, J. L. Foster, and C. L. Parkinson, Eds., Cambridge University Press, 191-219.

Kummerow, C., W. Barnes, T. Kozu, J. Shiue, and J. Simpson, 1998: The Tropical Rainfall Measuring Mission (TRMM) sensor package. *J. Atmos. Oceanic. Technol.*, **15**, 809-817.

Mohr, K. I., and E. J. Zipser, 1996: Mesoscale convective systems defined by their 85-GHz ice scattering signature: Size and intensity comparison over tropical oceans and continents. *Mon. Wea. Rev.*, **124**, 2417-2437.

Spencer, R. W., H. M. Goodman, and R. E. Hood, 1989: Precipitation retrieval over land and ocean with the SSM/I: Identification and characteristics of the scattering signal. *J. Atmos. Oceanic Technol.*, **6**, 254-273.

Williams, E. R., S. A Rutledge, S. G. Geotis, N. Renno, E. Rasmussen, and T. Rickenback, 1992: A radar and electrical study of tropical "hot towers". *J. Atmos. Sci.*, **49**, 1386-1395.

Zipser, E. J., 1994: Deep cumulonimbus cloud systems in the tropics with and without lightning. *Mon. Wea. Rev.*, **122**, 1837-1851.

Zolman, J. L., E. J. Zipser, and K. I. Mohr, 1998: A comparison of tropical mesoscale convective systems in El Nino and La Nina. *J. Climate* (submitted).

# ELECTRIC FIELD PROFILES AND LIGHTNING IN STORMS WITH FREQUENT POSITIVE CLOUD-TO-GROUND LIGHTNING

D. R. MacGorman[1], W. D. Rust[1], P. Krehbiel[2], R. Thomas[2], W. Rison[2], M. Lockwood[3], W. Beasley[3], K. Eack[4]

[1] National Severe Storms Laboratory, Norman, Oklahoma, U.S.A.
[2] Langmuir Laboratory, New Mexico Institute of Mining and Technology, Socorro, New Mexico, U.S.A.
[3] School of Meteorology, University of Oklahoma, Norman, Oklahoma, U.S.A.
[4] Los Alamos National Laboratory, Los Alamos, New Mexico, U.S.A.

ABSTRACT: Eight balloon soundings of the electric field have been obtained in severe storms in which the majority of ground flashes lowered positive charge to ground, instead of the more usual negative charge. The majority of the soundings have data gaps. These storms occurred in Oklahoma, Texas, and Kansas on four days. Cloud-to-ground lightning data from the U.S. National Lightning Detection Network indicate that, in each of two severe storms on one day, the dominant polarity of ground flashes switched multiple times during the storm. On all other days, the majority of ground flashes were positive continually throughout most of the lifetime of the storm. Preliminary analyses of the soundings are compared with published soundings from storms that produced primarily negative ground flashes. Though some features of several of the electric field profiles appear different from those obtained from storms dominated by negative ground flashes, the electric field profiles in storms dominated by positive ground flashes did not have a single, clear consistent pattern. Lightning also was mapped in three dimensions for one of the isolated storms in which a sounding was obtained and for several other severe storms that occurred in central Oklahoma during field operations. Cloud flash rates often were more than an order of magnitude larger than ground flash rates, particularly during periods when the storms produced severe weather.

## INTRODUCTION

The field program of the MCS Electrification and Polarization Radar Study (MEaPRS) in spring 1998 employed balloon soundings of the electric field and thermodynamic parameters, airborne and standard Doppler radars, a polarimetric radar, airborne microphysical probes, a deployable lightning mapping system from New Mexico Institute of Mining and Technology (NMIMT), and the U.S. National Lightning Detection Network (NLDN). This paper concerns an adjunct experiment added to MEaPRS on a noninterfering basis: an experiment to acquire data on the electrical structure of warm-season thunderstorms in which the majority of cloud-to-ground flashes lower positive charge to ground, instead of the usual negative charge.

The existence of such storms has been documented over the last two decades (see review by MacGorman and Rust 1998), though they comprise a small fraction of all warm-season thunderstorms. Studies to date have been limited to documenting the occurrence of such storms and examining storm characteristics during periods in which storms produced positive ground flashes. Positive ground flashes have been shown to dominate lightning ground flash activity in and near the convective cells of some severe storms and some squall lines. Such behavior often is associated with the production of large hail (e.g., MacGorman and Burgess 1994), though Carey et al. (1998) showed that the charge carried by hail probably is not responsible.

Although electric field profiles or lightning structure have been measured in many storms (e.g., Stolzenburg et al. 1998), no one thus far has acquired such data in the convective cells of storms in which it is known that positive ground flashes dominated. The only electric field profiles and three-dimensional lightning structure obtained from regions in which most ground flashes were positive were obtained from anvils and from the stratiform region of mesoscale convective systems. However, the kinematics and microphysics of these regions are much different from those of deep convective cells, so the electrical structures may well be different, too.

Four hypotheses have been offered in attempting to explain domination by positive ground flashes in terms of a storm's electrical structure (see MacGorman and Rust 1998, Carey et al. 1998): (1) The charge structure is such that some upper positive charge is shifted horizontally well beyond lower negative charge. (2) The positive charge often found below negative charge in the lower part of the storm is enhanced to the point that it, instead of the usual negative charge, becomes the source of charge for ground flashes. (3) Upper positive charge descends

through negative charge in some region and can then produce positive ground flashes. (4) The vertical sequence of charge polarity in the storm is different from that in storms in which most ground flashes are negative.

A primary goal of our study was to begin evaluating these hypotheses by obtaining electric field profiles through storms that produce frequent positive ground flashes, with corresponding radar observations of the storms. A second goal was to map positive cloud-to-ground flashes relative to storm structure and electric field profiles to develop a better understanding of the processes responsible for the flashes.

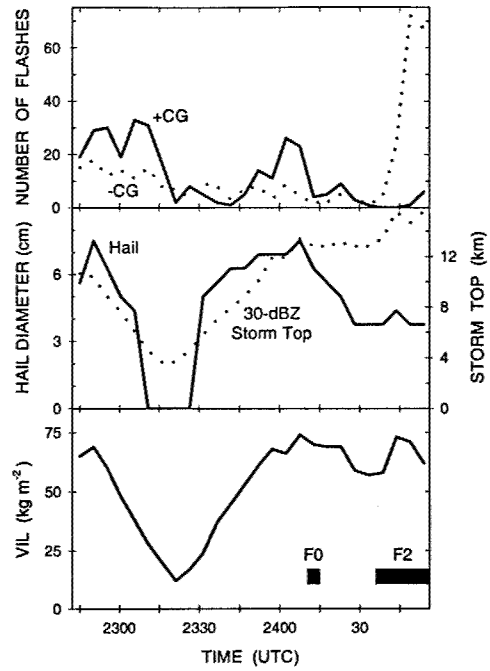


*Figure 1. Storm parameters and ground flashes (per 5 min) for a storm near Pink, Oklahoma on 8 June 1998. The balloon sounding was at 2352 – 0007 UTC. The maximum hail size that the NSSL algorithm estimates is 7.6 cm. Bars indicate the time of tornadoes, labeled with their F-scale (0=weak, 2=strong, 5=violent).*

## OVERVIEW OF DATA SETS

Several suitable storms and storm systems occurred within the operational area of MEaPRS. A total of eight balloon soundings of the electric field were obtained on four days; the majority had data missing from some layer or stopped before reaching the top of the storm. On June 8, two soundings were obtained in the strong convection of different isolated supercell storms. On June 19, one sounding was obtained through the anvil of another isolated storm. Two soundings were obtained in or near the convective line of each of two severe squall lines (on the evening/morning of May 14/15 and May 24/25) that produced mostly positive ground flashes. The remaining sounding was in the transition zone between the convective line and stratiform region of the squall line on May 25.

Storms occurred within range of the NMIMT three-dimensional lightning mapping system on five days. However, only two of these were days on which soundings were obtained (the days with isolated severe storms), and one sounding was far enough from the network that only the plan location of lightning could be used. The lightning mapping system had not yet been installed on the two days with squall lines. Lightning mapping data also were acquired for positive ground flashes on three other days with isolated storms; soundings were not obtained from these storms because of other program priorities, malfunction of the balloon-borne instruments, or logistical obstacles in trying to drive to the storms in time to observe positive ground flashes.

WSR-88D Doppler radar data were collected for all cases. Doppler radar data were collected from the NOAA P3 aircraft on May 24-25, along with data from in situ microphysical probes. Polarimetric radar data were collected from an NSSL radar on June 8 and on two other days for which lightning mapping data were obtained for positive ground flashes.

## DATA ANALYSES

Though all the supercell storms in our study produced continual cloud flashes for extensive periods, the two June 8 storms were the least prolific producers of positive ground flashes among the cases in this study; positive ground flashes outnumbered negative ground flashes only sporadically in both storms. In the first, positive ground flashes had outnumbered negative ground flashes just before the balloon was launched, but negative ground flashes outnumbered positive ground flashes during most of the flight. In the second storm (Fig. 1), positive ground flash rates exceeded negative ground flash rates throughout the flight, though negative ground flashes became much more frequent roughly 0.5 h after the flight. In all other cases in this study, positive ground flashes comprised more than 50% of all ground flashes for most of the life of the storm or storm system, and the percentage sometimes exceeded 90% for substantial periods. Figure 2 shows an example of ground flash activity for one of the other storms.

The flight into the 6/08 P storm (Figs. 3 and 4) was interesting in several respects. There is no tracking information for this flight, but the balloon was launched into the weak echo region of the supercell storm, and the

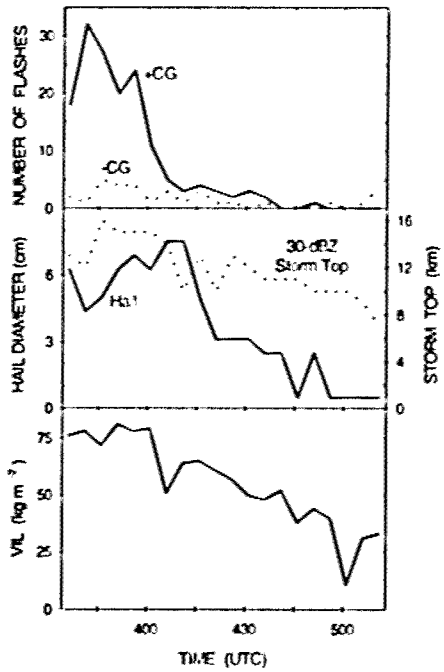


*Figure 2. Storm parameters and ground flashes (per 5 min) for a storm near Kremlin, Oklahoma on 25 May 1998. The balloon sounding was at 0409 – 0436 UTC.*

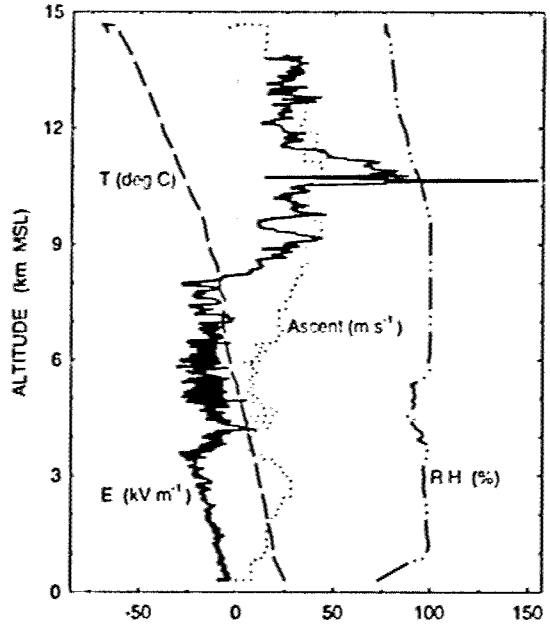


*Figure 3. Sounding of a supercell storm near Pink, Oklahoma on 8 June 1998 at 2352 – 0007 UTC. E is along the instrument axis; a thin trace indicates a vertical E. The wider trace at 3.5 – 7 km MSL indicates that the horizontal component of E is larger there.*

ascent rate (up to 45 m $s^{-1}$) indicates that the balloon flew through a strong updraft. Except for a low charge density from the ground to 3 km MSL, the first major charge region encountered by the balloon was a positive charge having a lower boundary at 8 km. The next large charge density encountered was a large positive charge, not the negative charge encountered in other published soundings of strong convection. If the 6/08 P sounding did in fact remain in the weak echo region of the storm, then the positive charges are in the substantial reflectivity that extended over the weak echo region. Negative charge was still higher. It is possible that, as in most storms, negative charge still occurred beneath an upper positive charge in unsampled regions of heavy precipitation beside the weak echo region.

This inference of elevated positive charges with negative charge above them is consistent with inferences drawn from the structure of intracloud lightning in similar storms. As shown by Krehbiel et al. (this preprint volume) when most ground flashes are positive in supercell storms, the vertical polarity of bilevel cloud flashes near the strong updraft appears to be inverted from that of most such flashes: The lower level of such a lightning flash is inferred to neutralize positive charge at the height of positive charge in the 6/08 P sounding, and the upper level is inferred to neutralize a thin layer of negative charge at the height of negative charge in the sounding.

A summary of the electric field soundings in all but one of the storms that produced frequent positive ground flashes is shown in Fig. 4. In the one balloon sounding not shown (one into an updraft on May 14, 1998), the electric field was less than 10 kV $m^{-1}$ from the ground up to an altitude of approximately 4.5 km MSL, where the balloon burst. Except for the low density of negative precipitation charge shown below 3 km MSL for case 6/08 P, only the larger field excursions are shown. In constructing this summary, subjective judgements were made to omit relatively small changes in E and changes which could have been caused by passing through charge, but which could also have been caused by approaching or moving away from larger charges (as occurs when charge geometry cannot be approximated as an infinite layer).

Support for more than one of the hypotheses concerning charge structure can be found in the set of soundings shown in Fig. 4, because there are similarities, but also substantial differences, among the soundings. For example, the 6/08 P sounding into a strong updraft and the two soundings into anvils all appear consistent with inverted thunderstorm charge structure, with the main lower charge being positive, and the main upper charge and

interior anvil charge being negative. However, as mentioned previously, it is possible that negative charge lies below positive charge in the unsampled region of heavy precipitation beside the updraft, so the 6/08 P sounding also could be consistent with upper positive charge extending horizontally beyond lower negative charge. This second interpretation is more consistent with the two other soundings into strong updrafts (6/08 S and 5/25 K3); both appear to have a typical profile, in that a large field excursion due to negative charge is just above the lowest positive charge. However, we find it difficult to reconcile the second interpretation with the two soundings through anvils. It may be that positive ground flashes can be produced by multiple, radically different charge distributions.

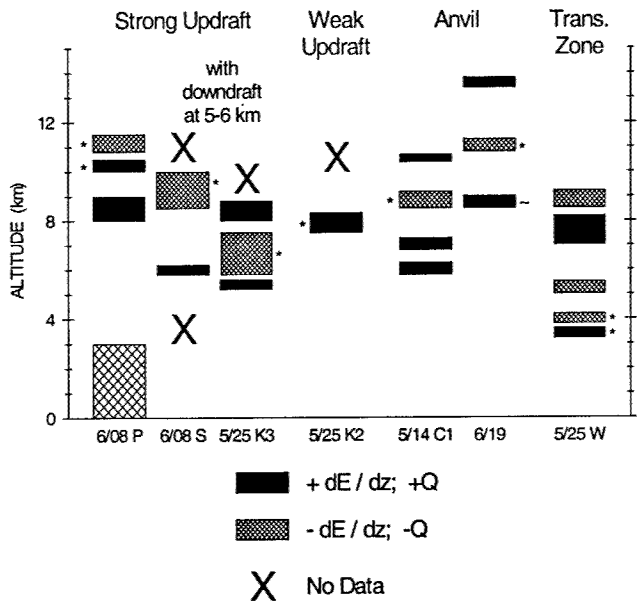


*Figure 4. Summary of dE/dz for seven balloon soundings in 1998. Except for the small charge density below 3 km on 6/08 P, the magnitude of charge density estimated for these dE/dz was 0.5–2.7 nC m$^{-3}$. * denotes the largest change in E for each sounding (always ≥50 kV m$^{-1}$); two for one sounding indicate two equal values. ~ denotes a rough estimate of height; this dE/dz occurred within a 2.8 km layer of missing data, and the upper boundary shown is where data resumed.*

CONCLUDING REMARKS

These soundings and lightning observations provide the first such observations for storms in which the majority of ground flashes lower positive charge to ground. More soundings and better coincident data sets of electric field profiles and lightning are necessary to make progress evaluating hypotheses concerning the production of positive ground flashes in warm-season thunderstorms. However, it is impossible to measure all the relevant storm and lightning parameters with the spatial and temporal resolution needed to unambiguously determine why positive ground flashes are produced by a given storm. What is needed is a combination of observations, theory, and numerical models such as has been used to improve understanding of tornadogenesis: Observations and theory were used to suggest and evaluate hypotheses and to place bounds on the behavior of numerical cloud models. Numerical cloud models were used to provide a complete self-consistent set of observables to test and refine hypotheses and to indicate what future measurements were needed to discriminate further among hypotheses. The observations described in this paper and the modeling described by Mansell et al. (presented at this conference) make a start in this direction.

ACKNOWLEDGMENTS: We thank Dave Jorgensen and Ron Holle for providing weather guidance to the mobile laboratories. We thank balloon crew members: Aaron Bansemer, Lee Coleman, Nick Demetriades, Beth Karl, Tim Lang, Ted Mansell, Heidi Morris, Jim O'Brien, Ivy Winger, and Kevin Young. We thank Leslie Cain and Dennis Nealson for maintaining the mobile laboratories and Terry Schuur for operating NSSL's multiparameter radar. We give special thanks to Maribeth Stolzenburg for processing the sounding data and to her and Tom Marshall for their valuable contributions to balloon data acquisition. This research is supported in part by NSF grant ATM9807179.

REFERENCES

Carey, L. D., and S. A. Rutledge, Electrical and multiparameter radar observations of a severe hailstorm. *J. Geophys. Res.*, *103*, 13979-14000, 1998.

MacGorman, D. R., and W. D. Rust, *The Electrical Nature of Storms*, Oxford Press, 422 pp., 1998.

MacGorman, D.R., and D.W. Burgess, Positive cloud-to-ground lightning in tornadic storms and hailstorms. *Mon. Weath. Rev.*, *122*, 1671-1697, 1994.

Stolzenburg, M., W. D. Rust, and T. C. Marshall, Electrical structure in thunderstorm convective regions: 3. Synthesis, *J. Geophys. Res.*, *14097-14108*, 1998.

# THUNDERSTORM ACTIVITY OVER LAND AND SEA REGIONS OF INDIA AND THE SENSITIVITY OF WET-BULB AND SEA SURFACE TEMPERATURES TO THEIR OCCURRENCE

G. K. Manohar, S. S. Kandalgaonkar and M. I. R. Tinmaker
Indian Institute of Tropical Meteorology, Pune, India

ABSTRACT : Thunderstorms over the tropical land and sea regions of the Indian sub-continent are characterized by their seasonal occurrence during the premonsoon (M-A-M) and monsoon (J-A-S) seasons. Monthly data on the number of thunderstorm days (THN), surface mean maximum wet-bulb temperatures (Tw) and mean sea surface temperatures (SST) for a period of 11 years (1970-1980), over several land stations across the latitude range 8°-30°N and at one island station, Port Blair (PBL) and Minicoy (MNC) each in the Bay of Bengal and Arabian Sea, have been used for this study. For the two data sets (THN and Tw / SST), at these two categories of locations, we present the results of their monthly (January-December) mean latitudinal (8°-30°N) and latitude-belts averaged seasonal variation. The seasonal variation of the Tw, SST and THN at these two locations has shown clear signal of its semiannual oscillation over land and sea areas. The central focus, therefore, of this study was the issue of the sensitivity of the occurrence of THN to Tw / SST. This issue is similar to the numerous sensitivity studies of lightning and the occurrence of the thunderstorms with that of the Tw on the land regions in the tropics (Williams, 1992; Williams et al., 1992 and Jayaratne, 1993). This information is an exceedingly important result towards documenting the response of tropical convection to modest changes in surface thermodynamics over land and oceans. The results of the sensitivity analysis of THN to Tw / SST are presented. The month to month SST variation showed that the peak SST heating occurs usually in the month of April. The SST then systematically cools down from the month of May until about July-August. It is worthwhile to note that the period of significant SST heating precedes the onset of normal monsoon (1 June) by about 30-45 days. It is proposed that the use of SSTs may well be made as a proxy for wet-bulb temperatures over the oceans for oceanic convection and monsoon studies where they are usually not available.

## INTRODUCTION

The tropical region of the earth is now well understood as a central player in the convective overturn of the atmosphere. Thunderstorms over land and sea regions of the Indian subcontinent are characterised by their seasonal occurrence during the premonsoon (M-A-M) and the monsoon (J-J-A-S) seasons. Very few studies are reported in the literature in connection with the time and space variation of the thunderstorms over the Indian region. Any information regarding the variation of thunderstorm activity and its relation with the parameters like wet-bulb temperature, sea surface temperature would be useful in understanding the role of these thunderstorms, in tropical convection and global electric circuit. The results of one such study made over the Indian region are presented in this paper.

## DATA

Monthly data of number of thunderstorm days (THN) and mean maximum wet-bulb temperature (Tw) of 78 Indian stations and mean sea surface temperatures (SST) at Port Blair (PBL) and Minicoy (MNC) island station, each in Bay of Bengal and Arabian sea form the data set for this study. These data are used to study the monthly mean latitudinal (8°-30°N) variation and latitude belts averaged seasonal variations of THN and Tw over the Indian region. SST data at PBL and MNC are used to study the issue of sensitivity of SST to the occurrence of oceanic thunderstorms and also their seasonal variation.

## RESULTS

The seasonal variation of the Tw, SST and THN at these two categories of locations (land and ocean) has shown clear signal of its semiannual oscillation which is in phase with each other. This result itself explains the prominence convection over land and sea region (Figures 2 and 3). The results of the sensitivity analysis of THN to Tw/SST are shown in Figures 1 and 4. The occurrence of THN per 1°C rise in Tw was more pronounced in the lower latitudes. These results are in good agreement with the results of Williams (1992), Williams et al (1992) and Jayaratne (1993). Month to month variation of SST showed that the peak SST heating occurs usually in the month of April. The SST then systematically cools down from the month of May until July-August. It is worthwhile to note that the period of significant SST heating precedes the onset of normal monsoon (1st June) by about 30-45 days.

## CONCLUSIONS

It is proposed that the use of SSTs may well be made as a proxy for wet-bulb temperatures over the oceans for oceanic convection and monsoon studies where they are usually not available.

ACKNOWLEDGEMENTS : The authors are thankful to Dr. A.S.R. Murty and Dr.Mrs. A.M.Selvam and Director for their constant support of our research activity.

## REFERENCES

Jayaratne, E.R., Conditional instability and lightning incidence in Galborone, Botswana, *Meteorol. Atmos. Phys.*, **52**, 169-175, 1993.

Williams, E.R., The Schuman resonance : A global tropical thermometer, *Science*, **256**, 1184-1187, 1992.

Williams, E.R., S.A. Rutledge, S.G. Geotis, N. Renno, E. Rasmussen and T. Rickenbach, A radar and electrical study of tropical "Hot Towers", *J. Atmos. Sci.*, **49**, 1386-1395, 1992.

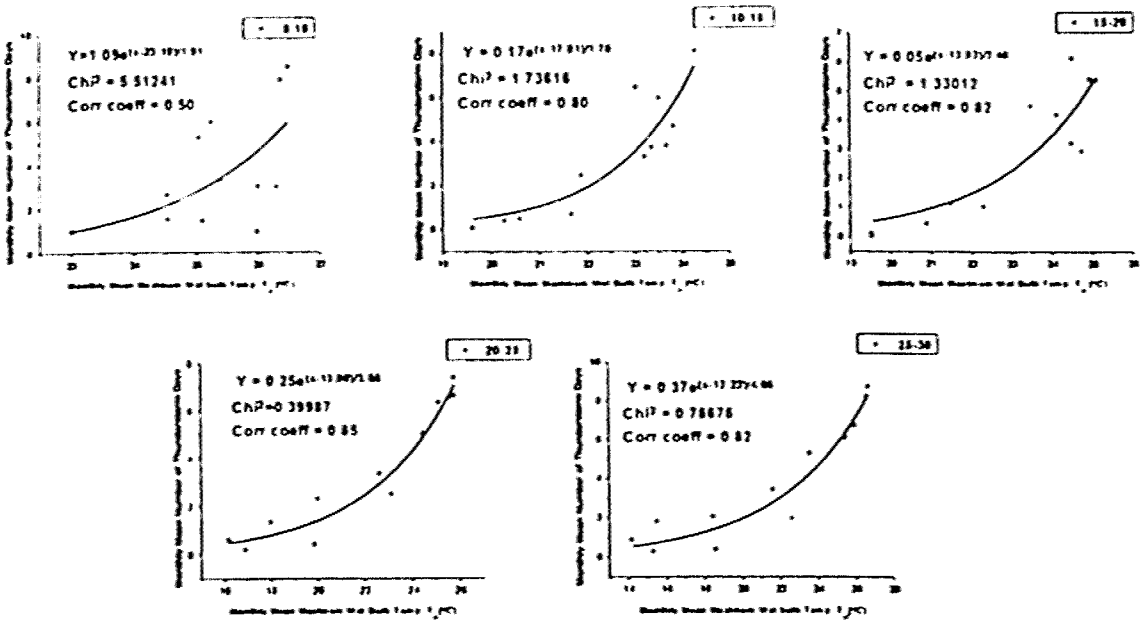


Figure 1 : The scatter diagram of X-Y plots of the monthly values of Tw-THN for the five latitude belts. A curve in each diagram is an exponentially growing best fit curve through the data points.

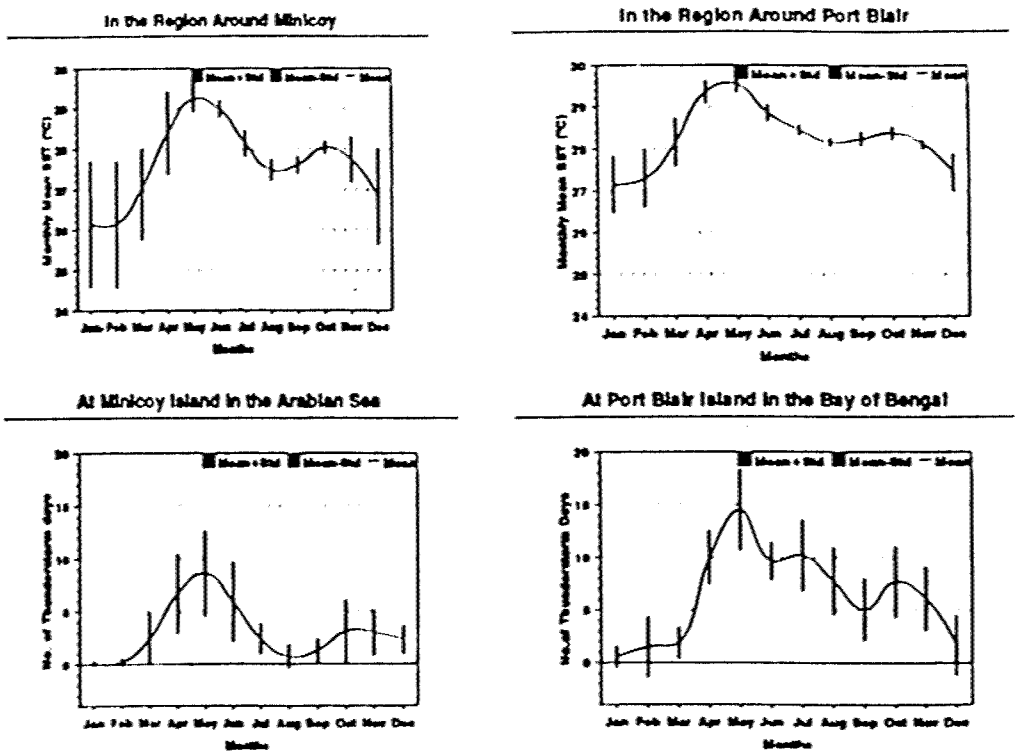


Figure 2 : Monthly mean SST (1955-1980), number of thunder-storm days at Minicoy and Port Blair island.

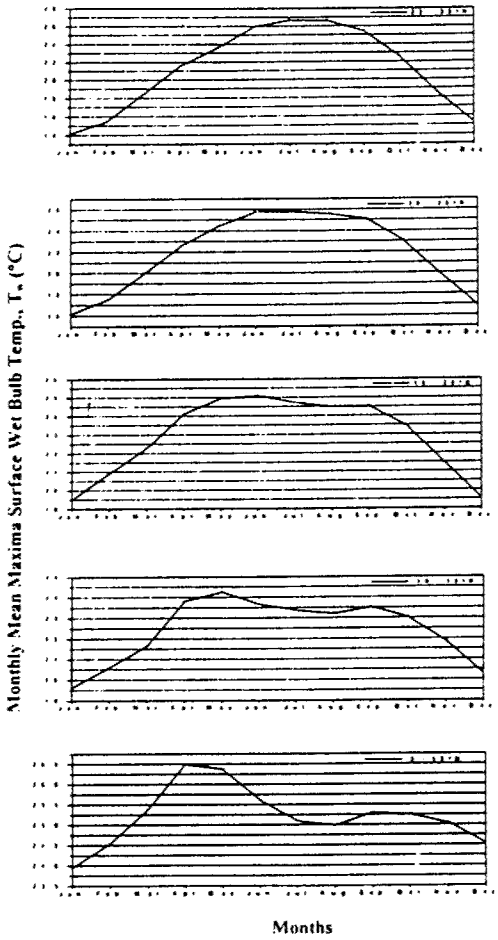


Figure 3 : Seasonal variation of monthly mean maximum surface wet-bulb temperature (Tw) for five latitude belts.

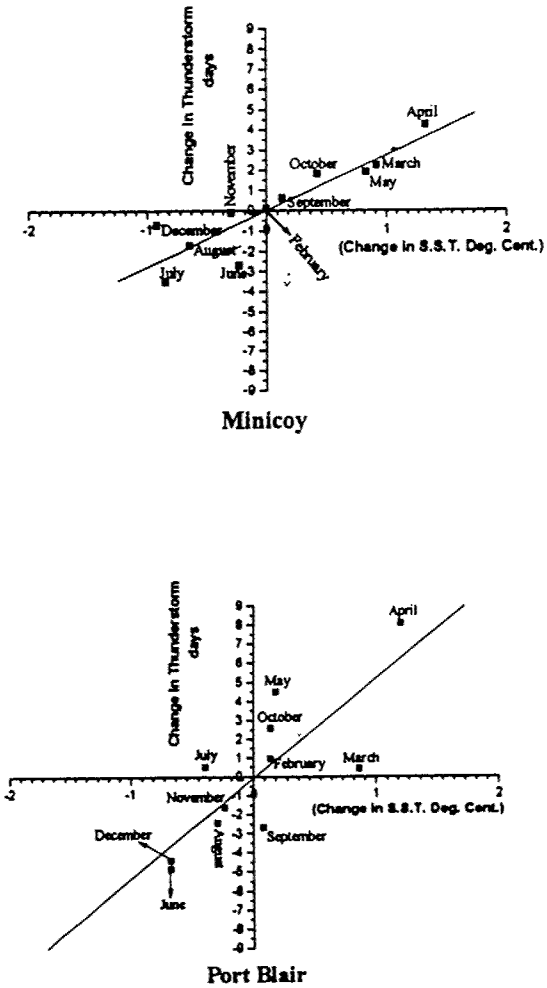


Figure 4 : Monthly change in the SST versus change in the number of thunderstorms days at Minicoy and Port Blair island.

# LIGHTNING ACTIVITIES OF WINTER THUNDERCLOUD OBSERVED BY DUAL-POLARIZATION DOPPLER RADAR ON THE HOKURIKU COAST OF JAPAN

Kouichirou Kami, Kazuo Shinjo, Tsutomu Sakai and Takeo Wakai

Research & Development Center , Hokuriku Electric Power Company
2-54 Hisakata-machi, Toyama 930-0848, JAPAN

**Abstract:** Lightning often occurs not only in summer but also in winter on the Hokuriku coast of Japan. Many damages of equipments and interruptions of power supply are caused by winter lightning. We have installed a dual-polarization Doppler radar ( C-band ) at Noto Peninsula in Hokuriku district to clear the relation between atmospheric activities and electrical activities of thunderclouds, and to establish a method of lightning forecast for winter season. In this paper, we describe an example of observation.

## 1 . Introduction

In order to clear the relation between atmospheric activities and electrical activities and to establish a method of lightning forecast in winter season, we have installed a dual-polarization Doppler radar ( C-band ) and have started observation of thunderclouds from November 1998.

## 2 . Observation and analysis Method

We have installed the radar at Hakui City on the Noto Peninsula ( 36° 54'36"N,136° 52'54"E ) . Table 1 shows the specifications of the radar, and Fig.1 shows the observation area. The observations have been carried out using the radar and Lightning Location System (LLS) covering the Hokuriku district.

Table 1. Specification of radar.

| | |
|---|---|
| Antenna | Parabola 4.39m ( in diameter ) |
| Frequency | 5320MHz |
| Repetition rate | 250~1180pps |
| Pulse length | 0.8$\mu$s ( dual-polarization Doppler )<br>2.0$\mu$s ( intensity ) |
| Peak power | 250kW |
| Antenna beam width | 0.95 degree |
| Maximum range | 120km( dual-polarization Doppler )<br>240km ( intensity ) |
| Minimum detectable signal | −108dBm below the peak power |

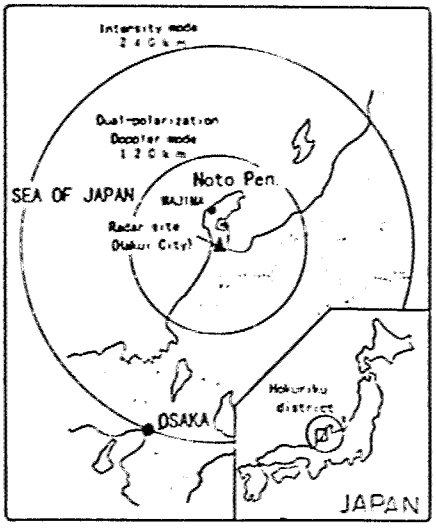


Fig.1 Radar observation area.

## 3. Case study

We study examples of observation during 14 to 15 December 1998. The meteorological conditions of occurrence of winter lightning have been cleared and have classified as follows ( Toshiyuki Hayashi et al., 1996 ), *type a ) Lightning by passage of a cold front, type b ) Lightning during winter monsoon pressure pattern with a meso scale low on the Sea of Japan, type c ) Lightning during strong winter monsoon pressure pattern, and type d) Lightning by passage of a synoptic low on the Sea of Japan* . This case corresponds with type d . Fig.2 and Fig.3 show weather charts ( surface and 700hPa ), and Fig.4 is the temperature profile at Wajima Weather Station, respectively, at 21:00JST ( JST=9hrs+UTC ) on 14 December 1998.

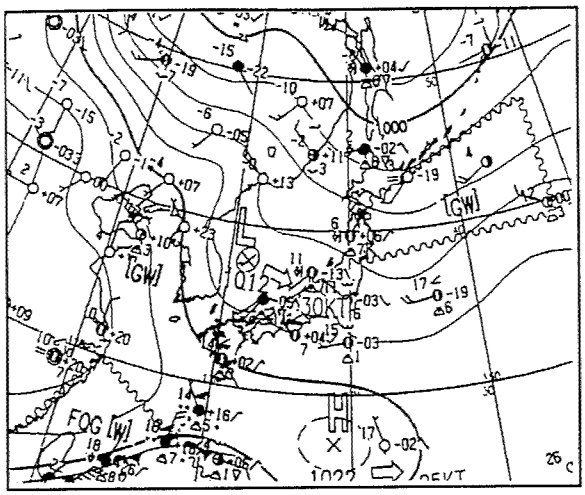

Fig.2 Weather chart ( surface analysis ).
( 21:00JST 14 December 1998 )

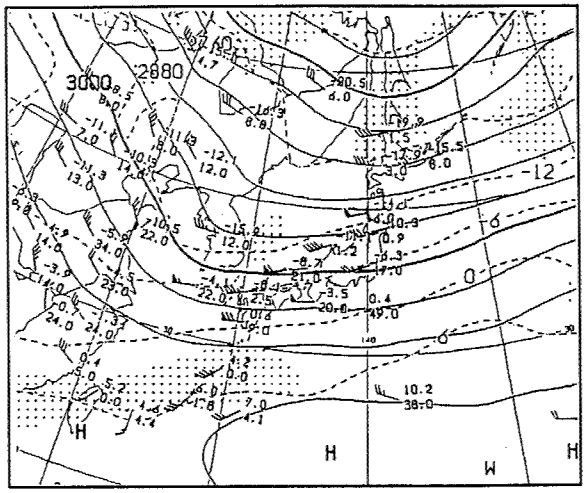

Fig.3 Upper level chart ( 700hPa analysis ).
( 21:00JST 14 December 1998 )

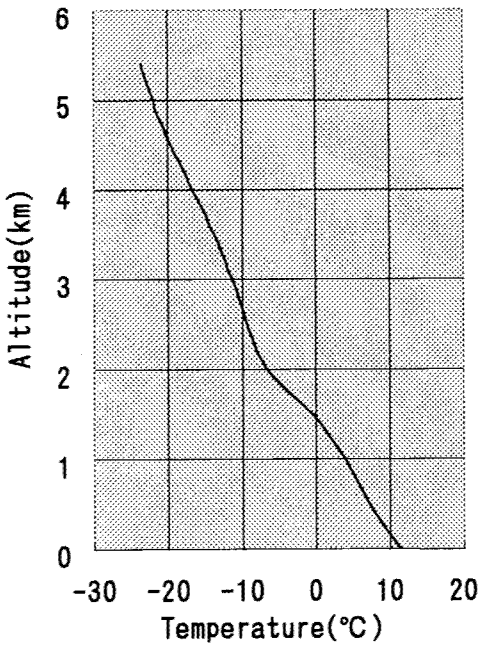


Fig.4 Vertical structure of temperature at Wajima.
(21:00JST 14 December 1998)

Fig.5 shows the time variation of the number of lightning discharges detected by the LLS from 12:00JST on 14 December to 06:00JST on 15 December 1998. The applied area is that of from latitude 36 degrees north to latitude 38 degrees north and from longitude 136 degrees east to longitude 138 degrees east. This area includes the observation area of the radar using dual-polarization Doppler mode. The square brackets in Fig.5 show the number of transmission line faults during each same term within the jurisdiction of the Hokuriku Electric Power Company. It can be seen from Fig.5 that the ratio of positive lightning discharges is higher than negative one, which are referred to as "Typical winter lightning".

Results of the radar observation from 00:40JST to 01:20JST on 15 December 1998 are as follows. This observation time is shown with an arrow in Fig.5. Fig.6 shows the CAPPI product of distribution of precipitation particles at the height of 2km and vertical cross section of the echoes on line A−B. The area of Fig.6 is shown with a small square in Fig.1. The white smeared portions show graupel regions and the black solid circles show lightning points detected by the LLS.

It can be estimated from the temperature structure of Fig.4 that the temperature of the height of 3km above the sea level was -10°C. The echo was formed over the coast line at 00:40JST, and included graupel region with the temperature of -15～-20°C at the height of 4～5km above the sea level. Non echo was observed at 00:30JST. The graupel region descended to the height of above 3km (below -10°C ) at 00:50JST, and positive lightning discharges were detected by the LLS during 10 minutes included the time. On the other hand, another graupel region occurred when it was 00:50JST at the height of 1～6km on the west of the place, where the graupel region was observed at first. The graupel region spread widely at 01:00JST, and negative lightning discharges were detected by the LLS. The graupel region descended to the height of below 3km ( above -10°C ) at 01:20JST, and one positive lightning discharge was detected by the LLS. After the time, this echo moved to the land and non lightning discharges were observed under this echo. Lightning discharges were most often detected by the LLS, from 10 to 20 minutes after that the graupel region with the temperature of -15～-20°C was observed at the height of 4～5km.

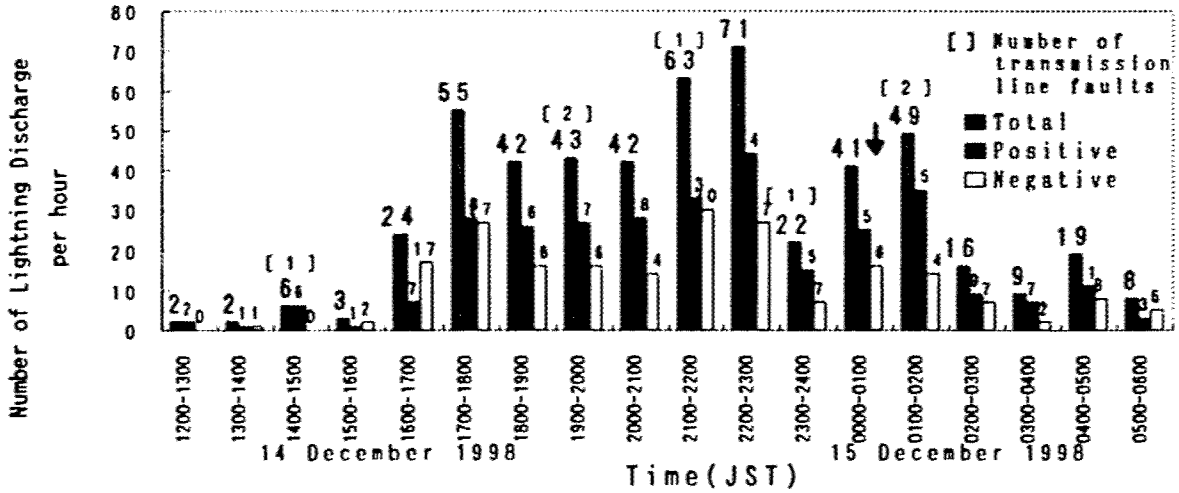


Fig.5 Time variation of lightning discharge frequency
during 12:00JST on 14 December to 06:00JST on 15 December.

The height of the echo top was about 9km above the sea level. The area with a reflectivity above 40dBZ was observed when it was 00:40JST at the height of 3.5~6.5km and it spread to the height of 1.5~7.0km at 00:50JST. The area descended to the height of 5.5km at 01:00JST, and the point with a reflectivity above 50dBZ was observed at the height of below 2.5km. Finally, the area with a reflectivity above 40dBZ descended to the height of below 2.5km at 01:20JST.

It is corresponds with other observation results in the Hokuriku coastal area ( H.Uyeda et al., 1996 ) that graupel region is elevated to the high altitude ( below -10°C ) before occurrence of lightning discharges, and also corresponds with another observation results ( T.Shimura et al., 1996 ) that high intensity area ( above 40dBZ in a reflectivity ) is observed in the mature stage of thunderclouds.

## 4. Conclusion

In this study, it is clarified that occurrence and development of graupel regions in thunderclouds is very important factor to forecast winter lightning discharges. Especially, we regard it is important that to remark an occurrence of graupel region at the temperature of -10~-20°C for improving of accuracy of lightning forecast. However, graupel region is not always observed by the radar when lightning discharges are detected by LLS. We continue to observe and to analyze distribution of precipitation particles when the lightning discharges are detected by LLS. An observation and an analysis of wind field and an analysis of the relation between the occurrence point of thundercloud and the topography are subjects for the future study.

## References

Toshiyuki Hayashi, Tsutomu Sakai and Kazuo Shinjo, Meteorological Condition and Lightning Activities in Hokuriku Area, Proceeding of 10th Int. Conf. on Atmospheric Electricity, Osaka, Japan, 584-587, 1996

H.Uyeda, T.Otsu, H.Kagaya, Y.Asuma, K.kikuchi, Z-I.Kawasaki and Y.sonoi, Characteristics of Winter Thunder Cluds Observed by a Dual-Polarization Doppler Radar, Proceeding of 10th Int. Conf. on Atmospheric Electricity, Osaka, Japan, 568-571, 1996

T.Shimura, G.Naito, F.Kobayashi, Relation between Polarity of Cloud-to-Ground Lightning Flashes and Radar Echoes due to Winter Thunderclouds over Hokuriku, Japan, Proceeding of 10th Int. Conf. on Atmospheric Electricity, Osaka, Japan, 564-567, 1996

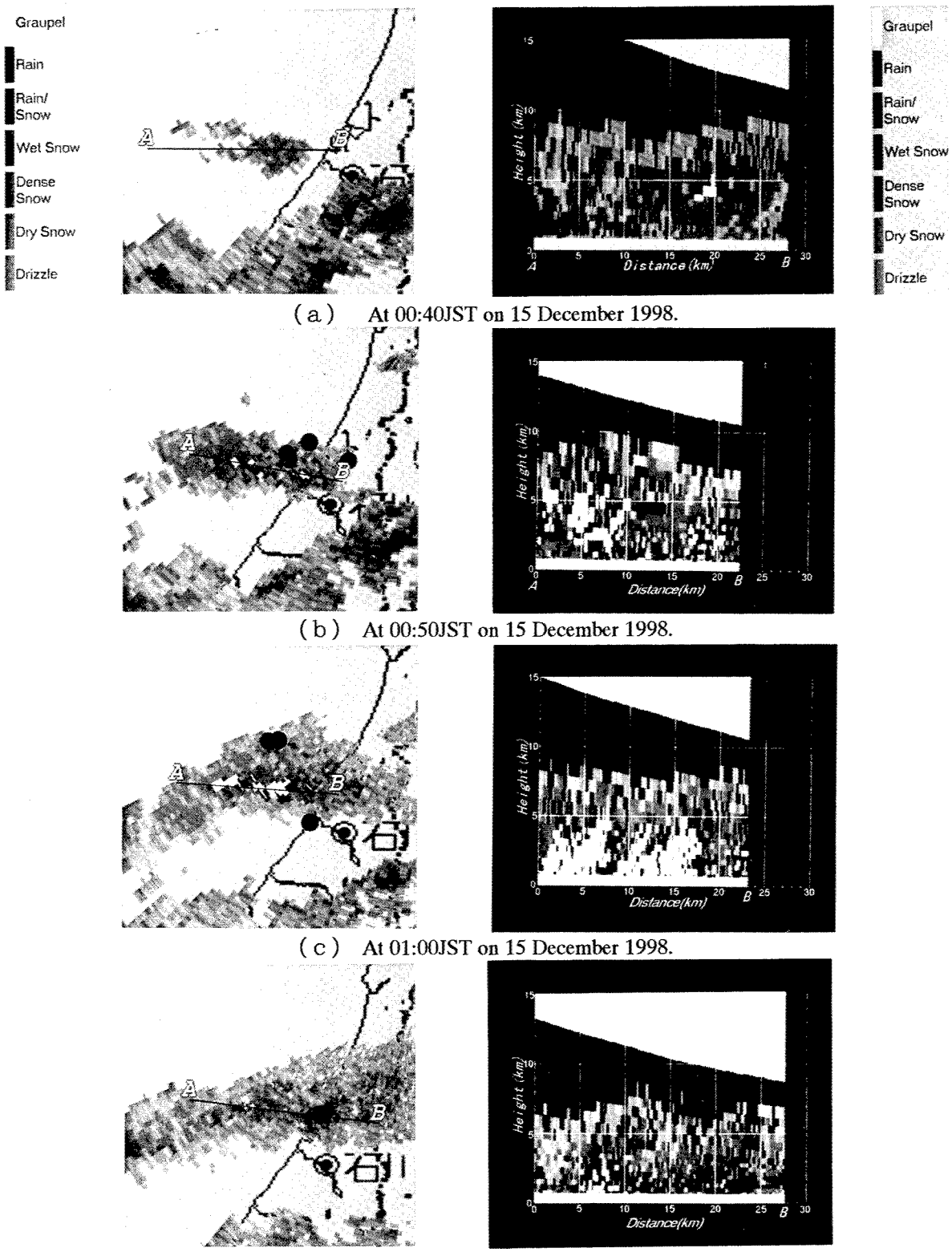


(a) At 00:40JST on 15 December 1998.

(b) At 00:50JST on 15 December 1998.

(c) At 01:00JST on 15 December 1998.

(d) At 01:20JST on 15 December 1998.

Fig.6 CAPPI product of distribution of precipitation particles at 2km height and vertical cross section of echoes on line A-B .

( The white smeared portion shows the graupel region.)

( The black solid circles show lightning points detected by LLS.)

Development of Heat Thunderstorms and Distribution of Lightning Strokes around the Northern Part of the Kanto Plain, Japan

[1]Tomoyuki Suzuki, [1]Fumiaki Kobayashi, [1]Takatsugu Shimura,
[2] Tadaomi Miyazaki ,and [3] Takeo Hirai

[1] Department of Geoscience, National Defense Academy, Yokosuka, Japan
[2] Department of Information Engineering, Maebashi Institute of Technology, Maebashi, Japan
[3] Lightning & Insulation Group Power Engineering R & D Center,
Tokyo Electoric Power Company, Yokohama, Japan

**ABSTRACT**: Doppler radar observation was carried out to investigate the generation and evolution processes of initial convective clouds of heat thunderstorms in the Kanto region of Japan in summer. The results of analysis in late August 1997 shows heat thunderstorms: (1) Initial convective echoes (hereinafter referred to as "first echo") were generated at the base of mountains in the evening. Most of the first echoes were generated at an altitude of 4 - 5 km AGL. (2) The first echoes which developed into meso-$\beta$ -scale thunderstorms were generated above the specific mountain areas. (3) CG strokes occurred after the mature stage cells.

## 1. Introduction

Heat thunderstorms often developed around the northwestern part of the Kanto plain in central Japan in the summer season. The greater Tokyo metropolitan area is often damaged by the lightning, hail, heavy rainfall and gusts from these thunderstorms. Therefore it is important to understand how the initial convective clouds which develop into meso-$\beta$ -scale thunderstorms are generated around the base of mountains. The aim of this research was elucidation of the following items: (1) The generation area of the first echoes. (2) The developing process of development the first echoes into meso-$\beta$ -scale thunderstorms. (3) The time and space relationship between the developing echoes and CG strokes.

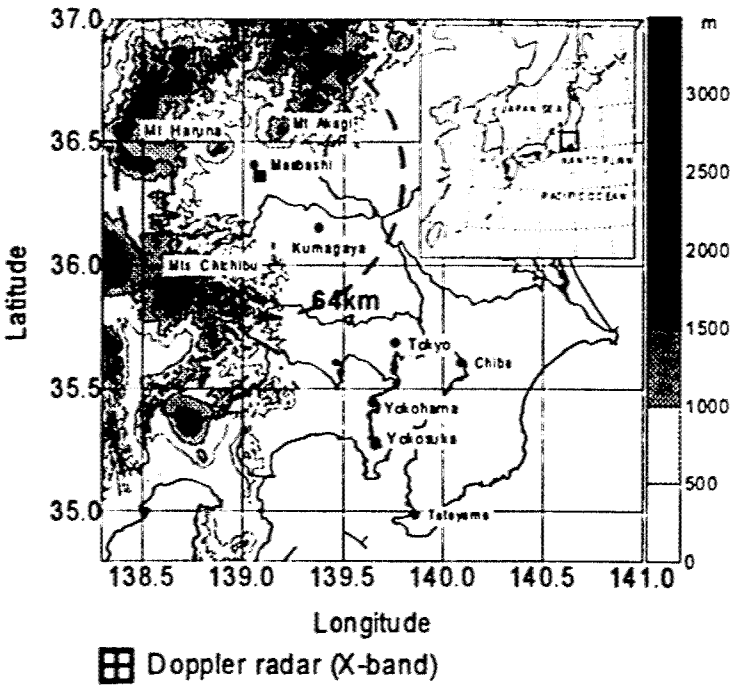


Figure 1. Observation area. The dashed line shows the maximum range of the radar.

## 2. Observation method

The special observations were carried out

from the middle of July to early September 1997 in the northwestern part of the Kanto plain using a Doppler radar, still camera, video camera, weather station, field mills, and GPS sonde (Fig. 1). The Doppler radar (X-band) was set up at Maebashi, Gunma prefecture in the northern part of the Kanto plain and CAPPI and RHI displays were obtained every 10 minutes. CG strokes were obtained by LPATS (Lightning Positioning And Tracking System) simultaneously. The analysis period was from 23 to 30 Aug. 1997, when a thermal trough passed over Japan.

Figure 2. Thunderstorm embryo

### 3. Results

Figure 2 shows a typical thunderstorm cloud embryo with a 3 km cloud top height, which developed into a thundercloud contained strong echoes (over 32 dBZ) about 15 minutes later. We defined the criteria of thunderclouds as a maximum echo intensity of at least 32 dBZ and a horizontal extension of more than 10km. We call the initial echo of the thunderclouds as " first echo ".

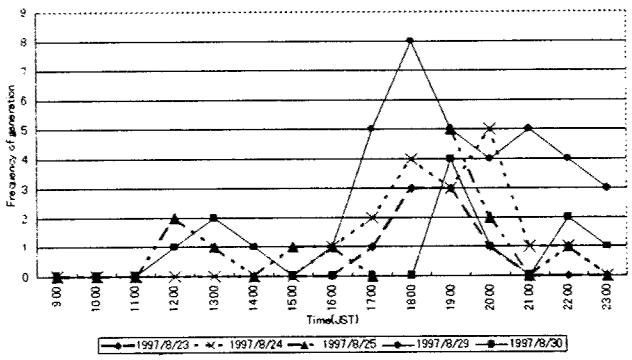


Figure 3. Frequency of first echoes generation from 23 to 30 Aug. 1997

### 3.1 First echo generation

Figure 3 shows frequency of first echoes generation per hour. Their generation started in the afternoon, and the highest frequency appeared in the evening (around 18 JST). The period of generation basically coincided with that of convergence between the northwesterly mountain wind and the southeasterly sea breeze. Figure 4 shows the altitude of first echoes. Many first echoes were generated at an altitude of 4 - 5 km. On this day, an altitude of 4 km was equal to the 0 ℃ temperature level. The distribution of the first echoes (Fig. 5) shows that generation occurred around the base of mountains facing the plain of Gunma prefecture. Especially, the first echoes which developed into thunderstorms with CG strokes were generated at low elevation (~500m above sea level). Although there has been little investigation of first echoes in Japan, there has been much in north America. For example, the investigation of first echoes in Colorado (e.g., Charles et al., 1983) reported first echoes appears at an altitude of 8 km (about -20 ℃) and that the cloud base is about 4 km. In Japan, however, it was at an altitude of 4 - 5km (around 0 ℃). It

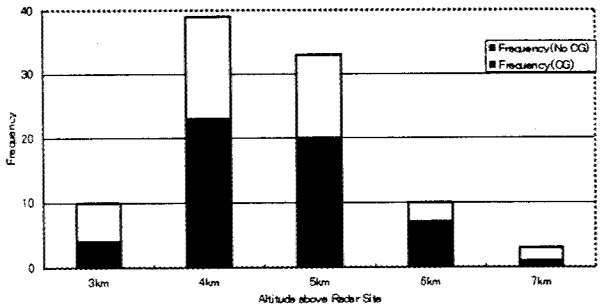


Figure 4. Frequency of first echoes generation altitude each time. CG indicate "Cloud to Ground strokes"

(around 0 ℃). It can also be noted that the cloud base is normally below 1 km in Japan. The altitude of first echo generation is lower than that of Colorado, because it is more wet in the lower layer than in the case of Colorado.

### 3.2 The process of development into meso-$\beta$-scale thunderstorms

We divide the mountain area up in consideration of the slope of mountains facing the radar site. The mountain area was divided into three sections: Mt. Akagi section, Mt. Haruna section, Mt. Chichibu section. We picked up the largest thunderstorms in each section on each day. As the results of this, it was found that the developing thunderstorms moving into the Metropolitan area were generated around the Mt. Akagi and the Mt. Chichibu section at the entrance to the Kanto plain. By contrast, few thunderstorm with development moved into the Metropolitan area around the Mt. Haruna section. Figure 6 shows the process of generation of first echoes with a size of several km and their development into meso-$\beta$-scale (100 km) thunderstorms. In this case, a convergence line several tens of km long is thought to have triggered the generation of the meso-$\beta$-scale thunderstorm. The first echo was generated because of the formation of convergence line between the northwesterly mountain wind and the southeasterly sea breeze. Echo cell groups developed with the generation of new echo cells over the gust front where was the northeast side of the old cells, and two hours later, a squall line-like echo system formed with a length about 120 km. Doppler velocity (Fig. 6) shows the formation of gust front around them. Accordingly, the mechanism of maintaining the generation of active echo cells was strong gusts from the dissipating (old) cells which caused the surface convergence.

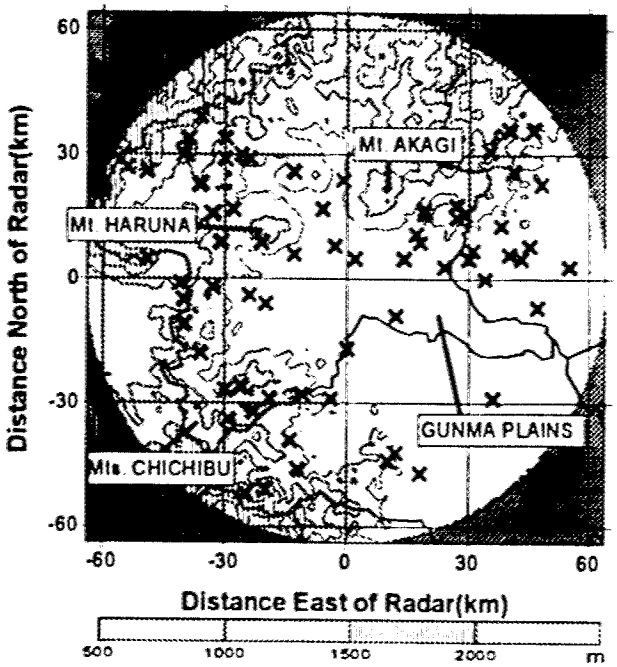


Figure 5. Location of the first echo generated from 23 to 30 Aug. 1997

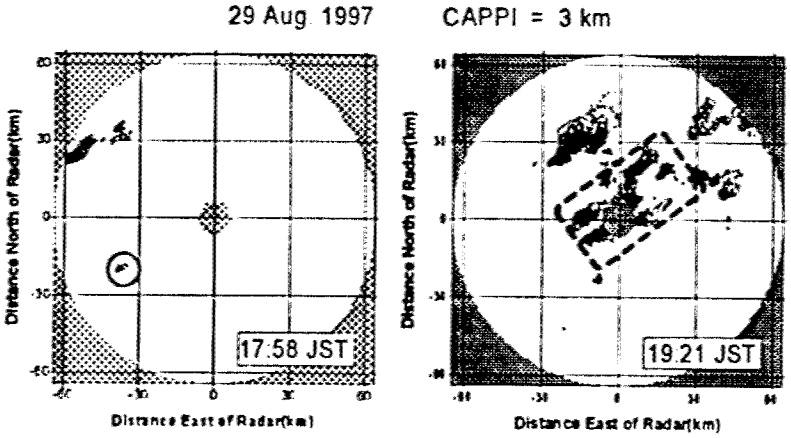


Figure 6 CAPPI image at 3 km AGL The left pannel shows first echo The right pannel shows a two line - shaped echo system

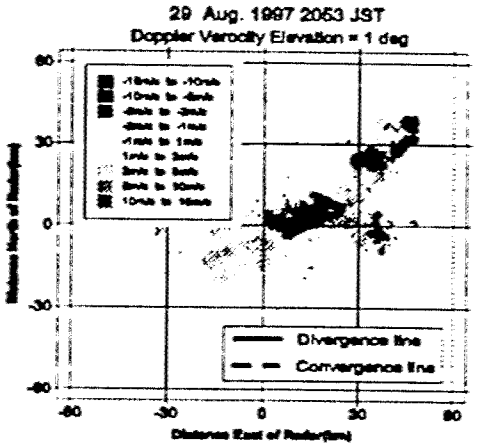


Figure 7. Doppler velocity, positive value indicates the radial velocity away from radar, and negative value, toward the radar.

### 3.3 The relationship between the vertical structure of thunderstorms and CG strokes

Figure 7 shows a case of thundercloud life-cycle and distribution of CG strokes. Many CG strokes occurred after the mature stage of development cells. In this case, CG strokes occurred in the strong echo area (over 32dBZ) and weak echo area (below 32dBZ) in each stage of the thundercloud. In another case, many CG strokes were concentrated in the strong echo area. It is thought that the difference of the CG distribution in echo area occurred as a results of the simultaneous presence of thundercloud at various stage of development.

### 4 Concluding remarks

(1) First echoes were generated at an altitude of 4 - 5km, at the base of mountains in the evening (around 18 JST).

(2) First echoes were generated at the base of mountains, but meso-$\beta$ -scale thunderstorms entering the greater Tokyo metropolitan area developed around the Mt. Akagi and the Mt. Chichibu sections.

(3) At the thunderclouds which developed in northern mountainous area of the Kanto region, CG strokes occurred in the both strong and weak echo region after the mature stage of cell development.


Reference

Charles A. Knight, William D. Hall and Philip M. Roskowski, Visual Cloud History Related to First Radar Echo Formation in Northeast Colorado Cumulus, *J. Appl. Meteor.*, **22**, 1022-1040, 1983


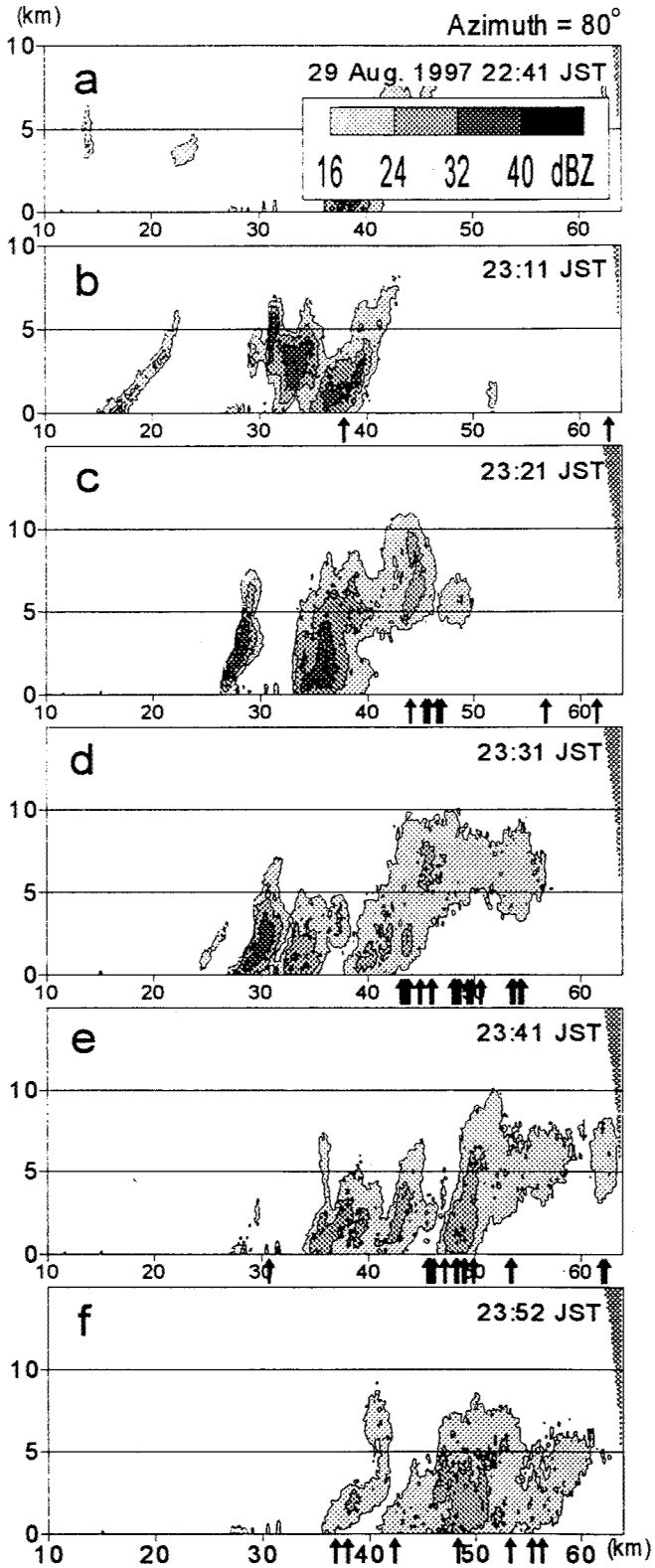


Figure 8. RHI from 22:40 JST to 23:52 JST. The arrows under the x axes show the location of CG strokes.

# TWO TYPES OF PGF-PRODUCING CLOUDS IN WINTER THUNDERSTORMS IN ISRAEL

Yoav Yair[1], Orit Altaratz[2], and Zev Levin[2]

[1]Department of Natural and Life Sciences, The Open University of Israel, Tel-Aviv, Israel
[2]Department of Geophysics and Planetary Sciences, Tel Aviv University, Tel-Aviv, Israel

## ABSTARCT

A study of the occurrence of positive ground flashes (PGF) in winter thunderstorms in Israel was conducted for the 1995/6-1997/8 seasons. We used data from 2 CGR lightning counters, an operational LPATS network and the Tel-Aviv University (TAU) weather radar. The study shows that PGFs occur primarily in events when the reflectivity pattern in a vertical cross-section of the cloud parallel to the prevailing winds, has a distinct tilted echo, with the PGFs located downwind of the main core of reflectivity. A relation between wind shear and PGF fraction was established. Other events show that very strong PGFs also occurred even though the wind shear was weak. In these events, the PGFs were located in regions of weaker reflectivity, typical of stratiform precipitation. RHI profiles of the active cells showed a bell structure with distinct bright bands. A time series showed that strong PGFs (with currents exceeding 100kA) occurred after successive CFs and NGFs. As the regions above the melting layer contain both supercooled water drops, graupel and ice crystals, we can assume that appropriate conditions for charge generation prevail, that possibly lead to the creation of an inverted dipole.

## INTRODUCTION

Levin et al. (1996) studied the occurrence of PGFs in winter thunderstorms in the Tel-Aviv area. The main finding from this study was that the long-term average of the PGF fraction [$R=PGF/(PGF+NGF)$] in thunderstorms was 0.25±0.05. Storms that exhibited high values of $R$ were usually associated with some level of vertical wind shear of the prevailing horizontal wind (a tilted dipole). Yair et al. (1998) modified the ratio to 0.16±0.08, and found a new equation relating the average PGF fraction in a given storm to the intensity of the vertical wind shear ($W$): [1] $R = 0.0305W + 0.073$. However, the correlation was relatively low (0.29), suggesting that the long-term average may actually be composed of different types of PGF-producing storms. Yair et al. (1998) argued that the fraction of PGF in a given storm may be masked by flashes occurring in events with no wind shear in the stratiform region (Holle et al., 1994), and by the transient nature of the dipole structure (Kitagawa and Michimoto, 1994). Lately, Altaratz (1997) studied the radar structure of thunderstorms in Israel, analyzing the reflectivity features of electrically active cells and the spatial and temporal relations between radar echoes and flash locations. The present work utilizes these radar images to further investigate the nature of PGF occurring in our region.

## DATA AQUISTION AND ANALYSIS

We used lightning strike positions and currents from the operational LPATS of the Israeli Electrical Company, which covers Israel and the eastern part of the Mediterranean Sea. Radar images were obtained from Tel-Aviv University's WR-100-5 Enterprise weather radar (5.6 cm). The method of analysis of individual cells is described in Altaratz et al. (1999). The radar scans of the entire volume were obtained for 5-minute intervals, and flashes that occurred within this period were designated on the PPI image and attributed to the nearest active cell. CAPPI images were produced for temperature levels responding to the heights of charge centers in the clouds (Williams, 1989). Vertical cross-sections were performed through the maximum reflectivity core of the cells, parallel to the wind direction at the relevant altitudes.

## RESULTS

The present work indicates that there are two main different types of PGF producing thunderclouds in winter storms in Israel. It is possible that there are other situations leading to positive ground flashes, but we focus this study on the two most distinguishable types. The following is an analysis of two such storms.

The storm of March 18th, 1998: a line of convective cells was approaching the Tel-Aviv coastline at 08:30 UTC. The wind shear in this event was 4.8 m $s^{-1}$ $km^{-1}$, corresponding to a PGF fraction of 0.22, according to equation (1). The cell presented in the analysis was located 22 km from TAU radar, and in the 30 minutes period it produced 3 CFs, 7 NGFs and 2 PGFs ($R$=0.22). The measured currents for the positive flashes were +48 and +65 kA. A CAPPI image of the cell at 08:25 shows that the ground locations of the ground flashes were removed downwind from the main convective core.

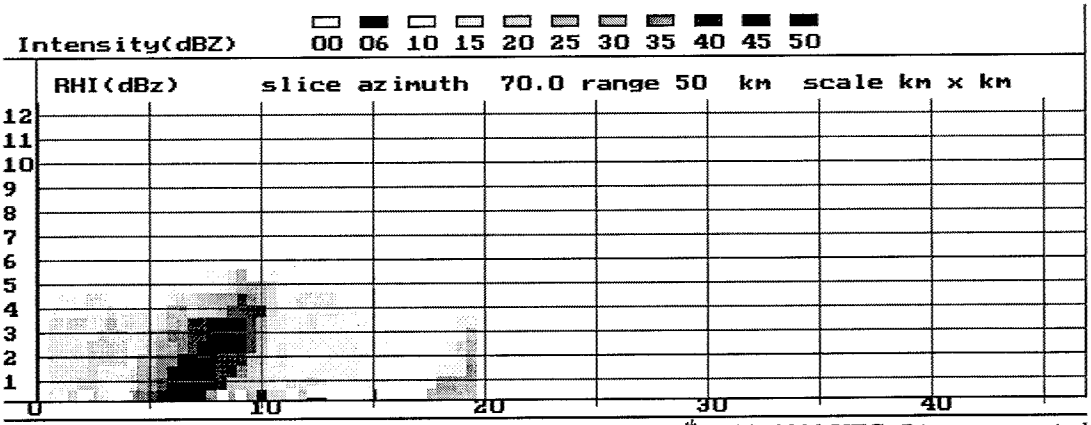


**Figure 1**: *RHI cross section of a PGF producing cell, March 18th 1998, 0830* UTC. *Distances are in km.*

The RHI cross section of this cell (Fig. 1), performed in the direction of the dominant wind vector (240), shows a distinct tilted echo, were the main reflectivity is offset from the vertical by the strong winds aloft (more than 35 m $s^{-1}$ at 6 km). This structure suggests that the mechanism of PGF formation is probably the displacement of the upper positive charge center with respect to the lower negative one, as reported by Brook et al. (1982). Engholm et al. (1990) found that the locations of negative ground flashes were displaced from the maximum reflectivity at low levels, and positive events were displaced further in the direction of the upper level wind. The low flash rate of this storm and the small total flash number, are probably the reason we do not observe this bipolar flash pattern. However, such a tilted echo in the vertical radar echo was also found in our previous study (Levin et al., 1996) and represents events with strong wind shears.

The storm of December 10th 1995: This case represents a different type of PGF producing thunderclouds. Three cells forming over the Mediterranean sea at ranges of 47-52 km from the TAU radar, were observed between 21:21-22:13 UTC. The cells evolved and generated lightning as they were drifting in the WSW synoptic wind. The wind shear in this event was moderate, at 1.78 m $s^{-1}$ $km^{-1}$, placing the expected value of PGF fraction at 0.12. Figure 2 presents the flash history as a function of time: a total of 123 flashes were measured in a 50 minutes period, of which 94 were IC flashes, 15 NGF and 14 PGF. It should be noted that PGFs usually cluster after successive CF and NGF, and exhibit much stronger currents. For example, the PGF at 21:40 peaked at 104 kA and was preceded by CFs and other PGFs; the PGF at 21:52 (98 kA) came after successive CFs and NGFs.

Figure 3 presents an RHI cross-section of the cell, which shows a bell-shaped echo with a central precipitation shaft (> 30 dBz) and a large horizontal, weakly precipitating area, associated with a melting layer (< 15 dBz). Such wide areas of weakly precipitating clouds are not uncommon in winter storms in Israel, where thunderclouds are usually embedded within a matrix of lower, less developed rain clouds.

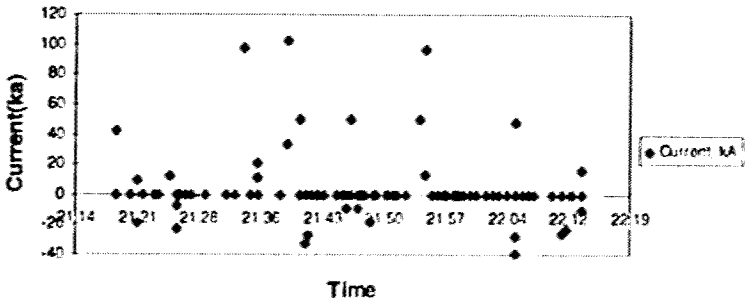


**Figure 2**: *Lightning currents as a function of time for the storm of December 10th, 1995.*

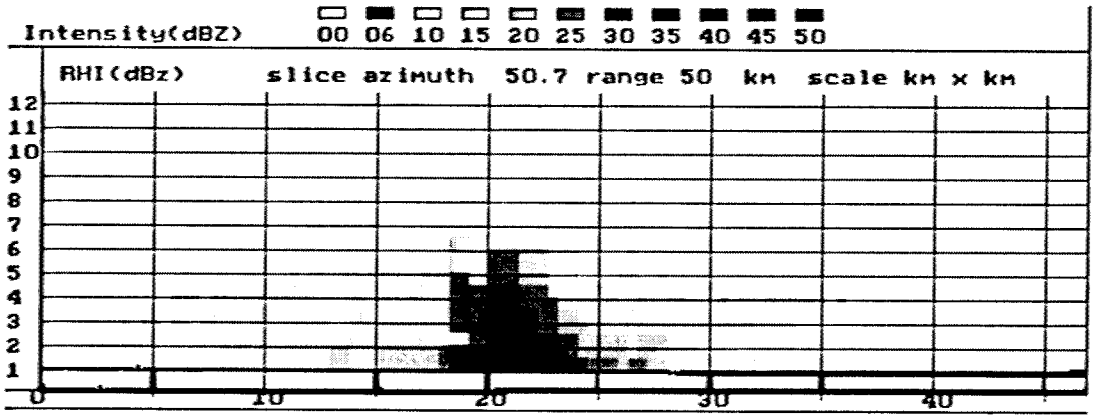


**Figure 3**: *a vertical cross-section of the December 10th 1995 storm.*

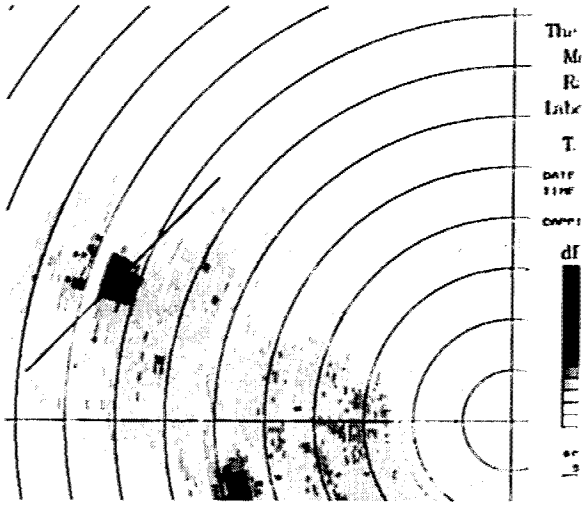

**Figure 4**: *CAPPI at 9000 feet of the storm of December 10th, 1995.*

The radar reflectivity features of the storm (Fig. 4) are similar to those found in the stratiform regions of MCSs in the US. The locations of lightning flashes are marked on top of the reflectivity map: IC flashes are empty circles (o), negative ground flashes are (*) and positive ground flashes are (+). It can be seen that the ground flashes are distributed at distances of 3-5 km from the main echo, with no special preference to the up-shear direction. The

straight dark line in Fig. 4 marks the orientation of the RHI cross section. The measured value of *R* in this particular storm (0.51) cannot be explained by a simple tilted dipole, and may better be explained by an inverted dipole forming in the stratiform precipitation region (Marshall and Rust, 1993). The charge structure in these wide areas was found to be complex and consisted of alternating shallow positive and negative layers (Bateman et al., 1995). Rutledge et al. (1990) and Williams et al. (1994) suggested that the lower positive charge layers are probably created by steady state local microphysical processes, and are not related to the charges generated within the main convective core. The formation of such a multi-layered charge structure in these stratiform regions may be explained by the laboratory experiments of Jayarante (1998). He found four sign reversals in areas where the mean droplet radius was less than 4 ì m, at temperatures between 0°C and –36° C. In order to verify that such layers indeed exist in clouds in our area, we need to conduct in-situ measurements of the electrical properties either by balloon or by airborne instruments.

## SUMMARY

In a continuing study of the nature of PGFs in thunderstorms occurring in the eastern Mediterranean, we combined radar images with lightning strike locations. This enabled the study of the spatial and temporal properties of electrically active cells. Two types of PGF producing clouds were observed during the study period: sheared convective cores that produced strong PGF downwind from the main (tilted) reflectivity maximum, and stratiform precipitating systems, that produced PGFs in the weak echo area around the main convective core. Further work in order to verify the electrical nature of the stratiform area must rely on in-situ airborne measurements.

## ACKNOWLEDGMENT

This research was supported by the Basic Research Foundation of the Israeli Academy of Sciences and Humanities.

## REFERENCES

Altaratz, O., 1997: On the relationship between meteorological parameters and lightning flashes as measured by radar and lightning detection systems. M. Sc. Thesis, 101 pp. Tel-Aviv University.

Altaratz, O., Z. Levin and Y. Yair, 1999: Electrical and radar observations of thunderstorms in the eastern Mediterranean. In: *Proceedings of the 11th ICAE meeting, Huntsville, USA*.

Bateman, M.G., W. D. Rust, B F. Smull and T. M. Marshall, 1995: Precipitation charge and size measurements in the stratiform region of two mesoscale convective systems. *J. Geophys. Res.*, **100**, 16,341-16,356.

Brook, M., M. Nakano, P. Krehbiel and T. Takeuti, 1982: The electrical structure of the Hokuriku winter thunderstorms. *J. Geophys. Res.*, 87, 1207-1215.

Engholm, C. D., E. R. Williams and R. M. Dole, 1990: Meteorological and electrical conditions associated with positive cloud-to-ground lightning. *Month. Weath. Rev.*, **118**, 2, 470-487.

Holle, R. L., A. I. Watson, R. E. Lopez and D. R. MacGorman, 1994: The life cycle of lightning and severe weather in 3-4 June 1995 PRE-STORM mesoscale convective system. *Month. Weath. Rev.*, 112, 8, 1789-1808.

Jayarante, E R., 1998: Possible laboratory evidence for multiple electric charge structure in thunderstorms. *J. Geophys. Res.*, **103**, 1871-1878.

Kitagawa, N. and K. Michimoto, 1994: Meteorological and electrical aspects of winter thunderclouds. *J. Geophys. Res.*, **99**, 10,713-10,721.

Levin, Z., Y. Yair and B. Ziv, 1996: Positive cloud-to-ground flashes and wind shear in Tel-Aviv thunderstorms. *Geophys. Res. Lett.*, **23**, 17, 2231-2234.

Marshall, T.C. and W. D. Rust, 1993: Two types of vertical electrical structure in stratiform precipitation regions of mesoscale convective systems. *Bull. Amer. Met. Soc.*, 74, 11, 2159-2170.

Rutledge, S. A., C. Lu and D. R. MacGorman, 1990: Positive cloud-to-ground lightning in mesoscale convective systems. *Jour. Atmos. Sci.*, **47**, 17, 2085-2100.

Williams, E. R., 1989: The tripole structure of thunderstorms. *J. Geophys. Res.*, **94**, 13,151-13,167.

Williams, E. R., R. Zheng and D. Boccippio, 1994: Microphysical growth state of ice particles and large-scale electrical structure of clouds. *J. Geophys. Res., 99, 10,787-10,792.*

Yair, Y., Z. Levin and O. Altaratz, 1998: Lightning phenomenology in the Tel Aviv area from 1989 to 1996, *J. Geophys. Res.*, **103**, 9015-9025.

# RELATION BETWEEN LIGHTNING ACTIVITY OF SUMMER AND WINTER THUNDERCLOUDS AND SURFACE ELECTRIC FIELD VARIATION, JAPAN

K. Michimoto[1], T. Shimura[2], and T. Suzuki[2]

[1]Air Weather Service H.Q., Defense Agency, Fuchu, Tokyo, JAPAN

[2]Department of Geoscience, National Defense Academy, Kanagawa, JAPAN

ABSTRACT: In winter, active convective clouds frequently form along the coastline of the Hokuriku district, in association with strong advection of Siberian air masses over the Sea of Japan. On the other hand, in summer, many thunderclouds form in the Kanto region in the afternoon every day. Summer and winter thunderclouds were investigated by field works, operation of the C- and X-band weather radars and a car-borne fieldmill. The investigation found a very close relation between the temporal variation of 3-dimensional radar echo and surface electric field magnitude detected by a car-borne fieldmill in the case of summer thunderclouds and winter convective clouds or thunderclouds. The study probed the close relation among radar echoes, quantity of thunderclouds and surface electric field magnitude in the summer and winter seasons. We think that summer thundercloud activity can basically be equated with winter thundercloud lightning activity, except that the magnitude of surface electric field under summer thunderclouds in the case of the Kanto region cannot be equated with that under winter thunderclouds in the case of the Hokuriku district in winter.

## INTRODUCTION

It is well known that lightning discharges from winter thunderclouds to ground have frequently occurred around Komatsu Airport, which is located in the Hokuriku district on the coastline of the Sea of Japan. Their electrical activity is generally very low and they most commonly exhibit only one or two lightning flashes throughout their whole duration. These are popularly called "Single-Flash Thunderclouds" (Michimoto,1993). On the other hand, in summer, many thunderclouds form in the Kanto region in the afternoon every day.

This paper compares the magnitude of surface electric field under summer thunderclouds in the Kanto region and that under winter ones in the Hokuriku district.

## OBSERVATIONS

We compare summer thunderclouds with winter ones in respect of influence on the surface electric field. Figure 1 shows the 35 dBZ echo at 2251 JST on 23th January 1990. The electric field was continuously recorded by a car-borne fieldmill. Figure 2 reproduces the record of the electric field, where time runs from right to left. The electric field reached a positive peak of 8 kv/m, and then a negative peak of 82 kv/m. Graupel fall was observed at that time.

Figure 3 shows the 35-to-45 dBZ echo at 2038 JST on 25th August 1998. The electric field was continuously recorded by a car-borne fieldmill. Figure 4 reproduces the record of the electric field, where time runs from right to left.

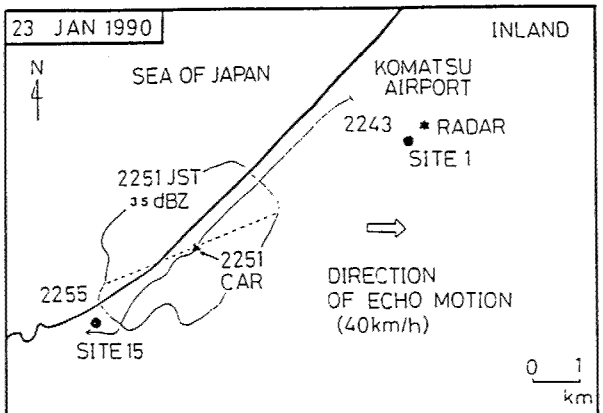


Figure 1. The 35 dBZ echo at 2251 JST on 23th January 1990.

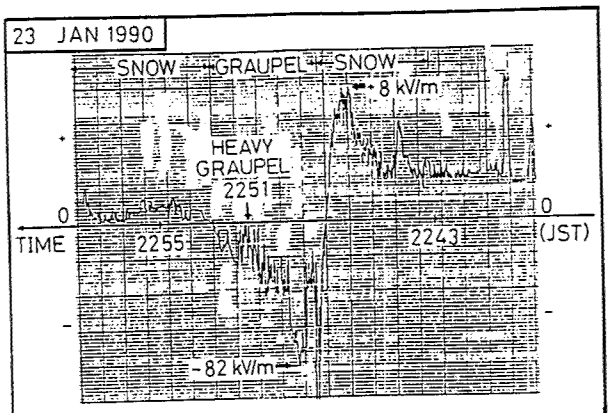


Figure 2. The record of the electric field on 23th January 1990.

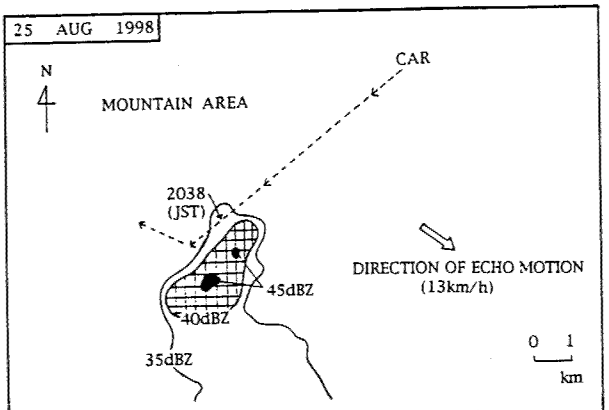


Figure 3. The 35-to-45 dBZ echo at 2038 JST on 25th August 1998.

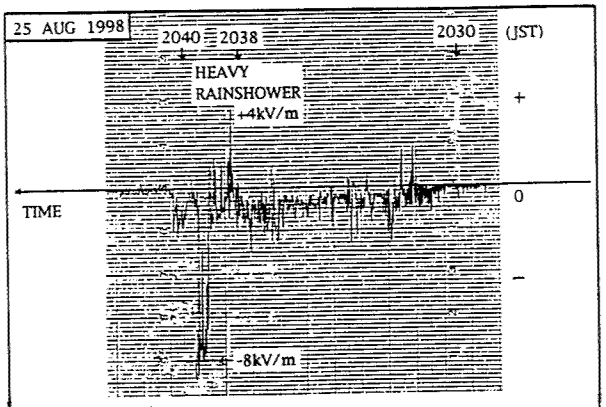


Figure 4. The record of the electric field on 25th August 1998.

The electric field reached a positive peak of 4 kv/m, and then a negative peak of 8 kv/m. Heavy rainshower was observed at that time with many lightning discharges near car.

DISCUSSION

Figure 5 indicates the variation of upper air temperature in each month. It can be seen that the -10 degree centigrade altitude has a wide variation, from 7 km in the summer season to 1 km in the winter season.

The lower part of this figure shows the electric field at the surface and the -10 degree centigrade altitude based on statistic values for 30 years at the Wajima Rawin-sonde station. Assuming that the magnitude of summer surface electric field is about 21 kv/m when the -10 degree centigrade altitude is about 7 km, that of the winter one will be in the range of 75-150 kv/m. The premise here is that the electric field is proportionate with the distance from the surface to the -10 degree centigrade altitude, which is distributed in a pancake-shaped plane of negative electrified particles (refer to from the schematic chart of thundercloud on the right side of Fig. 5).

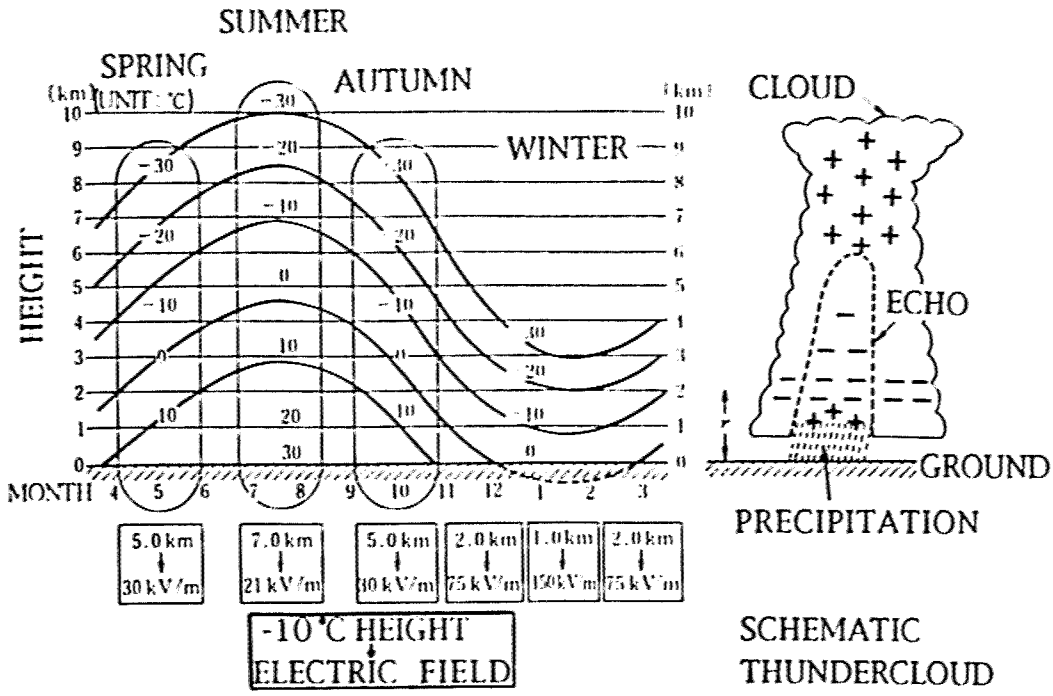


Figure 5. The variation of upper air temperature in each month. (The lower part of this figure shows the electric field at the surface and the right part, the schematic chart of thundercloud.)

Our two observations, one in summer and the other one in winter, each concerned the surface electric field and the -10 degree centigrade altitude. The actual readings for surface electric field ranged from -8 kv/m in summer to -82 kv/m in winter.

In the winter season, the surface electric field is very high, but the lightning activity is not very intense. In the summer season conversely, the surface electric field is not so high, but the lightning activity is quite intense. As the reason for this phenomenon, it is suggested that the -10 degree centigrade altitude is high enough in summer (about 7 km) and that the "pancake" of negative particles is not sufficiently affected by the magnitude of surface electric field.

In the winter season, on the other hand, we believe that the -10 degree centigrade altitude is so low (below 2 km), that the magnitude of surface electric field is very high. However, no lightning discharges occur because a sufficient charge separation cannot be performed in winter thunderclouds (Michimoto, 1993).

## CONCLUSION

Summer and winter thunderclouds were investigated by means of weather radars and a car-borne fieldmill around Komatsu Airport in the Hokuriku district and around the Kanto region, respectively.

The investigation concerned the surface electric field magnitude in the summer and winter seasons. We concluded that the magnitude of surface electric field under summer thunderclouds in the Kanto region cannot be equated with that of winter thunderclouds in the case of the Hokuriku district. Upper air temperature influences the surface electric field magnitude under thunderclouds. In particular, the -10 degree centigrade altitude greatly affects the surface electric field under summer and winter thunderclouds. We suggest that spring and autumn thunderclouds would be affected in a manner similar to summer and winter ones by the -10 degree centigrade altitude.

Further observations are planned for the future.

ACKNOWLEDGMENTS: The authors wish to express their great sincere thanks to the members of the Tokyo Electric Power Co. and Japan Radio Company for furnishing the LPATS data and the weather radar.

REFERENCE

Michimoto, K., A study of radar echoes and their relation to lightning discharges of thunderclouds in the Hokuriku district, Part II: Observation and analysis of "Single-Flash" thunderclouds in midwinter, J. Met. Soc. Japan, 71, 195-204, 1993.

# ELECTRICAL AND RADAR OBSERVATIONS OF THUNDERSTORMS IN THE EASTERN MEDITERRANEAN

Orit Altaratz[1], Zev Levin[1] and Yoav Yair [2]

[1]Department of Geophysics and Planetary Sciences, Tel-Aviv University, Tel-Aviv, Israel.

[2]Department of Natural Sciences, The Open University of Israel, Tel-Aviv, Israel.

## INTRODUCTION

The meteorological conditions for thunderstorm development in Israel have been reviewed by Levin et al. (1996). Most thunderstorms in our region occur between October and April and are usually associated with the passage of "Cyprus Lows", cyclones that originate in southern Europe, and travel over the northern part of the eastern Mediterranean Sea. A different, less prevalent, synoptic situation for the occurrence of thunderstorms is the Red Sea Trough, a tropical low pressure wave from the Red Sea that intrudes toward the Mediterranean Sea, bringing moist air from the tropics. Thunderclouds that form over the sea and the coastal area are typically with cloud base temperatures of about 5°C, and vertical dimensions of 6-8 km. Cloud top temperatures are found in the range of -30° C to -40°C and rarely below -50°C.

The resemblance between the winter thunderstorms in the eastern Mediterranean and those that occur in the western coast of Japan have been pointed out by Yair et al. (1998). The synoptic conditions in both areas are similar: cold, dry, continental air masses passing over relatively warm sea water, changing and becoming unstable as they approach the coast, generating convective clouds and thunderstorms. Levin et al. (1996) also showed that the tilted dipole mechanism, suggested by Brook et al. (1982) to account for the occurrence of positive ground flashes is probably active in storms producing a high fraction of PGFs in the Tel-Aviv area.

## MEASUREMENTS AND DATA ANALYSIS

Observations of lightning, that included the time, location, type and peak current of the lightning strikes were obtained from the Lightning Positioning and Tracking System (LPATS) operated by the Israeli Electrical Company. The system has five measuring stations and one central processing unit and its coverage range is 500 km from the center of Israel. It has a detection efficiency of 70-90% and a location accuracy of 500 meters.

The observations of precipitation were carried out with the 5.6cm, Enterprise WR-100-5 weather radar located at Tel-Aviv University. The radar's range is 200 km, ensuring the coverage of thunderclouds as they move from the Mediterranean Sea toward the coast.

The meteorological and synoptic conditions for each thunderstorm event were obtained from radiosondes released by the Bet-Dagan Meteorological station, which is located 8 km southeast to Tel-Aviv, and from synoptic maps.

The method of data analysis was based on: (a) The identification of convective cells within the radar's range (b) An analysis of the cell's characteristics (reflectivity, cloud top height, rain intensity) during its life cycle, and (c) The ascription of lightning strikes to the cell, (flashes were considered to be produced by a specific cell, if their maximal distance from the central echo did not exceed 10 km).

## RESULTS

An example of this method of analysis is presented for the storm that occurred at 24/3/96. This storm generated lightning over the sea and over the land during the afternoon, for several hours. Figure 1 shows the radar image of the storm from 19:01, with the lightning marks on it (PGF is marked by (+), NGF by (-), and CF by (o)). We followed the cell, marked by A(7) for 30 minutes, as it moved over the land with southwest winds.

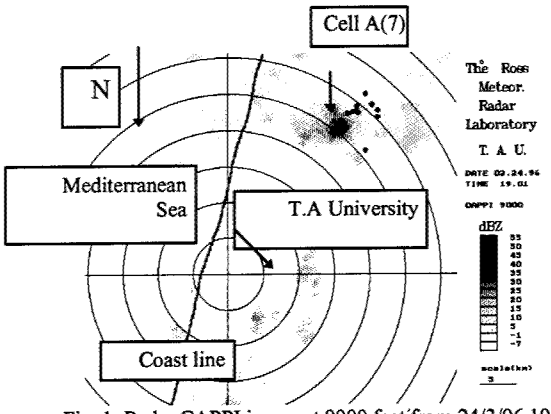

Fig. 1: Radar CAPPI image at 9000 feet from 24/3/96 19:01.

The cell generated 41 flashes during 35 minutes, consisting of 26 cloud flashes (CF), 12 negative ground flashes (NGF) and 3 positive ground flashes (PGF). Figure 2 shows four vertical cross-sections of the cell in different stages of its life cycle. In the first profile (18:52) the cell was in the developing stage. The strongest echoes were found in the middle part of the cell (45 dBZ at 3 km), and it did not produce any flashes. The cloud continued to develop and at 18:56 the maximum reflectivity reached 45 dBZ at the height of 3.3 km. At 19:01 it was 50 dBZ at 3.8 km. During the time interval between 18:56-19:00 the cell produced 14 flashes, and between 19:01-19:05 additional 12 flashes. The maximum lightning activity appeared at the mature stage of the cell. At this stage high reflectivity values (45-50 dBZ) were found at temperatures lower than -10°C.

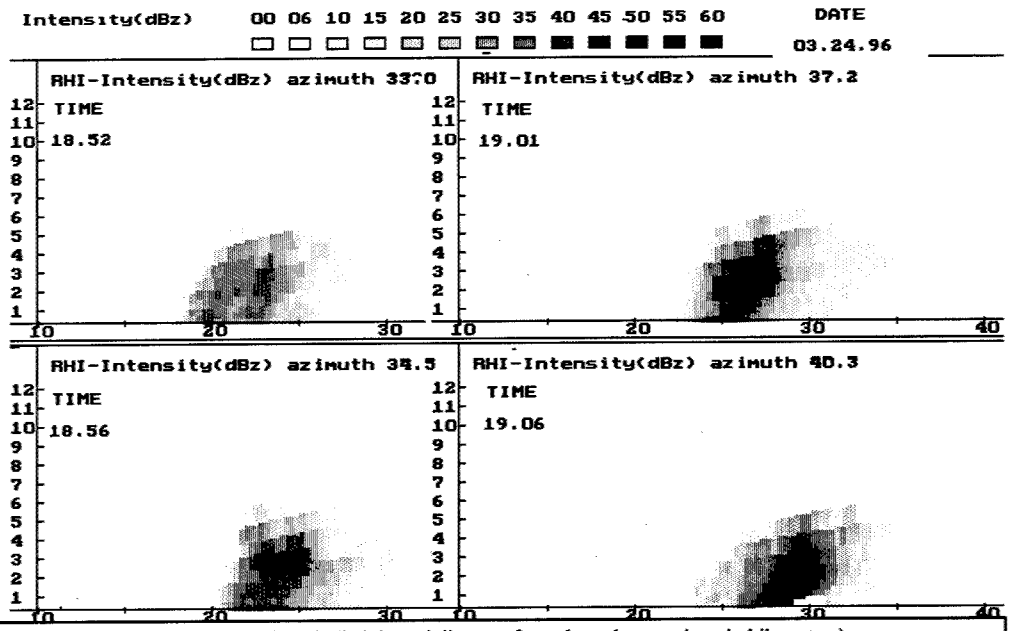

Fig2: Vertical profiles of the cell A(7), (height and distance from the radar are given in kilometers).

Figure 3 presents the change in time of two parameters of the cell A(7): the maximum radar reflectivity (in time intervals of 5 minutes), and the flashes that it produced (continuously in time). It is clearly evident that the peak in the flash rate was correlated in time with the maximum radar reflectivity of the cell. By looking again in the vertical cross sections we can see that these maximums happened in the mature stage in the life cycle of the cloud.

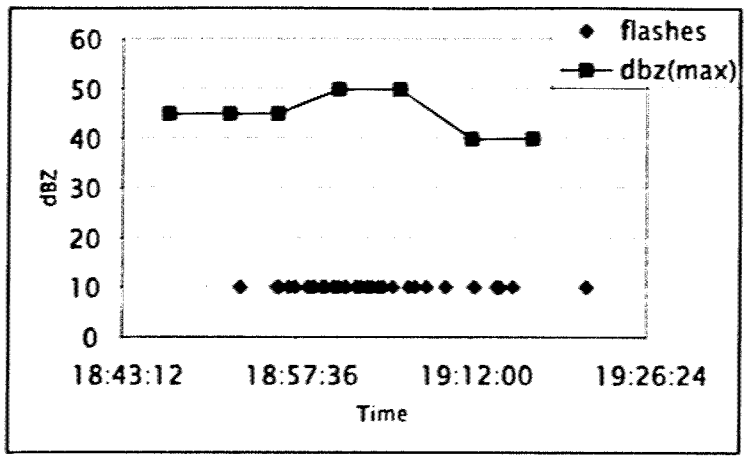


Fig3: Change in time of the maximum reflectivity and the flashes that the cloud A(7) produced

14 additional electrically active cells were analyzed using this method. The results are summarized in Table 1. In some of the cases the analysis was done for two or three cells together due of the difficulty of separating them in the radar image (they are marked in the table on the flash rate column). In those cases the values presented are of the stronger cell.

| Cell | Max height (km) | Max ref (dBZ) | Max rain intensity (mm/h) | Max ref. at the -10°c level (dBZ) | Max flash rate (#/5min) | Time between max ref And max flash rate (min) | Time between first echo and first flash (min) | Temp. level of 40 dBZ echo during the first flash (°C) | Temp. level of 30 dBZ echo during the first flash (°C) | Ref. at the -10°c level in the time of the first flash (dBZ) |
|---|---|---|---|---|---|---|---|---|---|---|
| 11/12/95 | | | | | | | | | | |
| A(1) | 8 | 52 | 82 | 47 | 11 (2 cells) | ---- | 10 | -13 | -22 | 42 |
| A(2) | 9 | 47 | 36 | 47 | 5 | 0 | ---- | -13 | -22 | 42 |
| A(3) | 9.5 | 52 | 82 | 47 | 22 (2 cells) | ---- | ---- | -1* | -10* | 32 |
| 24/3/96 | | | | | | | | | | |
| A(6) | 6.5 | 45 | 26 | 35 | 2 | 0 | 10 | -8 | -24 | 35 |
| A(7) | 7 | 50 | 59 | 50 | 14 | 0 | 10 | -15 | -25 | 45 |
| A(8) | 6.5 | 45 | 26 | 45 | 8 | 0 | 15 | -13 | -22 | 45 |
| 3/1/96 | | | | | | | | | | |
| A(9) | 9 | 50 | 26 | 45 | 17 | 0 | 10 | -9 | -16 | 40 |
| A(10) | ---- | 60 | 134 | 60 | 15 | ---- | 10 | -22 | -25 | 45 |
| A(11) | ---- | 60 | 134 | 55 | 11 | 0 | ---- | ---- | ---- | ---- |
| A(12) | ---- | 55 | 134 | 55 | 7 | 0 | ---- | ---- | ---- | ---- |
| 5/11/96 | | | | | | | | | | |
| A(13) | 10.5 | 55 | 134 | 50 | 7 (2 cells) | ---- | 10 | -27 | -27 | 50 |
| A(16) | 9.5 | 50 | 26 | 45 | 6 | ---- | ---- | ---- | -12 | 35 |
| A(17) | 8.5 | 50 | 59 | 45 | 4 | 0 | ---- | ---- | -3* | 40 |
| A(19) | 13 | 45 | 26 | 50 | 17 (3 cells) | ---- | ---- | ---- | -19 | 40 |

Table 1: Summary of radar reflectivity and lightning occurrence of the active cells

Note: 1) (*) The temperature levels of A(3),A(17) were exceptional so we decided not to include them in the conclusions.
2) A(10)-A(12) were too close to the radar to enable accurate height determination.

## DISCUSSION AND CONCLUSIONS

Based on the findings of the present study we can conclude several threshold values, that determine whether a convective cell in our region would become a thundercloud:

1) The top of the cloud has to be higher than 6.5 kilometers (at a temperature colder than -30°c).

2) The maximum intensity of the reflectivity needs to be higher than 45 dBZ.

3) The intensity of the reflectivity at the -10°c level is more than 35 dBZ.

4) The radar derived rain intensity is higher than 26 mm/hour.

We also found several parameters that define the beginning of the lightning activity:

1) The period between the first radar echo and the first lightning is about 10-15 minutes.

2) The top of the 40 dBZ echo should be higher than the -8°c level.

3) The top of the 30 dBZ echo should be higher than the -12°c level.

4) The reflectivity at the -10°c level is more than 32 dBZ at the time of the first discharge.

5) The vertical velocity of the top of the 40 dBZ echo during the 5 minutes prior to the first lightning is between 1.16-8.3 m/s.

The general characteristics of the electrical activity of thunderclouds, according to all the cells that were analyzed, showed that the beginning of the lightning activity and its maxima appeared in the mature stage of cloud development. Similar findings were reported by Fujita and Black (1988) and Lhermitte and Williams (1984). At the mature stage, the cells were developing upward as the radar echoes intensified while moving to higher altitudes. The first lightning occured 10-15 minutes after the first radar echo appeared (see Table 1). A similar delay was found by Levin and Tzur (1988) who used a numerical cloud model and calculated a 12-20 minutes delay. The peak of the electrical activity was well correlated in time with the maximum radar reflectivity. The variety of reflectivity intensities that appeared at this stage implied that a wide spectra of particle's sizes (and hence fall velocities) existed in the clouds. The heights of the maximum reflectivity indicated that there was a strong vertical flow in the clouds. All of these ensured a high number of particle interactions and an efficient charge separation process (Takahashi, 1984).

An interesting feature was the appearance of echoes stronger than 35-40dBZ at levels higher than the -10°C level. This indicated the appearance of graupel particles in the clouds. Dye et al. (1989) also found the threshold value of 40 dBZ above the –10°C, in thunderclouds in New Mexico.

This study points to further similarities between thunderclouds in the eastern Mediterranean and in western Japan. The microphysical properties described by Michimoto (1991), showed that the necessary conditions for the development of winter thunderclouds in Japan were: 1) fast vertical movement of the 40-50 dBZ echoes, and 2) cloud tops be at temperatures colder than –20°C . For thunderclouds in the Mediterranean we found that the analogous condition was a reflectivity threshold of 45 dBZ But in contrast to Japan our clouds need to reach temperatures of about –30°C . The difference probably arises due to the fact that Japan is slightly northerly to Israel, and therefore, colder temperatures are found at lower altitudes in the atmosphere.

**Acknowledgement**

This research was supported by the Basic Research Foundation of the Israeli Academy of Sciences and Humanities.

**References:**

Brook, M., Nakano, M., Krehbiel, P. and T. Takeuti,1982 : The electrical structure of the Hokuriku winter thunderstorms. *J. Geophys. Res.*, **87**, C2, 1207-1215.

Dye,J.,Winn,W.,Jones,J.and D.Breed,1989: The electrification of New-Mexico thunderstorms, 1. The relationship between precipitation development and the onset of electrification. *Quart. J. Roy. Meteor. Soc.*,**114**, 1271-1290.

Fujita,T.T.,and P.G.Black.1988: Monrovia microburst of 20 July 1986: A study of "SST" . in *Proceedings of the 15th Conference on Severe Local Storms , Am . Meteorol . Soc . , Baltimore,Md.*

Kitagawa, N. and K. Michimoto,1994 : Meteorological and electrical aspects of winter thunderclouds. *J. Geophys. Res.*, **99**, D5, 10713-10721.

Levin, Z. and I. Tzur, 1986: Models of the development of the electrical structure of clouds. In The Earth's Electrical Environment, Studies in Geophysics. National Academy Press, Washington DC.

Levin, Z., Y. Yair and B. Ziv, 1996: Positive cloud-to-ground flashes and wind shear in Tel-Aviv thunderstorms. *Geophys. Res. Lett.*, **23**, 17, 2231-2234.

Lhermitte,R.M.,and E.R.Williams,1984: Doppler radar and electrical activity observation of a mountain thunderstorm . in *Proceedings of the 22th Conference on Radar Meteorology, Zurich.*

Michimoto, K.1991: A study of radar echoes and their relation to lightning discharge of thunderclouds in the Hokuriku district, part 1: observation and analysis of thunderclouds in summer and winter. *J. Met. Soc.Japan*, **69**, 327-335.

Takeuti,T.,Z.Kawasaki,K.Funaki,N.Kitagawa,and J.Huse,1985: On the thundercloud producing the positive ground flashes. *J. Met. Soc.Jpn*, **63**, 354-358.

Takahashi,T.,1984: Thunderstorm electrification-A numerical study. *J. Atmos. Sci.*, **41**, 2541-2558.

Yair,Y.,Z.Levin and O. Altaratz, 1998b: Lightning phenomenology in the Tel Aviv area from 1989 to 1996, *J. Geophys. Res.*, **103**, 9015-9025.

# CLOUD-TO-GROUND LIGHTNING AT LOW SURFACE TEMPERATURES

Paul K. Moore and Vincent P. Idone

Department of Earth and Atmospheric Sciences
University at Albany, SUNY
Albany, New York, USA

ABSTRACT: A simple study was carried out to assess the absolute amount of cloud-to-ground (CG) lightning occurring at low surface temperatures in the continental U.S. The impetus for this study was the practical need to determine a lower operational temperature limit for certain lightning protection devices used in the telecommunication industry. These devices use a temperature dependent medium; a new lower limit of - 4°F had been proposed for design of these devices. Meteorological experience suggested that there was a negligible amount of lightning activity at this temperature and that this could be confirmed with CG lightning data from the National Lightning Detection Network (NLDN). Consequently, we examined the occurrence of CG lightning over the U.S. during the winter months of December-February for a total of six winters: 1988-89 through 1993-94. Three-hourly surface temperatures recorded at the nearest National Weather Service (NWS) reporting stations were correlated with all CG lightning events occurring below 32°F. Both the number of storm events and number of flashes were binned by temperature interval. We identified spurious flashes in clear air regions by examining radar maps and satellite imagery; such flashes were eliminated from the analysis.

We found hundreds of CG lightning storm events that occurred below 32°F over the six-winter period. Each storm typically consisted of just a few flashes though some occasionally contained hundreds of flashes. As anticipated, both the number of storm events and flashes fell dramatically with lower surface temperature. Out of 1,410,272 flashes recorded by the NLDN for the six winters studied, only 7,701 (0.55%) occurred below 32°F, 633 (0.045%) occurred at or below 13°F, and just 11 (0.00079%) occurred below 0°F. No CG strikes were observed at surface temperatures below - 4°F. A simple regression analysis yields (via 95% prediction bounds) an expected maximum number of flashes for $T \leq 9$°F of only 1046 nationwide for the entire six-winter period. This confirmed our expectation that such a low temperature limit was an extreme design constraint. As anticipated, CG lightning at low surface temperatures was most often associated with strong warm advection over a shallow, very cold surface layer. Most of this lightning occurred in the southeastern Great Plains, with the remainder extending northeastward into New England.

## INTRODUCTION

Our purpose in carrying out this study was to quantify the number of cloud-to-ground lightning flashes that occur over the continental U.S. at low surface temperatures. The impetus for this study was the practical need to determine what lower limit of temperature was appropriate for operation of a common type of surge suppression device used in the telecommunication industry. It had been proposed that such devices should be designed to operate at temperatures as low as - 4°F. Meteorological experience suggested that this was an extreme design constraint. The advent of the National Lightning Detection Network (NLDN) made it possible to directly address this question by correlating detected flashes with the nearest reported temperature available from primary and secondary reporting stations of the National Weather Service (NWS). In essence, this is what we have done.

## ANALYSIS

All temperature readings used in this study were obtained from 3-hour interval NWS surface maps available from the archives of the National Centers for Environmental Prediction. These temperatures are reported to 1°F and it is assumed that the temperatures are this accurate. The lightning data were obtained from archived NLDN observations available at the University at Albany (where the NLDN was originally developed) or, for the later years examined, from the present operators of the NLDN, Global Atmospherics, Inc., of Tucson, Arizona. The key flash parameters used in this study were the location and date/time of occurrence of each flash.

In correlating the lightning and temperature data fields, we started by imposing certain restrictions to help make the data set manageable. First, we limited the temperatures to values less than 32°F; this seemed like a natural upper limit. Given that even much lower temperatures were of primary interest here, we limited the analysis to those months of the year generally considered the coldest: December, January and February. To obtain a statistically valid sample, we examined a total of six winter seasons: 1988-1989 through 1993-1994.

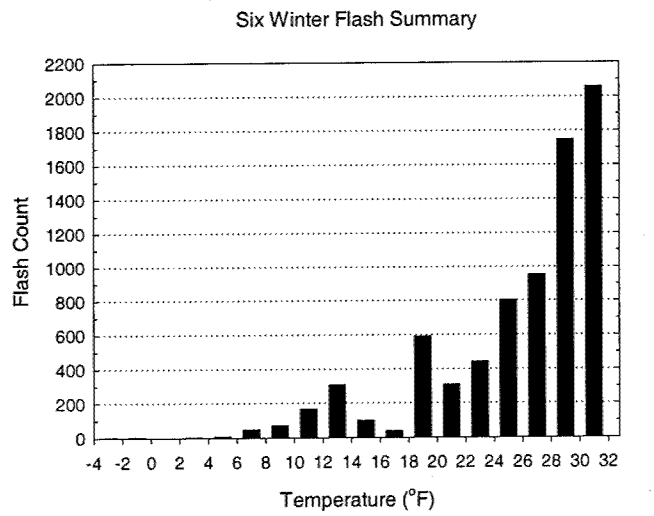


**Figure 1.** Summary of flash count versus temperature for the six winter seasons studied. Temperature bin interval is 2 degrees F.

We correlated the two data fields directly by inspection; we did not rely on a computer program to perform this procedure. This was a tedious task, as even during the winter season when the relative amount of lightning activity is much less, there are still a large number of individual flashes. Nonetheless, all lightning storm events (individual flashes to clusters of several hundred flashes) were identified in space and time over the six winters, guided by the temperature maps wherein regions with $T \geq 32^{\circ}$F were excluded. In the colder regions, each group of flashes was assigned an appropriate temperature. Occasionally, a group of flashes would be nearly equidistant from two NWS reporting stations with different temperatures; in this case, the lower of the two temperatures was used, reflecting the basic premise of this study. As we were using 3-hourly temperature summaries, we examined the lightning data in 3-hour windows centered on the map times. Hence, temperature assignments were updated only every three hours for long-lived events.

The location accuracy of the NLDN was not a significant factor in assigning temperatures to flashes given the large separation between NWS reporting stations and a typical flash location uncertainty of 4-8 km [*Cummins et al.*, 1998]. We do not consider the issue of detection efficiency as significant in this study, as should be apparent from the results presented below.

We note that in examining the data, a number of flashes were observed located many kilometers (~ 50 km or more) into clear-air regions as verified by coincident satellite imagery and radar maps. A total of 92 such flashes were observed. Such spurious events were excluded from the subsequent analysis.

## RESULTS

Hundreds of storm events were identified in this analysis, yet the quintessential results can be summarized in a few simple plots. In Figure 1, we show a histogram plot of the total flash count as a function of temperature. Here each temperature bin coincides with a 2°F increment, with the 31°F bin corresponding to those flashes assigned a temperature of either 31°F or 30°F, and so on. The total number of flashes found below 32°F for all six winters was 7,701. In comparison, the total number of flashes observed by the NLDN for the same period, regardless of temperature, was 1,410,272. Hence, only 0.55% of all observed flashes occurred below 32°F. Only 633 flashes (0.045%) were detected at or below 13°F and just 11 flashes (0.00079%) occurred below 0°F. No CG strikes were observed to occur for surface temperatures at or below - 4°F.

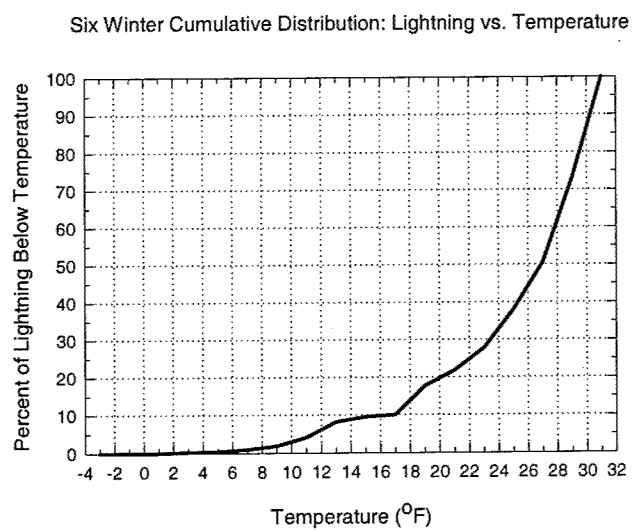


**Figure 2.** Cumulative distribution plot for the total of 7,701 flashes observed at $T < 32$ F.

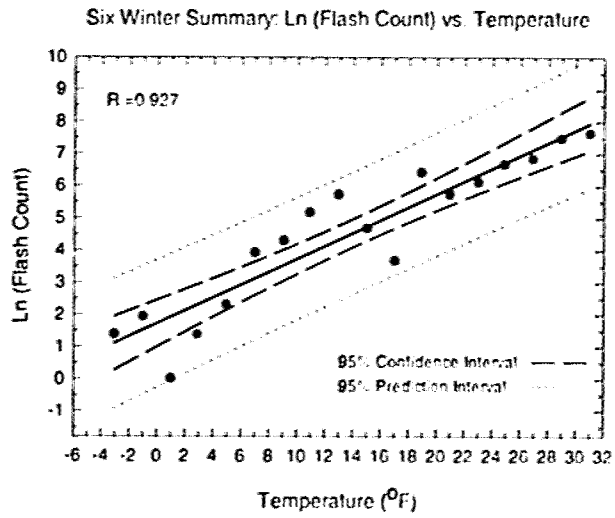


**Figure 3.** Regression analysis for Ln (Flash Count) versus temperature

In Figure 2, we present the cumulative distribution function of observed lightning flashes below 32°F as a function of temperature. From Figures 1 and 2, it is apparent that there is a dramatic decline of lightning activity with surface temperature, as expected. In Figure 3, we present the result of a simple regression analysis using the observed number of flashes as a function of temperature. Included are the 95% confidence and prediction bounds. The regression line in Figure 3 gives flash count, $N$, as a function of $T$ in °F as $N$=5.5*exp{0.2*$T$}. (Note that we took the liberty of assigning $N$=1 for the observed value of zero at 1°F to avoid the problem of obtaining minus infinity with the logarithmic transform used. A direct non-linear regression of the same type of exponential function performed on the original $N$ versus $T$ data yields a similar, but slightly different equation, this being $N$=13.3*exp{0.164*$T$} with R=0.979.)

In Figure 4, we present a geographic summary of all flashes that occurred for temperatures at or below 26°F for the full six-winter period of the study. (We show only this subset of the flashes because plotting all 7,701 flashes yields too busy a plot.) Finally, in Figure 5, we present a plot of all lightning activity that occurred for $T \leq 13$°F, this corresponding to about the 8% "coldest" lightning in our data set.

## DISCUSSION

Based upon Figures 1 – 3, it is apparent that the amount of lightning falls roughly exponentially with temperature for $T < 32$°F. The number of flashes at very low temperatures, say less than 10°F, is trivial in comparison with the warm season threat. This would be so even if the NLDN was operating at a detection efficiency of only 60%, a reasonable lower bound based upon results from 1993 as presented in *Idone et al.*, [1998]. For the proposed design lower limit of – 4°F, the 95% prediction bounds of Figure 3 yield a maximum number of flashes nationwide for the six year period of just 24; for $T \leq 9$°F, the corresponding count would be 1046. This suggests that there is a negligible probability of any surge suppression device having to deal with a flash at such low temperatures. Further perspective on these results can be gained by considering that the yearly flash count for the U.S. has been of the order of ten million flashes as reported recently by *Orville and Silver* [1997].

Though our study did not involve detailed meteorological analyses of the storm events as in *Moore and Orville* [1990] or *Holle and Watson* [1996], we can say that the usual situation encountered was that of a shallow cold layer at the surface with strong warm advection aloft. The geographic summary of flash locations in Figure 4 indicates clearly that lightning during the winter is most prevalent over a portion of

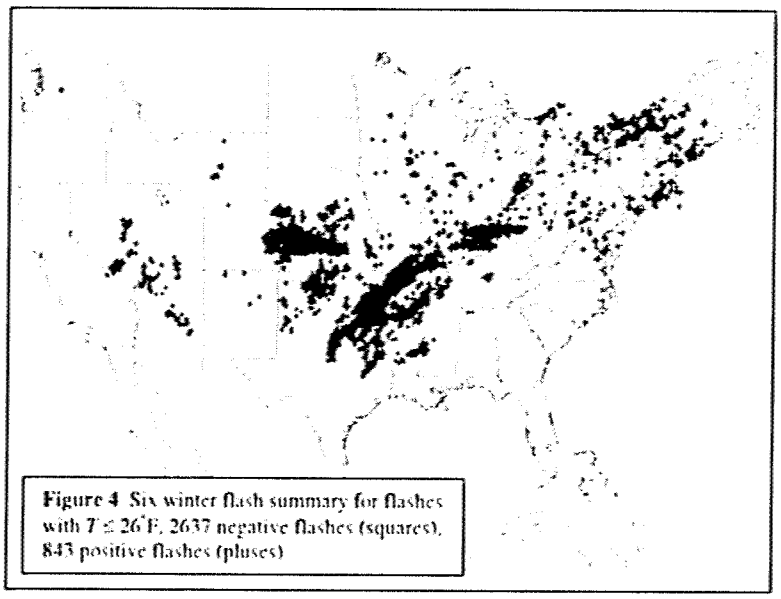

**Figure 4** Six winter flash summary for flashes with $T \leq 26$°F, 2637 negative flashes (squares), 843 positive flashes (pluses)

the U.S. that extends from the Northeast, through the Ohio River Valley and into the southeastern Great Plains. Certainly, the bulk of the lightning, including that lightning at the lowest temperatures, occurs mainly in the southeastern Great Plains. This observation is consistent with the strong potential for set up of the conditions described above. Some of the more intense events were closely associated with stationary surface fronts.

Further in-depth study of the meteorological aspects of lightning at such low surface temperatures is certainly warranted. It may also be worthwhile to investigate how well the observed exponential trend continues between flash count and simple "dry" surface temperature for warmer temperatures relative to more sophisticated thermodynamic considerations such as those discussed in *Williams* [1995].

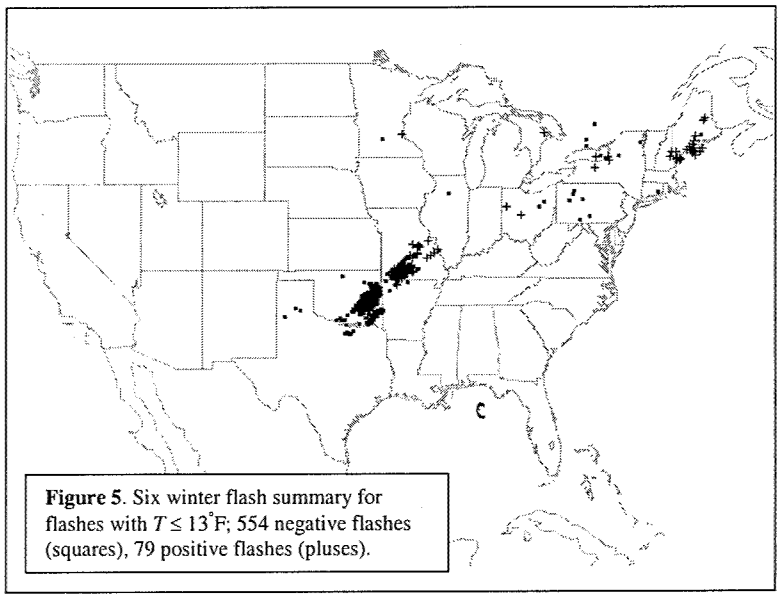

**Figure 5**. Six winter flash summary for flashes with $T \leq 13^{\circ}$F; 554 negative flashes (squares), 79 positive flashes (pluses).

CONCLUSION

Based on six winter seasons of data, we found a total of 7,701 flashes that occurred at local surface temperatures below 32°F. The decline of flash count with temperature is exponential with no flashes observed for $T < -4^{\circ}$F. Only 633 flashes were observed nationwide for $T \leq 13^{\circ}$F for the six seasons, suggesting that the overall threat of lightning at such low surface temperatures is essentially minimal. The geographic distribution of observed flashes is mainly along a swath from New England through the southeastern Great Plains. Most of the "coldest" lightning occurred in the southeastern Great Plains.

ACKNOWLEDGEMENTS: The authors are grateful to Mr. Donald Turner and Northern Telecom, Inc., for funding this study. We also thank Mr. Ken Cummins and associates at Global Atmospherics, Inc., for gracious assistance in these efforts.

REFERENCES

Cummins, K. L., M. J. Murphy, E. A. Bardo, W. L. Hiscox, R. B. Pyle, and A. E. Pifer, A combined TOA/MDF technology upgrade of the U.S. National Lightning Detection Network, *J. Geophys. Res.*, 103, 9035-9044, 1998.

Holle, R. L., and A. I. Watson, Lightning during two central U.S. precipitation events, *Mon. Weather Rev.*, 11, 599-614, 1996.

Idone, V. P., D. A. Davis, P. K. Moore, Y. Wang, R. W. Henderson, M. Ries, and P. F. Jamason, Performance evaluation of the U.S. National Lightning Detection Network in eastern New York, 1. Detection efficiency, *J. Geophys. Res.*, 103, 9045-9055, 1998.

Moore, P. K., and R. E. Orville, Lightning characteristics in lake-effect thunderstorms, *Mon. Weather Rev.*, 118, 1767-1782, 1990.

Orville, R. E., and A. C. Silver, Annual Summary: Lightning ground flash density in the contiguous United States: 1992-1995, *Mon. Weather Rev.*, 125, 631-638, 1997.

Williams, E. R., Meteorological aspects of thunderstorms, in *Handbook of Atmospheric Electrodynamics*, edited by H. Volland, pp. 27-60, CRC Press, Inc., Boca Raton, Florida, 1995.

# LIGHTNING IN SUPERCELL STORMS

Gerhard Reuter* and Steven Kozak

University of Alberta, Edmonton, Canada

## INTRODUCTION

Severe convective storms are often associated with lightning strike activity. How are cloud-to-ground (CG) lightning strikes related to the storm structure? CG lightning occur mostly downshear of the main radar reflectivity core in supercell storms, while in multicell storms the lighting strikes near the radar reflectivity core (Ray et al. 1987). In developing supercells, CG lightning was found mostly on the storm's left side with respect to its track (Keighton et al., 1991). Holle et al. (1994) found that there were more lightning strikes per precipitation core area, when compared with the remainder of the storm area. Rust et al. (1981) found that increases in radar reflectivity magnitudes were correlated with increases in CG lightning strikes. Rutledge and MacGorman (1988) observed that maximum CG activity is approximately correlated with the period of most intense rainfall with a delay on the time scale of hours.

In this conference paper the spatial and temporal patterns of lightning and precipitation are investigated for four Alberta hailstorms. Storm 1 and storm 2 occurred on 19 August 1992, while storm 3 and storm 4 formed on 30 July 1993. All four cases were long-lived hailstorms of quasi-supercell structure that moved across central Alberta. The Alberta Forestry Lightning Network (Kozak, 1998) had direction finders that synthesized the position and timing of the CG lightning strikes. All four storms were monitored by operational weather radar located at Carvel (53.34° N, 114.09° W). This C-band radar takes volume scans at intervals of 10 minutes by scanning at 24 different elevation angles from 0.4° to 24.6°.

## SPATIAL ORGANIZATION OF LIGHTNING STRIKES

At all times, both storms 1 and 2 remained well-defined entities that were easily tracked on the Constant Altitude Planar Position Image (CAPPI) maps that depict radar reflectivity at 2 km above ground. The shape of the 30 dBz echo remained close to an ellipse with its major axis pointing in the downwind direction (i.e. north-east). On each CAPPI map (produced every 10 minutes), a geometric center could be marked at the intersection of the major and minor axes of the ellipse, which closely approximated the storm area. The storm area was then divided in four equal quadrants: Right Front (RF), Left Front (LF), Right Back (RB) and Left Back (LB).

Fig. 1 (a) shows the time history of CG lightning strikes (#STR in $min^{-1}$) for storm 1. From 0040 to 0210 UTC the lightning frequency was relatively low, ranging from 0.5 to 2 $min^{-1}$. From 0210 to 0330 UTC, #STR increased to 5 $min^{-1}$. For the next 30 minutes, the lightning strikes frequency subsided, before developing a new peak of 5.5 $min^{-1}$ at 0430 UTC. The lightning diminished rapidly, ceasing at 0520 UTC. A total of 574 CG lighting strikes accumulated during the 4½ hours. Fig. 1a also shows the relative contributions of the lighting strike frequency from each of the four quadrants. Most of the lightning strikes occurred in the two back quadrants, with very few strikes in its front (i.e. downshear) side. From 0040 to 0210 UTC, the RB storm quadrant had slightly more lightning strikes than the LB quadrant. During this time, the maximum radar echo was located in the LB quadrant. After 0210 UTC, the maximum precipitation shifted into the LB quadrant, which was accompanied by an increase of lightning in the RB quadrant. Throughout the remainder of the storm's lifetime, the largest relative contribution towards lightning came from the RB quadrant.

Storm 2 (Fig. 1b) was similar to storm 1 in that it developed multiple peaks in CG lightning frequencies. In both storms, most of the lightning occurred in the two back quadrants (i.e. at the upshear side of the storms). The left quadrants of the storms (i.e. the northwest flank) had more lightning than the right quadrants (i.e. the southeast flank).

Storm 3 and Storm 4 developed over the radar area on 29-30 July 1993. Again, the storms could be tracked on the radar imagery and the shape of the intense radar echo was close to an ellipse. The relative contributions of the four storm quadrants towards the CG lightning strike frequency are plotted in Fig. 2. In both storms, most of the lightning strikes occurred in the two back quadrants (i.e. in the upshear side of the storms). In fact, very little lightning was found ahead of the geometric storm center. However, the relative importance of LB and RB quadrants differed for the two cases. In Storm 3, the two back quadrants contributed roughly equally. However, in Storm 4 far more lightning strikes occurred in the LB quadrant than in the RB quadrant.

We compare the total number of CG lightning strikes that accumulated throughout their observing period for the four storms (Table 1). Storm 1 and storm 2, which occurred on 19 August 1992, had more lightning strikes than those associated with the storms forming on 30 July 1993. For storms 1, 2 and 3, about 85% of their total lightning strikes were recorded at the back two quarters (i.e. in the south-west or upshear side). In storm 4, the back half contributed 60%; still higher than the frontside. Storms 1, 2, and 4 had more lightning on left flank (i.e. northwest side), while storm yielded more lightning on the right flank (i.e. south-east side).

* *Corresponding author e-mail address: Gerhard.Reuter@Ualberta.ca*

**Table 1. Total number of CG lightning strikes and the relative contribution of the four quadrants.**

| Storm | #1 | #2 | #3 | #4 |
|---|---|---|---|---|
| #STR | 574 | 278 | 176 | 109 |
| **Back** | **84%** | **86%** | **86%** | **60%** |
| Front | 16% | 14% | 14% | 40% |
| **Left** | **56%** | **65%** | **43%** | **60%** |
| Right | 44% | 35% | 57% | 40% |
| **LB** | **49%** | **57%** | **37%** | **43%** |
| RB | 35% | 29% | 49% | 17% |
| FF | 7% | 8% | 6% | 23% |
| RF | 9% | 6% | 8% | 17% |

## CORRELATION OF RAINFALL AND LIGHTNING

Two radar parameters often used for severe storm forecasting in Alberta are the maximum height of the 40 dBz reflectivity (denoted by H) and the maximum radar reflectivity above 2 km. Using the Marshall-Palmer $Z= 200 R^{1.6}$, the latter is converted to maximum rainfall rate (R). The Z-R conversion becomes problematic in heavy convective rain and hail (Xin et al. 1997). Fig. 3 compares the timing of the lightning strikes with the evolution of H and R for storm 1. In the first 2 hours, the maximum height H of the 40 dBz increased from 7 to 10.5 km, while the maximum rainfall rate R intensified from 40 to 80 mm $h^{-1}$. This rapid growth in rainfall had no immediate impact on the number of lightning strikes (#STR), which oscillated around 1 $min^{-1}$. However, from 2 to 3.5 h, #STR increased dramatically from 0.5 to 5 $min^{-1}$.

Fig. 4 compares the radar observations with the number of lightning strikes for storm 2. In the first hour of the observing period, the increase in #STR coincided with the increasing H and R. Thereafter, the ups and downs in H did not coincide with those in #STR. Similarly, changes in R and #STR were not correlated.

The analysis for storm 3 and storm 4 are depicted in Figs. 5 and 6. In both cases, the maximum height of the 40 dBZ was deep varying between 10 and 12 km for most of the storms' lifetime. The 12 km level for H, coincided with the tropopause for that day. Also R remained fairly uniform, ranging from 60 to 100 mm $h^{-1}$. These high values were indicative for large hail, which indeed were observed for both storm cells. More variability was indicated in the number of lightning strikes. The correlation between radar and lightning parameters were weak for both storms.

We computed the Correlation Coefficient of #STR versus H, and #STR versus R with various time delays. For a given time delay of $\Delta t$, H at time t was correlated with #STR at time $t+\Delta t$ for all times t. For delay times of less than 40 minutes, H and #STR were negatively correlated for storm 1 (Fig. 7a). However, with a delay of 80 minutes, the correlation coefficient between H and #STR became about +0.6. Similarly, R was uncorrelated with #STR for time delays less than 1 hour. The best correlation of +0.4 occurred for a delay of 100 min. The findings for storm 2 were similar (Fig. 7b). Significant positive correlation occurred only for a delay of 70-100 min.

Both storms 3 and 4 had positive CC between #STR and R for delay times of 0-20 minutes (Fig. 8). A 20 minute delay is still within the typical convective timescale of cumulus development. There was also positive correlation between #STR and H for a delay of 0-30 min. The highest CC value was +0.6 for a 30 min delay.

## CONCLUSIONS

CG lightning strike observations were analyzed for four severe Alberta hailstorms. The number of lightning strikes per $min^{-1}$ varied significantly throughout the lifetime of the four storms. There were half-hour periods of very intense lightning activity, interspersed with periods of only few lightning strikes. The spatial distribution of the lightning strikes within the radar echo region was far from uniform. About 60-85% of the lightning strikes occurred on the upshear side (i.e. on the southwest side of the northeast moving storms). Of the four storm quadrants, the left back quadrant tended to have the most lightning strikes. The right front quadrant usually had the fewest lightning strikes (see Table 1).

For the two storms on 30 July 1993 the lightning strike frequency was correlated with radar-derived rainfall parameters with an optimal delay of about 10-30 minutes. This agreed with the notion that coupling of precipitation and lightning parameters should occur within a period of 30 minutes, which is the time span of a typical thunderstorm cell. The two supercell storms on 19 August 1992 did not indicate that precipitation growth was followed by an increase in the number of lightning strikes for delay times less than an hour. However, the lightning tended to be correlated with the precipitation recorded 90 minutes earlier. A similar finding was reported by Rutledge and MacGorman (1988).

## REFERENCES


Holle, R.L., A.I., Watson, R.E. Lopez, D.R. MacGorman, and R.Oritz, 1994: *Mon. Wea. Rev.*, **122**, 1798-1808.

Keighton, S.J., H.B. Bluestein, D.R. MacGorman, 1991: *Mon. Wea. Rev.*, **119**, 1533-1556.

Kozak, S., 1998: Analysis of lightning in Alberta thunderstorms. *M.Sc.Thesis., Univ. of Alberta*, 120 pp.

Ray, P.S., D.R. MacGorman, and W.D. Rust, 1987: *J. Geophys. Res.*, **92**, 5713-5724.

Rust, W.D., W.L. Taylor, and D.R. MacGorman, 1981: *Bull. Amer. Meteor. Soc.*, **62**, 1286-1293.

Rutledge, S.A. and D.R. MacGorman, 1988: *Mon. Wea. Rev.*, **116**, 1393-1408.

Xin, L., G.W. Reuter and B. Larochelle, 1997: *Atmos.-Ocean*, **35**, 513-521.



***ACKNOWLEDGEMENTS:*** *This research was supported by grants from the Natural Sciences and Engineering Research Council and Environment Canada.*

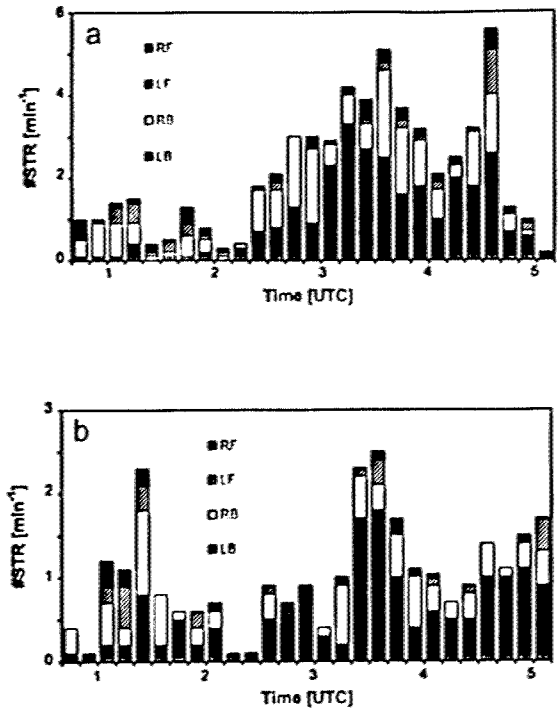


*Figure 1. Time history of number of lightning strikes per minute within each of the four quadrants (Right Front, Left Front, Right Back, and Left Back) for storm 1 (a) and storm 2 (b) on 19 August 1992.*

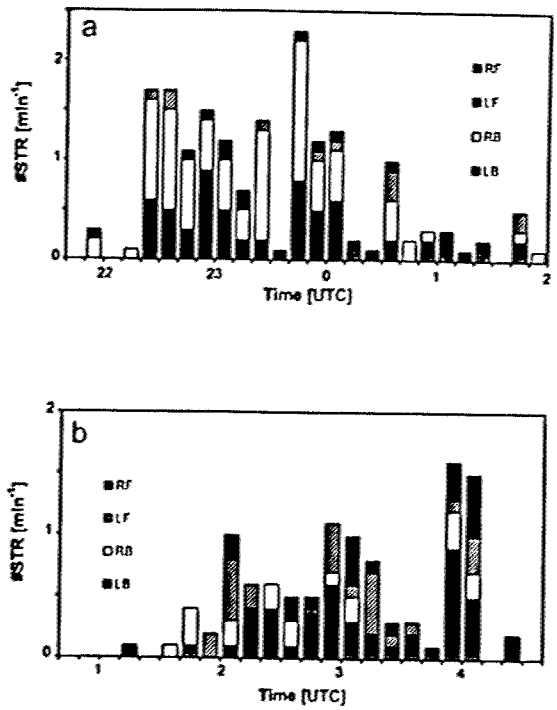


*Figure 2. Time history of number of lightning strikes per minute within each of the four quadrants (Right Front, Left Front, Right Back, and Left Back) for storm 3 (a) and storm 4 (b) on 30 July 1993.*

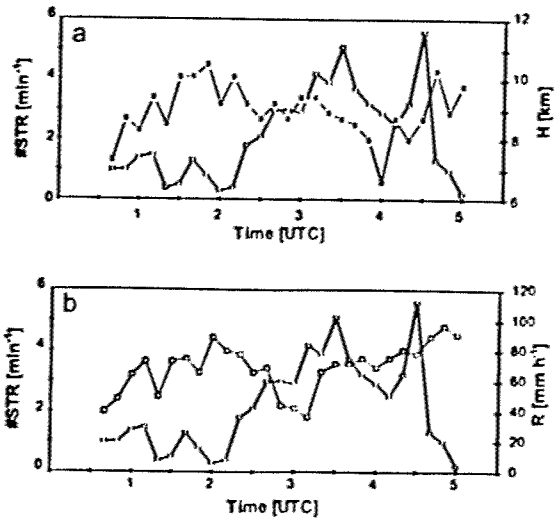


*Figure 3. Number of lightning strikes #STR (circles) compared with (a) maximum 40 dBz height H (crosses), and (b) maximum rainfall rate R (squares) for storm 1.*

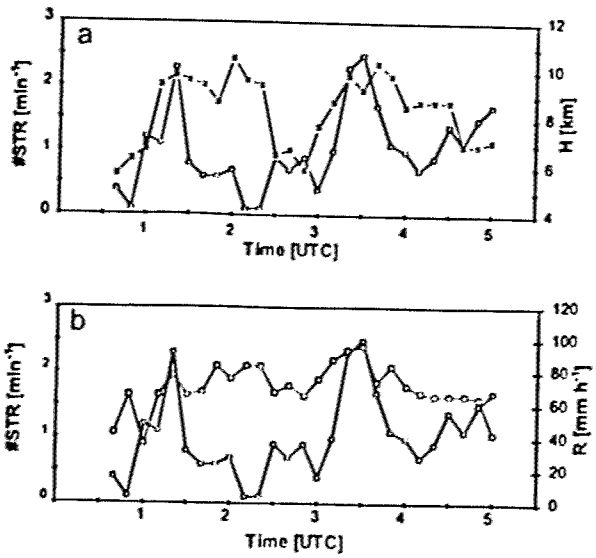


*Figure 4. Number of lightning strikes #STR (circles) compared with (a) maximum 40 dBz height H (crosses), and (b) maximum rainfall rate R (squares) for storm 2.*

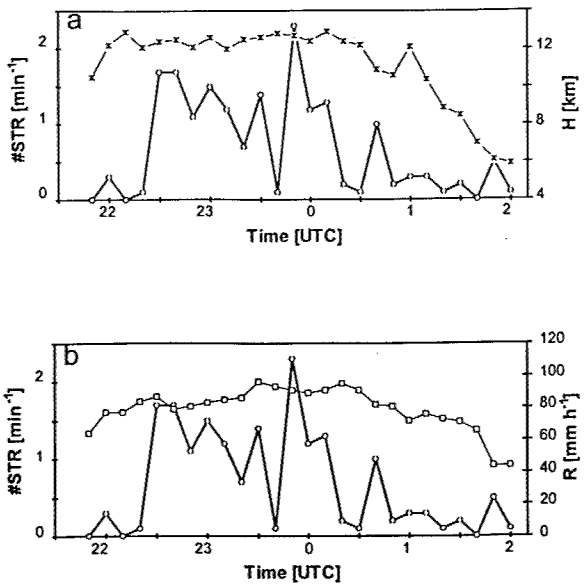


*Figure 5. Number of lightning strikes #STR (circles) compared with (a) maximum 40 dBz height H (crosses), and (b) maximum rainfall rate R (squares) for storm 3.*

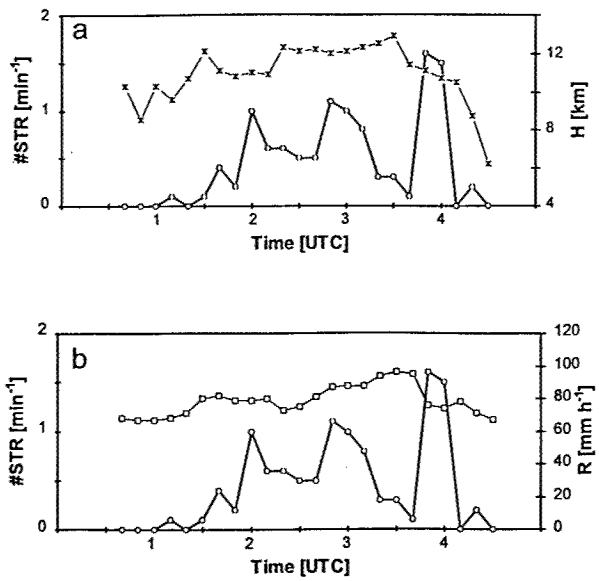


*Figure 6. Number of lightning strikes #STR (circles) compared with (a) maximum 40 dBz height H (crosses), and (b) maximum rainfall rate R (squares) for storm 4.*

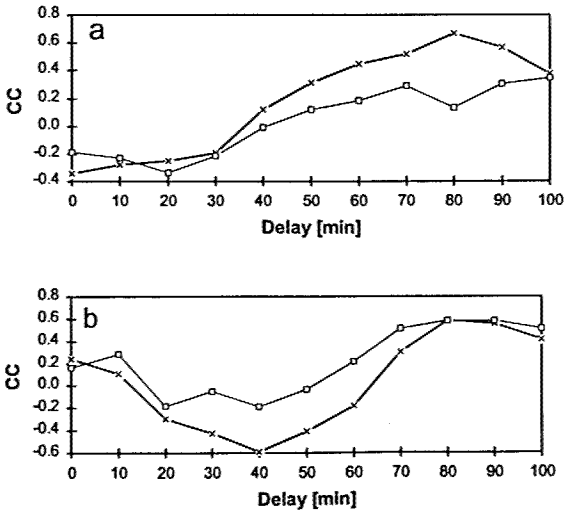


*Figure 7. Correlation coefficient (CC) plotted versus time delay of lightning strikes with maximum 40 dBz height H (crosses) and maximum rainfall rate R (squares) for (a) storm 1, and (b) storm 2 of 19 August 1992.*

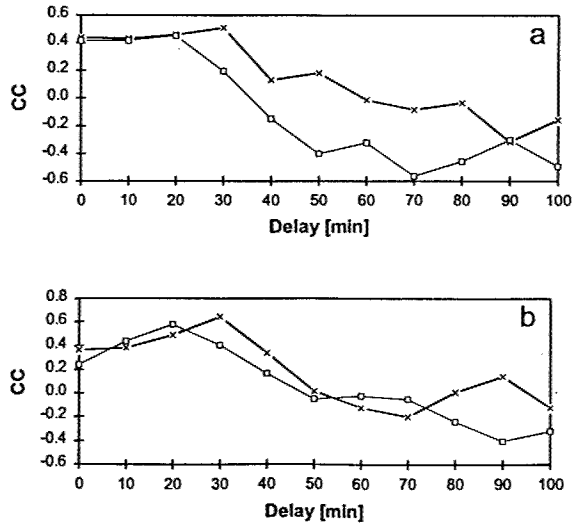


*Figure 8. Correlation coefficient (CC) plotted versus time delay of lightning strikes with maximum 40 dBz height H (crosses) and maximum rainfall rate R (squares) for (a) storm 3, and (b) storm 4 of 30 July 1993.*

# POLARIMETRIC RADAR OBSERVATIONS AND CLOUD MODELING STUDIES OF LOW LIGHTNING PRODUCING CONVECTION IN THE FORT COLLINS FLASH FLOOD

Walter A. Petersen, Lawrence D. Carey, and Steven A. Rutledge

Department of Atmospheric Science
Colorado State University
Fort Collins, Colorado 80523

**ABSTRACT:** Several recent studies have noted the presence of frequent lightning in flash flood-producing convection. However, heavy convective precipitation ultimately responsible for the Fort Collins flash flood of 28 July 1997 occurred with relatively little concomitant lightning activity. Analysis of CSU-CHILL multiparameter radar observations combined with cloud modeling simulations suggests that warm rain microphysics coupled with accretional growth of ice near the freezing level led to efficient precipitation production in the flood convection. However, the precipitation process may have suppressed electrification processes by rapidly removing precipitation ice mass and cloud water from the mixed phase region of the convection.

## 1. INTRODUCTION

On the night of 28 July 1997 the city of Fort Collins (FCL), Colorado, experienced heavy convective precipitation that resulted in a devastating flash flood (Petersen et al., 1999). In contrast to several recent studies (e.g., Bauer-Messmer et al. 1996; Holle and Bennet, 1998; Soula et al., 1998), lightning activity in the FCL convective system was relatively scarce. Only 20 cloud-to-ground (CG) lightning flashes were detected by the National Lightning Detection Network (NLDN) over the 6-hour duration of the precipitation event (Petersen et al., 1999). Further, visual observations from several locations in FCL coupled with a distinct lack of frequent, audible, thunder suggest that the *total* lightning flash rates (e.g., including intra-cloud [IC] flashes) were also small.

The CSU-CHILL dual-polarized radar and National Weather Service WSR-88D radars were operational on the night of the FCL flood, providing a robust data set for combined analyses of storm precipitation, kinematics, microphysics and electrification. This study presents a summary and interpretation of the radar observations set within the framework of cloud modeling simulations. Cloud simulations were conducted using a cylindrical cloud model with parameterizations for non-inductive charging based on Takahashi (1978), and "four-ice" bulk microphysics (cloud ice, snow, graupel, frozen drops; Ferrier, 1994). No lightning parameterization is included in this version of the model. The cloud model was coupled to a microwave scattering model (e.g., Vivekanandan et al., 1993; Bringi et al., 1997) for simulating multiparameter radar variables including reflectivity (Z), differential reflectivity (ZDR), linear depolarization ratio (LDR), and specific differential phase (KDP).

## 2. SUMMARY OF OBSERVATIONS

On the night of the flood, convection over FCL organized into a compact quasi-stationary rainfall system characterized by short lived (15-30 min.), training convective cells (Petersen et al., 1999). A time-height profile of the *maximum* radar reflectivity observed in a cylinder of 10 km radius, centered on FCL is shown in Fig. 1 The occurrence times of CG lightning are also indicated. Note that *maximum* values of Z ≥50 dBZ occurred below the height of the -10°C level and that echo tops of 13-14 km were not uncommon. In the *mean* however the majority of the precipitation mass was situated below the -10C level (e.g., Petersen et al., 1999). Local maxima in Z (≥ 50 dBZ) were often located between the 5°C and -10°C levels (2.5-5.3 km). When these maxima occurred coincident in time with Z ≥ 40 dBZ located well above the -10°C level, CG lightning occurred (Fig. 1). During the last 90 minutes of the event, ~50% (13 cm) of the maximum storm accumulated rainfall (26 cm) occurred, yet only 7 CG lightning flashes were detected by the NLDN. During this period of heavy rainfall local maxima in Z (≥ 52 dBZ) were situated *both above and below* the height of the freezing level. CSU-CHILL polarimetric radar data (Fig. 2) suggest that large ice particles were formed between 0°C and -10°C after raindrops, lofted in the updraft (x=0.5-2; Fig. 2), froze in the 0° to –10°C region of the clouds. This process is evinced in Fig. 2 by the presence of: 1) values of ZDR ≥ 1dB and KDP ≥ 1°/km (not shown) extending to near the -5°C level (4.2 km); 2) an overlying LDR "cap" (e.g., Bringi et al., 1997) between 0° and -10°C; and 3) difference reflectivity-derived ice fractions (FI) of 60% near the top of the KDP and ZDR columns, approximately collocated with the LDR cap. The LDR maximum and FI located near the freezing level between x=-1 and x=0 in Fig. 2, also suggest that large ice particles (perhaps frozen drops) collected rain and cloud water as they descended along the edge of the updraft.

The precipitation process in this case (lofting of raindrops, freezing of raindrops and further accretional growth of frozen drops/hail at temperatures ~-5°C) was undoubtedly very efficient (e.g., Takahashi and Kuhara, 1993). From an electrification viewpoint, recent multiparameter radar observations suggest that lofted freezing/frozen raindrops often appear as a precursor to lightning activity when observed at temperatures ≤ -10°C in tropical convection (e.g., Bringi et al., 1997; Carey et al., 1999). Indeed, Fig. 1 suggests that the cell depicted in Fig. 2 continued to grow into the mixed phase region of the cloud and later produced two CG's during the dissipating stage of its lifecycle.

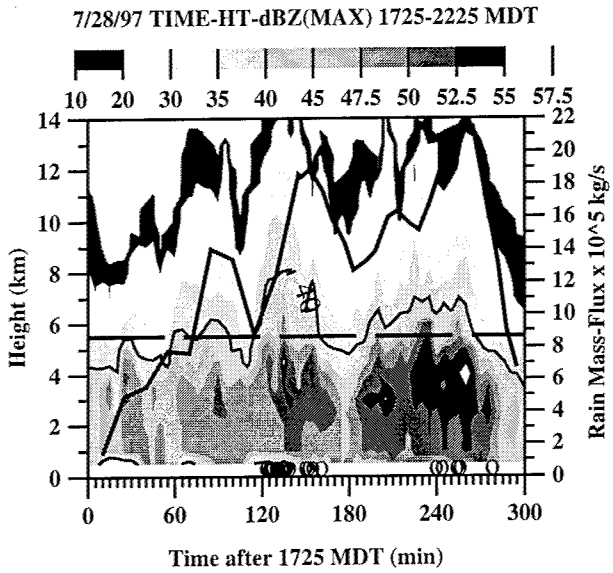


**Figure 1**. WSR-88D (KCYS) time-height (left ordinate) series of maximum Z (shaded) and rain mass-flux (right ordinate) over FCL. CG flash times indicated by circles on x-axis. Z=40 dBZ contoured, and -10°C isotherm is indicated by a dashed line.

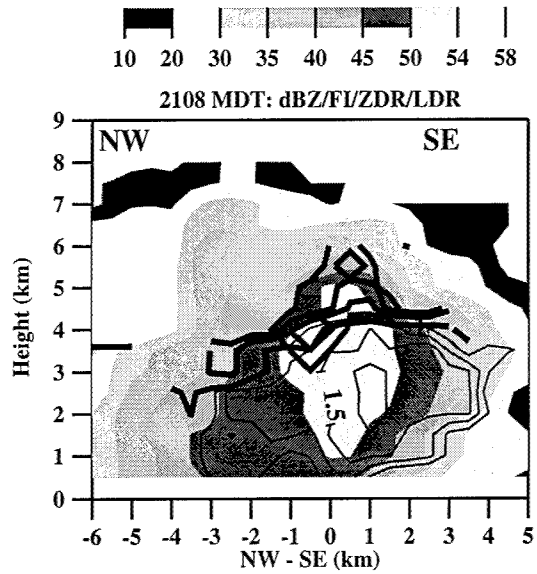


**Figure 2**. CSU-CHILL 2108 MDT cross-section of Z (shaded), ZDR (light solid line), LDR (bold grey line). and FI (bold black line). 0°C level indicated by hash mark at ~3.5 km. Contour intervals: ZDR 0.25 dB beginning at 1 dB; LDR 0.5 dB from –24.5 dB; FI contoured at values of 0.2, 0.6 and 0.8.

## 3. MODEL SIMULATIONS

Model simulations were conducted to relate cell-scale electrical and microphysical properties to the bulk observational characteristics of the clouds (e.g., made from multiparameter radar). Sensitivity studies were also conducted through application of small perturbations to the model thermodynamic environment and/or cloud base forcing. Variations of cloud-water (CW) autoconversion thresholds were also applied in an attempt to assess the possible effect of rapid rainfall production and a reduced inflow CCN concentration (e.g., rain-cleansed air) on cloud microphysics and electrification. Microphysical profiles from select periods of the model cloud lifecycles were provided as inputs to a microwave scattering model that generated multiparameter radar variables as a function of time and height for comparison to the CSU-CHILL radar observations.

The cloud simulation shown in Figs. 3a-c (R1) is approximately representative of the deepest convection and heaviest rainfall phase of the event (e.g., times 120-160, 190-280 in Fig. 1), and will be the focus of further discussion herein. Initial "gust front" forcing for this simulation was inferred from Doppler radar observations. The forcing was comprised of a maximum 4 $ms^{-1}$ updraft centered at 0.4 km AGL, applied over a duration of $10^3$s. The tropical character of the sounding (very moist, weak conditional instability) combined with the occurrence of numerous rain events near FCL on 28 July (Petersen et al., 1999) justified the use of a lower CW autoconversion threshold (0.5 g $kg^{-1}$) in order to replicate rapid rainfall production (analogous perhaps, to lowering the CCN count in water saturated, "rain-cleansed" air).

The vertical structure of Z in R1 (Fig. 3a) resembles that of the observations (Figs. 1-2). R1 rainwater (RW) mixing ratios (Fig. 3a) developed rapidly between 1 and 3 km in association with CW autoconversion and collision-coalescence processes. Moderate frozen drop/hail (FD) mixing ratios dominated the R1 mid-level reflectivity maxima, and were generated as the result of contact freezing of lofted rainwater by smaller mixing ratios of cloud-ice (CI) and snow (SN). A brief positive feedback occurred between the development of FD's and CI due to parameterized rime-splintering processes active between the –3°C and -8°C levels. Graupel (GR) mixing ratios increased due to the freezing of smaller raindrops and the riming of SN, but were advected to higher levels of the cloud in the updraft. During development of the R1 mid-level reflectivity core (1000-1300s; Fig. 3a),

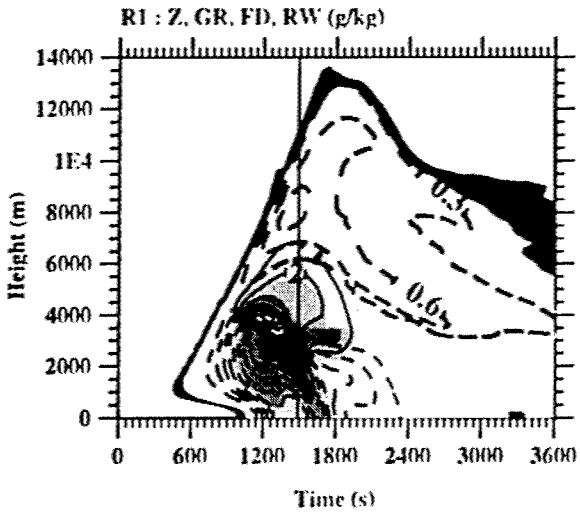


Figure 3a. Simulation-R1 time-height series of Z (shaded) with mixing ratios of GR (thick-dash; contoured every 0.3 g/kg); FD (solid line; contoured every 1 g/kg); and RW (thin-dash; contoured every 0.5 g/kg) overlaid. Time of electrical breakdown is indicated by a vertical line at t=1486 s.

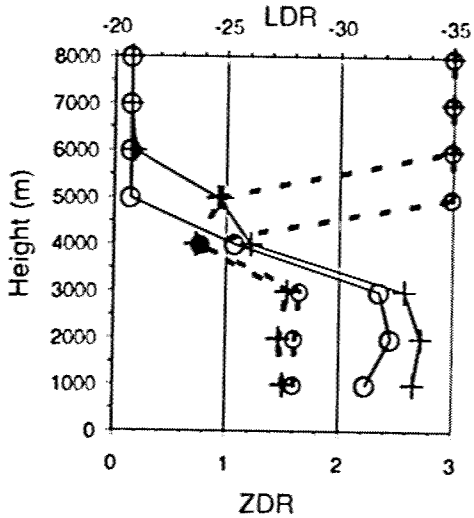


Figure 3b. Simulated R1 and R2 ZDR (dB; solid lines; values on lower x-axis) and LDR (dB; dashed lines; values on upper x-axis) vs. height. Composited from model times t=1080-1560s. R1 values indicated by (o), R2 values by (+).

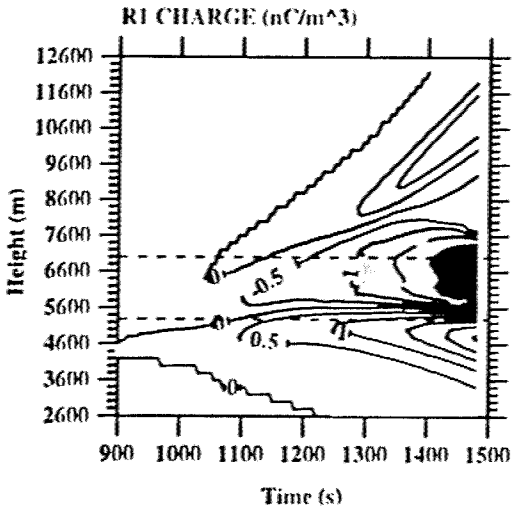


Figure 3c. Time-height series of R1 simulated charge densities ($nCm^{-3}$). Negative charge densities are shaded every -1 $nCm^{-3}$. Contour interval 0.5 $nCm^{-3}$. Height of -10°C and -20°C levels (in cloud) indicated by dashed lines.

moderate values of ZDR and KDP extended to the 4 km level (consistent with the presence of rainwater), and were overlaid by a weak LDR cap (Fig. 3b). Development of the LDR cap took place as significant quantities of rainwater began to freeze resulting in a parameterized decrease in FD orientation stability (e.g., "wobble" that

tends to increase when raindrops freeze rapidly; Bringi et al., 1997). Non-inductive charging (Fig. 3c) was initiated in R1 at ~900s when growing populations of FD, GR, CI and SN began to collide in presence of cloud water. Eventually, a tripolar charge structure developed (Fig. 3c) in association with: 1) ascending positive charge resident on SN and IC; 2) a relatively stationary layer of negative charge that resided on high density FD's in the –15°C to -25°C region; 3) negative charge resident on graupel in the –20°C to –30°C region, (reducing the net positive charge density associated with cloud ice and snow); and 4) lower positive charge center due to charge reversal microphysics and resultant positive (negative) charge transfer to frozen drops/hail (cloud ice, snow). Electrical breakdown (127 kV/m) occurred in the model at 1486s (~7 min. after initial development of the LDR cap) at an elevation of 5800m. Near the time of electrical breakdown the echo core was collapsing due to the rapid fallout of FD mass, and CW contents (not shown) were virtually depleted (<0.5 g/kg). Cessation of non-inductive charging in the model would have occurred within 1-3 minutes. Hence the model cloud, while significantly electrified, would only have produced a few lightning flashes at most.

Model sensitivity studies utilizing the same cloud base forcing as R1, but larger CW autoconversion thresholds exhibited small changes in cloud microphysical, dynamical and electrical structure. For example, when the autoconversion threshold was increased by a factor of four (2 g/kg; run R2), first-echo heights increased 1 km relative to R1, slightly higher Z and LDR were observed above the 0°C level (Fig. 3b), and electrical breakdown occurred ~30s earlier. Delays in RW formation in R2 resulted in both a 1 $ms^{-1}$ increase in the updraft magnitude below the 0°C level and slightly deeper penetration of CW and RW (note increased ZDR at 5 km in Fig 3b) into the mixed phase region. This resulted in 1 g/kg increases in FD mass just above the freezing level, but only a one minute increase in the duration of $Z \geq 40$ dBZ above the -10°C level (relative to R1), and virtually no change in the maximum height of the 40-45 dBZ contour. Hence, non-inductive charging was slightly enhanced when the CW autoconversion threshold was increased and rainwater formation was delayed.

Not unexpectedly, modeled cloud structures exhibited a strong sensitivity to small changes in both the temperature and moisture stratification at low levels in the sounding, and to small perturbations in the forcing strength. For example, when gust front forcing was reduced from 4 $ms^{-1}$ to 2 $ms^{-1}$ no significant cloud development occurred. Forcing of 3 $ms^{-1}$ resulted in a deep cloud possessing a top of nearly 11 km and a peak Z of 52 dBZ near the 0°C level. However, reflectivities were $\leq 40$ dBZ above the -10°C level, and while exhibiting some electrification and 50 mm $hr^{-1}$ rainfall rates, the electric field strengths never reached breakdown magnitudes (consistent with several time periods shown in Fig. 1).

## 4. CONCLUSIONS

Combined analyses of multiparameter radar observations and cloud/microwave radar scattering simulations suggest that warm rain microphysics coupled with accretional growth of ice near the freezing level led to efficient precipitation production in the convection responsible for the Fort Collins flash flood. Though the most intense observed and modeled convection electrified to the point of producing lightning, the precipitation process may have "short-circuited" electrical charge generation and lightning production in the clouds. Model simulations suggest that this could have occurred through the rapid removal of precipitation ice mass and cloud water from warmer regions of the convection either prior to, or just after, extension of the precipitation mass into the mixed phase region of the cloud and accompanying development of space charge via non-inductive charging processes.

## 5. REFERENCES


Bauer-Messmer, B., J. A. Smith, M. L. Baeck, and W. Zhao, 1997: Heavy rainfall: Contrasting two concurrent Great Plains thunderstorms. *Wea. Forecasting*, **12**, 785-798.

Bringi, V.N., K. Knupp, A. Detwiler, L. Liu, I. J. Caylor, and R. A. Black, 1997: Evolution of a Florida thunderstorm during the Convection and Precipitation/Electrification Experiment: The case of 9 August 1991. *Mon. Wea. Rev.*, **125**, 2131-2160.

Carey, L. D., and S. A. Rutledge, 1999: C-band polarimetric radar studies of tropical island convection: On the relationship between precipitation and lightning. Submitted, Mon. Wea. Rev.

Ferrier, B.S., 1994: A double-moment multiple phase four-class bulk ice scheme. Part I: Description. *J. Atmos. Sci.*, **51**, 249-280.

Holle, R. L., and S. P. Bennett, 1997: Lightning ground flashes associated with summer 1990 flash floods and streamflow in Tucson, Arizona: An exploratory study. *Mon. Wea. Rev.*, **125**, 1526-1536.

Petersen, W.A., L.D. Carey, S. A. Rutledge, J. C. Knievel, N. J. Doesken, R. H. Johnson, T. B. McKee, T. Vonder Haar, and J. F. Weaver, 1999: Mesoscale and radar observations of the Fort Collins flash flood of 28 July 1997. *Bull. Amer. Meteorol. Soc.*, **XX**, XX-XX.

Soula, S., H. Sauvageot, G. Molinie, F. Mesnard, and S. Chauzy, 1998: The CG lightning activity of a storm causing a flash flood. *Geophys. Res. Lett.*, **25**, 1181-1184.

Takahashi, T., 1978: Riming electrification as a charge generation mechanism in thunderstorms. *J. Atmos. Sci.*, **35**, 1536-1548.

Takahashi, T., and K. Kuhara, 1993: Precipitation mechanisms of cumulonimbus clouds at Pohnpei, Micronesia. *J. Meteorol. Soc. Japan*, **71**, 21-31.

Vivekanandan, J., R. Raghavan, and V. N. Bringi, 1993: Polarimetric radar modeling of mixtures of precipitation particles. *IEEE Trans. Geo. Remote Sensing*, **31**, 1017-1030.

# OBSERVATIONS OF THUNDERCLOUDS AND LIGHTNING ACTIVITY IN WINTER BY DUAL POLARIZATION RADAR AND SAFIR

Y.Sonoi[1], H.Uyeda[2], Z.I.Kawasaki[3], Y.Maekawa[4], S.Fukao[5], T.Takahashi[6]

[1] Technical Research Center The Kansai Electric Power Company, INC.Japan
[2] Department of Geophysics Faculty of Science, Hokkaido University, Japan
[3] Department of Electrical Engineering Faculty of Engineering, Osaka University, Japan
[4] Department of Communication Engineering Osaka Electro-Communication University, Japan
[5] Radio Atmospheric Science Center Kyoto University, Japan
[6] School of International Studies Obirin University, Japan

ABSTRACT : It is very important for the protection of electric power systems to comprehend the productive mechanism and the characteristics of lightning discharges in winter season. From these points of view, the authors have been investigating the thunderclouds in winter using a dual polarization Doppler radar, SAFIR (System de Surveillance et d' Alerte Fudre par Radioelectrique, in French) and other observational instruments. In this paper, we denote that the relationship between electrical polarities of cloud to ground lightning discharges (in the following of this paper, almost abbreviated as CG lightning) and the internal structure of thunderclouds, and that the statistically analyzed lightning characteristics observed by SAFIR and other equipment around the coast of Wakasa Bay located in the Northern Kin-ki District, and that also the relationship between lightning occurrence and the meteorological upper atmospheric temperature.

## 1. INTRODUCTION :

The authors have observed thunderclouds in winter using a C or an X band dual polarization Doppler radar from 1989 [*Maekawa et al.*, 1992. 1993., *Sonoi et al.*, 1995]. And additionally, we started observational investigations of lightning characteristics using SAFIR from 1991. In these observational period, we have proposed that there is a intimate relationship between lightning occurrence and the mixing process of graupel and ice crystals and that short lifetime winter lightnings are caused by immediate downfall of precipitation particles, especially graupel. In this paper,we denote newly discovered knowledge in these years. Namely, the polarity of CG lightning is negative when a mass of graupel was lifted up to 1~2 km altitude before and after the lightning discharge occurred, although the polarity was positive when a mass of graupel fell down before the lightning discharge was produced. And by the statistically analyzed data of SAFIR, thirty five thunderstorms days and 4,427 flashes were recorded and the total number of CG lightning were 975 of which 42.3 percents were positive polarity from 1st Dec. in 1996 to February 28th in 1997. Also, we will propose that there is some relationship between lightning occurrence and the temperature of the 500hPa pressure altitude.

## 2. Observation method

Observations on the relationship between the electrical polarities of CG lightning and internal structures of lightning clouds were carried out around the Wakasa Bay for two winter seasons using dual polarization Doppler radar. The location of the observatinal area is shown in Fig.1. Specifications of the radar are shown by *Uyeda et al.* [1991]. The statiscally analyzed lightning data of SAFIR were studied in the area (N:35°~37°, E:134°~137°) including the Wakasa Bay. Specifications and the observed locations of lightning discharges are shown by *Z.I.Kawasaki et al.* [1994]. And the meteorological data of upper atmospher of Wajima observatory which is located in Noto Peninsular northwest-ward away from the center of the Wakasa Bay were utilized.

## 3. Results

### 3.1 The relationship between the electrical polarities of CG lightning and internal structure of thunderclouds

The populations of thunderclouds observed by dual polarization radar were 12 in the first season

and 15 in the second season. Among observed thunderclouds, several clouds were chosen for detailed analyses of vertical structure of radar reflectivity $Z_H$, deferential reflectivity factor $Z_{DR}$. Figure 2 shows

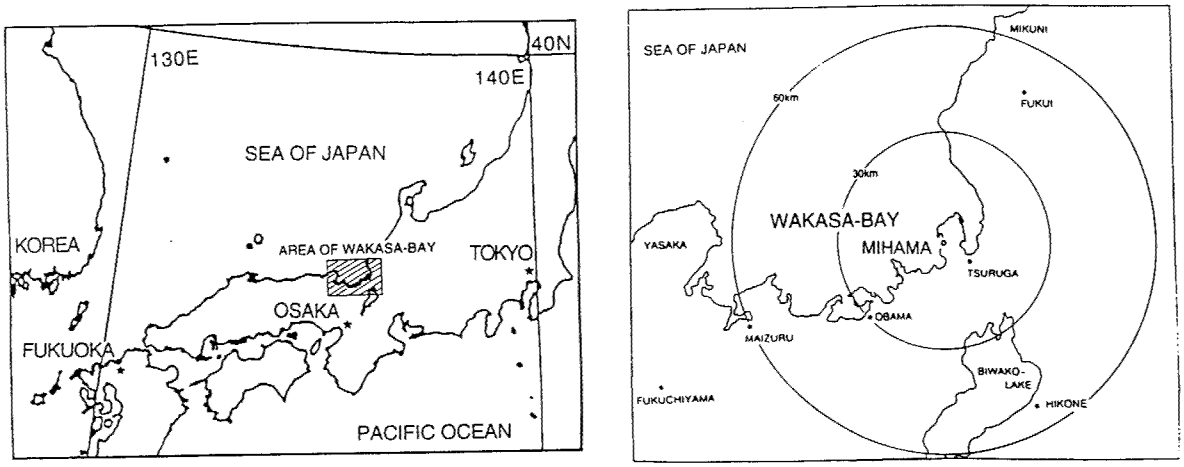


Fig.1 Location area of observation using dual polarization Doppler radar, SAFIR and other observational instruments.

the RHI (Range Height Indicator) of thundercloud producing a negative CG lightning observed on 6th Jan. in 1994. The negative flash was located at 1532JST (lightning location is indicated by an arrow in Fig.2(b)), and Fig.2(a) shows the RHI at 1524JST, Fig.2(b) shows the RHI at 1535JST, respectively. In both figures, $Z_{DR}$ of the precipitation particles in the regions encircled by a solid line were equale or less than 0 dB. Namely, there were occupied by graupel particles mainly in these encircled regions, and note that graupel core regions were maintained at the height of 1～1.5 km after the lightning discharge occurrence. On the other hand, when or before the positive lightning occurred, most graupel particles fell down to the low altitude in almost cases.

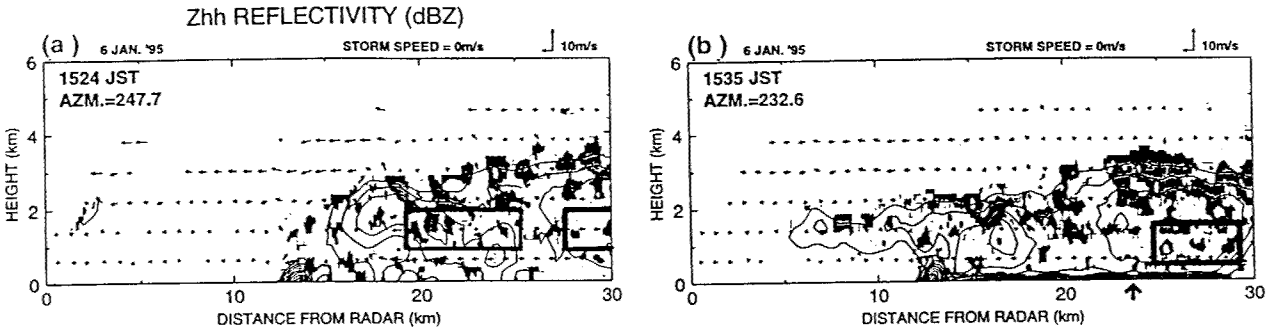


Fig.2 The RHI observed (a) at 1524JST and (b) 1535JST on 6th Jan. in 1994.

3.2 The statiscally analyzed lightning characteristics observed by SAFIR

We show that the daily change of the populations of lightning discharges including cloud discharges and positive or negative CG lightning discharges in Fig.3. In this figure, lightning discharges activity were peculiar on the 1st, 2nd, 21st, 22nd and 23rd in Dec. 1996. On the whole, occurrence frequency of lightning discharges decreased from Dec. in 1996 to Feb. in 1997. And there was a meaningful difference of the rate of CG lightning discharges between these fashes on 2nd and those of on 22nd in Dec. 1996, for example, on the 22nd, the rate of CG lightning discharges for all discharges was rather highly 44.4%, although there were few CG lightning on 2nd.

3.3 Difference of the thunderclouds activity in various aereas (i.e. on the sea and near the land.) where lightning discharges occurred

In the Fig4., we show that (a) the lightning discharge located by SAFIR at from 0500 to 0510JST, (b) the C band conventional radar reflectivity observed at 0505JST, (c) the transitions of the heights of CAPPIs (the height of CAPPI– L is 2 km and that of CAPPI– M is 4 km) and the echo top for the

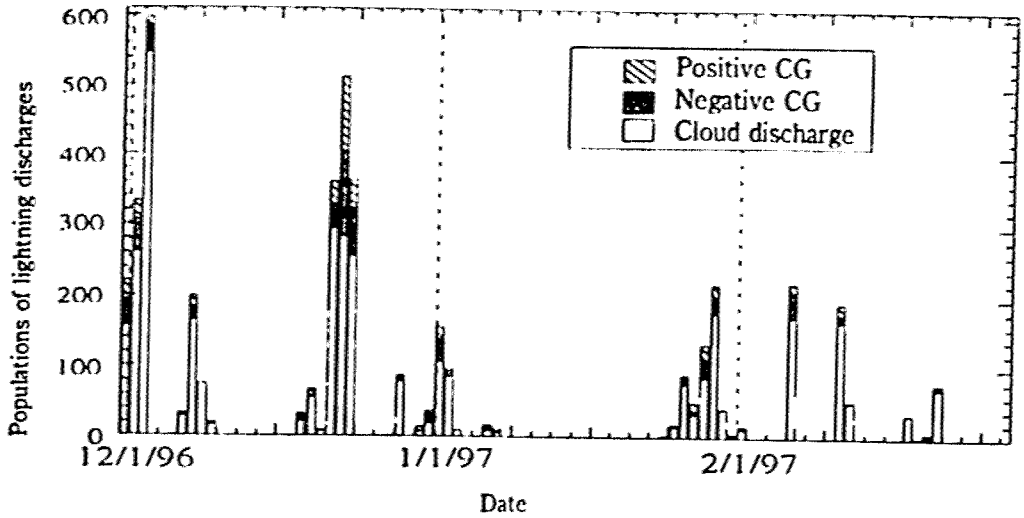


Fig.3 The daily populations of lightning discharges from 1st Dec. 1996. to 28th Feb. 1997.

thundercloud cell encircled and marked A (near the Tango Peninsula) observed from 0440 to 0510JST, by this C band radar and also (d) the same data, but for another thundercloud cell B (on the sea of Wakasa Bay), on 23rd Dec. in 1996. In Fig.4(a), the circles, the triangles and the small crosses indicate positive CG lightning, negative CG lightning and cloud discharges, respectively.

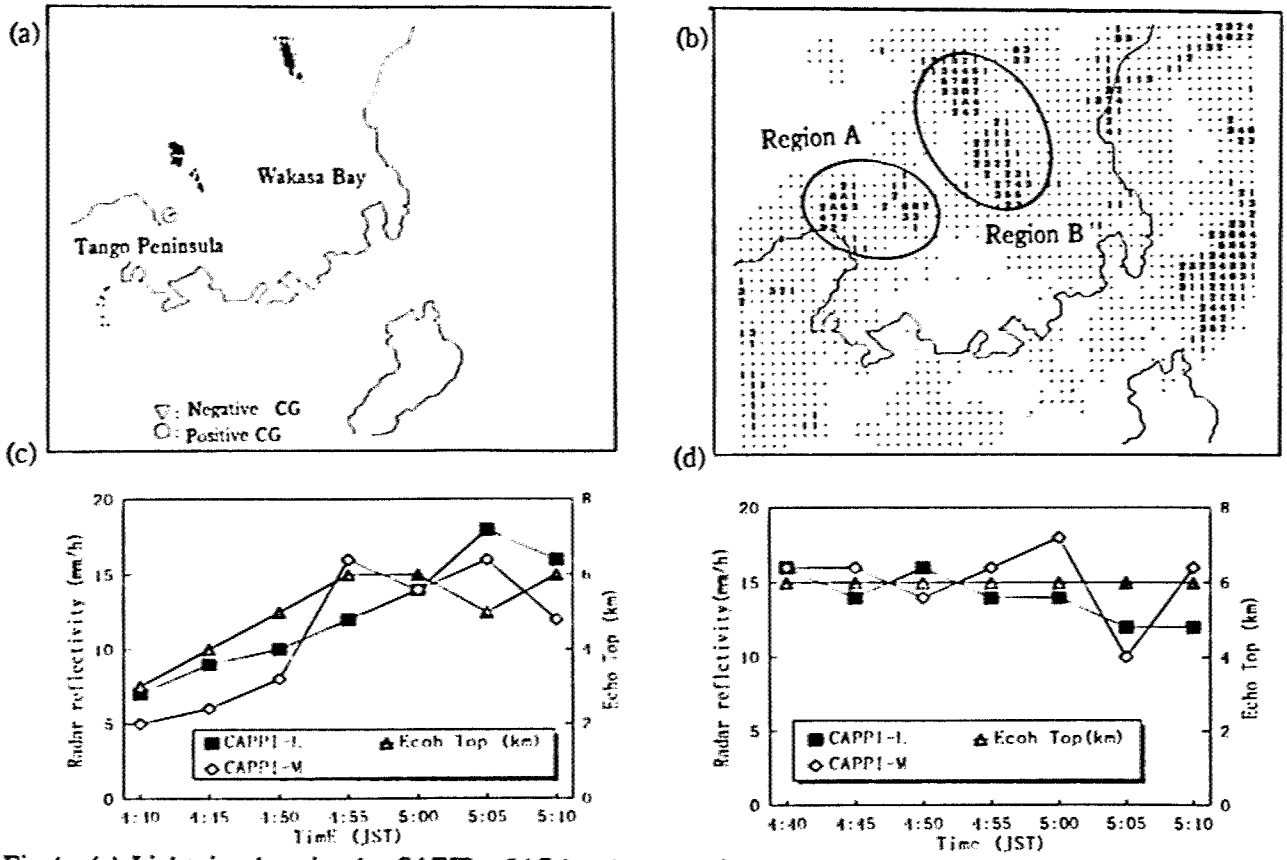


Fig.4 (a) Lightning location by SAFIR (b)C band conventional radar reflectivity (c)Transitions of the CAPPI-L(at 2 km altitude), CAPPI-M(at 4 km altitude) and the height of echo top in the region A. (d) Transitions of the CAPPI-L, CAPPI-M and the height of echo top in the region B. at about 0500JST, 23rd Dec. in 1996.

## 4.Discussion and Concluding Remarks

### 4.1 The relationship between electrical polarities of CG lightning and internal structure of thunderclouds

In two winter seasons, we observed 27 thunderclouds by dual polarization radar. From statiscal analyses, the average heights of graupel particles core 10 minutes before the lightning were 0.7 km for positive and 1.6 km for negative CG lightning discharges. As many investigators says, we often observed positive CG lightning in winter thunderclouds. Several reasons are proposed for many positive CG lightning in winter thunderstorms, that is to say, rapid downfall of graupel particles that are charged negative before lightning, the leaned clouds structure by strong wind and the positive pocket charge at the bottom of thunderclouds, and so on. Our Observational results in this paper demonstrate the first reason, but we don't consider simply that only one mechanism produce positive CG lightning discharge.

### 4.2 The ratio of CG lightning against cloud discharges

We investigated several meteorological factors for the reasons why and how CG lightning discharges will increase on some days, though cloud discharges dominate on another days. With our analysis results, when many positive CG lightning occurred, the height of −10 degrees were at rather high altitude, and also the equivalent potential temperatures indicated rather high value(K), although these results are not sufficient to clalify the productive mechanisms for many CG lightning discharges.

### 4.3 The diffrence of thunderclouds transition in various aereas

In Fig.4(c), the reflectivity of CAPPI−L and CAPPI−M were increasing gradually to the lightning occurrence time (about 0500JST), therefore, we consider that the thundercloud cell A was produced by the conflict and convergence of wintermonsoon wind that contained much vapor, to or around the Tango Peninsula. Also in Fig.4(d), for the thundercloud cell B, the both of reflectivity repeated up−and−down motion, and the height of echo top was maintained at the almost constant high altitude. For this phenomenon, we suppose that the cell B was supplied a large amount of vapor continuously from the rather warm Tsushima ocean current.

### 4.4 The relationship between lightning occurrence and the upper atmospheric temperature

Though we abbreviate the definite figures for want of space, we consider there is some relationships between lightning discharges occurrence and the upper atmospheric temperature. Especially, when the temperature at 500hPa altitude lower −30 degrees, there is a tendency to occure lightning discharges. However, lightning discharge phenomena in winter is a very peculiar, and then we will have to investigate using several observational instruments and consider electrically as well as meteorologically.

## References


(1)Fukao,S. *et al.*, Dual Polarization Radar Observation of Thunderclouds on the Sea of Japan in the Winter Season, *Geophys. Res. Lett.*, Vol.18, No.2, pp.179-182, 1991.

(2)Maekawa,Y. *et al.*, Dual Polarization Radra Observations of Anomalous Wintertime Thunderclouds in Japan, *IEEE Trans. Geosci. and Remote Sensing*, Vol.30, No.4, pp.838-844, 1992.

(3)Maekawa,Y., *et al.*, Distribution of Ice Particles in Wintertime Thunderclouds Detected by a C Band Dual Polarization Radar : A Case Study, *J. Geophys. Res.*, Vol.98, No.D9, pp.16613-16622, 1993.

(4)Sonoi,Y., et al., Dual Polarization Radar Observation of Thunderclouds in Winter Season, *J. Geomag. Geoelectr.*, Vol.47, No.10, pp.999−1010, 1995.

(5)Uyeda,H., et al., Observation of vertical structures of convective snow clouds with a dual−polarization radar in Hokkaido,Japan. Proc. 25th Int. Con. on Radar Meteorology, 717−720, 1991.

(6)Z−I.Kawaski etal., SAFIR operation and evaluation of it's performance, *Geophys. Res. Lett.* Vol.21, No.12, pp.1133−1136, 1994.

# A POSSIBLE MECHANISM OF GUSHES OF RAIN OR HAIL AFTER LIGHTNING

N. Singh and Avinash Mohan
Department of Physics
Nehru College, Chhibramau 209721, INDIA

ABSTRACT

Radar observations inferred that the lightning often followed by a rapidly intensifying echo and then a gush of rain or hail at the ground. This has been explained by several theoretical explanations. The present work explains that developed break even electric field gives rise to the lightning, which ionizes the gases in clouds. The ions get attached to the nuclei of water or ice, so that Gibb's free energy for formation of critical nuclei is reduced. Hence the nucleation rate and equilibrium concentration of critical water nuclei are increased. Also, the increased electric field enhances the nucleation rate of water droplets and at the same time reduces the relaxation time. The growth of electric field is provided due to non-inductive charging mechanism. Thus, the phenomenon of rain gush after lightning is explained.

## INTRODUCTION

Moore et al. (1962) observed an abrupt fall of rain at high rates sometimes occurring after a lightning stroke. They inferred that the lightning as more probably the cause rather than the effect of rain gush and that it may cause the sudden formation of heavy rains. Theoretical (Paluch and Sartor, 1973, Levin and Ziv, 1974) and experimental (Jayratne and Saunders, 1984) work suggested that polarization charging of precipitation particles is sufficient to explain rapid growth of electric field in clouds.

The present model assumes non-inductive charging in thunder-clouds developing high electric field (break even electric field, Marshall et al. 1995). This results in lightning producing avalanche of energetic ions. The effect of ions in the enhancement of nucleation rate (Sharma et al., 1992) and also, the effect of developed high electric field to enhance nucleation rate and reduce the relaxation time (Sharma et al., 1992; Singh and Mansoori, 1998) are additive to explain the observed phenomenon of rain or hail gushes after lightning.

## THEORETICAL CONSIDERATION

The electric field inside a thundercloud usually limited to values less than the break even field suggests that there is a charge rearrangement caused by break even process. It is observed that lightning usually occurs and reduces the resultant electric field to a value near or below the break even value ($E_{bc}$) varying as function of altitude.

The parallel plate capacitor model (Kumar and Mukku, 1992) is used to calculate electric field growth due to non-inductive charging process.

The lightning flash generated by charge separation in clouds consists of several individual strokes. Each of the estimated 500 lightning strokes occurring around the globe per sec. deposits about $10^5$ J/m into the lightning channel upto length 10 km and radius $10^{-3}$ to $10^{-2}$ m. The radially propagating shock waves produced due to high pressure and temperatures (30000 K) within lightning channel, ionizes the atmospheric species such as $N_2$, $O_2$, $H_2O$, $CO_2$ etc. to give atoms H, O, OH, CO etc.

Even though the lightning discharge destroys a large electric dipole, the lightning may cause the formation of very high space charge density and a very high electric field locally. On this basis we conceive of an electrically accelerated nucleation process as the process (a) and (b) described below:

(a) EFFECT OF IONS ON CLOUD CONDENSATION AND ICE NUCLEATION

Water molecules form clusters with ion at the centre. The condensation takes place at lower supersaturation ratio because the necessary energy for nucleus formation is attained at smaller radii due to addition of electrostatic energy term $3(Ze)^2/5\ r_W$ given as

$$\Delta G'_W = \Delta G_W + 3(Ze)^2/5\ r_W \qquad (1)$$

The nucleation rate $J'_W$ and equilibrium concentration $C(n'^*_W)$ of critical nuclei are given by

$$J'_W = (\alpha_c/\rho_W)[3N^3 M_W\ \sigma_{W/V}/\pi]^{1/2}\ (e_{sat.W}/RT)^2\ S_{V,W}\ \exp\ [-\Delta G'^*_W/kT] \qquad (2)$$

and, $$C(n'^*_W) = C(1),\ \exp\ [[-\Delta G'^*_W/kT] \qquad (3)$$

Expressions (1), (2) and (3) are also applicable to ice glaciation with respective constants.

(b) NUCLEATION RATE INDUCED BY ELECTRIC FIELD

Electric field generated (~ 10 esu) near the lightning channel affects the rate of nucleation (Sharma et al., 1992). The factor of enhancement $R_E$ varying with electric field is given by

$$R_E = 1 + (\tau_o/\tau_N) \qquad (4)$$

Similarly $R'_E$ and $R'_{E/O}$ are the factor of enhancement in ion induced and ion induced vs homogeneous nucleation. Notation is defined in Table 3. Primes indicate the ion induced while asterisk, the critical values.

RESULT AND DISCUSSION

Different parameters of homogeneous and ion induced heterogeneous nucleation are given in Table 1.

Table 1: Ion Induced Nucleation Parameters at 273 K.

| $S_{V,W}$ | $r_W^*$ (Å) | $r'^*_W$ (Å) | $\Delta G^*$ ($\times 10^{-12}$ erg) | $\Delta G'^*$ ($\times 10^{-12}$ erg) | $\ln[c(1)_0/c(\eta_W^*)]$ | $\ln[c(1)_0/c(\eta'^*_W)]$ | ln J | ln J' |
|---|---|---|---|---|---|---|---|---|
| 1.5 | 27.37 | 4.55 | 21.97 | 4.66 | 583.1 | 123.6 | -527.5 | -68.0 |
| 2.0 | 16.01 | 4.83 | 7.52 | 4.50 | 199.5 | 119.5 | -143.6 | -63.6 |
| 2.5 | 12.11 | 5.15 | 4.30 | 4.36 | 144.2 | 115.6 | 58.05 | -59.5 |

It is evident from Table 1 that at a given temperature with increase in supersaturation ratio, the radius of critical nucleus and Gibb's free energy decreases in ion induced heterogeneous nucleation and hence nucleation rate and equilibrium concentration of critical nuclei are enhanced. Thus, $r'^*_W < r^*_W$, $\Delta G'^*_W < \Delta G^*_W$, $c(\eta'^*_W) > c(\eta_W^*)$ and $J'_W > J_W$.

At a given temperature (273 K) and electric field (10 esu) the different parameters in electric field induced nucleation are given in Table 2.

Table 2: Electric Induced Nucleation Parameters at 273 K and 10 esu.

| $S_{V.W}$ | $r_W^*$ (Å) | $r'^*_W$ (Å) | $\tau_{ON}$ ($\mu$.sec) | $\tau'_{ON}$ ($\mu$.sec) | $R_E$ | $R'_E$ | $R'_{E/C_0}$ |
|---|---|---|---|---|---|---|---|
| 1.005 | 2225.00 | 4.286 | 52580.00 | 5.519 | 8.83 | 179.28 | 93100.00 |
| 1.050 | 227.50 | 4.311 | 1995.00 | 5.566 | 25.47 | 178.78 | 9440.00 |
| 1.500 | 27.37 | 27.270 | 87.59 | 87.080 | 71.55 | 71.69 | 71.97 |

From Table 2, it is evident that the enhancement factor varies linearly with electric field. At a given temperature and electric field the enhancement factor decreases with increase in supersaturation ratio. The radius of critical nuclei and the relaxation time decrease with increase in electric field. Thus, $\tau'_{ON} < \tau_{ON}$ and $R'_{E/0} > R'_E > R_E$.

Table 3: Notation for Equations (1) to (4).

| Variable | Definition |
|---|---|
| $Z$ | Charge number |
| $e$ | Electronic charge |
| $\alpha_c$ | Condensation coefficient |
| $M_W$ | Molecular weight of water |
| $\sigma_{W/V}$ | Surface free energy at vapour water interface |
| $e_{sat.W}$ | Saturated water vapour pressure |
| $S_{V.W}$ | Supersaturation ratio of vapour over liquid water |
| $k$ | Boltzmann constant |

| | |
|---|---|
| $T$ | Temperature |
| $\eta_W$ | Number of water molecules in an embryo |
| $R_E$ | Enhancement factor in electric field |
| $\tau_O$ | Relaxation time (homogeneous) |
| $\tau_N$ | Relaxation time (heterogeneous) |
| $C(1)_O$ | Concentration of water vapour molecules. |
| $\rho_W$ | Density of Water |

## CONCLUSIONS

Thus, electric field developed in thunderstorms produces the lightning. Near the lightning channel numerous ions are produced. These ions take part in nucleation process. At the same time, the external electric field also take part simultaneously to increase the nucleation process in vary much less time. This explains the observed phenomenon of 'rain gush' after lightning.

## REFERENCES


Jayratne, E.R. and C.P.R. Saunders, The 'Rain Gush', lightning and low positive charge center in thunderstorms, J. Geophys. Res., 89, 11816-11818, 1984.

Kumar, P. and V.N.R. Mukku, Model study of electric field growth in thunderstorms, J. Radio & Space Phys., 21, 229-233, 1992.

Levin, Z. and A. Ziv, The electrification of thunderclouds and the rain gush, J. Geophys., Res., 79, 2699-2704, 1974.

Marshall, T.C., M.P. McCarthy and W.D. Rust, Electric field magnitudes and lightning initiation in thunderstorms, J. Geophys. Res., 100, 7097-7103, 1995.

Moore, C.B.; B. Vonnegut, J.A. Machado and H.J. Survilas, Radar observations of rain gushes following overhead lightning strokes, J. Geophys. Res., 67, 207-220, 1992.

Paluch, I.R. and J.D., Sartor, Thunderstorm electrification by the inductive charging mechanism, I. Particle charges and electric fields, J. Atmos. Sci., 30, 1166, 1973.

Sharma, A.R., N. Singh and S.D. Pandey, Effect of atmospheric ions on the nucleating behaviour of partially wettable, water insoluble curved substrate, J. Radio & Space Phys., 21, 10-17, 1992.

Sharma, A.R., N. Singh and S.D. Pandey, On the equivalence of external electric field to supersaturation ratio in water vapour condensation, J. Radio & Space Phys., 21, 218-228, 1992.

Singh, N. and M.I. Mansoori, Variation of nucleation rate in an electric field, Abstract Book, p. 22, 68th Annual Session, Nat. Acad. of Sci. (India), CDRI, Lucknow, Oct. 23-25, 1998.

# RESULTS OF ELECTRICAL FIELD STRENGTH INVESTIGATIONS IN CONVECTIVE CLOUDS

A.A.Sinkevich, Ju.A.Dovgaluk, Yu.Ph.Ponomarev, and V.D.Stepanenko

A.I.Voeikov Main Geophysical Observatory, St.Petersburg, Russia

ABSTRACT: Relatively small number of electrical field strength investigations in convective clouds were carried out due to danger of aircraft traverses through them and great cost of investigations. Measurements of electric field strength, made by the flying laboratory Il-14 in Russia are analyzed. The electric field strength within the Cu med clouds was found not usually to exceed 600 V/m, mounting to 75 kV/m within the Cu cong-Cb clouds.The impact of crystallizing agent yields an average double electric field strength compared with the natural cycle of cloud development.

## INTRODUCTION

The electrical field strength structure of convective clouds that is result of electrical charge structure has long been the interest of many investigators. Different technique (surface electrical field measurements, balloon measurements and aircraft measurements) were used to measure electrical characteristics of Cu clouds to model its charge distribution and to obtain typical electrical field strength. Aircraft-laboratories provide possibility to observe cloud development and to measure a lot of microphysical characteristics. At the same time quantity of such investigations is rather low due to high price of experiments and danger for aircraft traverses through Cu. Of cause, there are serious problems to obtain Cu electrical field strength if measurements are carried out in the neighbourhood with Cu. Aircraft charging due to cloud particles aircraft hitting is a serious problem too [Imanitov ,1987].Aircraft experiments had shown that typical electrical field strength within Cu hum -Cu med constitutes 540-1100 V/m [Imanitov and Chuvaev, 1957]. Imanitov et al.,1971 had shown that electrical field strength can reach several hundreds kV/m in Cb and presented typical charge distribution within thunderstorm. Series of aircraft experiments were carried out by Michailovsky et al. He had paid attention to the depends between cloud living stage and electrical field strength (E). He had shown that E usually was equal to 3-11 kV/m in neighbourhood of Cu cong- Cb clouds in mature stage and reached -9 - 18 kV/m during clouds dissipation [Michailovsky, and Kashleva,1990; Galperin et al,1985]. Simple charge models containing 2 dipole or 3-tripole structure were discussed in many scientific publications [Nikandrov,1981]. Rust and Marshall (1996) had showed that thunderstorm charge structure is rather complicated and there are several charge regions within cloud. Stolzenburg et al.(1998) had shown that electrical field strength can reach 100-200 kV/m within thunderstorm clouds, it has complicated height structure and depends on cloud type and measured zone (that is updraft or downdraft). Cloud seeding significantly changes cloud microphysics and increase of electrical field strength was observed during aircraft experiments in India [Murty A.S.R. et al.,1985]. 7 cloud seeding experiments carried out in USSR had shown that increase in E after seedings can reach 1.5-20 times [Imanitov and Chuvaev, 1957]. Michailovsky et al. in accordance with aircraft experiments results had shown the increase in E after seedings with crystallizing reagents and reagents for dynamic

seedings [ Michailovsky and Kashleva,1990; Galperin et al,1985]. Field experiments had shown that seeding can lead to E increase or decrease in dependence of reagent amount [Stepanenko and Galperin, 1983].

## INVESTIGATION AND DATA PROCESSING METHOD

Clouds investigations were carried out with the help of Il-14 aircraft laboratory [Zvonarev et al, 1986] in 1982-1985. Electrical field strength was measured by aircraft electric flow meter [Imanitov et al,1971]. The device measures electrical field strength within the range 10-250000 V/m with relative accuracy better than 5%.

We present results of vertical electrical field component measurements in Cu med, Cu cong and Cb (E) [Ponomarev, and Sinkevich,1997]. Aircraft traverses through clouds were carried out. Maximum registered E in every cloud are analyzed. 232 E measurements are analyzed below. Usually several traverses through Cu were carried out and its living stage (developing, mature, dissipating) was registered. We don't present results of E measurements in Cu hum, because electrical field strength in them is rather small and don't exceed 50-200 V/m. Due to small number of measurements within Cb they are united with Cu cong. Usually, maximum electrical field strengths were observed in Cb. Data processing included statistical E analyze for clouds at different living stages. Measurements at different relative heights from cloud base were analyzed simultaneously, that is different groups were formed for the measurements within the layer from cloud base to the relative height of 1 km over cloud base, from 1 km to 2 km and so on.

## ELECTRICAL FIELD STRENGTH IN Cu med

19 traverses were carried through Cu med. 13 traverses were made through developing clouds and 6 - through mature. Averaged E is nearly the same for developing clouds and clouds in mature stage 240-260 V/m (the stage when no variations in cloud height were registered). Electrical field strength varied from 90 to 600 V/m and in every case was a positive value that means that positive charges were in cloud tops. Greater E values were registered near central cloud part in comparison with their boundaries. E fluctuations were registered. Mostly, their horizontal length was equal to 0.2-1.5 km.

## ELECTRICAL FIELD STRENGTH IN Cu cong -Cb

213 traverses were made through Cu cong - Cb to measure electrical field strength. 97 traverses were made through clouds having height 1-2 km, 92 traverses - through clouds having height 2-3 km, and 23 - through clouds having height greater than 3 km. Results show that averaged value of electrical field strength depends on cloud living stage and relative height from cloud base. Maximum E values are usually registered in clouds in mature living stage and in dissipating clouds. Averaged E amount up to 16-20 kV/m at relative height 2-3 km, at the same time in developing clouds it equals nearly 2 kV/m. We would like to mention that rather great electrical fields can present in dissipating clouds - E>30 kV/m in 28% of cases, in 22% of cases such fields were registered in clouds being in mature stage. At the same time mode of electrical field strength varies usually within the limits 1.2-4.0 kV/m. It means that such clouds are not dangerous for aircrafts in most cases. Electrical field strength was a positive value in 96% of cases. It means that positive charge was higher than aircraft.

Electrical field strength values were lower at heights 1-2 in comparison with height 2-3 km. Averaged E value varies from 1.2 to 3.4 kV/m. Electrical field strength mode constitutes 2.0-2.5 kV/m. Only 12% of clouds in mature and dissipating stages had electrical field strength greater than 10 kV/m. Developing clouds have lower values of electrical field strength. Maximum E did not exceed 6.5 kV/m. Negative E values were registered with probability less than 5%. Probably, it was the result of precipitation positive charge. Small E values were the result also of the fact that clouds with smaller heights were included in this group in comparison with the group discussed above. We obtain data only for dissipating clouds for lower layer. Registered E values are small here and did not exceed 1 kV/m.

## ELECTRICAL FIELD STRENGTH IN Cu AFTER SEEDING

24 Cu cong were seeded and 30 Cu cong were not seeded. Traverses through clouds were made from developing stage up to their dissipation. Different characteristics were measured. Detailed data is available [Bekryaev et al.,1987],[Sinkevich and Ponomarev, 1995]. Measurements were carried out at chosen heights in the upper cloud parts. Averaged values of E in dependence from time of the experiment starting were calculated and temporal E dependence was analyzed. Two curves were analyzed:the 1 - for seeded clouds, the 2 - for clouds in natural cycle of development. Difference between two curves is obvious. Electrical field strength remains practically constant during all duration of observations for clouds without seedings and some E increase is fixed only at 18 min of observations. We think, that is the result of natural crystallizing process in cloud and precipitation formation. Averaged electrical field strength was equal to nearly 15 kV/m at the beginning of experiment for seeded clouds. One can observe E increase in 5 min after seeding which reaches nearly 30 kV/m at 10-12 min. During 10-12 min averaged E remain constant and then one can observe its reduction to the value less than 5 kV/m. Aircraft observations had shown that increase of electrical field strength coincide with crystals appearance in Cu cong clouds.

## CONCLUSIONS

Aircraft experiments had shown that electrical field strength constitute 1-3 kV/m in Cu mostly. E averaged value depends on cloud living stage reaching its maximum in dissipating clouds and clouds in mature stage. E can significantly increase at these stages reaching several tens of kV/m. Cloud seeding with crystallizing reagent lead to E increase nearly 2 times in 10-12 min after reagent introduction.

ACKNOWLEDGMENTS: Experiments were supported by Rosgidromet Department of Cloud Seeding. Data analyze and preparation of the paper were supported by Russian Fund of Basic Investigations.

## REFERENCES

Bekryaev V.I., Yu.F. Ponomarev, A.A. Sinkevich, and E.V. Chubarina, The results of investigations of the process of convective clouds crystallization after seeding, Leningrad, Gidrometeoizdat, Voprosy fiziki oblakov, Aktivnye vozdeistviya, Collection of articles, 131-136, 1987.

Galperin,S.M., et al., Cu clouds electrization in natural cycle and after seeding, Collection of articles, Voprosy atmosphernogo electrichestva, Leningrad, Gidrometeoizdat, 76-102, 1985.
Imanitov I.M., E.V. Chubarina, and Ya.M. Shvartz, Clouds Electricity. Leningrad, Gidrometeoizdat, 92, 1971.
Imanitov,I.P. and A.P. Chuvaev, Results of electrical processes investigations in thunderstorms, Collection of articles, Investigations of clouds, precipitation and thunderstorm electricity, Leningrad, Gidrometeoizdat,13-16, 1957.
Imanitov,I.P., et al., Clouds electricity, Leningrad, Gidrometeoizdat, 92, 1971.
Michailovsky, Y.P. and L.V. Kashleva, Conditions of the beginning of Cu clouds organized electrization by the aircraft investigations data , Gidrometeoizdat, Trudy MGO, 527, 51-58, 1990.
Murty A.S.R. et al., Warm cloud electrical and thermodynamical responses to salt seeding, 4 WMO Scientific Conference on Weather Modification, Geneva, 11, 493-496, 1985.
Nikandrov, V.Y., Meteorological aspect of Cu cloud electrization, Leningrad, Gidrometeoizdat, 41, 1981.
Ponomarev Yu.Ph., and A.A.Sinkevich, Electrification of convective clouds over the northwest of Russia. J. Meteorology and Hydrology, 6,73- 80,1997.
Rust W.D., and T.C. Marshall, On abandoning the thunderstorm tripole charge paradigm, J. Geophysical Research, 101, 23499-23504, 1996. Stepanenko, V.D. and S.M. Galperin S.M, Radiotechnical methods of thunderstorm investigations, Leningrad, Gidrometeoizdat, 203, 1983.
Sumin Y.P. and Y.M. Shvartz, Electrical fields within Cu clouds vicinity, Gidrometeoizdat, Trudy MGO, 278, 113-132, 1972.
Sinkevich,A.A. and Yu.F. Ponomarev, Studies of physical effectiveness of Cu seeding with crystallizing reagent, BNIGMI MCD, dep 1181, GM 95, 75- 81, 1995.
Stolzenburg M., W.D. Rust, and T.C. Marshall, Electrical structure in thunderstorm convective regions. 3.Synthesis. J.of Geophysical Research,103, Nd12, 14097-14108,1998.
Zvonarev V.V., V.S.Lyadov, Yu.F.Ponomarev, A.A. Sinkevich, and V.D. Stepanenko, Characteristic features of the MGO aircraft laboratory IL-14, Leningrad, Gidrometeoizdat, Trudy MGO, 497, 51-52,

# STUDIES OF FLORIDA THUNDERSTORMS USING LDAR, LLP, AND SINGLE DOPPLER RADAR DATA

Gregory S. Forbes[1] and Steven G. Hoffert[2]

[1]Department of Meteorology, Penn State University, University Park, Pennsylvania, U.S.A.
[2]Template Software, Inc., Dulles, Virginia, U.S.A.

ABSTRACT: The paper summarizes results from research conducted on thunderstorms in the vicinity of the Kennedy Space Center (KSC), Florida, between 1993 and 1998. The focus of the research was to identify procedures that would assist weather forecasters at the Cape Canaveral Air Station (CCAS) in real-time detection and forecasting of the lightning threat to launches and daily ground operations at KSC/CCAS sites. The research was divided into three topics: (1) studies aimed at improving the forecasting of the initial cloud-ground (CG) lightning threat, (2) studies aimed at improving the forecasting of the end-of-storm termination of the CG lightning threat, and (3) studies of the location of CG strikes relative to the thunderstorm radar echo and to lightning discharges aloft. Only the first two topics are covered in this preprint

## METHODOLOGY

The research was conducted using the KSC Lightning Detection and Ranging (LDAR) system, the KSC LLP system for detection of ground strikes, Doppler radar data from the NWS WSR-88D radar at Melbourne, FL, and the KSC surface mesonet. Results were obtained for 76 cases, including 53 for which archived radar data were available and utilized. Most cases comprised more than one thunderstorm. Additional details of the methodology and results can be found in the publications by Forbes and Hoffert cited in the references at the end of the paper.

## STUDIES OF INITIAL LIGHTNING THREAT

Because of the proximity of KSC/CCAS to the coastline and to many rivers and bays, the sea-breeze front and multiple river breeze fronts can serve as lifting mechanisms to trigger and focus convective activity. Furthermore, outflows from inland thunderstorms can trigger eastward-moving gust fronts that serve as additional convective triggers. Often these mesoscale boundaries initiate convection *in situ* over the KSC/CCAS complex or promote reorganization of storms propagating into the area.

Convective initiation is enhanced when there is an imminent collision between two or more mesoscale boundaries, as has been shown by a number of researchers:

- Boundaries may be detected as arcs of cumulus clouds on satellite imagery or fine lines on radar reflectivity
- Convection may develop between the approaching boundaries when the air between them is conditionally unstable and already contains cumulus clouds
- Convection usually develops within 50 minutes of collision of mesoscale boundaries and within 20 km of the point of collision
- Convection shows some preference for developing on the side of the collision point above the stronger (colder, deeper) outflow
- Convective rolls (cloud streets) that intersect other mesoscale boundaries can also initiate thunderstorms
- The KSC surface mesonet can be useful in anticipating new convective development from progagating gust fronts or other mesoscale boundaries. Individual mesoscale boundaries may initiate convection when moving into (1) localized temperature hot spots and /or (2) maximum surface convergence, or (3) regions where the rate of short-term (~15 minute) temperature increase and/or convergence increase are maximum.

Once convective clouds have been initiated within the KSC/CCAS complex, the forecasting issues become largely ones of determining whether or not the clouds will grow large enough to develop lightning and where the storm will move. The issue of whether or not a convective cloud will develop lightning has been addressed through use of WSR-88D radar reflectivities and Doppler velocities. In addition, conceptual models based upon studies of the cloud dynamics and physics of lightning formation are invoked.

Initial lightning aloft is imminent (within 5 minutes) when:

- Radar reflectivity of 30 dBZ or greater develops at or grows vertically above about 7 km over KSC/CCAS in summer. This is indicative of the existence of sufficient cloud water content at temperatures of -15 to -20°C to allow mixed-phase electrification processes to develop lightning.
- Storm-top divergence indicates a vigorous updraft and the prospect of continued growth, particularly when combined with low-level convergence.

Hoffert (1996) found that that the most reliable predictor of the initial CG lightning threat was the upward growth of the radar echo until radar reflectivity exceeded 30 dBZ at and above the -10°C level (about 7 km in summer), particularly when accompanied by storm-top divergence. This is effectively the so-called the "30 dBZ above 7 km" rule used at CCAS. He found:

- 100% probability of detection of cloud-ground strike-producing storms
- 15% false alarm rate with respect to lightning aloft
- 35% false alarm rate with respect to cloud-ground strike-producing storms
- 0.83 critical success index with respect to anticipating lightning aloft
- 0.65 critical success index with respect to anticipating cloud-ground strike-producing storms
- 4.6 minute average lead time relative to lightning aloft
- 7.8 minute average lead time relative to cloud-ground strikes

STUDIES OF END-OF-LIGHTNING THREAT

LDAR activity often becomes sporadic during the dissipation stage of thunderstorms, with sometimes several minutes elapsing between discharges. Table 1 shows the probability of a future cloud-ground strike from the storm (including extrapolation of its movement) as a function of the time elapsed since the last LDAR activity (Forbes, 1993). The likelihood of a future cloud-ground strike becomes progressively low once LDAR activity has ceased in the storm for more than 3 minutes.

TABLE 1

PROBABILITY OF A FUTURE CLOUD-GROUND STRIKE
FROM A STORM DETECTED BY LDAR
AS A FUNCTION OF THE LENGTH OF TIME
SINCE THE MOST RECENT LDAR ACTIVITY

| Inactive Period (min) | Probability (%) |
|---|---|
| 1 | 46 |
| > 1 | 22 |
| > 2 | 13 |
| > 3 | 7 |
| > 4 | 5 |
| > 5 | 3 |
| > 6 | 2 |
| > 7 | 1 |
| > 8 | 0.5 |

Hoffert (1998b) examined the end-of-storm lightning threat stratified on the basis of the storm structure and characteristics during this stage:

- Cellular debris - low-topped convective cells embedded within stratiform reflectivity layers
- Non-cellular debris - stratiform reflectivity layer without significant embedded convective cells and often

accompanied by a bright band

- Precipitating debris - characterized by strongly descending reflectivity pockets or layers
- Non-precipitating debris - characterized by stationary or slowly descending reflectivity pockets or layers with weak reflectivity below them

Table 2 (Hoffert, 1998b) indicates the relative threat of cloud-ground strikes from combinations of these storm characteristics.

TABLE 2

RELATIVE RISKS OF CLOUD-GROUND LIGHTNING
BASED UPON END-OF-STORM DEBRIS CHARACTERISTICS

| | *Precipitating Debris* | *Non-Precipitating Debris* |
|---|---|---|
| *Cellular Debris* | Most CG<br>Highest Risk | Isolated CG<br>Moderate Risk |
| *Non-Cellular Debris* | Isolated CG<br>Moderate Risk | Least CG<br>Lowest Risk |

In cases with embedded convective cells and/or precipitating debris, the highest risk of cloud-ground strikes was located

- where 35 dBZ reflectivity extended to or above the -10°C level
- where 30 dBZ reflecitivity occurred below the freezing level and extended downward to near the surface

In cases of descending precipitating debris, the highest risk of cloud-ground strikes was found

- where there was 30 dBZ or weaker reflectivity above the freezing level
- where there was 30 dBZ or stronger reflectivity below the freezing level and extending to near the surface
- when/where there was rapid descent of the reflectivity layer in time
- where there was a steep slope of the reflectivity layer
- where there were downward bulges/streaks/curtains of higher reflectivity
- where and when there was bright band development
- where and when anvils merge
- where there was strong mid-level convergence
- where there was large spectrum width in mid-level velocities

Hoffert (1998b) concluded that the probability of cloud-ground strikes remains greater than 5% as long as there is still lightning aloft. However, clues based upon radar and field mill readings can allow termination of cloud-ground lightning warnings on some occasions even when lightning continues aloft. See Hoffert (1998b) for additional details.

- Cloud-ground lightning does not generally occur more than 2 km beyond the region having 20 dBZ radar reflectivity at low levels, but there are notable exceptions.
- Field mill readings typically remain above 1kV/m for tens of minutes or more after ground strikes have ended at a site and did not appear to give a reliable indication of the end-of-lightning threat

Several-minute gaps between incidents of LDAR bursts aloft proved to be the most reliable indication that the CG threat had ended during the dissipating stages of a storm. CG lightning was also found to be unlikely when echo greater than 20 dBZ at low levels had moved more than 2 km away from a site.

A limiting factor in the end-of-storm studies was uncertainty over whether LLP-indicated CG strikes were valid. Hoffert (1998b) found that there were numerous inconsistencies between LDAR and LLP indications of cloud-ground strikes during this end-of-storm stage. He found that this difficulty in determining what were and were not true cloud-ground lightning strikes was a limiting factor in assessing the true probabilities of cloud-ground strikes during this stage. Approximate rules for designating a ground strike based on LDAR:

- At least 2 LDAR points below 3 km with at least one LDAR point below 2.1 km
- Lowest LDAR point must be within slant distance of not more than 2 km from another LDAR point

## LOCATION OF CG STRIKES RELATIVE TO RADAR ECHOES AND LIGHTNING ALOFT

Several of the publications cited in the references illustrate the typical evolution of in-cloud (IC), CG, and cloud-air (CA) discharges, with LDAR events overlaid onto radar reflectivity cross-sections of storms. Forbes (1993) and Forbes and Hoffert (1995) give statistics indicating the probability of a CG lightning strike at various distances beyond the area previously experiencing LDAR-detected discharges. Space does not permit reproduction of that material here.

## ACKNOWLEDGMENTS

Research was supported by NASA Kennedy Space Center contracts NAG10-0187, NAG10-1054, and NAG10-0137. Forbes' participation in the research was partially funded through the NASA/ASEE Summer Faculty Fellowship Program, under NASA Grant NGT-60002. Assistance by Carl Lennon and Launa Maier of KSC, John Madura and Frank Merceret, KSC Weather Projects Office, the USAF 45th Weather Squadron, NWSO/MLB, the AMU, and NYMA and other NASA contractors is greatly appreciated.

## REFERENCES

Forbes, G.S., 1993: Lightning studies using LDAR and LLP data and applications to weather forecasting at KSC. NASA CR-194678, pp. 165-194.

Forbes, G.S., 1994: Lightning studies using LDAR and companion data sets. NASA CR-197448, pp. 205-233.

Forbes, G.S. and S.G. Hoffert, 1995: Lightning forecasting studies using LDAR, LLP, field mill, surface mesonet, and Doppler radar data. NASA CR-199891, pp. 195-224.

Forbes, G.S. and S.G. Hoffert, 1998: Research on Forecasting of Lightning at the Kennedy Space Center: Summary and Supplemental Forecasting Guidelines. Final Report, NASA Contract Rept. NAG10-0187, 26pp + app.

Forbes, G.S., S.G. Hoffert, and M.L. Pearce, 1996: Lightning forecasting studies at Kennedy Space Center using WSR-88D and companion data sets. *Preprints, 15th Conf. Wea. Analysis and Forecasting*, Norfolk, VA, Amer. Meteor. Soc., 447-450.

Hoffert, S.G., 1996: On the short-range forecasting of lightning at the Kennedy Space Center. M.S. Thesis, The Pennsylvania State University, 111pp.

Hoffert, S.G., 1998a: Studies of lightning and non-lightning convective clouds over the John F. Kennedy Space Center. *Preprints, 16th Conf. Wea. Analysis and Forecasting*, Phoenix, AZ, 129-131.

Hoffert, S.G., 1998b: The threat of cloud-ground discharges emanating from lightning aloft during the decaying stages of convection. Progress Report, NASA Contract NAG10-0187, 35 pp.

Hoffert, S.G. and G.S. Forbes, 1996: Ongoing studies to improve short-term prediction of lightning at KSC using WSR-88D and companion data. Progress Report, NASA Contract NAG10-0187, 54 pp.

Hoffert, G.S. and G.S. Forbes, 1997: Lightning forecasting studies at Kennedy Space Center. Interim Progress Report, NASA Contract NAG10-0187, 31 pp.

Hoffert, S.G. and M.L. Pearce, 1996: The 29 July 1994 Merritt Island, FL microburst: A case study intercomparing Kennedy Space Center three-dimensional lightning data (LDAR) and WSR-88D radar data. *Preprints, 18th Conf. Severe Local Storms*, San Francisco, CA, Amer. Meteor. Soc., 424-427.

Pearce, M.L. and S.G. Hoffert, 1997: The Snap Weather Information Integrated Forecast Tool (SWIIFT): Next generation software for research and operational meteorology. *Preprints, 13th Conf. Interactive Information Processing Systems*, Long Beach, CA, Amer. Meteor. Soc., 269-272.

# COMBINED DUAL-DOPPLER, MULTIPARAMETER RADAR, AND LIGHTNING OBSERVATIONS OF A SEVERE CONVECTIVE STORM

Timothy J. Lang[1], Steven A. Rutledge[1], and Patrick C. Kennedy[2]

[1]Department of Atmospheric Science, Colorado State University, Fort Collins, CO
[2]CSU-CHILL National Radar Facility, Greeley, CO

ABSTRACT: During the evening of 1 July 1998, a powerful severe convective storm passed through the plains of northeastern Colorado. The storm featured large hail and a possible tornado. Throughout a significant portion of its lifetime, the storm produced large amounts of intracloud (IC) lightning, as measured by a network of electric field change meters, but little cloud-to-ground (CG) lightning, as measured by the National Lightning Detection Network. The CG lightning that did occur during this time was predominantly positive in polarity. This storm passed through the dual-Doppler network formed by the CSU-CHILL multiparameter radar and the newly installed HOT radar, providing approximately two hours of combined dual-Doppler, multiparameter radar, and lightning observations during significant portions of the storm's mature and decay phases. This level of radar and lightning observations for a severe storm is largely unprecedented, and it provides a wealth of data with which to explore the relationships between the microphysical and kinematic structures of a severe storm and the lightning it produces. Key topics to be examined include relating the microphysical structure, as inferred from multiparameter radar, to the kinematic structure, as inferred from dual-Doppler analysis, for the two hours that these data are available. These radar analyses then will be compared to the amount, type, and predominant polarity of lightning produced, and the results will be discussed in light of previous, less-detailed observational studies of similar storms.

## INTRODUCTION

Past research (See Lang et al. 1999 for a review.) has shown that most non-severe convective storms in the mid-latitudes last less than two hours, and have peak total lightning flash rates of at most 10 $min^{-1}$ and peak cloud-to-ground (CG) lightning flash rates of approximately 2 $min^{-1}$ or less. The vast majority of CG lightning (> 90% or more) transfers net negative charge to ground. However, there is a class of severe thunderstorms which have long (> 2 hour) lifetimes, and which can produce significant quantities of positive CG lightning, greater than 50% positive in fact, and sustained total flash rates of over 15 $min^{-1}$. There also appears to be a class of thunderstorms which are distinguished by relatively low CG production, positive or negative, during significant portions of their lifetimes. In fact, these low-CG thunderstorms share many characteristics - such as high IC flash rates, significant hail production, and other severe weather phenomena - with predominantly positive CG producing severe storms. However, their CG signature is similar to that of ordinary cells.

During the evening of 1 July 1998 (local time), a severe thunderstorm occurred in the eastern plains of Colorado near Greeley. This thunderstorm was sampled by the CSU-CHILL multiparameter Doppler radar, the HOT Doppler radar, one field change meter (FCM), and the National Lightning Detection Network (NLDN). This resulted in over two hours of combined dual-Doppler, multiparameter radar, and electrical observations. Analysis of these data is in preliminary stages, and we report initial findings from the first half hour of the most intensive observation period, 0038-0108 UTC. During this time period, the storm appeared to be a low-CG intense thunderstorm.

## ANALYSIS METHOD

The CSU-CHILL radar is a dual-linearly polarized Doppler radar with a beamwidth of 1° and a wavelength of 11.1 cm. The HOT radar is a vertically polarized Doppler radar with a beamwidth of 1.2° and a wavelength of 11.1 cm. The baseline formed by the radars is 47.8 km in length. Both radars scanned synchronized plan-position indicator (PPI) sector volumes with repeat times of 6 minutes during the analysis time period (0038-0108 UTC), resulting in 5 combined dual-Doppler and multiparameter radar volumes. Radar data were edited for noise and clutter by using thresholds on the radar reflectivity, total power, noise-corrected power, and correlation coefficient fields. Sidelobe contamination and velocity folds typically were edited manually. Specific differential phase ($K_{dp}$) was estimated first by filtering the differential phase field using a 21-point running mean filter, then applying a finite differencing technique. Data were gridded to Cartesian space using variable radius filters, with 1 km x 1km resolution in the horizontal and 0.5 km resolution in the vertical.

Radar reflectivity and $K_{dp}$ were used in concert to differentiate between regions of rain only, hail only, and mixed phase precipitation. Areal coverage of these precipitation types then were estimated following the method of Carey and Rutledge (1998).

Dual-Doppler synthesis was performed using the National Center for Atmospheric Research CEDRIC analysis software. Storm motion was assumed to be from 304° at 8.2 m $s^{-1}$. Regions with beam crossing angles less than 30° were not included in the analysis. Downward integration with 0 m $s^{-1}$ as the upper boundary condition was done to estimate vertical motion. We corrected for particle fallspeed contamination using a common fallspeed-reflectivity relationship.

CG data from the NLDN were available for the grid region during the entire 30-minute period of this analysis. For a more detailed review of current NLDN capabilities see Cummins et al. (1998). Total flash rate data from a FCM located at the CHILL radar are available, but these data were affected by an unexpected noise source at the site. So far attempts to filter this noise source, which likely is masking many flashes, have been unsuccessful. At this point, although the storm was within range of the sensor (30-40 km) during this period, all we can say is that, from the standpoint of the FCM, the storm was electrified.

## OBSERVATIONS

Fig. 1a shows a horizontal cross-section at 0.5 km AGL of CSU-CHILL radar reflectivity during the 0050-0056 UTC radar volume. Also shown are the ground-strike locations and polarities of all NLDN CG lightning that occurred during the period 0038-0108 UTC. Remarkably, there were but 4 positive CG flashes and no negative CGs during this period. Moreover, 2 of these 4 positive CG flashes did not meet the 10 kA peak current threshold recommended by Cummins et al. (1998) to distinguish between misinterpreted intracloud (IC) flashes and real positive CG flashes. This is an extremely low total CG flash rate (well under 1 $min^{-1}$) relative to typical thunderstorms, but is similar to CG observations of intense thunderstorms by Lang et al. (1999) and other researchers. Fig. 1b shows a vertical cross-section of CHILL reflectivity through 17.0 km east of the CHILL radar.

Table 1 shows key radar-derived statistics for this storm, averaged over the 5 volumes during the 0038-0108 UTC time period. From Fig. 1 and Table 1 it is apparent that this storm was very intense. The numbers, where a comparison is possible, place the storm on a par with, or perhaps stronger than, other intense Colorado thunderstorms observed by the CHILL radar and analyzed by Carey and Rutledge (1998) and Lang et al. (1999). It also is comparable to intense storms in other regions. Immediately after this time period, at 0115 UTC, the National Weather Service issued a tornado warning on this storm which lasted for about an hour.

TABLE 1. Radar-derived statistics for the 1 July 1998 (local time) storm, averaged over the 5 volumes from 0038 to 0108 UTC (2 July).

| Statistic | Value |
|---|---|
| Maximum rain rate ($K_{dp}$) at 0.5 km AGL | 164.8 mm $h^{-1}$ |
| Area of heavy rain ($R \geq 60$ mm $h^{-1}$) at 0.5 km AGL | 77.0 $km^2$ |
| Area of hail at 0.5 km AGL | 72.8 $km^2$ |
| Area of $\geq 50$ dBZ at 0.5 km AGL | 125.4 $km^2$ |
| Maximum reflectivity | 68.5 dBZ |
| Max height of 60 dBZ contour | 10.5 km |
| Maximum updraft speed | 41.8 m $s^{-1}$ |
| Height of max updraft speed | 8.5 km |

## CONCLUSIONS

During the 30-minute period for which analysis has been completed, the storm of 1 July 1998 was very intense from both a dynamical and a microphysical perspective. It featured high rain rates, high peak radar reflectivities, significant hail production, and very fast updraft speeds. However, it produced very little CG lightning - perhaps as few as 2 positive CG flashes and no negative CG flashes - during this same time period. This behavior is similar to intense storms studied by Lang et al. (1999) and other researchers. Except for the low positive CG flash rates, it is also similar to predominantly positive CG producing storms studied by Carey and Rutledge (1998) and other researchers.

An explanation for the dearth of negative CGs sometimes observed in intense thunderstorms was first offered by MacGorman et al. (1989). They suggested that intense updrafts can elevate major charge regions, favoring ICs over CGs. This hypothesis has been confirmed in part by later observational and modeling work (e.g., Stolzenburg et al. 1998, Ziegler and MacGorman 1994). Given the great magnitudes of both the speed and depth of

the updraft in the 1 July 1998 storm, we suggest that this elevated charge mechanism may have been active during this time. Alternatively, the high rainfall rates may have allowed precipitation current to substitute for negative CG lightning current. This cannot be ruled out as yet, although Lang et al. (1999) analyzed a similar storm where this precipitation current mechanism most likely could not have been responsible for low negative CG rates.

It is not clear why this storm also produced few positive CGs during this time period, given that it was so similar in intensity to other predominantly positive CG producing storms. Carey and Rutledge (1998) found evidence supporting a precipitation unshielding mechanism in a predominantly positive CG producing storm. If this mechanism were active in the 1 July 1998 storm, it may have been that not enough precipitation had fallen out to unshield the upper positive charge region and allow for enhanced positive CG flashing. Although analysis of later time periods is not completed yet, CGs did become more prevalent later.

We plan to continue work on this case and will present these results, as well as work on later time periods of this storm, at this conference.

REFERENCES


Carey, L. D., and S. A. Rutledge, 1998: Electrical and multiparameter radar observations of a severe hailstorm. *J. Geophys. Res.*, **103**, 13979-14000.

Cummins, K. L., Murphy, M. J., Bardo, E. A., Hiscox, W. L., Pyle, R. B., and A. E. Pifer, 1998: A combined TOA/MDF technology upgrade of the U. S. National Lightning Detection Network. *J. Geophys. Res.*, **103**, 9035-9044.

Lang, T. J., Rutledge, S. A., Dye, J. E., Venticinque, M., Laroche, P. and E. Defer, 1999: Anomalously low negative cloud-to-ground lightning flash rates in intense convective storms observed during STERAO-A. Accepted in *Mon. Wea. Rev.*

MacGorman, D. R., Burgess, D. W., Mazur, V., Rust, W. D., Taylor, W. L., and B. C. Johnson, 1989: Lightning rates relative to tornadic storm evolution on 22 May 1981. *J. Atmos. Sci.*, **46**, 221-250.

Stolzenburg, M., Rust, W. D., and T. C. Marshall, 1998: Electrical structure in thunderstorm convective regions. Part III: Synthesis. *J. Geophys. Res.*, **103**, 14079-14108.

Ziegler, C. L., and D. R. MacGorman, 1994: Observed lightning morphology relative to modeled space charge and electric field distributions in a tornadic storm. *J. Atmos. Sci.*, **51**, 833-851.


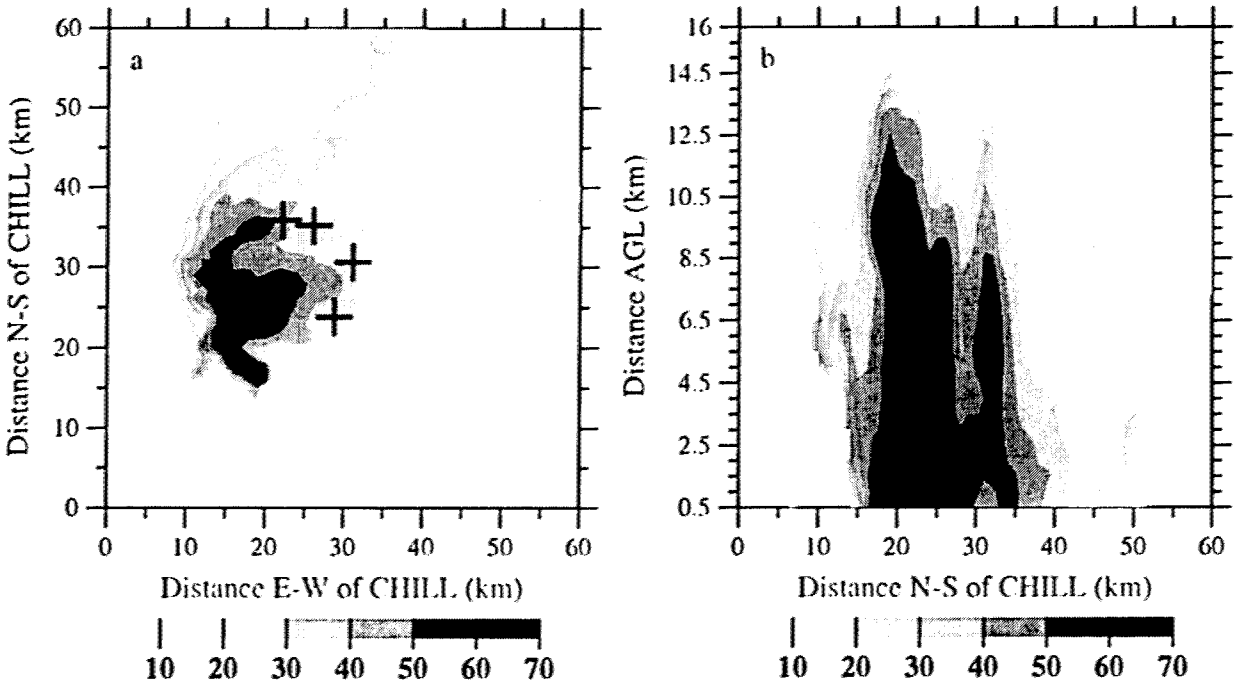


Figure 1. a) Horizontal cross-section of CSU-CHILL radar reflectivity at 0.5 km AGL for the volume lasting from 0050 to 0056 UTC. Also shown are the ground strike locations and polarities of all NLDN-detected CG lightning that occurred during the period 0038-0108 UTC. b) Vertical cross-section of CSU-CHILL radar reflectivity at 17.0 km east of the CHILL radar.

# RELATIONSHIP BETWEEN INITIAL DEVELOPMENT OF PRECIPITATION AND ONSET OF CLOUD ELECTRIFICATION AND THE OBSERVED BEHAVIOUR OF POINT DISCHARGE CURRENT DURING "RAIN" AND "NO-RAIN" SITUATIONS IN THE THUNDERSTORMS AT PUNE

S. S. Kandalgaonkar, M. I. R. Tinmaker and G. K. Manohar
Indian Institute of Tropical Meteorology, Pune, India

ABSTRACT : Thunderstorms are known to be more severe in the tropics and subtropics than elsewhere. The observations of lightning and precipitation show that the thunder clouds are the seat of intense cloud electrification and precipitation development. As the storm forms and dissipates several complex cloud physical and electrical processes such as charge separation, precipitation formation, occurrence of lightning and point discharge current are taking place. The understanding of the time sequence between these processes (i.e. initial development of precipitation and onset of cloud electrification) is important as the convection, electrification and precipitation are the remarkable aspects of thunder clouds. In addition to this, in thunderstorm activity the reports of occurrence of precipitation associated with point discharge current (PDC) are quite common. Measurements have shown that these precipitation elements are electrically charged bodies and normally deposit positive charge to the Earth's surface (Williams and Heckman, 1993). A pertinent question that surrounds this situation is the interaction (scavenging and attachment) between the PD ions and precipitation elements near the ground surface and its likely effect on PDC. It appears that very little information on this intuitively appealing problem is available in literature (Price, 1993). This short communication describes the results of the above two studies by using one-minute interval data of electric field, rainfall and PDC during the evolution of 14 and 21 thunderstorms which occurred at Pune (18°32'N, 73°51'E, 559 m asl).

The results of the first part of the study are presented in the form of one table and figure. The combined result of this study indicated in-cloud development of precipitation at least 3-7 minutes in advance of electric field intensification. Our result suggests that in most cases precipitation development in thunderstorms is initiated well before the electric field begins to intensify. This results appears to be in good agreement with the results of earlier studies (Dye et al., 1986, 1989).

The results of the second part of the study are presented in one table giving average PDC for every half a kilo width of electric field in the range −7.0 to +6.5 k $Vm^{-1}$. We also present scatter diagrams of one-minute interval values of PDC vs. electric field drawn over the "two" situations. Our results strongly suggest that PDC of both polarities in "rain" is reduced than that in "no-rain". The reduction for negative current was more obvious.

## INTRODUCTION

The thunderstorm is an important weather phenomenon for the understanding of the many issues related with atmospheric electricity and weather. As the storm forms and dissipates several complex cloud physical and electrical processes such as charge separation, precipitation formation, occurrence of lightning and point discharge current are taking place. The understanding of the time sequence between these processes is an important aspect as convection, electrification and precipitation are the remarkable features of the thunder cloud. Also, precipitation associated with the occurrence of PDC, is quite common during the thunderstorms. These precipitation elements are electrically charged bodies (Williams and Heckman, 1993) hence they must be having some influence on point discharge ions. As very little information is available in the literature (Price, 1993) on this problem, the present study has been taken up by considering the observations of electric field, PDC and rainfall intensities during the thunderstorm environment at Pune.

## DATA

One-minute interval data of electric field, PDC and rainfall during the evolution of 14 and 21 thunderstorms which occurred at Pune during the year 1973 form the data set for this study. Cloud electrification and initial precipitation relationship were studied for 14 thunderstorms while 21 thunderstorms were studied to investigate the likely effect of precipitation on point discharge ions. For this purpose the data of electric field,

PDC and rainfall intensity during rain and no-rain situations on individual days were scanned and separated into half-a-kilo interval width of electric field ranging from -7.0 to +6.0 k V $m^{-1}$.

## INSTRUMENTATION

The vertical component of electric field was measured by the potential equalization method using ($P_o$-210, 6 μ Ci) radioactive source and suitable electronic recording system. A Platinum/10% iridium needle nearly 4 cm long with 0.25 mm radius of the needle tip consisted the PD element in measurement of PDC. Rainfall intensity is measured by using the float type rain gauge coupled with a LVDT system and an electronic circuit that converts the displacement of the float into electrical signal.

## RESULTS

The results of the first part of the study are given in Table 1 and Figure 1(a-f). The downward arrow (↓) in Fig. 1 (a-f) indicates the time of registration of initial precipitation, while the upward arrow (↑) in the same figure indicates the time when initial electric field intensified. From this table it is seen that out of 14 storm days, on 9 days initial precipitation preceded the intensification of cloud electrification, while on 4 days precipitation lagged behind electrification and there was only one day on which precipitation and cloud electrification occurred simultaneously (see Fig. 1b).

The results of the second part of the study are presented in Table 2. This table presents average PDC for every half kilo width of electric field, in the range -7.0 to +6.0 k $Vm^{-1}$ (total no of intervals 26). Out of these 26 intervals, the average magnitude of PDC on 21 occasions is less, on three it is more and on two occasions it is just the same, in rain and no-rain situations. This comparison thus suggests that PDC in rain is reduced. This result is also clear from Figure 2, a scatter plot of electric field versus PDC in rain and no-rain situations. The two curves in Figure 2 indicate that for the same electric field width the no-rain curve overlays that for the rain curve. It is noted that PDC of both polarities in rain is reduced. This reduction of PDC in rain may be due to ion attachment of charged precipitation elements near the ground surface.

## CONCLUSION

The combined result of the first part of the study indicated in-cloud development of precipitation at least 3-7 minutes in advance of electric field intensification. The tendency of occurrence of such cases was found to be 64%.

The results of the second part of the study suggested that precipitation elements while approaching the ground surface cause depletion in PDC.

ACKNOWLEDGEMENTS : The authors are thankful to Dr. A.S.R. Murty and Dr.Mrs. A.M.Selvam and Director for their constant support of our research activity.

## REFERENCES

Dye, J.E., J.J. Jones, W.P. Win, T.A. Cerni, B. Gardiner, D. Lamb, R.L. Petter, J. Hallet and C.P.R. Saunders, Early electrification and precipitation development in a small isolated Montana cumulonimbus, *J. Geophys. Res.*, **91**, 1231-1247, 1986.

Dye, J.E., W.P. Win, J.J. Jones and D.W. Breed, The electrification of New Mexico thunderstorms. 1. Relationship between precipitation development and the onset of electrification, *J. Geophys. Res.*, **94**, 8643-8656, 1989.

Price, C., Global surface temperatures and the atmospheric electrical circuit, *Geophys. Res. Letters*, **20**, 1363-1366, 1993.

Williams, E.R. and S.J. Heckman, The local diurnal variation of cloud electrification and the global diurnal variation of negative charge on earth, *J. Geophys. Res.*, **98**, 5221-5234, 1993.

Table 1 : Chronological details of thunderstorms at Pune during 1973

| Dates of thunderstorms | Time of registration of initial precipitation at the ground (IST) A hr. | Time when initial electric field intensified and became maximum (IST) B hr. | Maximum electric field (k $Vm^{-1}$) | Amount of rainfall (mm) | A-B (min) Category I | A-B (min) Category II |
|---|---|---|---|---|---|---|
| 03.04.1973 | 1757 | 1801 | +8.29 | 2.0 | -04 | -- |
| 08.04.1973 | 1850 | 1850 | -6.22 | 0.4 | 00 | -- |
| 22.05.1973 | 1517 | 1457 | -6.48 | 26.6 | -- | +20 |
| 31.05.1973 | 1655 | 1658 | +6.22 | 0.6 | -03 | -- |
| 02.06.1973 | 2136 | 2134 | +3.88 | 2.0 | -- | +02 |
| 03.06.1973 | 1659 | 1709 | +5.51 | 5.6 | -10 | -- |
| 04.06.1973 | 1529 | 1535 | +5.99 | 18.3 | -06 | -- |
| 05.06.1973 | 2157 | 2032 | +5.63 | 0.7 | -- | +85 |
| 06.06.1973 | 1755 | 1833 | -4.53 | 12.5 | -38 | -- |
| 27.06.1973 | 1942 | 1918 | -9.72 | 3.5 | -- | +24 |
| 30.06.1973 | 1501 | 1527 | -2.69 | 11.1 | -26 | -- |
| 19.09.1973 | 1420 | 1506 | -7.31 | 61.2 | -46 | -- |
| 01.10.1973 | 1515 | 1526 | +4.25 | 2.0 | -11 | -- |
| 04.10.1973 | 1440 | 1637 | -6.98 | 22.7 | -117 | -- |

One-minute interval variation of electric field

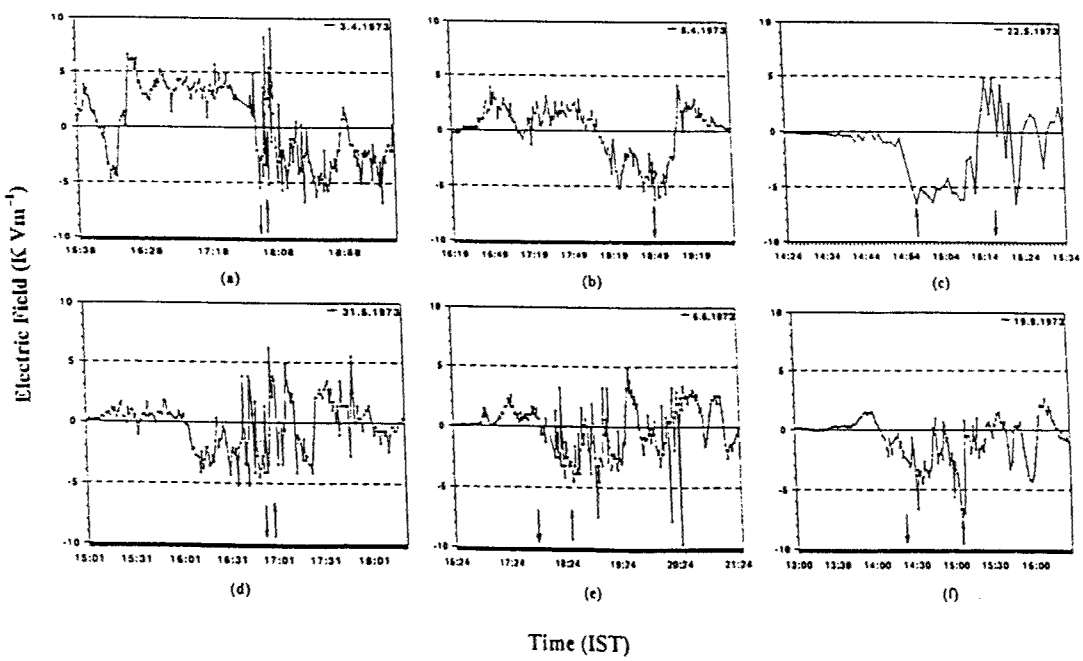


Figure 1(a-f) : One-minute interval field data for thunderstorms at Pune on six representative days.

Table 2 : Statistical details of the variation of average PDC in rain and no-rain situations based on 21 thunderstorms

| Range of electric field k $Vm^{-1}$ | Magnitude of PDC (μA) | | | Av. Precipitation intensity mm $hr^{-1}$ |
|---|---|---|---|---|
| | No-rain | Rain | Reduction | |
| -7.0 to -6.5 | 1.35 | 0.45 | 0.90* | 12.70 |
| -6.5 to -6.0 | 1.54 | 1.50 | 0.04* | 1.80 |
| -6.0 to -5.5 | 1.34 | 1.54 | 0.20 | 6.18 |
| -5.5 to -5.0 | 1.24 | 1.63 | 0.39 | 1.66 |
| -5.0 to -4.5 | 0.90 | 1.03 | 0.13 | 4.36 |
| -4.5 to -4.0 | 0.93 | 0.80 | 0.13* | 3.86 |
| -4.0 to -3.5 | 0.70 | 0.66 | 0.40* | 8.21 |
| -3.5 to -3.0 | 0.57 | 0.58 | 0.01 | 5.76 |
| -3.0 to -2.5 | 0.54 | 0.33 | 0.21* | 3.62 |
| -2.5 to -2.0 | 0.38 | 0.25 | 0.13* | 3.60 |
| -2.0 to -1.5 | 0.34 | 0.24 | 0.10* | 3.36 |
| -1.5 to -1.0 | 0.57 | 0.17 | 0.40* | 2.05 |
| -1.0 to -0.5 | 0.42 | 0.12 | 0.30* | 6.55 |
| -0.5 to 0.0 | 0.21 | 0.07 | 0.14* | 9.93 |
| 0.0 to 0.5 | 0.08 | 0.06 | 0.02* | 4.93 |
| 0.5 to 1.0 | 0.08 | 0.08 | 0.00 | 3.16 |
| 1.0 to 1.5 | 0.20 | 0.15 | 0.05* | 1.95 |
| 1.5 to 2.0 | 0.33 | 0.20 | 0.13* | 2.66 |
| 2.0 to 2.5 | 0.37 | 0.30 | 0.07* | 3.09 |
| 2.5 to 3.0 | 0.48 | 0.45 | 0.03* | 1.71 |
| 3.0 to 3.5 | 0.55 | 0.46 | 0.09* | 2.70 |
| 3.5 to 4.0 | 0.58 | 0.54 | 0.04 | 2.30 |
| 4.0 to 4.5 | 0.78 | 0.59 | 0.19* | 3.90 |
| 4.5 to 5.0 | 0.72 | 0.70 | 0.02* | 0.60 |
| 5.0 to 5.5 | 0.87 | 0.76 | 0.11* | 0.45 |
| 5.5 to 6.0 | 1.62 | 0.83 | 0.79 | 0.30 |

* indicates the reduction cases.

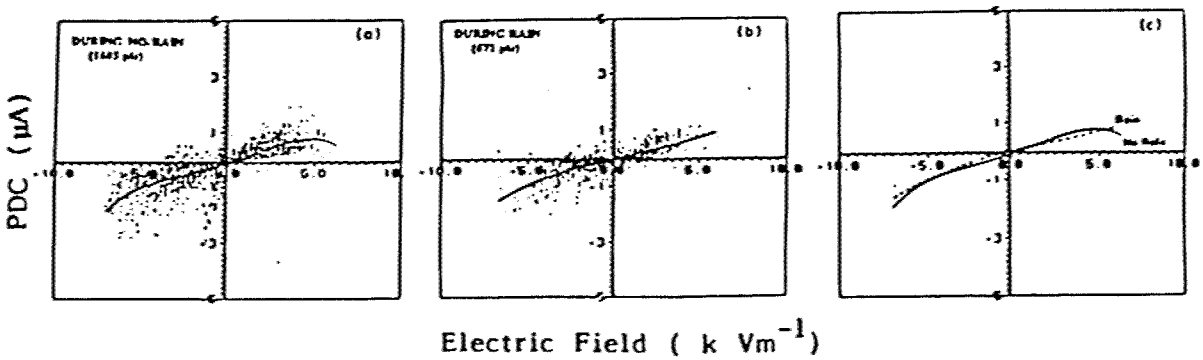


Figure 2 : Scatter plot of electric field versus PDC and curve fit for (a) no-rain situation (b) rain situation (c) no-rain and rain situations shown together.

# Electric Field Profiles in a Mesoscale Convective System with Multiple Bow Echoes 25 May 1998 during the MCS Electrification and Polarization Radar Study (MEaPRS)

W.D. Rust[1], T.C. Marshall[2], M. Stolzenburg[2], D.P. Jorgensen[3], T.R. Shepherd[4], and D.R. MacGorman[1]

[1]NOAA, National Severe Storms Laboratory, Norman, Oklahoma, U.S.A., (dave.rust@nssl.noaa.gov)
[2]Department of Physics and Astronomy, University of Mississippi, University, Mississippi, U.S.A.
[3]NOAA, National Severe Storms Laboratory, Boulder, Colorado, U.S.A.
[4]Cooperative Institute for Mesoscale Meteorological Studies, University of Oklahoma/NSSL, Norman, OK, U.S.A.

*Abstract:* Two mobile laboratories for mobile ballooning and a NOAA P-3 instrumented aircraft equipped with airborne Doppler radar were used to probe a mesoscale convective system (MCS) on 25 May 1998. The main convection region was aligned east to west (along the Kansas border) with storm motion from 287° at 15 m $s^{-1}$. The overall structure of the MCS was deep convection on the south side with a transition zone and large stratiform region on the north side. The MCS produced a series of eight bow-shaped radar echoes that moved rapidly during the night from 0000 UTC to 1200 UTC. Two electric field profiles were accomplished in the convective regions of two successive convective bow echoes. The magnitude of the maximum measured electric field, E, was about 100 kV $m^{-1}$. The majority of the ground flashes in the convective region were positive. A third sounding was made in the transition zone about 100 km north-northeast of the soundings in the convective region. Very few transition-zone soundings are in the literature: This one shows a peak E = 100 kV $m^{-1}$ and an inferred five regions of charge, with positive lowermost. Another profile was made into the rearmost part of the stratiform precipitation region about 55 km north-northeast and downwind of the transition zone launch site. The peak E magnitude was about 25 kV $m^{-1}$; there were three alternating charge regions, with negative lowest. The final sounding was just at the back edge of the stratiform region. The E was less than 5 kV $m^{-1}$ along the flight path. Maximum reflectivity in the stratiform rain region was 35-40 dBZ, about typical for mid-latitude MCSs. The electric field and inferred charge regions from the soundings are combined with Doppler derived horizontal winds and reflectivities.

## INTRODUCTION AND INSTRUMENTATION

As a continuation of our research on electrical aspects of mesoscale convective systems (MCSs), we conducted a field project named *MCS Electrification and Polarization Radar Study* (MEaPRS) during spring 1998 in the southern Great Plains. A primary objective of MEaPRS was to collect data from the convective region, transition zone, and stratiform region of the same MCS to determine the E profiles and charge distribution through an entire system. These data also add to the very few published soundings in the transition zone of an MCS. Background on MCSs and previous results leading to MEaPRS are found in Ch. 8 of MacGorman and Rust [1998], where details from the literature are cited. Newer results are in Stolzenburg et al. [1998a-c]. The MCS we describe here does not fit the simple two-dimensional conceptual model of an MCS. It was highly three-dimensional in structure and had several convective regions that were on the southern side of the MCS, moved rapidly to the east, evolved into bow echoes from strong straight-line rear inflow winds, and produced stratiform precipitation to their north. See http://mrd3.nssl.ucar.edu/MEaPRS/May24/May24.html for a summary of the structure and evolution of this MCS. Jorgensen and Smull [1993] described the nonelectrical aspects of MCSs with bow echoes. The limited objectives of this case study are to begin to determine if the electric field profiles in this unusually structured MCS can be linked by the flow within the system, fit the conceptual model of an MCS put forth by Stolzenburg et al. [1994], etc.

We collected pseudo-dual-Doppler radar data on the MCS with the NOAA P-3 aircraft, whose radar we had just modified for improved unambiguous velocity measurement. Three-dimensional wind fields were constructed from the radar radial velocity data using the pseudo-dual-Doppler techniques described in Jorgensen et al. [1996]. We used two mobile laboratories from the Joint Mobile Research Facility (see http://www.nssl.noaa.gov/jmrf/) for carrying data receivers and recorders and two cargo trucks for carrying helium, an inflated balloon, and other supplies for inflating and launching balloons. Stolzenburg et al. [1998b] reviewed our ballooning technique, but there are two important changes: (1)The electric field meters were suspended from a hydrophobic nylon line (called waxed nylon), instead of monofilament line; (2) Our radiosonde system was modified to use the global positioning system (GPS) for wind finding and calculating balloon location using Vaisala RS80-15G radiosondes; the system is called Mobile GPS and Loran Atmospheric Sounding System (MGLASS) and was developed by the National Center for Atmospheric Research. Details of procedures for data collection and summaries of operations can be found at

http://www.nssl.noaa.gov/projects/meaprs/. We coordinated the P-3 and mobile laboratories for data acquisition as much as weather conditions and air traffic control constraints allowed.

## MCS STRUCTURE, OBSERVATIONS, AND BRIEF DISCUSSION

The MCS initiated about 0000 UTC on 25 May 1998 along a quasi-stationary warm front that stretched west to east near the Oklahoma-Kansas border. The convective storms were severe with strong winds, large hail, mesocyclones, and several tornadoes. The extraordinary feature of this MCS was its eight bow-echo convective regions that developed starting about 0330 UTC and moved sequentially across the region. These cells became our targets for balloon soundings in the convective region. At 0410, a tornado was confirmed in the cell just to our north, and other cells with mesocyclones were nearby during the balloon flights into the convection. Our preliminary look at data from the National Lightning Detection Network revealed that there was a high percentage of positive ground flashes in the convection, which is somewhat atypical for MCSs. (See Fig. 2 of MacGorman et al., this preprint.) The severe weather and flooding from the supercells in the area controlled our intercept options. Figure 1 shows the system at the start of soundings in the convection and the locations of the other launch sites used later. A sounding was obtained in two successive bow-echo convective regions. Afterwards, the mobile laboratories went northward for a transition zone and a stratiform region soundings.

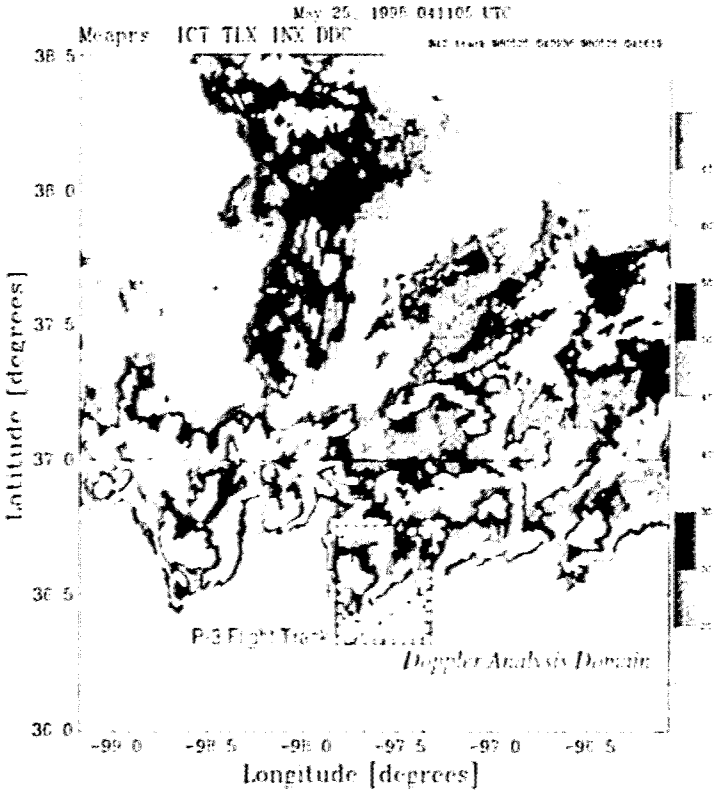


Fig. 1: Radar base-scan composite of MCS with multiple convective regions, 25 May 1998, 0411 UTC. The black box shows the pseudo-dual-Doppler analysis domain. The P-3 track is black line with wind barbs in the box. The circle-over-plus icons denote all three balloon launch sites. Only the southern site was in use at this time. The Doppler domain is in Oklahoma; the northern balloon sites are in Kansas (N37.0° is boundary.)

*Kremlin2 sounding in convective region, 0409 UTC:* (The convective region balloon launches are called Kremlin1, 2, and 3.) When the first balloon in the convective region failed at launch, we launched a second one nine minutes later in moderate to heavy rain. It went toward the west (i.e., back) side of the storm core, which contained 65 dBZ reflectivities and was moving from 287° at 15 m s$^{-1}$. The sounding (Fig. 2) indicates that the balloon did not encounter substantial charge until it reached 7.1 km MSL, after which it was in positive charge until 7.8 km. The data stopped at about 9 km. The humidity profile suggests the instrumentation was in and out of cloud, and future analysis of balloon tracking may show where the balloon went out of and then back into the cloud. This partial profile of E is remarkably similar to one in an isolated supercell two weeks later [MacGorman et al., this conference], but it was in the convective cell all the way up.

*Kremlin3 sounding in convective region, 0459 UTC:* This sounding (not shown) was into the next developing bow echo (in time and westward along the line). The balloon was launched at the leading edge of a core with reflectivities up to 65 dBZ. The balloon initially went SW in the outflow, but the wind veered sharply. By about 2.2 km MSL, the balloon was headed NE and was apparently in the storm's convective region. Radio interference caused loss of E data from about 1 to 3.5 km MSL. The balloon was in updraft much of the height above 4 km. At about 6 km, the balloon descended, followed shortly by rapid ascent. This sounding also went to only 9 km MSL. The E structure is more complex and indicates more charge regions than were in Kremlin2, but both of these are partial soundings. The profile does not clearly fit the pattern reported previously for soundings either in or outside of the updraft in a convective region [Stolzenburg et al., 1998c].

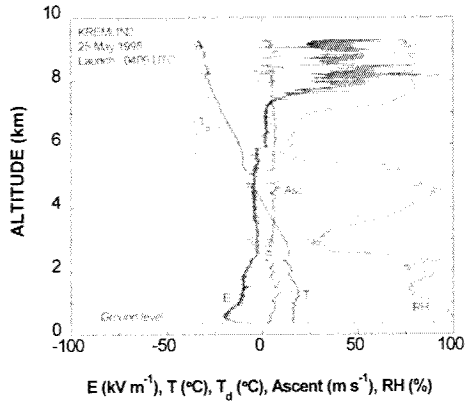


Fig. 2. Sounding in back side of convective region of bow-echo MCS. Data quit at 9 km. Still-air ascent of balloon was about 6 m s$^{-1}$. Symbols are E, electric field; T, temperature; $T_d$, dewpoint temperature; Asc, ascent; RH, relative humidity.

*Wellington1 sounding in developing transition zone, 0749 UTC:* This sounding was 100 km NNE of the convective launch site, behind the convection, and where a transition zone normally develops. The flight track shows the balloon was initially close to convection, but in the transition to stratiform precipitation at all times. This stratiform region failed to develop rearward, probably because the MCS was starting to dissipate or the convective storms were moving rapidly away from the launch site. The sounding is in Fig. 3 and a vertical cross-section radar image in Fig. 4. We infer that five substantial regions of charge were in the cloud.

*ElDorado sounding on back edge of stratiform region, 0842 UTC:* We launched this sounding 55 km NNE of Wellington and in the back part of the stratiform region. The back side was dissipating, presumably from the intrusion of dry air, as the MCS moved rapidly away. There was little rain, and the radar base scan shows about 20 dBZ over the balloon launch site. Above the ground there was a 170-m deep layer of negative charge and a kilometer of positive charge, with the latter probably on the light rain. Such low density charge is often seen in the precipitation beneath stratiform regions. The balloon apparently entered the cloud at about 5 km MSL. The E profile (Fig. 5) indicates only three charge regions in the cloud: a positive between two negatives. As few as three charges have been inferred from E this far back in the stratiform region of other MCSs, but sometimes more charge layers have been observed. Although we do not have many such profiles to compare it with, we obtained a nearly identical profile near the back edge of an MCS in an earlier year. In storm-relative coordinates, the flow above 4.5 km AGL (about 4.9 km MSL) was away from the convective line (e.g., Fig. 6). Below 4.5 km, there was some small amount of flow toward the convective line. Mostly, however, the storm relative flow below 4.5 km was weak and dominated by downward motion, indicative of a decaying stratiform rain region. We are still analyzing data to see if the upper three charges in Wellington1 could have advected to be the three in ElDorado at the back edge of the MCS.

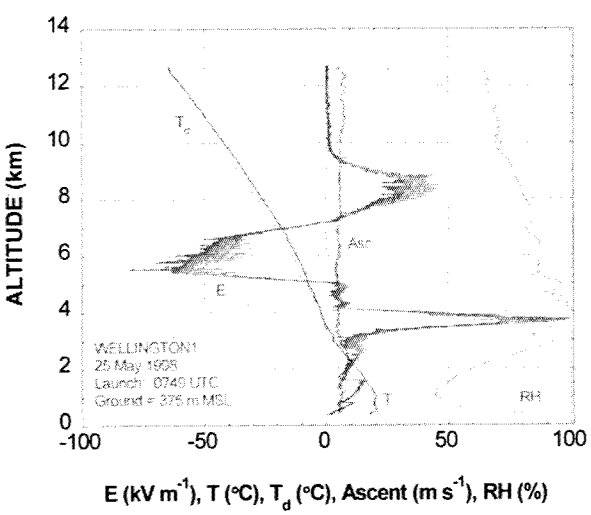


Fig. 3. Sounding in transition zone of bow-echo MCS. Still-air ascent of balloon was about 6 m s$^{-1}$. Symbols are E, electric field; T, temperature; $T_d$, dewpoint temperature; Asc, ascent; RH, relative humidity.

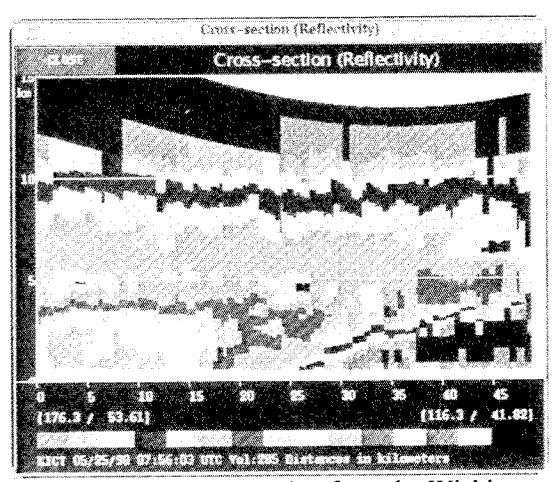


Fig. 4. Vertical cross section from the Wichita, Kansas, WSR-88D showing region of storm along which the balloon (the x at ≈22, 3.6 km) is moving (toward the right) in the transition zone and is at the altitude of the peak E (in Fig. 3) at about 3.6 km.

*Wellington2 sounding on back edge of stratiform region, 0857 UTC:* The back edge of the stratiform was over the Wellington launch site. The radar and tracking data show that this final balloon sounding (not shown) may have been in cloud with about 10 dBZ reflectivity, but this was mostly an out-of-cloud profile. All E were less than 5 kV m$^{-1}$.

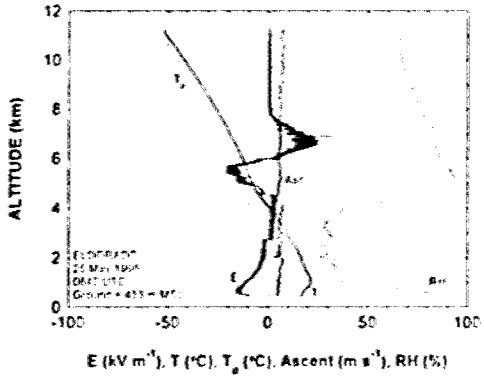


Fig. 5. Sounding in back side of stratiform region of MCS. The launch site was about 55 km from the transition zone site. Still-air ascent of balloon was about 6 m $s^{-1}$. Symbols are E, electric field; T, temperature; $T_d$, dewpoint temperature; Asc, ascent; RH, relative humidity.

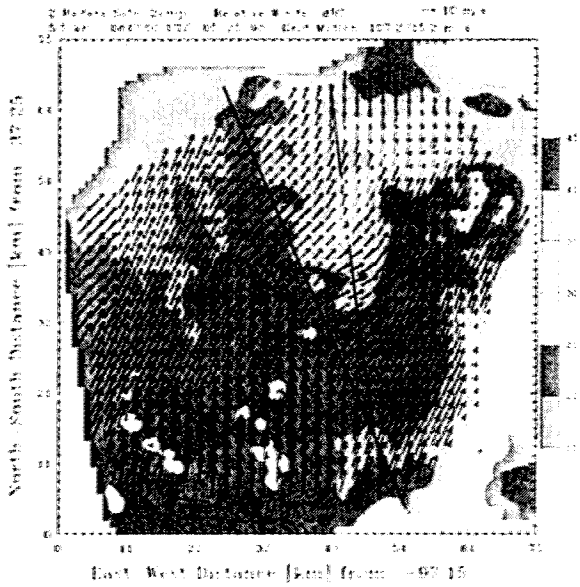

Fig. 6. Wind analysis from P-3 radar for ElDorado.

## CONCLUDING REMARKS

The soundings of electric field and the Doppler radar records constitute the main data base from which we infer characteristics of the MCS. As of this preprint, many analyses are ongoing. Future work will include: refining the placement of the balloon track in the radar reflectivity and flow fields, a more detailed comparison of the E profiles with the conceptual model, determining whether the MCS or parts of it had atypical electrical structure, determining if it is possible to link the convection, transition zone, and stratiform together since the profiles are aligned with the dominate flow, and an overall placement of this rather unusual MCS in the context of MCS electrification in general.

## ACKNOWLEDGMENTS

We thank Bill Beasley, Mike Biggerstaff, Ken Eack, and Dick Orville for their help and Ned Chamberlin for his work on GLASS. We thank balloon crew members: Aaron Bansemer, Lee Coleman, Nick Demetriades, Beth Karl, Tim Lang, Montra Lockwood, Ted Mansell, Heidi Morris, Natalie Murray, Jim O'Brien, Ivy Winger, and Kevin Young. We thank the crew of the P-3 for their critical roles in data collection. We are indebted to Roger Brown and Bim Wood for radar interpretation to help us balloon safely around the severe weather. Leslie Cain and Dennis Nealson maintained the mobile laboratories. This work is supported in part by NSF ATM9807179 and an NSSL Director's grant.

## REFERENCES

Jorgensen, D.P., and B.F. Smull, Mesovortex circulations seen by airborne Doppler radar within a bow-echo mesoscale convective system. *Bull. Amer. Meteor. Soc., 74*, 2146-2157, 1993.

Jorgensen, D. P., T. Matejka, and J. D. DuGranrut, Multi-Beam Techniques for Deriving Wind Fields from Airborne Doppler Radars. *J. Meteor. and Atmos. Physics*, 59, 83-104, 1996.

MacGorman, D.R., and W.D. Rust, The Electrical Nature of Storms. Oxford University Press, New York, 403 pp, 1998.

Marshall, T.C., and W.D. Rust, Two types of vertical electrical structures in stratiform precipitation regions of mesoscale convective systems. *Bulletin Amer. Meteor. Soc., 74*, 2159-2170, 1991.

Stolzenburg, M., T.C. Marshall, W.D. Rust, B.F. Smull, Horizontal distribution of electrical and meteorological conditions across the stratiform region of a mesoscale convective system. *Mon. Weath. Rev., 122*, 1777-1797, 1994.

Stolzenburg, M., W.D. Rust, B.F. Smull, and T.C. Marshall, Electrical structure in thunderstorm convective regions, 1, Mesoscale convective systems. *J. Geophys. Res. Vol. 103*, 14,059-14,078, 1998a.

Stolzenburg, M., W.D. Rust, and T.C. Marshall, Electrical structure in thunderstorm convective regions, 2, Isolated storms. *J. Geophys. Res., 103*, 14,079-96, 1998b.

Stolzenburg, M., W.D. Rust, and T.C. Marshall, Electrical structure in thunderstorm convective regions, 3, Synthesis. *J. Geophys. Res., 103*, 14,097-14,108, 1998c.

# CLOUD-TO-GROUND LIGHTNING CHARACTERISTICS OF A MAJOR TROPICAL CYCLONE TORNADO OUTBREAK

Eugene W. McCaul, Jr.[1], Dennis Buechler[2], and Steven J. Goodman[3]

[1]Universities Space Research Association, Huntsville, Alabama, U.S.A.
[2]University of Alabama in Huntsville, Huntsville, Alabama, U.S.A.
[3]National Aeronautics and Space Administration, Marshall Space Flight Center, Huntsville, Alabama, U.S.A.

## 1. INTRODUCTION

It is well known that most tropical cyclones (TCs) that make landfall along the Gulf coast of the United States spawn at least a few tornadoes (McCaul 1991). Although most landfalling TCs generate fewer than a dozen such tornadoes, a small proportion produce large swarm outbreaks, with as many as 25 or more tornadoes. Usually, these major outbreaks occur in large, intense hurricane-strength TCs (Novlan and Gray 1974; McCaul 1991), but on 15-17 August 1994 Tropical Storm Beryl spun off 37 tornadoes along its path from the Florida panhandle through the mid-Atlantic states. Some 32 of these tornadoes occurred on 16 August 1994 from eastern Georgia to southern Virginia, with most of these taking place in South Carolina. Beryl's 37 tornadoes moved it into what was at that time fifth place historically in terms of TC tornado productivity (Vescio *et al.* 1996).

The Beryl outbreak is especially noteworthy in that at least three of the tornadoes achieved peak intensity of F3 on the Fujita damage intensity scale. Although no fatalities resulted from the Beryl outbreak, at least 50 persons suffered injuries, and property damages totalled more than $50 million (Vescio *et al.* 1996). The Beryl outbreak is a good example of a TC whose greatest danger to the public is its post-landfall severe weather. In this respect, and in the character of its swarm outbreak of tornadoes, it resembles another large tornado outbreak spawned by a relatively weak TC, Hurricane Danny of 1985 (McCaul 1987). In the Danny outbreak, numerous shallow mini-supercell storms were found to have occurred, and it was noted that, because of the storms' relatively shallow depth, cloud-to-ground (CG) lightning was negligible. Better observations of future TC tornado outbreaks, especially with modern surveillance tools such as Doppler radars and the National Lightning Detection Network (NLDN), were recommended.

Although the Beryl tornado outbreak is not the first set of TC-spawned tornadic storms to be observed with the NLDN, it is one of the largest and likely the most intense such outbreak. The purpose of this paper is to document the NLDN-derived CG lightning characteristics of Beryl's tornadic storms, and to see how they compare with observations of CG lightning activity in other types of severe storms. In particular, we attempt to quantify the CG flash rates of TC tornadic cells, and to discover if there are any characteristics of their CG activity that may be useful to operational forecasters seeking to distinguish which cells are most likely to produce severe weather.

## 2. DATA ANALYSIS

Two principal types of data were analyzed in this study. The tornadic storms themselves were identified and characterized using regional radar mosaic imagery and single Doppler radar data from Columbia, South Carolina. The CG lightning activity of the storms so identified, as well as of the entire system of Beryl's remnants, was then studied using NLDN data.

To determine which storm cells were responsible for the tornadoes, we inspected the time series of regional 15-min radar reflectivity mosaic images from 1200 UTC 16 August to 0300 UTC 17 August 1994, and located tornadoes reported in Storm Data for August 1994 within these radar images. In general, it was possible to identify readily which echoes were responsible for the tornadoes. Using this method, we identified 12 separate tornadic cells that produced 29 tornadoes within the region of interest. We also documented the approximate times of cell genesis and lysis, and characteristic cell motion vectors for each cell, along with the numbers of tornadoes, the onset and demise of each cell's tornadic activity, and the maximum damage intensity of the tornadoes on the Fujita scale.

Once all the tornadic cells were identified and catalogued, we proceeded to study individual cell characteristics using available Doppler radar and NLDN data. The WSR-88D Doppler at Columbia (KCAE), was convenient for the purpose of radar documentation of the storms. KCAE was located close to the center of Beryl's tornado activity, with many of the tornadic storms passing within 30 km of the radar, and at least one tornado sighted visually from the collocated NWS office. A relatively complete archive of level 3

graphical radar data was obtained from KCAE.

According to our analyses, three of the strongest tornadic cells, storms 2, 3 and 4 (see Table 1), passed within 30 km of KCAE, and produced tornadoes for many hours. KCAE was able to observe these cells while they were producing tornadoes at ranges as small as 10 km and as great as 150 km from KCAE. We performed complete radar time-height and NLDN time series analyses of them for the period 1500 UTC to 2148 UTC, the latter time corresponding to the time the last cell exited the unambiguous velocity range of KCAE, approximately 148 km north of the radar. Radar parameters documented in this analysis include storm-relative mesocyclone rotational velocity $V_R$, rotational shear vorticity $\zeta$, mesocyclone core diameter $\phi$ (measured across the couplet of strongest inbound and outbound velocities), as well as range, elevation angle and altitude. Time series of WSR-88D estimated echo top heights $z_T$ and vertically integrated liquid $VIL$ were also recorded for each cell.

In the NLDN part of the study, we identified CG flashes as a function of time for each tornadic cell, using moving spatial windows whose size was designed to contain only the flashes from single cells, with minimal loss of peripheral flashes and minimal contamination by flashes from nearby cells. Separate counts were maintained for both negative and positive polarity CG flashes. All counts were tabulated as a function of time at intervals corresponding to the radar volume scan times, usually separated by 6 min intervals. These time intervals are roughly comparable to those used in other published studies of NLDN storm analyses, where 5 min sampling times are customary.

## 3. RESULTS AND DISCUSSION

The lightning histories of the 12 identified tornadic cells are summarized, along with the other echo-related parameters, in Table 1. For each cell, the lightning data includes the times of first and last CG lightning flashes and total numbers of flashes of positive and negative polarity.

Inspection of Table 1 shows that six of the 12 cells were multiple tornado producers. Storms 2, 3 and 4 accounted for 15 of the 29 tornadoes studied in this paper, with storm 4 spawning eight of these. Storms 3 and 4 both produced F3 intensity tornadoes. Although storm 2 produced four tornadoes, the strongest being F2 in intensity, it was tornadic for the longest time interval, more than 6.5 h. In fact, storm 2 was identifiable on radar for a remarkable 11 h, although it was not particularly strong during the first 3 h. These cell longevity statistics resemble those of the most intense midlatitude supercell outbreaks (see e.g., Knupp *et al.* 1996), and differ radically from those usually attributed to TC convective cells over the ocean, where cell lifetimes are seldom longer than about 35 min (Parrish *et al.*, 1984).

Storm 3 was the most active CG producer, generating 310 total flashes during a 5.5 h period. Three of the tornadic cells, all single tornado producers, generated no CG lightning at all. The flash rate for storm 3 can be characterized as moderate, averaging only about one flash per minute, but for the other cells, flash rates were weaker, even for the strong supercell storms 2 and 4.

Almost all the CGs from Beryl's tornadic cells were negative in polarity; only 24 of 788 total flashes from those cells were positive. Despite their modest flash rates, the tornadic cells were by far the most electrically active storms within Beryl's remnants. During the period of time considered here, only 337 of 1125 total CG flashes in all of Beryl's remnants in Georgia and the Carolinas occurred in non-tornadic storms. Thus, at least for this particular TC, the occurrence of noticeable lightning activity tended to suggest that a storm cell had tornadic potential.

We selected storms 2, 3 and 4 for detailed radar and NLDN analysis. Time-height analyses of radar- and NLDN-derived storm parameters were constructed and will be shown at the conference, for these storms. Parameters plotted in these analyses include the contoured field of mesocyclone vorticity $\zeta$ estimated from twice the radar-observed rotational shear, along with the time series of $VIL$ and total CG flashes per radar volume scan. Also included are the times and F-scale intensity ratings of the tornadoes produced by each storm.

For each storm, typical $VIL$ values were less than 45 kg m$^{-2}$, although storm 2 produced a brief peak of 55 kg m$^{-2}$. In several instances, tornadoes are reported even while $VIL$ values are less than 20 kg m$^{-2}$, especially when the storms are at ranges greater than about 80 km from KCAE. Echo top heights (not shown) are usually 11 km or less, although occasional brief pulses to 13-14 km are noted with each storm. The typical $VIL$ and echo top heights found in storms 2-4 are smaller than the typical values found in Great Plains supercells, but are consistent with those found in miniature supercells. The analyses show that each of the storms exhibited pulsing variations in rotation, VIL and other storm intensity parameters.

In each of these three storms, variations in CG lightning rate appeared to correlate well with $VIL$ changes. At longer ranges from the radar, however, the $VIL$ data tended to show a decreasing trend. Nevertheless, the $VIL$ of storm 2 displays an increase after about 2110 UTC, but it does not reach values seen during 1715-1825 UTC. In contrast, the CG rates reach their maxima in this storm after 2110 UTC. This suggests that the tendency for $VIL$ to decrease with range may be a result of the radar's undersampling of the mini-supercell storm volume, especially at low levels, as the storms recede from the radar. These undersampling problems become particularly noticeable when the mini-supercells move beyond approximately 100 km range from the radar. On the other hand, the NLDN data appear to be relatively free of such location bias, and may thus be very useful in monitoring the severity of storms moving from one radar surveillance zone to another.

In general, it is found that even the strong TC-spawned mini-supercells were characterized by low to moderate CG flash rates. The CG rates tend to be highest when the storms are at their strongest overall. However, there are instances where CG rates declined during tornado events. The first F3 tornado from storm 4, for example, is accompanied by a drop in CG rates to near zero at 1750 UTC. At the same time, this storm's $VIL$ actually increases slightly. In Great Plains tornadic supercells, negative relationships between CG lightning flash rate and tornadoes have also been observed (see e.g., MacGorman *et al.*, 1989; MacGorman 1993). Perez *et al.* (1997) have noted that increases in CG rates prior to tornadogenesis may be the result of pulses of updraft that act to enhance vortex stretching at low levels.

## CELLS, TORNADOES, AND LIGHTNING
## T. S. BERYL OUTBREAK, 16 AUG 94

| ECHO HISTORY[1] | | | | | TORNADOES[2] | | | | CG LIGHTNING[3] | | | |
|---|---|---|---|---|---|---|---|---|---|---|---|---|
| ID | 1ST TORNADO | MVT[4] | BEG[5] | END[5] | NUM | MAX | BEG[5] | END[5] | NEG | POS | BEG[5] | END[5] |
| 1 | Govan SC | 174@15 | 1330 | 1730 | 2 | F-2 | 1509 | 1702 | 53 | 1 | 1502 | 1711 |
| 2 | McEntire SC | 177@09 | 1345 | 0045 | 4 | F-2 | 1730 | 0002 | 157 | 5 | 1734 | 0001 |
| 3 | Columbia SC | 160@13 | 1445 | 2330 | 3 | F-3 | 1753 | 2122 | 304 | 6 | 1545 | 2114 |
| 4 | Neeses SC | 170@11 | 1445 | 2100 | 8 | F-3 | 1620 | 2100 | 130 | 3 | 1612 | 2002 |
| 5 | Hartwell GA | 147@13 | 1530 | 1830 | 1 | F-1 | 1739 | 1739 | 0 | 0 | --- | --- |
| 6 | York SC | 163@12 | 1715 | 2330 | 3 | F-2 | 2150 | 2245 | 75 | 1 | 1811 | 2130 |
| 7 | Lexington GA | 134@17 | 1715 | 1845 | 1 | F-2 | 1815 | 1815 | 0 | 0 | --- | --- |
| 8 | Ware Shoals SC | 140@19 | 1815 | 2030 | 1 | F-0 | 1940 | 1940 | 1 | 1 | 1929 | 1929 |
| 9 | Winnsboro SC | 156@12 | 1845 | 0000 | 3 | F-2 | 2144 | 2320 | 33 | 4 | 1932 | 2244 |
| 10[6] | Cowpens SC | 160@20 | 2145 | 2215 | 1 | F-1 | 2156 | 2202 | 0 | 0 | --- | --- |
| 11 | Hickory NC | 162@15 | 2300 | 0100 | 1 | F-2 | 2236 | 2245 | 2 | 0 | 2323 | 2329 |
| 12 | Lomax NC | 158@08 | 2200 | 0100 | 1 | F-0 | 0015 | 0015 | 11 | 3 | 2358 | 0113 |

Note 1: Source: NOWRAD mosaics 1200-0300 UTC 16-17 August 1994
Note 2: Source: Storm Data, August 1994
Note 3: Source: National Lightning Detection Network
Note 4: Cell motions (m/s) are 1 h means during mature phase of storm
Note 5: All times UTC are on 16 August or 17 August 1994
Note 6: Cell identification and radar history poorly defined

TABLE 1: Tabulation of echo histories, tornado histories, and CG lightning histories for 12 tornadic storms in Tropical Storm Beryl on 16 August 1994.

Another potentially important mechanism that could lead to suppression of CG rates during tornadoes is the so-called vortex-valve effect, which mandates a weakening of updraft aloft when vorticity maximizes at the surface. If this effect is important, then it suggests the possibility of constructing CG-based diagnostic parameters that might be useful in identifying storms that are undergoing tornadogenesis. Exclusive use of CG rates to identify imminent tornadogenesis does not appear promising, however, because decreases in CG activity may result from many processes, and may simply indicate storm dissipation.

An important aspect of the Beryl storms for which we have no data is intracloud (IC) lightning activity. Spratt *et al.* (1998) and Williams *et al.* (1998) have found that some storms exhibit increased IC lightning rates at times of greatest updraft strength, and that this characteristic may be a more reliable indicator of changes in storm severity than are CG rates. Further documentation of the IC lightning activity in TC mini-supercell tornado outbreaks and similar events is desirable.

## 4. SUMMARY AND OUTLOOK

NLDN CG lightning activity has been examined in detail here for the first time in a major TC tornado-swarm event. CG rates for most of the mini-supercell tornadic storms were weak to moderate, usually less than 1 flash per minute, with some of the short-lived tornadic cells showing no CG activity at all. In general, CG flash rates tended to indicate overall storm severity, but in some of the supercells there were brief decreases in CG activity during tornadoes, similar to what has been reported in some Great Plains tornadic storms. Almost all the CG activity was of negative polarity.

Because the NLDN data give indications of fluctuations in storm intensity that are relatively reliable regardless of storm location, they are especially useful in monitoring the evolving severity of mini-supercells, whose radar signatures typically degrade rapidly with range from radar sites. Because the tornadic supercells tended to have long cell lifetimes, the full spans of which could not be examined in detail in some cases by any one radar, we recommend that forecast and warnings meteorologists pay special attention to any persistent echo, especially when either (a) Doppler radar indicates the echo contains a mesocyclone that is intensifying, or (b) NLDN indicates increasing CG activity in the echo, if it is distant from radars. We also recommend deployment of proposed spaceborne geostationary total lightning detection sensors, which will permit thorough study and monitoring of many additional TC severe weather outbreaks.

## 5. REFERENCES


Knupp, K., R. L. Clymer, E. McCaul, and K. Pence, 1996: Structure and evolution of the 1994 Palm Sunday tornadic storms and their near mesoscale environment. *Preprints*, 18th Conf. Severe Local Storms, San Francisco, Amer. Meteor. Soc., 42-46.

MacGorman, D. R., D. W. Burgess, V. Mazur, W. D. Rust, W. L. Taylor, and B. C. Johnson, 1989: Lightning rates relative to tornadic storm evolution on 22 May 1981. *J. Atmos. Sci.*, **46**, 221-250.

MacGorman, D. R., 1993: Lightning in tornadic storms: A review. *The Tornado: Its Structure, Dynamics, Prediction, and Hazards*, C. R. Church, Ed., Amer. Geophys. Union Press, 173-182.

McCaul, E. W., Jr., 1987: Observations of the Hurricane "Danny" tornado outbreak of 16 August 1985. *Mon. Wea. Rev.*, **115**, 1206-1223.

McCaul, E. W., Jr., 1991: Buoyancy and shear characteristics of hurricane tornado environments. *Mon. Wea. Rev.*, **119**, 1954-1978.

Novlan, D. J., and W. M. Gray, 1974: Hurricane-spawned tornadoes. *Mon. Wea. Rev.*, **102**, 476-488.

Parrish, J. R., R. W. Burpee, F. D. Marks, Jr., and C. W. Landsea, 1984: Mesoscale- and convective-scale characteristics of Hurricane Frederic during landfall. *Preprints*, 15th Conf. Hurr. and Trop. Meteor., Miami, Amer. Meteor. Soc., 415-420.

Perez, A. H., L. J. Wicker, and R. E. Orville, 1997: Characteristics of cloud-to-ground lightning associated with violent tornadoes. *Wea. Forecasting*, **12**, 428-437.

Spratt, S. M., D. W. Sharp, S. J. Hodanish, 1998: Observed relationships between total lightning information and Doppler radar data during two recent tropical cyclone tornado events in Florida. *Preprints*, 19th Conf. Severe Local Storms, Minneapolis, Amer. Meteor. Soc., 659-662.

Vescio, M. D., S. J. Weiss, and F. P. Ostby, 1996: Tornadoes associated with Tropical Storm Beryl. *Nat. Wea. Digest*, **21**, 2-10.

Williams, E., B. Boldi, A. Matlin, M. Weber, S. Hodanish, D. Sharp, S. Goodman, R. Raghavan, and D. Buechler, 1998: The behavior of total lightning activity in severe Florida thunderstorms. submitted to *Atmos. Res.*

# TOTAL LIGHTNING ACTIVITY ASSOCIATED WITH TORNADIC STORMS

Steven J. Goodman[1], Dennis Buechler[2], Stephen Hodanish[3], David Sharp[3], Earle Williams[4], Bob Boldi[4], Anne Matlin[4] and Mark Weber[4]

[1]NASA Marshall Space Flight Center
[2]The University of Alabama in Huntsville
[3]National Weather Service, Melbourne, FL
[4]MIT Lincoln Laboratory, Lexington, MA

ABSTRACT: Severe storms often have high flash rates (in excess of one flash per second) and are dominated by intracloud lightning activity. In addition to the extraordinary flash rates, there is a second distinguishing lightning characteristic of severe storms that seems to be important. When the total lightning history is examined, one finds sudden increases in the lightning rate, which we refer to as lightning "jumps," that precede the occurrence of severe weather by ten or more minutes. These jumps are typically 30–60 flashes/min$^2$, and are easily identified as anomalously large derivatives in the flash rate. This relationship is associated with updraft intensification and updraft strength is an important factor in storm severity (through the accumulation of condensate aloft and the stretching of vorticity). In several cases, evidence for diminishment of midlevel rotation and the descent of angular momentum from aloft is present prior to the appearance of the surface tornado. Based on our experience with severe and tornadic storms in Central Florida, we believe the total lightning may augment the more traditional use of NEXRAD radars and storm spotters. However, a more rigorous relation of these jumps to storm kinematics is needed if we are to apply total lightning in a decision tree that leads to improved warning lead times and decreased false alarm rates.

## INTRODUCTION

Use of total lightning for severe storm identification and warning has been operationally tested during several severe weather episodes at the Melbourne, FL (MLB) National Weather Service Office. The most realistic approach has been to use the data to assess the character of a storm's updraft intensity as an additional proxy-quantity of parameters. The updraft maximum aloft systematically precedes manifestations of severe and hazardous weather at the surface by 5–20 minutes. This becomes more important for storms poorly-sampled by radar, either spatially or temporally, or storms that are marginally severe or tornadic. This is true for the existence, magnitude, trend, and density of lightning with each proving to be more valuable than the corresponding cloud-to-ground (CG) signal in most cases. Importantly, application is made according to the appropriate peninsular Florida tornado regime and different signals become more significant (of more weight) for assessing updraft character and subsequent tornado potential. Therefore, when blending data from a variety of sensors according to a given tornado environment, total lightning data is uniquely applied. Attempts are now being made to develop a (rule-based) decision tree for tornado warning issuance in east central Florida which would incorporate total lightning along with indicators from other sensors (mainly radar). Total lightning signatures are additions to a series of "weighting factors" that can tip the scales of confidence for the warning meteorologist.

## DATA AND METHODOLOGY

Our on-going (since 1997) observations in Central Florida are acquired using the Lightning Imaging Sensor Data Application Display (LISDAD), a system jointly conceived and

developed by MIT/Lincoln Laboratories, NWS forecasters at the Melbourne, FL WSO, and NASA MSFC scientists (Weber et al., 1998). LISDAD ingests full tilt volume scans from the Melbourne NEXRAD, the total lightning activity from the KSC Lightning Detection and Ranging (LDAR) system; and the ground strikes detected by the National Lightning Detection Network (NLDN).

The LDAR is a unique system that maps the 3-D VHF radiation produced by all lightning, thus allowing us to compute the total flash rate (from LDAR) and the CG fraction (from NLDN) as a function of the storm life-cycle. LDAR flash rates are computed by associating the individual VHF sources in time and space to produce discrete lightning flashes. The individual lightning flashes are then clustered in time and space to individual storm cells. The storm cells are identified and tracked automatically using the National Severe Storms Laboratory Storm Cell Identification and Tracking (SCIT) algorithm. From these data we generate time series of radar characteristics (maximum reflectivity, vertical integrated liquid water (VIL), radial shear, radar cloud top height, etc.) and lightning activity (jump rate, peak rate, total flash rate vs. ground strike only flash rate, updated minute by minute). We then relate the storm attributes to reports of severe weather. The entire storm history for each cell can be displayed in a pop-up box (in real time or in playback mode after the fact).

## RESULTS

Of the observed tornadic storms (during events which produced at least one known F2+ tornado to include the 22-23 February 1998 East Central Florida Tornado Outbreak), most were noted to achieve a flash rate of at least 120 fpm prior to the tornado (Figure 1). These storms tended to be the most electrically active storms in the area during their intense mesocyclone phase. Many, in fact, exceeded this lower threshold with some attaining flash rates in excess of 500 fpm and were in stark contrast to other surrounding non-tornadic storms. It could be argued that with the dominance of intracloud lightning activity, the ratio of intracloud to CG lightning could be higher for these tornadic storms. In general, the higher the total flash rate, the more vigorous the updraft and greater the potential for tornado. Storms with flash rates of at least 120 fpm would automatically be placed in the suspect category and would be further examined for radar clues and changes in flash rate trends.

Of more operational importance is the occurrence of a so called lightning "jump". For previous pulse-severe storm studies, a jump was defined as "an increase in total lightning over a time period of at least 2 minutes, in which the total flash rate increases at least 50 flashes during the entire lightning jump period". Continuous flash rate information can be a very useful complement to radar. This is especially true for fast moving developing storms which have tornadic potential which are moving through small counties. The rate of radar data refresh is no better than 5-minutes and trends in the lightning flash rate can help fill the anxious void. With further dramatic increases in flash rate, the warning meteorologist could come to decision before waiting for the next "deciding scan" and thus add several minutes to lead time. This is considered to be an important factor.

Several observations have been made of tornadic storms with more dramatic ramp-ups in lightning activity. Storms which experience rate increases of more than 100 fpm over a 10 minute period or those which continually trend upward to 120-150 fpm prior to tornado stand out as significant. Although little is really known about the relative values due to the size of the sample data set, general conclusions regarding the observance of a significant jump-up in flash rate points to a greater likelihood of tornadic development through the deepening and

strengthening of the parent mesocyclone circulation. The larger the increase, the greater the chances. It is interesting that during the February 23 outbreak, some storms continued to experience a flash rate increase even during tornado. It is surmised that perhaps this was associated with cyclic mesocyclones. That is, the current tornado-producing mesocyclone suffers from the occlusion process while a new updraft forms south of the original. The lightning rate associated with the updraft vigor of the developing mesocyclone is combined with the lightning rate of the original storm until such time that they can be separately distinguished.

Another potentially promising signal relates to a noteworthy decrease in total flash rate just prior to or during tornado. In some cases, this may be related to the collapse of the bounded weak echo region which already has a correlation to tornado occurrence. For storms associated with moderate to strong mesocyclones, already having experienced a minimal flash rate threshold of at least 120 fpm and also experienced a discernible lightning jump, if a distinct decrease becomes evident (especially if in the vicinity of 100 fpm or more), then the confidence of the warning meteorologist would likely improve as angular momentum aloft is perceived to be lowered towards the surface. This was noted with several of the tornadic storms, but not all of them. Some storms achieved tornado without experiencing this decrease or perhaps the signal was masked by other contributing factors. However, these storms were still marked by the relative high flash rates and lightning jump. In fact, there may be some merit in realizing the length of time a storm is able to maintain an excessive flash rate (for example a rate of 200 fpm or more) and its tornadic potential.

## CONCLUSIONS

Our initial time-height observations of tornadic storms in Central Florida show dramatic increases in lightning activity in association with the rapid vertical growth of the storm updraft. This lightning activity is extraordinarily high, and is overwhelmingly dominated by intracloud flashes. Based on our limited sample, the sudden lightning jumps nearly always precede the descent of the mesocyclone circulation. However, exceptions to this rule have been found and the characteristics of these storms are being analyzed at this time.

## REFERENCES

Weber, M. E., E. R. Williams, M. M. Wolfson, and S. J. Goodman, 1998. An Assessment of the Operational Utility of a GOES Lightning Mapping Sensor. MIT/Lincoln Laboratory Project Report NOAA-18, 13 February, 1998, 108 pp.

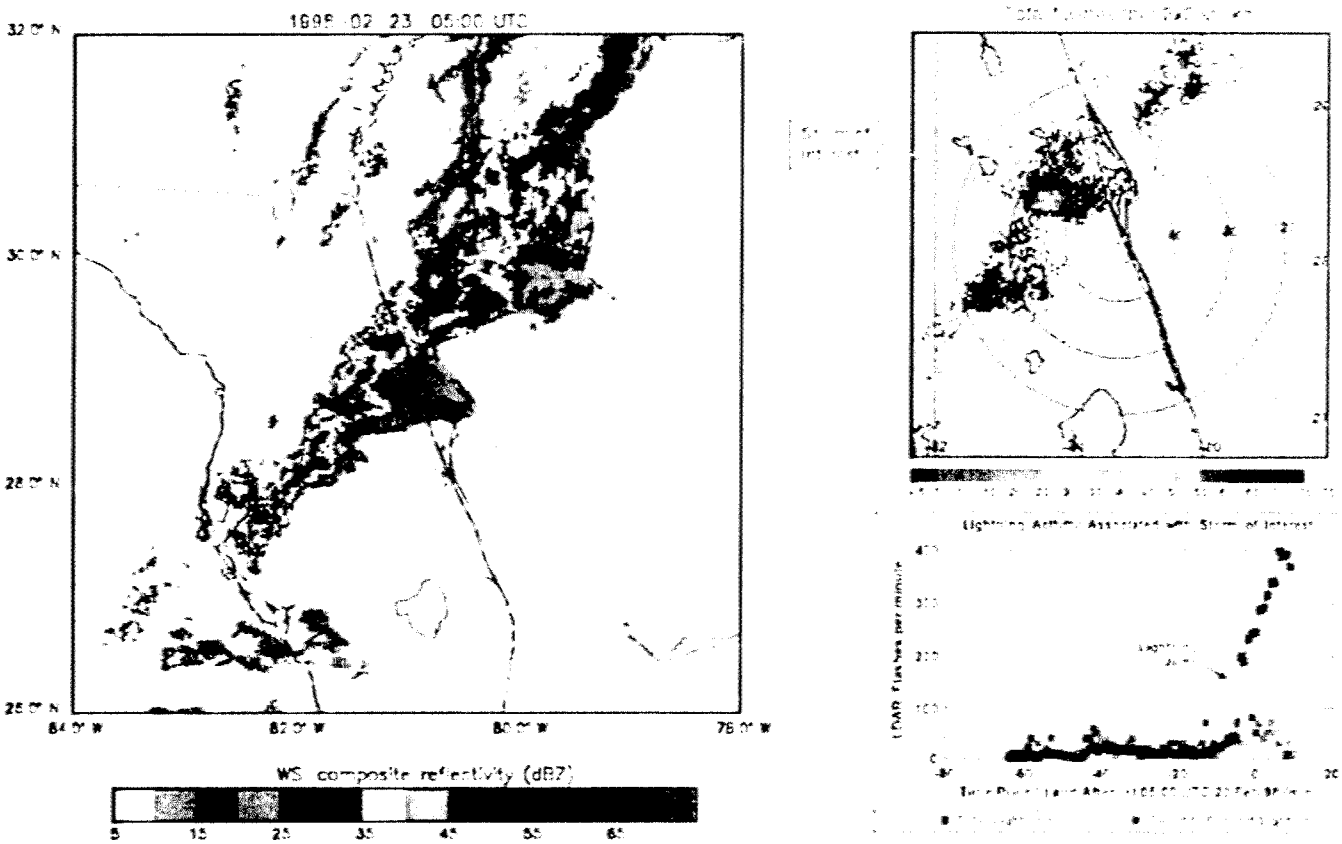


Figure 1. February 23, 1998 Central Florida tornado outbreak storms at 0500 UTC. Composite reflectivity in 5 dBZ steps (left); LDAR flash density (per 2 km x 2 km grid) over 5-min period (upper right); and time series of LDAR and cloud-to-ground lightning flash rates per min prior to the tornado (lower right).

# The 1997-98 El Nino Event and Related Lightning Variations in the Southeastern United States

D. E. Buechler[1], S. J. Goodman[2], E. W. McCaul[3], and K. Knupp[1]

[1]University of Alabama in Huntsville
[2]NASA Marshall Space Flight Center, Huntsville, Alabama
[3]Universities Space Research Association

ABSTRACT: The El Nino Southern Oscillation (ENSO) is a climate anomaly responsible for world-wide weather impacts ranging from droughts to floods. In the United States, warm episode years are known to produce above normal rainfall along the Southeast US Gulf Coast and into the Gulf of Mexico, with the greatest response observed in the October-March period of the current warm-episode year. The 1997-98 warm episode, notable for being the strongest event since 1982-83, presents our first opportunity to examine the response to a *major* ENSO event and determine the variation of wintertime thunderstorm activity in this part of the world. Due to the recent launch of a lightning sensor on NASA's Tropical Rainfall Measuring Mission (TRMM) in November 1997 and the expanded coverage of the National Lightning Detection Network (NLDN), we are able to examine such year-to-year changes in lightning activity with far greater detail than ever before.

## INTRODUCTION

Within the United States and adjacent coastal waters, the greatest number of thunderstorm days in the winter months (December-February) occurs along the Southeast Gulf Coast from East Texas to the Florida Panhandle and over the warm waters of the Gulf Stream. In a typical winter there will be approximately 5-10 thunderstorm days (WMO, 1953), which represents 8-16 percent of the 60 or more annual thunderstorm days that occur in the most active regions of the southeast U.S. Synoptic-scale frontal passages and Gulf coast cyclogenesis interact with the atmosphere/land-ocean temperature contrasts to produce the unstable air mass (and vertical motion forcing) favorable for the development of thunderstorms. The only other region in the entire Northern Hemisphere with similar environmental conditions and winter thunderstorm day frequency is the central Mediterranean.

## DATA AND METHODOLOGY

There are two primary lightning data sets employed in this study. A 10-year data base of U.S. cloud-to-ground lightning activity from the National Lightning Detection Network provides information on flash location and polarity within the CONUS and nearby oceans (Cummins et al., 1998). Modifications have been made to the individual NLDN sensors, their locations, and the overall network configuration over the past 10 years. While the impacts (e.g., detection efficiency, accuracy) of these changes are still being carefully examined by our group and others, the total cloud-to-ground lightning frequency in the Southeast U.S. and extending approximately 400 km into the Gulf of Mexico can be considered consistent and unbiased for the purpose of inter-annual comparisons since 1996. However, some statistics such as thunderstorm day frequency and thunderstorm hours are relatively unaffected by the modifications of the network design and can be reliably determined over the 10-year period of record.

The second lightning data set is the total lightning activity observed from space by the NASA Lightning Imaging Sensor (LIS). LIS was launched in November 1997 aboard the Tropical Rainfall Measuring Mission (TRMM) into a 35 degree inclination orbit. The LIS offers a global, low-latitude perspective on lightning activity during the ENSO winter, as well as an independent estimate of lightning activity 3-4 times per day within the Gulf of Mexico basin. Due to TRMM's precessing orbit, the entire diurnal cycle is sampled during the three-month winter season.

The lightning data and derived attributes are binned into 0.5 degree and 2.5 degree grids over the 3-month December-February periods for analysis. The lightning characteristics are then compared with rainfall estimates derived from other instruments on TRMM and from the Defense Meteorological Satellite Program (DMSP) Special Sensor Microwave/Imager (SSM/I), synoptic reanalysis from the National Centers for Environmental Prediction (NCEP), and National Weather Service 1200 UTC daily weather maps.

RESULTS

Figure 1 shows a comparison of the 1997-98 seasonal lightning observed by the LIS and rainfall derived from the SSM/I. Globally, enhanced rainfall and lightning are associated with continental storm systems in the Gulf of Mexico, Western Atlantic Gulf Stream, SE Brazil, Central Africa, and Northern Australia. In most of these regions there is at least a 100 mm monthly increase in rainfall compared to the 30-year average. In the eastern Pacific Ocean there is heavy rainfall (more than 300 mm above average), but a distinct lack of lightning. We believe the absence of lightning there is attributable to the weaker vertical motions and shallower depth of the mixed phase precipitation within oceanic storms. The structure of these storms are being examined in more detail using the TRMM Precipitation Radar (PR) and Microwave Imager (TMI), and are being addressed in another paper (Driscoll et al., this conference).

We can provide a regional focus on the enhancement of 1997-98 storminess by examining the variation of lightning activity in the Southeast US as determined from the NLDN. The difference in lightning activity between winter 1997-98 and winter 1996-97 alone is significant (Fig. 2). The broad region in the Gulf with an increase of more than 1500 flashes year-to-year represents an increase that is 2.5 standard deviations from the 10-year mean (to be shown at the conference). In other words, there is a statistically significant increase of lightning frequency in the Gulf in the winter of 1997-98. There is nearly a 300% increase in lightning days year-to-year (35 days in 1997-98 vs. 10-13 days in 1996-97) and a 300% increase in lightning hours (150 hours vs. 50).

In the Gulf of Mexico, the upper level (200 mb) jet anomaly during the 1997-98 ENSO is 16 m/s, nearly 30 percent stronger than the 12 m/s anomaly associated with the 1982-83 ENSO. The strong jet was responsible for increased coastal cyclogenesis, rainfall, and severe weather. From the 1200 UTC NOAA Daily Weather Map we determined the number of cyclones, cyclogenesis events, and frontal passages within the Gulf of Mexico region (Figure 3). We find a good correlation between warm ENSO events (86-87, 90-91, 94-95, and 97-98) and cyclogenesis within the Gulf of Mexico Basin. There were 20 winter cyclones (and frontal passages) identified within the Gulf during the December 1997-February 1998 period, which is the greatest number of such systems observed since 1987. On February 22, 1998 a major nocturnal tornado outbreak killed 41 people in Central Florida, the greatest number of fatalities in one day there since February 1983, when the ENSO driven upper level jet anomaly was stronger than normal.

## CONCLUSIONS

The increased southeastern U.S. thunderstorm activity in 1997-1998 is directly attributable to the long lived convective systems which are supported by the stronger synoptic-scale forcing associated with the stronger than normal upper level jet stream. Over land the picture is less clear where we note that not every ENSO has the same regional impact. The preferred location of the fronts, jet stream and other mean meteorological features in any given ENSO event will have a strong influence on the resulting location, duration, and frequency of storms. A simple statement that an El Nino (La Nina) will occur does not encapsulate these features. TRMM will allow us to extend this initial regional ENSO analysis to other parts of the world, using both satellite and NCEP data bases.

## REFERENCES


Cummins, K. L., M. J. Murphy, E. A. Bardo, W. L. Hiscox, R. B. Pyle, and A. E. Pifer, A combined TOA/MDF technology upgrade of the U.S. National Lightning Detection Network, J. Geophys. Res., 103, 9035-9044, 1998.

WMO (World Meteorological Organization), World Distribution of Thunderstorm Days, WMO No. 21, TP.6 and supplement, Geneva, 1953.


El Nino Winter December 1997-February 1998

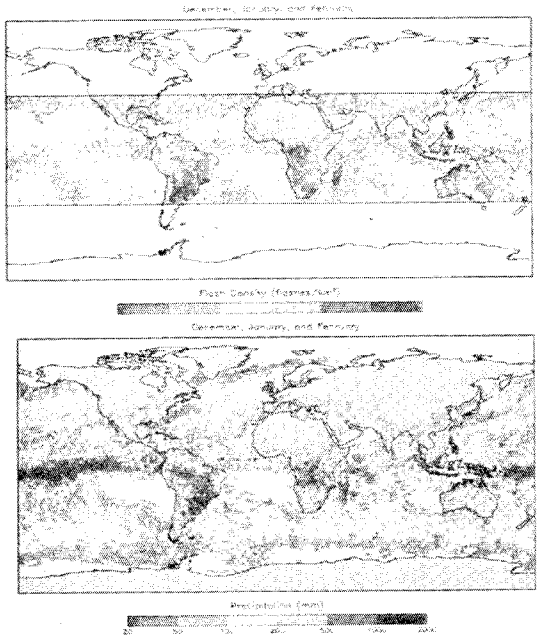

Fig. 1. Seasonal distribution of lightning and rainfall during 1997-98 ENSO winter period December 1997-February 1998 derived from observations made by the NASA Lightning Imaging Sensor (LIS), top; and the DMSP Special Sensor Microwave/Imager (SSM/I), bottom.

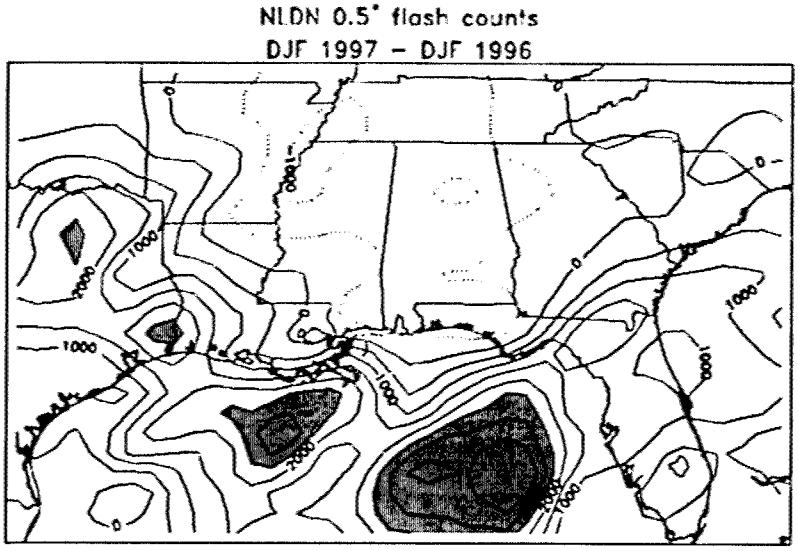


Fig. 2. Year-to-year difference (DJF 97-98 minus DJF 96-97) in wintertime cloud-to-ground lightning frequency. Positive anomalies (shaded) in increments of 500 flashes; positive differences greater than 2000 flashes in darker shading. Negative anomalies are dashed.

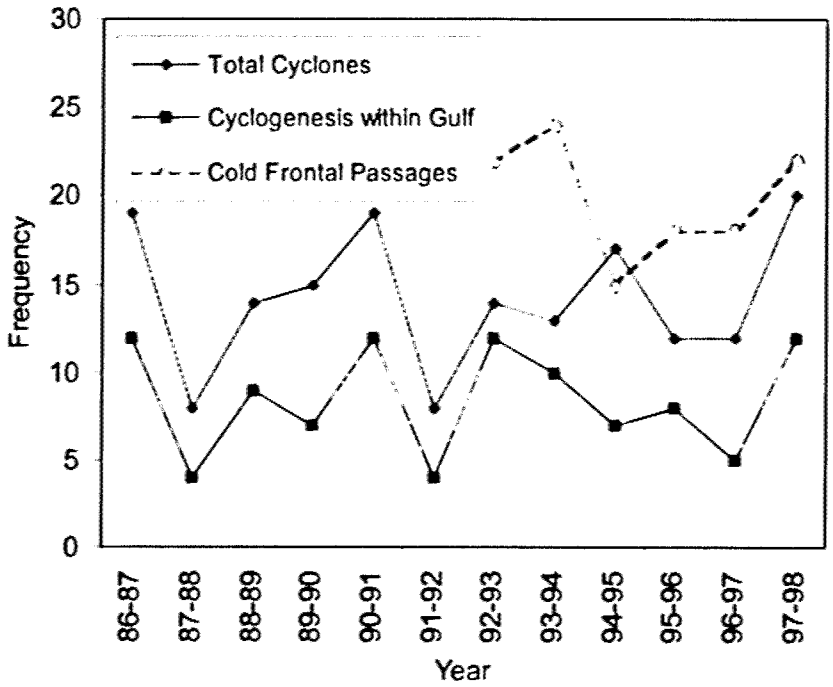


Figure 3. Synoptic scale cyclones and fronts during DJF 1997-98 in Gulf of Mexico Basin.

# A COMPARISON BETWEEN LIGHTNING ACTIVITY AND PASSIVE MICROWAVE MEASUREMENTS

Kevin Driscoll

Global Hydrology and Climate Center, Huntsville, Alabama

ABSTRACT: For more than a decade, space-based passive microwave radiometers have been used to infer a variety of climatological information, including precipitation, cloud water content, and cloud ice content. The microwave frequencies at 37 and 85 GHz are particularly useful in identifying storm systems with high ice content, due to the properties of ice which cause the scattering of upwelling radiation from the surface of the Earth. An examination of data from the Lightning Imaging Sensor and the TRMM Microwave Imager suggests that storms with the highest frequency of total lightning also possess the most pronounced microwave scattering signatures at 37 and 85 GHz. A total of 292 individual thunderstorms were examined, and a log-linear relationship was shown to exist between the number of optical lightning pulses produced by each storm and the corresponding microwave brightness temperatures. This relationship is consistent throughout the seasons in a variety of regimes, suggesting that there is a global dependence between lightning activity and cloud ice content.

## BACKGROUND

The Tropical Rainfall Measuring Mission (TRMM) is an ongoing program designed to study tropical rainfall and the associated release of energy. The TRMM satellite, which was launched into a orbit in November 1997, is a platform that houses several instruments which are being used to measure both meteorological and climatological parameters over the tropics between $\pm 35^{\circ}$ in latitude [*Kummerow, et al., 1998*]. By examining data from two of these instruments, the Lightning Imaging Sensor (LIS) and the TRMM Microwave Imager (TMI), it is now possible to characterize the relationship between lightning activity and the microwave signatures of storms that occur around the globe.

The data set from the Lightning Imaging Sensor consists of the optical events that are observed while making overpasses of active thunderstorms. Data recorded by this instrument includes the time of the lightning event, its radiant energy, and its location. The LIS instrument itself is a compact staring imager, and the $600 \times 600$ km$^2$ field-of-view allows the sensor to observe a point on the Earth or a cloud for approximately 80 seconds as it passes overhead in a low-earth orbit. The instrument has a temporal resolution of 2 ms and a spatial resolution of approximately 5 km. The instrument records lightning activity by detecting momentary changes in the brightness of the clouds as they are illuminated by lightning discharges. Due to the sensitivity and dynamic range of the sensor, it can detect lightning even in the presence of bright, sunlit clouds. The LIS instrument detects "total" lightning, since cloud-to-ground, intracloud, and cloud-to-cloud discharges all produce optical pulses that are visible from space [*Christian et al., 1992*].

The other data set used in this study is obtained from the TRMM Microwave Imager. The TMI is a passive microwave sensor, which measures the amount of radiation emitted from the Earth's surface and atmosphere. The TMI data is reported in the form of brightness temperatures, which are obtained from the radiation measurements using Planck's radiation law. Cloud water, cloud ice, and rain produce anomalies in the background radiation of the Earth (and the brightness temperatures) which makes TMI data an excellent resource for studying storms, weather, and climate. The radiometer measures the upwelling radiation at the microwave frequencies of 10.7, 19.4, 22.2, 37.0, and 85.5 GHz. The brightness temperatures are measured at both vertical and horizontal polarizations at all frequencies except 22.2 GHz, where only the vertical polarization is obtained. The swath width of the TMI is 780 km wide, but the spatial resolution is much smaller, ranging from 5 km at 85.5 GHz to 45 km at 10.7 GHz. Brightness temperatures obtained from the 37 and 85 GHz channels are particularly sensitive to cloud ice

due to the scattering properties of ice at these higher frequencies. The lower frequencies are most useful in detecting rain and water vapor over the oceans.

By studying thunderstorms with LIS and TMI data, much can be learned about the role of thunderstorms in atmospheric circulation and latent heat release. The relationship between lightning activity and cloud ice is important, particularly since the density of ice hydrometeors is related to the rainfall rate at the surface. Should a useful relationship exist between lightning activity and cloud ice, measurements of lightning activity may be used to estimate convective rainfall and latent heat release.

## METHODOLOGY

Several orbits of LIS lightning data were indiscriminately chosen for comparison with the TMI microwave measurements. Within each of these orbits, there are brief periods when the LIS instrument observed multiple thunderstorms in approximately the same region of the globe. These groupings of thunderstorms are referred to as "regional weather scenes". Information on the lightning activity and the microwave brightness temperatures associated with these regional weather scenes were extracted from the LIS and TMI data files on a storm-by-storm basis. Comparisons between the LIS and TMI data were only made for storms exhibiting lightning activity.

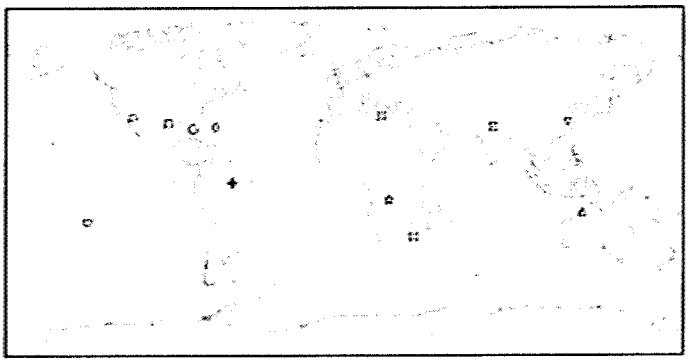

Figure 1. The approximate locations of the various "regional weather scenes" that contain thunderstorms examined in this study. The symbols shown at the centers these weather scenes correspond with the "plot symbols" used in Table 1, Figure 3, and Figure 4.

From eleven orbits of LIS and TMI data, twelve separate "regional weather scenes" were chosen for examination. These twelve weather scenes represent a broad sampling of storms from a variety of seasons and regimes, and their locations are shown in Figure 1. As described in Table 1, the number of storms associated with a weather scene ranged from 14 to 39 thunderstorms, and many of these storms were observed at different times during the diurnal cycle. Most of the weather scenes included a variety of storms producing low to medium

TABLE 1. A Listing of the "Weather Scenes" Included in this Study.

| Plot Symbol | Location | Latitude | Longitude | Date of Observation | Observation Time | Number of storms |
|---|---|---|---|---|---|---|
| □ | Southeastern US / Texas & Louisiana | 30 N | 94 W | January 22, 1998 | 04 12 UTC | 25 |
| ○ | Florida Peninsula | 27 N | 81 W | March 9, 1998 | 08 27 UTC | 36 |
| ◇ | Atlantic Ocean / off eastern coast of US | 28 N | 69 W | March 22, 1998 | 00 49 UTC | 17 |
| ⧗ | South of Himalayas / Nepal & India | 28 N | 78 E | April 9, 1998 | 05 38 UTC | 22 |
| ✣ | Amazon / Northwestern Brazil | 01 S | 60 W | June 11, 1998 | 21 07 UTC | 39 |
| ⋈ | Indian Ocean / off SE coast of S Africa | 29 S | 36 E | July 4, 1998 | 00 04 UTC | 19 |
| ⬭ | South Pacific Ocean | 21 S | 137 W | July 20, 1998 | 04 14 UTC | 17 |
| ▽ | Eastern China | 31 N | 118 E | August 2, 1998 | 10 47 UTC | 29 |
| ⌓ | Southwestern US / Arizona | 33 N | 113 W | August 6, 1998 | 00 24 UTC | 31 |
| ⌘ | Mediterranean Sea | 34 N | 19 E | November 22, 1998 | 09 08 UTC | 18 |
| △ | Northwestern Australia | 17 S | 126 E | November 22, 1998 | 09 38 UTC | 14 |
| ☆ | Central Africa / Dem Rep of the Congo | 10 S | 23 E | November 22, 1998 | 15 40 UTC | 25 |

levels of lightning activity, although two of these regional weather scenes contained several storms that produced extremely high levels of lightning activity.

One example of a weather scene is a convective system that was observed in March of 1998 over the Florida Peninsula, as shown in Figure 2. A majority of the thunderstorms in this example produced medium to high levels of lightning activity, and were part of a severe weather system that spawned several tornadoes a few hours prior to the TRMM satellite overpass. Note that there are depressions in the brightness temperatures coincident with regions of lightning activity. Additionally, the largest brightness temperature depressions correspond with the storms producing the highest amount of lightning activity.

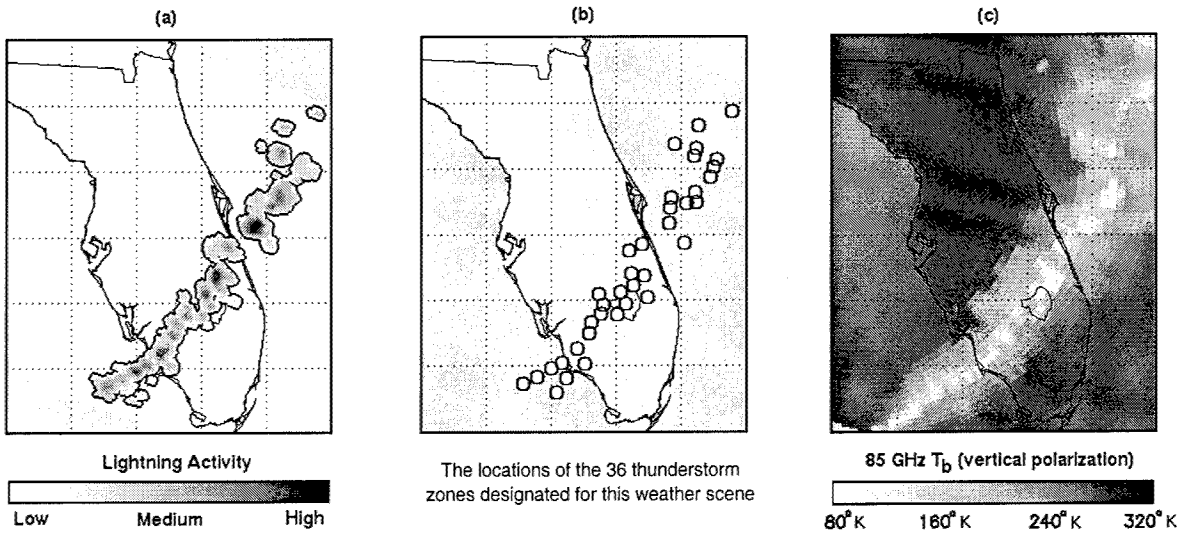


Figure 2. A depiction of data from one of the regional weather scenes, including maps of (a) the LIS lightning activity, (b) the locations of the individual "thunderstorm zones", and (c) the TMI 85 GHz brightness temperatures.

Small circular regions within a weather scene were declared to be "thunderstorm zones" if the region included a sufficient density of optical pulses. LIS and TMI data associated with these thunderstorm zones were extracted for a circular region around the point of peak optical pulse density. In order to be consistent, these circular regions were all defined with a diameter of almost 21 km, which corresponds with an area of approximately 350 $km^2$. The size chosen for these regions is large enough to encompass one or more adjacent measurements from the TMI as well as a majority of the optical lightning pulses which illuminate the cloud-tops of the storms. For each of these storm zones, the TMI brightness temperatures for the vertically polarized 37 and 85 GHz channels were extracted along with the corresponding LIS data.

When examining the LIS and TMI data sets, some differences were evident in the geolocated positions of the TMI data relative to the "true" positions of storms. The TMI is designed to scan with a constant angle of incidence, which intercepts the storms at a constant angle of 52.8° from horizontal. Each TMI measurement is mapped to a location corresponding with the intersection of the scan vector and the Earth's surface. Because the higher TMI frequencies are most sensitive to cloud ice at the top of the cloud, the geolocated position of data associated with tall storms can be geolocated more than 10 km away from the location directly underneath the cloud-top. This causes a misalignment with the LIS lightning data because the optical pulses observed by the LIS instrument have been corrected for this slant-path error and are mapped to a location underneath the illuminated cloud top. As a result, the geolocated positions of the 37 and 85 GHz TMI measurements were slightly adjusted in order to improve their alignment with the LIS data.

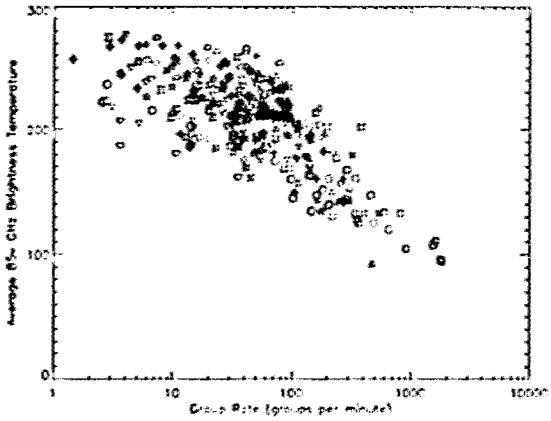


Figure 3. A scatter plot showing the observed relationship between LIS lightning activity and 85 GHz brightness temperatures.

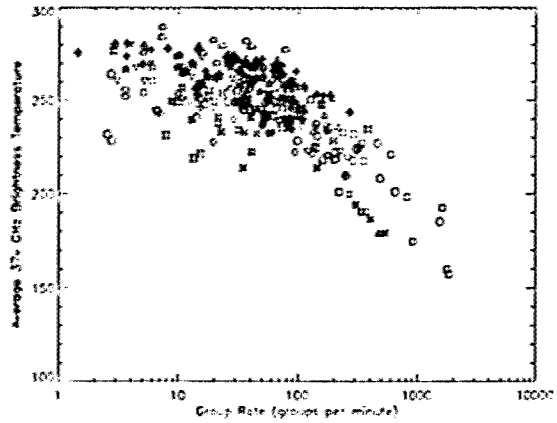


Figure 4. A scatter plot showing the observed relationship between LIS lightning activity and 37 GHz brightness temperatures.

## RESULTS

The frequency of LIS "groups" (i.e., optical lightning pulses) were compared with the average 37 and 85 GHz brightness temperatures for the 292 thunderstorm zones from the 12 weather scenes. The brightness temperatures were found to decrease as the group rate increased, as shown in Figures 3 and 4. Since these lowest brightness temperatures represent areas where the ice concentrations are greatest, the thunderstorm zones with the highest optical pulse rate must also contain the highest amount of cloud ice. The amount and distribution of lightning is believed to be directly related to the presence of large ice particles in the mixed phase region of a given thunderstorm, and it is no surprise that lightning activity is frequently coincident with decreased 37 and 85 GHz brightness temperatures, where scattering processes are dominating.

The expression which best captures this relationship between the brightness temperatures, Tb, and lightning activity, L, is

$$Tb\ 85 = 330 - 70 \cdot \log_{10}(L), \quad L > 20 \text{ groups/minute}$$

$$Tb\ 37 = 330 - 45 \cdot \log_{10}(L), \quad L > 20 \text{ groups/minute}$$

where the brightness temperatures are provided in degrees Kelvin. For thunderstorm zones associated with lightning activity below 20 groups/minute, the brightness temperatures are not as well correlated with the lightning activity. Some of this scatter can be attributed to the brief observation period, since LIS can only observe a thunderstorm zone for approximately 80 seconds as it makes an overpass. Despite these minor irregularities, the correlation between lightning activity and brightness temperature is quite good. The relationship between lightning activity and cloud ice content should also be just as good.

It is important to remember that these relationships were developed from a sampling of storms from a variety of regimes, suggesting that there is a global dependence between lightning activity and cloud ice content. Given that prior research has shown that a relationship exists between ice aloft and surface rainfall, future research should concentrate on the relationships between lightning activity and convective rainfall and latent heat release.

## REFERENCES

Christian, H.J., R.J. Blakeslee, and S.J. Goodman, Lightning Imaging Sensor (LIS) for the Earth Observing System, NASA Technical Memorandum 4350, MSFC, Huntsville, AL, February, 1992.

Kummerow, C., W. Barnes, T. Kozu, J. Shiue, and J. Simpson, The Tropical Rainfall Measuring Mission (TRMM) Sensor Package. J. Atmos. Ocean Tech., Vol. 15, No. 3, 1998, pp. 809-817.

# HIGH-ALTITUDE AIRCRAFT-BASED ELECTRIC-FIELD MEASUREMENTS ABOVE THUNDERSTORMS

M.G. Bateman[1], R.J. Blakeslee[2], J.C. Bailey[3], M.F. Stewart[4], and A.K. Blair[4].

[1]Universities Space Research Association, Huntsville, Alabama, U.S.A.
[2]NASA, Marshall Space Flight Center, Huntsville, Alabama, U.S.A.
[3]Raytheon ITSS, Huntsville, Alabama, U.S.A.
[4]The University of Alabama at Huntsville, Huntsville, Alabama, U.S.A.

ABSTRACT: We have developed a new set of eight electric field mills that were flown on a NASA ER-2 high-altitude aircraft. During the Third Convection And Moisture EXperiment (CAMEX-3; Fall, 1998), measurements of electric field, storm dynamics, and ice microphysics were made over several hurricanes. Concurrently, the TExas-FLorida UNderflights (TEFLUN) program was being conducted to make the same measurements over Gulf Coast thunderstorms. Sample measurements are shown; typical flight altitude is 20 km. Our new mills have an internal 16-bit A/D, with a resolution of 0.25 V/m per bit at high gain, with a noise level less than the least significant bit. A second, lower gain channel gives us the ability to measure fields as high as 150 kV/m.

## INTRODUCTION

The Tropical Rainfall Measuring Mission (TRMM) satellite is a low Earth orbiting satellite that includes a precipitation radar, microwave, visible, and infrared imagers, and the lightning imaging sensor (LIS). In order to provide ground validation for TRMM (specifically LIS), we have developed a new set of eight electric field mills that were flown on a NASA ER-2 high-altitude aircraft. Additionally, the ER-2 carried a Doppler radar, microwave and millimeter radiometers, and a conductivity probe (Gerdien type). This suite of instruments provides us with much information about a storm's dynamics, microphysics, and electrical nature. In several cases, the ER-2 flew over a storm as the TRMM satellite flew overhead. Some of the questions that these measurements will help us address include: dependence of lightning on the updraft and storm dynamics, relationship of lightning and ice microphysics, and lightning-current relationships.

## INSTRUMENTATION

Previously aboard the ER-2, we had flown two mills that output an analog voltage proportional to the field strength. Our new mills have an internal computer and 16-bit A/D that sends digital data to an onboard data system. The mills also have improved shielding that greatly reduces noise in the data. The field mills have an internal calibrator, which applies a known voltage to the rotor. The data system cycles the calibration voltage on and off every half hour during data collection. These calibrations show up as square "pulses" on the half hour.

We now are able to fly eight mills; using their separation in the $x$, $y$, and $z$ directions we can extract the $E_x$, $E_y$, and $E_z$ components and the charge on the aircraft, $Q$. Since we now have more than four mills, we can take advantage of redundancy to assess the quality of our measurements.

## OBSERVATIONS

Sample electric field data are shown. Each plot has three traces: (1) electric field from an upward pointing mill, (2) electric field from a downward pointing mill, and (3) the difference of these two.

These two mills were installed in the Q-bay of the ER-2, which is located directly behind the cockpit, mounted on the vertical centerline of the aircraft. By symmetry, the third trace shown in each plot is proportional to the vertical component of E ($E_z$). These data are uncalibrated, but the units approximate kilovolts per meter (kV/m). Typical flight altitude was 20 km.

Shown in Fig. 1(a) are electric field measurements from a flight over Hurricane Bonnie on 26 Aug 1998, prior to landfall. During the illustrated overpass, the airplane flew over two charge centers, one at 1508 and one at 1518. A lightning flash occurred during the first crossing, which essentially neutralized the charge center. Note that there are only a few lightning flashes seen on this entire plot.

Shown in Fig. 1(b) are electric field data from a pass over Hurricane Georges as it made landfall over mountains on the island of Hispaniola. The aircraft made its nearest approach to the eye at about 2318, turned around at about 2327, and passed near the eye again at about 2332. During this time the pilot, Dee Porter, reported a layered cloud extending up from the eye. He said that the lightning in the region of the eye (estimated about 185 km in diameter) was "continuous." The ER-2 was flying a line (E-W then W-E) across the hurricane about 55 km perpendicular from the eye at an altitude of about 20 km. During this time, the pilot said that upward discharges (presumably blue jets) were occuring at about one per minute. He said he could watch them propagate, that they were single filament, and that they were purple. He also commented that all the lightning he saw was contained in the eye, rather than in the feeder bands where hurricane lightning usually occurs. As the hurricane was passing over mountains, we speculate that orographic lifting is the cause for the unusual lightning in and around the eye.

Shown in Fig. 1(c) are electric field data from a typical active thunderstorm over Florida. The lightning flash rate is 1–3 per minute, quite a contrast from the hurricane examples.

We are in the process of calculating the geometric calibration coeffiecients for the new field mills. This involves having the aircraft fly in a constant field region and execute a series of pitches and rolls. Then using a matrix inversion process, we can calculate the geometric factors [*Winn*, 1993; *Koshak et al.*, 1994].

## CONCLUDING REMARKS

We now have a large set of measurements from hurricanes and overland thunderstorms, which we are only beginning to analyze. These include measurements from the TRMM satellite, ER-2 aircraft, and ground-based radars. We expect that this dataset will allow us to develop (or refine) algorithms relating lightning to many other storm parameters, which can then be applied to existing and future satellite-based lightning measurements. We will also be able to provide validation for the TRMM satellite.

## REFERENCES

Koshak, W.J., J. Bailey, H.J. Christian, and D.M. Mach, Aircraft electric field measurements: Calibration and ambient field retrieval, *J. Geophys. Res.*, *99*, 22,781–22,792, 1994.

Winn, W.P., Aircraft measurement of electric field: Self-calibration, *J. Geophys. Res.*, *98*, 6351–6365, 1993.

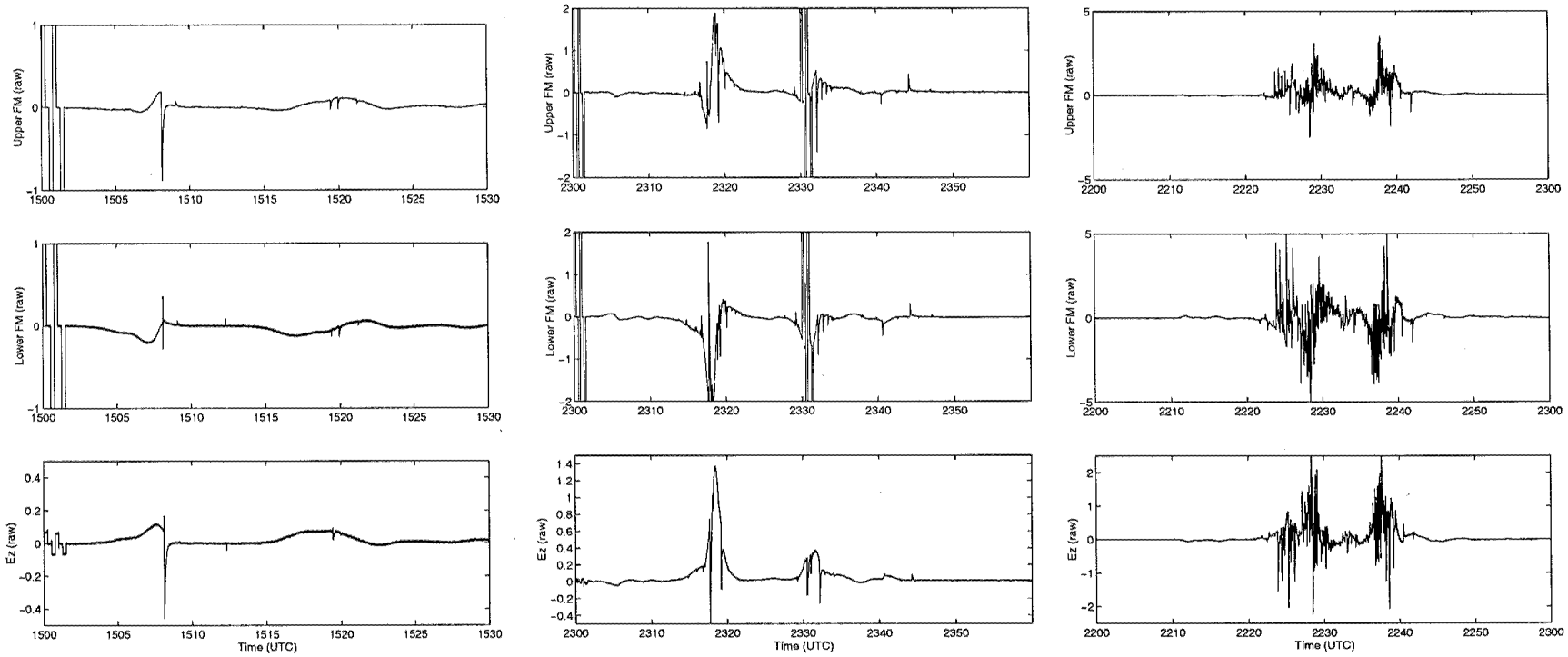


**Figure 1:** Electric field measurements: (a; left) above Hurricane Bonnie, 26 August 1998, (b; middle) above Hurricane Georges as it made landfall on the island of Hispaniola on 22 Sep 1998, and (c; right) above an active thunderstorm over Florida on 15 August 1998.

# LIGHTNING DISCHARGE LOCATIONS RELATIVE TO REFLECTIVITY AND UPDRAFT/DOWNDRAFT STRUCTURES IN A COLORADO THUNDERSTORM

J. E. Dye[1], T. Matejka[2], P. Laroche[3], E. Defer[3], G. Hubler[4], and S. A. Rutledge[5]

[1]National Center for Atmospheric Research, Boulder, Colorado USA
[2]NOAA National Severe Storms Laboratory, Boulder, Colorado USA
[3]Office Nationale d'Etudes et de Recherches Aerospatiales, Chatillon, France
[4]NOAA Aeronomy Laboratory, Boulder, Colorado USA
[5]Colorado State University, Ft.Collins, Colorado USA

ABSTRACT: The Stratospheric-Tropospheric Experiment: Radiation, Aerosols and Ozone (STERAO) Deep Convection project was conducted in NE Colorado in June/July 1996 to investigate the production of NOx (= NO + NO2) by lightning and vertical transport of chemical species by thunderstorms. Herein we report on the location of VHF sources along lightning channels detected by the ONERA lightning interferometer within the 10 July thunderstorm. The location of these sources is examined relative to the reflectivity determined from the Colorado State University CHILL multi-parameter radar and airflow structure derived from multiple Doppler radar analyses using NOAA WP3D tail Doppler radar and CHILL measurements. During the intense multicell stage of the storm most of the VHF lightning sources were in moderate updrafts with many sources also in the core updraft. Interestingly there were only a few VHF lightning sources in the main downdraft, although the paucity of sources in the downdrafts was not true during the entire storm lifetime. Results from this and other periods during the 5 hour storm history are presented.

## INTRODUCTION

An overview of the STERAO Deep Convection Project and results from the 10 July case are presented in more detail in Dye et al., (1999) including the intra-cloud and cloud-to-ground lightning history during the five hour lifetime of the storm. It is worth noting for the discussion that follows that this storm produced predominately IC lightning. The ratio of IC to total flashes was > 95% during most of the storm lifetime with periods up to 20 min or more no detected CG lightning. CG lightning was detected using the National Lightning Detection Network (NLDN) with the ONERA lightning interferometer used to detect total lightning. The 10 July storm was multicellular during the first 3 ½ hours of it's lifetime and but evolved to a low precipiation supercell strom with low and mid level rotation for the the last hour. During the multicell stage, one particularly intense cell had radar tops to 16.5 km MSL, which is unusually high for storms in northeastern Colorado. The cells of the storm extended 40 to 60 km along a line in the NW to SE direction, but was only 15 to 20 km across in the SW to NE direction. Thus, even though it was quite high it did not cover a particularly large area.

Several constant altitude horizontal sections (CAPPIs) at 10.5 km through the storm are displayed in Figure 1. VHF sources from the ONERA interferometer for a 5 min period centered on the time of the radar scan are superimposed as Xs on the CAPPIs. Segments of the

flight track of the Univ. of North Dakota Citation jet aircraft, which was flying at nominally 10.5 km, are also shown as a thin line on the appropriate panels. The panels depict much of the storm's lifetime and are separated by roughly one hour with panel a) at 2209 about 17 min after the first lightning, b) 2312, the most intense multicell stage, c) 0005, nearing the end of the multicell stage and d) 0128, during the supercell phase. [All times are in UTC.] The bold, solid lines show the lobes for interferometer (ITF) coverage. For cells close to the upper west edge of the ITF lobes the northern ITF site is much closer than the southern site which results in scatter and inaccuracies of the determined locations. We refer to this scatter as radial dispersion as it is along a radial from the closest site. It is evident for the NW cells in Figures a), b) and c).

As noted by Laroche et al., 1994 and others, negative leaders emit a lot of VHF radiation which can be detected by interferometric techniques. Because of the more continuous nature of positive leader propagation they do not radiate as much and hence are less detectable by the interferometer. In the plots shown below we must realize that we are primarily viewing locations of negative discharge processes, but the path of positive leaders can be partially inferred from the location of recoil streamers. Thus, our plots of VHF source locations probably shown most of the area in which lightning discharge processes have occurred during the 5 min time periods shown. Focusing our attention on cells where radial dispersion is not a problem, ie. the southeastern cells in panels b-d) we see that most of the sources are within the 25 dBZ radar contours, especially on the western side of the cells. In the intense multicell stage at 2312, and also at 0005 some sources do extend 20 to 25 km from the 25 dBZ contour. On one occasion sources extended 60 km from the core [See Stith et al., 1999], which is almost as far as the location of the Citation tracks seen Figures 1 a) and b), but this was rare.

Figure 2 presents derived vertical and horizontal winds during the 2312 intense multicell period from a 3 Doppler radar retrieval. The retrieval used the fore – aft scans from the P3 tail radar as the P3 flew beside the storm combined with those from CHILL. A 2 km grid was utilized for the retrieval thus some averaging occurs and actual vertical velocities are likely to be larger. Panel A) shows updrafts [2 to8 m/s light gray; >8 m/s dark gray] and downdrafts [-2 to -5 m/s horizontal hatching; <-5 m/s cross-hatching] superimposed on reflectivity contours for the 7.5 km MSL CAPPI. The 7.5 km CAPPIs were used because this is near the altitude where many lightning flashes originate. B) is the same as A) except VHF sources from the lightning interferometer are superimposed. C) shows the horizontal wind vectors with storm motion of u,v = 1.7, -5.5 m/s subtracted. Vector lengths correspond to the distance moved in 300 sec. The strongest updraft core with Doppler derived strengths of 18 m/s were located at approximately X,Y = 72,73 km from CHILL. As mentioned before these are lower limits and a factor of 2 less than the maximum updrafts found in a 3D cloud resolving model simulation of the storm. [Skamarock et al., 1999]

Note in Figure 2B that there were very few VHF sources in the downdraft core of the intense cell. Although it is difficult to tell from this black and white version of the figure, most of the sources were located in moderate updrafts and between the upcore updraft and the weaker downdraft centered at X,Y = 77,75. We are examining Doppler retrievals in comparison to VHF sources for other periods of the storm lifetime. Early results suggest that this pattern of a paucity of VHF lightning sources in the core downdraft was not present. The finding shown in Figure 2 is intriguing and clearly needs additional study.

REFERENCES

Dye, J. E. et al.; An Overview of the STERAO - Deep Convection Experiment with Results for the 10 July Storm, *J. Geophys. Res.*, submitted Jan. 1999.

Laroche, P; 3D mapping of lightning discharge within storms, *Internat. Aerospace and Ground Conf. On Lightning and Static Electricity*, Mannheim, Germany, 1994.

Skamarock, W.C. et al; Numerical simulations of the 10 July STERAO/Deep Convection experiment convective system: Dynamics and Transport, *J. Geophys. Res.*, submitted Jan.1999

Stith, J.; $NO_x$ Signatures from Lightning Flashes, Submitted to *J. Geophys. Res*, accepted after revision.

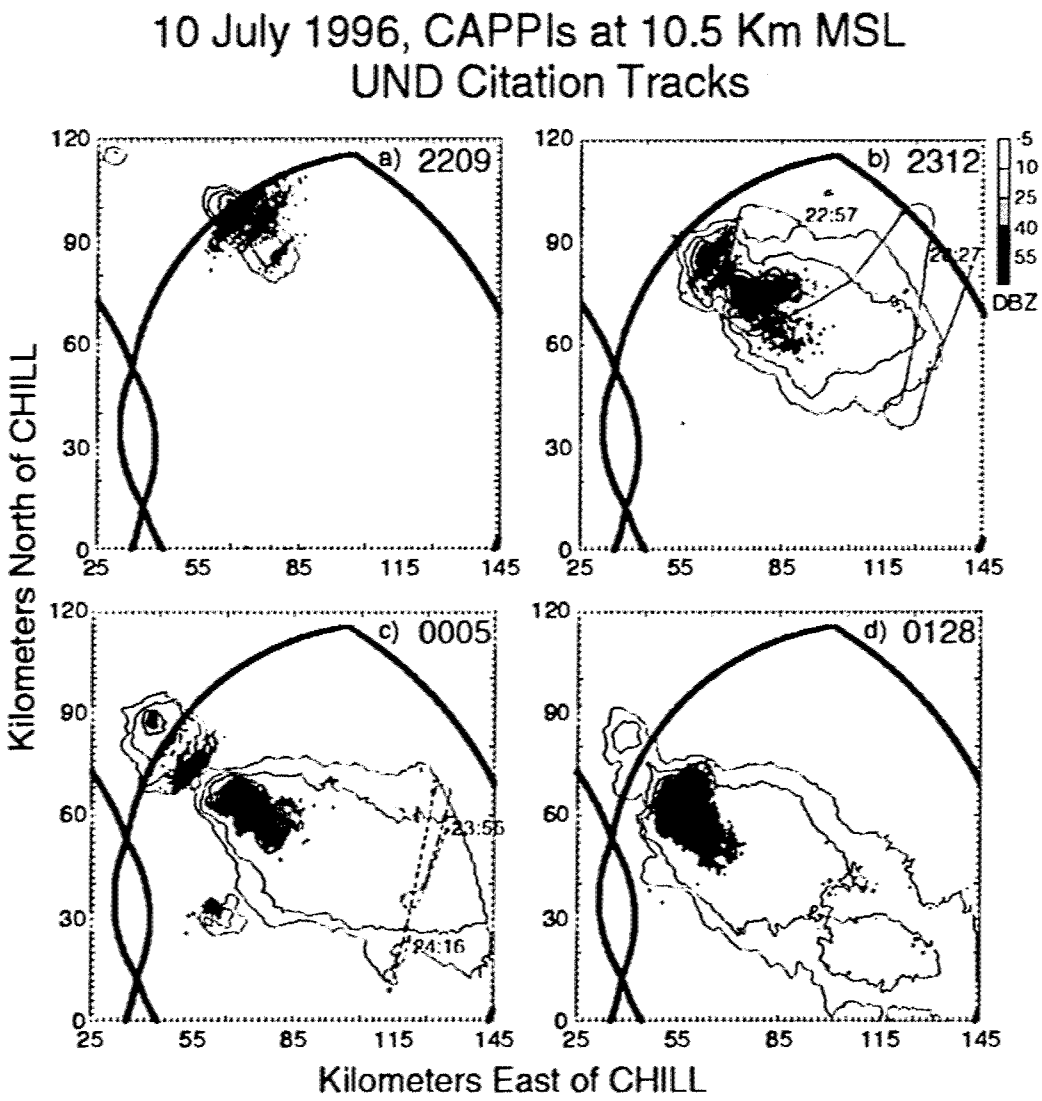


Figure 1. Constant altitude contours of radar reflectivity at 10.5 km MSL with VHF sources from lightning detected by the ONERA interferometer superimposed. See text for explanation.

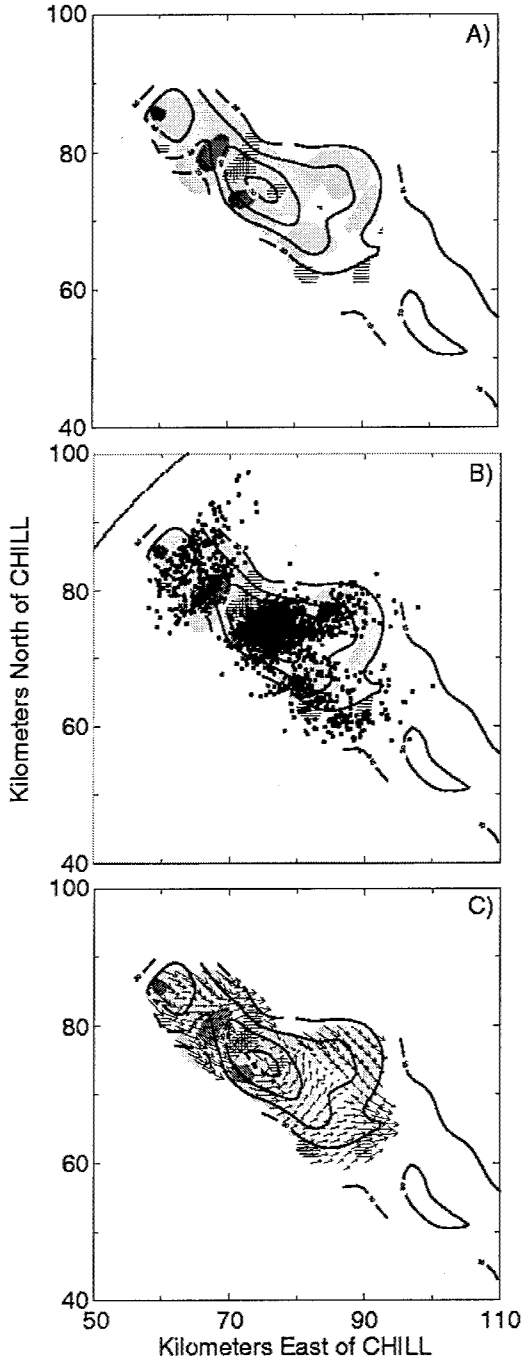


Figure 2. Doppler radar derived vertical and horizontal winds superimposed on radar reflectivity contours at 7.5 km MSL. A) Vertical winds with updraft regions of 2 to 8 m/s shown in light gray, updrafts >8 m/s in dark gray, downdrafts of -2 to -5 m/s shown by horizontal hatching and downdrafts <-5 m/s by cross-hatching. B) Same as A) but with interferometer located VHF sources from lightning channels superimposed. C. Same as A) but with horizontal wind vectors superimposed. Vector lengths correspond to the distance moved in 300 sec. Average storm motion of u,v = -1.7,5.5 m/s has been subtracted.

# Session VII:

# Fair Weather Electricity

# DATA PROCESSING AT SPECIAL DATA CENTER ON THE SURFACE LAYER ATMOSPHERIC ELECTRICITY, A I VOEIKOV MGO RC ARS

Ya M Shvarts, I A Petrenko, and G G Shchukin

A I Voeikov Main Geophysical Observatory Research Center for Atmospheric Remote Sounding, Voeikovo, Vsevolozhskiy rayon, Leningradskaya oblast, 188685, Russia

ABSTRACT. Measurements of atmospheric electric field potential gradient and polar air electric conductivity's are being continued at several meteorological stations of the Russia Hydrometeorological Service Special data center on the surface layer atmospheric electricity (SDC/AE) collects, processes and archives data of these measurements SDC/AE provides a safety of the archive and an access to it, including the archive of the WDC/AE. The operation of the SDC/AE are described The need is underlined for a resumption of the information exchange between the SDC/AE and the AE stations, which are placed beyond the Russia frontiers.

## INTRODUCTION

Over many years specialists of our institution attach great importance to regular ground atmospheric electric (AE) observations. Our position with respect to these observations was expressed, for example, in the reports which were presented to the 9th and 10th ICAE [*Shchukin et al, 1992, Klimin and Shvarts, 1996, Khlebnikova et al, 1996*]. First, it was shown the averaging of AE observation data can serve for revealing global processes that cover a substantial area of the globe, for example, the increase in Aitken nuclei concentration at the surface layer. Second, the existence of the correlation between the air electrical conductivity (AC) and the other parameters of the background air pollution confirmed the expediency of AC-characteristics for assessment of the background state of the atmosphere Third, it was shown the multivariate statistical analysis should be considered as independent research accompanying background air pollution monitoring The generalized historical data (monthly and annual means) only were used for the analysis owing to difficulties of an access to primary data (hourly means). Unfortunately, the plan for a modernization of our archive (the archive of the WDC/AE) [*Gordyuk and Tammet, 1992*] was not fulfilled Attacking this problem lies ahead.

## THE EXISTING SITUATION

Measurements of atmospheric electric field potential gradient V' and polar electric conductivities λp are being continued at four stations of the Russia Hydrometeorological Service (RHS). V' are measured at Voeikovo (near St.Petersburg), Irkutsk, Verkhnee Dubrovo (near Ekaterinburg) and Yuzhno-Sakhalinsk. λp are measured at Voeikovo and Irkutsk. A body of information on the surface atmospheric electricity diminished as compared with the similar information, which have been obtained yearly up to the middle 90s Special Data Center on the surface layer atmospheric electricity (SDC/AE) collects and processes data of these measurements The AE data over the period 1964-1989 were published in the WDC/AE monthly booklets in tabulated form - " Results of ground observations of atmospheric electricity (the world network). - St. Petersburg, Main Geophysical Observatory, 1966-1993". Beginning from 1990 up to 1996 the data processing were performed with IBM-370 compatible computer which was used mainly for processing of meteorological data . The results of the processing were stored on magnetic tape in the archive form. Subsequently, archive data were converted from the tapes to floppy disks of PC. In 1997 a

new system of processing and analysis of meteorological data was placed in operation by the RHS and the above-mentioned computer was removed from service. The system is based on using PC IBM. In connection with putting into operation of this system the development of a new technology for the collection, processing and accumulation of the AE data was required.

## DATA

Shown on the Fig.1 and Fig.2 are the courses of the annual means of V' and the total air electric conductivity λ over the period 1981-1996 years on evidence derived from the data of the observatories Voeikovo , Verkhnee Dubrovo , Irkutsk. These data demonstrate a modest rise of λ at Irkutsk and Voeikovo within the recent few years. It is supposed that this effect can be explained mainly by a decrease of an emission of aerosol-formed gases into the atmosphere due to a drop of the industrial production at the regions where the observatories are placed. It would be interest to compare our data with data of other atmospheric electric stations placed beyond the Russia frontiers.

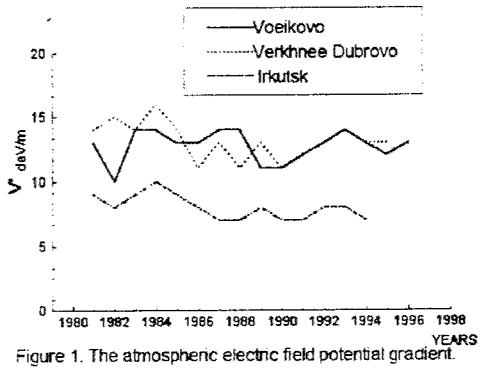

Figure 1. The atmospheric electric field potential gradient.

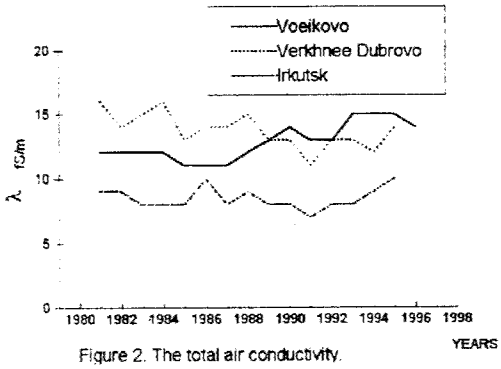

Figure 2. The total air conductivity.

## NEW SYSTEM

New AE data processing system was developed in two versions. The one is for the automated system for data recording and processing up to creating data bank. This system is designed for atmospheric electric stations, which are equipped by PC. The second is designed for processing data from stations, which are equipped by the chart recorders.

The software of the AE data processing consists of three program units: the primary data processing program for the automated system, the table creation program for processing both automated and non-automated system data and the file processing program for the non-automated station data entry.

The automated system operates at the atmospheric electric station Voeikovo. The primary archive and the main database are filled at the Voeikovo station since May, 1997.

The primary data processing includes the data accumulation in the primary archive in a form of binary files containing data in relative units up to 8 measuring channels with a sample period of 100 seconds. One file corresponds to 24-hour interval of measurements. File contains codes of quality of measurements for each of 100 seconds intervals. It can be changed by an operator in the case of violations, not recognized by the program (a fault of instruments, a switching in a mode of calibration). The program of the primary processing allows an automatic correction of estimated

average values by results of periodic calibrations of measuring instruments. The primary archive in addition to binary files involves a text file formed by the program of primary processing. Text file contains the coefficients of a binary file data recalculation from relative units to physical units.
The program provides graphic representation of measured values vs time both for a current data, and for any data of the primary database. The graphic representation of special measurements with period of sample 3 seconds is available too. The paper copy of any screen information is possible. The primary archive is transformed to the tables of hourly average values with the table creation program. Two sorts of the tables are available. First one is similar to the tables which were used earlier in the issues of WDC/AE. Second one is intended for an inclusion in standard databases. Excel- compatible format of tables provides a compatibility with other databases. The program of a conversion of the primary archive allows to enter meteorological data (codes of a cloud cover, speed and direction of a wind, information on the atmospheric phenomena) into the tables. For this purpose program handles files of conventional structure received from meteorological stations. The input information for the program of a secondary (main) database tables creation can be not only files of primary archive, but also atmospheric electric stations coded data.

The software of the SDC/AE data processing is intended for Windows 9x and NT systems. The programs are used at the Voeikovo station.
Thus changes in data processing in SDC/AE offers possibilities:

- to automate data processing and storing at the observatory Voeikovo,
- to automate and to unify a processing of data, received from other atmospheric electric stations, or stored in the 1964-1998 WDC/AE databases,
- opens the way for further operations on inclusion in the database of prior years data accumulated in the WDC/AE databases and a support of availability of data in the Internet network.

## CONCLUSIONS

The SDC/AE of MGO RC ARS appeals to ground atmospheric electric stations for a collaboration.

## REFERENCES

Gordyuk V.P. and H.F.Tammet. Modernization of the World Data Center for Atmospheric Electricity. In: Proceedings. 9th International Conference on Atmospheric Electricity. 1992. June 15-19, 1992. St.Petersburg, RUSSIA. A.I.Voeikov Main Geophysical Observatory. P. 46-49.

Khlebnikova E.I., E.N.Rusina, Ya.M.Shvarts. The Air Electrical Conductivity and Its Connection with Parameters of Background Air Pollution. In: Proceedings. 10th International Conference on Atmospheric Electricity. June 10-14, 1996. Royal Hotel Osaka, Osaka, Japan. P. 156-159.

Klimin N. N., Ya.M.Shvarts. Trends in the Surface Layer Atmospheric Electricity - The Evidence Estimated from Long-Term Measurements 1916-1992. Ibid. P. 152-155.

Shchukin G.G., Ya.M.Shvarts, L.V.Oguryaeva. Recordings of Atmospheric Electricity in Different Places. In: Proceedings. 9th International Conference on Atmospheric Electricity. 1992. June 15-19, 1992. St.Petersburg, RUSSIA. A.I.Voeikov Main Geophysical Observatory. P. 40-45.

# EFFECT OF COAGULATION ON THE PARTICLE CHARGE DISTRIBUTION AND AIR CONDUCTIVITY

Savita Dhanorkar and A. K. Kamra

Indian Institute of Tropical Meteorology, Pune, India

ABSTRACT: The ion-aerosol balance equations including the effect of the coagulation of charged aerosols are solved. The effect of coagulation on the steady state charge distribution of the singly and multiply charged aerosol particles is examined for different ionization rates and aerosol concentrations. When the aerosol concentration is large, the coagulation results in an increase in the fraction of charged aerosols and the increase continues upto a critical value of aerosol concentration. The polar conductivity computed from this charge distribution first decreases and then increases with the increase in aerosol concentration. The critical value of aerosol concentration at which the minimum in conductivity occurs shifts to the higher values of aerosol concentration for larger ionization rates.

## INTRODUCTION

The electrical conductivity of the atmosphere is determined by the concentration and mobility of ions. Therefore, a knowledge of the charge distribution on the aerosol particles is essentially required to understand the behaviour of polar conductivity. The diffusion of ions to the aerosol particles establishes a statistical charge distribution on the aerosol particles and leads to the depletion of the small air ions. The coagulation of aerosols is another important phenomenon which can significantly affect the charge distribution on the aerosol particles. Recently investigations have been made to study the effect of coagulation on dynamic behaviour of the charged aerosols (e.g. Adachi et al.,1981; Oron et al., 1989).

In this paper we consider both physical mechanisms, the coagulation of the charged aerosols and the particle charging, and calculate the steady state charge distribution on the submicron size particles from the ion-aerosol balance equations for multiply charged aerosols. The electrical conductivity of the atmosphere is estimated for the equilibrium conditions of charge distribution. The effect of coagulation on the behaviour of the electrical conductivity is also studied.

## STEADY STATE CHARGE DISTRIBUTION ON AEROSOLS

The ion-aerosol balance equations including the coagulation of the charged and uncharged aerosols are given by Dhanorkar and Kamra (1997). The steady state charge distribution on the monodisperse aerosol particles can be obtained from these equations. We have solved these equations for a system having a maximum of upto five elementary charges. The change in the size of aerosols due to coagulation is not considered in these calculations. We further assume that there is no direct production of the charged aerosols and that the attachment of ions and the coagulation of the aerosols are the only two mechanisms which lead to the formation of the charged aerosols.

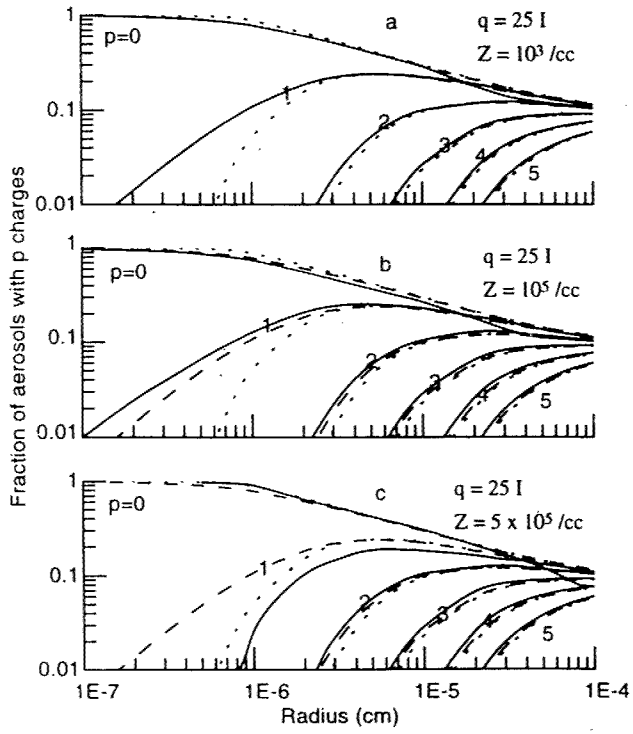


Figure 1. Fraction of aerosols with p charges as a function of radius for different values of aerosol concentrations according to Boltzman's distribution (.....), Hoppel's calculations (- - - - -), and present results ( ___ )

Fig. 1a shows the variation of the charge distribution of the aerosol particles calculated from the ion-aerosol balance equations using the size-dependent values of ion-aerosol attachment coefficients of Hoppel and Frick

(1986), for the ionization rate, q = 25 I and the total aerosol concentration, Z = $10^5$ particles/cm$^3$. The distribution on smaller particles (r < 0.1 μm) from our calculations is close to the one obtained by Hoppel (1985) where the coagulation of charged aerosols was not considered. However, for the larger aerosol particles ( r > 0.1 μm), coagulation results into the formation of somewhat higher number of charged aerosols. For example, the increase in the fraction of singly charged aerosols is 0.1% for r = 0.01 μm and 0.4% for r = 0.1 μm as compared to Hoppel's (1985) results. The fraction of the multiply charged aerosols also shows some increase in magnitude when the effect of coagulation is included.

The fraction of the charged aerosols increases for higher values of the total aerosol concentrations. For example, when Z = $10^5$ particles/cm$^3$, then for the same ionization rate, the coagulation of aerosols causes an increase of 19% in the fraction of singly charged aerosols for r = 0.01 μm and of 4% for r = 0.1 μm (Fig. 1b). The increase in the charged fraction of aerosols continues upto a critical value of the total aerosol concentration for given values of aerosol size and the rate of ionization. With the further increase in aerosol concentration, the charged fraction of aerosols decreases. For example, Fig. 1c shows that when the total aerosol concentration is equal to 5 x $10^6$ particles/cm$^3$ then for the same ionization rate, the coagulation process causes a decrease in the fraction of singly charged aerosols in the entire size range (0.001 μm < r < 1 μm). In this case, the fraction of singly charged aerosols decreases by 68% when r = 0.01 μm and by 18% when r = 0.1 μm when compared to Hoppel's (1985) results. It is worth noting that the fraction of singly charged aerosol particles becomes even less than that predicted by Boltzman's distribution. However, no such decrease is observed in the fraction of multiply charged aerosols for the total aerosol concentration considered by us. On the contrary, the fraction of the aerosols with two or more charges shows further increase in this case for aerosols of all sizes. The coagulation-induced change from enhanced to lower values of the fraction of charged aerosol particles as compared to that of Hoppel (1985), occurs for other values of the ionization rates as well but at different values of aerosol concentrations.

## VARIATION OF POLAR CONDUCTIVITY WITH AEROSOL CONCENTRATION

The polar conductivity has been computed from the size-mobility formula (Israël, 1971) using the charge distribution calculated here, for various values of the total aerosol concentration. As shown in Fig. 2a, the conductivity first decreases and then increases with the increase in the aerosol concentration. This trend in conductivity is in accordance with our earlier results (Dhanorkar and Kamra, 1997) where the contribution of multiply charged aerosols is not considered. The initial decrease and the subsequent increase in the polar conductivity with the increase in the aerosol concentration suggest the changeover of small ions to large ions as the main contributors to the conductivity. Moreover, as seen from Fig. 2a the critical value of aerosol concentration at which the minimum in conductivity occurs, is lower for the finer particles and increases with the mean size of aerosols. As shown in Figs. 2b and 2c, for ionization rates of 25 I and 50 I, respectively, the minimum in the polar conductivity shifts to the higher values of the aerosol concentration normally in the range of $10^5$ to $10^6$ particles/cm$^3$ for all values of the mean size of aerosols.

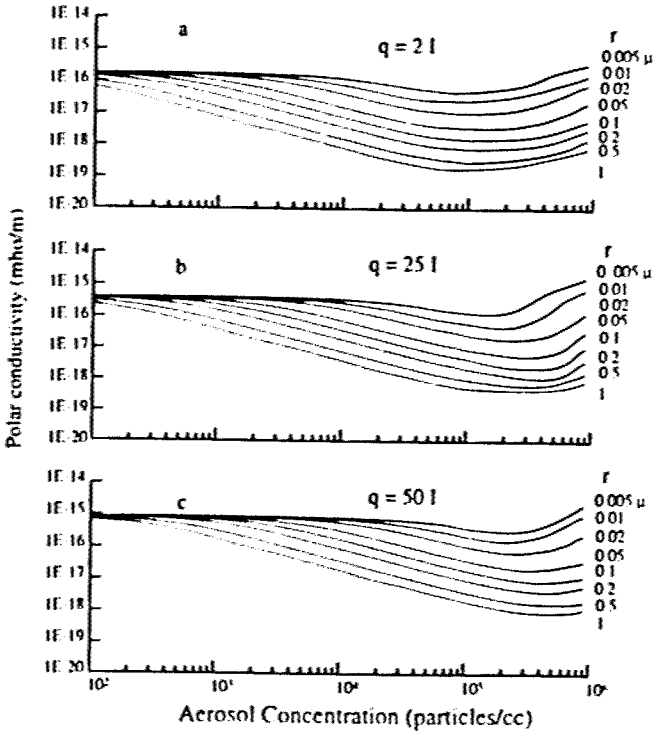


Figure 2. Variation of polar conductivity with aerosol concentration including the effect of coagulation of multiply charged aerosols

## CONTRIBUTION OF CHARGED AEROSOLS TO POLAR CONDUCTIVITY

Fig. 3a shows the percentage contributions of the small ions and of the charged aerosols to the polar conductivity for ionization rate of 25 I and the total aerosol concentration of $10^3$ particles /cm$^3$. In this case, the contribution of the singly as well as multiply charged aerosols to the polar conductivity is almost negligible ( < 0.1%). Therefore, the conductivity is mainly due to small ions in clean atmospheres where the aerosol concentration is small, e.g. over oceans or in the polar regions. However, the percentage contribution of the charged aerosols to the polar conductivity increases for higher values of aerosol concentrations. For example, Figs. 3b and 3c show that the contributions of charged aerosols significantly increase for the total aerosol concentration Z = $10^5$ particles/cm$^3$ and Z = 5 x $10^5$ particles/cm$^3$, respectively. In Fig. 3c, the contribution of the singly charged aerosols becomes even more than that of small ions if the mean radius of aerosols is > 0.06 μm. For aerosols having larger mean radii, the contribution of multiply charged aerosols also becomes appreciable and is almost comparable to that of the small ions.

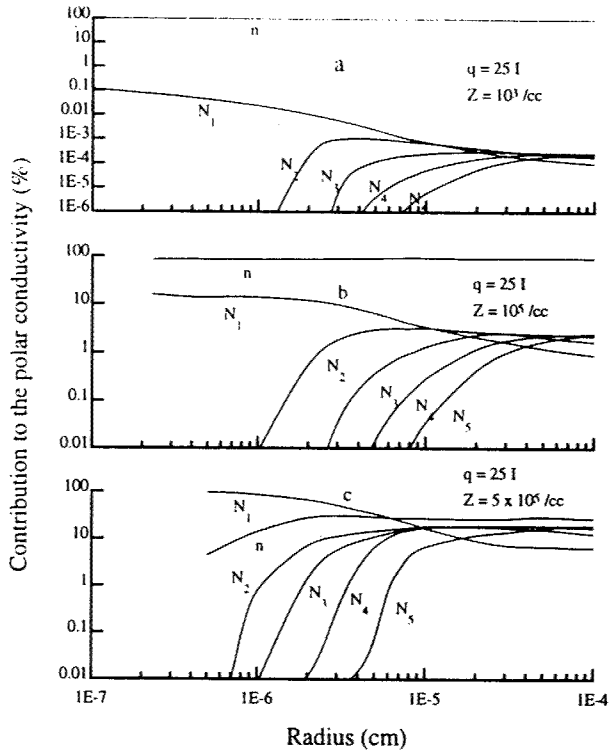


Figure 3. Variation of percentage contributions of small ions and charged aerosols to the polar conductivity as a function of the aerosol radius for different values of aerosol concentrations

## DISCUSSION

The earlier calculations of the particle charge distribution are primarily based on the diffusion theory of ions and can be well described by the Boltzman's statistics. The recent calculations of ion-aerosol attachment coefficient including the image-capture and three-body trapping effect give more precise estimate of the particle charge distribution on the smaller aerosol particles (Hoppel, 1977). However, in the urban polluted environment where the aerosol concentration may be as large or even larger than $10^6$ particles/cm$^3$, the effect of coagulation can cause a significant change in the charge distribution. In the present calculations, we include the effect of coagulation to calculate the equilibrium charge distribution on the monodisperse aerosols. Our results show that the effect of coagulation on the charge distribution is almost negligible and does not cause any significant change in it when the aerosol concentration is low. However, as the aerosol concentration increases, the coagulation causes an increase in the concentration of the singly as well as multiply charged aerosols upto a critical value of aerosol concentration. When the aerosol concentration exceeds this critical value, the concentration of singly and multiply charged aerosols begins to decrease. For a typical case of urban environment where the aerosol concentration is $10^5$ particles/cm$^3$ and ionization rate is 25 I, the effect of coagulation can cause an increase of 19% in the fraction of singly charged aerosols with their mean radius r ≈ 0.01 μm. However, when the aerosol concentration is 5 x $10^5$ particles/cm$^3$, the fraction of singly charged aerosols of the same radius decreases by 68%. Under such conditions, therefore, the present results can give more accurate estimates of the charged fraction of aerosols.

The increase in the concentration of charged aerosols continues upto a critical value of the aerosol concentration. But, when the aerosol concentrations are higher than this critical value, the coagulation process causes a decrease in the singly charged aerosols and the particle charge distribution starts approaching to the one described by the Boltzman's statistics. This condition is close to the one observed in a highly polluted environment. Our results suggest that for a given ionization rate, there exists a critical value of the total aerosol concentration for which the charge distribution on the aerosols closely agrees with the Boltzman's statistics.

Theoretical calculations of Dhanorkar and Kamra (1997) support their experimental observations (Dhanorkar and Kamra, 1992) that large ions substantially contribute to the electrical conductivity in highly polluted atmospheres. The polar conductivity computed here using the charge distribution obtained by including the effects of coagulation and of the multiply charged aerosols supports our earlier conclusion. Thus, the inverse relationship between the polar conductivity and aerosol concentration is observed only up to a critical value of aerosol concentration. This value of aerosol concentration is determined by the ionization rate and the mean size of the aerosols. When the concentration of aerosols exceeds this critical value, as may happen in the polluted atmospheres, the polar conductivity increases with the increase in the aerosol concentration. Under such conditions, the contribution of multiply charged aerosols to the polar conductivity becomes almost comparable or even exceeds that of small ions.

## CONCLUSIONS

The steady state particle charge distributions calculated from the ion-aerosol balance equations including the coagulation of multiply charged aerosols show variation with the aerosol concentration and the ionization rate and is close to the one obtained by Hoppel (1985) for the low aerosol concentrations. For the higher aerosol concentrations, however, the process of coagulation causes an increase in the concentration of the singly as well as multiply charged aerosols. This increase in the concentration of charged aerosols, however, continues only upto a critical value of aerosol concentration after which the distribution results into a decrease in the concentration of the singly charged aerosols. This critical value of the aerosol concentration is lower for the smaller ionization rates.

The polar conductivity computed from the charge distribution obtained here, supports our earlier conclusion that the inverse relationship between the polar conductivity and aerosol concentration is observed only up to a critical value of aerosol concentration which is determined by the ionization rate and the mean size of aerosols. In highly polluted conditions where the concentration of aerosols is higher than this critical value the concentration of the multiply charged aerosols becomes large and the polar conductivity increases with the increase in the aerosol concentration. Under such conditions of high pollution, the contribution of multiply charged aerosols to the polar conductivity becomes almost comparable or even larger than that of small ions and therefore must be taken in to account.

## REFERENCES


Adachi, M., K. Okuyama, and Y. Kousaka, Electrostatic coagulation of bipolarly charged aerosol particles, J. Chem. Eng. Japan, 14, 467-473, 1981.

Dhanorkar, S., and A. K. Kamra, Relation between electrical conductivity and small ions in the presence of intermediate and large ions in the lower atmosphere, J. Geophys. Res., 97, 20,345-20,360, 1992.

Dhanorkar, S., and A. K. Kamra, Calculation of electrical conductivity from ion-aerosol balance equations, J. Geophys. Res., 102, 30,147-30,159, 1997.

Hoppel, W. A., Ion-aerosol attachment coefficients and the diffusional charging of aerosols, Electrical Processes in Atmosphere, Ed. by H. Dolezalek and R. Reiter, 60-69, Dr. Dietrich Steinkopff Verlag, Darmstadt, 1977.

Hoppel, W. A., Ion-aerosol attachment coefficients, ion depletion, and the charge distribution on aerosols, J. Geophys. Res., 90, 5917-5923, 1985.

Hoppel, W. A., and G. M. Frick, Ion-aerosol attachment coefficients and the steady state charge distribution on aerosols in a bipolar ion environment., Aerosol Sci. & Techno., 5, 1-21, 1986.

Israël, H., Atmospheric Electricity, vol.1, pp. 1-317, Israël Program for Scientific Translations, Jerusalem, 1971.

Oron, A., J. H. Seinfeld and K. Okuyama, The dynamic behavior of charged aerosols, J. Collid & Interface Sci., 133, 57-65, 1989.

# NATURAL ATMOSPHERIC IONS AS ELECTROSTATIC SYSTEMS

V.V. Klingo

Voeikov MGO RCARS, St. Petersburg, Russia

ABSTRACT: Electrostatic parameters of atomic and molecular natural atmospheric ions have been calculated on a basis of the simplest quantum-mechanical approach. Electron wave functions of atomic orbitals are taken in the Slater-Zemer form. Necessary parameters have been determined for ions: $H^+$, $N^+$, $O^+$, and $O^-$. Classical analogues of diatomic molecules ions are found by a method of covalent bonds. The diatomic molecules ions $H_2^+$, $N_2^+$, $O_2^+$, and $O_2^-$ are three centers of charges with a experimental value of the distance between atomic nuclei.

Global investigations of electrical processes in clouds must involve an electrical structure of natural atmospheric gas ions. In particular, the adsorbed ions electric field stimulates homogeneous and heterogeneous mechanisms of an ice phase formation in clouds (Klingo, 1996). The ice emergence affects on the cloud processes including the electrical processes.

Electrostatic parameters of atomic and molecular ions are calculated on a basis of the simplest quantum-mechanical (quasi-classical) approach. Electrostatic model of water molecule have been constructed from such approach. Electron wave functions of atomic orbitals are taken in approximate but analytical well-know Slater-Zemer form. A radical part of this wave function has the following form:

$$\Psi_{nl}(r) = \frac{N_n}{a_o^{3/2}} \left(\frac{r}{a_o}\right)^{n-1} \exp\left\{-\frac{r}{a_o}\varsigma_{nl}\right\} ,$$

$$N_n = \left(2\varsigma_{nl}\right)^{\frac{2n+1}{2}} \left[(2n)!\right]^{-1/2} , \qquad \varsigma_{nl} = \frac{Z - S_{nl}}{n} \tag{1}$$

where $a_o$ is the Bohr radius, Z is the atomic number, $S_{nl}$ is the electron screening value of a given electron, n and l are the principal and angular-momentum quantum numbers.

An ion geometric dimension is the electron orbit radius $a_{nl}$ with the quantum numbers n and l, which identifies with the radius of the most remote sphere with the maximum probability of electron residence. One can neglect by insignificant spherical nonsymmetrical charge distribution in the presence of partially filled shells with $l \geq 1$. On account of the expression (1), radius $a_{nl}$ takes the form

$$a_{nl} = \frac{n^2 a_o}{Z - S} \tag{2}$$

where $S_{nl}$ is established on a basis of the Slater rules. The values $a_{nl}$ are listed for some atmospheric ions.

| Ion | $H^+$ | $N^+$ | $O^+$ | $O^-$ |
|---|---|---|---|---|
| $a_{nl}$, $m \cdot 10^{10}$ | 0.76 | 0.50 | 0.45 | 0.50 |

Thus, the gas atomic ion electrostatic model of definite chemical composition includes the point ion charge which is localized in spherical volume center with the radius $a_{nl}$.

Modern methods features of the electron structure molecules calculation in a quantum chemistry far deviate from the purpose in view of a present investigation. Basic principles will be only used. The molecule complex structure will be reduced to an electrical field source of sufficiently simple form. The molecule electrical structure is calculated at immovable atomic nuclei (the Born-Oppenheimer adiabatic approach). Molecules electron wave functions are linear combinations of atomic wave functions. The calculation of the molecule hydrogen positive ion is described in detail. Atomic nuclei with indexes $\alpha$ and $\beta$ dispose at distance R. $r_\alpha$ and $r_\beta$ are distances from this nuclei to a single electron. The electron wave function is written as

$$\Psi_{1S} = \alpha\Psi_\alpha + \beta\Psi_\beta \ ,$$

$$\Psi_j(r_j) = 2\gamma^{3/2} e^{-\gamma r_j} \ , \quad \gamma = \frac{\varsigma_{1S}}{a} \ , \quad \varsigma_{1S} = 1 \ , \quad j = \alpha, \beta \tag{3}$$

where $\Psi_j(r_j)$ is a normalized wave function of (1), $\alpha$ and $\beta$ are constant coefficients, they are equal by symmetry. The normalizing condition of the wave function $\Psi_{1S}$ gives

$$\alpha = \beta = \frac{1}{\sqrt{2(1 + I_{1S})}} \tag{4}$$

where $I_{1S}$ is the integral of overlap of bonding orbitals which has the form in coordinate system with center in the atomic nucleus of $\alpha$ index:

$$I_{1S} = \int \Psi_\alpha \Psi_\beta d\vec{r}_\alpha = 4\gamma^3 \int e^{-\gamma(r_\alpha + r_\beta)} d\vec{r}_\alpha \tag{5}$$

Integral $I_{1S}$ is found by means of the Fourier transformation.

$$\frac{e^{-\gamma r}}{r} = \frac{1}{2\pi^2} \int e^{i\vec{k}\vec{r}} \frac{d\vec{k}}{k^2 + \gamma^2} \tag{6}$$

Differentiating both part of (6) with respect to $\gamma$, we find the expression of $\Psi_j(r_j)$ (3). Inserting $\Psi_j(r_j)$ into (5), we obtain

$$I_{1s} = \frac{32\gamma^5}{\pi}\int\frac{e^{i\vec{k}\vec{R}}}{\left(k^2+\gamma^2\right)^4} \quad , \quad \vec{R} = \vec{r}_\alpha - \vec{r}_\beta \ . \tag{7}$$

taking into account the equality

$$\int e^{i\left(\vec{k}_1+\vec{k}_2\right)\vec{r}}\,d\vec{r} = 8\pi^3\delta\left(\vec{k}_1+\vec{k}_2\right)$$

Differentiating both part of (6) three times with respect to $\gamma^2$ on account of (7), we find the final expression of the overlap integral.

$$I_{1s} = \frac{\pi}{4}e^{-\gamma R_{1s}}\left(1+\gamma R_{1s}+\frac{1}{3}\gamma^2 R_{1s}^2\right) \tag{8}$$

The experimental value of the distance between ion hydrogen nuclei $R_{1S} = 1.06 \cdot 10^{-10}$ m, $\gamma R_{1S} = 2.0$, $I_{1S} = 0.459$. The electron orbitals radius at atomic nuclei is from (2) $a_{1S} = a_o = 0.529 \cdot 10^{-10}$ m.

Ion $H_2^+$ quasi-classical approach as electrical field source - electrostatic system includes two protons at the distance $R_{1S}$, which are surrounded by the general electron, and the same electron which is distributed between the protons. Electron «parts» a probabilistic meaning are $\alpha^2 = \beta^2 = 1/2(1+I_{1s})$ at each proton and $I_{1s}/(1+I_{1s})$ at a middle of axis between the protons. Numerical values of these point charges in charge electron units e are positive charges $0.657e^+$ at the protons and a negative charge $0.315e^-$ between the protons.

Electron orbitals of molecular ions $N_2^+$, $O_2^+$, and $O_2^-$ will be considered. Constructed electron wave functions these ions satisfy basic principles both quantum-mechanical description of electron systems and a formation of stable molecules with a covalent bond. Atomic electron shells subdivide into electron closed shells and valent shells. The wave functions of the closed shells to a considerable extent conserve electron configuration of isolated atoms. Each electron of the covalent bond ia ascribed to two nuclei.

$$\Psi_{2p} = \alpha\Psi_{\alpha,2p} + \beta\Psi_{\beta,2p} \tag{9}$$

where the wave functions are related to 2p-electrons of N and O atoms. They are taken from (1). The parameter $\zeta_{2p}$ in (9) equals semisum his values for neutral atom and corresponding ion. Normalization condition of $\Psi_{2p}$ in leads to expression (4) for $\alpha$ and $\beta$ with a replacement of the overlap integral $I_{1S}$ on $I_{2p}$.

$$I_{2p} = \frac{N_2^2}{a^4} \int r_\alpha r_\beta e^{-\gamma(r_\alpha + r_\beta)} dr_\alpha , \quad \gamma = \frac{\zeta_{2p}}{a_o} \tag{10}$$

The integral $I_{2p}$ is found by method which described above for $I_{1S}$ of (5) with sufficiently bulky calculations. A result of twice times differentiation (6) with respect to $\gamma$ is inserted into (10). The expression for $I_{2p}$ is obtained after differentiation (6) five times with respect to $\gamma^2$.

$$I_{2p} = \pi e^{-\gamma R} \left[ 12 + 12\gamma R + \frac{26}{9}(\gamma R)^2 + \frac{2}{3}(\gamma R)^3 + \frac{4}{45}(\gamma R)^4 \right] \tag{11}$$

The electrical field of the ions $N_2^+$, $O_2^+$, and $O_2^-$ will be added from the spherically symmetrical field of electron shells $1s^2 2s^2$ together with the atomic nucleus and the field of sum of 2p-electrons around and between the nuclei. The total sum of 2p-electrons in the ions $N_2^+$, $O_2^+$, and $O_2^-$ correspondingly equals 5, 7, and 9. The probabilistic distribution each from 2p-electrons for these ions is expressed as the distribution of 1s-electron in $H_2^+$ ion. For example, the ion $O_2^+$ consists of two positive charges $q^+$, which are equal $8e^+ - 4e^- - 7e^- / 2(1 + I_{2p})$, and the negative charge $q^-$, which is equal $7e^- I_{2p} / (1 + I_{2p})$. Calculation results of molecular ions parameters are represented in Table 1.

TABLE 1. Values of the parameter $\zeta_{2p}$ (1), the orbital radius $a_{2p}$ (2), the experimental distance between nuclei R, the overlap integral $I_{2p}$ (11), and the charges $q^+$, $q^-$ for the diatomic molecules ions

| Ion | $N_2^+$ | $O_2^+$ | $O^-$ |
|---|---|---|---|
| $\zeta_{2p}$ | 2.03 | 2.36 | 2.18 |
| $a_{2p} \cdot 10^{10}$ m | 0.519 | 0.448 | 0.484 |
| $I_{2p}$ | 6.54 | 3.52 | 4.54 |
| $R \cdot 10^{10}$ m | 1.26 | 1.34 | 1.34 |
| $q^+$ in e | 2.67 | 3.23 | 3.19 |
| $q^-$ in e | 4.34 | 5.45 | 7.38 |

Klingo, V.V. Influence of Adsorbed Atomic and Molecular Ions Electric Field on Ice Phase Formation in Clouds. Proceedings of The Fourteenth International Conference on Nucleation and Atmospheric AEROSOLS. Helsinki. – P. 322 – 325, 1996.

# ON FACTORS DETERMINING THE VARIATIONS OF THE ELECTRIC CHARACTERISTICS OF A SURFACE LAYER

A.I.Petrov, G.G.Petrova, I.N.Panchishkina

Department of Physics and Mathematics, Rostov-on-Don State Pedagogical University, Russia

ABSTRACT: During the study of electrode layer atmospheric – electrical characteristics were being studied within the other physical characteristics of atmosphere surface layer and upper layer of soil. Vertical profiles of polar conductivities in conditions of different atmosphere stratification for four points of observations with different contents of radon-222 in the soil and with different outcome of it into the atmosphere are presented in this study. Participation of convection and diffusion components of mechanical transfer current from atmosphere to earth in different conditions of thermal and dynamical unstability of surface layer was analyzed. The values of Dolezalek criteria for different conditions were estimated.

## INTRODUCTION

Electrical processes of lower atmosphere are inseparable part of all the physical processes in it. That is why the physical interpretation of atmospheric electrical measurement results is impossible without study of those conditions, within those in which the measurements were taken. The analyses of atmospheric electrical data together with the data of air surrounding physical condition gives favor to inner concern of nature of phenomenons being studied, which gives the possibility of analyzing the development of processes in electrode layer in this or other conditions. The mentioned mode gives the possibility to ensure so-called conditions of "fair whether", which is urgent for selection of atmospheric electrical data within the solving of global problems of atmospheric electricity, within the search of sun-earth connections or the connections of Earth electrical and magnetic fields. And the last, the usage of atmospheric electrical characteristics as pollution indicators of atmosphere in course of solving of ecological problems needs the knowledge of typical natural variations of these characteristics for the skill of differentiating from them the variations of antropoghenic nature. The discussed approach for solving atmospheric-electrical problems caused complex character of experimental studies of electrode layer of atmosphere, being carried out by us in course of last years. The complex of measurements and the points of study were presented earlier [Petrov et al., 1996]. Nevertheless, we should mention that Rostov-on-Don is a great industrial centre in black-soil steppe zone in the south of Russia. Settlements Pervomaiskoye and Mikhailovka (15 km apart each other) are situated in the Northern part of Rostov region, in agricultural zone far off from industrial centres. The measurements in the zone of Baikal Lake were taken in the settlement Bolshiye Koty, 18 km to the North from the source of the Angara River. The site of studies at Mikhailovka was located in some 200 metres from the bank of a small steppe river, and at the Baikal - at the same distance from the shore of the lake. In all the points of observations the sites were free of vegetation. The measurements were taken in summer months of 1989-1998 period.

## DISCUSSION OF THE RESULTS

As our data, so the data of other authors show, that one of the main factors defining the electrical condition of surface layer, is its stability [Petrov et al., 1996, Knudsen et al., 1989] and is connected at once with the mentioned intensity of turbulent mixing. The weakening of vertical movements after the sunset encourages the storage, in the nearest pre-ground layer in conditions of absence of wind, of different impurities, e.g. radioactive gases diffusing from the ground into the atmosphere. This leads to the growth of conductivity in surface layer in quiet nights in conditions of stable stratification of atmosphere (fig.1). Parameter of stability, so as the coefficient of turbulence, was calculated by the difference of air temperature at the height of 2 and 0.15 meter and the speed of wind at the height of 2 meters (according the method after Budiko). As it is seen from the mentioned figure, under the conditions of surface layer instability of (mainly in the day time hours with developed turbulence) the values of polar conductivities are not great and are constant according to the height in lower 5 meters of atmosphere. In conditions of stable stratification conductivity grows through the whole 5-meter layer, in particular, in the lowest layers of it. The highest conductivity on these layers is marked in Pervomaiskoye settlement, for which the highest concentration of radon is characteristically. Conductivity in Rostov-on-Don, in the whole, is lower than in other points due to the aerosol pollution contamination of industrial centre community air, but for the great quantity of radon in the soil, conductivity of atmosphere nevertheless sufficiently grows at once near the ground surface, while sufficiently lowering within the height. What for Mikhailovka settlement, with its relatively low concentration of radon-222 in the soil, marginal change of conductivity within the height, even with absence of noticeable turbulence mixing, is characteristically. The data of radon concentration on the measuring site at the Baikal are not obtained.

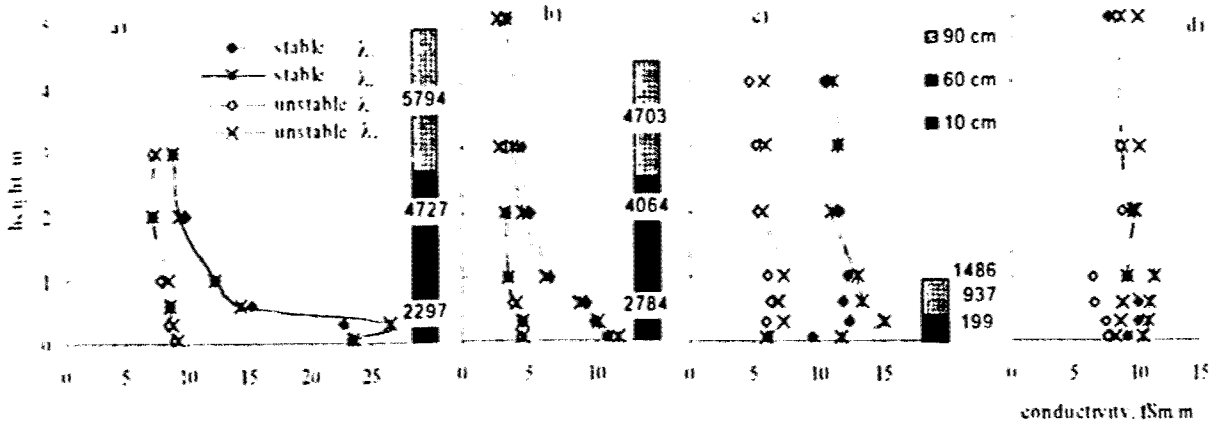


Fig.1. Vertical profiles of polar conductivities within unstable and stable stratification of surface layer of atmosphere: a) Pervomaiskoye site (1- 42 hours, 2 – 58 hours); b) Rostov-on-Don site (1 - 61 hours, 2 - 42 hours); c) Mikhailovka site (1- 45 hours, 2 - 182 hours); d) Baikal site (1 - 30 hours, 2 - 31 hours). - and radon-222 concentration in soil at different depth in these sites

Judging to the vertical profile of conductivity, the soil emanates here weakly. One should mention that the emission of soil gas into the atmosphere depends on the soil condition. At the Baikal site the radon concentration in the soil is either low, or the radon emission into the atmosphere is impeded. The last is possible due to the proximity of the shore of the lake the soil is soaked with moister to that condition that its pores are bridged and the gas exchange is hindered. Relatively high values of conductivity at the Baikal site, not taking in consideration supposed weak emanation of soil, are due to the exceptionally purity of air community, absence of aerosols. In course of radon-222 measurements it was noticed, that not always in night hours, without any wind, within ground surface radon is concentrated. The analyses of results detected the fact, that the distribution of soil temperature in course of depth influences the emission of radon from the soil provided other equal conditions. In course of quiet nights at Mikhailovka site, the more radon concentration in the ground layer was, the warmer the soil was at the depth of 20 cm in comparison to the 5-cm depth (fig.2). Within the following distribution of warmth in the soil, the warm air outcome from its depth, having lower density, emanates through the soil pores into the atmosphere and enriches the last with radon. This, on its turn, causes noticeable growth of conductivity lower than the level of 1 meter. The dependence of conductivity on the concentration of radon for quiet nights at Mikhailovka site is shown at figure 3. At Mikhailovka site at the bank of the river in night hours the fogs are frequent. One should mention, that for the foggy night hours the inclination of regression line of conductivity according to radon is less, so as to the scatter of points, what shows the activity of the other, not radon, mighty factor, affecting conductivity. In the studied phenomenon this is obviously aerosol. Out of figure 4 it comes, that in the conditions of presence of noticeable radon-222 concentration in the soil, being able to emanate from the soil into the atmosphere in the layer of 0.3-1 m there were high degree negative gradients of polar conductivities observable. But already within the coefficient of turbulence of 0.3 $m^2/c$ the gradients of the conductivities practically vanish (fig.4a,b). In condition of soil emanation absence any noticeable gradients in this layer are not formed even within weakening of turbulence mixing (fig.4c,d). The series of conductivity gradient regression of turbulence coefficient are approximated by logarithmic relationship.

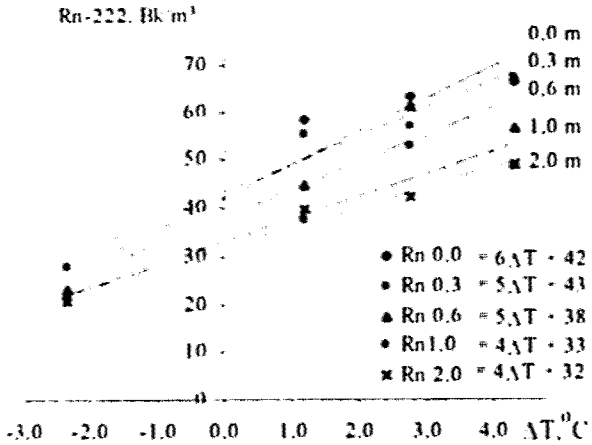


Fig.2. The concentration of radon-222 (Rn-222) in windless nights under the condition of variations i differences of soil temperatures (ΔT) at the depth of 20 and 5 cm (Mikhailovka site, 123 hours).

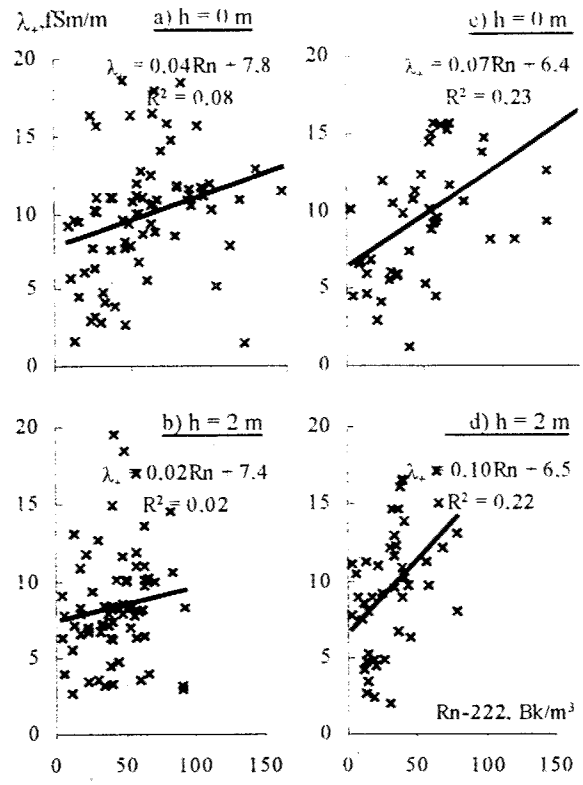


Fig.3. Lines of conductivity ($\lambda_+$) regression according to the radon-222 concentration (Rn-222) at Mikhailovka site at windless night hours: a, b – fog given (36 hours); c, d – clear nights (26 hours).

The tightest mode of connection with stratification of the surface layer and the intensity of turbulent mixing the processes of exchange in charge between the earth surface and the atmosphere is connected. The measuring by us directly of mechanical transfer current density from atmosphere to earth $i_t$ shows the growth within the intensity of turbulent mixing, if regarding its absolute notions (fig.5). Obviously, the diffusion component of mechanical transfer current $i_d$ here reveals itself. The density of the mechanical transfer current, as it is known, is $i_t = i_c + i_d$, where $i_d = K\dfrac{d\rho}{dz}$ - the diffusion current density ($K$ - the coefficient of turbulent diffusion $\rho$-space charge density), $i_c = \rho V$ -the convection current density ($V$ -the speed of vertical convection streams of air). As it is seen from figure 5 the value of $i_t$ in diffusion current absence (under $K$ =0) is equal to 0. Obviously, in these conditions the charge transfer from the atmosphere to the ground is conducted exceptionally by means of convection current. The acquired regression dependence allows evaluating the amount of this current density for the hours with $K \approx 0$. The nearest 0 values of $K$ are registered in windless hours with inverse air temperature distribution. As it comes out of figure 5 in the discussed conditions the density of convection component for the negative mechanical transfer current made in average -0.52 pA/m$^3$, and for positive one – 0.23pA/m$^3$. The regression equation is $i_t = a + b \ln K$ . Here $a$ and $b$ are any empirical coefficients.

Table 1, which presents the results of values averaged for different conditions of thermal and dynamic instability of surface layer, offers also the scheme of especial for this conditions mechanism of the charge transfer from the atmosphere to the ground. One should mention that the results, presented in the table, are averaged only for the periods when the negative current of mechanical transfer was observed. The results for positive notions $i_t$ are analogical, although the positive meanings through analyzed data make only 20 % of the all cases and figural notion of the latter 2-3 times lower in average than those for the negative current of mechanical transfer.

It was of interest to analyze how does the criteria $\Omega$, offered by Dolezalek [5], depends on the degree of atmospheric stability for evaluating the conditions of "fair whether" and being defined as $\Omega = i / i_\lambda$, where $i$ is the vertical electric "atmosphere-earth" current density, $i_\lambda$ is conductivity

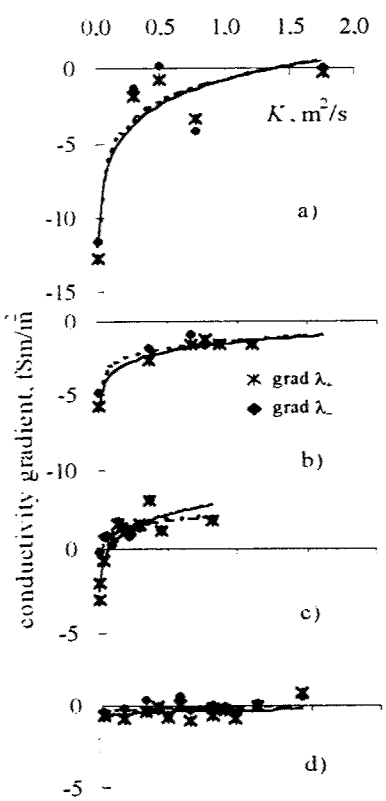


Fig.4. Dependence of conductivity gradient in the layer 0.3 – 1 m upon the coefficient of turbulence ($K$) in the surface layer: a) Pervomaiskoye site (169 hours); b) Rostov-on-Don site (108 hours); c) Mikhailovka site (395 hours); d) Baikal site (206 hours).

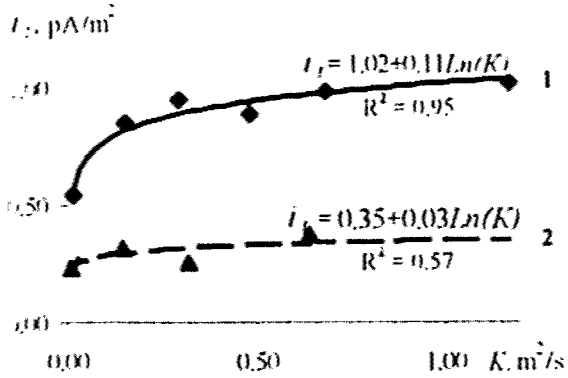


Fig.5. Dependence of mechanical transfer curren density ($i_t$) absolute values upon the coefficient of turbulence ($K$) at Mikhailovka site: 1 – for negative values of current density (469 hours); 2 – for positive values of current density (116 hours).

current density to the ground surface. So as $i = i_c + i_\lambda$, then $\Omega$ we may define as $\Omega = \frac{i_c + i_\lambda}{i_\lambda}$ and as follows $\Omega = 1 + \frac{i_c}{i_\lambda}$ If means $\Omega$ the nearer to 1, than less contribution to the transfer of a charge from the atmosphere to the earth surface the mechanical transfer current brings in comparison with the current of conductivity. It follows that provided $\Omega \approx 1$ one may neglect mechanical transfer of charges and regard the law of Ohm being applied for the surface layer. It is obvious from figure 6 that the nearest for 1 is criteria $\Omega$ under the conditions of surface layer stability. Within unstable stratificated surface layer the mechanical transfer current becomes comparable with the conductivity current, and $\Omega$ falls off from 1. It may occur, that the urgency of atmosphere lower layer stability must be included in the list of conditions, defining the state, so called concerning the atmospheric electricity, "fair whether".

| | U2<0,5 | U2>0,5 |
|---|---|---|
| | *windless nights* | *wnd nights* |
| T2-T0,5>0,3 | **-0,51** *0,00* $i_c$ ↓ | **-0,76** *0,20* $i_c$↓ $i_d$↻ |
| | *windless days* | *wnd days* |
| T2-T0,5<0,0 | **-0,28** *0,01* $i_d$ ↻ | **-1,04** *0,39* $i_d$↻ |

Table 1. The average values of mechanical transfer "atmosphere-earth" current density ($i_t$) for different conditions of thermal and dynamic instability of surface layer (Mikhailovka site).
$T_2$ and $T_{0,5}$ – meanings of air temperature at the height of 2 and 0,5 meters correspondingly; $U_2$ – the wind speed at the height of 2 meter; **-0,51**-the values of $i_t$, pA/m³; *0,01* – the coefficient of turbulence average values.

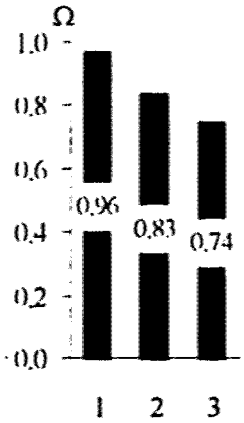


A schematic representation of:

a) $i_c$ ↓ - convection current; b) $i_d$ ↻ -turbulent diffusion current;

c) $i_c$↓ $i_d$↻ -mechanical transfer current with its components, the contribution of which is substantial in these conditions. Annotation: convection current under T2-T0,5 < 0 (daytime hours) is directed upward, i.e from the ground surface. That is why it doesn't bring any charge to the ground in daytime and thus it is not taken into consideration.

Fig.6. The Dolezalek criteria $\Omega$ under the different of the atmosphere surface layer stratification (Mikhailovka site): 1- stable stratification; 2 – neutral stratification; 3 – unstable stratification.

REFERENCES


Petrov, A.I., Petrova, G.G., and Panchishkina, I.N., Measurements of polar conductivities in the surface layer of the atmosphere, *in Proc.10th Int. Conf. Atm. Electricity*, 188--191, 1996.

Petrov, A.I., Petrova, G.G., and Panchishkina, I.N., Variations of vertical "atmosphere-earth" current components and its probable interpretation, *in Proc.10th Int. Conf. Atm. Electricity*, 548--551, 1996.

Knudsen, E., Israelsson, S., and Hallberg, B., Measurements of the electrode effect over flat, snow-covered ground, *J. Atm.Terr.Physics*, vol.51 № 6, 521--527, 1989.

# ON THE DESCRIPTION OF ATMOSPHERIC ELECTRIC FIELD AND CURRENT UNDER INHOMOGENEOUS CONDUCTIVITY

S.S. Davydenko, and P.A. Bespalov

Institute of Applied Physics of Russian Academy of Science,
46 Ulyanova st., 603600 Nizhny Novgorod, Russia

ABSTRACT: An approach to description of global electric processes under inhomogeneous distribution of atmospheric electric conductivity is elaborated. The conductivity is assumed to be varying arbitrary with latitude and increasing exponentially with altitude. Due to separation of variables established in a general equation describing an atmospheric electric potential, a set of the ordinary differential equations is obtained and solved by expansion into a generalized power series. A method of the eigenvalue spectrum evaluation and properties of the appropriate eigenfunctions are considered. To estimate responses of global atmospheric electric field and air-earth current to variations of latitude conductivity profile, a model of global electric circuit is constructed taking into account both the spatial conductivity distribution and electric sources connected with large-scale magnetospheric convection. Using the approach elaborated, an exact general solution of the problem is obtained. It is shown that latitude variation of terrestrial atmospheric conductivity leads to appearance of additional latitude homogeneous electric potential in the lower atmosphere with the magnitude of about 15% of the global ground-ionosphere voltage.

## INTRODUCTION

To construct an adequate model of global electric processes in the Earth's environment, one needs to know both electric sources distribution and electric properties of the media. As known, electric conductivity of terrestrial atmosphere depends significantly on the altitude above the planetary surface and on geo-coordinates of a measurement point. That dependence appears due to change of intensity of external ionization sources and differences in local meteorological conditions. Atmospheric conductivity at low heights, in the austasch layer, significantly depends on the near-surface turbulence, ground properties, Earth's radioactivity and has a complex spatial distribution. When receding from the ground, a contribution of the near-surface processes to the conductivity formation decreases and a cosmic rays become the main factor forming an exponential growth of the conductivity with altitude and its large-scale change with latitude.

A spatial variation of atmospheric conductivity leads to a significant complication in calculation of global circuit parameters and requires a complex numerical consideration. In some cases, however, it is useful to estimate an influence of the conductivity profile on a field and current distribution. In the present work, we elaborated a general method of calculation of electric field and current assuming atmospheric conductivity to be a product of two functions depending on the altitude and latitude respectively.

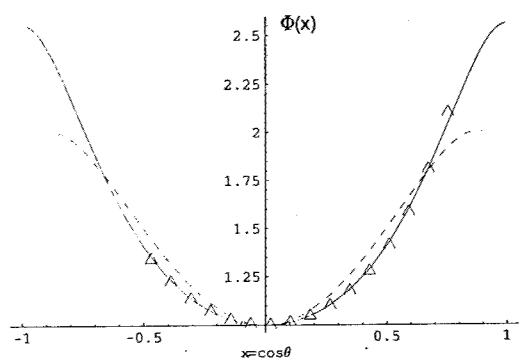


Figure 1: Results of atmospheric conductivity measurements [*Driscoll et al.*, 1996] (triangles) as compared to the conductivity profile considered by *Hays and Roble*[1973] (dashed line) and to the model distribution (3) under A = 1.14913 (solid line).

## DESCRIPTION OF THE MODEL

Let us suppose that a planet of radius $r_p$ and conductivity $\sigma_p$ is surrounded by atmosphere of height $h$ and conductivity

$$\sigma_a(r,\theta) = \sigma(r)\Phi(\theta), \tag{1}$$

where

$$\sigma(r) = \sigma_{a0}\exp(r/H), \tag{2}$$

$$\Phi(\theta) = \left(\frac{1+\mathcal{A}}{\sin^4\theta + \mathcal{A}}\right)^{3/2}. \tag{3}$$

Here $\sigma_{a0}$ is the conductivity at the planetary surface at the equator, $H$ is the scale height of the conductivity variation, $\mathcal{A}$ is a dimensionless parameter, $r$ and $\theta$ are a distance to the planetary center and a polar latitude angle respectively. A comparison of the latitude profile (3) under $\mathcal{A} = 1.14913$ with recent observational results and with one of the known conductivity distribution models is presented in Fig.1.

It is assumed that differential rotation of the well-conducted planetary plasma envelope provides the electric potential $U_a(\theta)$ at the upper atmospheric boundary $r_a = r_p + h$. Since we are looking for a stationary solution, the radial component of the electric current density must be continuous and a net current flowing through the upper atmospheric boundary must be zero. The above conditions and a continuity of the electric potential at the boundaries of the media present a set of boundary conditions of the problem.

## BASIC EQUATIONS AND GENERAL SOLUTION

Electric potential, field and current density in the model can be described by the equation for electric current density $\boldsymbol{j} = \sigma(r,\theta)\boldsymbol{E}$ and by the stationary continuity equation $\mathrm{div}\boldsymbol{j} = 0$. Taking into account that an electric field is potential, one can reduce these equations to the following second-order partial differential equation with respect to the electric potential $\varphi$:

$$\mathrm{div}(\sigma(r,\theta)\nabla\varphi) = 0. \tag{4}$$

Using the conductivity model (1) and presenting $\varphi(r,\theta)$ as a product of functions $\mathcal{F}(r)$ and $\mathcal{G}(\theta)$, one can separate variables and present the equation (4) as a set of the following ordinary differential equations:

$$(r^2\mathcal{F}'_r(r))'_r + r^2(\ln\sigma(r))'_r\mathcal{F}'_r(r) - \lambda^2\mathcal{F}(r) = 0, \tag{5}$$

$$((1-x^2)\mathcal{G}'_x(x))'_x + (1-x^2)(\ln\Phi(x))'_x\mathcal{G}'_x(x) + \lambda^2\mathcal{G}(x) = 0, \tag{6}$$

where $x = \cos\theta$, $\lambda$ is a real separation constant.

A general solution of the equation (6) can be presented as the power series

$$\mathcal{G}(x) = \sum_{k=0}^{\infty} a_k(x-1)^k. \tag{7}$$

Substituting (7) into the equation (6) and presenting the latitude conductivity profile as $\Phi(x) = \sum_{k=0}^{\infty}\phi_k(x-1)^k$, one can obtain the following recursion relation for the power series coefficients

$$a_k = -\frac{1}{k^2}\sum_{n=0}^{k-1} a_n\left\{\lambda\left(-\frac{1}{2}\right)^{k-n} + n\left(\phi_{k-n}(k-n) - \left(-\frac{1}{2}\right)^{k-n}\right)\right\}. \tag{8}$$

To find a general solution of the equation (6), one needs to determine an eigenvalues spectrum using the known properties of the solution. In our problem, such a property is a finiteness of eigenfunctions at the points $x = \pm 1$. In the same time, due to a symmetry of the latitude conductivity profile (3) with respect to the point $x = 0$, eigenfunctions of the equation (6) must be either even or odd. That possesses us to consider separately the conditions $\mathcal{G}(0) = 0$ and $\mathcal{G}'(0) = 0$ jointly with finiteness of the eigenfunctions at one of the point $x = \pm 1$ only. Taking into account the above properties, one can obtain a discrete eigenvalues spectrum $\lambda_j$ assuming $a_0 = 1$ and solving the equations

$$\sum_{k=0}^{\infty} a_k(-1)^k = 0, \qquad \sum_{k=1}^{\infty} k a_k(-1)^{k-1} = 0. \tag{9}$$

It should be pointed out that the equation (5) has a continuous eigenvalue spectrum, so eigenvalues of the problem coincide with eigenvalues $\lambda_j$ of the equation (6).

Using the obtained eigenvalues and relation (8), one can construct the appropriate eigenfunctions $\mathcal{G}_j(x)$ of the equation (6) and, in the similar way, general solutions $\mathcal{F}_j(r)$ of the equation (5), that is to obtain a general solution of the equation (4). It should be noticed that one of the most important properties of the eigenfunctions $\mathcal{G}_j(x)$ is their orthogonality, i.e. $\int_{-1}^{1}\mathcal{G}_j(x)\mathcal{G}_k(x)\Phi(x)dx = 0$ under $j \neq k$.

Now, one can estimate changes in a global electric pattern due to latitude variation of atmospheric conductivity. Let an external electric sources provides the electric potential

$$U_a(x) = D_0\mathcal{G}_0(x) + D_2\mathcal{G}_2(x) \tag{10}$$

at the upper boundary of the atmosphere $r_a$ [*Bespalov et al.*, 1996], then a general form of the solution is

$$\varphi(r,x) = \mathcal{F}_0(r)\mathcal{G}_0(x) + \mathcal{F}_2(r)\mathcal{G}_2(x), \tag{11}$$

where $\mathcal{F}_0(r)$ and $\mathcal{F}_2(r)$ are general solutions of the equation (5) under eigenvalues $\lambda_0$ and $\lambda_2$ respectively.

Under the given latitude conductivity profile (3), two lowest eigenvalues of the equation (6) are $\lambda_0 = 0$ and $\lambda_2 = \sqrt{6}$. The appropriate latitude eigenfunctions are

$$\mathcal{G}_0(x) = 1, \qquad \mathcal{G}_2(x) = P_2(x) - \left(\frac{231}{8}\mathcal{A} + 11\right)^{-1}\left(\frac{33}{5} + \frac{27}{5}P_4(x) - P_6(x)\right), \tag{12}$$

where $P_k(x)$ are the Legendre polynomials of the order $k$.

To determine the functions $\mathcal{F}_0(r)$ and $\mathcal{F}_2(r)$, one needs to substitute the radial conductivity profile (2) and the appropriate eigenvalue in the equation (5). A general solution of that equation under $\lambda_0 = 0$ is

$$\mathcal{F}_0(r) = A_0 + B_0\int \xi^{-2}\exp(-\xi)d\xi, \tag{13}$$

and under $\lambda_2 = \sqrt{6}$ is

$$\mathcal{F}_2(r) = A_2\mathcal{F}_{2,1}(r) + B_2\mathcal{F}_{2,2}(r), \tag{14}$$

where

$$\mathcal{F}_{2,1}(r) = \xi^2(\exp(-\xi)\xi^{-4})'_\xi, \qquad \mathcal{F}_{2,2}(r) = \xi^2\exp(-\xi)(\exp(\xi)\xi^{-2})'''_{\xi\xi\xi}. \tag{15}$$

Here $A_0$, $B_0$, $A_2$ and $B_2$ are constants depending on boundary conditions; $\xi = r/H$.

Substituting expressions (12) and (13)-(15) in the formula (11) and taking into account the discussed boundary conditions, an exact distribution of the electric potential was obtained. Using known values of atmospheric conductivity $\sigma_{a0} = 4,5\cdot 10^{-4}\ \mathrm{s}^{-1}$, total atmospheric height $h = 10^7$ sm, scale height of the conductivity variation $H = 6\cdot 10^5$ sm, Earth's interior conductivity $\sigma_p = 9\cdot 10^6\mathrm{s}^{-1}$ and Earth's radius $r_p = 6,37\cdot 10^8$ cm [*Volland*, 1987], the exact solution can be simplified and takes the form

$$\varphi_a(z,x) \approx D_0 + D_2\mathcal{G}_2(x)(1-\exp(-z/H)) \tag{16}$$

in the lower atmosphere ($z \ll h$), where $z = r - r_p$ is the altitude above the ground. Using (16), one can obtain distributions of the vertical electric field $E_{az}$ and current density $j_{az}$ in the lower atmosphere:

$$E_{az}(z,x) = -\nabla_z\varphi_a \approx -D_2\mathcal{G}_2(x)\exp(-z/H)/H, \quad j_{az}(z,x) \approx -\sigma_{a0}D_2\Phi(x)\mathcal{G}_2(x)/H. \tag{17}$$

To clear up an influence of the latitude conductivity variations, we solved the problem under the same boundary conditions assuming latitude-independent atmospheric conductivity. In that case, the equation (6) reduces to the Legendre equation with the spectrum of eigenvalues $\lambda_j^2 = j(j+1)$ and eigenfunctions $P_j(x)$. Using that eigenvalue spectrum, it is possible to find an asymptotic behavior of general solutions of the equation (5) and their first derivations under great values of the $\xi = r/H$:

$$\begin{aligned} &\mathcal{F}_{2k,1}(r) \sim 1 + o[\xi^{-1}], && \mathcal{F}_{2k,2}(r) \sim (-1)^{2k+1}\exp(-\xi)(\xi^{-2} + o[\xi^{-3}]); \\ &(\mathcal{F}_{2k,1}(r))'_r \sim j(j+1)\xi^{-2}/H + o[\xi^{-3}/H], && (\mathcal{F}_{2k,2}(r))'_r \sim (-1)^{2k}\exp(-\xi)(\xi^{-2}/H) + o[\xi^{-3}/H]), \end{aligned} \tag{18}$$

where $o[\xi^{-3}/H]$, $o[\xi^{-1}/H]$ are small terms of the appropriate order of magnitude.

The electric potential at the upper atmospheric boundary can be presented as a linear combination of the lowest even Legendre polynomials $U_a(x) = D_0 + D_2\sum_{k=0}^{3}\alpha_{2k}P_{2k}(x)$, where constants $\alpha_{2k}$ are defined by the expression (12). Taking into account the above values of $\sigma_{a0}$, $\sigma_p$, $H$, $h$ and $r_p$ and asymptotics (18), an exact distribution of electric potential in the lower atmosphere can be reduced to the following form:

$$\varphi_a^{(u)}(z,x) \approx D_0 + D_2\alpha_0\exp(-z/H) + D_2\mathcal{G}_2(x)(1-\exp(-z/H)). \tag{19}$$

Distributions of vertical electric field and current density corresponding to the potential (19) are

$$E_{az}^{(u)}(z,x) \approx D_2(\alpha_0 - \mathcal{G}_2(x))\exp(-z/H)/H, \quad j_{az}^{(u)}(z,x) \approx \sigma_{a0} D_2(\alpha_0 - \mathcal{G}_2(x))/H. \tag{20}$$

## DISCUSSION OF THE RESULTS

As seen from the expressions (16), (19) for electric potential and (17), (20) for vertical electric field and current density, a variation of atmospheric conductivity with latitude leads to appearance of an additional latitude-independent electric potential $\delta\varphi_a(z) = \varphi_a(z) - \varphi_a^{(u)}(z) \approx -D_2\alpha_0\exp(-z/H)$ and corresponding vertical electric field $\delta E_{az}(z) = E_{az}(z) - E_{az}^{(u)}(z) \approx -D_2\alpha_0\exp(-z/H)/H$ (see Fig.2). As follows from the expression (12), the coefficient $\alpha_0 = -(35A/8 + 5/3) \approx -0.15$, that is approximately equal to the ratio of the additional potential appearing near the ground to the voltage applied to upper boundary of atmospheric layer $D_2$. Assuming that the applied potential $U_a(x)$ is connected with a large-scale convection of the planetary plasma envelope, one can assume $D_2$ is of the order of unipolar potential $U = \dfrac{\mathcal{M}\Omega}{r_p c}$, where $\mathcal{M}$ and $\Omega$ are the dipole magnetic moment and angular velocity of the planet respectively, $c$ is the velocity of light [*Bespalov et al.*, 1996]. Since under the terrestrial conditions $U \approx 10^5$V, it appears that $\delta\varphi_a(0) \sim U\alpha_0 = 15$kV.

It should be noticed that more sophisticated models of atmospheric conductivity distribution can be used in the framework of the elaborated approach. In particular, longitude dependence of atmospheric conductivity and existence of the austasch layer can be naturally taken into consideration. The model can also take into account thunderstorms and other atmospheric electric sources as external currents with distributed magnitude in different regions of the atmosphere as well as the Earth's orography effect.

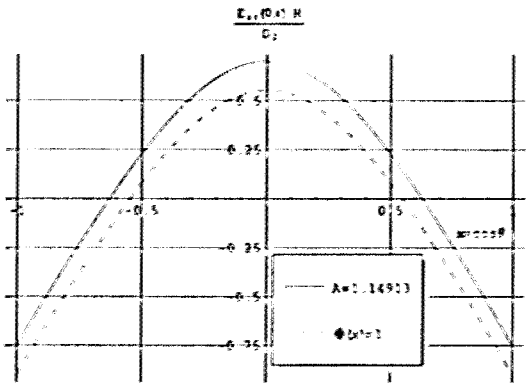

Figure 2: Normalized vertical electric field near the ground in the cases of latitude-independent atmospheric conductivity (dashed line) and model latitude conductivity profile (3) under A = 1.14913 (solid line).

## CONCLUSIONS

A new approach to the description of a global electric processes is elaborated. Considering an influence of the latitude profile of terrestrial atmospheric conductivity on global electric pattern, it is shown that the latitude conductivity variation leads to a significant redistribution of electric potential in the lower atmosphere, which is about 15% of the voltage applied to the atmospheric layer.

ACKNOWLEDGMENTS: The work was supported by RFBR grant No.98-02-16236 and by RAS grant for young scientist teams.

## REFERENCES

Driscoll, K.T., R.J. Blakeslee, J.C. Bailey, and H.J. Christian, Atmospheric Conductivity observations over a wide latitudinal range, in: *Proceedings of 10th International Conference on Atmospheric Electricity*, Osaka, Japan, 1996, P.176-179.

Hays, R.B., and R.G. Roble, A quasi-static model of global atmospheric electricity. 1. The lower atmosphere, *J.Geophys.Res.*, 84(17), 3291-3305, 1973.

Bespalov, P.A., Yu.V. Chugunov, and S.S. Davydenko , Planetary electric generator under fair-weather conditions with altitude-dependent atmospheric conductivity, *J.Atm.Terr.Phys.*, 58(5), 605-611, 1996.

Volland, H., Electromagnetic coupling between lower and upper atmosphere, *Physica Scripta*, T18, 289-297, 1987.

# GLOBAL VARIATIONS OF IONOSPHERIC POTENTIAL IN SURFACE LAYER

G.V.Kupovykh

Department of Physics,Taganrog State University of Radio Engineering,
Taganrog, Rostov region, Russia

ABSTRACT: Special features of the global variations of ionospheric potential in the surface layer have been studied by the models of the electrode effect. The changings of the eddy diffusion coefficient in twenty-four hours can explain the additional summer maximum in the duirnal variations of the electric field near the surface where the turbulent electrode effect takes place. Really it means that the variations caused by the turbulence diffusion are similiar to the unitary ones.

## INTRODUCTION

The observations of the atmospheric electric potential gradient above the ocean show the unitary variation with the period of twelve hours ( Carnegie curve) caused by the changings of the ionospheric potential [*Mauchly*,1926]. Usually the continental observations give different variations of the electric field near the surface [*Chalmers*,1957; *Kupovykh*,1996]. The common feature of the continental data is the appearance of the second maximum in diurnal variations of the electric field in the morning. The second maximum can not be explained by the effects of aerosol in the atmosphere,because the common regularity is not clear for all cases.The observations of the atmospheric electricity on the alpine station near Elbrus, where the concentrations of aerosol particles are small, show the appearance of the additional summer maximum (06-09) UT in atmospheric electric potential gradient ,but it does not appear in winter conditions [*Kupovykh*,1996]. When the strong turbulent mixing takes place,the values of the electrode effect at the height of 1-2 m depends on the eddy diffusion coefficient. [*Kupovykh, Morozov,*1992].

## MEASUREMENTS AND DATA ANALYSIS

The observations of the atmospheric electricity were made on the peak Cheget ( 3040 m above sea level) near Elbrus. In winter and spring the diurnal variations of the atmospheric electric field have the morning minimum (00-03) UT and the evening maximum (15-21) UT as the Carnegie curve.In summer the evening maximum is displaced to (18-21) UT and the second maximum of the electric field (06-09) UT takes place ( see Table 2,rows 2;3). There are not considerable concentrations of aerosol particles (less than $10^{9}$ $m^{-3}$) in the air and ionization rates are about 20 ion pair $\cdot$ $m^{-3}$ $\cdot$ $s^{-1}$ near the surface.

The average values of the eddy diffusion coefficient , calculated according to the meteorological dates ,are 0.8-0.9 $m^2 \cdot s^{-1}$ at the height of 1 m near the surface .In winter and spring the values of the diffusion coefficient are almost steady ,but in summer the diurnal variations take place ( see Table 2,row 4). All calculatons have been made according to informations for " fair-weather " conditions.

## THEORETICAL BACKGROUND

The steady-state governing equations for non-turbulent and turbulent surface layer are:

$$\frac{d}{dz}\left(\pm b_{1,2}\cdot n_{1,2}\cdot E - D(z)\cdot\frac{dn_{1,2}}{dz}\right) = q(z) - \alpha\cdot n_1\cdot n_2 \qquad (1)$$

and

$$\frac{dE}{dz} = \frac{e}{\varepsilon_0}\cdot(n_1 - n_2) \qquad (2)$$

where the notation is defined defined in Table 1. For nonturbulent case D(z) is zero and boundary conditions are $n_2(0)=0$, $E(0)=E_0$, $n_1(\infty)=n_2(\infty)=\left(q(\infty)/\alpha\right)^{-1/2}$. For the turbulent surface layer the eddy diffusion coefficient is D(z) and the boundary conditions are $n_1(z=z_0)=n_2(z=z_0)=0$, $n_1(\infty)=n_2(\infty)=\left(q(\infty)/\alpha\right)^{-1/2}$, $E(\infty)=j_0/\lambda(\infty)$, $\lambda(\infty)=\left(b_1\cdot n_1(\infty)+b_2\cdot n_2(\infty)\right)\cdot e$.

The exact form of the eddy diffusion coefficient is:

$$D(z)=D_1\cdot z, \quad D_1=u\cdot\frac{\aleph^2}{\ln z/z_0} \qquad (3)$$

The function of ionization rate is $q(z)=(7+4.8\cdot\exp(-2.362\cdot z))\cdot 10^6\ m^{-3}\cdot s^{-1}$.

TABLE 1. Notation for Equations (1)-(3)

| Variable | Definition | Baseline Value |
|---|---|---|
| $n_{1,2}$ | polar ions density | $\sim 10^9\ m^{-3}$ |
| E | electric field | $\sim 10^2\ V\cdot m^{-1}$ |
| $b_1$ | mobilities of positive ions | $1.2\cdot 10^{-4}\ m^2\cdot V^{-1}\cdot s^{-1}$ |
| $b_2$ | mobilities of negative ions | $1.4\cdot 10^{-4}\ m^2\cdot V^{-1}\cdot s^{-1}$ |
| $\alpha$ | recombination coefficient | $1.6\cdot 10^{-12}\ m^2\cdot s^{-1}$ |
| $z_0$ | parameter of roughness | $2.5\cdot 10^{-3}$ m |
| e | elementary charge | $1.6\cdot 10^{-19}$ C |
| $\varepsilon_0$ | electrical constant | $8.85\cdot 10^{-12}\ F\cdot m^{-1}$ |
| $j_0$ | electrical current density | $\sim 10^{-12}\ Amp\cdot m^{-2}$ |
| $\aleph$ | Karman constant | 0.43 |
| u | surface wind speed | $(0-6)\ m\cdot s^{-1}$ |

## THEORETICAL RESULTS AND DISCUSSION

The observations of the atmospheric electricity above the ocean have been made in conditions of the so-called classical electrode effect with uniform ionization rate and no aerosol (surface wind speed is not large). The thickness of the classical electrode layer is approximately 2-3 m. The average value of the electrode effect ($E/E_\infty$) is 1.4 at the height of 1 m and 1.1 at the height of 2 m. These results are almost independent of the electric field on the upper boundary of the electrode layer. Therefore the unitary variation of ionospheric potential shows itself well.(see Table 2,row 1).

In the continental observations of the atmospheric electricity the turbulent electrode effect usually takes place. The variations of the ionization rate and the aerosol can play an important part in electric state of surface layer. However , neither the action of aerosol particles nor the effects of atmospheric radioactivity but rather the variations of the eddy diffusion coefficient

determine the electrode effect and the variations of the electric field near the surface correspondingly.

The summer values of the eddy diffusion coefficient on the peak Cheget are presented in Table 2 (row 4), when there are the considerable daily changings of the meteorological parameters on the contrary to winter time data.

Using the model of the turbulent electrode effect the modeling of the Carnegie curve have been made at the height of 1 m ,where the electric field was measured. The experimental data of the electric field are presented in Table 2 (rows 2;3). The calculated values of the electrode effect and the electric field at the height of 1m are presented inTable 2 (rows 5;6). The theoretical results show that the appearance of the additional maximum (06 - 09) UT is caused by the turbulent diffusion in the surface layer. The increasing of the eddy diffusion coefficient increases the electrode effect near the surface.

TABLE 2. Diurnal Variations of Electric Field and Eddy Diffusion Coefficieht on the Peak Cheget (row 1-Carnegie curve; row 2- April; rows 3,4- August-September; row 5-electrode effect according to values of D; row 6- electric field at the height of 1 m according to values of D; <E> - average daily values of E) ; D-$m^2 \cdot s^{-1}$.

| N | UT | 00 - 03 | 03 - 06 | 06 - 09 | 09 - 12 | 12 - 15 | 15 -18 | 18 - 21 | 21 - 00 |
|---|---|---|---|---|---|---|---|---|---|
| 1. | E/<E> | 0.9 | 0.8 | 0.9 | 1.0 | 1.0 | 1.1 | 1.2 | 1.0 |
| 2. | E/<E> z ≈ 1 m | 0.7 | 0.8 | 1.0 | 1.0 | 1.0 | 1.3 | 1.3 | 1.0 |
| 3. | E/<E> z≈ 1 m | 0.8 | 0.9 | 1.2 | 1.0 | 1.0 | 1.0 | 1.1 | 1.0 |
| 4. | D z=1 m | 0.04 | 0.1 | 0.18 | 0.16 | 0.12 | 0.1 | 0.03 | 0.03 |
| 5. | $E/E_\infty$ z=1 m | 1.9 | 2.1 | 2.4 | 2.2 | 2.1 | 2.1 | 1.8 | 1.8 |
| 6. | E/<E> z=1 m | 0.8 | 0.9 | 1.0 | 1.0 | 1.0 | 1.0 | 1.2 | 1.1 |

## CONCLUSIONS

The theoretical and experimental results can be summarized as follows. The additional maximum in the unitary variation of the electric field is the result of the changings of the eddy diffusion coefficient due to meteorolgy. This effect can appear in "fair -weather "conditions on all continental stations when the turbulent mixing takes place .

## REFERENCES


Chalmers, J.A., Atmospheric Electricity, *Pergamon Press*, 421, 1967

Kupovykh, G., Negative space charge in surface layer, *Proc. 10 th Int.Conf. on Atm. Elect.*, 4,1996

Kupovykh, G.V. ,Morozov, V.N., Modelling of the electrode effect in surface layer, *Proc. 9 th Int. Conf. on Atm. Elect.*,2,615-618,1992

Mauchly ,S.J., Observation of the atmospheric electric potential gradient,*Res. of Dep.of Terr. Magn.*,6,1927

# A SENSOR FOR BALLOON MEASUREMENTS OF THE AIR CONDUCTIVITY

V I. Struminsky

Novosibirsk State University, Novosibirsk, RUSSIA

ABSTRACT: Small constant – altitude balloons are one of the best facilities of direct, long-duration experimental investigation of the stratospheric electricity. Because of the weight and power consumption limitations scientific equipment mounted on the payload that carried by the balloon should be as simple, light, economical as possible. A sensor for automatic conversion of the negative and positive components of the total electrical conductivity was especially designed for small balloon payload.

## INTRODUCTION

Electrical conductivity of the air can be measured by determination the rate of electric charge value decreasing on the surface of an insulating conductor with the equation [*Riecke*, 1903]

$$Q = Q_0 \exp\left(-\frac{\sigma t}{\varepsilon_0}\right)$$

where $Q_0$ is the initial positive electric charge; Q is the remaining charge after a time interval $t$; $\sigma$ is negative conductivity of the air, if the initial charge is positive or positive one, if the initial charge is negative; $\varepsilon_0$ is dielectric constant. This method has no wide field of applications in near - ground measurements because of relatively long time period of measuring process (some tens of minutes), but can be successfully applied to balloon and rocket investigations. The time of conductivity measurement with this method in the middle stratosphere is order of several seconds and in the mesosphere is of several tens milliseconds. Correct measurements in free atmosphere are possible only when the electric field strength generated by the charge of the conductor does not exceed appreciably the one existing in the environment. In another case the strong artificial electric field can modify significantly medium properties, in the first place, the spectra of ions mobility. It means, that the electric potential of conductor to the payload must be under several volts and less. Low value of the potential leads us to avoid traditional methods of charging the conductor using direct mechanical contacts because of perturbation caused by the contact potential difference and charge throw from the commutation circuit. Besides, low value of sensor potential makes possible to reduce its effect on the other measuring equipment, for instance, on the electric field meter operation.

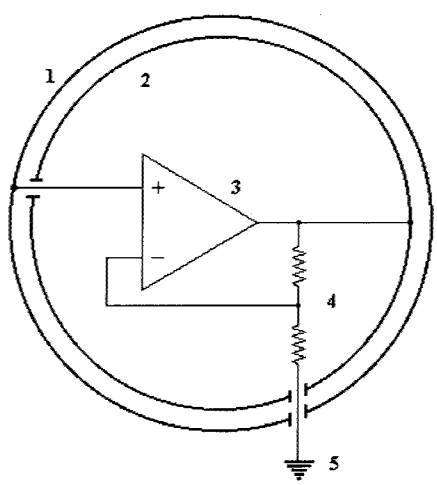


**Fig. 1. Spherical conductivity sensor.**

The best solution of the problem is charging the conductor without direct electrical contact between them and a voltage source.

Such sensor whose operation is provided by electric induction effect was developed especially for measurements under low electric potential of the "scattering body".

## SENSOR DESIGN

The sensor design is represented schematically in Fig. 1. The sensor consists of two insulated metal concentric spheres **1** and **2**, one inside another, high input impedance electronic comparator **3** and voltage divider **4**. The board with comparator and divider mounted on is located inside the internal sphere. Sensor "ground' is connected to payload body **5**. There are two grounded guard rings between

external and internal spheres for excluding direct electric charge flow from the inner sphere to the external.

Conductivity measurement is realized according to the method described in [*Struminsky, Frolow*, 1988].

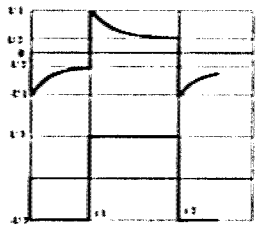

Fig. 2 Pulses sequence at the external sphere and at the sensor output

Let the positive voltage $U_3$ appears at the output of the comparator at the moment $t_1$ (Fig. 2). Further, the positive charge induced on the external sphere dissipates because of the negative air conductivity and the potential of the sphere decreases from $U_1$ level in the course of time. When the potential of the sphere achieves the level of comparator switching $U_2$ at the moment $t_2$, the comparator reverses its state and negative voltage is generated at the output. The process repeats itself, but now the positive conductivity causes the external sphere charge dissipation. Thus, the information about values of negative and positive conductivity components is contained in the duration of positive and negative comparator output pulses.

SHORT THEORY

As it was marked above, change of conductor charge with time is given by equation:

$$Q^{+} = Q_0^{+} \exp(-\tfrac{\sigma^{+} t}{\varepsilon_0})$$

Similar equation may be written for the negative conductor charge

$$Q^{-} = Q_0^{-} \exp(-\tfrac{\sigma^{-} t}{\varepsilon_0})$$

Electrical potential of the conductor relatively to the infinity is

$$\varphi^{+}(t) = \frac{Q_0^{+}}{C} \exp\left(-\frac{\sigma^{-} t}{\varepsilon_0}\right)$$

where C is the capacitance of the conductor. But in real balloon and rocket measurements the potential of conductor - conductivity sensor is measured relatively to another conductor (payload). If we charge these two conductors with the same charge value in opposite polarity the potential difference between the conductors is:

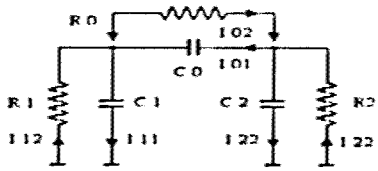


Fig. 3 Equivalent circuit of the sensor

$$U = \varphi_1 - \varphi_2 = Q_0\left(\frac{1}{C_1} + \frac{1}{C_2}\right)\exp\left(-\frac{\sigma t}{\varepsilon_0}\right)$$

$$\sigma = \sigma^{+} + \sigma^{-}$$

Let us consider the equivalent circuit of the sensor in Fig. 3, where $C_0$ is mutual capacity of the external sphere and payload (it is practically the mutual capacity of the external and the internal spheres). $C_1$ is capacity of the payload relatively to the environment; $C_2$ is the capacity of the external sphere. $R_1$ is resistance between the payload and the environment; $R_2$ is resistance between the external sphere and the environment. $R_0$ is

$$I_{02} = \frac{q_0}{R_0 C_0} = \alpha_0 q_0$$

$$I_{12} = \frac{q_1}{R_1 C_1} = \alpha_1 q_1$$

$$I_{22} = \frac{q_2}{R_2 C_2} = \alpha_2 q_2$$

$$I_{02} R_0 + I_{12} R_1 = I_{22} R_2$$

$$I_{22} + I_{02} = I_{01} + I_{21}$$

$$I_{01} + I_{12} = I_{11} + I_{02}$$

the resistor of known value, which is connected to the sensor in process of calibration. The Kirchhoff's equations system for this circuit is
where

$$\alpha_0 = (R_0 C_0)^{-1} \quad \alpha_1 = (R_1 C_1)^{-1} \quad \alpha_2 = (R_2 C_2)^{-1}$$

After transformation we have

$$\frac{dq_2}{dt}\left(1 + 2\frac{C_0}{C_2}\right) - \frac{dq_1}{dt}\left(1 + 2\frac{C_0}{C_1}\right) = -\left[\alpha_2 q_2\left(1 + 2\frac{R_2}{R_0}\right) - \alpha_1 q_1\left(1 + 2\frac{R_1}{R_0}\right)\right]$$

Solution is sought in the form

$$q_1,\ q_2 \sim \exp(kt)$$

$$k_{1\text{-}2} = \frac{C_0 C_1 C_2}{2(C_0 C_1 + C_0 C_2 + C_1 C_2)} *$$
$$* \left\{ [\alpha_0 R_0(\alpha_1 + \alpha_2) + \alpha_1 R_1(\alpha_0 + \alpha_2) + \alpha_2 R_2(\alpha_0 + \alpha_1)] \pm \sqrt{[\alpha_0 R_0(\alpha_1 + \alpha_2) + \alpha_1 R_1(\alpha_0 + \alpha_2) + \alpha_2 R_2(\alpha_0 + \alpha_1)]^2 - 4\alpha_1\alpha_2\left(1 + \frac{R_1}{R_0} + \frac{R_2}{R_0}\right)\left(1 + \frac{C_0}{C_1} + \frac{C_0}{C_2}\right)} \right\} \quad (1)$$

We can check the validity of solution when $C_0$ is equal to zero and $R_0$ is infinitely large. It corresponds to the case of two independently discharged capacitors $C_1$ and $C_2$.
In this case

$$k_1 = -\frac{1}{R_1 C_1}, \qquad k_2 = -\frac{1}{R_2 C_2}$$

When we calibrate the sensor with resistor of known value in nonconductive media ($R_1$, $R_2$ tend to infinity)

$$k_1 = -\left(R_0 C_0 + R_0 \frac{C_1 C_2}{C_1 + C_2}\right)^{-1}, \qquad k_2 = 0$$

(the last is particular case when the initial potentials equal to zero).
In common case an information concerning conductivity value is contained in (1). But this expression is too complicated for practical use. A simple solution may be obtained when $C_0 >> C_1 >> C_2$. If we calibrate the sensor with the resistor of known value $R_0$, we have

$$\ln \frac{U}{U_0} = -\frac{T_0}{R_0 C_0}$$

where $T_0$ is the pulse duration at the output. Further, taking into account that in process of conductivity measurement

$$\alpha_1 = \frac{1}{R_1 C_1} = \frac{\sigma^+}{\varepsilon_0}, \quad \alpha_2 = \frac{1}{R_2 C_2} = \frac{\sigma^-}{\varepsilon_0}$$

and the condition $C_0 >> C_1 >> C_2$, we obtain

$$k_1 = -\frac{1}{\varepsilon_0}\left(\sigma^+ \frac{C_1}{C_1 + C_2} + \sigma^- \frac{C_2}{C_1 + C_2}\right)^{-1}$$

If the conductivity components do not change significantly during one full cycle of the measurement $T_1$ is the pulse duration corresponding to positive conductivity measurement;

$$\sigma^+ \frac{C_1}{C_1 + C_2} + \sigma^- \frac{C_2}{C_1 + C_2} = -\frac{\varepsilon_0}{T_1} \ln \frac{U}{U_0} = \frac{\varepsilon_0 T_0}{R_0 C_0 T_1} \qquad \sigma^- \frac{C_1}{C_1 + C_2} + \sigma^+ \frac{C_2}{C_1 + C_2} = \frac{\varepsilon_0 T_0}{R_0 C_0 T_2}$$

$T_2$ is one corresponding to negative conductivity measurement.
The total conductivity is

$$\sigma = \sigma^+ + \sigma^- = \frac{\varepsilon_0}{R_0 C_0}\left(\frac{1}{T_1} + \frac{1}{T_2}\right)$$

We can calculate $\sigma^+$ and $\sigma^-$ separately

$$\sigma^+ = \frac{\varepsilon_0 T_0 (C_1 T_2 - C_2 T_1)}{R_0 C_0 T_1 T_2 (C_1 - C_2)} \qquad \sigma^- = \frac{\varepsilon_0 T_0 (C_1 T_1 - C_2 T_2)}{R_0 C_0 T_1 T_2 (C_1 - C_2)}$$

The advanced theory of sensor operation must include effects concerned with floating potentials, fhotocurrent from the sensor surface, diffusion velocities of light ions and some other.

## CONCLUSION

Description of simple spherical conductivity sensor is presented. A cylindrical version of the sensor was designed for rocket "mother – daughter" measuring system [*Struminsky*, 1986].

## REFERENCES


Riecke, E., Beitraege zur Lehre der Luftelektrizitaet. *Ann. Phys.* 12, 52 – 54, 1903

Struminsky, V.I., and A.S. Frolov, A method of measuring of gas medium conductivity, *A. C. SU #1392482*, 1988 (in Russian)

Struminsky, V.I., Horizontal component of mesospheric electric field from results of rocket experiment, *Cosmicheskie Issledovanya*, 24, N6, 938 – 941,1986 (in Russian)

# SEASONAL DEPENDENCE OF ELECTRICAL MOBILITY SPECTRA OF SMALL AIR IONS

Tiia-Ene Parts

Tartu University, Institute of Environmental Physics, 50090 Tartu, Estonia

ABSTRACT: Experimental results of the measurements of electrical mobility spectra of small air ions of one second of age during a period of 1986 to 1996 are presented. Temperature ~293 (+/-5) *K*, atmospheric pressure ~ 101.3 (+/- 1.5) *kPa*, relative humidity 30 to 80 % and chemical composition of the air were the most important variable circumstances in a fresh ventilated laboratory room at different seasons. It has been concluded that chemical composition of dominant small air ions does not particularly depend on the changes in air constituent due to several volatile, semivolatile organics and/or other air pollutant during the different seasons. The increase of water concentration in spring, summer and autumn should influence the electrical mobility of ions and consequently the chemical composition of later. The chemical reactions of water with most abundant gases and small ions in the air are discussed.

## INTRODUCTION

Air Electricity Laboratory of Tartu University has a long tradition of the investigation of charged particles in the air [*Tammet*, 1998; *Luts*, 1995; *Mirme*, 1994; *Salm et al.*, 1988; *Tamm et al.*, 1988]. Since 1975 the mobility spectra of small air ions have been measured in laboratory conditions by means of a special spectrometer for ions of one second of age [*Tammet et al.*, 1977]. Since 1985 the continuous measurement of mobility spectra of atmospheric ions was carried out in Tahkuse Observatory [*Hõrrak et al.*, 1994]. Our study of the influence of trace gases on the mobility spectra of small one second aged air ions was always accompanied by measurements of background spectra at different temperature, atmospheric pressure and relative humidity *i.e.* at the same experimental conditions [*Parts*, 1992]. The purpose of this work is to summarize the data of background and to bring out the most apparent peculiarities in mobility spectra at different seasons in laboratory experiments paying attention to chemical problems concerning the role of water in ion-molecular reactions.

## EXPERIMENTAL RESULTS AND DISCUSSION

The electrical mobility spectra of small air ions of one second of age were measured in laboratory conditions, that is at room temperature ~293 (+/-5) *K*, atmospheric pressure ~ 101.3 (+/- 1.5) *kPa* and relative humidity (RH) in the range of 30 to 80 *%*.

The period of the measurements extents to more than 10 years (1986 - 1996). The variability of temperature and atmospheric pressure indoors was small, +/-1.7% and +/-1.5%, respectively, comparing with RH variability +/-25%. The aspiration method allowed to achieve the sensitivity of experiments up to $10^{-9}$ (1 ppb), sometimes $10^{-10}$, for impurities like iodine, chlorine, pyridines and some other trace gases with high value of electron or proton affinity.

Figure 1 demonstrates the typical background mobility spectra at different seasons. The average data on mobilities are presented in Table 1.

The background mobility spectra *of positive ions* 1) has 2 remarkable peaks at 1.05 and 1.20 $cm^2V^{-1}s^{-1}$ with average mobilities 1.13 and 1.18 $cm^2V^{-1}s^{-1}$ in winter and spring, respectively; 2) has a predominant peak 1.25 $cm^2V^{-1}s^{-1}$ with average mobility 1.23 $cm^2V^{-1}s^{-1}$ in summer; and 3) has a large continuous transition from 1.00 to 1.40 $cm^2V^{-1}s^{-1}$ with average mobility 1.23 $cm^2V^{-1}s^{-1}$ in autumn.

Indoor positive ions are heavier, the average mobility is smaller in comparison to natural ions measured at Tahkuse [*Hõrrak et al.*, 1994].

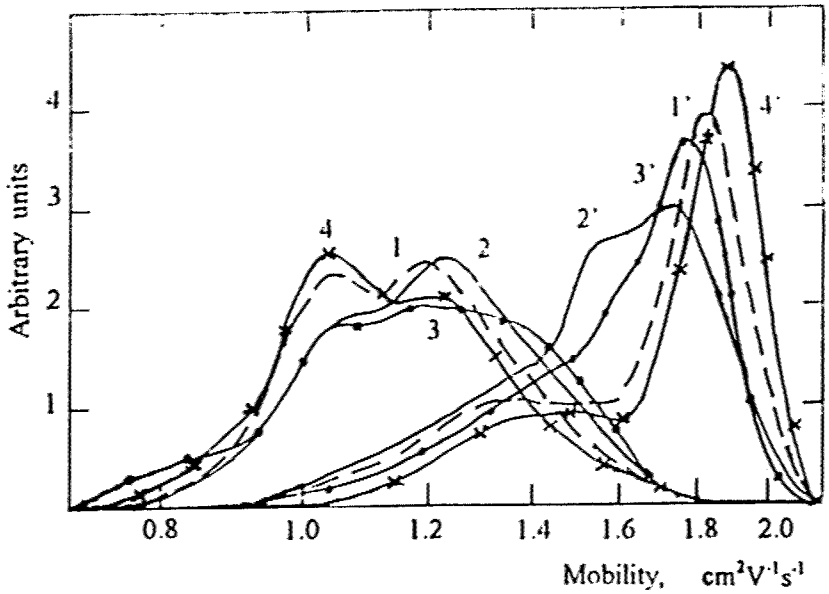


Figure 1.

The typical mobility spectra of one second aged small indoor ions in different seasons:

1, 2, 3, 4 - positive ions,
1', 2', 3', 4' - negative ions:

1, 1' - spring,
2, 2' - summer,
3, 3' - autumn,
4, 4' - winter.

The background spectra *of negative ions* 1) has the same tendency in winter and spring - two peaks appear at 1.50 and 1.90 $cm^2V^{-1}s^{-1}$ with average mobility 1.70 $cm^2V^{-1}s^{-1}$ in winter and 1.35 and 1.80 $cm^2V^{-1}s^{-1}$ with average mobility 1.67 $cm^2V^{-1}s^{-1}$ in spring; 2) has three different peaks ~1.35, 1.50 and 1.75 $cm^2V^{-1}s^{-1}$ with average mobility 1.60 $cm^2V^{-1}s^{-1}$ in summer either, 3) has one larger peak, predominantly at 1.75 $cm^2V^{-1}s^{-1}$ with average mobilities 1.68 $cm^2V^{-1}s^{-1}$ in autumn.

Indoor negative ions are smaller in comparison to natural ones in all seasons. Average mobility of natural negative ions is lower, < 1.55 $cm^2V^{-1}s^{-1}$ as presented by *Hõrrak et al.* [1994].

The most dominant peak for negative ions near 1.80 $cm^2V^{-1}s^{-1}$ is described by very small ions with masses m < 100 amu. This peak does not disappear in all experiments. The chemical composition of such ions was proposed to be $OH^-(HNO_3) = NO_3^-(H_2O)$ m = 80 amu or $OH^-(H_2O)_3$ m = 71 amu [*Parts*, 1990]. The later is thermodynamically the most stable smallest negative cluster in the air and could be responsible for peak 1.90 $cm^2V^{-1}s^{-1}$. The larger ions should be from the family $NO_3^-(HNO_3)_m(H_2O)_n$. The masses of clusters $NO_3^-(H_2O)_3$ and $NO_3^-(HNO_3)(H_2O)_3$ (m = 116 amu and m = 179 amu) amu are in a good correlation with mobilities 1.60 and 1.30 $cm^2V^{-1}s^{-1}$, respectively, and fit well with theoretical simulation presented by *Luts* [1995].

The most dominant positive ions of one second of age are the family of $NH_4^+(NH_3)_4(H_2O)_m$ and $H_3O^+(H_2O)_n$ [*Luts*, 1999]. The smallest of them have been observed in natural experiments at Tahkuse, never in laboratory conditions [*Tammet et al.* 1985]. Indoor small ions can deposit to room surfaces and that is one of the reason for differences in ion concentrations comparing to outdoors.

The increasing of nitrogen compounds, *e.g.* ammonia, nitrogen oxides, nitric acid in the air in winter caused by fuel combustion were observed in spectra. Mobility 1.00 $cm^2V^{-1}s^{-1}$ and ions $NH_4^+(NH_3)_4(H_2O)_{12}$ with m = 302 amu are the most abundant in winter. The higher concentration of water in summer reveals in the peak 1.25 $cm^2V^{-1}s^{-1}$ which corresponds to water content cluster $H_3O^+(H_2O)_9$, m = 181 amu.

TABLE 1. The average mobilities of dominant indoor air ions at different seasons.

| | Spring | Summer | Autumn | Winter |
|---|---|---|---|---|
| Positive ions: mobility, $K_+$ $cm^2V^{-1}s^{-1}$ | 1.18 | 1.23 | 1.23 | 1.13 |
| Negative ions: mobility, $K_-$ $cm^2V^{-1}s^{-1}$ | 1.67 | 1.60 | 1.68 | 1.70 |
| $K_-/K_+$ | 1.41 | 1.30 | 1.37 | 1.50 |

The changes in mobility spectra at certain unchangeable physical parameters, like temperature and atmospheric pressure indoors, are determinate particularly by size and the chemical composition of ions.

The influence of RH on mobilities in our experiments for one second aged ions is different to comparing with "younger" ones [*Thuillard*, 1995]. The chemical composition of one second small air ions is closer to natural than millisecond ones. In wintertime the central heating has an effect of decreasing RH in indoor air. Negative ions become lighter, average mobilities increases up to 1.80 $cm^2V^{-1}s^{-1}$. Positive ions become heavier, average mobility decreases up to 1.07 $cm^2V^{-1}s^{-1}$.

The experiments with artificial changes of RH [*Parts,* 1990; 1988] and seasonal variety of RH are in a good correlation. The increased RH get negative ions heavier, the average mobility decreases from 1.78 to 1.53 $cm^2V^{-1}s^{-1}$. The positive ions behaved in a different way, they went lighter. Mobility changed from average of 1.15 to 1.22 $cm^2V^{-1}s^{-1}$. In comparison with data by *Hõrrak et al.* [1994] average mobilities of natural ions were $K_- = 1.51$ $cm^2V^{-1}s^{-1}$ and $K_+ = 1.35$ $cm^2V^{-1}s^{-1}$.

It is known that chemical equilibrium between air constituents $H_2O$ - $NO_2$ - $HNO_3$ - $NH_3$ depends on water and $NO_2$ concentrations. Higher concentration of water leads to the enhance in nitric acid concentration and chemical reactions of later with ions affect the composition of air ions. The changes in this equilibrium should be the most important way to understand the changes in chemical composition of small air ions. Some aspects of the problem are presented by *Parts,* 1995.

The effect of temperature on the mobilities of dominant indoor 1 s ions in the range of 288 to 298 *K* is negligible, nevertheless sometimes observable. The Arrhenius law is remarkable for clustering reaction in the case of invariability of other physico-chemical parameters in our experiments. Ions of both polarity get heavier with increasing the temperature.

As the fact from the measurement of natural ion mobility spectra in the ground layer, the reduced average mobility falls with the growth of temperature in summer, especially for positive ions in the range of 15-25 C [*Salm et al.*, 1988]. In this case the role of air humidity was proposed by authors negligible. Authors have been suggested that the growth "of some kind of trace gases" causes the formation of larger cluster. As we know from atmospheric chemistry, the changes in the composition of air, due to the appearing of new trace gases, is negligible in

comparing with the concentration of most important constituents *e.g.* water, carbon oxides, sulphur dioxide, ammonia, nitrogen oxides, nitric acid, methane, formaldehyde, methanole, formic acid in the gas phase. Another situation is in the case of laboratory experiments and in the case of some chemical accident. In the point of view of gas phase composition, the natural situation in the ground layer of the atmosphere should be actually influenced by high variability of relative humidity, temperature, radiation which influence the chemical reactions of ions due to advantage in the formation of aerosol particles.

## CONCLUSIONS

The analysis of indoor air ions mobility spectra allows us to give following conclusions.

1) Changes in electrical mobility of small air ions do not usually depend on the changes in air constituent caused by several volatile, semivolatile organics and/or other air pollutant during the different seasons.

2) The increase of relative humidity indoors in spring, summer and autumn influences the electrical mobility of ions and consequently the chemical composition of later. First of all water has a strong effect on the system $H_2O$ - $NO_2$ - $HNO_3$ - $NH_3$ partial concentrations, on clustering reactions of ions, on aerosol particle formation.

ACKNOWLEDGEMENTS: The Estonian Science Foundation grant no. 1879 has in part supported this research. The author would like also to thank Dr Aare Luts for his support and kind presentation of his new results being in Press.

## REFERENCES

HÕRRAK, U., H. IHER, A. LUTS, J. SALM, H. TAMMET (1994) Mobility spectrum of air ions at Tahkuse Observatory, *J. Geophys. Res.*, 99, 10697-10700.

LUTS, A. (1999) Temperature variation of the evolution of positive small air ions at constant relative humidity, *J. Atm. Sol.-Ter. Phys.* (in Press).

LUTS, A. (1995) Mathematical simulation of the evolution of air ions. Ph.D. Thesis, Tartu, 149 p.

MIRME, A. (1994) *Electric aerosol spectrometry*, Ph.D. Thesis, Tartu, 129 p.

PARTS, T.-E. (1995) Small air ions as precursors of aerosol particles, *J. Aerosol Sci.*, 26, Suppl. 1., S319-S320.

PARTS, T. (1992) Organic nitrogen-containing trace gases in the atmosphere and their influence on the mobility spectra of small air ions, *Proc. 9th Int. Conf. Atmospheric Electricity, 1992*, St.Petersburg, 536-539.

PARTS,T. (1990) On the nature of negative small air ions of an ageing time of one second, *Acta et comm. Univ. Tartuensis*, 880, 52-60.

PARTS, T. (1988) On the nature of the small positive air ions, *Acta et comm. Univ. Tartuensis*, 824, 69-77 (in Russian).

SALM, J., H. TAMMET, H. IHER, U. HÕRRAK (1988) The dependence of small air ion mobility spectra in the ground layer of atmosphere on temperature and pressure, *Acta et comm. Univ. Tartuensis*, 809, 87-94 (in Russian).

TAMM, E., A. MIRME, Ü. KIKAS (1988) Corona discharge as a generator of monodisperse aerosols in nanometer size, *Acta et comm. Univ. Tartuensis*, 824, 123-131 (in Russian).

TAMMET, H. (1998) Reducion of air ion mobility to standard coditions. *J. Geophys. Res. Atmospheres* 103, 13033-13937.

TAMMET, H., H. IHER, AND F. MILLER (1985) Mobility spectra of one-second-aged small air ions in natural air, *Acta et comm. Univ. Tartuensis*, 707, 26-36 (in Russian).

THUILLARD, M. (1995) Electric mobility measurements of small ions in the temperature range –40 –20 C at constant relative humidity of 87 %, *J. Aerosol Sci.*, 26, 219-225.

# THE STRING FLUXMETER: HOW TO MAKE AND HOW TO USE

V. I. Struminsky

Novosibirsk State University, Novosibirsk, RUSSIA

ABSTRACT: Undoubtedly, the electric field strength is the most often measured parameter of the atmospheric electricity. At the same time, many of researchers have limited possibilities to obtain industrially produced equipment for this purpose. This paper describes a simple easy-to-make string fluxmeter with sensitivity of 0.2 V/m and more, frequency range 0 - 50 Hz or wider.

The main advantages of the string fluxmeter are:

- relatively high frequency of electric field conversion;
- extremely small area of the sensitive electrodes;
- low power consumption.

These features make the string fluxmeter especially useful for electric field measurements in the medium with high level of conductive and convective electric currents, for instance, in the balloon and rocket experiments.

## INTRODUCTION

Methods of atmospheric electric field investigations historically developed from passive antennas to radioactive probes and at last to the "field mills". It is known that "field mill" is the electric field meter with flat or half-cylindrical rotating electrodes. These devices have wide applications in investigations of the atmospheric electricity. At the last time new class of electric field meters with vibrating metal electrode appeared which modulates electric field strength in the vicinity of other non-vibrating ones [*Struminsky*, 1981, 1984, 1991]. General features of these devices are extremely low area modulation of the sensitive electrode and relatively high modulation frequency. The first makes possible to use the instrument under conditions of high convective current level, the second – in a medium with high electrical conductivity.

Besides, these devices are appropriate for long-period atmospheric measurements due to leak-proofness and high operate reliability because of absence of rotating elements. The description of such instrument with vibrating string as field modulator is presented below.

## THEORY

We consider system of Fig. 1 consists of three metal strings running parallel to conductive surface **XY**, above which they are mounted. This construction is exposed in atmosphere with conductivity $\sigma$ where there is quasi-static electric field $\mathbf{E}_0$ whose vector is orthogonal to the **XY**. We assume also that in common case there are two kinds of current in the medium: conductive with density $\mathbf{j}_{cond} = \sigma\mathbf{E}_0$ and convective ones $\mathbf{j}_{conv} = \rho\mathbf{V}$, where $\rho$ is space charge density, **V** is the velocity of its motion.

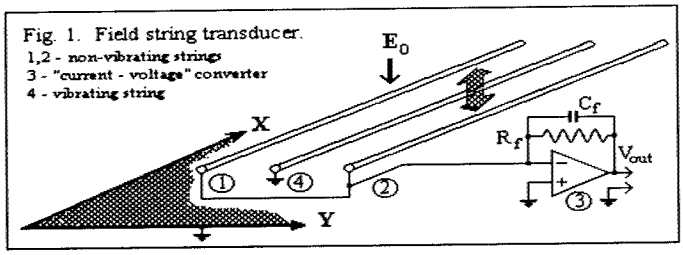


Fig. 1. Field string transducer.
1,2 - non-vibrating strings
3 - "current - voltage" converter
4 - vibrating string

Two insulated peripheral non-magnetic strings 1 and 2 are connected to the input of "current-voltage" converter 3. The middle ferromagnetic string 4 is grounded and vibrates in direction parallel to the field vector with angular frequency $\omega$. The string vibration causes electric field modulation in the vicinity of two non-vibrating strings and, consequently, electric charge induced on them. The current by

the alternating component of the induced charge is amplified and converted into voltage by "current-voltage" converter. Electric field strength near small segment of non-vibrating string with number $i$ and area $dS_i$ is

$$E_i = mE_0(1 + k_i \cos\omega t)$$

where $k_i$ is depth of field modulation above $dS_i$, $0 < k_i < 1$, $m$ is a factor of field distortion by the conductive strings, $m > 0$. The current to the string area $dS_i$ is

$$dI_i = \left(\varepsilon_0 \frac{\partial E_i}{\partial t} + \sigma E_i + \rho V\right) dS_i = (\varepsilon_0 k_i m E_0 \omega \sin\omega t + m\sigma E_0 + \sigma k_i m E_0 \cos\omega t + \rho V) dS_i \quad (1)$$

Convective component modulation in (1) is negligible because of absence of insulated string area modulation. Extracting from (1) only alternative components we obtain

$$dI_i = \left(\varepsilon_0 \frac{\partial E_i}{\partial t} + \sigma E_i + \rho V\right) dI_i^{\sim} = k_i m E_0 (\varepsilon_0 \omega \sin\omega t + \sigma \cos\omega t) dS_i$$

Total value of current to the surface of strings is

$$I^{\sim} = \int_s dI_i^{\sim} = mE_0(\varepsilon_0 \omega \sin\omega t + \sigma \cos\omega t) \int_s k_i dS = kmE_0(\varepsilon_0 \omega \sin\omega t + \sigma \cos\omega t)$$

$$I^{\sim} = kmE_0 \sqrt{\varepsilon_0^2 \omega^2 + \sigma^2} \sin(\omega t + \varphi) \qquad \varphi = \text{arc tg} \frac{\sigma}{\varepsilon_0 \omega} \quad (2)$$

Transfer function of the "current – voltage" converter (Fig. 1) is

$$V_{out} = -Z_f I^{\sim}, \text{ where } Z_f = \frac{R_f}{1 + j\omega R_f C_f} \quad (3)$$

From (2) and (3) we obtain

$$V_{out} = -kmE_0 R_f \sqrt{\frac{\varepsilon_0^2 \omega^2 + \sigma^2}{1 + \omega^2 R_f^2 C_f^2}} \sin(\omega t + \psi) \qquad \psi = -\left(\text{arc tg} \frac{\sigma}{\varepsilon_0 \omega} + \text{arc tg}\, \omega R_f C_f\right) \quad (4)$$

The average frequency of string vibration is about 300 Hz. Conductivity of near – ground atmosphere is about $10^{-14}$ Ohm$^{-1}$ m$^{-1}$. It follows therefrom that $\varepsilon_0^2\omega^2/\sigma^2 \sim 10^{10} >> 1$. Thus, we can rewrite the equations (4) as

$$V_{out} = -\frac{kmE_0 R_f \varepsilon_0 \omega}{\sqrt{1 + \omega^2 R_f^2 C_f^2}} \sin(\omega t + \psi) \qquad \psi = -\text{arc tg}\, \omega R_f C_f$$

Some parameters in the first equation are time-independent quantities. Therefore

$$\frac{kmR_f \omega \varepsilon_0}{\sqrt{1 + \omega^2 R_f^2 C_f^2}} = n = const \qquad V_{out} = -nE_0 \sin(\omega t + \psi)$$

Factor $n$ may be found by instrument calibration in artificial electric field of known strength.

INSTRUMENT DESIGN

Block diagram of the instrument is shown in Fig. 2. Two polarized electromagnets **3**, generator **4**

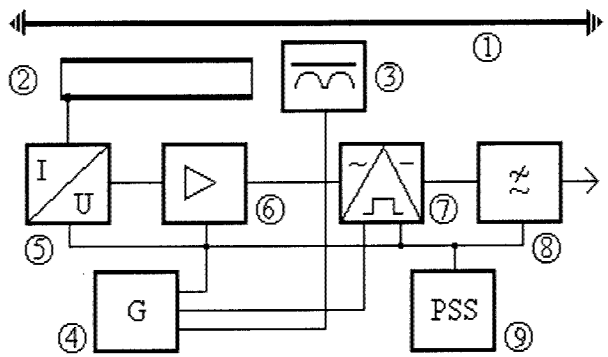


Fig. 2. Block diagram of the instrument

1 - grounded vibrating string
2 - insulated strings
3 - electromagnets
4 - generator
5 - "current - voltage" converter
6 - AC voltage amplifier
7 - phase-sensitive detector
8 - low freguency filter
9 - power supply source

and ferromagnetic string **1** are components of self – excited oscillator where vibrating string is positive feedback element. The string 18 sm. long and 0.4 mm across in diameter vibrates with amplitude about 1.5 mm and frequency about 300 Hz. Square pulses from generator output are applied to the phase – sensitive detector **7** as reference signal. Legitimate signal in the form of alternative current flows from the sensitive electrodes – insulated strings **2** into the input of "current – voltage" converter **5**. The output alternative voltage of the converter is applied to the input of linear amplifier **6**. Signal amplification is conducted largely in this unit, amplifier gain factor sets upper limit of the instrument range. Detector **7** performs full-wave rectification of the signal; the polarity of direct component at the output depends on the direction of the measuring electric field. Low frequency filter **8** suppresses the carrier modulation frequency. The filter has gain factor 3 for signal amplitude matching between them and the detector.

External appearance of the instrument and the cover destined for the control of transducer gain is shown in Fig. 3. The board with mounted on electronic components is located in the sealed pan inside the

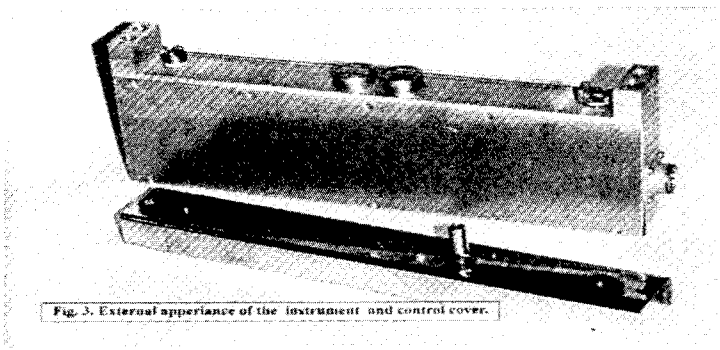

Fig. 3. External apperiance of the instrument and control cover.

metal box - instrument body. Non-vibrating tungsten strings holders mounted on ceramic insulators pasted in the instrument body. Electromagnets consist of shell –type magnetic circuit with central cylindrical permanent magnet and cylindrical coil. The upper path of the electromagnets must be shielded with thin non-magnetic foil.

Insulated flat electrode is mounted on shielded insulators inside the control cover.
Control cover enables to check in a repetitively manner the transducer gain during measurements by applying preset voltage to the inner electrode. The instrument may be connected to the data acquisition system at the distance about 50m. If more, it is desirable to use special signal transmission method ("voltage-current" converter at the sending part and "current-voltage" converter at the receiving ones).

Electronic circuit of the instrument is shown in Fig. 4. Temperature instability of the capacitors and resistors must be as low as possible. The "current-voltage" converter (IC OP-41) must be carefully shielded. If switching power source does not cause string vibration, it is necessary to exchange the winding leads of any electromagnet. If the polarity of the output voltage is not coincides to the measuring field sign the winding leads of the both electromagnets must be exchanged.

CONCLUSION

Gain stability of the string fluxmeter depends on some environment factors, primarily on temperature

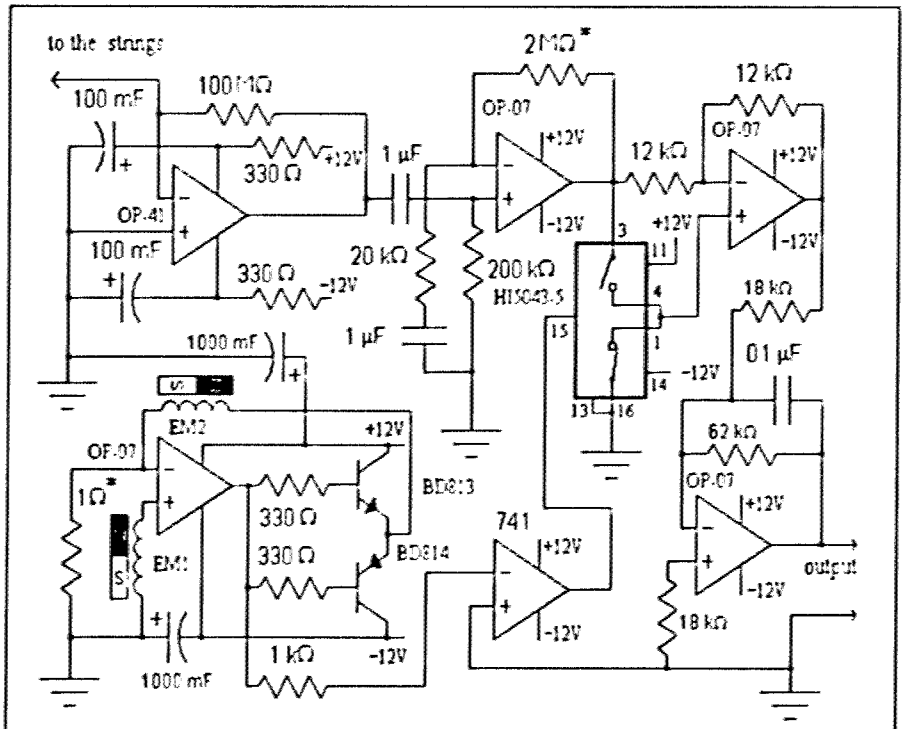

Fig. 4 Electronic circuit of the instrument

variations. These variations influence on the vibrating string tension, electromagnet coil resistivity, values of capacitors and resistors and so on. In this issue the simplest version of the instrument is described whose gain stability does not good enough for long-term measurements. It requires periodical gain check with the control cover. The advanced version of the instrument is equipped with units of string tension stabilization, self-compensation of vibration amplitude instability and some others. Gain instability of such device does not exceed 5% with temperature range –30 - +50° C.

REFERENCES:

Struminsky, V.I., An electrostatic field sensor, *A.C. SU # 830256*, 1981, (in Russian)
Struminsky, V.I., A device for electric field strength measuring, *A.C. SU # 1116399*, 1984 (in Russian)
Struminsky, V.I., A device for electric field strength measuring, *A.C. SU # 1661685*, 1991 (in Russian)

# STRUCTURES AND SPECTRA OF AEROELECRIC FIELD PULSATIONS

S.V.Anisimov[1], S.S.Bakastov[1], E.M.Dmitriev[1], E.A.Mareev[2]

[1]Geoelectromagnetic monitoring Laboratory, Geophysical Observatory, Shmidt Inst. of Earth Physics, RAS, Borok, Yaroslavl, Russia
Institute of Applied Physics RAS, Nizhny Novgorod, Russia

ABSTRACT: ULF pulsations of the atmospheric electric field are studied in terms of Kolmogorov-Obukhov turbulence description. The structural function method and fast Fourier transformation have been used for fair weather aeroelectric field data. It's shown that frequency spectra of aeroelectric field in the presence of large scale structures have decay slopes from -1.75 to -2.50, while the structural function index changes from 0.32 to 0.98. In the absence of large scale structures the slopes of aeroelectric field spectra were found to be steeper (approximately –3). Theoretical estimates for ULF pulsation spectra are presented taking into account turbulent mixing of the atmospheric space charge.

## INTRODUCTION

Aeroelectrodynamics of the lower atmosphere is associated with atmospheric dynamics and particularly with turbulence. Empirical data on the small scale turbulent structures of temperature and velocity demonstrate the "5/3 law" for spectra and "2/3 law" for structural functions with a good accuracy in the inertial subrange [*Tatarsky*, 1967]. The observable chaos of aeroelectric field pulsations in the ultra-low frequency (ULF) band is dominated by atmospheric turbulence [*Hoppel*, 1986]. *Makhdoomi and Raina* [1988] emphasized that a causal relationship exists between the fluctuating atmospheric electric elements and atmospheric turbulence in the surface layer. *Anderson* [1982] reviewed the theory of atmospheric space charge fluctuations when turbulent mixing and discussed possible behavior of space charge as a tracer of turbulent curls. *Anisimov et al.* [1990] found that atmospheric electric field pulsation spectra decrease according to the power-law function with the slopes close to –3. The experimental investigation with the use of the structural function method showed that spatio-temporal structures of atmospheric field with spatial scale ~10m occur in the surface layer [*Anisimov et al.*, 1994]. The use of structural-temporal method allowed us to discover submesoscale aeroelectrical structures generated by the turbulent flux [*Anisimov*, 1999]. The investigation of structural functions and frequency spectra relation is the main goal of this paper.

## EXPERIMENTAL METHOD

The database, originating from the results of 1994-1996 measured campaigns, has been the experimental foundation for analysis of structural and spectra characteristics of ULF aeroelectric field pulsations. This database has been formed from remote receiving of ULF pulsations by means of "field-mills" line consisting of five points, separated at a controlled distance $\Delta r$ from 5 to 30 meters each from another [*Anisimov et al.*, 1994]. A local data bank was stored at magneto-optical disk with a total volume about 300MB. The list of events included about 30 diurnal observations. The sampling rate was 10Hz and the resolution was 0.1V/m for the used database.

The search of aeroelectrical structures was the first step of the data analysis. The method of structural function $D(r)$ by Kolmogorov-Obukhov [*Tatarsky*, 1967] has been used for a display of aeroelectric field structures. For the locally homogenous and isotropic electric field $E$ the structural function of ULF pulsation with amplitude $\Delta E$ is written as

$$D_E(r)=\langle|\Delta E(r)-\Delta E(r+\Delta r)|^2\rangle. \quad (1)$$

It is known that in the inertial subrange the structural functions of temperature and velocity fluctuations $D(r)$ obey the "two thirds law" by Kolmogorov-Obukhov (Figure 1)

$$D(r)=Cr^{2/3}, \text{ for } l_0 \ll r \ll L_0, \quad (2)$$

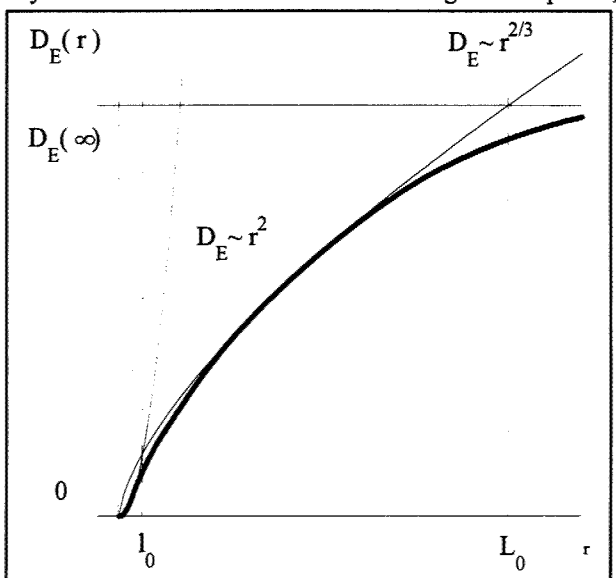


Figure 1. The plot of typical Kolmogorov structural function $D_E(r)$ and its general properties.

where $C$ is the structural constant, $l_0$ is the internal scale and $L_0$ is the external scale of inertial turbulent interval [*Tatarsky*, 1967]. Respective frequency spectra $S(\omega)$ are expressed in the form

$$S(\omega)=bC\omega^{-5/3}. \qquad (3)$$

The validity of Kolmogorov-Obukhov law is a fundamental property of meteorological fields. In the research of electric field pulsations the power approximations of structural function $D_E(r)\sim r_0^{D}$ and power spectrum of the field $S_E(\omega)\sim\omega^{-\alpha_S}$ are suitable. In a case of Kolmogorov-Obukhov law the decay slope $-\alpha_S$ and structural function power index $\alpha_D$ are coupled by the relation:

$$\alpha_D = \alpha_S - 1. \qquad (4)$$

The search of $\alpha_S$ and $\alpha_D$ relationship for electric field pulsations is one of the goals of present investigation. The computer program is used for structural function calculations and for its approximation by a power function. The frequency spectra $S_E(\omega)$ are calculated by means of fast Fourier transformation.

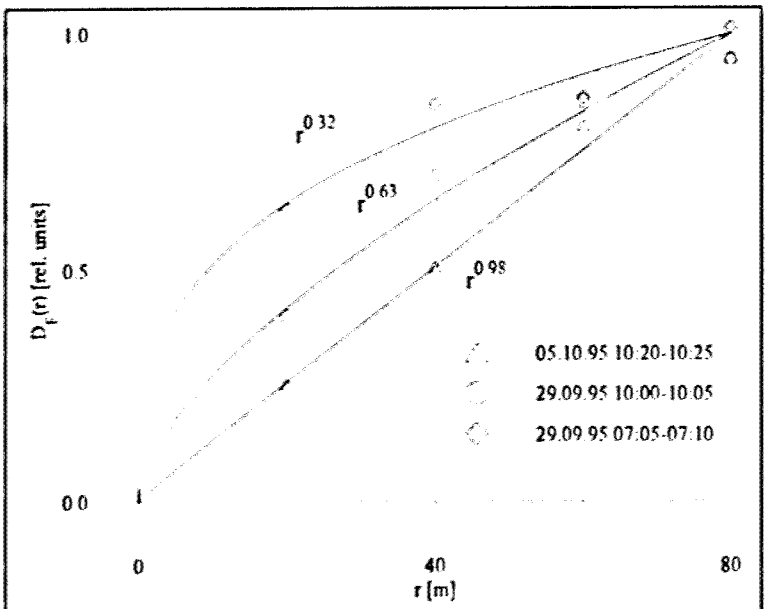

Figure 2. Plot of structural function variety with extreme observable index $\alpha_D$=0.32÷0.98.

EXPERIMENTAL RESULTS

It should be noted that temporal variability of aeroelectric field may be considered as a stationary random ergodic process. The ergodic assumption allows us to replace the ensemble averaging in Eq. (1) with the time averaging for period $T$, which must be more than the correlation time $\tau$ of a random process. In the inertial subrange of turbulent motion $\tau$~10s [*Anisimov et al.*, 1994], so we choose the time averaging $T$=300s for calculation of $D_E(r)$ according Eq. (1).

For analysis of $D_E(r)$ and $S_E(\omega)$ relation the aeroelectric field structures were located from database according to algorithm (1). The full number of allotted structures was more than 50. Figure 2 shows the structural function variety with the observed index boundary $\alpha_D$ from 0.32 to 0.98. The structural functions have been calculated for distance $\Delta r$=20m. The data corresponded to the fair weather conditions only.

Spectral decay slopes (power law approximation) were computed from log-log spectra plots. The extreme boundaries of spectral function are presented on Figure 3. It is seen, that $\alpha_S$ varied from 1.74 to 2.50 for examined structures. Two typical spectra averaged over five-minute interval for 06 Oct 1995 and for 29 Oct 1995 are shown on Figure 3.

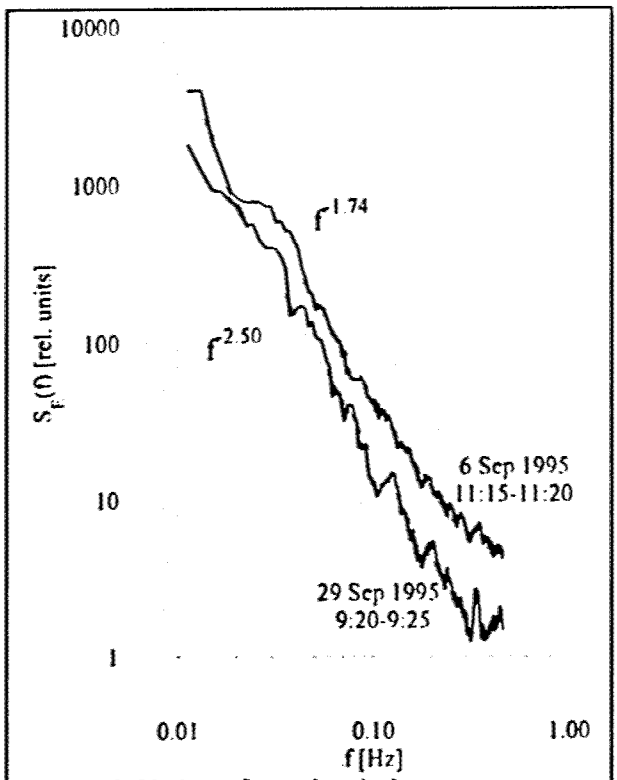

Figure 3. Variety of aeroelectrical structure spectra with extreme observable slopes $\alpha_S$=1.74÷2.50.

The correlation field of structural function power index $\alpha_D$ and spectra decay slope $-\alpha_S$ are shown on Figure 4. The coordinates of each point on the plot are determined by approximate values of powers for structural functions and spectra in the presence of

aeroelectrical structures. The $\alpha_D$ - $\alpha_S$ relation may be approximated as

$$\alpha_D \approx \alpha_S - 1.6\,, \qquad (5)$$

which slightly differs from the expression (4) by Kolmogorov-Obukhov.

It is important to note, that we have found some differences for spectra slopes of aeroelectrical structures and unstructured aeroelectrical noise in the surface layer. The Figure 5 presents spectra averaged over the period from $08^h50^m$ to $16^h30^m$ LT on 29 May 1995. Spectral decay slopes of 50 long time interval from ULF electric field pulsation data were calculated. The decay slope was close to 3.00 for these unstructured ULF pulsations. Therefore, one of the main conclusions of this work is that the power spectra of pulsations measured during large-scale aeroelectric structures fly-by, decay more slowly as compared to the case of "unstructured" ULF noise.

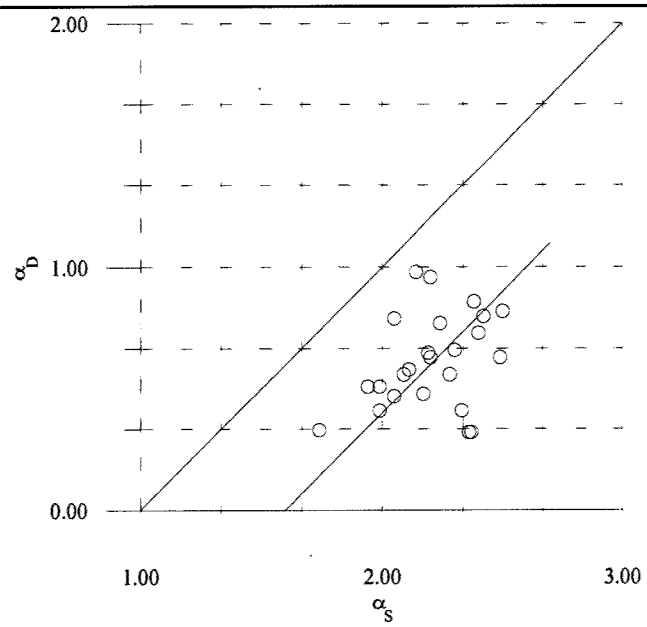


Figure 4. Indexes of power law approximations of spectra and structural functions for aeroelectrical structures.

THEORETICAL MODELS

To explain experimental results, we calculate power spectra of electric field $S_E(\omega)=\langle|E_z|^2\rangle$ for the two most interesting cases: 1) for stationary Kolmogorov turbulence (outer scale $L_0$) without large-scale structures; 2) for the drifting aeroelectrical structure (linear scale $L_1$, volume $V\sim L_1^3$, height over the grand $z_1$) occupied by the Kolmogorov turbulence with the outer scale $L_0<L_1,z_1$.

In the first case Fourier transformation on spatial and temporal variables could be used when analyzing the set of equations for the field and charge carriers. If aerosol density is negligible and all the charge is carried by the small ions only, one can obtain the following expressions for the electric field spectrum:

$$S_{ET}(\omega)=16\pi^2\frac{\gamma^2}{T_0^2}\int_{-\infty}^{\infty}\frac{k_z^4 s^2(\sigma_0 E_0)^2}{k^4|D(\omega,\boldsymbol{k})|^2}\langle T'T'^*\rangle d\boldsymbol{k}\,, \qquad (6)$$

$$S_{EV}(\omega)=16\pi^2\int_{-\infty}^{\infty}\frac{k_z^4(\sigma_0' E_0)^2}{k^4|D(\omega,\boldsymbol{k})|^2}\langle V_{Tz}V_{Tz}^*\rangle d\boldsymbol{k}\,. \qquad (7)$$

Where $D(\omega,\boldsymbol{k})=(s^2-k_z^2v_\alpha^2)^2+16\pi^2\sigma_0^2s^2$; $s=\omega-k_xv_0$; $v_0$ is the wind speed; $\sigma_0(z)$ is the stationary profile of the conductivity, characteristic scale of $\sigma_0$ change is assumed to be small as compared to $L_0$; $E_0$ is the vertical stationary electric field; $v_\alpha$ is the drift velocity of small ions in this field; $T_0$ is the air temperature; $\gamma$ is a constant equal a few tenths. Two expressions (6) and (7) correspond to different mechanisms of charge fluctuation generation. Equation (6) describes the generation of charge perturbations due to air temperature fluctuations, therefore it contains the temperature fluctuation correlator [*Anisimov et al.*, 1994]. Equation (7) describes the charge perturbations due to ion mixing on the inhomogeneous $\sigma_0(z)$ background. Being short in space, we present here the result of rather complicated calculations.

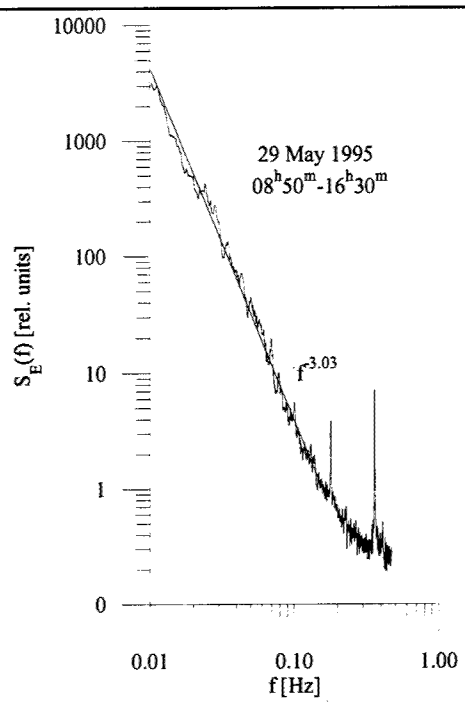


Figure 5. An example of spectrum for unstructured aeroelectric field noise.

In the inertial subrange $2\pi v_0/L_0 \ll \omega \ll 2\pi v_0/l_0$ one can get:

$$S_{ET}(\omega)=A_T\frac{C_T^2\gamma^2\sigma_0E_0^2}{\sigma_V T_0^2 v_0}\left(\frac{\omega^2}{v_0^2}+k_0^2\right)^{-4/3}\sim\omega^{-8/3}\,,$$

(8)

$$S_{E\Gamma}(\omega) = A_{\Gamma}\frac{\varepsilon^{2/3}\sigma_0'^2 E_0^2}{\sigma_{\Gamma}\sigma_0 v_0 v_a^2}\left(\frac{\omega^2}{v_0^2}+k_0^2\right)^{-7/3} \sim \omega^{-14/3}. \quad (9)$$

Here $A_T$ and $A_{\Gamma}$ are nondimensional constants of order of unity; $C_T^2=10^{-3}K^2/cm^{2/3}$; $\varepsilon=10^2 cm^2/s^3$; $\sigma_{\Gamma}$ is the dispersion of wind speed so that $\sigma_{\Gamma} \ll v_0$. We conclude that even in the simplest case of aeroelectrical structures absence a decay slope of a power spectrum of the field depends substantially on the mechanism of energy transfer from the aerodynamic turbulence to the electric energy of short period pulsations.

The calculations above have been fulfilled with an account of small ions only, which are passive but not conservative contaminants. As the result the space charge density spectrum differs from a comon Kolmogorov law. With the increase of aerosol particle content in the air the situation changes drastically. If aerosol density is sufficiently high so that all the charge is carried by heavy immobile particles, the space charge density may be considered as a passive conservative scalar. Then the 3-dimensional power spectrum of charge density in wave number space obey the classical Kolmogorov law $\langle\rho'\rho'^*\rangle \sim (k^2+k_0^2)^{-11/6}$, while for the spectrum of electric field the decay slope should be steeper: $\langle E'E'^*\rangle \sim 16\pi^2 k^{-2}\langle\rho'\rho'^*\rangle$, where Poisson equation is used. With the account of relation $k_z=\omega_0/v_0$ for the frozen turbulence in the inertial subrange it gives for the frequency spectra $S_E(\omega)\sim\omega^{-5/3}$. The latter conclusion agrees with the results by *Anderson* [1982]. However, if the signal at the point of measurement is generated by the turbulence inside the large-scale structure drifting far enough from this point, Fourier transformation for Poisson equation may not be used. One can show that in this case power spectra of space charge density and electric field at the point of observation have the same decay slopes. Particularly, for aerosol particle domination (which should be valid as a rule for aeroelectrical structures) we have: $S_E(\omega)\sim\omega^{-5/3}$, i. e. a decay slope of electric field spectrum is more smooth as compared to the case of homogeneous stationary turbulence.

## CONCLUSIONS

ULF pulsations of atmospheric electric field have been studied with the use of structural function method and fast Fourier transformation for fair weather conditions. It is shown that frequency spectra of aeroelectric field structures has slopes from -1.75 to -2.50 for the family of structural function power indices from 0.32 to 0.98. The decay slopes were found to be close to -3 for "unstructural" ULF noise in the surface layer. Theoretical estimates show that a decay slope of electric field pulsations spectrum depends on the particular mechanism of turbulent energy transfer and may vary from -5/3, through -8/3 (in the presence of small ions only), -11/3 (when Aitken nucleus dominate) and up to -14/3 (in inhomogeneous conductivity layer). Important information may be derived from the data on the correlation of electric field spectra and structural function rate indices.

ACKNOWLEDGEMENT: This work was supported partially by the Russian Foundation for Basic Research.

## REFERENCES

Anderson, R.V., The dependence of space charge spectra on Aitken nucleus concentrations, *J. Geophys. Res.*, 87, 1216-1218, 1982.

Anisimov, S.V., S.S.Bakastov and E.A.Mareev, Spatiotemporal structures of electric field and space charge in the surface atmospheric layer, *J. Geophys. Res.*, 99, 10603-10610, 1994.

Anisimov, S.V., E.A.Mareev and S.S.Bakastov, On the generation and evolution of aeroelectrical structures in the surface layer, *J. Geophys. Res.*, 1999 (accepted).

Anisimov, S.V., E.A.Mareev, and V.Y.Trakhtengerts, Characteristics of electric noises in the surfase atmospheric layer, *Res. Lett. Atmos. Electr.*, 10, 110, 1990.

Hoppel, W.A., R.V.Anderson and J.C.Willett, Atmospheric electrisity in the planetary Boundary Layer., in *The Earth's Electrical Environment*, edited by E.P.Krider and R.G. Roble, 149-165, National Academy Press, Washington, D.C., 1986.

Makhdoomi, B.A., and B.N.Raina, Correlation and spectra analysis on atmospheric electric parameters, in *Proceedings of the Eighth International Conference on Atmospheric Electricity*, 130–137, Uppsala, Sweden, 1988.

Tatarsky, V.I., Wave propagation in turbulent atmosphere (in Russian), 548pp., Nauka, Moscow, 1967.

# TURBULENT TRANSFER OF SPACE CHARGE IN THE ATMOSPHERIC SURFACE LAYER

Janet F. Barlow and R. Giles Harrison

Department of Meteorology, University of Reading, P.O. Box 243, Reading, RG6 6BB, U.K

**ABSTRACT**: Simultaneous measurements of electrical parameters and micrometeorological parameters were made near Reading,U.K.during July and August 1998. The diurnal cycle in the potential profile in the surface layer was observed to coincide with the daily cycle in atmospheric stability. Measurements of vertical wind speed $w$ and electric field $E$ were correlated. The covariance $<w'E'>$ gives the direct effect of turbulence on the electric field and showed a large positive peak during the daytime. Correlation with momentum flux ($-<u'w'>$) was observed during stable nocturnal periods. Spectral analysis of electric field data showed a dependence of spectral slope on aerosol mass concentration in the size range 0.1 to 15 ìm. For the frequency band 0.016 to 0.3 Hz, the spectral density $S(n)$ was proportional to $n^{-1.1}$ in the high aerosol case and $n^{-2.3}$ in the low aerosol case, showing qualitative similarity to the results of Anderson (1977) for space charge.

## Introduction

Turbulent transport of space charge in the surface layer is established as important in determining profiles of electrical parameters. Any realistic model of the electrode effect (e.g. Hoppel,1967) has to include the effects of turbulence and aerosol. Law (1963) deduced that there was a considerable convection current when examining measured profiles of ions. In addition, the nature of the turbulent transport of space charge is dependent on its composition (Anderson,1977), i.e. whether it is particulate or ionic.

These results underline the need to treat electrical and micrometeorological parameters as a coupled system in the atmospheric surface layer. This paper presents some results from a field campaign where the effects of turbulence and aerosol concentration on profiles of potential and electric field measurements were investigated.

## Field Campaign

Measurements were made in the U.K.at Sonning Farm, a semi-rural site near to Reading during July and August 1998. The site consists of gently sloping fields divided by shrubs and low trees. Fetch of wind in the direction of the prevailing wind was sufficient to assume equilibrium of surface layer fluxes with the ground. Traffic on a busy road to the south of the site presented a considerable source of particulate pollution with semi-diurnal fluctuation. Anti-cyclonic conditions prevailed for most of the measurement period, bringing warm days and strong convection.

## Instrumentation

Passive wire antennas of length 20m were used to sense atmospheric potential. Electrometers (Harrison, 1997) were used to measure the potential on each wire. Four antennas were mounted in a vertical array at heights 0.5, 1, 1.5 and 2m above the surface. Vertical profiles of temperature and wind were measured using fine wire platinum resistance thermometers and cup anemometers. Instruments were mounted at 0.4, 0.8, 1.6 and 3.2m heights. Aerosol mass concentration in the size range 0.1 to 15 ìm was monitored using an optical counter. An aspiration filter (Obolensky,1925) was used to measure space charge at 1.5m. Solar radiation was measured using a solarimeter and wind direction at 3m was measured using a wind vane. All instruments were logged at 1Hz and data was averaged and stored every 5 minutes.

An electrostatic fieldmill (Chubb Instruments, UK) was used to make fast response measurements of electric field at 2.85m. It was mounted adjacent to a sonic anemometer and platinum resistance thermometer. All three instruments were logged at 4Hz using the sonic anemometer in order to perform eddy correlation and calculate turbulence statistics.

**Results**

Data for periods with precipitation were rejected as then the passive wire antenna charges by contact with rain. Figure 1a) shows the time series of potential for a day with fair weather conditions (average windspeed at 3m less than $2ms^{-1}$, moderately high value of aerosol mass concentration M = 38 $\mu gm^{-3}$, few clouds) alongside solar radiation. Plotted points are 5 minute averages of 1 Hz data.Values of potential are low overnight but increase within a couple of hours of sunrise. The potential increases with height with a mean value of about 180V at 1m from 15:00 to 20:00 (British Summer Time). Fluctuations are correlated at different heights and increase in size with height.

Figure 1b) shows the gradient Richardson number

$$Ri = \frac{g/\theta \, \frac{\partial \overline{T}}{\partial z}}{\left(\frac{\partial \overline{U}}{\partial z}\right)^2} \qquad (1)$$

where $T$ is temperature and $U$ is wind speed. It represents the relative importance of buoyancy and wind shear in producing turbulence. Onset of turbulence in unstable conditions occurs when Ri<0.25. Turbulence is supressed in stable conditions when Ri>1. It can be seen from figures 1a) and 1b) that the potential starts to increase within an hour of the onset of turbulence. Values of potential reduce dramatically shortly before 21:00 BST when the atmosphere has returned to stable conditions. This suggests a strong link between potential gradient in the surface layer and local atmospheric stability.

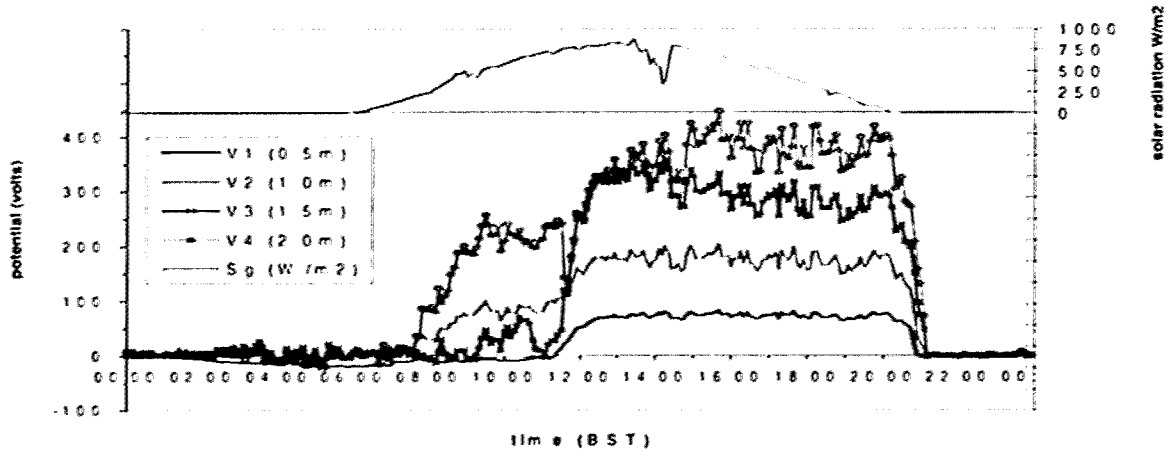


**Figure 1a): Solar radiation and potential profile for day 219 (7.8.98), fair weather conditions.**

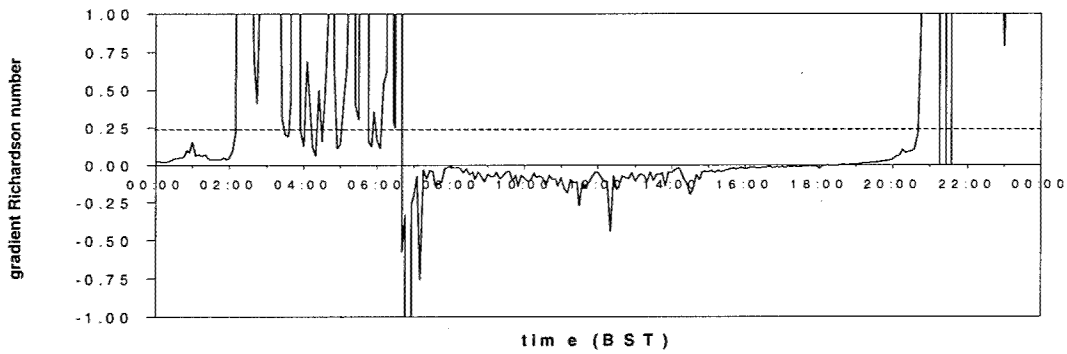


**Figure 1b): Gradient Richardson number stability parameter for day 219 (7th August 1998), fair weather conditions. Dotted line shows Ri = 0.25, the threshold for the onset of turbulence.**

Eddy correlation is the correlation between the vertical wind component $w$ and other quantities such as temperature $T$ or wind $u$. It is a direct measurement of turbulent fluxes in the boundary layer. A postive value for covariance $<w'T'>$ indicates the upward transport of heat due to turbulent eddies. The covariance between $w$ and electric field $E$ ($<w'E'>$) has been calculated, where $E$ is a point measurement made using the fieldmill. Positive correlation can be interpreted as the direct effect of turbulence in increasing the electric field.

Figure 2 shows $<w'E'>$ for day 221. Also shown are the momentum flux $-<u'w'>$ and the solar radiation $S_g$. During unstable daytime conditions the momentum flux is large and positive. The covariance $<w'E'>$ has its peak value when turbulence is strong. Smaller peaks occur at night and coincide with peaks in momentum flux. These are localised bursts of turbulence. Space charge due to trapping of radioactive gases near the surface in the nocturnal temperature inversion will be transported upwards and produce fluctuations in electric field.

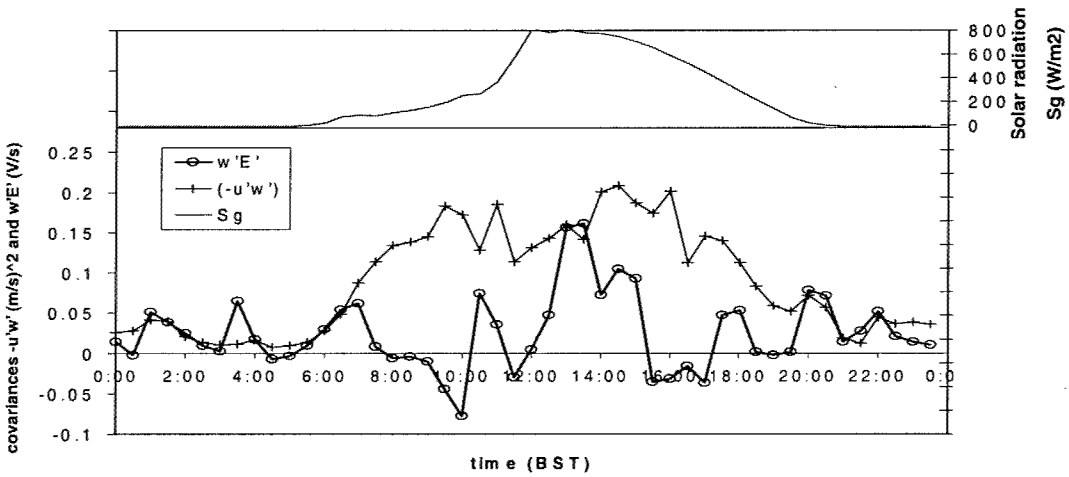


**Figure 2: Covariances for turbulent transport of heat <w'T'> and turbulent effect on electric field <w'E'>. Solar radiation $S_g$ also shown.**

Spectral analysis of wind data and passive scalar quantities such as temperature has shown that spectral density $S(n)$ varies with $n^{-5/3}$ at high frequencies ($n$). Anderson (1977) calculated that the log-log power law for space charge is $n^{-5/3}$ when space charge is particulate but is $n^{-11/3}$ when space charge is purely ionic. Electric field data measured by the fieldmill was analysed using an FFT program (1024 point

transform, Welch data windowing) to give spectral density. Figure 3 shows the spectra for periods of high and low aerosol concentration in the frequency range 0.016 to 0.3 Hz. $S(n)$ varies with $n^{-1.1}$ for the high aerosol period with aerosol mass concentration $M$ = 31ìgm $^{-3}$. For the low aerosol period, where $M$ = 12ìgm $^{-3}$, $S(n)$ varies with $n^{-2.3}$. This agrees qualitatively with Anderson's result for space charge that there is a steeper spectral slope when the air is cleaner.

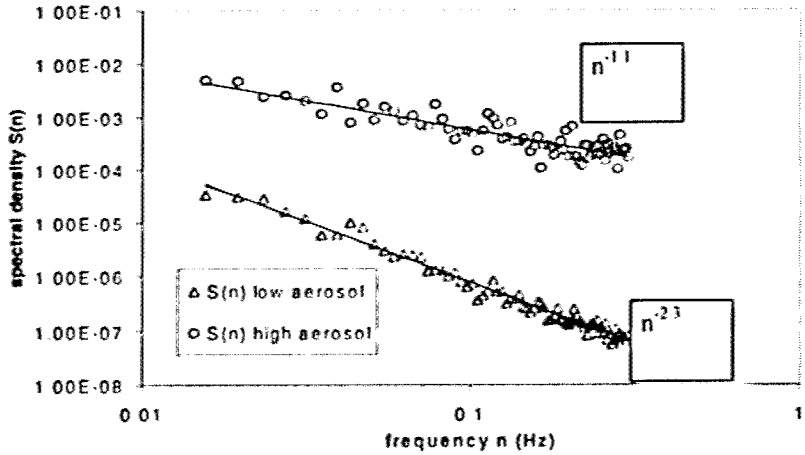


**Figure 3: Spectral density S(n) for periods of high and low aerosol mass concentration.**

## Conclusions

Measurements have shown a strong coupling between electrical and micrometeorological parameters. Future work could include the measurement of space charge fluxes directly by correlation of observed vertical wind fluctuations with space charge fluctuations.

## References


Anderson, R.V.(1977) Atmospheric electricity in the real world in "Electrical processes in Atmospheres", ed. H. Dolezalek and R. Reiter, Steinkopf Verlag, Darmstadt

Harrison, R.G. (1997) An antenna electrometer system for atmospheric electrical measurements, *Rev. Sci. Ins.*, 68 (3), 1599-1603

Hoppel,W.A.(1967) Theory of the electrode effect, *J.A.T.P.*, 29, 709-721

Law, J.(1963) The ionisation of the atmosphere near the ground in fair weather, *Q.J.R.M.S.*, 89, 107-121

Obolensky,W.N. (1925) Über elektrische Ladung in der Atmosphäre, *Ann. Phys. Lpz.*, 77, 644-666

Properties of Ion-induced Nucleation Obtained from Mobility Measurements

K. Hara, S. Nakae and K. Miura

*Department of Physics, Science University of Tokyo, Tokyo 162-8601, Japan*

**Abstract:** The ion-induced nucleation occurred at lower saturation ratio than that of homogeneous nucleation. The saturation ratios initiating growth of droplets differed in ion polarities. Electrical mobility of ions was examined relating to an ion-induced nucleation. It was measured with ion electrical mobility spectrometer of time-of-flight type. Measurements were made at various temperature and relative humidity. As a result, mobility of ions differed with different polarities under various conditions of atmosphere.

## 1. Introduction

The purpose of this research is to elucidate the mechanism of ion-induced nucleation in the stratosphere. Formation mechanisms of particle layer in the stratosphere have not yet been elucidated. One of the formation mechanisms at upper stratosphere is an ion-induced nucleation process. It seems likely for the following reasons: (a) little effect of Aitken particles transported from troposphere, (b) increase in ion-electron densities with altitude, (c) decrease in saturated vapor pressures of water and sulfuric acid.

The ion-induced nucleation processes were examined under the stratospheric conditions. The supersaturated condition was made by mixing the ionic air with hot vapor saturated with alcohol saturated vapor. The nucleation process was carried out with controlling the saturation ratio. It was confirmed that the ion-induced nucleation occurred at lower saturation ratio than that appears at homogeneous nucleation.

The experimental result is shown in Fig.1 [Hara *et al.*, 1997]. The saturation ratios initiating growth of droplets varied according to their polarity. The nature of ion species was examined by actual measurement of their electrical mobilities. The ion electrical mobility spectrometer (IMS) of time-of-flight type was made carefully. The ion species change in mass by the degree of ion-molecule reactions. The reaction rate depends on the atmospheric conditions including ions, such as temperature, relative humidity, pressure and neutral gas composition. The ion current was obtained with IMS and this dispersibility varied according to the drift time in the tube, temperature, relative humidity and pressure.

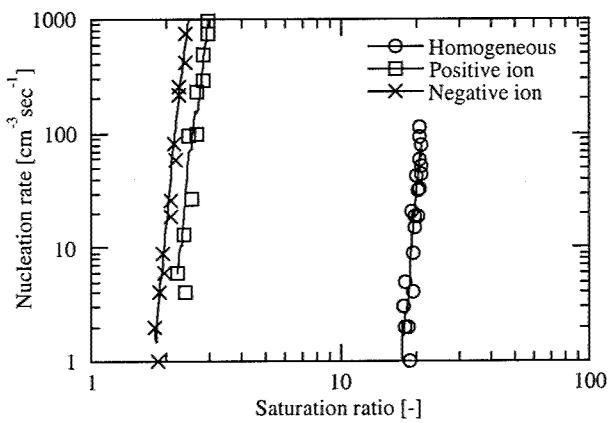


Fig. 1. Nucleation rate on homogeneous, positive and negative ion-induced nucleation

It was known that the electrical mobility spectra varied depending on the drift time of ions in the tube [Nagato and Ogawa, 1988].

In this paper, we report the electrical mobility measurements under the various temperature and relative humidity

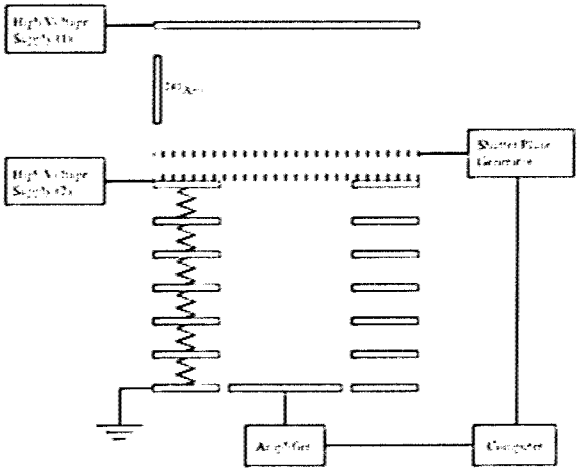

Fig. 2. Ion electrical mobility spectrometer with drift tube

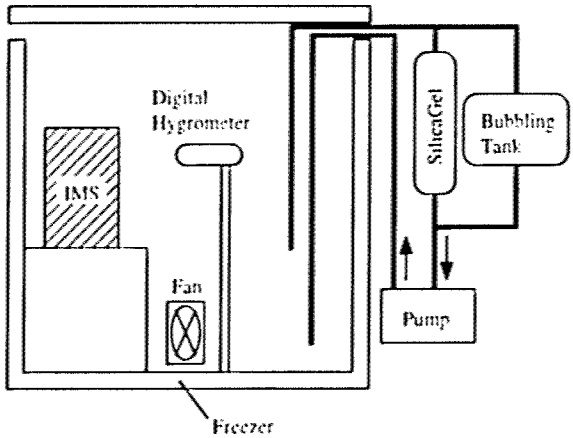


Fig. 3. Experimental chamber

## 2. Experimental

Electrical mobility of ions is measured by electrical mobility spectrometer of time-of-flight type. Figure 2 shows the ion mobility spectrometer with drift tube. This spectrometer consists of three parts, an ionization region, an electrical shutter region, and a drift region. In the ionization region, air is ionized by radiation emitted from $^{241}$Am, and then ion pairs are generated. Ion pairs are separated into positive and negative ions by an electric field supplied in the ionization region. The ion swarm is introduced into the drift region by the electrical shutter. After introducing the ion swarm to the drift region the drift velocity of ions attains to the constant by the collision with ions and molecules under the influence of a supplied electric field in the drift region. An electrical mobility, $k$, is determined from the drift velocity and the electric field in the drift region.

The experimental chamber is shown in Fig.3. This chamber is a freezer box, where temperature is variable from −40°C to room temperature. Relative humidity in the chamber is controlled with water bubbling tank and silica gel tube. Ion mobilities are measured with various conditions of temperature and humidity in the chamber.

Experimental points under various conditions are shown in Fig.4. The ranges of temperature and humidity are −36 to 36°C and 10 to 90 %, respectively. Measured mobilities, $k$, are converted into the values $k_0$ under the standard conditions using the Langevin rule, Eq.(1).

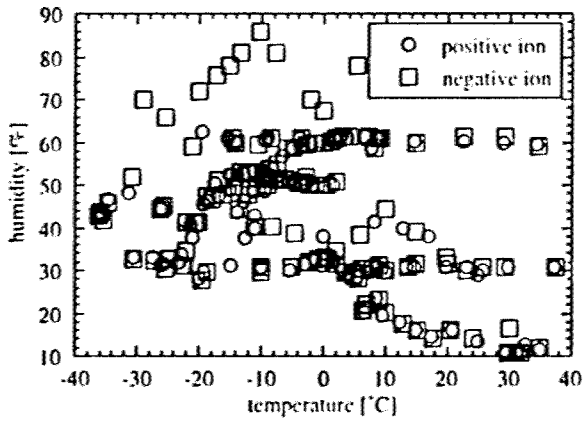


Fig. 4. Experimental conditions

$$k_0 = k \cdot \frac{p}{1013.25[\mathrm{hPa}]} \cdot \frac{273.15[\mathrm{K}]}{\theta} \tag{1}$$

where $p$ is pressure and $\theta$ is temperature on measured condition.

## 3. Results and Discussion

Figures 5–6 show the variations of mobility spectrum with temperature at narrow range of humidity. In the case of positive ions, mobilities gradually increase with decreasing temperature, and pass through a maximum at about 0 °C. With falls below 0 °C, mobilities decrease inversely. The width of mobility spectrum varies from wide to narrow with decreasing temperature. In the case of negative ions, mobilities shift from low to high values with decreasing temperature.

Figures 7–8 show the peaks of mobility spectra depending on the temperature with four ranges of humidity. In the case of positive ion, the mobilities shift from low to high value with decreasing temperature, and pass through a maximum at −10 to 10 °C. After passing through a maximum, the mobilities inversely shift to low value. Variations of peak mobilities have been small with increasing humidity. In the case of negative ion, the mobilities shift to high values with decreasing temperature at all range of humidity. However, mobilities depend largely on the temperature with increasing humidity.

Figure 9 shows the peak position of negative ions mobility spectra depending on humidity at four ranges of temperature. The mobilities shift to high values with decreasing humidity at all range of temperature. In this case, mobilities depend largely on the humidity with increasing temperature. In the case of positive ions, mobility spectra have not clearly depended on humidity.

It is supposed that the variation of mobilities with humidity might conceivably result from differences in clustering of water molecules, and also, it is supposed that the influence of temperature is related to ion-molecule reaction rate.

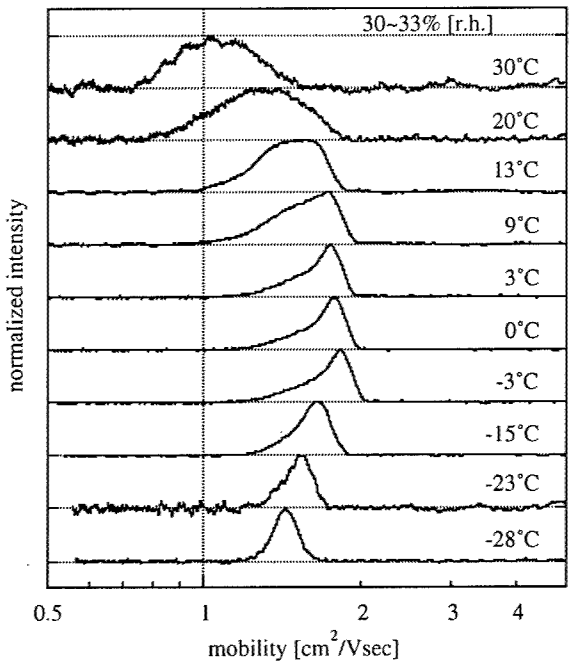


Fig. 5. Variation of positive ion mobility spectrum with temperature

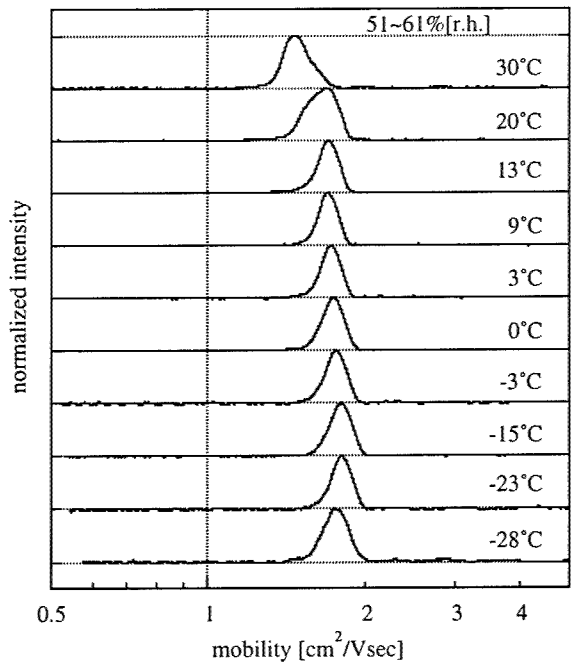


Fig. 6. Variation of negative ion mobility spectrum with temperature

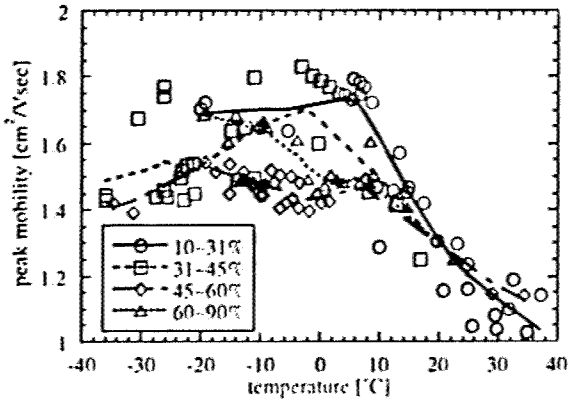


Fig. 7. Peak position of positive ion mobility spectra depending on temperature

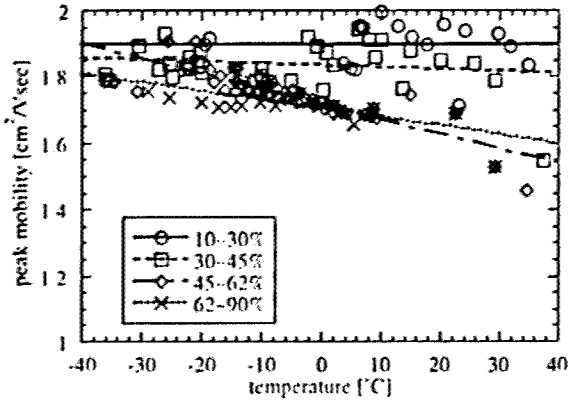


Fig. 8. Peak position of negative ion mobility spectra depending on temperature

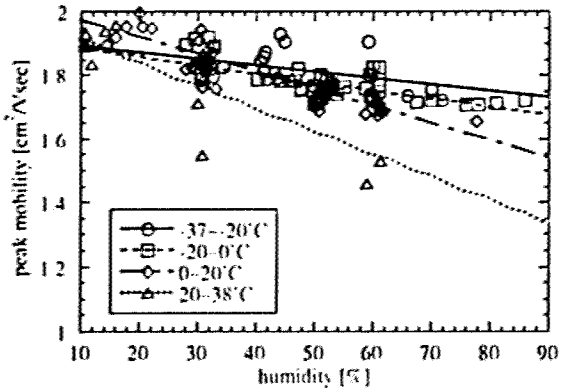


Fig. 9. Peak position of negative ion mobility spectra depending on humidity

## 4. Conclusion

Electrical mobility of ions was measured with ion electrical mobility spectrometer of time-of-flight type. It was found that the mobility of ions differed with different polarities at the various conditions. In the case of positive ions, mobilities increase with decreasing temperature, and pass through a maximum, then fall off inversely. In the case of negative ions, mobilities shift to high value with decreasing temperature and humidity. It is supposed that mobility shift is caused by the influence of the clustering of water molecules and ion-molecule reaction rate.

## References

Hara, K., S. Nakae, and K. Miura, Properties of ion nucleation in the atmosphere, *J. Atmos. Electr., 17, 53-58, 1997*

Nagato, K., and T. Ogawa, Atmospheric ion mobility spectra near the ground, *Planet.Space Sci., 36, 163-176, 1988*

# ENHANCED FAIR-WEATHER ELECTRIC FIELDS SOON AFTER SUNRISE

T. C. Marshall[1], W. D. Rust[2], M. Stolzenburg[1], W. Roeder[3], and P. R. Krehbiel[4]

[1] Department of Physics and Astronomy, University of Mississippi, University
[2] NOAA/ERL/National Severe Storms Laboratory, Norman, OK
[3] USAF 45th Weather Squadron, Patrick AFB, FL
[4] Physics Department, New Mexico Institute of Mining and Technology, Socorro

## INTRODUCTION

The typical fair weather electric field at the ground is between -100 and -300 V $m^{-1}$. At the NASA Kennedy Space Center and US Air Force Cape Canaveral Air Station (abbreviated hereinafter as KSC) the electric field at the ground sometimes reaches -400 to -1200 V $m^{-1}$ within an hour or two after sunrise on days that otherwise seem to be fair weather. (Throughout this study we use the following convention for electric field polarity: a positive, upward electric field causes an upward force on a positive charge.) We refer to the enhanced negative electric fields as the "sunrise enhancement." To investigate the sunrise enhancement at KSC we measured the electric field ($E$) in the first few hundred meters above the ground before and during several sunrise enhancements. From these $E$ soundings we can infer the presence of charge layers and determine their thickness and charge density.

## INSTRUMENTATION

We measured the electric field in the first several hundred meters above the ground with an electric field meter (EFM) carried by a tethered balloon. A schematic of the EFM, rigging system, and tethered balloon is in Figure 1. For this experiment we set the upper limit of the EFM at ±5000 V $m^{-1}$ with a resolution of 1 V $m^{-1}$. The $E$ data were telemetered to a receiving system carried in our mobile lab parked at the tether site. Atop the mobile lab, at 2.9 m above the surface, are sensors to measure temperature, humidity, wind speed, and wind direction. On each measurement day we began making $E$ soundings before sunrise and continued making soundings for the next few hours. The network of electric field mills at KSC provided $E$ data near the ground to determine when and where sunrise enhancements occurred. These downward facing, rotating vane mills are located at an altitude of 1.0 m. The $E$ values shown in this paper from the KSC field mills are one-minute averages.

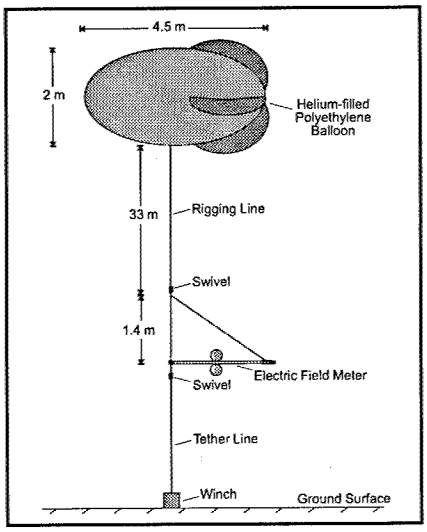


**Figure 1.** The tethered balloon sounding system. The winch holds 1000 m of line.

## DATA AND DISCUSSION

In our analysis of the $E$ soundings, we assume that the charges are approximately distributed in horizontal layers. We make this assumption to calculate an effective charge density and layer depth for the charge layer by using a one-dimensional approximation to Gauss's law. We also assume that the ground represents a flat conductor. The total $E$ at any location is due to the induced charges on the conducting surface as well as on the charges in the air. Using the flat conductor assumption and the infinite horizontally stratified charge assumption, it is easy to show that $E$ at any altitude is due only to the charge above the measurement altitude.

On September 7, 1996, we made 13 ascent $E$ soundings adjacent to KSC Mill 18, beginning shortly before sunrise and continuing for about 3 hours. There was a sunrise enhancement beginning about 1143 UT; at KSC Mill 18 the enhancement peak magnitude was about 900 V $m^{-1}$ at 1230 UT. Ephemeris sunrise was at 1104 UT, but the sunshine did not strike the ground at the tether site until 1120 UT. During part of the morning there was a thin fog layer a few meters above the surface near the tether site.

Figure 2 shows the first 6 soundings made on September 7. These early soundings, made before the enhancement began, were similar to soundings made on non-enhancement days in the following ways: (1) the largest $E$ was found at the lowest altitude of 1.3 m, (2) there was a positive charge layer located close to the ground (below about 20 m altitude), (3) the $E$ magnitude was less than 200 V $m^{-1}$ above 50 m altitude, and (4) the charge density of the layer was between 0.05 and 0.2 nC $m^{-3}$ and was larger before local sunrise than after.

Figure 3 shows the later soundings made on September 7, and Figure 4 shows the deduced charge densities and layer thicknesses based on the $E$ soundings, along with the KSC Mill 18 $E$ data and the meteorological data from the tether site. In Figure 4 there is a time lag between the beginning of the local sunrise enhancement (1143 UT) and the beginning of increased fluctuations in the meteorological parameters (relative humidity, wind speed, and wind direction) at 1217 UT. The $E$ soundings in the period between 1143 and 1217 UT, #7 and #8, were similar to the pre-enhancement soundings (Fig. 2) except that the charge density increased from about 0.06 nC m$^{-3}$ in sounding #6 to 0.12 nC m$^{-3}$ in sounding #8.

As Figures 3 and 4 show, the $E$ soundings and charge layer characteristics on September 7 changed substantially shortly before the sunrise enhancement reached its local maximum at 1230 UT. Sounding #9, which began at 1219:40 UT, was substantially different from the previous ascent soundings and was made at about the time that the fluctuations in the meteorological parameters began. Subsequent $E$ soundings (#10-13) were similar to sounding #9 and were different from the soundings made before the increase in meteorological fluctuations. Together, soundings #9-13 show (1) an increased $E$ magnitude at the ground, (2) a deepening positive charge layer (increasing from 20 m before the enhancement to 170 m), and (3) a corresponding decline in charge density as layer thickness increased.

Data collected on four other days further reinforce the validity of the correlations found in the data presented above for September 7: the local charge density begins to increase at the same time as the beginning of the local sunrise enhancement while the charge depth and the meteorological parameters remain roughly constant, and, when the local meteorological parameters begin to show substantial fluctuations and just before the local maximum in the sunrise enhancement, the charge layer depth increases while the charge density decreases.

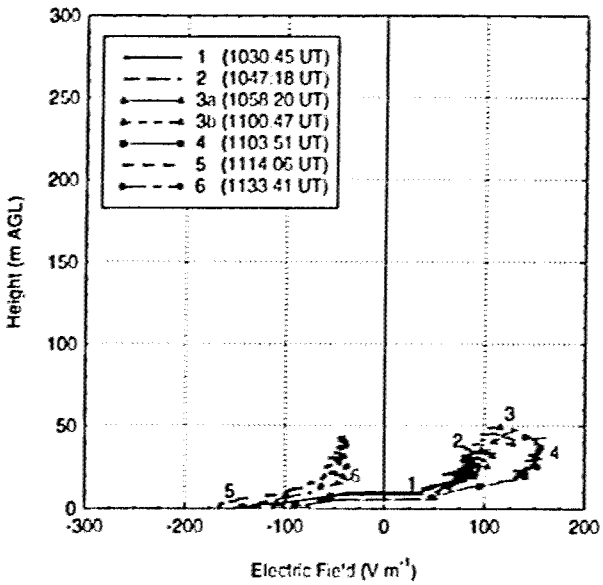


**Figure 2.** First six balloon soundings of electric field made on September 7, 1996, from near KSC Mill 18.

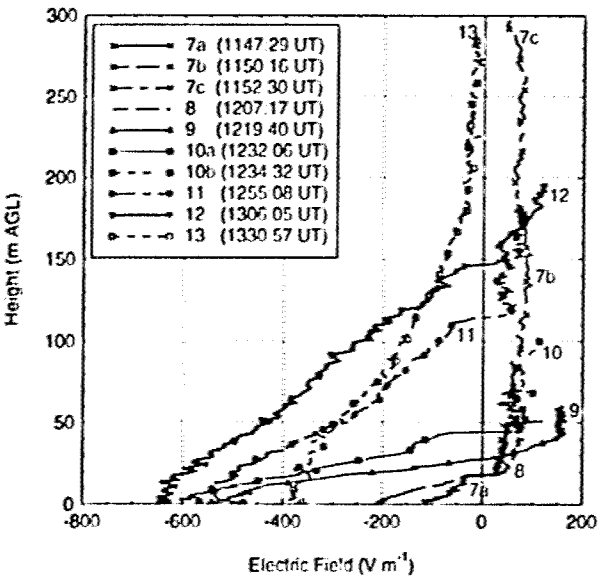


**Figure 3.** Last seven balloon soundings of electric field made on September 7, 1996, from near KSC Mill 18.

## HYPOTHESES

A workable hypothesis must explain the increase in charge observed between 1.3 m and 200 m above ground. The approximate one-dimensionality of the charge distribution and the approximate flatness of the ground lead to the conclusion that the field measured by the KSC mills and the balloon-borne field meter is due only to charge above these instruments. The additional charge must move into the charge layer from one of three places: from above, from the side, or from below. We can rule out charge entering the layer from above, for we would have seen this in the balloon soundings. The possibility that the charge enters from the side will be called the advection hypothesis, while the possibility that the charge enters from below will be called the convection hypothesis.

**The advection hypothesis:** The advection hypothesis depends on the presence of nearby, denser charge. In this hypothesis we envision the denser charge is initially over water to the west of the KSC field mill network. Since there is usually less radioactivity in water than in soil [*Mühleisen*, 1961], the positive electrode layer charge density should be higher over water than over land. The coincidence between the change in the wind direction to

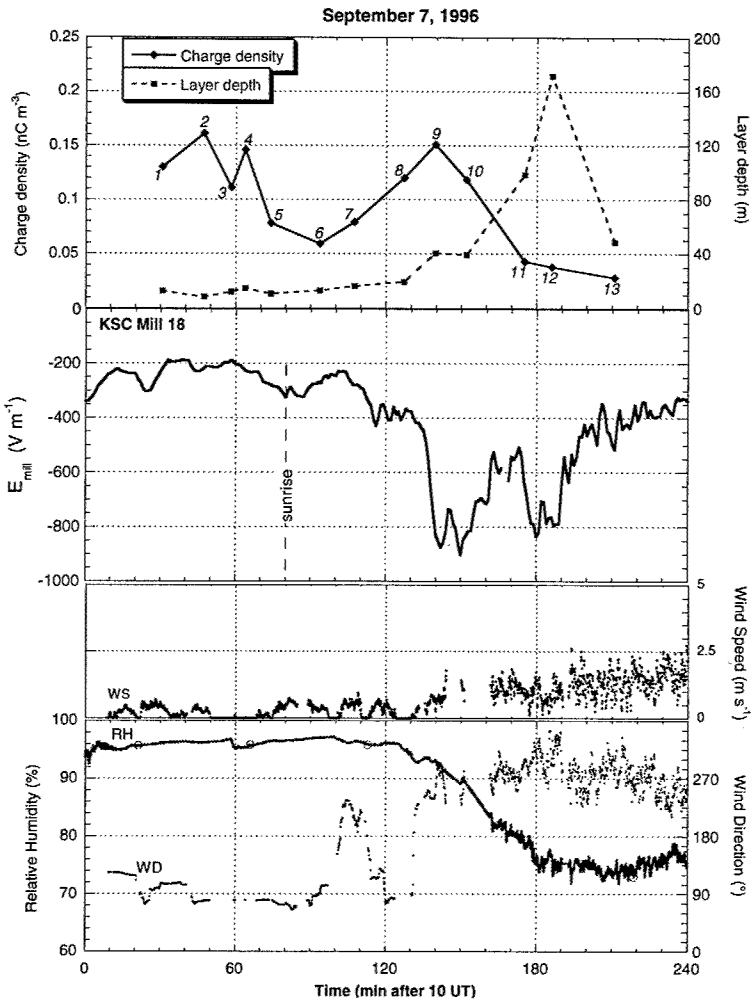


**Figure 4. Top panel** shows charge density and charge layer depth pairs deduced from each balloon sounding on September 7, 1996. Sounding numbers are marked along the charge density curve, and points are plotted at the beginning time of the ascent. **Middle panel** is electric field data from KSC Mill 18. The time marked "sunrise" is when sunlight first reached the ground at the tether site, a few meters away from Mill 18. **Bottom two panels** are other meteorological measurements made at the tether site with instruments mounted atop the mobile laboratory at 2.9 m height. There are gaps in these data between 1210 and 1245 UT.

roughly westerly at the balloon tether site (beside KSC Mill 18) and changes in the depth and density of the charge layer suggests that, during the sunrise enhancement at Mill 18, enhanced positive charge is being advected eastward from the Indian River to Merritt Island and the KSC field mill network.

Two facts in the balloon sounding data do not agree with the advection hypothesis. First, the charge density and layer depth would not change until the advected charge arrived; the arrival is indicated by the wind shift and the increase in turbulence in the meteorological data. However, the wind shift and the increase in turbulence occurred 5-30 minutes after the local charge density had begun increasing rather than occurring at the same time as the local enhancement in $E_{mill}$. Second, the advection hypothesis does not fit with the strong positive electrode layer that existed before the sunrise enhancement began; the pre-enhancement electrode layer characteristics were similar to the electrode layer over water reported by *Mühleisen* [1961]. Although we have no measurements of the charge characteristics over the Indian River, the similarity between our land measurements and those by *Mühleisen* [1961] over water makes the advection hypothesis seem unlikely to work as described.

**The convection hypothesis:** The convection hypothesis depends in part on the location of charge in a nonturbulent electrode layer and the relative positions of the $E$ measuring instruments. In this hypothesis we envision a dense layer of positive charge growing below 50 cm shortly before dawn on days without turbulence, as found by *Hoppel* (1967).

When nonturbulent, convectively stable conditions are established before sunrise, a substantial electrode layer of positive charge can form in addition to the usual electrode layer spread through the first 10 to 20 m. This additional charge layer would be located below 50 cm and, therefore, below the KSC field mills (at 1 m) and below the lowest altitude sampled by our EFM (1.3 m). The KSC mills would not be influenced by this additional portion of the electrode layer, since the additional charge would be located below the mills. At sunrise, solar

heating of the ground begins to change the temperature profile and small-scale convection begins. This convection would transport the denser charge at the surface upward. Initially, convection would occur on a very shallow scale of only centimeters. After a while the mixing would reach above the level of the KSC mills and would increase the positive charge above the mills. The amount of time this takes is unknown, but perhaps it corresponds to the 20 minutes between local sunrise and the beginning of the sunrise enhancement evident in the KSC mill data. As deeper mixing occurs, more positive charge from the pre-sunrise electrode layer would be transported above the KSC mills, thereby increasing the $E$ value measured. The KSC mills would see the results of convective mixing before our meteorological instruments (at an altitude of 2.9 m). The development of a convectively stable layer below a temperature inversion at night followed by convective mixing of the stable layer from the bottom upward after sunrise is a well known phenomenon.

Potential weaknesses in the convection hypothesis can also be pointed out. First, the enhancement is different in magnitude at different mills. Second, some of the mills nearer water have the larger field enhancements. We might expect that the convection hypothesis would give similar enhancements at all locations. A possible resolution of these problems is that the meteorological conditions needed to build up an enhanced electrode layer might be different at different mills. For example, since locations near water are topographically lower, they may be more protected from light breezes than other sites, thereby favoring a more enhanced electrode layer. Furthermore, the nearby water would favor the growth of larger cloud condensation nuclei and fog; these would also lead to a more enhanced electrode layer. KSC Mill 18, where most of our data were collected, is a good example of such a low-lying mill site: it is located in a shallow depression only a couple of meters from the eastern edge of a marsh.

## CONCLUSIONS

We used a tethered, instrumented balloon to collect fair-weather electric field data in the lowest few hundred meters above the ground before, during, and after 17 sunrises at the Kennedy Space Center. From the $E$ soundings we determined the density and thickness of the charge layer just above the surface of the earth. At our tether site the layer charge density began increasing at about the same time as the beginning of the local enhancement in the electric field magnitude at the ground. These changes began well before there was any change in the charge layer thickness above the tether point or any substantial change in relative humidity, wind direction, or wind speed measured at a height of 2.9 m at the tether site. Shortly (10-20 minutes) before the peak in the local surface $E$ enhancement, the layer charge density decreased while the charge layer thickness increased; these changes were coincident with a substantial decrease in relative humidity, a shift in the average wind direction, and increased fluctuations in relative humidity, wind speed and direction at 2.9 m. The typical decrease in charge density was from 0.2 to 0.05 nC $m^{-3}$ while the charge layer thickness increased from less than 20 m to almost 200 m.

We present two hypotheses, both based on enhanced electrode layers in the absence of radioactivity, to explain the observations. The convection hypothesis, in which there is local upward mixing of denser low-lying electrode layer charge, seems to fit more of the data, thus we prefer it over the advection hypothesis to explain the KSC sunrise enhancement. However, it seems possible that a combination of both processes may be needed to explain the relative magnitudes of the $E$ enhancements and the timing of the enhancement onsets. Indeed, the convection hypothesis relies heavily on turbulent mixing (associated with convection), and turbulent motions include horizontal as well as vertical transport. The stronger enhancement at some KSC field mills may be supplemented by advection of denser charge from above adjacent water or marshes. In some cases, this advection would only need to occur over distances of a few meters, rather than the 1000 m or more needed to bring charge from the Indian River.

***Acknowledgments:*** This experiment would not have been possible without the logistical support of John Madura at NASA/KSC. Phillip Gemmer, Amy Rust, Les Showell, and A1C Angela Carter helped collect the data, and Patrick Stoller helped analyze the altitudes. We thank Computer Sciences Raytheon Corp for providing helium. We appreciate the guidance of Professor C. B. Moore with the speculation concerning advection of an enhanced electrode layer from the Indian River. We also appreciate John Willett for his comments and suggestions on this work. This research was supported by the USAF 45th Weather Squadron and by NASA/KSC.

## REFERENCES

Mühleisen, R., Electrode effect measurements above the sea, *J. Atmos. Terr. Phys.*, *20*, 79-81, 1961.
Hoppel, W. A., Theory of the electrode effect, *J. Atmos. Terr. Phys.*, *29*, 709-721, 1967.

# ON ELECTRIC PROPERTIES OF RADIATION FOG

S. Israelsson

Meteorology, Department of Earth Sciences, University of Uppsala, Uppsala, Sweden.

ABSTRACT: The results from 9 field studies of the electrical and meteorological properties of radiation fog are presented. The radiation cooling and turbulence is controlling radiation fog. About 1 hour before sunset the negative radiation balance leads to a cooling of the surface layer, which leads to a reduction in the turbulent diffusion and an increasing concentration of radioavtivity in the lowest layer. The shallow layer of enhanced ionization can cause a reversed electrode effect with a stratum of negative space charges. Periods of significant fog develoment appeared to occur when wind speeds dropped below 0.5 - 1 $ms^{-1}$ below 10 m. There is also in radiation fog a distinct tendency of quasi-periodic oscillations of the meteorological and electrical parameters on a time scale longer than 10 min. Fog formation starting also above the ground and an attachment of ions to the fog droplets occurs, which leads to negative space charge density in the radiation fog, 30 - 100 $pCm^{-3}$, and a sedimentation current on average -1.4 $pAm^{-2}$. Both the conductivity and electric potential gradient in radiation fog are on the average reduced to one-third of their values in fog-free air. For conductivity by reason of the attachment of small ions to the fog particles. That leads to that the conduction current will be reduced to one-tenth of the the value in fog-free air. The effect of radiation fog on the potential gradient is normally a consequence of the change of the conductivity. But in the present study the potential gradient decreases in the radiation fog.

## INTRODUCTION AND PAST INVESTIGATIONS

There is controversy in the literature concerning radiation fog formation. One set of observations suggests that fog forms during a lull in turbulence, while other observations suggest that increased turbulence leads to fog formation (*Welch et al.*, 1986). Generally, radiation fog forms in fair-weather after nocturnal surface cooling lowers the temperature to the dew point. Results by *Bott et al.*, (1990) elucidated the strong interaction between the radiatively induced dropletgrowth and their gravitational settling is responsible for a distinct reduction of the liquid water content.

An overview of the electric phenomena in the lower atmosphere is given by *Hoppel et al.*, (1986). The conductivity decreases markedly in fog by reason of the attachment of small ions to fog particles, rendering the ions much less mobile. A source of space charge at ground level is the electrode effect. The primary source of ions in the atmospheric surface layer is radioactivity originating from the ground. In nocturnal temperature inversions the radioactive gases can be trapped in a concentrated layer close to the ground, see *Israelsson et al.*, (1973). *Crozier* (1963a) showed that the space charge can reverse from positive in the lowest 10 to 20 cm to negative above, yielding a reversed electrode effect. Measurements of all pertinent parameters are needed during a fog event to formulate a physical theory that adequately accounts for the observations. Measurements of space charges in fog are sparse and do not provide a uniform picture. Studies (see *Israel,* 1973) show that the droplet charge limit increases in proportion to the radius of the particle. In wet mist it has often been found (*Chalmers,* 1967) that there is a current to the earth frequently of opposite sign to the potential gradient, so that there could not be a conduction current. Under misty conditions *Borra et al.*, (1997) demonstrate the occurrence of unipolar negative point discharges with current densities between -1 to -10 $pAm^{-2}$. The attachment of negative ions to droplets coupled with the sedimentation are shown to be efficient and could account for the sub-$nCm^{-3}$ space charges observed in the mist layer. In fog the conductivity is usually reduced to 1/3 of the value in mist-free air. Accordingly one would expect that in fog there would be an increase in the potential gradient or a reduction in in the air-earth current or both simultaneously. But in some case contradictory effects are observed. For fog one must distinguish between two different influences on the air-earth current. One is the reduction of the conductivity and changes the potential gradient or both. The other influence stems in a modification by falling electrically charged fog particles, the sedimentation current.

## THEORETICAL CONSIDERATIONS

The various currents that flow near the ground can be expressed as $J_M = J_E + J_C + \varepsilon_0 dE/dt$, where $J_M$ is the total Maxwell current measured by a horisontal plate antenna. $J_E$ is the conduction current, $J_C$ is the convection current and $\varepsilon_0 dE/dt$ is the displacement current, which does not involve any charge transfer. The last term is in most cases in fair-weather conditions fairly small. In the present study we used the mean turbulent flux, the current $J_c$, $w'Q'$, where $w'$ is the vertical velocity fluctuations and $Q'$ is the turbulent fluctuation of the space charge density. We here use $J_s$, the sedimentation current, which is a function of falling charged particles influenced by the gravitation expressed by $v_s Q$, where $v_s$ is the sedimentation velocity and Q is the space charge density of the fog. The convection current $J_C$ can be splitted into $J_{c'}$, the turbulent current and the sedimentation current $J_s$. Thus $J_C = J_{c'} + J_s$.

In radiation fog the mean turbulent current is fairly limited due to that the eddy-diffusion coefficients are small and lie between $10^{-2}$ to $10^{-4}$ $m^2s^{-1}$. This leads to the following expression:

$$J_M = J_E + J_S \qquad (1)$$

## RESULTS AND DISCUSSIONS

The measurements were made at the Marsta Observatory (59°55'N, 17°35'E) located in very flat farming area 10 km north of Uppsala, Sweden. The nearest forest is more than 1 km away from the observatory. The very flat surroundings with very few obstacles lead to an occurrence of radiation inversions with fog. A map of the observatory is presented by *Israelsson et al.*, (1973). The micrometeorological parameters wind, temperature and humidity were continuously recorded with standard instruments.

For measurements of the space charge density two identical instruments (Obolensky filters) were constructed which, apart from minor modifications, are copies of the Anderson apparatus (see *Anderson*, 1966). The instrument is shown schematically in a previous paper (*Knudsen et al.*, 1989). The α-activity of the air was recorded by ionization chambers which have been presented in previous papers, see *Israelsson et al.*, (1972). We measured the electric potential gradient with a radioactive collector and a field mill at a height of 1 m, the electric polar conductivity ( $\lambda^+$ and $\lambda^-$ ) with aspiration condensers. The critical mobility of the conductivity meter was $2 \cdot 10^{-4}$ $m^2V^{-1}s^{-1}$. The vertical current density was measured according to the Kasemir-Dolezalek system (*Israel*, 1973). We also used horizontal long-wire antenna, see Israelsson et al., (1994).

Results from 9 field studies of the electrical and meteorological properties of radiation fog are presented. The data have been treated in the following way. First the fast fluctuations of the different parameters were studied. Then the hourly mean-values were determined and finally the mean-values from the 9 fog cases were calculated. In the present paper we only present one diagram, Figure (1), from a case where hourly mean values are used.

The study shows that about 1 hour before sunset the negative radiation balance leads to a cooling of the surface layer, which leads to a reduction in the turbulent diffusion and an increasing concentration of radioavtivity in the lowest layer. Fog formation starting above the ground at this time. The present study shows that the the radiation fog is preceded by a period of the growth of subvisible droplets. This growth to visible size requires 1 to 2 hours. Surface cooling decreases is about 1-2 °C per hour. Relative humidity increases in the lower 10 m to saturated conditions. A very weak ground fog in the lower levels develops in this period. But the fog development is coupled with the destabilization of the lower atmosphere and with increases in turbulent mixing. The fog formation started above the ground which has been observed in several field studies (e.g., *Jiusto and Lala*, 1983).

We observed that the first phase of fog development appears to have been associated with periods of marked cooling and with relative lulls in the wind. There is also a tendency for fluctuations on the time scale of 10 or more minutes in wind below 10 m. The oscillations were also observed in the other meteorological and electrical parameters. Oscillations of 10-20 min. have been shown for meteorological parameters by *Brown and Roarch*, (1976) and *Borra et al.*, (1997). The slow oscillations are in our cases dependent on the surrounding orography and the meso-scale structure of the atmosphere.

Results by *Bott et al.*, (1990) elucidated the strong interaction between the radiatively induced dropletgrowth and their gravitational settling is responsible for a distinct reduction of the liquid water content. Fog can forms several meters above the ground due to that strong temperature inversion reduces the net thermal emission on the lowest few meters.

Our unfiltered data show turbulent variations of the space charge density before sunset and pronounced slow variations after sunset in stable stratification and radiation fog.

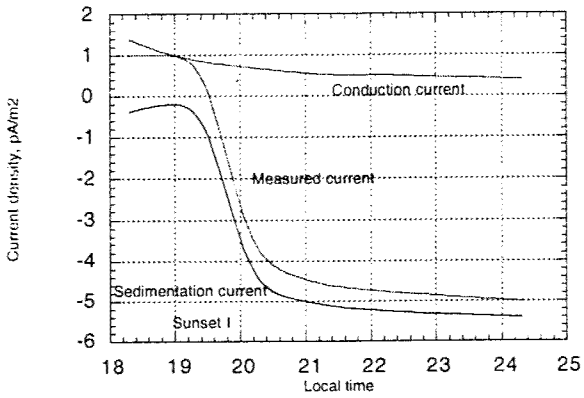


Figure (1). Hourly mean values of the different currents in radiation fog.

Figure (1), represents hourly mean values from one of the cases, May 3, from measurements of the different current densities according to Equation (1). The visibility in the fog is less than 100 m. The diagram shows that before sunset the measured current and the conduction current densities agree very well. But near sunset the measured current and the sedimentation current densities approach each others. The sedimentation current density will be negative. Our observations indicate that the space charge density will be negative and the polar conductivity, potential gradient and conduction current decrease about one hour before the visiual observation of radiation fog. This shows a modification by falling electrically charged fog particles and therefore a sedimentation current appears. The conductivity in radiation fog is in our 9 cases on the average reduced to 0.31 of its value in fog-free air by reason of the attachment of small ions to the fog particles. The potential gradient is reduced to on an average 0.29 of its value in fog-free air. The conduction current is in the same way on the average reduced to 0.09. The sedimentation current ($J_S$), calculated according to Equation (1), in the radiation fog is on an average -1.4 $pAm^{-2}$. This current density is caused by the direct interaction of two physical processes, i.e. the radiatively induced growth of the larger particles and their subsequent gravitational settling. Gravitational settling of charge droplets also emerge as an important factor. This is in agreement with observations by (*Chalmers*, 1967), who found that in wet mist it often a current to the earth frequently of opposite sign to the potential gradient, so that there could not be a conduction current, which is in agreement with our results. Under misty conditions *Borra et al.*, (1997) demonstrated the occurrence of unipolar negative point discharges. The attachment of negative ions to droplets coupled with the sedimentation are shown to be efficient and could account for the sub-$nCm^{-3}$ space charges observed in the mist layer.

*Hoppel et al.*, (1986) described the atmospheric-electric fog effect and they used the words "typical example of successful forecast of both onset and dissipation of fog". In their diagram the conductivity decreased during the fog as was expected. But the potential gradient growthed which is in opposite to the present results. The different electrical properties of the fog can be explained by the differences in the fog formations. The building up of radiation and advection fog is quite different from meteorological point of view.

The dropletgrowth velocity depends on the supersaturation and therefore it is a function of the time. Generally, radiation fog forms under high pressure and stable conditions after nocturnal surface cooling lowers the temperature to the dew point. Our observations show that the fog seems at first stage to be coupled with the stabilization of the lower atmosphere with decreasing turbulence. But during the developing of the fog the destabilization with increasing in turbulent mixing seems to play a role. This is in agreement with observations by *Jiusto and Lala* (1982) and *Welch et al.*, (1986).

The attachment of ions to cloud particles reduces their concentration and the electrical conductivity. *Phillips* (1967) and *Griffithes et al.*, (1974) concluded that a decrease in conductivity of about 3 orders of magnitude occurred under highly electrified conditions. This decrease was found to be sensitive to variations in the liquid-water content and the electrical field but only slightly affected by changes in altitude, particle charge, and the manner in which the charge is distributed over the size spectrum.

As a summary our observations indicate that the space charge density will be negative and the polar conductivity and potential gradient decrease about one hour before the visual observation of radiation fog. This also leads to a decreasing conduction current in the radiation fog but at the same time an increasing negative sedimentation current can be noted, showing the importance of the gravitation settling.

ACKNOWLEDGEMENTS: The study was supported in part by grants from the Swedish Natural Science Foundation.

REFERENCES

Andersson, R.A., Absolute measurements of atmospheric charge density, *J. Geophys. Res.* 71, 24, 5809, 1966.

Borra, J.-P., R.A. Roos, D. Bernard, H. Lazar, A. Goldman and M. Goldman, Electrical and chemical consequences of point discharges in forest during mist and a thunderstorm. *J. Phys. D: Appl. Phys.* 30, 84-93, 1997.

Bott, A., U. Sievers, and W. Zdunkowski, A radiation fog model with a detail treatment of the interaction between radiative transfer and of microphysics. *J. Atm. Sciences*, Vol. 47, No 18, 1990.

Brown, R. and W. T. Roach, The physics of radiation fog:II- a numerical study. *Quart. J. R. Met. Soc.* 102, 335-354, 1976.

Chalmers, J.A., *Atmospheric Electricity*, 2nd ed. Pergamon Press, Oxford, 1967.

Crozier, W. D., Electrode effect during nighttime low-wind condition. *J. Geophys. Res.*, 68, 3451-58, 1963a.

Griffith, R.F., J. Latham, and V. Myers, The ionic conductivity of electrified clouds. *Q. J. R. Meteorolog. Soc.* 100, 181-190, 1974.

Hoppel, W., R.V. Anderson, and J.C. Willett., Atmospheric electricity in the planetary boundary layer, in The Earth's Electrical Environment, *Studies in Geophysics*, National Academy Press, USA, p. 149-165, 1986.

Israel, H., *Atmospheric Electricity II*, Fields, charges and currents U.S. Dept. of Commerce, Springfield, 1973.

Israelsson, S., E. Knudsen, E. Ungethum and L. Dahlgren, On the natural a-activity of the air near the ground. *Tellus*, 24, 368-379, 1972.

Israelsson, S., E. Knudsen, and E. Ungethum, On the natural beta-activity of the air in the atmospheric surface layer. *Atm. Environment*, Pergamon Press, Vol 7, 1127-1137, 1973.

Israelsson, E., Knudsen and H. Tammet, An experiment to examine the covariation of atmospheric vertical currents at two separate stations. *J. Atm. Electr.*, Vol.14, No 1, 63-73, 1994.

Jiusto, J.E., and G.G. Lala, Radiation fog field programs- recent studies. ASRC-SUNY, Publ. No. 869, 1983.

Knudsen, E., Ungethüm, E. and Israelsson, S., A new space charge measuring system. *Gerl. Beitr. Geoph.* 83, 1974.

Knudsen, E., K. P. S. C. Jayaratne, and S. Israelsson, An investigation of sources of errors by space charge measurements using the Obolensky filter method. *J. Atm. Terr. Physics*, Vol.51, 527- 531, 1989.

Philips, B.B., Ionic equilibrium and the electrical conductivity in thunderclouds. *Mon. Weather Rev.* 95, 854-862, 1967

Welch, R.M., M.G. Ravichandran and S.K.Cox, Prediction of quasi-periodic oscillations in radiation fogs. Part I: Comparison and simple similarity approaches. *J. Atm. Sciences*, Vol. 43, No. 7, 633-651, 1986.

# MEASUREMENT OF ATMOSPHERIC ELECTRICAL CONDUCTIVITY DURING MONSOON PERIOD

Jagdish Rai, Adarsh Kumar and A. K. Singh*

Department of Physics, University of Roorkee, Roorkee-247 667, India

ABSTRACT: A Gerdian condenser was employed to study the positive conductivity during the monsoon period of 1996. Some meteorological parameters like temperature, wind speed, relative humidity, rainfall and atmospheric pressure were also measured simultaneously. The average value of conductivity for the months of June, July and August 1996 were found to be $26.71\times10^{-16}$, $37.55\times10^{-16}$ and $40.62\times10^{-16}$ mhos/m respectively. The average rainfall for the above three months was 6.5 mm, 170.8 mm and 715.0 mm respectively. The increase of conductivity with the increase in monthly rainfall has been attributed to the fact that the rain contains charged particles, which increases conductivity near ground surface. The conductivity increases with temperature and relative humidity for the entire monsoon period. It may be attributed to the condensation of droplets on aerosols, which influences the magnitude of ionization and ionic mobility near ground surface. Our results have been discussed in light of the existing theoretical and experimental studies.

## INTRODUCTION

The man's activity in a world of rapidly growing population may lead to inadvertent changes of the climate on a local basis and even on a global scale. Since the governing conditions of the human life style and the increasing air pollution are on an average related together and may have influence on the atmospheric electrical parameters, therefore, it is considered that parallel with the problem of pollution by industrial sources, vehicular traffic etc, the surface electrical parameters may also be altered [*Agarwal et al.* 1995]. Various investigators have studied the effect of air-pollution and meteorological changes on atmospheric conductivity [*Makino and Ogawa,* 1985; *Agarwal et al.* 1995 and many others], nothing is known regarding its variation during monsoon period. Therefore the authors thought to study it. The positive electrical conductivity during the monsoon period of June, July and August, 1996 were measured and the studies were made in relation with the changes in meteorological parameters like temperature, relative humidity and wind speed.

## MEASUREMENT TECHNIQUES

For the measurement of conductivity, Gerdien's cylinder [*Mukku,* 1982] was used. Gerdien's cylinder is a cylindrical capacitor consisting of a central electrode (conducting rod) and an outer electrode (cylindrical tube). When the air consisting of ions is sucked, the ions of opposite polarity are attracted by the electrodes. The charge collected by the electrode is fed to the ground through a high resistance. The voltage drop across the resistor is measured by an electrometer amplifier. The outer electrode was kept at a voltage of 30V.

The critical mobility inside the cylinder is given by [*Mukku,* 1982]

$$\omega_c = \frac{M \ln(R/r)}{2\pi L V} \qquad (1)$$

where, L is the length of the cylinder, R the radius of outer electrode, r the radius of inner electrode, V the voltage applied across the electrodes of the capacitor, M (= $\pi R^2 V$) aspiration rate and v the velocity of the air being aspirated

The ion having mobility greater than this critical mobility are captured by the central electrode. The ions having less mobility than the critical mobility are mostly removed by the aspiration. A fraction of ions with mobility less than $\omega_c$ is also collected. If $\omega/\omega_c$ is the fraction of ions with mobility less than the critical mobility that are being captured, then,

* Registered for Ph.D. Degree in the Department of Earth Sciences, University of Roorkee, Roorkee, India

$$i = Men\omega/\omega_c = \frac{M\sigma}{\omega_c} \quad (2)$$

here, $\sigma$ $(= ne\omega)$ is conductivity of air, n the number of ions per unit value and e the electron charge. From Equation (2) we have

$$\sigma = i\omega_c/M \quad (3)$$

The calculated value of the $\omega_c$ comes out to be $2.66\times10^{-4}$ $m^2V^{-1}sec^{-1}$. By noting the ionic current the conductivity of air can be calculated by using Equation (3).

The observations of positive conductivity were made on the top of the building (12 meters from ground) housing Physics Department of the University of Roorkee, Roorkee (29°51'N, 77°53'E, 275 meters above sea level), India. The daily mean values of electrical conductivity for the monsoon season were obtained by averaging electrical conductivity at every 5 minutes interval during the coarse of particular day. Meteorological data for temperature, relative humidity, wind speed and rain fall were obtained on normal meteorological instruments installed at the National Institute of Hydrology, Roorkee, India which is situated in the university campus.

## RESULTS AND DISCUSSIONS

Figure 1 shows the variation of atmospheric electrical conductivity for the months of June, July and August, 1996. The electrical conductivity for the three consecutive months were in the ranges of (16.86 - 37.11), (11.30-64.93) and (16.91-59.11) $\times 10^{-16}$ mhos/m respectively while the relative humidity was found to be within limits of (65-96), (67-94) and (86-95) for June, July and August. For the above three months the average conductivity was $26.71\times10^{-16}$, $37.55\times10^{-16}$ and $40.62\times10^{-16}$ mhos/m respectively. The atmospheric electrical conductivity in the month of June is positively correlated with relative humidity, while in the months of July and August, it is negatively correlated. Table 1 shows daily rainfall data for the months of June, July and August. As seen from Table 1, it rarely rained in the month of June except the last four days. The average rainfall for the above three months was 6.55 mm, 170.8 mm and 715.0 mm respectively. It has been found that the conductivity increases with increasing monthly rainfall. It has been attributed to the fact that the rain contains charged particles, which increases conductivity near ground surface. The increased relative humidity is due to the increased moisture content of the atmosphere. It is well known that the electrical conductivity of the moist air is more than that of the dry air.

However, July and August are the months of rain. Condensation of water molecules starts on aerosol particles. The atmospheric ions attached to the droplets and aerosols decrease the mobility of these ions. Thus the increasing relative humidity decreases the atmospheric electrical conductivity by decreasing the mobility of charge carriers. *Bhartendu* [1971] also found that the changes in relative humidity are inversely related to atmospheric electrical parameters.

The figure shows that during the three months of monsoon the conductivity has a negative correlation with temperature. *Nizamuddin et al.* [1982] found that with the onset of solar eclipse of March 7, 1980 an increment in both types of conductivity was reported. It is well known that the solar eclipse event is followed by a decrease in temperature. This has been attributed to the increased relative humidity in the atmosphere and hence the increase in atmospheric conductivity. However the conditions during monsoon period are quite different. During this period the water droplets are formed in the atmosphere thereby increasing the total aerosol concentration. A rise in temperature vaporizes the existing droplets and a decreasing temperature creates more droplets due to increased condensation. Thus the increasing temperature decreases the aerosol concentration there by decreasing ionic mobility and hence the decrease in the electrical conductivity.

Our results for unipolar conductivity and wind speed show a positive correlation for the entire monsoon period and an enhancement was noted with increasing wind speed. This finding is in agreement with the work of *Mukku* [1982] where he has reported that wind influences conductivity mostly in the short-term range. The high wind speed removes the larger particles faster and thereby increasing the mobility of smaller charged particles. The increased mobility increases the electrical conductivity. The

best fit regression line between conductivity and wind speed (WS), temperature (T) & relative humidity (RH), have been obtained from the three months data and those are given by

$\sigma = (9.01356\ WS + 13.6932) \times 10^{-16}\ Sm^{-1}$

$\sigma = (-0.012\ T + 34.94) \times 10^{-16}\ Sm^{-1}$

$\sigma = (-0.217\ RH + 53.69) \times 10^{-16}\ Sm^{-1}$

TABLE 1. Daily rain fall data for the months of June, July and August

| Date (June'96) | Rainfall (mm) | Date (July'96) | Rainfall (mm) | Date (August'96) | Rainfall (mm) |
|---|---|---|---|---|---|
| 11 | 0.2 | 1 | 0.3 | 1 | 7.8 |
| 12 | - | 2 | - | 2 | 18.6 |
| 13 | - | 3 | - | 3 | 11.4 |
| 14 | - | 4 | - | 4 | 31.0 |
| 15 | - | 5 | 32.1 | 5 | - |
| 16 | - | 6 | - | 6 | - |
| 17 | - | 7 | - | 7 | - |
| 18 | - | 8 | - | 8 | 3.2 |
| 19 | - | 9 | - | 9 | 11.6 |
| 20 | - | 10 | 15.2 | 10 | 1.4 |
| 21 | 0.3 | 11 | 21.4 | 11 | 1.6 |
| 22 | - | 12 | 4.2 | 12 | 0.2 |
| 23 | - | 13 | 4.0 | 13 | 76 |
| 24 | - | 14 | - | 14 | 23.5 |
| 25 | 3.1 | 15 | 7.4 | | |
| 26 | - | 16 | - | | |
| 27 | 20.4 | 17 | 5.0 | | |
| 28 | 3.2 | 18 | - | | |
| 29 | 0.5 | 19 | 32.2 | | |
| 30 | 14.2 | 20 | 11.2 | | |

ACKNOWLEDGEMENT: Authors are thankful to the University Grants Commission, New Delhi and the Indian Space Research Organization, India for financial support.

REFERENCES

1. Agarwal, R.R., Rai, J. and Varshneya, N.C., Effect of ionization and particulate pollutants on GEC parameters over the Indian subcontinent, *Indian J. Radio and Space Phys.*, 24; 159, 1995.
2. Bhartendu, S., Correlation of electric potential gradients at land station and their implication on the classical picture of atmospheric electricity, *Pure and App. Geophys.*, 84, 13, 1971.
3. Makino, M. and Ogawa, T., Quantitative estimation of global circuit, *J. Geophys. Res.*, 90, 5961, 1985.
4. Mukku, V.N.R., Study of electrical conductivity and ions in relation to global electrical and local meteorological parameters, *Ph.D. Thesis*, University of Kashmir, India, 1982.
5. Nizamuddin, S., Ramanathan, R., Rao, A.M., Khera, M.K., Makhdomi, B.A., Raina, B.N., Rafiqi, A.R., Mukku, V.N.R., Goel, R.K., Pathak, P.P., Rai, J. and Varshneya, N.C., *Proceedings of International Symposium on Solar Eclipse*, Indian National Science Academy, 48, 263, 1982.

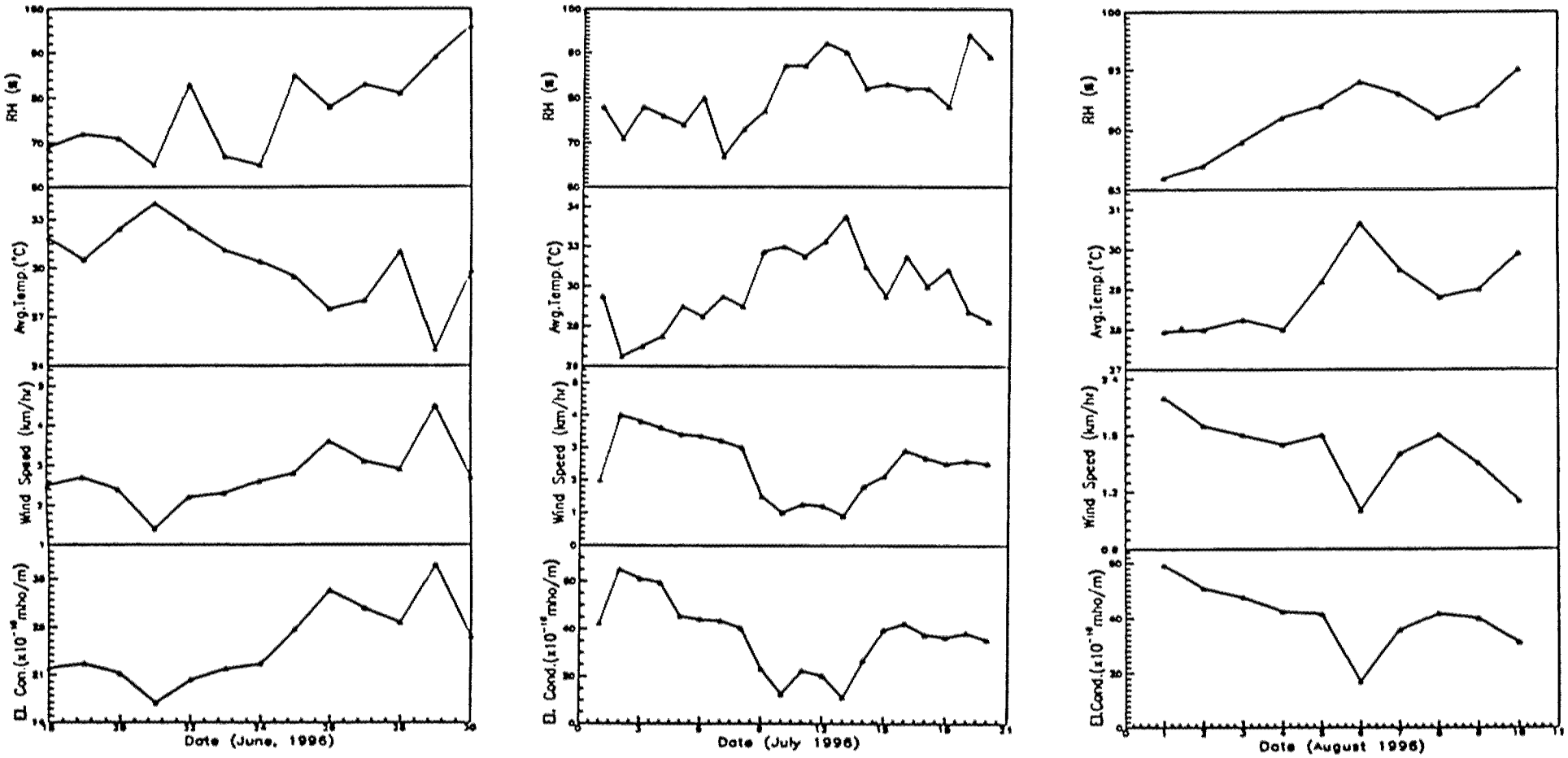
RH (%)
Avg.Temp.(°C)
Wind Speed (km/hr)
El. Con.(x10$^{-16}$mho/m)
Date (June, 1996)
RH (%)
Avg.Temp.(°C)
Wind Speed (km/hr)
El. Cond.(x10$^{-16}$mho/m)
Date (July 1996)
RH (%)
Avg.Temp.(°C)
Wind Speed (km/hr)
El.Cond.(x10$^{-16}$mho/m)
Date (August 1996)

FIGURE 1.

# THE ATMOSPHERIC ELECTRIC FOG EFFECT

J.C.H. van der Hage[1] and T.F. de Bruin[2]

[1] Institute for Marine and Atmospheric Research Utrecht (IMAU), Netherlands.
[2] Netherlands Institute for Sea Research (NIOZ), Netherlands.

## ABSTRACT

The onset and the dissipation of fog is always accompanied by variations of the electric conductivity of the air. Fog forecasts by various authors, made on the basis of this effect are discussed. In the urban environment of Utrecht these forecasts prove to be unreliable. Forecasting may perhaps be applied with more succes in marine environments. One case study of the atmospheric electric fog effect on the North Sea is presented.

## INTRODUCTION

The correlation between the onset or the dissipation of fog and accompanying variations of the electrical conductivity of the air is called the atmospheric electric fog effect. This effect is caused by the scavenging of small ions from the air by fog droplets. Fog droplets grow on condensation nuclei; and the droplets scavenge small ions more efficiently then the original dry particles did.

Several authors (Anderson et al., Ottevanger, Lemcke, Tijm) have attempted to make use of the atmospheric electric fog effect for short range forecasting of the onset and the dissipation of fog. Their results are compared in table I of this report.

Fog events can also be forecasted on the basis of optical techniques. The merits of the optical- and the electrical methods are discussed in this report.

## FORECASTING FOG FROM CONDUCTIVITY MEASUREMENTS

The fog forecasts discussed in this report are actually hindcasts. They were made after the actual observations of fog events by comparison with simultaneous observations of air conductivity and by defining forecast criteria in such a way that optimum results for the given set of data were obtained. In table I the differences between Utrecht 1 and Utrecht 2 originate in different criteria applied to the same data set. Utrecht 3 refers to another data set.

Table I

| Station | % score no-change | % score onset | % score dissip. | % score total |
|---|---|---|---|---|
| Argentia | 95 | 91 | 91 | 88.7 |
| Lakehurst | 91 | 76 | 95 | 89.3 |
| Norfolk | 98 | 89 | 100 | 91.7 |
| Pensacola | 89 | 76 | 100 | 86.5 |
| De Bilt | -- | 62 | -- | -- |
| Utrecht 1 | 22 | 48 | 83 | 43 |
| Utrecht 2 | 18 | 71 | 64 | 54 |
| Utrecht 3 | -- | 92 | -- | 42 |

The criteria used by the various authors to forecast the onset of fog displayed in table I are summarized below. With regard to criteria for dissipation and persistence please refer to the original papers.

## CRITERIA FOR PREDICTING THE ONSET OF FOG

1- Anderson and Trent (Argentia, Lakehurst, Norfolk, Pensacola)

Difference between dry bulb and dewpoint temperatures below 2° F.
Conductivity decreasing to approximately 2/3 normal.
Electric field increasing in the fair weather direction.

2- Ottevanger (De Bilt)

Conductivity decreasing to half the maximum value observed in the six hours preceding forecast time, the new conductivity value must be five relative units or less (one relative unit is estimated at $0.4*10^{-15}\ \Omega^{-1}m^{-1}$ by the present authors).

3- Lemcke (Utrecht 1, Utrecht 2)

Relative humidity at least 90% (Utrecht 1) or at least 95% (Utrecht 2). Conductivity decreasing more than 40% per hour (Utrecht 1) or more than 30% (Utrecht 2), this decrease must be at least $0.3*10^{-15}\ \Omega^{-1}m^{-1}h^{-1}$ in both cases. The new value for the negative conductivity must be $2*10^{-15}\ \Omega^{-1}m^{-1}$ or less in both cases.

4- Tijm (Utrecht 3)

Relative humidity at least 95%
Conductivity pos. or neg. less than $2.2*10^{-15}\ \Omega^{-1}m^{-1}$.

Anderson and Trent associate fog with a visibility less than one mile. By international agreement fog corresponds to a visual range below 1000m and that is the criterion that Ottevanger, Lemcke and Tijm have used in their forecasts. In those cases where visual range decreased to 1200m while fog was predicted Anderson and Trent would consider their forecast a succes whereas Ottevanger, Lemcke and Tijm would classify theirs as a failure. This is an additional cause for the comparatively low scores near Utrecht and De Bilt as far as the onset of fog is concerned.

Tijm (1994) points out that the reliability in predicting fog is not determined just by the percentage of true forecasts. In table 1, Utrecht 3 yields the highest onset score, referring to 37 fog events of which 34 (92%) were forecasted correctly. This high score is due to the criterion of $2.2*10^{-15}\ \Omega^{-1}m^{-1}$ which is hardly restrictive for the occurrence of fog in Utrecht. As a consequence fog was also forecasted on 40 other days without occurring. So there were more false forecasts than true ones in the Utrecht 3 experiment.

## VISUAL RANGE AND CONDUCTIVITY

Visibility and electrical conductivity of the air are correlated as they both decrease with increasing humidity due to the growth of the condensation nuclei. Ottevanger has compared his own atmospheric electric fog forecasts with forecasts for the same events based on visibility observations. He then scores 60% correct forecasts for the onset of fog Ottevanger has also compared the forecasts by Anderson and Trent with their reported visibility observations. He concludes that Anderson and Trent would have produced six correct forecasts out of ten when they would have based their predictions for the onset of fog on visibility data.

Ottevanger remarks that visibility observations are much easier and cheaper to perform than measurements of conductivity but this is only true for climatological stations where visibility is estimated on a synoptic routine basis. On stations where the human observer is replaced by instruments with automatic data registration, a conductivity meter is cheaper than optical instruments with the required specifications. For the onset of fog the visual range of interest lies between 1000m and 5000m. The dissipation of fog is associated with a visual range between 500m and 1000m. On many airports optical transmissometers with a measuring range of 50m-3200m are installed. These instruments produce suitable data for fog predictions but they have optical path lengths of 80m or 160m. Installation of instruments with such long baselines is difficult and expensive and, under some conditions, impossible.

## A CASE OF FOG ON THE NORTH SEA

In the afternoon of July 22, 1988 the Dutch research vessel "Aurelia" sailed into a very dense fog bank on the North Sea, north of the Doggersbank. To the officers on the bridge the

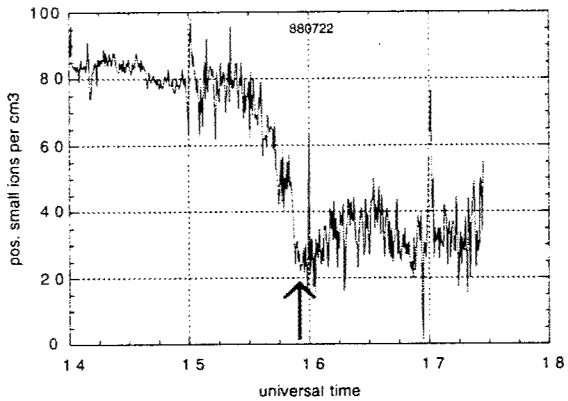


fig.1: Atmospheric electric fog effect observed on the research vessel AURELIA sailing on the North Sea on 22-7-1988. The concentration of positive small ions decreases strongly before fog is encountered. The conductivity of the air is roughly proportional to the concentration of positive small ions.
The arrow indicates when the AURELIA sailed into a fogbank. Fifteen minutes before that moment the conductivity had already decreased significantly. Registration stopped at 17.30h, still sailing in the fog.

fog came as a surprise but registrations of the air conductivity apparatus carried by the Aurelia show that about 15 minutes before encountering the fog, the electric conductivity of the air decreased in a significant way (see fig.1).

## CONCLUSIONS

The high scores obtained by Anderson and Trent on one side and the poor scores by Ottevanger, Lemcke and Tijm on the other, are partly due to the different criteria used by these authors in forecasting fog events and partly to the different aerosol composition in the atmosphere of Utrecht and De Bilt compared to the American stations.

In the urban environment of Utrecht and De Bilt the correlation between fog and conductivity is poor: fog is always correlated with low conductivity, but low conductivity is not correlated strongly with fog. Therefore forecasting fog from conductivity measurements is not satisfactory but it may be succesful in marine environments.

There are plans to build a large airport on an artificial island in the North Sea off the Dutch coast. Fog will be a great problem there; perhaps conductivity measurements can be useful as an additional forecasting parameter.

## REFERENCES


Anderson,R.V. and E.M. Trent, Evaluation of the use of atmospheric-electricity recordings in fog forecasting, Naval Res.Lab.report 6426, 1966.

Lemcke,C., Het atmosferisch electrisch misteffect. I.M.A.U report 79-6, Utrecht University, 1979.

Ottevanger,W.P.A.G., The atmospheric fog effect at De Bilt, Pageoph.**95**, p.221-225, 1972.

Tijm,A.B.C., Relatie tussen de conductiviteit van de lucht en het zicht. I.M.A.U report 94-2, Utrecht University, 1994.

# ION-AEROSOL INTERACTIONS IN ATMOSPHERIC AIR

**K.L. Aplin and R.G. Harrison**

Department of Meteorology, University of Reading, PO Box 243, Earley Gate, Reading, Berkshire, RG6 6BB, U.K.

**ABSTRACT:** Charged particles are continually generated in atmospheric air, and the interaction between natural ionisation and atmospheric particles is complicated. It is of some climatic importance to establish if ions are implicated in particle formation. Atmospheric ion concentrations have been investigated here at high temporal resolution, using Gerdien ion analysers at a site where synchronous meteorological measurements were also made. The background ionisation rate was also monitored with a Geiger counter, enabling ion production from natural radioactivity to be distinguished from other effects. Measurements at 1Hz offer some promise in establishing the atmospheric electrical influences in ionic nucleation bursts, although combinations of other meteorological factors are also known to be significant. High time resolution meteorological and ion measurements are therefore clearly necessary in advancing basic understanding in the behaviour of atmospheric aerosol.

## INTRODUCTION

Natural radioactivity and cosmic rays are a constant source of molecular ions in atmospheric air. Establishing the significance of these long-lived atmospheric ions is intimately linked with the importance of the atmospheric electrical system in atmospheric processes (Harrison, 1997), and the conventional view that the electrical properties of the atmosphere are completely insignificant is increasingly untenable. The ions produced are rarely single species, but form clusters of water molecules around a central ion. Atmospheric electrical fields lead to transport of small ions by vertical conduction processes. Typical atmospheric ion concentrations in unpolluted air and fair weather conditions are about 400-500 ions $cm^{-3}$.

It is of great interest to understand how ions could be implicated in particle production, and significant ion-induced nucleation of particles could be a relevant mechanism. Hõrrak *et al.* (1998) reported the spontaneous formation of intermediate size ions in atmospheric air, from a change in the ion mobility spectrum of urban air. Observations of direct aerosol formation in unpolluted marine air (O'Dowd *et al.*, 1996) and theoretical work on clustering reactions of ions (Castleman, 1982) suggest ions can be critical in gas-to-particle conversion processes.

If the volumetric ion production rate is $q$, the positive ion number concentration $n_+$, the negative ion concentration $n_-$ and if it is assumed that $n_+ = n_- = n$, then the variation of ion concentration with time is given by the equation

$$\frac{dn}{dt} = q - \alpha n^2 - \beta n Z - \gamma n \qquad (1)$$

where $\alpha$ is the ionic self-recombination coefficient, $\beta$ the ion-aerosol attachment coefficient (which varies with aerosol size and charge), $Z$ the aerosol number concentration and $\gamma$ the ion-induced nucleation coefficient. It has been usual to regard the aerosol and ions as distinct systems of particles, which interact purely by collisions. However the observations of Hõrrak *et al.* (1998)

now suggest that the γ-term could be significant in new particle events, and this would couple the time dependence in the ion concentration equations to time dependence in aerosol concentration. The simultaneous measurement of ion and aerosol concentration is therefore of importance.

## THE GERDIEN CONDENSER

Gerdien developed a method of measuring air conductivity from a cylindrical condenser in 1905. A voltage is applied between two cylindrical electrodes and the inner one is earthed via a sensitive ammeter (Harrison, 1997). In the tube, ions of the same sign as the polarising voltage are repelled by the outer electrode, and move in the electric field to meet the inner electrode where they cause a small current. In the Gerdien used for this work the currents are of order $10^{-15}$ A, and the conductivity is given by

$$\sigma = \frac{i\varepsilon_0}{CV} \tag{2}$$

where $C$ is the capacitance of the Gerdien, and $V$ is the polarising voltage across the electrodes. The Gerdien tube can be used to measure conductivity as long as the output current is proportional to the polarising voltage, indicating that a fixed fraction of the ions in the air are collected by the central electrode.

There exists a critical mobility $\mu_c$ such that only ions with $\mu > \mu_c$ contribute to the conductivity measurement. This is given by *e.g.* Wilkinson (1997)

$$\mu_c = \frac{(a^2 - b^2)\ln\left(\frac{a}{b}\right)u}{2VL} \tag{3}$$

where $a$ is the radius of the tube, $b$ is the radius of the central electrode, $u$ is the flow speed through the tube and L is the length of the tube. Operating the Gerdien at different critical mobilities is easily executed by varying the voltage or flow rate, and enables it to act as a simple and effective mobility spectrometer.

## GERDIEN CONTROL SYSTEM

A Microcontroller-based system for remotely controlling and logging the Gerdien data has been developed. This is clearly necessary for measurement of mobility spectra, as the voltage across the Gerdien has to switch to different values. By this method, one Gerdien tube can also be used to measure quasi-synchronous positive and negative air conductivity by cycling between positive and negative polarising voltages.

The microcontroller used in this application[1] is programmable in BASIC and has eight I/O pins, which can be wired up for communication with other computers, or for digital inputs to external circuits. The microcontroller is cheap and compact, and can simultaneously control the Gerdien and send the data to the serial interface of another computer. Once the program is downloaded to the microcontroller it runs for as long it is powered, and the program resumes its operation if the power is cut and then restored.

The electronic control circuit employed essentially comprises two relays, driven by VN10KM MOSFET transistors controlled by digital outputs from the microcontroller, and a

[1] BASIC Stamp 1, Parallax Instruments Inc., 3805 Atherton Road, Suite 102, Rocklin, California 95765, USA

LTC1298 12-bit analogue to digital converter. One relay (a changeover device) was connected to a positive and negative bias voltage. The other relay was a high input impedance reed relay, connected across the feedback resistor of the picoammeter. When this relay is on it shorts the picoammeter feedback resistor and provides a measurement of the picoammeter input offset voltage, overriding the state of the other relay so that no current measurement is made. The analogue-to-digital conversion is carried out by a sub-routine in the microcontroller program (Parallax, 1998) and enables the voltage output from the picoammeter to be logged.

| Name | Actions |
|---|---|
| Zero | Turns reed relay on to zero current amplifier<br>Sets other relay to "0" to reduce power consumption<br>Waits for 6s<br>Takes 5 readings of zeroed state of current amplifier at 1Hz<br>Sends readings to PC via serial protocol |
| + | Turns reed relay off to allow ion current measurements<br>Sets other relay to positive bias voltage<br>Waits 3 minutes<br>Takes 10 readings of ion current at 1Hz<br>Sends readings to PC via serial protocol |
| - | Sets relay to negative bias voltage<br>As + above and repeats forever |

Table 1: Outlines the actions performed by the program running on the microcontroller. The delay of three minutes after the change of bias voltage is required to allow complete recovery from the transient that occurs on switching.

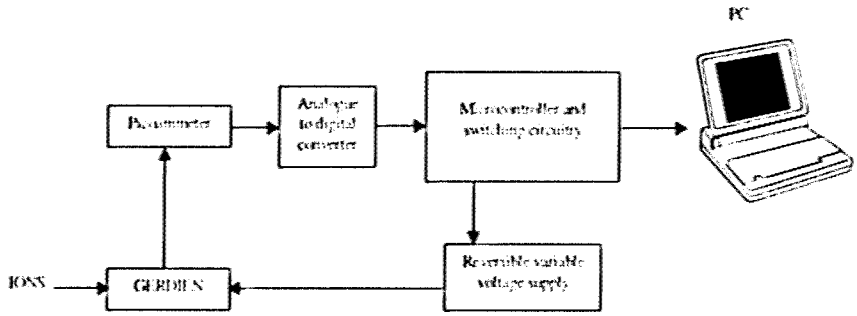


Figure 1: Schematic showing the integrated air ion measurement system

## RESULTS

Measurements of ion concentrations at different mobilities have been made in Reading by using the Microcontroller system to switch the Gerdien between two voltages of the same sign, -6V and –9V. Knowing the wind component into the Gerdien and the tube ventilation rate allows calculation of the critical mobility using (3). The ionic number density is approximated by

$$n = \frac{\sigma}{e\mu} \qquad (4)$$

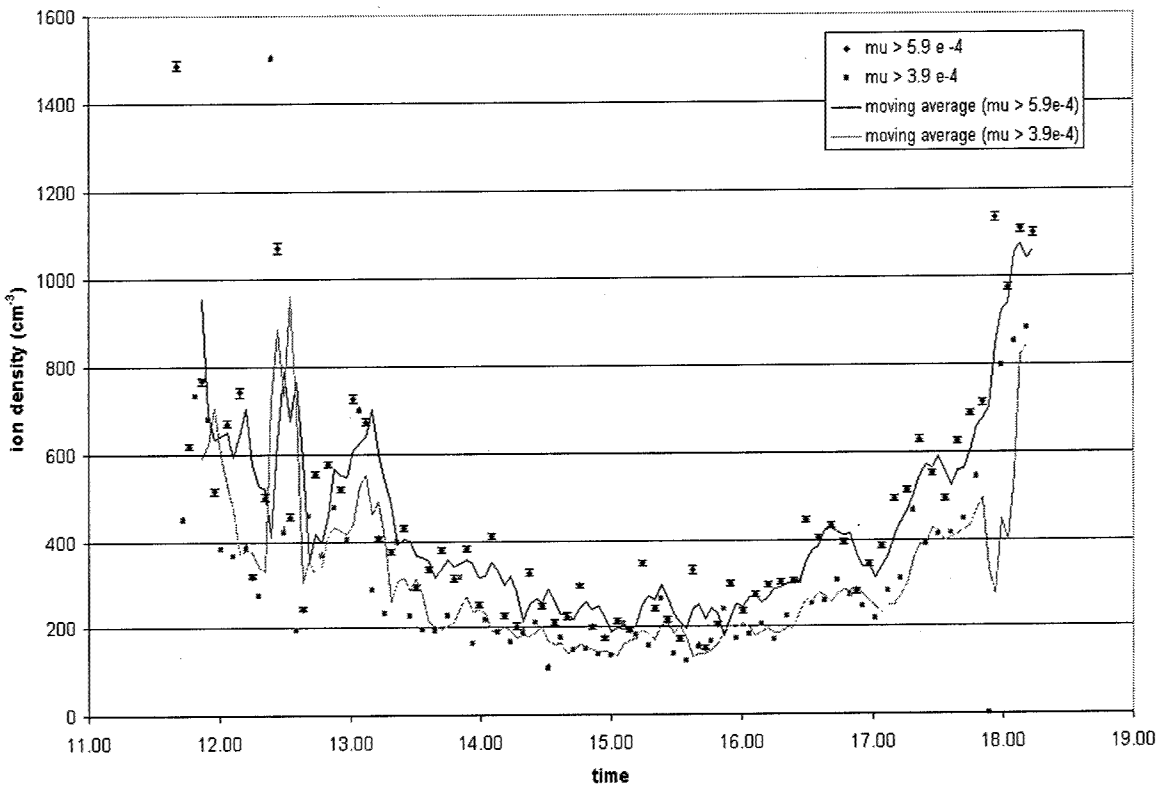


Figure 2: The negative ion number concentration at critical mobilities of 5.9 and 3.9 x $10^{-4}$ $Vm^{-2}s^{-1}$ for a typical day (23/2/99).

where $e$ is the electronic charge, $\mu$ the critical mobility and $n$ the concentration of ions with a mobility exceeding the critical mobility. The results are promising; for example the peak at about 12.30 shows a shift in the spectrum towards higher mass ions, perhaps implying a nucleation event.

## CONCLUSIONS

These results indicate that the microcontroller-based ion counter system is ideal for measuring high time and mobility resolution ion spectra, and the microcontroller system can easily be expanded, such as for controlling the fan. Synchronous measurement of mobility spectra and meteorological parameters will assist in the understanding of ion-aerosol interactions.

## REFERENCES

Castleman A.G. (1982), In: Schryer D.R., *Heterogeneous atmospheric chemistry*, AGU, Washington

Harrison R.G. (1997), Climate change and the global atmospheric electrical system, *Atmospheric Environment*, **31**, 20, 3483-3484

Hõrrak U. *et al.* (1998), Bursts of intermediate ions in atmospheric air, *J. Geophys. Res*, **103**, 13909-13915

O'Dowd C.D. *et al.* (1996), New particle formation in the environment, *Proc. 14th Int. Conf. on Nucleation and Atmospheric Aerosols,* Helsinki, Eds: Kulmala M. and Wagner P.E., Pergamon Press, 925-929

Parallax Inc. (1998), *BASIC Stamp® Manual*, Version 1.9

Wilkinson S. (1997), *Determination of the characteristics of urban atmospheric aerosol,* MSc. Dissertation, Department of Meteorology, University of Reading

# SOUTH POLE ELECTRIC FIELD RESPONSES TO CHANGES IN OVERHEAD IONOSPHERIC POTENTIAL

Brian A. Tinsley

W. B. Hanson Center for Space Science, University of Texas at Dallas,
FO22, Box 830688, Richardson, TX 75083-0688

ABSTRACT: Measurements of the vertical atmospheric electrical field *Ez* at the South Pole made between 1982 and 1986 have been analyzed, and the results reveal an important component due to extraterrestrial influences. The measurements are consistent with the theoretical expectation that the potential patterns in the polar caps that are measured by satellites, and that change with changes in solar wind parameters, are superimposed on the otherwise nearly uniform (but varying in time) global ionospheric potential due to low-latitude thunderstorm sources. The analysis technique was to calculate the overhead ionospheric convection potential from a satellite empirical model, using as inputs measured solar wind parameters, except that when the solar wind data were not available we used as inputs measured ground based magnetic disturbance parameters. We fitted the average low latitude *E* variation (the Carnegie curve) to the individually measured South Pole diurnal curves during the time intervals when the superimposed polar cap potential was near zero. We then subtracted the fitted Carnegie curves from the measured curves and performed a regression analysis of the residuals on the calculated superimposed polar cap potential values, averaging the data in three hour intervals. Positive correlations with correlation coefficients of about 0.5 were found. Most of the remaining variability in *Ez* can be attributed to local meteorologically induced noise and the day-to-day variability of the low latitude thunderstorm generators.

## INTRODUCTION

In the Antarctic summer it is possible to get very a good signal-to-noise ratio with the South Pole near-surface electric field (*Ez*) measurements, and in fair weather during winter they also have a higher signal-to-noise ratio than corresponding low latitude, low altitude near-surface measurements. The altitude is 2.8 km above mean sea level, and the site is on the Antarctic ice cap, with a desert climate, very low radon and aerosol content, and is thunderstorm free. In the summers the prevailing winds are generally light, flowing in a nearly constant direction, and relatively free from turbulent and convective motions [*Byrne et al.*, 1993]. Thus the conductivity fluctuations that produce space charge in the presence of the vertical current density density (*Jz*), and that when moved by winds produce meteorological noise on *Ez*, are considerably minimized compared to those for other sites not on polar ice caps.

The polar cap upper atmosphere generators are associated with magnetosphere-ionosphere convection processes and Birkeland currents of several million amperes that create horizontal potential differences across both the northern and southern polar cap ionospheres [*Richmond*, 1986; *Roble and Tzur*, 1986; *Heppner and Maynard*, 1987]. The energy source is the interaction of the solar wind with the magnetosphere, and resulting patterns of ionospheric potential are created as perturbations on the otherwise spatially uniform and global ionospheric potential ($\Phi$). The perturbation potential patterns are sun-aligned, and approximately centered on the geomagnetic poles. The potentials on the dawn sides of the north and south polar caps are 20-30 kV higher than on the dusk sides during geomagnetically quiet times, increasing to about 80 kV for average conditions, and reaching 150-200 kV during active conditions [*Boyle et al.*, 1997]. We designate the perturbation ionospheric convection potential above a ground site as $\Psi$.

Figure 1 is from *Hairston and Heelis* [1990] and shows examples of patterns from their empirical model, derived from satellite measurements, of the perturbation ionospheric convection potential. The example corresponds to a dawn-dusk potential difference of 76-77 kV, for the solar wind *By* component

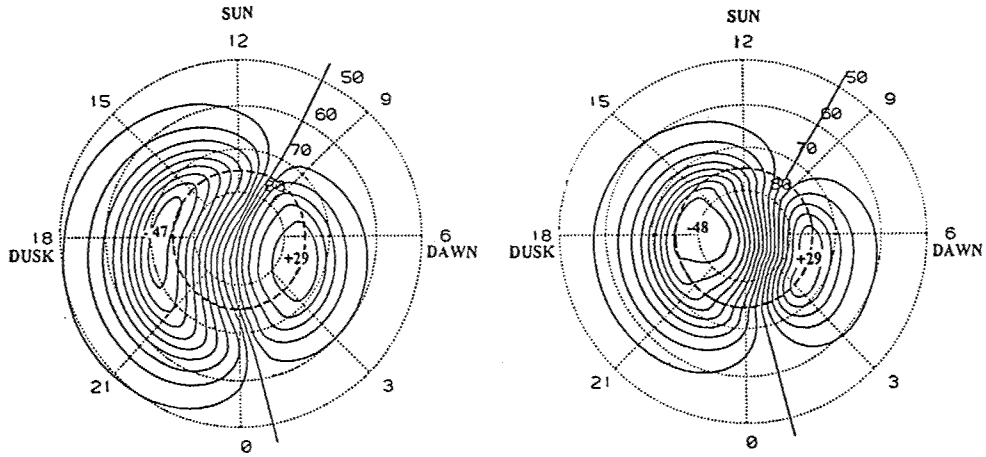


Fig 1. Two examples of polar cap ionospheric potential patterns from Hairston and Heelis [1990]. The pattern on the left is for the southern polar cap with By positive, or the northern polar cap with By negative. The pattern on the right is for the south with By negative or the north with By positive. The values of the potential maxima and minima are 29 kV and near -47 kV respectively, for a dawn-dusk potential difference near 76 kV. A power law parameter r, that determines the decay of the potential equatorward of the convection reversal boundary, was –6 for the left pattern and –5 for the right. Equipotentials are shown for 5 kV increments. The dashed line is the track of the south pole.

being either –7 nT or + 7 nT. The negative perturbation on the dusk side (with a minimum of –48 kV) is of greater amplitude than the positive perturbation on the dawn side (with maximum 29 kV).

The conductivity of the atmosphere increases rapidly with height above the surface, because the cosmic ray flux is rapidly attenuated below about 15 km, and the ionic mobility increases exponentially with height [*Roble and Tzur*, 1986]. This rapid increase in conductivity with height results in the ionospheric potential being essentially reached a few tens of km above the surface. This distance is considerably smaller than the horizontal scale of the convection pattern (~ 600 km), so that the geometry is essentially that of a plane parallel leaky capacitor, with the conductivity of the material between the plates increasing rapidly with distance from the lower plate. Thus, for a given vertical conductivity profile the potential gradient (vertical electric field *Ez*) at any altitude varies linearly with the overhead ionospheric potential. The ionospheric potential above the South Pole at a given time is the sum of the low-latitude ionospheric potential $\Phi$ for that time and the ionospheric convection potential $\Psi$ at that location for that time. The diurnal variation of $\Psi$ corresponds to the trace, as the Earth rotates, of the South Pole across the sun-aligned and magnetic-pole-centered ionospheric convection pattern, as indicated by the dashed lines in Figure 1. The total overhead ionospheric potential is $\Psi + \Phi$, with a diurnal variation that is the sum of the individual diurnal variations of $\Psi$ and $\Phi$. In the analysis that follows we do not consider the relatively large day-to-day variability of $\Phi$, but use the average over tens of days which is known as the Carnegie curve.

## RESULTS

South Pole measurements of varying quality were made from January 1982 through January, 1986. A data set of 27 days with minimum meteorological noise and free of instrumental malfunction was extracted for analysis. We calculated the overhead ionospheric convection potential $\Psi$ as hourly averages for the 27 days of good observations. The days used represent those of minimum meteorological noise in the Antarctic late spring and early fall. In Figure 2 the variation of the $\Delta Ez$ (the South Pole observed electric field *Ez* minus the Carnegie curve that has been scaled to the average of *Ez* for 4-6 and 14-16 hrs for the individual day) is compared to the calculated values of overhead ionospheric potential $\Psi$ for the

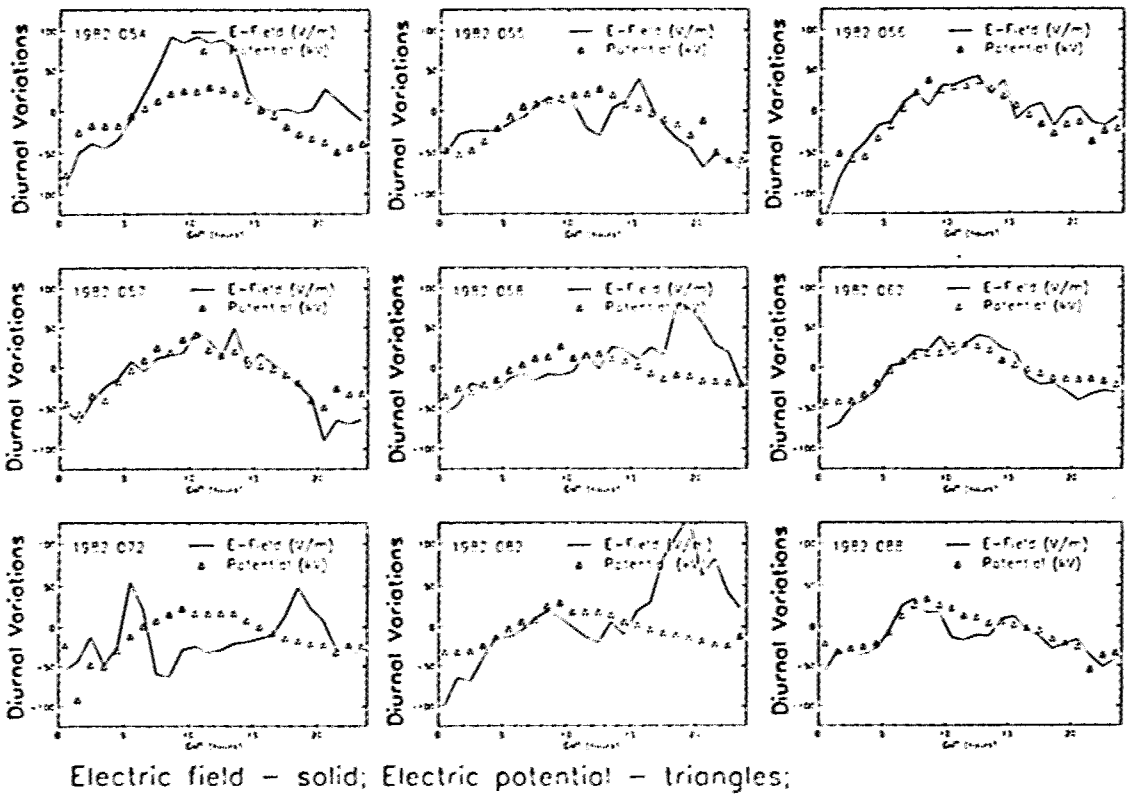


Fig. 2. Variations of near surface observed electric field $E_z$ for individual days minus the Carnegie curve normalized for that day (solid line, $\Delta E_z$), compared to the overhead ionospheric convection potential $\Psi$ (triangles) for the first nine days of the 27 days of good data.

first 9 of the 27 days of good data. For some of the days with the smoothest $E_z$ variation the correlation is readily apparent. In Figure 3 regression plots of $\Delta E_z$ against $\Psi$ are shown for the first 14 days and the last 13 days of the data set. Positive correlations with a slope of about 0.7 V m$^{-1}$ kV$^{-1}$ were found, with correlation coefficients of about 0.5. The correlations are partly due to $\Delta E_z$ following the diurnal variations of $\Psi$, and partly due to $\Delta E_z$ following the day-to-day variations of $\Psi$.

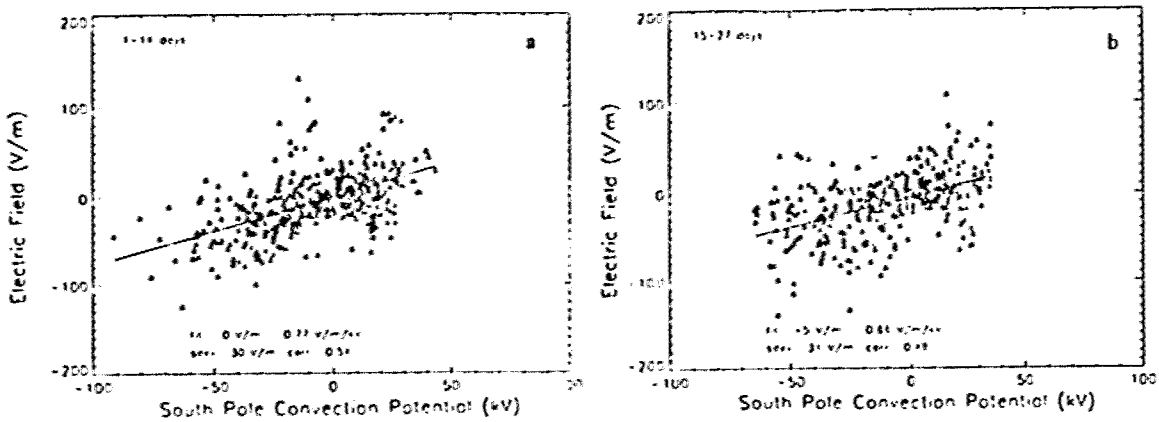


Fig. 3. (a) Regression of $\Delta E_z$ (South Pole observed $E_z$ minus normalized Carnegie Curve) on modelled overhead ionospheric convection potential $\Psi$ for the first 14 days of the data set; (b) the same for the remaining 13 days.

## CONCLUSIONS

The influence of magnetosphere-ionosphere coupling processes on the surface electric fields in the polar caps has been investigated. The results are basically consistent with what is expected theoretically, in that the surface field *Ez* is due to the superposition of the ionospheric convection potential pattern measured by satellites on the otherwise uniform global ionospheric potential due to low-latitude thunderstorm current sources. A regression analysis of the South Pole *Ez* minus the scaled Carnegie Curve was made on the overhead ionospheric convection potential, calculated from an empirical model based on satellite observations. Positive correlations with correlation coefficients of about 0.5 were found. In order to give a better interpretation of the residuals, information on simultaneous low latitude thunderstorm activity (global deep convection or Schumann resonances) are needed. Alternatively, simultaneous measurements of the surface *Ez* field at other suitable sites in the polar cap regions would allow separate evaluation of the day-to-day variability of both the ionospheric convection potential and the low latitude thunderstorm generated ionospheric potential. Further details can be found in *Tinsley et al.*, [1998].

ACKNOWLEDGEMENTS: We thank R. A. Helliwell for discussions and permission to use the South Pole electric field data, and Dr. T. J. Rosenberg for assistance in extracting electric field and ground wind data from datalogger tapes. This work was supported by the National Science Foundation, with grants DPP 9208937 and ATM 9504828.

## REFERENCES

Boyle, C. B., P. H. Reiff, and M. R. Hairston, Empirical polar cap potentials, *J. Geophys. Res., 102,* 111-125, 1997.

Byrne, G. J., J. R. Benbrook, E. A. Bering, A. A. Few, G. A. Morris, W. J. Trabucco and E. W. Paschal, Ground based instrumentation for measurements of atmospheric conduction current and electric field at the South Pole, *J. Geophys. Res., 98,* 2611-2618, 1993.

Hairston, M. R., and R. A. Heelis, Model of the high latitude ionospheric convection pattern during southward interplanetary magnetic field using DE-2 data, *J. Geophys. Res., 95,* 2333-2343, 1990.

Heppner, J. P., and N. C, Maynard, Empirical high-latitude electric field models, *J. Geophys. Res., 92,* 4467-4489, 1987.

Richmond, A. D., Upper-atmosphere electric field sources, in *The Earth's Electrical Environment,* pp. 195-205, Nat. Acad. Press, Washington, DC, 1986.

Roble, R. G., and I. Tzur, The global atmospheric-electric circuit, in *The Earth's Electrical Environment,* pp. 206-231, Nat. Acad. Press, Washington, DC, 1986.

Tinsley, B. A., Weiping Liu, R. P. Rohrbaugh and M. W. Kirkland, South Pole electric field responses to overhead ionospheric convection, *J. Geophys. Res., 103,* 26137-26146, 1998.

# STRATOSPHERIC BALLOON MEASUREMENTS OF CONDUCTIVITY AND ELECTRIC FIELDS ASSOCIATED WITH SFERICS IN BRAZIL

M. M. F. Saba, O. Pinto, Jr., I. R. C. A. Pinto, O. Mendes, Jr.

Instituto Nacional de Pesquisas Espaciais, São José dos Campos, SP, BRAZIL

ABSTRACT: Measurements of stratospheric conductivity and of electric fields associated with sferics, were obtained during two balloon flights carrying double-probe electric field detectors launched from Cachoeira Paulista, Brazil (geographic coordinates 22°44'S, 44°56'W) on 26 January 1994 and 23 March 1995. From data obtained in 1994, a linear relationship between the vertical quasi-DC electric field peak amplitude and the decay time constant of sferics was found for negative flashes. The results are compared to similar data for intracloud flashes. The data were supported by radar and METEOSAT satellite images. For the first time, positive and negative conductivity vertical profiles were obtained in Brazil. During the flight, at an average altitude of 27.5 km, the balloon passed over two thunderclouds as identified, by on-board video images and photographs. The simultaneous conductivity measurements and thundercloud on-board observations allowed to determine that the presence of clouds affects the stratospheric negative conductivity, producing a extended and cumulative drop after the balloon passed over each cloud. Based on data obtained in 1995 and on the present knowledge about the differences between positive cloud-to-ground and intracloud flashes, two methods to distinguish between them in balloon electric field data are presented: the first is based on an estimation of the charge destroyed in the event; the second is based on the ratio between the vertical quasi-DC and the VLF electric field. The behavior of the vertical quasi-DC electric field before and after large cloud-to-ground lightning flashes is discussed and attributed to the existence a shielding layer around the thunderstorm caused by a factor decrease of three or more in the conductivity inside the cloud.

## INTRODUCTION

It has been known for decades that understanding of the conductivity of the middle atmosphere is crucial for solving coupling problems between the lower atmosphere and the ionosphere [*Bering et al.*, 1980; *Hu et al.*, 1989]. This task has among others, two important aspects to be addressed: the determination of the atmospheric conductivity vertical profiles and the causes of conductivity variations in the stratosphere.

Two sorts of temporal variations in stratospheric conductivity have been observed at a constant altitude. First, temporal fluctuations of conductivity up to 30% of the mean value are commonly seen in fair weather [*Hu et al.*, 1989]. Second, some authors report that greater amplitude variations (up to 100% of the mean value) may occur during foul weather conditions.

To date very few *in situ* measurements of stratospheric vertical electric field associated with lightning flashes have been published [e.g. Burke, 1975; Holzworth and Chiu, 1982; Pinto et al., 1992]. The vertical electric field associated with lightning flashes have a typical signature of a sferic, that is, a rapid variation followed by a tail which lasts less than 10 seconds. The recovery curve (i.e. the return to the previous ambient field) depends on the local conductivity and, as it has a time constant different from the ambient relaxation time, it is probably influenced by electric charging processes inside the thundercloud.

## CONDUCTIVITY RESULTS

On 26 January 1994, a stratospheric balloon was launched from Cachoeira Paulista, carrying a double probe electric field detector to measure the conductivity in the stratosphere.

Negative and positive conductivity were measured each 10 minutes during about 5 hours in daytime. The first negative and positive conductivity profiles were obtained in Brazil. At float altitudes, the positive conductivity was found to be contaminated by photoelectric emission and, consequently, were not used in this paper. The negative conductivity measurements obtained at the balloon float altitude are also presented and discussed in terms of thunderstorm related variations. These observations may add valuable contributions to the very limited amount of conductivity data obtained over thunderstorms. As far as we know, this is the first conductivity data in the stratosphere supported by video images. The support of video images leave no space for doubts commonly present in this kind of study such as if the balloon was actually over the thunderstorm. Hu et al. [1989] have pointed out that the horizontal distance between the thunderstorm and the balloon may be crucial in determining the effect of the storm on the conductivity.

The negative and positive conductivity values obtained during the ascension of the balloon launched on Jan 26, 1994, in Brazil, showed almost the same value. On the other hand, when the payload was at an altitude of 25.8 km, $\sigma_+$ was higher than $\sigma_-$, probably due to the influence of the photoelectric effect [*Chakrabarty et al.,* 1994].

The values of scale height, 5.2 km for negative and 5.8 km for positive conductivity, are in general agreement with other measurements made in different parts of the world. During its drift westward, at an average altitude of 27.5 km, the balloon passed over two thunderclouds as identified by video on-board images. The variation of the negative conductivity in Figure 1 shows a systematic decrease when the balloon approaches a thundercloud. The conductivity drops by a factor of about 2 in the vicinity of the first thundercloud and by a factor of about 1.5 after the second thundercloud. The same tendency seems to occur in the vicinity of the third thundercloud.

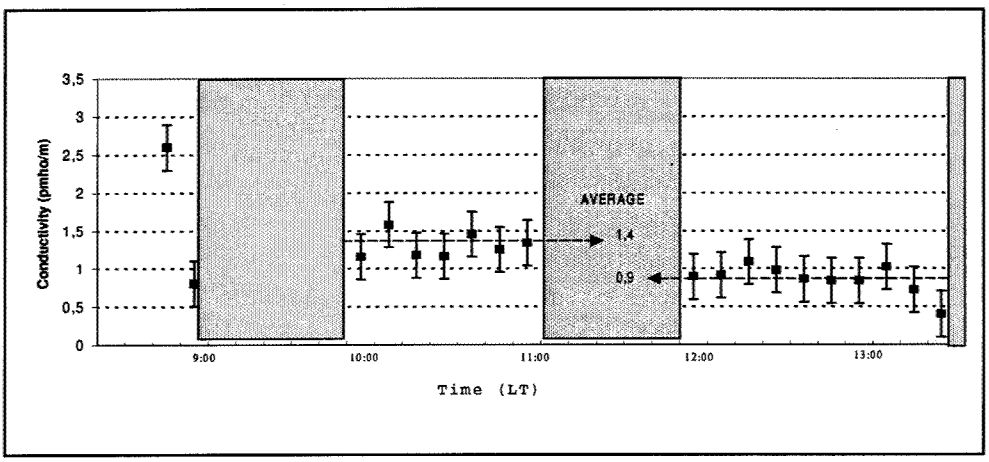


Figure 1. Negative conductivity measurements obtained on 26 January 1994.

Variations of this order in the stratospheric conductivity values have already been reported in some papers [*Bering et al.,* 1980; *Holzworth et al.,* 1986; *Pinto et al.,* 1988; *Hu et al.,* 1989]. The present measurements not only confirm the influence of thunderstorms on stratospheric conductivity, but also seem to reveal a sort of an extended and cumulative drop of $\sigma_-$ values after each thunderstorm. It seems that this influence is not limited to the space right above the thundercloud, but is prolonged along the direction of the stratospheric winds that conduct the balloon. In case of more than one thunderstorm, the drop on the $\sigma_-$ values would sum up. The same behavior in the conductivity was apparently seen by *Pinto et al.* [1988], although no images were available at that time.

It is known that penetrative cumulus convection is an effective source of atmospheric gravity. These waves are considered to be important for transport of momentum and substances across the tropopause because they are associated with strong vertical motions [*Sato et al,* 1995]. Considering that in our case the thunderclouds were in the mature stage, when updrafts dominate, it is very plausible to suppose that gravity waves were the responsible for the conductivity variations observed.

Even though the variations in conductivity values involved both space and time changes, which can no be easily separated, we suggest that the systematic decrease of the stratospheric conductivity may be explained by injection in the stratosphere of air parcels containing low concentration of small ions from the top of the thunderstorms, reducing the total concentration of small ions. Such parcels are known to be found in the interior of thunderstorms [*Makino and Ogawa,* 1985]. The mechanism above, however, could not explain the increase in the conductivity observed by other authors. This fact suggests that different mechanisms can be acting at different situations. It is also possible that the location of the balloon with respect to the storm may be fundamental to determine what kind of variation will occur.

## ELECTRIC FIELDS ASSOCIATED WITH SFERICS

On 23 March 1995, a 54000-$m^3$ balloon was launched at 1335 LT and drifted westward, as usual in this period of the year. During the flight, it passed over a thundercloud at an altitude of 32 km and registered a few but intense sferics. The flight on 26 January 1994, registered also several sferics when balloon passed over the thunderclouds. The payload in both flights was equipped with a double probe electric field detector to measure the vertical quasi-DC electric field and an antenna to measure the VLF electric field. The data were sampled every 50 milliseconds using two different gains [Saba et al., 1998].

Based on electric field data and on the present knowledge about the differences between positive cloud-to-ground and intracloud flashes, two methods to distinguish them are presented: the first is based on an estimate of the

destroyed charge in the event (smaller destroyed charges for intracloud flashes); the second is based on the peak amplitude ratio between the vertical quasi-DC and the VLF electric field (smaller ratios for intracloud flashes).

*Relationship between the Amplitude and Decay Time Constant of Sferics*

Figure 2 shows the relationship between the amplitude of the sferics associated with negative cloud-to-ground flashes and their decay time constants (Jan. 1994) Decay time constants were obtained from exponential curve fits for the first 60 data points after the electric field peak amplitude. As there is no other published relationship for negative flashes our results are shown with those obtained by Burke [1975] for intracloud flashes. The best fit lines, equations and correlation coefficients are also presented. In both cases the correlation coefficients are high, although the slope of the linear equations are very different. Such a different behavior cannot be explained by different ambient conductivity only; it must be associated with the different types of lightning considered in each case, indicating that the temporal variation of the charging process inside the cloud in each case may be quite different. At present, this process is not well known. It is also worth noting that for large sferics the decay time constant can be higher than the ambient relaxation time.

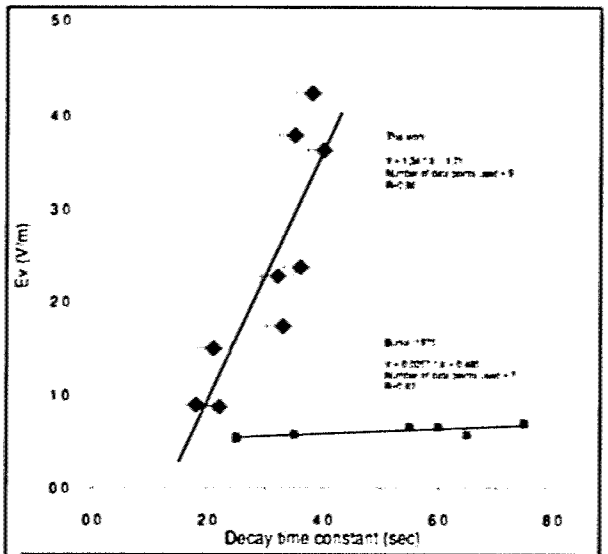


Figure 2. Sferic peak amplitude versus decay time constant

*The Behavior of the Vertical Electric Field during the Occurrence Sferics*

Figure 3 shows an 8-min. interval of continuous stratospheric vertical electric field data obtained at an altitude of 32.2 km on 23 March 1995. The two positive cloud-to-ground flashes, P1 and P2 and a third flash (cloud-to-ground or intracloud flash), originated in the same isolated thunderstorm, can be seen in the figure.

There are two points worth mentioning about Figure 3. First, the average value of the vertical electric field just before and just after the occurrence of P1 and P2 is not altered. This is in agreement with most balloon-borne electric field measurements recorded in literature. Second, the electric field shows an abrupt increase about 15 sec before the first flash (P1).

With respect to the first point, charges destroyed by P1 and P2 should have produced a decrease of at least 0.43 V/m in the vertical field, considering the measured conductivity scale height of 5.2 km [Saba et al., 1998]. Since this decrease was not observed, and considering that the vertical electric field resolution of our measurements was 0.15 V/m, we suppose that a screening layer around the thunderstorm should have reduced the variation of the electric field seen by an external observer. The estimated shielding factor associated with the screening layer would be equal or greater than 3. Considering that this factor is also related to the ratio between the conductivity inside and outside the thunderstorm [Volland, 1984], we found that the conductivity inside the cloud is lower than that outside by a factor of three or more.

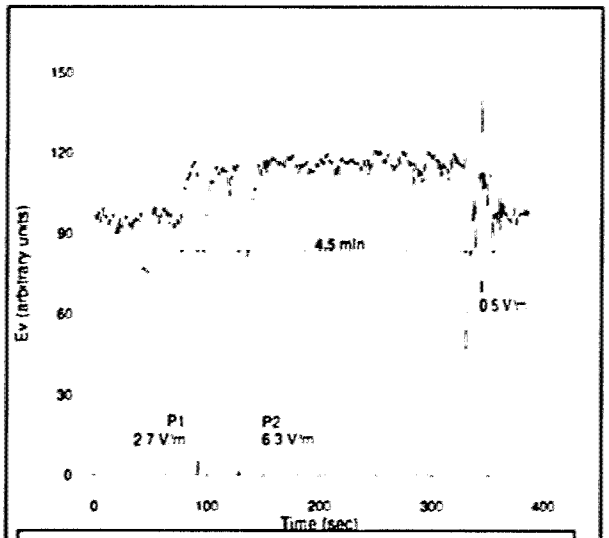


Figure 3. Vertical electric field obtained on March 23, 1995, showing three sferics and an abrupt increase around 70 s.

The second point related to Figure 3 is the occurrence of an abrupt increase in the electric field about 15 sec prior to the first positive flash. It was of about 0.28 V/m and remained for about 4.5 minutes. Although the actual process behind this phenomenon may be very complex, we suggest that this increase be related to a transient

shielding layer just above the cloud. It could have been produced in consequence of the large breakdown field. The necessary time to a transient shielding layer to be completely shielded (99%) was estimated by Brown et al. [1971] as approximately equal to five times the relaxation time constant at the shielding layer altitude. Considering the altitude of the top of the cloud (8 km), a complete shielding would occur at about 5 minutes. This value is of the same order of the 4.5 minutes interval indicated in Figure 3. A similar case (with an increase of about 0.3 V/m) seems to have been observed by Holzworth and Chiu [1982].

## CONCLUSIONS

The first negative and positive stratospheric conductivity profiles in Brazil were obtained. The scale heights are found to be in reasonable agreement with measurements in other parts of the world. We suggest that the extended and cumulative drop of $\sigma_-$ values after each thunderstorm is caused by the injection of air parcels in the stratosphere. We suppose that the persistence of this decrease along the trajectory of the balloon is due to the fact that the balloon passed exactly over the thunderclouds, and moved with these air parcels.

The criteria for identification of two lightning sferic signatures as being due to positive flashes were presented. A linear relationship between the amplitude and the decay time constant for negative lightning sferics was found to be different from the same relationship for intracloud sferics. The reason for such a difference is probably related to charging processes inside the thundercloud and remains to be investigated in more details.

The existence of a screening layer around the thundercloud could be the explanation sought for the fact that even after the occurrence of strong flashes the vertical electric field remains unaltered.

An intensification of the electric field inside the thundercloud could be a possible reason for the observed abrupt increase of vertical electric field about 15 sec prior the occurrence of a positive flash. This high intensity field may be responsible, or related to some of the emissions recently reported to occur over the top of thunderstorms. If so, the abrupt increase of the vertical electric field reported here and that reported by Holzworth and Chiu [1982] may be considered as one of the few electric field signatures associated with such emissions.

ACKNOWLEDGMENTS: The authors would like to thank the Fundação de Amparo à Pesquisa do Estado de São Paulo (FAPESP) for supporting the research through the projects 92/4774-2 and 93/0907-0.

## REFERENCES

Bering, E.A., T.J. Rosenberg, J.R. Benbrook, D. Detrick, D.L. Matthews, M.J. Rycroft, M.A. Saunders, and W.R. Sheldon, Electric fields, electron precipitation, and VLF radiation during a simultaneous magnetospheric substorm and atmospheric, *J. Geophys. Res., 85,* 55-72, 1980.

Brown, K. A., P. R. Krehbiel, C. B. Moore, and G. N. Sargent, Electrical screening layers around charged clouds, *J. Geophys. Res., 76*, 2825-2835, 1971.

Burke, H. K., Large scale atmospheric electric fields: comparisons with balloon data, Ph.D. thesis, Rice University, Houston, TX, 1975.

Chakrabarty, D.K., M. Lal, G. Beig, J.S. Sidhu, and S.R. Das, Balloon measurements of stratospheric ion conductivities over the tropics. *J. Atmos. Terr. Phys., 56,* 1107-1115, 1994.

Holzworth, R. H., and Y. T. Chiu, Sferics in the stratosphere, in *Handbook of Atmospherics*, vol. 2, edited by H. Volland, pp. 1-19, CRC Press, Boca Raton, Fl, 1982.

Holzworth, R.H., K.W. Norville, P.M. Kintner, and S.P. Powel, Stratospheric conductivity variations over thunderstorms, *J. Geophys. Res., 91,* 13,257-13,263, 1986.

Hu, H., R.H. Holzworth, and Y.Q. Li, Thunderstorm related variations in stratospheric conductivity measurements, *J. Geophys. Res., 94,* 16,429-16,435, 1989.

Makino, M., and T. Ogawa, Quantitative estimation of global circuit, *J. Geophys. Res., 90*, 5961-5966, 1985.

Pinto, I.R.C.A., O. Pinto Jr., W.D. Gonzalez, S.L.G. Dutra, J. Wygant, and F.S. Mozer, Stratospheric electric field and conductivity measurements over electrified convective clouds in the South American region, *J. Geophys. Res., 93,* 709-715, 1988.

Pinto, I. R. C. A., O. Pinto Jr., R. B. B. Gin, J. H. Diniz, and A. M. Carvalho, A coordinated study of a storm over the South American continent: 2. Lightning-related data, *J. Geophys. Res., 97,* 18205-18213, 1992.

Saba, M. M. F., O. Pinto Jr., I. R. C. A. Pinto, Stratospheric conductivity measurements in Brazil, *J. Geophys. Res.,* submitted, 1998.

Sato, K., H. Hashiguchi, and S. Fukao, Gravity waves and turbulence associated cumulus convection observed with the UHF/VHF clear-air Doppler radars, *J. Geophys. Res., 100*, 7111-7119, 1995.

Volland, H., *Atmospheric Electrodynamics*, Springer Verlag, New York, NY, 1984.

# EFFECT OF WIND ON HORIZONTAL WIRE ANTENNA COLLECTING ATMOSPHERIC AIR-EARTH CURRENT

R. Lelwala[1], T. J. Tuomi[2], S. Israelsson[3] and K. P. S. C. Jayaratne[1],

[1]Department of Physics, University of Colombo, Colombo 03, Sri Lanka.
[2]Finnish Meteorological Institute, Box 503, FIN-00101 Helsinki, Finland
[3]Meteorology, Department of Earth Sciences, Uppsala University, Uppsala, Sweden

ABSTRACT: The electromagnetic hydrodynamic structure of a horizontal long-wire antenna collecting fair weather atmospheric air-earth current is investigated. The model consists of a set of equations for the motions of air ions and the solution is found by shooting analytical techniques. The solution shows that the resultant effect of wind on the current collected by the antenna is zero. From our solution, the current collecting area, which is called the effective area of the wire antenna, is inversely proportional to the speed of air ions. On the other hand, the current is directly proportional to the speed of air ions. These two effects compensate each other to nullify the resultant effect.

In this case, the wire antenna should be kept at a considerably high level to avoid the electrode layer and the electrostatic mirror effect of the earth. The horizontal variation of wind is considered as constant and the logarithmic vertical wind profile was assumed. The solution was found numerically.

## INTRODUCTION

There are number of methods to collect the current from air: Wilson plate [*Israël 1973*], Burke and Few sensor [*Burke and Few 1978*] and horizontal wire antenna [*Kasemir, 1955; Ruhnke, 1969*]. Horizontal wire antenna is used to measure atmospheric air-earth conduction current and has been introduced in many atmospheric electricity observatories. Horizontal wire antenna is a well-insulated metal wire of radius about 0.5-1.5 mm spanned horizontally 1.5-3m above the ground surface. Its length is typically a few hundreds of meters, in some cases one-kilometer. The antenna potential is the same as that of the ground since one end of the wire antenna is connected to the earth through an operational amplifier with very high input impedance and very low input bias current. The effective area of an antenna collecting air-earth current is the ratio of the current collected by the antenna to the air-earth current density. This effective area is a rectangular plane surface above the wire antenna inclined by some angle. Air ions passing through this area are attached to the wire. Two different effective areas are defined for the displacement and non-displacement components of air-earth conduction current. The dynamic effective area is calculated considering that the air does not contain any space charge and the electric current flow lines match the electric field lines. Therefore, the dynamic effective area is not affected by wind. The static effective area is related to the non-displacement current, and it is calculated assuming that the wind-effected ion trajectories do not follow the electric field lines. Average values of vertical current density are calculated according to the *Kasemir-Ruhnke* [1959] model using dynamic effective area neglecting space charges in the lower atmosphere. *Tammet et al.* [1996] discussed the error of current density calculated with *Kasemir-*

*Ruhnke* [1959] model using dynamic effective area instead of the static effective area. In this paper static effective area will be considered.

## THEORY

In the calm atmosphere, air ions follow the vertical electric field lines and the electric current flow is vertical. When a horizontal wind component exists, current flow lines incline to the horizontal plane at an angle *arctan(kE/v),* where $k$ is the mobility of the air ions and $v$ is the horizontal wind speed. In the presence of the horizontal wire antenna, these current flow lines are modified by the surrounding electric field of the wire antenna as shown in the figure 1.

Assume that a horizontal wire antenna above the ground is in the fair weather atmospheric field of $E$ with a horizontal wind, $v_0$ perpendicular to the wire antenna. Let the z-axis of the right handed Cartesian rectangular coordinate system be along the wire antenna while x-axis is parallel to the current flow lines in the far field i.e. at an angle $arctan(kE/v_0)$ to the horizontal plane. The electric field on the surface of a horizontal wire of radius $r_0$ at height $h$ is given by,

$$E_0 = \frac{E\left(h/r_o\right)}{\ln\left(\frac{2h}{r_0}\right)} \tag{1}$$

The x and y components of the electric field acting on an air ion at the point $(x, y)$ are,

$$E_x = -\frac{\lambda x}{2\pi\varepsilon_0\left(x^2+y^2\right)} \qquad E_y = -\frac{\lambda y}{2\pi\varepsilon_0\left(x^2+y^2\right)} \tag{2}$$

where $\lambda = 2\pi\varepsilon_0 r_0 E_0$ is a constant and $E_0$ is the electric field on the wire surface. Therefore, the drift velocity components on the air ion are,

$$v'_x = -\frac{k\lambda x}{2\pi\varepsilon_0\left(x^2+y^2\right)} \qquad v'_y = -\frac{k\lambda y}{2\pi\varepsilon_0\left(x^2+y^2\right)} \tag{3}$$

The horizontal and vertical velocity components of the air ion are,

$$v_x = \frac{dx}{dt} = v' - \frac{Kx}{x^2+y^2} \qquad v_y = \frac{dy}{dt} = -\frac{Ky}{x^2+y^2} \tag{4}$$

Where $K = \frac{k\lambda}{2\pi\varepsilon_0}$ and $v' = \sqrt{v_0^{\,2} + (kE)^2}$

The solution is,

$$x = \frac{y}{\tan\left(\left(y-b\right)/s\right)} \tag{5}$$

Where $b$ is an arbitrary constant and $s = \frac{K}{v'}$.

## DISCUSSION

Equation (5) shows that when the $x$ coordinate goes to infinity *i.e.* $x \to \infty$, $y = b$, the current flow lines are parallel to the $x$-axis in the far field of the wire antenna. Since the solution contains the tan function, periodic current flow lines can be observed as shown in the Figure 1. Boundaries of the periodic current flow trajectories are shown with broken lines. All the current flow lines within the 1st periodic pattern converge onto the wire antenna. The wire antenna collects all the

air ions, which follow these lines. The boundary of the 1st periodic pattern defines the impact parameter, which leads to the definition of the effective area for the conduction current. Therefore this impact parameter is called as the "effective width" of the wire antenna. This limiting trajectory passes through the stagnation point. Therefore the effective width of the wire antenna can be found by substituting this point to Equation (5). When $y=0$, $b=n\pi s$ where $n=0,1,2,.....$ Here $b=\pi s$. $2b=2\pi s$ is the effective width of the wire antenna. Other values of $n$ define the boundaries of other repetitive patterns. $2b=2\pi s=2\pi K/v'$ predicts that the effective area is inversely proportional to the speed of air ions. The electric current is defined by $i=nqAv$, where $n$ is the volume charge number density, $q$ is the charge of a particle, $A$ is the cross sectional area perpendicular to the charge flow direction and $v$ is the wind velocity. This relation exhibits a linear proportionality of the current flow with the speed of air ion. These two effects nullify the affect of wind on the current collected with horizontal wire antenna. It gives the clue to extend the same conclusion to other types of antennae since this effect is independent of the shape of the antenna.

The lines of electric current flow rotate due to the horizontal wind. The angle of rotation is given by the $arctan(v/kE)$. This rotation restricts the selection of the shape of the wire antenna to a circular cross section, which has axial symmetry. In the vicinity of the wire surface, lines of electric current flow converge to meet the wire surface perpendicularly. Scale analysis shows that when the wind speed is greater than 1 m/s the ion stream reaching to the wire antenna is almost horizontal. In the calculation of the minimum required distance between two parallel wire antennas, rotation of the current should be considered in addition to the effective width of the wire antenna. This distance is important because the effective areas of two wire antennas should not overlap. For example, two parallel antenna with the same height is not suitable when the horizontal wind speed is greater than 1m/s.

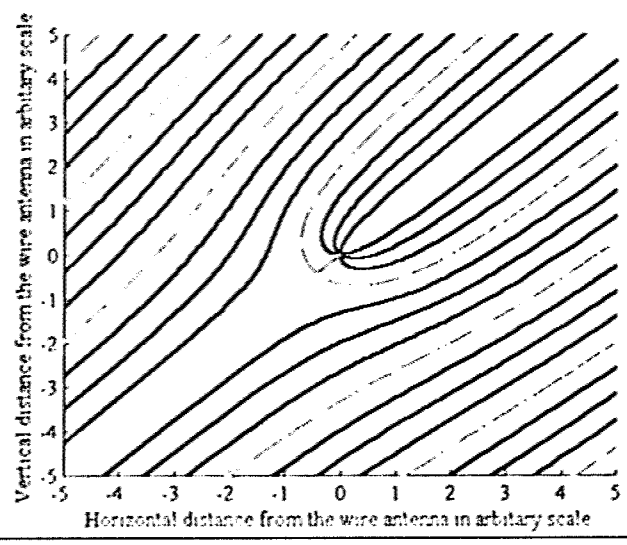


Figure 1. Electric Current flow lines in the vicinity of wire antenna when the wind speed is compatible with electrical drift velocity.

Figure (2) shows the variation of the effective width with the wind speed. In this case we have assumed the following values for each parameter. Vertical atmospheric electric field, $E=100V/m$; height of the wire antenna, $h=1m$; radius of the wire antenna, $r=10^{-3}m$; mobility of air ions, $k=1.5X10^{-4}m^2/Vs$. Under these conditions the wire antenna sustains its surface electric field at about $16kV/m$. When the wind velocity increases from 0.1 to 1m/s, the effective width descreases drastically from 50mm to 5mm. Effective width of the same antenna in the calm atmosphere calculated using the equation,

$$s_d = \frac{2\pi h}{\ln(2h/r)} \tag{6}$$

is about *83cm.* When the wind speed is higher than 1m/s the effective witdth of the wire antenna for conduction current is compatible with that of the convection current. It does not make a considerble effect on the measured value of the conduction current since the speed of air ions are increased by the wind.

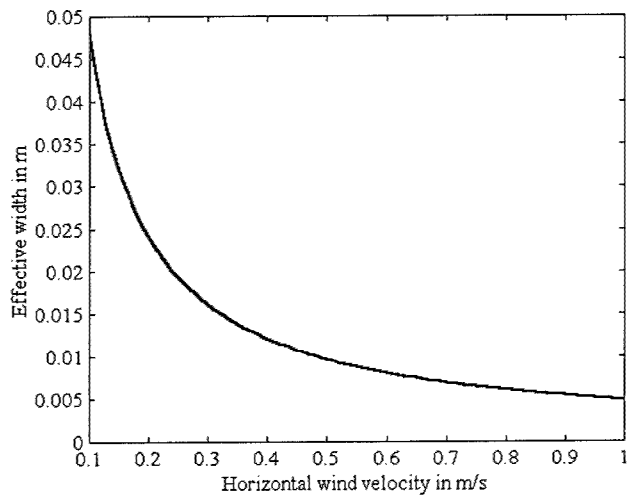


Figure 2. Variation of the effective width of the wire with the wind speed.

REFERENCES


Burke, H.K., and A.A. Few, Direct measurements of the atmospheric conduction current, *J. Geophys. Res.*83, 3093-3098, 1978.

Israel, H., *Atmospheric Electricity II*, U.S. Dept. of Commerce,Springfield, 1973.

Kasemir, H.W., and L.H. Ruhnke, Antenna problems of measurement of the air-earth current, in *Recent Advances in Atmos. Electricity* (ed by L.G. Smith), 137-147, Pergamon Press, London, 1959.

Kasemir, H.W., Measurements of air earth current density, in *Proc. Conf. Atmos. Electricity, Geophys. Res.* Pap. 42, pp. 91-95, Air Force Cambridge Res. Center, Bedford, Mass., 1955.

Ruhnke, L.H., Area averaging of atmospheric electric currents, *J. Geomagn. geoelctr.*, 21, 453-462, 1969.

Tammet, H., S. Israelsson, E. Knudsen and T.J. Tuomi, Effective area of a horizontal wire antenna collecting the atmospheric electric vertical current, *J. Geophys. Res.*, 101, 29671-29677, 1996.

# SYNERGETIC MODELS OF SPACE CHARGE STRUCTURES IN THE ATMOSPHERE

O.V. Mareeva[1], E.A. Mareev[2], S. Israelsson[3], S.V. Anisimov[4]

[1] State Pedagogical University, 603600 Nizhny Novgorod, Russia
[2] Institute of Applied Physics RAS, 603600 Nizhny Novgorod, Russia
[3] Geocentrum, Meteorology, Uppsala University, Sweden
[4] GEMM Laboratory, Shmidt Inst. of Earth Physics RAS, Borok, Yaroslavl, Russia

ABSTRACT: A dynamical nonlinear model of the formation of space charge structures has been developed, taking into account recombination and drift of small ions in the electric field. Quasi-stationary solutions in the form of the running wave of the space charge density are found. It is shown that non-stationary inhomogeneous distributions of space charge density are described under definite conditions by the Burgers equation. Estimations show that the found self-consistent solutions can be displayed in the boundary layer both under fair weather conditions and below thunderclouds. Theoretical results are confirmed by examples of the vertical electric field recording, which exhibit nonlinear behavior of the field.

## INTRODUCTION

The dynamics of electric field and space charge with characteristic times less than the local relaxation time of the atmosphere have attracted much attention recently. In particular, the experiments on ground-based remote receiving of electric field short period pulsations give evidence of spatio-temporal structures occurence in the surface layer [*Anisimov et al.*, 1994]. A model has been developed treating these structures formation in terms of light ions and aerosol turbulent mixing and drift in the external electric field [*Anisimov et al.*, 1999]. But the formation of nonlinear space charge structures in the atmosphere is still questionable.

Note that stationary distributions of electric field and space charge density in the lower atmosphere have been studied theoretically by many authors especially when the electrode effect considering (see [*Hoppel et al.*, 1986] for review). As to nonlinear dynamic models, just the first attempts of their developing are in progress now. *Qui et al.* [1994] investigated numerically the influence of ion attachment on the vertical distribution of the electric field and charge density below a thunderstorm. *Mareeva et al.* [1999] proposed a dynamical nonlinear model of the formation of space charge structures. In this paper we develope this model and compare it with the results of experimental observation.

## A MODEL DESCRIPTION

Our consideration is based on a simple model, in which conductivity is determined by ions with different signs and rather different mobilities. This model corresponds, specifically, to weakly ionized gas in the lower troposphere. Let us assume that ion losses are caused mainly by recombination. The system of equations that contains balance equations for densities of positive ($n_1$) and negative ($n_2$) ions and the Poisson equation is written down in the following form:

$$\frac{\partial n_1}{\partial t} + \mathrm{div}\, n_1 \mathbf{v}_1 = q - \alpha n_1 n_2 \tag{1}$$

$$\frac{\partial n_2}{\partial t} + \mathrm{div}\, n_2 \mathbf{v}_2 = q - \alpha n_1 n_2 \tag{2}$$

$$\mathrm{div}\mathbf{E} = 4\pi e(n_1 - n_2) \tag{3}$$

where $\mathbf{v}_{1,2} = \pm\mu_{1,2}\mathbf{E} + \mathbf{v}_0 + \mathbf{v}_T - D_{1,2}\nabla n_{1,2}/n_{1,2}$ are the velocities of ions determined by their drift in electric field $\mathbf{E}$, transport in the flow of neutral gas and diffusion; $\mu_{1,2}$ are the mobilities of positive and negative ions respectively; $q$ is the external source of ionization; $\alpha$ is the coefficient of ion recombination. Here and below adhesion of light ions to heavy aerosol particles is not taken into account.

Further it will be convenient to pass over from the system of equations (1) - (3) to the system for variables $\rho = e(n_1 - n_2)$ and $\sigma = e(\mu_1 n_1 + \mu_2 n_2)$ that characterize the density of the electric charge and the medium conductivity, respectively. Usually the mobility of negative ions in the

surface layer is slightly higher: $\mu_2 \simeq 2\cdot 10^{-4}\mathrm{m}^2/\ \mathrm{V}\cdot\mathrm{s}$, $\mu_1 \simeq 1.5\cdot 10^{-4}\mathrm{m}^2/\ \mathrm{V}\cdot\mathrm{s}$ [*Hoppel et al.*,1986], so that $\Delta\mu = \mu_2 - \mu_1 > 0$. The set of equations for the variables $\sigma$, $\rho$ and $E$ takes a form:

$$\begin{aligned} \frac{\partial\sigma}{\partial t} + \frac{\partial}{\partial z}(-\sigma E\Delta\mu \ &+ \ \mu_1\mu_2\rho E) = \\ = eq(\mu_1+\mu_2) \ &+ \ 4\pi a(\mu_1\mu_2\rho^2 - \sigma^2 - \sigma\rho\Delta\mu); \end{aligned} \tag{4}$$

$$\frac{\partial\rho}{\partial t} + \frac{\partial}{\partial z}(\sigma E) = 0 \quad ; \quad \frac{\partial E}{\partial z} = 4\pi\rho, \tag{5}$$

where $a = \alpha/4\pi e(\mu_1+\mu_2)$.

Let us search for the solution of the set (4)-(5) in a form of the stationary wave, propagating along the axis $z$ with a constant velocity $V$, so that the functions $\rho(\xi)$, $\sigma(\xi)$, $E(\xi)$ depend on the only variable $\xi = z - Vt$. Assuming that perturbations of ion densities are relatively small ($|n_1 - n_2| \ll |N|$, where $N = n_1 + n_2$) while the ion drift velocities $V_{1d}, V_{2d}$ are defined by the unperturbed homogeneous electric field $E_0$, we obtain the following equation:

$$\rho'_\xi(1 - \frac{V(V+\Delta V_d)}{V_{1d}V_{2d}}) = -4\pi\sigma\rho\frac{(V+a\Delta V_d)}{V_{1d}V_{2d}} - 4\pi(1-a)\frac{\rho^2}{E_0}, \tag{6}$$

where $\Delta V_d = V_{2d} - V_{1d}$. Equilibrium state of this equation is determined as follows:

$$\rho_0 = -\sigma_0 E_0\frac{(V+a\Delta V_d)}{(1-a)V_{1d}V_{2d}}. \tag{7}$$

It is seen from Eq.(7) that the equilibrium value of space charge density $\rho_0$ is not so high if $V \simeq -a\Delta V_d$. With the account of model boundary conditions $\rho(\xi\to-\infty) = 0$; $\rho(\xi\to\infty) = \rho_0$ we yield the following solution in the form of the running step:

$$\rho = \frac{\rho_0}{1+\exp(-\rho_0\xi/C)}, \tag{8}$$

where

$$C = \frac{AE_0}{4\pi(1-a)}; \ A = 1 - \frac{V(V+\Delta V_d)}{V_{1d}V_{2d}}. \tag{9}$$

The positive value of the step velocity corresponds to the motion along the external electric field while the negative one describes the step running against the field $E_0$. In the most interesting case $A \to 0$ the narrow (with the width $C/\rho_0$) step of the space charge density and electric field perturbation is formed. If $V = -\Delta V_d$, the step of the width $V_{1d}V_{2d}/4\pi(1-a)\sigma_0\Delta V_d$ is formed with the charge density "jump" $\rho_0 = \sigma_0 E_0\Delta V_d/V_{1d}V_{2d}$.

One should note that account of different ion mobilities in the above analysis is of importance, because in the case $\mu_1 = \mu_2 = \mu$ the requirement of a small width leads to the relation $V_d \simeq |V|$ and the following expression for the equilibrium charge density $\rho_0/e \simeq -4\pi\sigma(\gamma - \alpha/2)^{-1}$. Assuming $\alpha = 1.6\cdot 10^{-6}\mathrm{cm}^3/\ \mathrm{s}$, $\mu = 1.8\cdot 10^{-4}\mathrm{cm}^2/\ \mathrm{V}\cdot\mathrm{s}$, $\gamma = 4\pi\mu e = 3.2\cdot 10^{-6}\mathrm{cm}^3/\ \mathrm{s}$, we get: $|\ \rho_0/e\ | \simeq 1.5\cdot 10^3\mathrm{cm}^{-3}$. Therefore, in a case of the same ion mobilities under fair weather conditions over the land a sharp step could be formed if the space charge density is sufficiently high, much higher than for a common electrode effect. This condition may be realized however in more strong electric fields under thunderclouds.

## NONLINEAR EQUATION FOR CHARGE PERTURBATIONS OF FINITE MAGNITUDE

Deriving the nonlinear equation for the charge perturbations, we will proceed from the set of equations (4)-(5) in a case of the same ion mobilities. Denoting $I = \rho/e$ and assuming $|N| \gg |I|$, one can yield:

$$\frac{\partial^2 I}{\partial t^2} + (\alpha+\gamma)N\frac{\partial I}{\partial t} - V_d^2\frac{\partial^2 I}{\partial z^2} - V_d(4\gamma-\alpha)I\frac{\partial I}{\partial z} = -\gamma\alpha N^2 I - 2V_d\frac{\partial q}{\partial z}. \tag{10}$$

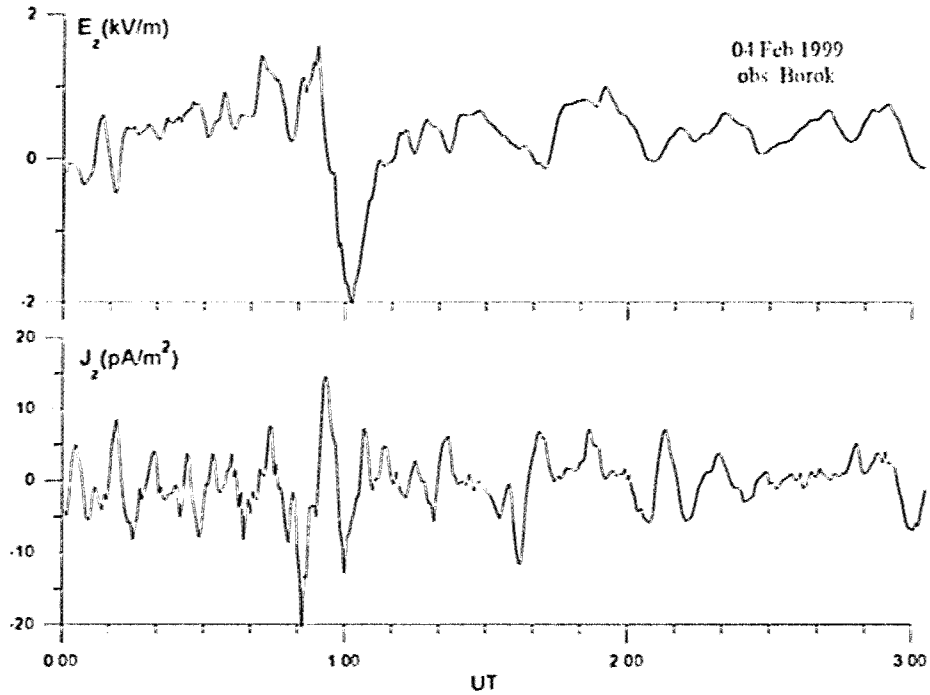


Figure 1 Plot of aeroelectric field and current variations

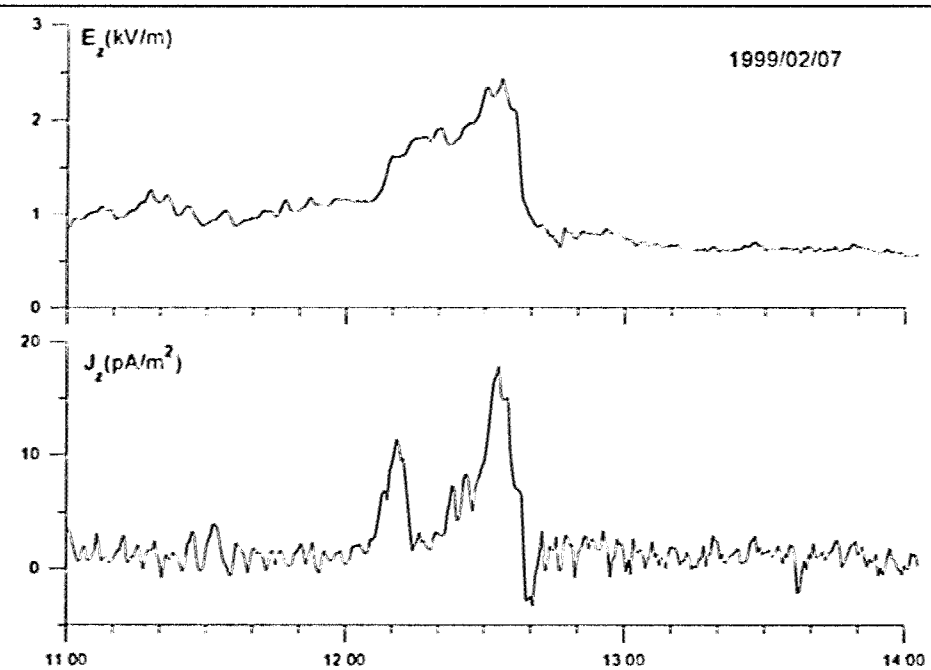


Figure 2 Plot of aeroelectric field and current variations

Here the relation $N^2 = 4q/\alpha$ and the condition of the constant value of the vertical electric current density $j = const = \gamma NE/4\pi$ have been used. Note that Eq. (10) has a simple solution when the intensity of ionization depends on the height exponentially. For instance, in a case $q = A + Q_0 \exp(z/l)$, where $z < 0$, $A$ and $Q$ are the constants, $l$ is the characteristic scale of intensity decrease (of order of 1 m), a negative space charge layer with the constant density $I = -V_d/2l\gamma \simeq -10^3$ near the ground surface should be formed. This phenomenon (reversal electrode effect) earlier has been observed in experiments and considered numerically (see e.g. [*Israelsson*, 1996]). Noted simple analytical estimations agree with these results.

In the absence of nonlinear term on the left hand side the solution of the Eq.(10) is the damped wave process. Comparison of the third and forth terms shows that nonlinearity is substantial when the parameter $R_e = I_0(4\gamma - \alpha)z_0/V_d > 1$, where $z_0$ is the characteristic scale of the charge density change, $I_0$ is its magnitude. The parameter $R_e$ is analogous to the Reinolds number in the common hydrodynamics of the viscous fluid, because it characterizes relative role of nonlinear and dissipative effects. It could be called the "electro-kinetic" Reinolds number in our consideration.

There are two characteristic times in the present problem: the time of charge relaxation $t_c = (\gamma N)^{-1}$ and the time of conductivity relaxation $t_r = (\alpha N)^{-1}$. In the most curious case $t_r \ll t_c$, when the characteristic time of space charge evolution of the process $T$ obeys the inequality $t_r \ll T \ll t_c$ and $q'_z = 0$, we derive the Burgers equation:

$$\frac{\partial I}{\partial t}(\alpha + 2\gamma)N - V_d(4\gamma - \alpha)I\frac{\partial I}{\partial z} - V_d^2\frac{\partial^2 I}{\partial z^2} = 0. \tag{11}$$

In the framework of this equation the nonlinear evolution of the space charge density perturbation (i.e. put in the hump form) can be easily analysed [*Mareeva et al.*, 1999].

To illustrate the obtained theoretical results, we present two examples of electric field (and respective full vertical current density) temporal behavior, observed in the ground-based experiments at the Geophysical Observatory "Borok". One can see on the Fig. 1,2 the nonlinear solitary wave forms with sufficiently high magnitude and characteristic times from 10 to 30 min. With the account of the wind speed of order 1 m/s it corresponds to the spatial scale of order of 1 km.

## CONCLUSIONS

A dynamical nonlinear model of the formation of space charge structures has been developed, taking into account recombination and drift of small ions in the electric field. Quasi-stationary solutions in the form of the running wave are found. The dynamical stationary state and wave velocity turned out to depend substantially on the difference of mobilities of positive and negative ions. It is shown that non-stationary inhomogeneous distributions of space charge density are described by the modified Burgers equation. Its solution depends upon the effective "electro-kinetic" Reynolds number. The found self-consistent nonstationary structures can be revealed in the boundary layer. Their parameters are defined by meteorological conditions and can give the signature of nonlinear processes of electric interaction in the atmosphere. A model developed has been applied to the interpretation of the vertical electric field and current observation.

## REFERENCES


Anisimov, S.V., S.S. Bakastov and E.A. Mareev, Spatiotemporal structures of electric field and space charge in the surface atmospheric layer, *J. Geophys. Res.*, 99, 5, 10603-10610, 1994.

Anisimov, S.V., E.A. Mareev and S.S. Bakastov, Generation and evolution of aeroelectric structures in the surface atmospheric layer, *J. Geophys. Res.*, 104, 1999 (accepted).

Hoppel, W.A., R.V. Anderson and J.C. Willett, Atmospheric electricity in the planetary boundary layer, in: *The Earth's Electrical Environment,* ed. by E.P.Krider and R.G.Roble, Washington: D. C., National Academy Press, 1986. P. 149-165.

Qie, X., S. Soula and S. Chauzy, Influence of ion attachment on the vertical distribution of the electric field and charge density below a thunderstorm, *Ann. Geophys.*, 12, 1218-1228, 1994.

Mareeva, O.V., and E.A. Mareev, Nonlinear structures of electric field and space charge in the surface atmospheric layer, *Geomagnetizm and Aeronomy*, N4, 1999.

Israelsson, S., Space charge layers created by corona and electrode effects at ground level below thunderclouds, *Proc. X Int. Conf. on Atmospheric Electricity*, Osaka, 1996, p. 140-143.

Mareev, E.A., S. Israelsson et al., Studies of an artificially generated electrode effect at ground level, *Ann. Geophys.*, 14, 1095-1101, 1996.

# CLASSIFICATION OF NATURAL AIR IONS NEAR THE GROUND

U. Hõrrak, J. Salm, and H. Tammet

Institute of Environmental Physics, University of Tartu
18 Ülikooli St., Tartu, 51014, Estonia

ABSTRACT: The structure of air ion mobility spectrum recorded at Tahkuse Observatory, Estonia, during 14 months, is studied using factor analysis. The air ions in a mobility range of 0.00041–3.2 $cm^2 V^{-1} s^{-1}$ (diameters 0.36–80 nm) are divided into five classes: small and big cluster ions, intermediate ions, light and heavy large ions. The boundaries between the classes are 1.3 $cm^2 V^{-1} s^{-1}$, 0.5 $cm^2 V^{-1} s^{-1}$, 0.034 $cm^2 V^{-1} s^{-1}$, 0.0042 $cm^2 V^{-1} s^{-1}$. Five factors correlated with respective ion classes explain 92% of total variance. According to their physical nature, the intermediate and large ions are called aerosol ions. The classification of air ions according to their mobility leads to a correlated classification of atmospheric aerosol particles according to size. The 1.6 nm boundary diameter between clusters and aerosol particles is confirmed, and the boundary diameters between the nanometer particles, the ultrafine particles and the Aitken particles as classes of tropospheric aerosol are estimated to be 7.4 nm and 22 nm.

## INTRODUCTION

The concepts of small and large air ions have a perceptible physical background. Problems arise when trying to specify the concept of intermediate ions and settle the mobility boundaries. The boundaries defined in atmospheric electricity textbooks are rather conventions. A natural classification is assumed to explain coherent behavior of air ions inside class intervals and relative independence of the ions of different classes. A requirement to measurements used in the verification of the classification is that the recorded air ion mobility fractions should be narrow when compared with mobility classes. The analysis of the statistical behavior of fraction concentrations requires thousands of mobility spectra recorded during at least one full year. First measurements that simultaneously satisfy both of these requirements have been carried out at Tahkuse Observatory where a 20-fraction air ion mobility spectrometer covering a mobility range of 0.00041–3.2 $cm^2 V^{-1} s^{-1}$ is running almost continuously since 1988 [*Hõrrak et al.*, 1994].

The large and intermediate ions are charged aerosol particles, and their mobility is correlated with the particle diameter. Thus the problem is related to the atmospheric aerosol particle size classification. As well as in the case of mobility measurements, the measurements of particle size distribution in a wide size range have been episodic and the boundaries between the particle size classes are conventional. Obviously the air ion mobility data contains the largest available statistical information about long term variations of tropospheric aerosol size spectrum. Thus the analysis of mobility spectra at Tahkuse Observatory could provide essential information about natural classification of atmospheric aerosol particles according to their size.

## INSTRUMENTATION AND MEASUREMENTS

The instrumentation at Tahkuse Observatory consists of three original multichannel aspiration mobility analyzers. Air is sucked into the analyzers through an opening in the gable of a building at a height of about 5 m from the ground. High trees around the building shield the electric field and suppress the electrode effect asymmetry of polarities [*Hõrrak et al.*, 1994].

Table 1 describes the scheme of mobility fractions. All 20 fraction concentrations of positive air ions and 20 fraction concentrations of negative air ions were measured every 5 minutes. The hourly averages and standard deviations of air ion fraction concentrations inside the hourly periods were recorded together with simultaneously measured values of wind direction, wind speed, atmospheric pressure, temperature, relative humidity, and concentration of $NO_2$. The present analysis is based on the data collected during the period from September 1, 1993, to October 27, 1994. Due to occasional pauses in the measurements, about 16% of the possible measuring time was lost, and 8615 hourly mobility spectra of both signs are available.

TABLE 1. Air ion fractions, estimates of equivalent diameter ranges assuming single charged particles, and proposed classes of air ions.

| Fraction number | Mobility $cm^2 V^{-1} s^{-1}$ | Classes of ions | Diameter nm |
|---|---|---|---|
| 1 | 2.51–3.14 | Small cluster ions | 0.36–0.45 |
| 2 | 2.01–2.51 | | 0.45–0.56 |
| 3 | 1.60–2.01 | | 0.56–0.70 |
| 4 | 1.28–1.60 | | 0.70–0.85 |
| 5 | 1.02–1.28 | Big cluster ions | 0.85–1.03 |
| 6 | 0.79–1.02 | | 1.03–1.24 |
| 7 | 0.63–0.79 | | 1.24–1.42 |
| 8 | 0.50–0.63 | | 1.42–1.60 |
| 9 | 0.40–0.50 | Inter-mediate ions | 1.6–1.8 |
| 10 | 0.32–0.40 | | 1.8–2.0 |
| 11 | 0.25–0.32 | | 2.0–2.3 |
| 12 | 0.150–0.293 | | 2.1–3.2 |
| 13 | 0.074–0.150 | | 3.2–4.8 |
| 14 | 0.034–0.074 | | 4.8–7.4 |
| 15 | 0.016–0.034 | Light large ions | 7.4–11.0 |
| 16 | 0.0091–0.0205 | | 9.7–14.8 |
| 17 | 0.0042–0.0091 | | 15–22 |
| 18 | 0.00192–0.00420 | Heavy large ions | 22–34 |
| 19 | 0.00087–0.00192 | | 34–52 |
| 20 | 0.00041–0.00087 | | 52–79 |

Average concentrations of negative and positive small ions are 245 $cm^{-3}$ and 274 $cm^{-3}$. The concentration of large ions diminishes towards higher mobilities due to a reduction of charging probability and concentration of aerosol particles. The shape of their mobility spectrum is in accordance with calculations based on the theory of bipolar charging of aerosol particles by diffusion of cluster ions. Average concentration of intermediate ions is about 50 $cm^{-3}$. Occasional bursts of intermediate ions up to about 900 $cm^{-3}$ occur during daytime. The intermediate ions are formed probably by diffusion charging of nanometer aerosol particles generated by photochemical nucleation process. Another process responsible for the generation of intermediate ions is the growth of small ions under special environmental conditions. The variation coefficient of the hourly average values of concentration is about 50% for small ions, 70% for large ions, and up to 130% for intermediate ions. At night-time, intermediate and large air ions show a lower variation coefficient of 50–60%.

FACTOR ANALYSIS

Fraction concentrations of air ions are interpreted as a set of closely correlated variables. Greater part of the measurement information about correlated variables can be represented by a considerably smaller number of new variables, called the principal components, or factors. The analysis was carried out both in terms of the original values of the 20 fraction concentrations and of their logarithmically rescaled values, and the results are nearly the same. The eigenvalue problem was solved for the correlation matrix which is equivalent to preliminary standardization of variables, or analysis of relative variations. The principal components were transformed to well interpretable factors with dominating positive factor loadings using the VARIMAX procedure. The factor analysis was carried out separately for positive and negative ions. The results are presented in Figure 1 for positive ions, the results for negative ions being very similar.

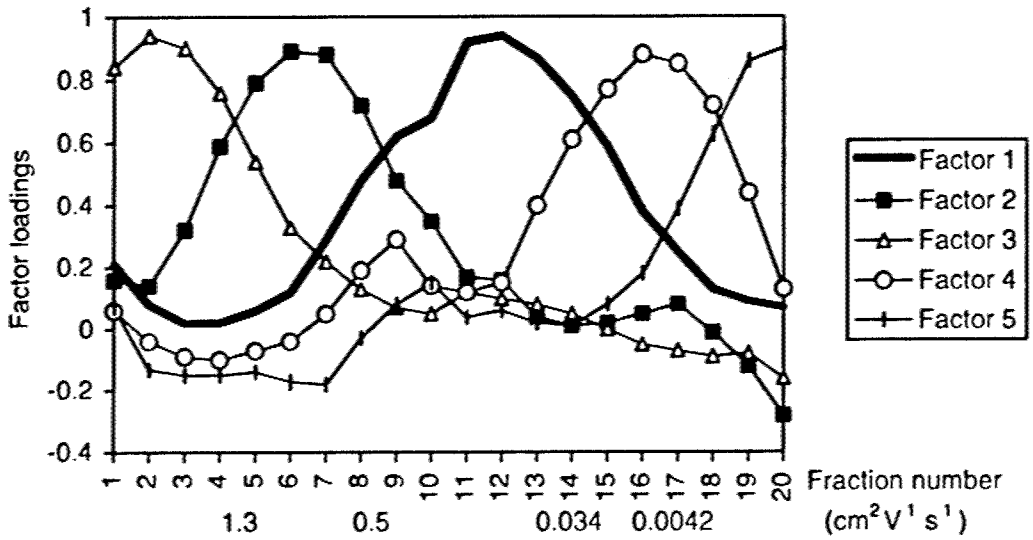


Figure 1. Factors of air ion mobility spectrum for positive ions.
The mobility and diameter boundaries of fractions are given in Table 1.

The first five principal components explain 92% of the total variance and each of the five factors presents at least as much variance as the average for one fraction concentration. The subsequent 14 principal components explain only 8% of the total variance. A part of this variation is caused by instrument noise. Thus the mobility spectrum has five essential degrees of freedom, and the set of 20 fraction concentrations can be relatively well described by only five factors representing at least 92% of all the measurement information.

Factor 1 (see Figure 1) is highly correlated with intermediate ions (fractions 9–14) and thus can be called the "burst factor" of intermediate ions. It accounts for 24% of the total variance. Factor 2 is highly correlated with big cluster ions (fractions 4–8), Factor 3 with small cluster ions (fractions 1–4), and Factor 4 with light large ions (fractions 15–18). They account for approximately equal variances, 20%, 18% and 17%. The contribution of Factor 5, associated with heavy large ions (fractions 18–20), is the lowest, 13%. This factor is correlated inversely with cluster ions (fractions 2–7). Factor 2, correlated highly with big cluster ions (fractions 5–8), is correlated negatively with heavy large ions (fractions 19–20).

## DISCUSSION AND CONCLUSIONS

The analysis of the correlations between the factors and air ion fraction concentrations shows that all the air ions can be divided into two wide classes: cluster ions with mobilities above 0.5 $cm^2 V^{-1} s^{-1}$, and aerosol ions with mobilities below 0.5 $cm^2 V^{-1} s^{-1}$. Aerosol ions are particles with physical properties of macroscopic bodies. The cluster ions can be divided into two subclasses (small and big cluster ions), and the aerosol ions into three subclasses (intermediate ions, light and heavy large ions). This classification, given in Table 1, is still to a certain extent conventional and the boundaries are not exactly determined because the factors have crossloadings (any variable is correlated with more than one factor, see Figure 1).

A mobility of 0.5 $cm^2 V^{-1} s^{-1}$ or a diameter of 1.6 nm is the same boundary, which has been considered physically as the boundary between molecular clusters and macroscopic particles [*Tammet*, 1995]. The same value of 0.5 $cm^2 V^{-1} s^{-1}$ was also formerly considered as the lower boundary of small air ions [e.g., *Hõrrak et al.*, 1994].

The above classes of air ions could be physically characterized as follows:

- *Small cluster ions*: mobility 1.3–2.5 $cm^2 V^{-1} s^{-1}$, estimated diameter 0.36–0.85 nm and mass 30–400 u. The core of a cluster could contain an inorganic molecule and be surrounded by one layer of water molecules. After recombination, the cluster would be destroyed and separated back to molecules.
- *Big cluster ions*: mobility 0.5–1.3 $cm^2 V^{-1} s^{-1}$, estimated diameter 0.85–1.6 nm and mass 400–2500 u. The core of a cluster could contain an organic molecule and be surrounded by a layer of water molecules. In the case of intensive nucleation events (bursts) the enhanced concentrations were recorded simultaneously with intermediate and light large ion concentrations. As distinct from aerosol ions, collisions between cluster ions and ambient gas molecules are considered to be elastic [*Tammet*, 1995].
- *Intermediate ions*: mobility 0.034–0.5 $cm^2 V^{-1} s^{-1}$, diameter 1.6–7.4 nm. The corresponding class of aerosol particles: the *nanometer particles*. Some intermediate ions are a product of ion–induced nucleation: nucleating vapor condenses to cluster ions, which grow to the size of intermediate ions called the *primary aerosol ions*. Particles born in the neutral stage in the process of gas-to-particle conversion, or nucleation, and charged by attachment of cluster ions, are called the *secondary aerosol ions*.
- *Light large ions*: mobility 0.0042–0.034 $cm^2 V^{-1} s^{-1}$, diameter 7.4–22 nm. The corresponding class of aerosol particles: the *ultrafine particles*. They are often in a quasi-steady state of stochastic charging with cluster ions.
- *Heavy large ions*: mobility < 0.0042 $cm^2 V^{-1} s^{-1}$, diameter > 22 nm. The corresponding class of aerosol particles could be called the *Aitken particles*. They are, as a rule, in a quasi-steady state of stochastic charging with cluster ions, and some of them may carry multiple charges.

ACKNOWLEDGEMENTS: This research was supported by the Estonian Science Foundation grants nos. 1879, 3326, and 3050.

## REFERENCES

Hõrrak, U., H. Iher, A. Luts, J. Salm, and H. Tammet, Mobility spectrum of air ions at Tahkuse Observatory, *J. Geophys. Res.*, ***99***, 10,679–10,700, 1994.

Tammet, H., Size and mobility of nanometer particles, clusters and ions, *J. Aerosol Sci.*, ***26***, 459–475, 1995.

# ATMOSPHERIC ELECTRICITY AS A FACTOR OF DRY DEPOSITION OF PARTICULATE POLLUTION

H. Tammet[1] and S. Israelsson[2]

[1]Institute of Environmental Physics, University of Tartu, Tartu, Estonia
[2]Geocentrum, Meteorology, University of Uppsala, Uppsala, Sweden

ABSTRACT: The electrical deposition is known in case of unattached radon daughter clusters which are unipolarily charged and of high mobility. The role of the electrical forces in deposition of aerosol particles is estimated comparing the fluxes of particles carried by different deposition mechanisms in a model situation. The ratio of electrical and diffusion deposition fluxes decreases about ten times only when the mobility decreases thousand times from the values characteristic for small ions to the values characteristic for large ions. The electrical flux of fine particles can dominate on the tips of leaves and needles even in a moderate atmospheric electric field of few hundreds V/m as measured over the plain ground surface. Unlike the diffusion deposition, the electrical deposition is essentially non-uniform: the plate out on the tips of leaves and especially on needles of top branches of conifer trees is more intensive than on the ground surface and electrically shielded surfaces of plants. The knowledge of deposition geometry could improve our understanding of air pollution damages of plants.

## INTRODUCTION

The turbulent diffusion approaches zero on the surface of plant leaves and needles. *Porstendörfer* [1994] writes: "3.3.1. *Deposition processes*. In general, the dry deposition of aerosol particles is governed by the physical processes of sedimentation by gravity, impaction by inertial forces, interception and Brownian diffusion". Two mechanisms, impaction and interception, are considered together below and called the aerodynamic deposition. All four non-electrical mechanisms together are called the mechanical deposition. The electrical mechanism of deposition is neglected by *Porstendörfer* [1994] as is common in the literature about aerosol deposition.

The electrical deposition has been considered when discussing deposition of radon daughters, considerable amount of which are carried by positive small ions [*Wilkening*, 1977; *Willett*, 1985; *Tammet and Kimmel*, 1998]. The electrical mobilities of aerosol particles are three orders of magnitude less than the mobilities of small ions, and they are not unipolarily charged. However, the diffusion coefficient of the aerosol particles is low as well, and the relative effect of electrical field could appear considerable. *Schneider et al.* [1994] showed how the particles are deposited on the faces and eyes of people exposed to a strong electric field e.g. near a computer display. New discussion was started by *Henshaw et al.* [1996], who published an impressive demonstration of the enhanced deposition of radon daughters in the vicinity of electric power cables indoors, and explained the effect by the electrical deposition of dust particles carrying the attached fraction of radon daughters. Additionally, *Henshaw et al.* [1996] pointed out the problem of the electrostatic deposition of radon daughters as a possible mechanism of the environmental effect of HV power lines.

The hypothesis by *Henshaw* was not accompanied by a theoretical model of the effect. A quantitative theoretical estimate is required to decide, under which conditions the electrical deposition should be considered or could be neglected.

ESTIMATES OF COMPONENTS OF DEPOSITION VELOCITY

The deposition velocity is defined as the ratio of the deposition flux to the surface area. Specific deposition velocities caused by gravity, aerodynamic effect (impaction and interception), Brownian diffusion and electric field are denoted below as $u_G$, $u_A$, $u_D$, and $u_E$.

The deposition velocities $u_G$ and $u_E$ of uniformly charged particles over a plain surface are easy to estimate:

$$u_G = mgB, \qquad u_E = EZ = EqB,$$

where $g$ is the gravitational acceleration, $E$ is the electric field, $m$, $q$, $B$, and $Z$ are respectively the mass, charge, mechanical and electrical mobility of the particle.

The natural ground is mostly covered by plant canopy. The electric field is strongly enhanced on the tips of leaves and on needles of plants. Deposition to specific elements of plants depends on their geometry. The shapes and positions of leaves and needles are variable. Thus a model of a needle is considered as a cylinder or wire of radius $R$ at distance $H$ from the horizontal plain surface. The field on the surface of a long wire is

$$E = \frac{H}{R\ln(2H/R)}E_0,$$

where $E_0$ is the undisturbed atmospheric electric field over the plain surface. The field on the surface of a short needle is a little enhanced when compared with the estimate above. Numeric examples will be given for a long wire with $R = 0.5$ mm and $H = 7$ cm. In this occasion, $E = 25\ E_0$.

If the particles are not uniformly charged, the probability $p_i$ of a particle to carry the charge $q = ie$ should be considered and the deposition velocity is to be calculated as a sum: $u_E = E\sum_{i=1}^{\infty} p_i Z_i$, where $Z_i$ is the mobility of a particle with a charge $ie$.

The aerodynamic deposition on a cylinder is estimated according to a simplified model fitting the empirical data presented by *Fuchs* [1964] and numerical results by *Wessel and Righi* [1988]:

$$u_A = \left[\left(\frac{\mathrm{Stk}}{0.6+\mathrm{Stk}}\right)^2 + \frac{r}{R}\right]\frac{v}{\pi},$$

where $r$ is the particle radius, $v$ is the air flow velocity, and Stk is the Stokes number:

$$\mathrm{Stk} = \frac{vmB}{R}.$$

The Brownian deposition on a cylinder is estimated according to the Churchill-Bernstein equation for heat transfer translated according to *Eckert and Drake* [1972] to the terms of diffusion as explained by *Tammet and Kimmel* [1998]:

$$u_D = \frac{kTB}{2R}\left(0.3 + \frac{0.62\,\mathrm{Re}^{1/2}\,\mathrm{Sc}^{1/3}}{\left(1+(0.4/\mathrm{Sc})^{2/3}\right)^{1/4}}\right)\left(1+\left(\frac{\mathrm{Re}}{282000}\right)^{5/8}\right)^{4/5},$$

where Re and Sc are the Reynolds number and Schmidt number:

$$\mathrm{Re} = \frac{2Rv}{\mu}, \qquad \mathrm{Sc} = \frac{\mu}{kTB},$$

$k$, $T$ and $\mu$ being the Boltzmann constant, temperature, and kinematic viscosity of the air.

The deposition velocities are not exactly additive. A rough approximation is used below to estimate the combined mechanical deposition velocity $u_M$:

$$u_M = \sqrt{u_G^2 + u_A^2 + u_D^2}$$

## DISCUSSION AND CONCLUSIONS

The critical field strength is defined as that which makes the velocity of electrical deposition equal to the velocity of some other specific deposition. Different critical field strengths can be related to the gravitational, Brownian, aerodynamic, and joint mechanical deposition. The velocity of electrical deposition is proportional to the field strength. Thus the relative effect of the electric field is easy to estimate when the critical field strength is known. Some examples illustrating the quantitative role of the electrical deposition are given in Figures 1 and 2 below.

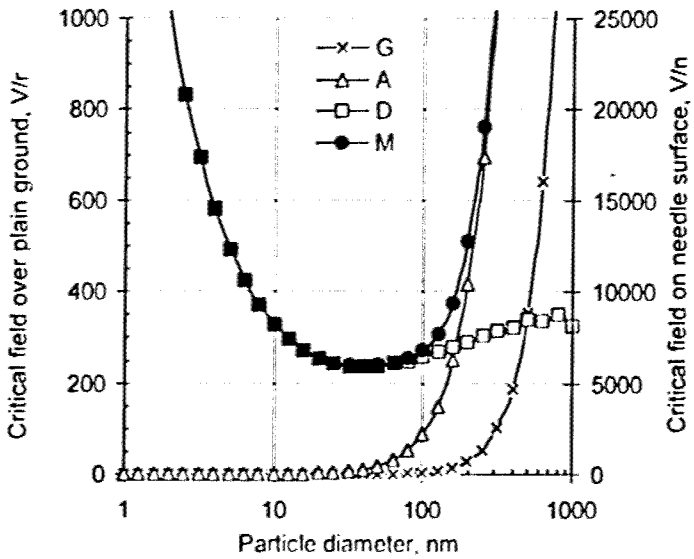


Figure 1. Critical electric field against different mechanisms of deposition:
G – gravitational,
A – aerodynamic,
D – diffusional,
M – joint mechanical.
Assumptions:
Standard atmospheric conditions.
Cylinder diameter 1 mm,
height 7 cm,
particle density 2 g/cm$^3$,
$\lambda_1/\lambda_2 = 2$.
Wind velocity 1 m/s.

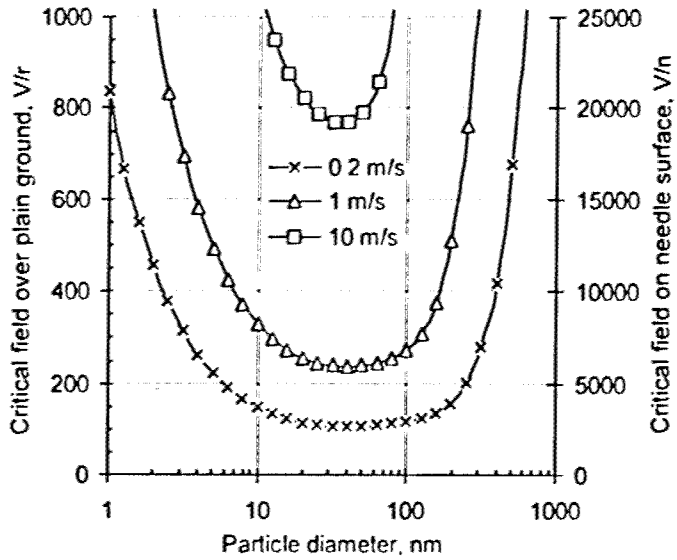


Figure 2. Critical electric field against joint mechanical deposition depending on the wind velocity.
Assumptions:
Standard atmospheric conditions.
Cylinder diameter 1 mm,
height 7 cm,
particle density 2 g/cm$^3$,
$\lambda_1/\lambda_2 = 2$.

According to Figure 1, the gravitational mechanism has a secondary role in aerosol particle deposition and can play some part only at extremely weak wind. Aerodynamic sedimentation and Brownian diffusion are essential mechanisms of mechanical deposition of particles. The aerodynamic deposition is essential in case of particles of diameter above 100 nm. In the size range of large air ions the aerodynamic deposition is negligible and the Brownian diffusion dominates as the mechanism of mechanical deposition. In case of uniformly charged particles, the electrical mobility and diffusion coefficient are proportional to each other. Thus the dependence of the critical electric field on the particle size is weak in the size range of Langevin ions.

Figure 2 illustrates the role of electric deposition compared with joint mechanical deposition depending on the wind velocity. The critical field strength is lowest in the particle diameter range of 10–200 nm which consists of most of the atmospheric aerosol particles. The role of the electrical deposition essentially depends on the wind velocity. In case of a low wind of about 1 m/s or less, the critical field is comparable to the normal atmospheric electrical field, and electrical deposition of aerosol particles has considerable role as a factor of redistribution of deposit on different elements of the plants. In a strong wind about 10 m/s or more, the electrical deposition can be considerable only in a thunderstorm situation or on the top branches of trees.

The electrical deposition of aerosol particles should be considered when discussing enhanced pollution damages of the top branches of conifer trees.

ACKNOWLEDGEMENTS: This research was supported by the Estonian Science Foundation grant no. 3050 and by the Swedish Institute Visby Programme.

REFERENCES

Eckert, E.R.G., and R.M. Drake, *Analysis of Heat and Mass Transfer*, McGraw-Hill, Tokyo, 1972.

Fuchs, N.A., *The Mechanics of Aerosols*, Pergamon Press, Oxford, 1964.

Henshaw, D.L., A.N. Ross, A.P. Fews, and A.W. Preece, Enhanced deposition of radon daughter nuclei in the vicinity of power frequency electromagnetic fields, *Int. J. Radiat. Biol.*, ***69***, 25–38, 1996.

Porstendörfer, J., Properties and behavior of radon and thoron and their decay products in the air, *J. Aerosol Sci.*, ***25***, 219–263, 1994.

Schneider, T., M. Bohgard, and A. Gudmundsson, A semiempirical model for particle deposition onto facial skin and eyes. Role of air currents and electric fields, *J. Aerosol Sci.*, ***25***, 583–593, 1994.

Tammet, H., and V. Kimmel, Electrostatic deposition of radon daughter clusters on the trees, *J. Aerosol Sci.*, ***29***, S473–S474, 1998.

Wessel, R.A., and J. Righi, Generalized correlations for inertial impaction of particles on a circular cylinder, *Aerosol Sci. Technol.*, ***9***, 29–60, 1988.

Wilkening, M.H., Influence of the electric fields of thunderstorms on radon-222 daughter ion concentrations, In *Electrical Processes in Atmospheres*, 54–59, Steinkopff, Darmstadt, 1977.

Willett, J., Atmospheric-electrical implications of $^{222}$Rn daughter deposition on vegetated ground, *J. Geophys. Res. D*, ***90***, 5901–5908, 1985.

# THE LIMITS OF AIR ION MOBILITY RESOLUTION

H. Tammet

Institute of Environmental Physics, University of Tartu, Estonia

ABSTRACT: An innovation by *Loscertales* [1998] forced the revision of the theory of the diffusion-limited mobility resolution. Traditionally, the limit of resolution has been estimated according to the ratio of the thermal energy $kT$ to the work of the electric field expressed as $qV$, where $q$ is the ion charge and $V$ is the voltage between electrodes. This is correct when the electric field is transverse to the air flow. Otherwise, the term $qV$ should be replaced by the term $qEL$, where $L$ is the Lagrangian length of the passage of an ion through the air in the mobility separation zone. The work $qEL$ exceeds $qV$ in the longitudinal or inclined field analyzers which promise further improvement of the mobility resolution when compared with traditional transverse field instruments. The inclined field method can be accomplished as proposed by *Loscertales* [1998] or by using inclined grids as suggested in the present paper.

## INTRODUCTION

Understanding of the limits of mobility resolution is important because of increasing interest in the nanometer particle and airborne cluster research during the present decade. The resolution of existing mobility spectrometers does no fully satisfy the requirements of analytic instruments, and any improvement promises new applications of ion mobility spectrometry.

Three factors limit the resolution: (1) finite width of electrodes and slits of a differential analyzer, (2) background noise of the measured electric current, (3) air ion diffusion, or Brownian motion, in a mobility analyzer. Primitive estimates of the limits of resolution due to electrode width are simple and well known, but far from faithful. The reason for this is that these estimates neglect the possibility of mathematical inversion. Possibility of computational enhancing of the resolution is limited by the noise of the measured electric current. Thus the first two factors should be discussed together. The problem is mathematically complicated and no satisfactory solution is known up to now.

The third factor is physically the most fundamental and is discussed in many papers. A review of publications has been given by *Flagan* [1998]. However, the problem seems not to be exhausted. Recently *Loscertales* [1998] suggested a new idea to make an aspiration condenser in which the electric field is inclined relative to the air flow, and he showed that the commonly accepted resolution limit can be surpassed in a new instrument. The proposal by Loscertales makes it necessary to revise some concepts and correct misunderstandings in the common theory of diffusion-limited mobility resolution.

## STANDARD INTERPRETATION OF DIFFUSION-LIMITED RESOLUTION

Brownian diffusion of air ions results in a Gaussian dispersion of coordinates of air ions in a uniform separating field inside an analyzer. Although the images of the mobility lines are not Gaussian, they can well be approximated by Gaussians. The mobility resolution is measured by the ratio of the Gaussian standard deviation $s_Z$ to the center of the mobility line $Z_o$: $d = s_Z/Z_o$.

In a simplest mobility analyzer the mobility is measured by the drift on an ion during a predetermined time or by the time (TOF method) of drifting a predetermined distance. *Zeleny*

[1929] showed that the Brownian motion or diffusion of ions limits the resolution of the simplest mobility analyzer to the value

$$\mathrm{d} = \mathrm{d}_\circ = \sqrt{2\frac{kT}{qV}}\ , \tag{1}$$

where $q$ is the ion charge and $V$ is the voltage between the beginning and the end of the drift path. Solutions of specified problems have been given by *Tammet* [1970], *Stolzenburg* [1988], *Rosell-Llompart* [1996] and others.

The resolution of a specific analyzer can be written as $\mathrm{d} = f \times \mathrm{d}_0$, where the factor $f$ exceeds the value of 1 in any classic aspiration or TOF mobility analyzer. E.g., $f = \sqrt{1 + h^2 / l_\circ^2}$ in a plain aspiration condenser with a plug flow, where $h$ is the distance between the electrodes and $l_0$ is the length of the condenser.

The value of $\mathrm{d}_0$ is determined by the ratio of the average thermal energy of an ion and the work of the electric field separating the ions. The resolution limit $\mathrm{d}_0$ has a fundamental physical nature: the ratio of the standard deviation of the ion flight distance to the average flight distance in the free molecule regime is expressed by the same Equation 1, and the solution for the free molecule regime can be immediately transformed to the solution of the macroscopic problem by using simple mechanical and probabilistic calculations [*Tammet*, 1970].

## INNOVATION BY LOSCERTALES

*Loscertales* [1998] proposed a new method improving the diffusion-limited mobility resolution by means of the longitudinal electric field in an aspiration mobility analyzer. The plain Loscertales analyzer is explained in Figure 1. The plates are not equipotential and the electric field is not perpendicular to the air flow as assumed in traditional mobility analyzers. The deviation from a traditional analyzer is characterized by the ratio of longitudinal and transverse components of the electric field, Lo = $E_x$ / $E_y$, called the Loscertales number below. When discussing the diffusive broadening of the mobility lines or the transfer function, the flow rate of ionized air is assumed negligible compared with the neutral sheath air flow rate. The electric field between the plates is inclined but uniform, and the voltage $V$ between any pair of facing points in Figure 1 is the same along the plates. Due to the Brownian diffusion, the cloud of simultaneously entering particles of mobility $Z$ expands during the passage as illustrated in Figure 1. The center of the cloud is deposited at the distance

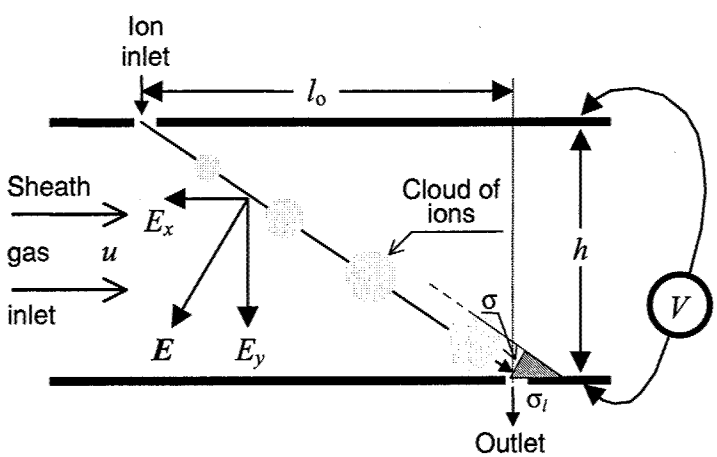


Figure 1. The plain Loscertales mobility analyzer.

$$l = \left(\frac{uh}{ZV} - \mathrm{Lo}\right)h\ . \tag{2}$$

The mobility $Z_0$ of ions emerging through the outlet corresponds to the length of the analyzer $l_0$.

The mobility resolution $\mathrm{d} = \mathrm{s}_Z / Z_0$ is to be estimated according to the Brownian standard deviation of the sedimentation length $\mathrm{s}_l$ and taking note of the derivative

$$\frac{\mathrm{s}_l}{\mathrm{s}_Z} \approx \left|\frac{\mathrm{d}l}{\mathrm{d}Z}\right| = \frac{uh^2}{Z_0^2 V} . \tag{3}$$

In a traditional analyzer $|\mathrm{d}l/\mathrm{d}Z| = l/Z$ and $\mathrm{d} = \mathrm{s}_l / l_0$. When the analyzer is too short, the denominator $l_0$ suppresses the resolution. In a Loscertales analyzer the derivative $|\mathrm{d}l/\mathrm{d}Z|$ remains finite even if the length of the analyzer approaches zero. Thus a further increase in resolution is possible. Calculations [*Loscertales*, 1998; *Tammet*, 1998] yield the result

$$f = \sqrt{1 + \frac{l_0^2}{h^2}} \Big/ \left(\mathrm{Lo} + \frac{l_0}{h}\right). \tag{4}$$

The value of the Loscertales number has no upper limit and the situation $f < 1$ is possible which seems to be paradoxical from the viewpoint of traditional interpretation explained above.

## REVISION OF THE STANDARD INTERPRETATION

The standard interpretation is based on the assumption that the term $qV$ equals the work done by electric field in separating the ions. The assumption is correct when the electric field is transverse to the air flow as expected in the classic aspiration method. The assumption fails in the Loscertales analyzer, where the work of the electric field $W > qV$. So the apparent paradox can be easily solved. It should be pointed out as a little known fact that the limit of resolution expressed as $\mathrm{d}_0$ was surpassed a century ago in an instrument by *Zeleny* [1898] who proposed the method of parallel velocities. In this instrument the voltage $V$ is applied between two grids, and the ionized air flows through the grids parallel to the electric field. The average velocity of ions between the grids is $v = EZ - u$, where $u$ is the air flow velocity, and the mobility is calculated as $Z = h/Et + u/E$, where $h$ is the geometric, or Eulerian, drift of ions. The resolution limit of the method is

$$\mathrm{d} = \sqrt{2\frac{kT}{qE(h + ut)}} . \tag{5}$$

When compared with Equation 1, the expression of the work of the electric field, $W = qV$, is replaced by $W = qE(h + ut)$. The quantity $L = h + ut$ can be interpreted as the Lagrangian distance of ion drift in the separation region and the work of the separating field can be written as $qEL$. Thus the essence of revision of the standard interpretation of the diffusion-limited mobility resolution is that the drift distance in the resolution calculation should not be considered as a geometric distance but as the Lagrangian distance of passage of ions through the air.

Unfortunately, the parallel flow method has no known applications today because it does not allow injection and extraction of ions with air flows.

## METHOD OF INCLINED GRIDS

The proposal of Loscertales to make an aspiration analyzer with non-equipotential electrodes has not materialized due to troublesome technical problems. A combination of the grid method of Zeleny and the non-equipotential electrode method of Loscertales promises easier technical realization of the instrument. The schematic design of the new instrument is explained in Figure 2. The orientation of the electric field in the analyzer is the same as in the Loscertales analyzer, and the diffusion-limited resolution is determined with the same equations. As distinct from the Zeleny grid instrument, the new analyzer has inlet and outlet slits for ions like the tra-

ditional DMA-s. The ions to be separated do not pass through the grids and there is no harmful effect of adsorption of ions on the grids. To the contrary, the adsorption is even useful as a means of additionally cleaning the sheath air. An essential advantage of the method is that the grids suppress the turbulence and maintain the plug flow profile. The required total voltage in the inclined grid instrument is less than in the Loscertales instrument, and the voltage dividers are short and simple. Sheath air can be easily cleaned from background ions by inclusion of additional grids into the air flow before the analyzer.

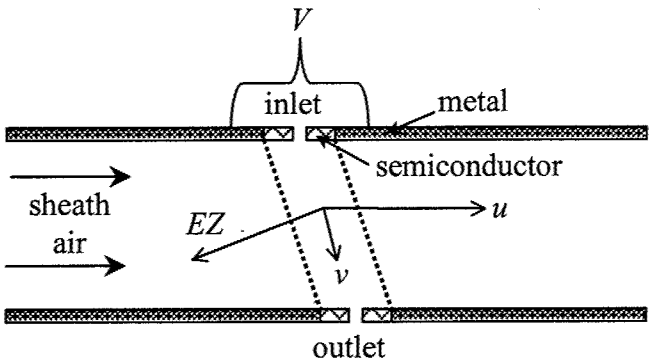


Figure 2. Mobility analyzer with inclined grids

CONCLUSIONS

The limit of resolution estimated according to the ratio of the thermal energy $kT$ to the work of the electric field expressed as $qV$ is correct when the electric field is transverse to the air flow. Otherwise, the work of the electric field exceeds $qV$ and can be expressed as $qEL$, where $L$ is the Lagrangian drift of the ion through the air. Longitudinal or inclined field analyzers promise further improvement of the mobility resolution when compared with traditional transverse field instruments. Actually, the improved resolution is characteristic of the oldest flow-through-grids method by *Zeleny* [1898]. However, the Zeleny grid method does not allow injection and extraction of ions with air flows. This disadvantage is prevented in the inclined field method suggested by *Loscertales* [1998]. The instrument of Loscertales is difficult to manufacture, but the same theoretical advantages can be achieved in a simpler instrument with inclined grids as suggested above.

ACKNOWLEDGEMENTS: This research was supported by the Swedish Institute Visby grant and by the Estonian Science Foundation grant no. 3050.

REFERENCES

Flagan R.C., History of electrical aerosol measurements, *Aerosol Sci. Technol.*, ***28***, 301–380, 1998.

Loscertales, I.G., Drift differential mobility analyzer, *J. Aerosol Sci.*, ***29***, 1117–1139, 1998.

Rosell-Llompart, J., I.G. Loscertales, D. Bingham, and J. Fernandez de la Mora, Sizing nanoparticles and ions with a short differential mobility analyzer, *J. Aerosol Sci.*, ***27***, 695–719, 1996.

Stolzenburg, M., *An ultrafine aerosol size distribution measuring system*, Ph.D. thesis, University of Minnesota, 1988.

Tammet, H., *The aspiration method for the determination of atmospheric-ion spectra*, IPST, Jerusalem, 1970.

Tammet, H., Optimal length of the plain Loscertales mobility analyzer, *J. Aerosol Sci.*, ***29***, S63–S64, 1998.

Zeleny, J., On the ratio of velocities of the two ions produced in gases by Röngten radiation, and on some related phenomena, *Philos. Mag.*, ***46***, 120–154, 1898.

Zeleny, J., The distribution of mobilities of ions in moist air, *Phys. Rev.*, ***34***, 310–334, 1929.

# AEROELECTRICAL MEASUREMENTS IN GEOELECTROMAGNETIC COMPLETE SET OF GEOPHYSICAL OBSERVATORY "BOROK"

S.V.Anisimov, S.S.Bakastov, E.M.Dmitriev, E.B.Anisimova

Geoelectromagnetic monitoring Laboratory, Geophysical Observatory, Shmidt Inst. of Earth Physics, RAS, Borok, Yaroslavl, Russia

ABSTRACT: Atmospheric electricity is an integral part of the Earth's electromagnetic environment. An extensive database, which obtained on long-term ground aeroelectrical measurement, is a background for experimental research of the solar-terrestrial relationship. Mid-latitude Geophysical Observatory "Borok" (58.03°N, 38.97°E) is equipped with the installation for geoelectromagnetic monitoring including aeroelectric, geomagnetic and radiophysics measurements. The basic data logging system is an 16-th channel analog to digital converter with sampling rate 10Hz and final storage data on CD. Local data bank is created as result of continuous observations.

## INTRODUCTION

Geophysical studies of solar-terrestrial relationships have shown the need for essentially new approach to appreciate of aeroelectrical processes in the Earth's environment. The global electrical circuit has the properties determinable by physical parameters of the magnetosphere, ionosphere, atmosphere and litosphere. Long-term ground-based aeroelectrical measurements simultaneously with geoelectromagnetic observations are necessary for database creation and experimental investigations of atmospheric electrical response to solar flares and related events.

The mid-latitude Geophysical Observatory "Borok" (58.03°N, 38.97°E) is one of a kind experimental complex for the study of the Earth's electromagnetic environment [*Anisimov et al.*, 1992]. Geomagnetic measurements have been continuously conducted at the Observatory for the last three decades. Aeroelectrical observations started in 1985. Long-term observations at Borok enable to analyze the ecologically essential variations of geophysical fields. Actually, Borok represents a good example of a "geophysical preservation zone" with a low level of man-made electromagnetic disturbances, natural background of seismic noise, absence of industrial pollution and stable water regime. Since 1957 the Observatory "Borok" has been the main center in the former USSR for collecting, storage and propagation of geomagnetic data. Aeroelectrical information is kept in the form of photo/paper records, and analog magnetic tapes. The digital acquisition system was developed in 1996. So the Observatory with its huge data archive is unique for exploration of solar-terrestrial relationship and investigating the effect of human activity on aeroelectrical environment.

## EXPERIMENTAL FACILITY

The observatory is equipped with an experimental unit for the field digital recording of a wide class of electromagnetic signals. The experimental complex comprises a set of sensors, amplifiers, analog filters, time and acquisition systems (Figure 2). It gives the possibility to record variations in a wide frequency range of the following geophysical fields:

- atmospheric electric field with the help of electrostatic fluxmeter;
- vertical atmospheric electric current by the current collector;
- atmospheric pressure by the microbarograph;
- 3-component of magnetic field in network of Samnet magnetometers;
- 3-component of ULF magnetic field by induction magnetometers;
- 3-component of telluric currents;
- riometric observations of cosmic noise absorption at frequency 32 MHz;
- multi-frequency Doppler sounding.

Figure 1. Electrostatic fluxmeter ("field mill")

***The electrostatic fluxmeter*** (Figure 1). For precise measurements of the atmospheric electric field, an electrostatic generator is used as a sensor [*Anisimov and Krylov*, 1980]. A quasi-static electric field is transformed into AC signals by means of periodic screening/unscreening of the sensor-based electrodes during rotation of the grounded plate. The electrostatic fluxmeter is designed according to the principle of a constant area of the sensor-based electrode. The construction enables

increasing of sensitivity by a differential method of the measurement. For calibration of the device, a calibrating plate is used, which is mounted at a fixed distance from the sensor-based electrodes. Main technical parameters are

- dynamic range for DC electric field ~80db;
- electric field noise $0.1 V/Hz^{1/2}$;
- power supply ~220V, 50W.

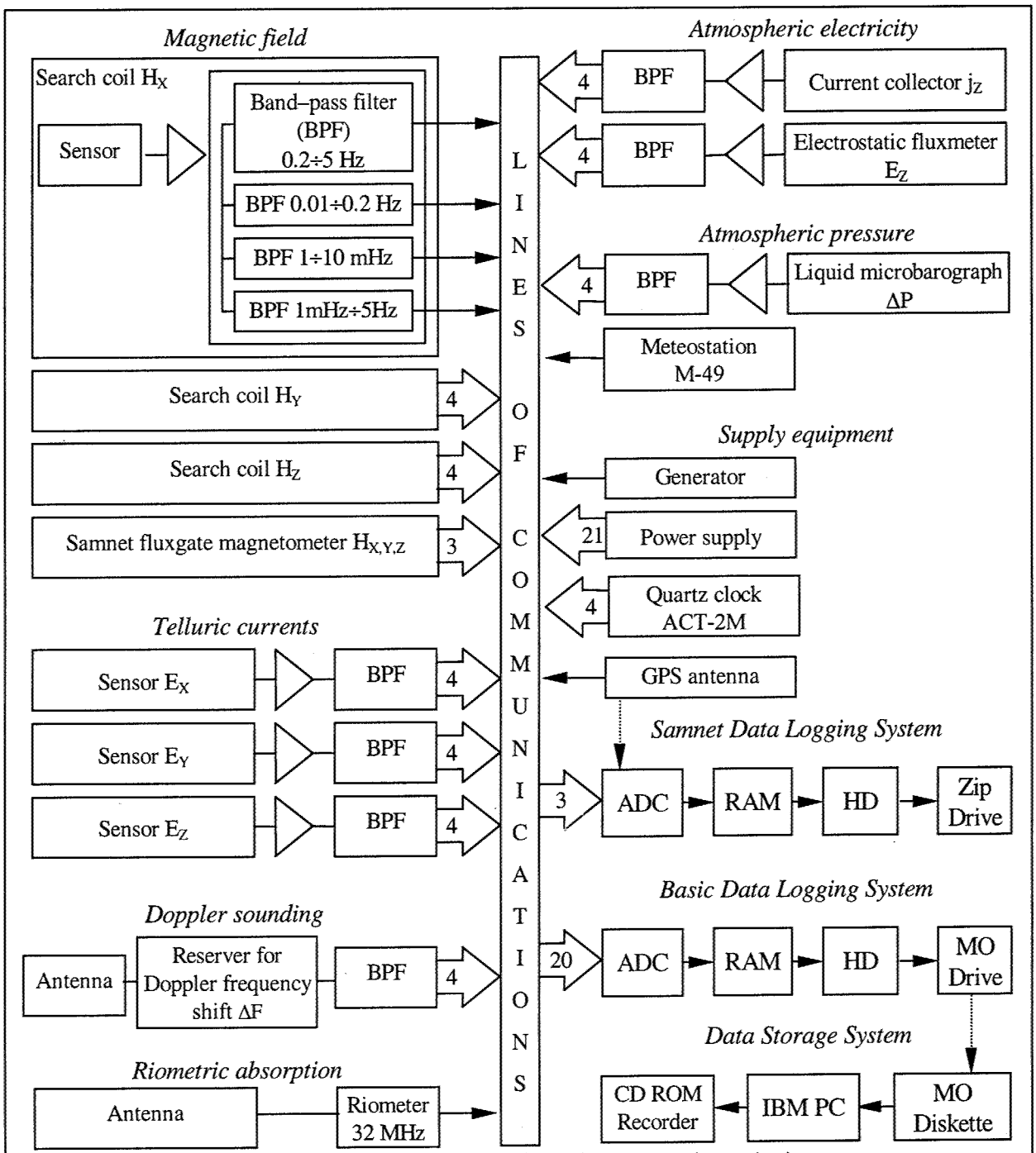

Figure 2. Experimental complex of Geoelectromagnetic monitoring.

***The current collector***. The vertical current in the atmosphere surface layer is measured using the method of voltage difference at a given stable resistor, connecting the sensor with the ground. The device comprises a current-collecting sensor, amplifier and a block of band-pass filters. Technical data are

- sensitivity ~$10^{-13}$A/m;
- dynamic range ~$10^{-13}$÷$10^{-9}$A/m.

Some common analysis of aeroelectric current measurements was given at *Tammet et al.*, 1996.

***The liquid microbarograph*** is suitable for the long-term recording of infrasound pressure variations with high sensitivity [*Bovsherov et al.*, 1979]. The microbarograph consists of 2 chambers with a measuring condenser. The pressure difference in chambers results in the difference of liquid levels and, consequently, in the imbalance between capacities of measuring condensers. While recording the infrasound pulsations, one chamber is connected with the atmosphere and the other is connected to a cylinder with a constant volume of air.

- Output sensitivity ~150mV/Pa.

***The fluxgate magnetometer.*** The instrument measures 3 components of the Earth's magnetic field with sampling interval of 1s and resolution 0.1nT. Fluxgate magnetometer is a part of Samnet network, operating in the UK, Faroe Islands, Iceland, Norway, Sweden, Finland and Russia. It is one of the 6 UK National scientific facilities for investigation of solar-terrestrial relations, which will also be included into a research of the correlation between the atmospheric electric field and substorm activity in progress.

***The induction magnetometer*** has been developed for recording the ULF magnetic field [*Anisimov et al.*, 1982]. The linear frequency response of magnetic sensors allows to compensate the spectral inhomogeneity and large dynamic range of magnetic pulsation intensity. The transformation coefficient of the induction sensor with preamplifier is about 1V/(nT·Hz). Some technical data of magnetometer are

- frequency range $10^{-3}$÷3Hz;
- magnetic field noise 0.5 pT/Hz$^{1/2}$;
- power supply ±12V, 0.25W.

***The telluric currents***. Geoelectromagnetic set has been supplemented with 3 component telluric current measurements, using 300m baseline between lead electrodes and 400m borehole. Threshold sensitivity of geovoltmeter is ~0.01μV/m, band width is 0.001÷5Hz. The method of differential measuring is used for telluric current observation.

## DATA LOGGING SYSTEM

The data logging system includes precision quartz clocks, a computer, equipped with analog to digital converter (ADC) and magneto-optical disk drive (MOD), and computer of storage system, equipped with MOD drive and CD ROM recorder. The scheme of the data logging system is presented in Figure 3.

***The quartz clocks*** generate a series of synchronizing impulses that are used in ADC. The 10 Hz impulses determine the sampling rate of ADC. Other impulses with the periods 1 s, 1 min and 1 h are used as time-markers. The main characteristic of clocks is

- current accuracy ~0.001 s/day.

***The analog to digital converter*** PCL-818L type is used to transform the observed analog signal into digital form in real time. 4 digital channels are occupied by time impulses. 16 analog channels are used for data reading. Characteristics of analog channels are

- 12 bit resolution;
- channel full range — ±5V;
- absolute accuracy — 0.01%;
- sampling rate — 10Hz.

***The magneto-optical disk drives is*** employed as intermediary storage of digital data and to copy the data on a hard disk of the storing computer later on. The main characteristics of MOD

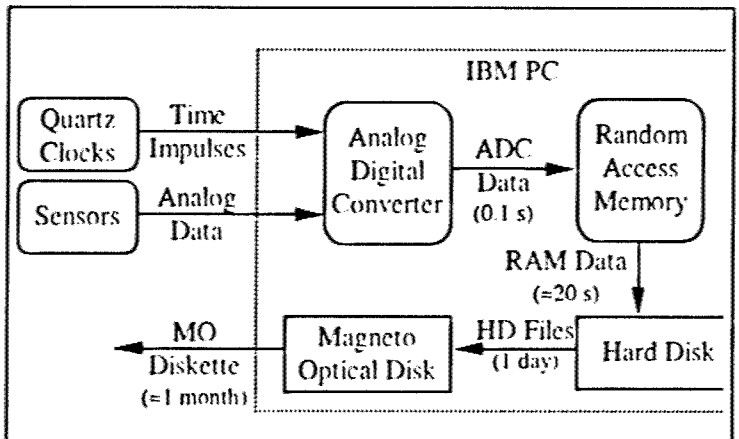


Figure 3. Scheme of processes employed to convert analog data

are

- diskette size — 640MB;
- speed of data transmission ~ 4MB/s;
- access time ~ 20ms.

***The CD ROM recorder*** is used for preparation of CD–copy of the data at final digital format. The main parameters of the CD ROM recorder are

- CD–R disk size — 640MB;
- speed for writing — 300kB/s.

CONCLUSIONS

The goal of aeroelectrical measurement as a part of geoelectromagnetic monitoring device is to create an extensive database for experimental investigations of the global electric circuit. The Geophysical Observatory "Borok" is equipped with the unique experimental complex for aeroelectrical, geomegnetic and radiophysics measurements with high resolution and sampling rate 10Hz. The experimental complex was tested and used in the series of international research programs as International Geophysical Year, STEP, STEP GBRSC, 210°-meridian, GAEM, SAMNET and others. Figure 4 shows the fragment of amplitude–time registration of geophysical fields at "Borok" Geophysical observatory.

ACKNOWLEDGEMENT: The authors would like to thank Dr.D.Milling from University of York for his help in progress of magnetic field measurements at Observatory. The development of Geoelectromagnetic monitoring set was supported partially by the Russian Foundation for Basic Research (RFBR).

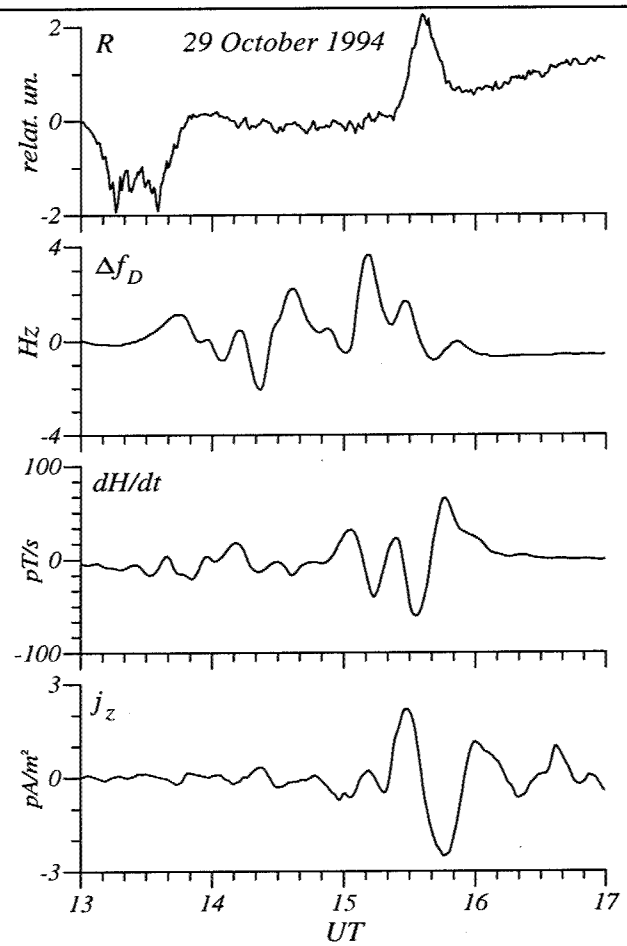


Figure 4 The plot of ground–based mid–latitude records of vertical aeroelectric current density variations – $\Delta j_z$, long period geomagnetic pulsations – dH/dt, Doppler frequency shift $\Delta f_D$ for $f_D$=4.625MHz, riometric absorption of cosmic noise R for $f_R$=32MHz, corresponding to the event of 29 October 1994.

REFERENCES

Anisimov, S., V.Pilipenko and O.Pokhotelov, STEP Reference Observatory: Borok, *STEP GBRSC news*, **4**, 3, 1-3, 1992.

Anisimov, S.V., Yu.E.Borovkov, V.I.Goncharov, V.F. Ruban, and N.N.Rusakov, High-sensitive search-coil magnetometer with M-DM amplifier, *Geomagnetic research* (in Russian), **30**, 43-45, 1982.

Anisimov, S.V., and S.M.Krylov, Sensor of Earth's electric field variations, in *Electromagnetic field structure of ULF pulsations* (in Russian), 158-163, 1980.

Bovsherov, B.M., A.I.Grachov, S.O.Lomadze, and A.K.Matveev, Liquid microbarograph, *Atmospheric and Oceanic Physics* (in Russian), **15**, 11, 1215-1218, 1979.

Tammet, H., S.Israelsson, E.Knudsen, and T.J.Tuomi, Effective area of horizontal long-wire antenna collecting the atmospheric electric vertical current, *J. Geophys. Res.*, **101**, 29,671-29,677, 1996.

# SIMULATION OF THE UNIVERSAL-TIME DIURNAL VARIATION OF THE GLOBAL ELECTRIC CIRCUIT CHARGING RATE

D. Mackerras[1], M. Darveniza[1], R. E. Orville[2], E. R. Williams[3], and S. J. Goodman[4]

[1] Department of Computer Science and Electrical Engineering, University of Queensland, Australia.
[2] Department of Meteorology, Texas A & M University, College Station.
[3] Parsons Laboratory, Massachusetts Institute of Technology, Cambridge.
[4] Earth System Science Division, NASA, Huntsville, Alabama.

ABSTRACT: A global lightning model that includes diurnal and annual lightning variation, and total flash density versus latitude for each major land and ocean, [*Mackerras et al.*, 1998] has been used as the basis for simulating the global electric circuit charging rate. A particular objective has been to reconcile the difference in amplitude ratios [AR=(max-min)/mean] between global lightning diurnal variation (AR ≈ 0.8) and the diurnal variation of typical atmospheric potential gradient curves (AR ≈ 0.35). A constraint on the simulation is that the annual mean charging current should be about 1000 A [*Makino and Ogawa*, 1985; *Kasemir*, 1994]. The global lightning model shows that negative ground flashes can contribute, at most, about 10-15% of the required current. For the purpose of the charging rate simulation, it was assumed that each ground flash contributes 5 C to the charging process. It was necessary to assume that all electrified clouds contribute to charging by means other than lightning, that the total flash rate can serve as an indirect indicator of the rate of charge transfer, and that oceanic electrified clouds contribute to charging even though they are relatively inefficient in producing lightning. It was also found necessary to add a diurnally invariant charging current component. By trial and error it was found that charging rate diurnal variation curves in Universal time (UT) could be produced with amplitude ratios and general shapes similar to those of the potential gradient diurnal variation curves measured over ocean and arctic regions during voyages of the Carnegie Institute research vessels.

## INTRODUCTION

A review of the global electric circuit has been given by *Adlerman and Williams* [1996]. The mean atmospheric potential gradient diurnal variation curves obtained over oceans and the arctic are believed to represent the diurnal variation of ionospheric potential substantially free from the obscuring effects of atmospheric pollution over land. One of the curves used as a basis for comparison was the mean annual curve (the "Carnegie curve") obtained from Figure 9 of *Whipple and Scrase* [1936], shown here as curve 2 in Figure 1d. Potential gradient curves for the northern winter (November, December, January, and February), the equinox (March, April, September, and October), and the northern summer (May, June, July, and August) were obtained from *Israël*, [1973, Figure 149]. As the fair-weather part of the global circuit can be represented as a linear resistance, the diurnal variation in UT of the potential gradient over oceans and the arctic can be assumed to represent without distortion the variation of the charging rate. It was also assumed that the time lag between any charging source contribution and the response of the ionospheric potential is much less than 1 hr.

We have attempted to simulate the global electric circuit charging rate on the basis of the global lightning model given by *Mackerras et al.* [1998] and a set of assumptions stated below. A test of the correctness of the simulation is to compare the diurnal variation in UT of the simulated charging rate curves with those of the potential gradient curves for each of the four periods noted above.

As noted by *Williams and Heckman* [1993], electrified clouds contribute to charge transfer by processes other than lightning, especially point discharge current and conduction current over land. Other processes are probably important over oceans. The simulation therefore includes a charge transfer component associated with electrified clouds by processes other than lightning.

A useful measure for a diurnal variation curve is its amplitude ratio (AR) = (maximum - minimum)/mean. A particular problem is to reconcile AR ≈ 0.35 for the Carnegie curve with AR ≈ 0.8 for the global lightning diurnal variation. The minimum for both curves occurs at about 0 to 4 hr UT when the local time in the Pacific Ocean is mid-afternoon. Then the global lightning rate is about 0.5 of the mean and the potential gradient is about 0.85 of the mean. It is possible that this difference is partly explained by the Pacific Ocean making a major contribution to global charging but only a relatively small contribution to global lightning.

## ASSUMPTIONS MADE IN SIMULATING THE CHARGING RATE

Negative ground flashes were assumed to lower an average 10 C of negative charge to ground and to be 50% efficient in causing the pumping of charge towards the ionosphere [*Anderson and Freier*, 1969], so contributing 5 C per ground flash to the charging rate. Positive ground flashes were neglected. All electrified clouds were assumed to contribute to charge transfer, driving positive charge towards the ionosphere, by point discharge, conduction current and similar processes. The total flash rate was used as a measure of the presence of electrified clouds. Over land a charge transfer $q_{nl}$ per total flash (all cloud and ground flashes) was assumed. Over oceans, electrified clouds were assumed to be present in similar numbers to those over adjacent land at the same latitude, and to contribute similar amounts of charge transfer. However, electrified clouds over oceans have much lower efficiency in producing lightning than those over land, with the exception of the North Atlantic Ocean. Hence a correction factor, $\beta$, was needed to obtain the charging contribution of oceanic electrified clouds. These factors were obtained by comparing the total flash density (TFD) over the ocean with that over adjacent land at the same latitude on each side of the ocean, given by *Mackerras et al.* [1998]. For example, for the South Atlantic Ocean, the TFD over the adjacent lands is about 6.7 times that over the ocean at the same latitude, so the contribution to charge transfer is 6.7 $q_{nl}$ C per total flash. For the other oceans, the correction factors were: North Atlantic Ocean: 1, Indian Ocean: 5.4, North Pacific Ocean: 9, and South Pacific Ocean: 8.4.

Other charging sources were assumed to be represented by a constant current source, implement by a fixed current density, $j_g$, from each element of area on Earth. The individual sources may not be diurnally-invariant; it is only necessary to assume that the global summation of all these sources is diurnally-invariant.

## METHOD

The global lightning model [*Mackerras et al.*, 1998] was based on two 12-month records of global lightning from DMSP satellites [*Orville and Henderson,* 1986], one 24-month record of global lightning by the ISS-b satellite [*Kotaki et al.,* 1981] and five years of records of CGR3 lightning counter registrations at stations between 60°N and 27°S [*Mackerras and Darveniza*, 1994]. The model provided estimates of the hourly flash densities $N_{gh}$ and $N_{th}$ for ground and total flashes, respectively, in each 5°×5° (in latitude and longitude) element of area, $a(\lambda)$, of the surface of Earth between 65°S and 65°N, where $\lambda$ is the mean latitude of the element. The model was modified to include calculation of the hourly charge transfer contribution, $Q_h$, from each element, using equation (1), for each hour (UT) of the day on a typical day in each month, and in each month of the year. Summations of charge transfer were made for each hour (UT) for the whole year and for three four-month periods corresponding to the northern winter, the equinox, and the northern summer. From these summations, the diurnal variation curves in UT and their amplitude ratios were obtained and compared with the potential gradient curves. The quantities $q_{nl}$ and $j_g$ were varied on a trial and error basis to determine whether the amplitude ratios and general form of the charging rate curves could be made to match those of the potential gradient curves, as well as resulting in the required mean annual current of about 1000 A. For land, $\beta = 1$ in equation (1). The factor 3600 converts the last term to the charge contribution per hour.

$$Q_h = 5\, N_{gh}\, a(\lambda) + \beta\, q_{nl}\, N_{th}\, a(\lambda) + 3600\, j_g\, a(\lambda) \qquad (1)$$

## RESULTS

It was found that, with $j_g = 0$, amplitude ratios for the charge transfer curves were about 0.47 (range 0.46 to 0.5), leading to the conclusion that a match of amplitude ratios would require a non-zero $j_g$. In subsequent trial and error simulations, it was found that a reasonable match could be obtained with $j_g = 0.65$ pA m$^{-2}$, active between 65°S and 65°N, corresponding to a global current of about 300 A, and with $q_{nl} = 3.7$ C per total flash. The mean current from ground flashes was 73 A, the mean current from non-lightning processes associated with electrified clouds was 624 A, and the mean total global current was 997 A. The amplitude ratios are given in Table 1 and the comparisons between the charging rate curves and the potential gradient curves for the three 4-month groups and the whole year are given in Figure 1. The root mean square (rms) differences between the simulated charging rate curves and the potential gradient curves range from 0.07 to 0.12, and are given in Table 1.

## DISCUSSION AND CONCLUSIONS

All curves have a minimum between 0 and 5 hr UT, corresponding to mid-afternoon local time for the Pacific Ocean. All curves have a tendency to three local maxima, the first 6-10 hr UT corresponding to mid-afternoon for Indonesia/Asia, the second 12-16 hr UT corresponding to mid-afternoon for Africa/Europe, and the third 17-22 hr UT corresponding to mid-afternoon for the Americas. This third local maximum tends to be weaker in the charging rate curves than the potential gradient curves, suggesting that the global lightning model total flash rate for the Americas, especially North America may be too low.

*Monahan* [1983] stated that the bursting of whitecap bubbles over oceans releases positive charge into the air at a rate that is a function of wind speed. The range of global whitecap current estimates in Table 1 of *Monahan* [1983] is 293 A to 750 A depending on the assumptions made. These currents are in the correct order to account for the required constant current component of charging current, even allowing for some inefficiency in the charge transfer process. Over land, a possible contributor to the constant current component is the Austausch (eddy diffusion) generator [*Kasemir*, 1956, 1994]. Charges carried by rain are also possible contributors to the charge transfer process.

It is clear that there is an arbitrary element in the choice of assumptions on which this simulation was based. Other mixes of assumptions could also result in simulated charging current diurnal variation curves that resemble the potential gradient curves. The simulation does not, but probably should, include charge transfer by electrified clouds with no lightning. However, the simulation does strongly suggest that oceanic electrified clouds must contribute to global charging at a rate much greater than would be expected from their lightning activity alone. The simulation also shows that an AR of about 0.35 cannot be achieved without a global charging current component (here estimated to be about 300 A) that is not related to lightning or electrified clouds, and whose global summation is diurnally invariant, or approximately so.

ACKNOWLEDGMENTS: We acknowledge with gratitude the contributions of all persons and organizations participating in the world-wide survey using CGR3 instruments. We thank R. W. Henderson for the supply of the first DMSP data set and for his assistance, and staff at the NASA Marshall Space Flight Center for supplying the second DMSP lightning data set. The project has been financially supported by the Australian Electrical Research Board, the Australian Research Grants Scheme, and University of Queensland grants.

## REFERENCES

Adlerman, E. J., and E. R. Williams, Seasonal variation of the global electrical circuit, *J. Geophys. Res.*, *101*, 29,679-29,688, 1996.

Anderson, F. J., and G. D. Freier, Interactions of the thunderstorm with a conducting atmosphere, *J. Geophys. Res.*, *74*, 5390-5396, 1969.

Israël, H., *Atmospheric Electricity*, vol. II, *Fields, Charges, Currents*, Nat. Sci. Found., Washington, D. C., 1973. (Translated from German by D. B. Yaakov and B. Benny, Israel Program for Sci. Transl., Jerusalem.)

Kasemir, H. W., Der Austauschgenerator, *Arch. Meteorol. Geophys. Bioklimatol.*, *9*(3), 357-370, 1956.

Kasemir, H. W., Current budget of the atmospheric electric global circuit, *J. Geophys. Res.*, *99*, 10,701-10,708, 1994.

Kotaki, M., I. Kuriki, C. Katoh, and H. Sugiuchi, Global distribution of thunderstorm activity observed with ISS-b, *J. Radio Res. Lab. Jpn.*, *28*, 49-71, 1981.

Mackerras, D., and M. Darveniza, Latitudinal variation of lightning occurrence characteristics, *J. Geophys. Res.*, *99*, 10,813-10,821, 1994.

Mackerras, D., M. Darveniza, R. E. Orville, E. R. Williams, and S. J. Goodman, Global lightning: Total, cloud and ground flash estimates, *J. Geophys. Res.*, *103*, 19,791-19,809, 1998.

Makino, M., and T. Ogawa, Quantitative estimation of global circuit, *J. Geophys. Res.*, *90*, 5961-5966, 1985.

Monahan, E. C., Positive charge flux from the world ocean resulting from the bursting of whitecap bubbles, in *Proceedings in Atmospheric Electricity*, Edited by L. H. Ruhnke and J. Latham, pp. 85-87, Deepak, 1983.

Orville, R. E., and R. W. Henderson, Global distribution of midnight lightning: September 1977 to August 1978, *Mon. Weather Rev.*, *114*, 2640-2653, 1986.

Whipple, F. J. W., and F. J. Scrase, Point discharge in the electric field of the earth, *Geophys. Mem.*, *7*, (68), 1-20, 1936.

Williams, E. R., and S. J. Heckman, The local diurnal variation of cloud electrification and the global diurnal variation of negative charge on Earth, *J. Geophys. Res.*, *98*, 5221-5234, 1993.

TABLE 1. Comparison of simulated charging rates (curves 1) and potential gradients (curves 2).

| Period (Figure) | Curve | Maximum | | Minimum | | Ampli-tude Ratio | Rms diff-erence |
|---|---|---|---|---|---|---|---|
| | | Value | hr UT | Value | hr UT | | |
| N. Winter | 1 | 1.14 | 18 | 0.80 | 1 | 0.34 | 0.07 |
| (Fig. 1(a)) | 2 | 1.21 | 18, 19 | 0.855 | 3, 4 | 0.355 | |
| Equinox | 1 | 1.15 | 14 | 0.79 | 1 | 0.36 | 0.07 |
| (Fig. 1(b)) | 2 | 1.18 | 19 | 0.87 | 2, 3 | 0.31 | |
| N. Summer | 1 | 1.14 | 14 | 0.81 | 1 | 0.34 | 0.12 |
| (Fig. 1(c)) | 2 | 1.18 | 21 | 0.86 | 3,4 | 0.32 | |
| Year | 1 | 1.13 | 14 | 0.80 | 1 | 0.34 | 0.07 |
| (Fig. 1(d)) | 2 | 1.195 | 19 | 0.85 | 3 | 0.345 | |

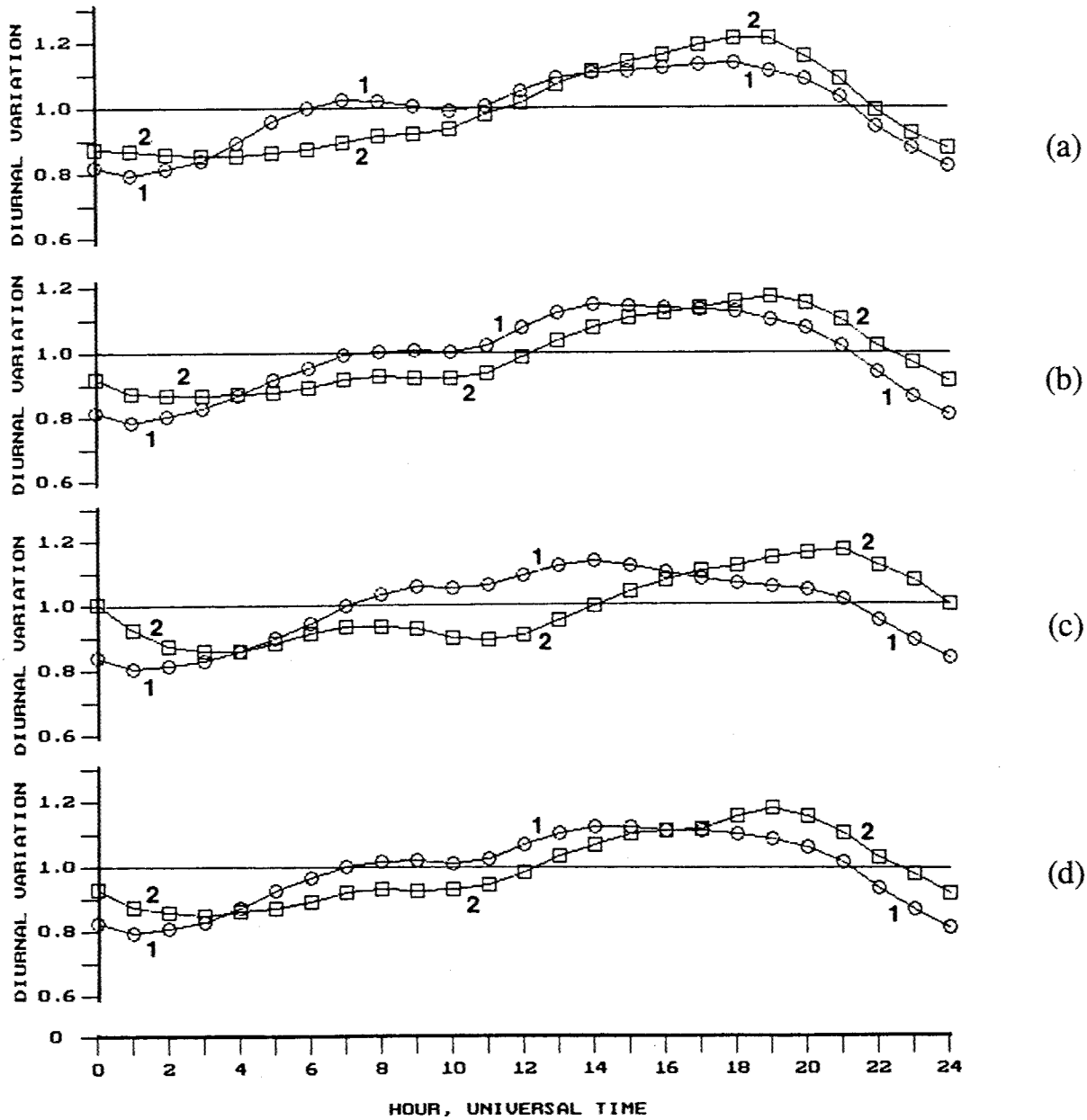


Figure 1. Diurnal variation in universal time (UT) of the simulated charging rates (curves 1) and the potential gradients (curves 2), for the periods (a) Northern Winter, (b) Equinox, (c) Northern Summer, and (d) Year.

# A STUDY OF THE ATMOSPHERIC ELECTRICAL PARAMETERS AND THE METEOROLOGICAL CONDITIONS DURING SOME INTENSE AIR POLLUTION EPISODES IN ATHENS

D. A. Retalis[1] and A. D. Retalis[2]

[1]National Observatory of Athens, Institute of Meteorology and Physics of the Atmospheric Environment, P.O. Box 20048, GR-118 10 Athens, Greece
[2]Integrated Information Systems S.A., Department of GeoInformation and Environmental Studies, 72-74 Salaminos Str., Kallithea, GR-175 76 Athens, Greece

ABSTRACT: In this study the variations of the air electrical parameters (large and small ions and conductivity) and the meteorological conditions during some intense air pollution episodes (smoke and $SO_2$) in Athens, for the period 1971-1985, were examined. It was found out that, during intense air pollution episodes, the large ions concentration were increased from its normal value, while small ions concentration and air conductivity were decreased. Synoptic weather conditions prevailing during the occurrence of episodes were investigated in details for the period 1984-1985. It was noticed that the onset of these episodes was found to have been associated with a warm air advection from the south-west or with the withdrawal of a cold air mass that had been previously established over Greece.

## INTRODUCTION

In Athens-Greece measurements of both positive and negative conductivity of the air, small and large ions concentration have been made regularly since 1968 at the National Observatory of Athens (NOA). NOA (ö=37°58' N, ë=23°43'E, h=107 m above msl) is located on the rather flat top of Nymphs Hill in the centre of Athens, facing the Acropolis, about 30 m higher than surrounding city. In Greece, the particulate air pollution (smoke) and the indirect influence of gaseous air pollution (sulfur dioxide) and wind speed on air electrical parameters has been examined by Retalis D.[1977], Retalis et al. [1991] and Retalis D. and A. Retalis [1998]. In this study the variations of the above mentioned electrical parameters and the meteorological conditions during some intense air pollution episodes (smoke and $SO_2$) in Athens, for the period 1971-1985, were examined.

## AIR ELECTRICAL PARAMETERS VARIATIONS DURING EPISODE DAYS

Data of smoke and $SO_2$ concentrations from the NOA station were used. The data were taken from climatological bulletin published by NOA. The selection of the intense air pollution episodes was based on the occurrence of concentrations higher than 200 ì gr/m$^3$, during the cold period and for the time period 1971-1980. Sixteen (16) episodes were selected. Smoke and $SO_2$ concentrations during the episode days at NOA station (1) and the University Club station (2), which is located in the center of Athens (h=88m above msl), are presented in Table 1.

Table 1. Smoke and $SO_2$ concentrations during the episode days at NOA and the University Club station.

| Episode Days | 6/11/1971 (1) | 17/12/1971 (2) | 18/12/1971 (3) | 19/12/1971 (4) | 10/11/1972 (5) | 29/11/1972 (6) | 15/1/1973 (7) | 8/12/1973 (8) | 18/12/1973 (9) | 19/12/1973 (10) | 12/12/1974 (11) | 11/1/1975 (12) | 13/1/1975 (13) | 18/1/1975 (14) | 24/1/1975 (15) | 30/12/1975 (16) |
|---|---|---|---|---|---|---|---|---|---|---|---|---|---|---|---|---|
| Smoke (1) ìgr/m$^3$ | 208 | 203 | 257 | 205 | 226 | 253 | 316 | 218 | 209 | 205 | 205 | 239 | 217 | 220 | 227 | 206 |
| $SO_2$ (1) ìgr/m$^3$ | 375 | 281 | 617 | 467 | 354 | 602 | 542 | 445 | 355 | 403 | 550 | 797 | 680 | 645 | 631 | 665 |
| Smoke (2) ìgr/m$^3$ | 431 | 238 | 544 | 576 | 438 | 658 | 514 | 433 | 390 | 369 | 234 | 542 | 542 | 362 | 295 | 649 |
| $SO_2$ (2) ìgr/m$^3$ | 404 | 407 | 711 | 692 | 341 | 774 | 626 | 449 | 383 | 539 | 345 | 936 | 863 | 749 | 538 | 573 |

The concentrations of large and small ions (positive and negative) and the air electrical conductivity (positive and negative) were taken from the atmospheric electricity bulletin published by NOA. Large ions concentration has been recorded for the period 1969-1977, small ions concentration has been recorded for the period 1968-1972 and air electrical conductivity measurements have been taken for the period 1968-1980. The mean monthly values, named as normal values, for the corresponding periods were estimated. The variations of these parameters during the sixteen episodes were examined, and their deviations from their normal values were estimated, respectively.

It was found out that the positive large ions concentration was increased at a rate of 16-45% above its normal value, while the negative one by 12-55%. Positive small ions concentration was reduced by 14-51% below its normal value and 12-55% for negative, respectively. Positive polar conductivity was reduced by 17-58% below its normal value, while negative one by 8-54%. The results are better interpreted in Figures 1-3.

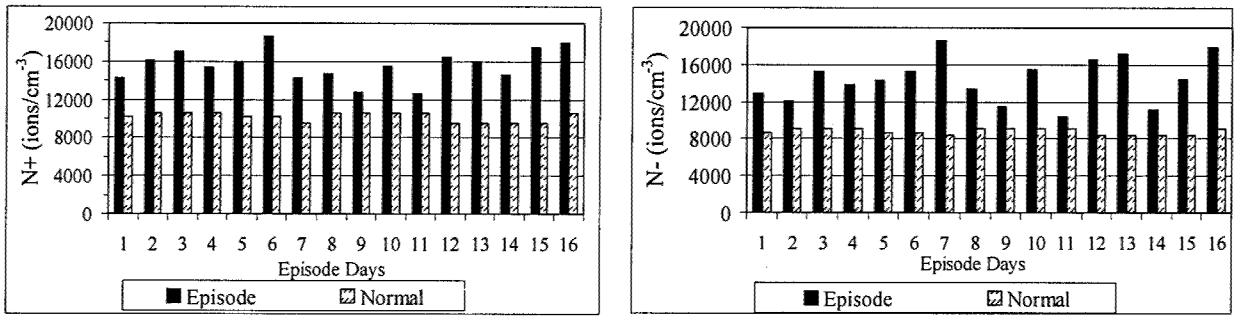


Figure 1. Histograms of large (positive and negative) ions concentration variations during the episode days and their normal values.

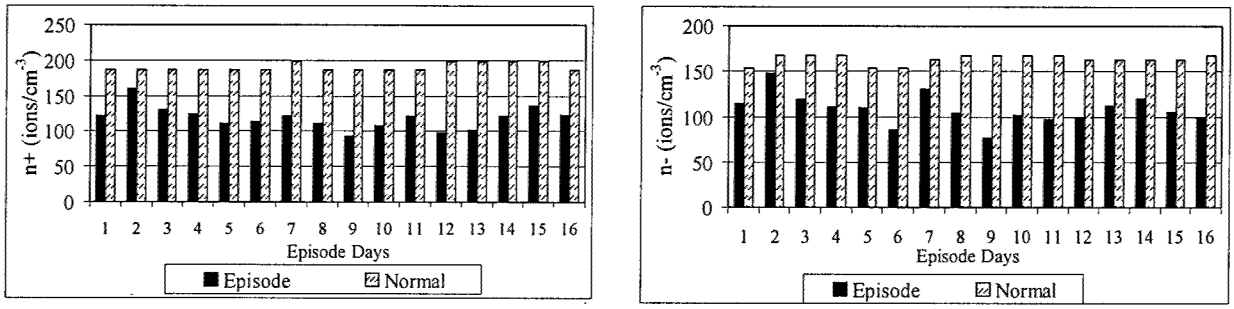


Figure 2. Histograms of small (positive and negative) ions concentration variations during the episode days and their normal values.

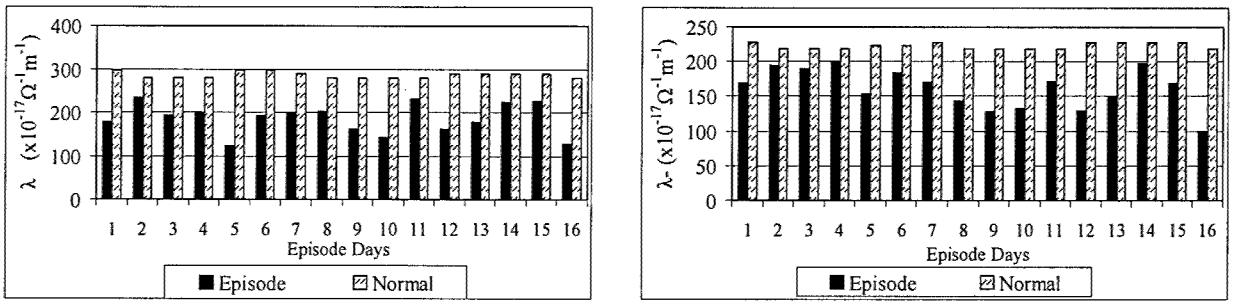


Figure 3. Histograms of polar (positive and negative) conductivity concentration variations during the episode days and their normal values.

## METEOROLOGICAL CONDITIONS DURING SELECTED EPISODES

The meteorological conditions during the sixteen episodes in Athens were also examined. It is well known that the wind speed is the main factor that controls the dispersion of pollutants in an urban area. Therefore, it was the first parameter to be examined. Hourly measurements of wind velocity and direction were available at NOA. It was found that, during the episode days, the meteorological conditions were characterized by fair weather conditions, with calm (11 days) or very low wind velocities (<0.5 m/s) from south-southwest directions. The analysis of the radiosoundings for the episode days, which depicted strong inversions, indicates supportive meteorological conditions for the development of atmospheric pollution episodes.

Synoptic weather conditions prevailing during the occurrence of episodes have been investigated in details by Pissimanis et al. [1991]. Emphasis was given to the importance of spells of weather in providing conditions that give rise to inversion of temperature at or near ground level, and hence to risks of severe incidents of air pollution. Much attention was given to the anticyclonic conditions, associated with pronounced stability during ground level radiation inversions, when the same sampling sites show high concentration of both smoke and $SO_2$.

For this reason, two other intense air pollution episodes lasting a total of 7 days in the cold months were selected for the period 1984-1985. Episodes were considered in which the smoke concentration was at least 250 ì gr/m$^3$ at two stations (Patission and Ministry) in the center of Athens for three or more days. The first one (E1) occurred on October 5-9, 1984 and the second one (E2) was occurred on January 19-21, 1985 (Table 2). During these episodes, the positive conductivity of the air was reduced from its mean value at a rate of about 23-29% for episode E1 and 3-19% for episode E2, while the negative conductivity was decreased from its mean value by 19-25% for E1 and 15-30% for E2, respectively.

Table 2: Smoke concentrations and conductivity concentrations during two selected episodes

| Dates | Smoke concentration (ìgr/m$^3$) | | ë, (×10$^{-17}$ Ù$^{-1}$m$^{-1}$) | ë- (×10$^{-17}$ Ù$^{-1}$m$^{-1}$) |
|---|---|---|---|---|
| | Patission Station | Ministry Station | | |
| 5/10/1984 | 380 | 360 | 261,5 | 199,0 |
| 6/10/1984 | 362 | 261 | 258,3 | 202,1 |
| 7/10/1984 | 344 | 360 | 241,7 | 197,9 |
| 8/10/1984 | 422 | 324 | 243,8 | 212,5 |
| 19/1/1985 | 395 | 400 | 232,3 | 158,3 |
| 20/1/1985 | 347 | 323 | 262,5 | 190,6 |
| 21/1/1985 | 385 | 311 | 280,2 | 193,8 |

The onset of these episodes was found to have been associated with a warm air advection from the south-west or with the withdrawal of a cold air mass that had been previously established over Greece. It was found that in the first episode (E1), on the first episode day an advection of an extended warm air mass originating from Sahara desert was taking place on an anticyclonic trajectory over the central or southern Mediterranean towards Greece. This warm air advection area had already extended over almost the whole country. Therefore, a considerable temperature rise had started to occur at 850 mb level over Athens, between 0200 LST of the first (20° C) and the second episode day (22° C) and between the day before the onset of the episode (18° C) and the first episode day.

The onset of the episode (E2) occurred at the last stage of the withdrawal of a well-pronounced cold air mass, generally towards the east and its subsequent substitution by a warmer anticyclonic air mass from the central Mediterranean. The passage of the cold air mass during the days preceding the first episode day can be verified from the temperature variation at 850 mb, (one day before the episode it was 0° C, the first day was 1° C and second day was 4° C) and the deviations of the daily maximum

temperatures from the corresponding mean maximum monthly temperature (two days before the episode –6.5° C, one day before –4.5° C and first day -1° C).

## DISCUSSION

The air electrical conductivity variations is almost exclusively due to the changes of small ion concentration. According to the relation:

$$\Lambda = \lambda_+ + \lambda_- = e\sum_i n_+ k_+ + e\sum_i n_- k_- \quad (1)$$

where $ë_+$ and $ë_-$ are the positive and negative conductivity, respectively, $n_+$, $n_-$ are the positive and negative small ions concentration, $k_+$, $k_-$ are correspondingly their mobility and e is the element electrical charge ($e=1.602 \times 10^{-19}$ Cb).

In urban polluted areas small ions concentration is given by [Israel, 1971]:

$$n_1 = \frac{q}{\eta_{12} N_2 + \eta_{10} N_0} \quad (2)$$

and

$$n_2 = \frac{q}{\eta_{21} N_1 + \eta_{20} N_0} \quad (3)$$

where $n_1$, $n_2$ are positive and negative small ion concentration, correspondingly, $q$ is the number of small ion production, $Í_0$ is the uncharged nuclei concentration, $Í_1$, $Í_2$ are positive and negative large ion concentration, correspondingly and $ç_{10}$, $ç_{12}$, $ç_{20}$, $ç_{21}$ are the attachment coefficients of small ions to the large ones and to the uncharged nuclei.

In these relations it is obvious that small ions concentration and hence air electrical conductivity is reversely proportional to the number of nuclei and hence to the degree of air pollution. This means that an increase of air pollution leads to a reduction of small ions and to the becoming, by attachment, large ions.

## CONCLUSIONS

The variations of the positive and negative large and small ions concentration and air electrical conductivity along with the meteorological conditions during some intense air pollution episodes (smoke and $SO_2$) in Athens, for the period 1971-1985, were examined. It was found out that during these episodes, the conductivity of the air and the small ions concentration were reduced from their normal values, while the large ions concentration were increased, respectively. Emphasis was given to the meteorological conditions that give rise to risks of severe incidents of air pollution and especially to the anticyclonic conditions. Synoptic weather conditions prevailing during the occurrence of episodes were investigated in details for two selected episodes during the period 1984-1985. The onset of these episodes was found to have been associated with a warm air advection from the south-west or with the withdrawal of a cold air mass that had been previously established over Greece.

## REFERENCES


Israel Ç., Atmospheric Electricity, Jerusalem: Israel Program For Scientific Translations, Vol. É, 1971.

Pissimanis D., Karras G. and Notaridou V., On the meteorological conditions during some strong smoke episodes in Athens, *Atmos. Environment.*, 25B, 193—202, 1991.

Retalis D., On the relationship between small ions concentration and (1) smoke, (2) sulfur dioxide and (3) wind speed, *Pure Appl. Geophys.*, 115, 575--581, 1977.

Retalis D., A. Pitta, and P. Psallidas, The conductivity of the air and other parameters in relation to meteorological elements and air pollution in Athens, Meteorol. Atmos. Phys., 46, 197--204, 1991.

Retalis D. and A. Retalis, Effects of air pollution and wind on the large-ion concentration in the air above Athens, *J. Geophys. Res.*, 103, 13,927—13,932, 1998.

# IONOSPHERIC POTENTIAL AS A MEASURE OF GLOBAL TEMPERATURE VARIATION

Ralph Markson[1] and Daniel Vogel[2]

[1]Airborne Research Associates, Weston, Massachusetts, U.S.A.
[2]Carnegie Mellon University, Pittsburgh, PA

**Abstract:** This report covers the final phase of an investigation of the relationship of ionospheric potential (Vi) to global temperature. Twenty reliable Vi balloon soundings were obtained at Orlando, Florida in March 1998. These were compared with hourly temperature measurements from South America and Africa, the major global thunderstorm regions. By using hourly time resolution METAR temperature data it is possible to do lag correlation analysis at hourly intervals. While data analysis is still being conducted (March 1999), some preliminary conclusions have emerged. A major complication in the analysis is that both temperature and Vi follow well established quasi-sinusoidal diurnal cycles that are out of phase. This can lead to apparent correlation between temperature and Vi depending on when the measurements are made and the lag. To minimize this effect, the Vi and temperature data were normalized. The tentative conclusion is that the inherent variation of Vi, caused by factors in addition to temperature, prevents this parameter from being used as a short term measure of continental scale temperature variation. However, equatorial temperatures before the time of the Vi measurements are positively correlated with Vi. It appears that Vi variation may be most useful for studying global change on seasonal and annual "climatological" time scales rather than short period "weather" time scales.

## A. Introduction

Williams [1992] has shown from Schumann resonance (SR) data that global thunderstorm activity is well correlated with monthly averages of tropical surface air temperature variations. He also reports high correlation between simultaneous SR and Vi measurements.

Since thunderstorm currents support a significant fraction of Vi, the measure of DC global circuit intensity, and thunderstorm activity is stimulated by surface temperature, we have been conducting an investigation of whether global temperature variation can be monitored through measurement of Vi. The Vi data are obtained through electric field balloon soundings. Initial results in Phase I of this program showed good correlation when low latitude hourly temperature values were used with maximum correlation for temperatures several hours before the Vi measurements [Markson and Lane-Smith, 1994]. Subsequently, using a different measuring system, simultaneous Vi data were obtained over two diurnal cycles with soundings in Weston, Massachusetts and Darwin, Australia to verify the hypothesis that a single measurement under favorable local meteorological conditions is globally representative [Markson et al., 1996]. Most of these intercontinental cross-hemisphere comparisons supported this basic global circuit hypothesis, however, there was evidence that sometimes local conditions at Weston affected the $V_i$ soundings and there were some problems with the instrumentation due to inclusion of a conductivity sensor. Markson and Price [1996] reported significant positive correlation between 69 Vi measurements made on 29 days over a 7 year period and daily average global temperature.

During March 1998, a series of 20 reliable Vi soundings were made from Orlando, Florida in clean air with an improved measuring system. From the shape of the profiles, and the fact that up (balloon) and down (parachute) soundings made with the same system about 50 miles apart closely tracked each other, these data appear to be reliable.

Temperature data were obtained for all stations from 45N to 45S latitude and the averages of all observations in 15° square latitude/longitude bins were stored. These measurements from Africa and South America, the major global thunderstorm generator regions in March (determined by IR satellite imagery) have been analyzed relative to Vi values.

## B. Methodology

The Vi data are obtained in the standard manner from electric field profiles [Clark, 1958; Markson, 1976]. An aircraft or balloon rises from the ground while measuring the vertical electric field in a fair-weather region with minimal clouds and preferably low humidity. The potential at the top of the sounding is determined by integrating the field. From the top of the sounding, or from the altitude where the signal becomes too small to be reliable (typically at about 1 V/m near 12 km with these measurements) the remainder of the potential is determined from the product of electric field intensity at

apogee times electrical scale height at that height [Markson, 1976].

An electric field measuring system was developed using a VIZ radiosonde. An electrometer with 3 T ohm input impedance was used. The instrument was housed in styrofoam for thermal insulation and testing showed that the system was insensitive to the expected temperature variation. Radioactive probes (200 uC) positioned 2.5 m above and below the sonde provided inputs to the differential circuit. Ten calibration voltages spanning the range 1-500 V were applied to the system both in the laboratory and before launch. This produced a calibration curve for each sonde that was used in data reduction. It was determined that the radioactive probes caused a 6% loading of the circuit and this was added to the measured plus extrapolated potential to determine Vi. The ambient electric field was measured at the time of launch and provided the ground level data point for the sounding. From the instrumentation standpoint it is estimated that the accuracy of the measurement is +/- 3%. However, another source of error can exist associated with the path of the sounding. If the balloon is launched from a region with different columnar resistance than the columnar resistance in an adjacent region it drifts into, error will be introduced into the integrated potential [Markson et al. , 1996].

Hourly METAR temperature data were obtained from the WSI Corporation. Satellite and ground measurements have only 3 or 6 hour time resolution limiting their usefulness in lag correlation studies. Hourly time resolution is needed for analysis because both temperature and Vi undergo significant (about 30% peak-to-peak) diurnal variations and their values are influenced by the time of the observations.

**C. Results and Discussion**

Because the major thunderstorm regions contributing to the global circuit are over Africa and South America, the experimental design called for obtaining data near the time of maximum thunderstorm activity in these regions. Eleven measurements were made during the African maximum thunderstorm period and nine were made during the complementary American time period. The maximum heating in both continents during March 1998 was at about 3:30 p.m. local time and the measurements were made over a period of about 2-3 hours centered at 16:30 UT for the African thunderstorms and 21:30 UT for the American thunderstorms. These times were about 6:00 p.m. local time for both central Africa (Zaire) and central South America (the Amazon).

Figure 1 depicts the Carnegie curve diurnal variation which is normalized to show the percent variation. This classic curve appears to be the most reliable estimate of the average diurnal variation of the global circuit from all ionospheric potential sounding programs going back 40 years [Clark, 1958; Fischer, 1962; Markson, 1976; 1985; 1986] as well as average fair-weather measurements at Mauna Loa Observatory [Cobb, 1968]. The normalized average diurnal temperature variation over Africa and South America from the acquired March 1998 temperature data base is also shown. The close parallelism is striking and the phase difference between maxima is seen. The times of the soundings and Vi magnitudes are also shown.

There are several mechanisms affecting the role of heating on convective development and Vi that must be considered. Temperature, which triggers convection, leads thunderstorm development. The storms must develop to the mature stage before they become significant electrical generators. Also, outflows from earlier storms will set off subsequent storms in nearby regions. A chain reaction can occur with storms continuing into the evening hours. Another factor is that the area of radiation shielding from cirrus and mid-level residue clouds will grow and cause a decrease in ground level temperature in that region. Thus one would expect the maximum positive correlation between Vi and temperature hours or more before the time of the soundings. Time lag analysis was conducted to investigate these effects

Another critical factor arises because temperature and Vi follow similar diurnal variations, but the temperature maximum occurs 3 hours before the Carnegie curve maximum. This means that for measurements made in the interval from 16 UT until 19 UT temperature will be decreasing while Vi is rising and they will be negatively correlated. Similarly, in correlating Vi with temperature several or more hours before the sounding, both curves are rising and a positive correlation will exist. Between about 06 UT and 15 UT measurements made at different times will produce a positive correlation because both parameters will get larger as time advances. These effects were seen in the lag correlation analysis which indicated strong positive correlations when the lag times were in the rising part of the curves with a reversal to negative correlation for lag times after 16 UT when the temperature curve starts to decrease.

In order to minimize this effect, the data were "normalized" assuming the curves in Fig. 1 represented expected average values. A normalization factor was determined for each sounding from the curves, e.g., Vi measurements made at 19 UT (maximum in Carnegie curve) would have been

divided by 1.19. The temperature data at the time of the measurement were treated the same way. Whereas the initial results with unnormalized data indicated strong correlation between Vi and temperature with lags of several hours, using the normalized data these correlations disappeared.

Since similar comparisons between Vi and temperature in Phase I showed positive correlation, it is necessary to consider the different result. In that study most of the measurements were made near in the time period of the peak in the Carnegie curve so some of the positive correlation would have arisen from the diurnal cycle phenomena which was not recognized at that time. Another factor was that the temperature measurements all came from stations within 15° of the equator because it was felt that temperature in the equatorial belt would have the greatest influence on the global electrical generator.

To investigate this possibility, we are rerunning the analysis using only temperature between the equator and 15° S (satellite imagery shows few high clouds north of the equator in March). Preliminary results indicate a positive correlation between low latitude temperature over both continents and Vi.

Figure 2 summarizes results from the different analyses for lags of 0, 4 and 8 hours. Fig. 2a is the unnormalized analysis using temperatures from most of the African and South American continental areas. There is negative correlation at lag 0 and positive correlation at lag 4 and lag 8. In Fig. 2b the normalization procedure for both variables has been applied and the apparent significant correlation between temperature and Vi vanishes at all lags. In Fig. 2c only the equator to 15° S temperatures across Africa and South America are used and both variables are normalized. Now the relationship between temperature and Vi becomes evident. For lag 0 there is a negative correlation, probably due to shielding from the initial convective development. For lag 4 the correlation is +0.49 which exceeds the 95% confidence level. For lag 8 the correlation is +0.75 which exceeds the 99.9% confidence level.

## D. Conclusion

The relationship of Vi to temperature is more complex than originally assumed. Analysis must allow for the sinusoidal out-of-phase diurnal variation of each parameter. Temperature is correlated positively with Vi most strongly over a period of hours before the Vi measurements. The correlation is negative at lag 0, presumably because of cooling due to shielding of solar radiation by cirrus and other residue clouds from earlier convective activity. Monitoring of Vi would probably be of most use in global change studies on monthly, seasonal and climatological time scales rather than shorter time scales.

## Acknowledgments

This work was funded by the National Science Foundation SBIR Program under Contract DMI-9304487. We thank Lothar Ruhnke for help developing the instrumentation, Robert Boldi and Earle Williams for numerous discussions on scientific and analysis problems and Richard Ferris for providing support at the MIT Field Site in Orlando where the measurements were made.

## References

Clark, J.F., The fair-weather atmospheric electrical potential and its gradient, *Recent Adv. In Atmos. Elect.*, Ed. L.G.Smith, pp. 61-73, Pergamon, New York, 1958.

Cobb, W.E., The atmospheric electric climate at Mauna Loa Observatory, Hawaii, *J. Atmos. Sci.*, 25, 470-480, 1968.

Fischer, H.-J., Die Elektrische Spannung zwischen Ionosphare und Erde, Ph.D. thesis, Tech. Hoch. Stuttgart, 124 pp., 1962.

Markson, R., Ionospheric potential variations obtained from aircraft measurements of potential gradient, *J. Geophys. Res.*, 81, 1980-1990, 1976.

Markson, R., Aircraft measurements of the atmospheric electrical global circuit during the period 1971-1984, *J. Geophys. Res.*, 90, 5967-5977, 1985.

Markson, R., Tropical convection, ionospheric potentials and global circuit variation, *Nature*, 320, 588-594, 1986.

Markson, R. and D.R. Lane-Smith, Global change monitoring through the temporal variation of ionospheric potential, Fifth Symp. on Global Change Studies, 279-287, AMS, Boston, 1994.

Markson, R. and C. Price, Ionospheric potential as a proxy index for global temperature, Proc. Tenth Int. Conf. on Atmos. Elect., Osaka, Japan, 632-635, Int. Comm. Atmos. Elect., 1996.

Markson, R., L.H. Ruhnke and E.R. Williams, Global scale comparison of simultaneous ionospheric potential measurements, Prod. Tenth Int. Conf. on Atmos. Elect., Osaka, Japan, 628-631, 1996.

Williams, E.R., The Schumann resonance: a global tropical thermometer,*Science*, 256,1184-1187, 1992.

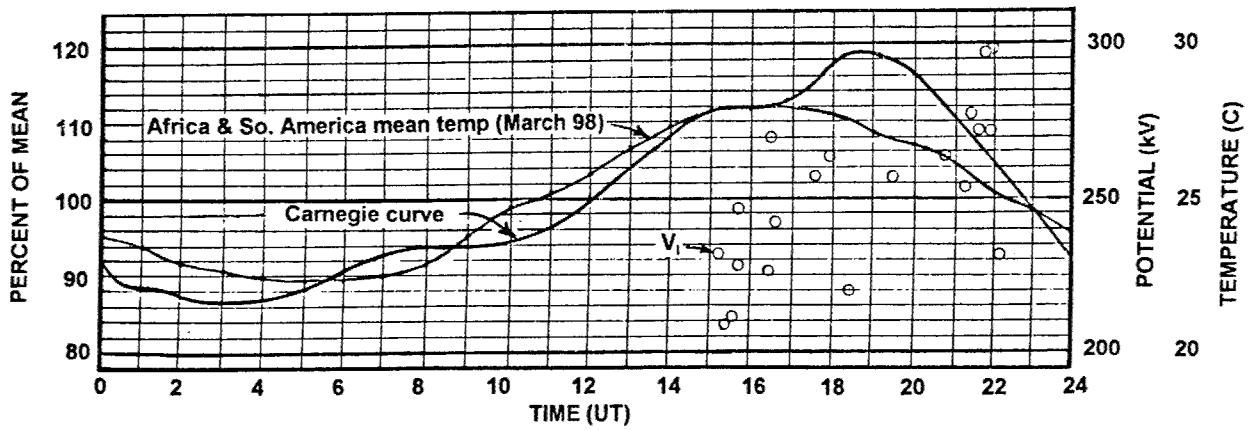


Figure 1. Normalized Carnegie curve and average diurnal temperature variation over Africa and America during March 1998. Ionospheric potential values shown at time of their measurement.

Fig. 2a

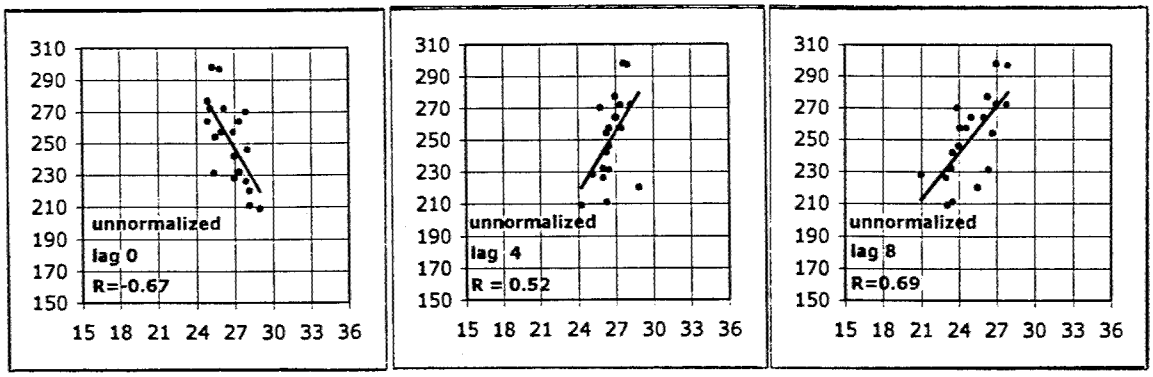


Fig. 2b

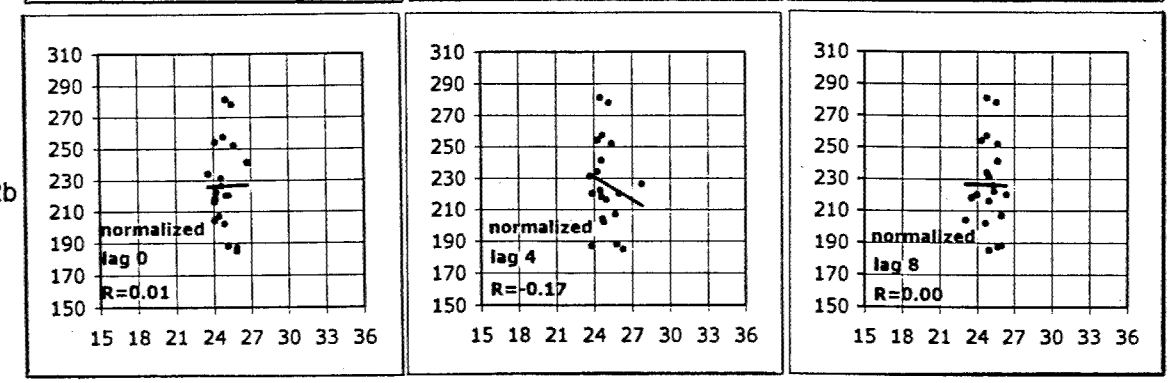


Fig. 2c

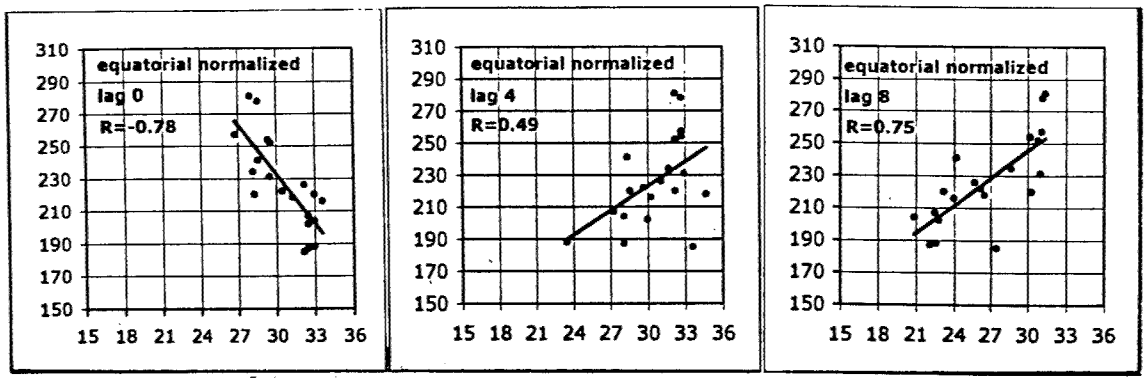

# EVIDENCE FOR THE ABSENCE OF CONDUCTIVITY VARIATIONS ABOVE THUNDERSTORMS

Jeff C. Bailey[1], Richard J. Blakeslee[2], and Kevin T. Driscoll[3]

[1]Raytheon ITSS, Global Hydrology and Climate Center (GHCC), Huntsville, Alabama, U.S.A.
[2]NASA Marshall Space Flight Center, GHCC, Huntsville, Alabama, U.S.A.
[3]University of Alabama in Huntsville (UAH), GHCC, Huntsville, Alabama, U.S.A.

ABSTRACT: In recent years, atmospheric conductivity and electric field measurements over thunderstorms have been made at 20 km with a high altitude aircraft. After compensating for the effects of aircraft charging induced by external electric fields no significant variations in ambient conductivity above thunderstorms have been found. These Gerdien results contrast strongly with the large (and frequent) conductivity variations reported in studies using relaxation probe techniques.

## INTRODUCTION

Over the past decade, atmospheric conductivity and electric field measurements have been made over thunderstorms at an altitude of 20 km from a NASA high altitude ER-2 aircraft. During these missions, the polar conductivities ($\sigma_-$ and $\sigma_+$) were simultaneously acquired using a pair of Gerdien probes (Fig. 1). Above thunderstorms, conductivity measurements can be affected by charge induced on the aircraft (and hence on the air intake tubes of the conductivity probes) by external storm electric fields, introducing measurement error. In these circumstances, theory (*Swann*, 1914) indicates that some ions with the same sign as the induced charge will be deflected from the air stream reducing the measured conductivity of that polarity. The theory also predicts that for the opposite polarity, the additional ions that are attracted by the induced charge are all collected on the intake tube rather than the inner electrode, leaving the ambient measurement unaltered. In this paper we show that the aircraft data support the validity of this theory. More importantly, we find no evidence for significant variations or departures of the ambient conductivity above thunderstorms from that found in undisturbed conditions as has been reported in some investigations (e.g., *Holzworth et al.*, 1986).

## MEASUREMENTS

In addition to the conductivity measurements, the vertical electric field and the aircraft self charge were measured using two electric field mills installed nearly symmetrically on the top and bottom of the aircraft (Fig. 1). The ER-2 navigation system provided measurements of position (from which we can derive geomagnetic latitude, $\Lambda$), pressure (P), and temperature (T). The measurements were collected during the COHMEX (1986), CaPE (1991), STORM-FEST (1992), TOGA COARE (1993) and CAMEX-1, 2 (1993 ,1995) field campaigns. This extensive data set includes more than 330 overflights of electrified storms (> 170 over storms producing lightning) and represents a broad sample of storm types, seasonal regimes, and geographical distribution. Additional data sets have recently been acquired during TEFLUN-A, B and CAMEX-3 (1998) and TRMM-LBA (1999).

## ANALYSIS

The difference between the measured conductivity, $\sigma$, and an estimate of the undisturbed conductivity, as a function of $E_x$ (horizontal component of the electric field along the fuselage of the aircraft) is needed to validate the theory and examine actual conductivity variations. In processing the data $\sigma$ and $E_x$ are averaged to 1 second resolution (these data are acquired with 0.1 s resolution). Lightning transients are not used due to too rapid variations, but the recovery periods from lightning transients are used. The undisturbed conductivity was derived through a normalization procedure. First, the measured conductivity data is normalized to the pressure and temperature of the standard atmosphere at 20 km using the following relation (*Driscoll et al.*, 1996),

$$\sigma(P_{20}, T_{20}, \Lambda) = \sigma(P, T, \Lambda) \cdot \left(\frac{P_{20}}{P}\right)^{-1.01+0.4\cos\Lambda} \left(\frac{T_{20}}{T}\right)^{2.20-0.4\cos\Lambda} \quad (1)$$

Next we normalize to a 45° geomagnetic latitude using *Neher* (1967) data (Fig. 2). A linear fit to the normalized fair weather conductivity (i.e., $\sigma$ located far from thunderstorm) is applied to the thunderstorm regions to provide a normalized undisturbed $\sigma_U$ ($P_{20}, T_{20}, \Lambda_{45}$). Finally, the normalization process is reversed to provide $\sigma_U$ ($P, T, \Lambda$). Figure 3 illustrates this normalization procedure.

At this point, $\sigma_U$ - $\sigma$ (I-D in figure 3) is derived and plotted as a function of $E_x$ (Fig. 4). Errors in $E_x$ on the order of 150 V/m are suggested by the data. Timing errors that cause $E_x$ and $\sigma$ to be mis-aligned can contribute to this error. Also, fast recoveries from lightning can significantly affect the calculated averaged $E_x$ field values. Uncertainties in the field mill geometric form factors may also contribute to this error. Turbulence over thunderstorms can cause errors in the navigation data ( $P, T, \Lambda$). An empirical fit to the data in Fig. 4 is applied to compensate for the effects of aircraft charge on the conductivity measurements to establish the magnitude of conductivity variations above thunderstorms. An example of this application to the data is illustrated in Figure 5.

## RESULTS AND CONCLUSIONS

The aircraft observations, in agreement with theory, show reductions proportional to the magnitude of the aircraft self charge for conductivity of the same polarity as the self charge and little change (perhaps slight enhancement) for conductivity of opposite polarity. The results presented in this paper show the necessity of obtaining simultaneous, high time resolution (at least 1 second) measurements of $\sigma$, E (or Q), P, T, and $\Lambda$ to most properly interpret conductivity measurements over thunderstorms.

No significant variations or departures from the expected undisturbed conductivity have been found above thunderstorms after compensating for the effects of aircraft charging induced by external electric fields.

The conductivity over thunderstorms is found to vary by no more than 10-20 %. Most of the variations that remain after applying the compensation discussed above are probably due to data and analysis errors (see discussion of errors above).

These Gerdien results contrast strongly with the large (and frequent) conductivity variations reported in studies using relaxation probe techniques (e.g., *Holzworth et al.*, 1986, *Hu et al.*, 1989). No known mechanism has yet been established which can account for these polar conductivity variations which can increase or decrease and can exceed a factor of 2.

## REFERENCES


Driscoll, K.T., R.J. Blakeslee, J.C. Bailey, and H.J. Christian, Atmospheric Conductivity Observations over a Wide Latitudinal Range, 10th International Conference on Atmospheric Electricity, June 10-14, 176-179, 1996.

Neher, H.V., Cosmic ray particles that changed from 1954 to 1958 to 1965, *J. Geophys. Res.*, *72*, 1527-1539, 1967.

Holzworth, R.H., K.W. Norville, P.K. Kinter, and S.P. Powell, Stratospheric conductivity variations over thunderstorms, *J. Geophys. Res.*, *91*, 13,257-13,263, 1986.

Hu, H, R. H. Holzworth, and Y. Q. Li, Thunderstorm related variations in stratospheric conductivity measurements, *J. Geophys. Res.*, *94*, 16429-16435, 1989.


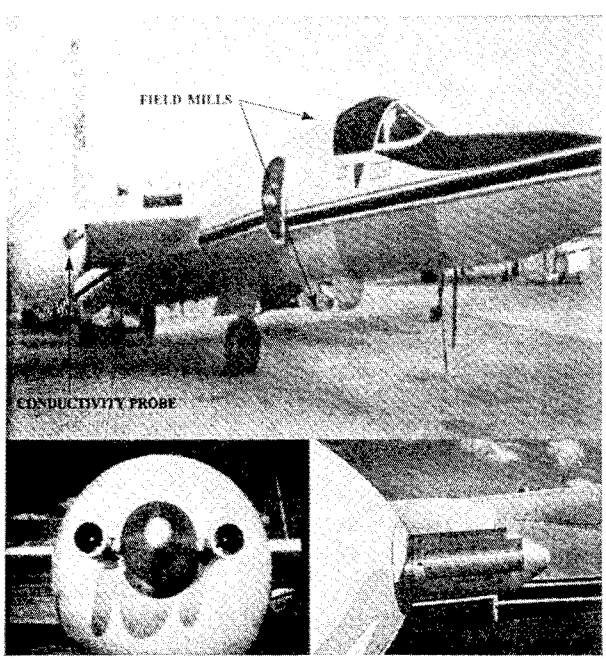


**Figure 1:** Picture of ER2 aircraft showing conductivity probe and field mill locations.

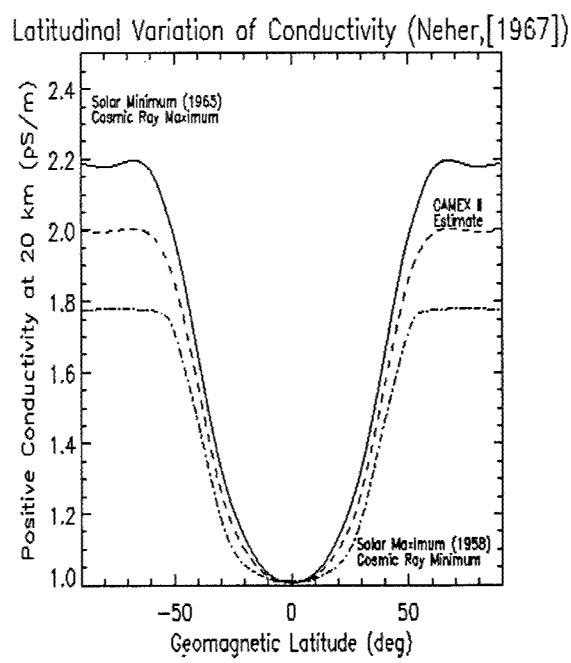


**Figure 2:** Conductivity as a function of geomagnetic latitude and solar cycle.

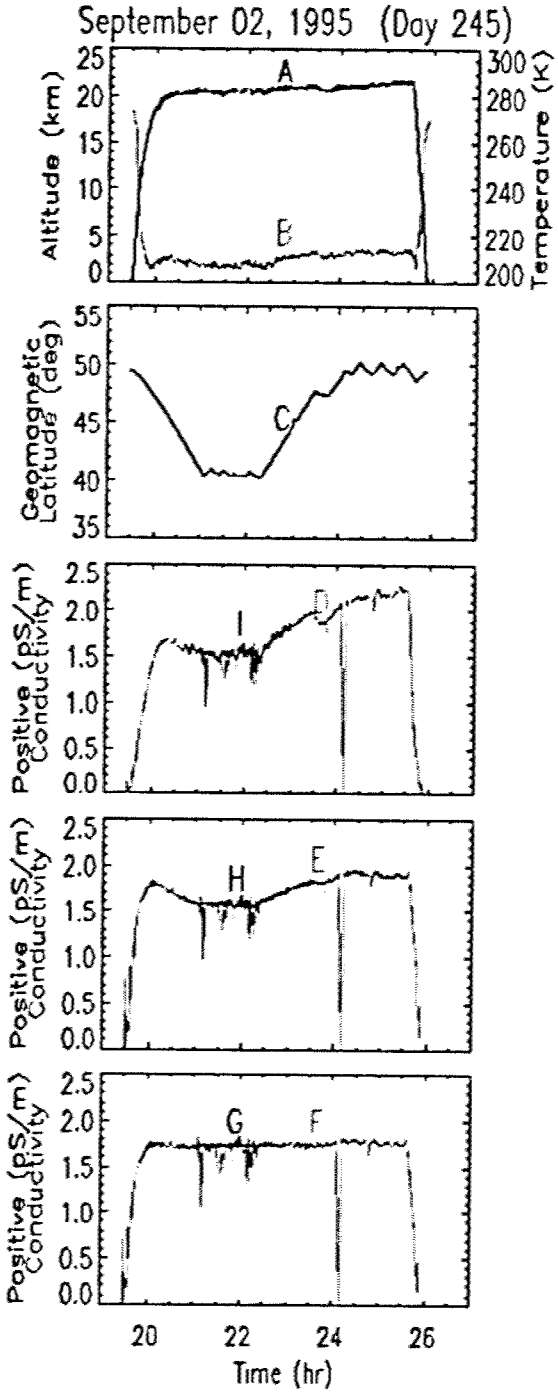


Figure 3a: Example of normalization procedure (A - altitude, B - Temperature, C - Geomagnetic Latitude, D - Measured conductivity, E - Conductivity normalized to 20 km (P, T) by Eq. 1, F - Conductivity normalized to 45 degree Geomagnetic Latitude from Neher data, G - Fit of undisturbed fair weather (FW) conductivity (dark line), H - Reverse normalize FW conductivity (dark line) to 20 km from Neher data, I - Reverse normalize FW conductivity (dark line)to the measured P, T, and geomagnetic latitude).

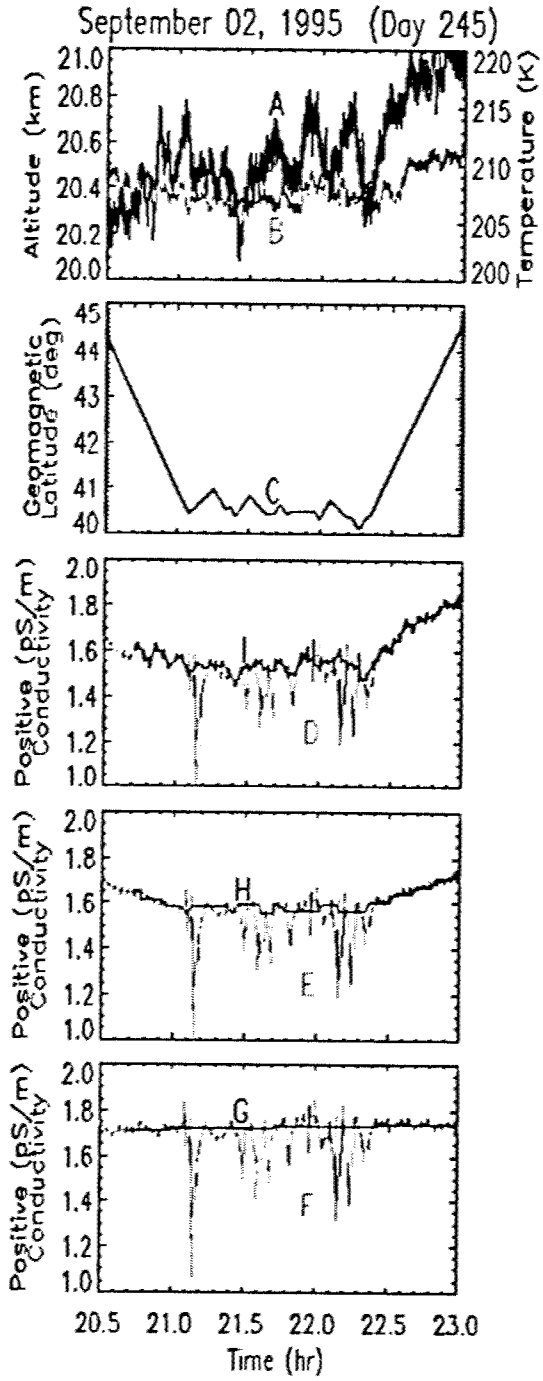


Figure 3b: Enlargement of Figure 3a around the storm cells of interest. Notation is the same as that in Figure 3a.

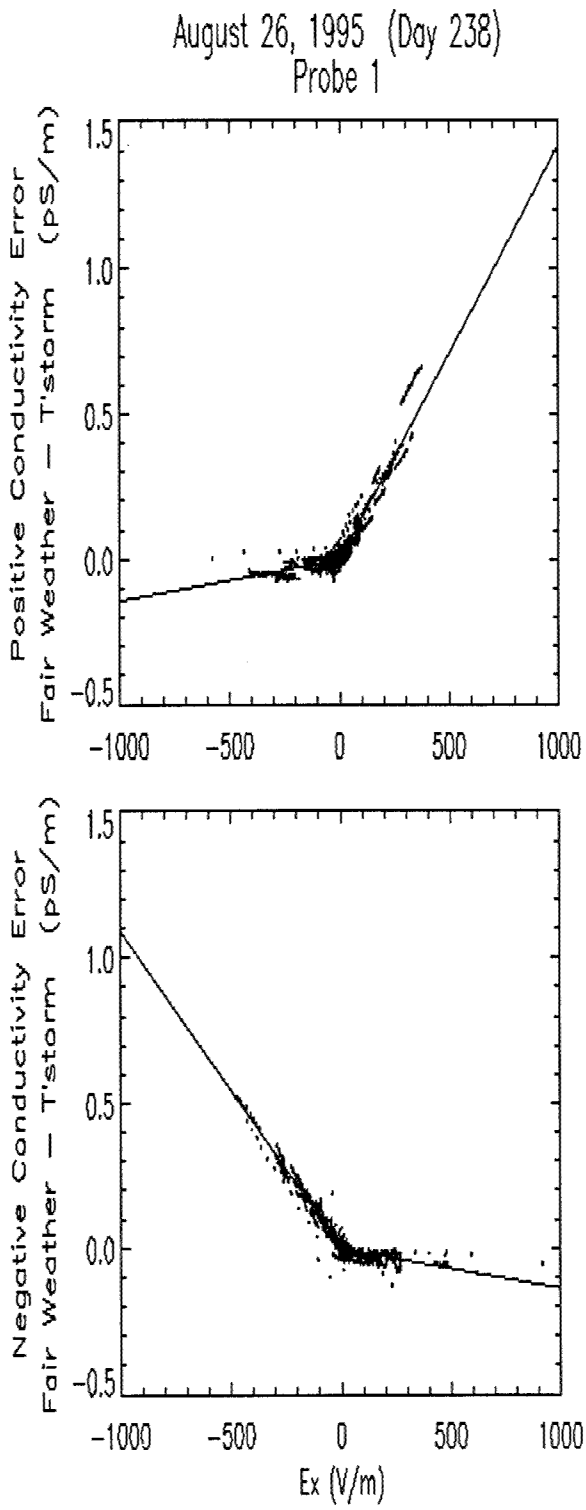


**Figure 4:** Conductivity Error (I-D of fig. 3) versus Ex. The linear fits have been used to correct for the conductivity errors.

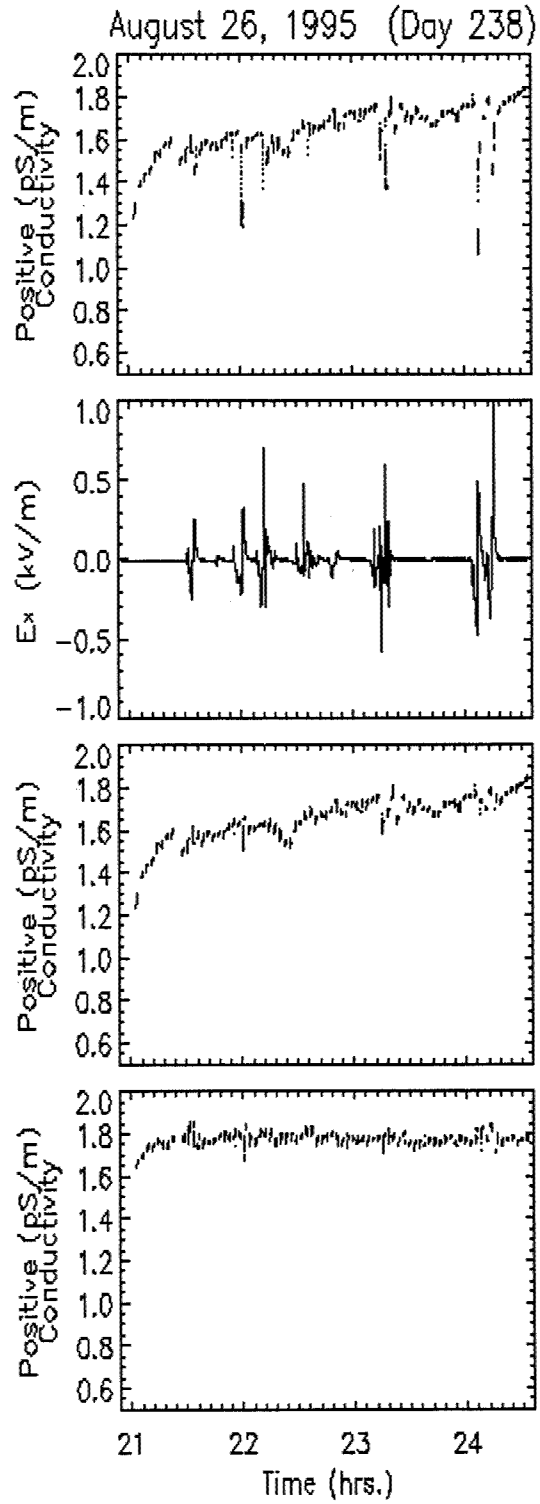


**Figure 5:** Removal of self charge caused errors on the measured conductivity (From top to bottom: Measured conductivity, Ex, Corrected conductivity using data from Fig. 4, Conductivity corrected and normalized to 45 degrees Geomagnetic Latitude).

# Session VIII:

# Global Lightning; Chemistry

# Enhanced $NO_x$ by Lightning in the Upper Troposphere and Lower Stratosphere Inferred from the Global $NO_2$ Measurements of the Upper Atmosphere Research Satellite (UARS)

N.T. SANGER[1], R. ZHANG[1], R. E. ORVILLE[1], X. TIE[2], W. RANDEL[2], AND E.R. WILLIAMS[3]

[1]Department of Meteorology, Texas A&M University, College Station, Texas
[2]National Center for Atmospheric Research, Boulder, CO
[3]Parsons Lab, MIT, Cambridge, MA

ABSTRACT: This paper focuses on a possible link between lightning activity and the UARS $NO_2$ data on a global scale. The $NO_2$ data from the Upper Atmosphere Research Satellite (UARS) are analyzed for the entire year of 1993 and compared to the seasonal and global lightning distribution inferred from the Optical Transient Detector (OTD). The comparison of the two data sets reveals that there is a strong correlation between increased lightning activity and higher observed levels of $NO_2$ in the upper troposphere and lower stratosphere. Enhanced $NO_2$ mixing ratios above the background level are consistently found in areas of elevated lightning activities. This correlation is strongest during the summer months in the Northern and Southern Hemispheres and in the tropics regions. Moreover, the results indicate that expected background levels of $NO_2$ mixing ratios generally correspond to areas of little or no lightning activity.

## 1. Introduction

Nitrogen oxides $NO_x$ ($NO + NO_2$) play a vital role in the atmosphere [Crutzen, 1970]. $NO_x$ is a major controlling factor for the hydroxyl radical OH, and are primarily responsible for the tropospheric formation of ozone $O_3$ [Warneck, 1987]. There are several anthropogenic and natural sources of $NO_x$ in the troposphere. The anthropogenic sources include aircraft emissions, biomass burning, combustion, and vertical transport from deep convection. The natural sources include releases from soils and lightning discharges and downward flux from the stratosphere. $NO_x$ is extremely reactive in the atmosphere with a short chemical lifetime. Typical mixing ratio in a clean atmosphere is between 0.03 - 0.1 ppb, and its mixing ratio is about 0.1 to 0.3 ppb in the upper troposphere [Warneck, 1987]. However, rapid vertical transport of these low altitude sources in the form of deep convection and lightning can result in a higher concentration of $NO_x$ in the upper troposphere [Ehhalt et al., 1992; Ridley et al., 1996]. The role of lightning in the global production of nitrogen oxides has been the subject of considerable investigations [Price et al., 1997a, b]. Globally, estimates of total lightning production range from 1Tg N/yr (terragram nitrogen per year) to more than 200 Tg N/yr [Biazar and McNider, 1995].

In this paper we analyze global $NO_2$ measured by the Upper Atmosphere Research Satellite (UARS). The $NO_2$ data are then compared with global and seasonal lightning data inferred from the Optical Transient Detector data (OTD).

## 2. Data Sources

The UARS satellite is the largest single atmospheric science space mission ever launched and contains ten instruments measuring constituents, winds, temperature, energetic particles, and solar irradiance. Measurements extend from the upper troposphere to the thermosphere [Rood, 1994]. The UARS observatory provides simultaneous, coordinated measurements of atmospheric internal structure and measurements of the external influences acting upon the upper atmosphere. In addition, the combination of orbit and instrument design provides nearly global coverage. The spatial resolutions are half a scale height in the vertical (2.5 to 3.0 km) and 500 km in latitude. Longitude resolutions range from 1000 km to zonal means. The 500 km latitude resolution translates into about 1 minute time resolution along the satellite track.

The two instruments critical to the data analyzed in this paper are the Improved Stratospheric and Mesospheric Sounder (ISAMS) and the Halogen Occultation Experiment (HALOE). The objective ISAMS is to measure the vertical distribution in the 15 to 80 km region of $CO_2$, $N_2O$, $NO_2$, $N_2O_5$, $HNO_3$, $O_3$, and $H_2O$, $CH_4$, and CO with a height resolution of 4 km and a horizontal resolution of 400 km. The objective of HALOE is to measure the vertical distribution of $O_3$, HCl, HF, $CH_4$, NO, and $NO_2$ over an altitude range of 10 to 65 km, with a height resolution of 2 km. In the data taken from these two instruments, the 100 mb level was chosen to be analyzed over the entire globe.

To demonstrate the correlation of enhanced $NO_2$ concentration and high lightning activities, the UARS $NO_2$ data in 1993 are compared to seasonal and global lightning distributions inferred from OTD in 1996. The OTD is the first space-based sensor capable of detecting and locating lightning events in the daytime as well as during the nighttime, which can be used to inferred the global lightning distributions [Nesbitt et al., 1999]. We assume that there is little change in annual variability of global lightning distribution.

## 3. Results

*UARS $NO_2$ Data*

The results of the UARS were analyzed in the following monthly groups: (December, January, and February), (March, April and May), (June, July, and August), (September, October and November).

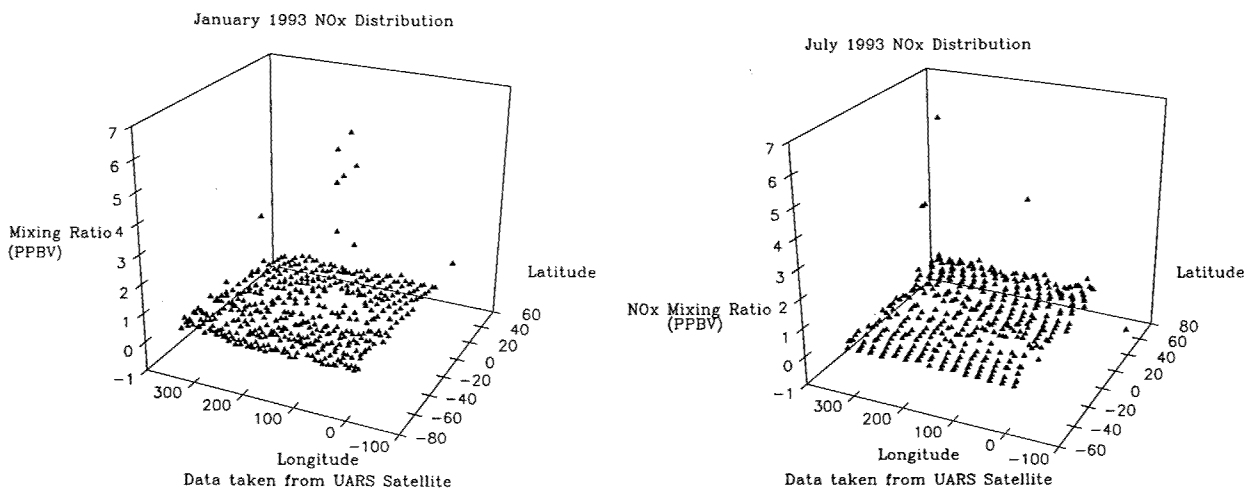


Figure 1. UARS $NO_2$ data for the months of January (left) and July (right) in 1993.

*a. (December – February)*

The best representation of typical $NO_2$ values for this period of interest is the month of January (Figure 1). During the month of January, $NO_2$ data spans from 66.4°S to 43.5° N. The typical $NO_2$ mixing ratio in the Southern Hemisphere from 66.4°S to 30.2.°S is 0.34 ppb. The maximum mixing ratio is 1.09 ppb. The typical mixing ratio from 29.9° S to 10.0°S is 0.57 ppb with a maximum of 6.25 ppb. From 9.6°S to 0.2°S, the average mixing ratio is 0.75 ppb with a maximum of 5.0 ppb. In the Northern Hemisphere tropics from 0.2°N to 10.5°N the typical mixing ratio is 0.65 ppb. The highest mixing ratio is 4.0 ppb. From 11.3°N to 29.9°N, the $NO_2$ typical values decrease markedly to 0.06 ppb. From 30.2°N to 43.5°N, the average mixing ratio is 0.08 ppb. Except in the region between 60 and 70°S, where anomalous higher $NO_2$ mixing ratios occur, the majority of the high mixing ratios (greater than 0.5 ppb) occurred over the land masses of South America, Africa, and Australia.

*c. (March – May)*

The best model of typical mixing ratio patterns for this time period is seen in May. In May, the $NO_2$ data are analyzed from 49.1° S to 42.2° N. In the area from 42.0°N to 30.1°N, the average mixing

ratio is 0.13 ppb and the maximum value is 0.48 ppb. From 29.8°N to 10.4°N, the typical mixing ratio is 0.24 ppb and the maximum value is 3.0 ppb. In the tropical region from 10°N to 0.06N°, the mean mixing ratio is 0.7 ppb and the highest value is 3.5 ppb. The average mixing ratio between 1.0°S and 9.5°S is 0.5 ppb. The maximum mixing ratio in this area is 1.3 ppb. From 10.3°S to 29.9°S, the average mixing ratio is 0.08 ppb with an extreme of 1.55 ppb. In the mid-latitude region from 30.2°S to 48.9°S, the typical mixing ratio is 0.08 ppb and the maximum value is 0.48 ppb.

*d. (June-August)*

The optimum $NO_2$ mixing ratio depiction for these four months is seen in July (Figure 1). The $NO_2$ data covers 65.4°N to 43.7°S. In the mid-latitude region from 65.4°N to 30.0°N, the typical mixing ratio is 0.32 ppb with a maximum of 3.88 ppb. From 29.7°N to 10.0°N, the mean mixing ratio is 0.4 ppb and the extreme value is 6.6 ppb. The average and maximum mixing ratio for the area between 9.7°N to 0.1°N is 0.2 and 0.8 ppb respectively. The typical mixing ratio from 0.3°S to 9.8°S is 0.3 ppb with a maximum of 1.24 ppb. For the tropical region of 10.3°S to 29.8°S, the average and extreme mixing ratio is 0.12 ppb and 0.77 ppb respectively. The average mixing ratio for the mid-latitude area between 30.1°S and 43.7°S, the average mixing ratio is a meager 0.04 ppb with a maximum of 0.42 ppb.

*c. (September-November)*

The most apt example of the typical $NO_2$ distribution for these two months is November. The $NO_2$ data cover 30.0°S to 49.5°N. For the tropical region from 30.0°S to 10.3°S, the typical mixing ratio is 0.09 ppb with a maximum of only 0.34 ppb. The average and maximum mixing ratio from 9.9°S to 0.1°S is 0.13 ppb and 0.79 ppb respectively. From 0.3°N to 9.8°N, the mean mixing ratio is 0.17 ppb and the maximum value is 0.96 ppb. For the tropical region covering 10.12°N to 29.9°N, the average and extreme mixing ratio is 0.04 ppb and 0.4 ppb respectively. In the mid-latitudes from 30.1°N to 49.5°N, the average mixing ratio is 0.1 ppb while the maximum is 0.94 ppb.

*Correlation Between UARS $NO_2$ and Lightning Activity*

Figure 2 shows seasonal distributions of UARS $NO_2$ mixing ratios with values greater than 0.5 ppb observed in the northern and southern hemispheres. It is clear from Figure 2 that the highest frequency of higher mixing ratios of $NO_2$ occurs in the summer months of both hemispheres. Figure 2 also presents an analysis of cases of $NO_2$ mixing ratios greater than or equal to 0.5 ppb compared to cases expected lightning areas inferred from OTD. In the months of January, October, and December, an anomalous region of higher $NO_2$ mixing ratios occurs between 60 and 70 °S, which contributes to most of the observed high $NO_2$ mixing ratios. Otherwise, over 70% of the observed cases of higher mixing ratios are within the regions of expected higher lightning activities. This is particularly true in July when about 75 % of 47 cases of higher $NO_2$ mixing ratios corresponds to frequent lightning areas. In addition, even for the month of January more than 70% of these higher $NO_2$ cases outside the 60 and 70°S region are found in the land masses of South America, Africa, and Australia. Moreover, for $NO_2$ mixing ratios greater than 1 ppb more than 90% of the cases are located in high lightning activity areas.

Hence, the analysis of the UARS data shows a strong correlation between lightning and observed levels of $NO_x$ in the upper troposphere and lower stratosphere. The highest $NO_x$ values are consistently found in areas of frequent lightning. These areas include the Southern Hemisphere land masses of South America, Australia, Africa, and Indonesia in the month of January. In the month of July, the Northern Hemisphere land masses of North America, Europe, Asia, and Africa experience a higher number of lightning flashes. Moreover, in areas of little or no lightning activity, the observed levels of $NO_2$ are normal.

## 5. Conclusion

The results reveal that there is a strong correlation between increased lightning activity and higher observed levels of $NO_x$ in the upper troposphere and lower stratosphere. Enhanced $NO_2$ mixing ratios above the background level are consistently found in areas of elevated lightning activities. This correlation is strongest during the summer months in the Northern and Southern Hemispheres and in the

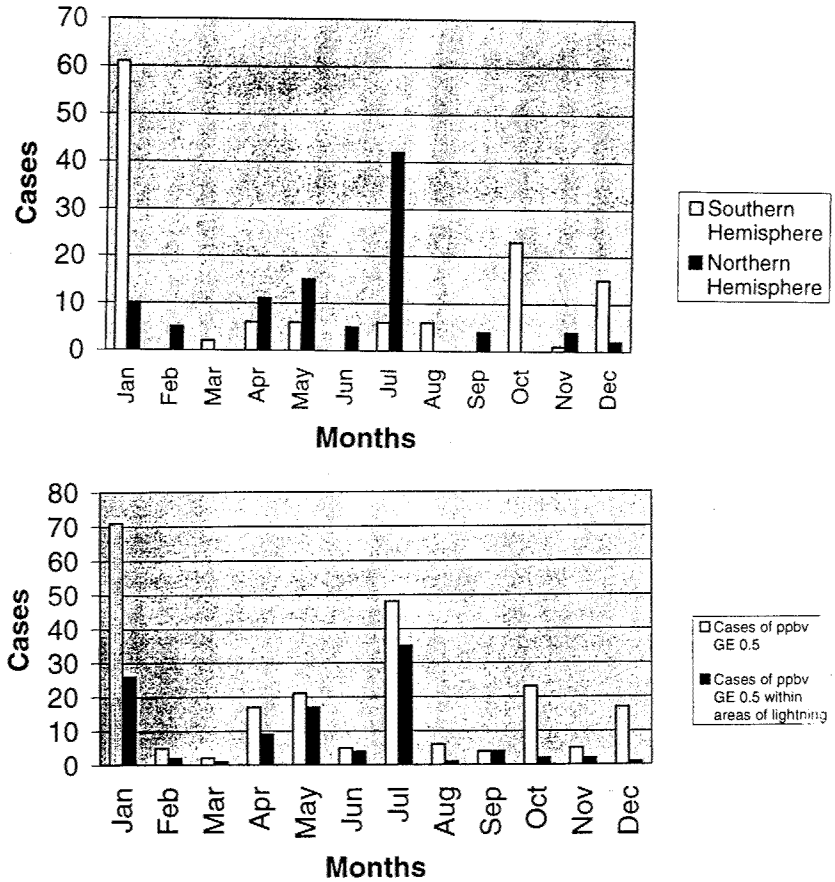


Figure 2. Frequencies of UARS NO2 mixing ratios greater than 0.5 ppb in the northern and southern hemispheres (top) and in expected lightning areas (bottom).

tropics regions. Moreover, the results indicate that expected background levels of $NO_2$ mixing ratios generally correspond to areas of little or no lightning activity.

## References


Biazar, A.P., and R.T. McNider, Regional estimates of lightning production of nitrogen oxides, *J Geophys. Res, 100*, 22,861-22,874, 1995.

Crutzen, P.J., The influence of nitrogen oxides on the atmospheric ozone content, *Q. J. R. Metrolo. Soc., 96*, 320-327, 1970.

Ehhalt, D.H., F. Rohrer, and A. Wahner, Sources and distributions of $NO_x$ in the upper troposphere at northern mid-latitude, *J Geophys. Res, 97*, 3725-3738, 1992.

Goldebaum, G.C., and R.R. Dickerson, Nitric oxides production by lightning discharges, *J. Geophys. Res., 98*, 18,333-18,338, 1993.

Nesbitt, S.W., Zhang, R., and R.E. Orville, Seasonal and global $NO_x$ production by lighting estimated from the optical transient detector (OTD), *J. Geophys. Res.*, submitted, 1999.

Price, C., J. Penner, and M. Prather, NOx from lightning. 1. Global distribution based on lightning physics, *J. Geophys. Res., 102*, 5929-5941, 1997a.

Price, C., J. Penner, and M. Prather, NOx from lightning. 2. Constrained from the global atmospheric electric circuit, *J. Geophys. Res., 102*, 5943-5951, 1997b.

Rood, R.B., Editorial on UARS Satellite, *J. Atmos. Sci., 51*, 2781-2782, 1994.

Ridley, B.A., J.E. Dye, J.G. Ealega, J. Zheng, F.E. Grahek, and W. Rison, On the production of active nitrogen by thunderstorms over New Mixico, *J. Geophys. Res., 101*, 20,985-21,005, 1996.

Warneck, P., *Chemistry of the Natural Atmosphere*, Academic Press Inc., 1987.

Evaluation of NOx produced by storms Based on 3D VHF Lighting Mapping

P. Laroche, E. Defer, P. Blanchet, C. Théry
Office National d'Etudes et de Recherches Aerospatiales
92322 Chatillon Cedex - France

Abstract

The evaluations of NOx production by lightning within storms are commonly based on modeling, laboratory and field experiments. To apply laboratory experiment and physical modeling to observed storms or at global scale, authors use schematic representation of a lightning flash. We describe the actual observed 3D structure of a lightning flash derived from VHF lightning mapping and we comment a method for the evaluation of NOx production.

## 1. Introduction

NOx (NO and $NO_2$) produced by lightning flashes are the natural sources of those species transported in the upper troposphere by storm clouds. Evaluation of lightning NOx effect on atmospheric chemistry is a complex and undetermined issue. The purpose of this paper is to show how a detailed description of the actual 3D structure of the lightning flashes can be used to evaluate their production.

## 2. Actual structure of lightning discharge within a storm

We have conducted observations of Central Florida storms with a 3 dimensional lightning mapper (Laroche *et al*, 1994). We interpreted the informations from this equipment to derive the actual length of the discharge.

### 2.1. Electromagnetic signals emitted by a lightning flash

A lightning flash consists in propagating discharge channels in which currents of different magnitude flow. The most energetic events in a flash are :

⇒ *the return stroke processes*, first and subsequent, which are observed for the Cloud to Ground flash (CG) (few 10 kA up to more than 100 kA). They radiate in low and hight frequency (up to 10 MHz) but are quiet in VHF.

⇒ *the negative stepped and dart leader* preceding the first or subsequent return stroke of a CG. Those leader discharges exhibit current up to 10 kA. They radiate strongly in VHF.

⇒ *the recoil streamer* processes which are the strongest events of an intra-cloud flash (IC), (up to 50 kA) radiate strongly in VHF. Recoil streamers are also observed during CG.

⇒ *the spider discharges*, so called because they exhibit long visible horizontal channels near the base of clouds. They radiate strongly in VHF. Despite that their current was not directly evaluated, the light they emitted indicates that they are highly thermalized and exhibit current of several kA.

⇒ *the positive leaders*, so called because they propagate in the direction of the electric field are thermalized and exhibit currents up to few kA. They do not radiate in HF nor in VHF.

One lightning flash exhibits several of those five types of components. All those five components may produce NOx because they are thermalized and dissociated gas channels in which NO can be freezed out if the cooling of the channel is fast enough (Chameides *et al*, 1977). In an intra-cloud flash all the components but the return stroke are present.

### 2.2. Observations

The VHF interferometer is tuned in the Nav aid band ( 110-118 MHz). It provides up to 4000 different location per second with a 23 µs time resolution (*Laroche et al.*, 1994). Within a radius close to 60 km, of an azimuth-elevation measuring station, we retrieve the XYZ location of emitted sources with a resolution of about 500 m. Basically, we observed three types of VHF sources : isolated sources, clusters of randomly organized set of locations and successive locations showing an organized propagation.

Three basic types of discharges upon the five indicated above, are identified by the temporal and spatial characteristics of the VHF source location.

a) The recoil streamer process is known to last from 10 µs up to 400 µs (Proctor *et al*, 1988). The shortest events are identified by our system as isolated locations. The events longer than 23 µs are identified as a continuous and organized propagating phenomena. Their mean velocity is between $10^7$ m.s$^{-1}$ and $6 \times 10^7$ m.s$^{-1}$.

b) The downward negative stepped leader is known to have a typical stepping rate between 15 and about 100 µs. As several branches propagate simultaneously, the corresponding XYZ successive locations have a random aspect due to the fact that the equipment provides the centroid of the impulsive VHF sources which radiate during a time window. The overall event which lasts few milliseconds, has, nevertheless, random XY locations scattered on a short distance (few km). The upward negative stepped leader is observed the same way as the downward event. It propagates upward and initiates the cloud to ground part of a positive flash. For both types of events the mean velocity is few $10^5$ m.s$^{-1}$.

c) The spider discharge which spatial and temporal characteristics of spider discharge VHF signature is quite similar to this corresponding to a negative stepped leader (mean velocity few $10^5$ m.s$^{-1}$) .

## 3. Evaluation of NOx produced by observed storms

### 3.1. Evaluation of lightning channel length

Negative discharges (they propagate in the opposite direction of the electric field) in a lightning flash are the more energetic components. The identification of the nature of a component depends on the time resolution and on the accuracy of the lightning mapper. For short or faint radiation lasting less than a time window (23 µs in our case), we are able to localize single location whose nature is not identified. Finally we identify :

⇒ stepped leaders of the negative CG.
⇒ recoil streamer processes.
⇒ spider discharges.
⇒ single locations.

To evaluate the NOx produced by a storm, we compute the length of the discharge as a function of space and time. We give on figure 1 the length per 500 m altitude step for the entire life of a single storm cell. To evaluate the length corresponding to single location, we assume that this radiation is due to a recoil streamer process which typical velocity is $2 \times 10^7$ m.s$^{-1}$. The typical length of a single location would so be 460 m which is about the mesh dimension. The vertical distributions of the discharges length confirm the phenomenological behavior of the flash components whose identification is not directly related to their height in the cloud :

⇒ the cumulative stepped leader length peaks around 2 km AGL (Above Ground Level).
⇒ the cumulative recoil streamer process peaks between 5 and 7 km AGL.
⇒ the cumulative spider discharge process peaks around 4 km AGL.
⇒ the cumulative Single location peaks around 6 km AGL.

The distribution with altitude of the single location length is similar to the distribution of the length of the recoil streamer. This is a preliminary justification of identifying single location as short duration recoil streamer.

We have made global calculation for several storms observed with our equipment with the same settings. We obtain the values on the table below :

| Event | Receivers Threshold (dBm) | Number of locations | Storms duration (hours) | #Flashes | Total length (km) | Peak Flash rate (Fl.mn$^{-1}$) | Mean Flash rate (Fl.mn$^{-1}$) | Mean length/flash (km) |
|---|---|---|---|---|---|---|---|---|
| 08-17-92 | -75 | 44 329 | 2.5 | 3505 | 77986 | 50 | 23.4 | 22.3 |
| 08-14-92 | -75 | 93 900 | 3 | 6362 | 115000 | 100 | 35.3 | 18.1 |
| 08-01-92 | -75 | 256 308 | 4 | 14835 | 363377 | 120 | 61.8 | 24.5 |

As the lightning mapper does not "see" the return strokes and the positive leaders, our first evaluation of the channels length ignores those two types of discharge. It has been verified that the number of locations our lightning mapper is able to display, depends on the sensitivity setting of the receivers. We obtain, for those three events, a

mean flash length of 22.5 km, mainly intra cloud, which obviously is larger than the one applied by Liaw *et al* (1990), mainly on the base of observation of return strokes.

To get a more relevant total length lightning channel evaluation, we just consider the most currently admitted lightning phenomenology :

⇒ recoil streamers propagate within the channel of the VHF quiet positive leader (Mazur, 1989).

⇒ return strokes mainly propagate within the branches of the negative leader to equilibrate the potential of those conductive channels.

So to get a more reliable evaluation of the total length of IC as well as CG we simply need to multiply by a factor of two our first level evaluation. That provides a **mean total length per flash of 45 km**.

3.2. NOx produced by electrical discharge

Many experimental and theoritical studies have been made to evaluate the production of NOx by lightning flashes (Ridley *et al*, 1994; Tuck, 1976). The field experiments identify a net production due to lightning (Noxon, 1976; Frantzblau *et al*, 1989). Liaw *et al* (1990) had analysed published works on NOx production by lightning. They attempted a normalization of the various evaluation on the base of general informations on lightning from Uman (1969) : $19.6 \times 10^{16}$ molecules.$J^{-1}$ for the production rate, $3.6 \times 10^{5}$ $J.m^{-1}$ for the energy deposition in the channel, a length of 7 km per stroke and 2 strokes per flash. For a permanent flash rate of 100 flashes per second, they finally proposed the following table :

| | for $4 \times 10^{8}$ $J.flash^{-1}$ | | | | for $5 \times 10^{9}$ $J.flash^{-1}$ | | | |
|---|---|---|---|---|---|---|---|---|
| Tg N/year | Max | Min | Mean | σ | Max | Min | Mean | σ |
| Theoritical | 23.6 | 0.5 | 5.8 | 7.7 | 295 | 6.6 | 72.2 | 96.2 |
| Laboratory | 2.4 | 0.5 | 1.6 | 0.8 | 30 | 5.9 | 19.1 | 10.0 |
| Field | 220 | 74 | 152 | 59.9 | 220 | 74 | 152 | 59.9 |

table from Liaw *et al* (1990)

Liaw *et al* (1990) discussed the amount of energy per flash and proposed $5 \times 10^{9}$ $J.flash^{-1}$ as a value which harmonized best the results of the various methods of evaluation.

To test our observations upon Liaw normalization, we need to propose a reasonable extension to derive a global budget. We obtained a mean flash rate of about 40 $Fl.mn^{-1}$. If we anticipate a CG ratio of 20 %, to obtain a permanent CG rate of 100 $Fl.s^{-1}$, we need to assume a permanent occurrence of 750 storm systems identical to the three described above. This is not too unrealistic, the permanent occurrence of 1500 storms being commonly stated. On that base the mean global flash rate would be 500 $Fl.s^{-1}$ which would lead to a global production of $978 \times 10^{12}$ $g.N.year^{-1}$ which is two order of magnitude larger than the most recently admitted value (Ridley *et al*, 1994). Our estimation must be tempered by energy consideration : leader phases are supposed to produce less per unit energy. Berton (1996) proposes for this type of flash component, a first evaluation of $10^{16}$ molecules $N.J^{-1}$. This would give about a total of **60 Tg $N.year^{-1}$** which is more relevant with other maximum evaluations but still 10 times greater than the most realistic evaluation based on situ measurements

## 4. Conclusions.

The use of 3D VHF lighting mapper is an efficient way to provide evaluation of NOx produced by observed storms. Such evaluation are based on parametrization of electrical discharge specific production ratio, which need to be validate with in situ NOx measurements.

**Acknowledgments**

This work was partially supported by a DGAC (Direction Générale de l'Aviation Civile) contract (C94.03).

## References


R. Berton. « Model estimate of NOx production during the cooling of a lightning flash » *Proceedings of the Comite Avion Ozone Symposium. Paris Oct. 1996*.

W.L. Chameides, D.H. Stedman, R.R. Dickerson, D.W. Rusch and R.J. Cicerone. « NOx production in lightning. » *J. Atmos. Sci.*, **34**, 143-149, 1977.

E. Franzblau and C. Popp. « Nitrogen Oxides Produced from lightning. » *J. Geophys. Res.*, **94**, 11,089-11,104, 1989.

P. Laroche, A. Bondiou, P. Blanchet, J. Pigère, M. Weber and R. Boldi. « 3D mapping of lightning discharge within storms. » *Int. Conf. on Lightning and Static Electricity Germany, 1994.ONERA TP n° 1994-186.*

Y.P. Liaw, D.L. Sisterson and L. Miller. « Comparison of Field, Laboratory, and Theoretical Estimates od Global Nitrogen Fixation by Lightning. » *J. Geophys. Res.*, **95**, n° D 13, 22,489-22,494, 1990.

V. Mazur. « Physical model of lightning initiation on aircraft in thunderstorms. » *J. Geophys. Res.*, **94**, 3,326-3,340, 1989.

J.F. Noxon. « Atmospheric nitrogen fixation by lightning. » *Geophys. Res. Lett.*, Vol 3, n° 8, 1976.

D.E. Proctor, R. Uytenbogaart, B. Meredith. « VHF Radio pictures of lightning flashes to ground. » *J. Geophys. Res.*, **93**, 1988.

B.A. Ridley, J.G. Walega, J.E. Dye, and F.E. Grahek. « Distributions of NO, NOx, NOy, and O3 to 12 km altitude during the summer monsoon season over New Mexico. » *J. Geophys. Res.*, **99**, 25,519-25,534, 1994.

A.F. Tuck. « Production of nitrogen oxides by lightning discharges. » *Quart. J. R. Met. Soc.*, n°102, 749-755, 1976.

M.A.Uman « Lightning » Elseivier 1969


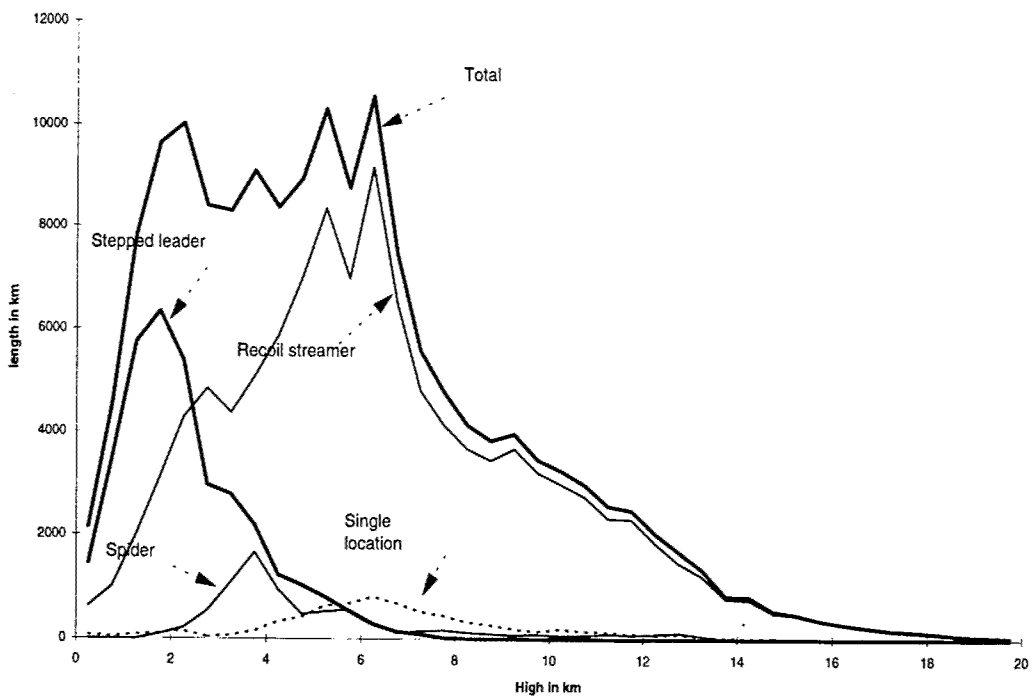


Figure 2. Storm situation of August 14 1992 : Cumulative channel length by 500m high

# IMPACT OF LIGHTNING DISCHARGE ON STRATOSPHERIC OZONE

B. Klumov
Institute for Geosphere Dynamics,
123098, Raspletina 7-13, Moscow, Russia
e-mail: klumov@idg.chph.ras.ru

**Abstract**

We have investigated the dynamics and chemical composition of the hot lightning channel at lower stratospheric altitudes. Two-dimensional gas dynamical code ZEUS-2D was used to calculate the expansion of the hot air channel. As the hot air channel expands, quenching occurs: the chemical composition of the gas stops changing and corresponds to the equilibrium composition at the moment of quenching. We focused our attention mainly on nitrogen oxides NO and $NO_2$ production by lightning as these minor constituents strongly affect on ozone. The temperature of NO quenching in lightning channel was found is about 2300-2500 K. At these temperatures NO mixing ratio in the channel is about 0.03 and weakly depends on the ambient air pressure. Later such lightning-produced column of NO spreads by turbulent diffusion processes with a typical timescale of the order of 100 s, forming the region with radial space scale of the order of 100 m, where NO mixing ratio far above then the ambient one. We calculated the photochemistry of the ozone in the region. It has been shown that strong ozone transient (on the order of a few minutes) depletion is formed in the region.

It is well known that lightning discharge process heats the channel gases up to a temperatures about $3 \times 10^4$K. At the temperatures both molecular oxygen and nitrogen are fully dissociated and are nearly single ionized. Subsequent rapid expansion of the hot air channel creates a column of the air with a strongly nonequilibrium composition. In particular a large amount of nitrogen oxides (NO, $NO_2$) is produced by the lightning discharge, these oxides may affect on the ozone layer.We can divide all physical processes occurring in the lightning channel according to the proper both characteristic speeds $v$ and characteristic times $\tau$ into three stages:

- lightning-breakdown processes: $v \sim 10^9 - 10^{10}$ cm/s, $\tau \sim 10^{-6}$ s.
- expansion of the hot channel, shock wave formation and propagation: $v \sim 10^5 - 10^6$ cm/s, $\tau \sim 10^{-3}$ s.
- cooling of the channel remnant by turbulent diffusion processes, formation of the air column with nonequilibrium composition, photochemistry processes: $v \sim 1 - 10^3$ cm/s, $\tau \sim 0.1 - 10^2$ s.

Obviously each stage creates an initial conditions for the next one. Let's consider in more detail last two stages.

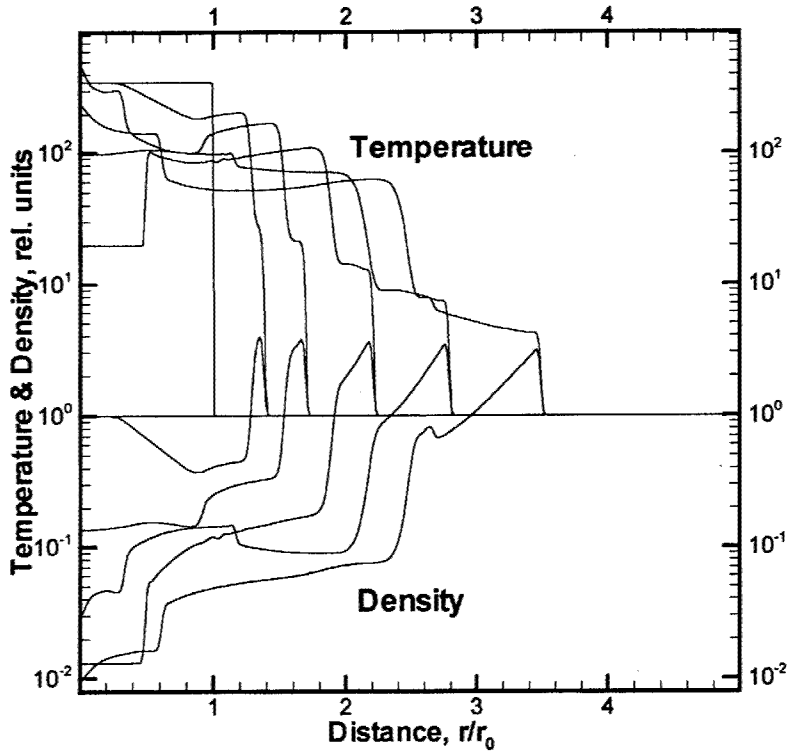


Figure 1. Radial profiles of the air density and temperature inside the lightning channel at various moments of time. Clearly seen the formation of the shock wave and its propagation. Final time corresponds to the time of about $5 \times 10^{-5}$s.

Without loss of generality we can take the typical initial lightning channel parameters as follows: temperature $T_h$ of the hot air $\simeq 3 \times 10^4$K, density of the hot air $\rho_h$ equals to the density of the ambient air $\rho_a$: $\rho_h \simeq \rho_a \simeq 10^{-4}$ g/cm$^3$ (notice that this condition is not evident, but weakly influences on the final result of the lightning NO production), so pressure $p_a$ of the ambient air $p_a \sim 0.1$ bar. Initial radius $r_0$ of the lightning channel $r_0 \simeq 10$ cm, length $L$ of the channel $L \simeq 5$ km. These parameters corresponds to energy of lightning $E_0 \simeq 2.5 \times 10^{16}$ erg, that appears to be is rather common for unit return stroke (for example, [1]).

Initial pressure $p_h$ inside the lightning channel is about $p_h \simeq$ 40 bar in our case (we taking into account full dissociation of the air and a single ionization of the oxygen and nitrogen atoms at the temperatures under consideration). You can see that $p_h/p_a \simeq 400 \gg (\gamma+1)/(\gamma-1) \sim 10$, where $\gamma$ is a ratio of specific heats, i.e. strong shock wave is generated during the lightning flash.

Initial velocity $D_0$ of the shock wave is determined from relationship: $D_0 \simeq \sqrt{2p_h/(\gamma+1)\rho_a}$. Initially $\gamma \simeq 1.2$ and $D \simeq 6 \times 10^5$ cm/sec. It should be emphasized that typical velocity of the return stroke propagation much greater; the velocity is about $10^9 - 10^{10}$ cm/sec, so the cylindrical explosion is the most appropriate approach for describing of the lightning channel expansion.

In the case shock wave velocity $D$ decreases with the radius $r$ of the shock wave front as: $D \simeq D_0 r_0/r$. Temperature $T_f$ behind the shock wave front is given by: $T_f \propto p_f/\rho_f \simeq p_f/\rho_a(\gamma-1)/(\gamma+1) \propto D^2 \propto 1/r^2$. In the relationships we neglect of $\gamma$ changing during hot lightning channel expansion, which may be important (note that $(\gamma-1)$ varies by factor of $\simeq 2.5$ during expansion). Note that in our calculations, described slightly below this effect is properly accounted for.

If the temperature of the gas is sufficiently high the thermochemical equilibrium take place, but rapid cooling result in some constituents can be "frozen" into the gas i.e.

quenching is occur. Let's consider the quenching of NO during rapid cooling of the initially equilibrium heated gas (similar problem of NO quenching during explosion was considered in [2], but there are some differences between our approaches).

The sink of NO in a hot air is controlled by the next reactions:

$$NO + N \rightarrow N_2 + O \tag{1}$$

(with rate constant $k_1 \simeq 3 \times 10^{-12}/\sqrt{T}\,\mathrm{cm}^3\mathrm{s}^{-1}$) and

$$NO + O \rightarrow N + O_2 \tag{2}$$

(with rate constant $k_2 \simeq 3 \times 10^{-15} T e^{19500\mathrm{K}/T}\ \mathrm{cm}^3\mathrm{s}^{-1}$)

So, the characteristic life time $\tau_{NO}$ of NO in the heated air is given by: $\tau_{NO} \simeq 1/(k_1[N] + k_2[O]) \simeq (k_2[O])^{-1}$. Thermochemical calculations show that we can to neglect the term $k_1[N]$ in comparison with the term $k_2[O]$ ($k_1[N] \ll k_2[O]$ for typical parameters of the heated air channel under consideration). It is easily to show that atomic oxygen O is in thermochemical equilibrium with molecular oxygen $O_2$ in our case, so $[O] = \sqrt{K_{eq}[O_2]}$ and $\tau_{NO} \sim 10^{-8} T[O_2] e^{-50000\mathrm{K}/T}$. Clearly seen that decrease of temperature of the hot air result in drastically increase of the establishment of NO equilibrium time. For parameters of the lightning channel cited above, $\tau_{NO} \sim 10^{-5}$ s at $T = 4000$K, $\tau_{NO} \sim 10^{-3}$ s at $T = 3000$K and $\tau_{NO} \sim 1$ s at $T = 2000$K.

So as the hot channel expands, quenching occurs: the chemical composition of the gas stops changing and corresponds to the equilibrium composition at the moment of quenching. Temperature of NO quenching is estimated from obvious relationship: $\tau_{NO} \simeq \tau_{cool}$, where $\tau_{cool}$ is characteristic cooling time of the heated air, depending on the temperature of the gas.

In our case $\tau_{cool} \sim r/v \sim 10^{-2} - 10^{-3}$ s, where $r$ is a radius of the expanded lightning channel ($r \sim 1$ m), and $v$ is a typical velocity of cooling wave ($v$ is defined by the rate of mixing processes). It is easily to estimate the temperature $T_q$ of NO quenching, in our case $T_q$ is about 2500 K. It should be noted that amount of NO "freezing" during expansion of the hot lightning channel is about of a few percents of the mass of the air heated above $T_q$ and the amount weakly depends on the $T_q$, NO yield per unit energy weakly depends on the ambient pressure. Notice that $NO_2$ production by lightning discharge is less effective than NO by a factor of about 100.

To calculate the amount of NO produced by lightning discharge more precisely we need to know the dynamics of the hot channel expansion. We use two-dimensional ZEUS code [3] to determine cited parameters.

Some results of our calculations are presented on the Figure 1. On the figure radial profiles of the density and temperature inside the lightning channel are depicted at various moments of time. By using these data one can to estimate the mass of the air heated to a temperatures above $T_q$.

Our calculations show that amount of NO produced by the lightning discharge is about 2-3 % of the initially heated air, that is the yield of NO molecules $P$(NO) may be evaluated

as 50-75 eV/molecule. It is interesting to compare the result with NO yield for both plasmatron [4] and explosion [2]. Note that vibrationally-excited molecular nitrogen is used to produce NO in the plasmatron - appears to be this method is the most energetically cheap. For plasmatron $P(\mathrm{NO}) \simeq 10$ eV/molecule, while for explosion $P(\mathrm{NO}) \simeq 150$ eV/molecule. Additional estimates of $P(\mathrm{NO})$ can be found, for example, in [5].

It should be emphasized that NO is produced mainly from an ohmic heated lightning channel rather than by a shock wave emanating from return stroke. Note that NO yield per energy unit depend only slightly on the pressure of the ambient air and is about the same at various altitudes of troposphere and lower stratosphere.

Thus a lightning discharge produces a large amount of NO in the expanded lightning channel, the level of NO far above the ambient NO level. Subsequent turbulent diffusion processes reduces NO mixing ratio in the channel, creating a column of the air with a significant excess of NO around channel remnant. Concentration $n_{\mathrm{NO}}$ of NO can be estimated from the solution of the 2D diffusion equation with no chemistry, the solution is given by: $n_{\mathrm{NO}}(r,t) \propto \exp(-r^2/Kt)/t$, where $K$ - turbulent diffusion coefficient, which can be evaluated as: $K \simeq 8t^{1.6}$ cm$^2$/s [6]. By using previous results on $P(\mathrm{NO})$ one can easily estimate typical radial scale $r_D$ of the column of the air where the concentration of NO is significantly above than ambient one: $r_D \sim 100$ m. The typical life time of the column $\tau_D$ with respect to diffusion spreading is estimated from: $r_D \simeq \sqrt{Kt} \simeq 3\tau_D^{1.3}$, or $\tau_D \sim 300$ s. Excess of NO creates a local and transient ozone depletion in the column via bimolecular reaction: $\mathrm{NO} + \mathrm{O_3} \rightarrow \mathrm{NO_2} + \mathrm{O_2}$ with the rate $k_3 \simeq 4 \times 10^{-12} \exp(-1560\mathrm{K}/T)$ cm$^3$s$^{-1}$. Note that the life time $\tau_{\mathrm{NO_2}}$ of the $\mathrm{NO_2}$ in the photolysis process: $\mathrm{NO_2} + \mathrm{h}\nu \rightarrow \mathrm{NO} + \mathrm{O}$ is about 100 s at tropospheric and lower stratospheric altitudes and is of the order of life time $\tau_D$ of the disturbed column. So we can estimate the radius of the column $r_{\mathrm{O_3}}$ in which ozone almost completely depleted: $[k_3 n_{\mathrm{NO}}(r_{\mathrm{O_3}}, t)]^{-1} \simeq \tau_{\mathrm{NO_2}}$. The radius $r_{\mathrm{O_3}}$ is of the order of 100 m for the typical lightning discharge. Consequently, lightning discharge can cause local (typical radial scales are on the order of 100 m) and transient (on the order of a few minutes) loss of ozone.

**References**


1. Ogawa T., Lightning currents, in *Handbook of Atmospheric Electrodynamics*, p. 93-136, CRC Press, 1995

2. Zel'dovich Y.B. and Raizer Y.P. *Physics of Shock Waves and High-Temperature Hydrodynamic Phenomena*, Academic Press, NY, 445 pp., 1966

3. Norman M.L. and J.M. Stone *The ZEUS-2D Code for Astrophysical Fluid Dynamics Simulations*, Astrophys. Journal Suppl., V. 80, 753-790, 1992

4. Rusanov V.D . and Fridman A.A., *Physics of Chemically Active Plasma*, Nauka, pp. 415, 1984

5. Lawrence M.G. et al, *Lightning and Atmospheric Chemistry: the Rate of Atmospheric NO Production*, in Handbook of Atmospheric Electrodynamics, p. 189-202, CRC Press, 1995

6. *The Natural Stratosphere*, CIAP Monograph, Washington, 1975

# AN ESTIMATION OF NITRIC OXIDE VARIATION CAUSED BY LIGHTNING OVER A BULGARIAN AREA BASED ON EXPERIMENTAL AND MODEL DATA

Staytcho I. Kolev

National Institute of Meteorology and Hydrology-Bulgarian Academy of Sciences, Sofia, Bulgaria

ABSTRACT: Recently has been qualitative confirmed by direct observation of enhanced levels of nitric oxides (NOx) in and around the active thunders clouds, as the lightning can alter radically the chemical composition of the air .On the base of both experimentally obtained data of lightning activity over Sofia area for ten year period and modelled accepted magnitudes of energy and frequency of strokes ,it has been estimated the variation of nitric oxides production due to lightning. It has been presented the yearly and mean monthly runs of nitric oxides at ground measured contents and the parallel lightning frequencies, as well and their calculated trends for the studied period 1982-1995. The obtained values has been partly compared with the published ones. Especially attention has been paid to some discrepancies and it has been discussed the possible explanation connected with the limitations associated with measuring procedures.

## INTRODUCTION:

In the recent years, investigators have taken a more direct approach to estimating the nitrogen fixation rate by lightning. Field measurements have focused on attempting to find a correlation between electrical activity and the levels of gaseous nitrogen oxides (i.e. NO and NO2) within and in the vicinity of thundercloud. Lightning can radically alter the chemical composition of the atmosphere as a whole. One of the measurements providing strong evidence that nitrogen oxides were produced by thunderstorms were those obtained by Noxon (1976). Later Drapcho et al. (1983) observed a sudden increase in NO and NO2 levels at the ground during a thunderstorm which was apparently produced by a nearby cloud-to-ground lightning flash. In situ NO measurements within active clouds have been reported by Davis and Chameides (1984) and the NO levels thus measured were found to be one or two orders of magnitude higher in active clouds than in clear air which has to disturb ratio NO/NO2. In order to establish quantitatively the rate of this nitrogen process it is necessary to determine the magnitude of two parameters which control it (Borucki and Chameides, 1984). These parameters are the number of NO molecules produced per Joule of discharge, and the number of joules dissipated by lightning per second.

## METHOD

The lightning discharge frequency for the Sofia area has been estimated on the base of data available at the Sofia and Burgas stations for the period 1982-1995. For the aim of the present study is used the approach of proceeding climate data, i.e. days with registered thunderstorm and its intensity as a duration in hours. As an useful information has been utilized the partly measuring with a lightning flash counter. The Sofia station is situated in a mountain valley and the climate is of continental type. Spectrophotometer, Karl Zeiss SPECOL 9 was used in determining NO2. Sampling duration was 1/2 hour. The sensitivity of the method is 0.1 microgram in the measured solution. The daily mean value is the arithmetic mean from the daily measurements. The monthly mean value is the arithmetic mean

Fig.1 The run of thunderstorm days and NO2 content at Sofia station

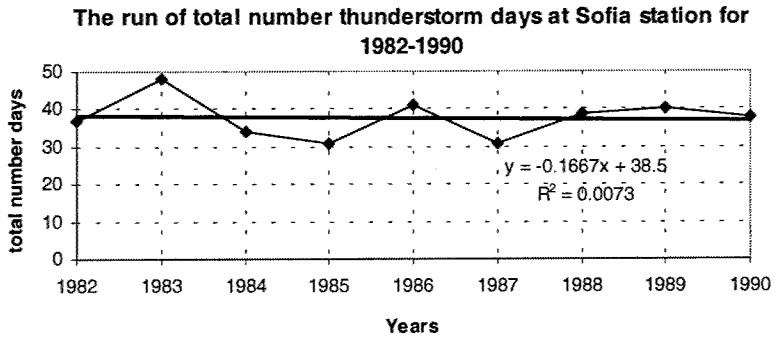


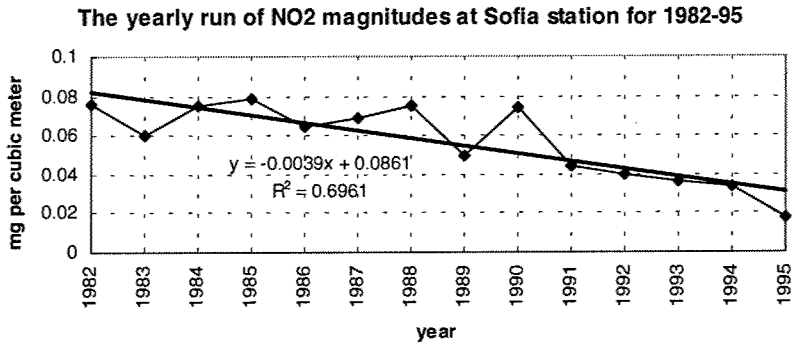


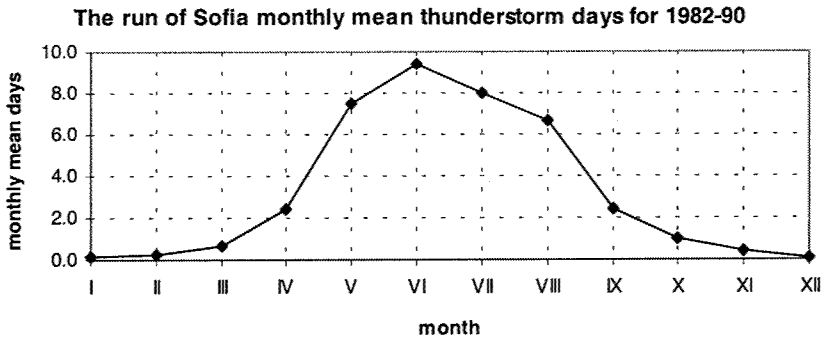


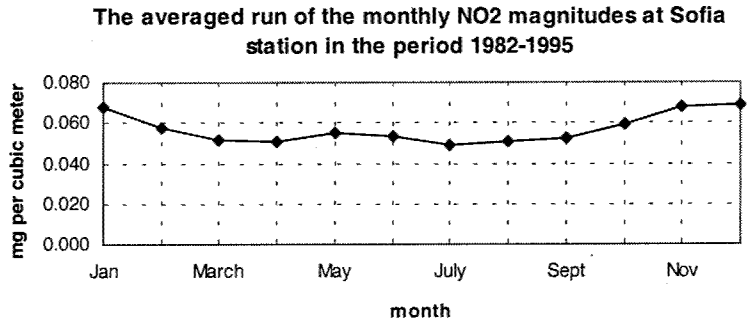

Fig.2 The run of thunderstorm days and NO2 content at Burgas station

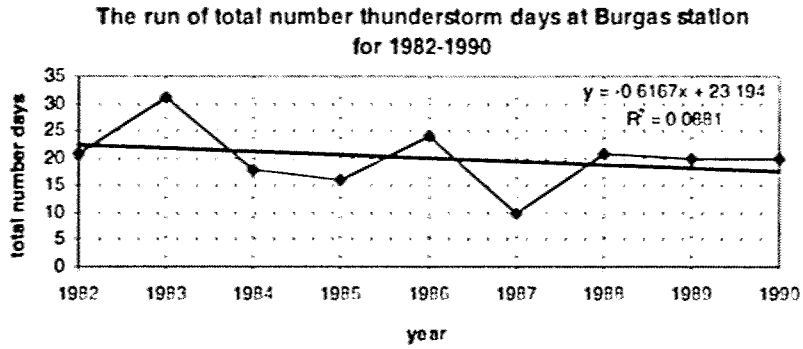


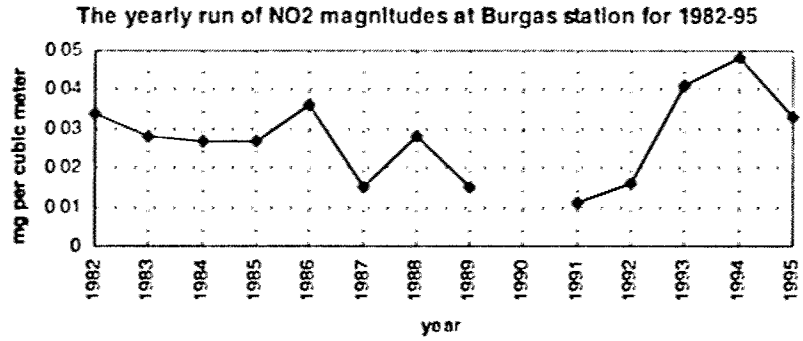


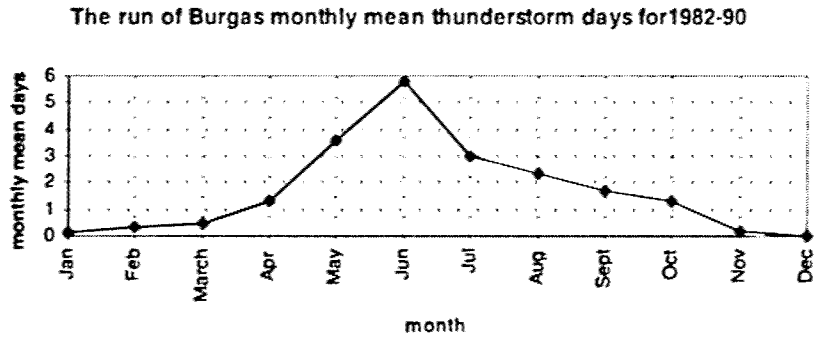


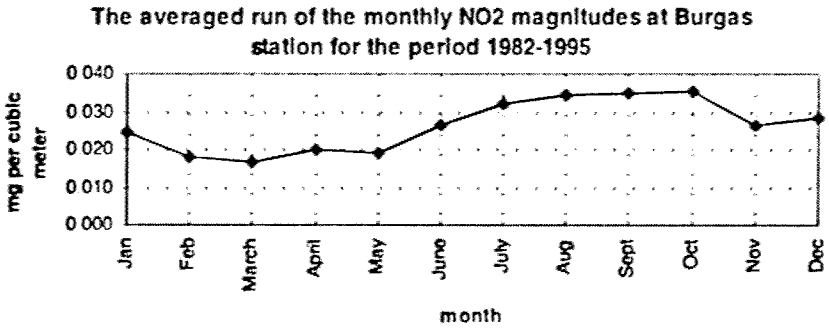

of daily data. Annual mean concentrations are the arithmetic mean calculated with 12 monthly values by WDCGG(1997). The Burgas station, equipped similarly, is situated at the Black sea coast and the climate is influenced by the sea.

RESULTS:

On the base of the primary data of thunderstorm days have been calculated the number of flashes, their mean energy and the expected production of NOx by them, using Kolev(1988), Price (1997). At fig.1 and 2 are presented the runs of the yearly total number and monthly mean thunderstorm days and corresponded yearly and averaged monthly runs of NO2 contents for the two stations.The comparisons of the trends between the primary obtained measured data show an absence of any correlation between thunderstorm activity and NO2 content to the both stations.

DISCUSSIONS AND CONCLUSIONS:

The calculated values of NOx produced by lightning over the region show an enough good agreement with the published data by Price (1997) .The discrepancy on the presented figures is due to the next probably reason. If NO2 were distributed uniformly throughout the troposphere , it would correspond to concentrations of NO2 at ground less than measured and would imply daytime average mixing ratios of NO smaller than device sensitivity. The most of the produced NO and NO2 are in the upper atmosphere. The colder temperatures at these levels would allow a larger ratio NO/NO2. These results have to be taken in considerations during future experiments dealing with the role of lightning in atmospheric chemistry.

ACKNOWLEDGEMENTS: This work was supported by the National Fund "Science Researches" to the Ministry of Education, Science and Technology, Republic of Bulgaria, under grant NZ 624/1996 and by the Joint Agreement between The Royal Society of London and the Bulgarian Academy of Science.

REFERENCES:

Burucki W.J.,and W.L. Chameides, Lightning: Estimates of the Rates of Energy Dissipation and Nitrogen Fixation,*Revies of Geophysics and Space Physics,* **22**, 4, 363--372, 1984.

Price C. et al., NOx from lightning 1.Global distribution based on lightning physics, *Journal of Geophysical Research,***102**, No.D5, 5929--5941, 1997.

Kolev S.I. et al., A study of the variation of the number of Lightning discharges by various weather conditions,*in Proc. of 8th Intern. Conference on Atm. Electricity,* 620--624, 1988.

WDCGG No.12, WMO WDCGG DATA REPORT,GAW DATA,Published by The Japan Meteorological Agency in Co-operation with the World Meteorological Organization, March, 1997

Noxon, J.F., Atmospheric nitrogen fixation by lightning,*Gephys.Res.Lett.*,3,463-65,1976.

Drapcho, D.L. et al.,Nitrogen fixation by lightning activity in a thunderstorm, Atmos. *Environ.*,17,729-734,1983

Davis, D.D. and W.L. Chameides, in Proc.VII Int. Conf. on Atmos.Electricity, Albany, NY,1984

# Recent results from the FORTE rf payload

Abram R. Jacobson[1]

[1]Los Alamos National Laboratory, Los Alamos, NM, U. S. A.

ABSTRACT: This work compares contemporaneous observations of lightning from two complementary systems. FORTE is a low-Earth-orbit satellite carrying radio-wave and optical instruments for the study of lightning. The radio receivers aboard FORTE observe very-high-frequency (VHF) emissions from the air-breakdown process preceding and (sometimes) accompanying large-scale current flow. Only VHF (and higher) emissions from lightning can reliably penetrate the ionosphere to a satellite, especially along grazing-incidence paths. The National Lightning Detection Network (NLDN) is a ground-based array of sensors in the continental United States (CONUS) observing the low-frequency (LF) and very-low-frequency (VLF) radiation from large-scale vertical currents. Prior to the launch of FORTE in 1997, essentially no work had been done on the statistical correlations between (a) ground-based LF/VLF and (b) spaced-based VHF remote sensing of lightning. During April – September 1998, FORTE was tasked with taking maximum triggered VHF data over and near the CONUS, and NLDN data was specially post-processed in a loosened-criterion mode providing enhanced detection range beyond the CONUS. We found during this campaign ~15,000 correlated NLDN/FORTE detections.

INTRODUCTION : The FORTE satellite (Fast On-Orbit Recording of Transient Events) was launched on 29 August 1997, and carried a highly versatile VHF receiver system. Initial FORTE observations of VHF lightning emissions revealed both Blackbeard-like transionospheric pulse pairs (TIPPs) and more diffuse emissions [*Jacobson et al.*, 1999]. The case was strengthened for a ground-reflection explanation of TIPPs. In addition, since a single satellite cannot determine the location of a VHF emission (other than to constrain that emission to lie within the small circle representing the Earth's limb seen from the satellite), there developed an interest in geolocating, by some other means than FORTE, emission centers associated with VHF signals seen by FORTE. This would allow an important advance in converting datastreams from a satellite into useful and quantitative information about radio emissions from lightning. Such information would include the absolute power and energy at the storm-located source of the VHF emission, as well as the height of the TIPP emission by interpreting the interpulse separation [*Jacobson et al.*, 1999].

In order to do this, we sought to rely on the association of at least some VHF pulses with low-frequency (LF)/very-low-frequency (VLF) sferics deriving from lightning discharges. The National Lightning Detection Network (NLDN) routinely monitors the continental United States (CONUS) and surrounding areas, detecting and geolocating (at >80% efficiency) cloud-to-ground vertical currents of the magnitude that radiate sensible sferics (>10 kA), and also detects and geolocates a certain lesser, though nonzero, fraction of intracloud currents [*Cummins et al.*, 1998; *Idone et al.*, 1998a; *Idone et al.*, 1998b]. The strategy was to seek statistically significant coincidences between NLDN strokes and FORTE VHF timestamps, and then to assign the sferic geolocation (latitude, longitude) to the VHF emission source. We did not know at the outset *how many* FORTE VHF events over the NLDN area should be expected to have an accompanying sferic detectable by NLDN.

RESULTS : Figure 1 shows the innermost coincidence distribution, from -0.2 ms to +0.2 ms, with a 10-μs bin size, for each class of coincident sferic, here restricting our attention to the VHF events having 1/e

width <10 μs. The secondary peak is entirely due to the "0" events, which are distant from the NLDN sensors and are contaminated by ionospheric pathing.

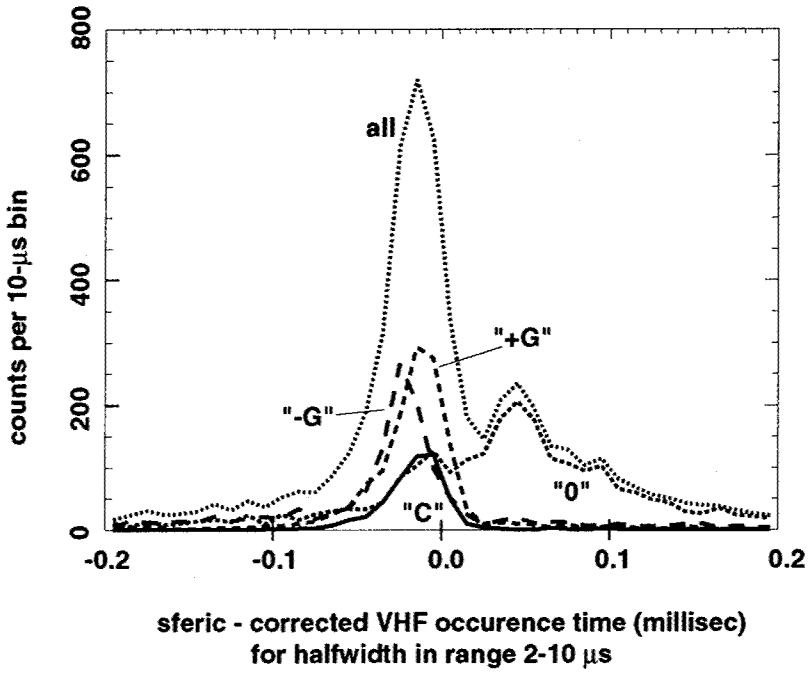


Figure 1: Histogram of NLDN discharge time minus VHF emission time, corrected for time-of-flight of the VHF to FORTE. The discharges are negative cloud-to-ground ("-G"), positive cloud-to-ground ("+G"), intracloud ("C"), and untyped long-range ("0").

On the basis of our findings on a prompt-coincidence peak, we will now accept as "valid coincidences" all those for which the NLDN-FORTE timestamp lag is in the range -0.3 to +0.3 ms. This criterion results 14,985 valid coincidences over the entire six-month campaign. This means we have 14,985 FORTE events that we believe we can geolocate on the basis of their NLDN coincidence.

Figure 2 shows histograms of the total energy emitted (assumed isotropic) in the FORTE VHF pulses, totaled over both time and the 22-MHz bandwidth centered on 38 MHz. Here the VHF pulse energies associated with intracloud and with positive cloud-to-ground discharges are virtually identical. The peak of energies for these two energetic classes of events is at ~0.6 joules in 22 MHz, for a spectral densityof .03 joules/Megahertz. This is similar to the quoted typical energy density in the low VHF in TIPPs observed by Blackbeard [*Holden et al.*, 1995; *Massey and Holden*, 1995; *Massey et al.*, 1998]. One should bear in mind that these FORTE TIPPs' are collected near the radio-noisy CONUS, while Blackbeard's TIPP's were collected largely in quieter equatorial regions. We also note that the Blackbeard TIPPs' source energy was estimated on the basis of assumed, not determined, distances from Blackbeard to the radio emitter.

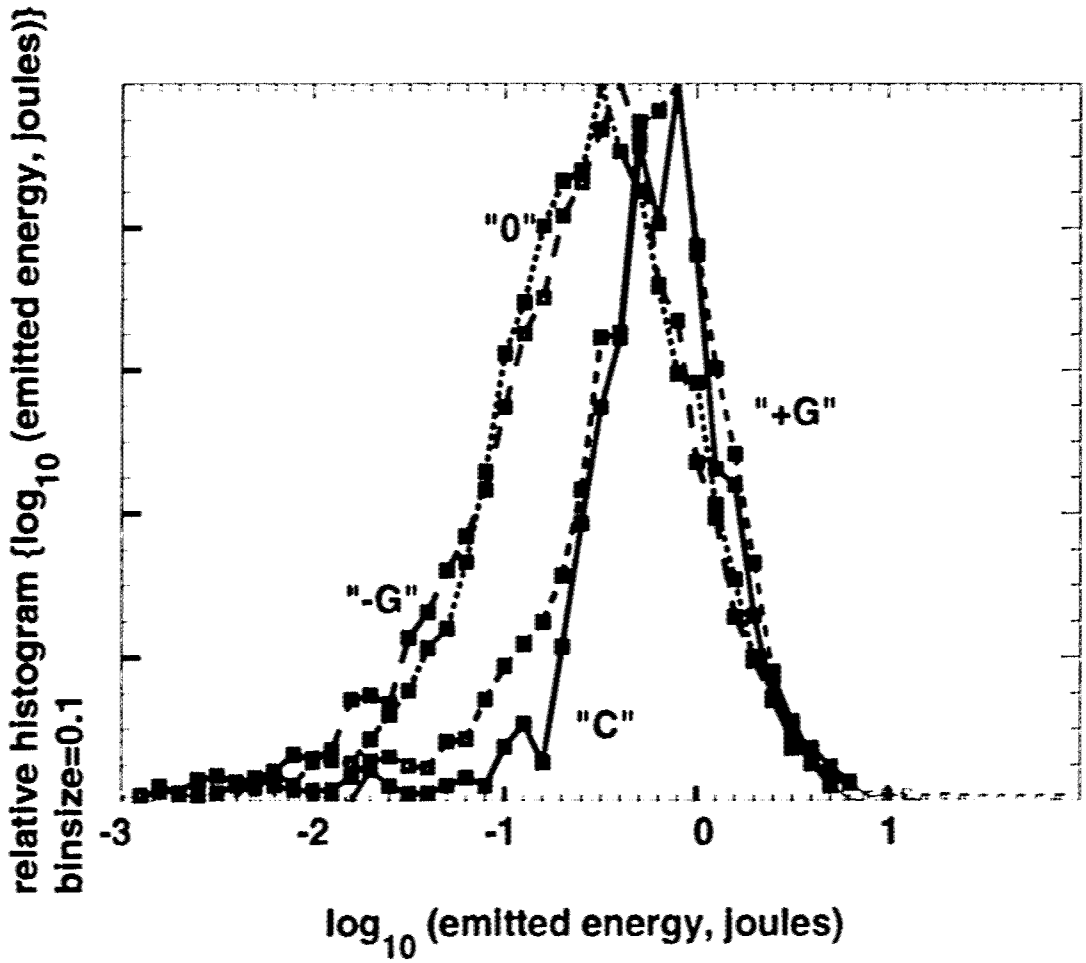


Figure 2: Histograms of total emitted energy in 22-MHz band centered on 38 MHz. Each histogram is separately normalized.

The height of TIPP emissions can be inferred from the time separation of the two pulses in a TIPP, given the geolocation furnished by NLDN. Figure 3 shows the distributions of emission height above ground for both northern CONUS/Canada continental storms and southern/maritime storms. The difference in emission height between these two regions probably reflects the difference in isotherm heights.

On the basis of this and other work on the NLDN/FORTE relationship, we have a good basis to conclude:

(a) NLDN-FORTE coincidences which rise above the accidental coincidence level are prompt within ~40 μs, except for the NLDN strokes which are further than 600 km from the nearest participating NLDN sensor.
(b) FORTE-observed VHF emissions in the North America sector are often as strong as, or stronger than, Blackbeard-observed TIPPs.
(c) Satellite-observed VHF emissions are much more likely to be associated with intracloud sferics than with cloud-to-ground sferics. Satellite-observed VHF emissions are more likely to be associated with positive- than with negative-cloud-to-ground sferics.
(d) Satellite-observed VHF emissions associated with intracloud sferics tend to be narrower in pulsewidth than are VHF emissions associated with either polarity of cloud-to-ground sferics.

(e) TIPPs that are associated with NLDN sferics are even more likely to be associated with intracloud sferics.

(f) TIPPs that are associated with NLDN sferics display a region-dependent emission-height distribution, suggestive of the height-versus-latitude of key isotherms, e.g. -20 C, in the troposphere. Over the CONUS/Canadian interior above 45 deg N, the half-points of the distribution are at roughly 6 and 9 km, and the peak is at 7-8 km. Over the southern maritime region, the peak is at >13 km, and the distribution is broader. We have no statistically significant evidence, amongst the TIPPs which are associated with NLDN sferics, for TIPP-emission heights above 15 km.

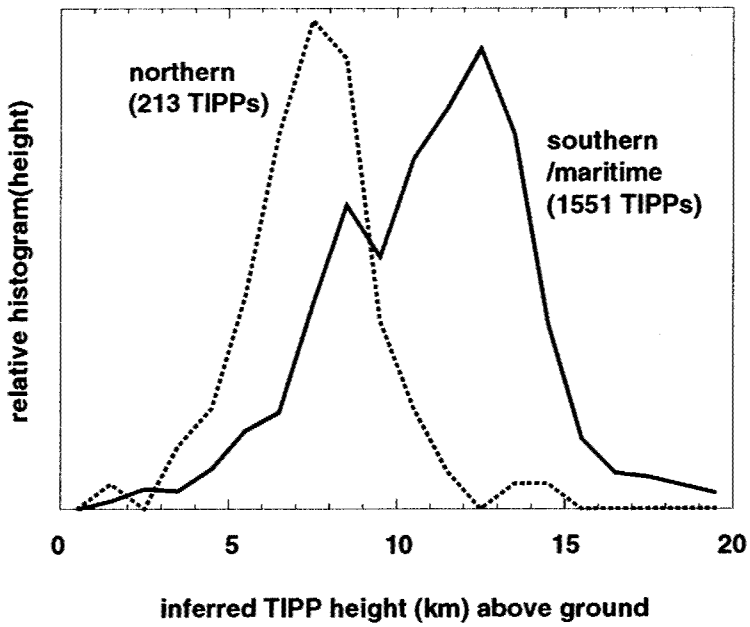


Figure 3: Histograms of inferred TIPP emission height. Each histogram is separately normalized.

Acknowledgement: This work was performed under the auspices of the U. S. Dept. of Energy.

REFERENCES

Cummins, K.L., M.J. Murphy, E.A. Bardo, W.L. Hiscox, R. Pyle, and A.E. Pifer, Combined TOA/MDF technology upgrade of U. S. National Lightning Detection Network, *J. Geophys. Res.*, *103* (D8), 9035-9044, 1998.

Holden, D.N., C.P. Munson, and J.C. Devenport, Satellite observations of transionospheric pulse pairs, *Geophys. Res. Lett.*, *22* (8), 889-892, 1995.

Idone, V.P., D.A. Davis, P.K. Moore, Y. Wang, R.W. Henderson, M. Ries, and P.F. Jamason, Performance evaluation of the U. S. National Lightning Detection Network in eastern New York 1. Detection efficiency, *J. Geophys. Res.*, *103* (D8), 9045-9055, 1998a.

Idone, V.P., D.A. Davis, P.K. Moore, Y. Wang, R.W. Henderson, M. Ries, and P.F. Jamason, Performance evaluation of the U. S. National Lightning Detection Network in eastern New York 2. Location accuracy, *J. Geophys. Res.*, *103* (D8), 9057-9069, 1998b.

Jacobson, A.R., S.O. Knox, R. Franz, and D.C. Enemark, FORTE observations of lightning radio-frequency signatures: Capabilities and basic results, *Radio Sci.*, *in press*, 1999.

Massey, R.S., and D.N. Holden, Phenomenology of transionospheric pulse pairs, *Radio Sci.*, *30* (5), 1645-1659, 1995.

Massey, R.S., D.N. Holden, and X.-M. Shao, Phenomenology of trans-ionospheric pulse pairs, *Radio Science*, *submitted*, 1998.

# THUNDERSTORM AND LIGHTNING STUDIES USING THE FORTE OPTICAL LIGHTNING SYSTEM (FORTE/OLS)

D. Suszcynsky[1], M. Kirkland[1], P. Argo[1], R. Franz[1], A. Jacobson[1], S. Knox[1], J. Guillen[2], J. Green[2], and R. Spalding[2]

[1]Los Alamos National Laboratory, Space & Atmospheric Sciences Group, MS D466, Los Alamos, NM 87545
[2]Sandia National Laboratories, Sensors and Electronics Dept., MS 0972, Albuquerque, NM 87185

ABSTRACT: A summary of FORTE/OLS satellite observations and analysis is presented with emphasis on correlating the OLS data with the FORTE/VHF and National Lightning Detection Network (NLDN) data sets. General statistics for the photo-diode (PDD) data are presented. Optical signals are detected both as individual events and as sequences of events associated with cloud-to-ground (CG) and intra-cloud (IC) flashes. The optical signals in concert with the associated VHF signals can be used to discriminate between CG and IC strokes and can also be used to deduce values for the mean cloud scattering delay of the emitted light. The benefits of a dual phenomenology approach to the detection and identification of lightning from space are discussed. PDD/NLDN correlation statistics are analyzed and used to estimate the sensitivity of the PDD to different types of lightning.

## INTRODUCTION

Space-based observations of lightning and thunderstorms in both the radio frequency (RF) and optical parts of the electromagnetic spectrum have been made since the 1960s. These efforts have resulted in significant insight into the phenomenology and science of lightning at the thunderstorm level, primarily through studies of global flash rate distributions/estimates and through statistical characterizations of observed lightning signals from either RF or optical waveform measurements (e.g. see review by *Goodman and Christian* [1993]). However, significant progress in conducting satellite-based studies of lightning at the stroke level has been limited, in particular, because dual phenomenology (joint RF/optical) measurements with sufficient time resolution (< 10 μs) have not generally been available. This situation was recently remedied with the Aug. 29, 1997 launch of the Fast On-Orbit Recording of Transient Events (FORTE) satellite. The satellite carries VHF broadband radio receivers and an Optical Lightning System (OLS) that provide dual phenomenology, high-time resolution observations of lightning transients on a routine, automated basis. This paper presents an overview of thunderstorm and lightning studies conducted to date using the FORTE/OLS. The operation of the OLS as both a collective system and as individual instruments, and the analysis of its data in tandem with other data sets allows us to study basic lightning emission processes, the effects of clouds on the propagation of light transients, and general lightning phenomenology at the stroke level.

## INSTRUMENTATION

FORTE is situated in a nearly circular, 70°-inclination orbit of approximately 825-km altitude. The instrumentation used for this study includes the two narrower-band 20 MHz FORTE VHF receivers as described in *Jacobson et al.*, [1998], and the FORTE/OLS sensor package. OLS consists of two instruments: (1) a broadband silicon photodiode detector (PDD) which is described in *Kirkland et al.*, [1999], and (2) a narrow-band CCD array called the Lightning Location System (LLS) that provides imaging and geolocation of optical transients. The PDD is a broadband (0.4 - 1.1 micron) silicon photodiode detector that collects amplitude versus time waveforms of lightning transients. The instrument has an 80° field-of-view which provides a footprint of about 1200-km diameter and is usually configured to collect 1.92 ms records with 15 μs time resolution. A data record is typically collected whenever the detected signal exceeds a preset, noise-riding, amplitude threshold for 5 or more consecutive samples. This protocol eliminates false triggers due to energetic particles. The PDD provides 12-bit sampling with a piece-wise linear dynamic range covering 4 orders of magnitude and with a sensitivity of better than $10^{-5}$ W/m$^2$. Several background compensation modes allow the instrument to be operated both at night and at a reduced sensitivity in the day. The LLS is a narrowband (10 Angstrom FWHM at 777.4 nm), 128 x 128 pixel CCD imager that geolocates optical transients to within a pixel size of 10 km x 10 km. The field-of-view of LLS is comparable to that of the PDD. The instrument reports event location and time-integrated amplitude (energy) whenever the time-integrated signal in any one pixel exceeds the pre-set threshold level for one or two successive sample periods (1 sample period = 2.38 ms). Once triggered, the signal levels for the entire array are read out. An anti-glint filter ignores signals which persist for more than 2 sample periods.

## OBSERVATIONS

Table 1 presents statistics on 592307 PDD waveforms collected from Sept. 7, 1997 through Feb. 16, 1999 (*Kirkland et al.*, [1999]). Particle and noise events have been removed from the data set. The source peak power and source energy estimates are arrived at by assuming a point source at the subsatellite point (when geolocation is not available) with no atmospheric extinction and a satellite altitude of 825 km. The geolocations of many of these events are routinely determined by both NLDN and FORTE/LLS reports. Consequently, the events can be associated with and analyzed in terms of meteorological data sets such as NEXRAD radar and satellite imagery.

TABLE 1. PDD statistics on 592307 lightning events collected from Sept. 7, 1997 to Feb. 19, 1999.

| Quantity | Minimum | Median | Maximum |
|---|---|---|---|
| Peak Irradiance ($W/m^2$) x $10^{-3}$ | 0.04 | 0.12 | 460 |
| Est. Source Peak Power (GW) | 0.34 | 1.0 | 3900 |
| Energy ($J/m^2$) x $10^{-6}$ | 0.36 | 0.70 | 56000 |
| Est. Source Energy (MJ) | 0.003 | 0.60 | 480 |
| Effective Pulse Width (μs) | 37 | 540 | 1740 |

Figure 1 demonstrates the basic phenomenology of CG optical signals at the stroke and flash level and compares the signals to simultaneous observations of the FORTE/VHF instruments and the NLDN array. Figure 1a shows a sequence of four consecutive PDD triggers that occur over a 0.25 s time interval. The vertical spikes are actual PDD waveforms that appear compressed because of the large time scale displayed. The triangles mark the NLDN-reported times of three strokes of a three-stroke negative CG flash. Figure 1b shows a corresponding sequence of three consecutive VHF waveforms collected over the same time interval. Figures 1cde present the detailed comparison of the three VHF/optical pairs in the flash. The VHF waveforms are displayed on an arbitrary amplitude scale to facilitate time comparisons with the optical waveforms. In each case the VHF trigger is seen to precede the optical trigger by up to a few 100's of μs, depending on how the time delay is measured (*Suszcynsky et al*, [1999]). Figures 1fgh show the spectrograms for the three VHF records displayed in figures 1cde. The spectrograms plot the signal power expressed in dBm (color bar) as a function of frequency and time and show features that are uniquely characteristic of CGs (see DISCUSSION). The arrows below the spectrograms indicate the NLDN-reported stroke times and aid in the identification of lighting type. The data is also populated with examples of likely IC flashes, although the NLDN array is generally insensitive to IC activity. Instead, we identify candidate IC flashes by searching for time intervals (1 ~ 10 ms) between successive triggers that are characteristic of IC activity. As with the CG example, the VHF signal precedes the optical signal by ~ 10 - 100 μs and the spectrograms show features that are unique to IC's (see DISCUSSION).

## DISCUSSION

The characteristics of the optical and VHF waveforms and spectrograms for CG and IC pulses can be associated with specific types of lightning activity by comparing the data to NLDN ground truth and the previous literature on ground-based measurements of optical and VHF emissions from lightning. The details and vindication of these associations are discussed in *Suszcynsky et al.*, [1999]. Briefly, the VHF spectrograms can be used almost exclusively to determine detected lightning types. The spectrogram shown in figure 1f is typical of first return strokes. The first 500 μs of the record contains VHF emissions associated with a stepped leader, followed by a 100 μs burst of additional VHF associated with the actual return stroke. The spectrogram in figure 1h is typical of subsequent strokes and shows VHF radiation from the dart leader, terminating at the time of the return stroke. For return strokes, the optical signatures do not show characteristics that can be used to uniquely discriminate between first and subsequent strokes. However, there is a tendency for subsequent stroke optical signals to be more symmetric about the peak than for first return strokes. This may be due to a contribution of the dart leader to the overall optical signal. The VHF spectrogram signals for IC flashes (not shown) are characterized by impulsive bursts of radiation with durations on the order of 1 - 20 μs (*Jacobson et al.*, [1999]; *Suszcynsky et al.*, [1999]). The corresponding optical signatures for IC pulses are generally weaker and more highly structured than those for CGs, although they are not unique predictors of IC activity.

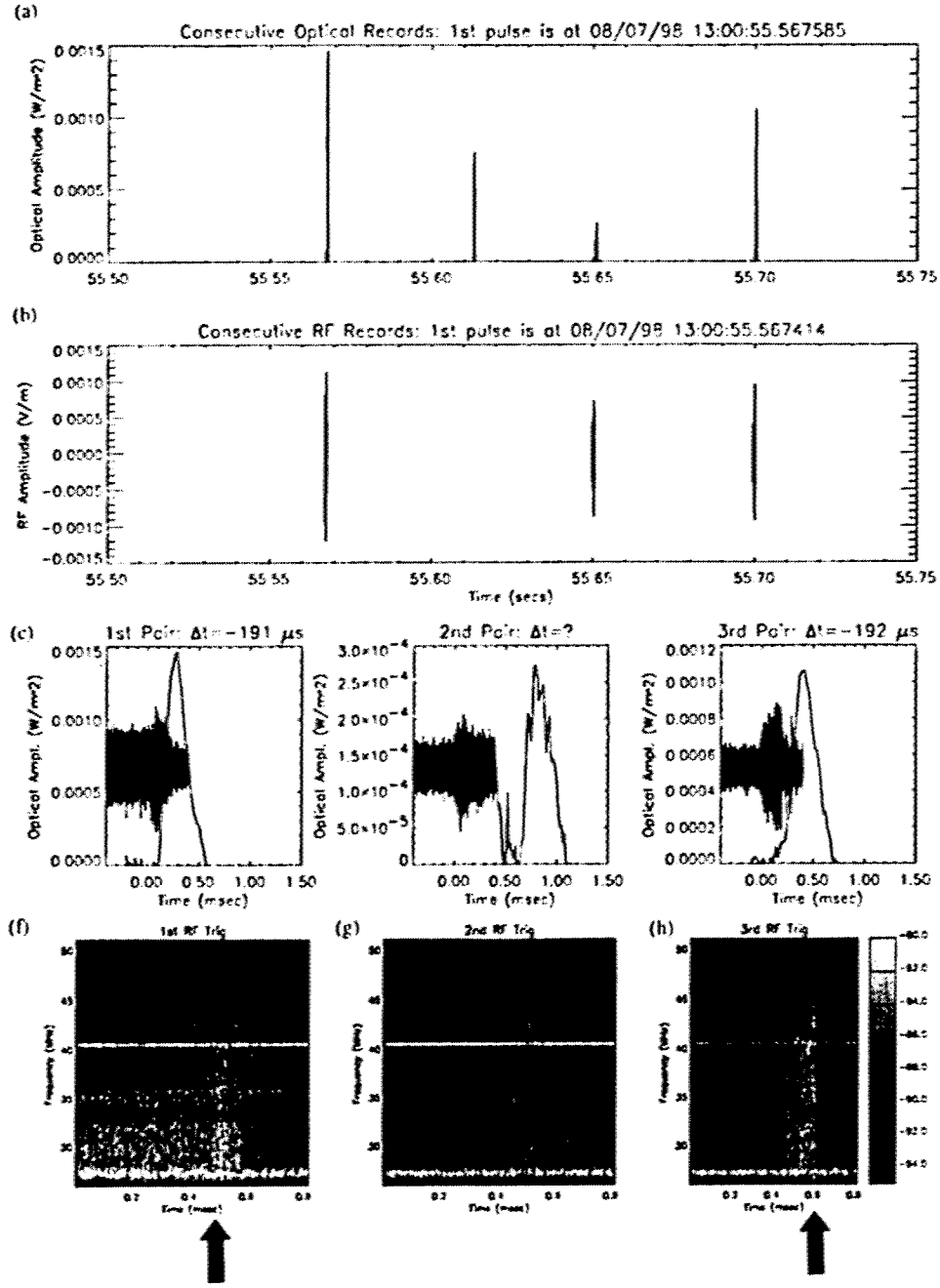


Figure 1. Example of a -CG flash. (a) Optical triggers, (b) coincident VHF triggers, (cde) detailed view of VHF/optical pairs, (fgh) VHF frequency-time spectrograms corresponding to VHF events (cde).

It is already clear from this initial analysis that a consideration of VHF signatures of lightning in tandem with optical data can greatly enhance a satellite's ability to discriminate lightning types from space. Some discrimination information can be found in the optical waveforms, however, the bulk of the discrimination capability in the FORTE instruments seems to lie in the interpretation of the VHF spectrograms. By analyzing a set of 237 randomly selected VHF and optical lightning trigger pairs, we find that we can distinguish between initial return strokes, subsequent return strokes and intra-cloud discharges at a better than 90% confidence level.

The degree to which the VHF signal precedes the optical signal is also an important parameter to measure since the delay in the arrival of the optical signal at the satellite can be related to the mean scattering delay of light due to

its propagation through the clouds, $<\Delta t_{scatt}>$. More generally, the light will experience both a delay and a broadening during its transit through the cloud. An experimental determination of $<\Delta t_{scatt}>$ can be used to "truth" existing light propagation models and can be facilitated by studying PDD lightning triggers that are in time coincidence with NLDN-reported events. To this end, $<\Delta t_{scatt}>$ was estimated by measuring the broadening of the optical pulses due to cloud transit, $w_{FORTE} - w_{source}$. The width of the detected optical pulse, $w_{FORTE}$ , was measured by integrating the full optical waveform over time and then dividing by the peak irradiance to arrive at an effective pulse width (*Mackerras et al.*, [1965]). The effective pulse width at the source, $w_{source}$, was estimated to be about 200 μs based on previous ground measuements of CG events (e.g. *Mackerras et al.*, [1965]).

Using the above technique, a $<\Delta t_{scatt}>$ value of 143 μs was measured for the 237 VHF/optical pairs mentioned above (*Suszcynsky et al.,* [1999]). The 237 correlations were found to be almost exclusively associated with CG strokes based on comparisons with NLDN data and with the stroke taxonomy illustrated in figure 1. Using the same $<\Delta t_{scatt}>$ measurement technique on the entire PDD data set, *Kirkland et al.*, [1999] found a mean $\Delta t_{scatt}$ of about 447 μs. The discrepency between the two results is apparently a function of lighting type. *Kirkland et al.* [1999] did not distinguish between CG and IC-sourced light. Since IC pulses are the predominant type of lightning and since the IC light signals detected by FORTE are generally broader and more structured than those associated with CGs, the inclusion of IC light in the *Kirkland et al*, [1999] statistics tends to bias the estimate for $<\Delta t_{scatt}>$ to larger values than those associated with just CGs. In fact, when the Kirkland et al. [1999] analysis is redone to include only those PDD triggers for which there was a NLDN negative CG report, we find a $<\Delta t_{scatt}>$ of about 203 μs, much closer to the 143 μs value measured for the 237-event study. The $<\Delta t_{scatt}>$ results are also in general agreement with the *Thomason and Krider*, [1982] model. For a light transient sourced at the center of a cloud of optical depth 200 and water drop diameter of 10 μ (moderate maritime cumulonimbus (Cb)), the model predicts a $<\Delta t_{scatt}>$ of about 51 μs (15 km increased path length) while the predicted value for an optical depth of 400 (strong maritime Cb) is 130 μs (39 km increased path length).

Finally, in order to estimate the relative sensitivity of the PDD to different types of lightning signals, a correlation study between the PDD and NLDN data sets was carried out for the April - July, 1998 time interval. Events were termed coincident if the PDD detected a lightning event within 5 ms of a reported NLDN event within the PDD field-of-view. Using these criteria, the PDD detected 5.5% (3623/65979) of the -CG events that were available for detection, 8.3% (651/7844) of the +CG events, and 14.5% (201/1383) of the IC events. Since 85% of the PDD triggers collected for this study had no associated NLDN correlations, and since NLDN is generally insensitive to IC activity, we conclude that the PDD predominantly detects in-cloud activity. "In-cloud" activity in this paper is defined as IC lightning and the in-cloud portion of CG lightning, including K-events which are known to produce optical emissions that can rival those of return strokes (*Goodman et al.*, [1988]). These results are consistent with the $<\Delta t_{scatt}>$ measurement comparison discussed above.

ACKNOWLEDGEMENTS: This work was supported by the US Dept. of Energy. The authors would also like to acknowledge the contributions of the Marshall Space Flight Center to the design/fabrication of the LLS instrument.

REFERENCES

Goodman, S. J., H. J. Christian, and W. D. Rust, A comparison of the optical pulse characteristics of intracloud and cloud-to-ground lightning as observed above clouds, *J. Applied Meteor., 27*, 1369-1381, 1988.

Goodman, S. J. and H. J. Christian, Global Observations of Lightning, in Atlas of Satellite Observations Related to Global Change, Cambridge University Press, ed., 191-219, 1993.

Jacobson, A. R., S. O. Knox, R. Franz, D. C. Enemark, FORTE observations of lightning radio-frequency signatures: capabilities and basic results, submitted to *Radio Sci.*, 1998.

Kirkland, M. W., D. M. Suszcynsky, R. Franz, J. L. L. Guillen, J. L. Green, Observations of terrestrial lightning at optical wavelengths by the photodiode detector on the FORTE satellite, submitted to *J. Geophys. Res.*, 1999.

Mackerras, D., Photoelectric observations of the light emitted by lightning flashes, *J. Atmos. Terr. Physics, 35*, 521-535, 1973.

Thomason, L. W. and E. P. Krider, The effects of clouds on the light produced by lightning, *J. Atmos. Sci., 39*, 2051-2065, 1982.

# DETECTION RATES OF LIGHTNING GENERATED RADIO EMISSIONS BY FORTÉ

R.S. Zuelsdorf[1], A.R. Jacobson[2], M. Kirkland[2], R.J. Strangeway[1], C.T. Russell[1]

[1]Institute of Geophysics and Planetary Physics, University of California, Los Angeles, U.S.A
[2]Los Alamos National Laboratory, Los Alamos, New Mexico, U.S.A.

ABSTRACT: Near-continuous observation at 38 and 130 MHz by the FORTÉ satellite has enabled a global investigation of the radio processes associated with lightning. Using FORTÉ data acquired between 1 November 1997 and 31 August 1998 we are able to determine the rates of RF detection for the entire globe during the months sampled. Here we present rate maps of all detected RF signals, signals with the characteristic 2nd pulse of a TIPP, and hard TIPPs of the kind previously detected by the ALEXIS spacecraft - those in which the peak power as detected in the 130 MHz centered band is at least 30% of the peak power detected in the 38 MHz centered band. Areas of greatest detection are the continental equatorial regions and from Indonesia up into India, but moderate levels of detection persist even over the oceans. Whereas the rate of detection of lightning with the characteristic second pulse of a TIPP is about half the rate of all detected RF pulses, the rate of hard TIPP detection is a small fraction of total RF detection. Analysis of the data three months at a time reveals the migration of lightning occurrence northwards from November throughout August. We also monitor the background noise in the eight 1-MHz sub-bands of both 20 MHz bands. By comparing the levels of background noise with the peak amplitude of the natural pulses detected, we determine what portion of the lightning generated signals is lost in the background noise.

## INTRODUCTION

The Los Alamos satellite FORTÉ provides the first near-continuous space observation of lightning generated radio emissions. Launched into its 800 km 70 degree inclination orbit on 29 August 1997, the VHF radio receivers on FORTÉ serve to continue the mission started with the Blackbeard instrument on board the ALEXIS satellite. From 1993 to 1997 Blackbeard detected short bursts (4 microseconds) of paired VHF radio noise which were dubbed Trans-Ionospheric Pulse Pairs (TIPPs) [*Holden et al.*, 1995]. These signals were about 100 times more powerful than regular RF lightning emissions. When the detection of these pulses were plotted over the globe it was established that TIPPs are clearly associated with lightning activity [*Zuelsdorf et al.*, 1997]. In 1997 when the first FORTÉ data were recorded and analyzed it was soon discovered that the new satellite was detecting in abundance what Blackbeard saw occasionally. The number of TIPPs FORTÉ detected in a day of observation approximately equalled what Blackbeard detected in a month. It was soon discovered that FORTÉ was detecting two distinct flavors of TIPPs: hard TIPPs with the power detected in the 130 MHz centered band being at least 30% of that in the 38 MHz centered band, and soft TIPPs with the signal power more predominant at low frequencies. Because Blackbeard required the signal integrated over its entire bandwidth, less than 75 MHz, to exceed a threshold value before a triggered sample was recorded, it is believed that Blackbeard detected the harder variety of TIPP [*Jacobson et al.*, 1998].

In addition to the detection of TIPPs, the greater sensitivity of FORTÉ has allowed it to detect other lightning generated signals that were previously missed by Blackbeard. These signals are associated with intracloud and cloud-to-ground lightning activity. Making use of this data, we are able to plot the worldwide detection rates of lightning generated RF signals and show how the rates and locations of occurrence vary seasonally. The rates and extent of RF lightning is of interest in comparison with optical lightning detectors such as the Lightning Imaging Sensor (LIS). Here we show that lightning generated RF signals are detected over a much wider area than optical emissions. We also plot the occurrence maps of soft and hard TIPPs. Although all TIPPs are generated in lightning producing regions of the world, the detection rates of hard TIPPs are much less than the rates for soft TIPPs. The regions of hard TIPP detection are very similar to those determined from Blackbeard.

## INSTRUMENTATION

FORTÉ monitors RF emissions by means of its two RF receivers. Until recently these receivers could be tuned to two different 22 MHz bands in the 20-300 MHz range. For this study, one receiver was tuned to a center frequency of 38 MHz, while the other was tuned to a center frequency of 130 MHz. Sampling is performed at 50 Msamples/sec. Typically 400 ms records are recorded for each receiver for each triggered event: 100 ms of pre-trigger samples and 300 ms of post-trigger samples, for a total of .8 seconds. The memory on FORTÉ allows for approximately 2000 events between downloads, that when combined with several downloads a day enables the detection of 10,000 events per day.

FORTÉ can trigger on a signal in either its high-band, low-band, or a combination of both. In this case, low-band triggering was used. The triggering mechanism used utilizes eight 1-MHz sub-bands embedded in the 38 MHz centered band. If the signal in usually 5 of the 8 sub-bands exceeds the threshold value, the system triggers. The threshold value is usually 20 dBm over the background in each sub-band. The background levels are averaged over a period of 2.2 ms and are recorded every 4 seconds. FORTÉ is able to retrigger within microseconds of recording an event, thus essentially allowing a continuous observation of VHF activity.

The two receivers are tied to FORTÉ's single two-polarization log-periodic antenna. The attitude of the spacecraft is designed so that an approximate VHF null is placed on the limb of the earth as seen be FORTÉ and with maximum reception at the nadir. At the equator this gives a footprint with an arc-diameter of approximately 6100 km. The 3 dB footprint however has a 40 degree half angle as measured from the spacecraft. This is equivalent to an arc-diameter of approximately 1400 km at the equator, or 12.6 degrees of longitude. Reception falls off rapidly for any signal outside this 3 dB region. The low-band triggering receiver could be set to either linear polarization of the antenna, but little to no difference was seen between the polarizations for low band.

## RESULTS

We utilize the near-continuous observation of FORTÉ to generate rate of detection maps for all RF generated lightning signals (including TIPPs), for all TIPPs, and for only hard TIPPs. Figure 1 is a contour map of all lightning generated RF detected signals. The contours are the base 10 logarithm of the number of signals detected per second per steradian. Blackened areas are regions of insufficient sampling. Although the varying thresholds throughout the globe (there are more anthropogenic background signals over

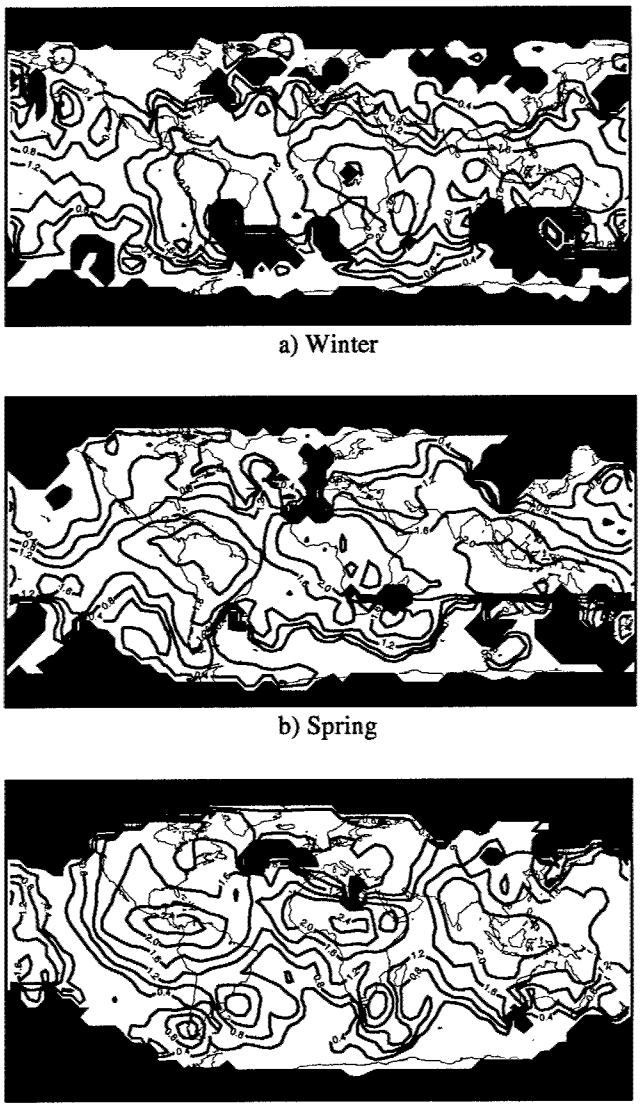

a) Winter

b) Spring

c) Summer

Figure 1. Contours of all RF lightning detection. Contours in $\log_{10}$(events/sec/steradian)

Figure 2. Contours of total TIPP detection in Spring
$\log_{10}$(events/sec/steradian)

industrial regions than non-industrial regions) prevent rigorous inter-regional comparison, they do not prevent the detection of the seasonal variation over fixed geographic regions. Panel a,b, and c represent northern hemisphere winter, spring, and summer respectively. We can observe the migration of lightning northward during these seasons. It is easy to see the vast increase in North American lightning activity from winter to summer. Although we see that lightning is mainly an equatorial and continental phenomenon, we do see more activity than expected over the distant oceans given the narrow 3 dB footprint. Figure 2 and Figure 3 are the representations of all TIPP and only hard TIPP detection respectively for the spring months. We see that the regions of detection are more or less the same, although the rates are different: TIPP rates are about 1/2 of the total RF, whereas hard TIPP detection is a much smaller fraction.

As mentioned, different levels of background radiation throughout the world make inter-regional comparisons difficult for Figures 1 through 3. Figure 4 is a map of the background noise observed in the 39 MHz sub-band. Contours are in mV/m, representing the amplitude of the electric field incident upon the antenna. The noise is more widespread in this sub-band than the others, but is displayed here because it clearly shows the problem in detecting RF lightning over developed regions.

Figure 5 is an attempt to account for background noise by plotting only the summer RF signals with an incident field greater than .18 mV/m. This value is just over the median value of the RF lightning distribution over the eastern U.S. and is sufficiently large to be detected over the threshold everywhere. Thus if we believe the amplitude distribution is essentially the same for all continental regions, Figure 5 allows for inter-region comparison. We can see that for the northern hemisphere summer lightning rates over North America are comparable to Indonesia, but greatly exceed those over Africa, which do not even register on the plot. An alternative explanation is that storms over Africa are not as powerful as the North America or Indonesia storms. Also missing is the oceanic activity. Again this can be indicative of less powerful processes in oceanic lightning.

Figure 3. Contours of hard TIPP detection in Spring
$\log_{10}$(events/sec/steradian)

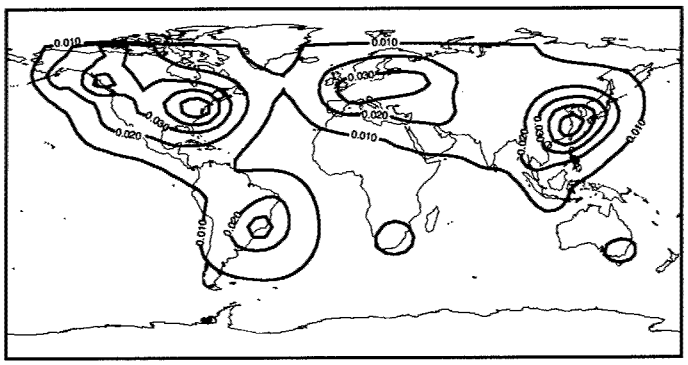

Figure 4. Contours of background radiation
at 39 MHz (mV/m)

SUMMARY

The use of the FORTÉ satellite allows for the near continuous observation of all lightning generated VHF signals, including TIPPs. Using data running from November 1997 throughout August 1998, we have produced rate of detection maps for all RF lightning signals, all TIPPs, and hard TIPPS. We observe a seasonal migration in RF lightning and see that hard TIPPs represent a small subset of that activity. As one might expect, most lightning activity was detected over continents and near the equator, however given the 3 dB footprint we detect more oceanic activity than would be expected from signals "leaking" from the continents. When we attempt to compensate for background radiation by plotting only signals sufficiently over the antrhopogenic signals, only North America and Indonesia show strong activity. This indicates that either the rates in these regions are greater than in Africa or the signals are stronger. The lack of ocean activity may likewise indicate either lower rates or a less powerful process.

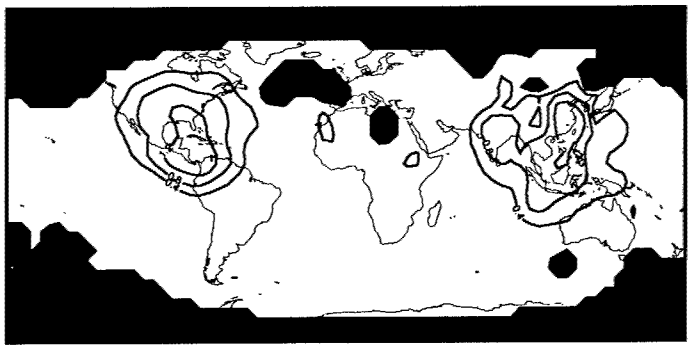

Figure 5. Contours of all RF lightning detection
with an amplitude greater than .18 mV/m
$\log_{10}$(events/sec/steradian)

ACKNOWLEDGEMENTS: This research was supported in part by a grant from the University Collaboration Research Program of the IGPP/LANL.

REFERENCES

Holden, D.N., C.P. Munson, and J.C. Devenport, Satellite observations of transionospheric pulse pairs, *Radio Science*, 30, 1645-1659, 1995.

Jacobson, A.R., S.O. Knox, R. Franz, and D.C. Enemark, FORTÉ observations of lightning radio-frequency signatures: capabilities and basic results, submitted to *Radio Science*, 1998.

Zuelsdorf, R.S., R.J. Strangeway, C.T. Russell, C. Casler, H.J. Christian, and R.C. Franz, Transionospheric pulse pairs (TIPPs): their geographic distribution and seasonal variations, *Geophys. Res. Lett.*, 24, 3165-3168, 1997.

**Satellite Observations of Transient Radio Impulses from Thunderstorms**

P. E. Argo, M. Kirkland, A. Jacobson, R. Massey, D. Suszynsky, K. Eack, T. J. Fitzgerald, D. Smith
Space and Atmospheric Sciences Group, Mail Stop D466, Los Alamos National Laboratory, Los Alamos, New Mexico 87545

ABSTRACT: Transient radio frequency emissions from thunderstorms detected by satellites were first reported in 1995. The nature and source of these emissions remained a mystery until the launch of the FORTE satellite in 1997. FORTE, with its more sophisticated triggering and larger memory capacity showed that these emissions were connected to major thunderstorm systems. The analysis reported here, connecting FORTE RF events with ground based lightning location data from the National Lightning Detection Network (NLDN), shows that localized regions within thunderstorms are responsible for the creation of the satellite detected RF signals. These regions are connected with the areas of strong radar returns from the NEXRAD Doppler radar system, indicating that they are from regions of intense convection. We will also show data from several storms detected in the extended Caribbean, in which the height profile of the source regions can be determined. Although as a single low earth orbit satellite FORTE cannot provide global coverage of thunderstorm/lightning events or locate single lightning flashes, follow-on satellite constellations should be able to provide detailed information on global lightning in near real-time.

INTRODUCTION

Over the past several years we have reported observations of transient radio impulses observed by Earth-orbiting satellites. The first reported observations (Holden, et al., 1995), from the ALEXIS/Blackbeard satellite, indicated the existence of brief (a few microseconds long) pulses, often seen as pairs of pulses that were dispersed in such a way to imply that they had undergone trans-ionospheric propagation. Blackbeard's memory and triggering limitations constrained detections to a few events per orbit. With the limited data set available from the Blackbeard observations it was not clear whether the source of these pulses was anthropogenic or natural. With the advent of the FORTE satellite, with its multi-channel triggering, increased sensitivity and enlarged memory configuration, we often acquire thousands of narrow pulse events during a single transit of the tropics or a few tens to hundreds of events observed during transits of the United States. From these recurrent emissions we were able to show that the pulse dispersion and pulse pair separation are consistent with a model of a source at high altitude (8-20 km) and a subsequent reflection from the ground (Jacobson, et al.,1999a). In addition, we often detected more classical structured emissions believed to come from normal lightning activities.

The FORTE observations have allowed us to collect a wealth of data on RF emissions emanating from thunderstorm regions. With the multi-channel trigger we are able to detect not only the very bright TIPP events observed by Blackbeard, but also weaker distinct pulses and diffuse RF emissions from lightning processes. A complex and involved analysis routine has been used to sort through the FORTE data, and to identify various forms of RF lightning returns (Jacobson, et al, 1999a,b). These tend to fall into three categories: 1) the pair of narrow RF pulses believe to be representative of a high altitude (8-20 kilometer) discharge and its reflection from the ground (TIPPs); 2) an extended train of apparently distinct and discrete pulses (believed to correspond to recurrent leader emissions); and 3) many dispersed traces, overlapping with each other and with poor contrast between peak and median instantaneous intensity, typical of diffuse lightning emissions.

This paper is intended not to provide rigorous scientific observations on the development or the characteristics of thunderstorms, since the sparseness of FORTE overpasses (both temporally at one location and in global coverage) do not lend themselves to that. Rather we will try to show how a follow-on system capable of global coverage could provide a rich data set in both individual storm development and in global storm conditions. It is important to note that the lightning flashes discussed in this paper are not just the TIPP events usually discussed in the FORTE and Blackbeard data, but also include the more classical structured and diffuse emissions. We will show that there are distinct differences between the continental thunderstorms and those detected in the tropical Caribbean.

OBSERVATIONS

The ground based lightning detections and locations in this study are done using historical data provided by the National Lightning Detection Network (NLDN) (Cummins et al.,1998). This network, which utilizes more than 100 sensors, has a median location accuracy of about 500 meters, and a CG flash detection efficiency of 80% to 90% for

stroke currents greater than 10 kA. The wide-band magnetic direction finders were designed to optimize detection of cloud-to-ground strokes, and in fact minimize the detection of intracloud strokes.

In this paper we will discuss a subset of the FORTE detections that are coincident with lightning strokes detected and geolocated by the National Lightning Detection Network. Using this coincidence to identify a location of the source of the FORTE detected signal, we find that the sources of these events are not only connected to the thunderstorm, but also usually come from very localized regions within the thunderstorm. For storms over the continental United States, where Doppler radar data are available, the localized regions of FORTE detected lightning are spatially coincident with regions of strong Doppler radar echoes. Since the strong radar echoes come from the regions of intense convection within the thunderstorm, we surmise that these same regions are responsible for the FORTE events, indicating that the lightning activity creating strong FORTE RF signatures is occurring in the strong convective regions within thunderstorm systems. Although in most cases the NLDN network is detecting lightning from an extended region around these discrete patches of strong convection, the majority of NLDN lightning locations also are in these regions.

*May 26, 1998*

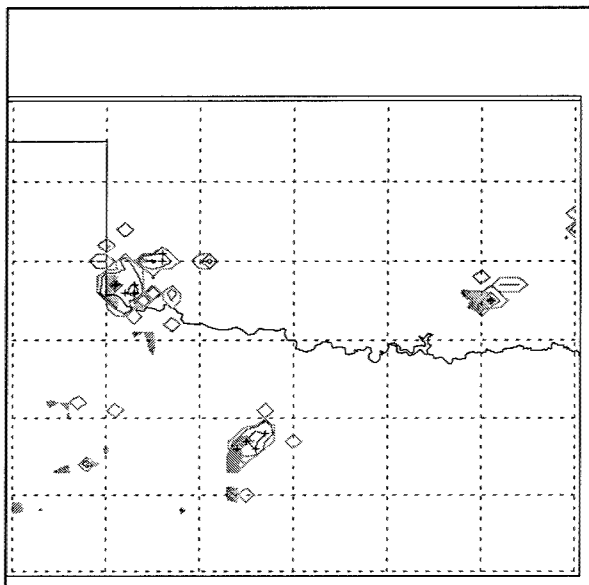

Figure 1. A map of the Texas panhandle region for 0500UT May 26, 1998 showing the relationship of the strong (>45dBz) NEXRAD radar echoes in gray, the NLDN lightning strike density (contours), and the FORTE detections (+'s).

At approximately 0500UT on May 26 the FORTE satellite was descending along the West Coast of the United States, and detected emissions from a pair of storms in Texas. Figure 1 is the radar reflectivity map taken at 0500UT and the combined NLDN and FORTE lightning detections during the overpass period. In Figure 1 the black pluses are the geolocated FORTE detections (locations gotten from the connection to NLDN lightning strikes), and the contours show the NLDN strike density. The NEXRAD data for echo strengths above 45 dBZ are plotted in gray. Note that generally there is an indication that the FORTE detections occur in the regions of highest radar return. During this time, as seen in the NEXRAD map, most of north Texas was undergoing stormy conditions. Two larger regions showed strong reflectivity echoes, one just east of the panhandle (on the Oklahoma border), and the other was north of Dallas. Smaller regions of strong echoes trailed westward across the state. The FORTE and NLDN returns come from the two regions connected to the high reflectivity echoes. The closeness of detected locations is striking in this case, where the time differences between maps were only a few minutes. In this case not a single TIPP event was identified and localized to this storm.

*Caribbean Storms*

We were also able to use FORTE/NLDN coincidence data for lightning events occurring over the extended Caribbean region (including the west Atlantic and east Pacific). In this area the NLDN data has reduced accuracy, and is unable to classify events, but still has geolocation capabilities acceptable for the requirements of this study. The lightning events observed over this Caribbean region were parts of larger ensembles of events clearly coming from storm systems, as observed both by NLDN and the FORTE overpasses. Using a geolocation technique described by Argo et al (1999) and the few FORTE/NLDN coincidence geolocations, we could connect a larger set of FORTE lightning detections to the given storm. Using this larger data set we will show how FORTE could be used to study macro-scale storm characteristics.

We chose nineteen storm systems within the extended Caribbean tropics (including the Western Atlantic and the Eastern Pacific) that had distinct and separable FORTE lightning data as well as NLDN/FORTE coincidences. Figure 2 shows the locations of these storms as the black asterisks. In all these cases the amount of FORTE data far

exceeded the number of coincidences with the NLDN system, and we used the geolocation technique described in Argo, et al (1999) to include this larger data set. In all of these events the ratio of TIPP events to total lightning events was at least 50%, and in several cases was greater than 70%. This is distinctly different from the CONUS storms discussed above, where this ratio was generally less than 10%. By using the time differences between the pair of pulses in the TIPP events we determine the height of the RF emission region, using the model discussed in Jacobson, et al (1999a). Figure 2 also shows the height distributions for these emission regions for all of the events. Although the values are normalized to the maximum count in the height distribution for each event, thee were from twenty to almost one hundred events in the peak bin for each storm selected. There is a tendency for the peak heights to be greater than 12 kilometers, in agreement with Jacobson, et al (1999b), but distinctly different from what the authors found for the ensemble of CONUS storms, where the height of the peak was about 8 km. In almost all profiles there is evidence of a bimodal distribution, with a lower peak at 5 to 7 kilometers. We are not sure whether this is real, or is an artifact of not isolating storm data sufficiently. One storm region was observed twice, several days apart. These observations are marked in Figure 2 by letters **a** and **b**. Another storm, marked as **c** and **d** in Figure 2, was observed at two times separated by almost 24 hours. In both cases the storm height profiles were very similar.

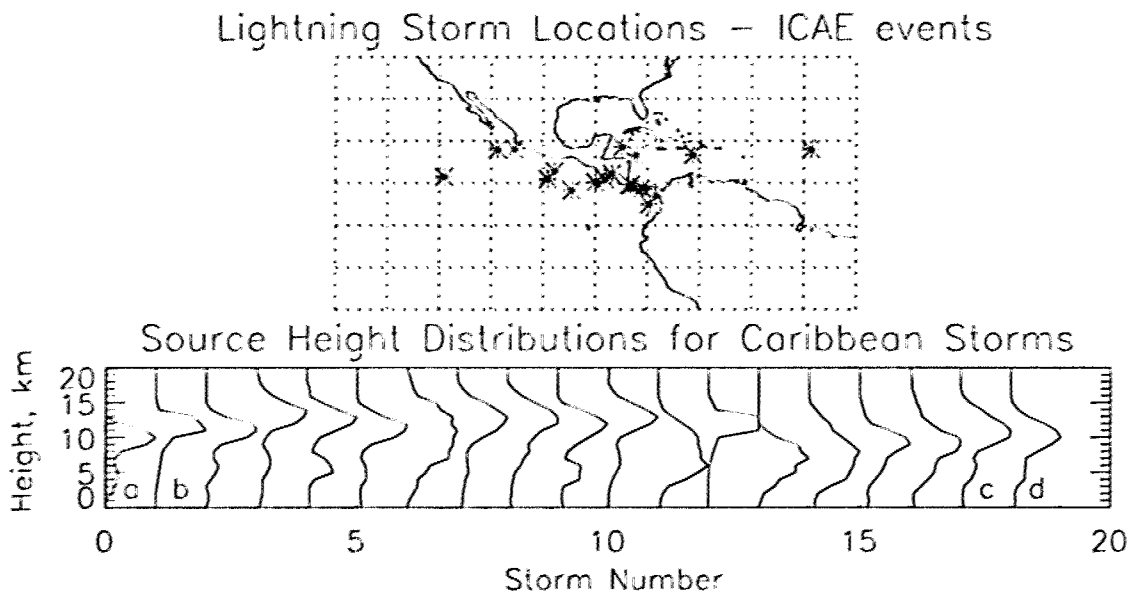


Figure 2. Nineteen storms in the extended region selected both by NLDN/FORTE coincidences and the use of recurrent-emission characteristics to do autonomous geolocation. The map shows the storm locations, the lower figure shows the height distributions of the discrete emissions that we could identify. Note that most storms have the most emissions at heights significantly above 10 kilometers.

## DISCUSSION

We have studied several storm cases where many of the FORTE RF detections are coincident (to within several hundred microseconds) of an NLDN located flash. In each case the locations of the FORTE/NLDN detected flashes are nearly coincident with the strong radar echoes detected by the NEXRAD Doppler radar system, indicating that this lightning activity is occurring in the locations of strong convective regions.

FORTE overpasses of tropical regions show a distinctly different character than those found in continental U.S. storms. We see far more RF triggers (often thousands), and many more are the narrow TIPP events. Smith (1998) determined that the source height from the one tropical storm observed was significantly higher than those observed in local thunderstorms (15 to 17 kilometers as opposed to 8 to 10), and Jacobson has shown for the ensemble of NLDN coincidences that the southeastern maritime storms had similar differences in height distributions than the inland continental storms. In the nineteen storms observed in this study we found a variety of height distributions, most showing peaks well above ten kilometers. In addition, the tropical storms are far more efficient at producing the

TIPP events (50-75% of the detections were TIPPs), again in contrast to the inland continental storms where usually fewer than 10% were identified as TIPPs.

SUMMARY

The FORTE satellite observations of the RF emanations from thunderstorms have significantly increased our understanding of the phenomenology of these events. The ability to detect and store several thousand events between downlinks has allowed us to observe complete passages of major thunderstorm systems. This in turn led to the corroboration of the model that the twin TIPP pulses were actually a single pulse and its reflection off of the ground. With this knowledge, we could then study the causative thunderstorm sources.

In this paper we have studied a subset of the FORTE detections that are coincident with lightning strokes detected and geolocated by the National Lightning Detection Network. Using this coincidence to attach a location to the source of the FORTE detected signal, we are able to show that the sources of these events are not only connected to the thunderstorm, but come from very localized regions within the thunderstorm. A further connection, using continental images from the NEXRAD weather radar network, was shown between the FORTE sources and strong Doppler radar echoes. Since the strong radar echoes come from the regions of intense convection within the thunderstorm, we conclude that these same regions are responsible for the FORTE events. This result is similar to that found in the earlier work done by Smith (1998), in which he showed that TIPP events are produced by singular, isolated, intracloud electrical discharges that occur in intense regions of thunderstorms. These intense regions appear to support electric fields an order of magnitude higher than those previously expected, or detected. Smith postulates that these large fields have not been detected by *in situ* measurements primarily because the regions are so compact that instruments have not reached them.

Although the FORTE satellite RF detection capabilities have extended our understanding of the VHF emissions from thunderstorms, and have shown that satellite borne RF detectors can provide lightning measurements of the convective core of the thunderstorm, the use of a low earth orbit satellite for global synoptic studies of thunderstorm morphology is hampered by the fact that such a satellite passes a thunderstorm at best a couple of times a day for durations of less than fifteen minutes. Early next century (~2003) a constellation of FORTE-like sensors will be flown by DOD/DOE , and will potentially be capable of providing global lightning detection coverage. Because the use of multiple coincidence detections will allow the constellation to unambiguously locate each lightning event, we will not have the problems of separating out closely co-located storms. In addition, the possibility of measuring TIPP time separations would allow us to follow the time evolution of the source altitude profiles, as well as the global differences in source altitude characteristics. We hope to be able to provide hourly maps of the global lightning, along with information such as the source height distributions.

REFERENCES

Argo, P.E., A. Jacobson, S. Knox, Geolocation of recurrent-emission lightning storms using the FORTE satellite, submitted to *J. Geophys. Res.*, 1999

Cummins, K., Murphy M., Bardo E., Hiscox W., Pyle R., Pifer A., A combined TOA/MDF technology upgrade of the U.S. National Lightning Detection Network, *J. Geophys. Res.*, 103,9035-9044,

Holden, D. N., C. P. Munson, and J. C. Devenport, Satellite observations of transionospheric pulse pairs, *Geophys. Res. Lett.*, 22, 889-892, 1995.

Jacobson, A.R.,S. Knox, R. Franz, and D. Enemark, FORTE observations of lightning radio-frequency signatures: Capabilities and basic results, *Radio Sci.*, in press, 1999a

Jacobson, A.R., K.L. Cummins, M. Carter, P. Klingner, D. Roussel-Dupre, S.O. Knox, FORTE observations of lightning radio-frequency signatures: Prompt coincidence with National Lightning Detection Network sferics, submitted to *J. Geophys. Res.*, 1999b

Smith, D. A., Compact intracloud discharges, Ph.D. Dissertation, Dept. of Electrical Engineering, University of Colorado, Boulder, 1998.

Smith, D. A., X. M. Shao, D. N. Holden, C. T. Rhodes, P. R. Krehbiel, M. Stanley, M. Brook, R. Thomas, Observations and analysis of distinct thunderstorm radio emissions, J. Geophys. Res., 104, 4189-4212, 1999.

# OPERATION OF AN ARRAY OF FIELD-CHANGE DETECTORS TO PROVIDE GROUND TRUTH FOR FORTE DATA

Robert S. Massey[1], Kenneth B. Eack[1], Marc H. Eberle[1], Xuan-Min Shao[1], David A. Smith[1], and Kyle C. Wiens[2]

[1]Space and Atmospheric Sciences Group, Los Alamos National Laboratory
Los Alamos, NM
[2]Department of Physics, New Mexico Tech, Socorro, NM

ABSTRACT: We have deployed an array of fast electric-field-change sensors around the state of New Mexico to help identify the lightning processes responsible for the VHF RF signals detected by the FORTE satellite's wide-band transient radio emission receivers. The array operates continuously, and provides us with locations and electric-field waveforms for events within New Mexico and into surrounding states.. We are particularly interested in events for which there are coincident FORTE observations. For these events, we can correct both the array and FORTE waveforms for time of flight, and can plot the two waveforms on a common time axis. Most of the coincident events are from cloud-to-ground discharges, but the most powerful RF emitters are a little-studied class of events variously called "narrow bipolar events" and "compact intra-cloud discharges". We have therefore focussed our attention on these events whether or not FORTE was in position to observe them.

## Introduction

Los Alamos National Laboratory has built and flown two satellites that have wide-band VHF radio receivers on board. The first of these satellites (named ALEXIS) has a receiver dubbed "Blackbeard" that recorded a 75 MHz analog bandwidth, and was usually tuned to 25-100 MHz or 100-175 MHz. This receiver has a video trigger circuit whose trigger level must to be set quite high to avoid triggering on communications and other non-geophysical signals, and as a result, only the most powerful transient radio signals are recorded. The surprising (at the time) result was that almost all events detected were very brief (a few microseconds duration), and occurred in pairs separated by 10-100 μs. We dubbed these events "TIPPs", for "trans-ionospheric pulse pairs" [Holden *et al* 1995, Massey and Holden 1995]. Radiation like that expected from ordinary lightning (intracloud or cloud-ground) was only rarely seen. The FORTE satellite, also built by Los Alamos for the Department of Energy, has several instruments capable of detecting lightning emissions. Two instruments detect optical emissions, while a package of VHF receivers detects radio emissions from 30-300 MHz. A multi-band trigger circuit allows FORTE to trigger on much weaker transients than Blackbeard, and as a result, FORTE most commonly triggers on intracloud and cloud-ground (CG) lightning events, though Blackbeard-style short-duration TIPPs are also recorded.

Using an array of electric-field-change sensors, Smith *et al* [1999] were able to show that TIPP events were the same narrow-bipolar events first described by Le Vine [1980]. By geolocating the events using differences in the measured times of arrival, Smith *et al* [1999] were able to show that these events occurred within thunderstorm regions with radar reflectivities exceeding 50 dBZ, and that they occurred within the cloud, in the region just above the negative charge layer.

With the utility of a field-change array proven, we deployed four field-change sensors in New Mexico, at Los Alamos, Socorro (at New Mexico Tech), Tucumcari (at Mesa Technical College), and Roswell (at Eastern New Mexico University), which form a rough square with sides of 200 km.

## Array design

Each station consisted of a flat-plate antenna under a rain-shielding dome, an integrating amplifier, a bipolar trigger circuit, and a PC with a 1 mega-sample/s digitizer and a GPS timing card. The

trigger thresholds are controlled by a D/A card in the PC. The digitizer runs constantly, so that pre-trigger samples can be obtained. When an event triggers the system, the PC records 4-12 milliseconds of post-trigger and 4 milliseconds of pre-trigger data. The trigger pulse is time-tagged by the GPS card. The PCs use the Linux operating system, and have Internet connections over which data are transferred to a central PC at Los Alamos. Each night, header files containing the time-stamps are downloaded, coincident events are identified, and the corresponding waveform files are downloaded. The waveform data for an event are cross-correlated to provide fine-scale relative timing, and the locations are determined by minimizing the chi-squared timing error. Locations thus determined were compared to NLDN-provided locations [Cummins, 1998], and for events within our array's nominal coverage, most locations agreed within 10 km.

The stations operated continuously, with very few outages, from May 15 through October 1998. As many as 4000 events were located per day, with a total of more than 100,000 events during the season.

## FORTE description

The FORTE satellite contains optical and radio instruments capable of detecting lightning emissions. In this paper we use data from the two "TATR" receivers, which have an analog bandwidth of 22 MHz, and are tuned (for these data) to center frequencies of 38 and 130 MHz. The output from each receiver is digitized at 50 mega-samples/second with 12-bit precision. A multi-band triggering circuit identifies transient events to be recorded in memory and transferred to the ground station. The primary antenna system is a crossed pair of 10-meter long log-periodic antennas. The antenna is nadir-pointing. The pattern has a null at the limb of the earth, though we still detect signals from near the limb. An on-board GPS receiver provides timing and location information.

## Coincidences with FORTE

Coincidences between the array data and FORTE events were identified by the requirement that the difference in trigger times be less than 10 milliseconds. These candidate events were analyzed to remove the propagation time (including ionospheric delays in the FORTE data) from the event to FORTE and to an array station. For most events, the resulting waveforms were coincident to within a few tens of microseconds. The largest uncertainty in these calculations was the event location (which could contribute as much as 33 μs error). The locations of the array stations and FORTE were determined by GPS receivers to a few hundred meters.

From May 15 through September, there were 15 coincidences where FORTE observed a negative CG, 77 coincidences with positive CGs, and 8 coincidences with positive narrow bipolar events. Jacobson [1999] has shown that FORTE is a more efficient collector of positive CGs than negative CGs, but the number of events in the present study is too small to conclude that we are seeing that effect.

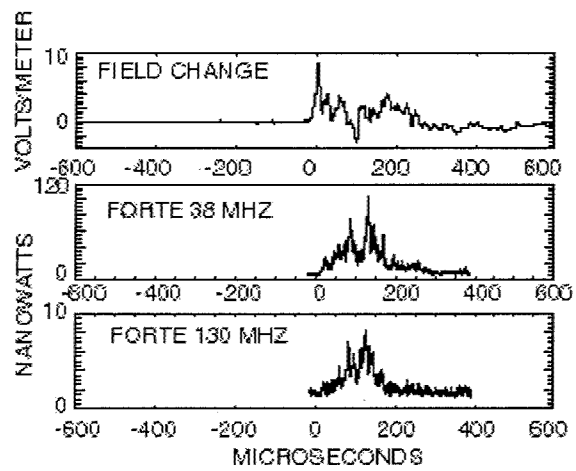


**Figure 1. Waveforms from a positive CG event on May 15, 1998. The top waveform is the electric field recorded at the Los Alamos station. The middle and bottom waveforms are the dispersion-corrected RF power fluxes observed at FORTE. The time axes are corrected back to the event time.**

Examples of FORTE coincidences with these three lightning types are shown in Figures 1-3. Figure 1 shows a positive CG, figure 2 shows a negative CG, and figure 3 shows a positive narrow bipolar discharge.

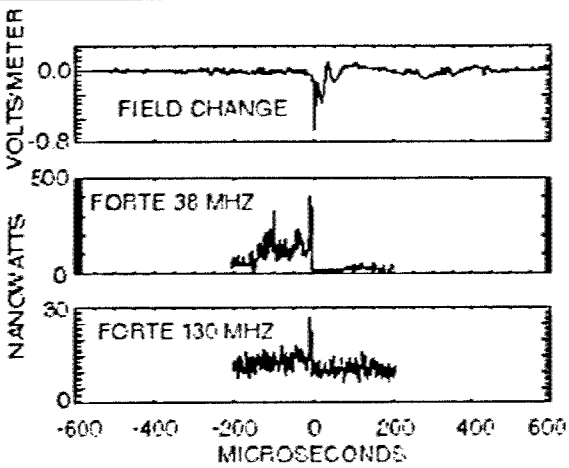


**Figure 2. Waveforms from a negative CG event on August 7, 1998.**

The positive CG of Figure 1 occurred during a series of storm systems over the Texas panhandle and western Oklahoma on May 15, 25, and 27. Lyons *et al* [1998] have noted that these storms produced an unusually high fraction of positive CG strokes, and in fact our array detected only positive CGs. At the time of these storms, the Tucumcari station was not yet operating, so we had only three stations, and these storms occurred at an azimuth for which we had poor range resolution. Fortunately, almost all events recorded by both FORTE and the array were also observed and located by the NLDN, so for these events we used the NLDN-derived locations rather than the array solutions. The storm on May 15 produced 40 out of our total of 100 array-FORTE coincidences. The timing relationship between the field change signature and the RF waveform for all events was similar to that shown in figure 1; that is, the RF emissions occurred throughout the field change waveform, with little RF power either before or after the field change signature.

Negative CG events like that shown in Figure 2 frequently had a sharper cutoff of the RF emissions than seen for positive CG events. This particular event appears to be a subsequent return stroke, with a very prominent spike and cutoff at the time of the return stroke. Examples of first return strokes, with prominent leader features, were also found.

Waveforms for narrow bipolar discharges were very distinctive in both the field change signature and the RF emissions. The two signatures were simultaneous within our timing error. For this event, both TATR receivers (A and B) were tuned to a center frequency of 38 MHz, but were connected to different linear polarizations of the antenna. The RF power was far higher than normally observed for CG events (note that the power scale is microwatts in this plot). The very brief duration of the sources suggest that they are small (< 1 km). The waveforms frequently contained reflections, which have been used by Smith *et al* [1999] to deduce the heights of the sources, which typically occur at about 8 km, though there is a wide range of heights. In figure 3, the signals in the electric-field waveform at just over 200 μs are the reflection from the ionosphere (called the "skywave") of the main signal. The ground reflection of the radio signal can be seen just a few microseconds after the main pulse in the lower two traces. The height determined by the skywave analysis is 7.0 km, while the height obtained from the RF reflection is 8.0 km. The elevation angle of FORTE as seen from the event location was 15°, which explains the small delay between the direct and reflected radio signals. The pulse at about 150 μs in the FORTE traces is apparently unrelated to the narrow bipolar event.

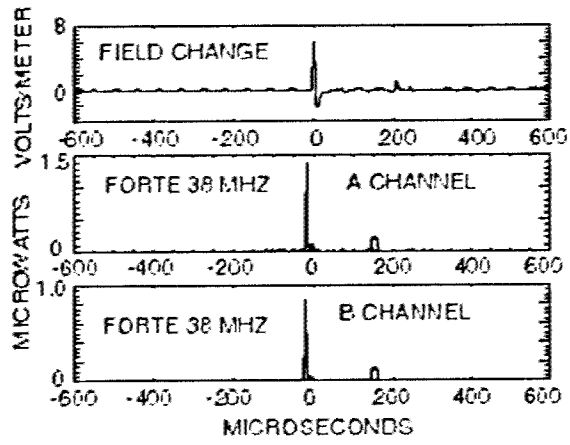


**Figure 3. Waveforms from a narrow positive bipolar event on July 1, 1998.**

## Discussion and plans

These data demonstrate the feasibility and utility of collecting coincident data with a ground-based array and FORTE. The timing and location accuracies are good enough that we can identify at what time in the field-change waveform the RF emissions occurred. The primary limitation of the system is the small number of coincident events collected. There are several reasons that the number of coincident events was so small. One problem was that, for most of the monsoon season, FORTE passes over New Mexico occurred during hours when there were no thunderstorms in the area. Another problem was that, for "ascending" passes (when the satellite was traveling northward), the on-board memory buffer would fill up with events that occurred over Central and Southern America, so the receiver halted until the memory was downloaded. The event rate over New Mexico simply couldn't compete with tropical systems.

To address these problems, we plan to install a 5-station array in Florida for the 1999 season. Stations will be located at or near Kennedy Space Center, Boca Raton, Ft. Myers, Tampa, and Gainseville. The New Mexico array will continue to operate, with the addition of a fifth station. The use of five stations will allow us to know whether one of the GPS receivers is giving erroneous times, and if so, which one it is. Both arrays will be operated at lower trigger thresholds when FORTE is in view.

When FORTE is not in view, the stations will concentrate on collecting data on narrow bipolar events. These events are readily recognized by software in the controlling PCs, and we can command the PCs to record waveforms only from these events (while recording trigger times for all events).

Because the PCs are on the Internet and running Linux, we can easily change the modes of operation, and we welcome ideas for joint efforts with other groups studying lightning or thunderstorms in New Mexico and Florida.

This work was performed under the auspices of the U.S. Department of Energy.

## References

Cummins, K. L, M. J. Murphy, E. A. Bardo, W. L Hiscox, R. B. Pyle, and A. E. Pifer, A combined TOA/MDF Technology Upgrade of the U. S. National Lightning Detection Network, *J. Geophys. Res.*, 103(D8), 9035-9044, 1998.

Holden, D. N., C. P. Munson, and J. C. Devenport, Satellite observations of transionospheric pulse pairs, *Geophys. Res. Lett.*, 22(8), 889-892, 1995.

Jacobson, A. R., Recent results from the FORTE RF payload, *Proc 11th International Conf. On Atmospheric Electricity,* 1999

Le Vine, D. M., Sources of the Strongest RF Radiation from Lightning, *J. Geophys. Res.* 85(C7), 4091-4095, 1980.

Lyons, W. A., T. E. Nelson, E. R. Williams, J. A. Cramer, and T. R. Turner, Enhanced Positive Cloud-to-Ground Lightning in Thunderstorms Ingesting Smoke from Fires, *Science,* 282(5386), 77-80, 1998.

Massey, R. S., and D. N. Holden, Phenomenology of transionospheric pulse pairs, *Radio Sci.*, 30(5), 1645-1659, 1995.

Smith, D. A., , X. M. Shao, D. N. Holden, C. T. Rhodes, P. R. Krehbiel, M. Stanley, M. Brook, R. Thomas, Observations and analysis of distinct thunderstorm radio emissions, Accepted *J. Geophys. Res.*, for publication in 1999.

# INVESTIGATION OF POSSIBILITIES TO OBTAIN THE INFORMATION ON THUNDERSTORM CLOUDS BY SATELLITE RADAR TRMM.

V D Stepanenko
A I Voeikov Main Geophysical Observatory
Karpysheva str., St Petersburg, 194621, Russia
Ph: (812)2478670; Fax(812)2478661

ABSTRACT. Results of theoretical estimations indicates the possibility to obtain the information on thunderstorm clouds using the satellite radar TRMM at the global scale and the advisability of joint application of its data and lightning imeging sensor (LIS) data.

## INTRODUCTION

Graund-based and airborne radars are the important technical methods of remote detecting and investigation of the thunderstorm clouds. It is well known that 2-santimiter radar which is used in the framework of the american-jupanese TRMM project for production of information on precipitation in tropical and subtropical regions contributes significantly to obtaining of satellite data for the precipitation at the global scale.

It is also known about application of LIS with 5-10 km geometrical resolution for the ground surface seted onto the satellite TRMM. While TRMM radar having narrow scaning directionality diagramme of the antenna is capable of giving the qualitative knowledge of the cumuli-nimbus clouds which yield precipitation without lightnings and with lightnings much as is done on the ground-based meteorological radar data using, for example, empirical criterion $Y=H_{max}\lg Z_{2}$, where $H_{max}$ – maximum of the upper boundary radioecho height, $Z_2$ – radar reflectivity for the level 2-2,5 km over zero temperature isoterm height [3]. On the basis of large volume of the statistical data derived using domestic weather radar and ground-based observations on the meteorological stations it was founded that when $Y<6$ thunderstorm phenomenon are not detected, when $6\leq Y\leq 25$ cumulinimbus clouds with both intensive rain and thunderstorm processes can be observed. While $Y>25$ probability of valid detection of the thunderstorm clouds $P>90\%$. As $Y\geq 40$ ultraintensive thunderstorm-hale clouds in the middle latitudes are usually detected. With consideration for the mentioned above theoretical estimations are presented in this report. Results of this estimations indicates the possibility and the advisability to obtain the information on the thunderstorm clouds using the 2-centimetre radar TRMM at the global scale.

## RESULTS AND DISCUSSION.

In the first stage the estimations of geometrical and energy radar resolution was performed. Its main technical characteristics are: $\lambda$=2cm, power of pulse

$P_t$=23kW, pulse duration after its compression $\tau$=1,7μs, beam width $\theta$=0,7°, directionality coefficient of the antenna G=46 dB, losses in the input-output chanal K=-4dB, angle of antenna scaning $\gamma$=20° produses the band observation L=220km on the Earth surface. If $\gamma$=40-45° then L≈500-600 km, pulse frequency F=3,5 kHz, sensitivity of receiver $P_{min}=4*10^{-14}$W.
Radar geometrical resolution can be estimated using its technical parameters and orbit characteristics [1]. The culculation results of this resolution for the mentioned $\gamma$ assuming that the Earth surface is plane are presented in the Table 1.

Table 1.

Geometrical resolution РЛС TRMM (x, y, h) according to the angle of sighting $\delta$

| $\delta$° | 90 | 85 | 80 | 75 | 70 | 65 | 60 | 55 | 50 | 45 | 40 |
|---|---|---|---|---|---|---|---|---|---|---|---|
| x, km | 3,65 | 2,87 | 1,44 | 0,97 | 0,73 | 0,59 | 0,50 | 0,44 | 0,39 | 0,35 | 0,33 |
| y, km | 3,65 | 3,67 | 3,71 | 3,78 | 3,87 | 4,03 | 4,22 | 4,46 | 4,77 | 5,16 | 5,69 |
| h, km | 0,25 | 0,54 | 0,89 | 1,22 | 1,56 | 1,93 | 2,33 | 2,77 | 3,26 | 3,82 | 4,16 |

Here x – resolution in the plane witch is perpendicular to the scaning plane, y – resolution in the plane witch is parallel to the scaning plane, h – altitude resolution. It is seen from the table that x is the most for 90° (when observing in nadir) and forms 3,65 km, with reducing of $\delta$ the value of x is decreased to 0,35 km for $\delta$=45°. As for value of Y, it slightly increases with enhancing of $\delta$.

Now we'll carry out estimation of the radar probability detection $W_r$ for precipitation clouds including the thunderstorm clouds. According to [3,4] $W_r$ is ratio of quantity of events of meteoobject detection to real quantity at the same region. Estimation will be provided according to [3]. Value of $W_r$ depends not only on reflectivity and geometrical sizes of meteoobjects but also on technical radar parameters, distance of this meteoobjects from radar, propagation radio wave conditions etc. Firstly it is necessary to determine value of $Z_{min}$ using the main radar equation for clouds and precipitation (energetic resolution). The folowed model of sloud was used: vertical size of supercooled part of this cloud is 5 km, The lower boundary of cloud is 0,2 km, everage liquid water content are W=0,1 g/m$^3$, 0,3 g/m$^3$, 1,0 g/m$^3$. The vertical dimantion of rain area H=1 km, 2 km, 3 km, 4 km, 5 km. Further values of $Z_{min}$ close to Earth surface was culculated, assuming that rain rate is constant through the height. Attenuation of radio waves in clouds and precipitations was taken into account. Results of culculations are presented in tables 2 and 3.

On the basis of experimental data reflectivity of thunderstorm clouds formed in the middle latitudes is in the range from 1-10 mm$^6$/m$^3$ to $10^5$-$10^6$ mm$^6$/m$^3$. Therewith first gradation includes only 16% of all events. Comparing this findings with culculation results presented in the tables 2 and 3 it is possible to state that thunderstorm clouds arised in the subtropical and tropical regions will be detected by satellite radar TRMM with a very high probability approaching 95-100% at the band of view of the Earth surface L=220 km. As for

case when L > 500 km, to determine mentioned above probability it is necessary take into account the influence of impeded echo signals for thunderstorm clouds located on the edge of band of view, e g when angle of sighting $\delta \approx 40\text{-}45°$.

Table 2.
Minimum values of reflectivity $Z_{min}$ for the upper boundary rain clouds witch can be detected by TRMM radar

| $\delta°$ | 90 | 70 | 45 |
|---|---|---|---|
| $Z mm^6/m^3$ | 10,7 | 11,7 | 48,0 |

Table 3.
Values of $Z_{min}$ [$mm^6/m^3$] close to the Earth surface for the different conditions

| $\delta°$ | W | H, km | | | | |
|---|---|---|---|---|---|---|
| | $g/m^3$ | 1 | 2 | 3 | 4 | 5 |
| 90° | 0,1 | 8,6 | 8,6 | 9,6 | 9,6 | 10,7 |
| | 0,3 | 10,7 | 10,7 | 10,7 | 11,7 | 11,7 |
| | 1,0 | 17,7 | 19,0 | 20,4 | 23,2 | 24,6 |
| 45° | 0,1 | 21,8 | 21,8 | 23,2 | 23,2 | 24,6 |
| | 0,3 | 33,9 | 35,6 | 35,6 | 37,3 | 39,0 |
| | 1,0 | 383 | 467 | 706 | 923 | 1286 |

## CONCLUSIONS

Using the 2-centimetre TRMM radar all thunderstorm clouds located in the place of satellit radar view are practicable detected. In the initial stage it is advisable to detect this clouds by empirical criteria Y for the ground-based weather radar. Further this criteria should be refined on the basis of synchronous radar and LIS data especially for detecting of very dengerous ultraintensive thunderstorm clouds. It is hoped that integrated application of these data will allow to obtain further insight into the processes of forming of discharging phenomenons in the different clouds and therefore to improve the quality ultrashort-term prediction of thunderstorms

## REFERENCES


1. Tropical Rainfall Measuring Mission (TRMM), edit. J. Simson. NASA, 1988.
2. Atlas D. And all. The outlook Precipitation Measurements from Space. Proc. 20th Conf. On Radar Meteor. Boston, December, 1981, p.484-489.
3. StepanenkoV.D., Galperin S.M. Radiotechnical methods of thunderstorm investigations, Leningrad. Gidrometeoizdat, 203, 1983.
4. StepanenkoV.D. Radar detection of thunderstorm clouds from sattelite. Trudy MGO, 534, 87-93, 1991
5. Newsletter on Atmospheric Electrisity. V.8, N1, June 1997, p.16.

# EL NIÑO RELATED MERIDIONAL SHIFTS IN THE GLOBAL POSITION OF THE WORLDWIDE THUNDERSTORM ACTIVITY

G. Sátori and B. Zieger
Geodetic and Geophysical Research Institute
of the Hungarian Academy of Sciences, Sopron, Hungary

ABSTRACT: The self-consistent behaviour of the frequency level and semiannual intensity variations of the first three Schumann resonance (SR) modes observed at Nagycenk (47.6°N, 16.7°E) indicates a southward shift in the global position of the lightning activity in warm El Niño years (1994, from March 1997 to April 1998) and a northward shift in cool La Niña years (1996, (1998)). The third SR mode has a crucial role in recognizing these meridional shifts due to the special angular distance of Nagycenk with respect to the African thunderstorm region. The diurnal zonal redistribution of the worldwide thunderstorm activity manifests in characteristic daily frequency patterns. The preserved daily frequency patterns with changing frequencly levels in the same months of the different years imply that the meridional shifts of the lightning activty exist in worldwide sense on the ENSO time scale. The estimated shifts are about 4-8° in latitude. The authors suggest that there are two temperature dependent and quasi-synchronous global oscillations in the atmosphere-ocean-land system. One of them is the El Niño Southern Oscillation (ENSO) known already, which is basically a zonal oscillation, the other is a meridional oscillation manifested in the average position of the land related global lightning activity which can be monitored by Schumann resonances.

## INTRODUCTION

Schumann resonances are eigenmodes of the Earth-ionosphere cavity, excited by lightning discharges [*Schumann*, 1952] . The field distributions include nodal lines where the electric or magnetic field vanishes and the frequency has singularity. Lightning activity is concentrated in specific source areas. In case of an extended source, the "nodal line" means the place, where the superposed field of the individual lightnings has a minimum and the frequency exhibits a quasi-singular behavior. Since the lightning activity generally maximises in the local afternoon, the mode structures, i.e. the field distributions attached to the active thunderstorm region move around the Earth in universal time. The daily frequency patterns are practically the manifestation of this motion.

The Nagycenk Observatory (47.6°N, 16.7°E, Hungary) gets into nodal position if the equivalent dipole corresponding to the African thunderstorm region is at about 8°N latitude. (39.2° is the angular distance between the source and the nearest nodal line of the third mode, in case of the vertical electric field component, Ez). Thus the frequency and amplitude/intensity variations of the third mode observed at Nagycenk (NC) are particularly sensitive to meridional motions of the African thunderstorm region.

## SR FREQUENCY VARIATIONS

The main purpose of this paper to present and interpret the frequency level variations observed on the ENSO time scale. The mean frequency levels for the first two modes were higher in 1994(1995) and in the first part of 1998. They reached a minimum level in the second part of 1996 and the first part of 1997. In the second part of 1998 the frequencly level started decreasing again. The difference between the highest and lowest mean frequency levels is only about 0.04 Hz

for the first mode and 0 06 Hz for the second mode. In case of the first two modes the magnitude of the long-term frequency level variation was less than their diurnal frequency ranges while for the the third mode the dramatic frequency level variation of about 0 6 Hz occurred in interannual relation surpasses its own diurnal frequency ranges. The long-term frequency level variation of the third mode (0.6 Hz) is ten times (or even more) higher than in case of the first two modes (0.04 Hz and 0.06 Hz).

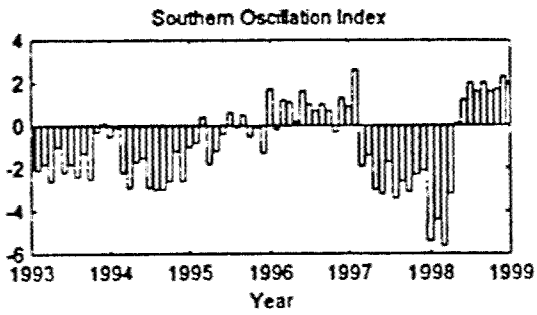


Figure 1.

The frequeny level variations of the first two modes occur on the ENSO time scale (warm periods-higher frequency level; cool periods-lower frequency level). Warm El Niño periods are indicated by negative values of the Southern Oscillation Indices (SOI) as depicted in Figure 1. It is the dramatic frequency level variation of the third mode between 1995 and 1997 that will show us that all these frequency level variations are related to meridional drifts of the African thunderstorm region with respect to the observer at NC.

Figure 2 shows the monthly means of the diurnal frequency variations of the first mode measured at NC under El Niño and La Niña conditions in months of January. The daily frequency patterns are preserved, only the frequency levels are shifted as shown here. The preserved daily frequency patterns with changing frequency levels on the ENSO time scale are observed in each season of the different years. As the daily frequency pattern is determined by the daily zonal redistribution of the worldwide thunderstorm activity, this implies that not only the African thunderstorm region exhibits meridional shifts on the ENSO time scale.

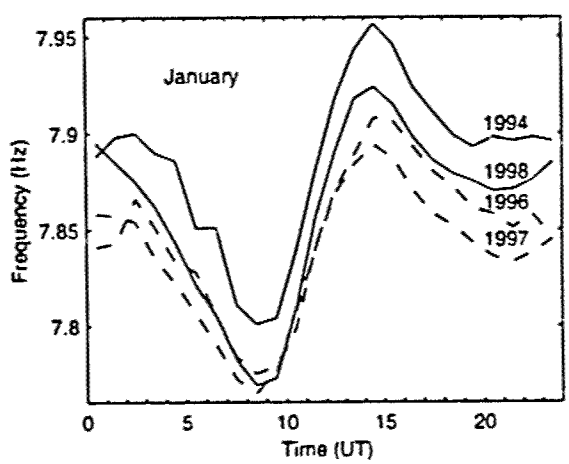


Figure 2.

In other words, the zonal redistribution of the worldwide thunderstorm activity on the diurnal time scale occurs at more northward latitudes in the cooler La Niña period and at more southward latitudes in the warm El Niño phase.

The meridional shifts on the ENSO time scale are estimated to be of about 4-8°, because larger meridional shifts ( e.g. the annual north-south migration of the global thunderstorm activity) cause detectable zonal shifts of nodal regions with respect to the observer, i.e. the nodal crossings occur in other hours of a day and the daily frequency pattern is not preserved any more. The lower limits of shifts is determined by the frequency resolution of data.

In principle NC can get into nodal position by the third mode twice during the north-south annual migration of the African thundersorm region. In spite of this fact, the dramatic frequency level variations of the third mode are rarely observed or only for some days (hours) at NC on the

seasonal time scale. This may mostly be attributed to the random-like getting over the equivalent dipole on the 8°N latitude which is crucial from the point of view of the nodal position of NC.

## SR AMPLITUDE/INTENSITY VARIATIONS

SR amplitude/intensity variations can be observed if the intrinsic source intensity changes and/or the source-observer distance varies. The semiannual variation of SR amplitude/intensity, which was predicted by *Williams* [1992] and observed by *Sátori and Zieger* [1996], *Füllekrug and Fraser-Smith* [1997], *Nickolaenko et al.*, [1998], is a signature of the semiannual variation of the surface air temperature in the tropical land regions with maxima around equinox months due to the semiannual variations in solar insolation [*Williams*, 1994]. Therefore the semiannual SR amplitude/intensity variation can be considered a semiannual modulation of the lightning activity in the tropics.

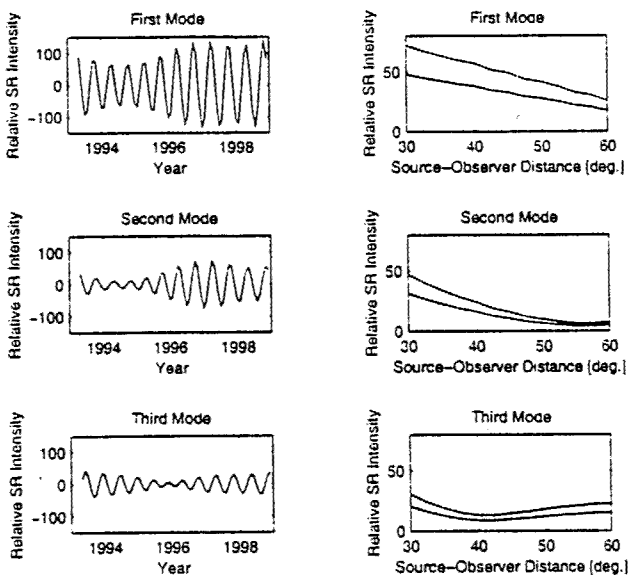


Figure 3.

Figure 3a shows the semiannual variations extracted by digital filtering technique from the monthly means of SR (squared) amplitudes measured at 1200-1600 UT (The African thunderstorm region is activated.) at Nagycenk for the first three modes of the vertical electric field component Ez. The finite impulse response (FIR) band-pass filter applied here was designed with the Parks-McClellan algorithm to assure optimum transfer charahteristics in the ± 10% period range around half a year. The magnitude of the semiannual variation changes on the ENSO time scale for each mode.

They show minima for the first two modes in 1994 and an other one for the first mode in 1997/1998 when the frequency level indicates a more southward position of the African thunderstorm region (warm period). Maxima are found in the second half of 1996 and 1998 when the frequency level indicates a northward shift (cold period). The magnitude of the semiannual variation for the third mode had a minimum between 1995 and 1997 just in the same time interval when the frequency level of the third mode indicated that the source region had crossed the latitude of 8°N. These results also support the ENSO related north-south meridional drifts of the Aftican thunderstorm region.

Figure 3b shows the theoretical spatial distribution of Ez calculated for the first three modes [*Nickolaenko and Rabinowicz*, 1974; *Jones and Joyce*, 1989]. A source intensity modulation of ± 20 % was applied here to represent the semiannual modulation of SR intensity with an arbitrary magnitude at the source. It can be seen that the magnitude of the modulation (the difference between the two curves) also depends on the angular distance between the source and the observer. At a source-observer distance between 39.2° and smaller than 54.7°, where the latter is the angular distane between the source and the nearest nodal line in the field distribution of the

second mode, when the source starts shifting towards the observer, the magnitude of the modulation starts increasing for the first two modes, while for the third mode, it decreases at first and then increases again. The average angular distance between the equivalent dipole of the African thunderstorm region and Nagycenk varies around 39°; therefore the changes in the magnitudes of the semiannual SR intensity variations can be interpreted as north-south drifts of the African thunderstorm region with respect to Nagycenk on the ENSO time scale.

## CONCLUSIONS

The self-consistent behaviour of the frequency level and semiannual intensity variations of the first three SR modes on the ENSO time scale gives a strong evidence for a meridional oscillation in the global position of the lightning activity in the longitudinal range where the African thunderstorm region is situated. The frequency level variations with preserved daily frequency patterns in the same months (seasons) of the different years studied here imply that the ENSO related meridional oscillation is present not only in the African thunderstorm region. The estimated magnitude of the meridional oscillation is about 4-8° in latitude. The main conclusion is that the global lighning activity has a southward drift under El Niño conditions and a nortward drift under La Niña conditions as shown here by SR observations during two warm and two cold episodes. It seems that the latitudinal range of meridional oscillation in the global position of lighning activity depends both on the duration and importance of the ENSO episods. As lightning activity is a temperature dependent and land related phenomenon, the authors suggest that the driving mechanism of this meridional oscillation is the El Niño related equatorial extra heating (southward drift) and the north-south asymmetry of land-ocean distributions (northward drift).

ACKNOWLEDGEMENTS: This research was supported by the Hungarian Science Foundation, T023111 and the U.S.-Hungarian Joint Found, JF554.

## REFERENCES

Füllekrug, M. and A.C. Fraser-Smith, Global lightning and climate variability inferred from ELF magnetic field variations. Geophys. Res. Lett. 24, 2411, 1997.

Jones, D. Ll. and G. S. Joyce, The computation of ELF radio wave field in the Earth-ionosphere duct. J. Atmos. Terr. Phys. 51, 233, 1989.

Nickolaenko, A. P. and L. M. Rabinowicz. Speeding up the convergence of the zonal harmonic series representation in the Schumann resonance problem. J. Atmos. terr. Phys. 36, 979, 1974.

Nickolaenko, A.P., G. Sátori, B. Zieger, L. M. Rabinowicz and I. G. Kudintseva. Parameters of global thunderstorm activity deduced from the long-term Schumann resonance records. J. Atmos. Sol. Terr. Phys. 60, 387, 1998.

Sátori, G. and B. Zieger, Spectral characteristics of Schumann resonances observed in Central Europe. J. Geophys. Res. 101, 29,663, 1996.

Schumann, W. O. Über die strahlungslosen Eigenschwingungen einer leitenden Kugel, die von einer duftschicht und einer Ionosphärenhülle umgeben ist. z. Naturforsh. 7a, 149, 1952.

Williams, E. R. The Schumann resonance: A global tropical thermometer. Science 256, 1184, 1992.

Williams, E. R. Global circuit response to seasonal variations in global surface air temperature. Mon. Weather Rev. 122, 1917, 1994.

# A NEW SCHUMANN RESONANCE STATION IN THE NEGEV DESERT FOR MONITORING GLOBAL LIGHTNING ACTIVITY

C. Price[1], M. Finkelstein[1], B. Starobinets[1], and E. Williams[2]

[1]Department of Geophysics and Planetary Sciences, Tel Aviv University, Israel
[2]Parsons Laboratory, MIT, Cambridge, USA

ABSTRACT: Due to increasing interest in global lightning activity, and its connection to the global climate system, a new field site has been established in the Negev Desert, Israel, to monitor the Schumann resonances on a continuous basis. As the result of a joint Israel-United States project, we are now monitoring the three components (horizontal N-S and E-W magnetic field; and vertical electric field) of the extremely low frequency (ELF) electromagnetic waves (1-50 Hz) produced by lightning. Data has been archived since February 1998, and the initial analysis indicates that the monitoring site is very "clean" with low anthropogenic noise levels. We observe all 7 modes of the Schumann resonance between 1-50 Hz on a regular basis. In addition, due to the location of our station (30N, 34E), we are north of Africa, and equi-distant between Asia and South America, the three main source regions of thunderstorm activity around the globe. Due to this geometry the individual magnetic detectors can easily be used to distinguish between the different source regions during the day, to study the dynamics and variability of each source region separately. We have noticed an interesting periodicity of approximately 5-days in global lightning activity. On a global scale, our Schumann resonance signals have been compared with simultaneous observations in California, and a daily correlation of 0.92 indicates that our measurements are truly global in nature.

## INTRODUCTION

In 1952 Schumann predicted that the earth-ionosphere cavity should have specific resonant frequencies that are determined primarily by the dimensions of the earth (Schumann, 1952). These resonant frequencies were predicted to occur at 8, 14, 20, 26, ... Hertz and are excited by lightning discharges around the globe. The wavelength of the first resonant mode (8Hz) is equivalent to the circumference of the earth (~40,000 km). Balser and Wagner (1960) were the first of many to observe the existence of these extremely weak resonant electromagnetic waves, now known as the Schumann Resonances (SR).

There are different reasons researchers are interested in the SR. Many are interested in understanding the propagation of electromagnetic waves in the earth-ionospheric waveguide, to gain insights into the structure and variability of the ionosphere. We are primarily interested in the SR as a tool to study the variability of global lightning activity. The interest in global lightning activity is growing in a number of fields in geophysics. There is increasing evidence that the earth's climate is changing. However, long-term changes are often hard to detect above the noise in the climate system using conventional methods. Satellites that do monitor these changes are limited in their temporal and spatial sampling of the earth. The SR, via its connection to global lightning activity, is also related to tropical convection and rainfall, upper tropospheric water vapor, and surface temperatures. Hence it may be possible to use the global electric circuit, regulated by lightning activity, to track changes in the earth's climate (Williams, 1992; Price, 1993; Markson and Price, 1999). In addition, ELF transients are related to the fairly recent discoveries of sprites and elves (Bocippio et al., 1995), and sprites appear to provide a link between tropospheric processes in thunderstorms and mesospheric processes in the upper atmosphere. Furthermore, global and regional lightning variability are important for studying the production of nitrogen oxides by lightning (Price et al., 1997). Although satellites are a valuable source for studying global and regional lightning activity, satellites sample only a fraction of the total lightning. Finally, there is interest in the continuous monitoring of ELF signals in the atmosphere due to the recent findings in Japan that anomalous ELF signals are detected days to weeks prior to large earthquakes (Hata et al., 1996).

FIELD SITE

Due to the above mentioned interests in global lightning activity and ELF measurements, a new field site has been established in the Negev Desert, Israel, to monitor the Schumann resonances on a continuous basis (Figure 1). The field site is located near the town of Mitzpe Ramon (30N, 34E), at the astronomical observatory of Tel Aviv University. The desert site is very remote with very low levels of anthropogenic noise. Furthermore, interference from nearby thunderstorms is minimal, with only a few days per year associated with local thunderstorms.

At the site we have buried two magnetic detectors that monitor the horizontal north-south and east-west magnetic components of the electromagnetic waves. In addition, we have an electric field spherical antenna to monitor the vertical electric field. The ELF data are sampled at 250 Hz using a 16-bit A/D converter. The raw time-series data are saved and archived every 5-minute period, each file being time-stamped using a GPS clock. All analysis of the time-series data is left for post-processing. The ELF time-series data are collected in the bandwidth of 1-50 Hz, using a notch filter at 50 Hz. The notch filter is needed primarily for the electric field component to prevent saturation of the preamplifier. In our monitoring mode we archive only one 5-minute file every hour, supplying 24 files per day. However, during certain field campaigns such as SPRITES'98 and SPRITES'99 all the raw data is saved to make comparisons between the visibly observed sprites in the United States and the ELF transients monitored in Israel. No threshold method is used for the detection of transients. All the data is collected. The data are transferred via modem to the Tel Aviv University campus once a week, where the data are archived on CD-ROMs. In compressed form we can save all three components from a month on a single 650MB CD.

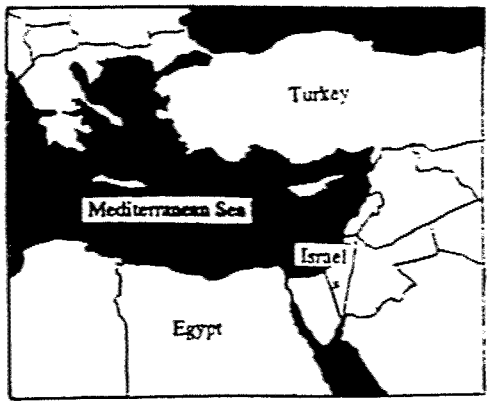


**Figure 1**: *Location of Israel in the Eastern Mediterranean with the SR site indicated be the X.*

INITIAL RESULTS

Figure 2 shows a typical example of the ELF data collected over a short 8-second period. In addition to the background signal with an amplitude of a few pico -Tesla (pT), a large ELF transient is also seen in this time-series. Figure 3 shows the power spectrum of such a time series over a 5-minute period. During post processing the spectrum is calculated for every 20-second period, and the final spectrum shown here is the average of 15 spectra. The ability to see all the SR modes between 1-50 Hz implies that our site has very low levels of anthropogenic noise.

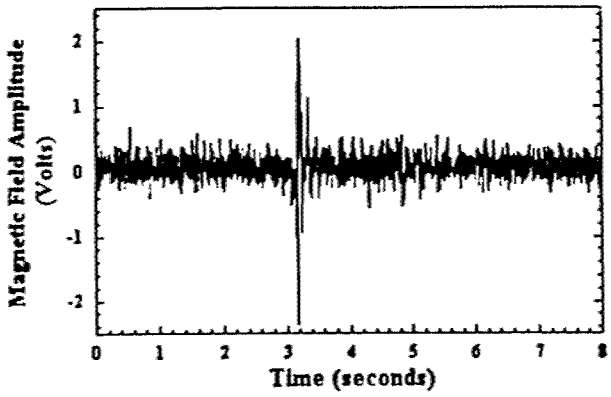


**Figure 2**: *An 8 second sample of the magnetic ELF data showing the background signal together with a transient Q-burst.*

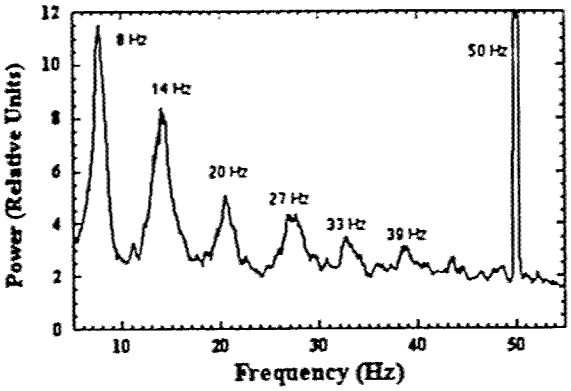


**Figure 3**: *A typical power spectrum for the north-south magnetic component of the SR. Note the power line signal at 50 Hz.*

The Schumann resonance represent global lightning activity because the ELF waves that produce these resonant modes manage to propagate, within the earth-ionospheric cavity, a few times around the planet before dissipating. In order to check this hypothesis we compared our SR data from the Negev Desert against SR data collected simultaneously in California (M. Fullekrug, personal communication). The overall amplitude of the SR at each station was calculated using both magnetic components of the ELF field. The comparison for the period 14 February – 28 March, 1998 is shown in Figure 6. The SR data collected at the two stations used completely different instrumentation, data analysis procedures and sampling methods. Nevertheless, the agreement is remarkable. Using all the data regardless of data quality the daily correlation between the data sets is 0.88. However, at least on the Israeli side we know which days were associated with nearby thunderstorm activity resulting in local noise at our station. These days are represented by the dotted lines in Figure 6. If we neglect these days the correlation increases to 0.92. This implies that the SR measurements at the new Israeli site are truly global measurements, allowing us to study the global variability of the climate system from a single location on the earth's surface.

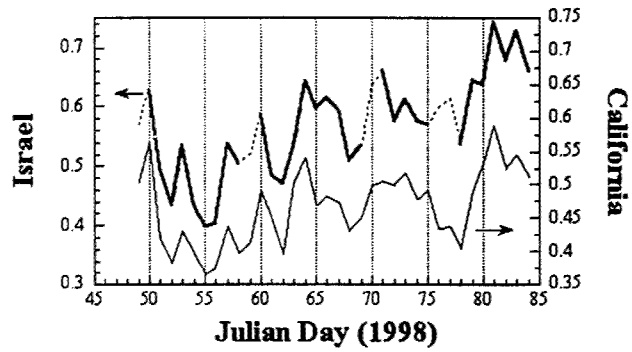


**Figure 6**: *Daily comparison between the SR 8 Hz magnetic field amplitude in Israel (upper curve) and California (lower curve) from 14 February –28 March, 1998.*

SUMMARY AND CONCLUSIONS

Since February 1998 a new Schumann resonance monitoring station has been collecting continuous ELF data in the Negev Desert, Israel. The raw time series' of all three components of the electromagnetic waves are saved every 5 minutes, with all spectral analysis done during post processing. Our site has very low levels of anthropogenic noise, allowing us to routinely observe all seven SR modes between 1-50 Hz. In addition, our daily mean SR observations agree remarkably well with simultaneous measurements made in California (r=0.92). We are therefore confident that our SR data represent *global* lightning activity. Due to the location of the observation site we can easily distinguish between the different tropical thunderstorm centers using different detectors at different universal times. From our initial analysis we have noticed an 5-day periodicity in both regional and global lightning activity.

ACKNOWLEDGMENTS: This work was supported by the Israel-United States Binational Science Foundation (BSF) under grant number 95-00441.

REFERENCES

Balser, M., and C. A. Wagner, 1960: Observations of the earth-ionosphere cavity resonances, *Nature*, 188, 638.

Bocippio, D.J., E.R. Williams, S.J. Heckman, W.A. Lyons, I.T. Baker and R. Boldi, 1995: Sprites, ELF transients and positive ground strokes, *Science*, 269, 1088.

Hata M., X. Tian, I. Takumi, S. Yabashi and A. Imaizumi, 1996: ELF horizontal magnetic flux precursor of the moderate M5.8 Yamanashi '96 inland earthquake - a general approach to electromagnetic wave precursor, *J. Atmos. Electr.*, 16, 199-220.

Markson, R., and C. Price, 1999: Ionospheric potential as a proxy index for global temperatures, *Atmos. Res.*, in press.

Price, C., 1993: Global surface temperatures and the atmospheric electric circuit, *Geophys. Res. Lett.*, 20, 1363.

Price, C., J. Penner and M. Prather, 1997a: NOx from lightning, Part I: Global distribution based on lightning physics, *J. Geophys. Res.*, 102, 5929.

Schumann, W.O., 1952: Uber die strahlungslosen eigenschwingungen einer leitenden kugel, die von einer luftschicht und einer ionospharenhulle umgeben ist, *Z. Naturforsch.*, 7a, 149.

Williams, E.R., 1992: The Schumann Resonance: a global tropical thermometer, *Science*, 256, 1184.

# SCHUMANN RESONANCES AND THE TEMPORAL-SPATIAL DYNAMICS OF GLOBAL THUNDERSTORM ACTIVITY

V.Mushtak[1], R.Boldi[2], and E.Williams[1]

[1]Department of Civil and Environmental Engineering, MIT, Boston, Massachusetts, U.S.A.
[2]MIT Lincoln Laboratory, Lexington, Massachusetts, U.S.A.

ABSTRACT: A two-dimensional computational ELF technique has been applied to interpret variations of peak frequencies of Schumann resosnances (SR) observed at the MIT experimental site (West Greenwich, Rhode Island). The spatial-temporal dynamics of global thunderstorm activity has been simulated on the basis of general meteorological data. It is shown that the proposed models provide a reasonable qualitative agreement between computed and observed variations for SR I to IV. Some inverse task diagrams has been constructed as an instrument for distinguishing between day-to-day thunderstorm scenarios.

## INTRODUCTION

From the very beginning of the ELF research, the parameters of SR (peak frequencies and amplitudes as well as quality factors) have been considered as valuable information suitable for monitoring global thunderstorm activity. As a rule, the monitoring procedures have been based on spherically symmetrical (regular) models of the Earth-ionosphere wave-guide, in the limits of which models the SR parameters depend only on source's characteristics and the source-observer distance. But the analysis of ELF data accumulated at the Rhode Island site since 1994 shows that such a dependence is not sufficient, and some other factors are to be taken into account to interpret observed variations of the SR parameters. It was assumed that asymmetries of the wave-guide are also responsible for the observed phenomena.

## PROPAGATION MODEL

The assumption has been tested by means of an approach suggested by *Madden and Thompson* [1965] and developed by *Kirillov et al.* [1997]. The method is based on a two-dimensional telegraph equation (TDTE)

$$\mathrm{div}\,[\mu_0 \mathrm{H}_{\perp}(\theta,\varphi)]^{-1}(\theta,\varphi)\mathbf{Grad}\,U(\theta,\varphi) + \omega^2\varepsilon_0[H_{\zeta}(\theta,\varphi)]^{-1}U(\theta,\varphi) = \Lambda(\omega,\theta,\varphi,\theta^*,\varphi^*)$$

formulated in an arbitrary system of spherical co-ordinates (the right part of the equation being a two-dimensional analogue of a three-dimensional source) with propagation parameters in the form of complex characteristic altitudes which are analogous to those introduced by *Greifinger and Greifinger* [1972] for simplified determining ELF eigenvalues from aeronomical profiles. In its general formulation, the TDTE method is suitable for taking into account any asymmetries of the wave-guide, but some considerations listed by *Galejs* [1970] suggest that the most important are the differences between "grossly averaged day and night hemispheres". Exploiting such a model provides an additional advantage, since it allows keeping at least a limited (azimuthal) symmetry of the wave-guide, which, in its turn, permits to obtain an analytical solution realizable without any time-consuming numerical integration algorithms. Since there still is no reliable procedure of extracting ELF propagation parameters directly from experimental observations, we estimated them on the basis of representative day and night aeronomical profiles.

FIG.1a. Peak Frequency vs. UT, SR I

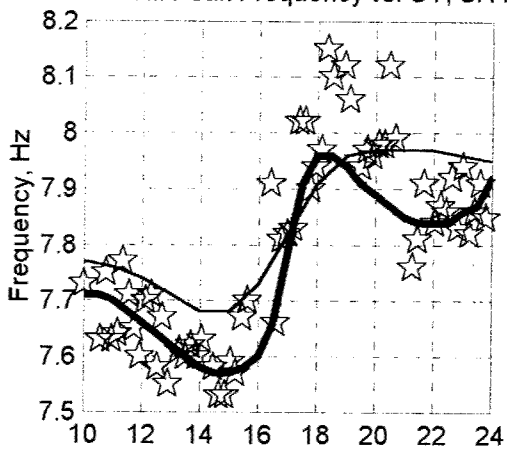


FIG.2a. Inv.Task Diagram, 2000 UT, SR I

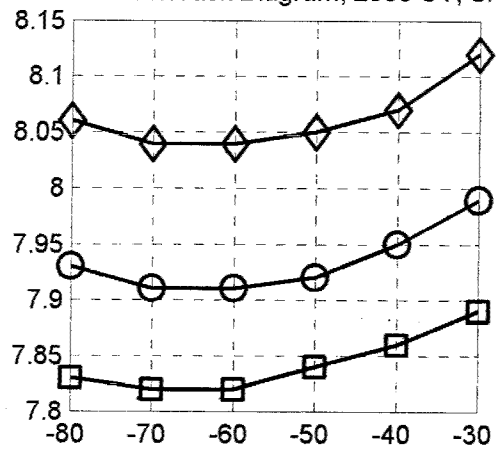


FIG.1b. Peak Frequency vs. UT, SR III

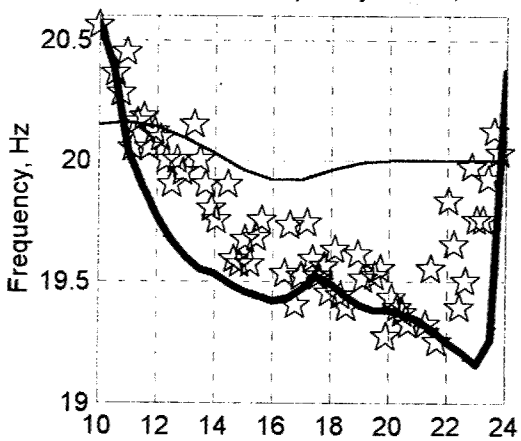


FIG.2b. Inv.Task Diagram: 1600 UT, SR III

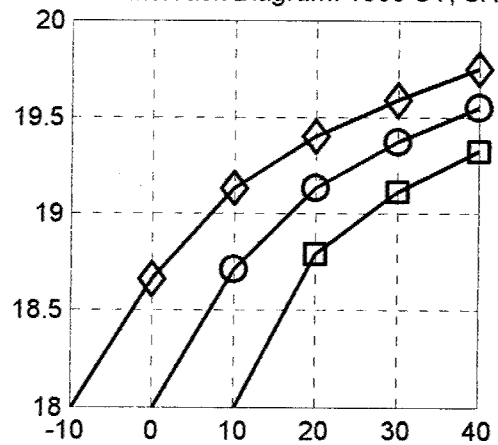


FIG.1c. Peak Frequency vs. UT, SR IV

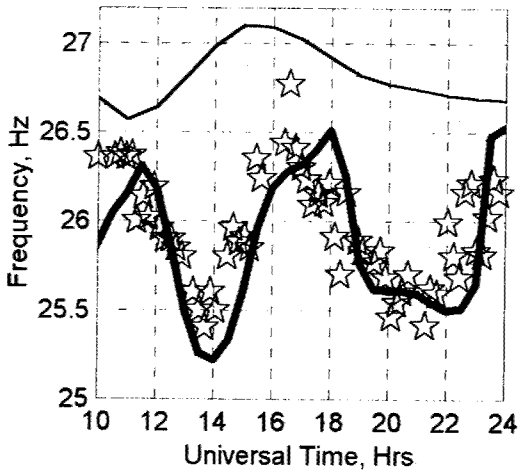


FIG.2c. Inv.Task Diagram: 1500 UT, SR IV

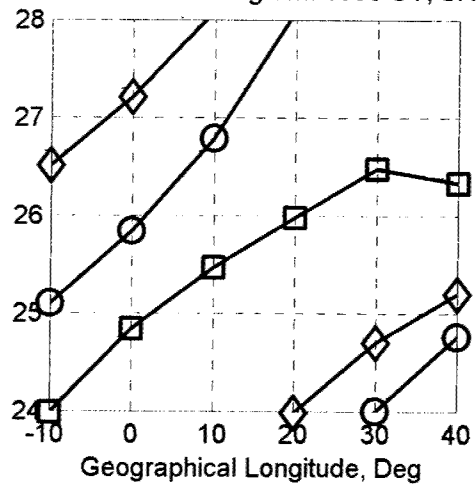

## GLOBAL THUNDERSTORM ACTIVITY MODEL

The model of the activity has been constructed taking into account the most general features of the spatial-temporal dynamics of this geophysical process, namely: the presence of three major global thunderstorm areas; the presence of kernel thunderstorm regions moving predominantly westward within each of the areas during its prevailing activity; latitudinal migration of the major areas with season, and an approximately Gaussian-like dependence of the total activity of each major area on the local time. The parameters of the model (the geographical limits and seasonal latitudinal migration of the major areas as well as the sizes, relative activities and longitudinal dynamics of the kernel regions) have been estimated on the basis of available meteorological, satellite and VLF data.

## THEORY AND EXPERIMENT CONCLUSIONS

A series of modeling simulations has been carried out to test the influence of the day/night asymmetry of the Earth-ionosphere wave-guide on the diurnal-seasonal variations of Schumann resonanses. Since the peak frequencies (PF) are the most susceptible to the source position and, therefore, are of the main interest from the point of view of monitoring global thunderstorm activity, special emphasis has been laid on these parameters. It was found that during the period of prevailing contribution of Asian activity there was rather a poor agreement between the observed and calculated dynamics of PF, which can be caused by two factors. Firstly, the Asian area is the most remote from the RI site, so it is essentially 'shielded' by the background activity even during its maximum intensity; secondly, geophysical properties of this land-maritime-archipelago area are too specific to be adequately described by the above-mentioned model. On the contrary, the continental - African and American - major areas produce PF variations which are in a qualitative (and, sometimes, also quantitative) agreement with simulated ones. An example (December 13, 1996; SR I, III-IV; the vertical electric component) is shown in Fig.1: pentagrams – experimental results, bold curves – simulations with a day/night model of the wave-guide; for comparison there are also shown simulations with a spherically symmetrical wave-guide (thin curves). In Fig.2 are shown some examples of inverse task diagrams – December values of peak frequencies vs. the longitude of the center of the American (Fig.1a) and African (Fig.1b, 1c) kernel regions for three latitudinal levels: 20°S (diamonds), 10°S (circles), and at the equator (squares).

Reasonable qualitative agreement between theoretical results and experimental observations shows that the proposed models satisfactorily reflect the most general features of generating SR in the Earth-ionosphere cavity. Nevertheless, to be used in an inverse task procedure, the propagation parameters need to be specified in a more adequate manner (for instance, on the basis of analyzing transients produced by lightnings reliably localized by means of some independent – satellite or meteorological - technique).

## REFERENCES


Galejs, J., Frequency Variations of Schumann Resonances, *J.Geophys.Res.*, **75**,3237--3251,1970.

Greifinger C., and Ph. Greifinger, Approximate Method for Determining ELF Eigenvalues in the Earth-Ionosphere Wave-Guide, *Radio Sci.*, **13**, 831—837, 1972.

Kirillov V., V. Kopeykin, and V. Mushtak, ELF Electromagnetic Waves within the Earth-Ionosphere Wave-Guide, *Geomagnetizm I Aeronomiya*, **37**, 114-120, 1997 [in Russian].

Madden, T., and W. Thompson, Low Frequency Electromagnetic Oscillations of the Earth-Ionosphere Cavity, *Rev. of Geophys.*, **3**, 211-254, 1965.

PERIODIC VARIATIONS OF SOLAR AND TROPOSPHERIC ORIGINS IN SCHUMANN RESONANCES

B. Zieger and G. Sátori

Geodetic and Geophysical Research Institute of the Hungarian Academy of Sciences, Sopron, Hungary

ABSTRACT: Long-term periodic variations in Schumannn resonance parameters were studied in the period range from 5 days to half a year. Dynamic spectra of daily Schumann resonance amplitudes and frequencies were computed for the first three modes and were compared with dynamic spectra of solar wind speed and geomagnetic indices such as Kp and DST. Several periodicities were identified including 108 days, 73 days, 47 days, 27 days, 20 days, 13.5 days and 9-10 days. The most significant correlation between Schumann resonance parameters and solar wind speed (or geomagnetic activity) was found at the period of 13.5 days (half a solar rotation period). This implies a solar influence on the upper boundary of the Earth-ionosphere waveguide most probably through energetic particles (MeV protons and electrons).

## INTRODUCTION

Schumann resonances are electromagnetic standing waves excited by lighting discharges in the Earth-ionosphere cavity. The observed intensity and frequency of Schumann resonances depend not only on the source intensity and the source-observer distance but also on the physical parameters of the Earth-ionosphere waveguide. Recently it was discovered that high energy particle precipitation cause changes in the Schumann resonance parameters [*Schlegel and Füllekrug*, 1999]. During such events the amplitude and frequency of Schumann resonances increase whereas the attenuation decreases. Schumann resonance frequencies and amplitudes have been recorded continuously for the vertical electric component at the Nagycenk Observatory (47.6°N, 16.7°E), Hungary since May 1993. This uniquely long homogenous data set allows to study long-term variations in Schumann resonance parameters. The annual and semiannual variations of Schumann resonance amplitudes were reported and discussed earlier [*Sátori and Zieger*, 1996]. In the present study, we identify periodicities in Schumann resonance amplitudes and frequencies in the period range from 5 days to half a year and discuss their possible origin.

## METHOD

Instead of conventional Fourier spectograms we applied a series of bandpass convolution filters to construct dynamic spectra. The central period of the bandpass filters with ±5 % relative band width was varied in steps of 5 % of the central period in order to ensure full coverage in the frequency range. We used a complex ideal bandpass filter tapered by the Hanning window, where the real and imaginary parts were the in-phase and out-of-phase components of the filter, respectively. The length of each filter was 12 times the central period which provided sufficiently good transfer characteristics in the frequency domain (see Figure 1).

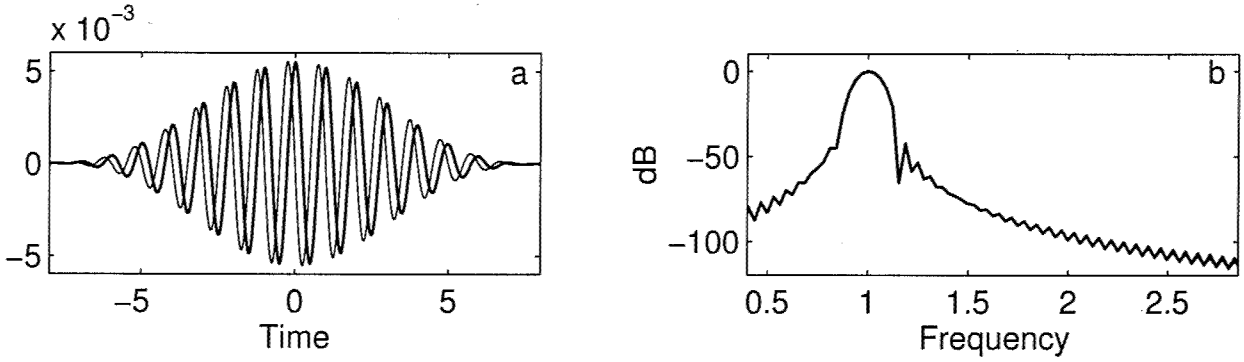


Figure 1. Real (thick line) and imaginary (thin line) parts of the bandpass filter in time (a) and frequency (b) domains. Time and frequency are given in units of the central period and central frequency, respectively.

Applying both the real and imaginary parts of the convolution filters, the instantaneous complex wave vector is obtained at each point of the dynamic spectrum matrix. The magnitude and phase of the complex wave vector determines the instantaneous amplitude and phase in the corresponding frequency band. The main advantage of this

method against the Fourier technique is that the frequency resolution can be freely selected, while in case of Fourier transformation the frequency resolution is determined by the selected time window, i. e. the time resolution. The time resolution of dynamic spectra calculated with convolution filtering is changing from one frequency band to the other according to the effective length of the corresponding bandpass filter. Taking the scalar product of two normalized complex dynamic spectra, a dynamic cross-spectrum can be derived, which is particularly suitable for identifying common periodicities in two variables.

RESULTS

We calculated the dynamic spectra of Schumann resonance parameters (using daily average amplitudes and daily median frequencies for the first three modes) in the period range from 5 days to 225 days. The dynamic spectra were normalized to the average power in the above mentioned period range to allow the comparison of different variables. The upper panel of Figure 2 depicts the dynamic spectrum of the amplitude of the first Shumann resonance mode. Very similar dynamic spectra were obtained for the second and third modes as well (not shown here). Lot of periodicities occur especially between 5 and 30 days. These periodic variations are not continuos but they appear intermittently. At longer periods the strongest periodicities are found at about 50 days, 70 days, 100 days and half a year. It should be noted that the time resolution at longer periods is inferior because of the longer filters, and the amplitudes are somewhat decreased at the beginning and end of the dynamic spectra for the same reason.

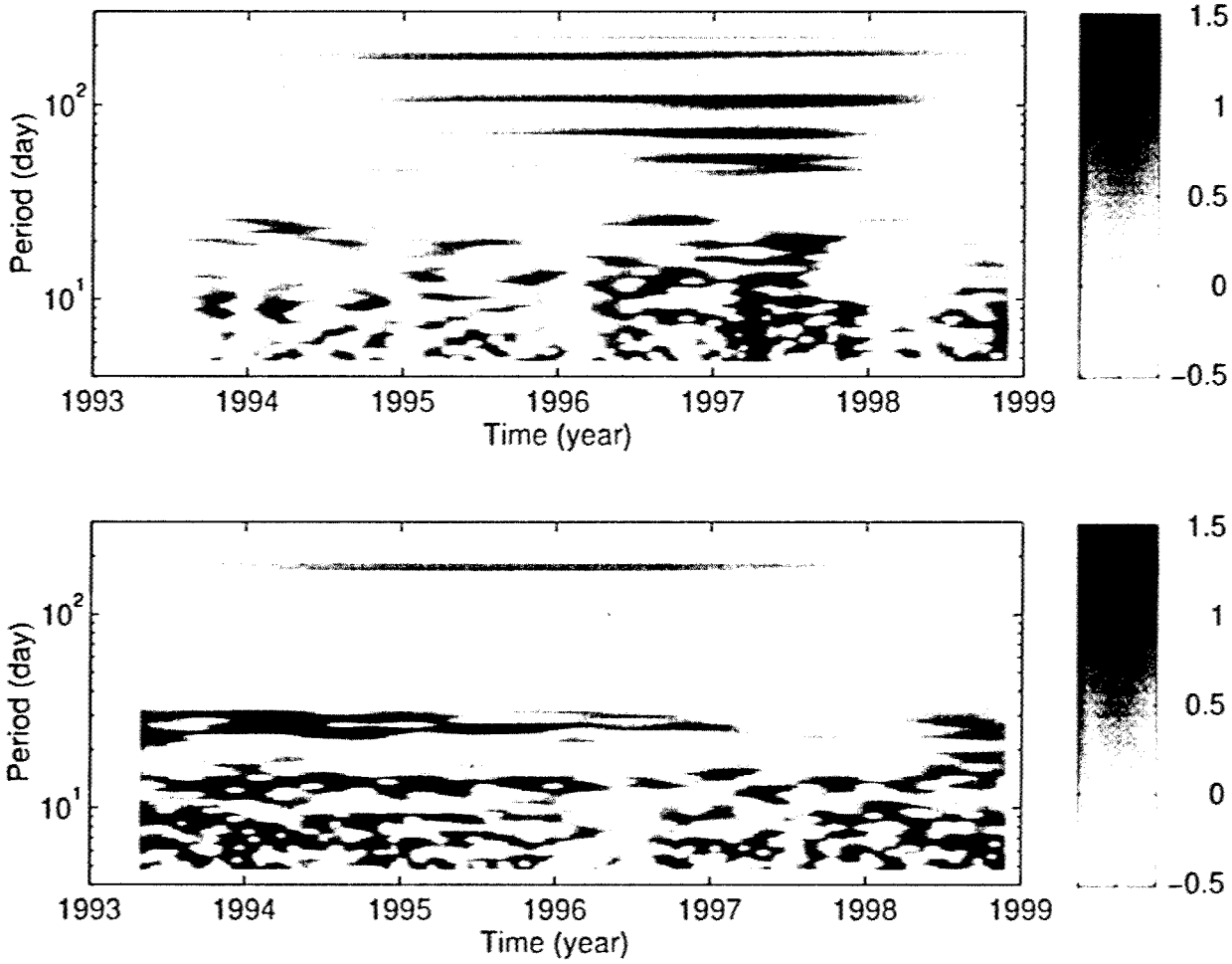


Figure 2. Normalized dynamic spectra of the amplitude of the first Schumann resonance mode (upper panel) and that of the geomagnetic index Kp (lower panel). The logarithmic intensity scales on the right are given in powers of 2.

The lower panel of Figure 2 shows the dynamic spectrum of the geomagnetic activity index Kp. Such dynamic spectra were computed also for solar wind speed and DST. In this period range, geomagnetic activity (as well as solar wind speed) is dominated by the harmonics of the solar rotation period (27 days, 13.5 days, 9 days etc.). Note that the half solar rotation period (13.5 days) is sometimes higher than the fundamental 27-day periodicity. The 13.5-day periodicity in solar wind speed and geomagnetic activity occurs mainly in the late declining phase of the solar cycle when the heliospheric current sheet is flat and tilted and two high speed solar wind streams hit the Earth during one solar rotation, originating from different magnetic hemispheres [*Mursula and Zieger*, 1996]. At higher periods, the most significant periodicity in geomagnetic activity is the well-known semiannual variation [*Russell and McPherron*, 1973].

In order to identify the dominant periodicities more accurately, we calculated so-called average spectra by averaging the amplitudes in each period band. The average spectra of the amplitudes of the first three Schumann resonance modes is shown in the upper panel of Figure 3. The dominant periodicities are fairly similar for the three modes, including 185, 152, 108, 73, 55, 47, 27, 20, 13.5, 10.4 and 8.6 days. The error of these period values is ±5 %, as the relative band width of the bandpass filters was ±5 % of the central period and the central period was varied in steps of 5 %. In the period range of 5 to 30 days, the most dominant periodicity of Shumann resonance amplitudes is the 20-day periodicity which is clearly separated from the 27-day spectral peak. Similar average spectra were calculated from the dynamic spectra of solar wind speed, Kp, and DST (see lower panel of Figure 3). There are strong periodicities in the Schumann resonance amplitudes which are completely absent in solar wind speed and geomagnetic activity, such as 108, 73, 47, 20 and 10 days. The latter periodicities are most probably of tropospheric origin. The harmonics of the solar rotation period are clearly present in the average spectra of Schumann resonance amplitudes. Note that the spectral peak at 13.5 days is higher than the spectral peak at 27-days indicating that the half solar rotation periodicity is a fundamental periodicity.

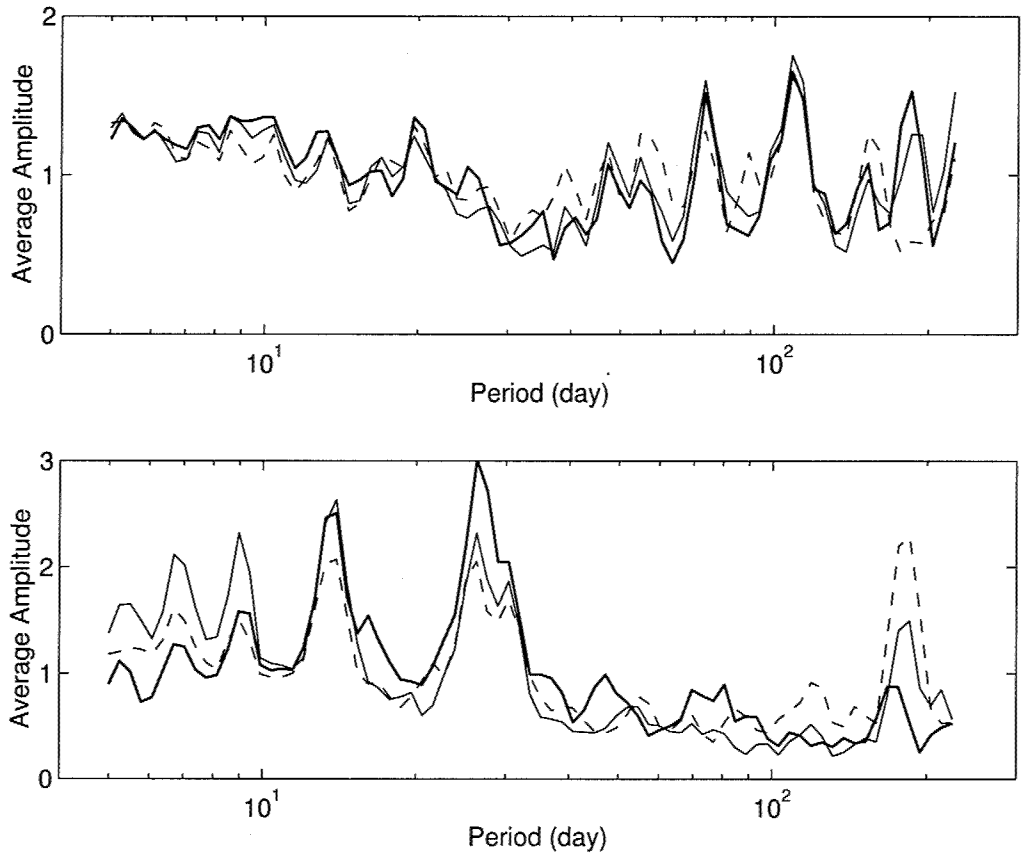


Figure 3. Upper panel: Average spectra of the amplitudes of the first (thick line), second (thin line) and third (dashed line) Schumann resonance modes; Lower panel: Average spectra of solar wind speed (thick line), Kp (thin line) and DST (dashed line).

We calculated dynamic cross-spectra between the Schumann resonance parameters and geomagnetic activity/solar wind speed in order to check if the common periodicities found in the average spectra are correlated. The dynamic cross-spectrum of the amplitude of the first Schumann resonance mode and Kp is shown in Figure 4. Highest average correlation was found at the period of 13.5 days. During the time interval studied, six episodes of enhanced 13.5-day variation occurred in Shumann resonance amplitudes and each of them was in phase with the 13.5-day variation of geomagnetic activity (or solar wind speed). Similar 13.5-day variation was identified also in the frequency of Schumann resonances.

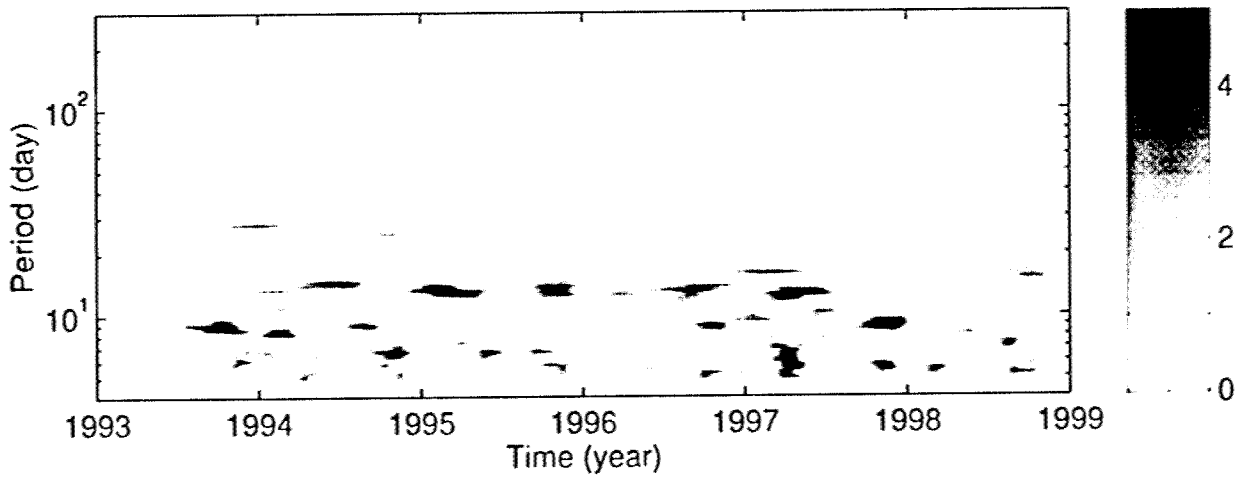


Figure 4. Dynamic cross-spectrum of the amplitude of the first Schumann resonance mode and Kp. The linear intensity scale on the right is given in units of the average power in the full period range.

## CONCLUSIONS

We identified the dominant periodicities in Schumann resonance parameters in the period range from 5 days to half a year. The harmonics of the solar rotation period are present both in the amplitude and frequency of Schumann resonances. The half solar rotation period was found to be the most dominant common periodicity in Schumann resonance parameters and geomagnetic activity (or solar wind speed). We suggest that the 13.5-day variation of Schumann resonance parameters are caused by energetic particles (protons, electrons > 1MeV) modulating the conductivity of the upper wall of the cavity resonator. The periodicities of 108, 73, 47, 20 and 10 days identified in Schumann resonance amplitudes may be driven by tropospheric processes, and be related to changes in the global lightning activity.

ACKNOWLEDGEMENTS: This research was supported by the Hungarian Science Foundation and the U.S.-Hungarian Joint Fund under grants T023111 and JF554, respectively. B. Zieger acknowledges support by the Danish Research Council and also by the Hungarian Ministry of Culture and Education under the Hungarian State Eötvös Fellowship.

## REFERENCES

Füllekgrug, M. and A.C. Fraser-Smith, Further evidence for a global correlation of the Earth-ionosphere cavity resonances, *Geophys. Res. Lett.*, 23, 2773-2776, 1996

Mursula, K. and B. Zieger, The 13.5-day periodicity in the Sun, solar wind, and geomagnetic activity: The last three solar cycles, *J. Geophys. Res.*, 101, 27077-27090, 1996

Russell, C.T. and R.L. McPherron, Semi-annual variation of geomagnetic activity, *J. Geophys. Res.*, 78, 92-108, 1973

Sátori, G. and B. Zieger, Spectral characteristics of Schumann resonances observed in Cenatral Europe, *J. Geophys. Res.*, 101, 29663-29669, 1996

Schlegel, K. and M. Füllekrug, Schumann resonance parameter changes during high energy particle precipitation, *J. Geophys. Res.*, in print, 1999

# COMPARISONS OF LONG-TERM SCHUMANN RESONANCE RECORDS IN EUROPE AND NORTH AMERICA

G. Sátori[1], E.R. Williams[2], B. Zieger[1], R. Boldi[3], S. Heckman[4], K. Rothkin[2]

[1]Geodetic and Geophysical Research Institute, Sopron, HUNGARY
[2] MIT, Parsons Laboratory, Cambridge, Ma, U.S.A.
[3] MIT, Lincoln Laboratory, Lexington, Ma, U.S.A.
[4] NASA, Hunstville, Alabama, U.S.A.

ABSTRACT: Two stations at a distance comparable with the wavelength in the Schumann resonance (SR) frequency range, one in Europe (Nagycenk, Hungary) and one in North America (West Greenwich, Rhode Island) have simultaneously monitored the natural vertical electric and horizontal magnetic field components in the frequency range of 3-25 Hz. This is a unique opportunity, as Schumann resonance stations are scarce and even fewer station have records with 5-6 year durations. The main purpose of this paper is to make comparisons in the SR time series measured simultaneously at the two field site, thereby providing access to global behavior on the seasonal and interannual time scales. The comparative measurements described here point out distinct differences in the nature of convection in South America and in Africa, and reveal new aspects about the behavior of tropical continental convection on the ENSO time scale.

## INTRODUCTION

Long term comparative measurements of the global electrical circuit have historically been quite scarce on account of local noise problems and the difficulty in obtaining measurements of ionospheric potential on a continous basis. Schumann resonance measurements largely overcome both these difficulties, and a growing interest in global change has encouraged new monitoring efforts. The major cornerstone of atmospheric electricity has been constructed around the universal diurnal cycle of global tropospheric convection. In this paper, coordinated measurements at remote locations in Hungary and in Rhode Island for a 6 year period are used to investigate aspects of global convection on the seasonal and the interannual time scales.

## INSTRUMENTATION-METHODOLOGY

In each field station a ball antenna and two induction coils are used for the measurement of the vertical electric field component and the horizontal magnetic field components, respectively. Spectral analysis applied by the two observatories are different. The actual peak frequencies of the first three modes and the corresponding amplitudes are determined by the complex demodulation technique at Nagycenk (NC), whereas Fourier analysis is applied to compute the spectral powers, and Lorentzian spectral fits are then used to determine the frequencies and the Q-factors for the first eight resonance modes in Rhode Island (RI).

## COMPARISONS

Figure 1 shows the geographical position of Nagycenk and West Greenwich with respect to the main tropical thunderstorm regions. Africa is the dominant source region for the European observatory and South America for the North American field site.

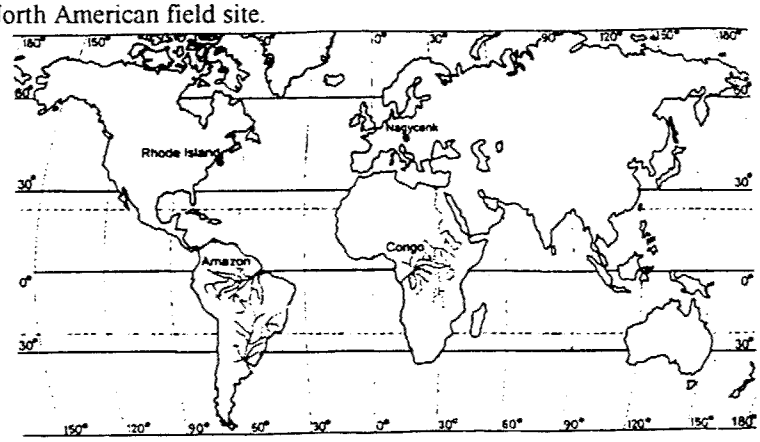


Figure 1. The geographical position of the two SR observatories (Nagycenk, Hungary and West Greenwich, Rhode Island) showing also the Amazon and Congo regions.

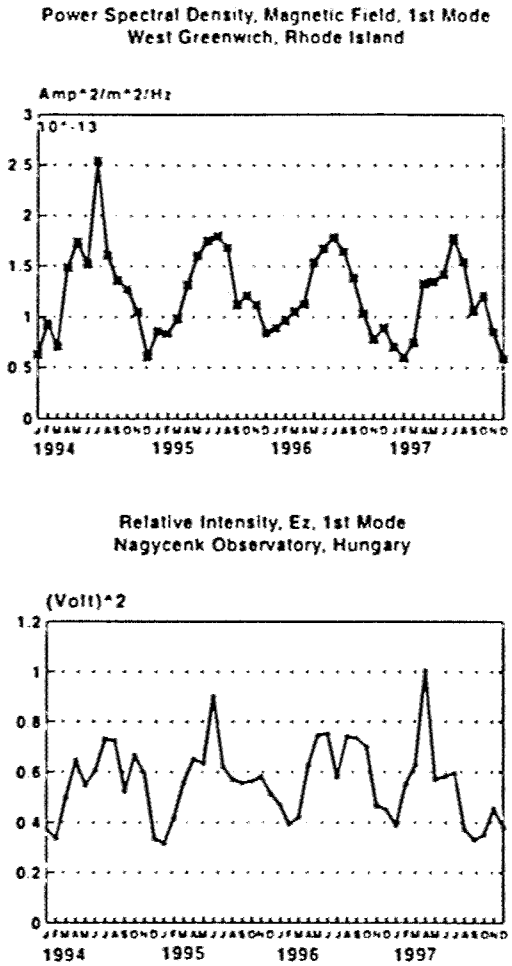


Figure 2.

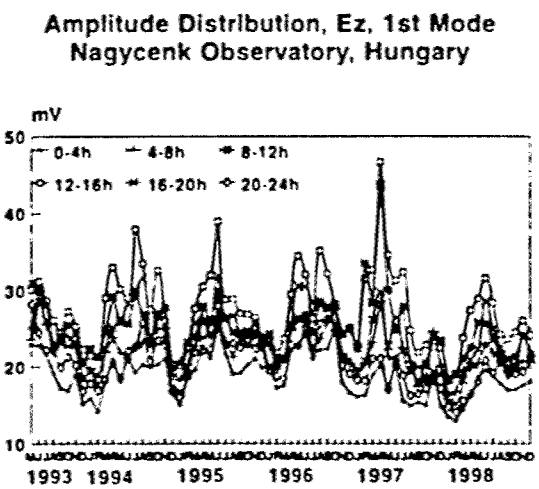


Figure 3.

The Ez records in Hungary and magnetics in Rhode Island are clearly consistent in amplitude and phase on the annual time scale, as indicated by Fig.2. The maxima in NH summer and the approximate factor-of two overall variation are consistent with ongoing observations of lightning from space with the Optical Transient Detector (OTD). The relative roles of source proximity effect and intrinsic source variation remain an issue for this time scale as well, and it is likely that their relative contributions are different at the two locations. The North American source is particularly strong in summer, perhaps as strong as any tropical source *Fullekrug and Fraser-Smith* [1998]. A portion of the substantial SR intensity variation is attributable to the source proximity effect in Rhode Island while the majority in Hungary is likely due to intrinsic variation of the global lightning activity. The signature of the tropical semiannual temperature variation is well pronounced in the vertical electric field component at Nagycenk [*Sátori and Zieger*, 1996] with maxima near equinox months in 1993, 1994, 1995 and 1997 but with different magnitudes in different 4-hour segments of the UT day as shown in Fig.3. The most pronounced semiannual signal is found in the 12-16 UT interval and lends further evidence for Africa as the primary source of the latter signal. Only a weak indication of the semiannual variation is present in the Rhode Island record. Figure 4. shows the annual and semiannual sinusoidal components of the SR intensities for Rhode Island (line with stars) and Nagycenk (line with circles) extracted by digital filtering technique. As each time series was normalized by its own median value both the magnitudes and phases are comparable. The annual wave is dominant for RI and they are almost in phase in the two stations with summer maxima, the semiannual waves with near equinoxial maxima are present only in Nagycenk records. The phase of the semiannual wave with summer (winter maxima) at RI implies its subharmonic nature without physical meaning. Figure 5. shows the filtered semiannual waves in the 12-16 UT and 20-24 UT intervals at Nagycenk. Their magnitudes are higher in that time interval when Africa dominates the lightning activity. Even the smaller late evening semiannual signal is rather attributable to the rest activity of Africa than South America.

Measurements of the horizontal magnetic field components were also started in Hungary at the end of 1996. Figure 6a,b show that the semiannual waves with near equinoxial maxima are also present in magnetics in this European station.

The distinct differences in semiannual behaviour between Hungary and Rhode Island naturally invited a closer examination of the respective source regions.

The two largest rivers in the world (by discharge volume) drain these two source regions: the Amazon

and the Congo. The limits of the Amazon basin correspond closely with Brazil's borders and likewise the Congo is largely contained within the former Zaire. Hydrological [*Amerasekera et al.*, 1997] and climatological meteorological information for these two countries [*Marques*, 1992; and *de Halleux*, 1979] have therefore been compared to shed light on the semiannual component on a scale appropriate for the global Schumann resonances.

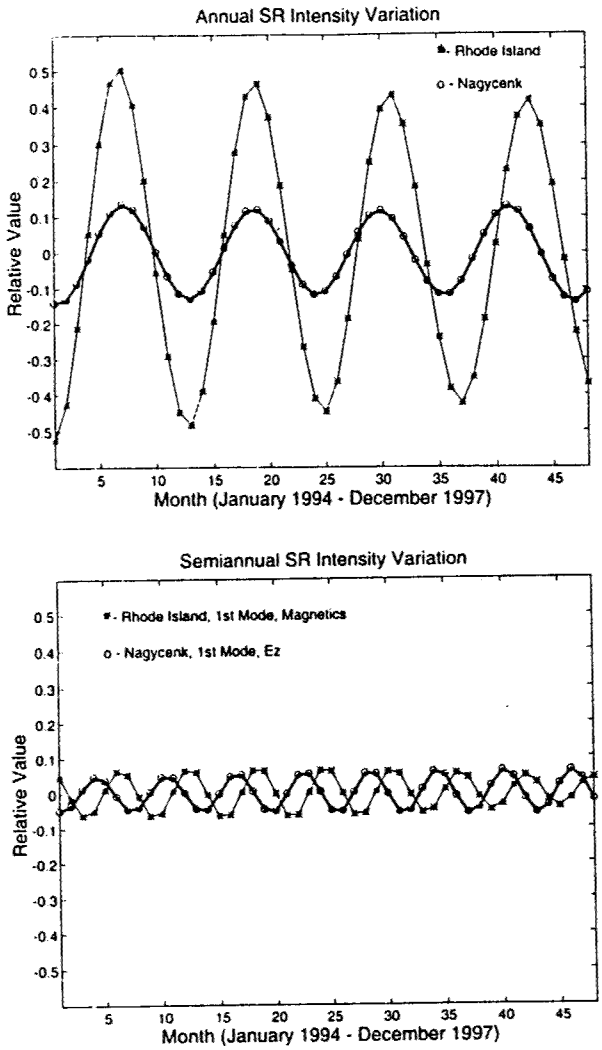


**Figure 4. Annual-semiannual SR intensity variations extracted by filtering technique. (above)**

Marked differences were found in the comparisons of seasonal maximum surface air temperature, with nearly all stations in Zaire showing double-peaked seasonal behavior, whereas fewer than 20% of 26 stations within 5 degrees of the equator in Brazil showed such an effect. Seasonal variations of rainfall [*Figueroa and Nobre*, 1990] likewise show a far more prevalent characteristic in Zaire than in Brazil. On a basin scale, the collective behavior is self consistent: the seasonal discharge record for the Congo is double-peaked, whereas the Amazon record shows a single broad maximum in July with little hint of semiannual behavior.

The physical explanation for the marked differences in Schumann resonance intensity documented in Fig.2 and Fig.4 may lie in the hydrological observations [*Meade et al.*, 1991 and *Amerasekera et al.*, 1997]. The difference in annual precipitation between these two great basins is only 30% but the runoff to rainfall ratio for the Amazon is 2.5 times greater than for the Congo. This observation suggests that the Amazon basin is much closer to fluid saturation (and hence prone to greater runoff) than the Congo. This also strongly suggests that Amazon (and the South American continent of which the Amazon is a large piece), will behave more like an ocean than a land surface, and hence respond less strongly than Africa to the well known semiannual variation in solar insolation in the tropical region [*Williams*, 1994]. The tropical oceans show very little response on the semiannual time scale. The contrast in convective response in Africa and Brazil on the semiannual time scale is consistent with the like contrast in their response on the diurnal time scale [*Park*, 1990] .

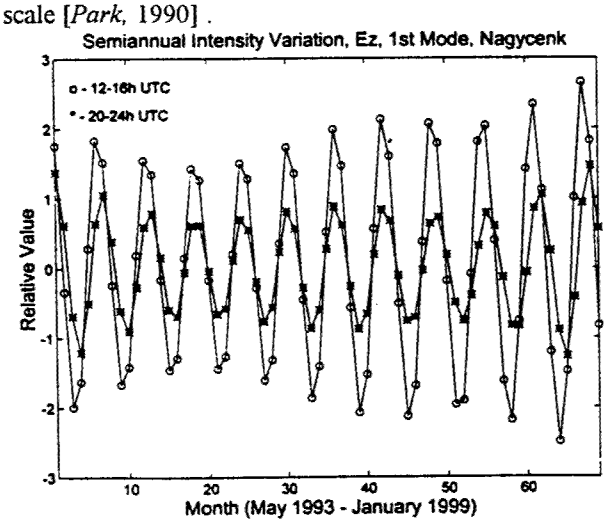


Figure 5. Semiannual waves of Ez at Nagycenk filtered for different segments of a day. (right )

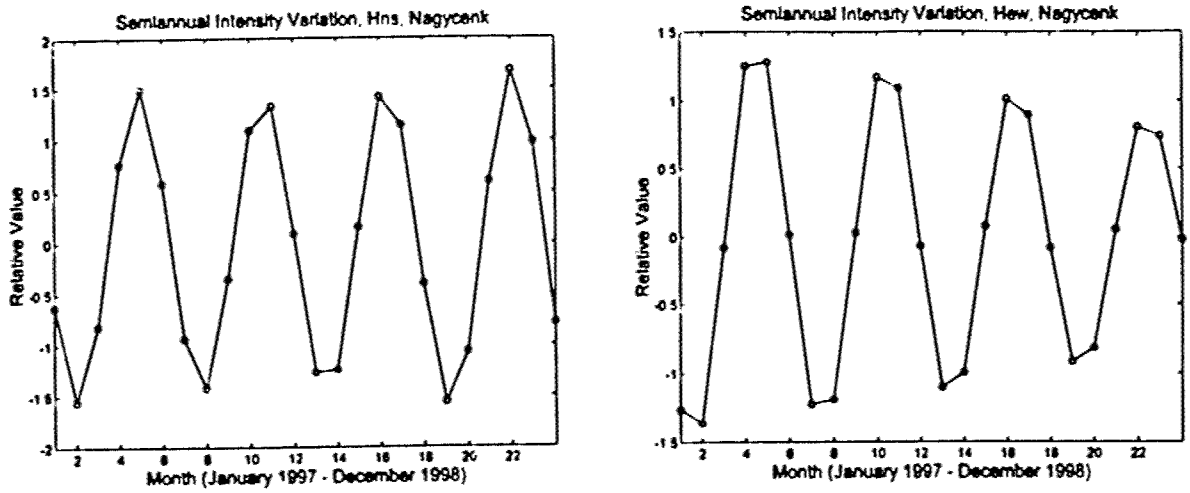


Figure 6. Semiannual intensity variations of the magnetics at Nagycenk extracted by filtering technique.

The interannual variation in SR intensity with a moderate increase in 1996 (see Fig 2) is correlated between the two stations, but is undramatic in comparison with the seasonal changes already discussed. The dominant contributor to interannual variability in the tropics, where lightning is most prevalent, is the El Niño phenomenon. Despite vigorous ENSO activity during the 1993-1998 period of coordinated SR measurements, the strong in-phase relationship between SR intensity and tropical temperature found earlier by *Williams* [1992] for an earlier epoch, is not apparent. In fact, in the present record, the behavior is opposite: the electric intensity in Hungary was low in the previous warm epoch (1993, 1994), high during the cool 1996, and again low in the latest intense warm El Niño phase between March 1997 and April 1998. Then it began to incrase in the recent cool La Niña phase (see Fig.3). Based on SR frequency and intensity observations at Nagycenk, *Sátori and Zieger* [1999] suggest meridional shifts of lightning activity in global sense with a southward (northward) displacement in the warm (cool) phase of the ENSO

ACKNOWLEDGEMENT: Discussion with E. Eltahir on issues of hydrology are much appreciated. This research was supported by the U.S.-Hungarian Joint Found, JF554 and the Hungarian Science Foundation, T023111.

REFERENCES

Amerasekera, K.N., R.F. Lee, E.R. Williams and E.A.B. Eltahir, ENSO and the natural variability in the flow of tropical rivers, *J. Hydrology, 200*, 24, 1997.

Ergo, A.B. and B. de Halleux, Catalogue Mondial des Donnees Climatiques Moyennes, Vol. II-L'Afrique, Fascicule I.,Premiere partie: Zaire, Musee Royal de L'Afrique Centrale, Tervuren, Belgium, 225 pp., 1979.

Figueroa, S. N. and C. A. Nobre, Precipitation distribution over Central and Western Tropical South America, *Climanalise*, 5(6), 36-45, 1990

Füllekrug, M. and A.C. Fraser Smith, Global lightning and climate variability inferred from ELF magnetic field variations, *Geophys. Res.Letter*, 24(19), 2411-2414, 1997.

Marques, J.C., Normais Climatologicas (1961-1990), Departamento Nacional de Meteorologia (INMET), Brasilia, Brazil, 84 pp., 1992

Meade, R.H., J.M. Rayol, S.C. Da Conceicao and J.R.G. Natavidade, Backwater effects in the Amazon River Basin, *Envir. Geol. Water Sci.*, 105-114, 1991.

Park, S., ISCCP Satellite Observations of the Diurnal Variation of Deep Tropical Convection, Master's Thesis, Center for Meteorology and Physical Oceanography, 1990

Sátori, G., and B. Zieger, Spectral characteristics of Schumann resonances observed in Central Europe, *J. Geophys. Res., 101*, 29,669, 1996

Sátori, G., and B. Zieger, El Niño related meridional oscillation of global lightning activity, *Geophys. Res. Letter*, in press, 1999

Williams, E. R., The Schumann resonance: A global tropical thermometer, *Science, 256*, 1184, 1992.

Williams, E. R., Global circuit response to seasonal variations in global surface air temperature, *Mon. Weather Rev., 122*, 1917, 1994

# GLOBAL LIGHTNING TRIANGULATION

**Martin Füllekrug**

Institut für Meteorologie und Geophysik
Johann Wolfgang Goethe Universität Frankfurt am Main
Feldbergstr.47, D-60323 Frankfurt/Main, Germany
Tel: (49) 69-798-23959, Fax: (49) 69-798-23280,
Elm: fuellekr@geophysik.uni-frankfurt.de,
WWW: http://www.geophysik.uni-frankfurt.de/~fuellekr/

## Introduction

Three GPS synchronized measurement stations recorded horizontal magnetic field variations in the ULF/ELF transition range from 4-200 Hz at Silberborn, Germany (51.8° N, 9.5° E), and 4-19 Hz at Hollister, California (36.8° N, 121.4° W), and at Lameroo, Australia (35.5° E, 140.6° E), during April 1998. The three station records exhibit simultaneous discrete excitations of Earth-ionosphere cavity (or Schumann) resonances which result from the constructive interference of electromagnetic waves which propagate with little attenuation in the spherical Earth-ionosphere waveguide (Schumann, 1952; Sentman, 1995). These Earth-ionosphere cavity resonances are mainly excited by particularly strong lightning flashes which can be triangulated by use of the orientation of the Poynting vector along the great circle path of propagation (see Figure 1).

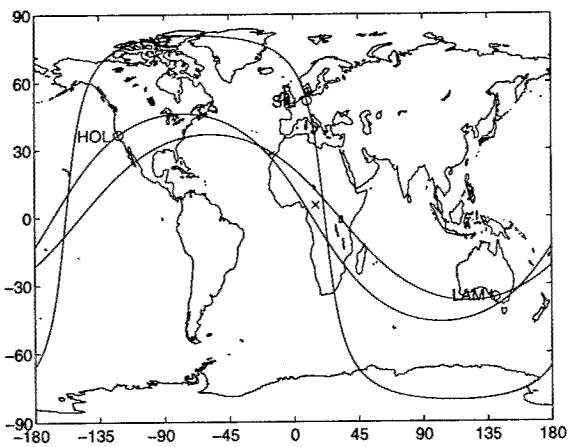


Figure 1: The orientation of the Poynting vector along the great circle path of propagation at Silberborn (SIL), Germany, Hollister (HOL), California, and Lameroo (LAM), Australia, are used to triangulate a lightning flash location in central Africa (x).

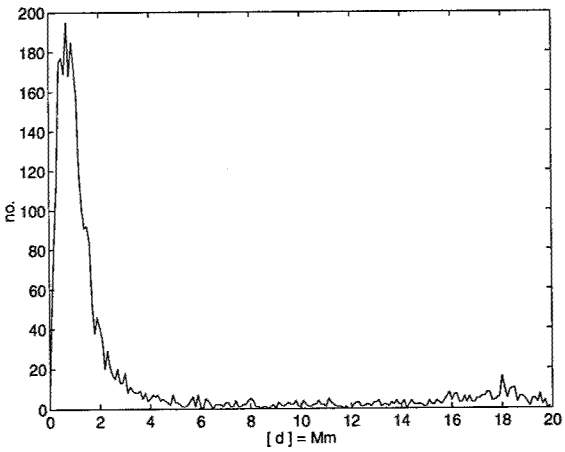


Figure 2: The validation of the triangulated lightning flash locations with lightning flash locations reported by the VLF time of arrival difference system of the British Meteorological Office indicates an accuracy of several hundered kilometers.

## Lightning flash triangulation

The great circle path crossing points of the three independently observed Poynting vector orientations determine two best fitting lightning flash locations on the Earth. The time of arrival difference between two stations is used resolve the hemispheric ambiguity. The derived lightning flash locations are validated with lightning flash locations reported by the VLF time of arrival difference system of the British Meteorological Office (Lee, 1986). The lightning flash location accuracy by use of Earth-ionosphere cavity resonances is on the order of several hundred kilometers (see Figure 2). The physical reason for the location error is threefold (Füllekrug & Sukhorukov, 1999). First, the lightning flash bearing deviation exhibits a rotational dependence at coastal stations as a result of the excitation of higher order modes in the vincinity of the sharp conductivity contrast between the Ocean and the Earth's crust (see Figure 3). Second, the bearing deviation exhibits a diurnal variation which results from the anisotropic contribution of the ionosphere to the wave propagation, mainly apparent during night time conditions (see Figure 4). This bearing deviation $\Delta\varphi$ can be estimated

$$\Delta\varphi = \arctan \frac{1}{2k_0 n_E h_E}$$

where, $k_0$ is the free space wave number, $h_E$ is the height of the ionospheric E-region ~90 km, and $n_E$ is the refractive index of the nocturnal E-region. Third, random occurrences of sporadic D-layer ionization patches result in a statistical variability of the source triangulation accuracy (Pappert, 1985).

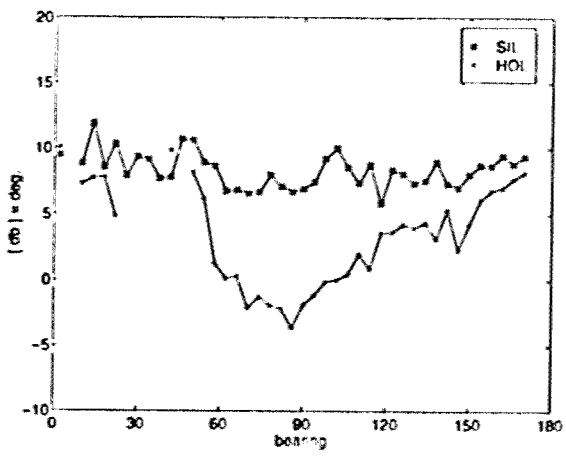


Figure 3: Rotational dependence of bearing deviations (db) at Silberborn (SIL), Germany, and Hollister (HOL), California. The rotational dependence at Hollister ~12° results from the nearby Pacific coast.

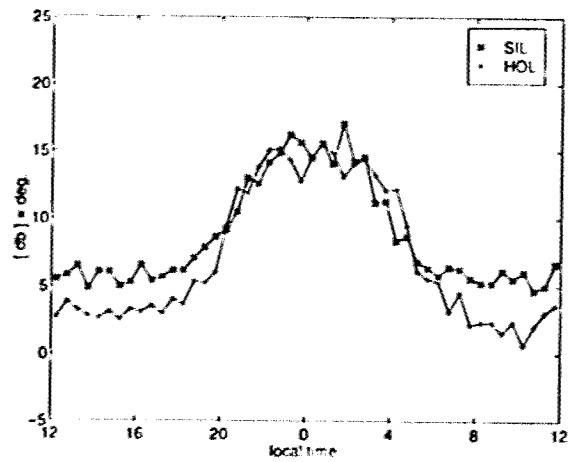


Figure 4: Mean diurnal variation of the bearing deviation (db) at Silberborn (SIL), Germany, and Hollister (HOL), California, ordered with respect to local time. The diurnal variation results from anisotropic contributions of the night time ionosphere.

## Global lightning activity

All triangulated lightning flashes represent an estimate of global lightning activity, depicted for April 28, 1998, in Figure 5. Since the horizontal magnetic field variations can easily be monitored continously, it is possible to determine the temporal evolution of particularly interesting thunderstorms, for example in central Africa, North America, and Australia (see Figure 6). The thunderstorms in North America and Australia exhibit a sharp rise of the flash rate and a decay within one day, while the high flash rate in Africa persists for 3-4 days and may be associated with a mesoscale convective system (Laing & Fritsch, 1997) or many individual thunderstorm cells.

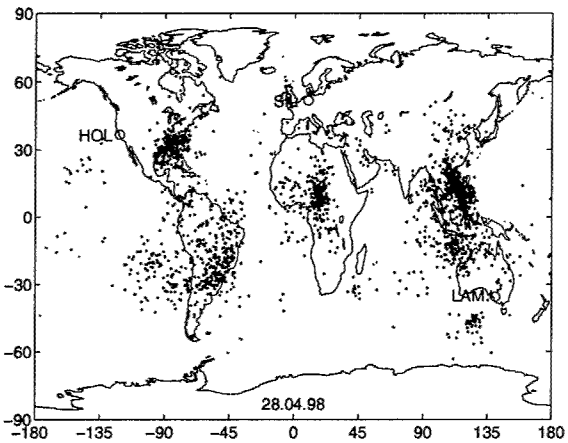


Figure 5: Lightning flash locations on April 28, 1998, triangulated from simultaneous observations of Earth-ionosphere cavity resonances at Silberborn (SIL), Hollister (HOL), and Lameroo (LAM).

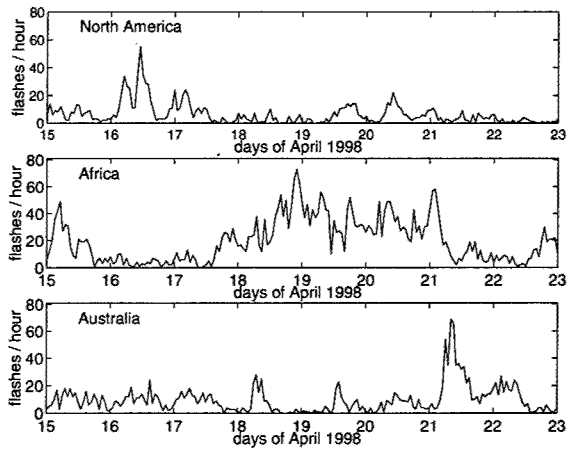


Figure 6: The number of lightning flashes per hour in North America and Australia exhibit a sharp rise of the flash rate and a decay within one day, while the high flash rate in Africa persists for 3-4 days.

# References


Füllekrug, M., & Sukhorukov, A.I. 1999. The contribution of anisotropic conductivity in the ionosphere to lightning flash bearing deviations in the ELF/ULF range. *Geophysical Research Letters*, .(in press), .

Laing, A. G., & Fritsch, J.M. 1997. The global population of mesoscale convective complexes. *Quart. J. Roy. Meteor. Soc.*, **123**, p. 389.

Lee, A.C. 1986. An experimental study of the remote location of lightning flashes using a VLF arrival time difference technique. *Quarterly Journal of the Royal Meteorological Society*, **Vol. 112**, p. 203–229.

Pappert, R.A. 1985. Calculated effects of traveling sporadic E on nocturnal ELF propagation: Comparison with measurement. *Radio Science*, **Vol. 20**(No. 2), p. 229.

Schumann, W.O. 1952. Über die strahlungslosen Eigenschwingungen einer leitenden Kugel, die von einer Luftschicht und einer Ionosphärenhülle umgeben ist. *Zeitschrift für Naturforschung*, **Vol. 7a**, p. 149 und 250.

Sentman, D.D. 1995. Schumann Resonances. *In:* Volland, H. (ed), *Handbook of Atmospheric Electrodynamics*, vol. I. CRC Press, Boca Raton.

# THE EUROPEAN LIGHTNING NOX PROJECT – FIRST RESULTS OF THE FIELD EXPERIMENT 1998

U. Finke#, P. Laroche+, H. Höller*, H. Huntrieser*, T. Fehr*

# Institut für Meteorologie und Klimatologie, Universität Hannover, Germany
+ Atmospheric Environment Research Sec., ONERA, Chatillon, France
* Institut für Physik der Atmosphäre, DLR – Oberpfaffenhofen, Wessling, Germany

ABSTRACT: The European lightning NOx project investigates the production and transport of NOx in thunderstorms. In summer 1998 a 3-month field experiment was organized in Central Europe. A unique set of instruments were used including two aircraft for in-situ chemical measurements, 3-dimensional high-resolution lightning mapper, and polarimetric radar for cloud observation. During the various anvil crossings extraordinary high concentrations of nitrogen oxide (exceeding 20ppbV) have been observed. The spiky nature of the signal and the observation of lightning in the near vicinity of the flight path are strong indicators for the NOx being produced by lightning.

## INTRODUCTION:

Nitrogen oxides (NOx = NO and $NO_2$) play an important role in atmospheric chemistry and ozone conversion. Lightning is a significant natural source of NOx but its contribution to the global budget is still uncertain to an order of magnitude. The residence time of NOx in the troposphere is below 10 days, and thus shorter than typical meridional transport times. Hence, despite the most lightning activity is met in the tropics, for the regional NOx budget at the mid latitudes one has to consider the regional lightning NOx production.

Basing on currently assumed emission rates the lightning NOx for Central Europe during the summer months is estimated to be of the same order of magnitude as the contribution from air-traffic. Recently field experiments have been performed in New Mexico (Ridley et al. 1996) and Southern Germany (Höller et al. 1999; Huntrieser et al. 1998) in order to narrow the uncertainty in the lightning NOx estimates.

## PROJECT EULINOX

The aim of the European Lightning NOx project (EULINOX) is the investigation of production and transport of NOx in thunderstorms on the cloud scale as well as on the regional (European) scale. This project is a cooperation between DLR (Germany), ONERA (France), NILU (Norway) and KNMI (Netherlands).

More detailed information on EULINOX can be found at http://www.pa.op.dlr.de/eulinox/.

## FIELD EXPERIMENT

A substantial part of EULINOX is the field experiment organized in summer 1998 in Central Europe. A unique set of instruments was available for chemical in-situ measurements in thunderstorm anvils, detailed mapping of the electric activity of the storm, and for the observation of the clouds dynamical structure and particle composition:

- Instruments for the measurement of chemical species (NOx, $CO_2$, CO, $O_3$) were installed on board of two aircraft. One jet aircraft (Falcon) used for measurements in the anvils of thunderstorm clouds and a second one (Do-228) for measurements in the boundary layer.
- Cloud structure was observed with the DLR polarimetric radar and with conventional Doppler radar from the German Weather Service.

- The positions of lightning discharges in the clouds were mapped with the high resolution VHF-interferometer (ONERA) inside the special observation area of 60km x 60km size in Southern Bavaria. The regional distribution of lightning was provided by an LPATS.
- Additional background data from satellites, synoptic observation data and numerical model analyses were available.

Numerical forecasts of chemical transport and trajectories were provided by the KNMI and NILU during the experiment. This greatly helped to plan the flight missions.

Altogether 7 research flights were performed with several penetrations of thunderstorm anvils. Enhanced NOx concentration and few spikes originating presumably from fresh lightning flashes were observed in these clouds.

Additionally flights on the European range revealed the background concentrations of the chemical species and the remains from past storms. The data from these measurements together with radar and lightning data will be used in chemical transport models in order to simulate the regional transport and conversion of the lightning produced NOx.

PRELIMINARY RESULTS

On the 21 July 1998 intense convective activity developed ahead of a cold front approaching the experimental area from the southwest. A few strong storms were moving over the experimental area and were well covered by the various observation systems. The Falcon aircraft entered the several storm anvils. Figure 1 shows the flight path of the Falcon during the crossing of an anvil at an altitude of 9000m. The radar reflectivity displayed on Fig. 1 shows the cloud shape at low altitudes (1000m). Distorted by the prevailing wind from southwest to northeast the anvil extended approximately 50km eastward beyond the visible cloud at low altitudes.

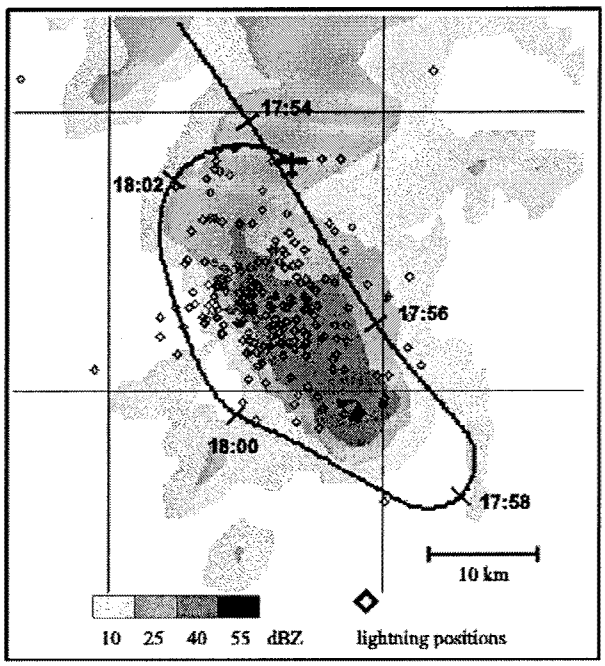


**Figure 1** Falcon flight track on the 21 July 1998, 17:53 – 18:03 UTC together with the radar reflectivity and the lightning detected during this time.

The NOx concentration observed during this anvil crossing is show on Figure 2. Maximum concentrations with spikes above 20ppbV were measured close to the storm center in the lee of the most recent lightning discharges (cf. Fig. 1).

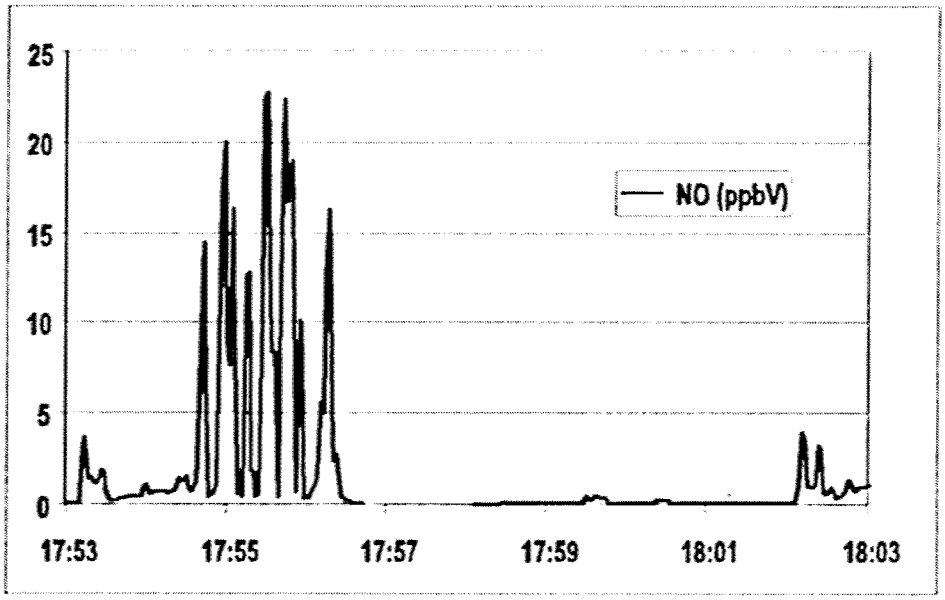


**Figure 2** Time series of NO concentration for the same time interval as in Fig. 1. Maximum concentrations above 20 ppbV were observed in the downwind area from fresh lightning discharges.

The further analyses of the collected data will be realized in the following steps:

1. Discrimination between lightning NOx and NOx transported from the boundary layer using the data from the trace gas measurements and the background concentration data.
2. Investigation of the electrical activity in the storm clouds in relation to the clouds structure and evolution stage.
3. Relating the electrical discharge activity detected by the 3D interferometer to the NOx observed in the clouds outflow.
4. Numerical simulations of the cloud dynamics and transport processes with a mesoscale cloud model (MM5).

ACKNOWLEDGEMNTS: The EULINOX project is sponsored by the Commission of European Communities in the context of the „Environment and Climate" Programme (Contract No. ENV4-CT97-0409).

REFERENCES

Höller, H., U. Finke, H. Huntrieser, M. Hagen, C. Feigl, 1999: Lightning produced NOx (LINOX) - experimental design and first results. *J. Geophys. Res.*, accepted for publication.

Huntrieser, H., H. Schlager, C. Feigl, H. Höller, 1998: Transport and production of NOx in electrified thunderstorms: Survey of previous studies and new observations at mid-latitudes. *J. Geophys. Res.* 103, 28,247-28,264.

Ridley, B. A., J. E. Dye, J. G. Walega, J. Zheng, F. E. Grahek, W. Rison, 1996: On the production of active nitrogen by thunderstorms over New Mexico. *J. Geophys. Res.* 101, 20,985-21,005.

# OPTICAL DETECTION OF LIGHTNING FROM SPACE

H. J. Christian

Global Hydrology and Climate Center, NASA-MSFC
977 Explorer Blvd., Huntsville, Alabama

Two primary detection techniques (optical and RF) have a proven capability for detecting lightning from low earth orbit. However, the lightning processes that generate the optical and RF signals are vastly different providing significantly different information content from each sensor type. Because of the intervening ionosphere, low frequency RF components do not reach satellite altitudes. As a consequence, many of the processes associated with the major energy release of a lightning event (i.e. return strokes, k-changes, recoil streamers, etc), in all likelihood contribute little to the RF signal arriving at the satellite. The optical output from lighting, on the other hand, has been shown to be highly correlated with the energetic, charge-transferring processes mentioned above. On the down side, the optical energy, while essentially unaffected by the atmosphere once it emerges from the cloud, is heavily scattered within the cloud. While there is little absorption by the cloud, the great optical depth makes the total light energy emerging from the cloud to be dependant on where in the cloud the lightning occurred. Analyses suggest that when lightning is confined to the lowest regions of the cloud, the light is strongly attenuated and detection becomes problematic. Fortunately, the vast majority of lightning flashes are comprised of channels that propagate through the middle of the cloud and higher. These flashes produce bright signals at the top of a cloud and are readily detectable.

Presently, we have two optical instruments in orbit. The Optical Transient Detector (OTD) has been orbiting the earth since April, 1995, while the Lightning Imaging Sensor (LIS) was launched on the Tropical Rainfall Measuring Mission (TRMM) in November of 1997. Both instruments are relatively small, solid state optical imagers, designed specifically to detect and locate lightning activity from low earth orbit with high detection efficiency and location accuracy. The basic features are discussed in Christian et al, [1989].

The OTD was launched on April 3, 1995 into a near circular orbit of 740 km with a $70^{o}$ inclination, providing an instantaneous field of view of 1300 x 1300 km. Since that time, it has been detecting lightning activity over most parts of the world, with approximately 10 km spatial resolution and better than 50% detection efficiency for both cloud to ground and intracloud lightning. In addition, the OTD transmits an image of the back ground scene every minute or so. This image is very valuable for determining background scene intensity, cloud types and for validation/correlation of satellite navigation via ground feature identification. Although the OTD is in a near polar orbit, it is not sun synchronous. Its orbit processes about 15 minutes a day relative to a given spot on the earth; it takes approximately 55 days to revisit a specific location at the same time of day. Thus it is necessary to sum over at least 55 days in order to develop global lightning distributions without diurnal bias.

The LIS is basically the same instrument as the OTD except that its sensitivity has been improved by a factor of three and that it is at a 350 km altitude orbit and with a $35^{0}$ inclination. This lower orbit increases the LIS spatial resolution to 4 km and decreases it field of view to 650 x 650 km. The improved sensitivity results in a detection efficiency approaching 90%. An important attribute of flying on TRMM is the simultaneous visible, IR, microwave, radar and lightning measurements. This provides an ability to test a number of hypotheses on the interrelationships between updrafts, ice formation, and lightning activity.

It images the scene much like a television camera however, because of the transient nature of lightning, its spectral characteristics, and the difficulty of daytime detection of lightning against brightly lit cloud backgrounds, actual data handling and processing is much different from that required by a simple imager. In order to achieve the performance goals required to meet the scientific objectives, the LIS combines a number off the shelf components in unique configurations. A wide field of view lens, combined with a narrow band interference filter is focused on a high speed charged coupled device (CCD) focal plane. The signal is read out from the focal plane into a real-time data processor for event detection and data compression. The resulting "lightning data only" signal is formatted, queued, and sent to the spacecraft for "real-time" transmission to ground stations. The overall instrument performance requirements are shown in table 1.

Table 1: LIS Performance Criteria

| | | | |
|---|---|---|---|
| Pixel IFOV (nadir) | 4 km | Measurement Accuracy | |
| FOV | 45° × 45° | location | 1 pixel |
| Wavelength | 777.4 nm | intensity | 10% |
| Threshold | 4.7 μJ $m^{-2}$ $sr^{-1}$ | time | tag at frame rate |
| SNR | 6 | Weight | 25 Kg |
| Array Size (2) | 128 × 128 | Power | 30 Watts |
| Dynamic Range | > 100 | Telemetry | |
| Detection Efficiency | ~ 90% | data rate | 8 kb/s |
| False Event Rate | < 5% | format | PCM |

The specific characteristics of the sensor design result from the requirement to detect lightning signals during the day. During the day, the background illumination produced by sunlight reflecting from the tops of clouds is much brighter than the illumination produced by lightning. Consequently, the daytime lightning signals tend to be buried in the background noise. Four techniques are implemented take advantage of the differences in the temporal, spatial, and spectral characteristics between the lightning signal and the background noise. First, spatial filtering is used which matches the instantaneous field of view (IFOV) of each detector element to the typical cloud-top area illuminated by a lightning stroke (i.e., ~10 km). Second, spectral filtering is obtained by using a narrow-band interference filter centered on a strong optical emission line (e.g., OI(1) at 777.4 nm) in the lightning spectrum. This method further maximizes the lightning signal relative to the reflected daylight background. Third, the LIS/OTD employs temporal filtering by taking 500 imaged per second. This takes advantage of the difference in lightning pulse duration (~ 400 microseconds) versus the background illumination which tends to be constant on the time scale of seconds.

Even with the three "filtering" approaches discussed above, the ratio of the background illumination to the lightning signal can still exceed 100 to 1 at the focal plane. Therefore, a fourth technique, a modified frame-to-frame background subtraction, is implemented to remove the slowly varying background signal from the raw data coming off the LIS focal plane. A detailed discussion on the measurement approach adopted for the LIS is presented later. The real-time event processor (RTEP) generates a precise measurement of the background scene imaged at each pixel of the focal plane array. This background scene is updated during each frame readout sequence and, at the same time, the background signal is compared with the off-the-focal-plane signal on a pixel-by-pixel basis. When the difference between these signals exceeds a selected threshold, the signal is identified as a lightning event and an event processing sequence is enabled. The implementation of this RTEP results in a $10^5$ reduction in data rate requirements (100MBPS to 8 KBPS) while maintaining high detection efficiency.

## INSTRUMENT DETAILS

The LIS consists of an imaging system, a focal plane assembly, a real-time signal processor and background remover, an event processor and formatter, power supply, and interface electronics are the six major subsystems of the sensor. The imaging system is a f/1.6 lens consisting of a beam expander, an interference filter and re-imaging optics. The 80° x 80° full angle LIS field of view is converged to less than 5° at the interference filter in order to minimize wavelength shifts due to non-normal incidence. The focal plane assembly, including the 128 x 128 element CCD array, preamplifiers, multiplexers, and clock and drive electronics provides subsequent circuits with an analog data stream of appropriate amplitude. As noted earlier, if after background removal, the difference signal for a given pixel exceeds a threshold, that pixel is considered to contain an event. Subsequently, the event is time tagged; location tagged, and passed to platform telemetry via the interface electronics to the spacecraft. The overall signal flow through the LIS instrument is depicted in Figure 1.

### Imaging System

The imaging system includes a fixed focus, wide angle lens consisting of a front negative group, a beam expander used to reduce the principal ray to less than 5° where the rays go through a 1nm bandwidth interference filter and a rear re-imaging group behind the bandpass filter. The need for the beam expansion optical system is driven by the incompatible requirements for a wide field of view and a narrow band interference filter needed in

order to meet signal/noise specifications. This problem occurs because the bandpass of interference filters shifts to shorter wavelengths for non-normal incidence. That is, if the wavelength of interest is incident upon the filter at an angle that shifts it beyond the filter bandpass, the signal will not be passed. Expanding the optical beam effectively compresses the incident angle and acheives the desired system performance. This optical system has an f-number of 1.6, is 20 cm long and 10 cm in diameter at its maximum width.

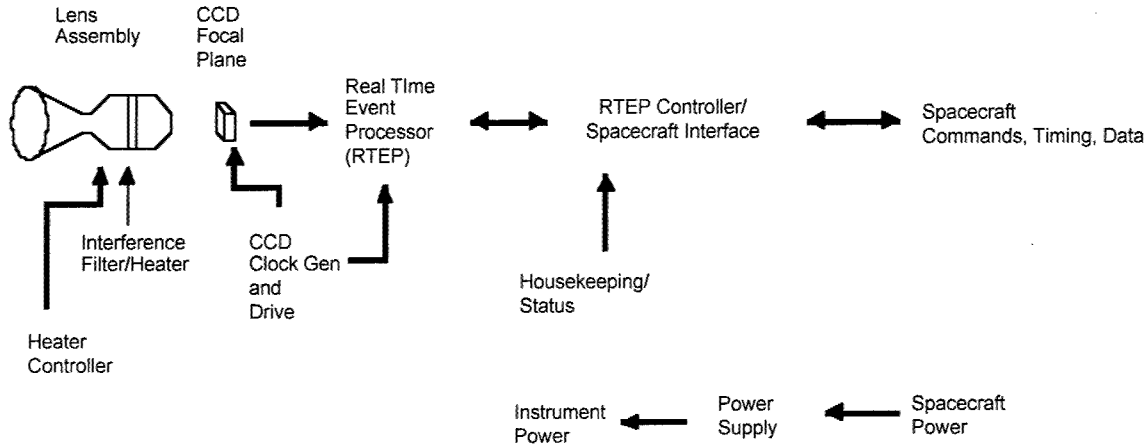


*Figure 1. Block diagram of the major elements of LIS*

## Real Time Event Processor

The need for off-the-focal plane signal processing by a real time processor (RTEP) in order to detect a lightning event has previously been addressed. Figure 2a demonstrates how the LIS RTEP extracts weak lightning flashes from an intense but slowly evolving background. The input signal is the video pixel stream produced by the CCD. The video signal associated with each pixel corresponds to the combined illumination of the quasi-static background scene and any optical transients that may have occurred during the frame period. (The height of the optical pulses is exaggerated for clarity.) The daytime background varies with sun angle, clouds, ground albedo, etc., and can reach in excess of 800,000 photo-electrons as compared to signal electrons which may be smaller than 6000 electrons. A lightning stroke occurs during a single frame producing a signal that is superimposed on top of the essentially constant background. The RTEP continuously averages the output from the focal plane over a number of frames on a pixel-by-pixel basis in order to generate a precise but evolving image of the background scene. This background scene is then subtracted on a pixel-by-pixel basis from the current video signal from the CCD to extract the candidate optical transients (lightning).

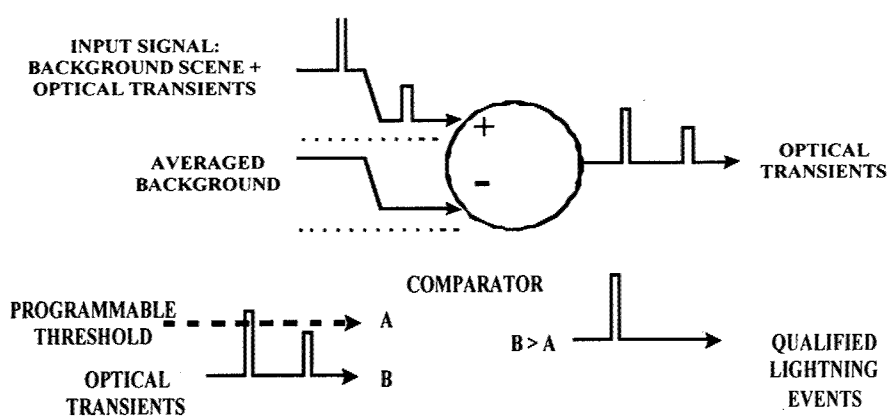


*Figure 2. (a) Extraction of weak lightning signals from background, and (b) thresholding of subtracted signal.*

Figure 2b depicts the subtracted signal. It consists of shot noise fluctuating about zero with occasional peaks due to lightning events. When a peak exceeds the level of the variable threshold, it is considered to be a lightning event and is processed by rest of the circuit. The threshold must be set sufficiently high that false triggers are kept to a small percent of the total lightning rate. Clearly, the threshold must be higher during daytime when shot noise is dominated by the solar background

The primary components of the real-time event processor include a closed loop tracking filter, a lightning event thresholder/selector, and a signal identifier. The tracking filter functions as a time domain low pass filter to produce a high-resolution measurement of the background scene. As part of the closed-loop operation, the background scene is subtracted on a pixel-by-pixel basis from the video signal input from the CCD. The residue is sent to the event thresholder/selector for evaluation. The residue is also passed through a limiter before being used to update the background average to ensure that a strong lightning does not contaminate the background average. If a large event were allowed to increase the background average for a particular pixel, its sensitivity for small lightning pulses would be cutoff until the averaging had reduced the background measurement to normal.

The residue (subtracted data) is amplified before being added with the old background value to produce an updated background value. The effective number of frames averaged is equal to 2/K-1, where K includes the residue analog amplification as well as the ADC/DAC conversion/scaling. Too high a fractional gain might permit lightning events to contaminate low background averages and would increase the processing noise. Too low a fractional gain would not allow the tracking filter to respond rapidly enough to changes in background intensity. In the baseline design, the frame averaging is set to two. Proper operation of the tracking filter requires that the background data are clocked synchronously with the video data and that the number of discrete storage elements in the background memory is exactly the same as the number of pixels in the focal plane array.

Since the original signal contains either background plus lightning or just background, the subtracted signal (residue) will be either a lightning signal, near zero or a false alarm as previously described. The residue signal is then digitized and compared with a threshold level (adaptive) in the thresholder/event selector. If the signal exceeds the threshold level, it is designated a lightning signal. The data formatter then appends pixel location and time information to the lightning intensity value and forwards it to the interface processor where it is encoded into a digital bit stream and sent to the spacecraft transmitter.

Analog/digital hybrid processing is used in a unique way that takes advantage of the strengths of each technology in order to provide high processing rates while consuming minimal power. While an all-digital approach is attractive for the higher integration and measurement stability it offers, no digitizers are available that achieve better than about 10.5 noise-free bits of dynamic range at 11 Megasamples/second. In the hybrid approach, the background subtraction and residue amplification are performed by analog circuits, with the residue (lightning event) digitized by an 8 bit, 11 Megasample/second converter. The background updating of the tracking filter is performed by digital logic, with the background image stored in digital memory. The background samples are converted back to the analog domain for analog subtraction by a 12 bit, 11 megasample/second digital-to-analog converter. The analog residue amplifier is a dual gain, piece-wise linear circuit that provides higher gain and more accuracy for the more prevalent low level signals, and compressed gain for the less frequent large signals. Considerable logic resources would be required to implement an equivalent high-speed digital multiplier in an all-digital design. In this hybrid implementation, a true 12 bits of resolution is achieved with the DAC, and is applied to just the background signal. The event pulses occur "on top" of the background, so the actual dynamic range is closer to 12.5 bits.

With the design as described, the LIS has met all design goals. Global lightning distributions have now been generated and presented as functions of time of day, season, and geographical location. Case studies of severe weather and hurricanes have been made. Comparisons have been made with the NLDN, and have revealed severe weather cases that we interpret as having very high ratios of intracloud lightning. These new sensors now enable thunderstorm studies to be conducted anywhere on the globe, under a multitude of conditions.

References

Christian H. J., R. J. Blakeslee, and S. J. Goodman, *The Detection of Lightning From Geostationary Orbit*, J. Geophys. Res., 94, 13,329-13,337, 1989

# An Optimal Relation of Radar Reflectivity to Lightning Rate

**S. Heckman**

**Global Hydrology and Climate Center**
**NASA Marshall Space Flight Center, AL 35812 USA**

## Introduction

Thunderstorms separate charge. Most places they lift positive charge or lower negative, a few places they lift negative or lower positive. The electrical generator is stronger in some parts of the cloud than in others. Our long term goal is to map this generator.

Cloud physicists tell us that uncharged ice and water particles become charged by collision, and that the charge transferred depends on size, temperature and humidity. There is still some disagreement about exactly how the charge transferred depends on size, temperature, and humidity. In principle, if we knew this ice physics, and also knew the distribution of particles everywhere in the storm, and the winds everywhere and the temperature and humidity everywhere, then we could compute everywhere the electrical power of the thunderstorm generator. In practice it is difficult to know all these things, particularly the distribution of particles, so it is difficult to use real thunderstorms to falsify cloud electrification theories.

We here take one small step towards computing that map of electrical generator power, by relating radar reflectivity profiles of 2000 storms to lightning flash rates of those storms. This small step by itself doesn't falsify any existing electrification theories; it merely places weak constraints on the relation of electric generator power to cloud ice.

## The Data and the Model

We use radar and lightning data from the TRMM satellite. The radar has 4 km horizontal and 1/4 kilometer vertical resolution. The lightning location resolution is about the same (3-6 km). The satellite sees many storms, but sees each only once. It provides for each storm a single snapshot of radar reflectivity and 80 seconds of lightning locations. This data can't possibly be used to map electric field and current density. We'll try instead to map their product, the power in volt amps per cubic meter.

We make the following three assumptions to create a tractable model: First, generator power for the storm system is the sum of generator powers of each 4km by 4km by 1/4 km radar cell. Second, generator power for each cell is a function only of radar reflectivity and temperature. Third, lightning flash rate is proportional to total generator power.

The first assumption is false. It is probable that generator power of each cell varies with variations in the ambient vertical electric field, which is not locally determined. The second assumption is false. At a given reflectivity and temperature, a cell in a storm growing in humid air with a shortage of ice condensation nuclei will contain a different distribution of cloud particles than a cell from a storm growing in drier air with abundant ice condensation nuclei. Even cells in the same storm at the same reflectivity and temperature may differ if they have different histories or have entrained different air. The third assumption is false. Some generator energy is dissipated by processes other than lightning, the average energy per flash is not constant from storm to storm, and energy may be stored for more than 80 seconds. We make these three assumptions anyway. Although they are false, we expect them to be approximately true. We don't yet know how poor that approximation may be; that is, we don't know how important the neglected variates are. But with neither a theory for nor a measurement of these missing variates, the best way to gauge their importance is to neglect them, and to see how much can be explained without them.

With the three assumptions, our model is

$$FlashRate \propto \sum_{cells} GeneratorPower(dbz, T)$$

The proportionality can be replaced with an equality if we are willing to measure generator power density in units of lightning flashes per second per meter cubed.

$$FlashRate = \sum_{cells} GeneratorFlashProductivity(dbz, T)$$

| | 10-15 | 15-20 | 20-25 | 25-30 | 30-35 | 35-40 | 40+ |
|---|---|---|---|---|---|---|---|
| 10+ km | 0 | 0 | 0 | 0 | 16. | 16. | 16. |
| 9 to 10 km | 0 | 0 | 0 | 0 | 0 | 0 | 0 |
| 8 to 9 km | 0 | 0 | 0 | .14 | .14 | .14 | .14 |
| 7 to 8 km | 0 | 0 | 0 | 0 | 0 | 0 | 0 |
| 6 to 7 km | 0 | 0 | 0 | 0 | 0 | 0 | 0 |
| 5 to 6 km | 0 | 0 | 0 | 0 | .19 | .19 | .19 |
| 4 to 5 km | 0 | 0 | 0 | 0 | .17 | .17 | .17 |
| 3 to 4 km | 0 | 0 | 0 | 0 | .08 | .13 | .13 |
| 2 to 3 km | 0 | 0 | 0 | 0 | .02 | .07 | .07 |
| 1 to 2 km | 0 | 0 | 0 | 0 | 0 | .19 | .25 |
| 0 to 1 km | 0 | 0 | 0 | 0 | 0 | 0 | .10 |
| -1 to 0 km | 0 | 0 | 0 | 0 | 0 | 0 | 0 |
| -2 to -1 km | 0 | 0 | 0 | 0 | 0 | 0 | 0 |
| -3 to -2 km | 0 | 0 | 0 | 0 | 0 | 0 | 0 |
| below -3 | 0 | 0 | 0 | 0 | 0 | 0 | 0 |

Table 1:
Inferred generator power density as a function of radar reflectivity and height above the freezing level. The units are lightning flashes per cubic kilometer. This is the inferred power that best predicts the observed flash rates in 200 storm systems, subject to the constraints that power is non-negative and a non-decreasing function of reflectivity.

The satellite's lightning imaging sensor tells us directly the flash rate of each storm. It's precipitation tells us directly the radar reflectivities. The precipitation radar also tells us the freezing level, so if we assume a lapse rate inside the storm, the precipitation radar indirectly tells us the temperature of each cell. This is enough information to invert for the unknown function $GeneratorFlashProductivity(dBZ, T)$.

We do the inversion by binning in radar reflectivity and temperature. We assume the unknown function FlashRate(dBZ, T) has one discrete value for each dBZ and temperature bin. Then the model reduces to

$$FlashRate = \sum_{bins} Volume(bin) GeneratorFlashProductivity(bin)$$

an equation with one unknown per bin. For each storm system we have a different flash rate, and a different number of cubic kilometers in each bin. This produces a simple linear system with one equation per storm system. So long as there are more storms than bins, this system is overdetermined. Table 1 shows the solution that minimizes the sum of absolute values of the errors, subject to the constraints that the solution must be everywhere non-negative, and that it must be a non-decreasing function of reflectivity.

Because the number of high reflectivity cells falls rapidly with height, Table 1 predicts a generator mostly located 1 to 2 kilometers above the freezing level. Higher altitudes contribute only about a third of the flashes, evenly divided between large contributions from rare high reflectivity cells more than 10 kilometers above freezing, and smaller contributions from more common high reflectivity cells between two and six kilometers above freezing. Table 1, if applied to any particular thunderstorm, produces a quite detailed map of that thunderstorm generator. But the details are almost certainly wrong. Only the gross features of the inversion have any chance of being true, details are almost certainly noise. In particular, the high altitude, high reflectivity contributions are inferred from a very small number of intense storms that produced a lot of lightning. Because only a few such storms went into the inversion, the high altitude high reflectivity results are suspect. Adding doubt to the high altitude results is the fact that $GeneratorFlashProductivity(dBZ, T)$ is here pushed hard against the constraint that it must be a non-decreasing function of reflectivity.

To avoid these dubious details, we grossly simplify Table 1. An obvious feature is a zero contribution from cells below the freezing level or with reflectivities less than 25 dBZ. This suggests a simpler predictor, in which all cells above the freezing level with reflectivities greater than 25 dBZ contribute some constant amount, that is, the lightning rate is proportional to the volume of storm above 25 dBZ and above the freezing level. Or perhaps proportional to volume above 30 dBZ and above freezing, or perhaps yet some other thresholds of temperature and reflectivity.

| | 25+ | 30+ | 35+ | 40+ | 45+ |
|---|---|---|---|---|---|
| 4km+ | 157 | 159 | 200 | 252 | 297 |
| 3km+ | 156 | 151 | 186 | 236 | 281 |
| 2km+ | 158 | 146 | 168 | 215 | 261 |
| 1km+ | 168 | 142 | 150 | 188 | 231 |
| 0km+ | 192 | 158 | 147 | 161 | 197 |
| -1km+ | 229 | 212 | 194 | 174 | 172 |

Table 2:
Sum of absolute errors of 30 models, in hundreds of flashes. Each model assumes that the lighting rate is proportional to the volume of cloud with reflectivity above some threshold and temperature below some other threshold. The constant of proportionality is optimized separately for each model. The lowest error is 142 hundred flashes, for the model flash rate is proportional to cloud volume greater than 30 dBZ, and higher than one kilometer above the freezing level. But it's not much lower than the errors for the models that instead have flash rate proportional to volume brighter than 35 dBZ and above the freezing level, or volume brighter than 30 dBZ and more than two kilometers above freezing.

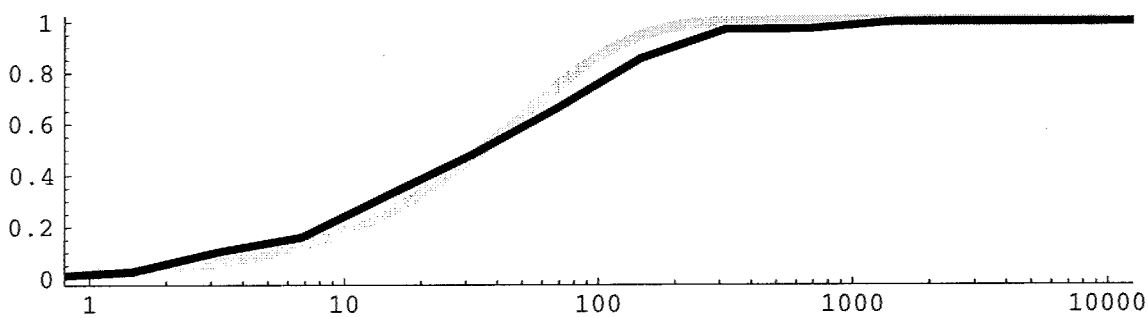

Figure 1:
The black line shows the observed chance of at least one lightning flash in our 80 second viewtime, as a function of the number of cubic kilometers above 30 dBZ and more than a kilometer above the freezing level. The gray line shows what that chance would be if the model were perfect, if lightning frequency really were exactly proportional to the volume.

Table 2 compares absolute deviations for 30 different combinations of threshold dBZ and threshold temperature (height above freezing). The best approximation of this sort is 0.00025 flashes per second per cubic kilometer above 30 dBZ and more than two kilometers above the freezing level. How good is this theory? That depends what you want to use it for. It's optimized to do well at predicting the total lightning rate. Let's test it at something slightly different; determining whether or not a certain storm will produce lightning. Because of the short viewtime of the satellite, we have to make that question "will a storm system produce at least one lightning flash in 80 seconds?" The black curve in Figure 1 shows observed chance of lightning versus the volume in cubic kilometers above 30 dBZ and more than one kilometer above freezing. The gray curve is $1-\exp(80*0.00025*volumeInCubicKm)$, which would be the chance of observing lightning if lightning frequency really were exactly proportional to volume above 30 dBZ and more than a kilometer above freezing.

**Future Work**

Our goal is still to map the generator. To that end, we plan to try to reduce the noise in the inversion sufficiently to test whether the high altitude contributions are real. We may also look for systematic features of storms that produced many more or many fewer flashes than predicted by the optimal threshold theory.

# OPTICAL TRANSIENT DETECTOR (OTD) OBSERVATIONS OF A TORNADIC THUNDERSTORM

D.E. Buechler[1], S.J. Goodman[2], H.J. Christian[2], K. Driscoll[1]

[1]The University of Alabama in Huntsville, Huntsville, AL.

[2] NASA Marshall Space Flight Center, Huntsville, AL.

ABSTRACT: Total lightning observations made by the Optical Transient Detector (OTD) of a tornadic thunderstorm that occurred over Oklahoma on 17 April 1995 are presented. The average flash rate of the tornadic storm during the 3.2 min observation period was 45 flashes $min^{-1}$, with a flash rate density of $1.16 \times 10^{-4}$ $s^{-1}$ $km^{-2}$. The total flash rate was almost 18 times higher than the cloud-to-ground rate measured by the National Lightning Detection Network (NLDN). In addition, total lightning rates were observed to decrease prior to tornadic development.

## INTRODUCTION

There have been few published reports of space-based lightning measurements of tornadic storms. The few that have been made come from instruments aboard Defense Meteorological Satellite Program (DMSP) satellites. Nighttime observations from the optical line scanner (OLS) on the DMSP often show streaks caused by lightning flashes recorded by the scanning sensor. Using OLS data, Orville and Vonnegut (1979) found flash rate densities during the 4 April 1974 tornado outbreak that were three times greater than during a Florida squall line. Turman and Tettlebach (1980) used a photodiode instrument, called the Piggyback Experiment (PBE), onboard two DMSP satellites. This device was capable of detecting only about the brightest 2% of the lightning flashes within its 650 km radius field of view. They found that the lightning flash rate densities of tornadic storms are significantly higher than for non-tornadic cases.

Recent studies on lightning activity within tornadic storms have generally focused on cloud-to-ground lightning observations (e.g., MacGorman and Burgess, 1994) due to the availability of such measurements. These studies suggest that variations in lightning activity may signal changes in storm evolution. This information combined with current measurements (e.g., radar data) may prove useful in forecasting severe weather. The intracloud lightning component of a storm is generally much larger than the cloud-to-ground component.

Recent results from Florida (Williams et al, 1999) suggest that "jumps" in total lightning measurements may be related to updraft intensification preceding tornado development. Lightning frequency and type (i.e., intracloud or cloud-to-ground) appears to be related to the dynamical and microphysical structure of thunderstorms (e.g., Goodman et al., 1988; Williams et al., 1989). A strong updraft promotes more frequent interactions between small and large ice hydrometeors within the mixed phase region of a thunderstorm, leading to electrification and lightning. The greater the interactions the more frequent the lightning. In addition, total (intracloud plus cloud-to-ground) lightning rates are greater than cloud-to-ground alone and may be a more sensitive indicator of change in storm character. Sferics and L-band radar observations of total lightning in tornadic storms suggest that intracloud processes dominate the total as storms become more severe (MacGorman et al., 1989). Thus, OTD measurements of total lightning should be significantly greater than only cloud-to-ground measurments in tornadic storms.

This paper describes the lightning activity observed by OTD of a tornadic thunderstorm in Oklahoma on 17 April 1995. The OTD instrument was specifically designed to optically detect lightning activity at storm (~10 km) scale resolution during both day and night. Although the field of view is in excess of $1.5 \times 10^{6}$ $km^2$, the OTD is in a low earth orbit which limits its viewing of any particular storm during an overpass to about 3 mins. Lightning flashing rates observed by OTD are compared to cloud-to-ground measurements obtained by the National Lightning Detection Network (NLDN).

RESULTS

On 17 April 1995, the OTD observed a tornadic thunderstorm (cell A) over Oklahoma from about 22:52:10 to 22:55:20 UTC. A unique feature of this storm is that it was followed throughout much of its life-cycle by VORTEX intercept teams, so that the times of tornadoes are well known. This storm produced 10 documented tornadoes between 21:00 and 01:00 UTC. All of the tornadoes were weak (F0-F1) and short-lived. One of the F1 tornadoes occurred at 22:56 UTC, about 1 min after the storm was observed by OTD. Another storm (cell B) was located about 55 km north of the tornadic cell. There were no reports of tornadic activity from cell B within an hour of the OTD overflight. The tornadic cell A and nontornadic cell B can be identified by their cold cloud tops in the GOES 8 IR image (Fig. 1). The two cells can not be discerned as two separate entities in the GOES 8 visible image, however, plots of cloud-to-ground lightning delineates two clusters associated with the two cells.

A total of 143 flashes were detected by OTD from the tornadic cell during the overpass, while the non-tornadic storm produced 74 flashes. Comparisons of flash statistics between cells A and B are shown in Table 1. During the entire period (~3.2 min) cell A was within the OTD field of view, an average flashing rate of 45 flashes $min^{-1}$ was observed. Only 8 cloud-to-ground flashes were recorded (3 negative and 5 positive) from cell A during this period resulting in a cloud-to-ground flash rate of 2.52 $min^{-1}$. All of the cloud-to-ground flashes were single stroke flashes, except for one two stroke positive flash. Assuming the OTD observed all the total lightning and that the NLDN accurately identified all of the cloud-to-ground flashes, a ratio of 16.9 intracloud to cloud-to-ground flashes is obtained (or 94% of the total flashes were intracloud). Similarly, 89% of the flashes in cell B were intracloud.

The time history of OTD and NLDN flash rates for tornadic storm A is shown in Fig. 1 for the OTD overpass. The flash counts are counted in 30 s intervals. Note that the OTD flash rate is about 1 flash $s^{-1}$ during the first minute of observation. The cloud-to-ground rate is much lower than this (generally less than 5 $min^{-1}$). Also note the decreasing OTD flash rate trend leading up to the observation of a tornado on the ground. A large increase in flash rates has been observed prior to tornadogenesis in severe storms in Florida (Williams et al., 1999). In this case however, OTD didn't observe the storm earlier and thus would have missed a rapid increase in the flash rate. The cloud-to-ground flashing rate is infrequent enough that no discernible pattern can be determined.

Using the number of OTD flashes per storm, the amount of time the storm was observed, and the size of the area where OTD events were detected, flash rate densities can be computed. An OTD flash rate density of $1.16\times10^{-4}$ flashes $s^{-1}$ $km^{-2}$ was observed for storm A, while storm B had a value of $0.92\times10^{-4}$ flashes $s^{-1}$ $km^{-2}$.

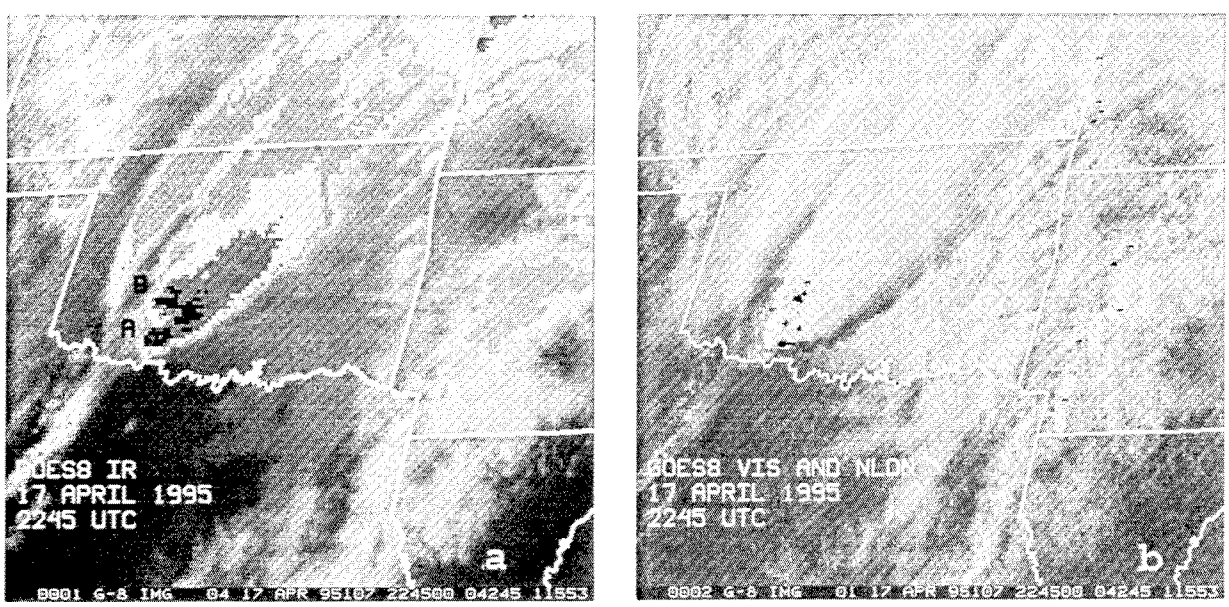


Figure 1. GOES 8 Infrared (a) and visible (b) satellite imagery of tornadic cell (labeled A) and nontornadic cell (labeled B). The cloud-to-ground locations are indicated on the visible image.

Table 1. OTD and NLDN cloud-to-ground statistics for cells A and B on 17 April 1995.

| | OTD Flashes | Negative CG flashes | Positive CG flashes | Storm Area ($km^2$) | OTD flash rate density ($s^{-1}$ $km^{-2}$) |
|---|---|---|---|---|---|
| Cell A | 143 | 3 | 5 | 6500 | $1.16\times10^{-4}$ |
| Cell B | 74 | 6 | 2 | 4200 | $0.92\times10^{-4}$ |

## SUMMARY AND CONCLUSIONS

Preliminary results of OTD observations of a tornadic thunderstorm observed just prior to tornado touchdown are presented. A presumably nontornadic thunderstorm located about 55 km north of the tornadic storm is also examined. The methodology of obtaining strokes and flashes from the OTD event measurements is presented and results from the two storms are calculated. From this small study, no definitive conclusions can be drawn about the differences in lightning activity between tornadic versus nontornadic storms. However, the high percentage of intracloud flashes produced by these storms is significant. During the ~3.2 min these storms were observed by OTD, they produced 94% (tornadic) and 89% (non-tornadic) intracloud lightning. The tornadic storm produced an flash rate of about 45 $min^{-1}$ (averaged over the OTD observation period) while the nontornadic storm yielded 23 flashes $min^{-1}$. This illustrates that cloud-to-ground networks can miss the majority of lightning in some storms.

Studies of the time history of lightning of individual cells are limited by the ~3 min observation time, which results form the low earth orbit of OTD. A geostationary version of OTD, could provide continuous coverage over a wide area at storm scale resolution (Christian, et al., 1992). The cloud-to-ground component of lightning in these storms is small (~10%). Thus, changes in total lightning rates (as opposed to only cloud-to-ground) may be a more sensitive indicator of changes in thunderstorm structure. Used in conjunction with other current observations (such as radar), severe storm warning capabilities may be improved.

## REFERENCES


Christian, H.J., R.J. Blakeslee, and S.J. Goodman, 1992: Lightning Imaging Sensor (LIS) for the earth observing system. *NASA TM-4350*, Available from Center for Aerospace Information, P.O. Box 8757, Baltimore Washington International Airport, Baltimore, MD 21240, 44 pp.

Goodman, S.J., D.E. Buechler, P.D. Wright, and W.D. Rust, 1988: Lightning and precipitation history of a microburst-producing storm. *Geophys. Res. Lett.*, **15**, 1185-1188.

MacGorman, D.R., D.W. Burgess, V. Mazur, W.D. Rust, W.L. Taylor, and B.C. Johnson, 1989: Lightning rates relative to tornadic storm evolution on 22 May 1981., *J. Atmos. Sci.*, **46**, 221-250.

MacGorman, D.R. and D. W. Burgess, 1994: Positive cloud-to-ground lightning in tornadic storms and hailstorms. *Mon. Wea. Rev.*, **122**, 1671-1697.

Orville, R.E. and B. Vonnegut, 1974: Lightning detection from satellites. *Electrical Processes in Atmospheres*. H. Dolezalek and R. Reiter, Eds., Steinkopff Verlag, 750-753.

Turman, B.N. and R.J. Tettelbach, 1980: Synoptic-scale satellite lightning observations in conjunction with tornadoes. *Mon. Wea. Rev.*, **108**, 1878-1882.

Williams, E.R., M.E. Weber, and R.E. Orville, 1989: The relationship between lightning type and convective state of thunderclouds. *J. Geophys. Res.*, **94**, 13213-13220.

Williams, E.R., B. Boldi, A. Matlin, M. Weber, S. Hodanish, D. Sharp, S. Goodman, R. Raghavan, and D. Buechler, 1999: The behavior of total lightning activity in severe Florida thunderstorms. Accepted for publication in *Atmospheric Research*

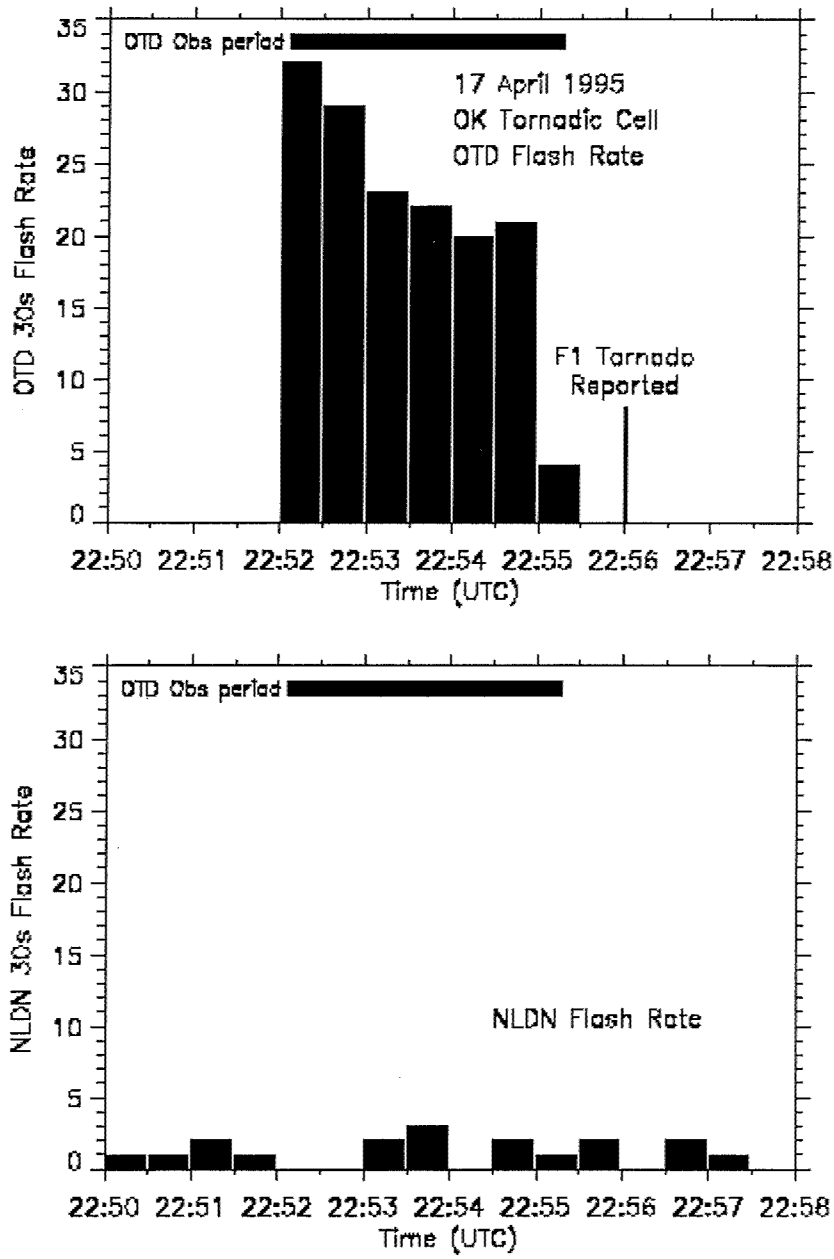


Figure 2. Time series of OTD and NLDN lightning flash rates for the tornadic thunderstorm of 17 April 1995. The time of tornado occurrence is indicated. Also shown is the time period when the OTD observed the storm.

# GLOBAL FREQUENCY AND DISTRIBUTION OF LIGHTNING AS OBSERVED BY THE OPTICAL TRANSIENT DETECTOR (OTD)

Hugh J. Christian[1], Richard J. Blakeslee[1], Dennis J. Boccippio[1], William L. Boeck[2], Dennis E. Buechler[3], Kevin T. Driscoll[3], Steven J. Goodman[1], John M. Hall[4], William J. Koshak[1], Douglas M. Mach[3], and Michael F. Stewart[3]

[1]NASA Marshall Space Flight Center, Huntsville, Alabama, U.S.A.
[2]Niagara University, Niagara, New York, U.S.A.
[3]University of Alabama in Huntsville (UAH), Huntsville, Alabama, U.S.A.
[4]CSC Huntsville, Huntsville, Alabama, U.S.A.

to the orbital precession of the satellite if the data is not averaged over a 55-day interval (e.g., see 5-day average data in Fig. 3). Therefore, the data was averaged using a 55-day sliding window in order to remove this bias.

## RESULTS AND DISCUSSION

The annual variation of the global flash rate for the period September 1, 1995, through August 31, 1996 is shown in Fig. 3 (i.e., the 55-day average). The OTD data reveal that the global flash rate achieves a maximum during the northern hemisphere summer of 54.4 flashes per second, a minimum of 28.6 flashes per second, and an average flash rate for the globe of 36.8 flashes per second. This average flash rate is less than half the traditional estimate of 100 flashes per second first proposed by *Brooks* (1925). Additionally, the OTD derived global flash rate is lower than most of the other published estimates of the average global flash rate, given that these prior estimates were all greater than 60 flashes per second (*Orville and Spencer,* 1979, *Kataki and Katoh*, 1983, *Mackerras et al.,* 1998). These prior estimates were reported with a range of uncertainty that approached a factor of two, which is the likely explanation for the discrepancy between the prior estimates and the results obtained from the OTD data.

The seasonal distribution and frequency of lightning activity are depicted in Fig. 4. In agreement with earlier studies, it is apparent that most lightning activity occurs over land. In an effort to quantify this percentage, the globe was divided into separate land and ocean components, and the annual flash rate was re-computed for both the continental and the oceanic regions as shown in Fig. 5. The oceanic lightning activity remained fairly constant throughout this period of observation with an average annual flash rate of 6.6 flashes per second (18%), while the flash rate for continental regions (82%) ranged from 24.2 to 49.0 flashes per second during the year.

By dividing the globe into latitudinal sections, a better understanding the annual variation in the global flash rate can be obtained. For example, by separately computing the flash rate for the northern and southern hemispheres, it is apparent that the maximum flash rate for each hemisphere occurs approximately six months apart and occurs during the corresponding summer season, as shown in Fig. 6. The maximum flash rate for the northern hemisphere, however, is significantly greater than that for the southern hemisphere. A further dissection of the hemispheres reveals that there are only minor differences in the magnitude of the flash rates associated with the region between the equator and 30° S latitude and the region between the equator and 30° N latitude. From this observation, it can be deduced that more lightning occurs in the region north of 30° N than in the region south of 30° S. Since there is generally more lightning activity over land than over water, and since there is more land mass north of 30°N than in the region south of 30° S, the reason for the difference in the maximum flash rates between the northern and southern hemispheres is understandable. Effectively, the lightning activity in North America and northern Asia is responsible for the imbalance in the annual cycle of the global flash rate observed during the summer months of the northern hemisphere.

Finally, by dividing the globe into latitude bands, stability of the flash rates for the tropics becomes apparent. As shown in Fig. 7, the frequency of lightning activity for the globe was subdivided into zones consisting of 5° S to 5° N latitude, 10° S to 10° N latitude, 20° S to 20° N latitude, and 30° S to 30° N latitude. On average, approximately 75% of all lightning occurs between 30° S and 30° N latitude zone. Although one might expect some variations based on semi-annual variation in precipitation near the equator, the flash rate for the tropics appears to remain fairly constant throughout the year.

## CONCLUSIONS

The OTD has now collected four years of data. In addition, the Lightning Imaging Sensor and the FORTE have been in orbit for over a year. Analysis of these new data sets should continue to improve the determination of the global flash rates and distributions, as well as to help characterize their seasonal and annual variability.

## REFERENCES


Brooks, C. E. P., The distribution of thunderstorms over the globe, *Geophys. Memo.*, *3*, No. 24, 147-164, 1925.

Goodman, S. J., and H. J. Christian, Jr., Global observations of lightning, in *Atlas of Satellite Observations related to Global Change*, ed. by R. J. Gurney, J. L. Foster and C. L. Parkinson, 191-219, Cambridge Univ. Press, 1993.

Kataki, M., and C. Katoh, The global distribution of thunderstorm activity observed by the Ionospheric Sounding Satellite (ISS-b), *J. Atmos. and Terr. Physics*, *45*, 843-847, 1983.

Levy, H., II, W. J. Moxim, and P.S. Kasibhatla, A global three-dimensional time-dependent lightning source of tropospheric NOx, *J. Geophys. Res.*, *101*, 22,911-22,922, 1996.

Mackerras, D., M. Darveniza, R. E. Orville, E. R. Williams, and S. J. Goodman, Global lightning: Total, cloud and ground flash estimates, *J. Geophys. Res.*, *103*, 19791-19809, 1998.

Orville, R.E., and D.W. Spencer, Global lightning flash frequency, *Mon. Weather Rev.*, *107*, 934--943, 1979.

Williams, E. R., The Schumann Resonance: A global tropical thermometer, *Science*, *256*, 1184-1187, 22 May 1992.

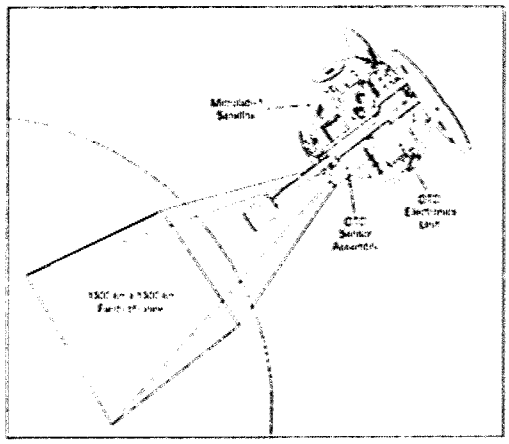

Fig. 1. A depiction of the OTD instrument and the Microlab-1 spacecraft as it orbits the Earth.

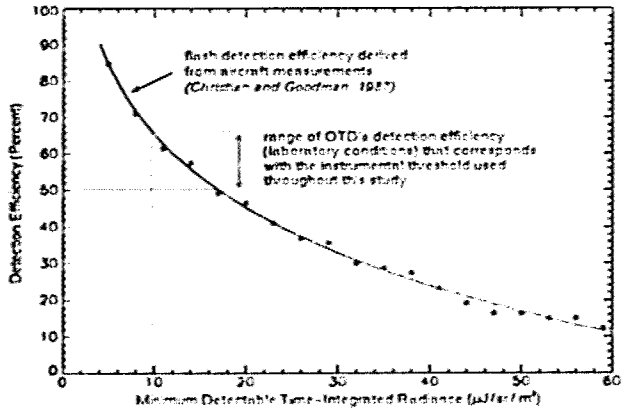


Fig. 2. Flash detection efficiency derived from laboratory radiometric calibration measurements.

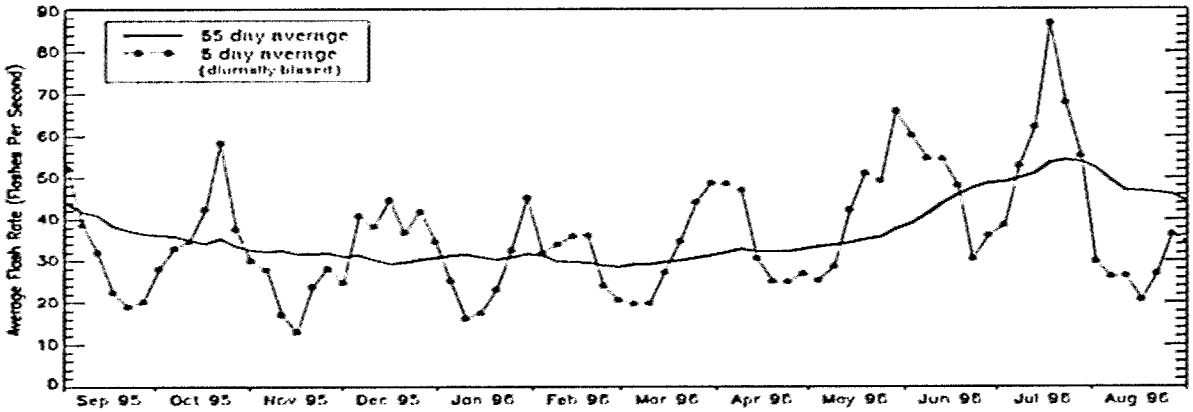


Fig. 3. The annual cycle of the global flash rate determined from OTD data for Sept. 1995 through Aug. 1996.

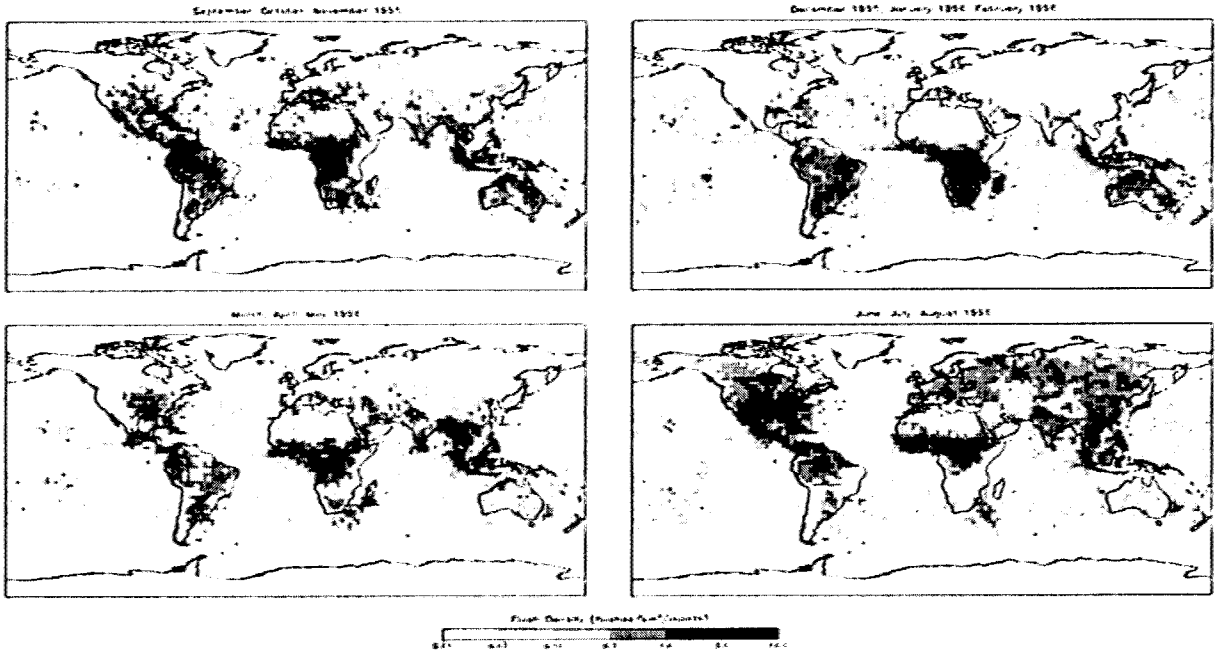

Fig. 4. Seasonal distribution of lightning activity as determined from OTD data.

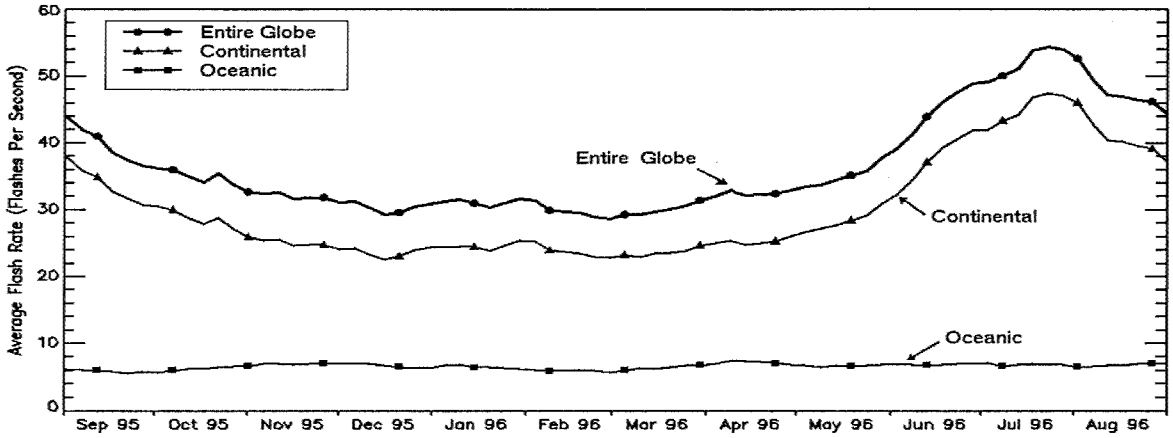


Fig. 5. The annual cycle of the global flash rate for continental and oceanic storms.

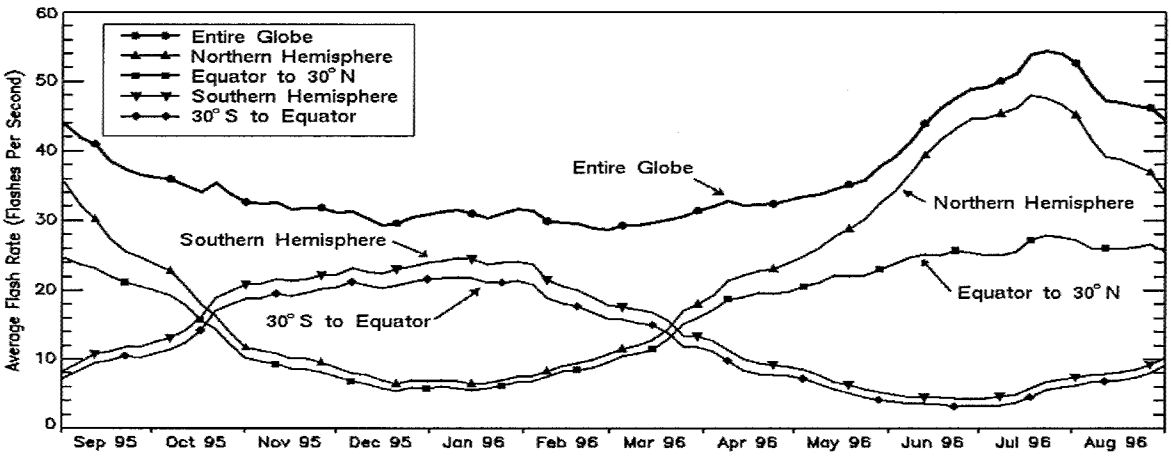


Fig. 6. The annual cycle of the global flash rate for the Northern Hemisphere, the Southern Hemisphere, the latitudes between 30° S and the Equator, and the latitudes between the Equator and 30° N.

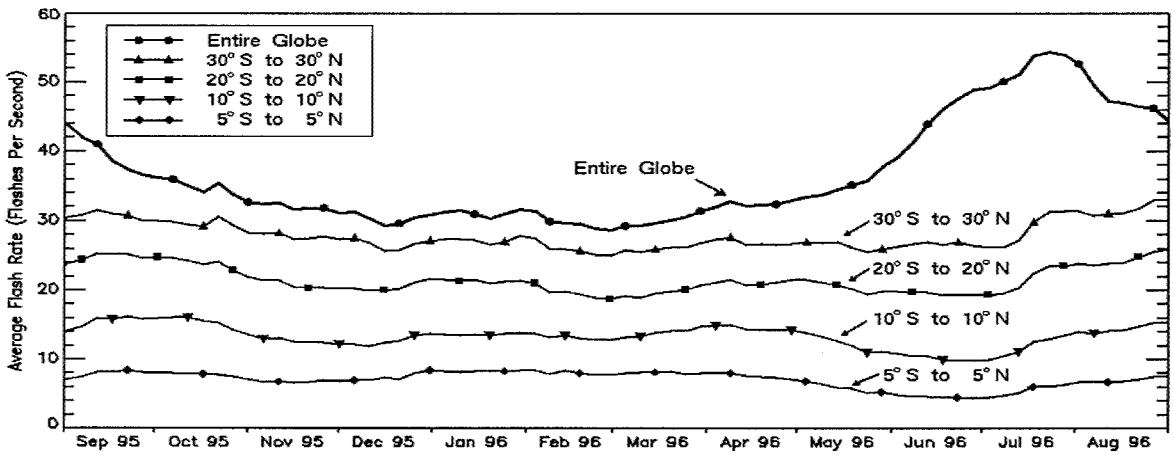


Fig. 7. The annual cycle of the global flash rate separated into various latitude zones.

# LIGHTNING PRODUCTION OF $NO_x$ IN A 3D STORM MODEL

J. H. Helsdon, X. Zhang, and R. D. Farley

Institute of Atmospheric Science, SD School of Mines & Technology, Rapid City, SD, USA

ABSTRACT: The 3D Storm Electrification Model (SEM) has been configured to account for the production of nitric oxide (NO) during a lightning flash, based on the energy dissipated. Following Borucki and Chameides (1984) we adopt a production rate of p(NO) = 9.2 x $10^{16}$ molecules/J. The lightning-produced NO (LNO) is distributed along the simulated channel and then transported with the storm flow. Chemistry involving 9 species and 18 reactions is included. The model simulations are being used to address a number of questions concerning the fate of LNO and other species within a storm, including their distribution within the storm structure. Results with a simpler set of chemical reactions within a 2D version of the model have indicated that the majority of the LNO and other species ends up in the upwind portion of the anvil. This 3D simulation, using the same storm as a basis, shows that there are significant concentrations of LNO both within the anvil and in the lower portion of the storm as it dissipates. Comparison between model concentrations of LNO and data from the recent STERAO project show reasonable agreement.

## INTRODUCTION

$NO_x$ (=NO and $NO_2$) has a important role in the photochemical reactions that determine the atmospheric $O_3$ concentration, and impact the ability of the atmosphere to oxidize and remove many trace species. Along with fossil fuel combustion, biomass burning, and soil microbial activity, lightning is a potentially important and also the least well known source of $NO_x$. During the last 20 years, there has been considerable research effort focused on the mechanisms and magnitude of lightning-produced $NO_x$ using theoretical calculations, laboratory measurements, and field observations. Questions concerning the details of how $NO_x$ is produced by lightning and its subsequent fate still remain. These questions have been addressed in global and regional chemical transport models by parameterizing the LNO using various methods and predicting the transport and evolution of related chemical species. It is this parameterization of the production of NO by lightning that is the weakest link in the chain. Our modeling efforts are directed toward mitigating this weakness by calculating the production of NO by lightning, that is simulated in the model, based on the physics of the lightning process itself. The simulation discussed below is the first such effort using our 3D SEM for a small, relatively simple storm that produces 18 lightning discharges.

## MODEL DESCRIPTION

The 3D SEM, developed at the South Dakota School of Mines and Technology, incorporates not only the cloud dynamics and microphysics, but also processes involved in cloud electrification and the intracloud lightning discharge. The inclusion of the lightning parameterization allows us to simulate $NO_x$ production and to trace the transport of the LNO and its reactants within and around the cloud.

The model domain is 20 km by 20 km in the X and Y directions and 16 km in the Z direction with a grid resolution of 400 m. The main dependent variables are: atmospheric wind, potential temperature, water vapor, cloud water, cloud ice, rain, snow, and graupel/hail. Each hydrometer category has a charge associated with it, governed by a charge conservation equation. The lightning scheme is as described in Helsdon *et al.* (1992) and includes the calculation of the energy dissipated by the flash. This energy dissipation is apportioned along the channel in a manner similar to the charge distribution. We use the value obtained by Borucki and Chemeides (1984) of p(NO) = 9.2 x $10^{16}$ molecules/J to calculate the production of NO by lightning. Table 1 shows the 18 chemical reactions involving 9 species used in the model. The reaction rates in Table 1 are taken from DeMore et al. (1997). The initial vertical profiles of all chemical species are derived from available observations, but are not taken from any specific case study. The model cloud is based on the 19 July 1981 CCOPE cloud.

## RESULTS AND DISCUSSION

The model was initially run for about 15 minutes without any air motion to allow the initial chemical profiles to come into steady-state balance. Temperature and moisture perturbations were then imposed to start convection. The first lightning flash occurred at 25.4 min simulation time, and the last at 28.5 min. The simulation was continued to 38 min, as the cloud dissipated, to trace the movement of the chemical species in the model wind field. For the lightning discharges, the charge transferred ranged from 2.51 to 6.87 C, channel lengths from 5.3 to 7.9 km, and energy dissipation from 9.08 to 22.77×$10^8$ J. Details of the discharges are listed in Table 2.

TABLE 1. Chemical Reactions and Their Rates

| | | | | | | | | | |
|---|---|---|---|---|---|---|---|---|---|
| (R1) | $O_3$ | + | $h\nu$ | | $\rightarrow$ | O | | | radiation dependent |
| (R2) | $O_3$ | + | $h\nu$ | | $\rightarrow$ | O1D | | | radiation dependent |
| (R3) | O1D | + | M | | $\rightarrow$ | O | + | M | $1.9\times10^{8}$ exp(390/T) |
| (R4) | O1D | + | $H_2O$ | | $\rightarrow$ | 2OH | | | $2.2\times10^{-10}$ cm$^3$ molecule$^{-1}$ s$^{-1}$ |
| (R5) | $NO_2$ | + | $h\nu$ | | $\rightarrow$ | NO | + | O | radiation dependent |
| (R6) | O | + | $O_2$ | + M | $\rightarrow$ | $O_3$ | + | M | $6.0\times10^{-34}$ [M]$^{\dagger\dagger}$(300/T)$^{2.3}$ cm$^3$ molecule$^{-1}$ s$^{-1}$ |
| (R7) | NO | + | $O_3$ | | $\rightarrow$ | $NO_2$ | + | $O_2$ | $2.0\times10^{-12}$ exp(-1400/T) cm$^3$ molecule$^{-1}$ s$^{-1}$ |
| (R8) | OH | + | OH | | $\rightarrow$ | $H_2O$ | + | $O_3$ | $4.2\times10^{-12}$ exp(-240/T) cm$^3$ molecule$^{-1}$ s$^{-1}$ |
| (R9)$^{\dagger}$ | OH | + | OH | + M | $\rightarrow$ | $H_2O_2$ | + | M | $k_0 = 6.2\times10^{-31}$ (300/T) |
| | | | | | | | | | $k_\infty = 2.6\times10^{-11}$ |
| (R10) | OH | + | $O_3$ | | $\rightarrow$ | $HO_2$ | + | $O_2$ | $1.6\times10^{-12}$ exp(-940/T) cm$^3$ molecule$^{-1}$ s$^{-1}$ |
| (R11) | OH | + | $HO_2$ | | $\rightarrow$ | $H_2O$ | + | $O_2$ | $4.8\times10^{-11}$ exp(250/T) cm$^3$ molecule$^{-1}$ s$^{-1}$ |
| (R12) | $HO_2$ | + | $HO_2$ | | $\rightarrow$ | $H_2O_2$ | + | $O_2$ | $2.3\times10^{-13}$ exp(600/T) cm$^3$ molecule$^{-1}$ s$^{-1}$ |
| (R13) | $HO_2$ | + | $HO_2$ | + M | $\rightarrow$ | $H_2O_2$ | + | $O_2$ | $1.73\times10^{-33}$ [M]$^{\dagger\dagger}$ exp(1000/T) cm$^3$ molecule$^{-1}$ s$^{-1}$ |
| (R14) | $HO_2$ | + | $O_3$ | | $\rightarrow$ | OH | + | $O_2$ | $1.1\times10^{-14}$ exp(-500/T) cm$^3$ molecule$^{-1}$ s$^{-1}$ |
| (R15) | $HO_2$ | + | NO | | $\rightarrow$ | OH | + | $NO_2$ | $3.5\times10^{-12}$ exp(250/T) cm$^3$ molecule$^{-1}$ s$^{-1}$ |
| (R16)$^{\dagger}$ | OH | + | $NO_2$ | + M | $\rightarrow$ | $HNO_3$ | + | M | $k_0 = 2.5\times10^{-30}$ (300/T)$^{4.4}$ |
| | | | | | | | | | $k_\infty = 1.6\times10^{-11}$ (300/T)$^{1.7}$ |
| (R17) | $CH_4$ | + | OH | | $\rightarrow$ | $2HO_2$ | + | CO + $H_2O$ | $2.45\times10^{-12}$ exp(-1775/T) cm$^3$ molecule$^{-1}$ s$^{-1}$ |
| (R18) | CO | + | OH | | $\rightarrow$ | $CO_2$ | + | $HO_2$ | $1.5\times10^{-13}$ [1 + 0.6×P(atm)] cm$^3$ molecule$^{-1}$ s$^{-1}$ |

$^{\dagger}$ k = cm$^3$ molecule$^{-1}$ s$^{-1}$

$^{\dagger\dagger}$ [M]: air density (molecule/cm$^3$)

Figure 1 is a composite showing the total cloud content (cloud water and cloud ice) and the NO field at four different times during the simulation. Although these are 3D model results, we only include a series of Y-Z cross sections because they reflect the major characteristics of the NO and cloud field. The $NO_2$ field is very similar in structure to that of NO, but with different values and is not shown here. We do not show the geometry of the lightning discharges here, but while they are primarily vertical, there are significant departures from the vertical orientation in response the influence of the horizontal electric field.

Figures 1A and E show the total cloud and NO field, respectively, at 26 min. The cloud is in the mature stage extending from 2 to 11.4 km. At this time the first four discharges have occurred and the LNO is prominent with a maximum value of 22.8 ppbv at 8 km in the center of the cloud. The LNO is distributed by the airflow and reacts with $O_3$ to form $NO_2$. In Figs. 1B and F (28 min) the cloud top extends to 12 km. As a result of 12 more discharges during this time interval, the NO maximum has increased to 35.8 ppbv. The region containing LNO is expanding because of the varying locations of the lightning discharges (see Table 2, 3$^{rd}$ column), variation in the airflow, and mixing.

After 28 min two additional discharges occur with their initiation points 1.6 km lower than the first discharges and termination points below cloud base. Figure 1G, at 30 min, shows the NO produced by these discharges lower in the cloud, while the earlier LNO has been transported into the anvil region. The maximum LNO concentration is 27.9 ppbv at 6.8 km. By 38 min, Fig. 1D shows that the remaining cloud is primarily a spreading anvil. Figure 1H shows a local maximum of around 2 ppbv LNO located in the downwind anvil near 10.5 km with another maximum of 6.3 ppbv at 4 km. Since this is a Y-Z cross section, the distribution of the LNO in the X direction is not shown.

Preliminary results from the Stratosphere-Troposphere Experiments: Radiation, Aerosols, and Ozone (STERAO) Project conducted in NE Colorado indicate that, for the storm of 10 July 96, NO concentrations were in the range of 3-4 ppbv with one peak value of 19 ppbv associated with a recent lightning discharge. The maximum value of NO produced in our simulation was 35.8 ppbv, comparable to the peak observation reported thus far from STERAO. Also measured during STERAO were maximum NO concentrations of 5 ppbv at 3.67 km, and 1.2 ppbv at 2.18 km. Although the 10 July storm had hundreds of discharges and our simulation only 18, our model results show that the concentration of NO decreases rapidly after the cessation of lightning. Contrary to the previous 2D results, the LNO injected lower in the cloud in the latter stages of the storm tends to remain at lower elevations, while the NO produced earlier in the storm tends to be transported to the anvil. This is not only a function of where the NO is produced, but also of the updraft/downdraft structure of the storm.

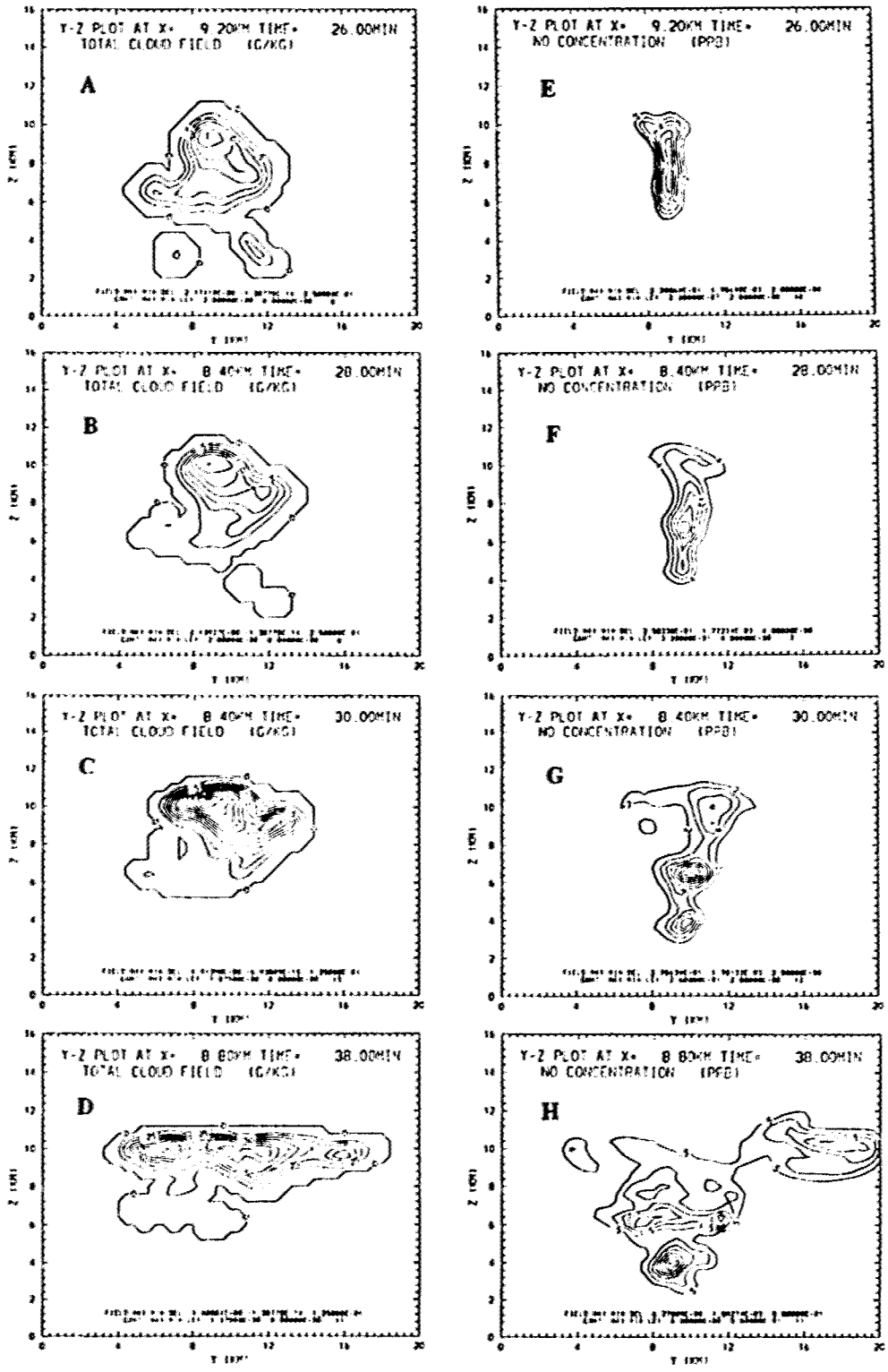


Figure 1. Total cloud field (A, B, C, and D) and NO concentration (E, F, G, and H) at 26, 28, 30, and 38 min, respectively. Contour intervals for the cloud field are 0.25, 0.25, 0.125, and 0.125 g/kg. The contour intervals for NO concentration are 2.0, 4.0, 2.0, and 0.5 ppbv. The Y-Z cross sections are taken at X = 9.2, 8.4, 8.4, and 8.8 km into the domain.

TABLE 2. Characteristics of the 18 Discharges

| Discharge Number | Time (mm:ss) | Starting Point (I, J, K) | Altitude Range (km) | Length (km) | Charge Transferred (C) | Energy Dissipated ($10^8$ J) |
|---|---|---|---|---|---|---|
| 1 | 25:24 | (25, 24, 21) | 10.4 - 5.6 | 5.8 | 2.74 | 9.13 |
| 2 | 25:36 | (26, 24, 21) | 10.4 - 5.6 | 6.2 | 2.77 | 9.24 |
| 3 | 25:45 | (24, 25, 21) | 10.0 - 5.2 | 5.3 | 4.09 | 12.71 |
| 4 | 26:00 | (25, 24, 21) | 10.4 - 5.6 | 5.3 | 2.65 | 9.68 |
| 5 | 26:03 | (23, 26, 20) | 10.0 - 5.2 | 5.7 | 2.71 | 9.08 |
| 6 | 26:12 | (25, 25, 20) | 10.0 - 5.2 | 5.8 | 2.51 | 9.24 |
| 7 | 26:21 | (23, 24, 21) | 10.4 - 5.2 | 6.2 | 4.05 | 14.22 |
| 8 | 26:27 | (24, 26, 20) | 9.6 - 4.8 | 5.7 | 4.12 | 13.92 |
| 9 | 26:30 | (26, 24, 20) | 10.0 - 5.2 | 5.7 | 2.68 | 9.39 |
| 10 | 26:39 | (22, 27, 19) | 9.6 - 4.8 | 5.7 | 2.90 | 11.12 |
| 11 | 26:45 | (25, 25, 20) | 9.6 - 4.8 | 5.5 | 4.52 | 14.56 |
| 12 | 26:57 | (23, 27, 19) | 9.6 - 4.4 | 6.4 | 4.34 | 15.94 |
| 13 | 27:09 | (23, 25, 19) | 9.6 - 4.0 | 7.9 | 6.87 | 22.77 |
| 14 | 27:18 | (21, 28, 19) | 9.6 - 4.8 | 5.8 | 2.71 | 10.54 |
| 15 | 27:27 | (25, 24, 19) | 9.6 - 4.4 | 5.7 | 3.79 | 13.44 |
| 16 | 27:42 | (22, 26, 18) | 9.6 - 4.4 | 5.9 | 4.46 | 16.64 |
| 17 | 28:12 | (23, 25, 17) | 9.2 - 4.0 | 6.0 | 5.36 | 19.81 |
| 18 | 28:30 | (21, 27, 17) | 9.2 - 4.0 | 6.7 | 4.68 | 16.90 |

## CONCLUSION

The 3D SEM was used to simulate $NO_x$ production by lightning. To our knowledge, this is the first effort to model lightning-produced $NO_x$ in a thunderstorm, based on the physics of the lightning discharge. Thus, the resulting solutions come from the physics of the situation and are not a function of arbitrarily assigned parameters. This simulation, employing total energy dissipation as the defining quantity for the production of NO by lightning, seems to generate reasonable results that agree favorably with observations. The set of chemical reactions considered, although still limited, should be sufficient to account the major behavior of lightning-produced $NO_x$ on the time scale of a thunderstorm for a relatively clean background environment. Based on these preliminary results, it would seem that any study of LNO must incorporate not only accurate production rates, but also the dynamic framework within which the lightning operates in order to make an accurate prediction of the spatial distribution of the LNO. Shortcomings of the current model include the lack of a cloud-to-ground discharge; the effect of the cloud on radiative transfer, which influences reactions (R1), (R2), and (R5) in the chemistry suite of Table 1; and lack of nonmethane hydrocarbons in the chemistry suite. These shortcomings will be addressed in future upgrades to the model.

ACKNOWLEDGMENTS: This work was supported by the Atmospheric Chemistry Division of the U. S. National Science Foundation under grants ATM-9322588 and ATM-9803762.

## REFERENCES

Borucki, W. J., and W. L. Chemeides, 1984: Lightning estimates of the rates of energy dissipation and nitrogen fixation. *Rev. Geophys.*, **22**, 363-372.

DeMore, W. B., S. P. Sander, D. M. Golden, R. F. Hampson, M. J. Kurylo, C. J. Howard, A. R. Ravishankara, C. E. Kold, M. J. Molina, 1997: Chemical kinetics and photochemical data for use in stratospheric modeling, Evaluation No. 12, *JPL Publ. 97-4*, 266 pp.

Helsdon, J. H., Jr., G. Wu, and R. D. Farley, 1992: An intracloud lightning parameterization scheme for a storm electrification model. *J. Geophys. Res.*, **97**, 5865-5884.

# Land-Ocean Differences in LIS and OTD Tropical Lightning Observations

D.J. Boccippio, W.J. Koshak, H.J. Christian, S.J. Goodman

Global Hydrology and Climate Center
NASA Marshall Space Flight Center, AL 35812

**Abstract.** Significant differences are known to exist on a global scale between continental and oceanic total lightning regional flash rates, suggesting differences in the properties of convective storms in these regimes. Lightning properties observed by the Optical Transient Detector (OTD) and Lightning Imaging Sensor (LIS) over land and ocean are compared, limited to analysis over the tropics in order to simplify physical interpretation. We find that the mean flash rates of individual storms over tropical land only exceed those over ocean by a factor of 2 (far less than the observed differences in regional flash rates). However, the average nearest neighbor distance of continental thunderstorms is half that over oceans. Cloud-top lightning optical radiance in oceanic storms is also twice as large as over land, suggesting either more energetic flashes over the oceans *or* less intervening cloud particles.

## 1. Introduction

The differences between continental and oceanic lightning flash rates pose a longstanding problem in atmospheric electricity. Global maps of lightning flash density, as compiled either from DMSP/OLS, OTD or LIS satellite measurements, are qualitatively different from other globally observed satellite fields, such as IR cloud top temperature and microwave-derived surface rainfall; the primary differences are a pronounced land bias and a relative paucity of oceanic lightning even in deep convective features such as the intertropical convergence zone (ITCZ). The land bias is readily visible in both daily observations and climatological composites, and the effects of continentality on the annual and diurnal modulation of lightning flash rates can be seen in 4-year composites of OTD data (Fig 1).

(Zipser, 1994) theorized that the differences are explainable by variations in characteristic updraft velocities of individual storms, and speculated that many oceanic deep clouds possess vertical velocities smaller than a "critical threshold" for the occurrence of lightning. In this study, we attempt to use the large and relatively unbiased statistical sample provided by OTD and LIS lightning measurements to more rigorously quantify the land/ocean differences in terms of both storm, flash and stroke observed properties in the two regimes, focusing on the tropics (22.5S 22.5N) in order to simplify physical interpretation.

## 2. Methodology

Data from both the OTD and LIS are used in this study. OTD data span a 770-day period beginning on 1 Nov 1996; this guarantees data collected at a uniform threshold (15 in OTD 8-bit units) and unbiased by diurnal aliasing (the window includes 14 satellite precessions through the local diurnal cycle). LIS data span 441 days (9 precessions through the local diurnal cycle) collected at various thresholds (the LIS instrument uses adaptive thresholding based upon the local background scene radiance). Any OTD orbits which triggered alerts during manual quality assurance inspections were excluded, and any OTD lightning data that received an automatic "TAC" quality index of less than 140 were excluded; this stringent filtering reduced sensor and radiation noise and mitigated the effects of the South Atlantic Anomaly (SAA).

A binary land/ocean mask was smoothed in order to generate tropical land, coast and ocean masks; the smoothing used here is extremely conservative and chosen to guarantee full "continental" and "oceanic" behavior and emphasize differences between the two (Fig 2). For all computed statistics which differed measurably between land and ocean, the equivalent coastal statistics fell between the land and ocean values. Regional subsets of the tropics were also defined as follows: Africa (all land, 25W-50E), South America (all land, 90W-30W), Maritime Continent (all coast, 80E-150E), West Pacific (all ocean, 120E-180E), Atlantic (all ocean, 75W-20E) and Indian Ocean (all ocean, 25E-120E). The OTD and LIS "area" data products were used to identify storm cells and derive per-storm flash rates. The area product assembles spatially contiguous optical flashes and is most analogous to a local region of electrified cloud (to the extent that flashes are confined to electrified cloud regions on the sensor pixel scales of about 9 km and 4 km, respectively).

OTD "area" products should be interpreted cautiously, at best, due to navigational drift over the course of individual satellite overpasses. LIS navigation is much stabler and LIS areas should represent a stable and robust storm metric.

Derived products including stroke/flash/area footprint and calibrated radiance are also considered in this study. Precise footprints are not included in the OTD dataset but were calculated for this study using the same pixel geolocation technique used operationally to generate LIS footprints. In the distributed OTD data, lightning radiance is calibrated by assuming one of three background radiances depending on whether the satellite is in day, twilight or night conditions. This can lead to significant errors in the calibrated lightning radiance. An improved technique was used to recalibrate these radiances by instead estimating the actual background radiance via the cosine of the local solar zenith angle (the empirical relationship was bootstrapped using the subset of OTD data in which lightning was observed at the precise time of a background scene snapshot). The improved technique leads to a significant reduction in the expected error of OTD calibrated radiances (Fig 3), and IDL code for its implementation is available from the author. LIS background radiances are operationally estimated directly from geolocation of the (more precisely navigated) background scene snapshots, yielding higher quality radiances in the distributed data. It should be remembered that these are measured cloud-top radiances; hence differences in this parameter either represent variability in the true lightning radiance *or* in the intervening cloud properties.

## 3. Results

Complete distributions of OTD and LIS area (storm), flash and group (stroke or recoil event) statistics were computed. The derived parameters typically span between 20-30 dB of dynamic range; for conciseness we present only the population means here. Derived parameters include: **Storm density:** the number of areas in the spatially subsetted region observed during the respective data windows (i.e., not adjusted for sensor viewtime). This parameter has units of [areas/sq km] and is useful only for relative intercomparisons. **Storm footprint:** the total areal extent of illumination for each area, [sq km]. **Storm radiance rate:** the total radiance output of each area divided by its viewtime [1e6 $\mu$J/sq km/ster/$\mu$m/s]. **Storm flash rate:** the number of flashes in each area divided by its viewtime, not adjusted for sensor detection efficiency [flashes/min]. **Nearest neighbor range:** the minimum distance to another area in the field-of-view [km]. The field-of-view sizes (roughly 700 and 1300 km for LIS and OTD, respectively) place limits on the usefulness of this calculation, and hence this parameter describes only the density of electrified convection at and below these scales. **Flash density:** As storm density, but for flashes [flashes/sq km]. **Flash footprint:** As storm footprint above [sq km]. **Flash radiance:** The total radiance of each flash, [1e6 $\mu$J/sq km/ster/$\mu$m]. **Flash duration:** Total duration of each flash, [ms]. **Groups/flash:** The number of 2-ms pixel groups in each flash, dimensionless. **Group footprint, radiance:** As flash footprint and radiance above.

The computed population means are summarized in Table 1. The most dramatic land/ocean differences are observed in storm flash rate (2.1:1 and 2.4:1 land/ocean ratios for LIS and OTD), storm nearest neighbor range (0.5:1 for both sensors at scales up to their field-of-view), flash footprint (0.7:1 for both sensors), flash radiance (0.5:1 for both sensors), flash duration (0.9:1 and 0.7:1) and groups/flash (0.6:1 for both sensors). Additionally, these means vary consistently between the three tropical continental regions, with Africa yielding the "most continental" values (highest storm flash rates, closest storm spacing, smallest flash footprints and radiances) and the Maritime Continent yielding the "most oceanic" values. With few exceptions, this variability is also observed by both sensors. While some slight variability exists between the storm flash rates of the three oceanic regions, the other parameters do not 'track' in the same manner as the three continental regions. It is also interesting to note the parameters which do *not* vary significantly between land and ocean, or between continents, namely the total storm footprint and radiance rate.

The twofold increase in mean per-storm flash rates over land is surprisingly low, given the order-of-magnitude differences in total regional flash rates observed in the OTD climatology. Increased density of storms at spatial scales below the sensor fields-of-view is also inadequate to explain the regional flash rates: twofold decreases in local nearest neighbor range imply only fourfold increases in total storm count, or eightfold increases in flash yield. The remainder of the difference must be accounted for by a higher density (over

| LIS | Land | Ocean | AF | SA | MC | PAC | ATL | IND |
|---|---|---|---|---|---|---|---|---|
| Storm density | .00301 | .00011 | .00272 | .00359 | .00123 | .00013 | .00013 | .00019 |
| Storm footprint | 727 | 729 | 745 | 710 | 756 | 727 | 730 | 748 |
| Storm radiance rate | .045 | .049 | .047 | .043 | .048 | .049 | .049 | .042 |
| Storm flash rate | 3.85 | 1.87 | 4.30 | 3.23 | 3.01 | 2.01 | 1.85 | 1.66 |
| Nearest neighbor rg ( 700 km) | 55 | 103 | 51 | 61 | 79 | 111 | 92 | 111 |
| Flash density | .02105 | .00027 | .02024 | .02204 | .00523 | .00035 | .00033 | .00043 |
| Flash footprint | 297 | 447 | 285 | 321 | 356 | 446 | 432 | 446 |
| Flash radiance | 0.72 | 1.58 | 0.66 | 0.82 | 0.98 | 1.60 | 1.50 | 1.35 |
| Flash duration | 260 | 282 | 257 | 266 | 286 | 298 | 283 | 276 |
| Groups/flash | 10.4 | 17.0 | 9.9 | 11.0 | 12.5 | 17.9 | 16.6 | 14.7 |
| Group footprint | 121 | 138 | 120 | 124 | 131 | 137 | 135 | 146 |
| Group radiance | .069 | .093 | .066 | .074 | .079 | .090 | .090 | .092 |
| **OTD** | | | | | | | | |
| Storm density | .00198 | .00014 | .00210 | .00174 | .00138 | .00021 | .00013 | .00021 |
| Storm footprint | n/a | n/a | n/a | n/a | n/a | n/a | n/a | n/a |
| Storm radiance rate | .009 | .007 | .009 | .011 | .010 | .007 | .007 | .006 |
| Storm flash rate | 2.96 | 1.21 | 3.02 | 2.78 | 2.64 | 1.08 | 1.49 | 1.15 |
| Nearest neighbor rg ( 700 km) | 69 | 105 | 66 | 76 | 88 | 105 | 97 | 110 |
| Nearest neighbor rg (1300 km) | 75 | 140 | 71 | 84 | 99 | 141 | 130 | 150 |
| Flash density | .01243 | .00040 | .01466 | .00781 | .00846 | .00055 | .00039 | .00057 |
| Flash footprint | 291 | 399 | 281 | 327 | 319 | 445 | 344 | 396 |
| Flash radiance | 0.19 | 0.38 | 0.18 | 0.24 | 0.23 | 0.44 | 0.31 | 0.34 |
| Flash duration | 149 | 202 | 142 | 171 | 177 | 212 | 186 | 191 |
| Groups/flash | 3.9 | 6.9 | 3.7 | 4.4 | 4.8 | 7.3 | 6.1 | 6.3 |
| Group footprint | 192 | 200 | 190 | 202 | 191 | 212 | 190 | 202 |
| Group radiance | .049 | .055 | .048 | .054 | .049 | .060 | .051 | .054 |

Table 1: Tropical population means for various LIS and OTD observables. Units are given in the text.

land) of storm clusters on scales larger than sensor fields-of-view. As an aside, we note that the characteristic differences in the largest 10% of vertical velocities in tropical land and ocean storms (as reported by (Zipser, 1994)) are between 2-3:1. The concordance of this this ratio with the LIS/OTD observed storm flash rate differences may be coincidental, but it is intriguing.

It is important to note that the current analysis does *not* address Zipser's hypothesis that many oceanic deep convective storms fall below a critical vertical velocity for lightning: we report only on those cells which are observably electrified. A tropical survey of the occurrence of all cells of comparable size to LIS/OTD areas would be required to identify the fraction of deep convective cells which are not lightning producers.

The implications of observed land/ocean differences in flash radiance, footprint, duration and group count are at present ambiguous. While the flash energetics of other low flash rate systems such as midlatitude winter storms and MCS stratiform regions are known to be larger than in higher flash rate convective cores, the total ice content of these systems is typically much smaller as well, and either property could lead to observed increases in cloud-top radiance (and related properties such as duration, footprint and group rate). Either inference is scientifically interesting, but without additional data constraints, we are unable to identify the primary cause.

# References

Zipser, E.J. 1994. Deep cumulonimbus cloud systems in the tropics with and without lightning. *Mon. Wea. Rev.*, **122**, 1837–1851.

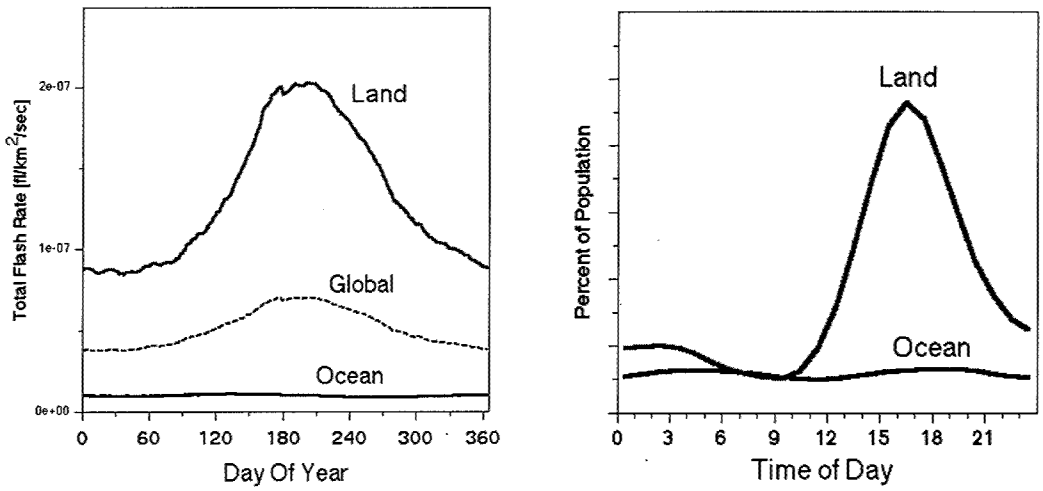


Figure 1: Smoothed annual and diurnal cycles of global total lightning flash rates. Annual cycle is composed of 4 years OTD data filtered using a 110-day moving average (two complete satellite precessions through the local diurnal cycle), and is adjusted with estimates of OTD detection efficiency.

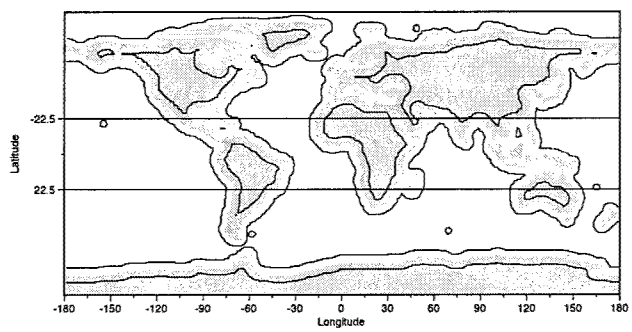


Figure 2: Land/coast/ocean mask used in this study.

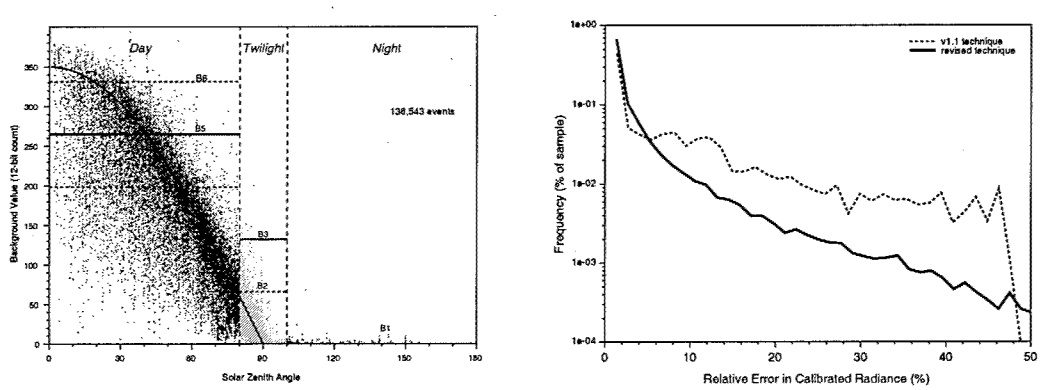


Figure 3: (a) Measured cloud background radiance (needed for AC calibration of lightning radiance) as a function of the local solar zenith angle. The continuous cosine fit is shown along with the three assumed radiances used in the distributed data (labelled B5,B3,B1). (b) Improvement in OTD calibrated lightning radiances using the solar zenith angle technique.

# Initial Comparison of the Lightning Imaging Sensor (LIS) with Lightning Detection and Ranging (LDAR)

Tomoo Ushio, Kevin Driscoll, Stan Heckman, Dennis Boccippio, William Koshak, Hugh Christian

Global Hydrology and Climate Center, Huntsville, Alabama, U.S.A.

**Abstract** The mapping of the lightning optical pulses detected by the Lightning Imaging Sensor (LIS) is compared with the radiation sources by Lightning Detection and Ranging (LDAR) and the National Lightning Detection Network (NLDN) for three thunderstorms observed during and overpasses on 15 August 1998. The comparison involves 122 flashes, including 42 ground and 80 cloud flashes. For ground flash, the LIS recorded the subsequent strokes and K-changes inside the cloud. For cloud flashes, LIS recorded those with higher sources in altitude and larger number of sources. The discrepancies between the LIS and LDAR flash locations are about 4.3 km for cloud flashes and 12.2 km for ground flashes. The reason for these differences remain a mystery.

**Introduction** Lightning is a transient, high current electric discharge occurring inside the cloud (cloud flash) or between the thunder cloud and the ground (ground flash). The electrical energy released by the flash is converted to heat, a shock wave, and Electro-magnetic radiation ranging from static field to x-rays. The strongest form of this radiation occurs in the visible wavelength. Recently, space borne optical sensors have been developed to detect the optical pulses produced by lightning during day and night. One of these instruments is the Lightning Image Sensor (LIS), which was launched into an orbit on 27 Nov. 1998 as a part of the TRMM(Tropical Rainfall Measuring Mission).

This paper will discuss the characteristics of lightning activity observed by LIS, NLDN, and LDAR for three thunderstorms. A comparison will be made between three sensors, showing temporal and spatial differences.

**Analysis** The TRMM satellite travels a distance of 7 kilometers every second as it orbits the Earth. With a field-of-view of 600[km]x600[km], LIS observes a point on the Earth for almost 90 seconds as it passes overhead. On the other hand, the LDAR is a stationary system located at the Kennedy Space Center (KSC) in Florida with an effective range of about one hundred kilometers. Since the LIS was launched into an orbit, there are only 4 days (or a total of about 6 minutes) where the LDAR detects lightning flashes within its effective range at the time LIS passes overhead. This paper examines the events of 15 August 1998. This event involved three main cells about 40 to 50 km west from the central station of KSC LDAR. The LIS passed overhead and observed thunderstorms in the center of its FOV for 80 seconds, beginning at 21:40 (UTC).

Even though the thunderstorm is within the effective range of LDAR, LDAR has limitations due to VHF signal attenuation, loss of below-horizon VHF sources and so on. The VHF source density detected by the LDAR system drops approximately 10 dB about every 70 km away from the LDAR central station mainly due to range attenuation [Boccippio, et al. 1999], and the location errors increases at a rate of r2. Poehler et al. [1977] estimate the location accuracies of within 1 km for the sources up to 50 km, and suggests that "acceptably good data" can be obtained out to about 40 km. In this case study, all the thunderstorms are equally located about 40 to 50 km away from the LDAR centroid. The effect of the attenuation can be relatively ignored.

Since any one flash produces more electro-magnetic pulses than can be resolved by LDAR, the sources must be grouped by flash. We calculated the density of the LDAR sources in the X-Y plain, and extracted the high density region of more than 7 sources in 14 square kilometer and within 0.4 second. If the region

selected are close each other in space and time, these regions are grouped as the same discharge event. If more than 5 LDAR sources are below 5 km in height, we classified the flash as a ground flash as opposed to a cloud flash.

The VHF radiation detectable by LDAR generally occurs during the negative breakdown process. For the negative ground flash, the VHF radiation sources from negative stepped leader goes downward to the ground. For the cloud flash, it does not reach to the ground. For positive ground flash, the VHF radiation does not go downward to ground, because the positive leader is silent in terms of VHF radiation. We are therefore unable to distinguish positive ground flash from VHF radiation observation alone. NLDN provides positive ground flash data, but the detection efficiencies of NLDN for positive ground flash has not yet been fully evaluated. In this analysis, the positive ground flashes are included with cloud flashes.

**Ground flash** In figure 1, one example of time sequence of x, y, and z of the 'events' , NLDN peak current, and LDAR sources for ground flash is shown. This flash begins at about 20.55 seconds (+177370820.677 TAI93) and lasts for about 450 milliseconds. (The NLDN also detects this flash as a negative ground flash which has the peak current of -32.7 kA and multiplicity of 3.) After the preliminary breakdown inside the cloud, the radiation sources propagate downward to ground for about 30 milliseconds. Consistent with the characteristics of VHF radiation for negative return stroke, the flash produce no VHF radiation. At the time of the return stroke or just after the NLDN first return stroke, LIS detects the optical signal. The NLDN and the radiation sources that go downward to ground, pin-point the time of first return stroke. Before the first return stroke, no optical pulses are emitted by the intra-cloud or stepped leader process. About 150 millisecond after the first return stroke, some optical pulses are emitted by subsequent return stroke or K-change inside the cloud. Since the VHF radiation during the dart leader is not as intense and the duration is short, the LDAR does not map the process well and we can not identify the process radiating the optical pulse. In all of the 24 cases that match with NLDN and LIS, the optical pulses are emitted by the first return stroke, subsequent stroke or K-changes between strokes. In 5 out of 24 , LIS detects optical signals from the intra-cloud process preceding the first return stroke. In all 21 cases, except for the flashes with multiplicity of 1, the optical pulses from subsequent strokes or K-changes are detected. LIS records the subsequent strokes or K-changes, rather than first return stroke and preliminary intra-cloud activity preceding first negative stepped leader.

Figure 2 shows the height distribution of the LDAR sources for ground flashes. Note that LIS records the flashes that have intra-cloud component with high altitude inside the cloud like K-change.

**Cloud flash** Figure 3 shows time sequences of the radiation pulses detected by LDAR and optical pulses by LIS for cloud flash occurring at 21:40:36 UT on August 15, 1998. The overall structure of the flash exhibits bi-level structure connected by single upward channel as observed by Shao et al. [1996]. The flash begins with horizontal activity lasting about 100 millisecond at an altitude of 10 km, and later propagates upward in the cloud. During the upward progression, some optical pulses are detected by LIS. In the later stage of the flash, the radiation sources distributed both in the upper and lower part of the cloud, indicating K-change occurs. At the end of the flash, one optical pulse is detected by LIS.

In figure 4, LDAR sources distribution for cloud flash versus height is shown. Note that more than 80% of the LDAR sources classified into flash are seen by LIS and at higher sources are more easily seen by LIS. It is suggested that the optical depth of the thundercloud reduces the light intensity of the lightning channel near cloud base.

**Spatial differences** The spatial difference is defined as the difference between the LIS flash centroid and the LDAR centroid, which is computed from all the radiation sources that occur during the flash. In figure 5, histograms of spatial difference for cloud and ground flashes are shown. The mean value of cloud and ground flash is 4.3 km and 12.2 km, respectively. The mean value for cloud flash is about 3 times smaller than those for ground flash. It is possible that the difference comes from channels extending outside the clouds themselves or a reflection from low altitude clouds neaby. However, the true reason for these discrepancies remain illusive.

## References


[1] Boccippio, D. J., S. Heckman, and S. J. Goodman, A diagnostic analysis of the Kennedy Space Center LDAR network, submitted, 1999

[2] Poehler, H., An accuracy analysis of the ldar system, Tech. Rep. CR-154631, NASA, 1977

[3] Shao, X. M., and P. R. Krehbiel, The spatial and temporal development of intracloud lightning, J. Geophys. Res., 101, 26641-26668, 1996


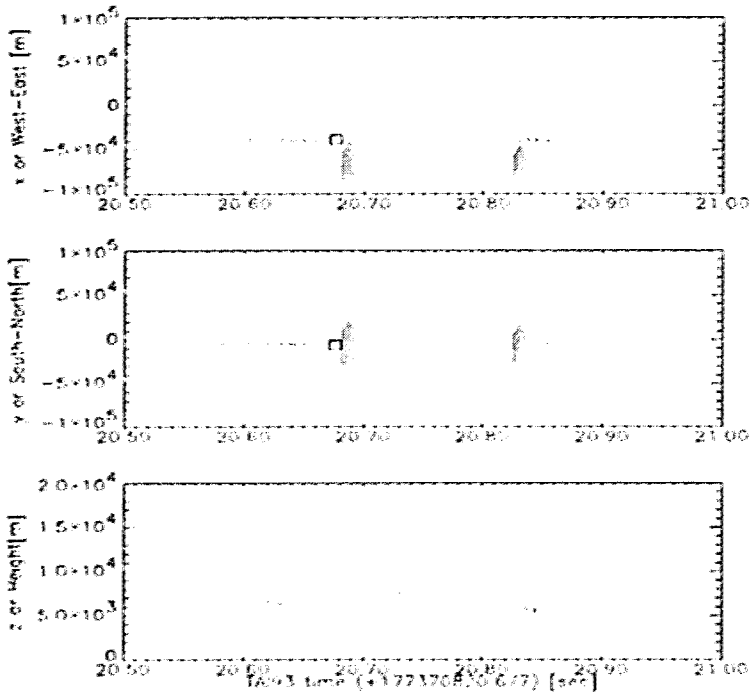


Figure 1: x (West-East), y (North-South), and z (altitude) of the radiation sources detected by LDAR, optical pulses by LIS (triangle) and the NLDN return stroke (square) versus time.

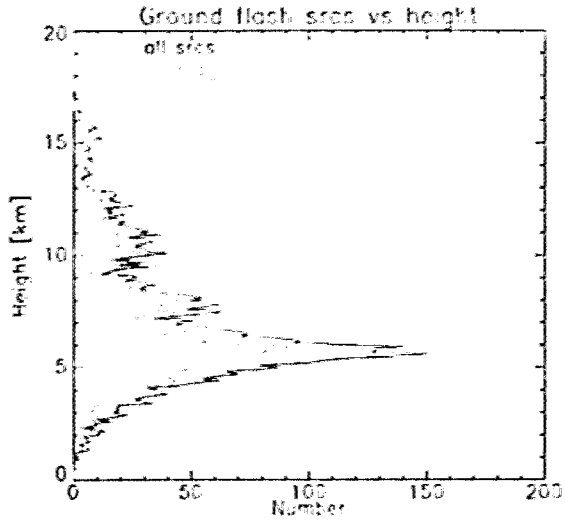


Figure 2: Height distribution of the LDAR sources for ground flashes.

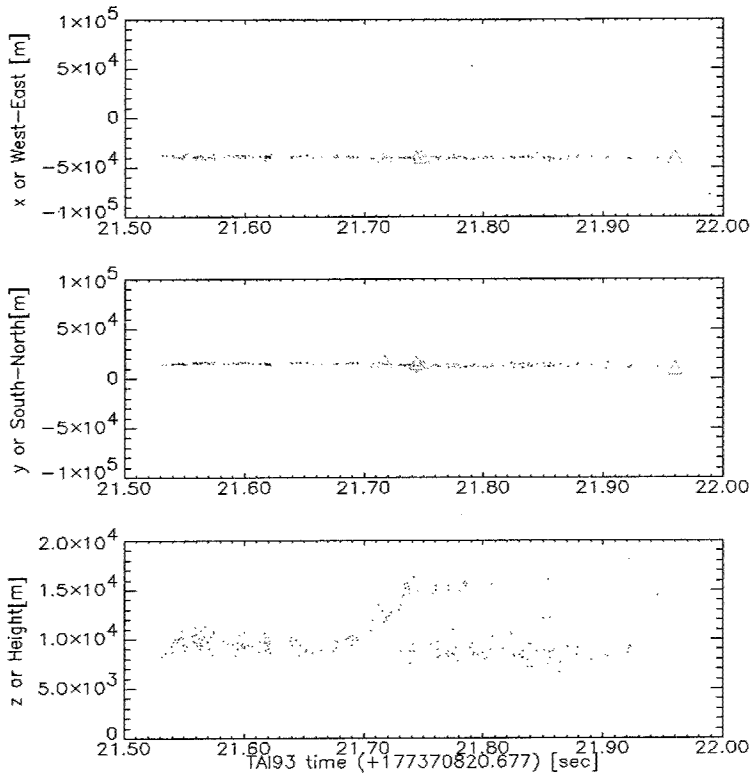


Figure 3: x (West-East), y (North-South), and z (altitude) of the radiation sources detected by LDAR, optical pulses by LIS (triangle) versus time.

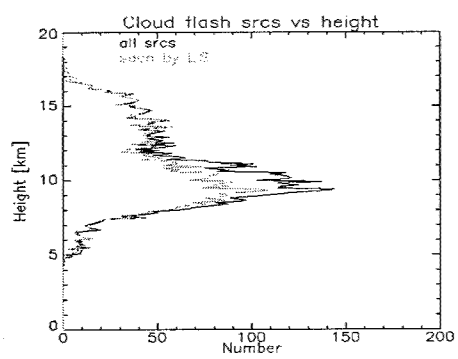


Figure 4: Height distribution of the LDAR sources for cloud flashes.

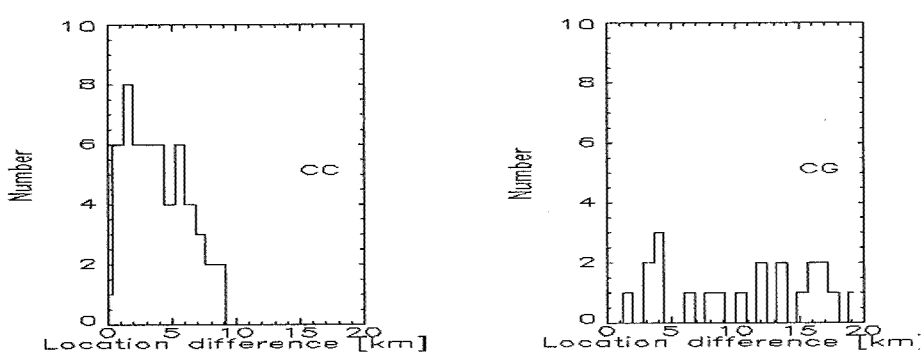


Figure 5: Spatial difference histogram of the LIS for cloud and ground flashes

# DIURNAL LIGHTNING DISTRIBUTION AS OBSERVED BY THE OPTICAL TRANSIENT DETECTOR (OTD)

Richard J. Blakeslee[1], Kevin T. Driscoll[3], Dennis E. Buechler[3], Dennis J. Boccippio[1], William L. Boeck[2], Hugh J. Christian[1], Steven J. Goodman[1], John M. Hall[4], William J. Koshak[1], Douglas M. Mach[3], and Michael F. Stewart[3]

[1]NASA Marshall Space Flight Center, Huntsville, Alabama, U.S.A.
[2]Niagara University, Niagara, New York, U.S.A.
[3]University of Alabama in Huntsville (UAH), Huntsville, Alabama, U.S.A.
[4]CSC Huntsville, Huntsville, Alabama, U.S.A.

ABSTRACT: Since April 1995, lightning activity around the globe has been monitored with the Optical Transient Detector (OTD). The OTD observations acquired during the one year period from September 1995 through August 1996 have been used to statistically determine the number of flashes that occur over the Earth during each hour of the diurnal cycle, expressed both as a function of local time and universal time. The globally averaged local lightning activity displays a peak in late afternoon (1500-1800 local time) and a minimum in the morning hours (0600-1000 local time) consistent with convection associated with diurnal heating. No diurnal variation is found for oceanic storms. The diurnal lightning distribution (universal time) for the globe displays a variation of about 35% about its mean as compared to the Carnegie curve which has a variation of only 15% above and below the mean.

## INTRODUCTION

Since April 1995, the Optical Transient Detector (OTD) has monitored lightning activity around the globe. The OTD is the first of the new generation space-based lightning sensors specifically designed to detect and locate lightning with a high detection efficiency. Therefore, OTD can provide quantitative statistics on the frequency and distribution of lightning worldwide when averaged over a sufficient time period. In this paper, we present results on the diurnal lightning activity derived from OTD observations during its first year in orbit.

One of the goals of improved space-based lightning measurements is to better understand the processes involved in sustaining the global electric circuit. Over the past 100 years, progress towards understanding the global electric circuit has been made at a very slow pace. At the early part of this century, researchers hypothesized that thunderstorms were responsible for the currents that circulate in the Earth's atmosphere between the highly conductive ionosphere and the surface of the Earth (*Wilson*, 1920). This discovery eventually led to the modern concept of the global electric circuit. However, the details that explain how thunderstorms contribute current to the global electric circuit have remained elusive, and the hypotheses that seek to explain a thunderstorm's role in the global electric circuit have not always been consistent with measurements. Therefore, as a second objective, this paper examines the global electric circuit implications of the OTD observations.

## MEASUREMENTS

The OTD was launched into a low-earth, 70° inclination orbit in April 1995 as a scientific payload on the MicroLab-1 satellite (recently renamed OV-1). The OTD sensor optically detects lightning flashes that occur within a 1300×1300 km$^2$ field-of-view during both day and night, with a detection efficiency estimated to be 50-66%. The orbital inclination and the instrumental field-of-view permit OTD to acquire lightning observations between 75° N and 75° S latitude. In addition, the OTD orbit precesses relative to the sun each day so that lightning is observed during all hours of the diurnal cycle. Figure 1 shows results from a simulation of the time of day when locations at 0°, 45°, or 70° latitude would be observed by OTD during a one month period. When averaged over a seasonal or annual time period sufficient data is available to calculate the diurnal lightning distributions.

## RESULTS

The averaged global lightning activity computed as a function of local time from the OTD observations for the period September 1, 1995 through August 31, 1996 is presented in Fig. 2 as a percentage departure from the mean. In this and subsequent figures the OTD data were summed and processed in hourly bins. The light colored bar surrounding the solid curve for each hourly estimate indicates the range of uncertainty. The average time of observation associated with each hourly bin is shown in the small insert figure. The OTD data reveals that, on average, local lightning activity peaks in the late afternoon (i.e., between 1500-1800 local time), and has a minimum in the morning (i.e., between 0600-1000 local). Not unexpectedly, the local-time lightning signal is dominated by convection associated with the diurnal heating from the sun. *Christian et al.* (1999, this issue) noted that 75% of all lightning occurs between the 30° S and 30° N latitude zone (i.e., the tropics and sub-tropics) consistent with this

result. Although not shown in Fig.2, the OTD analysis also shows that there is no diurnal dependence for oceanic lightning which maintains a fairly constant hourly rate.

Figure 3 presents the diurnal global lightning frequency compiled as a function of universal time from the same OTD observations shown in Fig. 2. There is considerably more structure and variability displayed in the lightning activity when plotted in terms of universal time as compared to local time. This simply reflects the integrated contributions being made to the global lightning activity from the major lightning producing centers of the world. This is more clearly illustrated in Fig. 4 in which the contributions from various regions of the Earth have been isolated following the approach of *Whipple and Scrase* (1936). In fact, the diurnal variation of total lightning frequency computed from the OTD observations is very similar to the earlier estimate of global thunderstorm occurrence derived by *Whipple and Scrase* (1936) as shown in Fig. 5.

The diurnal variation of the fair weather potential gradient over the oceans, traditionally referred to as the Carnegie curve, is shown in Fig. 6. This curve is well correlated in phase but not in amplitude with the distribution and timing of thunderstorms around the globe. The amplitude variation of both the global lightning (derived from the OTD measurements) and thunderstorms (derived from thunderday statistics) are considerably greater than the Carnegie curve. As shown in Fig. 4, the global flash rate from OTD has a variation of about 35% above and below the mean, while the Carnegie curve has a variation of only ±15% about the mean.

## DISCUSSION

The OTD observations have certainly better quantified the knowledge of the diurnal global lightning distribution and shown this distribution to be consistent with earlier thunderstorm statistics, yet the amplitude discrepancy with the Carnegie curve (and similar ionospheric potential measurements) remains. This result suggests that current sources other than or in addition to that from cloud-to-ground lightning significantly contribute to the global electric current budget. In addition, the global flash rates derived from OTD data (*Christian et al.*, 1999) further indicate that cloud-to-ground lightning (estimated to be between 12-16 flashes per second) would contribute considerably less than the 1000 A total current estimated to be flowing in the global electric circuit (*Muhleisen*, 1977).

In a pre-OTD modeling study, *Williams and Heckman* (1993), satellite-observed longitudinal distributions of electrical activity (from DMSP and ISS-b analyses) were convolved with local diurnal variations of cloud-to-ground lightning and point discharge current to produce universal time variations that were compared to the Carnegie curve. The predicted amplitude ratio (maximum-minimum/mean) for the lightning activity was found to be 2-3 times than the Carnegie curve, a result essential confirmed by the OTD results presented in this paper. On the other hand, the amplitude ratio for the diurnal variations of point discharge current showed good agreement suggesting that the primary source of current to the global electric circuit might be point discharge (corona currents). At this time, however, too little is know about the averaged diurnal distribution of local point discharge to establish the validity of this suggestion.

## CONCLUSIONS

Clearly many details do remain elusive concerning the global electric circuit and the role of thunderstorms in maintaining this circuit. The observations from OTD and other recently launched lightning sensors — e.g., the Lightning Imaging Sensor (LIS) on the Tropical Rainfall Measuring Mission (TRMM) — will contribute to this effort primarily by helping to isolating and quantify the role that lightning plays in the process. Already, as noted above, it appears that lightning may supply much less current to the global circuit than was believed even just a few years ago.

## REFERENCES


Christian, H. J., R. J. Blakeslee, D. J. Boccippio, W. L. Boeck, D. E. Buechler, K. T. Driscoll, S. J. Goodman, J. M. Hall, W. J. Koshak, D. M. Mach, and M. F. Stewart, Global frequency and distribution of lightning as observed by the Optical Transient Detector (OTD), Preprints, 11th International Conference on Atmospheric Electricity, Guntersville, Alabama, U.S.A., June 7-11, (see this issue), 1999.

Muhleisen, R., The global circuit and its parameters, in *Electrical Processes in Atmospheres*, edited by H. Dolezalek and R. Reiter, pp 467-476, Darmstadt, Germany, 1977.

Whipple, F. J. W., and F. J. Scrase, Point discharge in the electric field of the Earth, *Geophys. Mem.*, *68*, Meteorol. Off., Air Minis., London, 1936.

Williams, E. R., and S. J. Heckman, The local variation of cloud electrification and global diurnal variations of negative charge on the Earth, *J. Geophys. Res.*, *98*, 5221-5234, 1993.

Wilson, C. T. R., Investigations on lightning discharges and on the electric field of the Earth, *Phil. Trans. Roy. Soc. London*, *A221*, 73-115, 1920.

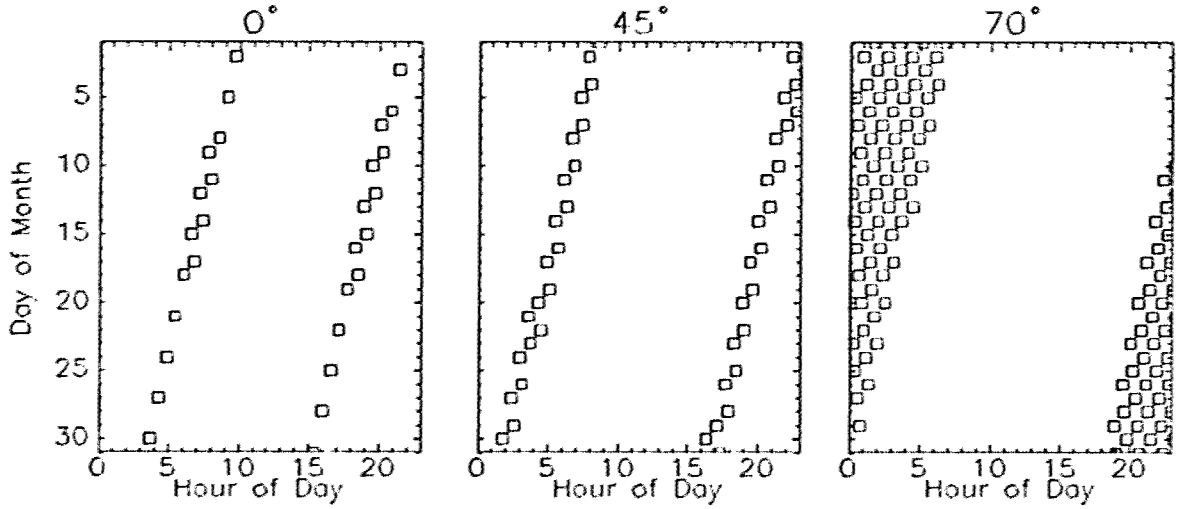


Fig. 1. Simulation of the time of day when locations on the Earth at 0°, 45°, and 70° latitude are observed by the OTD sensor during a one month period.

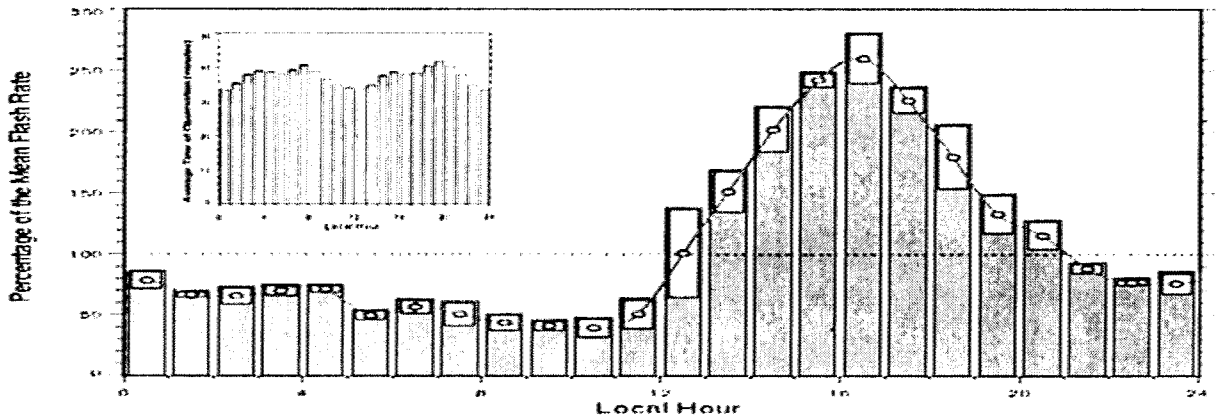


Fig. 2. Local-time variation of lightning activity averaged over the globe from OTD data for the one year period from September 1995 to August 1996. The average observation time associated with each bin is shown in the insert. The lighter colored bar surrounding the curve indicates the range of uncertainty.

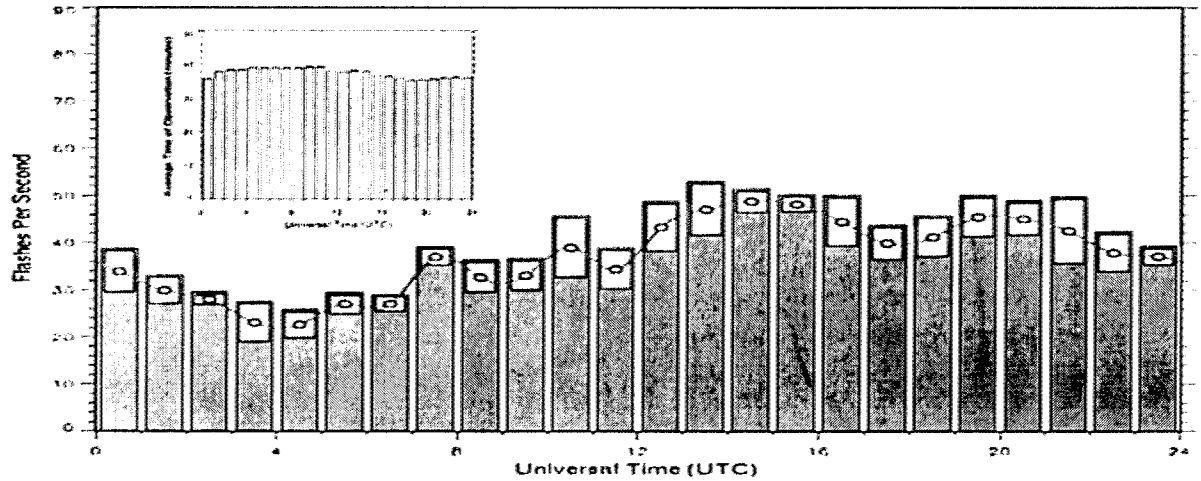


Fig. 3. The global diurnal lightning frequency derived from OTD data for the one year period from September 1995 to August 1996. The insert and error bars have the same meaning as in Fig. 2.

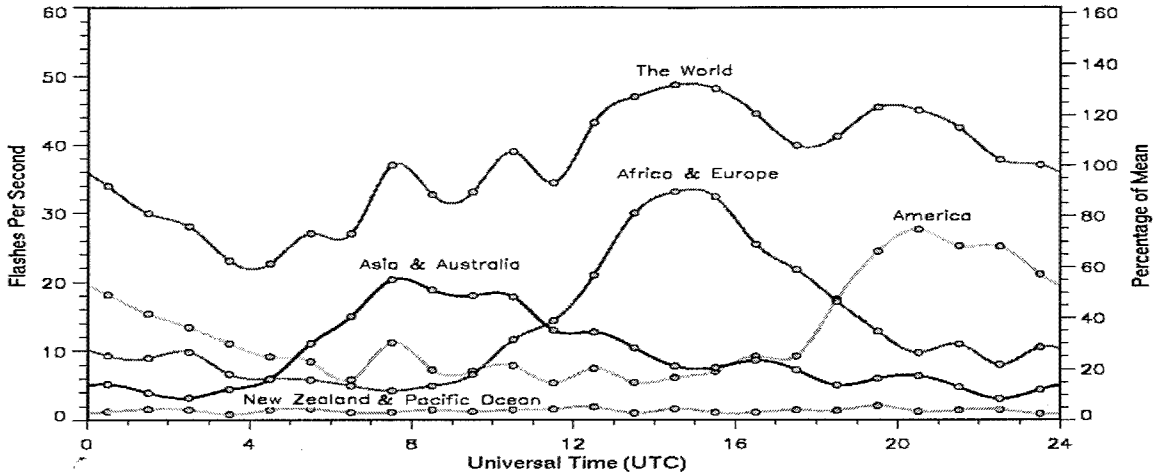


Fig. 4. The diurnal global lightning frequency as shown in Fig. 3 with the component contributions from America (30° W to 120° W), Africa and Europe (60° E to 30° W), Asia and Australia (150° E to 60° E) and New Zealand and the Pacific Ocean (120° W to 150° E).

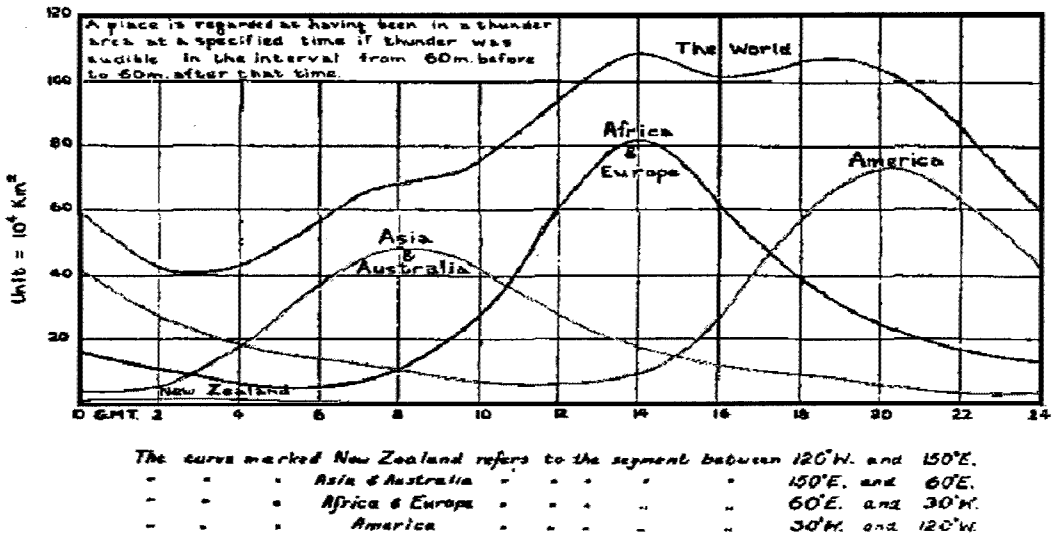


Fig. 5. The diurnal global thunderstorm occurrence and the corresponding contributions from the same regions of the Earth as used in Fig. 4 derived from thunderday statistics (from *Whipple and Scrase*, 1936).

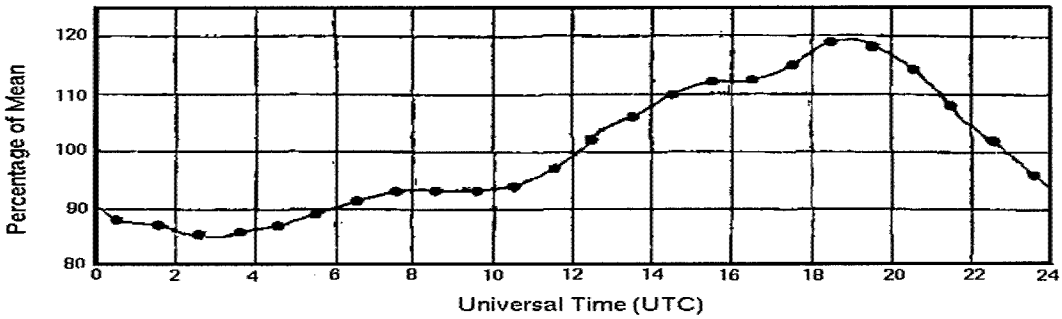


Fig. 6. The diurnal variation of the fair weather oceanic potential gradient commonly referred to as the "Carnegie Curve" (from *Whipple and Scrase*, 1936.

# THE LIGHTNING IMAGING SENSOR

Hugh J. Christian[1], Richard J. Blakeslee[1], Steven J. Goodman[1], Douglas A. Mach[2], Michael F. Stewart[2], Dennis E. Buechler[2], William J. Koshak[1], John M. Hall[3], William L. Boeck[4], Kevin T. Driscoll[2], and Dennis J. Boccippio[1]

[1]NASA Marshall Space Flight Center, Huntsville, Alabama, U.S. A.
[2]Earth Science Systems Laboratory, University of Alabama in Huntsville (UAH), Huntsville, Alabama, U.S.A
[3]CSC Huntsville, Huntsville, Alabama, U.S.A.
[4]Niagara University, Niagara, New York, U.S.A.

ABSTRACT: The Lightning Imaging Sensor (LIS) is a NASA Earth Observing System (EOS) instrument on the Tropical Rainfall Measuring Mission (TRMM) platform designed to acquire and investigate the distribution and variability of total lightning (i.e., cloud-to-ground and intracloud) between ±35° in latitude. Since lightning is one of the responses of the atmosphere to thermodynamic and dynamic forcing, the LIS data is being used to detect deep convection without land-ocean bias, estimate the precipitation mass in the mixed phased region of thunderclouds, and differentiate storms with strong updrafts from those with weak vertical motion.

## INTRODUCTION

Lightning measurements provided by the Lightning Imaging Sensor (LIS) on the Tropical Rainfall Measuring Mission (TRMM) offer an unique opportunity to develop combined data algorithms to investigate the electrical, microphysical, and kinematic properties of tropical thunderstorms. It is hypothesized that the type and frequency of lightning are intimately related to the microphysical (e.g., ice mass, liquid water content) and kinematic properties (e.g., updraft speed) of thunderstorm systems and to the environment (e.g., available buoyant energy). Recent evidence suggests that lightning activity can provide empirical estimates or bound the range of values for some geophysical properties such as the convective rain flux and rain rate, the vertical structure and distribution of storm mass, (convective) latent heating rates, the number and distribution of thunderstorms.

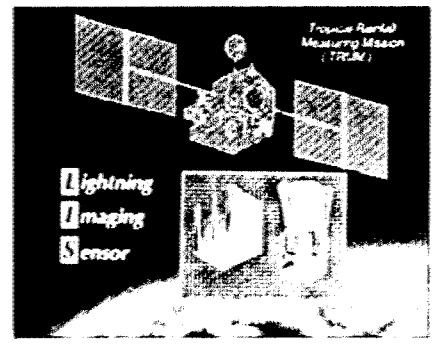


Figure 1. The Lightning Imaging Sensor integrated aboard the TRMM satellite.

## INSTRUMENT DESCRIPTION

The Lightning Imaging Sensor (LIS) is a scientific instrument that is integrated aboard the Tropical Rainfall Measuring Mission (TRMM) Satellite, as depicted in Fig. 1. On November 28, 1997, the LIS was launched into a low Earth orbit, and now circles the Earth at an altitude of 350 km. The inclination of this orbit is 35 degrees, thus allowing LIS to observe lightning activity in the tropical regions of the globe, as shown in Fig. 2.

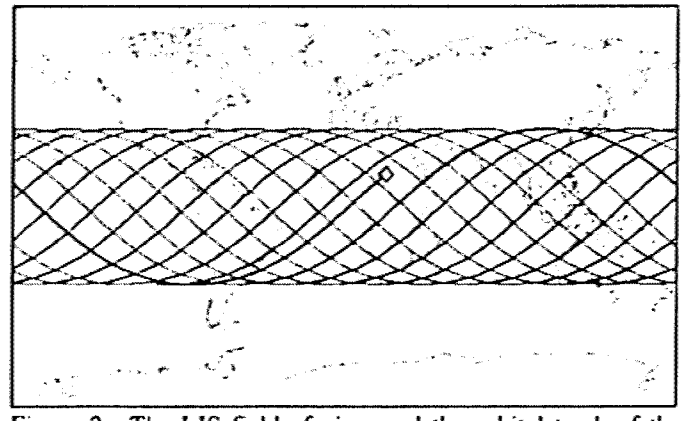

Figure 2. The LIS field-of-view and the orbital track of the TRMM satellite during a 24 hour period.

The LIS sensor contains an optical staring imager which is used to identify lightning activity by detecting momentary changes in the

brightness of the clouds as they are illuminated by lightning discharges [Christian et al., 1992]. Due to the sensitivity and dynamic range of the sensor, it can detect lightning even in the presence of bright, sunlit clouds. The LIS instrument detects "total" lightning, since cloud-to-ground, intracloud, and cloud-to-cloud discharges all produce optical pulses that are visible from space. Data recorded by this instrument includes the time of the lightning event, its radiant energy, and its location.

The primary component of the staring imager is the 128×128 charged coupled device (CCD) array which has a sampling rate slightly greater than 500 frames per second. The wide angle lens, combined with the 350 km altitude of the TRMM spacecraft, permit the sensor to view a 600 km × 600 km area of the Earth with a spatial resolution of between 3 and 6 km (3 at nadir, 6 at limb). Since the LIS travels around the Earth with a velocity greater than 7 km/s, the instrument can monitor individual storms and storm systems for lightning activity for almost 90 seconds as it passes overhead.

## DISCUSSION

The LIS instrument is one of five instruments on the TRMM platform. The other instruments include the TRMM microwave radiometer (TMI), the Visible and Infrared Scanner (VIRS), the Precipitation Radar (PR), and the Cloud and Earth Radiant Energy System (CERES) [Kummerow, 1998]. Each instrument provides a unique set of data that can be used to learn more about atmospheric circulation, weather, and climate. An example of data from four of these instruments is shown in Fig. 3. In this example, the TRMM spacecraft made an overpass over a weather system that spanned across parts of Texas and Louisiana on January 22, 1998. Data from VIRS instrument shows information on the cloud cover and cloud-top height, while the 85 GHz TMI data shows where cloud ice is most prevalent. Although the PR has a much smaller swath width, its data is extremely useful in quantifying the amount and location of precipitation. Also shown in Fig. 3 is the lightning data from the LIS instrument, which is coincident with the areas of producing the highest rainfall rates. By comparing the LIS data with data from the other instruments on TRMM, it is possible examine relationships between lightning activity and several important climatological parameters, including rainfall, latent heat release, and convection.

Data from the LIS is also being used to build a global lightning and thunderstorm climatology. As demonstrated in Fig. 4, the distribution of lightning activity in the tropics shows an affinity to land as well as some latitudinal variations according to the seasons. The solar flux and associated warming is believed be the dominant influence on this seasonal variation, and the relatively low frequency of lightning activity over the oceans can been attributed to weaker updrafts in oceanic storms. Since lightning activity is thought to be a sensitive indicator of climate change (even subtle temperature variations), the seasonal lightning climatologies found in Fig. 4, along with climatologies compiled in the future, will be used to test this theory.

## SUMMARY

The Lightning Imaging Sensor on TRMM has demonstrated that lightning activity can easily be detected from space. Simple comparisons of the LIS data with coincident TMI, PR, and VIRS data suggests that the detection of even a single discharge is significant and provides important information about storms, including estimates of the rate of precipitation, storm height, and the presence of ice. Further research should continue examine the role of lightning in the distribution of convective precipitation as well as the release and transport of latent heat.

## REFERENCES

Christian, H. J., R. J. Blakeslee, and S. J. Goodman, Lightning Imaging Sensor (LIS) for the Earth Observing System, NASA Technical Memorandum 4350, MSFC, Huntsville, Alabama, Feb. 1992.

Kummerow, C., W. Barnes, T. Kozu, J. Shiue, and J. Simpson, The Tropical Rainfall Measuring Mission (TRMM) Sensor Package. J. Atmos. Ocean Tech., Vol. 15, No. 3, 1998, pp. 809-817.

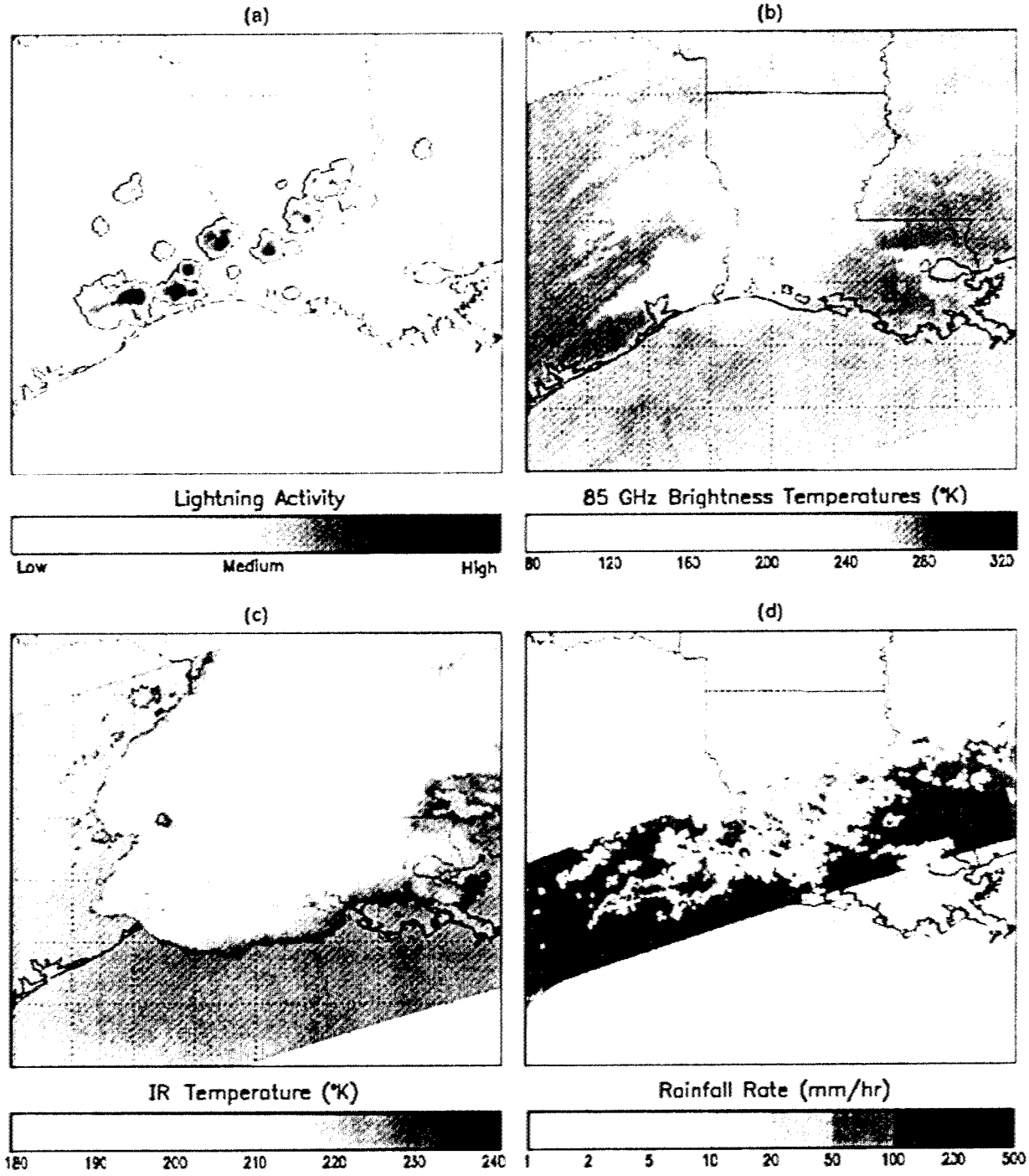


Figure 3. An example of (a) LIS, (b) TMI, (c) VIRS, and (d) PR data for storms in East Texas and Louisiana on January 22, 1998 at 0412 UTC.

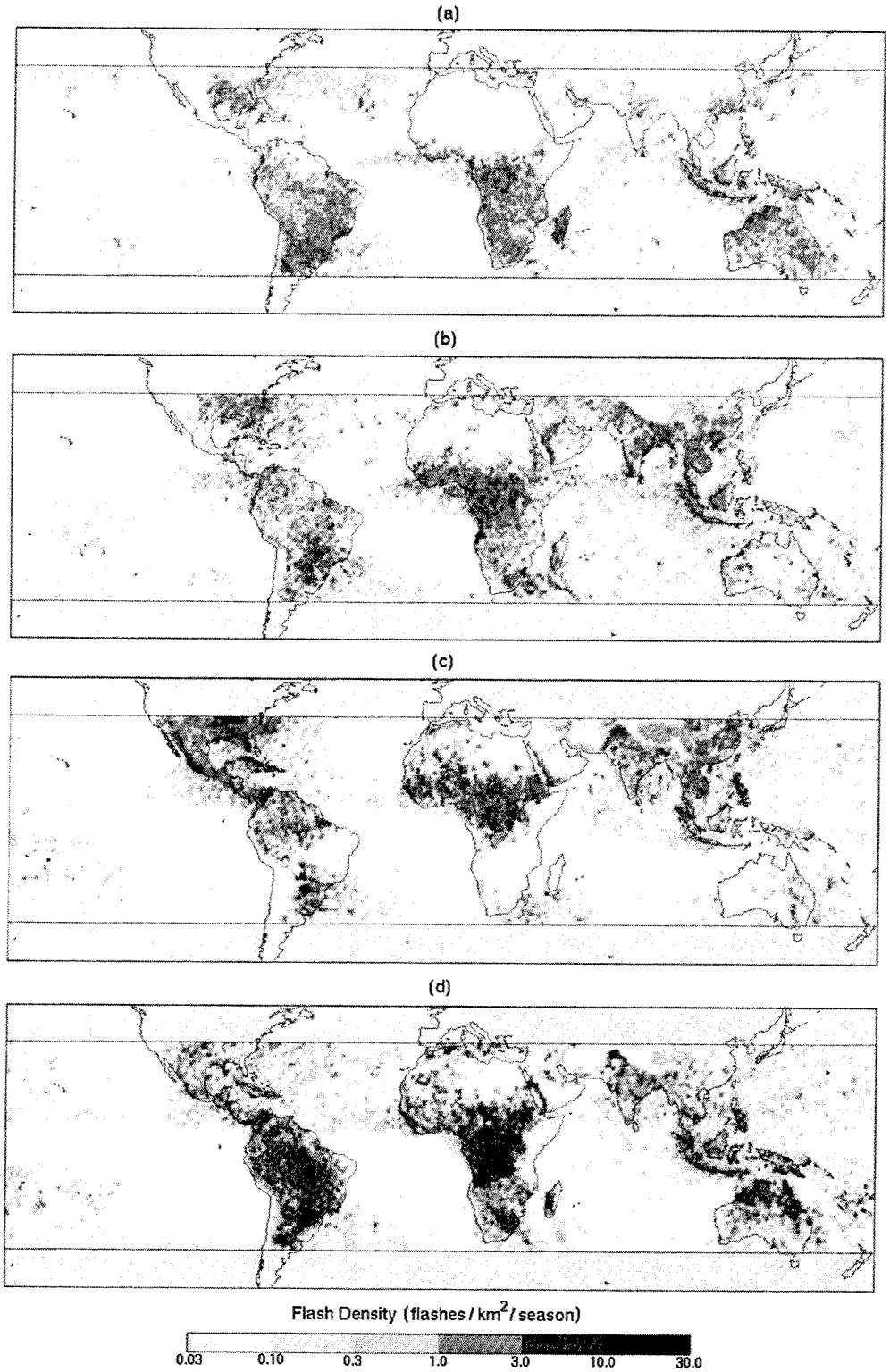


Figure 4. The 1998 seasonal distribution of lightning flashes as observed by LIS for (a) December, January, and February, (b) March, April, May, (c) June, July, and August, and (d) September, October, and November.

# GLOBAL LIGHTNING VARIATIONS CAUSED BY CHANGES IN FLASH RATE AND BY CHANGES IN NUMBER OF THUNDERSTORMS

[1]E. Williams, [1]K. Rothkin, [1]D. Stevenson and [2]D. Boccippio

[1]Massachusetts Institute of Technology, Cambridge, MA 02139 USA
[2]NASA Marshall Space Flight Center, Huntsville, AL 35806 USA

ABSTRACT: Observations from the Optical Transient Detector in space are used to examine the response of the number of storms and the total flash rate to thermodynamic forcing of deep convection on the diurnal and annual time scales. On the diurnal time scale, the flash rate appears to track with cloud bouyancy, and storm numbers dominate later in the cycle. On the annual time scale, almost all of the total lightning response is due to changes in the number of storms, with a negligible contribution from flash rate.

## INTRODUCTION

The lightning flash rate and the total flash count are frequently used measures of the electrical activity of thunderstorms. The flash rate is a widely recognized indicator of the strength of the storm updraft, with the highest flash rates occurring in severe storms (Williams et al, 1999). In climate studies and in the use of the global circuit as a diagnostic for global change (Williams,1992; Price, 1993; Markson and Lane Smith, 1994; Fullekrug and Fraser-Smith, 1997; Reeve and Toumi, 1999), one is concerned with the response of both lightning parameters to external forcing. If, for example, the thermally forced conditional instability of the atmosphere increases, does the mean flash rate per storm increase or do the numbers of storms increase or is the response a combination of these effects?

Attempts to answer this basic question with certain global data sets are faced with problems. The traditional meteorological measure of lightning, the thunder day, is wholly inadequate for this task, as days with a single lightning flash and days with tornadic supercells are not distinguished. The background Schumann resonances have been used in the climate context (Williams, 1992) but in this measurement the waveforms of individual lightning flashes overlap, preventing a discrete flash count. Furthermore, the integrated source parameter one extracts by this method (Heckman et al, 1998) cannot distinguish between 10 storms making 1 flash per minute and one storm making 10 flashes per minute.

Other data sets are better suited to address this issue. Foremost among these are the new optical measurements of lightning from space with the Optical Transient Detector (OTD) and the Lightning Imaging Sensor (LIS). This study is concerned with data from the OTD which provides flash rate data in the tropics and extratropics. Furthermore, these global observations provide access to lighning's response to forcing on the diurnal and the annual time scale. For climate studies, longer time scales are obviously of interest. The strategy pursued here is to understand the physical response on two widely separated time scales for which the forcing is well understood.

## OTD OBSERVATIONS

The OTD has been operating in low earth orbit since April, 1995. The details of the instrument and the measurement strategy are extensively described in other publications (Christian et al, 1996 ), including several papers in this Conference, and will not be repeated here. It is appropriate to point out that the typical observation time of the instrument over any given location is 2-3 minutes, an adequate interval to determine a thunderstorm flash rate. For purposes of this study, to guarantee adequate resolution of the diurnal and annual response, data were examined for three summer months (June-August , 1996) and three winter months (December, 1995, January-February, 1996). The influence of the diurnal cycle on the annual analysis was minimized by averaging over 55 days of data for each season.

In addressing the response of total lightning and lightning flash rate from a "storm", we need a storm observable. Let it be emphasized at the outset that "storm" is an ill-defined quantity in the multi-scale realm of turbulent atmospheric convection. No one measure is entirely adequate and in this study multiple measures of "storm" have been considered. The measure that probably conforms most closely to the isolated thunderstorm in meteorology (a deep convective element whose depth is comparable to its

height and whose overall lifetime is of order one hour) is the OTD "area" quantity. An "area" is defined solely in terms of optically-defined flashes. The centroid of every new flash initiates an "area" and any flash within 22 km (along latitude and longitude lines) of the initial flash is then included in that "area". Since the typical OTD viewtime is typically much shorter than a thunderstorm lifetime, no lifetime is assigned to "area". The 22 km scale, which admittedly is comparable to the pixel size of the OTD measurement (8-13 km) was chosen to bound the size of the majority of isolated thunderstorms.

The second measure of "storm" which is more removed from the meteorological entity is a 2°x2° patch in latitude/longtitude observed by OTD. Such patches are still substantially smaller than the nominal 1300km x 1300 km footprint of the sensor but considerably larger than the isolated thunderstorm. If any lightning is observed in the 2°x2° region, it is a "storm". Otherwise, it is not included in the collection of storms.

The behavior of "areas" and 2°x2° patches have been examined on both the diurnal and annual time scales and is described in the next section.

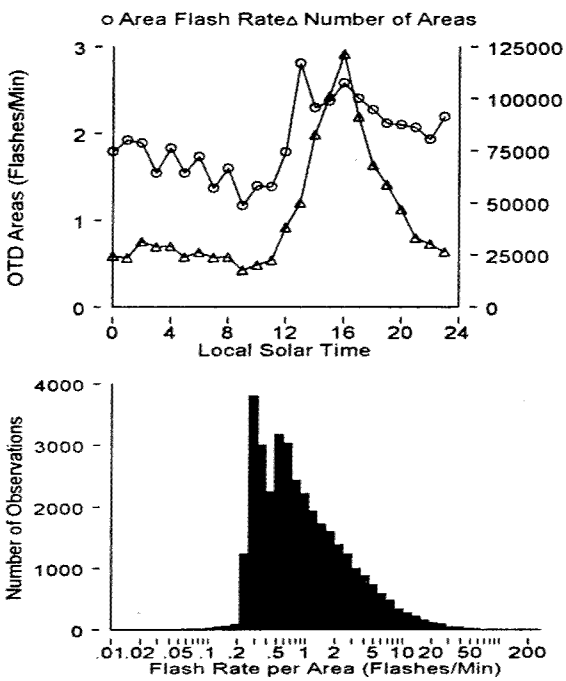


**Figure 1** Diurnal Variation and Flash Rate Distribution for OTD "Areas"

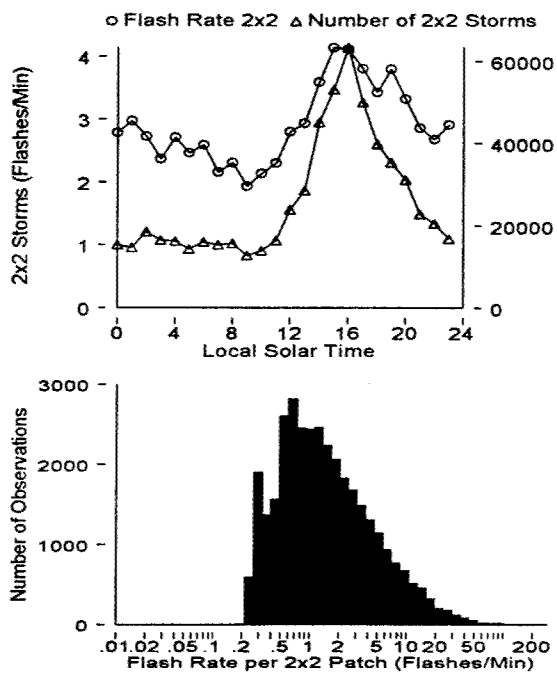


**Figure 2** Diurnal Variation and Flash Rate Distribution for 2°x2° Patches

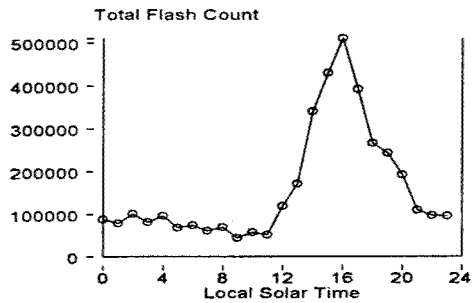


**Figure 3** Diurnal Variation of Total Lightning

| | OTD "Areas" | | 2°x2° Patches | | Total Flash Count |
|---|---|---|---|---|---|
| | Num. Areas | Flash Rate | Num. 2°x2° | Flash Rate | |
| Jan | 403678 | 2.2 | 205799 | 3.0 | 1331297 |
| Jul | 640144 | 2.0 | 409933 | 3.2 | 2510730 |

**Table 1** Annual Variation of Flash Rates (Flashes/Min), Number of Storms and Number of Flashes.

## RESULTS: DIURNAL TIME SCALE

To determine a collective diurnal variation, all observed "areas" and 2°x2° patches with lightning were binned in local solar time (regardless of location). We did not separate land areas from ocean areas as we expect the lightning activity and the overall response to be dominated by land anyway. Mean flash rate for each "area" was computed by taking the total number of flashes in that area and dividing by the appropriate viewtime. Mean flash rate for a 2°x2° patch was computed by taking the total number of flashes in that area (220kmx220km at the equator) and dividing by the viewtime.

The computed results for the diurnal variation of quantities pertaining to "area" is shown in Fig 1(a,b). Fig 1a shows the diurnal variation of number of "areas" and the diurnal variation of mean flash rate. The "area" flash rate declines from midnight till after dawn and then rises abruptly to peak in early afternoon before declining again through the afternoon. The overall mean is about 2 flashes/minute which is generally consistent with local thunderstorm observations. The overall amplitude variation of flash rate is appreciable, but still smaller than the diurnal variation in the number of "areas", a quantity that clearly peaks later in the afternoon. Fig 1b shows the distribution function of "area" flash rates, illustrating the mean near 2 flashes/minute but also a long tail at higher flash rates. Flash rates exceeding 1 flash per second (60 fpm), near the severe storm threshold (Williams et al, 1999), are exceedingly rare. The apparent cutoff at low flash rates is the direct result of the limited viewing time (ie., 1 flash in 3 minutes is 0.33 fpm).

Figure 2a shows the same pair of diurnal variations as in Fig 1, but now for 2°x2° patches instead of "areas". The number of 2°x2° patches shows an afternoon maximum similar to the behavior for "areas". The maximum flash rate is about 2 hours later in the diurnal cycle than for "areas" and the amplitude variation is somewhat greater. This difference is tentatively attributed to the large area of the 2°x2° patch and the misidentification of "storm" flash rate with number of true thunderstorms within the larger area. Figure 2b shows the distribution function of computed flash rates for all 2°x2° patches with lightning. The shape of this distribution is similar to the one for "areas", but its mean is clearly greater, owing to the larger area of the patches relative to the "areas". The diurnal variation of total flashes, the same result for 2°x2° patches as for "areas", is shown in Figure 3. The peak-to-trough variation in total lightning is nearly an order of magnitude, consistent with earlier local analyses (Williams and Heckman, 1993). Comparisons among Figures 1a and 2a and Figure 3 show that number of "storms" is still dominating over the flash rate effect in determining this large diurnal variation of total flashes.

## RESULTS: ANNUAL TIME SCALE

Numerous observations, with both optical and Schumann resonance methods (Fullekrug and Fraser-Smith, 1997; Satori et al, this Conf.), support the idea that the global lightning activity is maximum in NH summer and minimum in NH winter. The seasonal behavior of the DC global circuit appears to follow the same behavior (Adlerman and Williams, 1996). It is increasingly apparent that this annual cycle is strongly influenced by the extratropics and by the pronounced land/ocean asymmetry that is manifest primarily in the extratropics (Williams, 1994). The Earth's mean temperature is highest in July and lowest in January. The OTD flash analysis on the annual time scale has therefore centered on two months: January and July. Table 1 summarizes the relevent quantities for both "areas" and 2°x2° patches.

The general findings for the annual time scale are different than the diurnal results: the variation in number of storms (by either measure) completely dominates over mean flash rate in controlling the factor-of-two annual variation in total global lightning between summer and winter months. For example, the number of 2°x2° patches detected by OTD in July (640144) is nearly double the number for January (403678), but the mean area flash rates agree to within 10% (2.0 fpm vs 2.2 fpm). A self consistent picture is presented by the other numbers in Table 1.

## DISCUSSION AND CONCLUSIONS

On the diurnal time scale, both flash rate and number of storms make significant contributions to the variation of total lightning. The behavior of flash rate sheds new light on the link between conditional instability (ie., cloud bouyancy) and lightning. Earlier analyses (Price, 1993; Markson and Lane-Smith,1994) emphasized the lag in global circuit response from the time of maximum surface air

temperature, but here, as in the analysis of Williams and Heckman (1993), only total lightning and integrated global circuit sources were considered. The results in Figures 1a and 2a provide new evidence that flash rate follows more closely in phase with cloud buoyancy and CAPE (Convective Available Potential Energy), since wet bulb potential temperature, a good proxy for CAPE on the diurnal time scale (Williams and Renno, 1993), is known to peak in early afternoon (Albright, 1939) and to decline throughout the afternoon and into the early morning hours. The lag in peak total lightning into the late afternoon (see Fig. 3) is undoubtedly due to the nonlinear effects of outflow boundaries that increase the number of storms by destabilizing the atmosphere over a larger total area.

On the longer annual time scale, variations in the OTD flash rate are hardly detectable, and the dominant response to forcing is an increase in the number of thunderstorms, a result supported by all selections of OTD parameter to represent storms. If the annual time scale is representative of increasingly longer time scale behavior, then this result suggests that changes in cloud bouyancy will not be a contributor to changes in total lightning. In this same context, it remains to be shown whether the reported interannual variations in global lightning (Williams, 1992; Reeve and Toumi, 1999) are due to changes in flash rate or to changes in the numbers of storms. This question is difficult to answer with lightning observations from low earth orbit because of the aliasing effects of the pronounced diurnal cycle. An optical sensor in geostationary orbit would be well suited for this task.

REFERENCES

Adlerman, E. and E. Williams, Seasonal variation of the global electrical circuit, J. Geophys. Res., 101, 29679-29688, 1996.

Albright, J.C., Summer Weather Data, The Marley Company, Kansas City, Kansas, 153 pp., 1939.

Christian, H.J. et al, The Optical Transient Detector, 10th International Conference on Atmospheric Electricity, Osaka, Japan, June, 1996.

Fullekrug, M. and A.C. Fraser-Smith, Global lightning and climate variability inferred from ELF magnetic field variations, Geophys. Res. Lett., 24, 2411, 1997.

Heckman, S.J., E. Williams, and R. Boldi, Total global lightning inferred from Schumann resonance measurements, J. Geophys. Res., 103, 31775-31779, 1998.

Markson, R. and D. Lane-Smith, Global change monitoring through the temporal variation of ionospheric potential, AMS Conference on the Global Electrical Circuit, 273-278, Nashville, Tenn., 1994.

Price, C., Global surface temperatures and the atmospheric global circuit, Geophys. Res. Lett., 20, 1363, 1993.

Reeve, N. and R. Toumi, Lightning activity as an indicator of climate change, Quart. J. Roy. Met. Soc., (in press), 1999.

Satori, G., E. Williams, R. Boldi, K. Rothkin, S. Heckman and B. Zieger, Comparisons of long-term Schumann resonance measurements in Europe and in North America, this Conference.

Williams, E.R., The Schumann resonance: a global tropical thermometer, Science, 256, 1184, 1992.

Williams, E.R., Global circuit response to seasonal variations in global surface air temperature, Mon. Wea. Rev., 122, 1917-1929, 1994.

Williams, E., R. Boldi, A. Matlin, M. Weber, S. Hodanish, D. Sharp, S. Goodman, R. Raghavan and D. Buechler, The behavior of total lightning activity in severe Florida thunderstorms, Atmos. Res., (in press), 1999.

Williams, E., and S. Heckman, The local diurnal variation of cloud electrification and the global diurnal variation of negative charge on the Earth, J. Geophys. Res., 98, 5221-5234, 1993.

Williams, E.R. and N.O. Renno, An analysis of the conditional instability of the tropical atmosphere, Mon. Wea. Rev., 121. 21-36, 1993.

ACKNOWLEDGEMENTS

MIT thanks NASA Marshall Space Flight Center for support on Grant NAG8-935 to investigate observations from the OTD and for timely provision of the data tapes. Discussions with K. Driscoll, S. Goodman, S. Heckman and D. Mach are greatly appreciated.

# THE ROLE OF BOUNDARY LAYER AEROSOL IN THE VERTICAL DEVELOPMENT OF PRECIPITATION AND ELECTRIFICATION : ANOTHER LOOK AT THE CONTRAST BETWEEN LIGHTNING OVER LAND AND OVER OCEAN

E. Williams[1], D. Rosenfeld[2], N. Madden[1], C. Labrada[1], J. Gerlach[3] and L. Atkinson[3]

[1] Massachusetts Institute of Technology, Cambridge, Ma. 02139 USA
[2]The Hebrew University of Jerusalem, Jerusalem, Israel
[3]NASA Wallops Island Flight Facility, Wallops Island, Va USA

ABSTRACT: Comparisons are made between the cloud condensation nuclei (CCN) concentration in the boundary layer and radar/electrical observations of the vertical development of precipitation and lightning in both the 'break period' and 'monsoon' regimes in tropical Brazil. The initial radar echoes and the maximum flash rates are found to be higher when the CCN concentration is higher, characteristic of the 'break period' conditions. One possible explanation for both observations is the survival of cloud droplets against coalescence and their attainment of the mixed phase region aloft.

## INTRODUCTION

The order-of-magnitude contrast in lightning activity over land and over ocean is now well established on the basis of both optical observations from space (Orville and Henderson, 1986; Christian et al, 1996) and Schumann resonance observations (Huang et al, 1999). The traditional explanation for this notable contrast rests on temperature-controlled differences in instability and a resultant contrast in updraft speed for land and ocean storms. Certain problems with the traditional explanation have led to an examination of an alternative explanation proposed by D. Rosenfeld based on well established differences in the land/ocean aerosol concentration (Squires, 1958). This study was carried out in tropical Brazil, where distinct differences in meteorological regime and attendant cloud condensation nuclei have also been identified.

## DISCUSSION OF HYPOTHESES

Present hypotheses for the land/ocean lightning contrast share one assumption and are based on two common features. The assumption is that selective charge transfer in ice particle collisions and subsequent differential motions are causing cloud electrification and lightning. The two common features are that stronger updrafts are present in the continental storms and give rise to a more strongly developed mixed phase region, the seat of the charge separation process. Global observations with the TRMM radar strongly support this land/ocean contrast in mixed phase maturity. Fig 1 shows all observations of radar reflectivity greater than 40 dBZ at 7 km altitude for January 1998. The three main hypotheses are clearly distinguished by the microphysical basis for enhanced precipitation in the mixed phase region over continental regions.

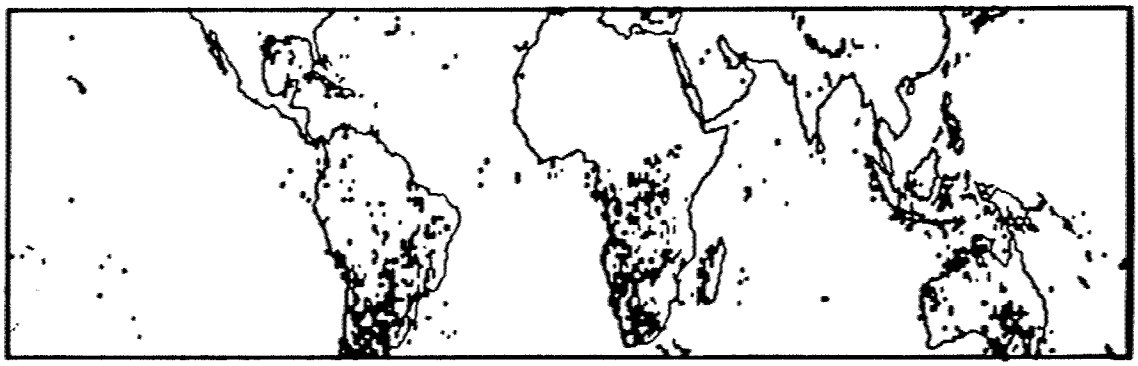

Figure 1 Locations of TRMM radar reflectivity >40 dBZ at 7 km altitude for January 1998

According to Williams et al (1992) and Rutledge et al (1992), the growth of graupel is sensitively controlled by the updraft speed. The radar reflectivity of the mixed phase region and the precipitation ice content are nonlinearly dependent on updraft speed in power law relationships. Larger CAPE (Convective Available Potential Energy) is available over land than over water.

According to Zipser and Lutz (1994 ), supercooled raindrops are necessary for mixed phase development, as they serve as nuclei for larger ice particles (graupel and hail) subsequently grown by the accretion of supercooled cloud droplets. A threshold updraft speed is needed to enable liquid drops to populate the mixed phase region. Larger updraft speeds are caused by larger CAPE over land.

The more recent hypothesis of D. Rosenfeld gives broader attention to cloud microphysics and is based on the well known land/ocean contrast in CCN. When boundary layer air is continental and dirty, the available liquid water in the storm updraft is shared amongst numerous small droplets, thereby suppressing mean droplet size and thwarting the coalescence process. This enables the cloud water to reach the mixed phase region to participate in generating additional cloud bouyancy, in the formation of precipitation, and in the separation of electric charge. In the cleaner oceanic regime, the condensation sites are few, the droplets large, and the warm rain coalescence process is very efficient.

The Rosenfeld hypothesis has physical appeal in its own right, but attention has also been called to problems with the more traditional hypotheses based on differences in instability (as measured by CAPE). First and foremost, CAPE values over tropical continental regions and over the warmer water of tropical oceans do not differ appreciably (Lucas et al, 1994). In Williams and Renno (1993), global maps of mean maximum wet bulb potential temperature show a substantial land/ocean contrast, but the histograms of CAPE values for land and warm ocean regions are not appreciably different. Furthermore, recent analysis (not shown) of the climatological wet bulb potential temperature over central Africa shows mean values of 21-22 C , which are less than the zero-CAPE intercepts in Williams and Renno (1993). This result is inconsistent with the land/ocean lightning contrast for Africa at midnight following Orville and Henderson (1986) and in recent LIS and OTD results.

## OBSERVATIONS IN BRAZIL

Observations designed to test the influence of aerosol on the vertical development and electrical activity of moist tropical convection were carried out in the TRMM/LBA field program near Ji Parana, Rondonia, Brazil. Radar measurements were obtained with the NASA TOGA C-band Doppler radar that operated round the clock for two months (January-February, 1999) in a deforested region of the southern Amazon basin.

The boundary layer aerosol was monitored continuously with an M1 Cloud Condensation Nucleus Counter (DH Huffman Associates) consisting of a diffusion chamber and an optical detection and counting scheme for cloud droplets nucleated by aerosol. The approximate 4-minute temporal resolution of the CCN concentration (particles per cubic centimeter) was well suited for comparisons with cloud scale ingestion of boundary layer air.

The lightning activity of the storms within about 50 km range of the TOGA radar was documented with an electric field mill (Mission Instruments) and two slow antennas of the New Mexico Tech design.

## RESULTS

The wet season weather in Rondonia, Brazil can be broadly classified as either 'monsoon' or 'break period', and this distinction is as clear cut as in earlier studies of lightning and rainfall in tropical Australia at a similar latitude (Williams et al, 1992; Rutledge et al, 1992). The monsoon regime, which is in reality the intertropical convergence zone over the South American continent, is characterized by widespread cloudiness, persistent rainfall, weak reflectivity in the mixed phase region, infrequent lightning and reduced surface air temperatures. The break period convection, occurring in the subsiding air adjacent to the ITCZ, is characterized by isolated thunderstorms, strong mixed phase reflectivity, frequent lightning, and higher surface air temperature. The global reflectivity map in Figure 1 suggests that the monsoon is prevalent in Rondonia in January.

An additional distinction between monsoon and break period conditions which is of cental importance in this study is the CCN population of boundary layer air. Figure 2 shows composite distributions of particle counts for four monsoon days (Jan 15,16,17 and 18) and four break period days (Jan 19,20,23 and 24). Each data sample represents a 4-minute integration with the CCN counter. In general, the boundary layer air in the monsoon regime is cleaner by a factor of 2-3 than in the break period regime. All of the monsoon values greater than 800 per cc occurred on January 18 in the presence of NNE airflow which probably carried smoke from numerous chimneys in Ouro Preto (a small town 10 km distant) over the TOGA radar site. The low CCN concentrations most typical of the monsoon (300-500 per cc) were not observed on break period days.

The heights of the first detection (10 dBZ threshold) of radar echo in developing cells were used as a test of the role of CCN populations in controlling the vertical development of precipitation. The SIGMET Echo Top Height algorithm was used for these determinations. By ingesting volume scan radar observations at 10 minute intervals and making movies of the echo top height product with 500 meter vertical resolution, it was

possible to document the first echo heights for hundreds of cases. Figure 3 shows the distributions of first echo heights on six monsoon days (Jan 6.12,15,16,17,and 18) and six break period days (Jan 13, 19, 20, 23, 24 and Feb 11). The mean height of first echo for break period days is approximately 2 km higher than for monsoon days. A substantial fraction of first echoes (more than 50%) in the break period developed within the mixed phase region. The great majority of first echoes in the monsoon regime were found in the subfreezing part of the cloud, indicating an efficient coalescence process.

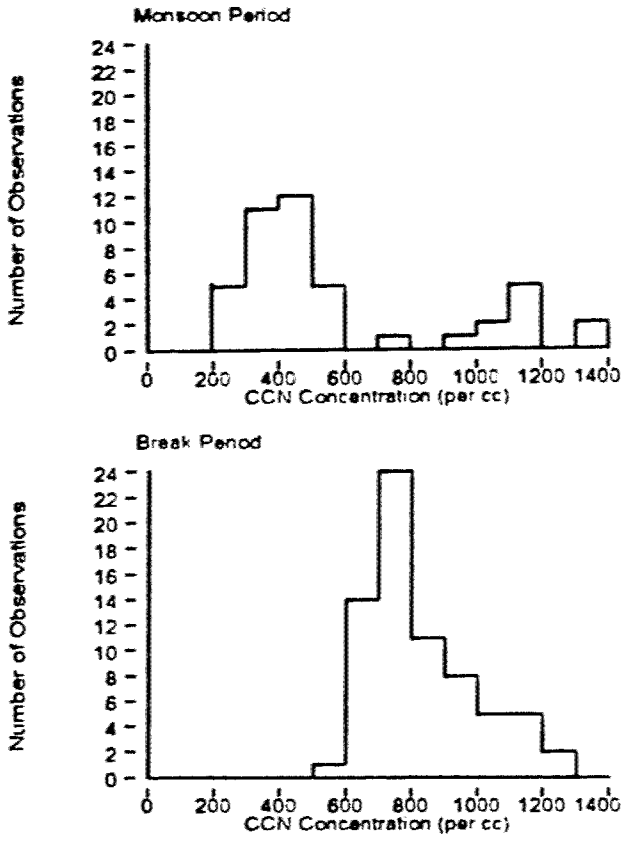


Figure 2 Distribution of CCN counts for monsoon and break period regimes.

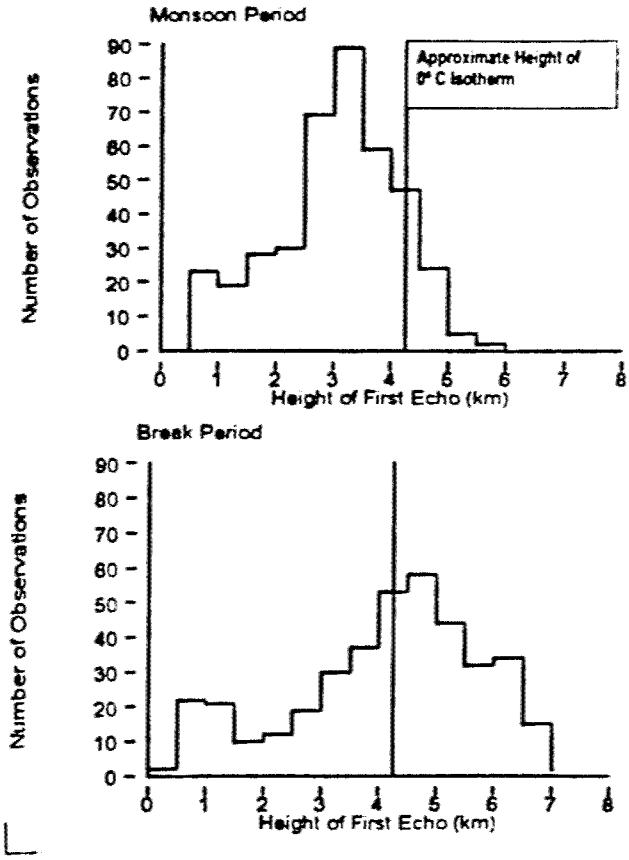


Figure 3 Distribution of first radar echo heights for monsoon and break period regimes.

In addition to these observations of the initial development of precipitation, comparisons were made of the CCN populations and the maximum lightning flash rate on individual days. For these comparisons, the daily mean CCN concentration was used. Figure 4 shows these comparisons for about 35 days from Jan-Feb, 1999. Despite the considerable scatter, a tendency for higher peak flash rates on 'dirty' days is apparent.

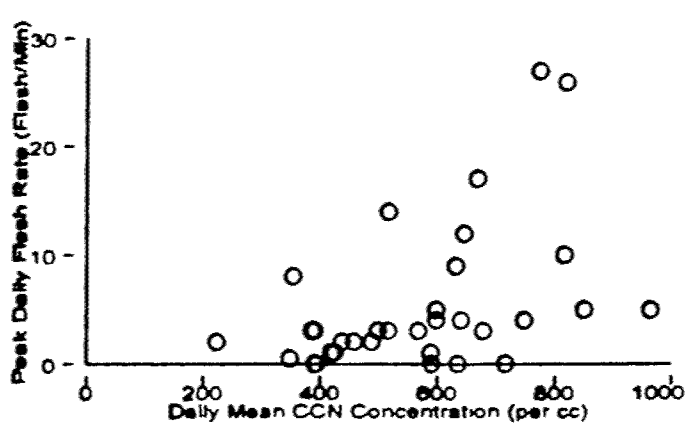


Figure 4 Maximum daily flash rates vs mean daily CCN concentration.

## DISCUSSION

The further clarificiation of the physical basis for differences in the vertical development of precipitation and lightning over land and over water requires revisitation of the hypotheses and a comparison with the new results. The abundance of warm rain first echoes in the monsoon regime (Fig. 3) would seem to support the Rosenfeld hypothesis: the available liquid water is shared among fewer droplets, leading to larger mean droplet sizes and favoring efficient coalescence. The collision/coalescence probability is well known to increase strongly with droplet size, due to inertial effects. The absence of larger mixing ratios in the monsoon regime(data not shown here) does not favor larger cloud water content as an explanation for preferential warm rain echoes.

The observation of higher peak flash rates in storms ingesting CCN-rich boundary layer air (Fig. 4) is consistent with all three hypotheses, and does not necessarily favor the aerosol hypothesis. By virtue of the larger fractional area of deep convection in the monsoon, the boundary layer air is in good communication with the tropospheric air. In the break period, the areal fraction is small and the boundary layer is further out of equilibrium with the troposphere. This lack of communication provides some explanation for both the greater instability and the higher CCN concentration in the break period. Further analysis is needed to sort out the effects of instability and aerosol. Indeed, the two quantities are not independent, as the aerosol control on mixed phase liquid water is also an appreciable influence on cloud buoyancy there because of the freezing process.

## CONCLUSIONS

Appreciable differences in CCN concentration, vertical development of precipitation and the peak lightning flash rate have been identified between the 'monsoon' and 'break period' regimes in tropical Brazil. It seems likely that the cleaner boundary layer air in the monsoon is stimulating an efficient warm rain coalescence process, leading to an abundance of first radar echoes at low levels in the developing clouds. The dirty air in the break period may keep droplet sizes small, enabling them to attain the mixed phase region where first echoes are often observed. The aerosol influence on mixed phase development and electrification in the mature phase of convection is also quite possible but sorting out the effects of the aerosol from the traditional instability issues will require further analysis of thermodynamic soundings and the remote observations of cloud droplet diameters (Rosenfeld and Lensky, 1998) for cases studied here.

## AKNOWLEDGEMENTS

The investigation of aerosol effects was stimulated by discussions with W. Lyons on their effects at midlatitude. We thank R. Barchet of Battelle Laboratories for loan of the CCN counter, and E. Betterton, G. Shaw, G. Roberts, P. Artaxo and S. Twomey for instruction in its operation. N. Renno assisted in innumerable ways, both theoretical and practical. R. Boldi provided considerable assistance with data acquisition and D. Rust loaned electric field instrumentation. Discussion with J. Fuentes and his students and D. Penney on thermodynamic data is greatly appreciated. Substantial assistance in the setup in Rondonia was provided by J.-L. Esteves, G. Carvallo and their associates. This work was funded by NASA Grant NAG5 4778 with encouragement from R. Kakar and O. Thiele.

## REFERENCES

Huang, E., E.R. Williams, R. Boldi, S. Heckman, W. Lyons, M.Taylor, T. Nelson and C. Wong; Criteria for sprites and elves based on Schumann resonance observations, J. Geophys. Res., (in press), 1999.

Lucas, C., E. Zipser, and M. LeMone, Reply to "Comments on "Convective Available Potential Energy in the Environment of Oceanic and Continental Clouds" ", J. Atmos. Sci., 53, 1212-1214, 1996.

Orville, R.E. and R.W. Henderson, Global distribution of midnight lightning: December 1977 to August 1978, Mon. Wea. Rev., 114, 2640-2653, 1986.

Rosenfeld, D. and I.M. Lensky, Spaceborne sensed insights into precipitation formation processes in continental and maritime clouds, Bull. Am. Met. Soc., 79, 2457-2476, 1998.

Rutledge, S.A., E.R. Williams and T.D. Keenan, The Down Under Doppler and Electricity Experiment (DUNDEE): Overview and preliminary results, Bull. Am. Met. Soc., 73, 3-16, 1992.

Squires, P., The microstructure and colloidal instability of warm clouds, Tellus, 10, 256-271, 1958.

Williams, E.R., S.A. Rutledge, S. G. Geotis, N. Renno, E. Rasmussen and T. Rickenbach, A radar and electrical study of tropical "hot towers", J. Atmos. Sci., 49, 1386-1395, 1992.

Williams, E.R. and N.O. Renno, An analysis of the conditional instability of the tropical atmosphere, Mon. Wea. Rev., 121, 21-36, 1993.

Zipser, E.J. and K. Lutz, The vertical profile of radar reflectivity of convective cells: a strong indicator of storm intensity and lightning probability, Mon. Wea. Rev., 122, 1751-1759, 1994.

# THE RELATIONSHIP BETWEEN THE BACKGROUND AND TRANSIENT SIGNALS IN SCHUMANN RESONANCES

E.Williams[1], D. Castro[1], R. Boldi[2], T. Chang[1] E. Huang[1], V. Mushtak[1], W. Lyons[3] T. Nelson[3], S. Heckman[4], and D. Boccippio[4]

[1]Massachusetts Institute of Technology, Cambridge, Ma., 02139 USA
[2]MIT Lincoln Laboratory, Lexington, MA 02173 USA
[3]FMA Research, Ft. Collins, CO 80524 USA
[4]NASA Marshall Space Flight Center, Huntsville, Al 35806 USA

ABSTRACT: Two distinct measures of the Earth's Schumann resonances--the background and the transients-- are studied through comparisons at the mesoscale and at the continental scale. A rough proportionality is shown between the far more abundant afternoon lightning activity and the larger positive mesoscale discharges that make sprites and simultaneously ring the Earth-ionosphere cavity to levels higher than the integration of all other lightnings.

## INTRODUCTION

The Schumann resonances of the Earth-ionosphere cavity provide a natural framework for global lightning studies from one or a few measurement sites. The 'background' and 'transient' resonsnces are distinct aspects of the same electromagnetic phenomenena. Historically, they have been investigated independently, with a few notable exceptions (Ogawa et al, 1966; Fellman, 1973; Lazebnyy and Nickolaenko, 1975). The twofold interest in global climate signals and the optical phenomena (sprites/elves) in the mesosphere (with which large positive SR lightning transients are associated) have reawakened interest in both aspects of SR. This study is concerned with the physical relationship between the background and the transient SR phenomena. This relationship is explored at the mesoscale in North America with observations of sprites and lightning from the National Lightning Detection Network (NLDN), and on a tropical continental scale (Africa, S. America) with single station SR measurements from West Greenwich, RI. The results support the idea that the background resonances are driven largely by lightning in late afternoon thunderstorms, and the transients are dominated by more energetic lightning in mesoscale convective systems (MCS') that predominate later in the diurnal cycle. A close relationship is found between these two lightning types on a global basis.

## MESOSCALE COMPARISONS

In an earlier study of positive ground flashes (CG's) during the End of Storm Oscillation in several Florida MCS' (Williams and Boccippio, 1993) it was noticed that larger numbers of late afternoon flashes were associated with larger numbers of positive CG's in the late evening. A later discovery (Boccippio et al, 1995) linked energetic positive CG's with both mesospheric sprites and Schumann resonance transients. To further clarify and quantify these relationships, further studies were carried out on MCS' in the Great Plains for which sprite observations and ground flash documentation by the NLDN were also available.

Storms were selected for which the sprite observation periods from the Yucca Ridge Observatory were reasonably complete and for which NLDN observations were available from beginning to end. The CG lightning history was determined by making 1000km scale NLDN maps at 30 minute intervals and then tracking forward and backward in time to identify the beginning and end of the CG activity. This analyis also enabled the selection of physical boundaries of the storms, which were checked against the Yucca Ridge logs to verify that sprites occurred over the respective lightning regions.

Total sprite counts against total flash counts are plotted for four MCS' in Fig 1a and sprite counts against positive CG counts appear in Fig 1b. Positive correlations are evident in both cases. The results in Fig 1b suggest that approximately one in every ten positive CG's produces a detectable sprite. The overall results in Fig 1 support a proportionality between CG lightning and both sprite and positive CG production.

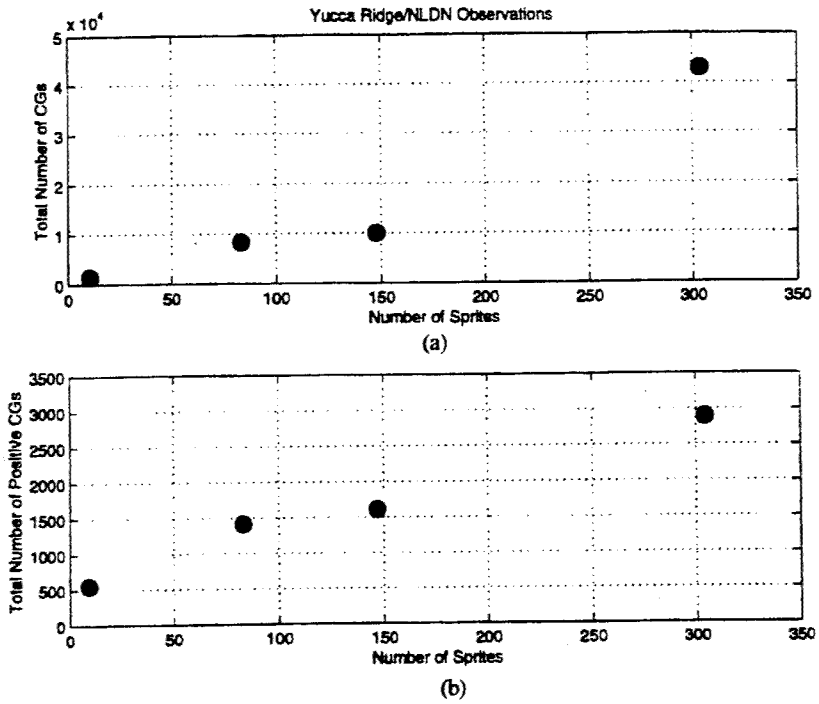


Figure 1 a)Total CG count vs total sprite count and b) Total positive CG count vs total sprite count.

CONTINENTAL SCALE COMPARISONS

A study of these lightning interrelationships on a global basis has been enabled by SR observations from MIT's ELF station in Rhode Island. Methods for analyzing both the background (Heckman et al, 1998) and the transients (Huang et al, 1999) have been described in some detail. The goal here is to combine the methods to compare background and transient response on individual days over Africa and S. America.

From the Rhode Island station, Africa lies nearly due east on a great circle path and S. America is south. If isotropic waveguide response is upheld, we expect the horizontal magnetic field from vertical lightning current in Africa to have a dominant NS component in RI. Likewise, the S. American lightning is expected to produce a dominant EW magnetic field. These predictions are consistent with the RI observations (in winter months when the global sources are well removed from the RI receiver) and with the classical behavior of the global electrical circuit (Whipple, 1929).

Fig 2 shows observations on a fairly typical winter day (Dec 14, 1996) in Rhode Island. Fig 2a shows the magnetic intensity variation on the NS magnetic coil and Fig 2b shows the EW intensity. The NS intensity is observed to peak at 15-16 UT, consistent with the well established time for late afternoon African lightning activity. Likewise, the well defined background maximum in the EW record is found at 20 UT, the approximate time for late afternoon activity in that continent.

Superimposed on the respective background curves in Fig 2 are the diurnal variations of the numbers of large positive transients mapped from Rhode Island in Africa (Fig 2a) and in S. America (Fig 2b) on the same day (Dec 14). (The acceptance criterion for a transient is a correlation coefficient between theoretical and measured wave impedance spectrum of 0.65 or greater.) Similar phase relationships between background and transient activity are apparent in both continents, with the transient activity lagging by several hours the maximum background intensity.

The number of S. American transients satisfying the acceptance criterion exceeds that of the African transients by more than a factor of 20. This result is attributable to waveguide attenuation and the strong decline in the distribution function of charge moments. Part of this 20-fold difference can be explained by the'slow tail' energy available in S. American events but largely dissipated in the case of African events, as discussed in Huang et al (1999).

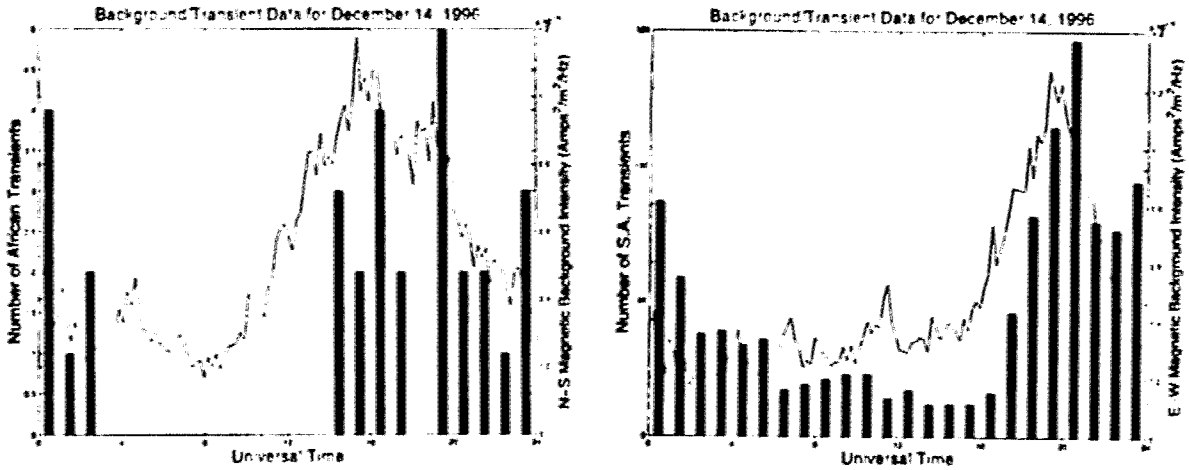


Figure 2 a)NS magnetic intensity and Africa transients, b) EW magnetic intensity and S.A. transients

To further quantify the relationship between the background and the transients, observations on 40 days were selected from December 1996, January 1997, and February 1997 for which both records were reasonably 'clean'. Figures 3 a and b show scatter plots of the daily number of positive transients versus the daily maxima in background intensity, for the African and S. American zones, respectively. Strong positive correlations are evident in both cases.

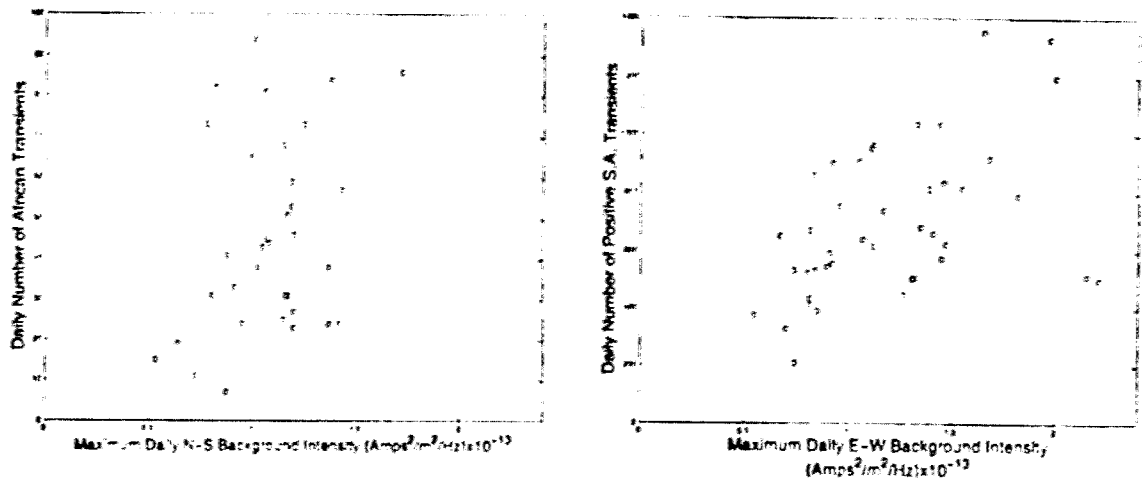


Figure 3 Background intensity vs daily transient counts for a) Africa and b) South America.

DISCUSSION

Three previous investigations of the relationship between the background and the transient SR were carried out more than 25 years ago without detailed knowledge of large positive ground flashes, mesospheric sprites, or the MCS' with which these extraordinary events are associated. Nor did these earlier investigators possess extensive capability for mapping the transients. Nevertheless, the earlier results on the distinct regional diurnal variations of the background and transient signals (Ogawa et al, 1966; Lazebnyy and Nickolaenko, 1975) agree with the present findings. Furthermore, the general finding that the background and transient signals are closely coupled (Fellman, 1973) stands out clearly in the present results. This study differs from that of Lazebnyy and Nickolaenko (1975) in the sense that our UT diurnal variations of transients is not flat and our transient populations, like the background signals, are dominated by continental regions.

The rough proportionality between the intensity of the background SR (representing the integration of ordinary afternoon lightning) and the numbers of large positive transients (mesoscale lightning later in the diurnal cycle) is welcome news to students of SR. This result suggest that the tail of the global lightning distribution (which is mappable from a single SR station) should serve as a quantitative measure of the total lightning distribution (which is more difficult to map from one or several stations).

## CONCLUSION

Based on both mesoscale and continental scale comparisons, the number of positive ground flashes and sprites is roughly proportional to the total lightning activity earlier in the diurnal cycle. Convective scale thunderstorms in the late afternoon which drive the background SR aggregate later in the diurnal cycle to form large mesoscale charge reservoirs. The large charge reservoirs are needed to make the energetic lightning flashes whose ELF signals stand out above all the others smaller lightning flashes.

## REFERENCES


Boccippio, D., E. Williams, S.J. Heckman, W.A. Lyons, I. Baker and R. Boldi, Sprites, ELF transients and positive ground strokes, Science, August, 1995.

Fellman, E., Analysis of Schumann resonances recorded simultaneously at two widely separated stations (in French), Doctoral thesis, Universitat des Saarlandes, 1973.

Heckman, S.J., E. Williams and R. Boldi, Total global lightning inferred from Schumann resonance measurements, J. Geophys. Res., 103, 31775-31779, 1998.

Huang, E., E. Williams, R. Boldi, W. Lyons, S. Heckman, T. Nelson and C. Wong, Analysis of sprites and elves with Schumann resonance methods, J. Geophys. Res., (in press), 1999.

Lazebnyy, B.V. and A.P. Nickolanenko, Daily variations of the number of VLF bursts according to synchronous observations at Karkov and Ulan-Ude, Geomagn. Aeron., 15, 218-219, 1975.

Ogawa, T., Y. Tanaka, T. Miura, and M. Yasuhara, Observations of natural ELF and VLF electromagnetic noises using ball antennas, J. Geomag. and Geoelec., 18, 81-92, 1966.

Whipple, F.J.W., On the association of the diurnal vaiation of electric potential gradient in fine weather with the distribution of thunderstorms over the globe, Quart. J. Roy. Met Soc., 55, 1-17, 1929.

Williams, E. and D. Boccippio, Microphysics and storm structure during the End of Storm Oscillation, Conf. on Severe Storms and Atmospheric Electricity, AMS, St. Louis, MO, 1993.


## ACKNOWLEDGEMENTS


These studies have been supported by the Physical Meteorology and Climate Dynamics Sections of the National Science Foundation (Grant ATM 963 3766), with assistance from J. Fein, R. Rogers, and R. Taylor. We thank T. Mitchell of the University of Rhode Island for continued use of the Rhode Island field station.

# LONG-TERM SR AND ELF TRANSIENTS OBSERVED IN A JAPANESE SITE

M. Hayakawa[1], A.P. Nickolaenko[1], Y. Hobara[1] and E. R. Williams[2]

[1]*The University of Electro-Communications, 1-5-1, Chofugaoka, Chofu-city, Tokyo 182, Japan*

[2] *Massachusetts Institute of Technology, Cambridge, Massachusetts 02139, USA*

Abstract – We deduce temporal variations of the level of the global lightning activity from the long-term Schumann resonance (SR) monitoring. We analyze the continuous analog records of the horizontal magnetic field component covering period from August 1967 to November 1970. The amplitudes of the first, second, and third SR modes were monitored at the Tottori observatory (35.5$^0$ N, 134.33$^0$ E). The experimental records show that the temporal changes of the SR amplitudes considerably vary from day to day. Meanwhile, the regular diurnal and longer scale variations appear in the data after applying the statistical processing. We found annual, biennial, and semi-annual components in variations of the global thunderstorm activity between 1967 and 1970. In addition the initial results from our new ELF station established In Moshiri, Hokkaido will be presented, in which we observe the SR and ELF transients associated with Sprite events during the winter lightning activity in Japan sea. These results will be compared with the long-term Tottori data.

## INTRODUCTION

This work is the extension of our previous results ( *Nickolaenko, Hayakawa and Hobara* 1996). In that publication we had treated the Schumann resonance records one year long: from September 1968 to August 1969. The analyses presented here are based on more complete data set monitored at the Tottori station (35.5$^0$ N, 134.33$^0$ E) from August 1967 to November 1970.

Schumann resonance (SR) occurs in the natural cavity formed by the surface of the Earth and the lower ionosphere and occupies the following peak frequencies: 8, 14, 20, 26, etc. Hz. A detailed description of the phenomenon and relevant measurement techniques may be found the following papers: *Nickolaenko, Hayakawa and Hobara* (1996), *Sentman* (1996), *Nickolaenko* (1997) and in the book by *Bliokh et al.* (1980). Our analysis is based on the long-term records carried out with an analog device regarded in literature as the SR mode tracker. Such a device monitored the current amplitudes of first three SR modes on the paper charts.

The main goal of our study is obtaining estimates for the level of the global thunderstorm activity (the main source of EM power observed in the SR band) as a function of time. We apply a simple and robust analysis for this purpose. It is based on the fact established both on the SR modeling (*Nickolaenko*, 1997) and processing of the experimental data (*Nickolaenko, Hayakawa and Hobara*, 1996, *Nickolaenko et al.*, 1998): the cumulative power observed in the wide frequency range that covers several SR modes is a relatively accurate (with an accuracy of some tens percent) estimate for the global thunderstorm activity. Therefore, we do not involve in the present analysis any distances between observatory and the global thunderstorms.

## DATA ACQUISITION AND PROCESSING

The original data were recorded from a horizontal solenoid magnetic antenna with the ferromagnetic core aligned along the North-South direction. Such an antenna has the main lobes of its angular pattern oriented along the East-West arc.

Data were picked from the paper tapes and integrated for each hour of a day. Correspondingly, the diurnal variations of the SR amplitudes are depicted with 24 points for each day. The relative gains of individual SR modes (channels of the tracker) were equalized before the measurements. Therefore, the amplitude of the resonance signal was measured in arbitrary units, but the units themselves remained the same for all three SR modes.

We applied the following procedure to obtain the estimates for the intensity of global thunderstorms. The amplitudes monitored during a particular month formed a statistical ensemble of data. The monthly averaged diurnal variations were obtained with the following procedure.

$$I(t) = \frac{1}{N}\sum_{k=1}^{N}\left[A_1^2(t,k) + A_2^2(t,k) + A_3^2(t,k)\right] \qquad (1)$$

Here, $I(t)$ is the function of time directly proportional to the diurnal variations of the global thunderstorm activity, $A_i(t,k)$ is the amplitude of $i$-th SR mode recorded at the time $t$ at a particular $k$-th day of the month.

We computed also the standard deviations $D(t)$ of the intensity estimates $I(t)$ in the following way. First, we computed the dispersions for individual modes:

$$D_i(t) = \frac{1}{N-1}\sum_{k=1}^{N}\left[A_i(t,k) - \langle A_i(t)\rangle\right]^2 \qquad (2)$$

where the monthly average diurnal variations of the $i$-th mode amplitude are found from:

$$\langle A_i(t)\rangle = \frac{1}{N}\sum_{k=1}^{N}\left[A_i(t,k)\right] \qquad (3).$$

Clearly, the data dispersion (2) equals zero in the case of regular diurnal variations reproducing itself from day to day. Otherwise, the non-zero standard deviation data appears from (2). Besides, the deviations obtained in such a way are very close to the values estimated using the source-observer distances found from the ratio of modal amplitudes recorded (see *Nickolaenko, Hayakawa and Hobara* 1996, *Nickolaenko* 1997, *Nickolaenko et al.* 1998).

We applied the above algorithm to process the data recorded from August 1967 to November 1970. Unfortunately, the data for some months during this period are absent. The Tottori records available cover the period of time up to December 1972, but the rest of the archive does not contain amplitudes of all three SR modes simultaneously. Therefore, we do not use these records in the present analysis.

We depict the survey of relative variations of the global thunderstorm activity in the following way in Fig.1. We divide the abscissa into separate vertical stripes. Each stripe in the upper frame is 24 hr long and it presents the average diurnal variations found from the SR records monitored during particular months of year. Each month is labeled below with its first letter.

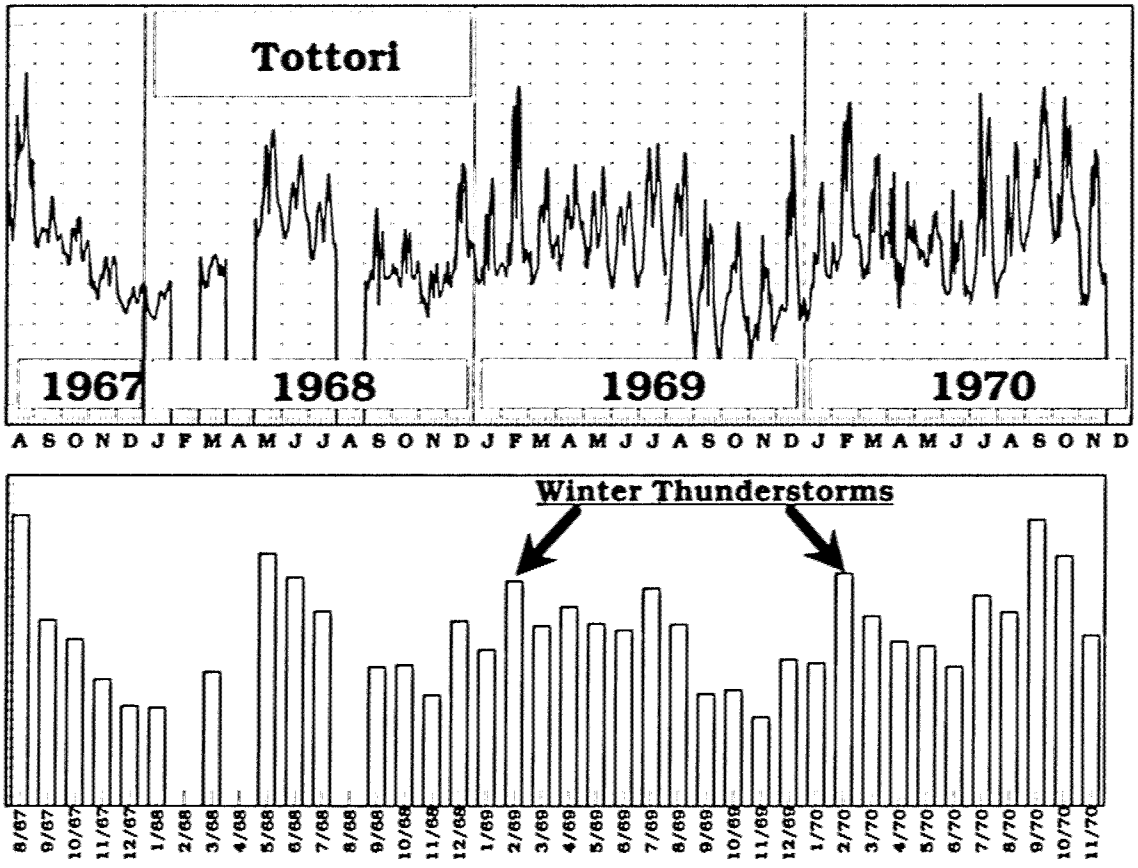


Fig. 1. Survey of the variations of the global thunderstorm activity deduced with from the SR records.

The abscissa starts from August 1967 in both the frames in Fig. 1. The following years are shown with the stripes for all 12 months (an absence of data recorded is shown by the gaps in the plots). Such a graph allows presenting averaged data in a rather compact form: one may see both the diurnal and annual variations in the upper frame of Fig. 1. Lower frame here depicts the "rectified" annual variations that we obtained after integration of the diurnal variations shown in the upper frame over the 24 hr periods.

Fig. 1 reveals a pronounced growth in the global lightning intensity during the summer (in the northern hemisphere). A distinct effect of the winter thunderstorms (during February) is seen clearly in the lower frame as well.

## CONCLUSION

To conclude the paper we repeat the main results.

1. Temporal variations of the global lightning activity may differ severely for the successive days.
2. The tendency is clear in the monthly averaged records towards regular diurnal amplitude variations.
3. The SR amplitudes monitored during period of 40 months reveal semi-annual, annual and biennial periodical components.

## OBSERVATION OF ELF TRANSIENTS AT MOSHIRI

We have started the continuous measurement in a low-noise site at Moshiri, Hokkaido from July, 1997, after the preliminary test observations at different places in Japan. We perform 3-component measurement (2 horizontal magnetic fields by using one set of induction coils and a vertical electric field using a ball antenna) with full calibration. Observed frequency range is from 0.1 Hz to 1 kHz. 24hr-SR frequency spectra averaged over each 10 minutes and ELF transients triggered by using the total horizontal magnetic field are recorded.

The purposes of this measurement are focused mainly on the detection of global warming and monitoring the global thunderstorm activities, and ELF radiation associated with sprite events during the winter lightning activity in Japan. We will present some examples of ELF transients possibly associated with sprites and SR results compared with Tottori data obtained 30 years ago.

## REFERENCES


Bliokh, P.V.,A.P. Nickolaenko, and Yu.F. Filippov. Schumann resonances in the Earth-ionosphere cavity, /ed. D. Ll. Jones, Peter Perigrinus, London, New York, 1980, 168 pp.

Nickolaenko, A.P., ELF/VLF propagation measurements in the Atlantic during 1989, J. Atmos. Terr. Phys., **57**, 1821-831, 1995.



Nickolaenko, A.P., ELF/VLF propagation measurements in the Atlantic during 1989, J. Atmos. Terr. Phys., **57**, 1821-831, 1995.



Nickolaenko, A.P., M. Hayakawa, Y. Hobara, Temporal variations of the global lightning activity deduced from the Schumann resonance data, J. Atmos. Terr. Phys., **58**, 1699-1709, 1996.

Nickolaenko, A.P., Modern aspects of Schumann resonance studies, J. Atmos. Solar-Terr. Phys., **59**, 805-816, 1997.

Nickolaenko, A.P., G. Satori, B. Zieger, L.M. Rabinowicz and ZI.G. Kudintseva, Parameters of global thunderstorm activity deduced from the long-term Schumann resonance records, J. Atmos. Solar-Terr. Phys., **58**, 387-399, 1998.

Sentman D.D., Schumann resonances, Handbook of atmospheric electrodynamics, /H. Volland—ed., vol. 1, Atmospheric Electricity, 267-298, CRC Press Inc., Boca Raton, London, Tokyo, 1995.

# Author Index

**Primary Author** Secondary Author


## A

**Adzhiev, A. ..... 424**
Agzagova, M. ..... 424
**Akpan, U. ..... 428**
**Altaratz, O. ..... 468**
Altaratz, O. ..... 460
**Amirov, A. ..... 142**
**Anisimov, S. ..... 571, 630**
Anisimov, S. ..... 614
Anisimova, S. ..... 630
**Aplin, K. ..... 598**
**Areitio, J. ..... 392**
Areitio, J. ..... 396
**Argo, P. ..... 680**
Argo, P. ..... 6, 672
**Armstrong, R. ..... 92**
Armstrong, R. ..... 84
Atkinson, L. ..... 754
Avila, E. ..... 268, 292

## B

**Bailey, J. ..... 646**
Bailey, J. ..... 527
Bakastov, S. ..... 571, 630
Baker, M. ..... 276
**Baranski, P. ..... 300**
**Barlow, J. ..... 575**
Bartels, D. ..... 388
**Bateman, M. ..... 527**
**Beasley, W. ..... 222**
Beasley, W. ..... 444
Bespalov, P. ..... 551
Bhalwankar, V. ..... 343
Black, M. ..... 400
Black, P. ..... 400
Blair, A. ..... 527
**Blakeslee, R. ..... 742**
Blakeslee, R. ..... 527, 646, 726, 746
Blanchet, P. ..... 14, 184, 656
**Blyth, A. ..... 363**
**Boccippio, D. ..... 254, 734, 738**
Boccippio, D... 172, 726, 742, 746, 750, 758
**Boeck, W. ..... 420**
Boeck, W. ..... 166, 726, 742, 746
Boldi, R. ..... 515, 698, 705, 758
**Bondiou-Clergerie, A. ..... 22, 184**
Bondiou-Clergerie, A. ..... 26, 335
**Borisov, V. ..... 127**
Brook, M. ..... 88
Brooks, W. ..... 180
**Buechler, D. ..... 519, 722**
Buechler, D. ..... 511, 515, 726, 742, 746
Bychkov, V. ..... 142
**Byerley, L. ..... 180**

## C

**Caranti, G. ..... 280, 347**
Caranti, G. ..... 292
Carey, L. ..... 436, 480
Carvalho, A. ..... 38, 42, 62, 408
Castellano, N. ..... 268
Castro, D. ..... 758
Cazetta, A. ..... 38
**Chang, D. ..... 372**
Chang, J. ..... 123
Chang T. ..... 758
**Chauzy, S. ..... 316, 320**
Chauzy, S. ..... 184, 384
**Chen, M. ..... 115**
Chen, M. ..... 18, 30
**Christian, H. ..... 715, 726, 746**
Christian, H. ... 166, 172, 722, 734, 738, 742
**Clodman, S. ..... 80**
Combal, B. ..... 320
Conforte, J. ..... 408
**Cooray, V. ..... 119**
Cooray, V. ..... 162
**Coquillat, S. ..... 320**
**Cramer, J. ..... 250**
**Crawford, D. ..... 154**
**Cummings, K. ..... 218**
Cummings, K. ..... 180, 250
Curran, E. ..... 200

## D

**D'Alessandro, F. ..... 226, 230**
Darveniza, M. ..... 634
Dash, J. ..... 264
**Datta, S. ..... 296**
**Davis, D. ..... 158**
Davis, D. ..... 22,50,58
Davis, M. ..... 376
**Davis, S. ..... 46**
**Davydenko, S. ..... 551**
De, U. ..... 296
deBruin, T ..... 595
**Defer, E. ..... 14**
Defer, E. ..... 335, 530, 656
Defoy, S. ..... 384
Delannoy, A. ..... 184

DeSordi, S. ..... 238
**Dhanorkar, S. ..... 539**
Diniz, J. ..... 38, 42, 62
Dmitriev, E. ..... 571, 630
Domingues, M. ..... 38
**Dong, W. ..... 107**
Dong, W. ..... 30
Dovgaluk, Ju. ..... 492
**Driscoll, K. ..... 523**
Driscoll, K. .... 646, 722, 726, 738, 742, 746
**Dye, J. ..... 530**

**E**
Eack, K. ..... 6, 222, 444, 680, 684
Eberle, M. ..... 684
Ebneter, A. ..... 260
**Ermakov, V. ..... 242**
Ezcurra, A. ..... 392, 396

**F**
Farley, R. ..... 288, 730
Fehr, T. ..... 712
Filho, A. ..... 62, 408
**Finke, U. ..... 712**
Finkelstein, M. ..... 695
Fitzgerald, T. ..... 680
Fleischhacker, P. ..... 260
**Forbes, G. ..... 496**
Fournier, G. ..... 218
Franz, R. ..... 672
Fukao, S. ..... 484
**Fullekrug, M. ..... 709**

**G**
Gallimberti, I. ..... 22
**Galvan, A. ..... 162**
Gardner, L. ..... 84
Gattaleeradapan, S. ..... 288
Georgis, J. ..... 320
Gerlach, J. ..... 754
**Goodman, S. ..... 515**
Goodman, S. .. 172, 254, 420, 511, 519, 634
..... 722, 726, 734, 742, 746
**Gourbiere, E. ..... 214**
Goshima, H. ..... 65
Goswami, K. ..... 296
Goto, Y. ..... 416
Gotschl, T. ..... 162
Green, J. ..... 672
Guillen, J. ..... 672
Gumley, J. ..... 226
**Guo, C. ..... 30, 211**
Guo, C. ..... 18

**H**
**Hale, L. ..... 150**
Hall, J. ..... 726, 742, 746
**Hallett, J. ..... 355**
Hamlin, T. ..... 172, 376, 432
**Handel, P. ..... 284**
**Hara, K. ..... 579**
Harlin, J. ..... 376, 432
Harms, D. ..... 238
Harrison, R. ..... 575, 598
**Hayakawa, M. ..... 762**
Hayakawa, M. ..... 96
**Heckman, S. ..... 719**
Heckman, S. ..... 254, 705, 738, 758
**Helsdon, J. ..... 288, 730**
**Herrero, I. ..... 396**
Herrero, I. ..... 392
Hinson, M. ..... 238
Hirai, T. ..... 456
Hobara, Y. ..... 96, 762
Hodanish, S. ..... 515
Hoffert, S. ..... 496
Hojo, J. ..... 10
Holden, D. ..... 6
**Holle, R. ..... 200**
Holler, H. ..... 712
Honma, N. ..... 416
**Horrak, U. ..... 618**
Huang, E. ..... 758
Hubler, G. ..... 530
Huffines, G. ..... 412
Huntrieser, H. ..... 712
Hussein, A. ..... 123

**I**
**Idone, V. ..... 50**
Idone, V. ..... 400, 472
**Ishii, M. ..... 10**
Isoda, H. ..... 54
**Israelsson, S. ..... 587**
Israelsson, S. ..... 428, 610, 614, 622
Ito, T. ..... 99
**Ivanovsky, A. ..... 111**

**J**
Jacobs, S. ..... 238
**Jacobson, A. ..... 668**
Jacobson, A. ..... 672, 676, 680
Janischewshyj, W. ..... 123
**Jayarante, R. ..... 308, 312**
Jayaratne, K. ..... 610
Jones, L. ..... 296
Jorgensen, D. ..... 507

## K


Kalov, R. ..... 424
**Kami, K. ..... 452**
**Kamra, A. ..... 343**
Kamra, A. ..... 539
**Kandalgaonkar, S. ..... 503**
Kandalgaonkar, S. ..... 448
Kassabova, T. ..... 324
**Kawasaki, Z. ..... 54, 176**
Kawasaki, Z. ..... 2, 18, 30, 34, 103, 484
Kennedy, P. ..... 500
Kirkland, M. ..... 672, 676, 680
**Kitagawa, N. ..... 207**
**Kithil, R. ..... 204**
**Klingo, V. ..... 543**
**Klumov, B. ..... 660**
Knox, S. ..... 672
Knupp, K. ..... 519
Kobayashi, F. ..... 380, 456
**Kolev, S. ..... 664**
**Kolpakov, A. ..... 332**
Kordi, B. ..... 123
**Koshak, W. ..... 192**
Koshak, W. ..... 726, 734, 738, 742, 746
Kozak, S. ..... 476
**Krasnitsky, Y. ..... 131**
**Krehbiel, P. ..... 376**
Krehbiel, P. ..... 88, 172, 432, 444, 583
Kumar, A. ..... 591
Kumykov, Kh. ..... 424
Kupovykh, G. ..... 555


## L


Labrada, C. ..... 754
**Lacerda, M. ..... 42**
Lalande, P. ..... 22, 26
**Lang, T. ..... 500**
**Laroche, P. ..... 656**
Laroche, P. ..... 14, 22, 58, 158, 530, 712
**Latham, J. ..... 363**
Lawson, R. ..... 260
**Lelwala, R. ..... 610**
Levin, Z. ..... 460, 468
**Liu, X. ..... 30**
Liu, X. ..... 18, 103, 107, 115, 339
Lockwood, M. ..... 444
Lojou, J. ..... 184
Lopez, R. ..... 200
**Lyons, W. ..... 84**
Lyons, W. ..... 92, 758


## M


**MacGorman, D. ..... 444**
MacGorman, D. ..... 222, 359, 507
**Mach, D. ..... 166**
Mach, D. ..... 420, 726, 742, 746
**Mackerras, D. ..... 634**
Madden, N. ..... 754
Madura, J. ..... 238
Maekawa, Y. ..... 484
Maliarova, L. ..... 332
**Manohar, G. ..... 448**
Manohar, G. ..... 503
**Mardiana, R. ..... 2**
**Mareev, E. ..... 272**
Mareev, E. ..... 571, 614
**Mareeva, O. ..... 614**
**Markson, R. ..... 188**
**Marshall, T. ..... 388**
Marshall, T. ..... 507
**Mason, B. ..... 264**
**Massey, R. ..... 684**
Massey, R. ..... 6, 680
Masuelli, S. ..... 347
Matejka, T. ..... 530
Matlin, A. ..... 515
Matsuura, K. ..... 2
**Mazur, V. ..... 26**
**McCaul, E. ..... 511**
McCaul, E. ..... 519
**Mendes, O. ..... 38**
Mendes, O. ..... 606
**Michimoto, K. ..... 464**
**Miki, M. ..... 65**
**Mitzeva, R. ..... 324**
Miyazaki, T. ..... 456
Miura, K. ..... 579
Mohan, A. ..... 488
**Molinari, J. ..... 400**
Molinie, G. ..... 384
Moore, C. ..... 88
**Moore, P. ..... 472**
Morales, C. ..... 372
**Morozov, V. ..... 69**
Morris, H. ..... 222
Murakami, M. ..... 2
**Murray, N. ..... 368**
**Murray, W. ..... 260**
**Mushtak, V. ..... 698**
Mushtak, V. ..... 758


## N


Nakae, S. ..... 579
Nakamura, K. ..... 30, 103, 146
**Nakano, M. ..... 146**
Nakano, M. ..... 30, 103

**Narita, K.** ..... **416**
Nelson, T. ..... 84, 92, 758
**Nierow, A.** ..... **246**
Nickolaenko, A. ..... 762
Noggle, R. ..... 180
Numphas, E. ..... 428

## O

**Oladiran, E.** ..... **428**
Olsen, W. ..... 372
**Orlov, A.** ..... **135**
Orlov, A. ..... 138
**Orville, R.** ..... **412**
Orville, R. ..... 368, 404, 634, 652
Ota, Y. ..... 2
**Otsuyama, T.** ..... **96**

## P

Panchiskina, I. ..... 547
**Parts, T.** ..... **563**
Peck, S. ..... 268
**Pereyra, R.** ..... **292**
Pereyra, R. ..... 280
**Peterson, W.** ..... **480**
Petrenko, I. ..... 536
**Petrov, A.** ..... **547**
Petrova, G. ..... 547
**Pinto, I.** ..... **408**
Pinto, I. ..... 38, 42, 62, 606
**Pinto, O.** ..... **62**
Pinto, O. ..... 38, 42, 408, 606
Ponomarev, Yu. ..... 492
**Price, C.** ..... **695**
Pyle, R. ..... 218

## Q

**Qie, X.** ..... **103**
Qie, X. ..... 30, 107

## R

**Rai, J.** ..... **591**
Rakov, V. ..... 99, 154
Rambo, K. ..... 154
Randel, W. ..... 652
Retalis, A. ..... 638
**Retalis, D.** ..... **638**
**Reuter, G.** ..... **476**
Richard, P. ..... 184
**Rison, W.** ..... **432**
Rison, W. ..... 88, 172, 376, 444
**Roeder, W.** ..... **238**
Roeder, W. ..... 583
Rosenfeld, D. ..... 754
Rothkin, K. ..... 705, 750
Roussel-Dupre, R. ..... 72
Roux, F. ..... 184
Ruhnke, L. ..... 26, 188
Russell, C. ..... 676
**Rust, D.** ..... **507**
Rust, D. ..... 222, 388, 444, 583
**Rutledge, S.** ..... **436**
Rutledge, S. ..... 480, 500, 530

## S

**Saba, M.** ..... **606**
Sakai, T. ..... 380, 452
Salm, J. ..... 618
**Sanger, N.** ..... **652**
Sardonia, J. ..... 238
Sathe, A. ..... 343
Sato, K. ..... 10
**Satori, G.** ..... **691, 705**
Satori, G. ..... 701
**Saunders, C.** ..... **268**
Saunders, C. ..... 324
Schnetzer, G. ..... 154
**Schroeder, V.** ..... **276**
Scott, R. ..... 432
Scuka, V. ..... 162
Shao, X. ..... 6, 684
**Sharp, A.** ..... **234**
Sharp, D. ..... 515
Shchukin, G. ..... 536
Sheperd, T. ..... 507
Shimizu, K. ..... 10
**Shimura, T.** ..... **380**
Shimura, T. ..... 456, 464
Shindo, T. ..... 65, 380
Shinjo, K. ..... 10, 452
**Shio, H.** ..... **328**
**Shostak, V.** ..... **123**
Showalter, R. ..... 246
**Shvarts, Ya.** ..... **536**
Silvani, X. ..... 320
Simond, N. ..... 384
**Sinkevich, A.** ..... **492**
**Singh, N.** ..... **488**
Singh, A. ..... 591
Sizhazhev, S. ..... 424
**Smith, D.** ..... **6**
Smith, D. ..... 680, 684
Solakiewicz, R. ..... 192
**Solomon, R.** ..... **335**
**Sonoi, Y.** ..... **484**
**Sorokin, A.** ..... **351**
Souders, C. ..... 246
**Soula, S.** ..... **384**
Soula, S. ..... 316
Soulage, A. ..... 184

Spalding, R. ..... 672
**Stanley, M. ..... 88**
Stapleton, M. ..... 154
Starobinets, B. ..... 695
**Stepanenko, V. ..... 688**
Stepanenko, V. ..... 492
Stevenson, D. ..... 750
Stewart, M. ..... 527, 726, 742, 746
Stewart, R. ..... 260
Stolzenburg, M. ..... 388, 507, 583
Stozhkov, Y. ..... 242
Strabley, R. ..... 84, 92
Straka, J. ..... 359
Strangeway, R. ..... 676
**Struminsky, V. ..... 559, 567**
Sugita, A. ..... 207
Sumi, S. ..... 30, 146
**Suszcynsky, D. ..... 672**
Suszcynsky, D. ..... 84, 92, 680
Suzuki, N. ..... 416
**Suzuki, T. ..... 456**
Suzuki, T. ..... 464
Symbalisty, E. ..... 72
Syssoev. V. ..... 138

## T

Takagi, N. ..... 18, 30, 99, 103, 115
Takahashi, S. ..... 207
**Takahashi, T. ..... 304**
Takahashi, T. ..... 484
Takeuchi, N. ..... 416
**Tammet, H. ..... 622, 626**
Tammet, H. ..... 618
Taylor, M. ..... 84
**Temnikov, A. ..... 138**
Temnikov, A. ..... 135
Thery, C. ..... 14, 184, 335, 656
**Thomas, R. ..... 172**
Thomas, R. ..... 88, 260, 376, 432, 444
Thomson, E. ..... 46
Tie, X. ..... 652
Tinmaker, M. ..... 448, 503
**Tinsley, B. ..... 602**
Titova, E. ..... 332
**Toracinta, R. ..... 440**
**Tuomi, T. ..... 196**
Tuomi, T. ..... 610

## U

Uman, M. ..... 99, 154
**Ushio, T. ..... 18, 738**
Ushio, T. ..... 103
Utkin, A. ..... 127
Uyeda, H. ..... 484

## V

**van der Hage, J. ..... 595**
Varela, G. ..... 268, 280, 292
Vogel, D. ..... 642

## W

Wada, A. ..... 65, 380
Wakai, T. ..... 452
Wang, C. ..... 30
**Wang, D. ..... 99**
Wang, D. ..... 18, 30, 103, 115
Watanabe, T. ..... 18, 30, 99, 103, 115
Weaver, K. ..... 260
Weber, M. ..... 515
Weinman, J. ..... 372
Wieland, C. ..... 260
Wiens, K. ..... 6, 684
**Willett, J. ..... 58**
Willett, J. ..... 22
**Williams, E. ..... 750, 754, 758**
Williams, E. .... 84, 515, 634, 652, 695, 698,
..... 705, 762
Winn, W. ..... 260
**Wolff, D. ..... 404**

## X

Xiao, Q. ..... 30
Xiushu, Q. ..... 18

## Y

**Yair, Y. ..... 460**
Yair, Y. ..... 468
Yan, M. ..... 339
**Yoshihashi, S. ..... 34**
Yoshihashi, S. ..... 54, 176
Yu, Y. ..... 103
**Yukhimuk, V. ..... 72**

## Z

**Zadorozhny, A. ..... 76**
**Zajac, B. ..... 436**
Zhang, G. ..... 30, 103
Zhang, R. ..... 652
Zhang, X. ..... 730
**Zhang, Y. ..... 339**
Zhang, Y. ..... 30, 115
Zhong, D. ..... 115
Zhou, L. ..... 115
**Zieger, B. ..... 701**
Zieger, B. ..... 691, 705
**Ziegler, C. ..... 359**
Zipser, E. ..... 404, 440
**Zuelsdorf, R. ..... 676**

## Subject Index


### A

Aeroelectric field
- measurements at Borok Geophysical Observatory ..... 630
- spectra of pulsations ..... 571
- structure of pulsations ..... 571

Aerosols
- and ball lightning creation ..... 142
- and the Carnegie curve ..... 555
- charged species in the mesosphere ..... 76
- charged species in tropospheric clouds ..... 135, 138, 359
- charges on ..... 539, 618
- coagulation of ..... 539
- condensation nuclei ..... *see condensation nuclei*
- diffusion coefficient of ..... 622
- dry deposition of ..... 622
- general references ..... 539, 555, 575, 591, 598, 614
- ion attachment of or interaction with ..... 272, 316, 539, 575, ..... 598
- land/ocean concentrations ..... 754
- mass concentration in the UK ..... 575
- mobility of ..... 347, 622
- scavenging of ..... 347
- in thundercloud development ..... 242, 359

Air pollution ..... 347, 536, 547, 563, 575, 622, 630, 634, 638
Air terminals ..... 211, 226, 230
Air to earth current ..... *see current (global atmospheric)*
Aircraft
- cloud seeding experiments in India ..... 492
- conductivity measurements ..... 646
- convective forecasting for ..... 246
- damage from Gulf cyclone ..... 372
- electric field measurements ..... *see electric field*
- emissions of NOx ..... 652
- lightning attachment to ..... *see lightning*
- measurements of NOx ..... 712
- measurements of particle charge and image ..... 260
- in study of MCSs ..... *see MCSs*
- microphysical measurements ..... 444
- observations of lightning optical emissions ..... 284
- observations of sprites, jets, elves ..... 80
- observations of thundercloud charging ..... 355
- safety in Australia ..... 234
- safety threats due to convective clouds ..... 246, 372, 492

Aircraft Total Lighting Advisory System (ATLAS) ..... 188
Airglow ..... 80
Aitken nuclei ..... 536, 579
Atmospheric chemistry of lightning ..... *see lightning*
Atmospheric ions ..... *see ions*

### B

Ball lightning ..... *see lightning*
Balloon sounding
- Brazilian with high altitude photographs ..... 606
- Brazilian with high altitude video images ..... 606
- of conductivity ..... *see conductivity*
- of electric fields ..... *see electric field*
- general references ..... 492
- and global temperature studies ..... 642
- of lightning-caused field changes ..... *see electric field change*
- of microphysical particles ..... 260

Bipolar pulses ..... 6, 10, 432, 684
Blue jets ..... *see jets*
Boundary layer ..... 551, 614, 754
Bow echoes ..... 368, 507

Breakdown field
- in dart leaders ..... 107, 111
- general references ..... 188, 226, 238, 276
- in negative leaders ..... 26, 38
- for red sprite initiation ..... 69, 72, 88
- and VHF emissions ..... 668

Bright bands ..... *see radar*
BLM (Bureau of Land Management) ..... 412

### C

CLDN (Canadian Lightning Detection Network) ..... 218, 250
Carnegie curve ..... 555, 602, 634, 742
Carnegie Institute research vessels ..... 634
Charge structure in thunderclouds
- dipolar ..... 308, 312, 432
- discussions in the 1930's ..... 176
- general references ..... 335, 428, 432
- in Kansas MCSs ..... 368
- lower positive center ..... *see lower positive charge center*
- negative center ..... *see negative charge center*
- in Pingliang China ..... 18
- tripolar ..... 188, 268, 304, 312
- upper positive center ..... *see upper positive charge center*

Climatology of lightning ..... 176, 184, 218, 234, 276, 392, ..... 412, 420, 428, 436, 440, 448, 695, 715, 726
Cloud droplet charge ..... 332, 347, 351
Cloud ice ..... 480, 730
Cloud seeding ..... *see aircraft (cloud seeding)*
Cloud-to-ground discharges
- general references ..... 10, 42, 46, 50, 69, 103 135, 172, 176, 180, 184, 188, 207, 218, 242, 246, 250, 335, 368, 376, 384, 400, 404, 408, 412, 428, 432, 436, 440, 444, 456, 460, 476, 480, 484, 496, 515, 519, 523, 606, 656, 664, 672, 676, 680, 684, 715, 722, 726, 738
- positive events ..... 62, 162, 606
- positive events producing sprites ..... 84, 88, 96
- positive events related to TLEs ..... 84
- ratio of positive to negative ..... 392, 428, 460
- simulation of leader electric fields of ..... *see leader*
- space sensor observation of ..... *see space sensors*
- in Spain ..... 392
- sprite-producing ..... 69, 84, 222
- and surface temperature ..... 448, 472

Cloud-top height ..... 184, 339, 372, 468
Cloud-top temperature ..... 468, 734
CIDs (Compact Intracloud Discharges)
- radar reflectivity associated with ..... 6
- radio frequency emissions from ..... 6, 684
- with respect to charge centers

Condensation nuclei ..... 595, 754
Conductivity
- above thunderclouds producing red sprites ..... 72
- above thunderstorms ..... 646
- altitude and latitude variation ..... 150, 551
- in the Austasch layer ..... 551
- balloon/rocket measurements ..... 559, 567, 606
- of distilled water ..... 320
- effects on coagulation ..... 359
- and fog ..... 587, 595
- Gerdien measurement of ..... 527, 591, 598, 646
- and global temperature studies ..... 642
- of the ground ..... 119
- measurements in Greece ..... 638
- measurements in Russia ..... 536
- mesospheric ..... 76

and negative leaders ..... 26
in positive leaders ..... 22
and rainfall ..... *see rainfall*
required for laser triggering of lightning ..... 65
spherical meter ..... 559
stratospheric ..... 606
and turbulent electric dynamo ..... 272
in surface layer ..... 547
Contact potential ..... 559
Convective charging mechanism ..... 288, 316
Corona current ..... *see current*
Cosmic rays ..... 242, 551, 598
Counters of lightning ..... *see flash counter*
Current
conduction ..... 76, 587, 598, 610, 634
convection ..... 272, 300, 316, 567, 575
corona ..... 188, 211, 316, 320, 416
global atmospheric ..... 551, 567, 587, 742
Maxwell ..... 150, 288, 300
moments at ELF ..... 88
point discharge ..... 503, 634
of return stroke ..... 34, 38, 42, 65, 119, 123, 196, 211, ..... 230,380, 392, 412, 460, 738
volume ionization ..... 351
Cyclone *(see also Hurricane)* ..... 372

D

Dart leader ..... *see leader*
DMSP (Defense Meteorological Satellite Program) ..722, 734
Deposition ..... 324
Detection efficiency
of CLDN system in Canada ..... 218
of direction finder network in Spain ..... 392
of LIS ..... 172, 715
of LLP-IMPACT system in Finland ..... 196
of LLP magnetic direction finder network in France ..... 384
of LPaTS network in Israel ..... 468
of long-range GAI lightning location network ..... 250
of NLDN ..... 680
of OTD ..... 440, 715, 726, 742
Differential reflectivity ..... *see radar*
Diffusion
in cloud models ..... 347
and droplet-ice collisions ..... 296
eddy ..... 316
in electric dynamo theory ..... 272
of ions ..... *see ions*
of water vapor ..... 324
Direction finders 62, 162, 192, 196, 218, 234, 250, 384, 392, ..... 396, 400, 404, 412, 476
Doppler radar ..... *see radar*
Downbursts ..... 368

E

ENSO (El Nino Southern Oscillation) ..... 519, 691, 705, 726
Electric field
balloon sounding of ..... 388, 444, 492, 583,507, 642
electrostatic ...10, 22, 26, 30, 42, 58, 69, 138, 166, 176, 188, .207, 211, 222, 238, 260, 272, 284, 288, 300, 316, 320, 335, .339, 347, 351, 368, 388, 396, 416, 444, 464, 488, 492, 551, .....555, 559, 567, 575, 598, 602, 614, 618, 622, 630, 719
fair weather ..... 176, 396, 536, 547, 555, 583, 587, 598, ..... 602, 610, 630, 634
in fog ..... 587
of leader ..... *see leader*
in lightning channel ..... 111
measurements above thunderstorms ..... 527646
mesospheric ..... 76
meter *(see also field mill)* ..... 222, 260, 368, 507, 559, ..... 567, 583, 630
propagation effect on ..... 119
quasi-electrostatic in sprite production ..... 72, 96
radiated ..... *see ELF, ULF, VLF, LF, HF, VHF, or UHF*
of Schumann resonances ..... *see Schumann resonance*
associated with sferics ..... 606
in snowstorms ..... 328
sunrise enhancement of ..... 583
Electric field change
array for FORTE ground-truth experiment ..... 684
balloon measurements ..... 222, 388
in Chinese Inland Plateau ..... 18, 103
measurements in Florida ..... 88
measurements in Japan ..... 10
measurements in New Mexico ..... 6
of RTL events ..... 22, 30, 58, 65, 115, 119
Electrical deposition ..... *see radon*
Electrode effect ..... 555, 575, 587, 614, 618
Elves ..... 80, 84, 695, 758
EOSO (End of Storm Oscillation) ..... 758
ELF (Extremely Low Frequency) radiated fields ..88, 96, 150, ..... 695, 698, 709, 758, 762
Eyewall ..... 400

F

Fair weather field ..... *see electric field*
False alarm rate ..... 515
Fast antenna
electric fields observed by ..... 10, 18, 107, 222
ground truth experiment for FORTE *see electric field change*
measurements at Kennedy Space Center ..... 46
measurements at Sea of Japan coast ..... 10, 65
FORTE (Fast On-orbit Recording of Transient Events) *see space sensors*
Field mill *(see also electric field meter)*
car-borne in Japan ..... 464
ground-based ..... 103, 166, 276, 396, 567, 571, 583, 630
Flash counter ..... 230, 460, 664
Flash density ..... 180, 214, 218, 230, 392, 412, 634, ..... 722, 734, 742
Flash rate ..... 176, 184, 234, 276, 300, 335, 363, 372, 384, 476, 480, 500, 515, 523, 634, 652, 664, 672, 676, 719, 722, ..... 726, 734, 742, 750, 754, 762
Fluxmeter ..... *see electric field (meter)*
Fog
atmospheric electric effect of ..... 595
and conductivity ..... *see conductivity*
radiation ..... 587
and triggered lightning ..... 238
Forecasting
and Bureau of Meteorology ..... 234
fog ..... 595
hurricane intensity ..... 400
and lightning flash rate ..... *see flash rate*
rainfall amount ..... 372, 384
weather at KSC, Florida ..... 496
of winter lightning ..... 452
Freezing level ..... 480

G

Geomagnetics and Schumann resonances ..... *see Schumann resonance*

Gerdien meter ..... *see conductivity*
Gibb's free energy ..... 488
GAI (Global Atmospherics Inc.). 192, 218, 250, 254, 404, 472
Global electric circuit ..... 176, 150, 300, 448, 551, 567, 587
..... 610, 630, 634, 642, 695, 705, 742, 750
Graupel ..... 260, 268, 284, 292, 296, 304, 308, 312
..... 324, 339, 355, 359, 372, 440, 464, 480, 484, 73 0
Gravity waves ..... 80

**H**

Hail ..... 200, 260, 288, 296, 308, 335, 372, 436, 476, 488,
..... 500, 730, 688
HF (High Frequency) radiated fields ..... 6, 656
HVPS (High Volume Precipitation Spectrometer) ..... 260
Hurricane *(see also Cyclone)* ..... 200, 400

**I**

Ice crystals ..... 260, 268, 284, 292, 296, 304, 308, 312, 324,
..... 335, 339, 355, 359, 363, 460, 484, 730
IMPACT sensors ..... 62, 196, 207, 218, 412
Interferometry
  in China ..... 18, 30, 107
  in Darwin, Australia ..... 2, 34, 54
  in Florida ..... 14, 88
  in Hokuriku coast of Japan ..... 34
  for lightning locating ..... 88, 107
  microwave ..... 65
  ONERA system ..... 14, 530, 713
  SAFIR used in Japanese winter storms ..... 484
  spaceborne ..... *see space sensors (ORAGES)*
  of spider lightning ..... 14, 656
  3-D channel mapping ..... 131
  at VHF/UHF ..... 34, 54, 107, 184, 335, 376, 656
Intracloud discharges
  compact ..... *see CIDs*
  discrimination from ground flashes ..... 62, 172,
  242, 335, 432, 460, 480, 523, 606, 656, 668, 672, 676, 715,
  ..... 722, 726, 738
  general references ..... 10, 18, 103, 184, 188, 242, 335, 246,
  ..... 432, 668
  inverted polarity ..... 376
  space observations of ..... *see space sensors*
  and tornadic activity ..... *see tornadoes*
Ionization rates
  and coagulation effects ..... 539
  for fair weather in Russia ..... 555
  related to sprites ..... 92
Ionosphere
  lightning RF penetration of ..... 669
  potential of ..... 176, 551, 555, 602, 606, 630, 634,
  ..... 642, 705, 742
  and Schumann resonance ..... *see Schumann resonance*
  and sprites ..... 96
  wave propagation effects of ..... 119, 250, 372, 715
Ions
  attachment/interaction to/with aerosols ..... *see aerosols*
  attachment to cloud droplets ..... 347, 351, 503
  attachment to fog droplets ..... 587
  and conductivity measurements ..... 591, 646
  diffusion of ..... 351, 539
  general references ..... 551, 559, 575, 591, 598, 610
  inducing nucleation ..... *see nucleation*
  in the mesosphere ..... 76
  method of covalent bonds for ..... 543
  mobility of ..... 347, 351, 539, 559, 563, 579, 587, 591,
  ..... 598, 614, 618, 626
  and positive leader propagation ..... 111
  production from cosmic rays ..... *see cosmic rays*
  recombination of ..... 316, 614
  small ..... 288, 347, 563, 595, 598, 614, 622, 638

**J**

Jets ..... 69, 80, 222

**K**

K-change ..... 103, 172, 715, 738
KDP (specific Differential Phase) ..... *see radar*
KSC (Kennedy Space Center) ..... 88, 166, 254, 496, 583, 738

**L**

La Nina ..... 691
Langmuir Laboratory ..... 260, 432
LTL (Laser Triggered Lighting) ..... 65
Latent heat ..... 268, 308, 372, 746
LCC (Launch Commit Criteria) ..... 238
Leader
  bi-directional development of ..... 26, 30, 34, 107, 115
  dart ..... 46, 107, 656
  modeling ..... 22, 26
  negative/stepped ..... 14, 26, 30, 34, 46, 54, 65, 107, 115
  ..... 154, 211, 656
  pilot system for ..... 26
  positive ..... 22, 26, 30, 34, 58, 107, 111, 115, 158, 656
  simulated electric field of ..... 226
  and strike probability ..... 230
  velocity of ..... *see velocity*
Lightning
  attachment to aircraft ..... 34
  ball ..... 142
  channel length ..... 38, 730
  charge ..... 38, 88, 380, 606, 730
  chemistry ..... 652, 656, 660, 664, 712
  climatology ..... *see climatology of lightning*
  cloud-to-ground ..... *see cloud-to-ground discharges*
  component definitions ..... 166
  counter ..... *see flash counter*
  current ..... *see current*
  damage and safety ..... 180, 200, 204, 207, 211, 214, 238
  detection from space ..... *see space sensors*
  imaging ..... *see OTD, LIS, FORTE*
  initiation by cosmic rays ..... 242
  initiation by uncharged raindrops ..... 320
  intracloud ..... *see intracloud discharges*
  land-ocean differences ..... 734, 754
  locating .2, 107, 62, 135, 166, 172, 184, 188, 192, 196, 207,
  218, 230, 250, 335, 368, 372, 376, 384, 392, 424, 444, 452,
  460, 468, 472, 519, 523, 530, 709, 656, 712, 715, 719, 738
  M-components ..... 42, 99, 154
  magnetic fields produced by ..... 65, 127
  mapping ..... *see interferometry*
  measurements of in the vicinity of strikes to a stack ..... 65
  multiple channel ..... 46
  optical emissions from ..... *see optical emissions*
  peak current ..... 38, 42, 84, 218, 380, 404, 412, 436
  protection ..... 211, 226, 230, 238, 472, 484
  return stroke ..30, 38, 42, 46, 50, 80, 99, 103, 115, 119, 123,
  ..... 154, 162, 226, 234, 396, 404, 428, 656, 715, 734
  rocket triggered ..... *see RTL*
  rod ..... 115, 211
  spider ..... *see interferometry*
  strikes to towers ..... 42, 123, 146, 180
  subsequent strokes ..... 42, 65

superbolt ..... 380
transmission line model for ..... 99, 123
video camera measurements of ..... 58, 65, 88, 416
LASI (Lightning and Storm Intensity) ..... 188
LDAR (Lightning Detection And Ranging) ..... 88, 166, 254, 432, 496, 738
LLP (Lightning Location and Protection, Inc.) 196, 384, 496
LIS (Lightning Imaging Sensor) ..... *see space sensors*
LISDAD (Lightning Imaging Sensor Data Application Display) ..... 254, 515
LPaTS (Lightning Positioning and Tracking System) ... 38, 62, 218, 230, 234, 412, 460, 468, 713
LDR (Linear Depolarization Ratio) ..... *see radar*
Long-range lightning detection ..... 250
Long-wire antenna ..... 610
Loop antenna ..... 65
Los Alamos National Laboratory ..... 684
LF (Low Frequency) radiated fields ..... 250, 372, 428, 606, 668, 709
Lower positive charge center ..... 18, 103, 268, 300, 316, 432


## M


M-components ..... *see lightning*
Magnetic direction finders ..... *see direction finders*
Magnetic field
of lightning ..... *see lightning*
measurements in Germany ..... 709
of Schumann resonances ..... *see Schumann resonance*
Magnetometer ..... 630
Mathematical inversion
related to ion mobility resolution ..... 626
for retrieving ground flashes on spherical/oblate earth ... 192
of sferics waveforms ..... 131
Maxwell current ..... *see current*
Melting layer ..... 460
MCCs (Mesoscale Convective Complexes) ..... *see MCSs*
MCSs (Mesoscale Convective Sytems)
in Brazil ..... 408
and electrification modeling ..... 284
in Florida ..... 758
in Kansas and Oklahoma ..... 222, 368, 507
sprites and elves production in ..... 84, 92
in Texas ..... 404
in Tropics ..... 440
in U.S. ..... 436
MEaPRS (Mesoscale Electrification and Polarimetric Radar Study) ..... 172, 368, 507
Mesosphere
charged aerosols in ..... *see aerosols*
conduction currents in ..... *see current*
conductivity in ..... *see conductivity*
electric fields in ..... *see electric field*
and the global electric circuit ..... *see global electric circuit*
ions in ..... *see ions*
and sprites ..... 695, 758
TLEs (Transient Luminous Events) ..... 84, 92, 96
Microlab-1 satellite ..... 184, 276, 440, 726, 742
Microphysical charging mechanisms ..... 188, 264, 268, 276, 280, 284, 288, 292, 296, 300, 304, 308, 312, 316, 324, 328, 332, 335, 339, 347, 351, 355, 359
Microwave
interferometry ..... *see interferometry*
brightness temperature and lightning flashing rate ..... 523
scattering model ..... 480
SSM/I (Special Sensor Microwave Imager) ..... *see SSM/I*
TMI (TRMM Microwave Imager) ..... *see TMI*
Mixed phase region ..... 440, 754
Mobility of ions ..... *see ions*
Mobility resolution ..... 626
Mobility spectrometer ..... 579, 618, 626
Multiplicity ..... 404, 408, 412


## N


Narrow Bipolar events ..... *see bipolar pulses*
NLDN (National Lightning Detection Network) ..... 192, 218, 222, 246, 250, 254, 368, 400, 404, 412, 444, 472, 480, 500, 511, 519, 530, 668, 672, 680, 722, 738, 758
NSSL (National Severe Storms Laboratory) ..... 408, 412
Negative charge center
general references ..... 6, 103, 188, 268, 304, 320, 339, 388, 432
temperature height of ..... 10
NO (Nitric Oxide)
amount produced by lightning ..... 530, 730, 652, 656, 660, 664, 712
diffusion of ..... *see diffusion*
3-D Storm Electrification Model (SEM) ..... 730
$NO_2$ (Nitrogen dioxide) ..... 530, 730, 652, 656, 660, 664, 712
$NO_x$ (Nitrogen oxides) ..... 530, 730, 652, 656, 660, 664, 695, 712, 726
Noctilucent clouds ..... 76
Non-inductive charging ..... 488
NALDN (North American Lightning Detection Network) 218
Nucleation
in cloud models ..... 347
of ice crystals using dry ice ..... 355
ion-induced ..... 579, 598
in thundercloud development ..... 242
rate ..... 579


## O


Optical (lightning) emissions
aircraft observations of ..... *see aircraft*
land-ocean differences ..... 734
observed in Northern India ..... 420
observed from satellite *(see also space sensors)* ..... 172, 176, 380, 672, 684, 715, 738
from red sprites, jets, or elves ..... 72, 80, 84, 96
from triggered lightning ..... *see RTL*
OLS (Optical Line Scanner) ..... *see space sensors*
ORAGES (French space interferometer) ..... *see space sensors*
OTD (Optical Transient Detector) ..... *see space sensors*
$O_3$ (Ozone) ..... 730, 660, 712, 726


## P


Photographic measurements of triggered lightning ..... *see RTL*
Pilot system ..... *see leader*
PBL (Planetary Boundary Layer) ..... *see Boundary layer*
Point discharge current ..... *see current*
Polar mesosphere summer echoes ..... 76
Pollution ..... *see air pollution*
Positive flashes ..... *see cloud-to-ground discharges*
Potential gradient ..... *see electric field*
Precipitation ..... *see rainfall, graupel, hail, snow*
PR (Precipitation Radar) on TRMM ... 372, 440, 527, 688, 754
Propagation effects on lightning radiated fields ..... 162, 119


## Q

## R


Radar
acoustic (sodar) ... 380
bright bands ... 460
differential reflectivity ... 480
doppler ... 276, 335, 359, 380, 400, 444, 452, 484, 496, 500, 507, 511, 527, 530, 680, 712
40 dBZ reflectivity above freezing level ... 372
general references ... 384, 436, 464, 472, 476, 484, 488, 606, 688
and electrification modeling ... 284
in Hokuriku district of Japan ... 380
images of hurricanes ... 400
and lightning flash rate ... *see flash rate*
linear depolarization ratio ... 480
and the MEaPRS field program ... 368
NEXRAD ... 515
reflectivity and occurrence of CIDs,
reflectivity and occurrence of sprites ... 88
and severe weather ... *see thunderstorms (severe)*
space ... *see PR on TRMM*
specific differential phase ... 480, 500
WR-100-5 Enterprise type in Israel ... 460, 468
WSR-88D type ... 404, 511
Radiation fog ... *see fog*
Radiometers ... 372, 527
Radiosonde ... 388, 468
Radon
electrical deposition of daughter clusters ... 622
general references ... 547, 598
mobility of daughter clusters ... 622
Rainfall
and air conductivity ... 591
droplet charge ... 300, 339, 343
droplet fracturing ... 238
droplet and lightning initiation ... 320
droplet size ... 324, 328, 339
in Eastern Mediterranean ... 468
and ENSO ... *see ENSO*
forecast improvement using lightning data ... 384, 372, 392
lightning relationships ... 184, 300, 392, 476, 488
observed by SSM/I ... *see SSM/I*
observed by TMI ... *see TMI*
observed by TRMM ... *see TRMM*
and Schumann Resonance ... *see Schumann resonance*
Z-R laws ... 384
Recoil streamer ... *see streamer*
Red sprites ... *see sprites*
Reynold's number ... 343, 347
Return stroke ... *see lightning*
Rime accretion rate ... 268
RTL (Rocket Triggered Lightning)
and air terminals ... *see air terminals*
altitude triggering technique of ... 30, 115
in Camp Blanding Florida ... 50, 99, 154
current measurements of ... 22, 55, 146
digital cameras for ... 30
field change measurements of ... 22, 30, 58, 65, 119
in Gansu, China ... 18, 30, 107
in Japan ... 146
and launch commit criteria ... *see LCC*
optical emissions from ... 50
rocket-and-wire technique of ... 22, 154, 158
sounding rockets for ... 22, 58
still and video cameras for ... 22, 58
streak photography of ... 30, 50, 58
stroke couplets in ... 50


## S


Satellite sensors ... *see space sensors*
Schmidt number ... 343
Schumann resonance ... 642, 691, 695, 698, 701, 705, 709, 750, 754, 758, 762
Sferics ... 131, 250, 372, 606, 668, 722
Shock wave ... 660, 738
Slow antenna ... 10, 30, 103, 115, 222
Snow ... 328, 480, 730
Sodar ... *see radar (acoustic)*
Solar wind ... 701
SAA (South Atlantic Anomaly) ... 440, 734
Southern oscillation ... *see ENSO*
Space charge
dynamical nonlinear model ... 614
general references ... 188, 211, 272, 316, 339, 359, 351, 416, 571, 575, 587, 610
Space sensors (for lightning detection)
FORTE ... 6, 668, 672, 676, 680, 684
LIS ... 166, 172, 176, 184, 254, 276, 363, 372, 420, 440, 523, 527, 676, 688, 715, 734, 738, 746, 750
OLS ... 722, 734
ORAGES ... 184
OTD ... 166, 184, 254, 363, 276, 446, 652, 715, 722, 726, 736, 734, 738, 742, 750
Space shuttle ... 80, 238
SSM/I (Special Sensor Microwave Imager) ... 372, 440, 734
Specific differential phase ... *see radar*
Spectrometer ... *see mobility spectrometer*
Spectrophotometer for $NO_2$ measurements ... 664
Sprites
aircraft observations of ... *see aircraft*
CCD TV camera observations of ... 72
and ground discharges ... *see cloud-to-ground discharges*
duration of ... 96
electric field necessary for ... 69
general references ... 695, 758, 762
and mesoscale convective systems ... *see MCSs*
quasi-electrostatic fields in ... 96
and radar reflectivity ... 88
satellite observations of ... 80
SPRITES'95 campaign ... 92
SPRITES'98 campaign ... 92
and VHF pulses ... *see VHF*
Stepped leader ... *see leader*
Streak photography of triggered lightning ... *see RTL*
Streamer ... 18, 111, 138, 211, 230, 432, 656, 715
String fluxmeter ... *see electric field (meter)*
Sublimation ... 268, 324
$SO_2$ (Sulfer dioxide) ... 638
Superbolt ... 380
Supercell ... 172, 359, 376, 476, 750
Supercooled water droplets ... 242, 296, 308, 355. 460
Surface layer ... 536, 547, 555, 571, 575, 614
SAFIR (system de surveillance et d' alerte fudre par radioelectrique) ... *see interferometry*


## T


Telegraph equation ... 698
Terminal velocity ... *see velocity*
Thunder ... 54, 176, 214, 284, 424, 436, 480
Thundercloud charges .. *see charge structure in thunderclouds*
Thunderstorm(s)
in Africa and South America ... 642, 691
in Australia ... 34
and ball lightning ... 142

in Canada producing hail ..... 476
charge density below ..... 614
in Colorado ..... 530
conductivity above ..... *see conductivity*
damage and safety ..... 200, 207
day ..... 230, 519, 664, 750
development in convective clouds ..... 424
discharges above ..... 69
in Eastern Mediterranean ..... 468
and El Nino ..... *see ENSO*
electric dynamos in ..... 272
in Europe ..... 712
in Finland ..... 196
in Florida ..... 18, 22, 58, 496, 738
heat type in Japan ..... 456
in India ..... 420, 448, 503
and the ionosphere ..... 602
and La Nina ..... *see La Nina*
and launch commit criteria ..... *see LCC*
microphysical charging of ..... *see microphysical charging mechanisms*
modeling of ..... 276, 335, 359, 363
in New Mexico ..... 18, 308, 432
in Nigeria ..... 428
nocturnal ..... 84
in Oklahoma ..... 388
observed by space sensors ..... *see space sensors*
and Schumann resonances ..... *see Schumann resonance*
and sea surface temperatures ..... 448,
severe ..... 207, 218, 234, 250, 372, 396, 436, ..... 444, 500, 515, 722
in Spain ..... 392
and sprites ..... 84, 88, 92, 222
summer type in Montana ..... 308
summer type in China ..... 30, 103
summer type in Poland ..... 300
in Sweden ..... 162
tornadic ..... *see tornadoes*
TIPP producing ..... 6, 680, 684
and wet bulb temperature ..... 448
winter type in Israel ..... 460, 468
winter type in Japan ..... 30, 34, 304, 380, 416, 452, 464
winter type in US ..... 519
Time-of-arrival
algorithm for lightning locating ..... 46, 54, 62, 107, 192
general references ..... 18, 38, 46, 54, 250, 254
system in Australia ..... 234
system of the British Meteorological Office ..... 709
system in Finland ..... 196
system in Japan ..... 10, 207
and the LASI system ..... 188
system in New Mexico ..... 6
system for North America ..... 218, 412
system in Oklahoma ..... 172, 376
system in Spain ..... 392, 396
and TIPP locating ..... 684
Tornadoes ..... 172, 200, 359, 368, 372, 404, 436, ..... 500, 511, 515, 722, 750
TLEs (Transient Luminous Events) ..... *see mesosphere*
TIPP (Transionospheric Pulse Pair) ..... 6, 668, 676, 684
Transmission line model ..... *see lightning*
Triboelectrification ..... 238, 328
Triggered lightning ..... *see RTL and LTL*
TRMM (Tropical Rainfall Measuring Mission) ..... 172, 176, ... 184, 276, 372, 404, 420, 440, 519, 523, 527, 688,715, 719, ..... 738, 746, 754
TMI (TRMM Microwave Imager) ..... 372, 404, 523, 527, 747
Turbulent electrode effect ..... *see electrode effect*

## U

UHF (Ultra High Frequency) radiated fields ..... 2, 34, 54, 184
ULF (Ultra Low Frequency) radiated fields ..... 150, 571, ..... 630, 709
UARS (Upper Atmosphere Research Satellite) ..... 652
Upper positive charge center ..... 6, 316, 339, 355, 432

## V

Velocity
of air aspiring through a Gerdien meter ..... 591
of air in electric dynamo theory ..... 272
associated with convection currents ..... 567
of ions ..... *see ions (mobility of)*
associated with K-changes
of leader ..... 46, 50, 54, 58, 111, 158
of microphysical cloud particles ..... 268, 276, 292, 308, 312 ..... 320, 328, 347, 355
of return stroke ..... 99
and sferic generation ..... 131
terminal ..... 343, 347
updraft ..... 339, 363, 515, 734, 746, 754
vertical in the Boundary Layer ..... 316, 571
VIL (Vertically Integrated Liquid) ..... 372
VHF (Very High Frequency) radiated fields ..... 2, 6, 10, 14, ..... 107, 150, 180, 184, 254, 335, 376, 432, 530, 656, 676, ..... 684, 738
VLF (Very Low Frequency) radiated fields ..... 92, 250, ..... 372, 428, 606, 709
Vorticity ..... 515

## W

## X

X-ray detector ..... 222
X-rays ..... 738

## Y

## Z

ZDR (differential reflectivity) ..... *see radar*
Z-R laws ..... *see rainfall*

# REPORT DOCUMENTATION PAGE

*Form Approved*
*OMB No. 0704-0188*

Public reporting burden for this collection of information is estimated to average 1 hour per response, including the time for reviewing instructions, searching existing data sources, gathering and maintaining the data needed, and completing and reviewing the collection of information. Send comments regarding this burden estimate or any other aspect of this collection of information, including suggestions for reducing this burden, to Washington Headquarters Services, Directorate for Information Operation and Reports, 1215 Jefferson Davis Highway, Suite 1204, Arlington, VA 22202-4302, and to the Office of Management and Budget, Paperwork Reduction Project (0704-0188), Washington, DC 20503

| 1. AGENCY USE ONLY *(Leave Blank)* | 2. REPORT DATE | 3. REPORT TYPE AND DATES COVERED |
|---|---|---|
| | June 1999 | Conference Publication |

**4. TITLE AND SUBTITLE**

11th International Conference on Atmospheric Electricity

**5. FUNDING NUMBERS**

**6. AUTHORS**

H.J. Christian, Compiler

**7. PERFORMING ORGANIZATION NAMES(S) AND ADDRESS(ES)**

George C. Marshall Space Flight Center
Marshall Space Flight Center, AL 35812

**8. PERFORMING ORGANIZATION REPORT NUMBER**

M–923

**9. SPONSORING/MONITORING AGENCY NAME(S) AND ADDRESS(ES)**

National Aeronautics and Space Administration
Washington, DC 20546–0001

**10. SPONSORING/MONITORING AGENCY REPORT NUMBER**

NASA/CP—1999–209261

**11. SUPPLEMENTARY NOTES**

Prepared for Global Hydrology Research Office
Proceedings of a conference held in Guntersville, Alabama, June 7–11, 1999

**12a. DISTRIBUTION/AVAILABILITY STATEMENT**

Unclassified–Unlimited
Subject Category 42
Standard Distribution

**12b. DISTRIBUTION CODE**

**13. ABSTRACT** *(Maximum 200 words)*

This document contains the proceedings from the 11th International Conference on Atmospheric Electricity (ICAE 99), held June 7–11, 1999. This conference was attended by scientists and researchers from around the world.

The subjects covered included natural and artificially initiated lightning, lightning in the middle and upper atmosphere (sprites and jets), lightning protection and safety, lightning detection techniques (ground, airborne, and space-based), storm physics, electric fields near and within thunderstorms, storm electrification, atmospheric ions and chemistry, shumann resonances, satellite observations of lightning, global electrical processes, fair weather electricity, and instrumentation.

**14. SUBJECT TERMS**

lightning, thunderstorms, storm physics, storm electrification, cloud electrification, shumann resonances, atmospheric chemistry, remote sensing, global electrical processes, electric fields

**15. NUMBER OF PAGES**

797

**16. PRICE CODE**

A99

| 17. SECURITY CLASSIFICATION OF REPORT | 18. SECURITY CLASSIFICATION OF THIS PAGE | 19. SECURITY CLASSIFICATION OF ABSTRACT | 20. LIMITATION OF ABSTRACT |
|---|---|---|---|
| Unclassified | Unclassified | Unclassified | Unlimited |

National Aeronautics and
Space Administration
AT01
**George C. Marshall Space Flight Center**
Marshall Space Flight Center, Alabama
35812